NSEL Report Series
Report No. NSEL-034
July 2014

Characterization of Behavior of Steel-Concrete Composite Members and Frames with Applications for Design

Mark D. Denavit
and
Jerome F. Hajjar

NSEL
NEWMARK STRUCTURAL ENGINEERING LABORATORY

Department of Civil and Environmental Engineering
University of Illinois at Urbana-Champaign

UILU-ENG-2014-1802

ISSN: 1940-9826

The Newmark Structural Engineering Laboratory (NSEL) of the Department of Civil and Environmental Engineering at the University of Illinois at Urbana-Champaign has a long history of excellence in research and education that has contributed greatly to the state-of-the-art in civil engineering. Completed in 1967 and extended in 1971, the structural testing area of the laboratory has a versatile strong-floor/wall and a three-story clear height that can be used to carry out a wide range of tests of building materials, models, and structural systems. The laboratory is named for Dr. Nathan M. Newmark, an internationally known educator and engineer, who was the Head of the Department of Civil Engineering at the University of Illinois [1956-73] and the Chair of the Digital Computing Laboratory [1947-57]. He developed simple, yet powerful and widely used, methods for analyzing complex structures and assemblages subjected to a variety of static, dynamic, blast, and earthquake loadings. Dr. Newmark received numerous honors and awards for his achievements, including the prestigious National Medal of Science awarded in 1968 by President Lyndon B. Johnson. He was also one of the founding members of the National Academy of Engineering.

Contact:
Prof. B.F. Spencer, Jr.
Director, Newmark Structural Engineering Laboratory
2213 NCEL, MC-250
205 North Mathews Ave.
Urbana, IL 61801
Telephone (217) 333-8630
E-mail: bfs@illinois.edu

This technical report is based on the first author's doctoral dissertation of the same title, which was completed in December 2012. The second author served as the dissertation advisor for this work.

The authors are grateful for the contributions others have made in the completion of this report. The finite element formulation presented in this report has been extended from the work of Cenk Tort. Prof. Roberto Leon and Prof. Tiziano Perea conducted the slender CFT beam-column experiments described in this report. The research on CFT bond was conducted with Prof. Xilin Lu and Jie Zhang. Prof. Donald White, Prof. Ronald Ziemian, Prof. Gregory Deierlein, and Prof. Andrea Surovek provided advice on the stability analysis and design portions of the work. Prof. Larry Fahnestock, Prof. James LaFave, Prof. Roberto Leon, and Prof. Arif Masud provided advice and guidance on this research. Valuable assistance was provided by many undergraduate researchers at the University of Illinois and Northeastern University, including Tarik Ata Rafi, Ezra Jampole, Stephen Palkovic, Abdulrahman Ragab, Alex Reiff, Rachel Back, Brian Beck, Steve Earl, and Elisa Livingston.

This material is based upon work supported by the National Science Foundation under Grant Nos. CMMI-0619047 and CMMI-0530756 as part of the George E. Brown, Jr. Network for Earthquake Engineering Simulation (NEES); the American Institute of Steel Construction; the Georgia Institute of Technology; and the University of Illinois at Urbana-Champaign. Computational analyses in this work were executed in part on the Extreme Science and Engineering Discovery Environment (XSEDE), which is supported by National Science Foundation Grant No. OCI-1053575. Any opinions, findings, and conclusions expressed in this material are those of the authors and do not necessarily reflect the views of the National Science Foundation or other sponsors.

The cover photographs are used with permission. The Trans-Alaska Pipeline photograph was provided by Terra Galleria Photography (http://www.terragalleria.com/).

ABSTRACT

Steel-concrete composite frames are seeing increased use in practice. Their excellent structural characteristics, including high strength, stiffness, and ductility, make them an appealing option for many building configurations. However, there exist gaps in the knowledge of behavior and the design provisions for these structures. This work seeks to document composite member and frame behavior and address key design issues through targeted studies utilizing advanced computational formulations and detailed examination of experimental results.

A three-dimensional distributed plasticity beam finite element formulation suitable for nonlinear static and dynamic analyses of steel-concrete composite frames has been developed. The formulation is suitable for both concrete-filled steel tubes (CFT) and steel reinforced concrete (SRC) members, as well as steel wide-flange and hollow structural steel sections that are part of composite frames. A mixed basis for the formulation was chosen to allow for accurate modeling of both material and geometric nonlinearities. The formulation utilizes uniaxial cyclic constitutive relations for the concrete and steel that account for the salient features of each material, as well as the interaction between the two, including concrete confinement and local buckling. The accuracy of the formulation was verified against a wide variety of monotonic and cyclic experimental results of composite members, demonstrating the capability of the formulation to accurately produce realistic simulations of element and frame behavior.

Aspects of the behavior of composite columns were assessed through an examination of results from a series of experiments on full-scale slender CFT beam-columns conducted by project collaborators. Additionally, comparative computational analyses were performed using the mixed beam formulation and detailed data interpretation focusing on the beam-column interaction strength was conducted.

Several aspects of the design of steel-concrete composite structures were examined. The natural bond behavior of CFT columns was investigated through an examination of prior experimental work and new provisions were developed for the assessment of natural bond strength of CFT connections. The in-plane stability behavior of steel-concrete composite members and frames was assessed through a parametric study on small non-redundant benchmark frames, leading to the development of new elastic flexural rigidities for elastic analysis of composite members; new effective flexural rigidities for calculating the axial compressive strength of SRC members; new Direct Analysis stiffness reductions for composite members; and new recommendations for the construction of the interaction diagram for composite members.

The seismic behavior of composite moment and braced frames was assessed through static pushover and incremental dynamic analyses. The analyses were performed on a suite of 60 archetype frames that were designed according to current design provisions. Connections were assumed to be strong; however, panel zone behavior for the moment frames and bond-slip behavior for SRC columns were included in the model. Using the analysis results, system performance factors were developed for the composite frames based on the methodology described in FEMA P695.

CONTENTS

Page

CHAPTER 1: INTRODUCTION 1
1.1 Objectives, Research Scope, and Organization 1

CHAPTER 2: LITERATURE REVIEW 4
2.1 Behavior of Composite Members and Frames 4
2.2 Modeling of Composite Members and Frames 8
2.3 Design of Composite Members and Frames 11

CHAPTER 3: MIXED FINITE ELEMENT MODELING OF COMPOSITE MEMBERS AND FRAMES 18
3.1 Introduction 18
3.2 Two- and Three-Dimensional Mixed Beam Finite Elements 18
3.3 Uniaxial Cyclic Constitutive Relations for Concrete 20
3.4 Uniaxial Cyclic Constitutive Relations for Steel 25
3.5 Concrete Filled Steel Tube Beam-Columns 36
3.6 Steel Reinforced Concrete Beam-Columns 43
3.7 Wide Flange Steel Beams 53
3.8 Wide Flange and Rectangular Hollow Structural Steel Braces 60
3.9 Connection Regions in Composite Special Moment Frames 60
3.10 Connection Regions in Composite Special Concentrically Braced Frames 63

CHAPTER 4: VALIDATION OF THE MIXED FINITE ELEMENT FORMULATION 66
4.1 Introduction 66
4.2 Description of Monotonic Loading Types 66
4.3 General Observations from the Validation Results 69
4.4 Circular Concrete-Filled Steel Tube Members 69
4.5 Rectangular Concrete-Filled Steel Tube Members 110
4.6 Steel Reinforced Concrete Members 156
4.7 Wide Flange Steel Beams 182
4.8 Wide Flange and Rectangular Hollow Structural Steel Braces 194

CHAPTER 5: NATURAL BOND BEHAVIOR OF CFT COLUMNS 204
5.1 Introduction 204
5.2 Existing Design Provisions 204
5.3 Experimental Studies 206
5.4 Proposed Design Formula 222
5.5 Distribution of Bond Stress along Column Height 224
5.6 Conclusions 229

CHAPTER 6: STABILITY ANALYSIS AND DESIGN OF COMPOSITE STRUCTURES....230
6.1 Introduction 230
6.2 Benchmark Frames 231
6.3 Fully Nonlinear Analysis of Benchmark Frames 235
6.4 Flexural Rigidity for Elastic Analyses 239
6.5 Nominal Axial Strength of Composite Columns 241
6.6 Nominal Flexural Strength of Composite Sections 245
6.7 Direct Analysis Method 247
6.8 Alternative Methods of Design 255
6.9 Aspects of Design Not Directly Addressed in this Study 256
6.10 Conclusions 259

CHAPTER 7: EXPERIMENTAL EVALUATION AND EVOLUTION OF BEAM-COLUMN INTERACTION STRENGTH 260
7.1 Full-Scale Slender Concrete-Filled Steel Tube Beam-Column Tests 261
7.2 Comparison of Experimental and Computational Results 265
7.3 Experimental Evaluation of the Beam-Column Interaction Strength 335
7.4 Experimental Validation of the Proposed Beam-Column Design Methodology .. 336
7.5 Cyclic Evolution of Beam-Column Interaction Strength 353

CHAPTER 8: SEISMIC PERFORMANCE FACTORS FOR COMPOSITE FRAMES ..358
8.1 Introduction 358
8.2 Seismic Force Resisting Systems 358
8.3 Selection and Design of Archetype Frames 359
8.4 Nonlinear Analysis Model 365
8.5 Static Pushover Analyses 366
8.6 Dynamic Response History Analyses 369
8.7 Evaluation of Seismic Performance Factors 377
8.8 Conclusions 383

CHAPTER 9: CONCLUSIONS 384
9.1 Modeling of Composite Members and Frames 384
9.2 Behavior of Composite Members and Frames 385
9.3 Design of Composite Members and Frames 386
9.4 Further Research Needs 387

REFERENCES.... 389

APPENDIX A: DETAILED BENCHMARK STUDY RESULTS 404
A.1 Evaluation of the Proposed Design Methodology 404
A.2 Alternative Methods of Design 507

APPENDIX B: DESIGN OF ARCHETYPE FRAMES 542
B.1 Index Archetype Configurations 542
B.2 Loads 544
B.3 Design Criteria 545
B.4 Design Process and Observations 552
B.5 Final Designs 553

APPENDIX C: DETAILED ARCHETYPE STUDY RESULTS 562
C.1 Static Pushover Analysis Results 562
C.2 Dynamic Response History Analysis Results 623

Chapter 1

INTRODUCTION

In steel and concrete composite construction, the two materials are integrated in structural members to combine their advantages. Composite structural members provide a cost-effective alternative to traditional structural steel or reinforced concrete beams, slabs, columns, and walls. This work investigates the behavior of composite frame structures, either braced or moment resisting, consisting of composite columns, steel or composite braces, and steel beams.

Structural steel has high strength, ductility, and is fast to erect. Reinforced concrete provides high rigidity and is economical, fire resistant, and durable. Different composite members provide different advantages through judicious use of these materials. Several types of composite columns exist, the most basic and common are steel-encased concrete (SRC) where a steel shape is encased with a concrete column and concrete-filled steel tubes (CFT) were an outer tube is filled with concrete. Concrete-filled tubes are generally designated by the shape of steel tube, i.e., rectangular and square (RCFT) or circular (CCFT).

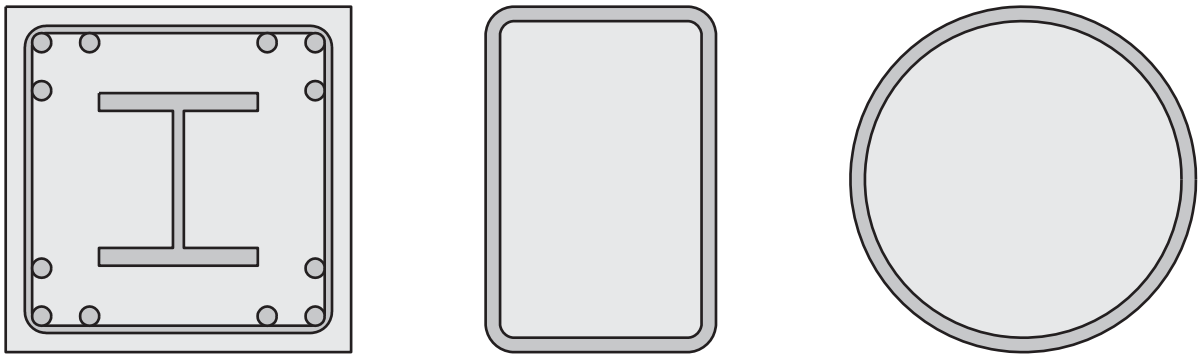

(a) SRC (b) RCFT (c) CCFT

Figure 1.1. Typical Steel and Concrete Composite Sections

1.1 Objectives, Research Scope, and Organization

Despite the potential advantages of composite frame structures, there remain gaps in quantitatively justified guidance for design of these structures. Specifically, the recently developed Direct Analysis method for stability design of steel structures (AISC 2010b) has yet to be validated explicitly for use with composite structures; there is little data to justify the structural system response factors (e.g., R, C_d, and Ω_o) given in the specifications (ASCE 2010; ICC 2012) for seismic design of composite frames; and little guidance is available regarding the value of stiffness that should be used in elastic analyses of composite frames. It is the goal of this work to characterize the behavior of composite frames under non-seismic and seismic loading and to develop rational design recommendations. An additional complimentary goal is to develop a comprehensive nonlinear analysis tool for composite frames. The accuracy of this tool will be crucial to the development of meaningful observations and recommendations.

A review of previous relevant research is presented in Chapter 2, including experimental studies, computational formulations, and design recommendations for composite frames. Among the experimental studies presented is a series of full-scale slender CFT beam-column tests performed at the NEES MAST facility at the University of Minnesota by project collaborators (Perea 2010; Perea et al. 2012). The specimens were subjected to varied and complex loading histories that included concentric axial loading, non-proportional loading subjecting the specimen to cyclic axial compression and uniaxial bending, non-proportional loading subjecting the specimen to cyclic axial compression and biaxial bending, and cyclic torsional loading.

The ability to perform accurate nonlinear simulations is a key component in the assessment of the behavior of structural systems. A three-dimensional distributed plasticity formulation for composite beam-columns suitable for nonlinear static and dynamic analyses of composite structural systems has been developed and is presented in Chapter 3. This model forms the basis of studies presented in later chapters. Two- and three-dimensional distributed plasticity mixed beam elements form the cornerstone of the model. A mixed basis for the formulation was chosen to allow for accurate modeling of both material and geometric nonlinearities. New uniaxial constitutive relations are developed for the concrete and steel elements to simulate the cyclic response of CFT and SRC beam-columns. The relations account for the salient features of each material, as well as the interaction between the two, including for concrete: varying levels of confinement within a section, cracking, crushing, and spalling, and for steel: cyclic plasticity, residual stresses, and local buckling. Models for wide flange steel beams, wide flange or rectangular hollow structural steel braces, and connection regions have also been developed to allow for the analysis of complete, three-dimensional composite frames. The formulation is implemented in the OpenSees framework (McKenna et al. 2000).

The accuracy of the formulation is validated against a comprehensive set of experimental results from monotonically and cyclically loaded specimens in Chapter 4. The verification confirms the capability of the formulation to accurately produce realistic simulations of element and frame behavior.

To ensure that the beneficial effects of the interaction between the steel and concrete composite frame are realized, it is important to have a comprehensive understanding of the composite action between the constituent materials, particularly in critical connection regions where load is transferred to the column from girders or braces. For CFTs, transfer of stress through natural bond, without the use of steel stud anchors or bearing mechanism, is often the most economical connection detail; however, efforts to characterize the bond strength are hindered by varying experimental results, even among similar specimens (Roeder et al. 1999). The natural bond behavior of CFTs is examined in Chapter 5, synthesizing past experimental research, developing a new formula for nominal bond strength, and investigating the distribution of slip and bond stress along the length of the column.

Chapter 6 investigates the use of the Direct Analysis method, established within the American Institute of Steel Construction (AISC) *Specification for Structural Steel Buildings* (AISC 2010b), for composite steel-concrete beam-columns, including both concrete-filled steel tube and steel reinforced concrete members. In addition, the chapter outlines recommendations for equivalent flexural rigidity to be used in elastic analyses for composite columns. Both the Direct Analysis recommendations and equivalent rigidity values were developed based on computational results from a comprehensive suite of analyses of benchmark frames. The validity of the elastic analysis and design approach is confirmed though comparisons to results of fully nonlinear analyses using distributed plasticity finite elements that explicitly model the key

phenomena that affect system response, including member inelasticity (e.g., concrete cracking and steel residual stresses) and initial geometric imperfections.

The series of full-scale slender beam-column tests conducted by project collaborators is examined in Chapter 7. Three aspects are considered. First, analyses are performed, investigating the ability of the mixed beam model to capture the complex behavior observed in the long and varied loading histories. Second, beam-column strength limits points are identified from the experiment results and comparisons are made to the proposed Direct Analysis beam-column design methodology. Third, experimental results from one specimen that was subjected to a special load history are examined in detail. Through a series of probes and subprobes, experimental interaction surfaces were determined and shown to evolve in size, position, and shape as the loading progressed. Corresponding computational results are presented, which showed a good correspondence with the experimental results, indicating that the finite element formulation is capable of predicting the complex behavior observed in CFT members.

The behavior of composite frames under seismic loading is investigated and rational system performance factors are developed in Chapter 8. Static pushover and dynamic response history analyses are performed on a suite of archetype frames that were designed according to current design specifications. The methodology described in FEMA P695 is utilized to determine system performance factors for the composite moment and braced frames that provide equivalent safety against collapse in an earthquake for buildings with different seismic force resisting systems.

The final chapter summarizes the work, draws conclusions, and provides recommendations for further research. Additionally, three appendices are included. Appendix A contains detailed results from the study described in Chapter 6. The design and details of the frames used in the Chapter 8 are presented in Appendix B. Appendix C contains detailed results from the study described in Chapter 8.

Chapter 2

LITERATURE REVIEW

Numerous studies have been conducted to assess behavior, formulate computational models, and develop design recommendations for steel-concrete composite systems. This literature review highlights key studies, starting with recent experimental work on frames and members, including a set of full-scale slender beam-columns tests conducted by project collaborators. An overview of the various computational models formulated for composite members is then presented, providing context for the analysis model used in this work. Finally, prior work aimed to develop design recommendations is summarized.

2.1 Behavior of Composite Members and Frames

2.1.1 Member Behavior Studies

A significant amount of experimental research on composite members has been performed over the past several decades. These studies have demonstrated the excellent behavior of composite members and have been used in the development of current design provisions. Databases that strive to catalog the many studies that have been conducted provide a means to examine the work as a whole. Several such databases have been developed (SSRC, Task Group 20 1979; Lundberg and Galambos 1996; Aho and Leon 1997; Kawaguchi et al. 1998; Nishiyama et al. 2002; Kim 2005; Goode 2008). Distinct from the other databases, Gourley et al. (2008) presents quantitative and qualitative summaries of many of the experimental and analytical research on composite members, connections, and frames that are reported in detail in the literature. Several key member studies are summarized in Table 2.1, many of these are used for the validation studies presented in Chapter 4.

2.1.2 Frame Behavior Studies

Prior experimental research on composite frames characterizes well the robust performance of composite systems and provides excellent examples of the behavior of composite members within indeterminate structures. Several key system studies are summarized below.

Kawaguchi et al. (2002) conducted an experimental study on portal frames subjected to constant axial load and cyclic lateral loading. The frames consisted of steel girders framing into square CFT columns with through-type diaphragm connections. The specimens were designed such that yielding occurred first in the columns and that the girders remained in the elastic range. Different width-to-thickness ratios (D/t = 21, 39, 54) were used along with different levels of axial load (15%, 30%, and 50% of the nominal axial strength). The specimens with high axial load exhibited significant strength deterioration and some pinching behavior was seen in the more concrete dominant specimens, however, the performance of the majority of specimens was good and stable hysteresis loops observed.

Table 2.1. Summary of Key Composite Member Studies

Reference	Summary
Virdi and Dowling (1973)	Monotonic biaxial proportionally loaded SRC beam-column tests
Bridge (1976)	Monotonic biaxial proportionally loaded RCFT beam-column tests
Tomii and Sakino (1979)	Monotonic non-proportionally loaded RCFT beam-column tests
Morino et al. (1984)	Monotonic biaxial proportionally loaded SRC beam-column tests
Shakir-Khalil and Zeghiche (1989)	Monotonic biaxial proportionally loaded RCFT beam-column tests
Grauers (1993)	Monotonic proportionally loaded RCFT beam-column tests
Lu and Kennedy (1994)	Monotonic four-point bending tests on RCFT beams
Ricles and Paboojian (1994)	Cyclic non-proportionally loaded SRC beam-column tests
Mirza et al. (1996)	Monotonic proportionally loaded SRC beam-column tests
Matsui and Tsuda (1996)	Monotonic proportionally loaded CCFT and RCFT beam-column tests
O'Shea and Bridge (1997)	Monotonic CCFT stub column tests with a broad range of material and geometric properties including very high strength concrete and very thin tubes
Schneider (1998)	Monotonic CCFT and RCFT stub column tests
Kilpatrick and Rangan (1999)	Monotonic proportionally loaded CCFT beam-column tests
Nakahara and Sakino (2000)	Cyclic non-proportionally loaded RCFT beam-column tests
Varma (2000)	Monotonic stub column tests on RCFT columns and cyclic non-proportionally loaded RCFT beam-column tests
Elchalakani et al. (2001; 2008)	Monotonic and cyclic pure bending tests on CCFT beams
Nishiyama et al. (2002)	Summaries of many studies on CFT members including: monotonic stub column tests, monotonic eccentrically loaded short column tests, cyclic non-proportionally loaded beam-column tests, and cyclic sub-assemblage tests
Ricles et al. (2004)	Cyclic tests on RCFT column/WF beam sub-assemblages
Sakino et al. (2004)	Monotonic stub column tests on CCFT and RCFT columns with a broad range of material and geometric properties
Wheeler and Bridge (2004)	Monotonic four-point bending tests on large CCFT beams
Marson and Bruneau (2004)	Cyclic non-proportionally loaded CCFT beam-column tests
Han and Yang (2005)	Cyclic non-proportionally loaded CCFT beam-column tests
Yang and Han (2006)	Monotonic proportionally loaded CCFT and RCFT beam-column tests constructed with recycled aggregate concrete
Liu et al. (2008)	Cyclic non-proportionally biaxially loaded RCFT beam-column tests
Bambach et al. (2008)	RCFT columns subjected to impact loading
Fujikura et al. (2008)	CCFT columns subjected to blast loading
Zhang et al. (2009)	Cyclic non-proportionally loaded CCFT beam-column tests
Han et al. (2010)	Monotonic stub columns tests on inclined and tapered CFT columns
Ou et al. (2011)	Monotonic tests of CFT column systems
Yang and Han (2012)	Monotonic tests of CCFT and RCFT columns subjected to partial compression

Herrera et al. (2008) investigated the behavior and seismic performance of a composite moment resisting frame. A four story, two bay, three-fifths scale frame was constructed and tested under hybrid pseudo-dynamic loading. The frame consisted of rectangular CFT columns, wide flange beams, and split tee moment connections. A series of four tests were performed on the structure corresponding to different seismic hazard levels. First, the frame was subjected to a ground motion representing a frequently occurring earthquake. The maximum roof displacement was measured as 0.6% of the building height and the structure remained primarily elastic. Second, the frame was subjected to a design basis earthquake. The maximum roof displacement was measured as 3.0% of the building height and the frame experienced inelastic deformation but no significant strength degradation. After this test the frame was straightened to eliminate the residual drift. Third, the frame was subjected to a maximum considered earthquake. The

maximum roof displacement was measured as 3.7% of the building height. Plastic hinges formed in the beams and a crack developed at the bottom of the first story middle column, resulting in a drop in shear capacity. Lastly, the frame was subjected to a second design basis earthquake, representing an aftershock. The maximum roof displacement was measured as 3.3% of the building height. The crack from the previous test propagated and another crack was formed, however the frame did not collapse.

Tsai et al. (2008) conducted tests on a full scale three story, three bay CFT buckling restrained braced (BRB) frame. Square CFTs were used for the two exterior columns and circular CFTs for the two center columns. BRBs were installed in the center bay only. Three types of moment connections were used in the exterior beam-column connections, specifically through beam, external diaphragm, and bolted end plate connections. Several types of BRBs were used in the frame, including single-core, double-cored, and all metal. A series of six pseudo dynamic tests were conducted subjecting the frame to ground motions of various intensities, and then a quasi-static cyclic load protocol was applied until fracture of the braces. The braces were replaced and another series of pseudo dynamic tests were performed. Throughout the testing sequence, the frame performed well. Vibration tests were conducted after each pseudo dynamic test to measure the changes in stiffness and damping, only minor changes were observed.

2.1.3 Full-Scale Slender Beam-Column Tests

Project collaborators (Perea 2010; Perea et al. 2012) conducted a series of full-scale slender concrete-filled steel tube beam-column tests at the NEES MAST Laboratory at the University of Minnesota. The specimens were selected to fill gaps in prior experimental research, particularly to have high member slenderness and high section slenderness (D/t ratio). Parameters in the experimental study include: section shape and size, member length, and concrete strength. Table 2.2 shows a test matrix with measured geometric and material properties. Specimen 1-C5-18-5 is shown prior to testing and during testing in Figure 2.1.

The MAST Laboratory allows for six degree-of-freedom (DOF) control through a rigid steel crosshead. For the main portion of testing, most specimens were kept in a fixed-free (K=2) configuration, achieved as follows. The beam-column bases were welded to a base plate which was bolted to the testing floor, providing a fixed connection. The beam-column tops were welded to a base plate with a hole for placing the concrete, which was bolted to the crosshead. The free condition was provided by control of the crosshead; allowing horizontal displacements and setting bending moments at the top to zero. Twisting deformation was constrained to zero due to the low torsional stiffness of the specimens.

The loading protocol for each specimen was divided into several load cases. The first three load cases were similar for each of the specimens. The first load case subjected the specimens to concentric load. The horizontal DOFs were held at zero force, allowing the specimen to displace transversely. The vertical DOF was loaded under displacement control until a critical load was reached or until the actuator load limits were reached. The second load case subjected the specimens to constant axial load (with different values being used for different subcases) and cyclic transverse displacements causing uniaxial flexure. The vertical DOF was under load control while the horizontal DOFs were under displacement control. The third load case had similar control to that of the second load case but the horizontal displacements were moved in a patterns causing biaxial flexure. These patterns were either sets of radially extending probes, figure eight patterns, or for one specimen set of probes and subprobes. In the probe patterns, a constant axial load was held and the horizontal displacements were increased with a

fixed ratio of X to Y displacement until a critical flexural strength was achieved, at which point the horizontal displacements were reversed.

Table 2.2. Full-Scale Slender Beam-Column Test Matrix

Specimen	*D or H* (mm)	*B* (mm)	*t* (mm)	f'_c (MPa)	F_y (MPa)	*L* (mm)
1-C5-18-5	141	---	3.15	37.9	383	5,499
2-C12-18-5	324	---	5.92	38.6	337	5,499
3-C20-18-5	508	---	5.92	40.0	328	5,525
4-Rw-18-5	508	305	7.39	40.7	365	5,537
5-Rs-18-5	508	305	7.39	40.7	365	5,537
6-C12-18-12	324	---	5.92	91.0	337	5,499
7-C20-18-12	508	---	5.92	91.0	328	5,534
8-Rw-18-12	508	305	7.39	91.7	365	5,553
9-Rs-18-12	508	305	7.39	91.7	365	5,553
10-C12-26-5	324	---	5.92	54.5	335	7,950
11-C20-26-5	508	---	5.92	55.8	305	7,995
12-Rw-26-5	508	305	7.39	56.5	406	7,957
13-Rs-26-5	508	305	7.39	57.2	383	7,969
14-C12-26-12	324	---	5.92	80.0	383	7,963
15-C20-26-12	508	---	5.92	80.0	293	7,976
16-Rw-26-12	508	305	7.39	80.7	381	7,957
17-Rs-26-12	508	305	7.39	80.7	380	7,963
18-C5-26-12	141	---	3.15	80.7	383	7,941

Additional load cases were performed on the specimens. These included cyclic torsional loading at different levels of axial compression; and concentric axial, cyclic uniaxial flexural, and cyclic biaxial flexural loading in a configuration having a fixed base and with the top fixed against rotation but free to translate (thus $K = 1$ with the CFT subjected to reverse curvature flexure).

The specimens were extensively instrumented with a variety of measurement systems. Of particular interest was the moment-curvature relationship of the composite section along the length of the column; thus redundant measurements were taken to provide a reliable data set. The MAST system itself includes 8 load cells and LVDTs (corresponding to the 8 actuators) which are reduced to force and displacement in the 6 degrees of freedom at the top of the column. String pots were used in two orthogonal directions at several locations along the length of the columns. LVDTs were placed in set of three to measure the elongation or shortening over a certain gage length at different locations on the section in order to measure curvature. Multiple LVDTs sets were placed at the base of the column, where the curvature was expected to be the highest, and on LVDT set was placed at the top of the column. Sets of strain gages were also used in a similar manner, with sets of three being placed at locations along the length of the column. The Metris K600 DDM coordinate measurement system with approximately 40 LEDs was used to measure the displacement of the base of the column. These measurements are useful for determining the curvature as well as identifying local buckling. Additionally, video and photographic data was collected during each test.

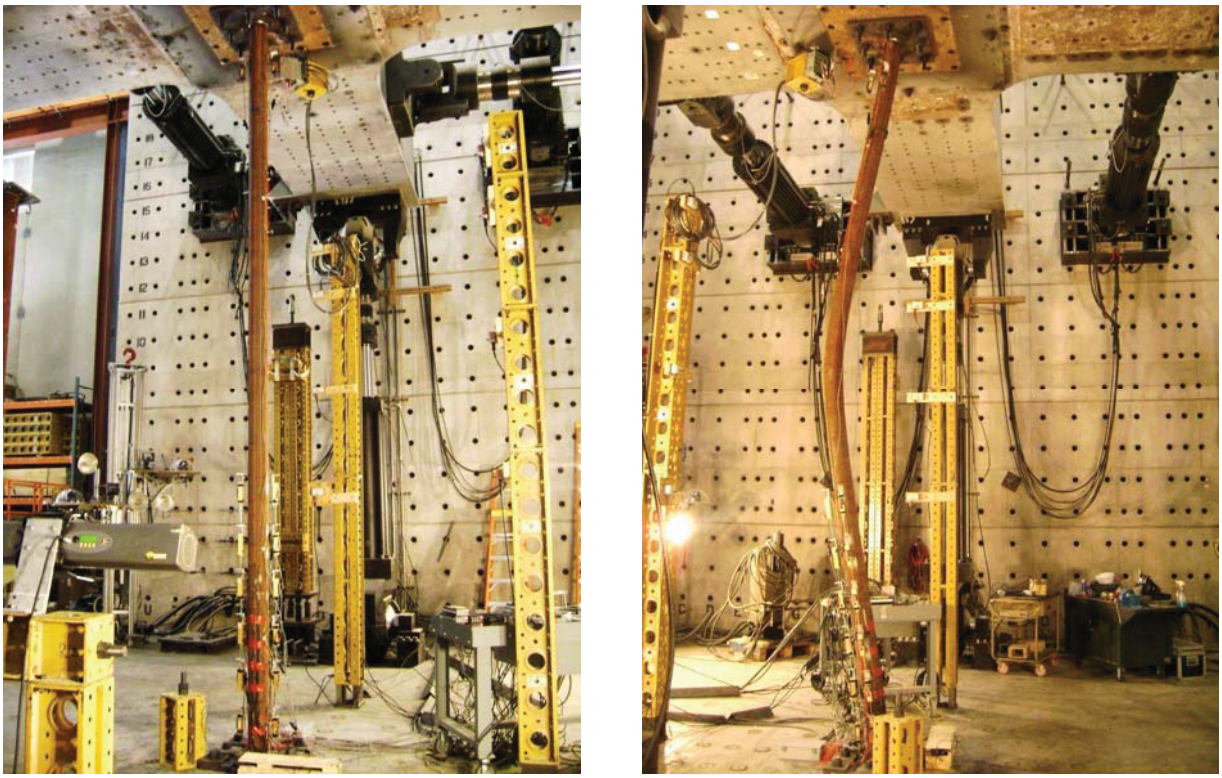

(a) Before Testing (b) During Testing

Figure 2.1. Specimen 1-C5-18-5

The tubes were instrumented during concrete placement to study the effects of wet concrete on CFT members. The hydrostatic pressure of the wet concrete causes the tubes of RCFT members to bulge leaving initial deformations and stresses. These were shown to cause premature local buckling of the steel tube as compared to tubes that were stiffened during pouring. Further analytical studies were conducted to derive stress and deformation limits, above which stiffeners should be used during pouring or special measures should be taken during design (Perea 2010; Perea et al. 2012).

2.2 Modeling of Composite Members and Frames

A number of different types of finite element formulations can be applied to frame structures using composite members. Beam elements reduce the three-dimensional behavior to one-dimension, utilizing a kinematic assumption (e.g., initially plane sections remain plane) to describe the deformations of any point within the member by the deformations of cross sections along the length of the member. Three-dimensional continuum analysis allows for detailed simulation of composite members. In this type of analysis, the concrete is commonly modeled with brick elements, while the steel is modeled with brick or shell elements (Schneider 1998; Johansson and Gylltoft 2002; Varma et al. 2002; Hu et al. 2003). The interface between the two materials may be modeled with gap and friction elements. Phenomena that are simplified for analysis using beam elements may be modeled explicitly. For example, confinement of the concrete can be modeled through the use of three-dimensional constitutive relations and local buckling of the steel member can be modeled through geometric and material nonlinear

behavior. Despite the improved accuracy and rationality, the computational expense prevents continuum analysis from being a viable option for analysis of complete three-dimensional frames.

Concentrated plasticity beam formulations model material nonlinearity only at hinges at the element ends while assuming elastic behavior between the hinges (Hajjar and Gourley 1997; El-Tawil and Deierlein 2001; Inai et al. 2004). Distributed plasticity beam formulations allow material nonlinearity throughout the element, monitoring inelasticity at specific integration points along the length of the element (Hajjar et al. 1998; Aval et al. 2002; Varma et al. 2002; Tort and Hajjar 2010b). In comparison to concentrated plasticity, distributed plasticity is more accurate and more computationally expensive, since inelasticity is traced at multiple points along the length of the element rather than just the element ends. While in many cases (e.g., double curvature of a beam-column) material nonlinearity is mostly limited to the element ends, the distributed plasticity approach is appealing because of its accuracy and generality.

In both the concentrated and distributed plasticity approaches, initiation and evolution of cross sectional behavior needs to be modeled. This may be accomplished in several ways. One option models section behavior through multiple surfaces and flow rules defined in stress-resultant space (Hajjar and Gourley 1996; El-Tawil and Deierlein 2001). In these formulations, elastic response is maintained if the loading point remains within the loading surface. Plastic deformation commences when the loading surface is breached with the level of deformation related to the distance between the loading surface and bounding surface. A second option, subdivides the two-dimensional cross section into many fibers that are each assigned a uniaxial material model (Hajjar et al. 1998; Aval et al. 2002; Varma et al. 2002; Tort and Hajjar 2010a). A kinematic assumption (e.g., initially plane sections remain plane) is used to determine the longitudinal strain at the centroid of each fiber. Based on this strain, the stress and modulus of each fiber are computed and aggregated to obtain the sectional response. The fiber approach is appealing because of the ability to account (either explicitly or implicitly) for all the salient features of composite members (e.g., concrete cracking, confinement, local buckling, etc.) through relatively simple uniaxial stress-strain models.

A further classification of beam elements relates to what variables are taken as the primary unknowns. This classification distinguishes displacement-based, force-based, and mixed elements. Mixed, in this case, indicates that both element displacements and stress resultants as taken as primary state variables. However, the term could also indicate other combinations of primary state variables (Hjelmstad and Taciroglu 2003). Displacement-based, also termed stiffness-based, elements regard nodal displacements as the primary unknowns (Hajjar and Gourley 1997; Aval et al. 2002; Alemdar and White 2005). Element deformations are computed using interpolation functions. Element equilibrium is satisfied only in a variational sense, i.e., element internal forces computed from the assumed displacement field do not strictly satisfy equilibrium. This type of formulation is considered easy to implement and to extend to geometric nonlinear behavior. However, the interpolation functions typically used for the deformations only model a linear curvature distribution along the length of the element. This is a significant limitation especially in the case where plastic hinges develop, causing severely nonlinear curvature distributions. Force-based, also termed flexibility-based, elements regard stress resultants as the primary unknowns (de Souza 2000; El-Tawil and Deierlein 2001; Alemdar and White 2005). Forces along the length of the element are computed using interpolation functions. Element equilibrium is strictly satisfied; however, the compatibility of deformations within the element is satisfied only in a variational sense. In comparison to displacement-based elements,

force-based elements are often more computationally expensive and have more elaborate state determination procedures. Mixed elements regard both element forces and nodal displacements as primary unknowns, allowing interpolation functions for both element deformations and stress resultants along the length of the element (Nukala and White 2004; Alemdar and White 2005; Tort and Hajjar 2010b). Despite the complexity of the state determination procedure, which is typically greater than for displacement- or force-based elements, the mixed method provides a favorable balance of accurate assessment of nonlinear curvatures along the length of the element and capability to include geometric nonlinearity directly.

2.2.1 The OpenSees Framework

The formulation developed in this research is implemented in the OpenSees framework. OpenSees is an object-oriented software framework for the analysis of structural systems (McKenna et al. 2000). Software patterns, implemented within the framework, represent the fundamental relationships necessary for nonlinear finite element analysis. The main abstractions include: *ModelBuilder*, which constructs objects and adds them to the domain; *Domain*, which is the aggregation of all nodes, elements, loads and constraints and contains the state of the structure; *Recorder*, which monitors and outputs defined parameters in the model; and *Analysis*, which moves the model from one state to another. These abstractions interact with specific elements through the common interface of the abstract *Element* class. The flexible, reusable, and extensible nature of the framework allows a minimum amount of new code that needs to be written for a new element or material to be implemented. For example, the implementation of a beam element, may only require the implementation of the state determination procedure within the natural coordinate system, since existing geometric transformations and cross section constitutive relations may be suitable (Scott et al. 2008).

In prior work, a number of elements have been implemented within the OpenSees framework ranging from brick and quadrilateral elements for continuum analysis, to beam, truss, and zero-length elements for frame analysis. Beam elements include: two- and three-dimensional elastic elements, concentrated plasticity elements, displacement-based distributed plasticity elements, and force-based distributed plasticity elements (McKenna et al. 2000). A wide variety of uniaxial materials for use in fiber sections also have been implemented. Materials include: elastic, elastically perfectly plastic, hardening, and several models specifically for concrete and steel, among others.

2.2.2 Uniaxial Constitutive Relations

Accurate constitutive models are necessary for the analysis of structural members. Analyses that use a fiber discretization to define section behavior rely on uniaxial material models that govern the behavior of the subdivisions of the cross sections. The need for uniaxial constitutive models for specific types or shapes of members typically arises from multi-dimensional behavior which affects the uniaxial response. For composite beam-columns, the dominant multi-dimensional effects are confinement of the concrete and local buckling of the steel. A number of uniaxial constitutive relations have been proposed for composite members, selected models are summarized in Table 2.3.

2.3 Design of Composite Members and Frames

A wide variety of behavior and differences in progression of damage are possible in composite members due to the range of relative proportions of steel and concrete permissible in these members. Composite members that are concrete dominant will behave more like reinforced concrete members while others that are steel dominant will behave more like structural steel members (Hajjar and Gourley 1996). Design provisions for composite members must account for this variation while simultaneously minimizing conflicts with structural steel and reinforced concrete provisions as well as bringing forth the advantages of composite design. Prior work in the development of design provisions for composite members is presented here, highlighting the aspects of design that will be addressed in this work. Related work on structural steel and reinforced concrete members is also presented to provide context.

Composite members have been included in the American Institute of Steel Construction (AISC) steel specification since the 1936 *Specification for the Design, Fabrication and Erection of Structural Steel for Buildings* (AISC 1936). However, the provisions only addressed composite beams until the 1986 *Specification for Structural Steel Buildings – Load and Resistance Factor Design* (AISC 1936), when provisions for composite columns and beam-columns were added based upon research consolidated through the Structural Stability Research Council (SSRC, Task Group 20 1979) and related venues in the 1960's through the early 1980's. The provisions for composite systems underwent incremental changes in subsequent specifications until major revisions and restructuring occurred for the 2005 *Specification for Structural Steel Buildings* (AISC 2005). Further additions were made for the 2010 *Specification* (AISC 2010b), mainly addressing the use of noncompact or slender tubes in concrete filled steel tube (CFT) members and expanded provisions on force transfer between the steel and concrete components.

Similarly, the 2010 AISC *Seismic Provisions for Structural Steel Buildings* (AISC 2010c) have undergone major revisions and restructuring, including integral incorporation of composite systems into the provisions for the first time. This expansion of provisions over the last five years was a culmination of a surge of research activities on composite systems that occurred worldwide from the late 1980's through the last several years; within the U.S. and Japan, this work was conducted especially as part of the U.S.-Japan Cooperative Earthquake Engineering Research Program, Phase 5 on Composite and Hybrid Structures, sponsored by the National Science Foundation (NSF), and subsequently by projects sponsored within the NSF George E. Brown, Jr. Network for Earthquake Engineering Simulation (NEES) as well as the American Institute of Steel Construction.

The development of the AISC provisions has also benefited from the approaches adopted in other international specifications for composite structures. Examples include the provisions in Australia (Standards Australia 1998), Canada (CSA 2009), and Eurocode 4 (CEN 2004). Relevant provisions within these specifications include approaches for the design of both composite members and connections.

Table 2.3. Summary of Proposed Uniaxial Constitutive Relations for Composite Members

Reference	Type	Steel Model	Concrete Model
Shams and Saadeghvaziri (1999)	CFT	n/a	Ratio of two 5th order polynomials, calibrated to the results of continuum analyses
Susantha et al. (2001)	CFT	n/a	Popovics' equation pre-peak, bilinear post peak, calibrated to experimental results
Elremaily and Azizinamini (2002)	CCFT	Elastic-perfectly plastic, shifted to account for hoop stress	Popovics' equation with confinement computed based on experimentally calibrated hoop stress
Sakino et al. (2004)	CFT	CCFT: elastic-perfectly plastic, shifted to account for hoop stress. RCFT: multi-linear model including strain hardening and local buckling	Sakino and Sun model with confinement computed based on experimentally calibrated hoop stress
Hatzigeorgiou (2008)	CCFT	Elastic plastic hardening model, shifted to account for hoop stress	Cubic equation pre-peak, bilinear post peak, calibrated to experimental results
Tort and Hajjar (2010a)	Cyclic RCFT	Shen incremental bounding surface steel plasticity model with modifications for cold forming and local buckling	Chang and Mander model with post peak behavior calibrated to experimental results
Denavit and Hajjar (2012)	Cyclic CCFT	Shen incremental bounding surface steel plasticity model with modifications for cold forming and local buckling	Chang and Mander model with confinement computed based on experimentally calibrated hoop stress
Mirza and Skrabek (1992)	SRC	Elastic plastic model with yield plateau and nonlinear strain hardening	Quadratic equation pre-peak, bilinear post peak with three regions of confinement
Sanz Picon (1992)	SRC	Elastic plastic model with yield plateau and nonlinear strain hardening	Kent and Park model for concrete confined by rectangular hoops
Elnashai and Elghazouli (1993)	Cyclic SRC	Bi-linear hardening model including the effect of flange local buckling	Mander model with three regions of confinement
El-Tawil and Deierlein (1996)	SRC	Elastic-perfectly plastic	Mander model with three regions of confinement
Chen and Lin (2006)	SRC	Multi-linear model including the effect of local buckling	Mander model with three regions of confinement
Denavit, Hajjar, and Leon (2011)	Cyclic SRC	Shen incremental bounding surface steel plasticity model	Chang and Mander model with three regions of confinement

2.3.1 Stability Analysis and Design

The general philosophy for stability design held by AISC for the past several decades is well stated in the current *Specification*: "any method that considers the influence of second-order effects (including P-Δ and P-δ effects), flexural, shear and axial deformations, geometric imperfections, and member stiffness reduction due to residual stresses on the stability of the structure and its elements is permitted" (AISC 2010b). Accordingly, a wide range of stability analysis and design procedures have been developed. They vary based on which effects are addressed in the analysis when determining required strength, and which effects are addressed in design equations, when determining available strength.

At one extreme, with design by "advanced analysis", all significant effects are accounted for through a material and geometric nonlinear analysis. Consequently, member strength checks are deemed to be satisfied automatically if the analysis shows that the structure supports the load (White et al. 2006). This approach is now enabled through Appendix 1 of AISC (2010b) More commonly, design methodologies that require only elastic analyses are employed. The AISC *Specification for Structural Steel Buildings* defines three specific methods: 1) the effective length method, 2) the first-order analysis method, and 3) the direct analysis method (AISC 2010b). The first-order analysis method is a simplified conservative version of the direct analysis method and will not be discussed; the other two methods are discussed below.

In the effective length method, a second-order elastic analysis is performed to determine required strengths. As specified within AISC (2010b), the structure is modeled with nominal geometry and a minimum horizontal notional load. The in-plane flexural buckling strength is based upon the product of the unsupported length and a factor, K, termed the effective length factor. A number of buckling models and K factor equations have been proposed over the years (Yura 1971; LeMessurier 1977; Baker 1987; ASCE 1997), however, the selection of which is appropriate for a given structure is not always obvious, and in some cases subtle differences in the model can produce significantly different results (White et al. 2006). In addition, no consensus approaches have been established for calculating effective length factors for composite beam-columns.

The direct analysis method provides an alternative and often more accurate strategy for addressing frame in-plane stability considerations (White et al. 2006). In this method, required strengths are determined with a second-order elastic analysis. However, members are modeled with a nominal reduced elastic stiffness and a nominal initial out-of-plumbness is included (the initial out-of-plumbness is often modeled using notional lateral loads). The in-plane flexural buckling strength is based upon the unsupported length of the column, eliminating the need to compute a K factor. Among the merits of the direct analysis method is that it provides a better representation of the structure's distributed forces and moments at the strength limit of the most critical member or members. The validity of the direct analysis method has been established through comparisons between fully nonlinear analyses and elastic analyses (Surovek-Maleck and White 2004a; b; Deierlein 2003; Martinez-Garcia 2002).

A schematic comparison of the direct analysis method and the effective length factor method is shown in Figure 2.2. This figure shows the loading path of a beam-column as obtained from three separate analyses. First is a distributed plasticity analysis, which is considered the most accurate since it includes both material and geometric nonlinearity. The other two are elastic analyses as specified for the effective length factor method and for the Direct Analyses method. Both elastic analyses include geometric nonlinearity and account for initial imperfections, but the elastic stiffness is reduced for the Direct Analyses method as shown by the lower initial stiffness. The critical load of the distributed plasticity analysis is indicated by the peak axial load, while the critical load for the elastic analyses is indicated by the intersection of the load path and a strength interaction diagram. The strength interaction diagram for the effective length factor method is based on an axial strength computed with a value of $K > 1$. For the Direct Analysis method the axial strength is computed with $K = 1$. Key points from this figure are: 1) the critical axial load is about the same for all three analyses indicating that all three are reasonably good methods for determining the strength limit point, although differences in accuracy exist; 2) the critical moment for the effective length factor method is less than the of the Direct Analysis method or the distributed plasticity analyses; 3) the critical moment from the

Direct Analysis method is closer to the critical moment of the distributed plasticity, but not equal.

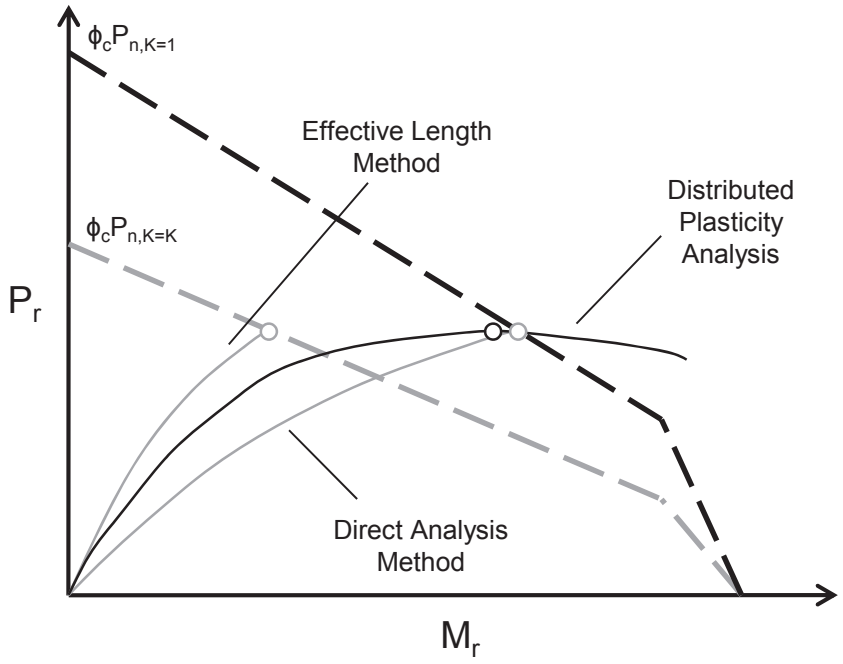

Figure 2.2. Comparison on In-Plane Beam-Column Interaction Checks

2.3.2 Elastic Flexural Rigidity

In elastic analyses, the behavior of cross-sections is represented by elastic rigidities (e.g., *EA*, *EI*, *GJ*). For structural steel, the use of the gross section properties and initial elastic stiffness (e.g., $EI = E_s I_s$) is widely considered safe and accurate for analysis and design. Concrete cracks in tension and experiences nonlinearity early in compression; thus, the elastic rigidities for first-order and second-order elastic analysis of steel-concrete composite members typically should be lower than that of the gross section properties and initial elastic stiffness. A variety of approaches and relations have been proposed to evaluate the elastic rigidity of composite members. The elastic rigidity recommendations from the studies highlighted below are summarized in Table 2.4. The different recommendations are not necessarily comparable since they were often developed with different objectives and for different purposes (e.g., determination of axial strength, assessment of deformations, and use in nonlinear formations).

Schiller, Hajjar, and Gourley (1994) summarized available elastic rigidity recommendation for RCFTs with a focus on use in nonlinear beam-column element formulations. Axial, flexural, shear, and torsional rigidity, were investigated separately making comparisons to available experimental results. It was determined that for axial and flexural elastic rigidities, using the gross section properties and initial stiffness were appropriate for the purpose of the elastic component of a concentrated plasticity element. However, an alternative

flexural rigidity was recommended for more general use within elastic analysis in which only a portion of the flexural rigidity from the concrete is included.

Table 2.4. Summary of Recommended Elastic Rigidities

Reference	Type	Expression	Notes
Schiller, Hajjar, and Gourley (1994)	Axial	$EA = E_s A_s + E_c A_c$	RCFT
	Bending	$EI = E_s I_s + 0.311 E_c I_c$	RCFT
	Bending	$EI = E_s I_s + E_c I_c$	RCFT – for use in concentrated plasticity beam-column elements
	Shear	$GA = \frac{G_s A_s}{2} + \frac{G_c A_c}{1.2}$	RCFT
	Torsion	$GJ = G_s J_s$	RCFT
Roeder et al. (2010)	Bending	$EI = E_s I_s + C' E_c I_c$ $C' = 0.15 + \frac{P}{P_o} + 2\frac{A_s}{A_s + A_c} \le 0.9$	CCFT
Tikka and Mirza (2006a; b)	Bending	$EI = 0.8 E_s I_s + 0.8 E_s I_{sr} + \frac{\alpha_c E_c I_c}{1 + \beta_d}$ $\alpha_c = 0.47 - 3.5\frac{e}{h}\left(\frac{1}{1 + 9.5\frac{e}{h}}\right) + 0.003\frac{l}{h} \ge 0$	SRC
AISC (2010b), Leon, Hajjar, and Kim (2007)	Bending	$EI_{eff} = E_s I_s + E_s I_{sr} + C_3 E_c I_c$ $C_3 = 0.6 + 2\left(\frac{A_s}{A_c + A_s}\right) \le 0.9$	CFT
	Bending	$EI_{eff} = E_s I_s + 0.5 E_s I_{sr} + C_1 E_c I_c$ $C_1 = 0.1 + 2\left(\frac{A_s}{A_c + A_s}\right) \le 0.3$	SRC
ACI (2011), MacGregor and Hage (1977)	Axial	$EA = E_c A_g$	RC
	Bending	$EI = 0.7 E_c I_g$	RC – Columns
ACI (2011), Khuntia and Ghosh (2004a; b)	Bending	$EI = E_c I$ $I = \left(0.80 + 25\frac{A_s}{A_g}\right)\left(1 - \frac{M_u}{P_u h} - 0.5\frac{P_u}{P_o}\right) \le 0.875 I_g$	RC – Columns

Roeder, Lehman, and Bishop (2010) investigated the flexural rigidity of CCFTs through comparisons to available experimental results either taking reported elastic rigidities or determining them through load-deformation results. Noting overestimations of the elastic flexural rigidity for members subjected only to flexural loading, a new expression was proposed where the concrete contribution depends on the axial load and the steel ratio.

Tikka and Mirza (2006a; b) developed expressions for the flexural rigidity of SRC members though parametric computational studies on composite beam-columns. Variations of concrete strength, steel strength, steel ratio, reinforcing ratio, column length, and load eccentricity were included in the study. An expression for the elastic flexural rigidity was proposed in which a factor of 0.8 is applied to the steel contribution and a factor which varies based on the eccentricity and length of the member is applied to the concrete contribution. Long term effects were accounted for by dividing the concrete contribution by $(1+\beta_d)$ where β_d is the ratio of dead load to total load.

The work of Leon, Hajjar, and Kim (2007) provides the basis for the effective flexural rigidities for computing the axial compressive strength of composite members that appear in the AISC *Specification* (AISC 2010b). Different expressions are provided for CFT and SRC columns and were developed based on comparisons to axial loaded column and beam-column tests.

The work of MacGregor and Hage (1977) provides the basis for the simple effective flexural rigidities for reinforced concrete members that appear in the ACI *Code* (ACI 2011). The flexural rigidity for columns is recommended as 70% of the product of the initial concrete modulus and the gross moment of inertia. The more complex expressions for the flexural rigidities that appear in the ACI *Code* are based on the work of Khuntia and Ghosh (2004a; b). These equations were developed based on parametric computational studies on concrete cross sections and take into account the effects of load and steel ratio. These rigidities are typically used within first-order or second-order analyses to obtain required strengths for design within the ACI *Code* (ACI 2011). Other studies have also focused on the flexural rigidity of reinforced concrete members (Mirza 1990; Elwood and Eberhard 2009).

2.3.3 Axial Compression-Bending Moment Interaction Strength

Prior to the 2005 AISC *Specification for Structural Steel Buildings* (AISC 2005), the axial and flexural strengths of composite beam-columns were based on calculations that determined an equivalent steel section. This approach had limitations in that it was not applicable to columns with steel ratios below 4% and it often underestimated the contribution of the concrete, particularly for concrete-dominant composite beam-columns with low steel ratios (Griffis 2005). The beam-column strength interaction provisions in AISC (2005) are based more directly on mechanics principles. The cross section strength may now be determined using one of two methods: the plastic stress distribution method, which is applicable to most common composite column cross sections; and the more general strain-compatibility method, which is comparable to approaches often taken to compute reinforced concrete section strength. The compressive strength for axially loaded columns including length effects is then computed using a column curve that is identical to that for steel columns, and an effective stiffness, EI_{eff}, that is based on a curve fit to experimental data (Leon et al. 2007). As a result of the new methodology, the range of applicability of the provisions was extended to members with steel ratios as low as 1%.

The 2010 *Specification* provides clarified requirements for constructing the axial load-bending moment interaction diagram for compact composite beam-columns. A number of methods satisfy these requirements and the commentary to the specification identifies three in particular. The first method involves utilizing the interaction equations derived for structural steel members. This method is simple although conservative, as it typically under predicts the contribution of the concrete. This is the method required for CFT members with noncompact or

slender tubes. The second method utilizes the plastic stress distribution method. The nominal strength interaction surface of the section is determined using the plastic stress distribution at several points along the interaction curve, and length effects are accounted for by using a reduction factor on axial strength at all points on the interaction surface that is calculated based on the case of pure compression (Leon and Hajjar 2008). The third method is an approach presented in AISC Design Guide 6 (Griffis 1992) based on the strain compatibility method.

Other approaches have been proposed in prior research for various member types [e.g. applicable only to RCFTs (Choi et al. 2006, 2008) or to CCFTs (Roeder et al. 2010)].

2.3.4 Seismic Design

A key component of seismic design in the United States is the allowance for inelasticity in structural elements subjected to severe earthquake ground motions. However, static elastic analysis is prevalent for seismic design in current practice. Seismic performance factors have been developed as a core component of these elastic analysis procedures to enable accounting for the nonlinear response seen in structures during earthquakes. These factors include: the response modification factor, R, used in reducing seismic forces as determined through elastic methods; the displacement amplification factor, C_d, used in amplifying displacements as determined through elastic methods; and the system overstrength factor, Ω_o, used to estimate the actual strength as compared to the design strength.

These three factors are tabulated for a variety of lateral force resisting systems in national codes (ASCE 2010; ICC 2012). However, the response modification factor for these systems were estimated based on limited data at the time they were codified. Original R factors were based largely on judgment and qualitative comparisons with known response capabilities of relatively few lateral-force-resisting systems (FEMA 2009). More recently, a methodology has been developed to provide a rational basis for determining system behavior factors which provide equivalent safety against collapse in an earthquake for buildings with different lateral-force-resisting systems (FEMA 2009). Equivalent safety is provided through an acceptably low probability of structural collapse common to all systems. Structural collapse is defined in the context of using incremental dynamic analysis, in which nonlinear time history analyses are performed at increase magnitudes of seismic loading until the structure achieves its peak strength; in this approach, no explicit modeling of collapse (e.g., including fracture) is typically included. Statistical data is generated through conducting these nonlinear collapse simulations on a set of archetype models with uncertainty approximated based on the level of knowledge of the particular system and accuracy of the analysis tool.

The requirements for specific composite lateral-force-resisting systems are given in the AISC *Seismic Specification* (AISC 2010c). The first edition of the AISC *Seismic Specification* published in 1992 did not address the design of composite systems. Subsequent editions in 1997, 2002, and 2005 included composite systems in Part II of the specification. In the 2010 edition of the *Seismic Specification*, Part II has been eliminated and both steel and composite lateral force resisting systems have been integrated in the main provisions. Composite systems, for example special moment frames with composite columns and steel beams, are expected to exhibit overall behavior that is similar to the corresponding structural steel system, since inelastic deformations will occur in much the same way, (i.e., flexural yielding of the girders in moment frames; brace buckling in brace frames) (Malley 2010).

Chapter 3

MIXED FINITE ELEMENT MODELING OF COMPOSITE MEMBERS AND FRAMES

3.1 Introduction

Accurate nonlinear formulations are necessary for the assessment of structures under seismic and other extreme loading. Distributed-plasticity beam elements strike a favorable balance of computational efficiency and accuracy for the analysis of frame structures. Further, the mixed formulation, treating both displacements and forces as primary variables, allows for accurate modeling of both the geometric and material nonlinearities that arise in steel-concrete composite members. The mixed beam element formulation serves as the cornerstone of analysis model used in this work. Accompanying it are uniaxial constitutive relations and connection models which combine to create a formulation suitable for modeling entire frames.

The models described in this chapter have been implemented within the OpenSees framework (McKenna et al. 2000) and are used in the studies described in the remainder of this dissertation. These studies have different goals and in some cases require different models, even for identical physical members. Notably, some studies pertaining to design require simpler models that follow assumptions common in the development of design recommendations (e.g., neglecting steel hardening and concrete tension), while other studies do not have such limitations and simply aim to capture the behavior as accurately as possible. To distinguish these similar but separate models, they will be termed "Proposed for Behavior" and "Proposed for Design" respectively. The validity of the models and their underlying assumptions are shown through comparisons between computation and experimental results presented in the following chapter.

3.2 Two- and Three-Dimensional Mixed Beam Finite Elements

In prior research, several mixed finite element formulations have been developed for two- and three-dimensional analysis of steel and composite members and frames (Nukala and White 2004; Alemdar and White 2005; Tort and Hajjar 2010b; Denavit and Hajjar 2010). The formulation by Nukala and White (2004) is intended for the analysis of steel structures and included section warping. The formulation by Tort and Hajjar (2010b) is intended for the analysis of rectangular CFT members and included slip between the steel tube and concrete core. The formulation by Denavit and Hajjar (2010) is suitable for use with a wide variety of steel and composite members and is adopted for use in this work.

The element stiffness and internal force are derived in the corotational frame using moderate rotation and small strain assumptions. Rigid body modes of deformation are accounted for solely in a geometric transformation. When accompanied with an exact transformation between the corotational and global frame the element is capable of capturing large displacement and rotation behavior. Cubic-Hermitian and linear interpolation function are used for the transverse and axial deformation fields respectively, while linear and constant interpolation functions are used for the bending moment and axial load fields respectively. The Green-

Lagrange strain measure is used to define the axial strains, while curvature is assumed to be the second derivative of the transverse deformation field. The axial strain at each of the fibers in the section is determined utilizing a kinematic assumption (i.e., initially plane sections remain plane), neglecting any slip occurring between the steel and concrete. In the mixed formulation, element compatibility and section equilibrium are satisfied with two equations beyond element equilibrium. The simultaneous solution of all three governing equations adds to the complexity of the state determination algorithm. The unbalance from the additional equations is converted to an unbalanced force at the global level and eliminated through the global solution iterations. A full derivation of this element is presented in the work of Denavit and Hajjar (2010).

3.2.1 Localization

Regions of beams and columns that experience large inelastic curvatures when subjected to severe loading are designated plastic hinges. The inelasticity generally occurs in certain critical locations (e.g., the member ends for reverse curvature bending) and over a finite length, which is termed the plastic hinge length. The plastic hinge length has important implications for finite element analyses (Attalla et al. 1994). Distributed plasticity models, such as the one adopted in this work, track inelasticity throughout the entire length of the element. For strain-hardening sections, the plastic hinge length develops naturally and can be observed in analyses. However, for strain-softening sections, to maintain equilibrium, typically only one section in the element will follow the softening path, while the others simply unload elastically. The portion of the element over which the softening section is applicable is dependent on the numerical integration weight assigned to the section which depends on the number of sections. This causes a loss of objectivity and computed results vary significantly based on the selected mesh density. This phenomenon is known as localization.

Localization has been studied in the context of force based beam elements (Coleman and Spacone 2001; Scott and Fenves 2006; Scott and Hamutcuoglu 2008). Two general solutions have been proposed, the first is the alteration of the softening slope of the constitutive relations, and the second is to ensure that the numerical integration is performed such that the softening effects are distributed along the appropriate length of the member, i.e., the integration weight assigned to the section which softens represents the physical plastic hinge length.

Scott and Hamutcuoglu (2008) present a specialized numerical integration scheme based on Lobatto quadrature but with the ability to prescribe the integration weights at the element ends. This approach was implemented for the mixed beam element and in many cases performed very well, eliminating the mesh dependency associated with localization. However, the special numerical integration scheme often made it more difficult to obtain convergent results. Thus, an approximate method of handling localization was adopted whereby the mesh density (i.e., number of elements per member and number of integration points per element) is selected such that the integration weight implied by Lobatto quadrature of the critical integration point (section highest moment) was approximately equal to the physical plastic hinge length. This approach, however, has limitations. Aspects of the physical behavior such as the moment gradient must be known a priori and often a mesh cannot be selected such that the region of expected inelasticity is represented by a single integration point or even a single element. Nonetheless, with careful selection of the mesh density, accurate results can be obtained for a vast majority of practical cases.

3.2.2 Constitutive Relations

The accuracy of the mixed beam formulation depends strongly on the ability of the constitutive relations to provide realistic estimations of the behavior of the constituent materials. Using the fiber method, the response of a cross section is governed by the aggregation of response from individual fibers and the uniaxial constitutive relations associated with them. In this work, the discretization of the various sections was defined using a single numeric parameter for two-dimensional analyses and two numeric parameters for three-dimensional analyses. The numeric parameters relate the nominal size of individual fibers to the section depth or width. For example, for a RCFT (H = 12 in, B = 8 in, t = 5/8 in) section in strong axis bending, the fiber discretization could be defined by specifying the nominal fiber size as $1/30^{th}$ of the section depth. In this case, the number of fibers through the thickness of the steel tube flange would be determined by dividing the thickness of the flange by the nominal fiber size (H/30) and rounding up to the nearest integer, in this case resulting in 2 (Equation 3.1).

$$2 \approx 1.25 = \frac{5/8\,\text{in}}{12\,\text{in}/30} = \frac{t}{H/30} \tag{3.1}$$

For the case of segments of the cross section that are circular in shape (e.g., reinforcing bars, circular steel tubes, and corners of rectangular steel tubes) the fiber discretization was defined by the number of fibers in the radial and circumferential directions. The number of fibers for these directions was selected such that the size of any individual fiber did not exceed the nominal fiber size.

In all cases, the fiber discretization was defined consistently such that the sum of the areas of the fibers exactly equaled that of the idealized geometry, and the sum of the moments of inertia of the fibers approached that of the idealized geometry as the nominal size of the fibers approached zero.

Relatively coarse fiber discretization schemes (i.e., approximately 20 fibers for a three dimensional analysis) have been shown to accurately predict the cyclic inelastic response of structural steel and reinforced concrete members (Kostic and Filippou 2012). In this study, relatively fine discretization schemes (i.e., nominal fiber size of $1/20^{th}$ or $1/30^{th}$ of the section depth) were selected since the initial stiffness was often of critical importance and the resulting number of fibers did not pose any computational problems.

Further, the uniaxial constitutive relations must be able to model arbitrary strain histories such as may be seen in static cyclic or dynamic loading. General steel and concrete uniaxial cyclic relations are presented in the next two sections. Application of these materials to specific steel and composite sections is presented in later sections.

3.3 Uniaxial Cyclic Constitutive Relations for Concrete

This section describes a general uniaxial concrete constitutive relation that has been adapted from the rule-based model of Chang and Mander (1994). The constitutive relation was designed for broad applicability, so in addition to defining typical input parameters, such as concrete strength and initial modulus, the analyst may select the monotonic backbone curve (either Popovics' or Tsai's equation as described below), whether to include or neglect the tensile strength, and whether to include or neglect spalling. The details and adaptations of how

this model is applied to specific composite members and to the "Proposed for Behavior" and "Proposed for Design" models are described in later sections.

3.3.1 Monotonic Concrete Stress-Strain Relation

A monotonic stress-strain relation serves as the backbone of the cyclic constitutive relation. Numerous such models have been proposed in the literature (Kent and Park 1971; Popovics 1973; Tsai 1988; Sheikh and Uzumeri 1980; Hoshikuma et al. 1997; Akiyama et al. 2010), two have been selected as options for this constitutive relation. The relations are defined using normalized values of strain, stress, and tangent as defined in Equation 3.2 for compression and Equation 3.3 for tension.

$$x = \frac{\varepsilon_c}{\varepsilon'_{cc}}; \quad y = \frac{f_c}{f'_{cc}}; \quad n = \frac{E_c \varepsilon'_{cc}}{f'_{cc}} \tag{3.2}$$

$$x = \frac{\left(\varepsilon_c - \varepsilon_{to}\right)}{\varepsilon'_t}; \quad y = \frac{f_c}{f'_t}; \quad n = \frac{E_c \varepsilon'_t}{f'_t} \tag{3.3}$$

where,

x = normalized strain
ε_c = strain
ε_{to} = tensile strain offset
ε'_{cc} = strain at peak stress in compression
ε'_t = strain at peak stress in tension
y = normalized stress
f_c = stress
f'_{cc} = peak stress in compression
f'_t = peak stress in tension
n = normalized modulus
E_c = initial modulus of elasticity

The first monotonic stress-strain relation is Popovics' equation (Equation 3.4) (Popovics 1973). This equation defines the stress-strain response based on three parameters: the initial modulus of elasticity, the peak stress, and the strain at peak stress.

$$y = \frac{rx}{r - 1 + x^r} \tag{3.4a}$$

$$r = \frac{n}{n - 1} \tag{3.4b}$$

The second monotonic stress-strain relation is Tsai's equation (Equation 3.5) (Tsai 1988). This equation defines the stress-strain response based on four parameters: the three parameters for Popovics' equation plus a parameter that controls the post-peak behavior, termed r (r_n in compression and r_p in tension). Tsai's equation is more accurate in cases of high confinement or

high strength since the post-peak response can be controlled directly. For the case of $r = n/(n–1)$, Tsai's equation simplifies to Popovics' equation.

$$y = \frac{nx}{D(x)} \tag{3.5a}$$

$$D(x) = \begin{cases} 1 + \left(n - \dfrac{r}{r-1} \right) x + \dfrac{x^r}{r-1} & \text{for } r \neq 1 \\ 1 + \left(n - 1 + \ln x \right) x & \text{for } r = 1 \end{cases} \tag{3.5b}$$

Both of these equations predict non-zero stress for all non-zero strains, however to model spalling in compression or cracking in tension, it is desirable to have zero stress and tangent at high strain levels. This is achieved by defining a critical normalized strain, x_{cr}, at which the stress-strain relation is overridden by linear degradation to zero stress. The slope of the linear degradation is equal to the tangent of the stress-strain relation at x_{cr}. Once the concrete has reached zero stress in tension it is said to have cracked and is no longer capable of sustaining tensile stress. Once the concrete has reached zero stress in compression it is said to have spalled and is no longer capable of sustaining any stress.

3.3.2 Initial Modulus of Elasticity

Various relations have been proposed for the initial modulus of elasticity for concrete. It is given in the AISC *Specification* (AISC 2010b) as Equation 3.6.

$$\begin{aligned} E_c \left[\text{ksi} \right] &= w_c \left[\text{lbs/ft}^3 \right]^{1.5} \sqrt{f'_c \left[\text{ksi} \right]} \\ E_c \left[\text{MPa} \right] &= 0.043 w_c \left[\text{kg/m}^3 \right]^{1.5} \sqrt{f'_c \left[\text{MPa} \right]} \end{aligned} \tag{3.6}$$

where,

w_c = weight of concrete per unit volume
f'_c = specified compressive strength of concrete

A similar relation (Equation 3.7) is given in the ACI *Code* (ACI 2011).

$$E_c \left[\text{psi} \right] = 33 w_c \left[\text{lbs/ft}^3 \right]^{1.5} \sqrt{f'_c \left[\text{psi} \right]} \tag{3.7}$$

Also given in the ACI *Code* is a simpler relation (Equation 3.8) applicable to normalweight concrete. This relation is used for the analyses described in this work. Note that Equation 3.8 is equivalent to Equation 3.7 for w_c = 144.0 lbs/ft^3 and to Equation 3.6 for w_c = 148.1 lbs/ft^3.

$$E_c\left[\text{psi}\right] = 57,000\sqrt{f'_c\left[\text{psi}\right]}$$
$$E_c\left[\text{ksi}\right] = 1,802\sqrt{f'_c\left[\text{ksi}\right]} \tag{3.8}$$
$$E_c\left[\text{MPa}\right] = 4,733\sqrt{f'_c\left[\text{MPa}\right]}$$

A distinction that should be noted is that E_c in stress-strain relations (e.g., Equation 3.4) is typically defined as the initial modulus while relations for the elastic modulus of concrete often define E_c as a secant modulus (e.g., from the origin to $0.45f'_c$ for Equation 3.7). This difference can be evaluated by determining the initial modulus, E_{ci}, that would yield a given secant modulus, E_{c45}. The ratio between the initial and secant modulus is shown in Figure 3.1 where the stress-strain relation is given by Popovics' equation (Equation 3.4), E_{c45} is given by Equation 3.8 , and ε_c is given by Equation 3.9 (see below). The difference is approximately 5% for normal strength concrete, reducing to less than 1% for high strength concrete. This small difference can be neglected in most cases.

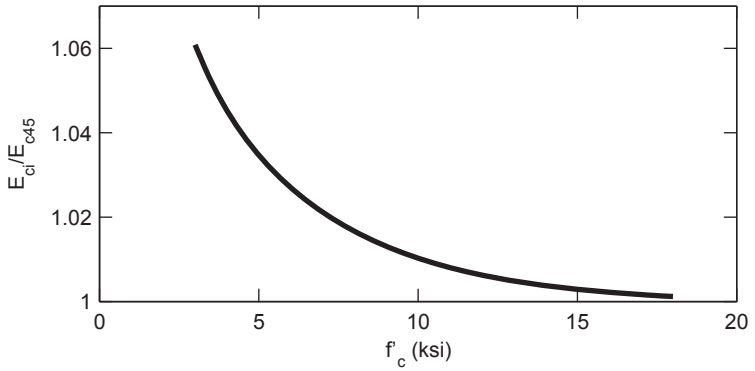

Figure 3.1. Comparison of Initial and Secant Modulus (E_{ci} and E_{c45})

3.3.3 Concrete in Compression

The compressive strain at peak stress for unconfined concrete, ε'_c, has been found to be a function of the compressive strength. Chang and Mander (1994) recommend Equation 3.9 to capture this behavior.

$$\varepsilon'_c = f'_c\left[\text{ksi}\right]^{1/4} / 710$$
$$\varepsilon'_c = f'_c\left[\text{MPa}\right]^{1/4} / 1150 \tag{3.9}$$

Lateral confining pressure provided by the steel tube in CFTs or the steel member and steel reinforcing in SRCs improves both the strength and ductility of the concrete. This effect is modeled by estimating the symmetric confinement pressure, f_l, or the confinement pressure in two orthogonal directions, f_{l1} and f_{l2}, based on the geometric and material properties of the section (as described later for each composite member) then applying a confinement model to compute the peak stress and strain at peak stress. The confinement model of Mander et al. (1988)

is selected in this work. For CCFTs, where a symmetric state of confinement (i.e., $f_{l1} = f_{l2}$) may be assumed, Equation 3.10 is utilized to compute the increased strength.

$$f'_{cc} = f'_c\left(-1.254 + 2.254\sqrt{1 + 7.94\left(f_l / f'_c\right)} - 2.0\left(f_l / f'_c\right)\right) \tag{3.10}$$

For SRCs, the state of confinement is unsymmetric and Equation 3.11 is utilized to compute the increased strength.

$$f'_{cc} = f'_c\left(1 + A\bar{x}\left(0.1 + \frac{0.9}{1 + B\bar{x}}\right)\right) \tag{3.11a}$$

$$\bar{x} = \frac{f_{l1} + f_{l2}}{2f'_c}; \quad \rho = \frac{f_{l1}}{f_{l2}}; \quad f_{l1} \le f_{l2} \tag{3.11b}$$

$$A = 6.8886 - \left(0.6069 + 17.275\rho\right)e^{-4.989\rho} \tag{3.11c}$$

$$B = \frac{4.5}{\frac{5}{A}\left(0.9849 - 0.6306e^{-3.8939\rho}\right) - 0.1} - 5 \tag{3.11d}$$

For both cases, the increase in strain at peak stress due to confinement follows the model by Richart et al. (1929) (Equation 3.12).

$$\varepsilon'_{cc} = \varepsilon'_c\left(1 + 5\left(f'_{cc} / f'_c - 1\right)\right) \tag{3.12}$$

For unconfined concrete Chang and Mander (1994) recommend the following expression for r_n (Equation 3.13) to be used in Tsai's equation for monotonic compressive backbone curve (Equation 3.5).

$$\begin{aligned} r_n &= \frac{f'_c[\text{ksi}]}{0.75} - 1.9 \\ r_n &= \frac{f'_c[\text{MPa}]}{5.2} - 1.9 \end{aligned} \tag{3.13}$$

In the presence of confining pressure, the post-peak degradation of concrete is more gradual and is modeled with a lower r_n value. For very low values of r_n, a spurious hardening behavior occurs in the pre-peak range. In order to accommodate these low values of r_n necessary to model high confinement pressures, two values of r_n are used; one prior to the peak stress being reached, r_{pre}, and one after the peak stress is reached, r_{post} (Equation 3.14). Continuity in stress and tangent are maintained since the transition occurs at the peak stress. Specific values of $r_{n,pre}$ and $r_{n,post}$ are given later in the context of each composite cross section.

$$r_n = \begin{cases} r_{n,pre} & x \le 1 \\ r_{n,post} & x > 1 \end{cases} \tag{3.14}$$

3.3.4 Concrete in Tension

Often the tensile response of concrete is neglected, however, modeling the tensile response of concrete has been shown to improve the accuracy of nonlinear finite element models for composite members (Gourley and Hajjar 1994). The shape of the stress-strain response of concrete in tension is similar to that of concrete in compression. Noting that, Chang and Mander (1994) recommended the using the same shape equations as the compressive response for the tensile response of concrete (i.e., Popovics' or Tsai's equation above) but with normalized variables defined with respect to tensile values for the peak stress, f'_t (Equation 3.15), and the strain at peak stress, ε_t (Equation 3.16). When Tsai's equation is used, the post-peak factor, r_p, is given by Equation 3.17 based on recommendations by Tort and Hajjar (2007).

$$\begin{aligned} f'_t[\text{ksi}] &= 0.19\sqrt{f'_c[\text{ksi}]} \\ f'_t[\text{MPa}] &= 0.50\sqrt{f'_c[\text{MPa}]} \end{aligned} \tag{3.15}$$

$$\varepsilon_t = 1.23\frac{f'_t}{E_c} \tag{3.16}$$

$$r_p = 4 \tag{3.17}$$

3.3.5 Concrete under Cyclic Loading

In the cyclic rule-based model of Chang and Mander (1994) the state determination procedure starts by using the strain increment to determine on which branch (or rule) of the stress strain response the fiber is currently located. Once the current rule is determined, state variables are updated as necessary then the stress and tangent are computed. Among the rules are the envelope curves in tension and compression are described in previous sections. The remaining rules are defined to provide transitions between the envelope curves for the case of load reversals and also transitions between transition curves for the case of partial load reversals.

A full description of the cyclic rules including all calibrated parameters, stress-strain relation for transition curves, and the shifting of the tensile envelope is available in Denavit and Hajjar (2010). This description is based upon the work Chang and Mander (1994) with minor modifications.

3.4 Uniaxial Cyclic Constitutive Relations for Steel

The primary features of the behavior steel components of composite members are plasticity, residual stress, and local buckling (in this work fracture is neglected). This section describes a uniaxial steel constitutive relation that accounts for these features and two additional, less complex steel constitutive relations that account for plasticity and residual stress (neglecting local buckling). The simpler models are more appropriate for the some studies conducted in this

work particularly those for the development of design recommendations. Details and adaptations of applying the models to specific composite or steel members are described in later sections.

3.4.1 Shen et al. Steel Material

The first steel model presented is based on the bounding-surface plasticity model of Shen et al. (1995). This constitutive relation is derived based on a set of hardening and flow rules that act on the incremental strain. Key features of the model are described below.

The total strain increment, $\Delta\varepsilon^t$, is decomposed into an elastic component, $\Delta\varepsilon^e$, and plastic component, $\Delta\varepsilon^p$ (Equation 3.18).

$$\Delta\varepsilon^t = \Delta\varepsilon^e + \Delta\varepsilon^p \tag{3.18}$$

The stress increment, $\Delta\sigma$, is defined as the product of the strain increment and a modulus (Equations 3.19 through 3.21). The appropriate modulus depends on which component (elastic, plastic, or total) of the strain is utilized. Further, the tangent modulus, E^t, may be written in terms of the elastic modulus, E^e, and the plastic modulus, E^p, (Equation 3.22).

$$\Delta\sigma = E^t\,\Delta\varepsilon^t \tag{3.19}$$

$$\Delta\sigma = E^e\,\Delta\varepsilon^e \tag{3.20}$$

$$\Delta\sigma = E^p\,\Delta\varepsilon^p \tag{3.21}$$

$$E^t = \frac{E^p E^e}{E^p + E^e} \tag{3.22}$$

The elastic component is assumed to hold a linear relationship (Equation 3.23).

$$\sigma = E^e\varepsilon^e \tag{3.23}$$

When the stress lies within the elastic range, the tangent modulus is assumed to be equal to the elastic modulus (the plastic modulus is taken as infinity). The size of the elastic range decreases monotonically with loading and is described by Equation 3.24.

$$\frac{\kappa}{\kappa_o} = \alpha - a\exp\left(-100b\bar{\varepsilon}^p\right) - \left(\alpha - a - 1\right)\exp\left(-100c\bar{\varepsilon}^p\right) \tag{3.24}$$

where,

κ = half of the current size of the elastic range
κ_o = half the initial size of the elastic range, taken as the yield strength, F_y
$\bar{\varepsilon}^p$ = effective plastic strain range, defined as the difference between the maximum and minimum plastic strains the material has experienced
α, a, b, c = material constants

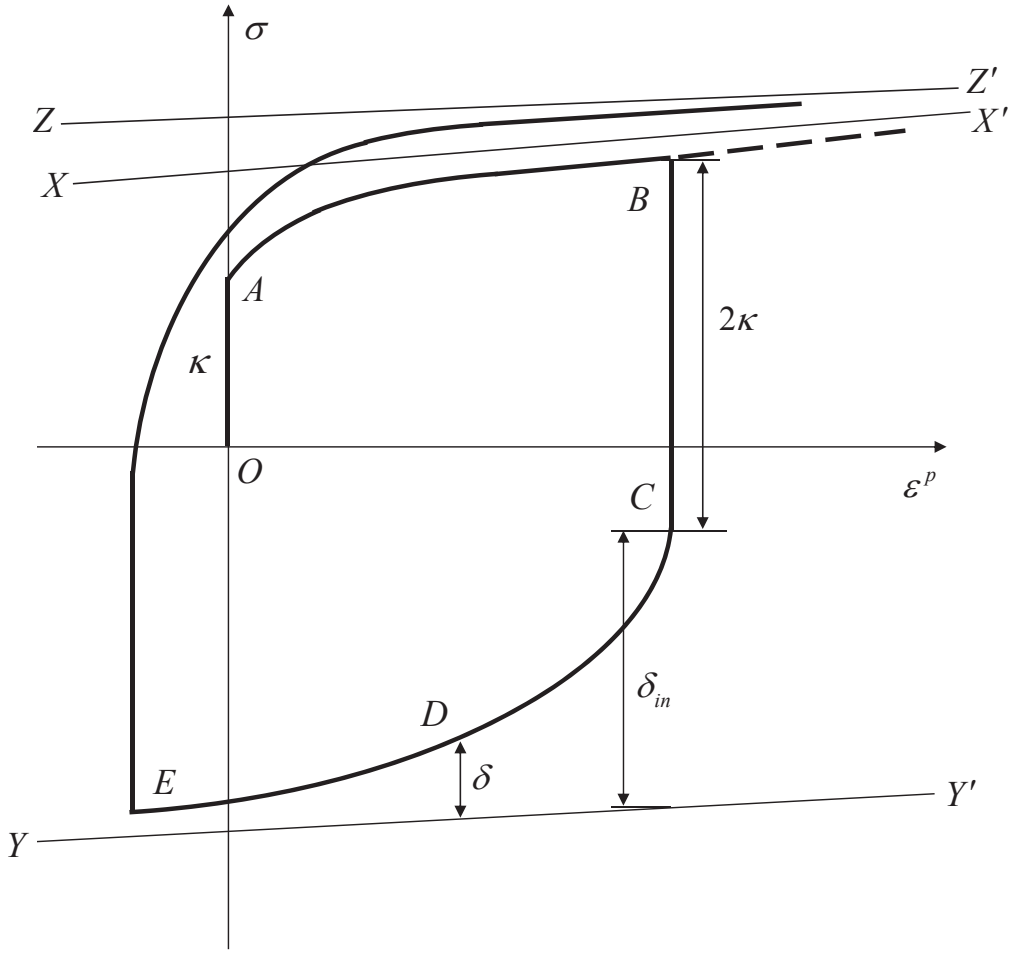

Figure 3.2. Uniaxial Cyclic Stress-Plastic Strain Curve

If the stress lies outside of the elastic range, the plastic modulus takes a finite value given by Equation 3.25.

$$E^p = E_o^p + h\frac{\delta}{\delta_{in} - \delta} \tag{3.25}$$

where,

E_o^p = slope of the bounding line

$h = e\delta + f$

δ = distance between the bounding surface and the current (loading) point

δ_{in} = value of δ at the point of initial yield in the current loading path

e, f = material constants.

The slope of the bounding line is assumed to decrease with the accumulated plastic work (Equation 3.26).

$$E_o^p = \frac{E_{oi}^p}{1 + \omega W^p} \tag{3.26}$$

where,

E_{oi}^p = initial slope of the bounding line, a material constant
W_p = accumulated plastic work (Equation 3.27)
ω = a material constant.

$$W^p(t) = \int_0^t \sigma(s)\,\varepsilon^p(s)\,ds \tag{3.27}$$

where,

t = a time parameter
s = variable of integration.

The size of the bounding line is assumed to increase with plastic strain (Equation 3.28).

$$\bar{\kappa} = \bar{\kappa}_\infty + (\bar{\kappa}_o - \bar{\kappa}_\infty)\exp(-\zeta\rho^2) \tag{3.28}$$

where,

$\bar{\kappa}$ = current size of the bounding line
$\bar{\kappa}_\infty$ = limiting value of the bounding line, taken at the ultimate tensile strength , F_u
$\bar{\kappa}_o$ = initial size of the bounding line, a material constant
ρ = half of the effective plastic strain range, $\bar{\varepsilon}^p$
ζ = a material constant

For better correlation to cyclic behavior that does not include full reversals, the virtual bounding line and memory line are introduced (Figure 3.3). Both the virtual bounding line and the memory line are assumed to lie parallel to the bounding line. The initial size of the memory line is taken as the yield strength of the steel and the size grows symmetrically with the loading point (i.e., the size of the memory line grows with the largest stress attained by the material). If a loading path reverses before reaching the memory line (e.g., Point B in Figure 3.3), the virtual bounding line is created outside the bounding line by the same amount the loading path was short of the memory line (e.g., line X_v-X_v' in Figure 3.3). Along the reversed path, until the memory line on the opposite side is reached (e.g., Point C in Figure 3.3), the plastic modulus is computed with respect to the virtual bounding line, not the bounding line, as described by Equation 3.29,

$$E^p = E_o^p + h\frac{\delta + \delta_v}{\delta_{in} - \delta} \tag{3.29}$$

where,

δ_v = distance between the virtual bounding line and the bounding line

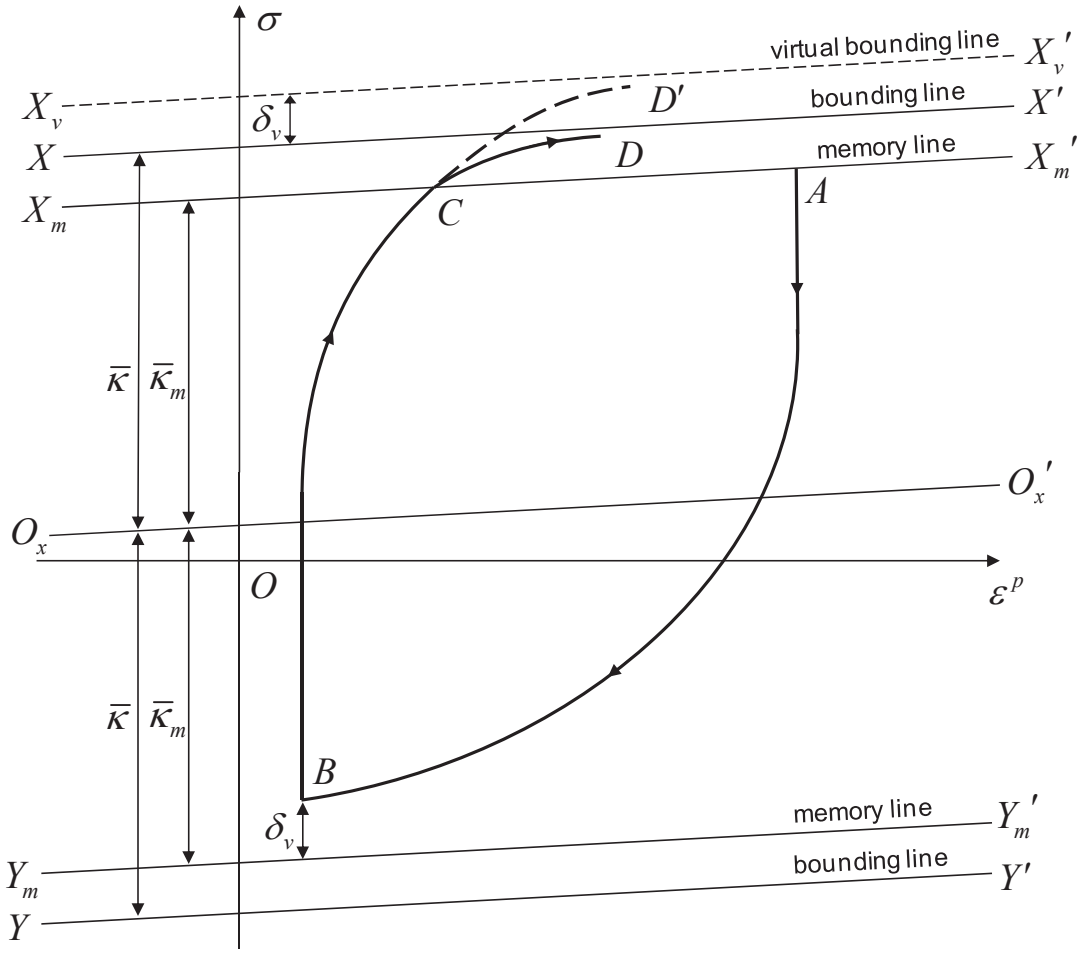

Figure 3.3. Definition of Virtual Bounding Line and Memory Line

First Plastic Excursion

The performance of the plasticity formulation under large monotonic strains is relatively poor, significantly overpredicting the stress. To correct for this, during the first plastic excursion (stresses greater than the yield strength) the trial stress computed by the incremental plasticity formulation is overridden by a prescribed stress-strain relation. This rule remains in effect until plasticity occurs in the opposite direction (i.e., the stress-strain response continues along the prescribed stress-strain relation even after small elastic unloading and reloading).

A suitable stress-strain relation would have an initial tangent equal to E_{sh}, and not exceed the ultimate stress. Kunnath et al. (2009) present a nonlinear equation which satisfies these requirements (Equation 3.29). This curve is used and performs well provided that $p > 2$. If $p \leq 2$, a bilinear equation is used; the first linear branch has slope of E_{sh} and final stress of $(F_y+F_u)/2$ and the section linear branch has a final stress of F_u and a final strain of ε_u (Galambos 2000).

$$\sigma_s = F_u + \left(F_y - F_u\right)\left(\frac{\varepsilon_u - \varepsilon_s}{\varepsilon_u - \varepsilon_{sh}}\right)^p \tag{3.29a}$$

$$p = E_{sh}\frac{\varepsilon_u - \varepsilon_{sh}}{F_u - F_y} \tag{3.29b}$$

where,

ε_u = strain at ultimate stress
ε_{sh} = strain at the initiation of strain hardening
E_{sh} = modulus at the initiation of strain hardening

Local Buckling

Under compressive loading steel components are susceptible to local buckling. In a detailed analysis with continuum or shell elements this behavior can be captured explicitly. In frame analyses with beam elements, this behavior can only be accounted for implicitly in the material constitutive relation.

To account for local buckling, the monotonic compressive response is modified to consist of three regions (Figure 3.4a). The first region is the model as described previously, beginning with the elastic behavior then continuing into plasticity. The second region is commences after the initiation of local buckling, which is assumed to be triggered when the compressive strain reaches a prescribed value, ε_{lb}. In this region the response from the plasticity model is overridden by linear strength degradation with a prescribed modulus, K_{slb}. The third region is a constant ultimate residual stress, F_{ulb}.

Under cyclic loading additional modifications are necessary to properly model the local buckling response. The first initiation of local buckling is triggered by the condition described in Equation 3.30. Upon unloading from tensile plasticity the strain at zero stress, $\varepsilon_{lb,ref}$, is computed assuming elastic behavior. This strain serves as the reference to determine the initiation of local buckling. Additionally, the stress must be greater than or equal to the constant ultimate residual stress.

$$\left(\varepsilon \leq \varepsilon_{lb} + \varepsilon_{lb,ref}\right) \text{and} \left(\sigma \leq F_{ulb}\right) \tag{3.30}$$

After the first initiation of local buckling, later local buckling is triggered when the trial strain and stress reach a boundary defined upon the previous unloading from local buckling. The boundary, shown graphically in Figure 3.4b, consists of the remainder of the local buckling response had the unloading not occurred for strains less than the unloading strain and the

unloading stress for strains greater than the unloading strain. These rules correspond to behavior observed experimentally by Fukumoto and Kusama (1985) for rectangular steel tubes. Further, to provide a smooth transition to the limiting stress, the bounding line in the compressive region (i.e., Line *Y-Y′* in Figure 3.2) is defined to be equal to the unloading stress.

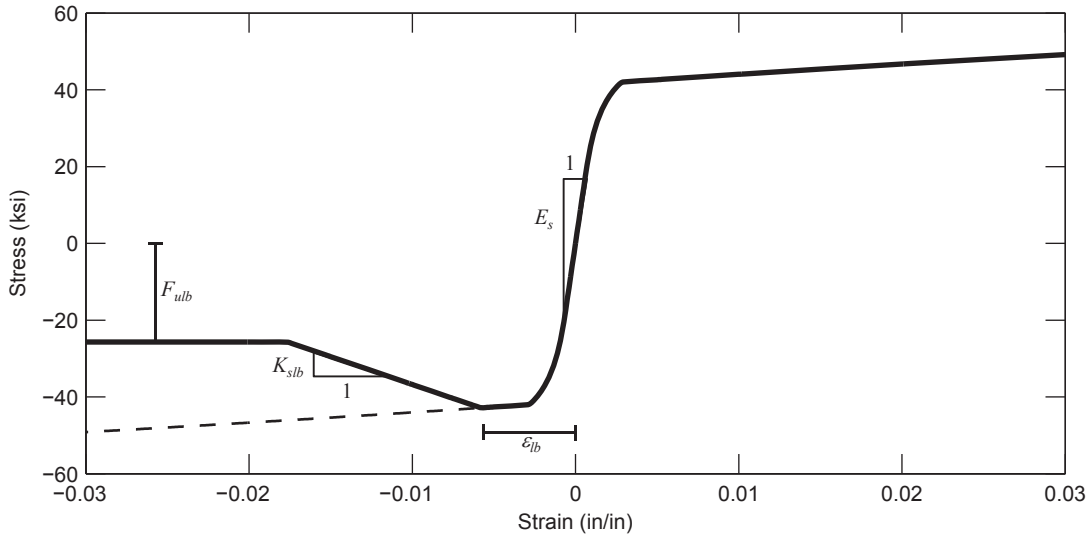

(a) Monotonic

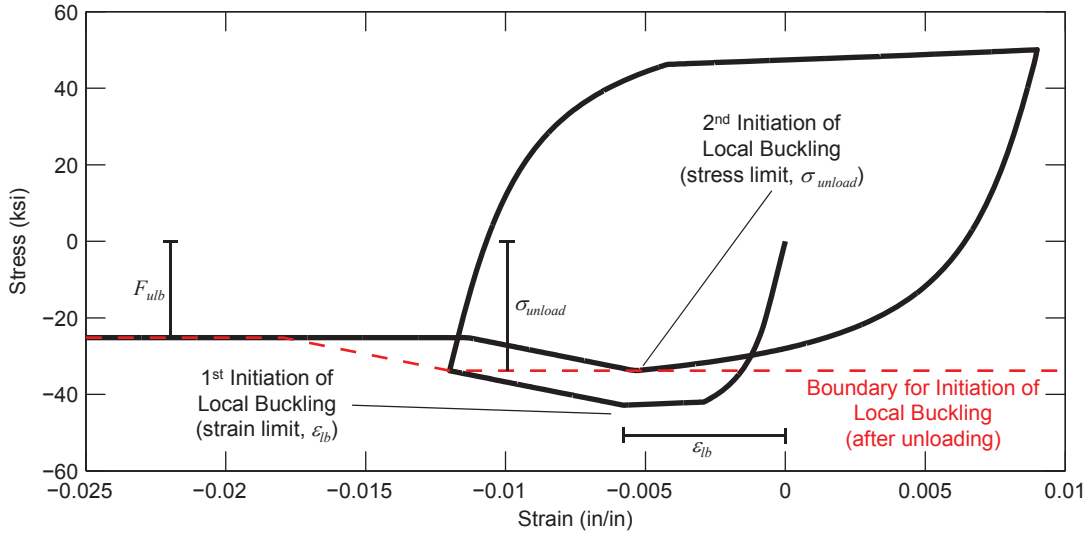

(b) Cyclic

Figure 3.4. Steel Stress-Strain Relationship including Local Buckling

To approximate the response of unloading of the buckled steel component, reductions in the size of the elastic range and plastic modulus for reloading back into tension can be reduced (Equations 3.31 and 3.32). Where the reduction factor for each is a function of the accumulated

plastic work (Equation 3.33). Specific values of the rate and limit of the reductions are given later in the context of each composite and steel cross section.

$$\kappa_{reduced} = \gamma_{\kappa} \kappa \tag{3.31}$$

$$E^{p}_{reduced} = \gamma_{E^p} E^{p} \tag{3.32}$$

$$\gamma_X = 1 - \alpha_X \sqrt{\frac{W^P}{F_y}} \geq \beta_X \tag{3.33}$$

where,

λ_X = reduction factor for value X
α_X = rate of the reduction
β_X = limit of the reduction

Material Constants

The material parameters required for the steel material model are given in Table 3.1 as reported in Mamaghani et al. (1996).

Table 3.1. Steel Model Material Parameters

Parameter	$F_y \leq 40$ ksi (276 MPa)	40 ksi (276 MPa) < F_y ≤ 52 ksi (359 MPa)	$F_y > 52$ ksi (359 MPa)
κ_o	1.15 F_y	1.13 F_y	1.06 F_y
a	–0.505	–0.528	–0.553
b	2.17	1.88	6.47
c	14.4	18.7	34.8
e	500	316	700
f	0.300 E_s	0.484 E_s	0.361 E_s
α	0.191	0.217	0.175
ω	3.08 / F_y	4.00 / F_y	2.67 / F_y
E^p_{oi}	8.96×10^{-3} E_s	1.01×10^{-2} E_s	7.85×10^{-3} E_s
ζ	9.89×10^{-4} / ε_y^2	1.52×10^{-3} / ε_y^2	8.04×10^{-3} / ε_y^2
M	–0.37	–0.052	0.00

Modifications for Cold-Formed Steel Members

Effects from the cold-forming process of the steel tubes should be included in a comprehensive constitutive relation, notably the smooth transaction between elastic and plastic response, rather than the formation of a significant yield plateau. To model these effects, the yield plateau is neglected and an initial plastic strain, $\overline{\varepsilon}^p_o$, is defined.

3.4.2 Abdel-Rahman and Sivakumaran Steel Material

The second steel model used in this work is based on the work of Abdel-Rahman and Sivakumaran (1997). This constitutive relation is more appropriate to model the steel tube of CFTs for some of the studies conducted in this work. This model was developed for cold-formed steel members accounts for the residual stress and gradual transition into plasticity though a multi-linear stress-strain relation (Figure 3.5). The increased yield strength in the corner region is accounted for directly by computing a different yield strength for the corner based on the geometry of the corner and material properties of the flat region (Equation 3.34). To extend this model for cyclic behavior, the backbone curve is defined in the context of a multi-surface kinematic hardening plasticity model (Mróz 1967).

$$F_{y,corner} = F_{y,flat} + \Delta F_{y,corner} \tag{3.34a}$$

$$\Delta F_{y,corner} = 0.6\left(\frac{B_c}{(r/t)^m} - 1\right) F_{y,flat} \tag{3.34b}$$

$$B_c = 3.69\left(\frac{F_{u,flat}}{F_{y,flat}}\right) - 0.819\left(\frac{F_{u,flat}}{F_{y,flat}}\right)^2 - 1.79 \tag{3.34c}$$

$$m = 0.192\left(\frac{F_{u,flat}}{F_{y,flat}}\right) - 0.068 \tag{3.34d}$$

where,

r = internal radius of the corner
t = thickness of the flat

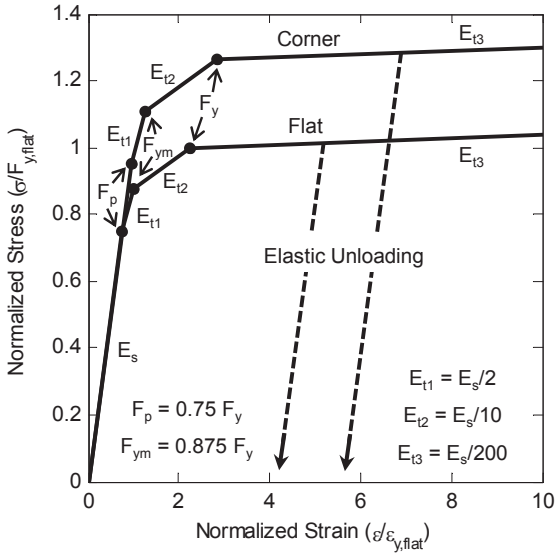

Figure 3.5. Abdel-Rahman and Sivakumaran Steel Material

3.4.3 Elastic-Perfectly Plastic Steel Material

The third steel model used in this work is a simple elastic perfectly plastic steel model, defined with an initial elastic modulus and yield strength (Figure 3.6). An elastic perfectly plastic relation is more appropriate to model the hot-rolled steel shapes and reinforcing steel for some of the studies conducted in this work.

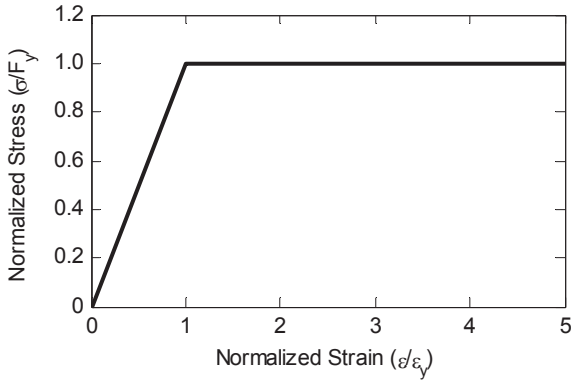

Figure 3.6. Elastic-Perfectly Plastic Steel Material

3.4.4 Steel Ultimate Stress

The majority of experimental reporting includes documentation of the steel ultimate strength. For the cases where it is not reported or otherwise unavailable, an empirical relation was developed to estimate the ultimate strength. This relation (Equation 3.35) was based on the yield strength and ultimate strength reported for a wide variety of steel coupon tests in published literature. Coupon tests from plate, wide flange sections, circular and rectangular tubes, as well as reinforcing steel were included in the calibration of this equation. It is noted that there is significant scatter in these results (Figure 3.7) and Equation 3.35 should only be used when other data is unavailable.

$$\begin{aligned} F_u &= F_y\left(1+187F_y\left[\text{ksi}\right]^{-1.61}\right) \\ F_u &= F_y\left(1+4190F_y\left[\text{MPa}\right]^{-1.61}\right) \end{aligned} \tag{3.35}$$

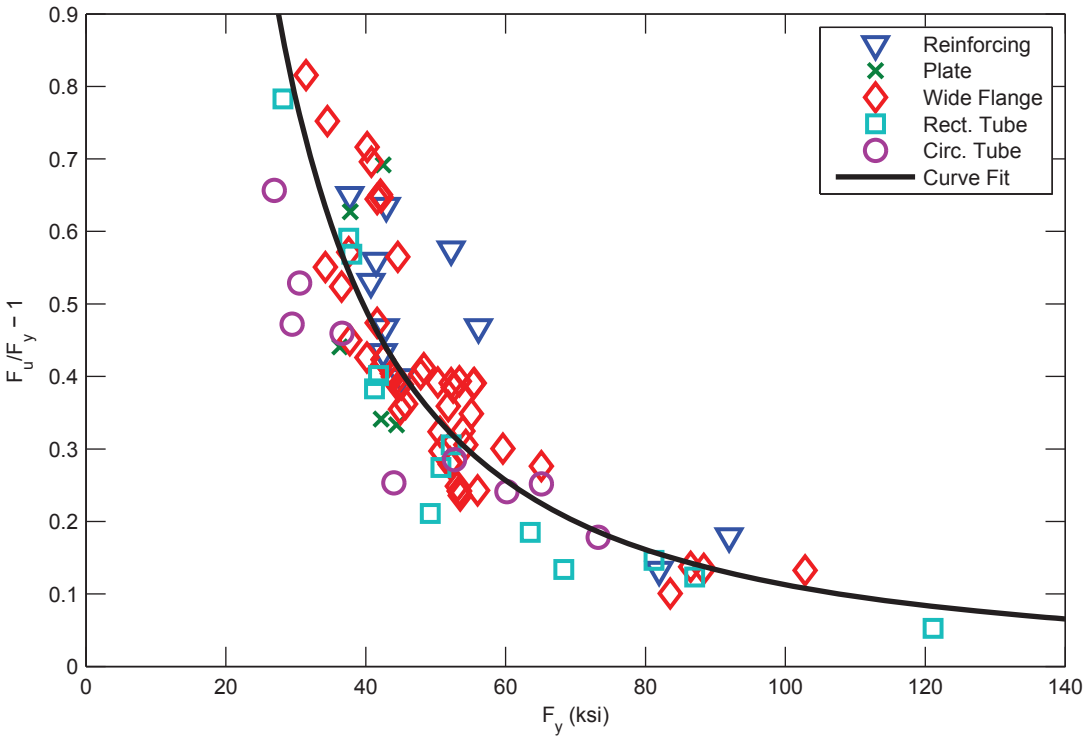

Figure 3.7. Calibration of the Empirical Relation for Steel Ultimate Stress

3.4.5 Residual Stress of Wide Flange Steel Members

For hot-rolled wide flange shapes, modifications were made to model the effects of residual stress within the steel section. The residual stress at a fiber is modeled explicitly as an initial elastic stress in the uniaxial constitutive relation. The Lehigh residual stress pattern (Figure 3.8a) (Galambos and Ketter 1959) is used to define the value of residual stress in the steel section with a maximum compressive residual stress of 30% of the yield strength occurring at the flange tips and a maximum tensile residual stress computed to ensure section equilibrium (Equation 3.36).

$$F_t = \frac{b_f t_f}{b_f t_f + t_w \left(d - 2t_f\right)} F_c \tag{3.36}$$

The Lehigh pattern incudes a linear variation in residual stress in the flange. To model this in an efficient manner, the residual stress in the flange is broken into a number of sectors with a step pattern used to establish the distribution across the section. An example of the implementation of this is shown in (Figure 3.8b) where dots represent individual fibers and the different colors represent different values of residual stress.

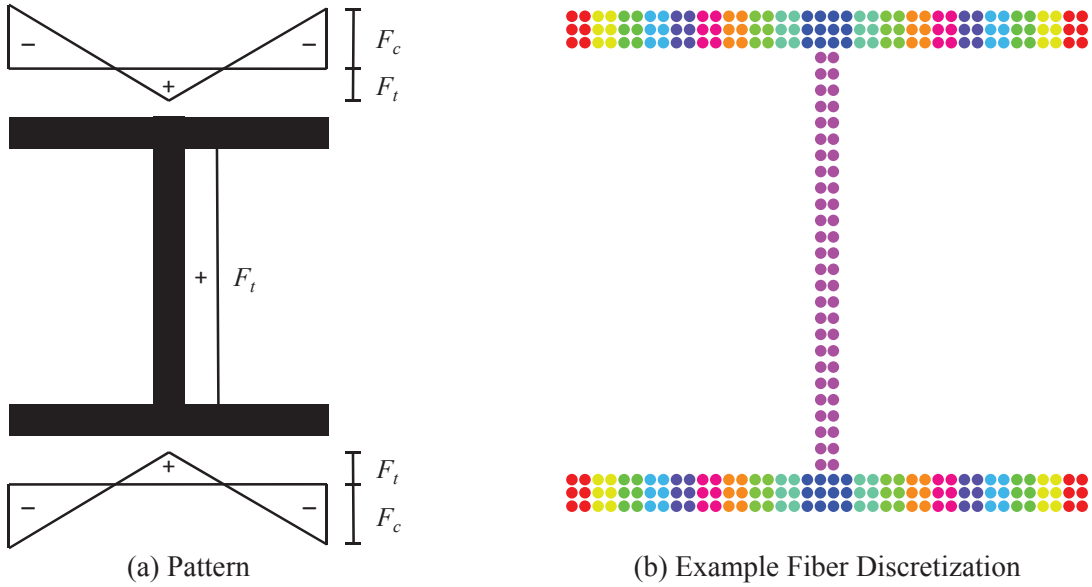

(a) Pattern (b) Example Fiber Discretization

Figure 3.8. Lehigh Residual Stress Pattern

3.5 Concrete Filled Steel Tube Beam-Columns

When CFT members are subjected to compression, both the steel tube and the concrete core expand laterally due to Poisson's effect. In the early stages, the steel tube expands at a greater rate than the concrete core (i.e., the Poisson's ratio is larger for the steel tube). However, as the loading continues the rate of lateral expansion of the concrete core increases due to micro-cracking and eventually a radial interaction occurs. The result of this interaction is a confinement pressure on the concrete and a hoop stress in the steel. For CCFTs the effect occurs early enough

to enhance the strength of the concrete. For RCFTs no strength enhancement is observed in part due to the resultant bulging of the faces of the tube due to the outward pressure from the concrete, but the confinement has a beneficial effect on the ductility of the concrete.

Upon further loading, local buckling will occur in the steel tube. Because of the presence of the concrete core, the steel tube only has the ability to buckle outward. This is in contrast to hollow tubular members that may also buckle inward, this is a higher mode of buckling that both delays the onset of local buckling and increases the compressive capacity (Bradford et al. 2002).

This section describes the fiber section model that reflects this behavior and is used in conjunction with the mixed beam finite element to model CFT beam-columns. The fiber section includes two different uniaxial materials for CCFT members (representing the steel tube and the concrete core) and three for RCFT members (representing the flat region of the steel tube, the corner region of the steel tube, and the concrete core). An example discretization is shown in Figure 3.9.

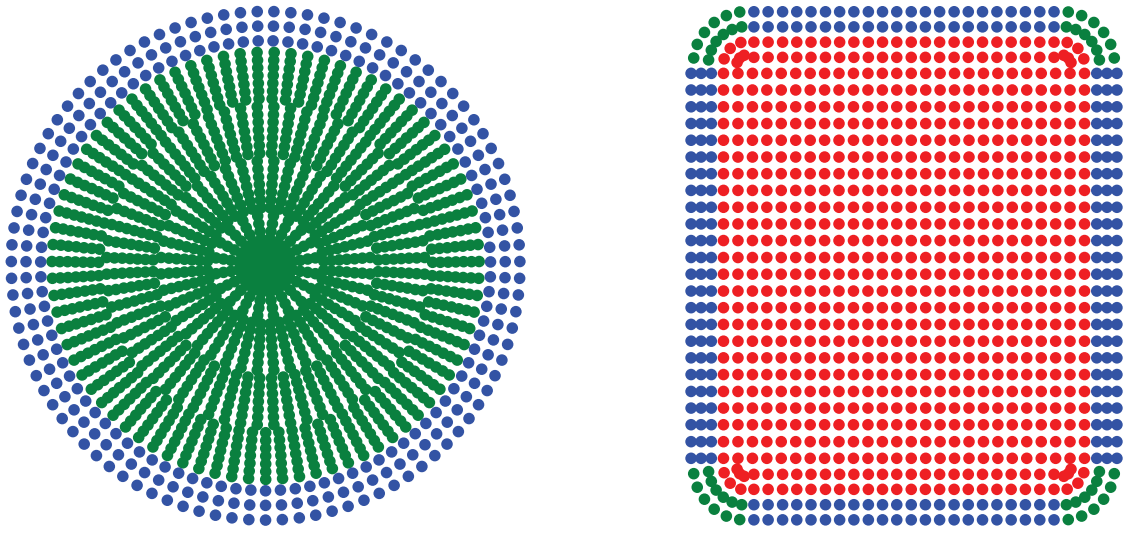

(a) CCFT (b) RCFT

Figure 3.9. Example Fiber Discretization for CFT Sections

3.5.1 "Proposed for Behavior" Model

For concrete-filled steel tubes, the parameters of the constitutive relations outlined earlier are given in Table 3.2 and Table 3.3 based on prior studies (Tort and Hajjar 2010a; Denavit and Hajjar 2012). Additional parameters specific to shape of the steel tube are presented below.

Circular Concrete-Filled Steel Tubes

The confining pressure, f_l, for the concrete core of CCFT members is computed by Equation 3.37 assuming a hoop stress equal to $\alpha_\theta F_y$, where α_θ is given in Equation 3.38 (Denavit and Hajjar 2012).

$$f_l = \frac{2\alpha_\theta F_y}{D/t - 2} \tag{3.37}$$

$$\alpha_\theta = 0.138 - 0.00174\frac{D}{t} \geq 0 \tag{3.38}$$

Due to lateral expansion of the concrete core the steel tube is under a state of biaxial stress. To account for this, the initial yield range is adjusted based on the level of hoop stress assumed to the present in the steel tube. The size of the initial yield surface is computed using Equation 3.24, noting the initial plastic strain. The size is then multiplied by the results of Equations 3.39 and 3.40 for the positive stress and negative stress yield limits respectively to obtain the size of the initial yield surface accounting for the biaxial state of stress. This adjustment is made only for the initial yield surface.

$$\alpha_{z,\text{positive}} = 0.5\left(\alpha_\theta + \sqrt{4 - 3\alpha_\theta^2}\right) \tag{3.39}$$

$$\alpha_{z,\text{negative}} = 0.5\left(\alpha_\theta - \sqrt{4 - 3\alpha_\theta^2}\right) \tag{3.40}$$

Table 3.2. Comparison of CFT Models

Parameter	Symbol	"Proposed for Behavior" Model	"Proposed for Design" Model
Initial Stiffness	E_c	Equation 3.8	same
Concrete Compressive Backbone Curve		Tsai's Equation, Equation 3.5	Popovics' Equation, Equation 3.4
Compressive Peak Stress	f'_{cc}	f'_c (RCFT) Equation 3.10 (CCFT)	same
Compressive Strain at Peak Stress	ε'_{cc}	Equation 3.9 (RCFT) Equation 3.12 (CCFT)	same
Compressive Post-Peak Shape Factor	r_n $r_{n,pre}$ $r_{n,post}$	Equation 3.14 Equation 3.13 Table 3.3	n/a
Concrete Tensile Backbone Curve		Tsai's Equation, Equation 3.5	none
Tensile Peak Stress	f_t	Equation 3.15	n/a
Tensile Strain at Peak Stress	ε_t	Equation 3.16	n/a
Tensile Post-Peak Shape Factor	r_p	Equation 3.17	n/a
Steel Model		Shen et al. (1995), Section 3.4.1	Abdel-Rahman and Sivakumaran (1997), Section 3.4.2

Rectangular Concrete-Filled Steel Tubes

There is a noted difference in the material properties between the corner region and the flat region of rectangular tubes. In the model this is accounted for with different values for the initial plastic strain (Table 3.3), yield stress (Equation 3.40), and ultimate stress (Equation 3.40) (Tort and Hajjar 2007).

$$F_{y,corner} = 1.09F_{y,flat} \tag{3.40}$$

$$F_{u,corner} = 1.03F_{u,flat} \geq F_{y,corner} \tag{3.40}$$

Table 3.3. Parameters for the Proposed for Behavior CFT Model

Parameter	Symbol	CCFT	RCFT
Initial Plastic Strain	$\bar{\varepsilon}_o^p$	0.0006	0.0006 (corner region) 0.0004 (flat region)
Strain Hardening Modulus	E_{sh}	$E_{sh} = \frac{E_s}{100}$	$E_{sh} = \frac{E_s}{100}$
Strain at Ultimate Stress	ε_u	$\varepsilon_u = 120\frac{F_y}{E_s}$	$\varepsilon_u = 120\frac{F_y}{E_s}$
Tube Slenderness Parameter	R	$R = \frac{D}{t}\frac{F_y}{E_s}$	$R = \frac{H}{t}\frac{F_y}{E_s}$
Strain at Local Buckling	ε_{lb}	$\varepsilon_{lb} = -0.2139R^{-1.413}\frac{F_y}{E_s}$	$\varepsilon_{lb} = -3.14\left(\frac{H}{t}\sqrt{\frac{F_y}{E_s}}\right)^{-1.48}\frac{F_y}{E_s}$
Local Buckling Softening Slope	K_{slb}	$K_{slb} = -\frac{E_s}{30}$	$K_{slb} = 3.22(0.08 - R)E_s \leq -\frac{E_s}{30}$
Local Buckling Ultimate Residual Stress	F_{ulb}	$F_{ulb} = \frac{0.17}{R}F_{lb} \leq F_{lb}$	$F_{ulb} = 1 + 7.31(0.08 - R)F_y \leq F_y$
Degradation of Plastic Modulus	γ_{E^p}	$\gamma_{E^p} = \left(1 - 10R\sqrt{\frac{W^p}{F_y}}\right) \geq 0.05$	$\gamma_{E^p} = \left(1 - 20R\sqrt{\frac{W^p}{F_y}}\right) \geq 0.05$
Degradation of Size of the Elastic Zone	γ_κ	$\gamma_\kappa = \left(1 - 15R\sqrt{\frac{W^p}{F_y}}\right) \geq 0.05$	$\gamma_\kappa = \left(1 - 30R\sqrt{\frac{W^p}{F_y}}\right) \geq 0.05$
Concrete Compressive Post-Peak Shape Factor	$r_{n,post}$	$r = 0.4 + 0.016\frac{D}{t}\frac{f_c'}{F_y}$	$r = 1.7\frac{H}{t}\sqrt{\frac{F_y}{E_s}}\frac{f_c'}{F_y}$

3.5.2 "Proposed for Design" Model

The parameters of the constitutive relations for the "proposed for design" model are given in Table 3.2. This model differs from the "proposed for behavior" model in several key ways that make is more suitable for studies aimed at developing design recommendations:

- Popovics' equation is used lieu of Tsai's equation for the concrete backbone curve, eliminating the need for the post-peak shape factor
- The tensile strength of concrete is neglected
- The Abdel-Rahman and Sivakumaran (1997) steel model is used in lieu of the Shen et al. (1995) steel model.

3.5.3 Plastic Hinge Length

In order to limit the ill effects of localization, the mesh density should be selected such that the integration weight associated with sections in critical (highest moment) locations should be representative of the plastic hinge length. An estimate of the plastic hinge length can be obtained by examining a prototypical cantilever beam-column (Figure 3.10a). The plastic hinge length may be approximated by Equation 3.41 normalized by the length from the point of maximum moment to the point of zero moment, L_i.

$$\frac{L_p}{L_i} = 1 - \frac{M_y}{M_u} \tag{3.41}$$

This expression requires values for the yield moment, M_y, and the ultimate moment, M_u. The ultimate moment has a relatively straightforward definition and can be obtained by performing a cross-sectional moment-curvature analysis and identifying the peak moment (Figure 3.10b). The yield moment, however, does not have an obvious definition, owing to the gradual transition to plasticity seen in the moment-curvature response. Prior studies have used different definitions to identify the yield moment. Elghazouli and Elnashai (1993) performed this type of study on partially encased composite columns and identified the yield moment as the moment at which the yield strain was reached in both the tensile and compressive extreme fibers. Bae and Bayrak (2008) performed this type of study on reinforced concrete columns and identified the yield moment as the moment at which the yield strain was reached in the compressive steel reinforcement.

In this study, the yield moment is defined directly from the moment-curvature response using an offset methodology analogous to that used to define the offset yield stress from tensile coupon tests that do not exhibit a clear yield point. The yield moment is defined as the moment that corresponds to the point of intersection of the moment-curvature response and a line parallel to the initially linear portion of the response. The slope of the parallel line is taken as the secant stiffness from zero moment to 45% of the ultimate moment. The offset is the distance between the origin of the moment-curvature response and the point of intersection of the parallel line and the zero moment axis. The offset is expressed in terms of curvature and is taken as $0.001/D$, where D is the overall section depth. This value was selected based on inspection of results from typical composite cross sections as the point at which the initiation of significant plastic deformations typically occurred.

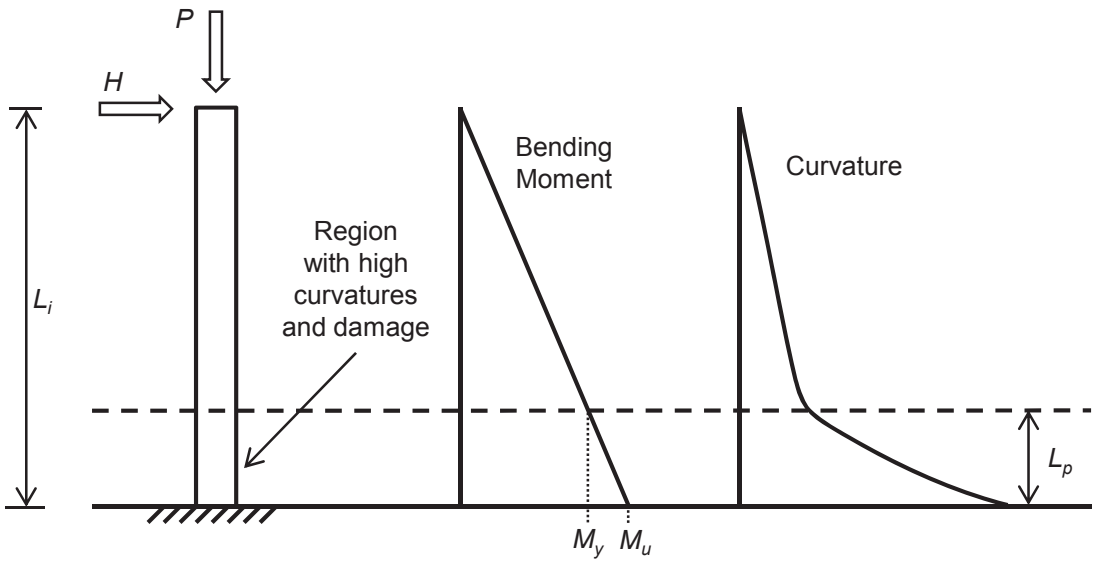

(a) Prototypical Beam-Column

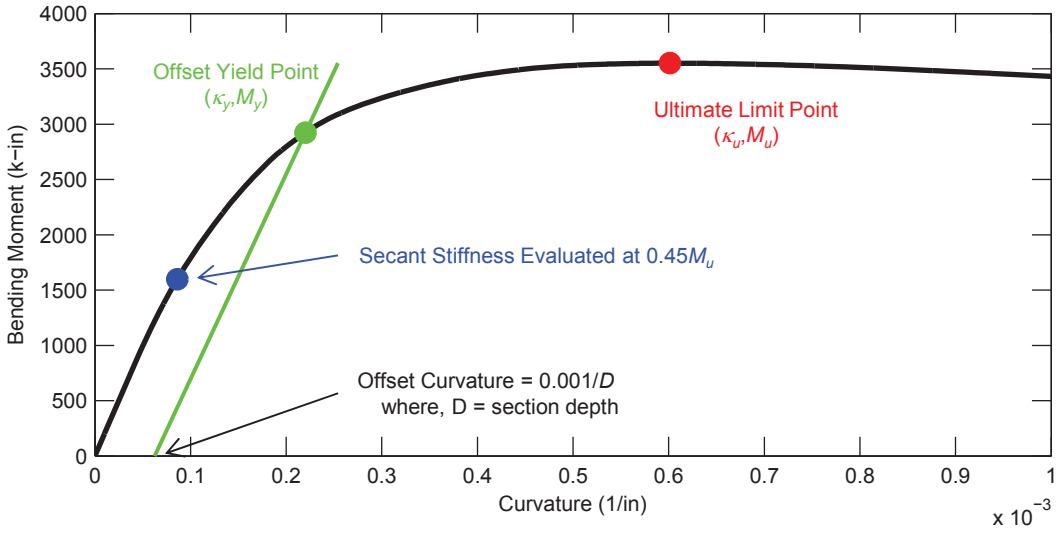

(b) Moment Curvature Results

Figure 3.10. Schematic of Methodology to Evaluate the Plastic Hinge Length

The plastic hinge length obtained from this methodology will vary with the given cross section as well as the applied axial load. Thus, in this work a parametric study was performed to document the variation of the plastic hinge length with material, geometric, and loading properties then provide simple approximate expressions for the plastic hinge length. The parametric study employs the same cross sections as used in Chapter 6 for another study. Five circular (HSS 7.000×0.500, HSS 10.000×0.500, HSS 12.750×0.375, HSS 16.000×0.250, and HSS 24.000×0.125) and five rectangular (HSS 6×6×1/2, HSS 9×9×1/2, HSS 8×8×1/4, HSS 9×9×1/8, and HSS 14×14×1/8) HSS sections are selected to span the range of permissible steel ratios and three concrete strengths (f'_c = 4, 8, 16 ksi) are selected for a total of 30 CFT cross sections. Steel yield strengths were taken as typical nominal values (F_y = 42 ksi for CCFT and F_y = 46 ksi for RCFT). The plastic hinge length is determined using the "Proposed for Behavior"

model for each cross section and for compressive axial loads ranging from zero to 50% of the cross section capacity; results are shown in Figure 3.11. Variations in the plastic hinge length are seen with steel ratio, concrete strength and axial load. The greatest variations occur with axial load for the more concrete dominant sections.

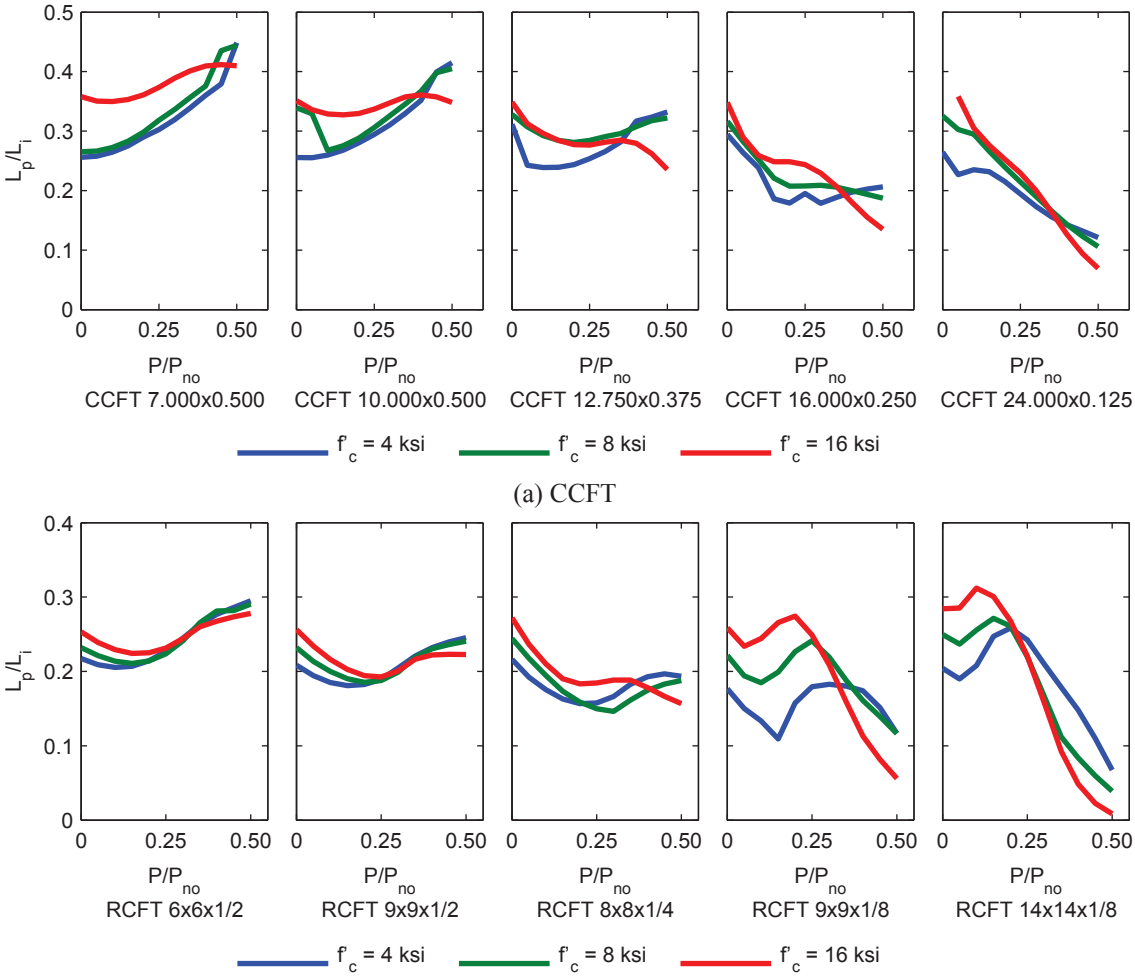

(a) CCFT

(b) RCFT

Figure 3.11. Plastic Hinge Length Results for CFT Sections

3.6 Steel Reinforced Concrete Beam-Columns

Several researchers have developed models specifically for use with SRC members (Mirza 1989; Sanz Picon 1992; Elnashai and Elghazouli 1993; El-Tawil and Deierlein 1999; Chen and Lin 2006). One defining feature among these models is the varying levels of concrete confinement assumed throughout the cross-section. For this model, five distinct regions are identified within the section (Figure 3.12a). Separate constitutive relations are defined for each of these regions; an example fiber discretization is shown in Figure 3.12b.

3.6.1 "Proposed for Behavior" Model

Three regions of concrete are defined based on the expected level of confinement pressure. The outermost concrete region of concrete, the cover concrete, is assumed to have zero confining pressure in either direction. Furthermore, it is allowed to spall. The critical strain at which the nonlinear stress-strain curve transitions to a linear degradation (Section 3.3.1) is given by Equation 3.42 (Mander et al. 1988).

$$x_{cr} = 2.0 \tag{3.42}$$

The concrete inside the lateral reinforcing bars is termed the medium confined concrete. The magnitude of the confining pressure provided by the lateral reinforcing bars is computed in two orthogonal directions with Equation 3.43.

$$f_{ly,medium} = K_e \rho_y F_{yr} \tag{3.43a}$$

$$f_{lz,medium} = K_e \rho_z F_{yr} \tag{3.43b}$$

where,

K_e = ratio of effectively confined cross sectional area to area of the core as defined by Mander et al. (1988)

ρ_y, ρ_z = volumetric ratios of the transverse reinforcing steel in either direction as defined by Mander et al. (1988)

F_{yr} = yield strength of the longitudinal reinforcement

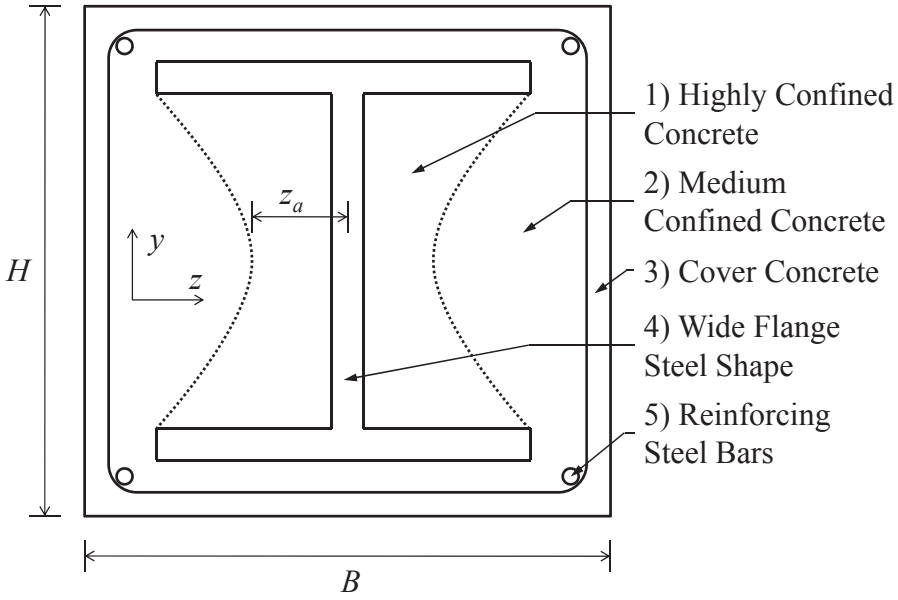

(a) Regions

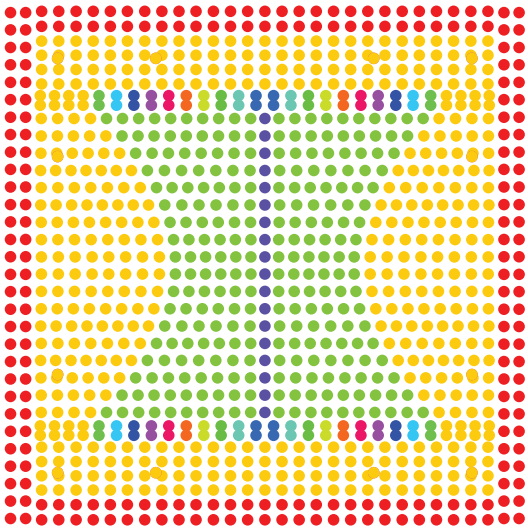

(b) Example Fiber Discretization

Figure 3.12. SRC Section

The concrete between the flanges is termed highly confined concrete. In this region, confining pressure is provided by both the lateral reinforcing bars and the steel shape. El-Tawil and Deierlein (1999) developed a mechanism model in which the confining pressure provided by the steel shape acts only in the y direction (defined in Figure 3.12a) and is computed considering the plastic moment capacity of the flange (Equation 3.44). The distance between the vertex of the parabola defining the boundary between the highly and medium confined concrete (Figure 3.12a) and the centerline of the steel section is described by Equation 3.45. This parabolic boundary is modeled explicitly with different constitutive relations on either side (as shown in Figure 3.12b). In contrast, the parabolic boundary between the cover and medium confined concrete is implicitly modeled, utilizing the factor K_e to provide average behavior. The difference in

handling these two boundaries exists to provide greater accuracy in modeling the boundary between the flanges while retaining the flexibility of different possible configurations of reinforcing steel.

$$f_{ly,high} = f_{ly,medium} + \frac{t_f^2 F_{ys}}{0.75\left(b_f - t_w\right)^2} \tag{3.44}$$

$$z_a = 0.50 b_f - 0.25\left(d - 2t_f\right) \geq 0.50 t_w \tag{3.45}$$

$$r_{n,post} = 0.75 \tag{3.46}$$

A comparison of the monotonic compressive response of the concrete in each of the three regions is shown in Figure 3.13.

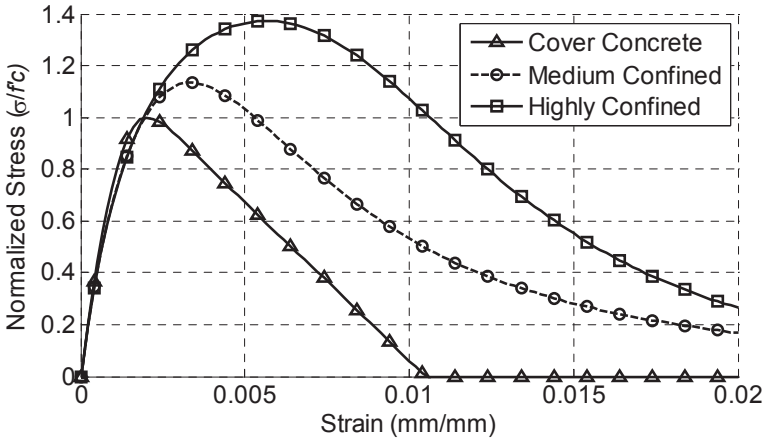

Figure 3.13. Concrete Constitutive Relations

The constitutive relation used for the wide flange steel shape and the reinforcing steel bars is based on the bounding-surface plasticity model of Shen et al. (1995) (Section 3.4.1). Residual stresses are defined as described in Section 0. The initial hardening modulus and strain at ultimate stress for the first plastic excursion are given by Equations 3.47 and 3.48 respectively, the same as described later in Section 3.7 for wide flange steel beams.

$$E_{sh} = \frac{E_s}{100} \tag{3.47}$$

$$\varepsilon_u = 120\frac{F_y}{E_s} \tag{3.48}$$

The confined concrete is assumed to prevent flange and web local buckling and thus, these effects have not been included. In contrast, the model by Elnashai and Elghazouli (1993) is for partially encased composite columns and includes flange local buckling since the concrete

only prevents inward buckling of the flange. For simplicity, the wide flange steel section is modeled with sharp corners (i.e., neglecting the fillets).

Buckling of the reinforcing steel bars is included in the model in the same manner as local buckling (described in Section 3.4.1). The softening slope, ultimate residual stress, and degradation parameters for the bar buckling model are as described in Equations 3.49 to 3.52, based on comparisons to a set of cyclic cantilever SRC column tests conducted by Juang and Hsu (2008). The experimental setup is shown in Figure 3.14, measured material and geometric properties for the specimens are given in Table 3.4, and results are shown in Figure 3.15. The parameters were adjusted until a good correspondence was seen for all specimens. Additionally, these tests were used to calibrate the bond-slip model described later in Section 3.9.

$$K_{lb} = -\frac{E_s}{100} \tag{3.49}$$

$$F_{ulb} = 0.2F_y \tag{3.50}$$

$$\gamma_{E^p} = \left(1 - 2.0\sqrt{\frac{W^p}{F_y}}\right) \geq 0.05 \tag{3.51}$$

$$\gamma_{\kappa} = \left(1 - 2.0\sqrt{\frac{W^p}{F_y}}\right) \geq 0.05 \tag{3.52}$$

Table 3.4. Material and Geometric Properties – Juang and Hsu 2008

Specimen	H (mm)	B (mm)	f'_c (MPa)	Steel Section	F_v (MPa)	Reinforcement Configuration	F_{vr} (MPa)	L (mm)	L/H
SRC100m	370	370	38.5	H200x100x5.5x8	312	2x-2y	529	2,320	6.3
SRC150m	370	370	38.5	H194x150x6x9	312	2x-2y	529	2,320	6.3
SRC200m	370	370	38.5	H200x200x8x12	312	2x-2y	529	2,320	6.3
SRC100c	370	370	38.5	H200x100x5.5x8	312	2x-2y	529	2,320	6.3
SRC150c	370	370	38.5	H194x150x6x9	312	2x-2y	529	2,320	6.3
SRC200c	370	370	38.5	H200x200x8x12	312	2x-2y	529	2,320	6.3

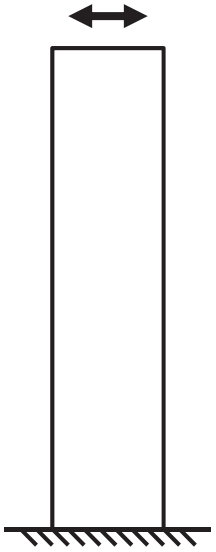

Figure 3.14. Experiment Setup – Juang and Hsu 2008

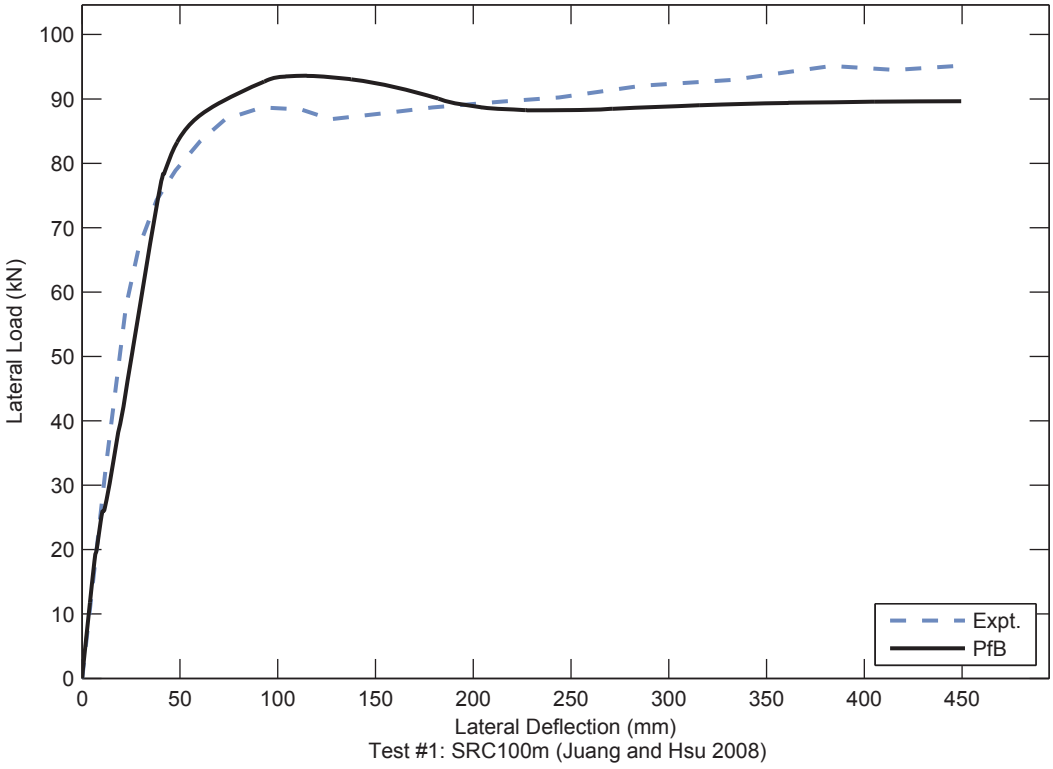

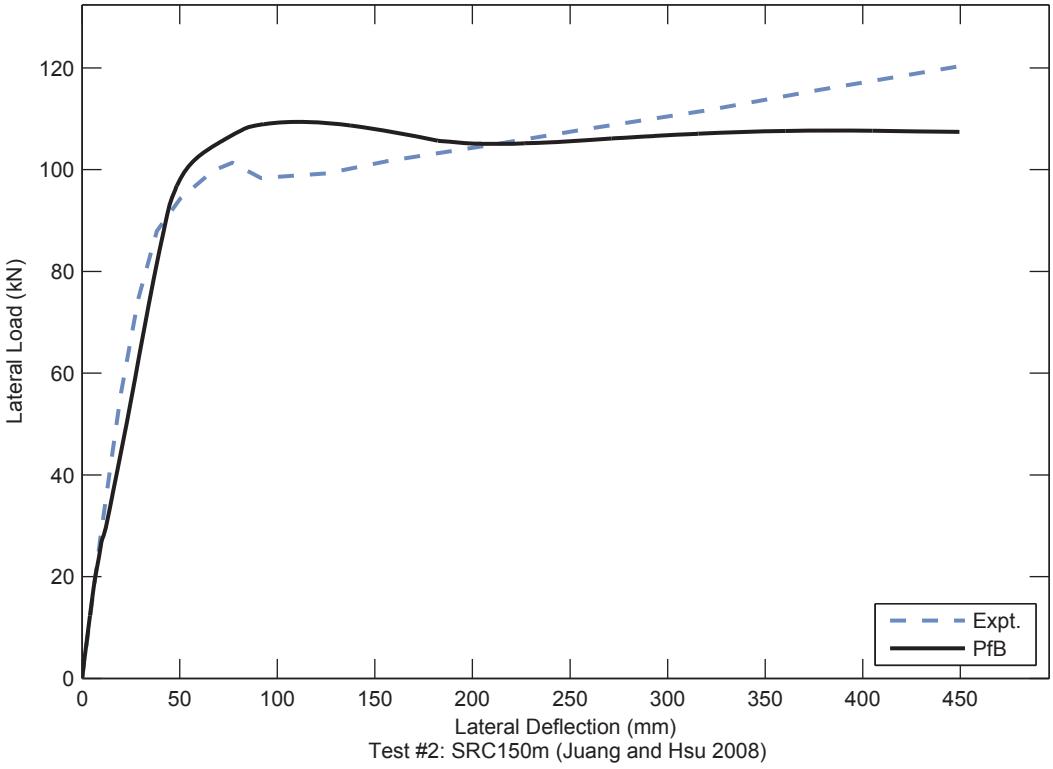

Figure 3.15. Cyclic SRC Results – Juang and Hsu 2008

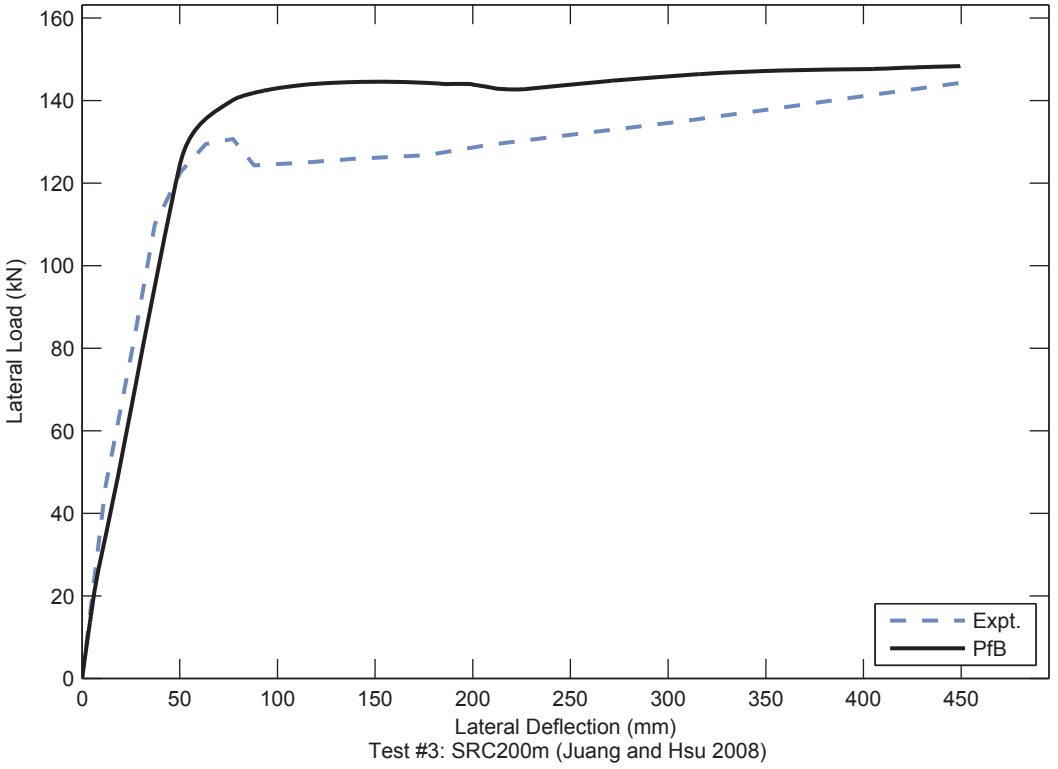

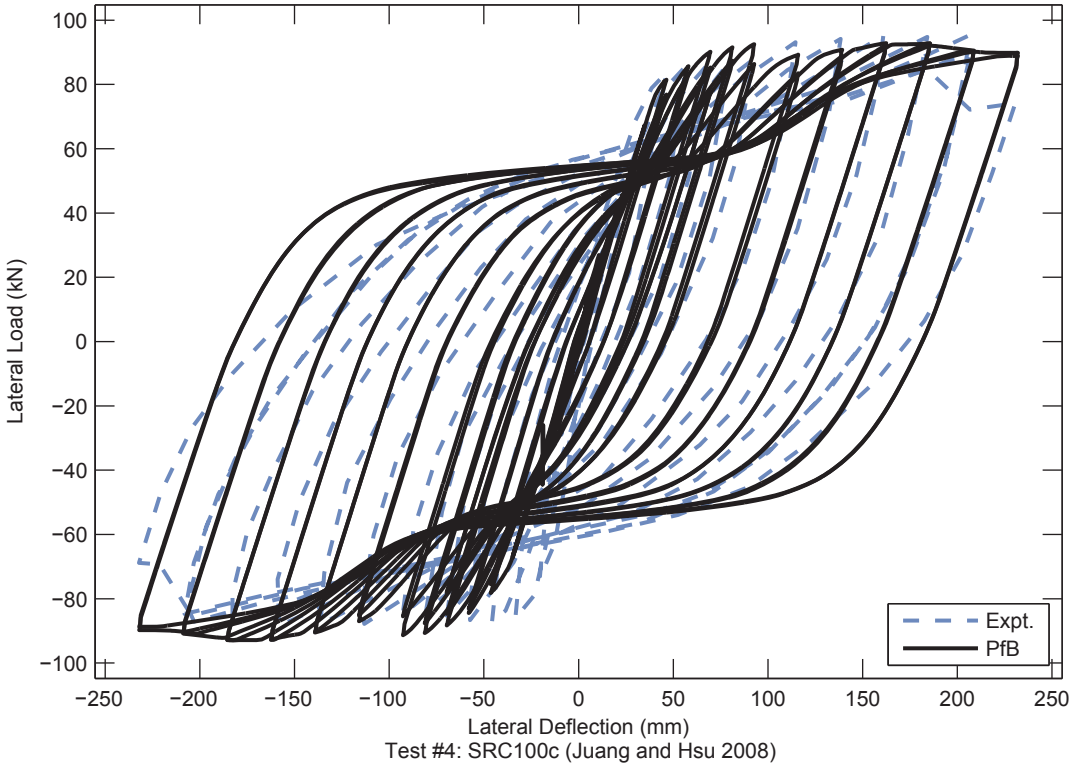

Figure 3.15. Cyclic SRC Results – Juang and Hsu 2008 (Continued)

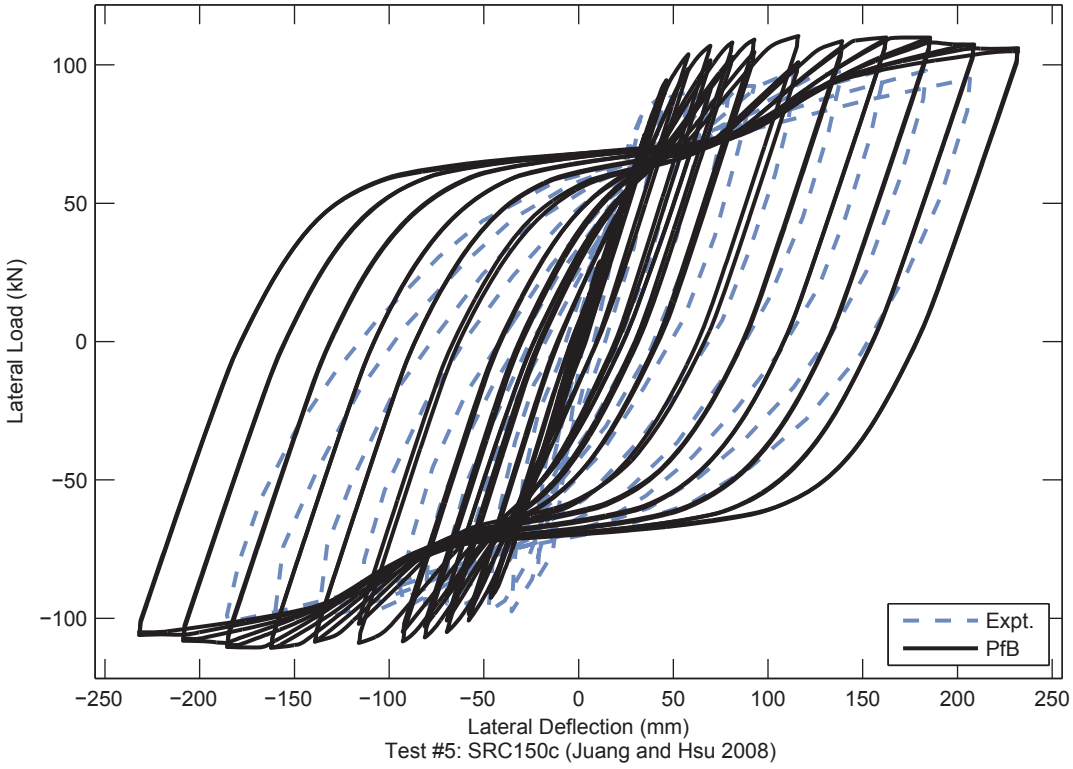

Test #5: SRC150c (Juang and Hsu 2008)

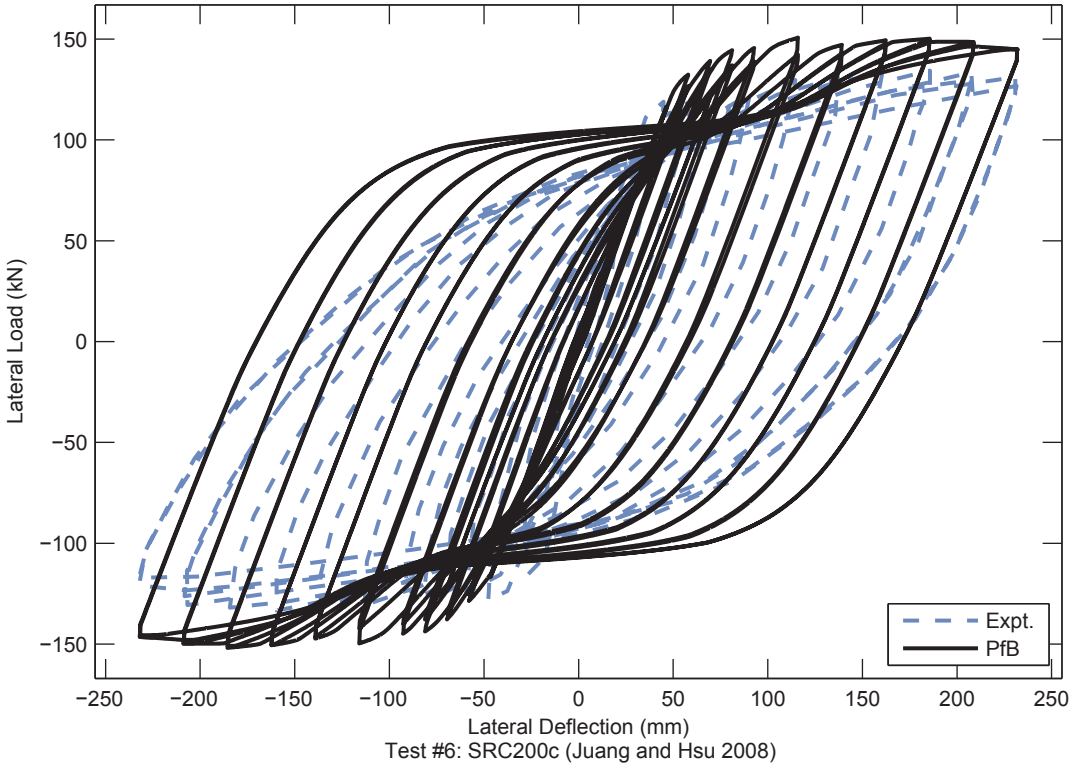

Test #6: SRC200c (Juang and Hsu 2008)

Figure 3.15. Cyclic SRC Results – Juang and Hsu 2008 (Continued)

3.6.2 "Proposed for Design" Model

The parameters of the constitutive relations for the "proposed for design" model are given in Table 3.5. This model differs from the "proposed for behavior" model in several key ways that make is more suitable for studies aimed at developing design recommendations:

- Popovics' equation is used lieu of Tsai's equation for the concrete backbone curve, eliminating the need for the post-peak shape factor
- The tensile strength of concrete is neglected
- An elastic-perfectly plastic steel model is used in lieu of the Shen et al. (1995) steel model for both the steel section and reinforcing bars.

Table 3.5. Comparison of SRC Models

Parameter	Symbol	"Proposed for Behavior" Model	"Proposed for Design" Model
Initial Stiffness	E_c	Equation 3.8	same
Concrete Compressive Backbone Curve		Tsai's Equation, Equation 3.5	Popovics' Equation, Equation 3.4
Compressive Peak Stress	f'_{cc}	f'_c (Cover) Equation 3.11 (Confined)	same
Compressive Strain at Peak Stress	ε'_{cc}	Equation 3.9 (Cover) Equation 3.12 (Confined)	same
Compressive Post-Peak Shape Factor	r_n $r_{n,pre}$ $r_{n,post}$	Equation 3.14 Equation 3.13 Equation 3.46	n/a
Concrete Tensile Backbone Curve		Tsai's Equation, Equation 3.5	none
Tensile Peak Stress	f_t	Equation 3.15	n/a
Tensile Strain at Peak Stress	ε_t	Equation 3.16	n/a
Tensile Post-Peak Shape Factor	r_p	Equation 3.17	n/a
Steel Model		Shen et al. (1995), Section 3.4.1	Elastic-Perfectly Plastic, Section 3.4.3

3.6.3 Plastic Hinge Length

A parametric study to determine the plastic hinge length of SRC columns was performed as described in Section 3.5.3 for CFT columns. The selected sections all had outside dimensions of 28 in. × 28 in.. Four wide-flange shapes (W14×311, W14×233, W12×120, W8×31), 3 reinforcing configurations (20 #11, 12 #10, 4#8), 3 concrete strengths (f'_c = 4, 8, 16 ksi) were used for a total of 36 sections each for strong and weak axis bending. Results are shown in Figure 3.16. For strong axis bending the normalized plastic hinge length ranges from 0.05 to 0.35. For weak axis bending the normalized plastic hinge length is typically higher, as expected since first yield of wide flange members occurs relatively earlier in weak axis bending, and ranges from 0.10 to 0.40.

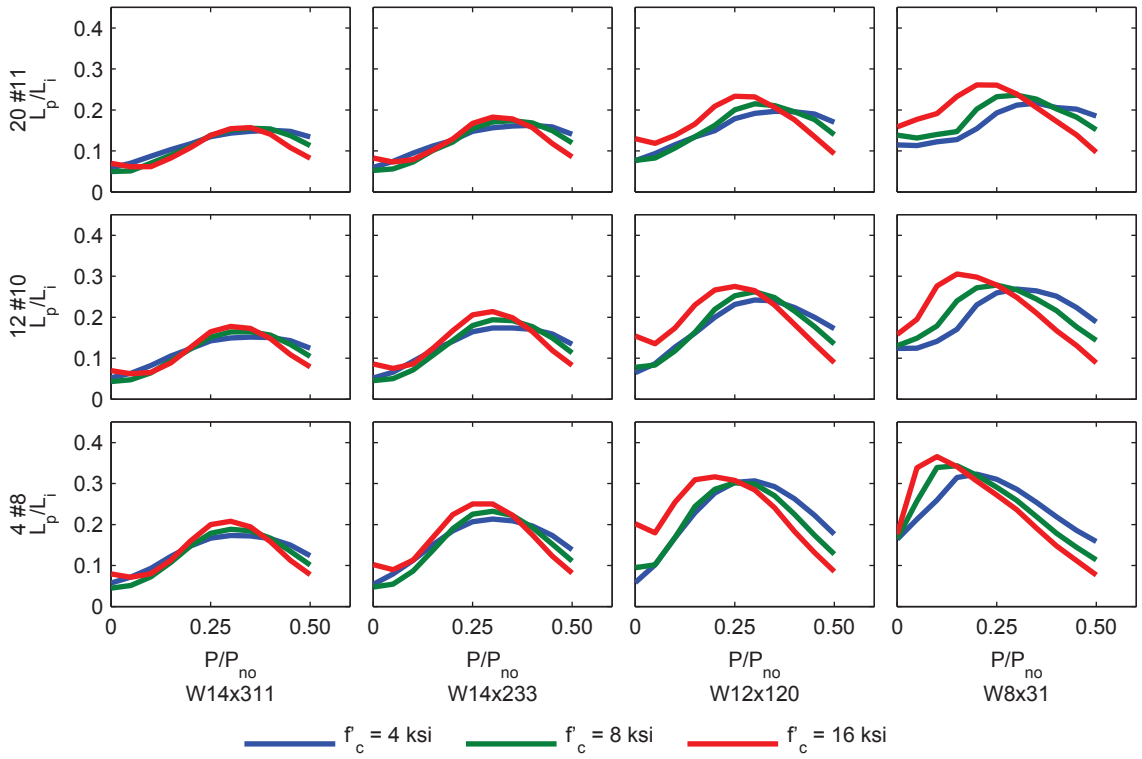

(a) Strong Axis Bending

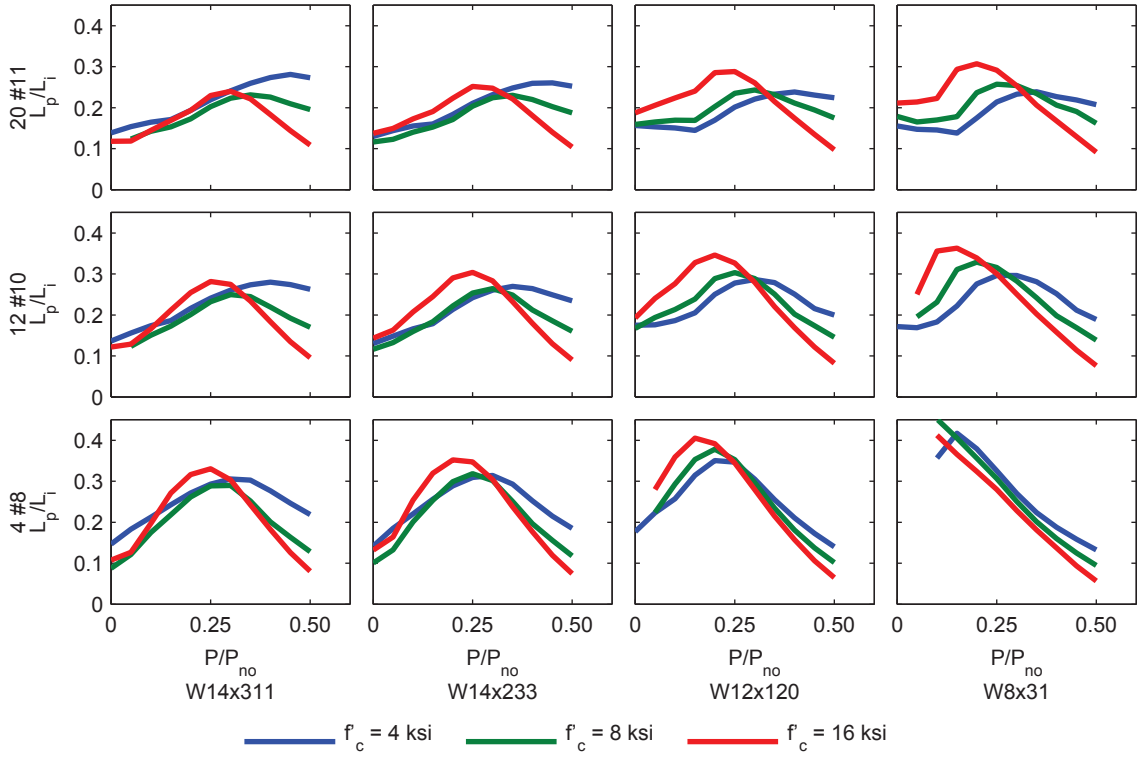

(b) Weak Axis Bending

Figure 3.16. Plastic Hinge Length Results for SRC Sections

3.7 Wide Flange Steel Beams

In order to analyze entire composite frames, especially seismically designed moment frames where inelasticity is expected to be primarily limited to the beams, accurate steel wide flange beam models are necessary. This section describes the fiber section model used in conjunction with the mixed beam finite element to model wide flange steel beams.

The uniaxial constitutive relation for the wide flange steel shape is based on the bounding-surface plasticity model of Shen et al. (1995) (Section 3.4.1). Residual stresses are defined as described in Section 0. The initial hardening modulus and strain at ultimate stress for the first plastic excursion are given by Equations 3.53 and 3.54 respectively. The yield plateau is neglected and the initial hardening modulus is taken as lower than typical experimentally measured values from coupon tests so that the computational results better match the experimental results at the member level. The strain at ultimate stress is taken as a standard value from the literature (Gioncu and Mazzolani 2001).

$$E_{sh} = \frac{E_s}{100} \tag{3.53}$$

$$\varepsilon_u = 120\frac{F_y}{E_s} \tag{3.54}$$

In wide flange steel beams, the onset of local buckling of the web or flange will cause degradation of the moment response. As with local buckling of the steel tube in CFTs, this response can be modeled explicitly in an analysis with continuum or shell elements. For beam formulations, it can be captured implicitly by modifying the uniaxial constitutive relation. The proposed modifications are as described in Section 3.4.1 with specific parameters (e.g., strain at local buckling, degradation slope) derived from experimental studies as described below. Additionally, since local buckling is the primary phenomenon causing softening at the section level, discussion the plastic hinge length will be included here.

Three point bending tests on steel beams have been performed by several researchers. Details of selected tests from the literature (Sawyer 1961; Lukey and Adams 1969; Smith and Adams 1968; Green et al. 2002) are shown in Table 3.6. The length of the plastic region can be related to the maximum moment obtained in these tests by Equation 3.55, which assumes a linear moment gradient.

$$\frac{L_p}{L_i} = 1 - \frac{M_p}{M_{\max}} \tag{3.55}$$

where,

L_p = plastic hinge length
L_i = distance from the point of maximum moment to the point of zero moment
M_p = plastic moment
M_{max} = maximum moment

An empirical expression for the plastic hinge length is derived by linear regression to the experimental data. The result of this regression is Equation 3.56 (coefficient of determination = 0.59).

$$\frac{L_p}{L_i} = 0.405 - 0.0033\frac{h}{t_w} - 0.0268\frac{b_f}{2t_f} + 0.184\left(\frac{F_u}{F_y} - 1\right) \tag{3.56}$$

Lay (1965) proposed expression for the wavelength for flange local buckling (Equation 3.57). The experimental data, the proposed expression, the expression by Lay (1965) are compared in Figure 3.17. Significant scatter is noted for both expressions. The mean absolute error in L_p/L_i for the proposed expression is 0.046 compared to 0.061 for the expression by Lay (1965), likely due the inclusion of the steel ultimate strength term.

$$L_p = 0.71 b_f \frac{t_f}{t_w}\left(\frac{h t_w}{t_f b_f}\right)^{1/4} \tag{3.57}$$

The plastic hinge length is related to the strain at local buckling by Equation 3.58, which was developed based on the idealized response of a beam under linear moment gradient (Kemp and Dekker 1991) where E_h is the steel hardening slope.

$$\frac{\varepsilon_{lb}}{\varepsilon_y} = 1 + \frac{E_s}{E_h}\frac{L_p}{L_i - L_p} \tag{3.58}$$

The softening slope, ultimate residual stress, and degradation parameters for the local buckling model are as described in Equations 3.59 to 3.62, based on comparisons to a set of cyclic cantilever wide flange beam tests conducted by Tsai and Popov (1988). The experimental setup is shown in Figure 3.18, measured material and geometric properties for the specimens are given in Table 3.7, and results are shown in Figure 3.19. The parameters were adjusted until a good correspondence was seen for all specimens.

$$K_{lb} = -\frac{E_s}{200} \tag{3.59}$$

$$F_{ulb} = 0.2 F_y \tag{3.60}$$

$$\gamma_{E^p} = \left(1 - 2.0\sqrt{\frac{W^p}{F_y}}\right) \geq 0.05 \tag{3.61}$$

$$\gamma_{\kappa} = \left(1 - 2.0\sqrt{\frac{W^p}{F_y}}\right) \geq 0.05 \tag{3.62}$$

Table 3.6. Three Point Bending Experiments on Wide Flange Steel Beams

Author	Year	Specimen	d	t_w	b_f	t_f	F_{yf}	F_{uf}	F_{yw}	F_{uw}	L_i	M_p	M_{max}
			in	*in*	*in*	*in*	*ksi*	*ksi*	*ksi*	*ksi*	*in*	*k-ft*	*k-ft*
Saw yer	1961	4	8.11	0.238	5.32	0.401	41.0	67.3	46.0	67.8	22.4	68.4	93.8
Saw yer	1961	5	8.11	0.238	5.32	0.401	41.0	67.3	46.0	67.8	30.3	68.4	91.2
Saw yer	1961	6	8.11	0.238	5.32	0.401	41.0	67.3	46.0	67.8	42.1	68.4	87.8
Saw yer	1961	7	5.05	0.237	4.99	0.357	41.5	66.3	56.5	71.8	21.2	34.2	51.5
Saw yer	1961	8	5.05	0.237	4.99	0.357	41.5	66.3	56.5	71.8	28.7	34.2	49.4
Saw yer	1961	9	5.05	0.237	4.99	0.357	41.5	66.3	56.5	71.8	40.0	34.2	49.0
Saw yer	1961	10	10.24	0.253	4.00	0.374	38.0	58.1	40.4	59.4	17.1	65.9	86.3
Saw yer	1961	11	10.24	0.253	4.00	0.374	38.0	58.1	40.4	59.4	23.7	65.9	90.7
Saw yer	1961	12	10.24	0.253	4.00	0.374	38.0	58.1	40.4	59.4	32.3	65.9	85.8
Saw yer	1961	13	12.08	0.284	6.56	0.454	38.8	64.1	47.3	67.0	27.7	146.8	183.1
Saw yer	1961	14	12.08	0.284	6.56	0.454	38.8	64.1	47.3	67.0	37.5	146.8	183.8
Saw yer	1961	15	12.08	0.284	6.56	0.454	38.8	64.1	47.3	67.0	52.2	146.8	187.2
Saw yer	1961	16	11.94	0.213	4.05	0.229	44.1	60.1	54.3	65.0	17.0	71.7	75.9
Saw yer	1961	17	11.94	0.213	4.05	0.229	44.1	60.1	54.3	65.0	22.8	71.7	71.8
Saw yer	1961	18	11.94	0.213	4.05	0.229	44.1	60.1	54.3	65.0	31.7	71.7	72.7
Saw yer	1961	19	8.11	0.292	8.05	0.431	41.2	67.5	44.6	68.0	33.9	105.7	126.7
Saw yer	1961	20	8.11	0.292	8.05	0.431	41.2	67.5	44.6	68.0	45.9	105.7	120.5
Saw yer	1961	21	8.11	0.292	8.05	0.431	41.2	67.5	44.6	68.0	64.0	105.7	113.8
Lukey & Adams	1969	A-1	9.86	0.301	8.01	0.425	41.3	69.3	44.8	69.8	68.5	133.3	183.8
Lukey & Adams	1969	A-2	9.86	0.301	6.93	0.425	41.3	69.3	44.8	69.8	58.0	118.4	167.4
Lukey & Adams	1969	B-1	7.88	0.175	4.04	0.208	54.1	71.1	57.5	77.2	30.6	40.7	45.8
Lukey & Adams	1969	B-2	7.88	0.175	2.91	0.208	54.1	71.1	57.5	77.2	20.4	32.6	37.9
Lukey & Adams	1969	B-3	7.88	0.175	3.39	0.208	54.1	71.1	57.5	77.2	24.7	36.1	41.0
Lukey & Adams	1969	B-4	7.88	0.175	3.70	0.208	54.1	71.1	57.5	77.2	27.5	38.3	40.9
Lukey & Adams	1969	B-5	7.88	0.175	3.81	0.208	54.1	71.1	57.5	77.2	28.5	39.1	41.4
Lukey & Adams	1969	C-1	9.86	0.181	4.01	0.207	54.1	74.6	51.1	70.2	27.0	53.3	59.6
Lukey & Adams	1969	C-2	9.86	0.181	2.90	0.207	54.1	74.6	51.1	70.2	18.9	43.3	54.3
Lukey & Adams	1969	C-3	9.86	0.181	3.38	0.207	54.1	74.6	51.1	70.2	23.0	47.6	55.7
Lukey & Adams	1969	C-4	9.86	0.181	3.68	0.207	54.1	74.6	51.1	70.2	25.5	50.3	56.6
Lukey & Adams	1969	C-5	9.86	0.181	3.54	0.207	54.1	74.6	51.1	70.2	24.4	49.1	56.0
Smith & Adams	1968	D-1	7.94	0.182	2.65	0.190	41.1	61.5	53.6	66.7	34.8	25.0	27.4
Smith & Adams	1968	D-2	7.94	0.182	2.66	0.189	42.0	62.2	54.6	68.3	51.4	25.5	27.5
Smith & Adams	1968	D-3	7.94	0.182	2.66	0.191	43.7	62.8	54.1	67.7	52.1	26.0	25.6
Smith & Adams	1968	D-4	7.94	0.185	2.66	0.193	40.7	60.5	55.5	68.3	73.0	25.7	27.0
Smith & Adams	1968	D-5	7.94	0.185	2.66	0.192	40.7	60.5	55.5	68.3	44.7	25.6	29.1
Smith & Adams	1968	D-6	7.93	0.183	2.64	0.188	44.3	64.1	55.1	68.7	17.4	26.2	34.3
Smith & Adams	1968	E-1	7.94	0.189	3.46	0.192	43.7	62.8	54.1	67.7	48.8	30.9	38.0
Smith & Adams	1968	E-2	7.93	0.182	3.46	0.189	41.1	61.5	53.6	66.7	73.2	28.9	31.5
Smith & Adams	1968	E-3	7.93	0.182	3.46	0.189	40.8	60.2	53.1	65.7	73.2	28.7	30.0
Smith & Adams	1968	E-4	7.94	0.182	3.46	0.188	40.8	60.2	53.1	65.7	102.5	28.7	31.1
Smith & Adams	1968	E-5	7.93	0.182	3.46	0.188	42.0	62.2	54.6	68.3	62.8	29.4	31.0
Smith & Adams	1968	E-6	7.93	0.183	3.46	0.189	44.3	64.1	55.1	68.7	24.4	30.7	36.9
Green, Sause, & Ricles	2002	3	12.00	0.390	6.00	0.519	81.4	90.9	87.8	94.1	54.0	328.4	386.9
Green, Sause, & Ricles	2002	4	20.89	0.388	5.99	0.519	88.0	100.1	88.8	100.2	54.0	747.8	797.2
Green, Sause, & Ricles	2002	4A	20.98	0.387	6.00	0.516	88.0	100.1	88.8	100.2	54.0	749.4	813.1
Green, Sause, & Ricles	2002	5	20.96	0.386	6.00	0.512	88.0	100.1	88.8	100.2	54.0	744.3	886.5
Green, Sause, & Ricles	2002	6	11.90	0.406	8.99	0.511	88.0	100.1	88.8	100.2	54.0	472.3	535.6

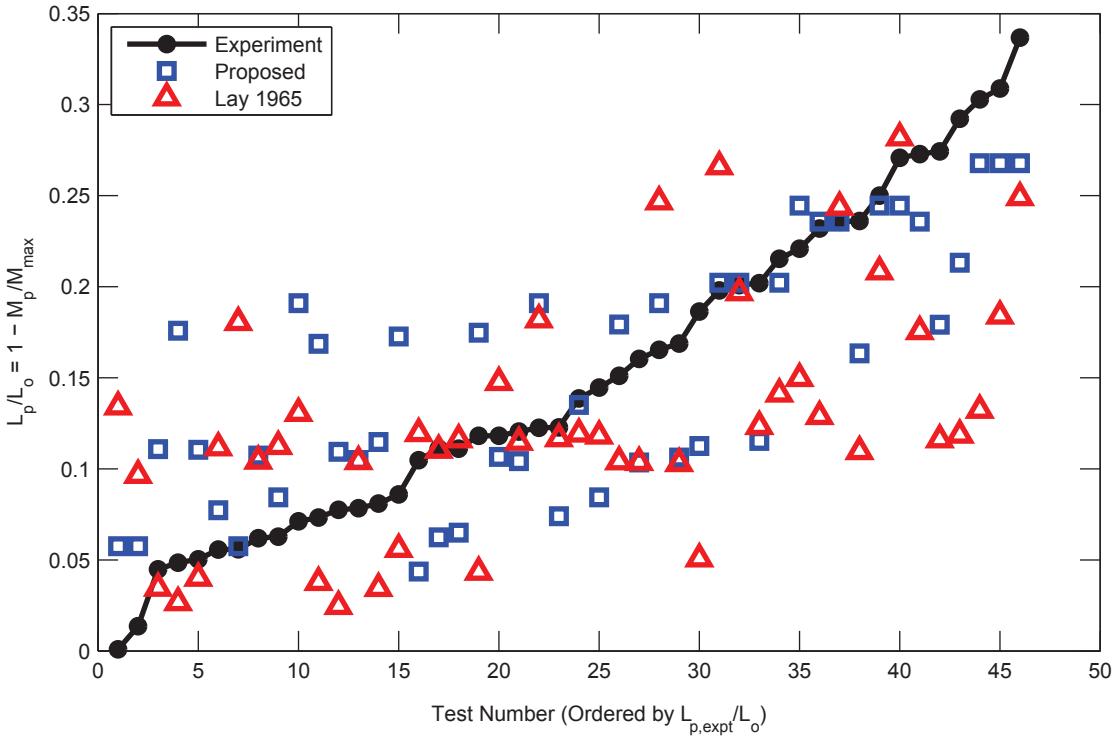

Figure 3.17. Comparison of Plastic Hinge Length for Wide Flange Steel Beams

Table 3.7. Material and Geometric Properties – Tsai and Popov 1988

Test #	Specimen	d *(mm)*	b_f *(mm)*	t_f *(mm)*	t_w *(mm)*	F_y *(MPa)*	L *(mm)*
1	1	455	153	13.3	8.0	263	1,557
2	8	526	165	11.4	8.9	333	1,494
3	9	460	154	15.4	9.1	256	1,598
4	10R	455	153	13.3	8.0	310	1,438
5	11	526	165	11.4	8.9	256	1,605
6	12	526	165	11.4	8.9	317	1,572

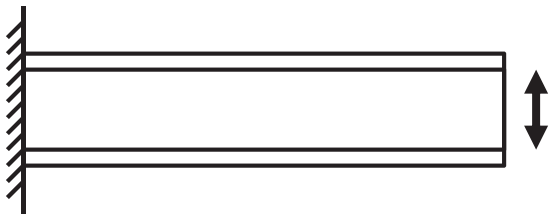

Figure 3.18. Experiment Setup – Tsai and Popov 1988

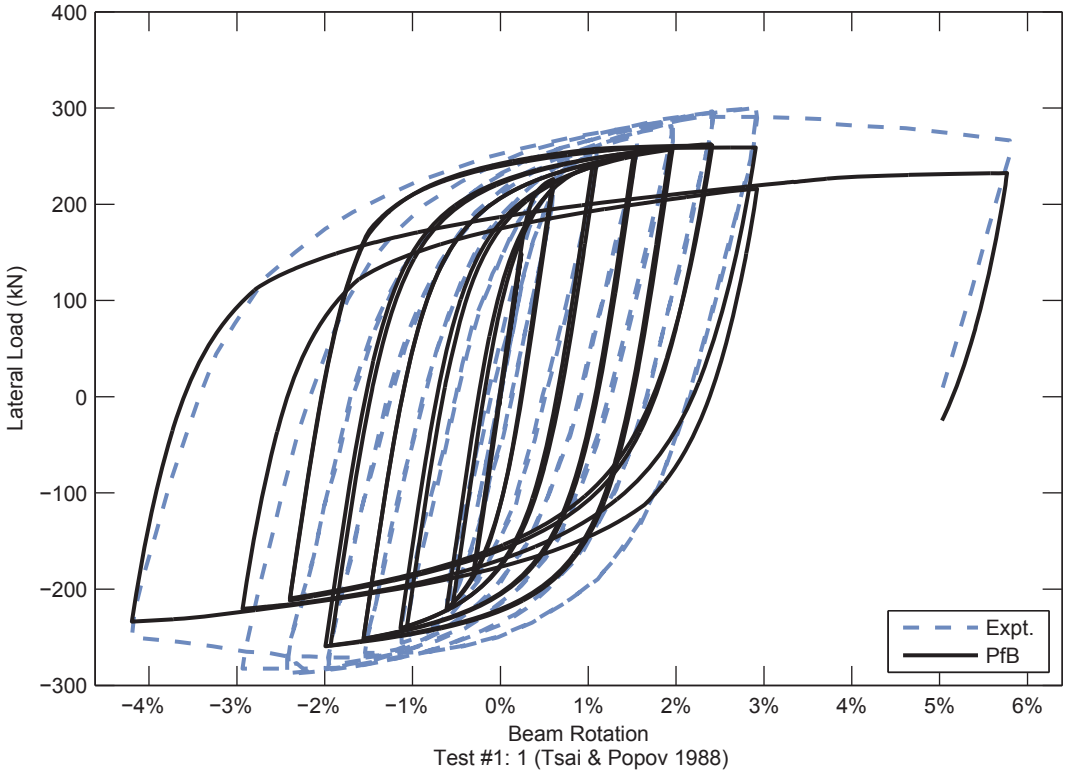

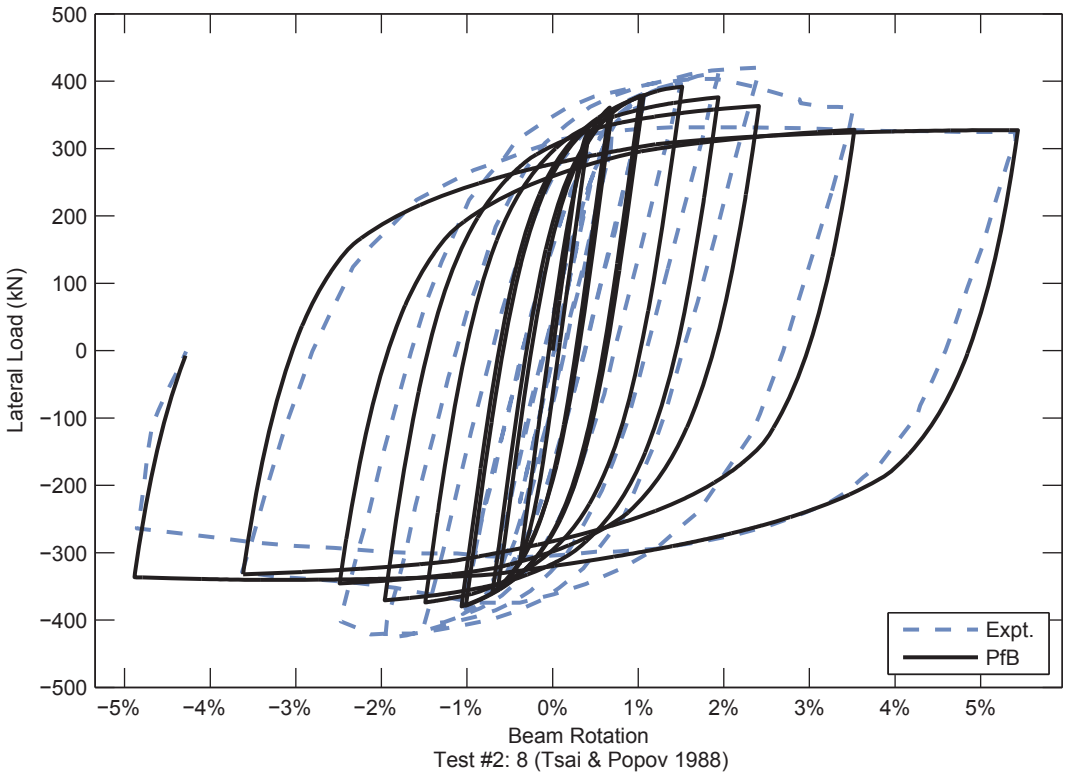

Figure 3.19. Cyclic WF Results – Tsai and Popov 1988

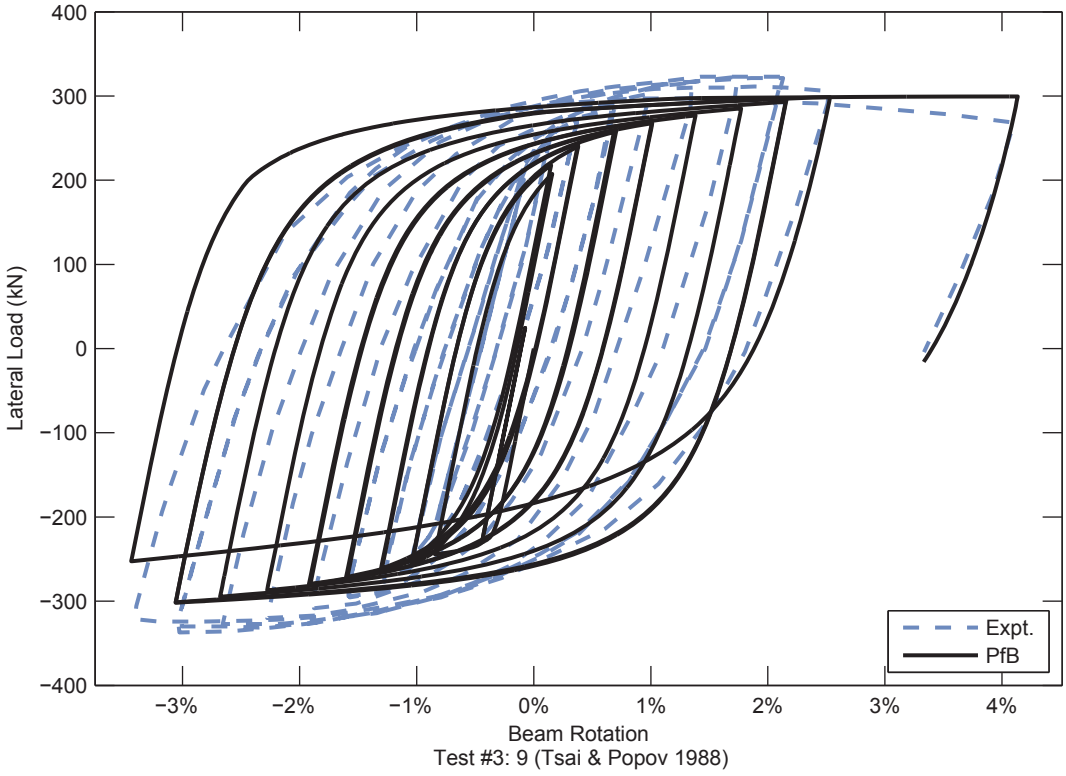

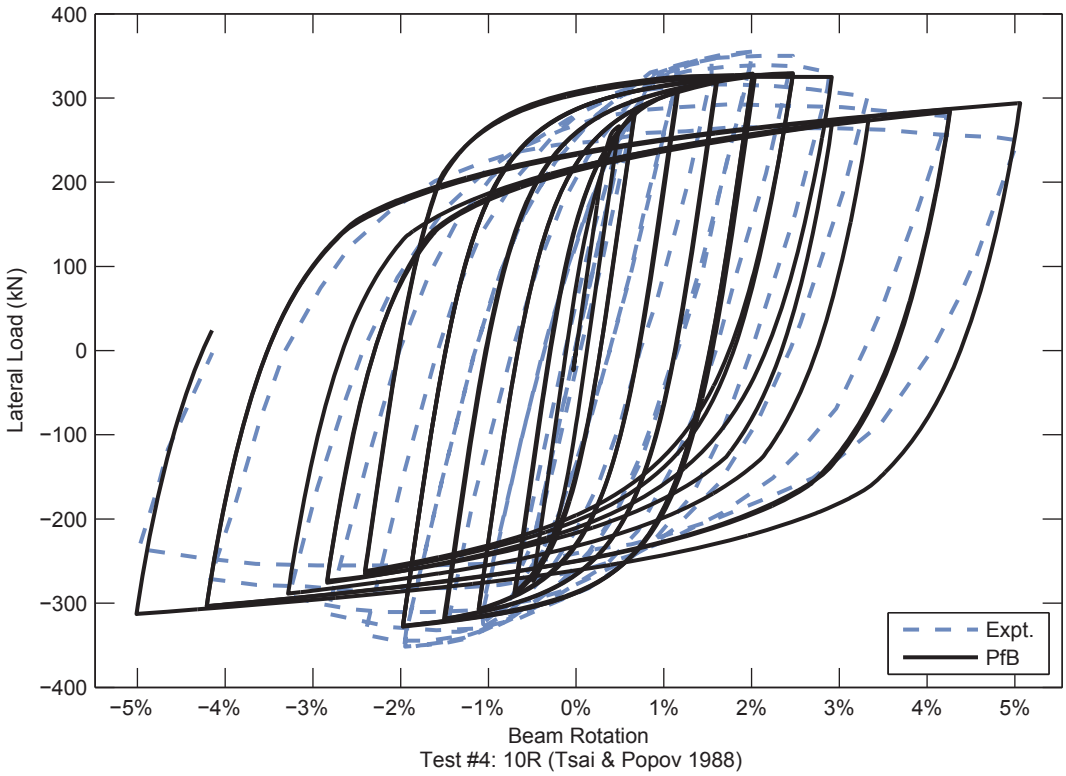

Figure 3.19. Cyclic WF Results – Tsai and Popov (Continued)

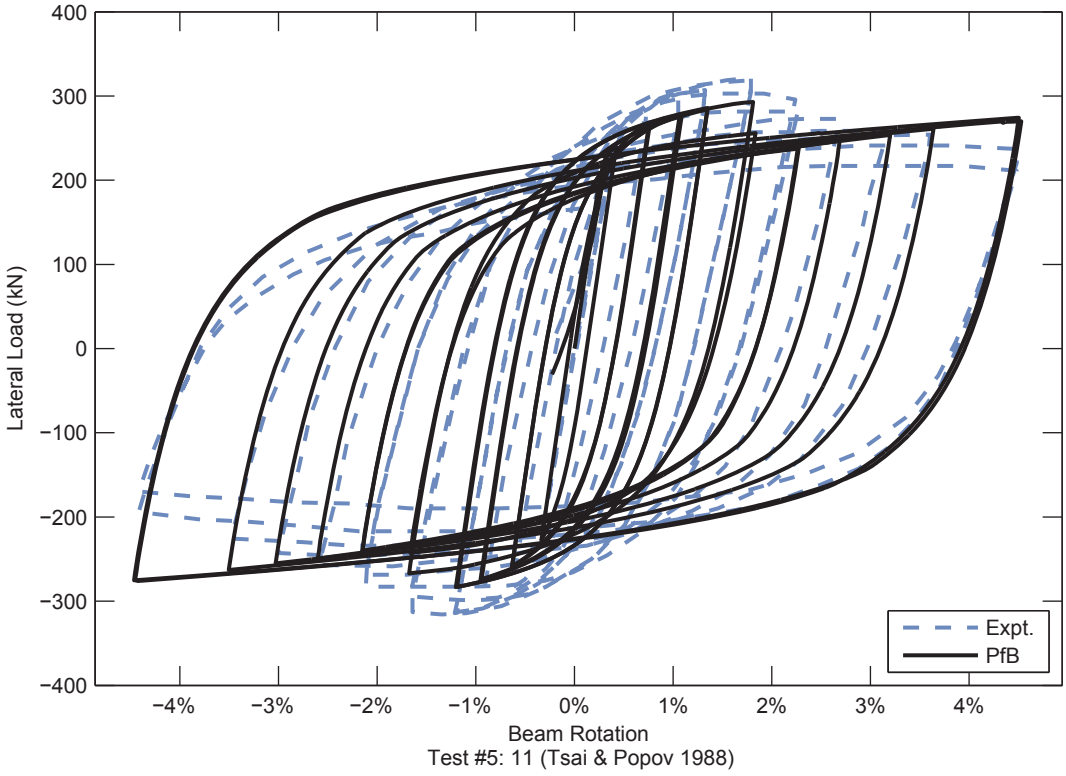

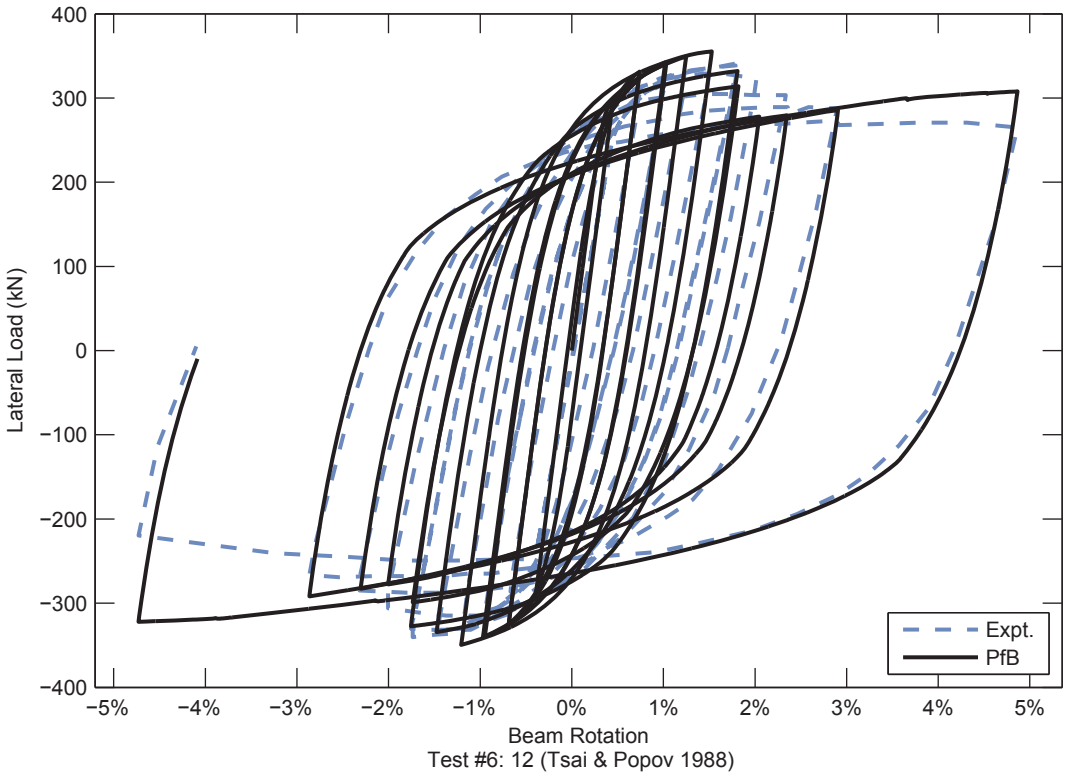

Figure 3.19. Cyclic WF Results – Tsai and Popov (Continued)

3.8 Wide Flange and Rectangular Hollow Structural Steel Braces

In braced frames, the primary inelastic response is yielding and buckling of the braces. The cyclic inelastic response of steel braces is modeled by including multiple elements along the length and explicitly modeling initial out-of-straightness in the brace. This technique has been shown to be accurately brace behavior (Uriz et al. 2008). An initial out-of-straightness equal to one thousandth of the brace length (L/1000) is used based on recommendations by Uriz et al. (2008) and standard construction tolerances (AISC 2010a).

The Shen et al. (1995) uniaxial constitutive relation (Section 3.4.1) is used. Residual stresses for wide flange braces are defined as described in Section 0, residual stress for rectangular HSS braces are defined with an initial plastic strain the same as for rectangular CFTs ($\bar{\varepsilon}_o^p$ = 0.0006 in the corner region, 0.0004 in the flat region). Local buckling is neglected. This is acceptable for the braces studied in this work since they were designed to be "highly ductile" (AISC 2010c) with low width-to-thickness ratios.

3.9 Connection Regions in Composite Special Moment Frames

Neglecting connection behavior in special moment frames can result in under-predictions of deformation and over-predictions of strength. Even at low loads, the elastic deformations of the panel zone can significantly contribute to the drift of the frame as a whole. In this work, the connection region of special moment frames is modeled as shown in Figure 3.20. Key components are a rigid link parallelogram model with a rotational spring representing the nonlinear panel zone behavior and elastic beam elements which serve to move the beam plastic hinges to specified locations. Nonlinear beam elements for the columns and beams as described in previous sections frame into this connection model. The connecting elements (e.g., split tees as shown in Figure 3.20) are not explicitly modeled since they are designed to not experience significant deformations, even under large frame deformations.

Panel zone models have been developed for in prior work for structural steel connections (e.g., Kim and Engelhardt 2002) reinforced concrete connections (e.g., Altoontash 2004), and composite connections (e.g., Kanatani et al. 1987; Muhummud 2003; Fukumoto and Morita 2005). The rigid link parallelogram model used in this work is the *Join2D* element implemented in the OpenSees framework by Altoontash (2004). The rotational spring representing the nonlinear panel zone behavior follows the recommendations of Muhummud (2003). A tri-linear constitutive relation defined by the peak panel zone shear strength, V_u, and the initial stiffness, K_e, as shown in Figure 3.21 is used. The model is extend for cyclic behavior, by defining the backbone curve in the context of a multi-surface kinematic hardening plasticity model (Mróz 1967). The peak shear strength and the initial stiffness are defined by superimposing contributions of the steel and concrete components as defined in Table 3.8 for RCFT columns and Table 3.9 for SRC columns.

Connecting elements can serve to strengthen the beam and force the location of the plastic hinge away from the column face. This has been observed in experiments on beam-to-column connections (e.g., Ricles et al. 2004). To model this, elastic beam elements are placed in between the panel zone element and the nonlinear beam element. The length of the elastic beam element is equal to the length of the connection. Section properties of the beam without adjustments for the connecting elements are used.

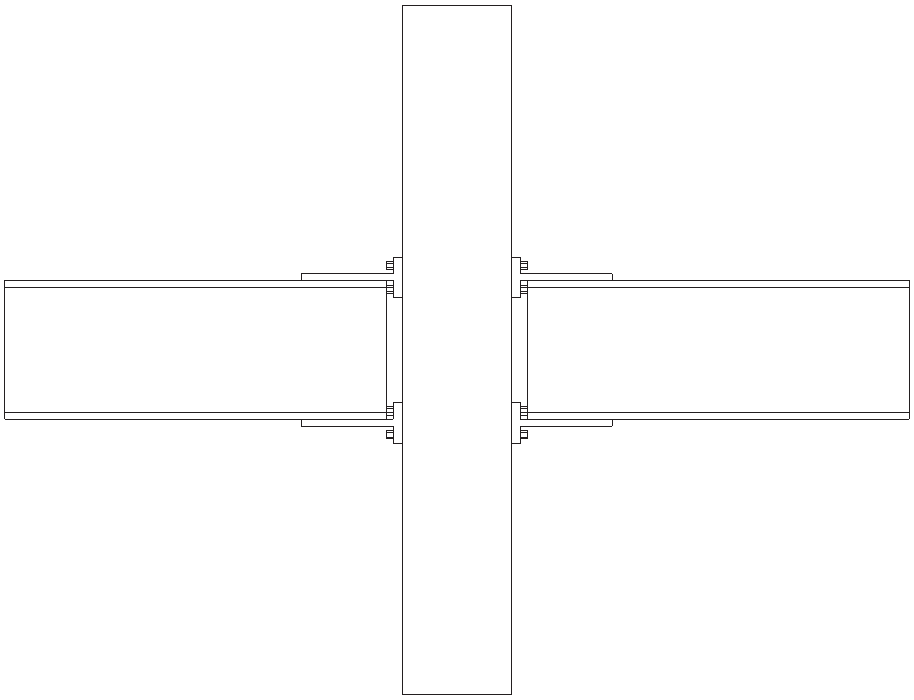

(a) Physical View

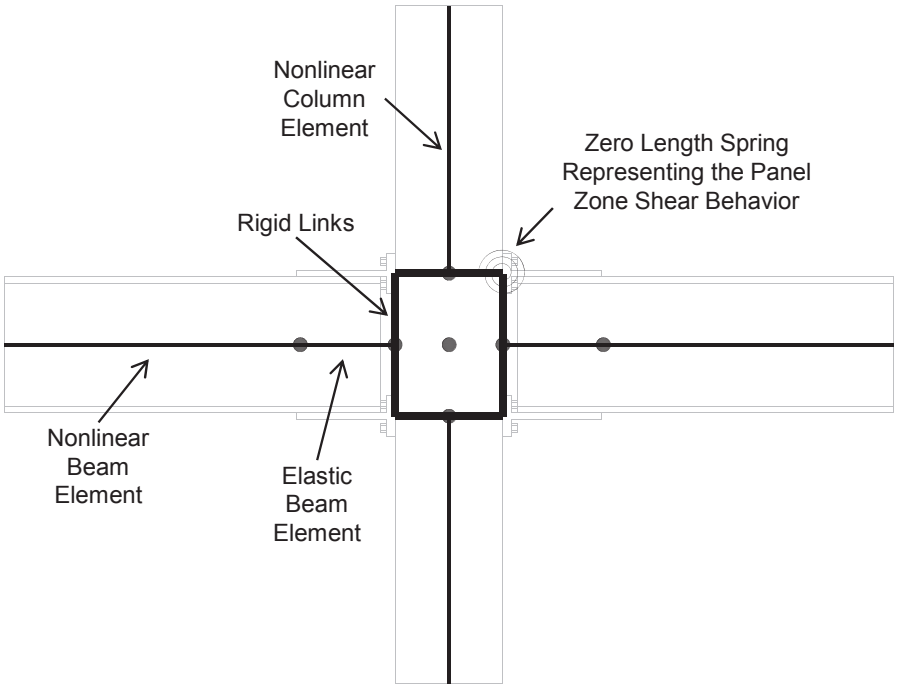

(b) Model View

Figure 3.20. Schematic of the Connection Region of Special Moment Frames

For SRC columns, strain-penetration effects were observed to reduce the stiffness by imparting fixed end rotations at the column ends (Ricles and Paboojian 1994; Juang and Hsu 2008). Thus, for these members, a simple rotational spring bond-slip model is included between the beam element and the joint as well as between the beam element and the base. An elastic constitutive relation is used with the rotational stiffness approximated by Equation 3.63 for strong axis bending. This stiffness was calibrated through comparisons between experimental and computational results for a series of cantilever column tests by Juang and Hsu (2008) presented in Section 3.6.1. This rotational spring bond-slip model is similar in nature to other models proposed for reinforced concrete columns (Sezen and Moehle 2003; Zhao and Sritharan 2007) although with a simpler constitutive relation.

$$K_{bs} = \frac{E_s I_s + E_s I_{sr} + 0.5 E_c I_c}{4H} \tag{3.63}$$

where,

H = overall depth of the section

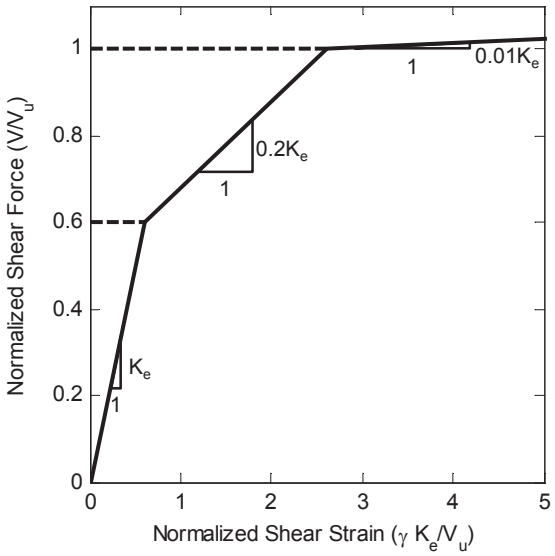

Figure 3.21. Panel Zone Shear Constitutive Relation

3.10 Connection Regions in Composite Special Concentrically Braced Frames

Connection regions in special concentrically braced frames have large gusset plates that serve to stiffen the connections. Hsiao et al. (2012) developed recommendations for modeling the connection region of steel special concentrically braced frames. Simplified versions of the model by Hsiao et al. (2012) are used in this work. The beam-to-column connection region is modeled as shown in Figure 3.22 and the mid-beam connection region is modeled as shown in Figure 3.23. Rigid links are used to model the region where the gusset plate stiffens the beam, brace, and column. The length of the rigid link along the column is equal to distance from the work point to the top of the gusset plate. The length of the rigid link along the brace is equal to distance from the work point to the physical brace. The length of the rigid link along the beam is equal to distance from the work point to column face plus 75% of the distance from the column face to the edge of the gusset plate. The column and beam frame directly into the rigid link whereas a moment release is used between the rigid link and the brace.

Table 3.8. Equations for RCFT Panel Zone Model

Component	Elastic Stiffness	Peak Shear Strength
Concrete Core	$K_e = G_c \frac{5}{6} \frac{S}{\tan(\alpha)} (B - 2t)$	$V_u = 0.885\sqrt{f_c'[ksi]}A_c$
Steel Tube	$K_e = G_s H 2t$	$V_u = 0.6F_y H 2t$
Doubler Plate	$K_e = G_s H_{flat} t_{doubler}$	$V_u = 0.6F_y H_{flat} t_{doubler}$
Total	$K_e = K_{e,concrete} + K_{e,steel} + K_{e,doubler}$	$V_u = V_{u,concrete} + V_{u,steel} + V_{u,doubler}$

Table 3.9. Equations for SRC Panel Zone Model

Component	Elastic Stiffness	Peak Shear Strength
Concrete	$K_e = G_c \frac{5}{6} \frac{S}{\tan(\alpha)} B$	$V_u = 0.474\sqrt{f_c'[ksi]}A_c$
Steel Shape	$K_e = G_s d t_w$	$V_u = 0.6F_y d t_w$
Doubler Plate	$K_e = G_s d_{doubler} t_{doubler}$	$V_u = 0.6F_y d_{doubler} t_{doubler}$
Total	$K_e = K_{e,concrete} + K_{e,steel} + K_{e,doubler}$	$V_u = V_{u,concrete} + V_{u,steel} + V_{u,doubler}$

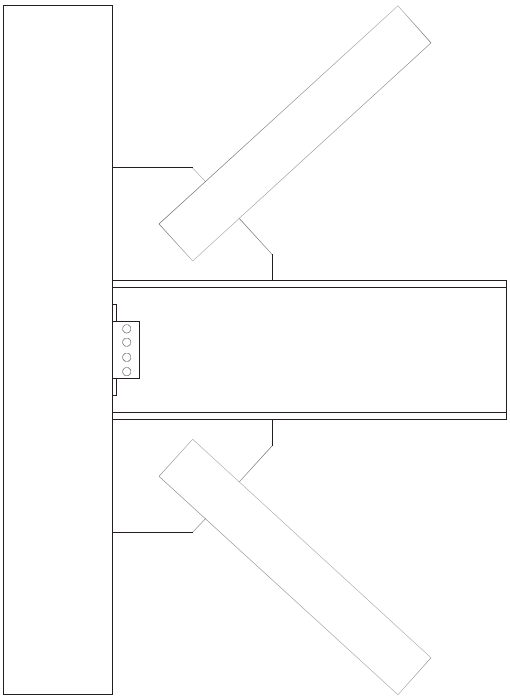

(a) Physical View

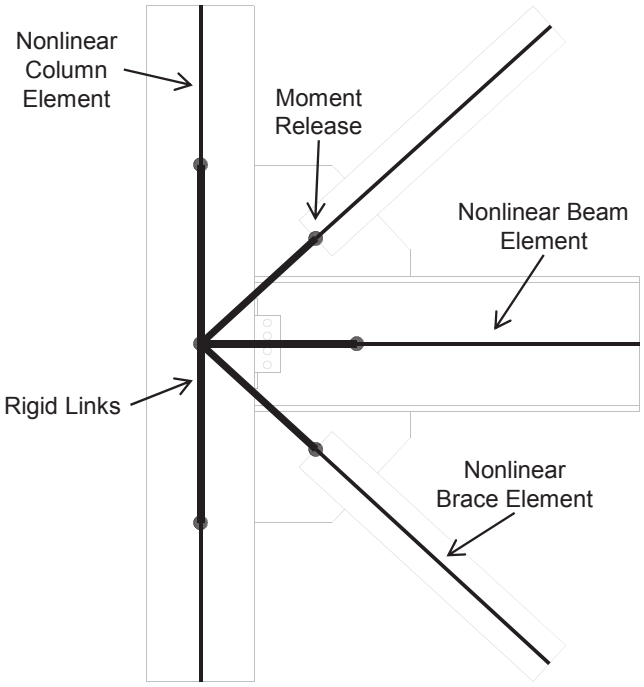

(b) Model View

Figure 3.22. Schematic of the Beam-To-Column Connection Region of Special Concentrically Braced Frames

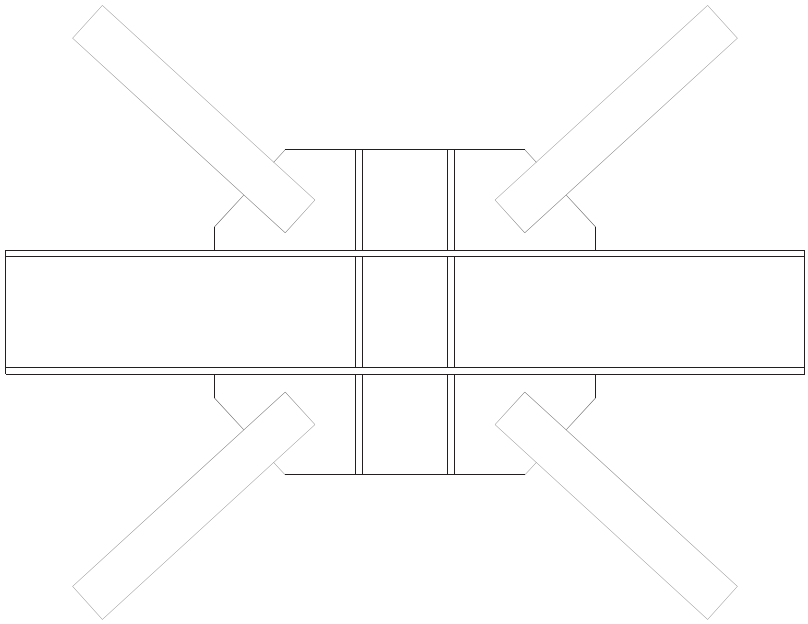

(a) Physical View

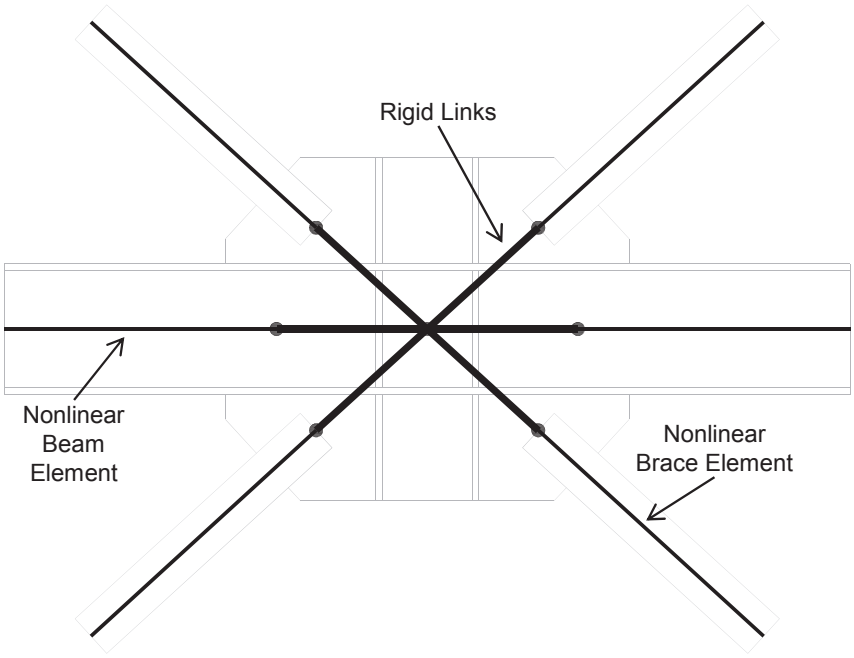

(b) Model View

Figure 3.23. Schematic of the Mid-Beam Connection Region of Special Concentrically Braced Frames

VALIDATION OF THE MIXED FINITE ELEMENT FORMULATION

4.1 Introduction

This chapter presents results of analyses using the mixed finite element formulation introduced in Chapter 3. The analyses are intended to provide a comprehensive investigation to the accuracy of the formulation. The geometric nonlinear aspects of the formulation were validated against theoretical solutions and trusted prior computational results of elastic members and frames in prior work (Denavit and Hajjar 2010). These comparisons will not be repeated here; rather the focus of the validation will be comparisons to experimental results.

The member and frame specimens analyzed in this study were chosen to have a broad range of loading and boundary conditions as well as material and geometric properties. The computational results are compared against the experimental results with quantitative comparisons made using various metrics computed from the resulting load-deformation response. These metrics include initial stiffness, peak load, deformation at peak load, and area under the curve. The fully nonlinear analyses are separated into sets based on member type and loading type. Over 250 specimens were analyzed; the number of experiments in each set is shown in Table 4.1.

Table 4.1. Summary of Validation Analyses

		Loading Type					
		SC	BM	PBC	NBC	Cyclic	Total
Member Type	CCFT	24	13	24	24	7	92
	RCFT	28	18	19	14	18	97
	SRC	---	---	39	---	8	47
	WF Beam	---	17	---	---	4	21
	Steel Brace	---	---	---	---	9	9
	Total	52	48	82	38	46	266

Note: SC = short column; BM = beam; PBC = proportionally loaded beam-column; NBC = non-proportionally loaded beam-column

4.2 Description of Monotonic Loading Types

Among monotonically loaded specimens, four common types of loading were identified (Figure 4.1): 1) short concentrically loaded (stub) columns (SC); 2) beams (BM); 3) proportionally loaded beam-columns (PBC); and 4) non-proportionally loaded beam-columns (NBC). For each of these types, the loading, control, and reported results are similar enough that the same analysis procedure may be used for all specimens. The analyses were run in two-

dimensions for all SC, BM, and NBC specimens. The PBC specimens were run in two-dimensions if the loading was on a principal axis and in three-dimensions otherwise.

Preliminary mesh refinement studies were performed. The results varied somewhat between the different loading types. For cross sections that exhibit hardening behavior, little accuracy was gained by using more than the minimum number of elements. The minimum number of elements was defined such that nodes exist wherever boundary conditions were located, loads were applied, or measurements were taken. For cross sections that exhibit softening behavior, strong mesh dependence is seen due to localization, with less accurate results occurring for meshes with higher density. Thus the minimum mesh density was used for these analyses as described in Table 4.2.

Table 4.2. Modeling Details for Monotonic Validation Studies

Loading Type	Dimensionality	Number of Elements	Number of Sections Per Element
SC	2D	1	3
BM (Direct)	2D	1	3
BM (Four-Point)	2D	4	3
BM (Three-Point)	2D	2	3
PBC	2D/3D	2	3
NBC	2D	1	3

Localization and mesh dependence are most evident for the NBC specimens since the axial loads were often large, making the softening response more drastic. Thus for the NBC tests, in addition to the analysis results using the beam element, analysis results using just one cross section are presented. The cross section analyses better reflect the ability of the constitutive relations to capture the behavior, while the beam element analysis results show the potential accuracy that may be obtained with the element in the presence of localization.

In all cases, the fiber discretization was selected such that the nominal depth of each fiber was $1/30^{th}$ of the section depth. For two-dimensional loading, the fibers were elongated in length (i.e. strips). For three-dimensional loading, the nominal width of each fiber was $1/30^{th}$ of the section width. The number of fibers in each component of the section was determined using these fixed ratios rounding up to the nearest integer as described in Chapter 3. For example for a W14x159 (d = 15.0 in, t_f = 1.19 in) in strong axis bending the number of fibers in each flange was 3 (Equation 4.1).

$$3 \approx 2.38 = \frac{1.19\,\text{in}}{15.0\,\text{in}/30} = \frac{t_f}{d/30} \tag{4.1}$$

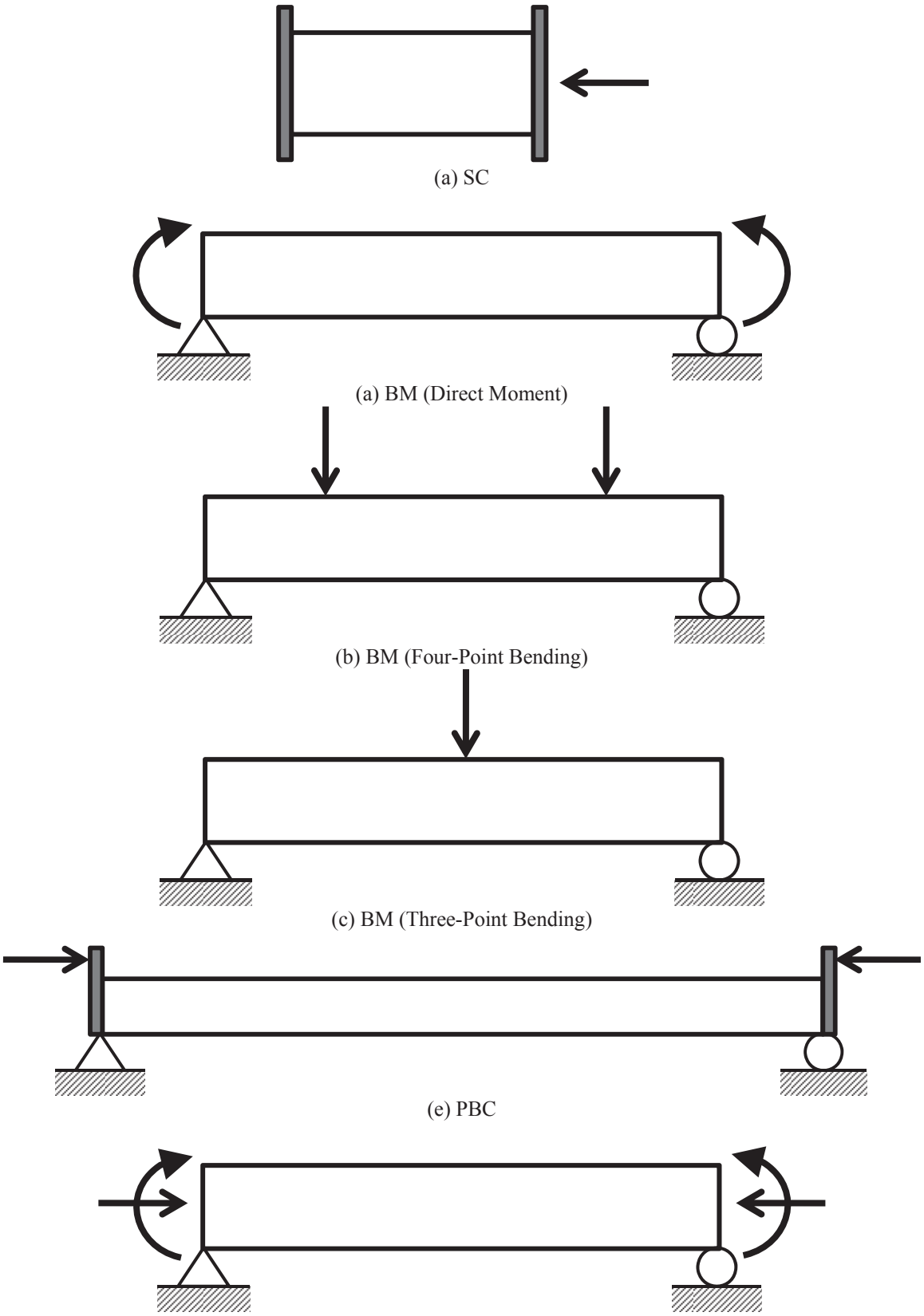

(a) SC

(a) BM (Direct Moment)

(b) BM (Four-Point Bending)

(c) BM (Three-Point Bending)

(e) PBC

(f) NBC

Figure 4.1. Experimental Setup of Monotonic Validation Tests

4.3 General Observations from the Validation Results

The "Proposed for Design" (PfD) and "Proposed for Behavior" (PfB) models are similar in the pre-peak range of all specimens and for the entire range of the BM and PBC specimens. However, the PfD exhibits stronger degradation than the PfB model for the SC and NBC specimens. This is caused primarily by the use of Popovics' equation rather than Tsai's equation for the monotonic concrete response. In the PfB model, Tsai's equation is used and the factor r is defined to account for the expected level of concrete confinement. The PfD is nonetheless suitable for developing design recommendations since it captures the pre-peak response including peak loads well, as will be seen in the remainder of this chapter.

The results of the NBC validation study clearly show the effects of localization. The analyses performed with the beam element show approximately the same peak strength but a much steeper softening response than the analyses performed with a single cross section. This is because with the beam element, once softening commences, the deformations are concentrated in only one of the three sections in the beam, increasing the curvatures at that section and accelerating the descent down the softening response of the cross section.

4.4 Circular Concrete-Filled Steel Tube Members

4.4.1 Monotonic Validation Results

The experimental results used in the monotonic validation of CCFT members were taken from a variety of sources, as shown in Table 4.3. Summary error statistics are given in Table 4.4; detailed results are presented in the remainder of this section.

The PfB model is very successful at predicting peak strength and area under the curve, as the median error is less than 5% for both of those metrics for all loading types with the exception of NBC specimens. It is logical that these metrics have less error than initial stiffness and deformation at peak strength since they were targeted in the calibration of the model. Initial stiffness and deformation at peak strength were not directly targeted in the calibration process and have comparatively larger errors. Errors in initial stiffness can likely be attributed to either discrepancies between computed and experimental values of the elastic modulus of the concrete core, as the elastic modulus of the steel tube does not exhibit significant variation, or experimental measurements that may be affected by seating or elastic deformations at the small deformation levels where initial stiffness is defined.

The following additional observations are made regarding the validation results:

- For some of the SC specimens (#7 and #17, Table 4.5) the peak does not occur until later in the experiment and post-peak degradation is not observed. The models, on the other hand, predict a comparatively early peak and some, albeit small, degradation. Since these two specimens have a low D/t ratio and local buckling is not active in that stage of loading, the early peak in the model can be attributed to an early peak in the concrete model. This could possibly be caused by the assumption that the confining pressure remains constant throughout the loading, instead of potentially increasing as the loading progresses. However, the loss in accuracy of peak strength and area under the curve are minimal because of this discrepancy.

- For other SC specimens (#1, #2, and #8, Table 4.5) hardening is observed after the initial post-peak degradation that is not captured by the model. This behavior is likely due to strain hardening in the steel or increases in confinement as the concrete crushes and expands outward; however, the resulting inaccuracy in the load-deformation results is minimal.
- For the direct moment BM specimens, the peak moment is underpredicted for the more slender sections ($D/t > 45$) and overpredicted for the more stocky specimens. However, the shape of the response (e.g., hardening slope) is captured well by the models. These inaccuracies could be the result of calibrating the uniaxial constitutive relations primarily to stub column tests where the concrete confinement and steel local buckling behavior are different. However, the average response is good and the entire response of the four-point bending BM specimens (Wheeler and Bridge 2004) is captured well.
- For the PBC specimens, the PfD model predicts a slightly higher load and slightly faster degradation than the PfB model, this is in contrast to the other types of loading where the PfB model typically predicted high peak strengths. This is possibly due to differences in the progression of stiffness between Popovics' equation and Tsai's equation with the selected r.
- For the NBC specimens, the experiments sometimes exhibit a significant hardening behavior that is not captured by the model, even in the cross section analyses. This is likely due to differences (e.g., bending moment) in the loading between NBC specimens and SC specimens against which the uniaxial constitutive relations were calibrated. The yield moment, however, appears to have been well captured by the model.

Table 4.3. References - CCFT Monotonic Validation

Loading Type	References	Results
SC	Bergmann (1994) Giakoumelis and Lam (2004) Han and Yao (2004) Han et al. (2005) O'Shea and Bridge (1997a; b) Yamamoto et al. (2000) Yoshioka et al. (1995)	Measured Material and Geometric Properties: Table 4.5 PfB Error Statistics: Table 4.6 PfD Error Statistics: Table 4.7
BM	Elchalakani et al. (2001) Ichinohe et al. (1991) Wheeler and Bridge (2004)	Measured Material and Geometric Properties: Table 4.8 PfB Error Statistics: Table 4.9 PfD Error Statistics: Table 4.10
PBC	Kilpatrick and Rangan (1999) Matsui and Tsuda (1996)	Measured Material and Geometric Properties: Table 4.11 PfB Error Statistics: Table 4.12 PfD Error Statistics: Table 4.13
NBC	Ichinohe et al. (1991) Nishiyama et al. (2002)	Measured Material and Geometric Properties: Table 4.14 PfB Error Statistics: Table 4.15 PfD Error Statistics: Table 4.16 PfB (section) Error Statistics: Table 4.17 PfD (section) Error Statistics: Table 4.18

Table 4.4. Summary Error Statistics – CCFT Monotonic Validation

Type	# of Spec.	Initial Stiffness			Peak Load			Deformation at Peak Load			Area Under Curve		
		Mean	Std.	Median	Mean	Std.	Median	Mean	Std.	Median	Mean	Std.	Median
SC	24	62.9%	89.0%	27.9%	-1.3%	6.8%	-0.9%	-44.2%	21.5%	-45.4%	6.0%	12.1%	1.8%
BM	13	17.1%	30.8%	16.8%	-3.4%	12.8%	-2.4%	---	---	---	-0.3%	14.3%	2.0%
PBC	24	-19.3%	25.5%	-10.1%	3.5%	5.3%	2.3%	11.5%	19.7%	14.6%	1.6%	4.7%	1.3%
NBC	24	9.5%	13.0%	7.4%	-7.5%	10.5%	-7.0%	-53.6%	27.0%	-55.9%	-12.9%	9.6%	-13.8%
NBC (section)	24	9.2%	13.0%	7.3%	-3.2%	9.7%	-3.3%	-29.7%	34.2%	-20.8%	0.6%	9.5%	-0.4%

(a) Proposed for Behavior

Type	# of Spec.	Initial Stiffness			Peak Load			Deformation at Peak Load			Area Under Curve		
		Mean	Std.	Median	Mean	Std.	Median	Mean	Std.	Median	Mean	Std.	Median
SC	24	73.3%	94.0%	36.4%	-2.2%	6.9%	-2.1%	-49.1%	23.4%	-46.2%	-29.2%	18.3%	-25.0%
BM	13	14.0%	29.6%	10.4%	-7.8%	13.9%	-5.7%	---	---	---	-3.6%	14.8%	-1.8%
PBC	24	-19.1%	25.6%	-9.2%	6.1%	4.6%	6.1%	1.9%	22.4%	5.9%	0.6%	5.7%	0.2%
NBC	24	17.6%	13.8%	17.4%	-10.6%	10.0%	-9.4%	-63.2%	23.9%	-65.0%	-44.2%	31.3%	-43.4%
NBC (section)	24	17.3%	13.9%	17.2%	-7.5%	9.7%	-5.9%	-50.4%	34.6%	-55.1%	-31.8%	29.7%	-26.7%

(b) Proposed for Design

Table 4.5. Material and Geometric Properties – CCFT Validation Set – SC

Test #	Author	Year	Specimen	D *(mm)*	t *(mm)*	D/t	F_y *(MPa)*	f'_c *(MPa)*	L *(mm)*	L/D
1	Yoshioka et al.	1995	CC4-D-4	450	2.96	152.0	41	283	1,350	3.0
2	Yoshioka et al.	1995	CC4-C-4	300	2.96	101.4	41	283	901	3.0
3	Yoshioka et al.	1995	CC4-A-4	149	2.96	50.4	41	283	448	3.0
4	Yoshioka et al.	1995	CC8-A-4	108	6.47	16.7	41	835	324	3.0
5	Yamamoto et al.	2000	C30A-4A	319	10.30	30.9	52	335	956	3.0
6	Yamamoto et al.	2000	C10A-2A	102	3.20	31.8	23	371	305	3.0
7	Giakoumelis & Lam	2004	C3	114	3.98	28.8	31	343	300	2.6
8	Giakoumelis & Lam	2004	C11	114	3.75	30.5	58	343	300	2.6
9	Han et al.	2005	CA2-1	100	1.87	53.5	85	282	300	3.0
10	Han et al.	2005	CA4-1	200	1.87	107.0	85	282	600	3.0
11	Han et al.	2005	CC1-1	60	2.00	30.0	90	404	180	3.0
12	Han et al.	2005	CB3-2	150	2.00	75.0	85	404	450	3.0
13	O'Shea & Bridge	1997	S30CS10A	165	2.82	58.5	114	363	578	3.5
14	O'Shea & Bridge	1997	S16CS80A	190	1.52	125.0	78	306	664	3.5
15	O'Shea & Bridge	1997	S10CS80B	190	0.86	220.9	75	211	664	3.5
16	O'Shea & Bridge	1997	S10CS50A	190	0.86	220.9	46	211	659	3.5
17	O'Shea & Bridge	1997	S30CS50B	165	2.82	58.5	48	363	581	3.5
18	O'Shea & Bridge	1997	R12CF1	190	1.11	171.2	110	203	662	3.5
19	O'Shea & Bridge	1997	S20CS50A	190	1.94	97.9	46	256	664	3.5
20	O'Shea & Bridge	1997	S16CS50B	190	1.52	125.0	54	306	665	3.5
21	O'Shea & Bridge	1997	S30CS80A	165	2.82	58.5	78	363	581	3.5
22	Bergmann	1994	RU11	324	5.60	57.8	92	444	1,000	3.1
23	Han & Yao	2004	scv2-1	200	3.00	66.7	59	304	600	3.0
24	Han & Yao	2004	sch2-1	200	3.00	66.7	59	304	600	3.0

Table 4.6. Comparison Metrics – CCFT Validation Set – SC – Proposed for Behavior

Test #	Initial Tangent (kN)			Peak Load (kN)			Strain at Peak Load (mm/mm)			Area Under Curve (kN)		
	Expt.	Model	Error	Expt.	Model	Error	Expt.	Model	Error	Expt.	Model	Error
1	6,450,090	5,197,120	-19.43%	6,876	7,458	8.47%	0.002640	0.002201	-16.63%	246.9	262.6	6.35%
2	3,241,150	2,493,580	-23.07%	3,263	3,543	8.58%	0.004027	0.002204	-45.26%	138.6	139.2	0.46%
3	623,879	723,963	16.04%	1,066	1,108	3.88%	0.010798	0.003488	-67.70%	52.9	51.7	-2.19%
4	646,948	611,141	-5.53%	2,439	2,446	0.30%	0.043436	0.038300	-11.83%	119.2	121.9	2.29%
5	1,434,340	3,975,240	177.15%	8,430	7,913	-6.12%	0.011874	0.005974	-49.69%	406.3	442.1	8.79%
6	102,098	326,641	219.93%	675	641	-5.02%	0.044211	0.021213	-52.02%	36.8	37.3	1.36%
7	121,696	463,951	281.24%	995	908	-8.74%	0.069693	0.025081	-64.01%	112.0	106.7	-4.71%
8	151,745	528,865	248.52%	1,072	1,089	1.51%	0.110078	0.005944	-94.60%	112.0	112.5	0.41%
9	314,446	403,816	28.42%	849	809	-4.76%	0.005835	0.003172	-45.64%	18.1	20.0	10.06%
10	1,204,630	1,468,710	21.92%	2,777	2,908	4.70%	0.005389	0.002632	-51.16%	58.5	59.8	2.13%
11	100,871	167,221	65.78%	440	410	-6.90%	0.007814	0.005413	-30.73%	11.3	11.3	0.10%
12	580,334	863,423	48.78%	1,755	1,793	2.19%	0.006907	0.003060	-55.70%	42.9	43.1	0.42%
13	859,890	1,217,960	41.64%	2,661	2,847	6.97%	0.003866	0.003478	-10.03%	18.6	25.3	36.12%
14	1,040,340	1,252,510	20.39%	2,602	2,410	-7.36%	0.003816	0.002585	-32.27%	16.4	21.9	33.76%
15	895,896	1,148,000	28.14%	2,453	2,185	-10.92%	0.003928	0.002551	-35.06%	14.5	17.0	17.43%
16	763,965	908,874	18.97%	1,341	1,387	3.40%	0.003578	0.002257	-36.93%	11.7	12.2	4.20%
17	730,417	856,303	17.23%	1,661	1,545	-7.00%	0.012866	0.003534	-72.53%	22.5	21.2	-5.86%
18	1,072,370	1,427,530	33.12%	2,993	3,188	6.53%	0.003278	0.002819	-13.98%	17.6	22.6	28.24%
19	810,896	1,035,890	27.75%	1,676	1,547	-7.69%	0.007022	0.002271	-67.66%	17.5	15.4	-11.69%
20	957,083	1,058,880	10.64%	1,691	1,745	3.19%	0.003760	0.002367	-37.06%	17.7	17.9	0.70%
21	824,362	1,035,190	25.57%	2,295	2,130	-7.17%	0.006012	0.003541	-41.09%	21.5	21.9	1.51%
22	1,463,430	4,259,290	191.05%	11,404	9,820	-13.89%	0.009078	0.003870	-57.37%	226.5	258.9	14.30%
23	1,834,870	1,348,430	-26.51%	2,387	2,339	-2.01%	0.003261	0.002724	-16.47%	78.6	75.2	-4.35%
24	835,396	1,348,440	61.41%	2,175	2,338	7.49%	0.006304	0.002763	-56.18%	70.9	74.2	4.70%
Mean			62.88%			-1.27%			-44.23%			6.02%
Standard Deviation			88.98%			6.79%			21.48%			12.10%
Median			27.94%			-0.85%			-45.45%			1.82%

Table 4.7. Comparison Metrics – CCFT Validation Set – SC – Proposed for Design

Test #	Initial Tangent (kN)			Peak Load (kN)			Strain at Peak Load (mm/mm)			Area Under Curve (kN)		
	Expt.	Model	Error	Expt.	Model	Error	Expt.	Model	Error	Expt.	Model	Error
1	6,450,090	5,547,410	-13.99%	6,876	7,391	7.49%	0.002640	0.002201	-16.63%	246.9	112.6	-54.39%
2	3,241,150	2,646,430	-18.35%	3,263	3,499	7.22%	0.004027	0.002305	-42.77%	138.6	63.8	-53.93%
3	623,879	772,762	23.86%	1,066	1,103	3.40%	0.010798	0.003283	-69.60%	52.9	36.3	-31.38%
4	646,948	631,315	-2.42%	2,439	2,412	-1.11%	0.043436	0.024267	-44.13%	119.2	121.0	1.52%
5	1,434,340	4,243,940	195.88%	8,430	7,859	-6.77%	0.011874	0.005154	-56.60%	406.3	362.8	-10.72%
6	102,098	339,894	232.91%	675	621	-7.94%	0.044211	0.007473	-83.10%	36.8	35.4	-3.91%
7	121,696	487,376	300.49%	995	876	-11.87%	0.069693	0.006818	-90.22%	112.0	97.8	-12.73%
8	151,745	565,582	272.72%	1,072	1,081	0.83%	0.110078	0.005284	-95.20%	112.0	86.2	-23.07%
9	314,446	431,516	37.23%	849	807	-4.96%	0.005835	0.003172	-45.64%	18.1	10.7	-41.19%
10	1,204,630	1,553,430	28.95%	2,777	2,893	4.17%	0.005389	0.002632	-51.16%	58.5	22.8	-61.09%
11	100,871	180,086	78.53%	440	409	-7.07%	0.007814	0.005112	-34.58%	11.3	9.4	-16.82%
12	580,334	916,194	57.87%	1,755	1,778	1.34%	0.006907	0.002760	-60.04%	42.9	19.2	-55.35%
13	859,890	1,293,190	50.39%	2,661	2,828	6.27%	0.003866	0.003285	-15.03%	18.6	18.5	-0.30%
14	1,040,340	1,330,450	27.89%	2,602	2,395	-7.94%	0.003816	0.002608	-31.66%	16.4	13.3	-18.68%
15	895,896	1,227,340	37.00%	2,453	2,186	-10.86%	0.003928	0.002551	-35.06%	14.5	11.5	-20.52%
16	763,965	977,419	27.94%	1,341	1,385	3.25%	0.003578	0.002281	-36.26%	11.7	8.6	-26.93%
17	730,417	927,124	26.93%	1,661	1,522	-8.36%	0.012866	0.003319	-74.20%	22.5	17.5	-22.30%
18	1,072,370	1,501,150	39.98%	2,993	3,189	6.54%	0.003278	0.002819	-13.98%	17.6	14.1	-20.12%
19	810,896	1,101,750	35.87%	1,676	1,533	-8.52%	0.007022	0.002318	-66.99%	17.5	10.5	-40.18%
20	957,083	1,131,950	18.27%	1,691	1,726	2.08%	0.003760	0.002392	-36.39%	17.7	11.5	-35.35%
21	824,362	1,113,810	35.11%	2,295	2,109	-8.09%	0.006012	0.003206	-46.67%	21.5	17.2	-19.96%
22	1,463,430	4,589,620	213.62%	11,404	9,700	-14.94%	0.009078	0.003371	-62.87%	226.5	143.6	-36.60%
23	1,834,870	1,444,030	-21.30%	2,387	2,313	-3.07%	0.003261	0.002802	-14.08%	78.6	38.7	-50.75%
24	835,396	1,444,110	72.87%	2,175	2,313	6.33%	0.006304	0.002763	-56.18%	70.9	38.3	-45.90%
Mean			73.26%			-2.19%			-49.13%			-29.19%
Standard Deviation			94.03%			6.94%			23.37%			18.27%
Median			36.43%			-2.09%			-46.15%			-25.00%

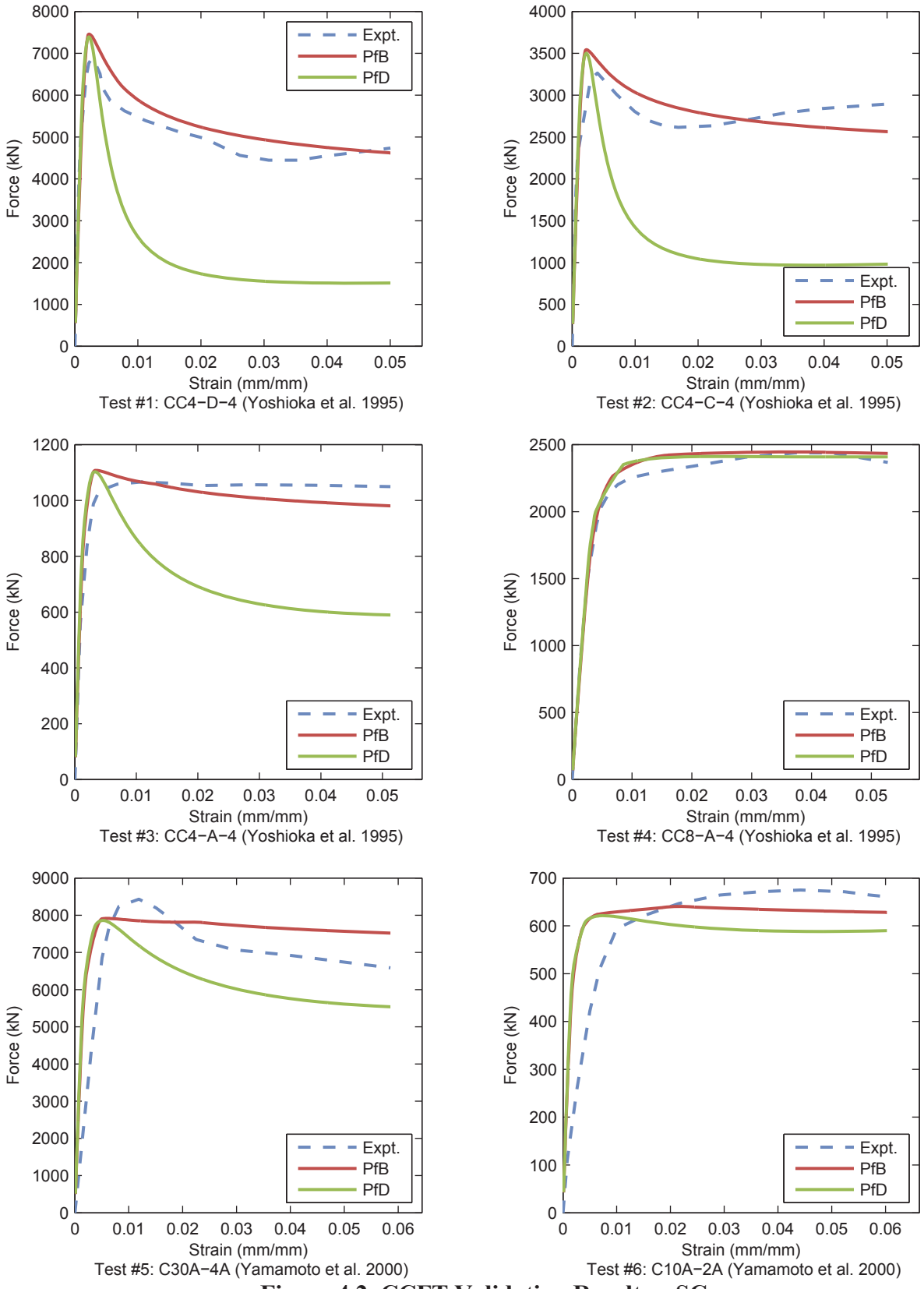

Figure 4.2. CCFT Validation Results – SC

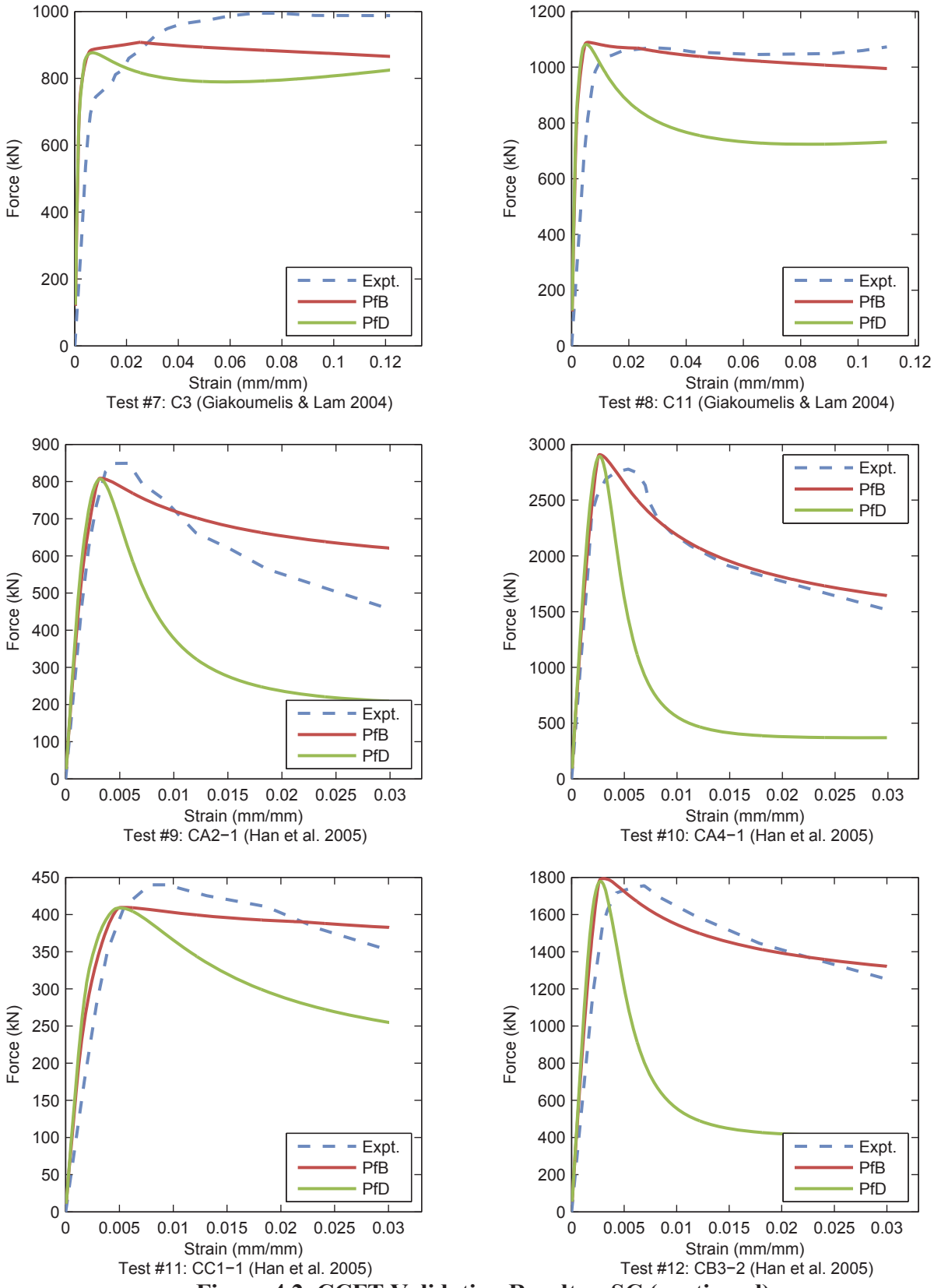

Figure 4.2. CCFT Validation Results – SC (continued)

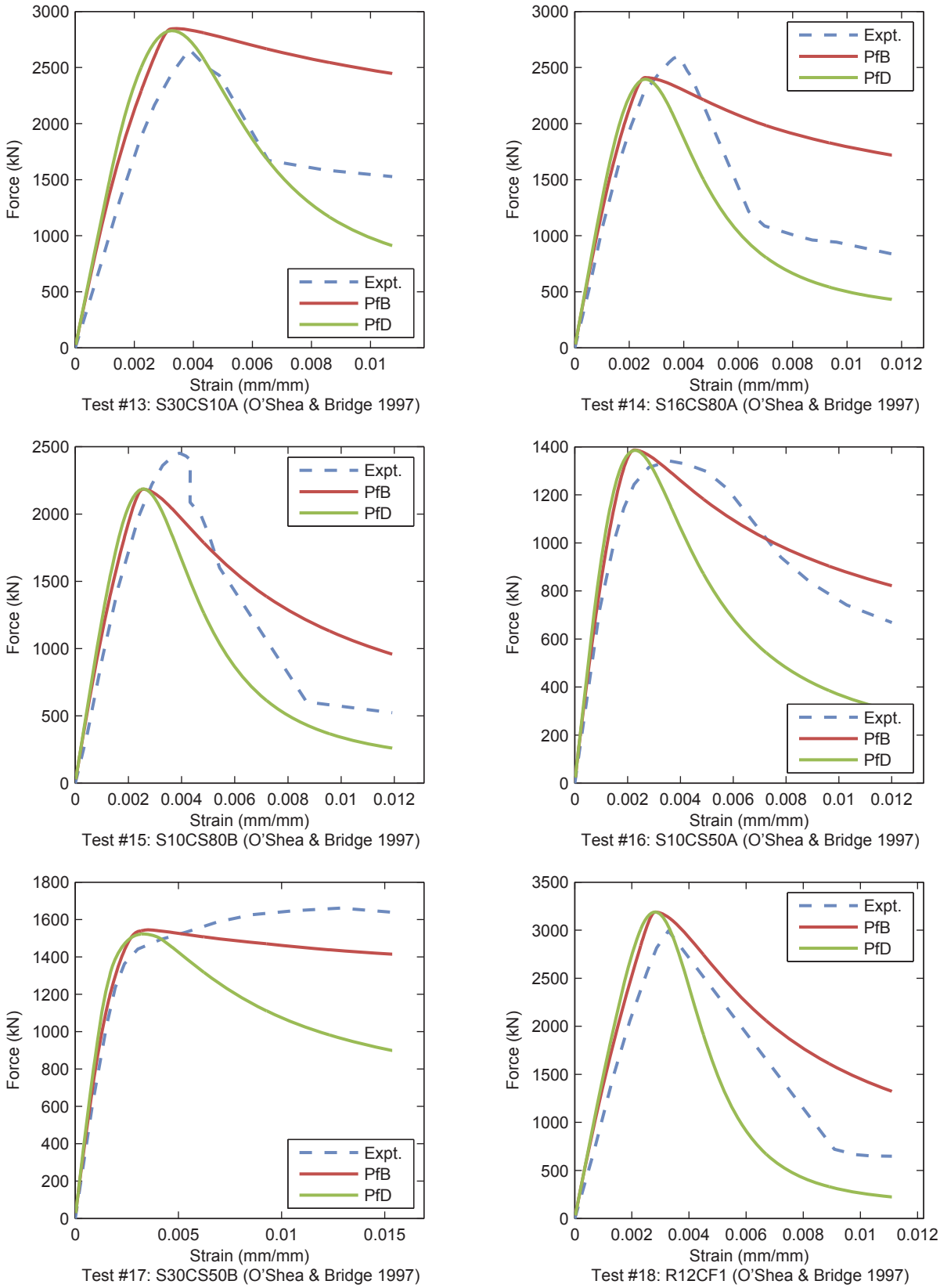

Figure 4.2. CCFT Validation Results – SC (continued)

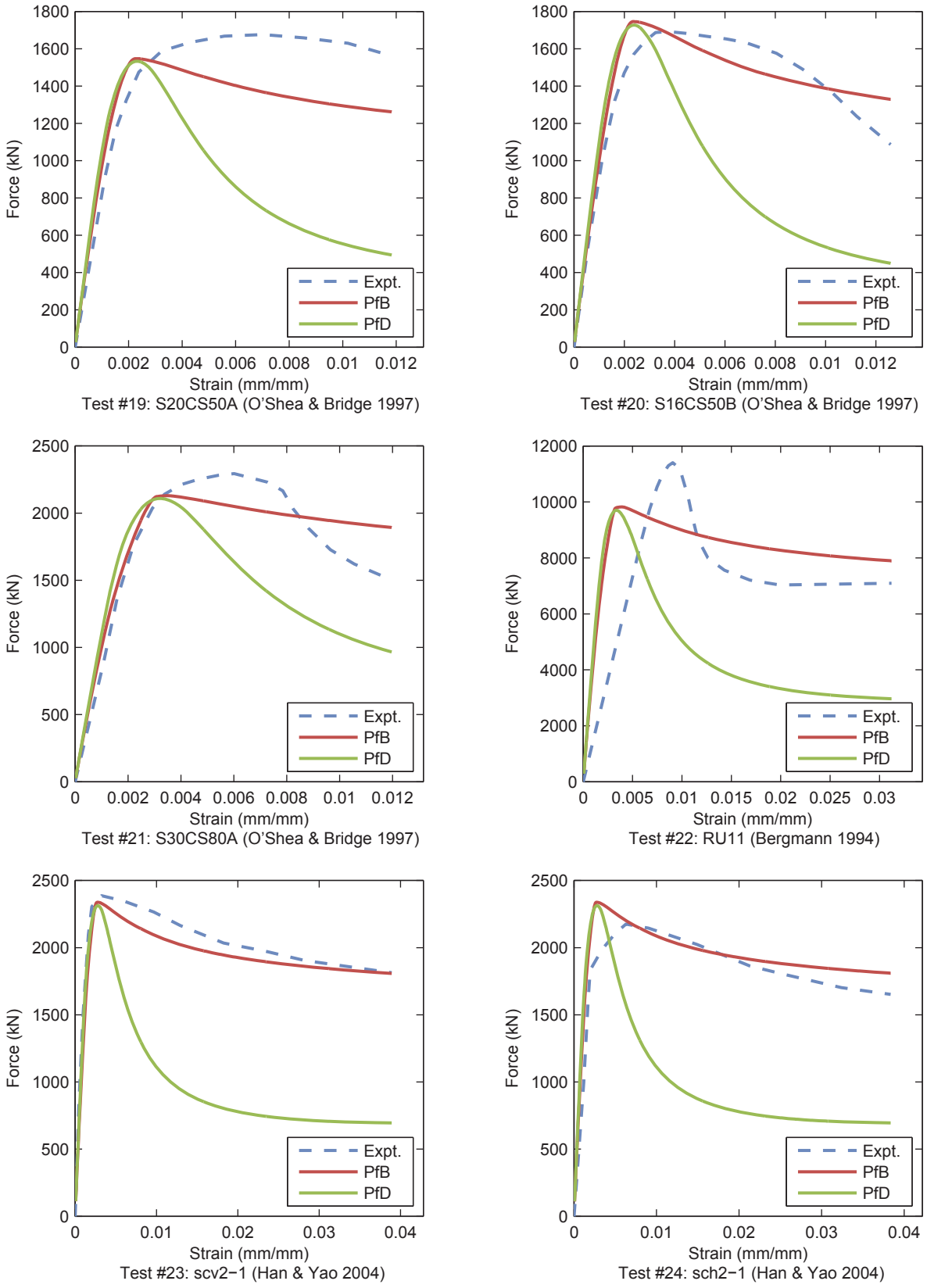

Figure 4.2. CCFT Validation Results – SC (continued)

Table 4.8. Material and Geometric Properties – CCFT Validation Set – BM

Test #	Author	Year	Specimen	Type of Loading	D (mm)	t (mm)	D/t	f'_c (MPa)	F_y (MPa)	Shear Span (mm)	Bending Span (mm)
1	Ichinohe et al.	1991	C06F0M	Direct Moment	300	6.23	48.2	58.8	436	---	600
2	Elchalakani et al.	2001	CBC0-C	Direct Moment	110	1.00	109.9	23.4	400	---	800
3	Elchalakani et al.	2001	CBC0-B	Direct Moment	110	1.25	88.3	23.4	400	---	800
4	Elchalakani et al.	2001	CBC0-A	Direct Moment	111	1.50	73.9	23.4	400	---	800
5	Elchalakani et al.	2001	CBC2	Direct Moment	89	2.79	31.8	23.4	432	---	800
6	Elchalakani et al.	2001	CBC6	Direct Moment	76	3.24	23.5	23.4	456	---	800
7	Elchalakani et al.	2001	CBC1	Direct Moment	102	2.53	40.2	23.4	365	---	800
8	Elchalakani et al.	2001	CBC3	Direct Moment	76	2.45	31.2	23.4	415	---	800
9	Elchalakani et al.	2001	CBC5	Direct Moment	61	2.44	24.9	23.4	456	---	800
10	Wheeler & Bridge	2004	TBP002	Four Point Bending	406	6.40	63.4	40.0	351	1,300	1,200
11	Wheeler & Bridge	2004	TBP003	Four Point Bending	406	6.40	63.4	55.0	351	1,300	1,200
12	Wheeler & Bridge	2004	TBP005	Four Point Bending	456	6.40	71.3	48.0	351	1,300	1,200
13	Wheeler & Bridge	2004	TBP006	Four Point Bending	456	6.40	71.3	56.0	351	1,300	1,200

Table 4.9. Comparison Metrics – CCFT Validation Set – BM – Proposed for Behavior

Test #	Initial Tangent			Peak Moment			Area Under Curve		
				(kN-m)					
	Expt.	Model	Error	Expt.	Model	Error	Expt.	Model	Error
1	63.39	53.35	-15.83%	369.50	319.82	-13.44%	49,926	44,360	-11.15%
2	1.73	1.27	-26.69%	7.61	6.01	-21.03%	590	456	-22.75%
3	1.65	1.52	-8.06%	9.09	7.27	-20.02%	282	230	-18.65%
4	2.06	1.74	-15.46%	11.77	9.43	-19.90%	1,093	881	-19.38%
5	1.35	1.85	37.23%	10.94	11.74	7.32%	1,198	1,349	12.62%
6	1.53	1.46	-5.12%	9.74	9.96	2.23%	838	894	6.67%
7	1.88	2.24	18.79%	11.38	11.65	2.37%	770	822	6.83%
8	0.95	1.24	30.72%	6.83	7.42	8.54%	652	737	12.94%
9	0.41	0.72	77.12%	3.97	4.87	22.75%	324	408	25.72%
Test #	**Initial Tangent**			**Peak Moment**			**Area Under Curve**		
	(kN-m/mm)			*(kN-m)*			*(kN-m-mm)*		
	Expt.	Model	Error	Expt.	Model	Error	Expt.	Model	Error
10	25.20	29.43	16.79%	469.98	458.71	-2.40%	31,515	31,326	-0.60%
11	26.60	30.75	15.60%	477.08	470.82	-1.31%	32,001	32,053	0.16%
12	30.54	44.40	45.35%	634.52	606.83	-4.36%	52,672	53,810	2.16%
13	30.01	45.48	51.55%	647.95	611.77	-5.59%	48,151	49,115	2.00%
Mean			17.08%			-3.45%			-0.26%
Standard Deviation			30.79%			12.84%			14.30%
Median			16.79%			-2.40%			2.00%

Table 4.10. Comparison Metrics – CCFT Validation Set – BM – Proposed for Design

Test #	Initial Tangent			Peak Moment (kN-m)			Area Under Curve		
	Expt.	Model	Error	Expt.	Model	Error	Expt.	Model	Error
1	63.39	53.63	-15.39%	369.50	293.31	-20.62%	49,926	41,864	-16.15%
2	1.73	1.23	-28.44%	7.61	5.66	-25.60%	590	433	-26.57%
3	1.65	1.49	-9.72%	9.09	6.95	-23.59%	282	223	-21.01%
4	2.06	1.73	-15.86%	11.77	8.48	-27.93%	1,093	824	-24.61%
5	1.35	1.86	37.81%	10.94	11.46	4.78%	1,198	1,315	9.74%
6	1.53	1.46	-4.78%	9.74	9.68	-0.56%	838	875	4.38%
7	1.88	2.24	18.90%	11.38	11.17	-1.83%	770	801	3.99%
8	0.95	1.24	31.17%	6.83	7.15	4.71%	652	715	9.65%
9	0.41	0.73	77.77%	3.97	4.74	19.42%	324	399	23.04%
Test #	**Initial Tangent** *(kN-m/mm)*			**Peak Moment** *(kN-m)*			**Area Under Curve** *(kN-m-mm)*		
	Expt.	Model	Error	Expt.	Model	Error	Expt.	Model	Error
10	25.20	27.82	10.41%	469.98	443.19	-5.70%	31,515	30,412	-3.50%
11	26.60	28.58	7.45%	477.08	454.96	-4.64%	32,001	31,124	-2.74%
12	30.54	41.10	34.57%	634.52	571.93	-9.86%	52,672	51,706	-1.83%
13	30.01	41.64	38.75%	647.95	579.99	-10.49%	48,151	47,365	-1.63%
Mean			14.05%			-7.84%			-3.64%
Standard Deviation			29.60%			13.86%			14.78%
Median			10.41%			-5.70%			-1.83%

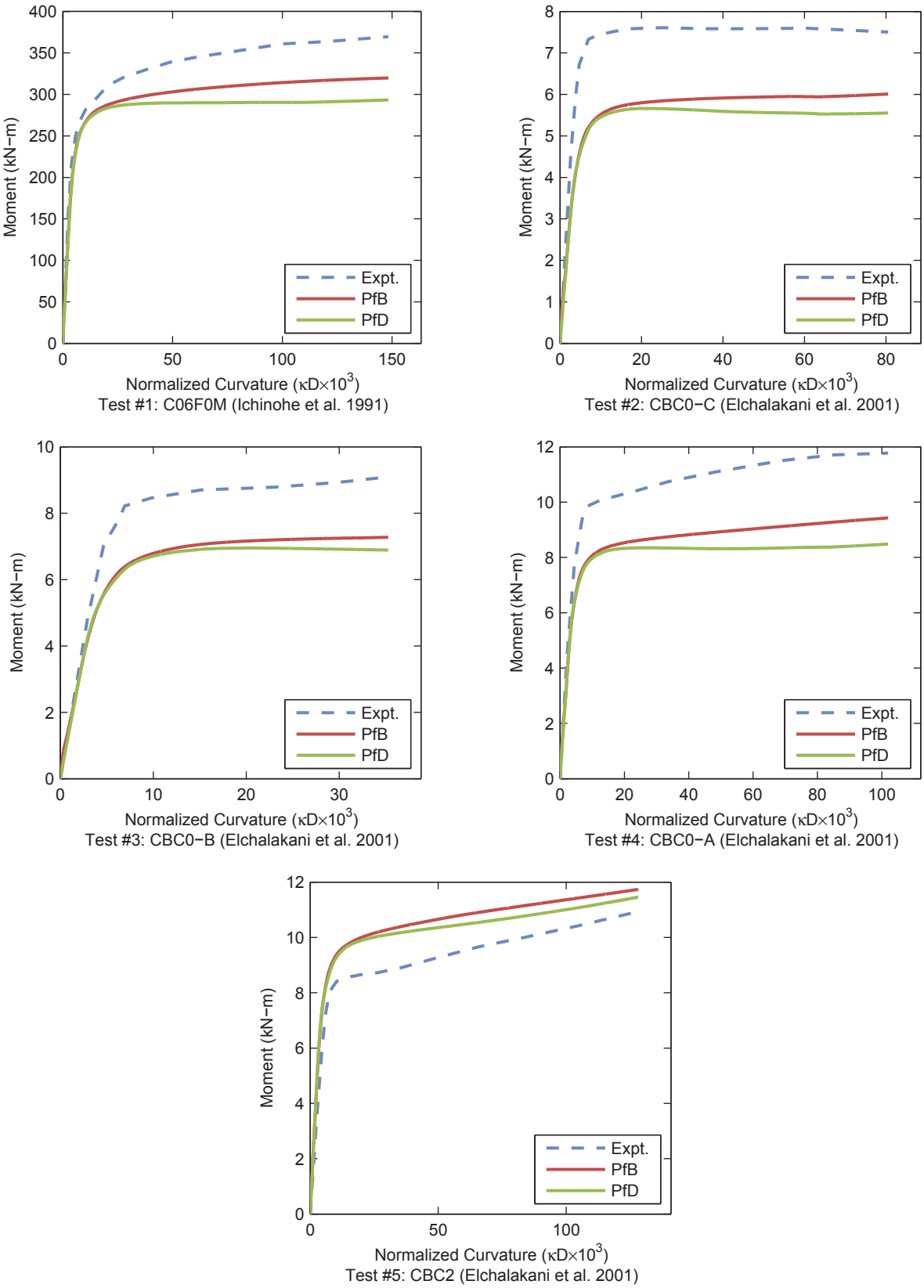

Figure 4.3. CCFT Validation Results – BM

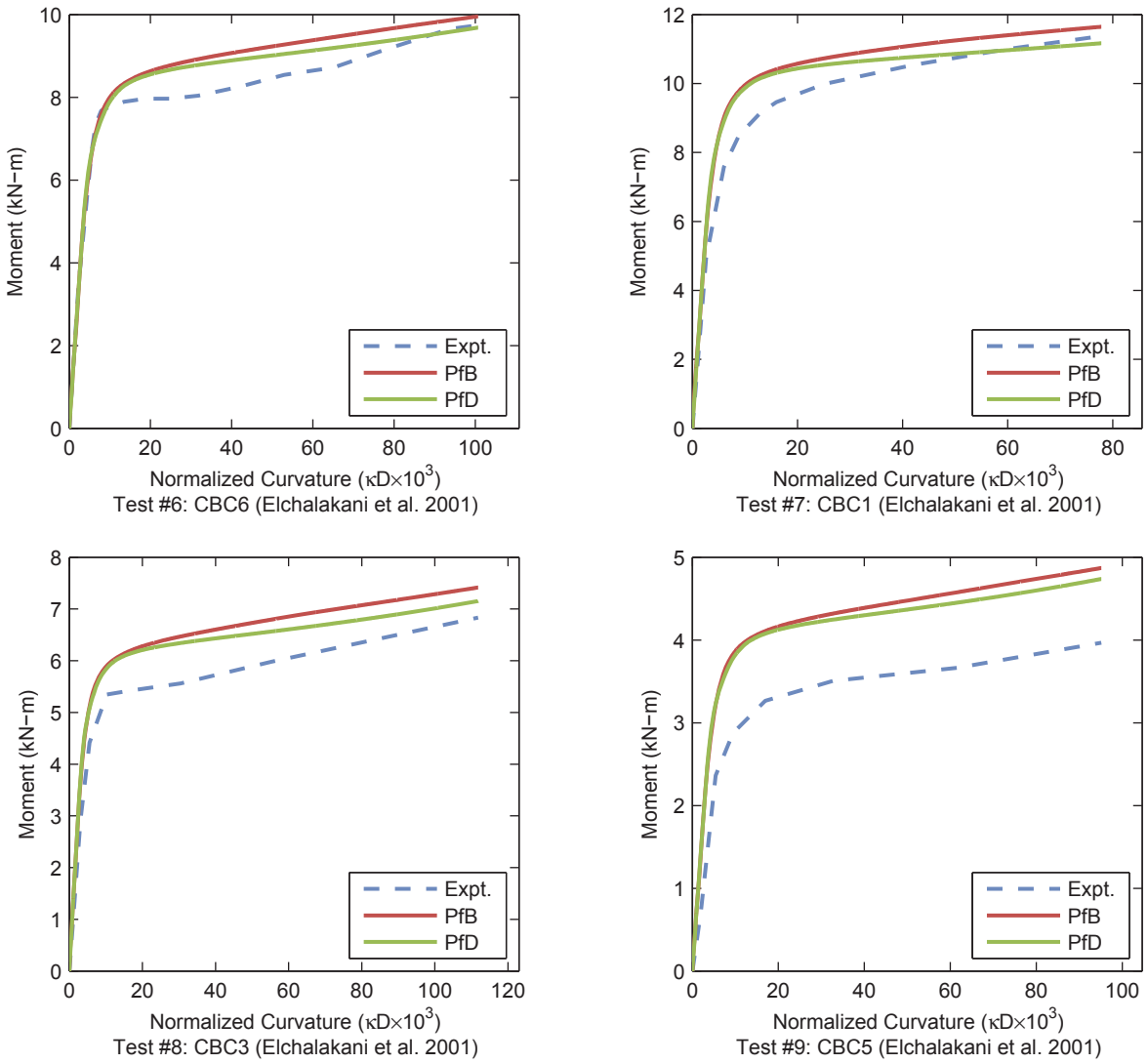

Figure 4.3. CCFT Validation Results – BM (continued)

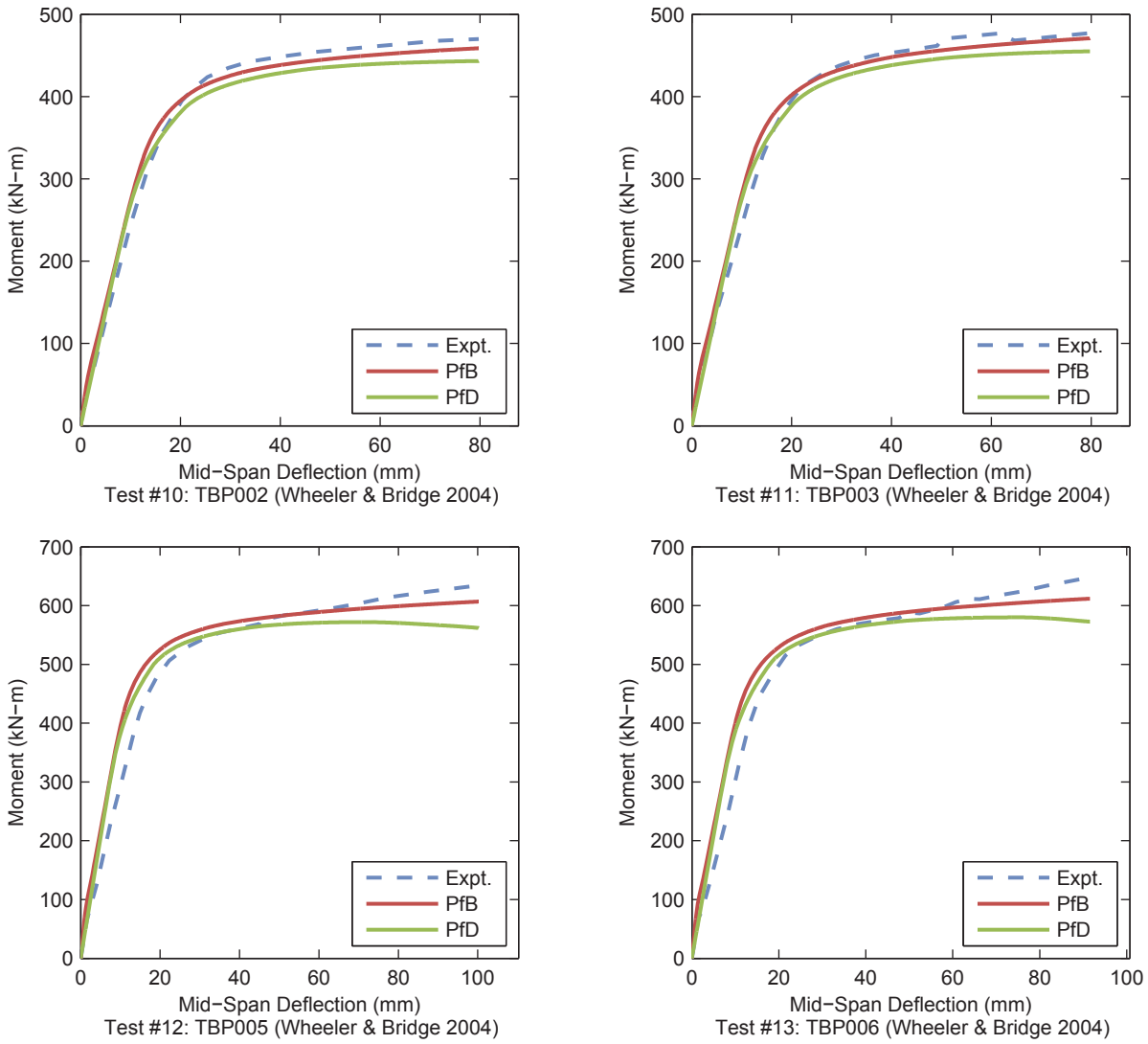

Figure 4.3. CCFT Validation Results – BM (continued)

Table 4.11. Material and Geometric Properties – CCFT Validation Set – PBC

Test #	Author	Year	Specimen	D (mm)	t (mm)	D/t	f'_c (MPa)	F_y (MPa)	L (mm)	L/D	e (mm)	e/D
1	Matsui & Tsuda	1996	C4-1	165	4.50	36.7	32	414	661	4.0	20.7	0.125
2	Matsui & Tsuda	1996	C4-3	165	4.50	36.7	32	414	661	4.0	62.0	0.375
3	Matsui & Tsuda	1996	C4-5	165	4.50	36.7	32	414	661	4.0	103.2	0.625
4	Matsui & Tsuda	1996	C12-1	165	4.50	36.7	32	414	1,982	12.0	20.7	0.125
5	Matsui & Tsuda	1996	C12-3	165	4.50	36.7	32	414	1,982	12.0	62.0	0.375
6	Matsui & Tsuda	1996	C12-5	165	4.50	36.7	32	414	1,982	12.0	103.2	0.625
7	Matsui & Tsuda	1996	C24-1	165	4.50	36.7	32	414	3,965	24.0	20.7	0.125
8	Matsui & Tsuda	1996	C24-3	165	4.50	36.7	32	414	3,965	24.0	62.0	0.375
9	Matsui & Tsuda	1996	C24-5	165	4.50	36.7	32	414	3,965	24.0	103.2	0.625
10	Kilpatrick & Rangan	1999	SC-0	76	2.20	34.5	58	435	802	10.6	15.0	0.197
11	Kilpatrick & Rangan	1999	SC-1	76	2.20	34.5	58	435	1,032	13.6	15.0	0.197
12	Kilpatrick & Rangan	1999	SC-2	76	2.20	34.5	58	435	1,262	16.6	15.0	0.197
13	Kilpatrick & Rangan	1999	SC-3	76	2.20	34.5	58	435	1,487	19.6	15.0	0.197
14	Kilpatrick & Rangan	1999	SC-4	76	2.20	34.5	58	435	1,717	22.6	15.0	0.197
15	Kilpatrick & Rangan	1999	SC-5	76	2.20	34.5	58	435	1,947	25.6	15.0	0.197
16	Kilpatrick & Rangan	1999	SC-6	76	2.20	34.5	58	435	2,172	28.6	15.0	0.197
17	Kilpatrick & Rangan	1999	SC-7	76	2.20	34.5	58	435	2,402	31.6	15.0	0.197
18	Kilpatrick & Rangan	1999	SC-9	102	2.40	42.4	58	410	1,947	19.1	10.0	0.098
19	Kilpatrick & Rangan	1999	SC-10	102	2.40	42.4	58	410	1,947	19.1	15.0	0.147
20	Kilpatrick & Rangan	1999	SC-11	102	2.40	42.4	58	410	1,947	19.1	20.0	0.197
21	Kilpatrick & Rangan	1999	SC-12	102	2.40	42.4	58	410	1,947	19.1	25.0	0.246
22	Kilpatrick & Rangan	1999	SC-13	102	2.40	42.4	58	410	1,947	19.1	30.0	0.295
23	Kilpatrick & Rangan	1999	SC-14	102	2.40	42.4	58	410	1,947	19.1	40.0	0.393
24	Kilpatrick & Rangan	1999	SC-15	102	2.40	42.4	58	410	1,947	19.1	50.0	0.492

Table 4.12. Comparison Metrics – CCFT Validation Set – PBC – Proposed for Behavior

Test #	Initial Tangent (kN/mm)			Peak Load (kN)			Deformation at Peak Load (mm)			Area Under Curve (kN-mm)		
	Expt.	Model	Error	Expt.	Model	Error	Expt.	Model	Error	Expt.	Model	Error
1	19,736.8	1,769.4	-91.04%	1,215.1	1,300.4	7.02%	6.47	5.04	-22.19%	23,993	25,172	4.92%
2	10,590.6	594.7	-94.38%	751.7	822.0	9.34%	8.78	6.07	-30.91%	21,102	22,064	4.56%
3	839.4	339.0	-59.61%	555.1	557.5	0.42%	12.61	7.12	-43.49%	10,229	10,091	-1.35%
4	241.1	189.4	-21.44%	947.8	1,011.5	6.71%	15.61	18.80	20.47%	61,013	64,493	5.70%
5	88.2	65.2	-26.15%	575.6	632.2	9.84%	19.87	25.14	26.50%	41,725	44,993	7.83%
6	40.3	37.3	-7.29%	389.6	442.7	13.64%	22.94	28.01	22.12%	28,329	31,142	9.93%
7	56.9	44.0	-22.61%	608.6	617.6	1.48%	33.69	43.51	29.17%	49,693	52,085	4.81%
8	17.6	15.8	-10.28%	347.2	402.2	15.82%	59.38	63.17	6.38%	28,974	32,476	12.09%
9	9.4	9.2	-2.17%	274.3	300.7	9.60%	65.00	72.81	12.02%	21,917	23,336	6.48%
10	89.0	85.7	-3.77%	245.3	250.9	2.32%	8.49	8.93	5.21%	9,536	9,118	-4.38%
11	51.2	50.9	-0.41%	208.0	219.6	5.57%	10.52	12.52	18.96%	10,457	10,357	-0.96%
12	37.8	33.5	-11.34%	182.1	190.6	4.68%	12.89	16.23	25.97%	8,760	8,881	1.38%
13	30.0	23.8	-20.65%	162.1	165.8	2.31%	13.41	19.76	47.33%	9,606	9,868	2.72%
14	19.7	17.6	-10.36%	141.6	144.0	1.65%	20.44	23.45	14.69%	8,941	8,948	0.07%
15	14.6	13.5	-7.15%	122.0	125.4	2.79%	23.79	27.01	13.52%	8,641	8,755	1.32%
16	12.0	10.8	-10.00%	106.6	109.9	3.06%	28.66	30.94	7.97%	7,066	7,263	2.78%
17	9.0	8.7	-2.83%	95.6	96.4	0.81%	30.93	35.33	14.26%	7,576	7,711	1.78%
18	66.7	58.7	-11.98%	360.7	343.1	-4.87%	15.66	19.93	27.31%	20,090	19,257	-4.15%
19	43.8	40.3	-8.00%	309.7	300.8	-2.85%	19.55	22.39	14.54%	15,551	15,195	-2.28%
20	33.8	30.9	-8.55%	274.6	267.9	-2.44%	20.02	24.24	21.10%	13,467	13,213	-1.89%
21	27.2	25.1	-7.75%	241.4	241.2	-0.08%	20.90	25.52	22.13%	17,354	16,670	-3.94%
22	23.6	21.1	-10.52%	220.6	218.9	-0.76%	26.58	26.59	8.16E-05	15,690	15,098	-3.77%
23	17.2	15.6	-9.39%	189.1	184.0	-2.70%	26.44	28.47	7.69%	13,315	12,712	-4.53%
24	13.0	12.1	-6.66%	158.5	158.2	-0.18%	25.92	30.10	16.12%	11,591	11,370	-1.90%
Mean			-19.35%			3.47%			11.54%			1.55%
Standard Deviation			25.54%			5.32%			19.75%			4.73%
Median			-10.14%			2.31%			14.62%			1.35%

Table 4.13. Comparison Metrics – CCFT Validation Set – PBC – Proposed for Design

Test #	Initial Tangent (kN/mm)			Peak Load (kN)			Deformation at Peak Load (mm)			Area Under Curve (kN-mm)		
	Expt.	Model	Error	Expt.	Model	Error	Expt.	Model	Error	Expt.	Model	Error
1	19,736.8	1,858.7	-90.58%	1,215.1	1,285.3	5.78%	6.47	3.42	-47.13%	23,993	23,553	-1.83%
2	10,590.6	597.8	-94.36%	751.7	810.7	7.85%	8.78	4.79	-45.42%	21,102	21,015	-0.41%
3	839.4	340.2	-59.48%	555.1	551.1	-0.73%	12.61	5.45	-56.72%	10,229	9,736	-4.82%
4	241.1	198.1	-17.85%	947.8	1,023.8	8.01%	15.61	18.24	16.87%	61,013	62,709	2.78%
5	88.2	64.3	-27.10%	575.6	636.6	10.59%	19.87	23.81	19.82%	41,725	44,263	6.08%
6	40.3	36.9	-8.31%	389.6	442.5	13.59%	22.94	27.67	20.65%	28,329	30,704	8.39%
7	56.9	45.4	-20.26%	608.6	642.7	5.60%	33.69	39.55	17.40%	49,693	53,465	7.59%
8	17.6	15.0	-14.82%	347.2	411.5	18.52%	59.38	56.89	-4.19%	28,974	33,013	13.94%
9	9.4	8.7	-7.07%	274.3	304.5	10.99%	65.00	66.86	2.86%	21,917	23,659	7.95%
10	89.0	89.7	0.74%	245.3	255.8	4.31%	8.49	8.08	-4.87%	9,536	8,590	-9.92%
11	51.2	53.0	3.61%	208.0	225.5	8.41%	10.52	11.56	9.87%	10,457	10,036	-4.02%
12	37.8	34.7	-8.41%	182.1	197.2	8.32%	12.89	15.27	18.47%	8,760	8,836	0.87%
13	30.0	24.4	-18.62%	162.1	172.5	6.46%	13.41	18.64	38.96%	9,606	9,800	2.01%
14	19.7	17.9	-8.78%	141.6	150.7	6.45%	20.44	21.51	5.21%	8,941	9,058	1.31%
15	14.6	13.7	-6.19%	122.0	131.8	8.04%	23.79	25.61	7.64%	8,641	8,887	2.84%
16	12.0	10.8	-9.60%	106.6	115.4	8.25%	28.66	29.96	4.54%	7,066	7,427	5.10%
17	9.0	8.7	-2.90%	95.6	101.1	5.68%	30.93	34.73	12.31%	7,576	7,861	3.76%
18	66.7	61.8	-7.36%	360.7	360.9	0.06%	15.66	16.68	6.57%	20,090	19,105	-4.91%
19	43.8	42.2	-3.69%	309.7	314.2	1.47%	19.55	20.35	4.09%	15,551	15,410	-0.91%
20	33.8	31.7	-6.11%	274.6	278.6	1.45%	20.02	22.15	10.65%	13,467	13,320	-1.09%
21	27.2	24.9	-8.59%	241.4	249.9	3.53%	20.90	23.39	11.95%	17,354	16,304	-6.05%
22	23.6	20.2	-14.09%	220.6	226.0	2.47%	26.58	24.13	-9.21%	15,690	14,805	-5.64%
23	17.2	14.6	-15.49%	189.1	188.7	-0.20%	26.44	26.38	-0.25%	13,315	12,643	-5.05%
24	13.0	11.3	-12.94%	158.5	161.3	1.78%	25.92	27.20	4.94%	11,591	11,196	-3.41%
Mean			-19.09%			6.11%			1.88%			0.61%
Standard Deviation			25.65%			4.61%			22.37%			5.71%
Median			-9.19%			6.11%			5.89%			0.23%

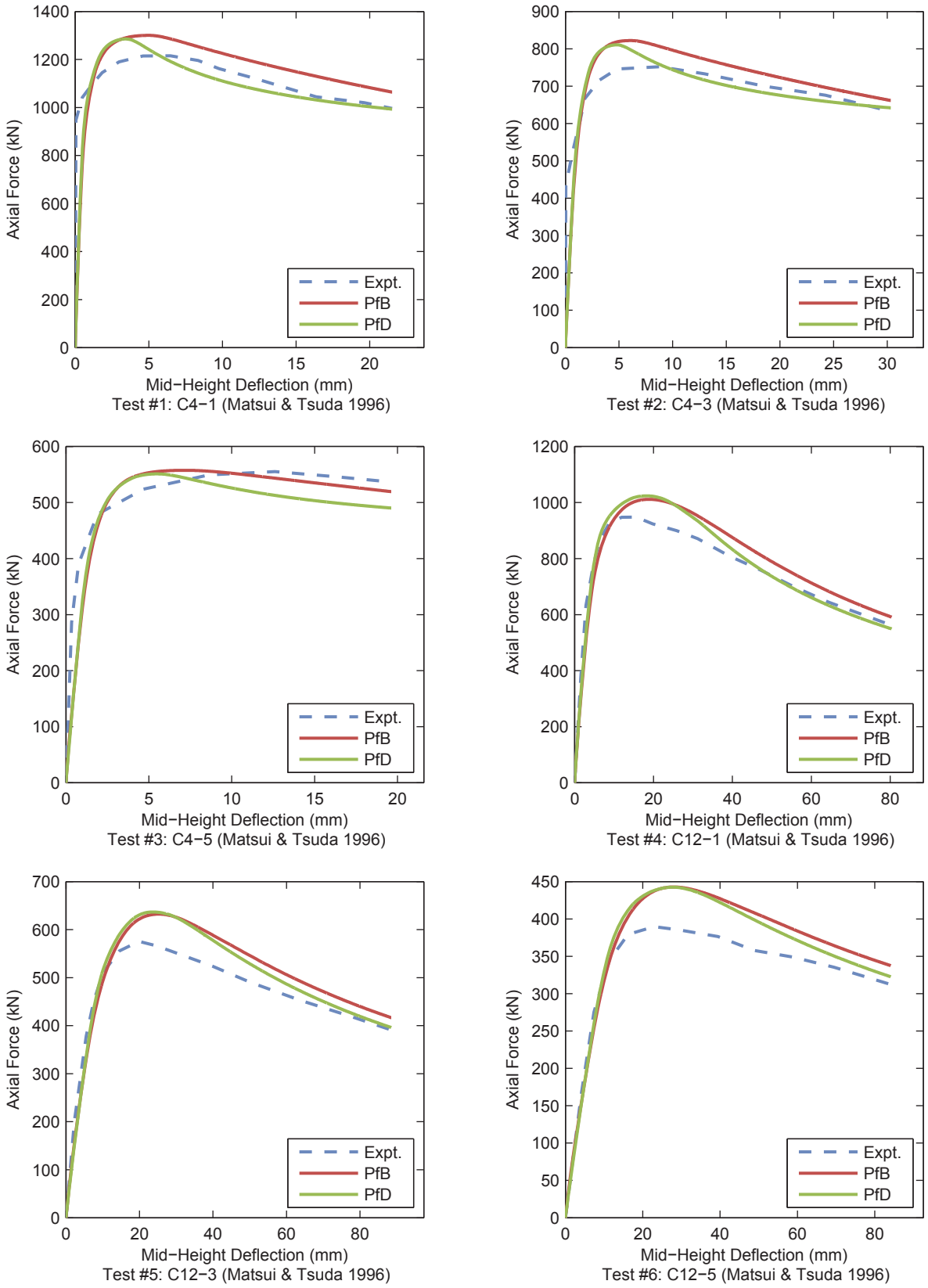

Figure 4.4. CCFT Validation Results – PBC

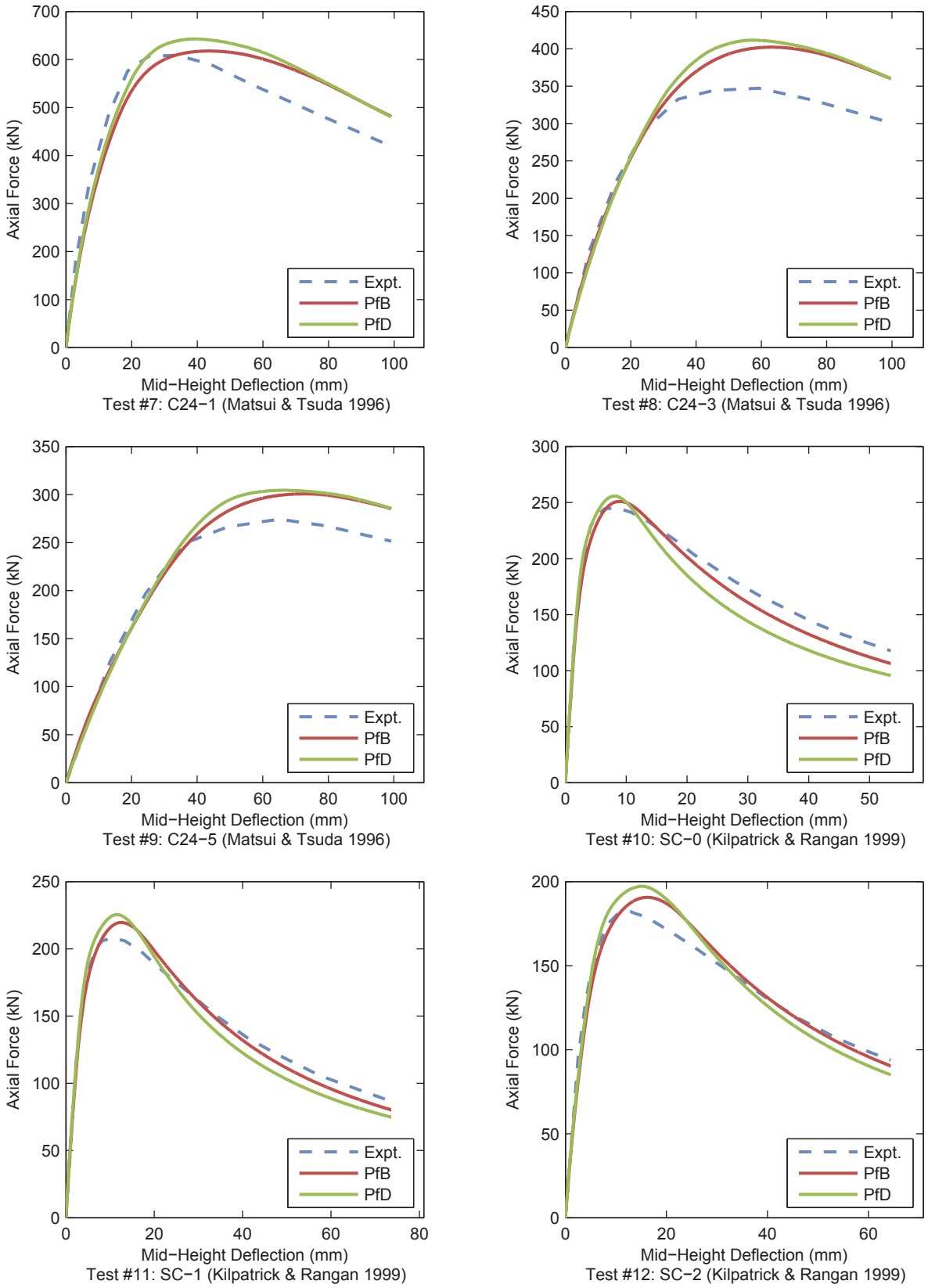

Figure 4.4. CCFT Validation Results – PBC (continued)

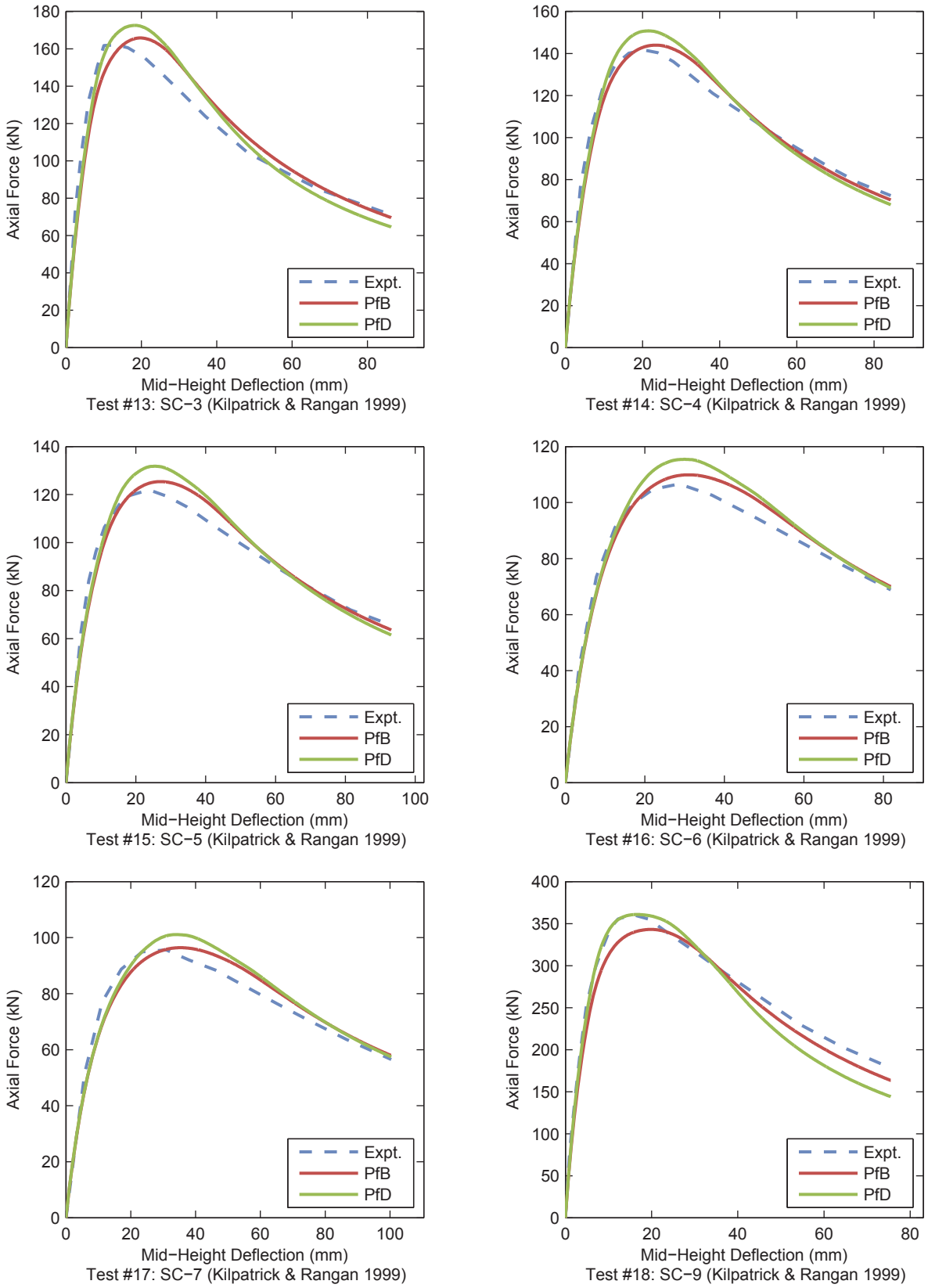

Figure 4.4. CCFT Validation Results – PBC (continued)

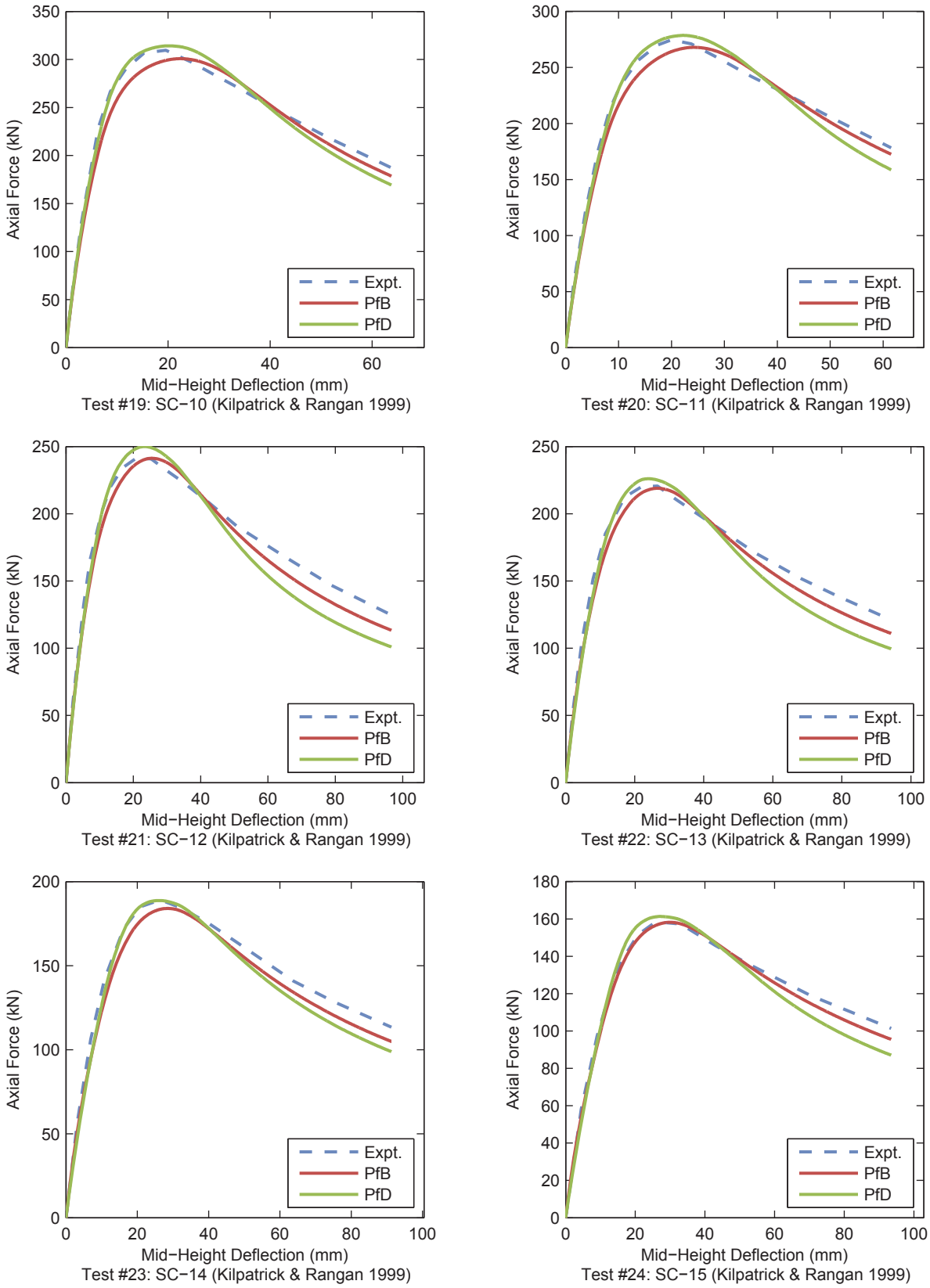

Figure 4.4. CCFT Validation Results – PBC (continued)

Table 4.14. Material and Geometric Properties – CCFT Validation Set – NBC

Test #	Author	Year	Specimen	D (mm)	t (mm)	D/t	f'_c (MPa)	F_y (MPa)	L (mm)	L/D	P (kN)	P/P_o
1	Ichinohe et al.	1991	C06F3M	300	5.83	51.5	64	420	600	2.0	1,932	0.30
2	Ichinohe et al.	1991	C06F5M	300	5.83	51.5	62	420	600	2.0	3,217	0.51
3	Ichinohe et al.	1991	C08F5M	300	8.40	35.7	65	401	600	2.0	3,481	0.48
4	Ichinohe et al.	1991	C12F5M	300	11.70	25.6	66	380	600	2.0	4,070	0.51
5	Nishiyama et al.	2002	EC4-A-4-035	150	2.96	50.7	40	283	450	3.0	363	0.35
6	Nishiyama et al.	2002	EC4-A-4-06	150	2.96	50.7	40	283	450	3.0	612	0.59
7	Nishiyama et al.	2002	EC4-C-2-035	300	2.96	101.4	25	283	900	3.0	832	0.34
8	Nishiyama et al.	2002	EC4-C-4-03	300	2.96	101.4	41	283	900	3.0	1,064	0.30
9	Nishiyama et al.	2002	EC4-C-4-04	300	2.96	101.4	41	283	900	3.0	1,418	0.40
10	Nishiyama et al.	2002	EC4-C-8-045	300	2.96	101.4	78	283	900	3.0	2,739	0.45
11	Nishiyama et al.	2002	EC4-D-4-04	450	2.96	152.0	40	283	1,350	3.0	2,943	0.40
12	Nishiyama et al.	2002	EC4-D-4-06	450	2.96	152.0	41	283	1,350	3.0	4,488	0.60
13	Nishiyama et al.	2002	EC6-A-4-02	122	4.54	26.9	40	579	366	3.0	274	0.20
14	Nishiyama et al.	2002	EC6-A-4-06	122	4.54	26.9	40	579	366	3.0	822	0.60
15	Nishiyama et al.	2002	EC6-C-2-06	239	4.54	52.6	25	579	717	3.0	1,772	0.60
16	Nishiyama et al.	2002	EC6-C-4-06	239	4.54	52.6	40	579	717	3.0	2,156	0.60
17	Nishiyama et al.	2002	EC6-C-8-03	239	4.54	52.6	78	579	717	3.0	1,547	0.30
18	Nishiyama et al.	2002	EC6-C-8-06	239	4.54	52.6	78	579	717	3.0	3,095	0.60
19	Nishiyama et al.	2002	EC6-C-4-025	239	4.54	52.6	41	579	717	3.0	907	0.25
20	Nishiyama et al.	2002	EC8-A-4-06	108	6.47	16.7	40	834	324	3.0	1,203	0.60
21	Nishiyama et al.	2002	EC8-C-4-015	222	6.47	34.3	40	834	666	3.0	753	0.15
22	Nishiyama et al.	2002	EC8-C-4-06	222	6.47	34.3	40	834	666	3.0	3,014	0.60
23	Nishiyama et al.	2002	EC8-C-4-03	222	6.47	34.3	41	834	666	3.0	1,515	0.30
24	Nishiyama et al.	2002	EC8-C-8-07	222	6.47	34.3	78	834	666	3.0	4,422	0.70

Table 4.15. Comparison Metrics – CCFT Validation Set – NBC – Proposed for Behavior

Test #	Initial Tangent			Peak Moment (kN-m)			Curvature at Peak Moment ($_{\kappa}Dx10^{3}$)			Area Under Curve		
	Expt.	Model	Error	Expt.	Model	Error	Expt.	Model	Error	Expt.	Model	Error
1	60.1	74.5	23.91%	381.9	340.2	-10.90%	112.7	20.1	-82.14%	43,219	38,886	-10.03%
2	62.0	66.1	6.53%	358.6	309.3	-13.76%	90.5	14.9	-83.58%	32,253	25,891	-19.73%
3	84.4	76.4	-9.51%	512.3	402.3	-21.47%	111.9	21.8	-80.49%	54,205	42,874	-20.90%
4	75.6	84.4	11.70%	705.4	484.6	-31.31%	143.6	35.9	-74.99%	88,221	65,696	-25.53%
5	6.9	9.0	29.42%	31.8	28.3	-11.17%	78.7	14.1	-82.10%	2,328	2,014	-13.47%
6	6.8	7.4	8.34%	26.6	24.0	-9.90%	79.4	10.2	-87.20%	1,951	1,432	-26.58%
7	46.0	48.4	5.33%	128.4	121.4	-5.52%	44.9	8.3	-81.50%	6,922	6,158	-11.04%
8	49.9	55.9	11.92%	149.8	150.7	0.64%	19.1	9.0	-52.73%	10,670	9,457	-11.37%
9	52.8	54.8	3.82%	156.2	151.0	-3.33%	19.4	7.6	-60.95%	11,829	8,862	-25.08%
10	52.3	64.1	22.52%	194.3	218.2	12.33%	9.5	7.4	-22.51%	9,209	7,656	-16.87%
11	154.7	161.8	4.58%	409.8	427.2	4.25%	7.2	6.5	-9.22%	25,384	21,337	-15.94%
12	148.5	146.1	-1.62%	347.1	365.8	5.38%	7.1	5.5	-22.81%	6,821	6,259	-8.24%
13	5.5	6.7	20.55%	46.8	43.6	-6.88%	64.7	44.5	-31.26%	2,834	2,771	-2.22%
14	4.9	5.7	16.17%	42.1	34.5	-18.11%	79.6	24.4	-69.30%	2,796	2,399	-14.18%
15	19.1	28.2	47.28%	130.2	128.6	-1.19%	37.6	16.6	-55.79%	9,128	8,628	-5.47%
16	28.1	30.5	8.48%	154.6	142.8	-7.66%	74.9	15.1	-79.90%	10,424	8,725	-16.30%
17	36.0	41.6	15.68%	217.2	217.4	0.07%	72.1	17.7	-75.43%	16,193	15,405	-4.87%
18	35.8	35.5	-0.75%	177.0	170.3	-3.83%	15.9	13.0	-18.47%	11,028	9,062	-17.83%
19	30.1	34.4	14.20%	171.6	186.4	8.59%	19.9	19.9	0.00%	2,621	2,981	13.73%
20	5.9	5.4	-8.25%	53.9	45.3	-16.03%	74.5	32.7	-56.10%	3,347	2,969	-11.31%
21	32.1	31.4	-2.36%	314.4	292.0	-7.13%	59.1	41.4	-29.90%	15,977	15,411	-3.55%
22	31.9	30.3	-5.00%	272.7	220.6	-19.13%	53.4	24.9	-53.37%	18,539	14,893	-19.67%
23	31.9	32.9	3.26%	293.6	284.3	-3.18%	42.4	30.4	-28.25%	10,281	10,351	0.68%
24	29.8	30.3	1.54%	261.4	204.0	-21.93%	40.0	20.2	-49.60%	14,667	11,054	-24.64%
Mean			9.49%			-7.55%			-53.65%			-12.93%
Standard Deviation			12.99%			10.50%			27.03%			9.57%
Median			7.44%			-7.01%			-55.94%			-13.83%

Table 4.16. Comparison Metrics – CCFT Validation Set – NBC – Proposed for Design

Test #	Initial Tangent			Peak Moment (kN-m)			Curvature at Peak Moment ($_{K}Dx10^{3}$)			Area Under Curve		
	Expt.	Model	Error	Expt.	Model	Error	Expt.	Model	Error	Expt.	Model	Error
1	60.1	78.8	31.00%	381.9	330.3	-13.51%	112.7	12.5	-88.87%	43,219	24,852	-42.50%
2	62.0	74.8	20.60%	358.6	292.1	-18.56%	90.5	9.2	-89.81%	32,253	6,624	-79.46%
3	84.4	87.1	3.26%	512.3	388.8	-24.10%	111.9	13.6	-87.86%	54,205	27,344	-49.55%
4	75.6	98.3	30.01%	705.4	467.8	-33.69%	143.6	16.6	-88.43%	88,221	50,941	-42.26%
5	6.9	9.4	35.04%	31.8	27.5	-13.43%	78.7	9.8	-87.60%	2,328	1,478	-36.51%
6	6.8	7.7	13.17%	26.6	22.8	-14.51%	79.4	7.2	-90.95%	1,951	425	-78.20%
7	46.0	49.2	7.12%	128.4	115.7	-9.91%	44.9	6.4	-85.72%	6,922	2,917	-57.86%
8	49.9	58.5	17.18%	149.8	145.9	-2.54%	19.1	6.8	-64.60%	10,670	2,587	-75.75%
9	52.8	57.5	8.90%	156.2	144.1	-7.79%	19.4	5.7	-70.40%	11,829	1,531	-87.05%
10	52.3	68.2	30.42%	194.3	208.2	7.19%	9.5	5.5	-42.54%	9,209	1,374	-85.08%
11	154.7	171.0	10.52%	409.8	414.4	1.11%	7.2	5.7	-21.25%	25,384	4,142	-83.68%
12	148.5	152.5	2.67%	347.1	345.9	-0.34%	7.1	4.2	-41.12%	6,821	1,750	-74.35%
13	5.5	6.8	22.42%	46.8	42.9	-8.46%	64.7	32.9	-49.14%	2,834	2,737	-3.41%
14	4.9	6.4	30.94%	42.1	33.7	-19.95%	79.6	21.0	-73.55%	2,796	2,299	-17.76%
15	19.1	30.2	58.15%	130.2	123.8	-4.86%	37.6	13.0	-65.46%	9,128	7,463	-18.24%
16	28.1	33.8	20.21%	154.6	135.5	-12.36%	74.9	11.0	-85.30%	10,424	5,459	-47.64%
17	36.0	44.0	22.38%	217.2	211.3	-2.72%	72.1	13.0	-82.00%	16,193	11,003	-32.05%
18	35.8	41.0	14.58%	177.0	161.4	-8.85%	15.9	8.5	-46.83%	11,028	2,265	-79.46%
19	30.1	35.4	17.73%	171.6	182.8	6.51%	19.9	17.0	-14.35%	2,621	2,975	13.51%
20	5.9	5.9	-1.09%	53.9	44.6	-17.20%	74.5	31.9	-57.25%	3,347	2,955	-11.71%
21	32.1	32.1	-0.11%	314.4	289.0	-8.07%	59.1	40.5	-31.50%	15,977	15,284	-4.34%
22	31.9	32.8	2.78%	272.7	216.0	-20.81%	53.4	21.6	-59.60%	18,539	14,272	-23.02%
23	31.9	33.9	6.23%	293.6	281.2	-4.21%	42.4	29.2	-31.20%	10,281	10,284	0.03%
24	29.8	35.1	17.62%	261.4	198.8	-23.95%	40.0	15.5	-61.32%	14,667	8,181	-44.22%
Mean			17.57%			-10.63%			-63.19%			-44.19%
Standard Deviation			13.82%			10.00%			23.86%			31.26%
Median			17.40%			-9.38%			-65.03%			-43.36%

Table 4.17. Comparison Metrics – CCFT Validation Set – NBC (section) – Proposed for Behavior

Test #	Initial Tangent			Peak Moment (kN-m)			Curvature at Peak Moment ($_{\kappa}Dx10^{3}$)			Area Under Curve		
	Expt.	Model	Error	Expt.	Model	Error	Expt.	Model	Error	Expt.	Model	Error
1	60.1	74.3	23.49%	381.9	345.5	-9.53%	112.7	29.8	-73.55%	43,219	41,435	-4.13%
2	62.0	66.0	6.43%	358.6	314.7	-12.24%	90.5	17.7	-80.39%	32,253	28,979	-10.15%
3	84.4	76.1	-9.76%	512.3	413.0	-19.39%	111.9	32.1	-71.35%	54,205	47,089	-13.13%
4	75.6	83.8	10.82%	705.4	508.0	-27.99%	143.6	73.6	-48.73%	88,221	72,697	-17.60%
5	6.9	9.0	29.20%	31.8	29.4	-7.54%	78.7	33.8	-57.10%	2,328	2,231	-4.13%
6	6.8	7.4	8.23%	26.6	25.1	-5.65%	79.4	17.5	-77.90%	1,951	1,855	-4.89%
7	46.0	48.4	5.24%	128.4	123.4	-3.92%	44.9	11.4	-74.65%	6,922	6,741	-2.62%
8	49.9	55.8	11.86%	149.8	153.7	2.62%	19.1	12.3	-35.81%	10,670	10,789	1.11%
9	52.8	54.9	3.91%	156.2	154.3	-1.26%	19.4	9.5	-51.08%	11,829	11,027	-6.78%
10	52.3	64.3	22.96%	194.3	224.3	15.46%	9.5	8.5	-10.03%	9,209	10,975	19.17%
11	154.7	162.0	4.71%	409.8	435.9	6.36%	7.2	8.1	12.65%	25,384	28,645	12.85%
12	148.5	146.6	-1.27%	347.1	376.7	8.54%	7.1	6.2	-12.81%	6,821	8,004	17.34%
13	5.5	6.6	19.80%	46.8	45.6	-2.68%	64.7	68.6	6.07%	2,834	2,839	0.18%
14	4.9	5.6	14.63%	42.1	37.9	-9.85%	79.6	62.0	-22.10%	2,796	2,774	-0.76%
15	19.1	28.1	46.80%	130.2	137.5	5.67%	37.6	30.3	-19.44%	9,128	10,364	13.54%
16	28.1	30.5	8.36%	154.6	152.3	-1.49%	74.9	24.0	-68.00%	10,424	10,670	2.35%
17	36.0	41.5	15.51%	217.2	225.5	3.78%	72.1	29.2	-59.47%	16,193	16,967	4.78%
18	35.8	35.6	-0.42%	177.0	181.9	2.73%	15.9	19.1	20.08%	11,028	11,742	6.47%
19	30.1	34.3	13.83%	171.6	189.7	10.52%	19.9	19.9	0.00%	2,621	3,004	14.64%
20	5.9	5.4	-9.53%	53.9	51.6	-4.29%	74.5	74.5	0.00%	3,347	3,346	-0.04%
21	32.1	31.2	-2.75%	314.4	300.5	-4.41%	59.1	59.1	0.00%	15,977	15,639	-2.12%
22	31.9	30.2	-5.39%	272.7	242.6	-11.04%	53.4	56.6	6.02%	18,539	17,314	-6.61%
23	31.9	32.8	2.91%	293.6	296.4	0.95%	42.4	42.4	0.00%	10,281	10,586	2.97%
24	29.8	30.2	1.21%	261.4	231.8	-11.30%	40.0	41.9	4.71%	14,667	13,645	-6.97%
Mean			9.20%			-3.16%			-29.70%			0.65%
Standard Deviation			12.96%			9.74%			34.20%			9.54%
Median			7.33%			-3.30%			-20.77%			-0.40%

Table 4.18. Comparison Metrics – CCFT Validation Set – NBC (section) – Proposed for Design

Test #	Initial Tangent			Peak Moment (kN-m)			Curvature at Peak Moment ($_{\kappa}Dx10^{3}$)			Area Under Curve		
	Expt.	Model	Error	Expt.	Model	Error	Expt.	Model	Error	Expt.	Model	Error
1	60.1	78.5	30.61%	381.9	332.3	-12.98%	112.7	13.7	-87.88%	43,219	29,689	-31.31%
2	62.0	74.7	20.34%	358.6	294.7	-17.83%	90.5	10.0	-88.98%	32,253	10,924	-66.13%
3	84.4	86.8	2.93%	512.3	393.4	-23.20%	111.9	15.1	-86.53%	54,205	34,510	-36.33%
4	75.6	97.9	29.47%	705.4	475.0	-32.66%	143.6	19.5	-86.41%	88,221	60,054	-31.93%
5	6.9	9.4	34.77%	31.8	28.0	-11.88%	78.7	11.3	-85.60%	2,328	1,814	-22.05%
6	6.8	7.7	12.85%	26.6	23.4	-12.12%	79.4	8.2	-89.70%	1,951	827	-57.60%
7	46.0	49.2	7.06%	128.4	117.0	-8.95%	44.9	6.8	-84.76%	6,922	4,080	-41.05%
8	49.9	58.4	17.11%	149.8	147.8	-1.34%	19.1	7.4	-61.10%	10,670	4,345	-59.28%
9	52.8	57.5	8.86%	156.2	146.1	-6.48%	19.4	6.2	-67.93%	11,829	2,761	-76.66%
10	52.3	68.4	30.77%	194.3	212.2	9.25%	9.5	5.9	-38.27%	9,209	1,985	-78.44%
11	154.7	171.0	10.55%	409.8	420.9	2.71%	7.2	6.2	-13.60%	25,384	6,105	-75.95%
12	148.5	153.0	3.03%	347.1	353.6	1.88%	7.1	4.5	-36.97%	6,821	2,493	-63.45%
13	5.5	6.7	21.83%	46.8	44.6	-4.74%	64.7	68.6	6.07%	2,834	2,809	-0.86%
14	4.9	6.3	29.68%	42.1	36.3	-13.80%	79.6	35.3	-55.60%	2,796	2,690	-3.79%
15	19.1	30.2	58.00%	130.2	129.8	-0.29%	37.6	17.1	-54.51%	9,128	9,379	2.76%
16	28.1	33.8	20.40%	154.6	141.2	-8.65%	74.9	12.5	-83.30%	10,424	8,117	-22.13%
17	36.0	44.0	22.32%	217.2	216.0	-0.57%	72.1	14.8	-79.46%	16,193	13,684	-15.50%
18	35.8	41.1	14.99%	177.0	167.6	-5.32%	15.9	9.4	-41.07%	11,028	3,582	-67.52%
19	30.1	35.3	17.32%	171.6	186.3	8.57%	19.9	19.8	-0.10%	2,621	3,002	14.53%
20	5.9	5.7	-3.13%	53.9	51.2	-5.04%	74.5	74.5	0.00%	3,347	3,329	-0.56%
21	32.1	32.0	-0.50%	314.4	297.5	-5.37%	59.1	59.1	0.00%	15,977	15,517	-2.88%
22	31.9	32.7	2.48%	272.7	234.5	-14.02%	53.4	40.1	-24.92%	18,539	16,841	-9.16%
23	31.9	33.8	5.95%	293.6	292.9	-0.23%	42.4	42.4	0.00%	10,281	10,527	2.39%
24	29.8	35.0	17.42%	261.4	216.3	-17.25%	40.0	20.0	-50.01%	14,667	11,811	-19.47%
Mean			17.30%			-7.51%			-50.44%			-31.77%
Standard Deviation			13.87%			9.74%			34.65%			29.71%
Median			17.22%			-5.92%			-55.06%			-26.72%

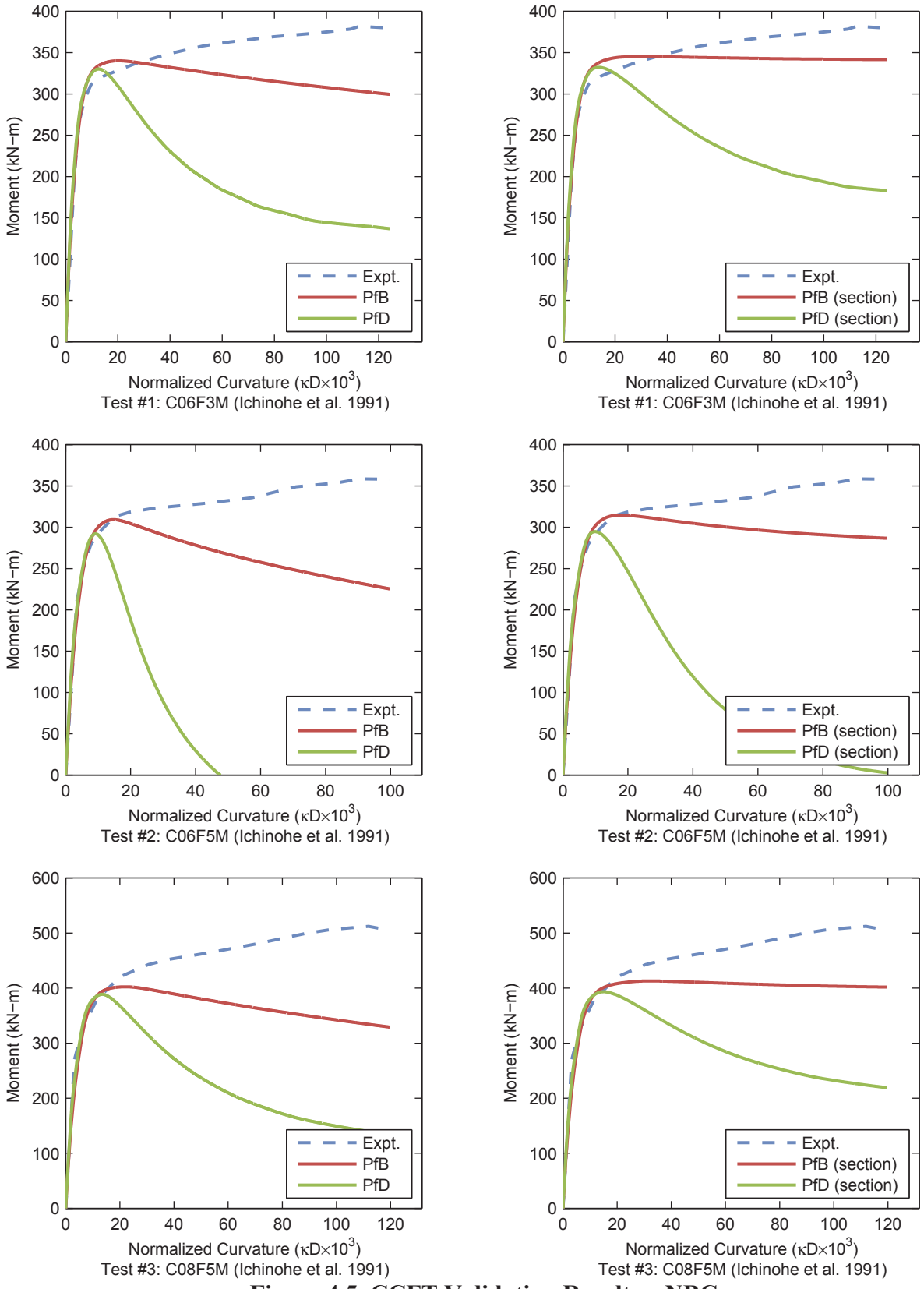

Figure 4.5. CCFT Validation Results – NBC

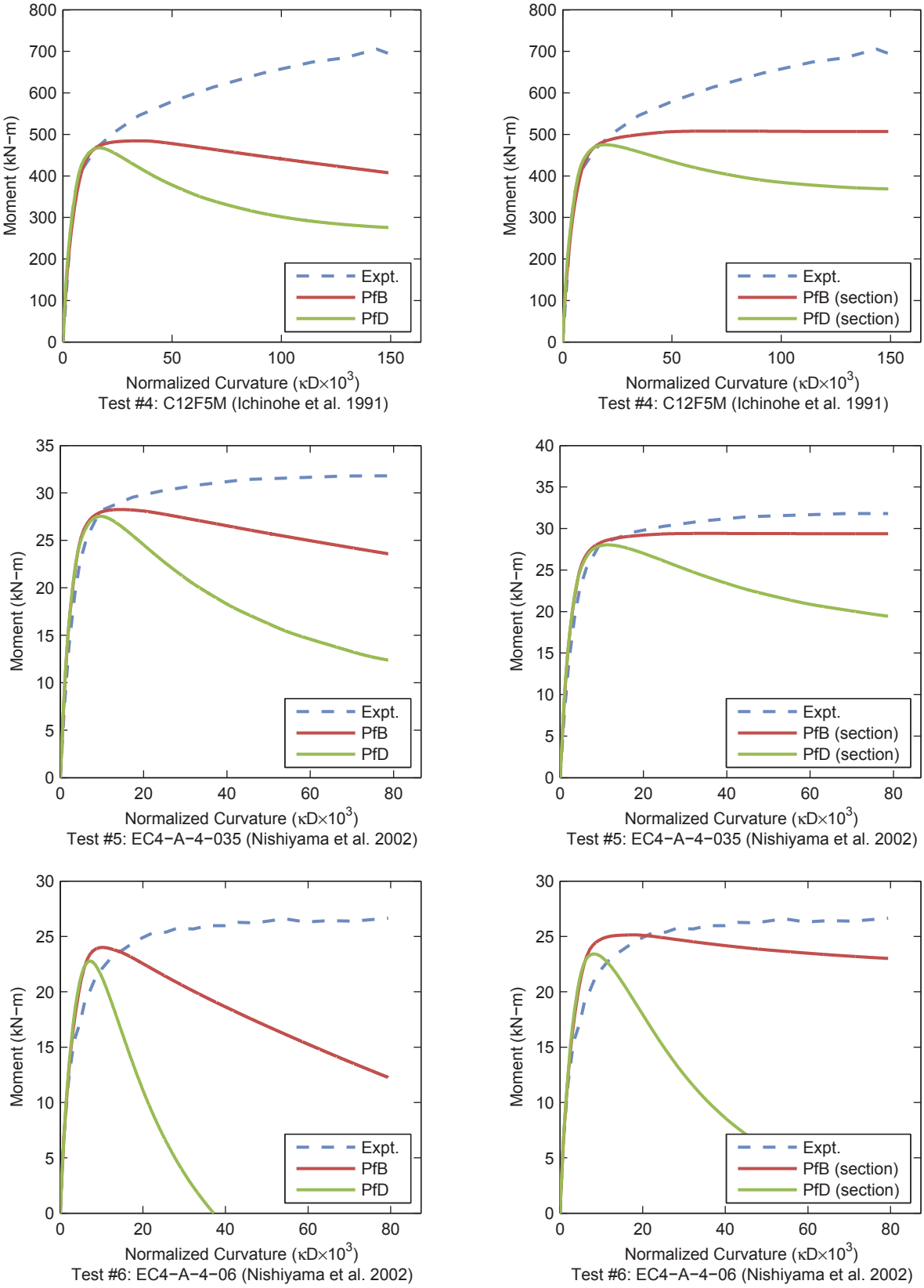

Figure 4.5. CCFT Validation Results – NBC (continued)

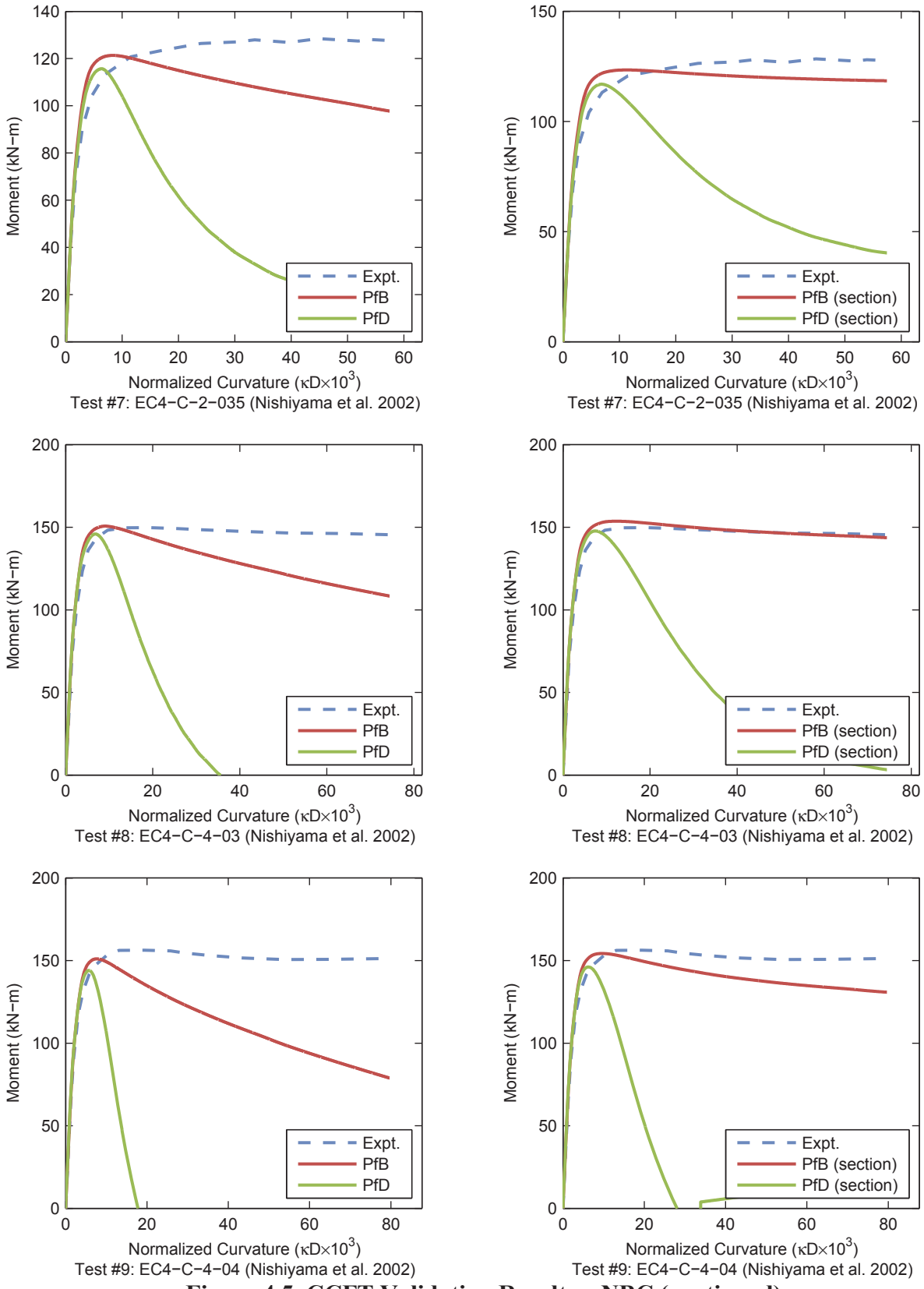

Figure 4.5. CCFT Validation Results – NBC (continued)

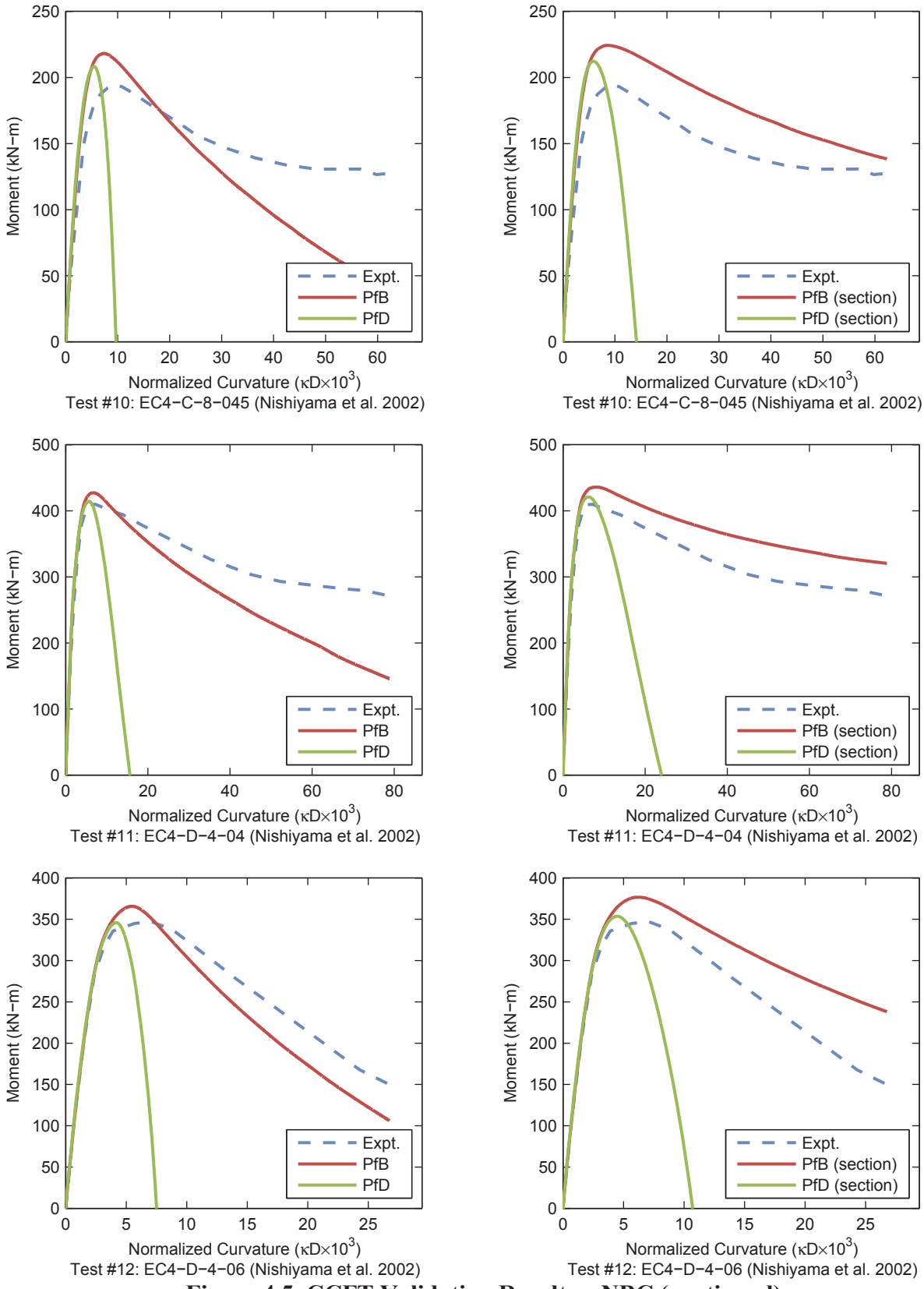

Figure 4.5. CCFT Validation Results – NBC (continued)

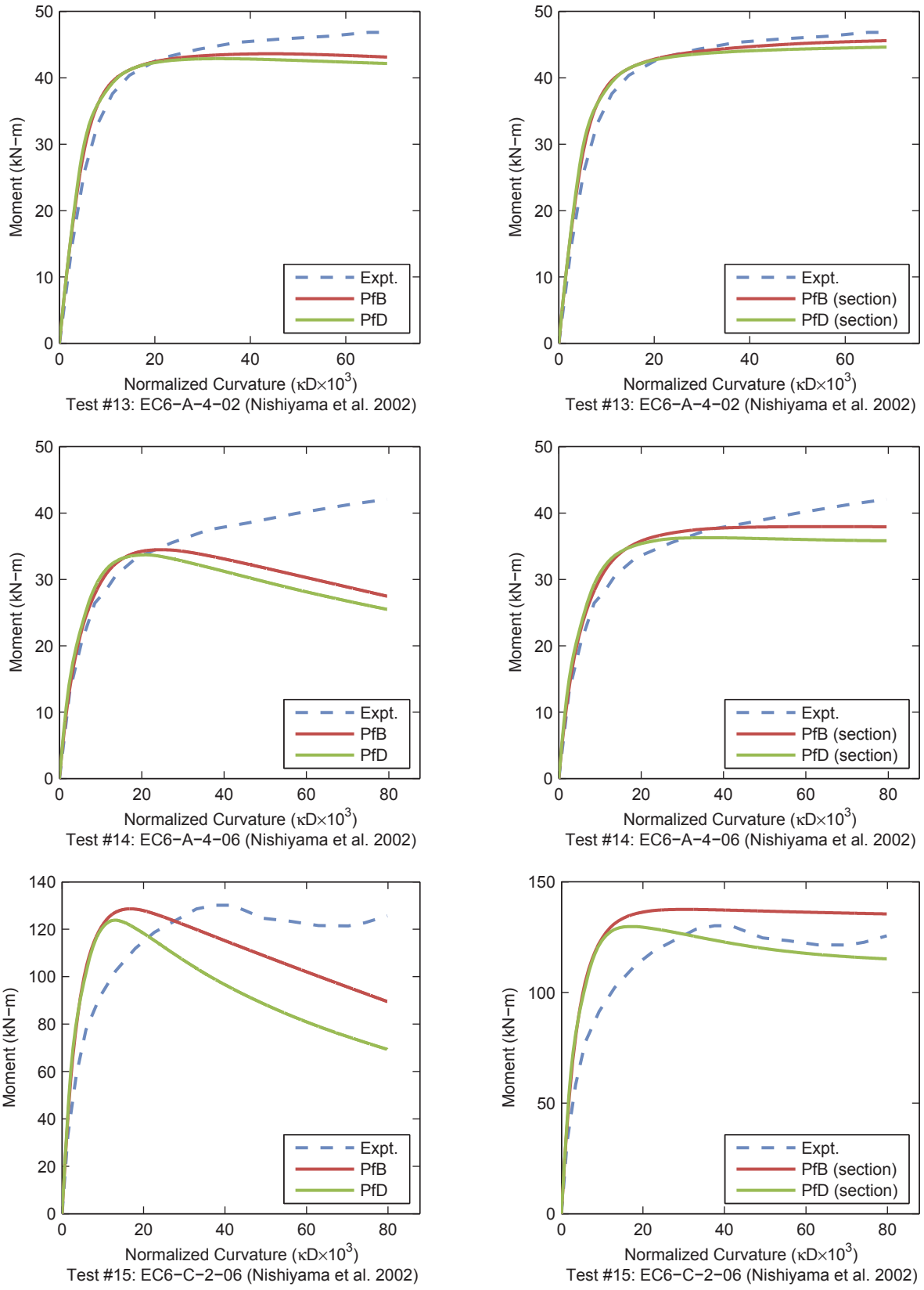

Figure 4.5. CCFT Validation Results – NBC (continued)

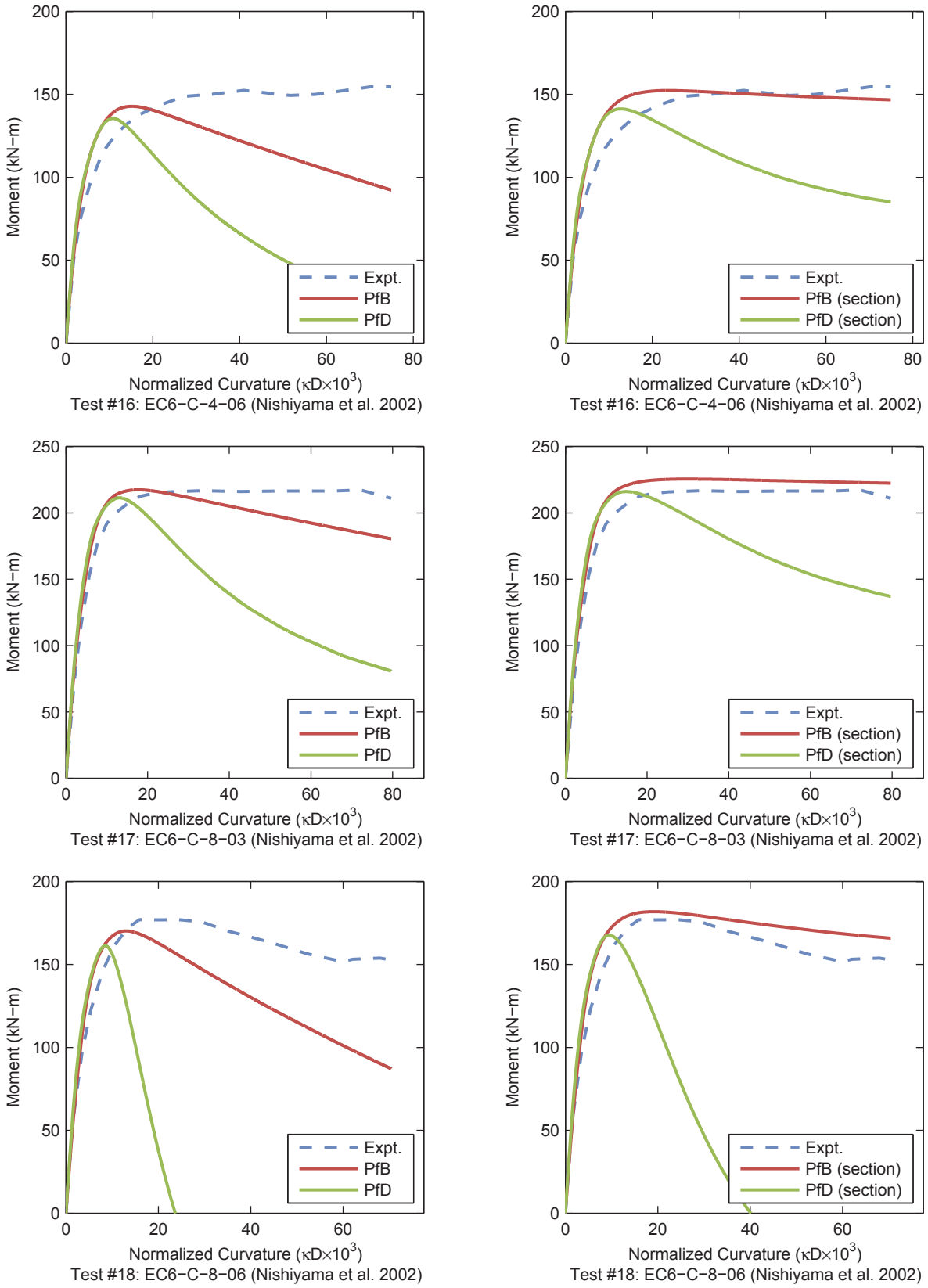

Figure 4.5. CCFT Validation Results – NBC (continued)

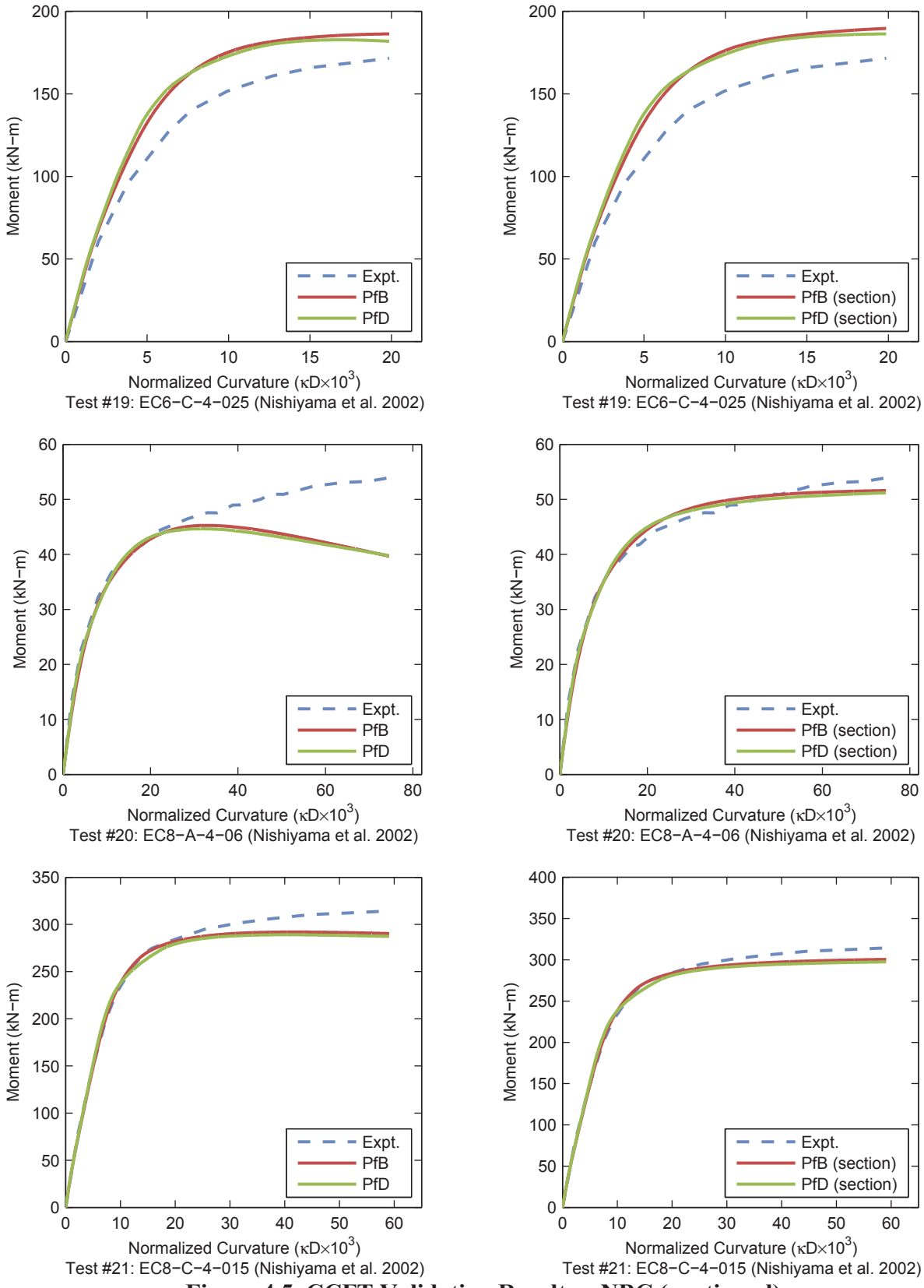

Figure 4.5. CCFT Validation Results – NBC (continued)

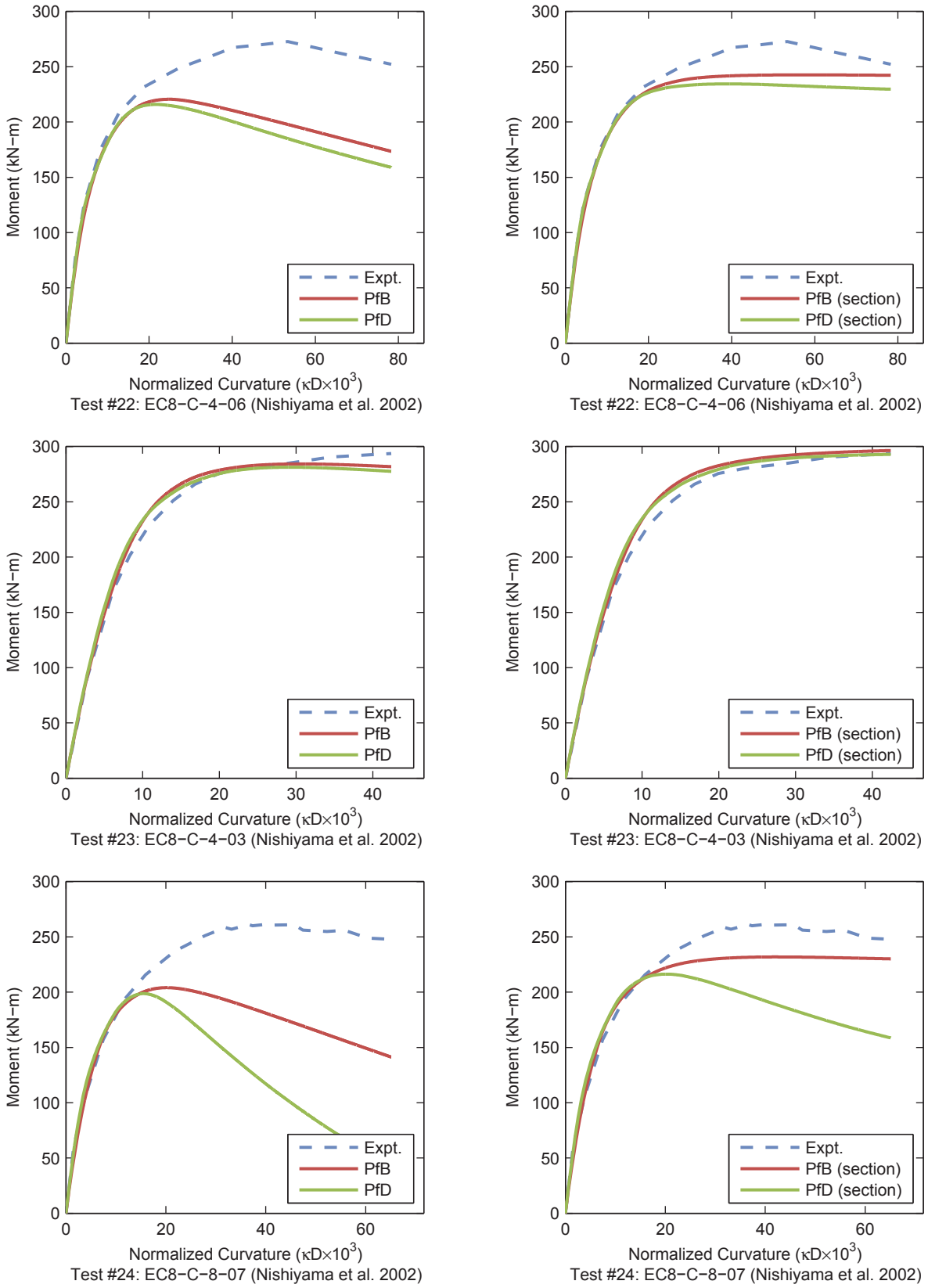

Figure 4.5. CCFT Validation Results – NBC (continued)

4.4.2 Cyclic Validation Results – Elchalakani and Zhao 2008

Elchalakani and Zhao (2008) performed a series of tests on CCFT members. The loading configuration was the same as the monotonic pure bending beam tests described above (Figure 4.1) and the same mesh density was used. Measured material and geometric properties of the specimens are given in Table 4.19, results are shown in Figure 4.6.

Table 4.19. Material and Geometric Properties – Elchalakani and Zhao 2008

Test #	Specimen	D (mm)	t (mm)	D/t	f'_c (MPa)	F_y (MPa)	Bending Span (mm)
1	F19I1	60	2.95	20.5	23.1	413	800
2	F11I1	87	2.28	38.3	23.1	473	800
3	F04I1	110	1.25	88.3	23.1	430	800
4	F01I1	109	1.05	104.1	23.1	457	800
5	F16I1	89	3.09	28.8	23.1	473	800
6	F15I1-S	76	2.35	32.4	23.1	370	800
7	F14I3	89	2.52	35.5	23.1	378	800

The following observations are made regarding the validation results:

- The model captures the experimental behavior well, accurately capturing the initial stiffness, peak strength, and unloading response.
- The specimens with thicker tubes exhibit fuller hysteresis loops while the specimen with the thinner tube exhibits a pinching behavior. With the addition of the reduced size of the elastic range and plastic modulus the model is able to capture this behavior well.

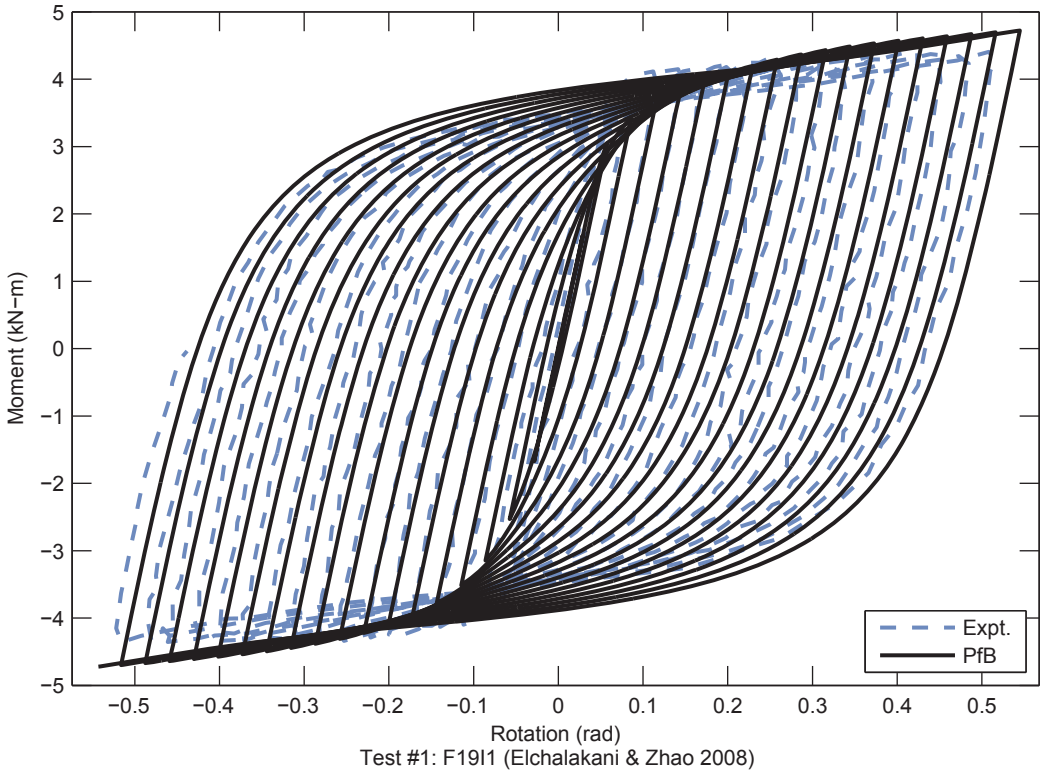

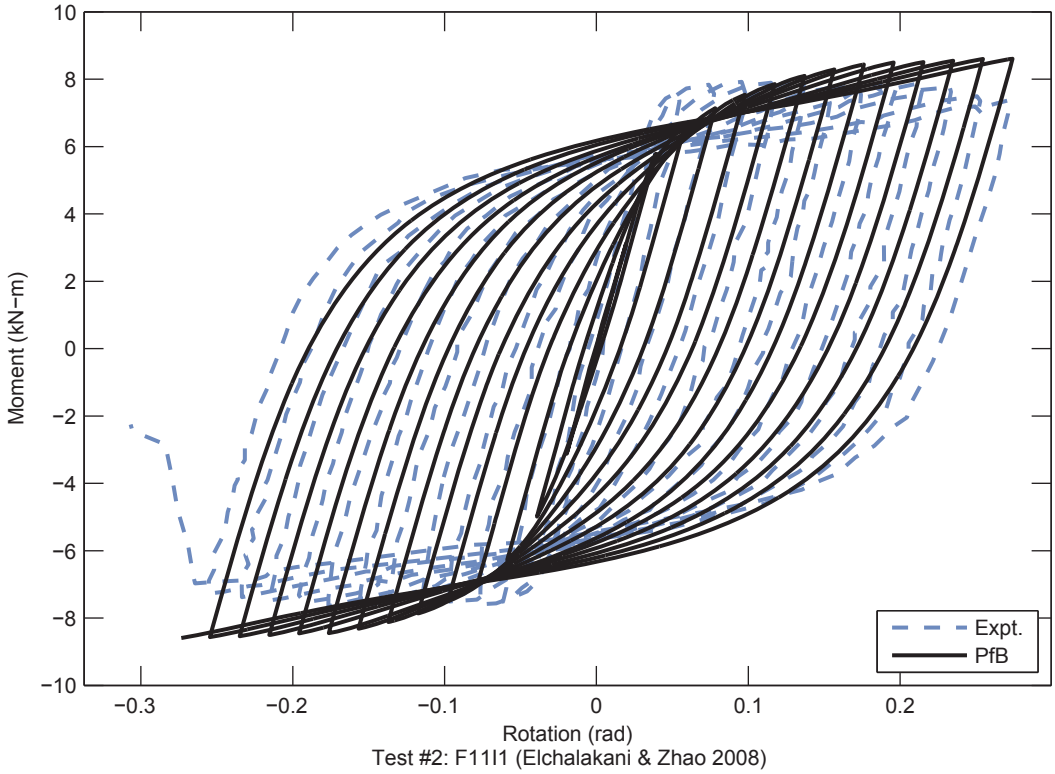

Figure 4.6. CCFT Validation Results – Elchalakani and Zhao 2008

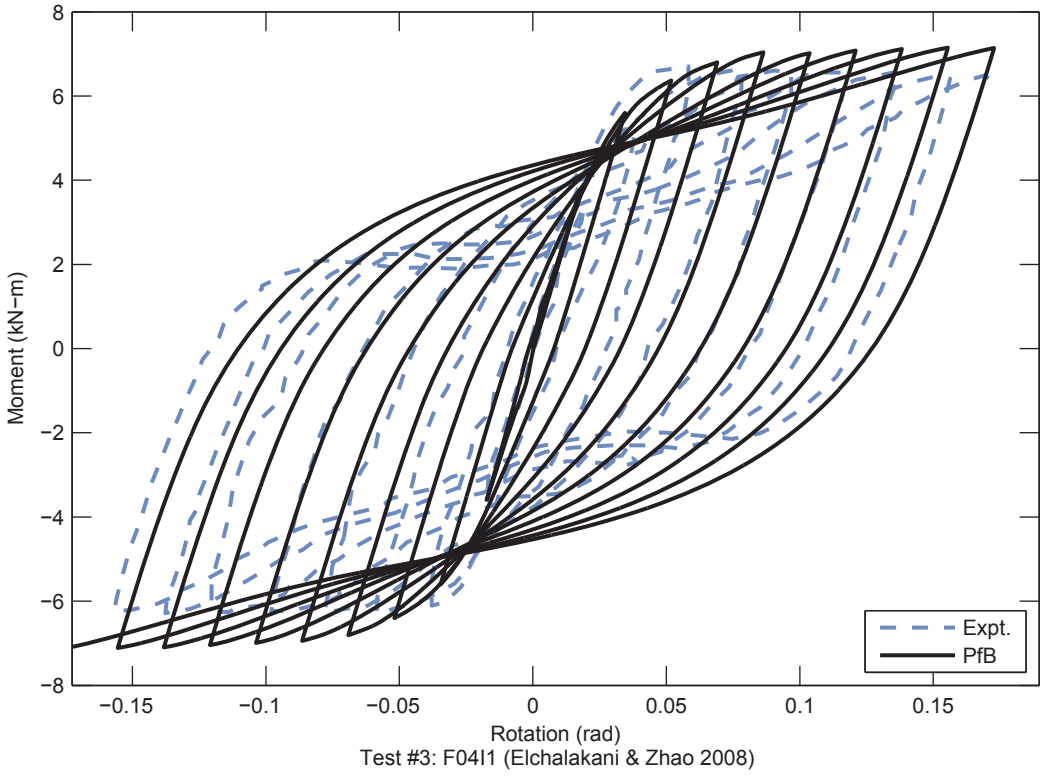

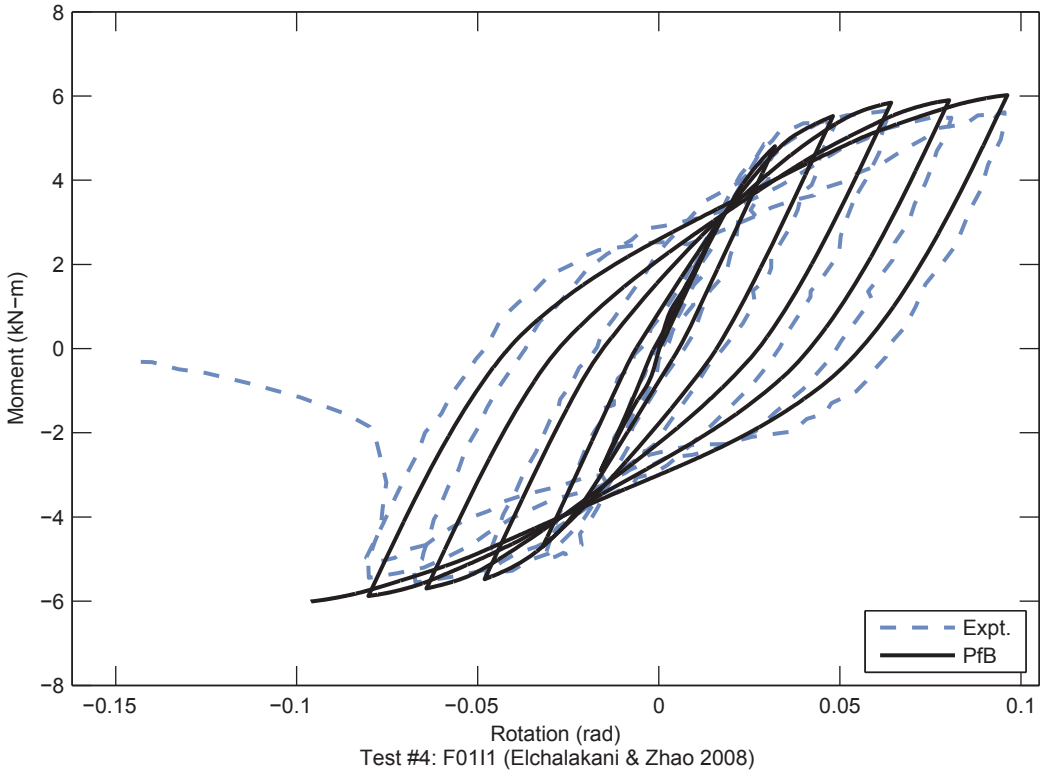

Figure 4.6. CCFT Validation Results – Elchalakani and Zhao 2008 (Continued)

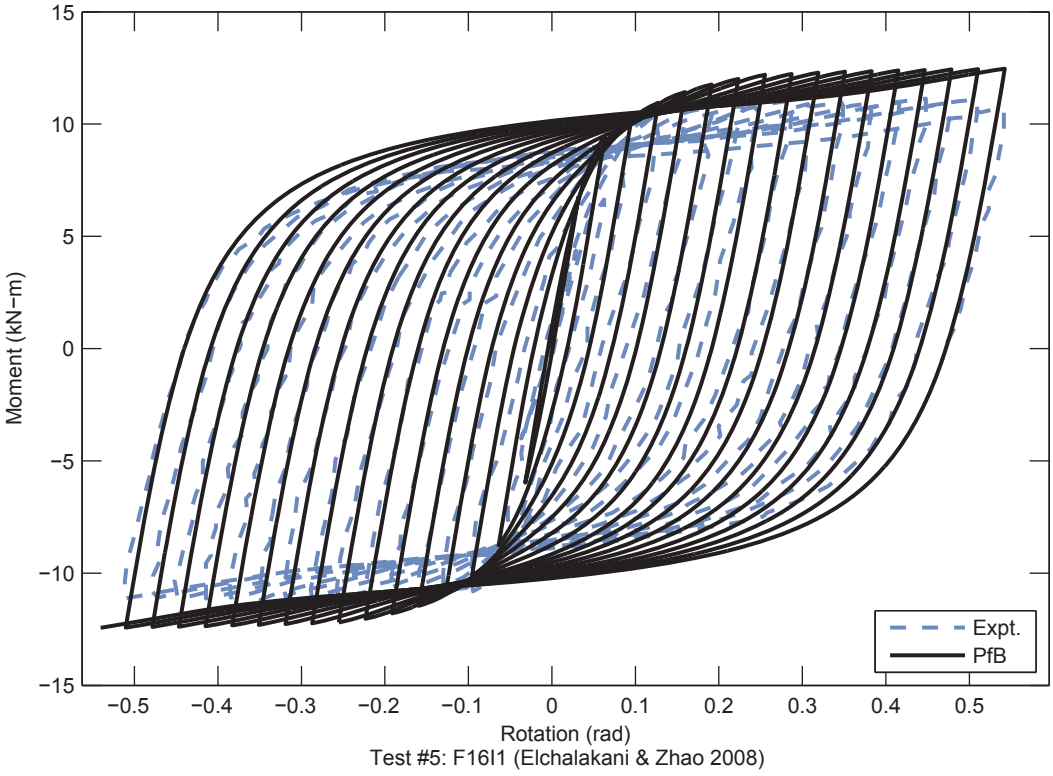

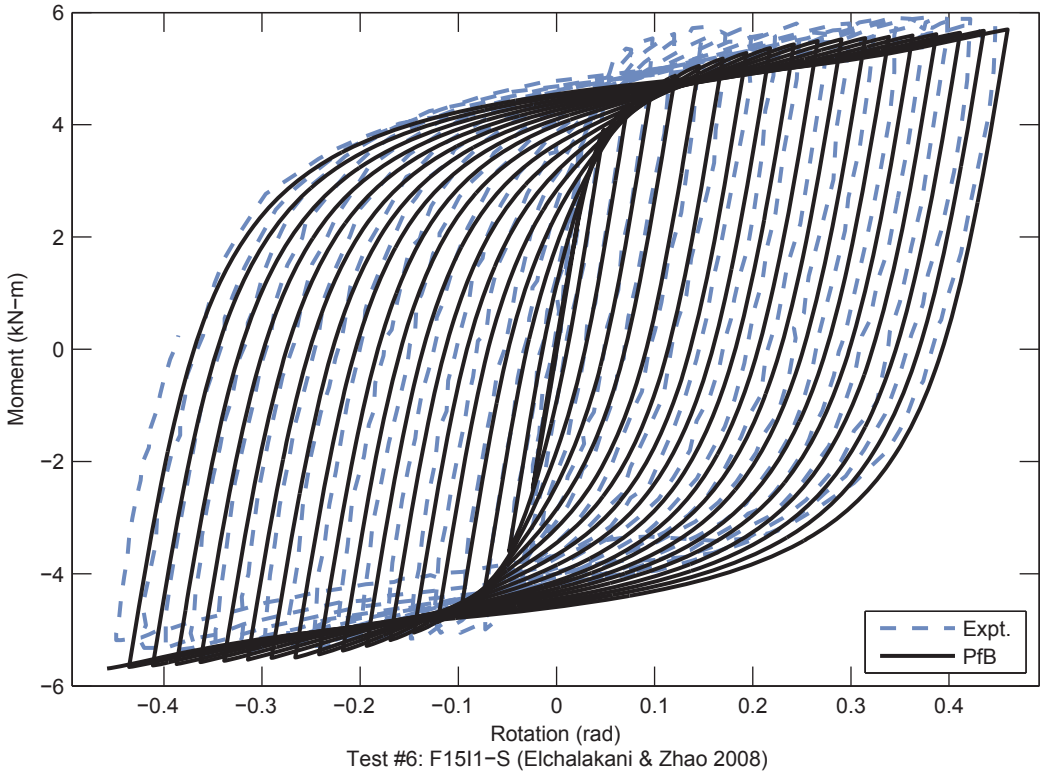

Figure 4.6. CCFT Validation Results – Elchalakani and Zhao 2008 (Continued)

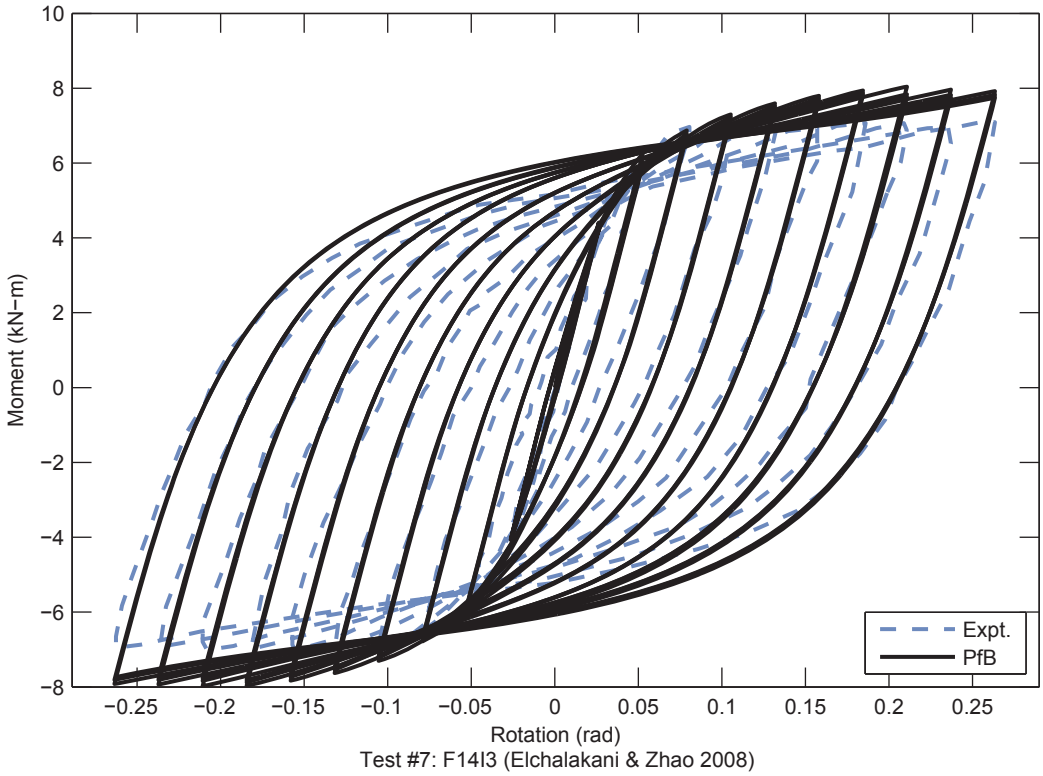

Figure 4.6. CCFT Validation Results – Elchalakani and Zhao 2008 (Continued)

4.5 Rectangular Concrete-Filled Steel Tube Members

4.5.1 Monotonic Validation Results

The experimental results used in the monotonic validation of RCFT members were taken from a variety of sources Table 4.20. Summary error statistics are given in Table 4.21; detailed results are presented in the remainder of this section.

Table 4.20. References - RCFT Monotonic Validation

Loading Type	References	Results
SC	Grauers (1993) Nishiyama et al. (2002) Schneider (1998) Tomii and Sakino (1979) Varma (2000)	Measured Material and Geometric Properties: Table 4.22 PfB Error Statistics: Table 4.23 PfD Error Statistics: Table 4.24
BM	Assi et al. (2003) Gho and Liu (2004) Lu and Kennedy (1994) Tomii and Sakino (1979)	Measured Material and Geometric Properties: Table 4.25 PfB Error Statistics: Table 4.26 PfD Error Statistics: Table 4.27
PBC	Bridge (1976) Grauers (1993) Shakir-Khalil and Zeghiche (1989)	Measured Material and Geometric Properties: Table 4.28 PfB Error Statistics: Table 4.29 PfD Error Statistics: Table 4.30
NBC	Nakahara and Sakino (1998) Tomii and Sakino (1979) Varma (2000)	Measured Material and Geometric Properties: Table 4.31 PfB Error Statistics: Table 4.32 PfD Error Statistics: Table 4.33 PfB (section) Error Statistics: Table 4.34 PfD (section) Error Statistics: Table 4.35

The PfB model is very successful at predicting peak strength and area under the curve, as the median error is less than 10% for both of those metrics for all loading types. Initial stiffness and deformation at peak strength were not directly targeted in the calibration process and have comparatively larger errors. The PfD model captures the pre-peak behavior as well as the PfB model, with median errors of peak strength less than 10% for all loading types. The following additional observations are made regarding the monotonic validation results:

- For some of the SC specimens (#5-#10, #16, #22-#24, Table 4.22), the experiments exhibit a sharp drop in strength immediately following the peak. The PfD model often captures this drop better than the PfB model, although the PfB model captures the area under the curve better. The PfD model is better capable of capturing the sharp drop because of the greater post-peak degradation in the concrete constitutive relation. After the sharp drop, the experiments often show an increase in strength as the confinement pressure increases. The PfB model assumes constant confining pressure and thus does not capture the sharp drop well but does capture the average behavior well.
- The response of the PfB model for the SC specimens is often near an elastic perfectly plastic response.

- For some of the BM specimens, a wavy response is observed from the PfB model. This is likely due to the peak being reached at successive integration points in the beam, possible because of the hardening behavior after the initial post peak degradation.
- For the biaxial loaded PBC specimens, the relative proportions of the displacements are not predicted correctly, indicating that the path taken by the specimen (in Y-Z lateral deformation space) in the model was different than in the experiment. The peak strengths, however, are captured well.

Table 4.21. Summary Error Statistics – RCFT Monotonic Validation

Type	# of Spec.	Initial Stiffness			Peak Load			Deformation at Peak Load			Area Under Curve		
		Mean	Std.	Median	Mean	Std.	Median	Mean	Std.	Median	Mean	Std.	Median
SC	28	47.0%	54.3%	30.1%	-1.7%	10.0%	-3.7%	-27.1%	30.7%	-32.9%	11.5%	15.4%	8.9%
BM	18	16.3%	20.5%	15.2%	-6.8%	7.7%	-4.5%	---	---	---	-3.0%	7.1%	-0.7%
PBC	19	-6.2%	15.7%	-7.3%	-1.3%	7.2%	-3.2%	9.4%	27.8%	4.3%	-6.7%	15.1%	-7.3%
NBC	14	2.9%	18.1%	8.4%	-5.4%	5.3%	-5.5%	-2.1%	25.0%	0.0%	-9.5%	13.7%	-7.3%
NBC (section)	14	2.9%	18.1%	9.5%	-2.3%	5.6%	-3.7%	91.7%	156.0%	42.2%	3.7%	10.9%	-0.3%

(a) Proposed for Behavior

Type	# of Spec.	Initial Stiffness			Peak Load			Deformation at Peak Load			Area Under Curve		
		Mean	Std.	Median	Mean	Std.	Median	Mean	Std.	Median	Mean	Std.	Median
SC	28	51.1%	55.6%	34.4%	-4.5%	11.2%	-6.7%	-37.2%	28.1%	-40.2%	-16.7%	8.7%	-15.6%
BM	18	15.8%	19.9%	14.5%	-10.2%	7.6%	-7.7%	---	---	---	-6.1%	7.1%	-4.3%
PBC	19	-6.1%	14.7%	-5.6%	-2.0%	6.8%	-5.2%	3.8%	26.2%	6.2%	-10.3%	14.7%	-7.1%
NBC	14	3.2%	18.1%	9.5%	-9.8%	6.3%	-9.7%	-34.4%	27.9%	-35.5%	-45.7%	25.1%	-46.1%
NBC (section)	14	3.3%	18.2%	9.9%	-8.3%	7.1%	-7.3%	-32.3%	34.0%	-32.9%	-32.0%	19.1%	-28.4%

(b) Proposed for Design

Table 4.22. Material and Geometric Properties – RCFT Validation Set – SC

Test #	Author	Year	Specimen	H (mm)	B (mm)	t (mm)	H/t	f'_c (MPa)	F_y (MPa)	L (mm)	L/H
1	Tomii and Sakino	1979	I-A	100	100	2.29	43.7	32	194	300	3.0
2	Tomii and Sakino	1979	II-A	100	100	2.20	45.5	21	339	300	3.0
3	Tomii and Sakino	1979	III-A	100	100	2.99	33.4	21	288	300	3.0
4	Tomii and Sakino	1979	IV-A	100	100	4.25	23.5	20	284	300	3.0
5	Grauers	1993	1 (stub)	120	120	5.00	24.0	47	304	500	4.2
6	Grauers	1993	2 (stub)	120	120	5.00	24.0	46	438	500	4.2
7	Grauers	1993	3 (stub)	120	120	5.00	24.0	96	327	500	4.2
8	Grauers	1993	4 (stub)	120	120	5.00	24.0	96	439	500	4.2
9	Grauers	1993	8 (stub)	120	120	8.00	15.0	103	323	500	4.2
10	Grauers	1993	27 (stub)	250	250	8.00	31.3	33	379	500	2.0
11	Schneider	1998	S1	127	127	3.15	40.4	30	356	611	4.8
12	Schneider	1998	S2	127	127	4.34	29.2	26	357	609	4.8
13	Schneider	1998	S3	127	127	4.55	27.9	24	322	610	4.8
14	Schneider	1998	S4	127	125	5.67	22.3	24	312	607	4.8
15	Schneider	1998	S5	127	127	7.47	17.0	24	347	611	4.8
16	Schneider	1998	R1	152	77	3.00	50.8	30	430	609	4.0
17	Schneider	1998	R2	153	77	4.47	34.2	26	383	611	4.0
18	Schneider	1998	R3	152	102	4.32	35.3	26	413	610	4.0
19	Schneider	1998	R4	153	103	4.57	33.4	24	365	611	4.0
20	Schneider	1998	R5	151	101	5.72	26.5	24	324	606	4.0
21	Schneider	1998	R6	152	102	7.34	20.8	24	358	609	4.0
22	Nishiyama et al.	2002	CR4-D-8	324	324	4.38	74.0	80	262	972	3.0
23	Nishiyama et al.	2002	CR4-C-4-1	215	215	4.38	49.1	41	262	645	3.0
24	Nishiyama et al.	2002	CR8-C-8	175	175	6.47	27.0	77	835	525	3.0
25	Nishiyama et al.	2002	CR4-D-2	323	323	4.38	73.7	25	262	969	3.0
26	Varma	2000	SC-32-46	305	305	8.6	35.5	110	259	1,200	3.9
27	Varma	2000	SC-32-80	305	305	8.9	34.3	110	560	1,200	3.9
28	Varma	2000	SC-48-46	305	305	5.8	52.6	110	471	1,200	3.9

Table 4.23. Comparison Metrics – RCFT Validation Set – SC – Proposed for Behavior

Test #	Initial Tangent (kN)			Peak Load (kN)			Strain at Peak Load (mm/mm)			Area Under Curve (kN)		
	Expt.	Model	Error	Expt.	Model	Error	Expt.	Model	Error	Expt.	Model	Error
1	590,005	407,643	-30.91%	497	464	-6.75%	0.003911	0.002015	-48.49%	8.2	8.8	8.31%
2	370,824	371,234	0.11%	511	483	-5.52%	0.003864	0.002052	-46.88%	10.6	11.5	8.61%
3	494,929	416,694	-15.81%	528	514	-2.67%	0.002664	0.003140	17.88%	11.0	12.0	9.23%
4	452,492	528,143	16.72%	665	630	-5.24%	0.029941	0.005090	-83.00%	19.1	18.1	-5.26%
5	457,681	805,212	75.93%	1,432	1,258	-12.18%	0.004022	0.002613	-35.04%	107.8	109.3	1.45%
6	620,722	793,765	27.88%	1,678	1,538	-8.33%	0.004519	0.004347	-3.82%	135.4	138.7	2.49%
7	464,012	975,585	110.25%	2,025	1,902	-6.05%	0.004886	0.002748	-43.75%	118.9	143.5	20.69%
8	423,604	972,370	129.55%	2,224	2,138	-3.89%	0.004986	0.003456	-30.68%	152.4	168.7	10.69%
9	537,809	1,174,980	118.48%	2,229	2,238	0.40%	0.005201	0.002932	-43.63%	146.4	155.3	6.10%
10	1,189,210	2,853,040	139.91%	4,850	4,684	-3.43%	0.004154	0.003621	-12.83%	358.1	404.9	13.06%
11	608,580	622,521	2.29%	914	993	8.55%	0.004278	0.002556	-40.24%	22.5	25.8	14.79%
12	687,148	701,761	2.13%	1,091	1,113	2.08%	0.007384	0.004119	-44.22%	29.6	31.7	7.07%
13	407,187	743,627	82.63%	1,109	1,042	-5.98%	0.003824	0.004174	9.15%	38.3	40.2	4.91%
14	282,032	819,694	190.64%	1,221	1,161	-4.91%	0.008028	0.005837	-27.29%	16.0	16.6	3.96%
15	579,948	965,852	66.54%	2,066	1,544	-25.28%	0.040458	0.008907	-77.98%	90.7	72.9	-19.70%
16	500,450	493,399	-1.41%	809	775	-4.25%	0.003704	0.001923	-48.07%	30.1	31.7	5.19%
17	470,542	622,692	32.34%	993	991	-0.15%	0.006273	0.003219	-48.68%	24.0	26.3	9.75%
18	804,107	738,418	-8.17%	1,142	1,206	5.62%	0.006172	0.003924	-36.42%	27.5	30.1	9.66%
19	428,859	738,208	72.13%	1,219	1,126	-7.66%	0.003998	0.003349	-16.24%	17.0	17.5	3.15%
20	507,945	815,564	60.56%	1,333	1,185	-11.08%	0.003486	0.004534	30.03%	40.2	37.9	-5.69%
21	535,500	947,628	76.96%	1,692	1,538	-9.10%	0.031919	0.006709	-78.98%	72.7	67.8	-6.69%
22	3,247,430	5,133,910	58.09%	7,153	9,324	30.35%	0.003090	0.002607	-15.64%	185.3	232.6	25.53%
23	1,263,160	1,964,160	55.50%	2,325	2,706	16.36%	0.002773	0.002222	-19.88%	85.6	113.0	32.09%
24	1,637,740	1,906,930	16.44%	5,430	5,496	1.21%	0.009577	0.005537	-42.19%	225.6	249.0	10.39%
25	3,189,110	3,389,110	6.27%	3,495	3,852	10.22%	0.002453	0.001996	-18.63%	117.3	169.3	44.38%
26	4,834,010	5,883,940	21.72%	11,576	11,738	1.40%	0.002444	0.002813	15.09%	86.7	119.9	38.31%
27	5,996,110	5,889,760	-1.77%	14,261	14,506	1.72%	0.002721	0.003632	33.48%	137.2	167.2	21.90%
28	4,886,390	5,449,770	11.53%	12,084	11,801	-2.34%	0.002820	0.002803	-0.60%	90.6	134.8	48.76%
Mean			47.02%			-1.67%			-27.06%			11.54%
Standard Deviation			54.28%			10.02%			30.70%			15.36%
Median			30.11%			-3.66%			-32.86%			8.92%

Table 4.24. Comparison Metrics – RCFT Validation Set – SC – Proposed for Design

Test #	Initial Tangent (kN)			Peak Load (kN)			Strain at Peak Load (mm/mm)			Area Under Curve (kN)		
	Expt.	Model	Error	Expt.	Model	Error	Expt.	Model	Error	Expt.	Model	Error
1	590,005	422,242	-28.43%	497	467	-6.05%	0.003911	0.002141	-45.27%	8.2	6.0	-26.87%
2	370,824	374,038	0.87%	511	459	-10.27%	0.003864	0.002253	-41.70%	10.6	9.0	-15.30%
3	494,929	417,103	-15.72%	528	495	-6.33%	0.002664	0.002600	-2.38%	11.0	9.9	-10.02%
4	452,492	526,042	16.25%	665	616	-7.30%	0.029941	0.002814	-90.60%	19.1	16.0	-16.03%
5	457,681	835,554	82.56%	1,432	1,228	-14.24%	0.004022	0.002613	-35.04%	107.8	79.5	-26.18%
6	620,722	829,604	33.65%	1,678	1,442	-14.07%	0.004519	0.002646	-41.45%	135.4	107.6	-20.49%
7	464,012	1,007,320	117.09%	2,025	1,875	-7.38%	0.004886	0.002748	-43.75%	118.9	83.6	-29.68%
8	423,604	1,007,210	137.77%	2,224	2,066	-7.11%	0.004986	0.002911	-41.62%	152.4	104.7	-31.30%
9	537,809	1,201,110	123.33%	2,229	2,226	-0.14%	0.005201	0.002932	-43.63%	146.4	105.1	-28.23%
10	1,189,210	2,967,420	149.53%	4,850	4,430	-8.68%	0.004154	0.002535	-38.98%	358.1	310.4	-13.32%
11	608,580	650,549	6.90%	914	937	2.48%	0.004278	0.002334	-45.44%	22.5	18.9	-15.96%
12	687,148	720,945	4.92%	1,091	1,044	-4.29%	0.007384	0.002626	-64.43%	29.6	25.9	-12.67%
13	407,187	755,788	85.61%	1,109	994	-10.35%	0.003824	0.002729	-28.63%	38.3	33.3	-13.14%
14	282,032	831,115	194.69%	1,221	1,117	-8.55%	0.008028	0.003423	-57.36%	16.0	14.9	-6.83%
15	579,948	977,466	68.54%	2,066	1,476	-28.56%	0.040458	0.003761	-90.70%	90.7	68.0	-25.10%
16	500,450	511,148	2.14%	809	812	0.33%	0.003704	0.002473	-33.24%	30.1	29.5	-2.04%
17	470,542	635,708	35.10%	993	942	-5.08%	0.006273	0.003996	-36.30%	24.0	23.0	-4.03%
18	804,107	756,924	-5.87%	1,142	1,130	-1.02%	0.006172	0.002616	-57.61%	27.5	25.5	-7.21%
19	428,859	750,730	75.05%	1,219	1,065	-12.68%	0.003998	0.002818	-29.51%	17.0	15.4	-9.31%
20	507,945	826,602	62.73%	1,333	1,143	-14.25%	0.003486	0.003534	1.35%	40.2	33.5	-16.61%
21	535,500	958,227	78.94%	1,692	1,481	-12.48%	0.031919	0.003952	-87.62%	72.7	63.5	-12.61%
22	3,247,430	5,398,270	66.23%	7,153	9,437	31.93%	0.003090	0.002607	-15.64%	185.3	121.4	-34.47%
23	1,263,160	2,057,630	62.90%	2,325	2,685	15.49%	0.002773	0.002318	-16.40%	85.6	64.4	-24.78%
24	1,637,740	2,011,890	22.85%	5,430	4,731	-12.86%	0.009577	0.003514	-63.31%	225.6	198.2	-12.12%
25	3,189,110	3,487,980	9.37%	3,495	3,893	11.41%	0.002453	0.002096	-14.56%	117.3	104.5	-10.87%
26	4,834,010	6,082,440	25.83%	11,576	11,757	1.56%	0.002444	0.002865	17.21%	86.7	71.2	-17.85%
27	5,996,110	6,129,760	2.23%	14,261	14,166	-0.66%	0.002721	0.002878	5.76%	137.2	110.4	-19.50%
28	4,886,390	5,672,250	16.08%	12,084	12,388	2.51%	0.002820	0.002834	0.47%	90.6	84.8	-6.39%
Mean			51.11%			-4.52%			-37.16%			-16.75%
Standard Deviation			55.56%			11.18%			28.07%			8.75%
Median			34.38%			-6.72%			-40.22%			-15.63%

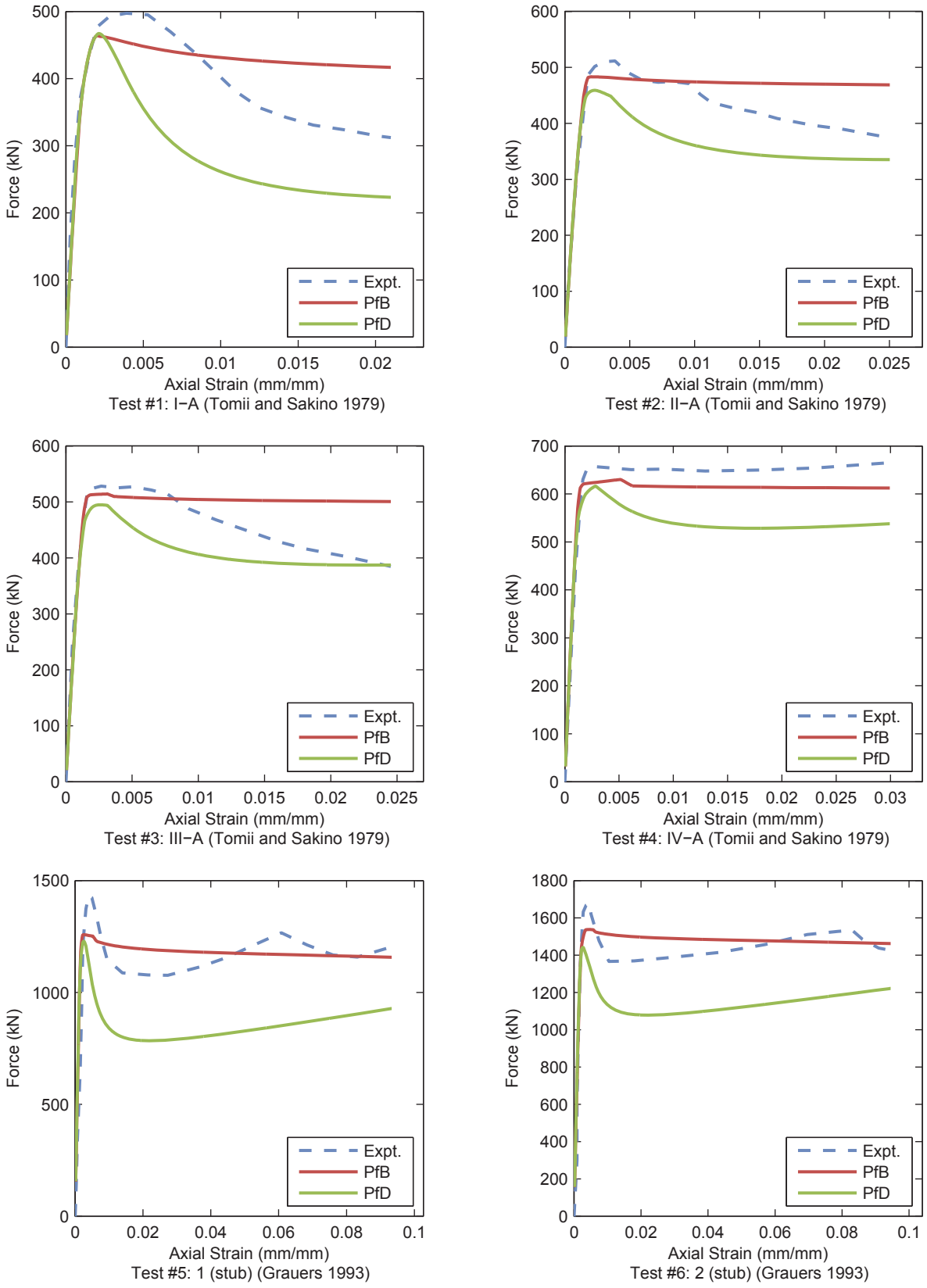

Figure 4.7. RCFT Validation Results – SC

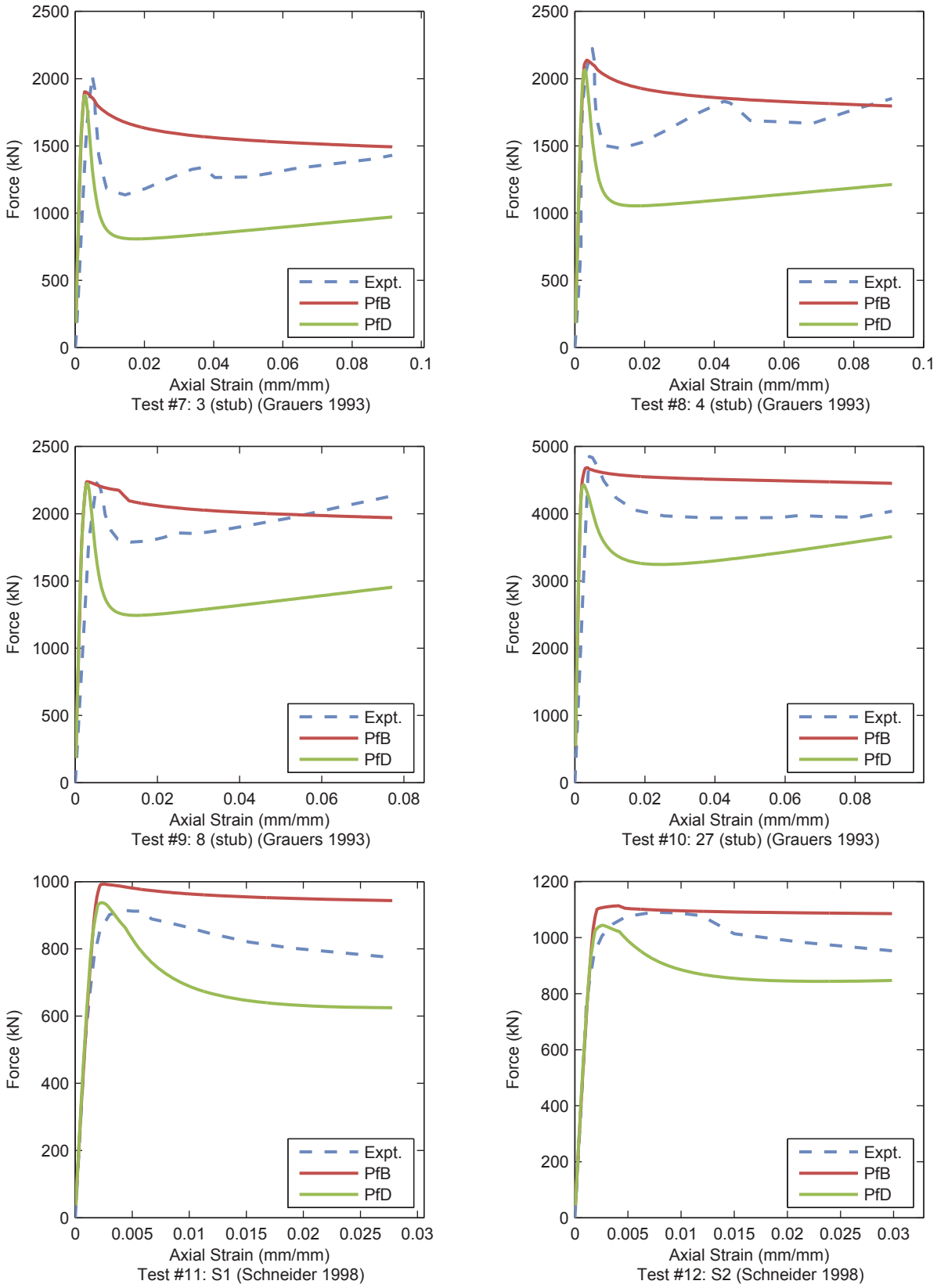

Figure 4.7. RCFT Validation Results – SC (continued)

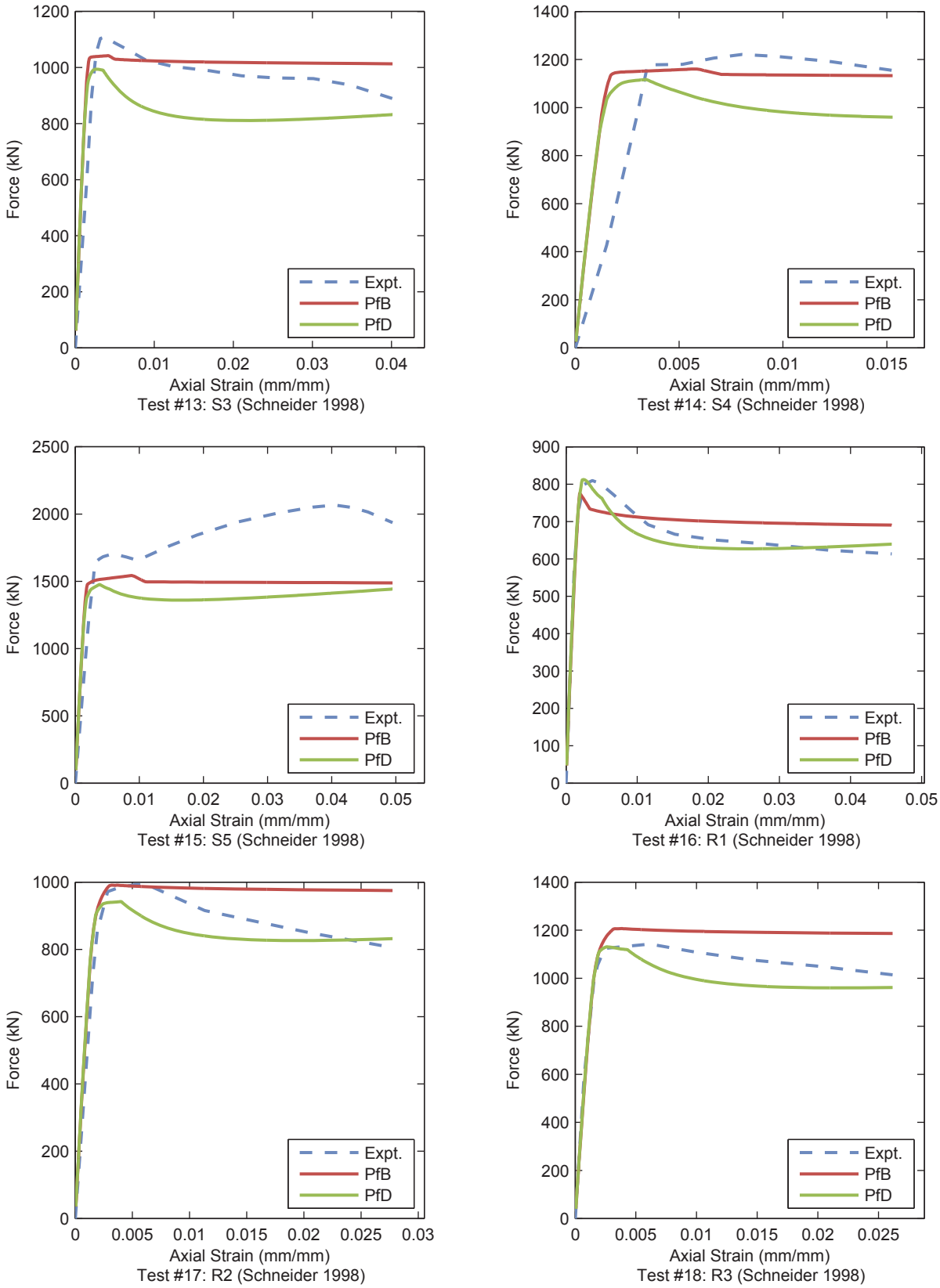

Figure 4.7. RCFT Validation Results – SC (continued)

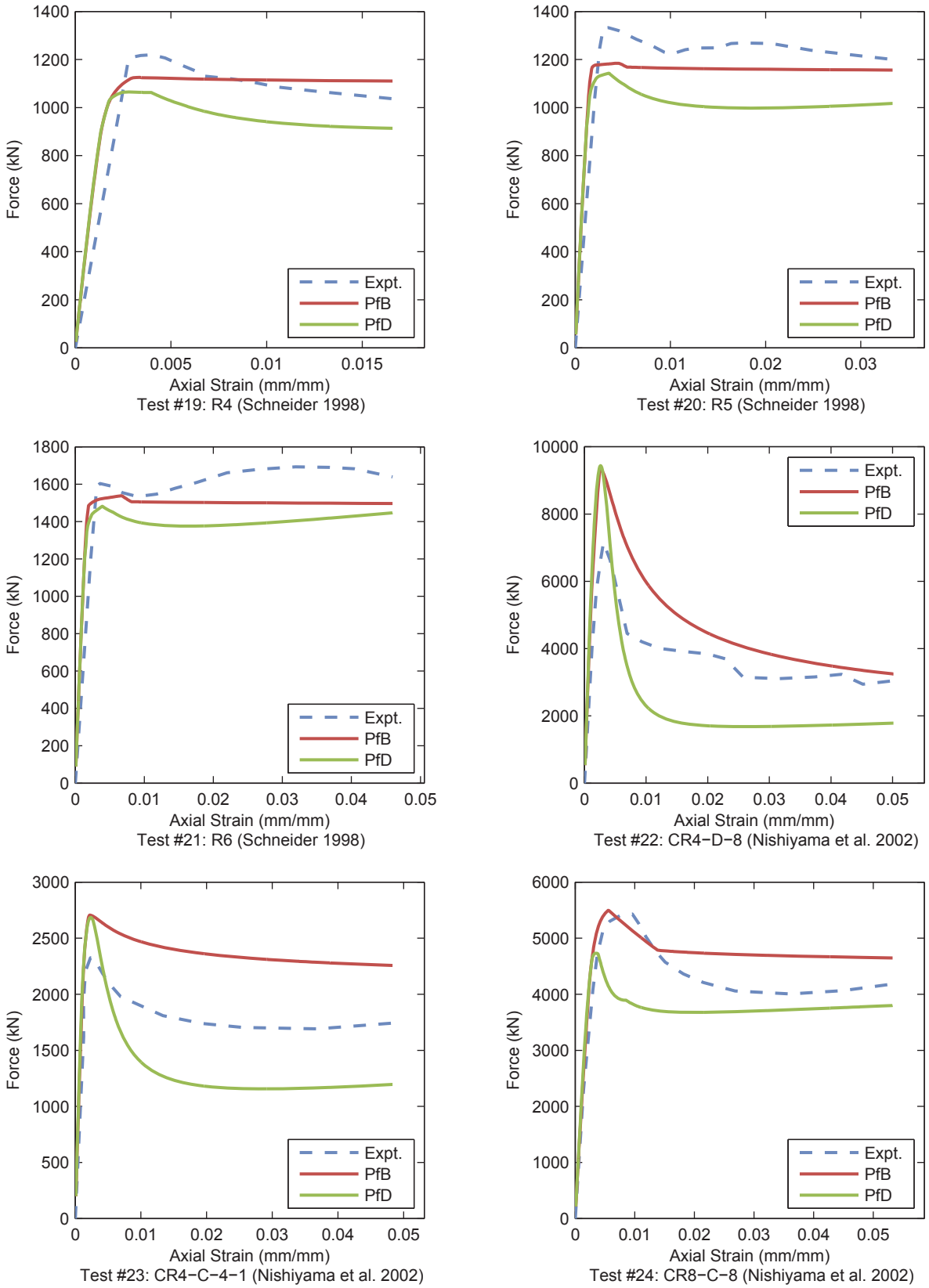

Figure 4.7. RCFT Validation Results – SC (continued)

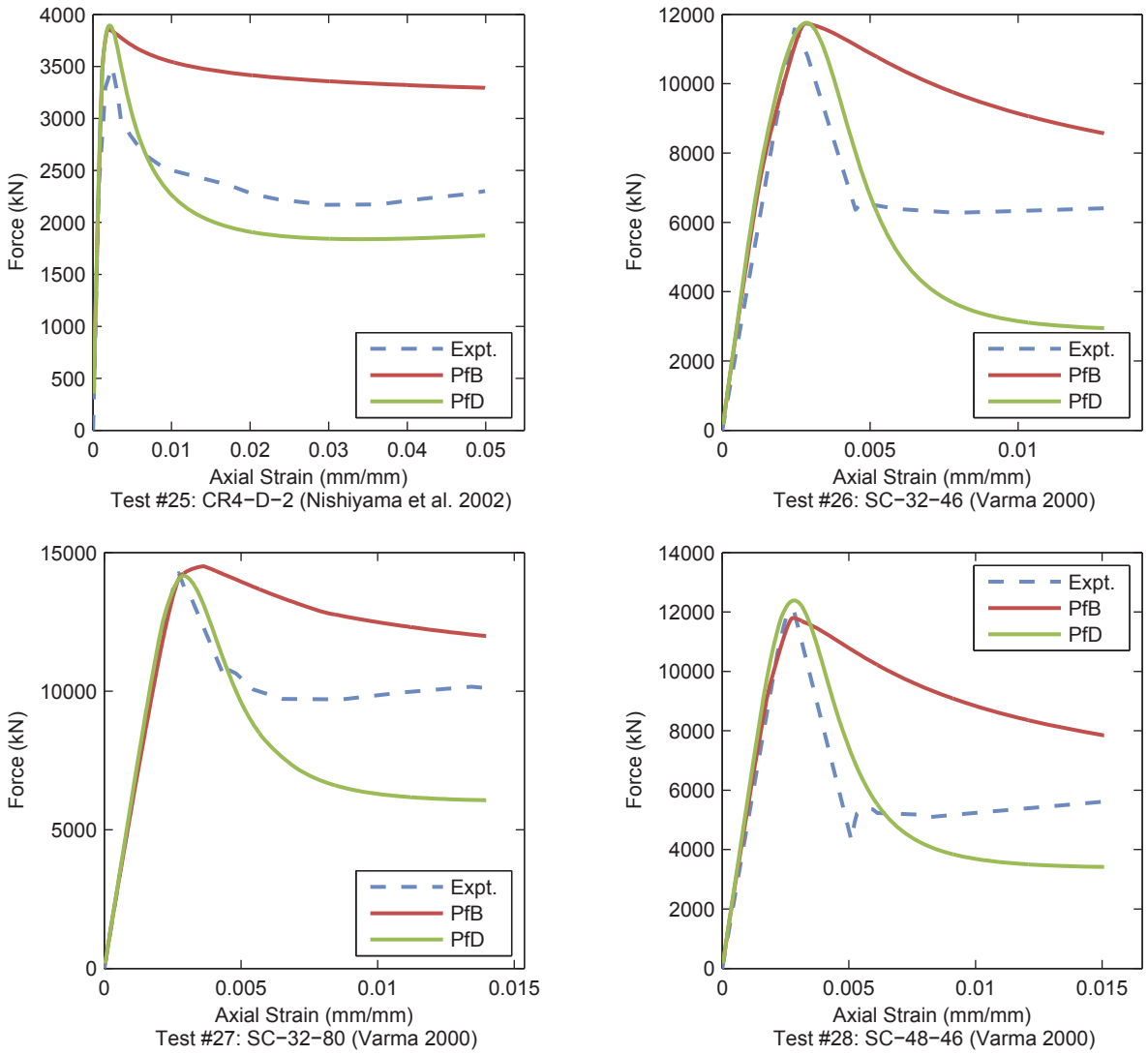

Figure 4.7. RCFT Validation Results – SC (continued)

Table 4.25. Material and Geometric Properties – RCFT Validation Set – BM

Test #	Author	Year	Specimen	Type of Loading	H (mm)	B (mm)	t (mm)	H/t	f'_c (MPa)	F_y (MPa)	Shear Span (mm)	Bending Span (mm)
1	Gho and Liu	2004	B02	Four Point Bending	150	150	4.87	30.8	56.3	438	365	730
2	Gho and Liu	2004	B04	Four Point Bending	150	150	4.84	31.0	87.5	438	365	730
3	Assi et al.	2003	B1C-SN	Four Point Bending	140	140	3.90	35.9	31.2	350	325	350
4	Assi et al.	2003	B1D-RN	Four Point Bending	200	100	4.70	42.6	31.2	360	325	350
5	Lu and Kennedy	1994	CB12	Four Point Bending	152	152	4.43	34.4	47.0	383	235	1,305
6	Lu and Kennedy	1994	CB13	Four Point Bending	152	152	4.43	34.4	42.8	383	463	1,305
7	Lu and Kennedy	1994	CB15	Four Point Bending	152	152	4.43	34.4	41.2	383	768	1,305
8	Lu and Kennedy	1994	CB22	Four Point Bending	152	152	8.95	17.0	46.9	467	236	1,305
9	Lu and Kennedy	1994	CB31	Four Point Bending	253	152	6.17	41.1	46.7	431	261	1,508
10	Lu and Kennedy	1994	CB35	Four Point Bending	253	152	6.17	41.1	44.3	431	1,276	1,508
11	Lu and Kennedy	1994	CB41	Four Point Bending	253	152	9.04	28.0	46.2	425	261	1,508
12	Lu and Kennedy	1994	CB45	Four Point Bending	253	152	9.04	28.0	43.8	425	1,276	1,508
13	Lu and Kennedy	1994	CB52	Four Point Bending	253	152	6.17	41.1	47.1	431	235	1,305
14	Lu and Kennedy	1994	CB53	Four Point Bending	253	152	6.17	41.1	42.1	431	463	1,305
15	Lu and Kennedy	1994	CB55	Four Point Bending	253	152	6.17	41.1	40.5	431	768	1,305
16	Tomii and Sakino	1979	II-0	Direct Moment	100	100	2.27	44.1	21.6	305	---	300
17	Tomii and Sakino	1979	III-0	Direct Moment	100	100	2.98	33.6	20.6	289	---	300
18	Tomii and Sakino	1979	IV-0	Direct Moment	100	100	4.25	23.5	18.6	284	---	300

Table 4.26. Comparison Metrics – RCFT Validation Set – BM – Proposed for Behavior

Test #	Initial Tangent (kN-m/mm)			Peak Moment (kN-m)			Area Under Curve (kN-m-mm)		
	Expt.	Model	Error	Expt.	Model	Error	Expt.	Model	Error
1	35.12	36.02	2.56%	91.77	79.27	-13.62%	1,153	1,050	-8.91%
2	44.22	36.90	-16.56%	102.53	81.39	-20.62%	1,380	1,123	-18.67%
3	9.92	14.44	45.49%	55.80	44.89	-19.56%	1,214	1,039	-14.37%
4	19.09	31.05	62.63%	97.06	75.46	-22.25%	2,087	1,758	-15.77%
Test #	**Initial Tangent**			**Peak Moment** (kN-m)			**Area Under Curve**		
	Expt.	Model	Error	Expt.	Model	Error	Expt.	Model	Error
5	14.74	16.03	8.78%	72.08	68.55	-4.91%	2,824	2,810	-0.51%
6	14.53	15.74	8.32%	71.59	65.75	-8.16%	1,578	1,508	-4.42%
7	14.57	15.60	7.11%	68.58	65.97	-3.81%	2,069	2,024	-2.19%
8	29.92	25.21	-15.73%	150.73	136.54	-9.42%	4,572	4,334	-5.21%
9	35.71	42.70	19.59%	209.88	206.25	-1.73%	7,562	7,810	3.28%
10	33.59	41.59	23.83%	206.67	204.66	-0.97%	8,456	8,611	1.84%
11	44.95	53.68	19.43%	280.36	271.25	-3.25%	8,147	8,539	4.81%
12	47.13	52.33	11.02%	282.49	270.01	-4.42%	12,831	12,806	-0.19%
13	18.28	18.57	1.59%	143.95	139.10	-3.37%	4,612	4,690	1.68%
14	15.10	18.20	20.57%	145.74	137.98	-5.33%	5,948	6,044	1.62%
15	17.89	18.06	0.96%	143.12	136.61	-4.55%	4,935	4,895	-0.81%
16	2.91	3.48	19.49%	11.21	12.08	7.78%	594	627	5.53%
17	3.36	4.31	28.15%	15.00	14.55	-2.98%	763	746	-2.14%
18	4.06	5.94	46.36%	19.37	19.01	-1.85%	971	966	-0.45%
Mean			16.31%			-6.83%			-3.05%
Standard Deviation			20.47%			7.70%			7.05%
Median			15.23%			-4.49%			-0.66%

Table 4.27. Comparison Metrics – RCFT Validation Set – BM – Proposed for Design

Test #	Initial Tangent (kN-m/mm)			Peak Moment (kN-m)			Area Under Curve (kN-m-mm)		
	Expt.	Model	Error	Expt.	Model	Error	Expt.	Model	Error
1	35.12	36.06	2.67%	91.77	75.95	-17.24%	1153	1011	-12.28%
2	44.22	36.79	-16.79%	102.53	78.16	-23.77%	1380	1073	-22.28%
3	9.92	14.20	43.08%	55.80	42.80	-23.30%	1214	1005	-17.22%
4	19.09	30.81	61.39%	97.06	71.36	-26.48%	2087	1695	-18.78%
Test #	**Initial Tangent**			**Peak Moment** (kN-m)			**Area Under Curve**		
	Expt.	Model	Error	Expt.	Model	Error	Expt.	Model	Error
5	14.74	15.98	8.44%	72.08	65.29	-9.42%	2824	2693	-4.65%
6	14.53	15.68	7.94%	71.59	63.16	-11.78%	1578	1466	-7.09%
7	14.57	15.56	6.81%	68.58	63.43	-7.52%	2069	1968	-4.90%
8	29.92	25.29	-15.47%	150.73	134.47	-10.79%	4572	4233	-7.42%
9	35.71	42.79	19.85%	209.88	202.26	-3.63%	7562	7479	-1.09%
10	33.59	41.71	24.20%	206.67	196.83	-4.76%	8456	8246	-2.48%
11	44.95	53.87	19.84%	280.36	267.20	-4.69%	8147	8274	1.56%
12	47.13	52.54	11.47%	282.49	260.31	-7.85%	12831	12333	-3.88%
13	18.28	18.54	1.45%	143.95	134.97	-6.24%	4612	4582	-0.64%
14	15.10	18.19	20.51%	145.74	135.57	-6.98%	5948	5931	-0.28%
15	17.89	18.06	0.92%	143.12	133.77	-6.54%	4935	4816	-2.41%
16	2.91	3.43	17.52%	11.21	11.21	0.09%	594	599	0.86%
17	3.36	4.24	26.27%	15.00	13.75	-8.35%	763	724	-5.03%
18	4.06	5.86	44.37%	19.37	18.68	-3.59%	971	961	-1.03%
Mean			15.80%			-10.16%			-6.06%
Standard Deviation			19.90%			7.60%			7.05%
Median			14.50%			-7.68%			-4.26%

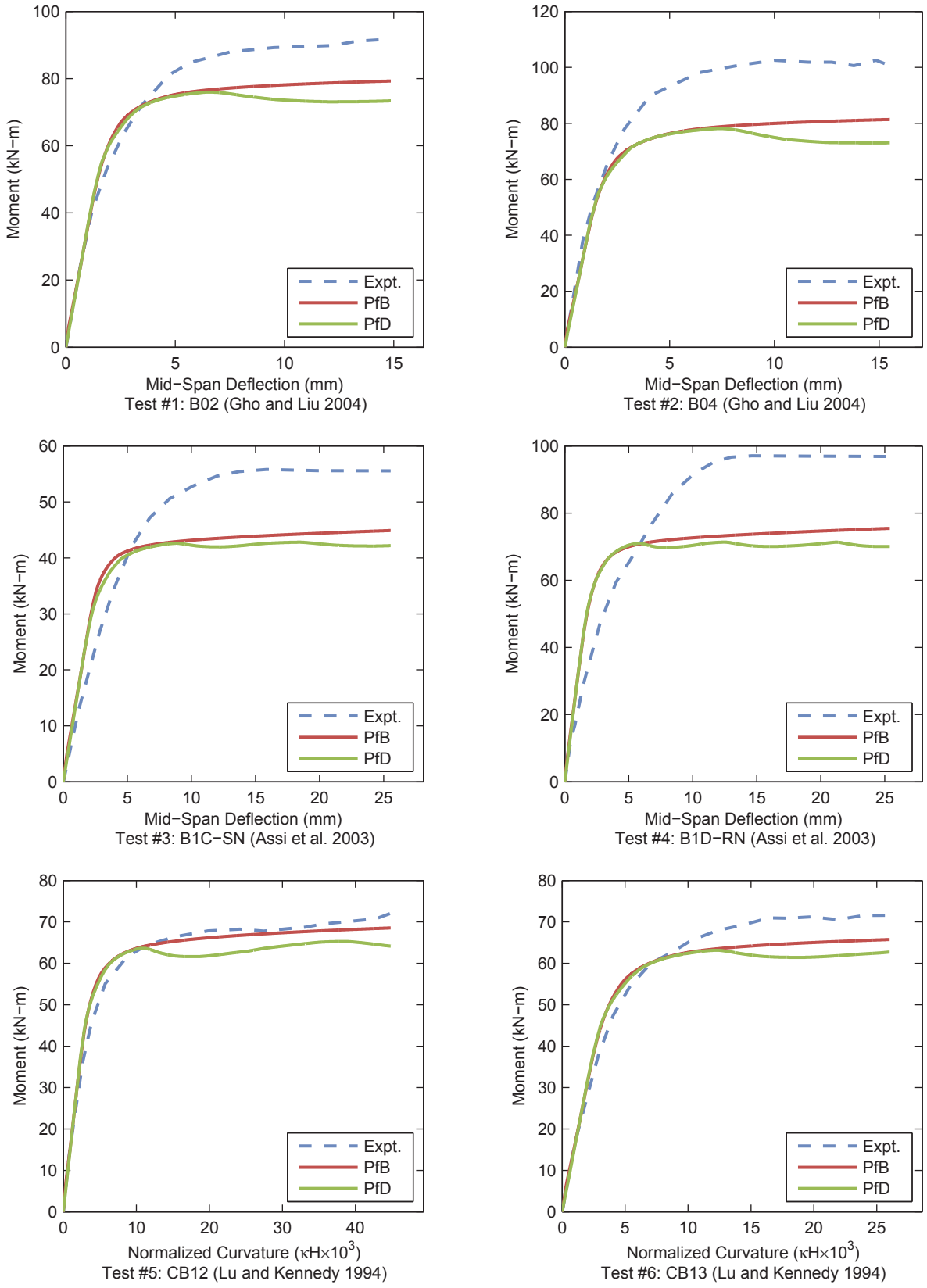

Figure 4.8. RCFT Validation Results – BM

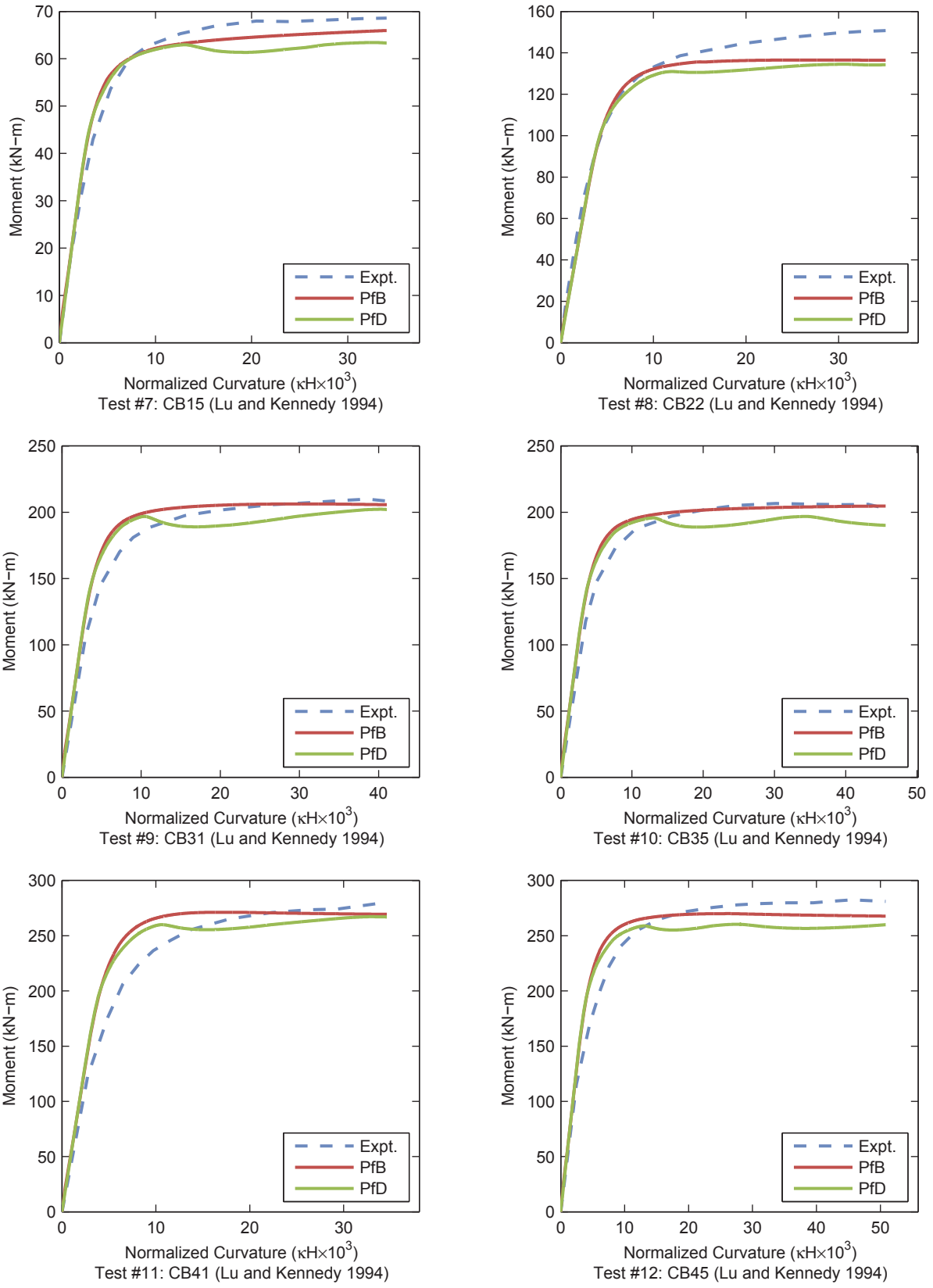

Figure 4.8. RCFT Validation Results – BM (continued)

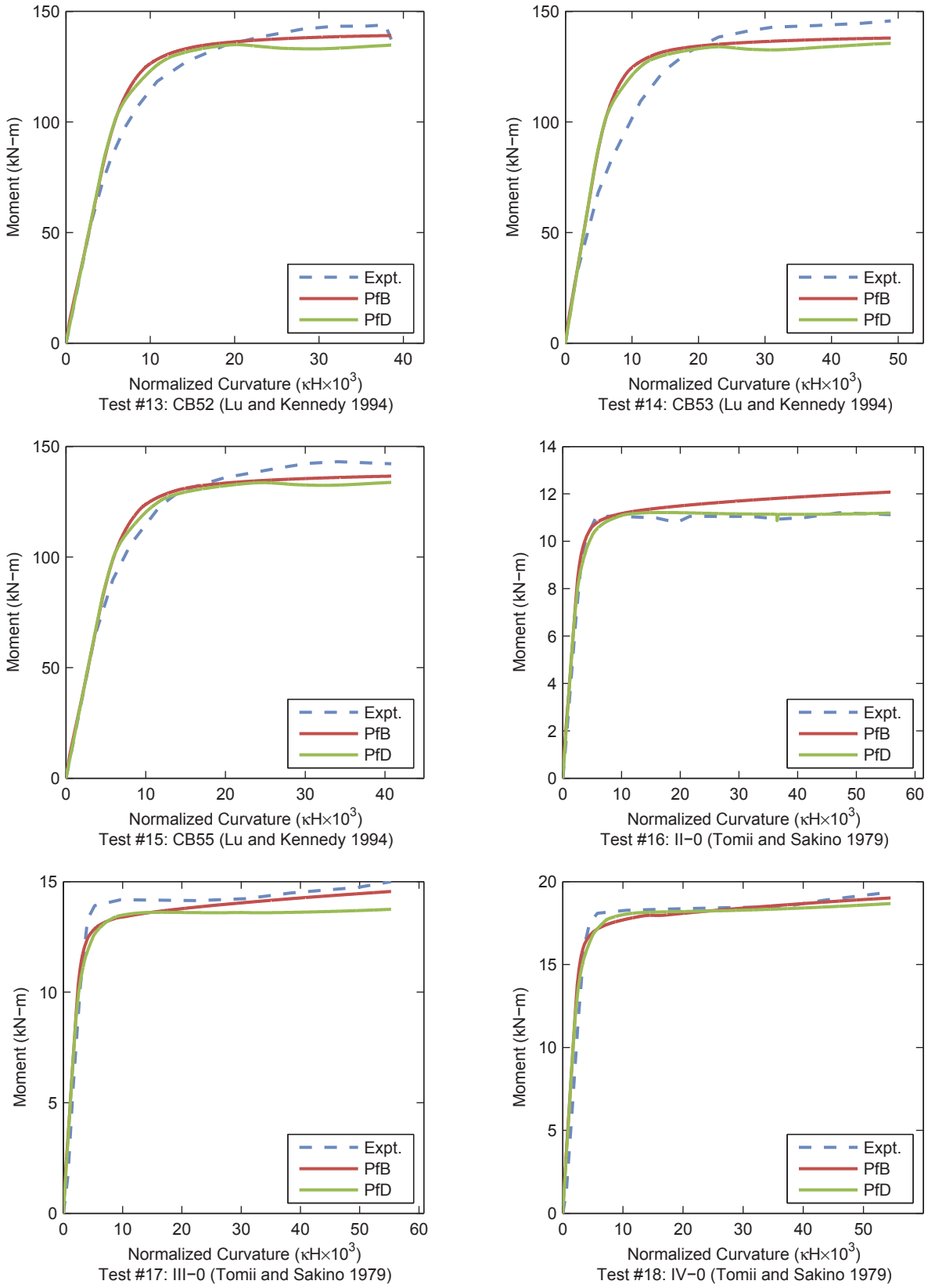

Figure 4.8. RCFT Validation Results – BM (continued)

Table 4.28. Material and Geometric Properties – RCFT Validation Set – PBC

Test #	Author	Year	Specimen	H (mm)	B (mm)	t (mm)	H/t	f'_c (MPa)	F_y (MPa)	L (mm)	L/H	e (mm)	e/H	angle (deg)
1	Grauers	1993	1 (column)	120	120	5.00	24.0	47	304	3,000	25.0	20.0	0.167	0
2	Grauers	1993	2 (column)	120	120	5.00	24.0	46	438	3,000	25.0	20.0	0.167	0
3	Grauers	1993	6 (column)	120	120	8.00	15.0	46	300	3,000	25.0	20.0	0.167	0
4	Grauers	1993	7 (column)	120	120	8.00	15.0	47	376	3,000	25.0	20.0	0.167	0
5	Grauers	1993	9 (column)	120	120	8.00	15.0	103	379	3,000	25.0	20.0	0.167	0
6	Grauers	1993	10 (column)	120	120	8.00	15.0	39	379	3,000	25.0	20.0	0.167	0
7	Grauers	1993	13 (column)	120	120	8.00	15.0	80	364	3,000	25.0	10.0	0.083	0
8	Bridge	1976	SHC-1	204	204	9.96	20.5	30	291	2,130	10.5	38.0	0.187	0
9	Bridge	1976	SHC-3	203	203	10.03	20.3	37	313	2,130	10.5	38.0	0.187	30
10	Bridge	1976	SHC-4	203	203	9.88	20.5	39	317	2,130	10.5	38.0	0.187	45
11	Bridge	1976	SHC-5	203	203	10.01	20.2	44	319	3,050	15.1	38.0	0.188	30
12	Bridge	1976	SHC-6	203	202	9.78	20.8	36	317	3,050	15.0	64.0	0.315	45
13	Bridge	1976	SHC-7	153	152	6.48	23.5	31	254	3,050	20.0	38.0	0.249	0
14	Bridge	1976	SHC-8	153	152	6.48	23.5	31	254	3,050	20.0	64.0	0.420	0
15	Shakir-Khalil and Zeghiche	1989	2	120	80	4.50	26.7	36	386	2,760	23.0	24.0	0.200	0
16	Shakir-Khalil and Zeghiche	1989	3	120	80	4.47	26.8	36	385	2,760	23.0	60.0	0.500	0
17	Shakir-Khalil and Zeghiche	1989	5	120	80	4.47	26.8	39	343	2,760	23.0	40.0	0.333	90
18	Shakir-Khalil and Zeghiche	1989	6	120	80	4.47	26.8	41	343	2,760	23.0	24.0 (z) 16.0 (y)	0.240	0
19	Shakir-Khalil and Zeghiche	1989	7	120	80	4.44	27.0	40	358	2,760	23.0	60.0 (z) 40.0 (y)	0.601	0

Table 4.29. Comparison Metrics – RCFT Validation Set – PBC – Proposed for Behavior

Test #	Initial Tangent (kN/mm)			Peak Load (kN)			Deformation at Peak Load (mm)			Area Under Curve (kN-mm)		
	Expt.	Model	Error	Expt.	Model	Error	Expt.	Model	Error	Expt.	Model	Error
1	66.5	51.4	-22.75%	596.5	568.7	-4.65%	24.77	24.24	-2.14%	56,332	51,716	-8.19%
2	49.7	50.0	0.63%	700.1	643.1	-8.15%	22.04	31.30	41.97%	69,857	64,758	-7.30%
3	81.5	64.6	-20.78%	770.1	715.9	-7.03%	23.91	23.31	-2.50%	74,184	68,104	-8.20%
4	80.6	63.8	-20.87%	876.9	778.4	-11.24%	22.04	30.23	37.16%	87,661	77,589	-11.49%
5	71.2	69.0	-3.13%	977.4	909.1	-6.99%	27.41	35.46	29.38%	100,871	92,830	-7.97%
6	60.0	62.8	4.73%	821.8	758.5	-7.70%	28.28	29.44	4.10%	80,314	73,585	-8.38%
7	182.4	129.4	-29.07%	1,157.3	1,019.5	-11.91%	14.42	25.16	74.47%	102,726	92,390	-10.06%
8	552.1	512.1	-7.25%	1,941.4	2,046.0	5.38%	10.83	11.30	4.29%	21,960	22,774	3.71%
9	549.2	516.1	-6.02%	2,219.4	2,301.2	3.69%	15.16	13.51	-10.88%	37,823	38,694	2.30%
10	545.4	515.4	-5.49%	2,186.9	2,354.3	7.66%	15.27	14.58	-4.55%	58,262	61,982	6.38%
11	274.0	249.3	-9.01%	2,055.0	2,209.6	7.52%	17.60	19.56	11.10%	30,608	31,603	3.25%
12	163.4	144.5	-11.58%	1,617.9	1,653.7	2.22%	29.27	26.29	-10.18%	38,429	38,478	0.13%
13	71.6	70.1	-2.14%	675.1	736.6	9.11%	19.79	23.24	17.40%	32,172	36,535	13.56%
14	41.9	42.5	1.34%	511.2	578.5	13.16%	31.82	29.64	-6.85%	25,697	28,325	10.23%
15	44.6	32.9	-26.20%	401.3	394.7	-1.66%	20.83	28.08	34.79%	8,736	8,075	-7.56%
16	13.1	13.6	3.32%	246.7	258.7	4.86%	34.77	38.66	11.20%	8,142	8,471	4.04%
17	11.3	10.0	-10.92%	208.1	201.1	-3.38%	33.30	33.30	-6.01E-07	4,404	4,140	-5.98%
18-Y	42.2	53.0	25.46%	265.6	254.2	-4.30%	15.30	8.84	-42.21%	3,423	2,079	-39.26%
18-Z	19.7	16.2	-17.89%	278.4	254.2	-8.69%	25.72	35.81	39.22%	9,996	8,789	-12.07%
19-Y	14.9	20.2	35.74%	167.3	162.0	-3.16%	25.61	13.99	-45.37%	5,327	2,514	-52.82%
19-Z	7.2	6.6	-9.02%	165.7	162.0	-2.22%	38.06	44.67	17.36%	8,016	7,575	-5.49%
Mean			-6.23%			-1.31%			9.42%			-6.72%
Standard Deviation			15.70%			7.22%			27.81%			15.13%
Median			-7.25%			-3.16%			4.29%			-7.30%

Table 4.30. Comparison Metrics – RCFT Validation Set – PBC – Proposed for Design

Test #	Initial Tangent (kN/mm)			Peak Load (kN)			Deformation at Peak Load (mm)			Area Under Curve (kN-mm)		
	Expt.	Model	Error	Expt.	Model	Error	Expt.	Model	Error	Expt.	Model	Error
1	66.5	52.8	-20.66%	596.5	560.6	-6.02%	24.77	25.60	3.36%	56,332	47,544	-15.60%
2	49.7	51.4	3.40%	700.1	645.1	-7.86%	22.04	29.31	32.97%	69,857	60,073	-14.01%
3	81.5	65.7	-19.42%	770.1	709.6	-7.85%	23.91	25.68	7.42%	74,184	63,994	-13.74%
4	80.6	64.7	-19.73%	876.9	790.4	-9.87%	22.04	27.45	24.58%	87,661	74,815	-14.65%
5	71.2	69.5	-2.34%	977.4	930.0	-4.85%	27.41	33.43	21.98%	100,871	84,744	-15.99%
6	60.0	63.7	6.23%	821.8	768.3	-6.51%	28.28	26.79	-5.28%	80,314	71,679	-10.75%
7	182.4	130.7	-28.32%	1,157.3	1,054.6	-8.87%	14.42	22.60	56.76%	102,726	85,739	-16.54%
8	552.1	521.1	-5.62%	1,941.4	2,030.8	4.61%	10.83	9.70	-10.46%	21,960	22,180	1.00%
9	549.2	528.1	-3.85%	2,219.4	2,259.8	1.82%	15.16	10.97	-27.65%	37,823	36,811	-2.68%
10	545.4	528.1	-3.17%	2,186.9	2,298.5	5.10%	15.27	11.68	-23.52%	58,262	56,606	-2.84%
11	274.0	255.4	-6.78%	2,055.0	2,178.7	6.02%	17.60	19.56	11.10%	30,608	31,281	2.20%
12	163.4	144.7	-11.45%	1,617.9	1,622.4	0.28%	29.27	25.69	-12.24%	38,429	37,803	-1.63%
13	71.6	71.2	-0.54%	675.1	737.5	9.24%	19.79	23.89	20.68%	32,172	34,056	5.85%
14	41.9	41.5	-0.91%	511.2	578.8	13.22%	31.82	28.81	-9.47%	25,697	27,475	6.92%
15	44.6	33.7	-24.48%	401.3	394.6	-1.69%	20.83	25.13	20.64%	8,736	8,176	-6.41%
16	13.1	13.1	-0.06%	246.7	258.3	4.69%	34.77	36.92	6.19%	8,142	8,485	4.21%
17	11.3	9.7	-14.02%	208.1	197.3	-5.20%	33.30	33.30	-6.01E-07	4,404	4,108	-6.72%
18-Y	42.2	51.8	22.75%	265.6	248.8	-6.35%	15.30	8.58	-43.94%	3,423	2,025	-40.84%
18-Z	19.7	16.1	-18.25%	278.4	248.8	-10.65%	25.72	35.45	37.81%	9,996	8,698	-12.98%
19-Y	14.9	19.6	31.99%	167.3	157.1	-6.08%	25.61	13.55	-47.09%	5,327	2,434	-54.31%
19-Z	7.2	6.4	-11.88%	165.7	157.1	-5.17%	38.06	44.05	15.72%	8,016	7,450	-7.06%
Mean			-6.05%			-2.00%			3.79%			-10.31%
Standard Deviation			14.71%			6.83%			26.17%			14.66%
Median			-5.62%			-5.17%			6.19%			-7.06%

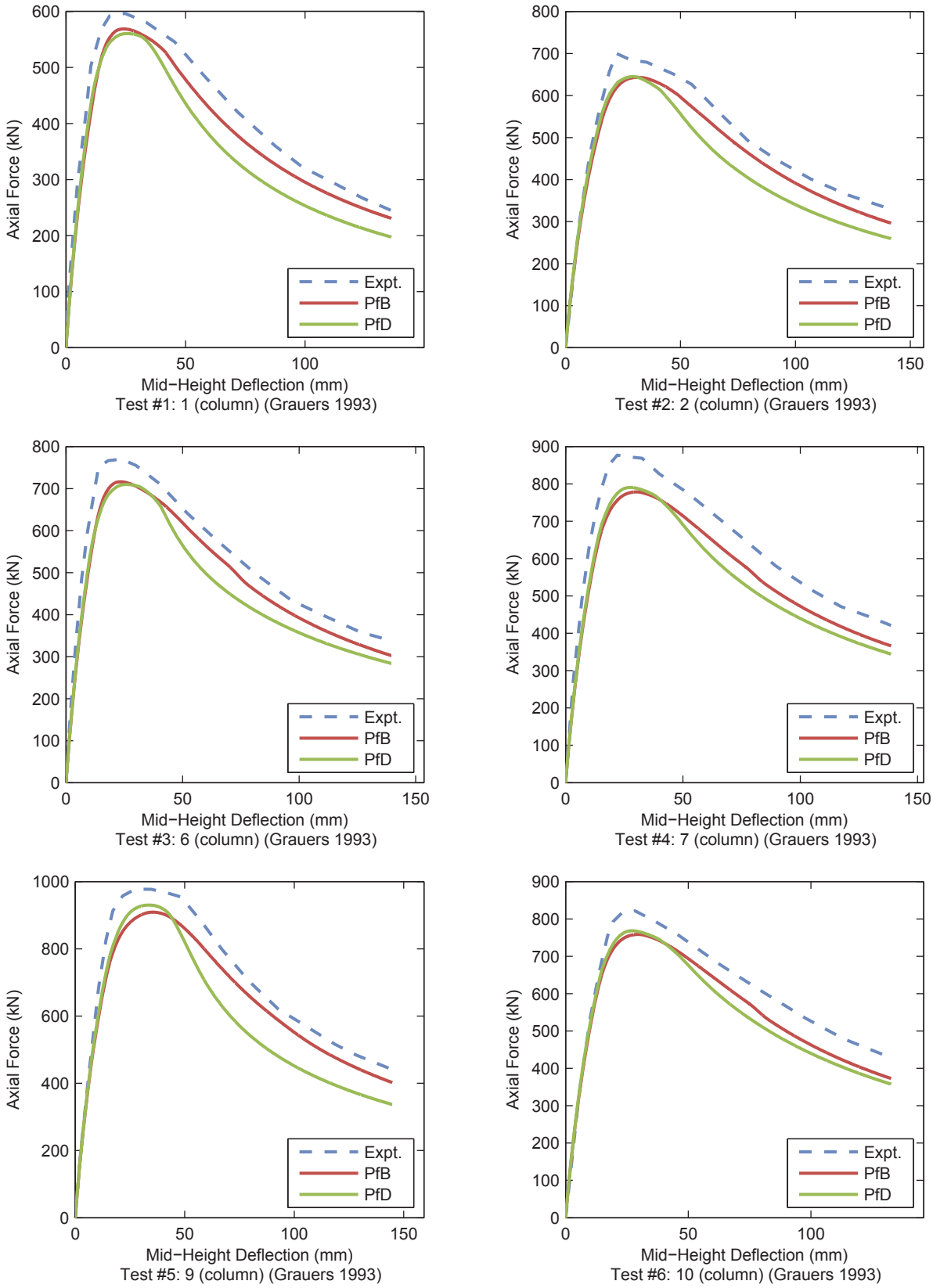

Figure 4.9. RCFT Validation Results – PBC

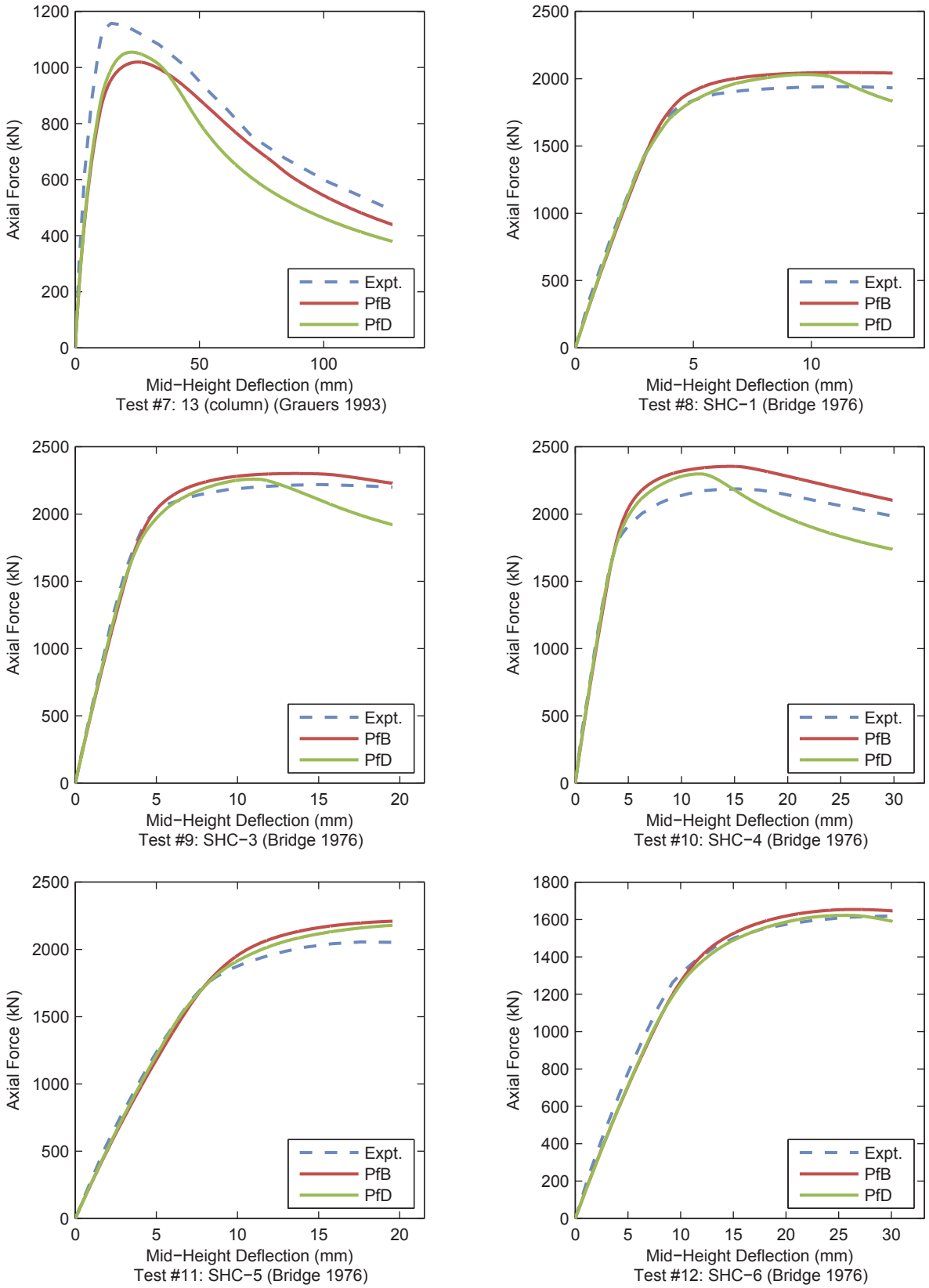

Figure 4.9. RCFT Validation Results – PBC (continued)

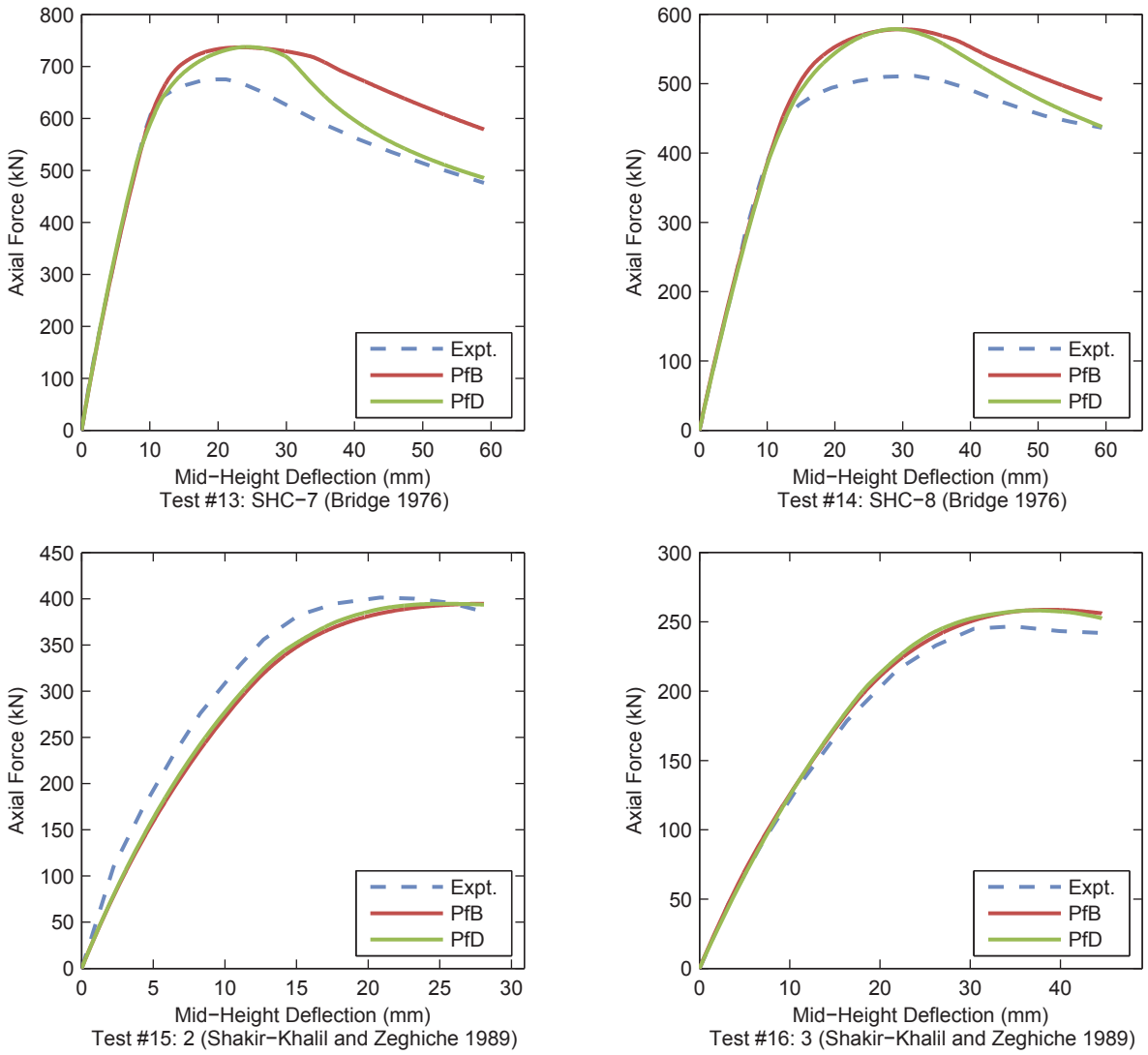

Figure 4.9. RCFT Validation Results – PBC (continued)

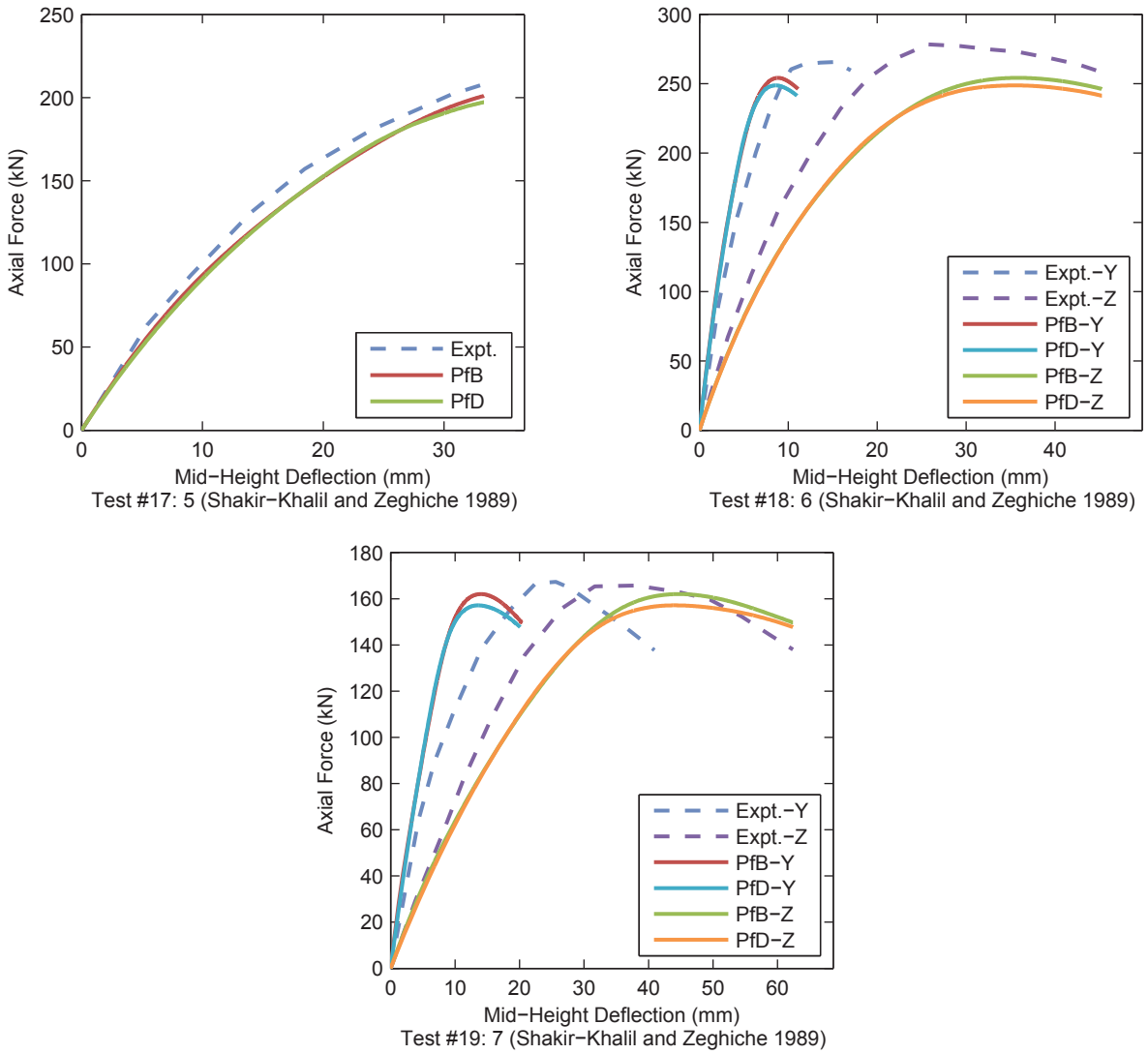

Figure 4.9. RCFT Validation Results – PBC (continued)

Table 4.31. Material and Geometric Properties – RCFT Validation Set – NBC

Test #	Author	Year	Specimen	H (mm)	B (mm)	t (mm)	H/t	f'_c (MPa)	F_y (MPa)	L (mm)	L/H	P (kN)	P/P_o
1	Tomii and Sakino	1979	III-1	100	100	2.98	33.6	21	289	300	3.0	51	0.10
2	Tomii and Sakino	1979	III-2	100	100	2.98	33.6	21	289	300	3.0	102	0.20
3	Tomii and Sakino	1979	III-3	100	100	2.99	33.4	21	288	300	3.0	153	0.30
4	Tomii and Sakino	1979	III-4	100	100	2.99	33.4	21	288	300	3.0	204	0.40
5	Tomii and Sakino	1979	III-5	100	100	2.99	33.4	21	288	300	3.0	255	0.50
6	Tomii and Sakino	1979	III-6	100	100	2.99	33.4	21	288	300	3.0	306	0.60
7	Nakahara and Sakino	1998	BR4-6-10-02	200	200	6.16	32.5	119	310	600	3.0	1,128	0.20
8	Nakahara and Sakino	1998	BR4-6-10-04-1	200	200	6.16	32.5	119	310	600	3.0	2,255	0.40
9	Nakahara and Sakino	1998	BR8-6-10-02	200	200	6.39	31.3	119	781	600	3.0	1,590	0.20
10	Varma	2000	BC-32-80-20	305	305	8.90	34.3	110	600	1,520	5.0	3,050	0.20
11	Varma	2000	BC-32-80-40	305	305	8.90	34.3	110	600	1,520	5.0	6,100	0.40
12	Varma	2000	BC-32-46-20	305	305	8.60	35.5	110	259	1,520	5.0	2,520	0.22
13	Varma	2000	BC-32-46-40	305	305	8.60	35.5	110	259	1,520	5.0	5,035	0.43
14	Varma	2000	BC-48-46-20	305	305	5.80	52.6	110	471	1,520	5.0	2,360	0.19

Table 4.32. Comparison Metrics – RCFT Validation Set – NBC – Proposed for Behavior

Test #	Initial Tangent			Peak Moment (kN-m)			Curvature at Peak Moment ($_{K}Hx10^{3}$)			Area Under Curve		
	Expt.	Model	Error	Expt.	Model	Error	Expt.	Model	Error	Expt.	Model	Error
1	4.04	4.68	15.89%	15.8	14.7	-7.11%	58.18	58.18	0.00%	836	807	-3.42%
2	4.27	4.97	16.44%	15.4	14.1	-8.51%	50.90	41.13	-19.18%	874	813	-6.99%
3	4.72	4.89	3.60%	14.6	13.5	-7.52%	8.78	11.52	31.17%	819	755	-7.79%
4	4.40	4.83	9.86%	13.3	12.5	-5.65%	15.55	9.25	-40.55%	756	698	-7.69%
5	4.69	4.76	1.49%	12.4	11.1	-10.46%	12.40	9.38	-24.34%	591	518	-12.37%
6	5.32	4.68	-12.09%	10.8	9.0	-16.32%	12.00	10.36	-13.68%	279	238	-14.58%
7	82.06	54.48	-33.61%	193.4	183.2	-5.30%	9.61	12.51	30.22%	6,802	6,667	-1.97%
8	83.02	53.10	-36.04%	186.3	188.6	1.22%	7.36	7.84	6.48%	5,920	5,845	-1.27%
9	49.31	52.09	5.64%	329.3	332.5	0.97%	15.48	12.69	-18.02%	10,184	10,305	1.19%
10	159.33	178.46	12.01%	926.0	900.2	-2.78%	18.32	10.72	-41.50%	193,199	97,784	-49.39%
11	164.99	178.67	8.29%	787.4	796.4	1.15%	8.59	8.59	0.00%	27,982	26,714	-4.53%
12	158.80	186.23	17.27%	600.1	532.8	-11.23%	8.30	9.62	15.95%	32,157	25,486	-20.75%
13	154.19	167.22	8.45%	544.0	543.8	-0.04%	4.83	6.37	31.98%	5,732	6,294	9.81%
14	132.02	162.53	23.11%	593.5	569.4	-4.05%	8.94	10.00	11.81%	37,434	32,333	-13.63%
Mean			2.88%			-5.40%			-2.12%			-9.53%
Standard Deviation			18.07%			5.27%			24.99%			13.74%
Median			8.37%			-5.48%			0.00%			-7.34%

Table 4.33. Comparison Metrics – RCFT Validation Set – NBC – Proposed for Design

Test #	Initial Tangent			Peak Moment (kN-m)			Curvature at Peak Moment ($_{K}Hx10^{3}$)			Area Under Curve		
	Expt.	Model	Error	Expt.	Model	Error	Expt.	Model	Error	Expt.	Model	Error
1	4.04	4.56	13.04%	15.8	14.0	-11.44%	58.18	35.96	-38.20%	836	770	-7.85%
2	4.27	4.82	13.06%	15.4	13.8	-10.64%	50.90	8.14	-84.00%	874	739	-15.37%
3	4.72	4.88	3.37%	14.6	13.0	-10.95%	8.78	6.96	-20.76%	819	650	-20.60%
4	4.40	4.83	9.98%	13.3	11.8	-11.38%	15.55	5.73	-63.18%	756	550	-27.29%
5	4.69	4.77	1.67%	12.4	10.0	-19.19%	12.40	5.20	-58.06%	591	349	-41.01%
6	5.32	4.66	-12.49%	10.8	8.1	-25.11%	12.00	4.23	-64.78%	279	140	-50.00%
7	82.06	54.72	-33.32%	193.4	181.8	-6.00%	9.61	9.00	-6.28%	6,802	3,930	-42.22%
8	83.02	53.18	-35.94%	186.3	179.5	-3.66%	7.36	5.65	-23.25%	5,920	1,078	-81.80%
9	49.31	53.78	9.06%	329.3	303.3	-7.91%	15.48	9.18	-40.70%	10,184	8,326	-18.24%
10	159.33	180.98	13.59%	926.0	852.1	-7.98%	18.32	8.57	-53.20%	193,199	63,236	-67.27%
11	164.99	185.48	12.42%	787.4	714.9	-9.20%	8.59	5.77	-32.79%	27,982	5,401	-80.70%
12	158.80	189.83	19.54%	600.1	538.4	-10.29%	8.30	7.97	-3.97%	32,157	8,632	-73.16%
13	154.19	167.78	8.82%	544.0	530.6	-2.47%	4.83	5.12	5.94%	5,732	2,821	-50.79%
14	132.02	161.33	22.20%	593.5	587.8	-0.95%	8.94	9.10	1.81%	37,434	13,781	-63.19%
Mean			3.21%			-9.80%			-34.39%			-45.68%
Standard Deviation			18.06%			6.33%			27.94%			25.13%
Median			9.52%			-9.75%			-35.49%			-46.11%

Table 4.34. Comparison Metrics – RCFT Validation Set – NBC (section) – Proposed for Behavior

Test #	Initial Tangent			Peak Moment (kN-m)			Curvature at Peak Moment ($_{K}Hx10^{3}$)			Area Under Curve		
	Expt.	Model	Error	Expt.	Model	Error	Expt.	Model	Error	Expt.	Model	Error
1	4.04	4.65	15.29%	15.8	14.9	-5.83%	58.18	58.18	0.00%	836	812	-2.84%
2	4.27	4.93	15.62%	15.4	14.6	-5.33%	50.90	59.44	16.79%	874	826	-5.49%
3	4.72	4.88	3.36%	14.6	13.9	-4.71%	8.78	58.49	565.85%	819	780	-4.73%
4	4.40	4.82	9.68%	13.3	12.8	-3.60%	15.55	59.65	283.56%	756	738	-2.38%
5	4.69	4.75	1.39%	12.4	11.3	-8.58%	12.40	16.11	29.94%	591	556	-5.84%
6	5.32	4.68	-12.15%	10.8	9.4	-12.56%	12.00	23.65	97.13%	279	252	-9.75%
7	82.06	54.41	-33.70%	193.4	186.3	-3.71%	9.61	16.73	74.18%	6,802	6,921	1.75%
8	83.02	53.10	-36.04%	186.3	191.7	2.90%	7.36	9.03	22.70%	5,920	6,606	11.59%
9	49.31	51.98	5.42%	329.3	335.5	1.87%	15.48	13.46	-13.06%	10,184	10,618	4.26%
10	159.33	178.27	11.89%	926.0	930.6	0.50%	18.32	13.33	-27.20%	193,199	205,630	6.43%
11	164.99	181.50	10.01%	787.4	846.2	7.47%	8.59	10.56	22.95%	27,982	35,330	26.26%
12	158.80	186.96	17.74%	600.1	559.4	-6.78%	8.30	15.70	89.22%	32,157	31,056	-3.42%
13	154.19	168.45	9.25%	544.0	574.4	5.59%	4.83	8.04	66.60%	5,732	6,900	20.38%
14	132.02	162.96	23.44%	593.5	593.6	0.02%	8.94	13.82	54.54%	37,434	43,178	15.34%
Mean			2.94%			-2.34%			91.66%			3.68%
Standard Deviation			18.11%			5.62%			156.01%			10.93%
Median			9.47%			-3.66%			42.24%			-0.31%

Table 4.35. Comparison Metrics – RCFT Validation Set – NBC (section) – Proposed for Design

Test #	Initial Tangent			Peak Moment (kN-m)			Curvature at Peak Moment ($_{K}Hx10^{3}$)			Area Under Curve		
	Expt.	Model	Error	Expt.	Model	Error	Expt.	Model	Error	Expt.	Model	Error
1	4.04	4.55	12.71%	15.8	14.0	-11.40%	58.18	10.76	-81.50%	836	770	-7.86%
2	4.27	4.81	12.76%	15.4	13.8	-10.51%	50.90	8.62	-83.07%	874	756	-13.46%
3	4.72	4.87	3.15%	14.6	13.1	-10.64%	8.78	7.49	-14.77%	819	677	-17.28%
4	4.40	4.83	9.84%	13.3	11.8	-10.92%	15.55	6.20	-60.11%	756	588	-22.30%
5	4.69	4.76	1.60%	12.4	10.1	-18.47%	12.40	5.61	-54.77%	591	391	-33.79%
6	5.32	4.65	-12.69%	10.8	8.2	-24.20%	12.00	4.59	-61.71%	279	167	-40.31%
7	82.06	54.59	-33.48%	193.4	183.4	-5.21%	9.61	9.48	-1.30%	6,802	4,732	-30.42%
8	83.02	53.21	-35.90%	186.3	181.4	-2.66%	7.36	5.93	-19.46%	5,920	1,406	-76.24%
9	49.31	53.72	8.96%	329.3	305.0	-7.38%	15.48	9.44	-39.05%	10,184	8,820	-13.39%
10	159.33	181.48	13.90%	926.0	874.4	-5.57%	18.32	9.52	-48.00%	193,199	146,789	-24.02%
11	164.99	188.33	14.15%	787.4	745.6	-5.31%	8.59	6.29	-26.78%	27,982	11,568	-58.66%
12	158.80	190.18	19.76%	600.1	556.5	-7.28%	8.30	9.15	10.26%	32,157	15,946	-50.41%
13	154.19	169.46	9.91%	544.0	552.9	1.64%	4.83	5.56	15.11%	5,732	4,217	-26.42%
14	132.02	161.07	22.01%	593.5	606.9	2.27%	8.94	10.16	13.63%	37,434	25,143	-32.83%
Mean			3.33%			-8.26%			-32.25%			-31.96%
Standard Deviation			18.18%			7.09%			34.04%			19.14%
Median			9.87%			-7.33%			-32.91%			-28.42%

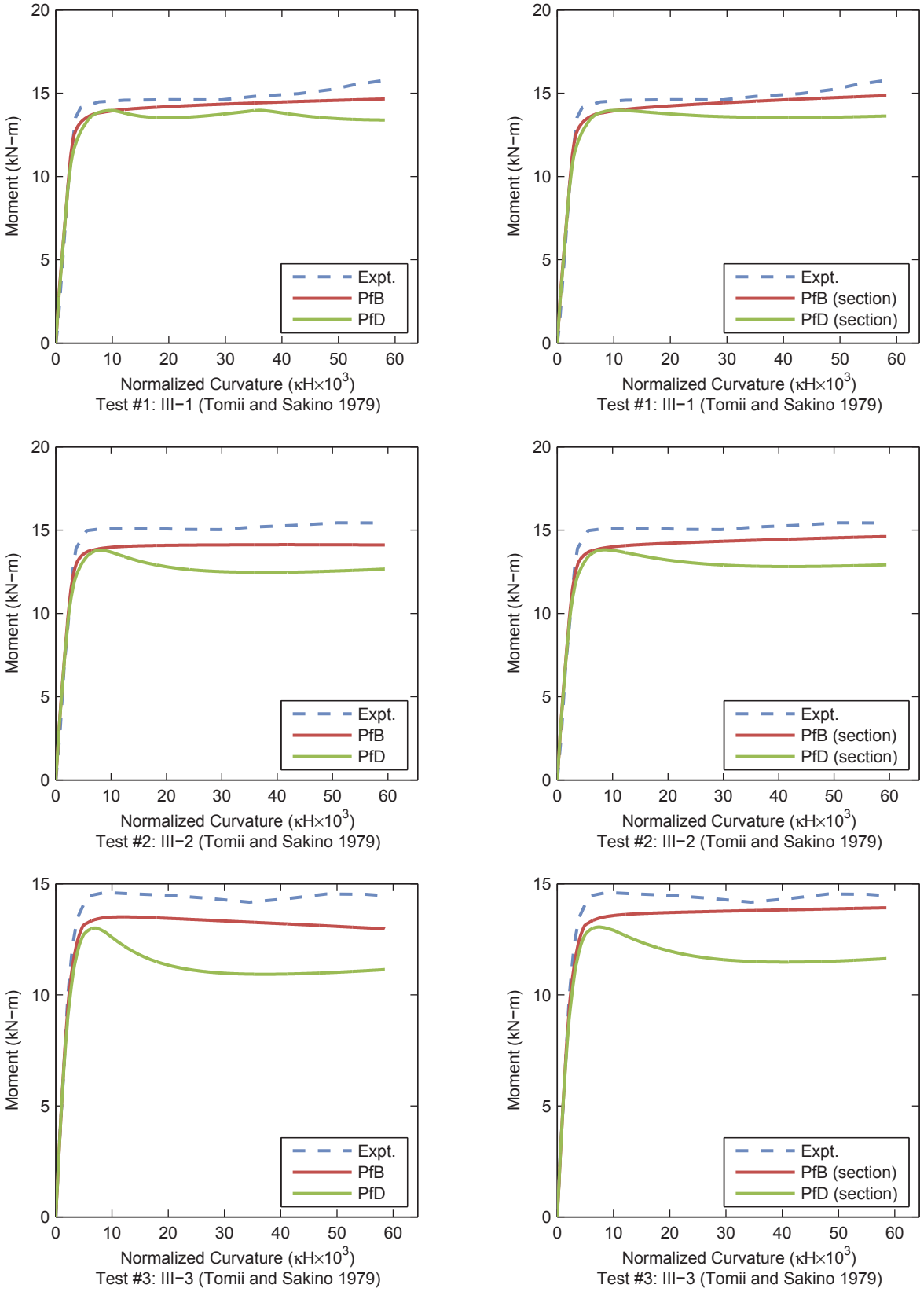

Figure 4.10. RCFT Validation Results – NBC

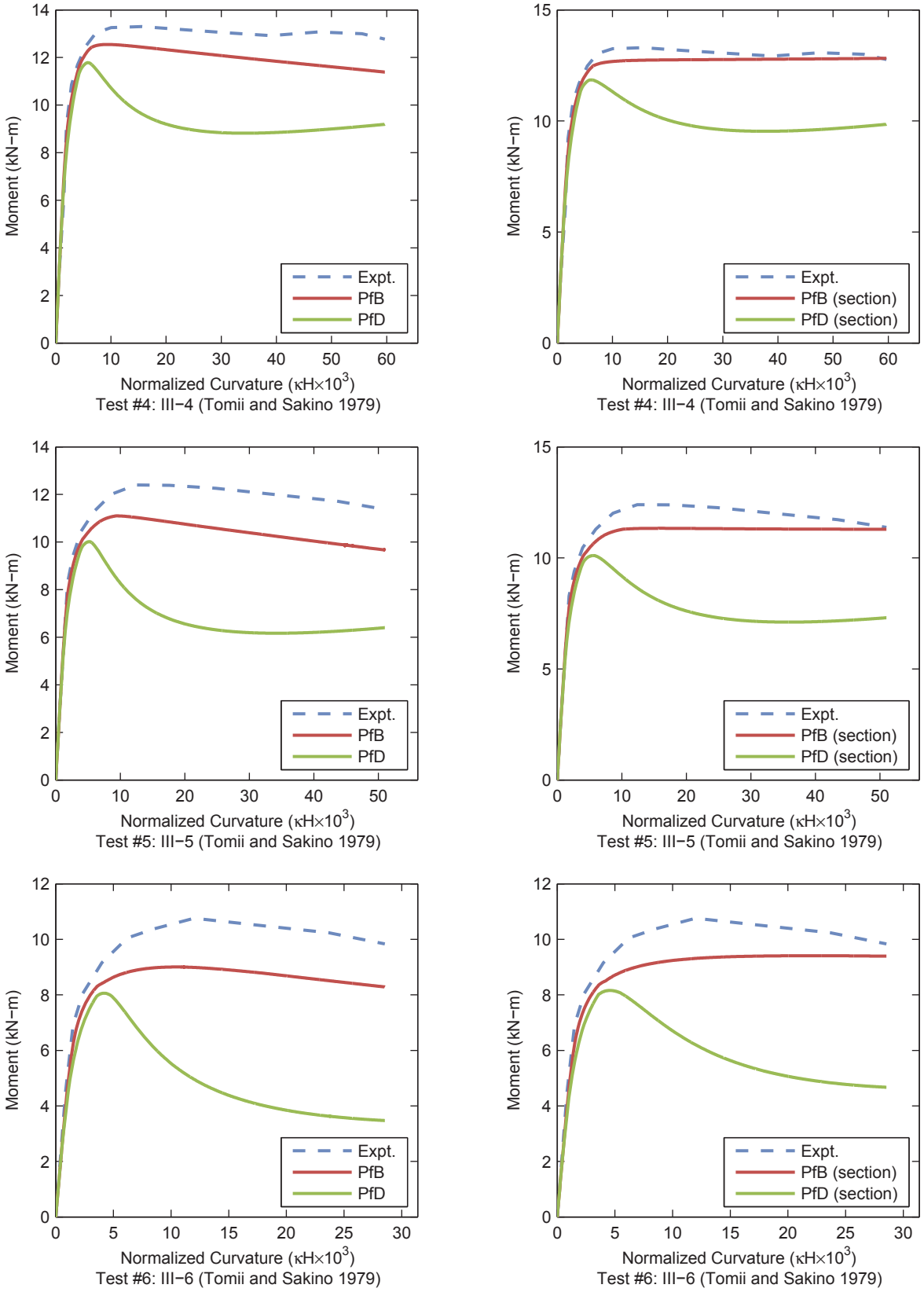

Figure 4.10. RCFT Validation Results – NBC (continued)

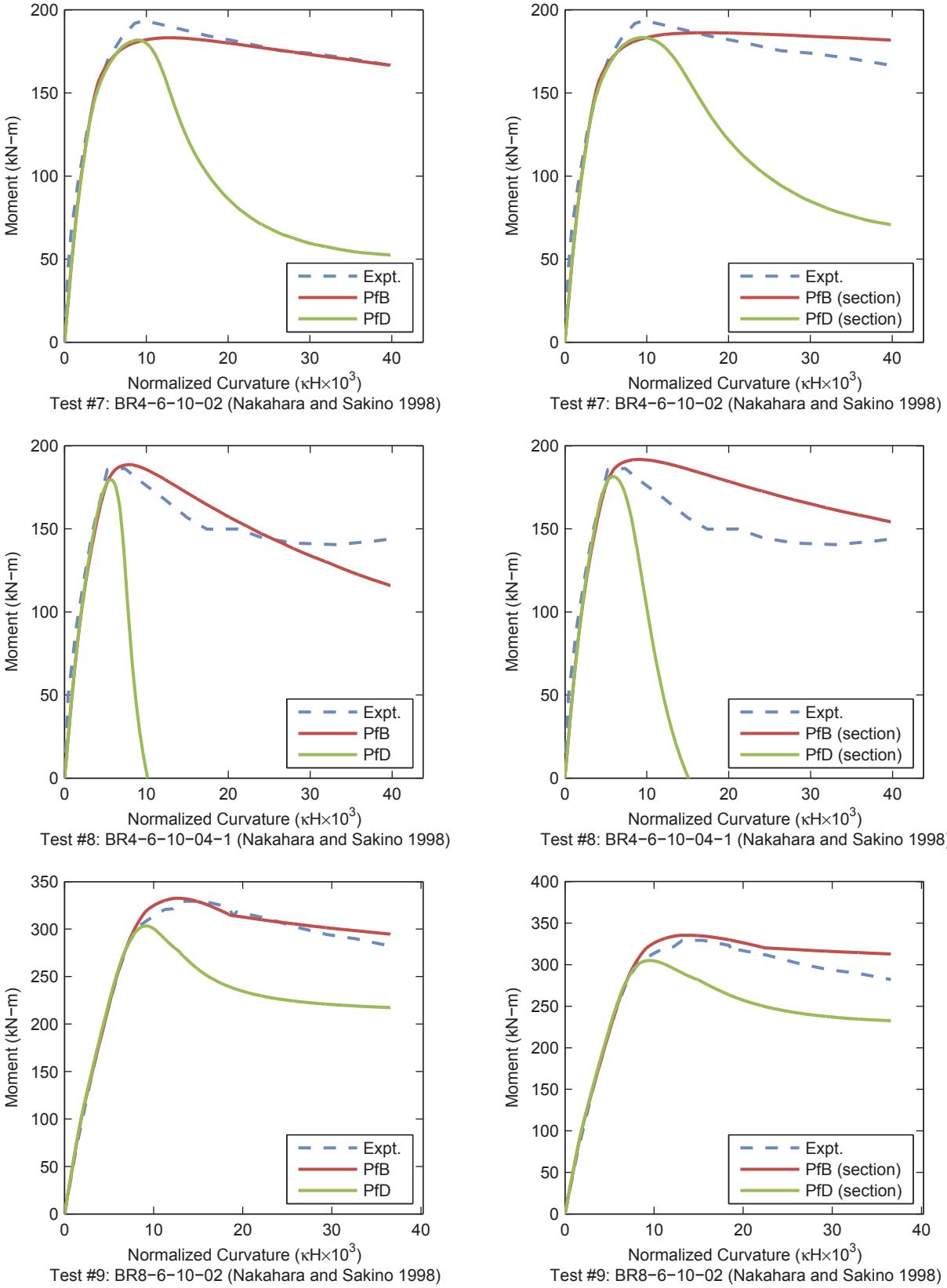

Figure 4.10. RCFT Validation Results – NBC (continued)

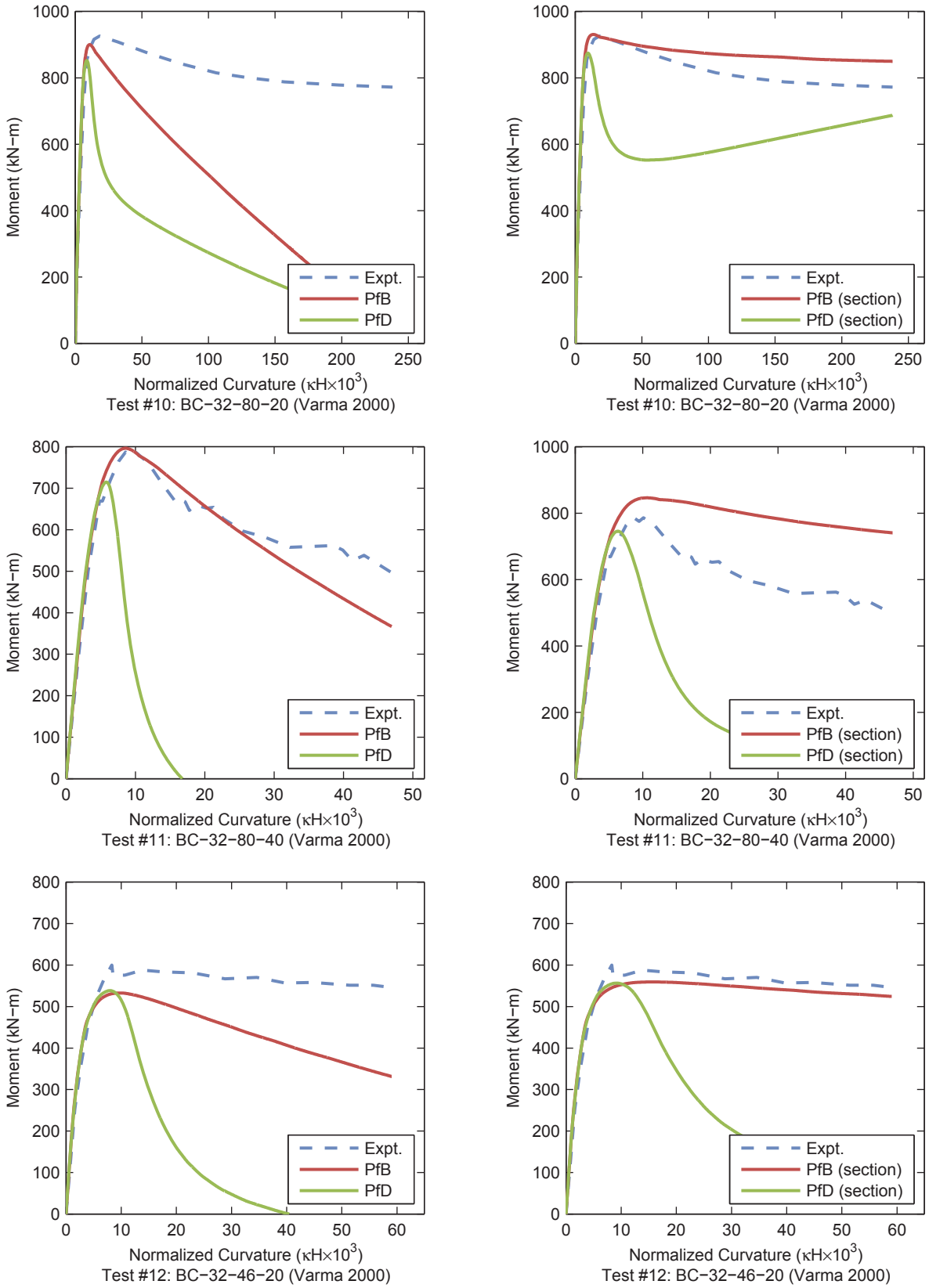

Figure 4.10. RCFT Validation Results – NBC (continued)

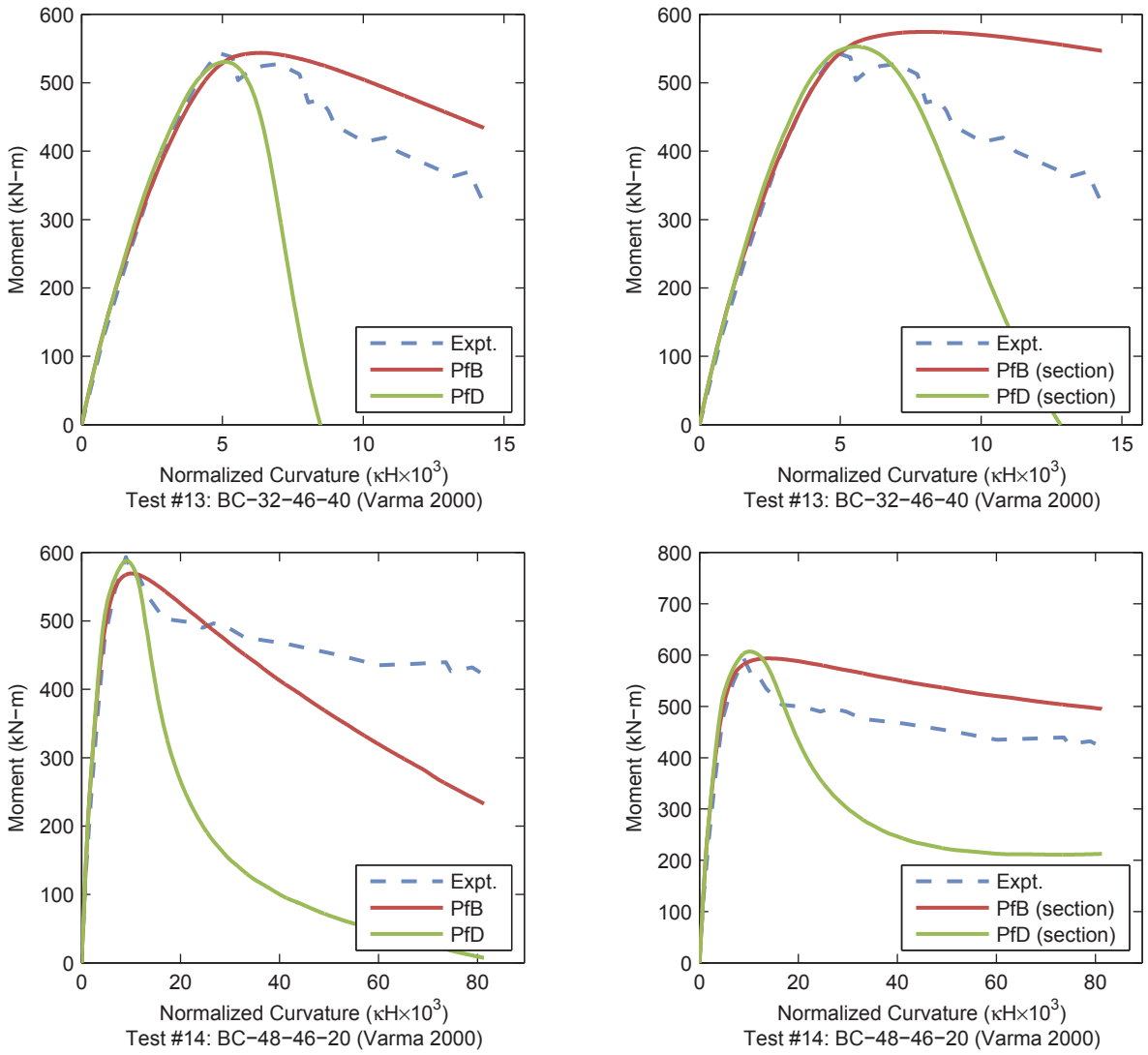

Figure 4.10. RCFT Validation Results – NBC (continued)

4.5.2 Cyclic Validation Results - Nakahara and Sakino 2000

Nakahara and Sakino (2000) performed a series of tests on RCFT members. The loading configuration was the same as the monotonic NBC tests described above (Figure 4.1) and the same mesh density was used. Material and geometric properties of the specimens are given in Table 4.36, results are shown in Figure 4.11.

Table 4.36. Material and Geometric Properties – Nakahara and Sakino 2000

Test #	Specimen	H (mm)	B (mm)	t (mm)	H/t	f'_c (MPa)	F_y (MPa)	L (mm)	L/H	P (kN)	P/P_o
1	BRA4-6-5-02	200	200	5.93	33.7	48	320	660	3.3	570	0.18
2	BRA4-6-5-04	200	200	5.93	33.7	48	320	660	3.3	1,140	0.36
3	BRA4-4-5-02	200	200	4.25	47.1	48	211	660	3.3	426	0.17
4	BRA4-4-5-04	200	200	4.25	47.1	48	211	660	3.3	851	0.35
5	BRA4-2-5-02	200	200	2.04	98.0	48	253	660	3.3	380	0.17
6	BRA4-2-5-04	200	200	2.04	98.0	48	253	660	3.3	761	0.34
7	BRA4-6-5-02-C	200	200	5.93	33.7	48	320	660	3.3	570	0.18
8	BRA4-6-5-04-C	200	200	5.93	33.7	48	320	660	3.3	1,140	0.36
9	BRA4-2-5-02-C	200	200	2.04	98.0	48	253	660	3.3	380	0.17
10	BRA4-2-5-04-C	200	200	2.04	98.0	48	253	660	3.3	761	0.34

For the specimens with high axial load and moderate H/t ratios (BRA4-6-5-04, BRA4-4-5-04, and BRA4-6-5-04-C) the degradation seen in the experiment is not captured as well as it is for the specimens with high axial load and high H/t ratios (BRA4-2-5-04 and BRA4-2-5-04-C). For the specimens with low axial load, the cyclic degradation is less drastic overall and the model captures the behavior very well for all H/t ratios. This is likely due to the relatively simple way local buckling is triggered in the steel constitutive relation. In addition to the scatter observed when deriving the expression for strain at local buckling, each fiber is independent and the state of the section as a whole is not taken into account in the local buckling model. Nonetheless, the specimens that were not captured well were intermediate cases, with more extreme cases showing better correlation.

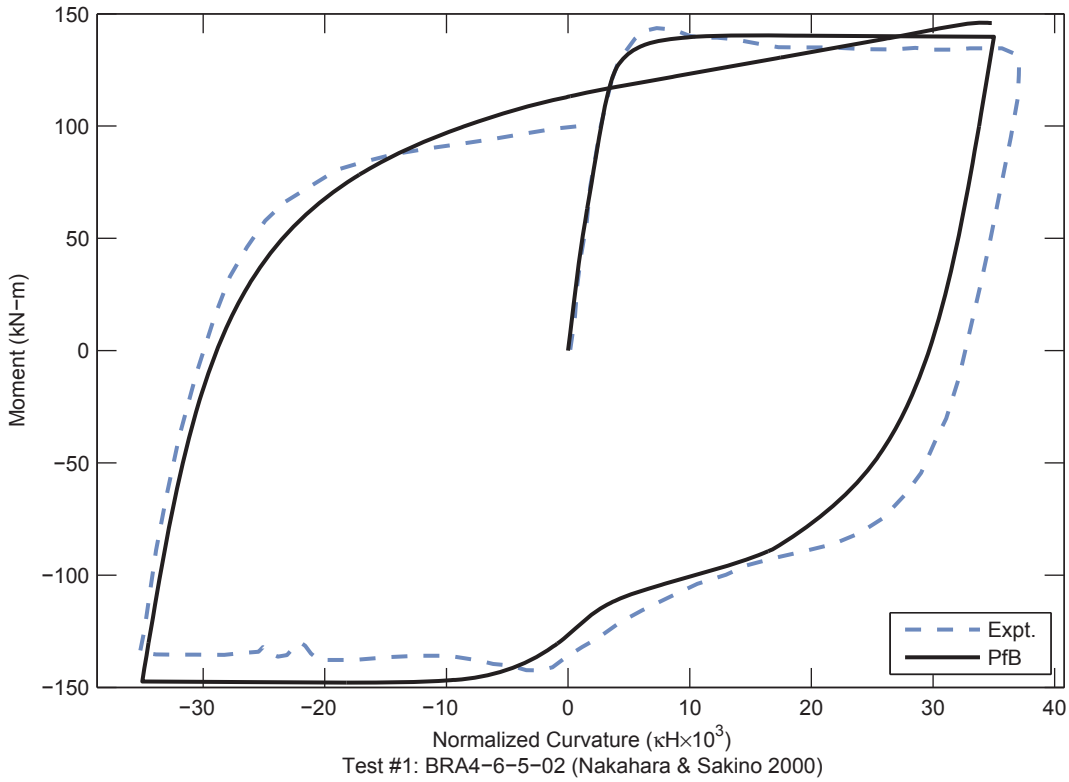

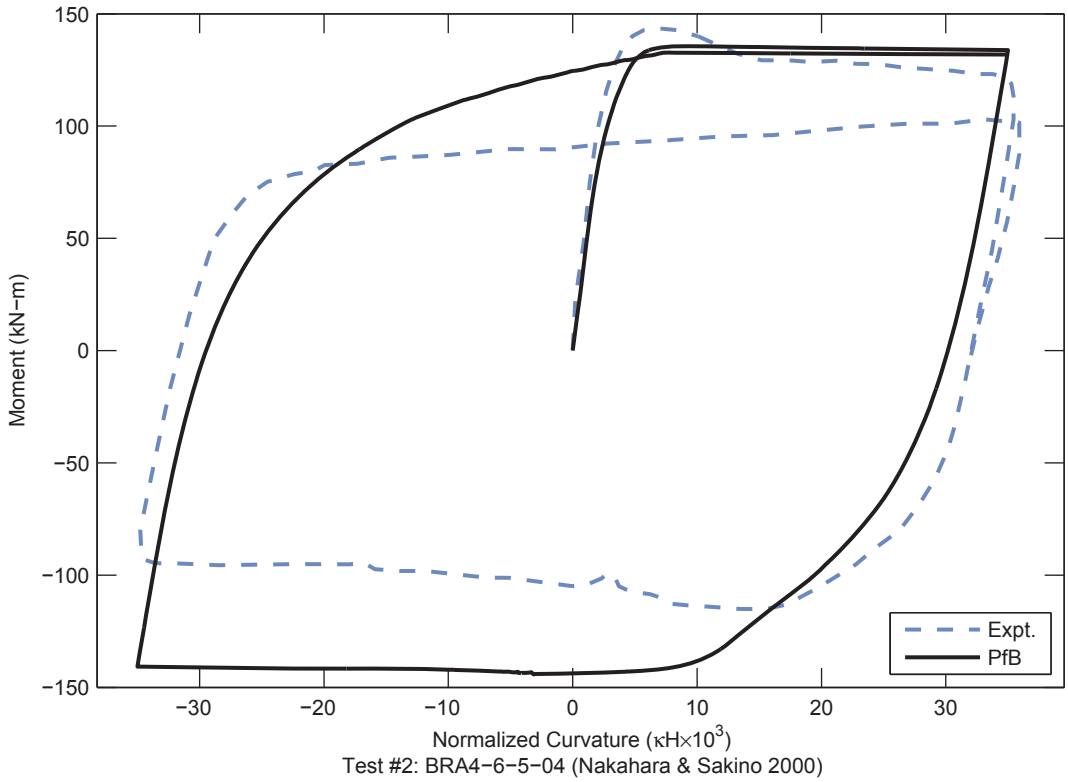

Figure 4.11. RCFT Validation Results – Nakahara and Sakino 2000

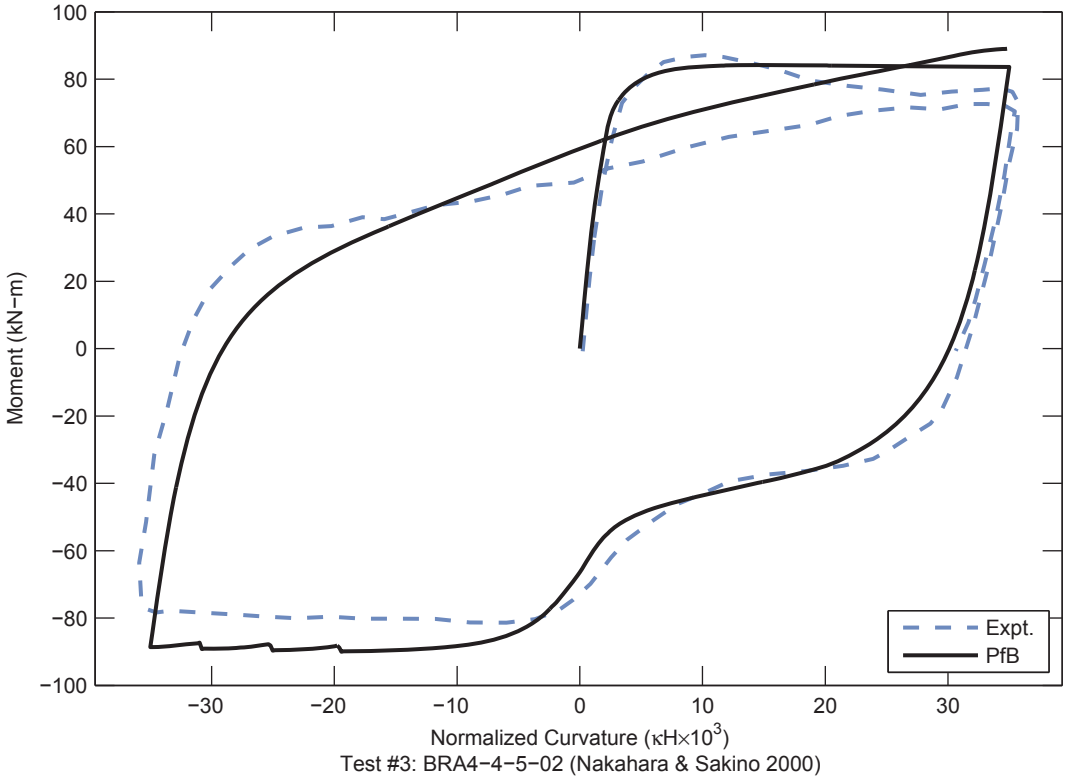

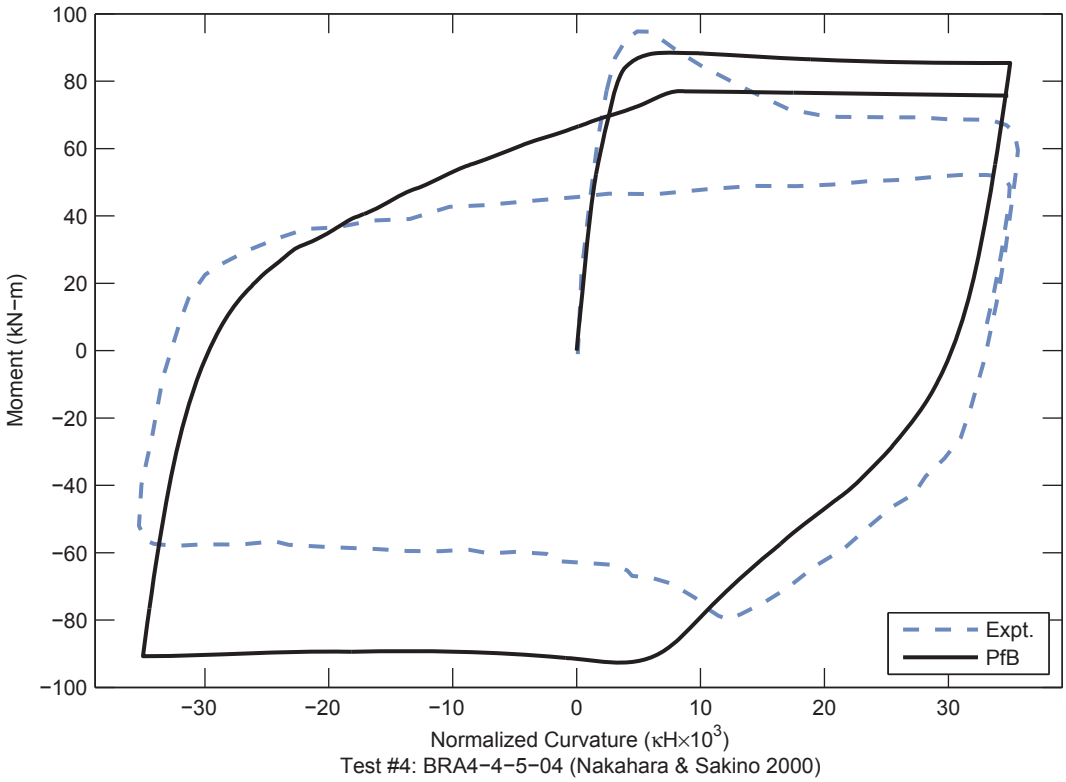

Figure 4.11. RCFT Validation Results – Nakahara and Sakino 2000 (Continued)

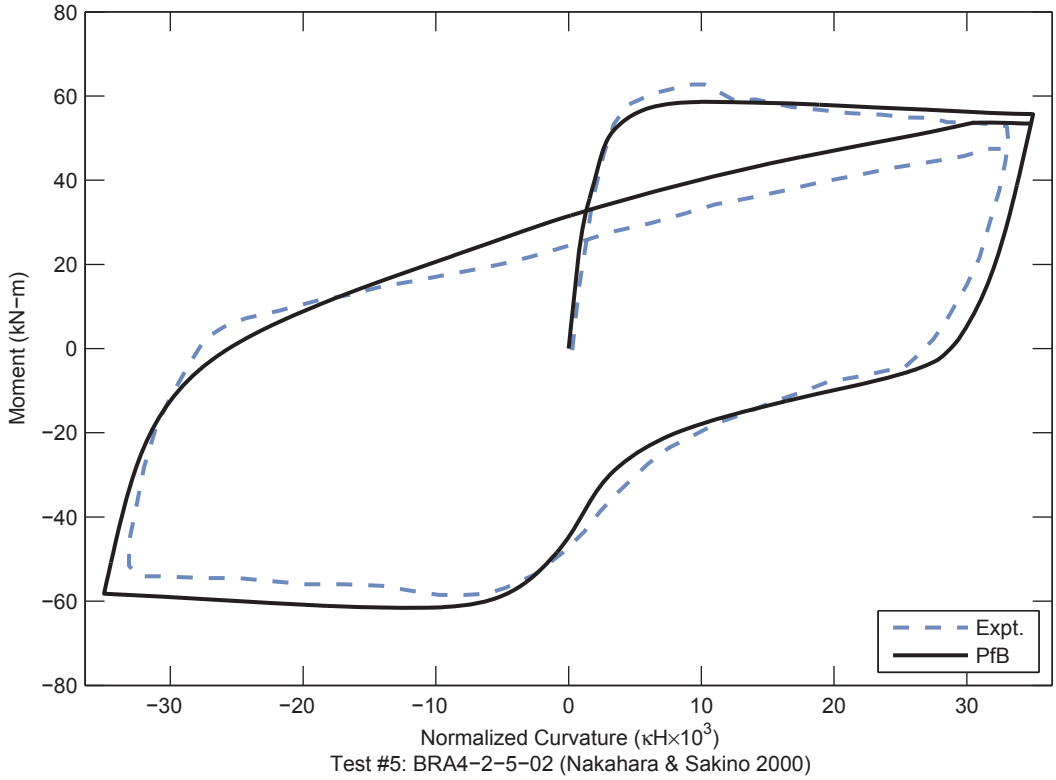

Test #5: BRA4−2−5−02 (Nakahara & Sakino 2000)

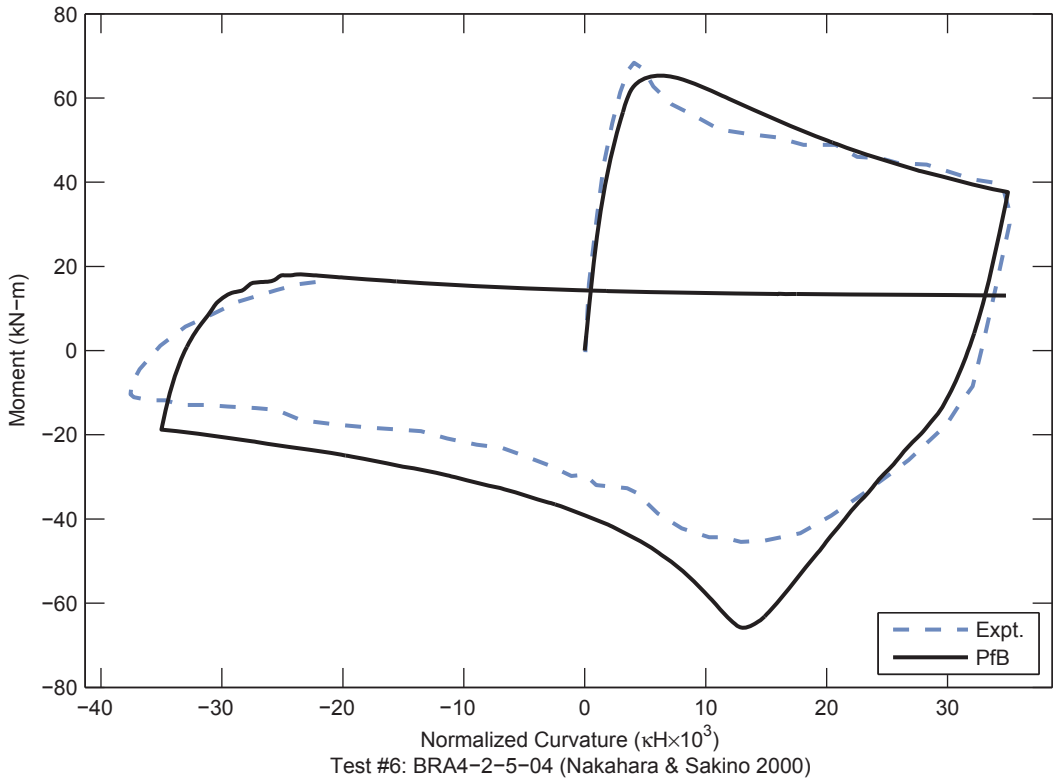

Test #6: BRA4−2−5−04 (Nakahara & Sakino 2000)

Figure 4.11. RCFT Validation Results – Nakahara and Sakino 2000 (Continued)

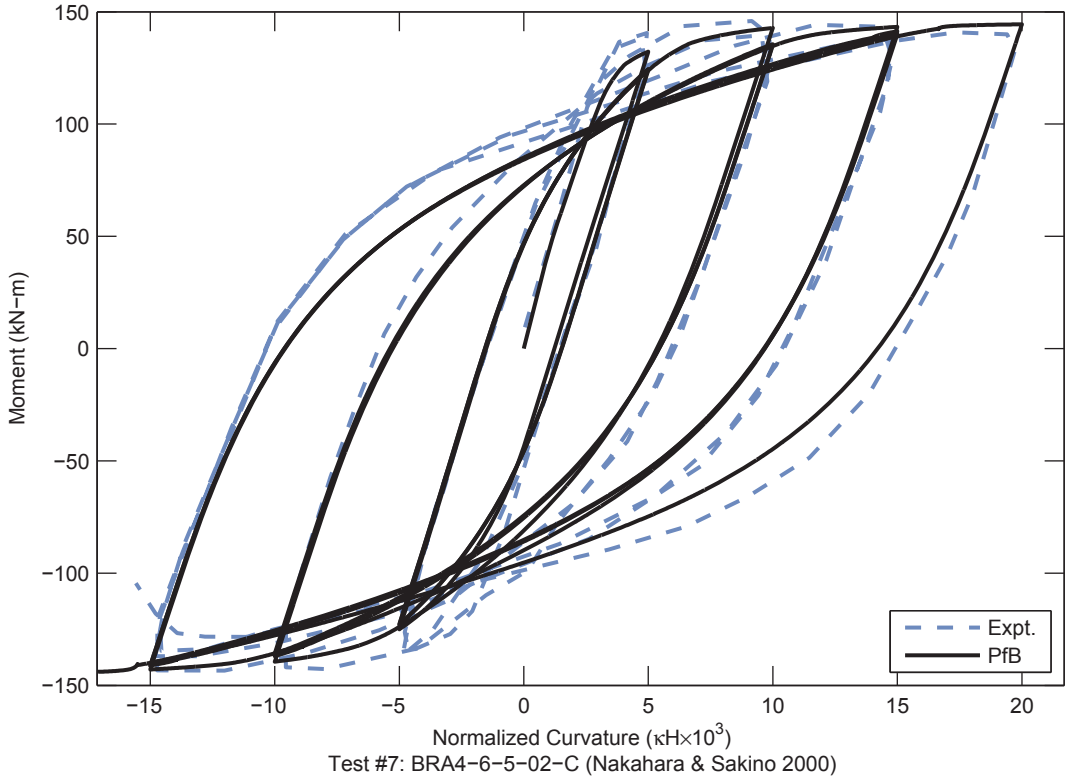

Test #7: BRA4−6−5−02−C (Nakahara & Sakino 2000)

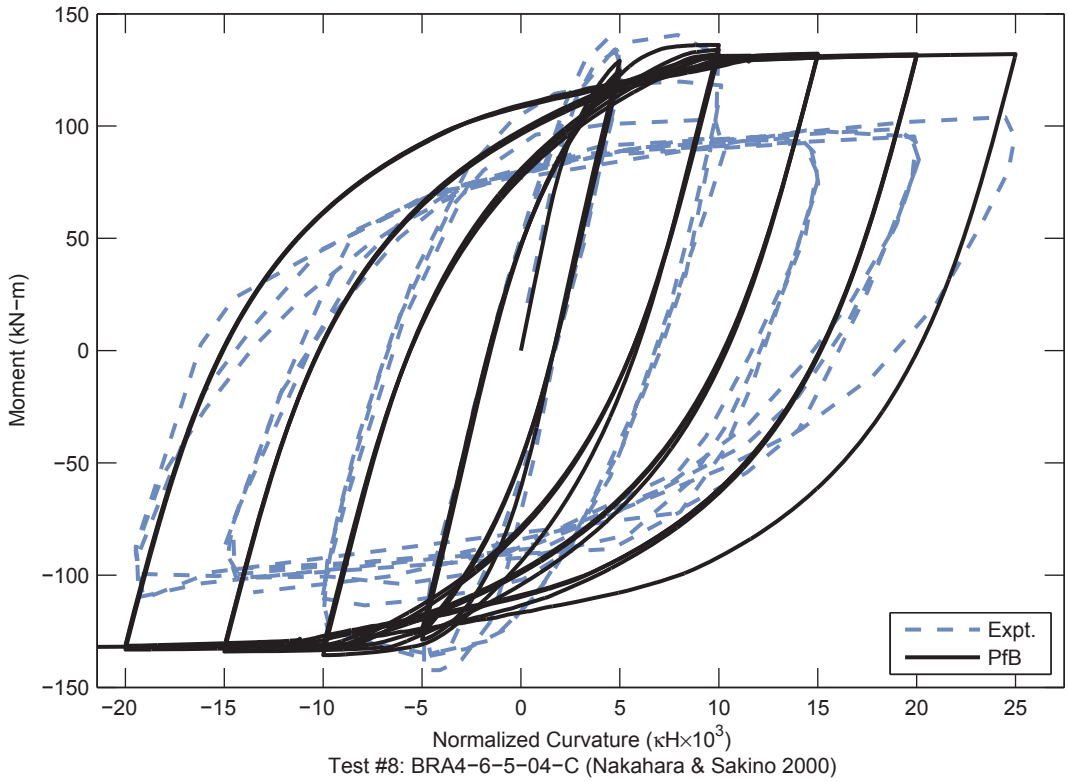

Test #8: BRA4−6−5−04−C (Nakahara & Sakino 2000)

Figure 4.11. RCFT Validation Results – Nakahara and Sakino 2000 (Continued)

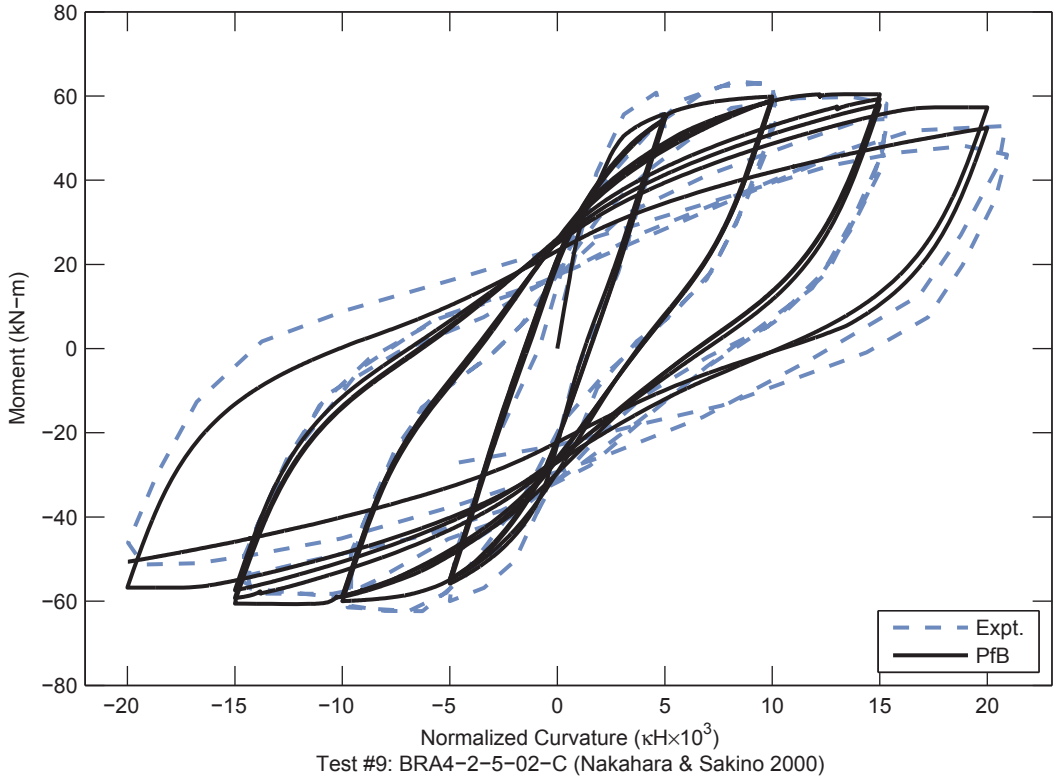

Test #9: BRA4−2−5−02−C (Nakahara & Sakino 2000)

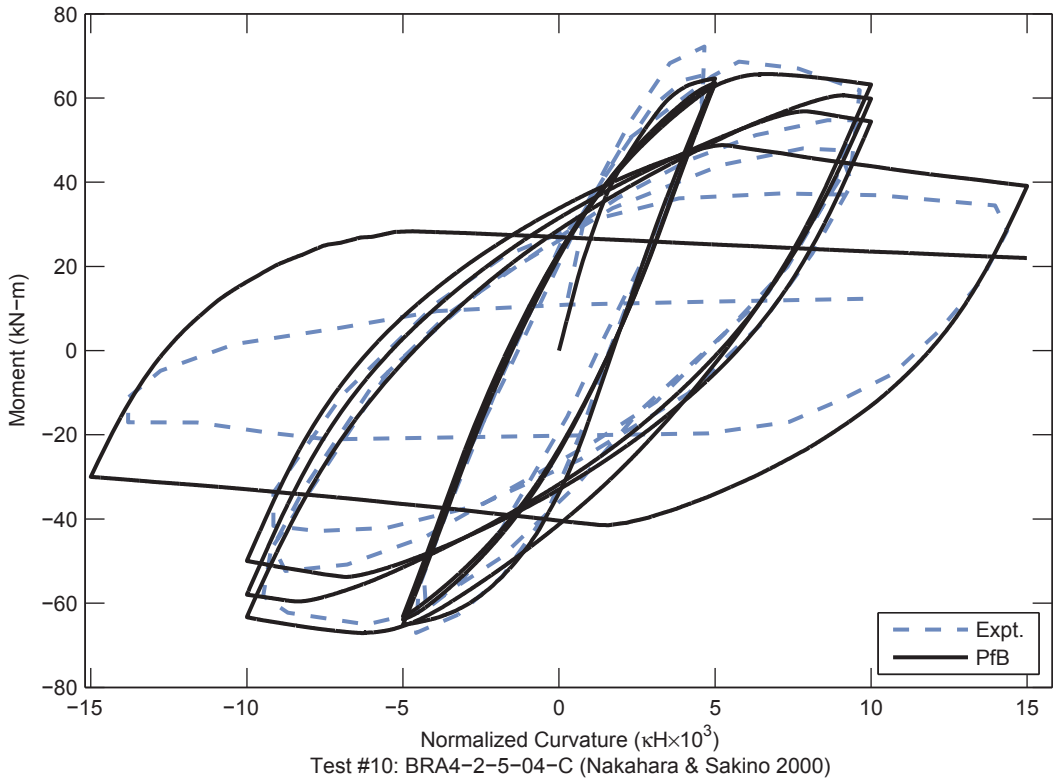

Test #10: BRA4−2−5−04−C (Nakahara & Sakino 2000)

Figure 4.11. RCFT Validation Results – Nakahara and Sakino 2000 (Continued)

4.5.3 Cyclic Validation Results - Varma 2000

Varma (2000) performed a series of non-proportionally loaded beam-column tests on RCFT members. A cantilever column was subjected to an axial compressive load applied by tension rods. An actuator then applied horizontal loads at the top of the specimen. The tension rods moved with the specimen creating a follower load. This was modeled by defining a stiff truss element connected to the top and to a secondary node at the base. The axial load was applied to the secondary node and transferred through the truss element to the top, applying a load roughly in line with the chord of the specimen as in the experiment. Two beam elements were used along the length, each with three integration points. Material and geometric properties of the specimens are given in Table 4.37, results are shown in Figure 4.13.

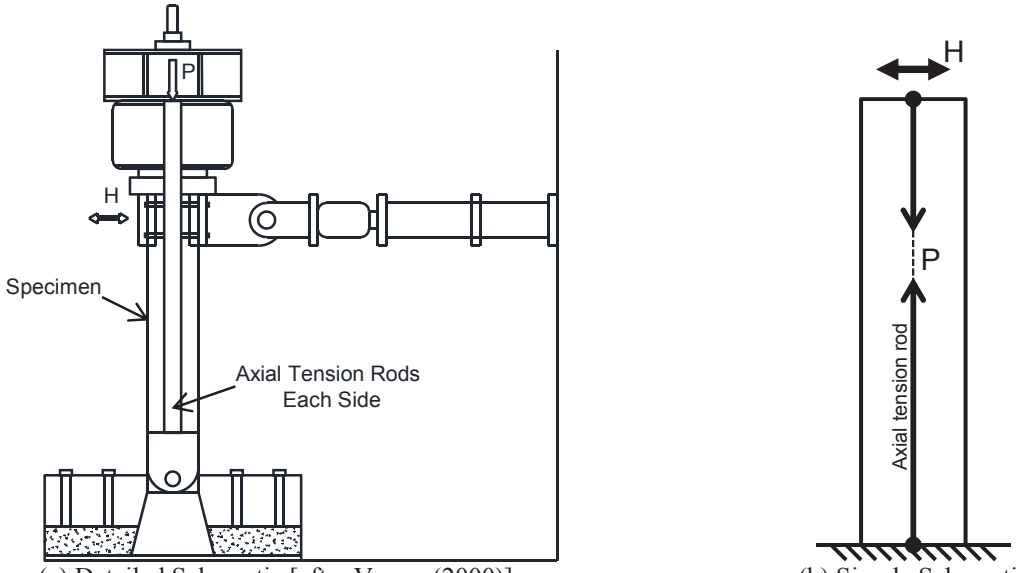

(a) Detailed Schematic [after Varma (2000)] (b) Simple Schematic

Figure 4.12. Experiment Setup – Varma 2000

Table 4.37. Material and Geometric Properties – Varma 2000

Test #	Specimen	H (mm)	B (mm)	t (mm)	H/t	f'_c (MPa)	F_v (MPa)	L (mm)	L/H	P (kN)	P/P_o
1	CBC-32-80-10	305	305	8.90	34.3	110	600	1,500	4.9	1,523	0.10
2	CBC-32-80-20	305	305	8.90	34.3	110	600	1,500	4.9	3,050	0.20
3	CBC-48-80-10	305	305	6.10	50.0	110	660	1,500	4.9	1,355	0.10
4	CBC-48-80-20	305	305	6.10	50.0	110	660	1,500	4.9	2,715	0.19
5	CBC-32-46-10	305	305	8.6	35.5	110	269	1,500	4.9	1,255	0.11
6	CBC-32-46-20	305	305	8.6	35.5	110	269	1,500	4.9	2,515	0.21
7	CBC-48-46-10	305	305	5.8	52.6	110	471	1,500	4.9	1,178	0.09
8	CBC-48-46-20	305	305	5.8	52.6	110	471	1,500	4.9	2,270	0.18

The following observations are made regarding the validation results:

- A generally good correlation is seen between the computational and experimental results.
- The peak loads are underpredicted by the model. This is possibly due to extra confinement provided by the footing that moved the plastic hinge up in the experiment.
- The unloading stiffness, yield upon unloading, cyclic degradation are captured well by the model.
- The experiment exhibits hardening behavior with the peak strength of each cycle occurring at the reversal. The models, however, show peaks being reached within the cycles and flat or softening behavior from the peak to the reversal. This has only a minor effect on the accuracy of the load-deformation curve as a whole.
- For some specimens (e.g., CBC-48-80-20) the degradation is overpredicted, for other specimens (e.g., CBC-48-80-10) it is underpredicted. For specimen CBC-48-46-10, the degradation under constant amplitude cycles is not captured. On average, however, the degradation is captured well.

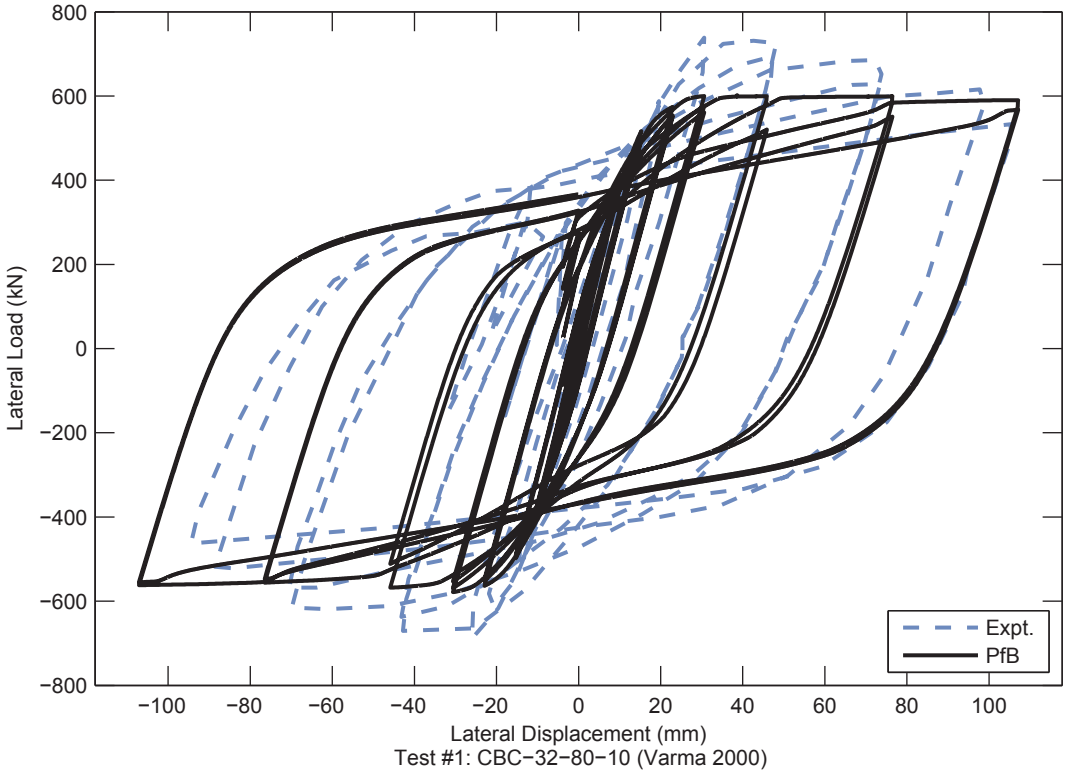

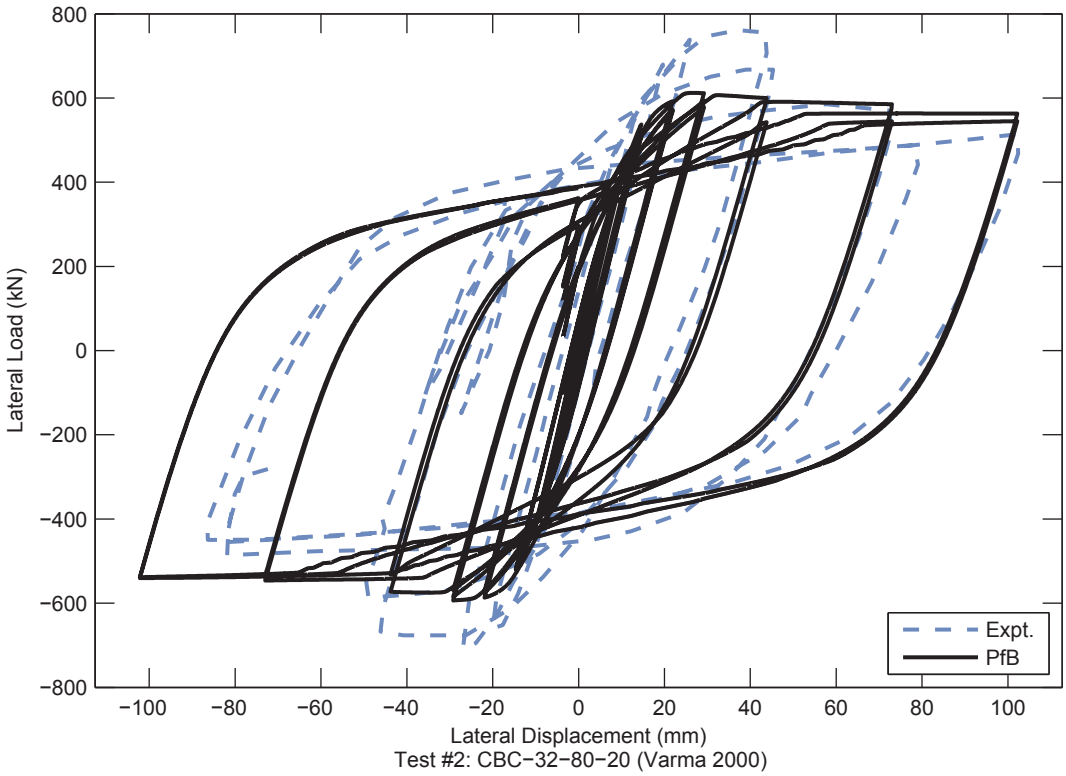

Figure 4.13. RCFT Validation Results – Varma 2000

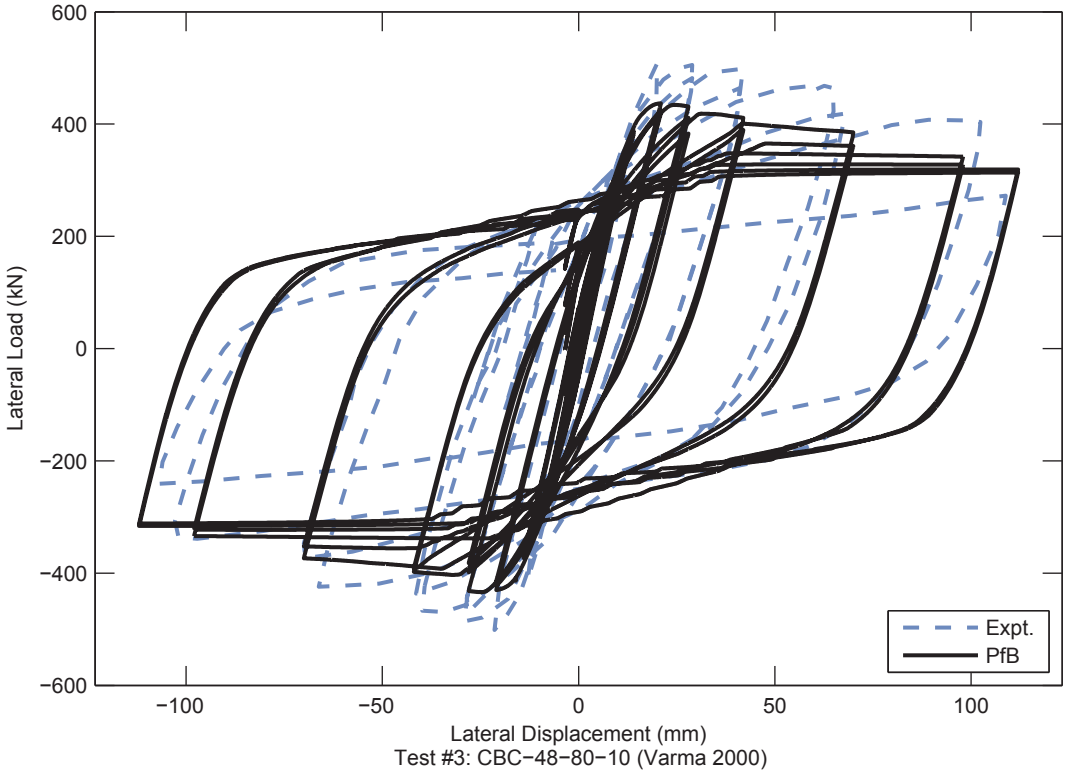

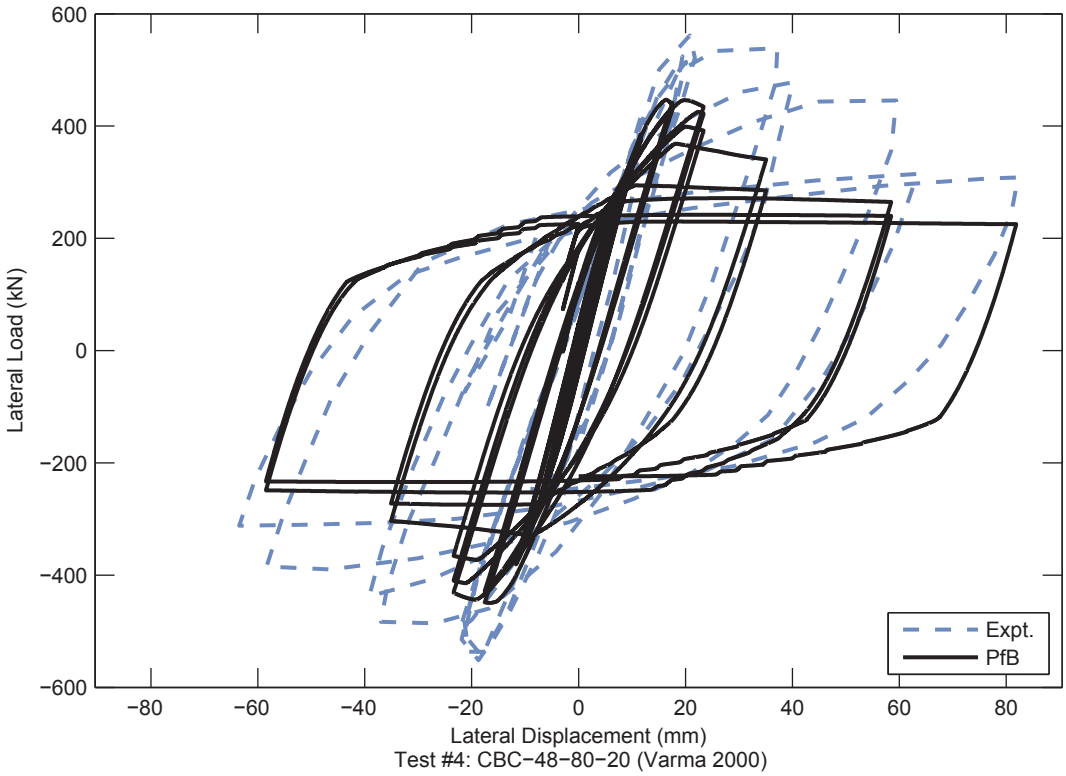

Figure 4.13. RCFT Validation Results – Varma 2000 (Continued)

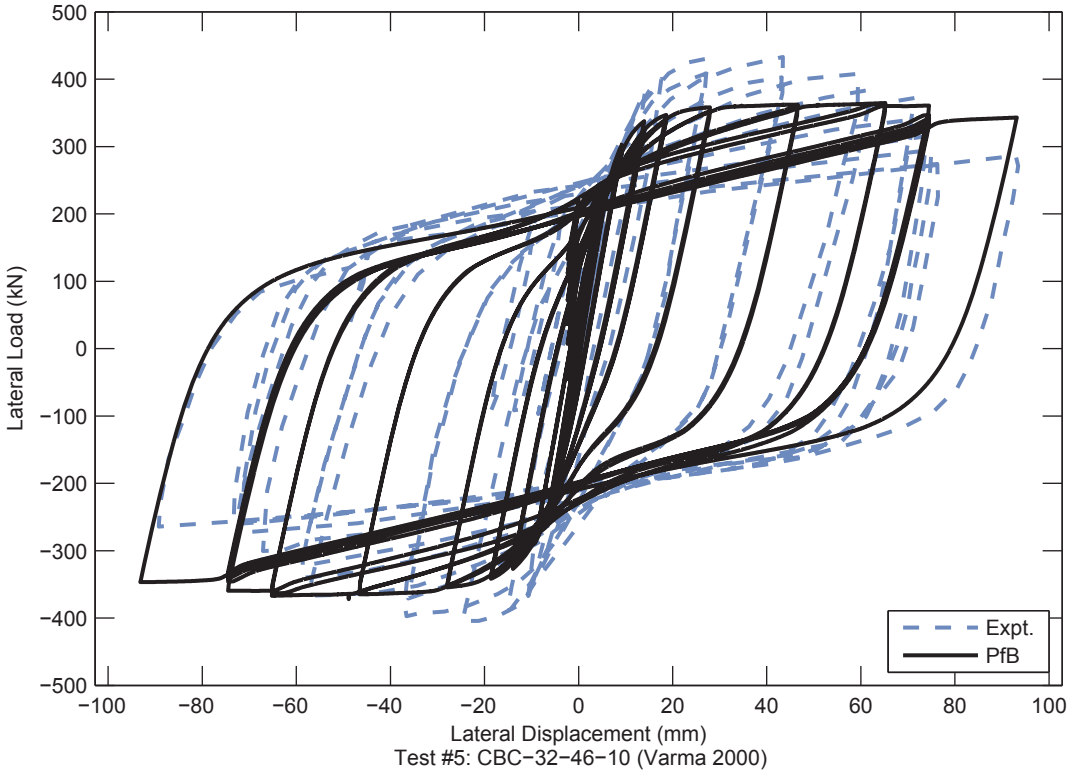

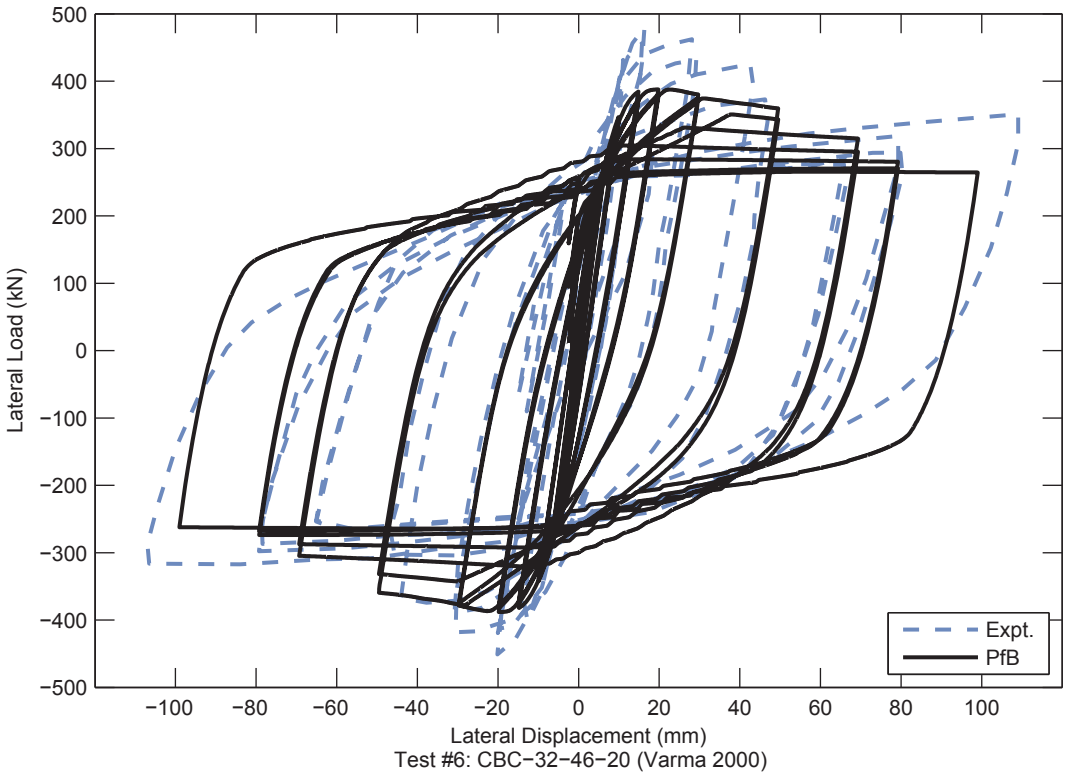

Figure 4.13. RCFT Validation Results – Varma 2000 (Continued)

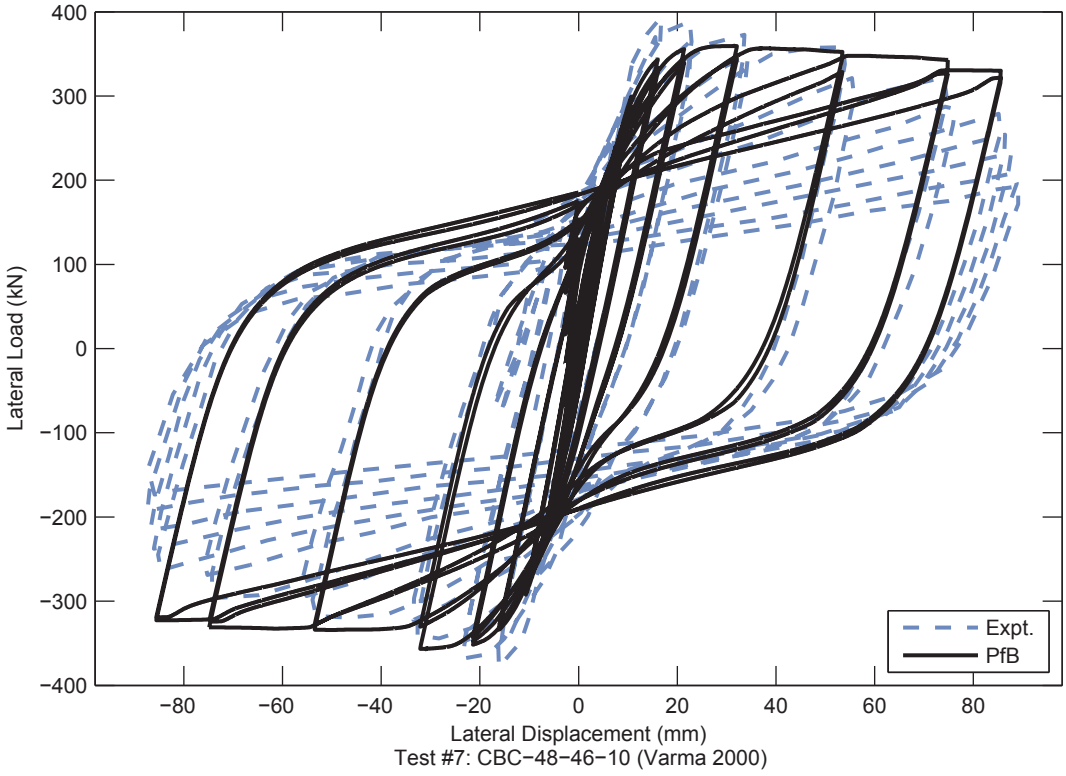

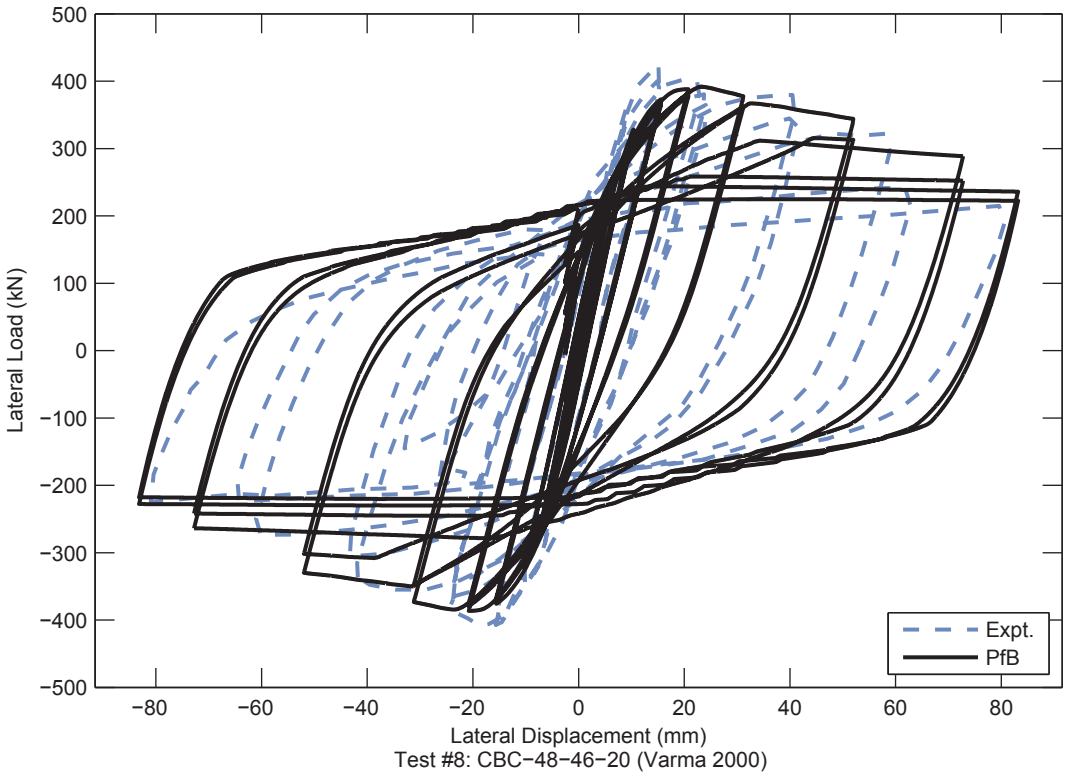

Figure 4.13. RCFT Validation Results – Varma 2000 (Continued)

4.6 Steel Reinforced Concrete Members

4.6.1 Monotonic Validation Results

The experimental results used in the monotonic validation of SRC members were taken from a variety of sources Table 4.38, including two series of tests that do not correspond to one of the four defined monotonic validation types.

Chen et al. (1992) present a series of concentrically loaded SRC column experiments. The test setup was similar to that of PBC columns with an eccentricity of zero. The initial out-of-straightness was not reported and was taken as $L/1000$ in the analyses. Four elements were used along the length of the column, each with three integration points.

Mirza et al. (1996) present a series of proportionally loaded SRC beam-column experiments. The experiment setup is similar to that of the four point bending tests but with a compressive axial load on the member (Figure 4.14). Four elements were used along the length of the column, each with three integration points.

Summary error statistics are given in Table 4.39; detailed results are presented in the remainder of this section.

Table 4.38. References - SRC Monotonic Validation

Loading Type	References	Results
PBC	Morino et al. (1984) Virdi and Dowling (1973) Wang (1999)	Measured Material and Geometric Properties: Table 4.40 PfB Error Statistics: Table 4.41 PfD Error Statistics: Table 4.42
Chen et al. (1992)	Chen et al. (1992)	Measured Material and Geometric Properties: Table 4.43 PfB Error Statistics: Table 4.44 PfD Error Statistics: Table 4.45
Mirza et al. (1996)	Mirza et al. (1996)	Measured Material and Geometric Properties: Table 4.46 PfB Error Statistics: Table 4.47 PfD Error Statistics: Table 4.48

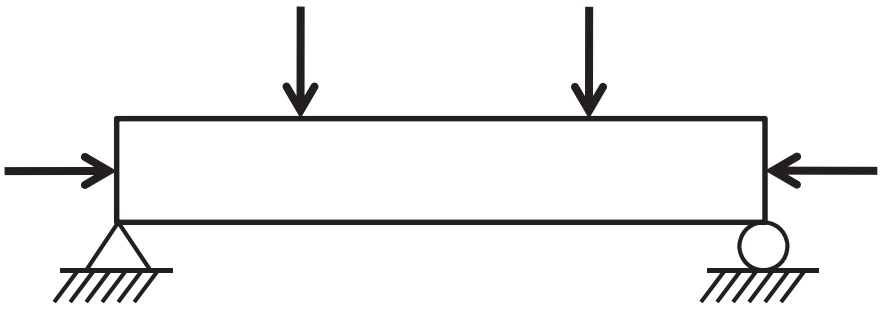

Figure 4.14. Experiment Setup – Mirza et al. 1996

The PfB model is very successful at predicting peak strength, deformation at peak load, and area under the curve, as the median error is less than 10% for those metrics for the PBC and Mirza loading types. The following additional observations are made regarding the monotonic validation results:

- For the biaxial loaded PBC specimens, the relative magnitudes of the displacements are predicted well.
- For some PBC specimens (#2 and #8, Table 4.40), the strength is significantly inaccurate. For others (#5, #18, #20, and #22, Table 4.40) it is somewhat inaccurate. However, overall, the peak strength is accurately predicted with median errors less than 5%.
- For the tests by Chen et al. (1992), the strength is well predicted except for two specimens (#2 and #3, Table 4.43). This discrepancy is possibly due to inaccuracy of the assumed initial imperfections.
- For the tests by Mirza et al. (1996), the shape of the response is distinctive. Post-peak behavior is not given in the experimental results, however, for some specimens the post-peak is seen because the model predicts the peak too early.

Table 4.39. Summary Error Statistics – SRC Monotonic Validation

Type	# of Spec.	Initial Stiffness			Peak Load			Deformation at Peak Load			Area Under Curve		
		Mean	Std.	Median	Mean	Std.	Median	Mean	Std.	Median	Mean	Std.	Median
PBC	36	37.9%	97.3%	40.8%	-2.2%	7.6%	-2.5%	-16.5%	52.8%	-7.7%	9.3%	37.1%	4.3%
Chen	7	51.1%	9.9%	50.2%	17.9%	13.5%	12.4%	-13.3%	8.8%	-15.9%	68.8%	38.2%	80.0%
Mirza	16	16.5%	24.4%	13.3%	1.1%	11.7%	0.4%	-5.7%	12.2%	-4.1%	5.9%	11.4%	5.9%

(a) Proposed for Behavior

Type	# of Spec.	Initial Stiffness			Peak Load			Deformation at Peak Load			Area Under Curve		
		Mean	Std.	Median	Mean	Std.	Median	Mean	Std.	Median	Mean	Std.	Median
PBC	36	12.5%	89.3%	12.2%	-2.8%	8.7%	-3.6%	-21.1%	51.7%	-12.4%	-6.3%	33.2%	-7.9%
Chen	7	59.6%	11.3%	59.4%	18.5%	13.4%	12.9%	-20.8%	7.6%	-22.7%	16.7%	28.7%	19.1%
Mirza	16	0.6%	19.3%	-3.2%	0.2%	11.4%	0.1%	-14.2%	9.8%	-12.6%	-8.4%	16.2%	-5.7%

(b) Proposed for Design

Table 4.40. Material and Geometric Properties – SRC Validation Set – PBC

Test #	Author	Year	Specimen	H (mm)	B (mm)	f'_c (MPa)	Steel Section	F_y (MPa)	Reinforcement Configuration	F_{yr} (MPa)	L (mm)	L/H	Bending Axis	e (mm)	e/D
1	Wang	1999	RSJ1	200	200	55.0	RSJ 102x102	310.0	n/a	n/a	4,000	20.0	strong	55.0	0.275
2	Wang	1999	RSJ3	200	200	45.0	RSJ 102x102	310.0	n/a	n/a	4,000	20.0	weak	55.0	0.275
3	Wang	1999	RSJ4	200	200	25.0	RSJ 102x102	310.0	n/a	n/a	4,000	20.0	biaxial	77.8	0.389
4	Wang	1999	RSJ7	200	200	25.0	RSJ 102x102	310.0	n/a	n/a	4,000	20.0	biaxial	123.0	0.615
5	Virdi and Dowling	1973	G	254	254	44.8	UC 6x6@15.7	314.7	2x-2y	309	7,315	28.8	biaxial	73.4	0.289
6	Virdi and Dowling	1973	H	254	254	48.9	UC 6x6@15.7	314.7	2x-2y	309	7,315	28.8	biaxial	146.8	0.578
7	Virdi and Dowling	1973	I	254	254	53.1	UC 6x6@15.7	314.7	2x-2y	309	7,315	28.8	biaxial	220.2	0.867
8	Morino et al.	1984	A4-45	160	160	21.1	H-100x100x6x8	293.0	2x-2y	387	924	5.8	biaxial	40.0	0.250
9	Morino et al.	1984	B4-45	160	160	23.4	H-100x100x6x8	287.0	2x-2y	387	2,309	14.4	biaxial	40.0	0.250
10	Morino et al.	1984	C4-45	160	160	23.3	H-100x100x6x8	308.0	2x-2y	387	3,464	21.7	biaxial	40.0	0.250
11	Morino et al.	1984	D4-45	160	160	21.2	H-100x100x6x8	293.0	2x-2y	387	4,619	28.9	biaxial	40.0	0.250
12	Morino et al.	1984	A8-45	160	160	33.6	H-100x100x6x8	303.0	2x-2y	387	924	5.8	biaxial	75.0	0.469
13	Morino et al.	1984	B8-45	160	160	33.3	H-100x100x6x8	311.0	2x-2y	387	2,309	14.4	biaxial	75.0	0.469
14	Morino et al.	1984	C8-45	160	160	24.6	H-100x100x6x8	305.0	2x-2y	387	3,464	21.7	biaxial	75.0	0.469
15	Morino et al.	1984	D8-45	160	160	22.9	H-100x100x6x8	302.0	2x-2y	387	4,619	28.9	biaxial	75.0	0.469
16	Morino et al.	1984	A4-60	160	160	21.1	H-100x100x6x8	293.0	2x-2y	387	924	5.8	biaxial	40.0	0.250
17	Morino et al.	1984	B4-60	160	160	23.4	H-100x100x6x8	287.0	2x-2y	387	2,309	14.4	biaxial	40.0	0.250
18	Morino et al.	1984	C4-60	160	160	23.3	H-100x100x6x8	308.0	2x-2y	387	3,464	21.7	biaxial	40.0	0.250
19	Morino et al.	1984	D4-60	160	160	21.2	H-100x100x6x8	293.0	2x-2y	387	4,619	28.9	biaxial	40.0	0.250
20	Morino et al.	1984	A8-60	160	160	33.6	H-100x100x6x8	303.0	2x-2y	387	924	5.8	biaxial	75.0	0.469
21	Morino et al.	1984	B8-60	160	160	33.3	H-100x100x6x8	311.0	2x-2y	387	2,309	14.4	biaxial	75.0	0.469
22	Morino et al.	1984	C8-60	160	160	24.6	H-100x100x6x8	305.0	2x-2y	387	3,464	21.7	biaxial	75.0	0.469
23	Morino et al.	1984	D8-60	160	160	22.9	H-100x100x6x8	302.0	2x-2y	387	4,619	28.9	biaxial	75.0	0.469

Table 4.41. Comparison Metrics – SRC Validation Set – PBC – Proposed for Behavior

Test #	Initial Tangent (kN/mm)			Peak Load (kN)			Deformation at Peak Load (mm)			Area Under Curve (kN-mm)		
	Expt.	Model	Error	Expt.	Model	Error	Expt.	Model	Error	Expt.	Model	Error
1	58.5	85.0	45.32%	959.7	979.9	2.10%	35.13	33.30	-5.20%	23,822	26,115	9.62%
2	39.9	72.3	81.08%	538.4	663.1	23.17%	25.35	25.35	6.31E-08	9,178	12,281	33.81%
3-Y	77.0	65.3	-15.12%	420.3	376.9	-10.33%	5.74	12.24	113.08%	1,333	3,049	128.64%
3-Z	76.6	55.9	-27.00%	419.7	376.9	-10.20%	16.68	16.68	0.00%	5,066	4,331	-14.51%
4-Y	64.6	62.0	-4.14%	248.9	239.1	-3.95%	-5.37	7.59	-241.42%	-1,716	1,131	-165.90%
4-Z	22.6	27.6	22.32%	250.3	239.1	-4.49%	20.47	20.47	9.77E-09	3,456	3,177	-8.08%
5-Y	21.7	29.2	34.21%	654.8	573.5	-12.41%	59.16	61.65	4.21%	27,739	26,349	-5.01%
5-Z	61.2	44.6	-27.13%	664.3	573.5	-13.67%	49.20	54.24	10.25%	25,302	24,297	-3.97%
6-Y	7.9	14.7	85.79%	344.1	372.0	8.11%	72.86	72.86	0.00%	16,154	18,406	13.94%
6-Z	10.7	21.9	105.40%	356.0	372.0	4.51%	60.60	61.06	0.76%	17,996	16,048	-10.83%
7-Y	5.9	9.0	51.36%	288.5	287.9	-0.19%	83.80	96.73	15.43%	23,171	23,784	2.64%
7-Z	7.6	12.8	69.94%	290.4	287.9	-0.84%	73.63	79.65	8.17%	16,063	19,934	24.10%
8-Y	147.3	559.4	279.89%	640.4	515.2	-19.55%	6.07	2.57	-57.60%	6,146	5,135	-16.44%
8-Z	128.9	428.5	232.44%	640.3	515.2	-19.54%	7.29	4.44	-39.16%	14,406	13,038	-9.49%
9-Y	54.3	93.5	72.13%	394.0	383.0	-2.80%	11.27	10.34	-8.29%	6,850	6,719	-1.91%
9-Z	42.9	72.1	68.11%	393.8	383.0	-2.76%	16.98	17.67	4.04%	16,248	16,442	1.19%
10-Y	39.6	41.9	5.73%	298.4	282.9	-5.17%	17.36	16.99	-2.16%	6,225	8,551	37.37%
10-Z	20.1	32.2	59.63%	298.8	282.9	-5.32%	37.67	31.65	-15.97%	28,527	28,563	0.12%
11-Y	37.6	23.1	-38.58%	204.9	198.9	-2.93%	19.50	22.92	17.56%	5,621	7,341	30.59%
11-Z	12.1	17.5	44.69%	204.8	198.9	-2.89%	49.57	48.68	-1.81%	24,130	23,817	-1.29%
12-Y	132.8	272.4	105.16%	376.5	378.8	0.62%	5.21	3.33	-36.15%	3,011	4,215	40.00%
12-Z	90.0	207.6	130.79%	378.5	378.8	0.08%	6.85	5.19	-24.16%	7,721	8,797	13.94%
13-Y	31.9	44.7	40.35%	297.7	291.5	-2.09%	15.85	12.96	-18.24%	5,069	8,817	73.93%
13-Z	26.2	34.6	31.89%	298.4	291.5	-2.31%	27.88	20.98	-24.75%	17,096	18,740	9.62%
14-Y	15.0	20.0	32.96%	199.3	198.3	-0.46%	23.34	21.44	-8.14%	6,403	8,596	34.24%
14-Z	8.2	15.3	86.35%	199.6	198.3	-0.62%	55.22	39.00	-29.37%	21,221	21,828	2.86%
15-Y	12.4	11.9	-4.35%	143.8	149.6	4.00%	30.79	31.24	1.46%	7,572	8,200	8.30%
15-Z	6.7	9.1	34.97%	144.3	149.6	3.69%	68.85	62.65	-9.00%	20,251	20,904	3.22%
16-Y	-134.3	468.0	-448.36%	523.0	553.7	5.86%	-2.92	3.40	-216.60%	5,942	8,120	36.65%
16-Z	417.4	603.3	44.56%	526.5	553.7	5.16%	4.31	3.78	-12.37%	13,288	14,633	10.13%
17-Y	50.6	77.1	52.14%	436.4	414.3	-5.05%	14.32	13.29	-7.21%	8,084	9,811	21.38%
17-Z	50.4	101.1	100.54%	436.0	414.3	-4.97%	17.76	15.31	-13.81%	17,347	17,752	2.33%
18-Y	32.5	34.1	4.85%	336.6	307.7	-8.59%	23.76	22.08	-7.07%	9,270	11,825	27.56%
18-Z	39.7	45.0	13.33%	337.5	307.7	-8.83%	30.58	26.62	-12.96%	31,133	29,358	-5.70%
19-Y	16.5	18.7	13.00%	220.9	217.0	-1.78%	26.02	29.37	12.89%	8,987	10,621	18.17%
19-Z	11.4	24.5	115.53%	222.0	217.0	-2.24%	50.97	38.44	-24.60%	26,852	26,592	-0.97%
20-Y	163.6	233.4	42.71%	444.9	411.6	-7.49%	5.84	3.78	-35.18%	5,557	5,501	-1.01%
20-Z	552.3	289.9	-47.52%	448.2	411.6	-8.18%	5.83	4.03	-30.90%	8,348	7,846	-6.00%
21-Y	27.0	38.1	41.22%	327.5	316.7	-3.32%	18.28	15.88	-13.09%	8,939	12,121	35.60%
21-Z	28.4	47.8	67.90%	326.8	316.7	-3.10%	20.30	16.72	-17.67%	18,378	19,197	4.46%
22-Y	12.3	16.7	36.39%	196.6	216.4	10.05%	28.60	27.49	-3.87%	8,713	11,004	26.30%
22-Z	16.5	21.0	26.82%	197.6	216.4	9.51%	35.62	32.00	-10.17%	18,667	19,901	6.61%
23-Y	11.7	9.8	-16.21%	160.3	162.8	1.60%	38.97	40.33	3.48%	10,261	10,692	4.21%
23-Z	10.7	12.6	16.98%	161.4	162.8	0.87%	47.75	51.44	7.74%	19,832	19,569	-1.33%
Mean			37.91%			-2.20%			-16.54%			9.30%
Standard Deviation			97.31%			7.63%			52.83%			37.09%
Median			40.79%			-2.54%			-7.68%			4.33%

Table 4.42. Comparison Metrics – SRC Validation Set – PBC – Proposed for Design

Test #	Initial Tangent (kN/mm)			Peak Load (kN)			Deformation at Peak Load (mm)			Area Under Curve (kN-mm)		
	Expt.	Model	Error	Expt.	Model	Error	Expt.	Model	Error	Expt.	Model	Error
1	58.5	82.9	41.75%	959.7	1,003.6	4.58%	35.13	30.39	-13.50%	23,822	27,044	13.53%
2	39.9	65.7	64.62%	538.4	692.3	28.58%	25.35	25.35	6.31E-08	9,178	12,614	37.44%
3-Y	77.0	52.7	-31.59%	420.3	375.9	-10.58%	5.74	12.18	111.94%	1,333	2,912	118.39%
3-Z	76.6	43.7	-43.00%	419.7	375.9	-10.45%	16.68	16.68	0.00%	5,066	4,156	-17.95%
4-Y	64.6	45.3	-29.90%	248.9	237.9	-4.41%	-5.37	7.62	-241.96%	-1,716	1,081	-163.02%
4-Z	22.6	17.8	-20.97%	250.3	237.9	-4.95%	20.47	20.47	9.77E-09	3,456	2,964	-14.24%
5-Y	21.7	22.4	2.85%	654.8	590.6	-9.81%	59.16	61.65	4.21%	27,739	25,812	-6.95%
5-Z	61.2	31.5	-48.59%	664.3	590.6	-11.10%	49.20	54.06	9.89%	25,302	23,852	-5.73%
6-Y	7.9	8.9	12.21%	344.1	382.9	11.28%	72.86	72.86	0.00%	16,154	17,866	10.59%
6-Z	10.7	12.4	15.82%	356.0	382.9	7.56%	60.60	61.02	0.68%	17,996	15,770	-12.37%
7-Y	5.9	5.5	-6.19%	288.5	293.9	1.88%	83.80	91.83	9.58%	23,171	23,576	1.75%
7-Z	7.6	7.8	2.74%	290.4	293.9	1.21%	73.63	75.60	2.68%	16,063	19,956	24.23%
8-Y	147.3	511.4	247.27%	640.4	487.2	-23.92%	6.07	2.18	-64.02%	6,146	4,103	-33.24%
8-Z	128.9	383.1	197.20%	640.3	487.2	-23.91%	7.29	3.65	-49.90%	14,406	10,926	-24.15%
9-Y	54.3	81.7	50.29%	394.0	378.3	-3.97%	11.27	9.61	-14.78%	6,850	5,275	-22.99%
9-Z	42.9	61.3	42.86%	393.8	378.3	-3.93%	16.98	16.12	-5.09%	16,248	14,803	-8.90%
10-Y	39.6	35.0	-11.69%	298.4	282.7	-5.24%	17.36	16.67	-4.02%	6,225	6,323	1.58%
10-Z	20.1	25.9	28.59%	298.8	282.7	-5.39%	37.67	30.93	-17.88%	28,527	25,323	-11.23%
11-Y	37.6	18.7	-50.28%	204.9	198.4	-3.18%	19.50	22.96	17.78%	5,621	6,165	9.67%
11-Z	12.1	13.5	11.76%	204.8	198.4	-3.13%	49.57	49.58	5.89E-05	24,130	22,297	-7.60%
12-Y	132.8	268.9	102.53%	376.5	360.6	-4.21%	5.21	2.32	-55.44%	3,011	2,933	-2.60%
12-Z	90.0	195.8	117.62%	378.5	360.6	-4.72%	6.85	3.51	-48.81%	7,721	7,005	-9.28%
13-Y	31.9	41.7	30.74%	297.7	288.6	-3.08%	15.85	11.56	-27.06%	5,069	5,896	16.30%
13-Z	26.2	29.9	13.96%	298.4	288.6	-3.30%	27.88	18.28	-34.43%	17,096	15,693	-8.21%
14-Y	15.0	16.8	12.21%	199.3	197.8	-0.72%	23.34	20.88	-10.54%	6,403	6,119	-4.45%
14-Z	8.2	11.5	40.80%	199.6	197.8	-0.88%	55.22	37.64	-31.84%	21,221	19,214	-9.46%
15-Y	12.4	9.1	-26.57%	143.8	149.7	4.10%	30.79	30.65	-0.45%	7,572	6,388	-15.64%
15-Z	6.7	6.1	-9.51%	144.3	149.7	3.79%	68.85	61.04	-11.34%	20,251	19,177	-5.30%
16-Y	-134.3	434.6	-423.53%	523.0	524.7	0.32%	-2.92	2.75	-194.26%	5,942	6,381	7.39%
16-Z	417.4	541.7	29.79%	526.5	524.7	-0.34%	4.31	3.05	-29.33%	13,288	12,197	-8.21%
17-Y	50.6	69.3	36.92%	436.4	408.6	-6.36%	14.32	12.37	-13.61%	8,084	7,738	-4.27%
17-Z	50.4	86.5	71.53%	436.0	408.6	-6.28%	17.76	13.97	-21.32%	17,347	15,346	-11.53%
18-Y	32.5	29.7	-8.84%	336.6	307.0	-8.80%	23.76	21.50	-9.52%	9,270	9,266	-0.05%
18-Z	39.7	36.5	-8.04%	337.5	307.0	-9.04%	30.58	25.74	-15.83%	31,133	26,827	-13.83%
19-Y	16.5	15.8	-4.37%	220.9	215.8	-2.34%	26.02	29.50	13.38%	8,987	7,709	-14.23%
19-Z	11.4	19.1	67.68%	222.0	215.8	-2.79%	50.97	39.74	-22.03%	26,852	24,100	-10.25%
20-Y	163.6	226.5	38.46%	444.9	393.3	-11.60%	5.84	2.85	-51.10%	5,557	4,257	-23.40%
20-Z	552.3	280.9	-49.14%	448.2	393.3	-12.26%	5.83	2.86	-50.93%	8,348	6,915	-17.17%
21-Y	27.0	35.0	29.51%	327.5	313.8	-4.21%	18.28	14.58	-20.23%	8,939	9,141	2.25%
21-Z	28.4	42.9	50.68%	326.8	313.8	-3.99%	20.30	14.92	-26.51%	18,378	17,014	-7.42%
22-Y	12.3	14.1	14.85%	196.6	215.8	9.75%	28.60	26.65	-6.82%	8,713	8,907	2.22%
22-Z	16.5	16.5	-0.17%	197.6	215.8	9.21%	35.62	30.73	-13.73%	18,667	18,172	-2.65%
23-Y	11.7	7.6	-34.89%	160.3	162.8	1.60%	38.97	39.76	2.02%	10,261	8,430	-17.84%
23-Z	10.7	8.7	-18.64%	161.4	162.8	0.87%	47.75	50.68	6.14%	19,832	17,734	-10.58%
Mean			12.49%			-2.82%			-21.09%			-6.35%
Standard Deviation			89.28%			8.71%			51.68%			33.19%
Median			12.21%			-3.62%			-12.42%			-7.90%

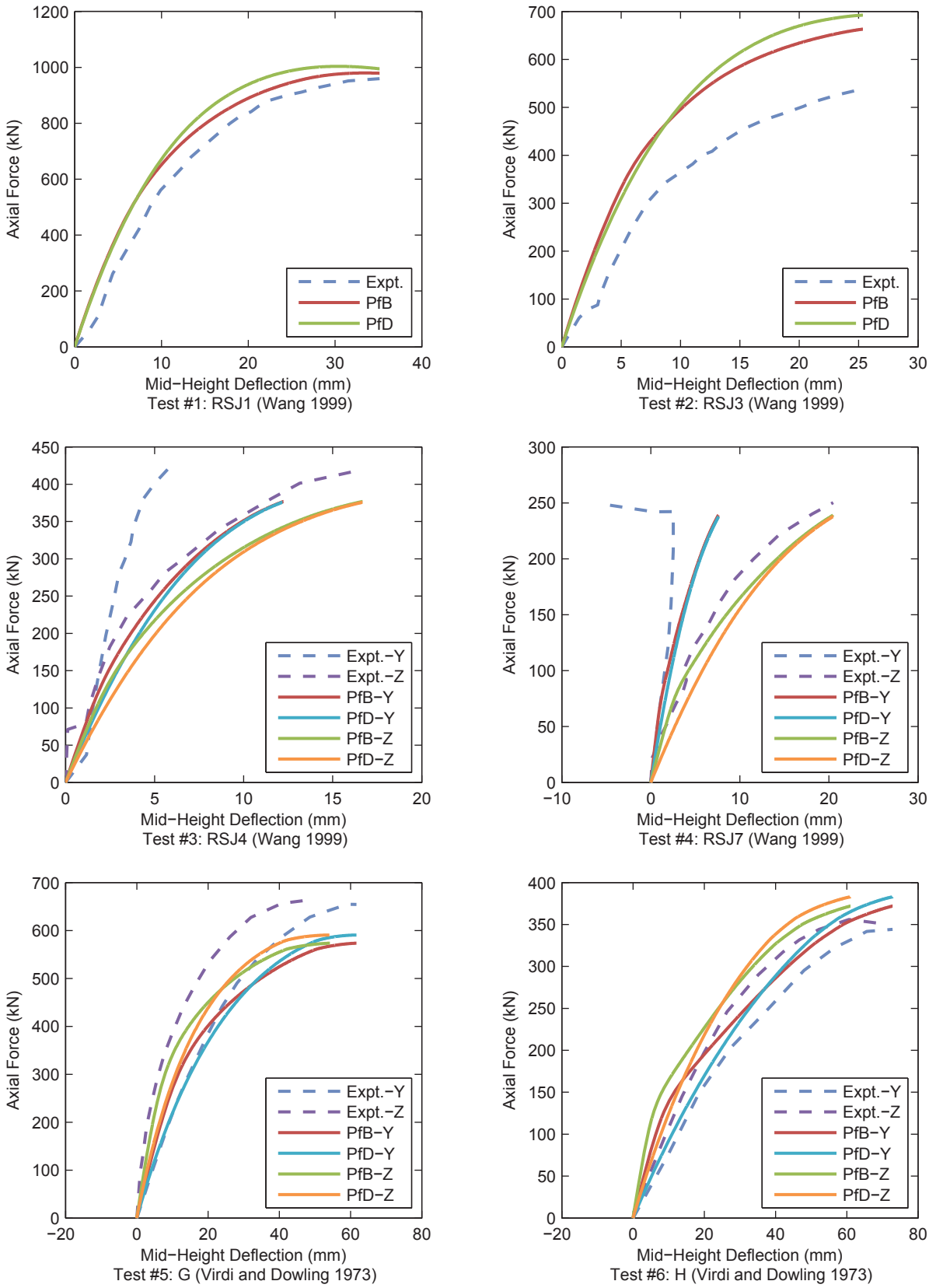

Figure 4.15. SRC Validation Results – PBC

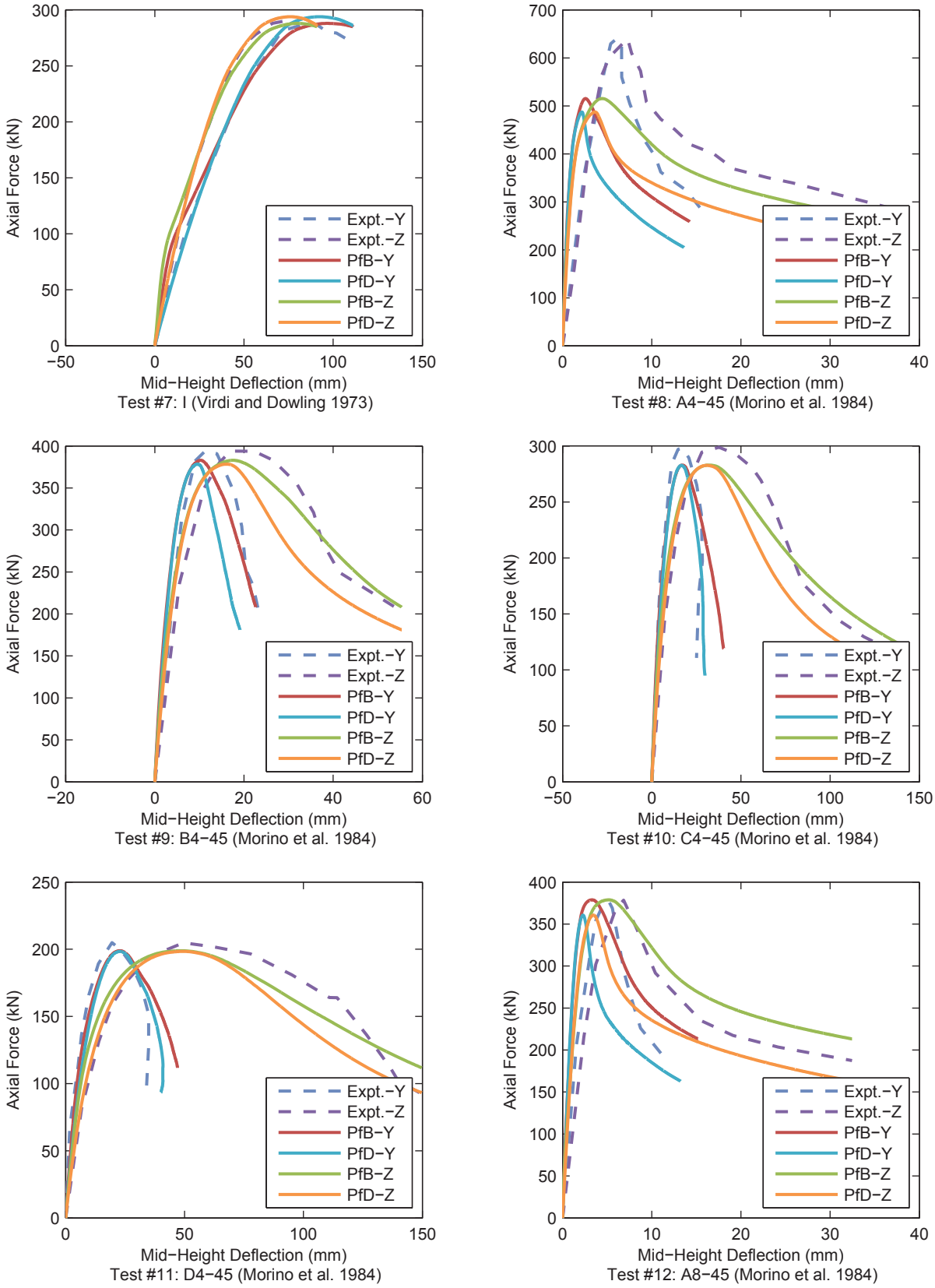

Figure 4.15. SRC Validation Results – PBC (continued)

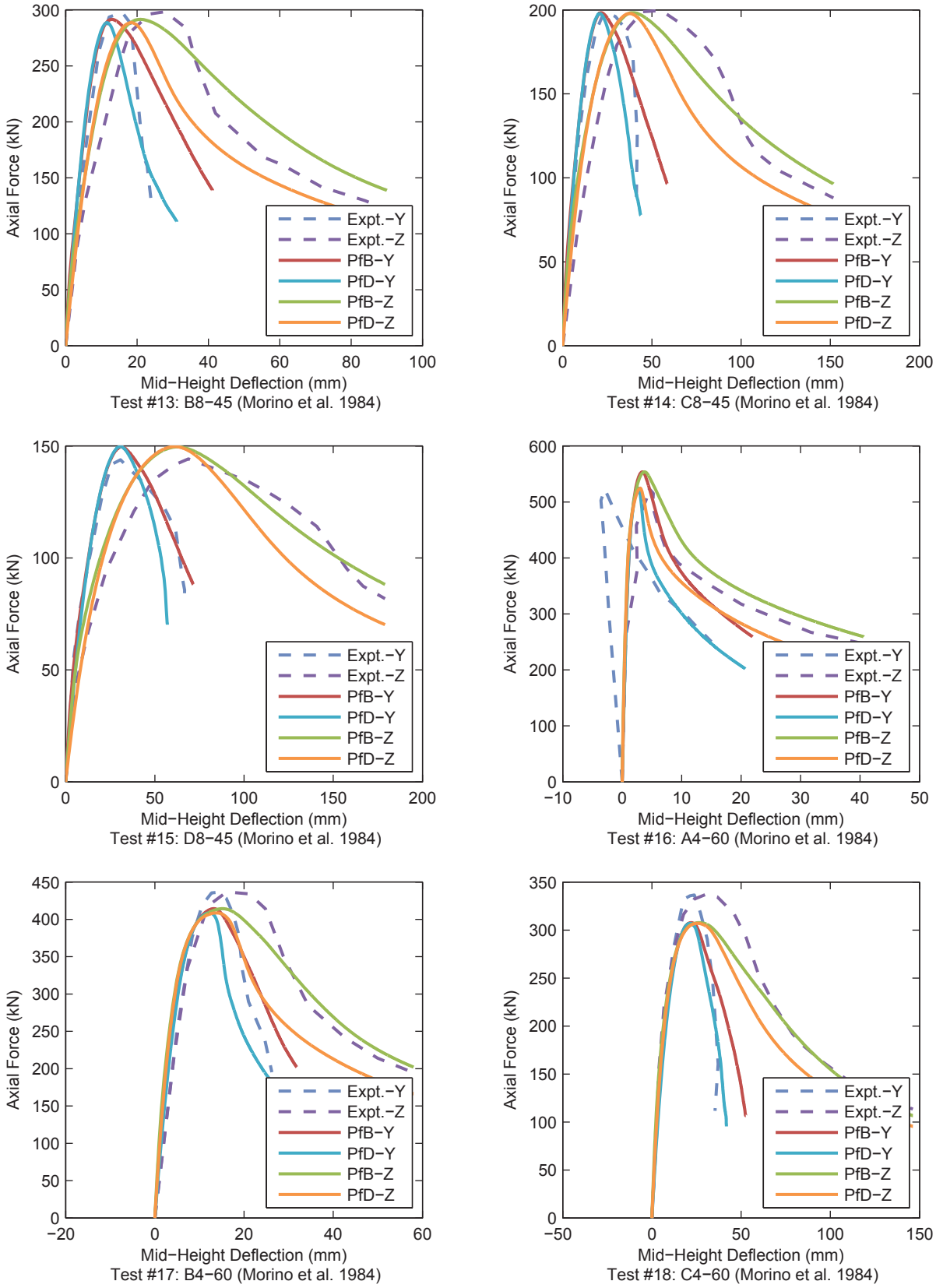

Figure 4.15. SRC Validation Results – PBC (continued)

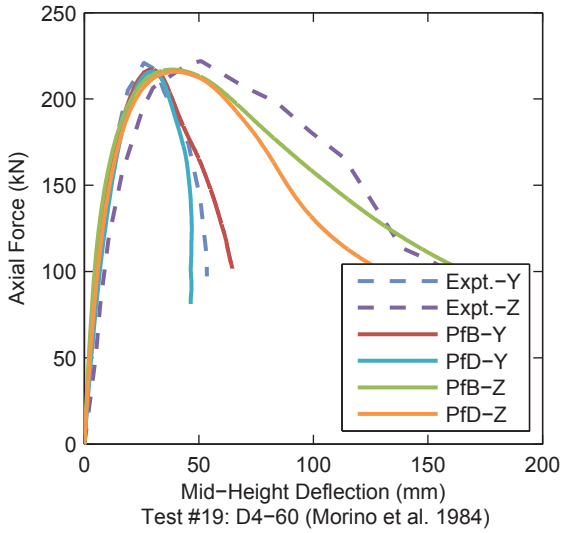

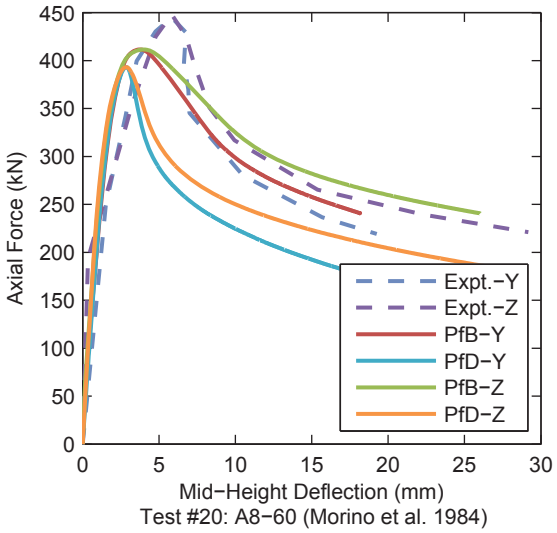

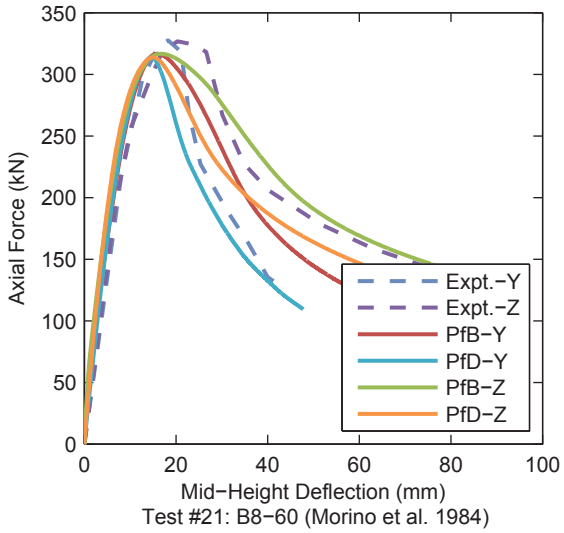

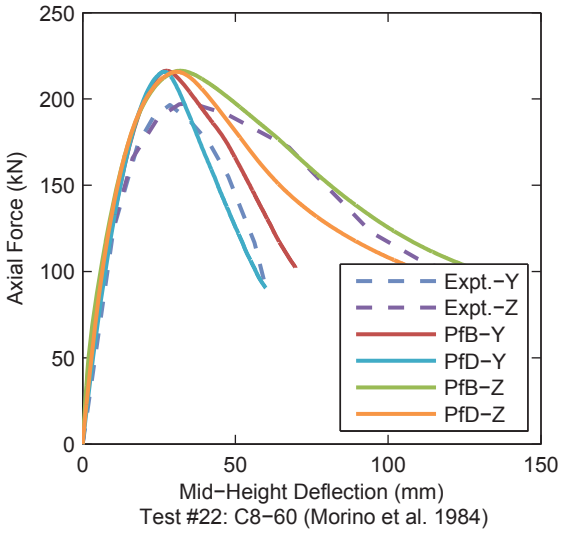

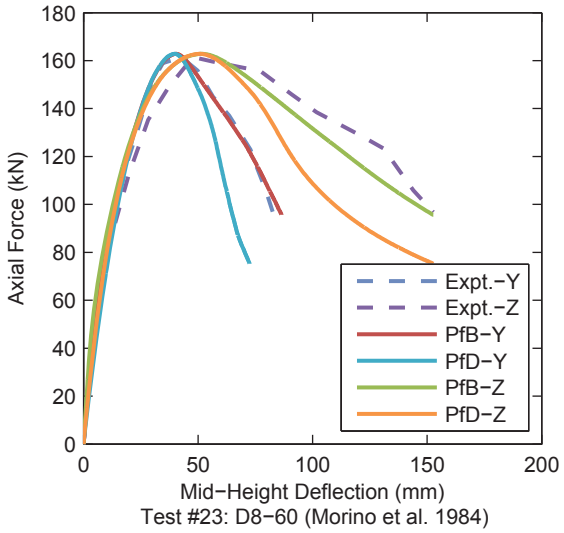

Figure 4.15. SRC Validation Results – PBC (continued)

Table 4.43. Material and Geometric Properties – SRC Validation Set – Chen et al. 1992

Test #	Author	Year	Specimen	H *(mm)*	B *(mm)*	f'_c *(MPa)*	Steel Section	F_y *(MPa)*	Reinforcement Configuration	F_{yr} *(MPa)*	L *(mm)*	L/H
1	Chen et al.	1992	S1	356	356	65.64	W8x40	376	2x-2y	414	4,572	12.9
2	Chen et al.	1992	S2	356	356	61.50	W8x40	376	2x-2y	414	4,572	12.9
3	Chen et al.	1992	S3	356	356	62.74	W8x40	376	2x-2y	414	4,572	12.9
4	Chen et al.	1992	S4	356	356	64.67	W8x40	376	2x-2y	414	4,572	12.9
5	Chen et al.	1992	S5	356	356	65.43	W8x67	376	2x-2y	414	4,572	12.9
6	Chen et al.	1992	S6	356	356	64.47	W8x28	248	2x-2y	414	4,572	12.9
7	Chen et al.	1992	S7	356	356	29.92	W8x67	376	2x-2y	414	4,572	12.9

Table 4.44. Comparison Metrics – SRC Validation Set – Chen et al. 1992 – Proposed for Behavior

Test #	Initial Tangent (kN)			Peak Load (kN)			Strain at Peak Load (mm/mm)			Area Under Curve (kN)		
	Expt.	Model	Error	Expt.	Model	Error	Expt.	Model	Error	Expt.	Model	Error
1	889	1,291	45.27%	8,501	9,555	12.40%	10.591300	8.902600	-15.94%	48721.5	87709.8	80.02%
2	763	1,264	65.62%	6,547	9,131	39.47%	9.725330	8.748750	-10.04%	75822.8	110436.0	45.65%
3	829	1,247	50.40%	6,716	8,985	33.79%	8.537340	8.723020	2.17%	53794.8	100629.0	87.06%
4	782	1,279	63.48%	8,111	9,413	16.05%	9.811920	9.021290	-8.06%	39594.9	86292.3	117.94%
5	1,046	1,474	41.01%	9,481	10,625	12.07%	10.167100	8.511510	-16.28%	51535.4	101652.0	97.25%
6	803	1,206	50.25%	8,180	8,420	2.93%	11.712600	9.285810	-20.72%	88020.8	91885.0	4.39%
7	832	1,180	41.73%	6,474	7,030	8.58%	9.447170	7.154240	-24.27%	81629.9	121680.0	49.06%
Mean			51.11%			17.90%			-13.31%			68.77%
Standard Deviation			9.91%			13.52%			8.84%			38.20%
Median			50.25%			12.40%			-15.94%			80.02%

Table 4.45. Comparison Metrics – SRC Validation Set – Chen et al. 1992 – Proposed for Design

Test #	Initial Tangent (kN)			Peak Load (kN)			Strain at Peak Load (mm/mm)			Area Under Curve (kN)		
	Expt.	Model	Error	Expt.	Model	Error	Expt.	Model	Error	Expt.	Model	Error
1	889	1,370	54.09%	8,501	9,597	12.89%	10.591300	8.106380	-23.46%	48721.5	58041.0	19.13%
2	763	1,338	75.33%	6,547	9,166	40.00%	9.725330	7.950120	-18.25%	75822.8	73973.1	-2.44%
3	829	1,321	59.36%	6,716	9,007	34.11%	8.537340	7.941260	-6.98%	53794.8	62498.0	16.18%
4	782	1,360	73.83%	8,111	9,493	17.03%	9.811920	8.153960	-16.90%	39594.9	58815.9	48.54%
5	1,046	1,547	47.97%	9,481	10,681	12.66%	10.167100	7.857770	-22.71%	51535.4	74070.7	43.73%
6	803	1,282	59.75%	8,180	8,559	4.63%	11.712600	8.248620	-29.57%	88020.8	56799.0	-35.47%
7	832	1,225	47.13%	6,474	7,008	8.25%	9.447170	6.849140	-27.50%	81629.9	103861.0	27.23%
Mean			59.64%			18.51%			-20.77%			16.70%
Standard Deviation			11.34%			13.36%			7.59%			28.72%
Median			59.36%			12.89%			-22.71%			19.13%

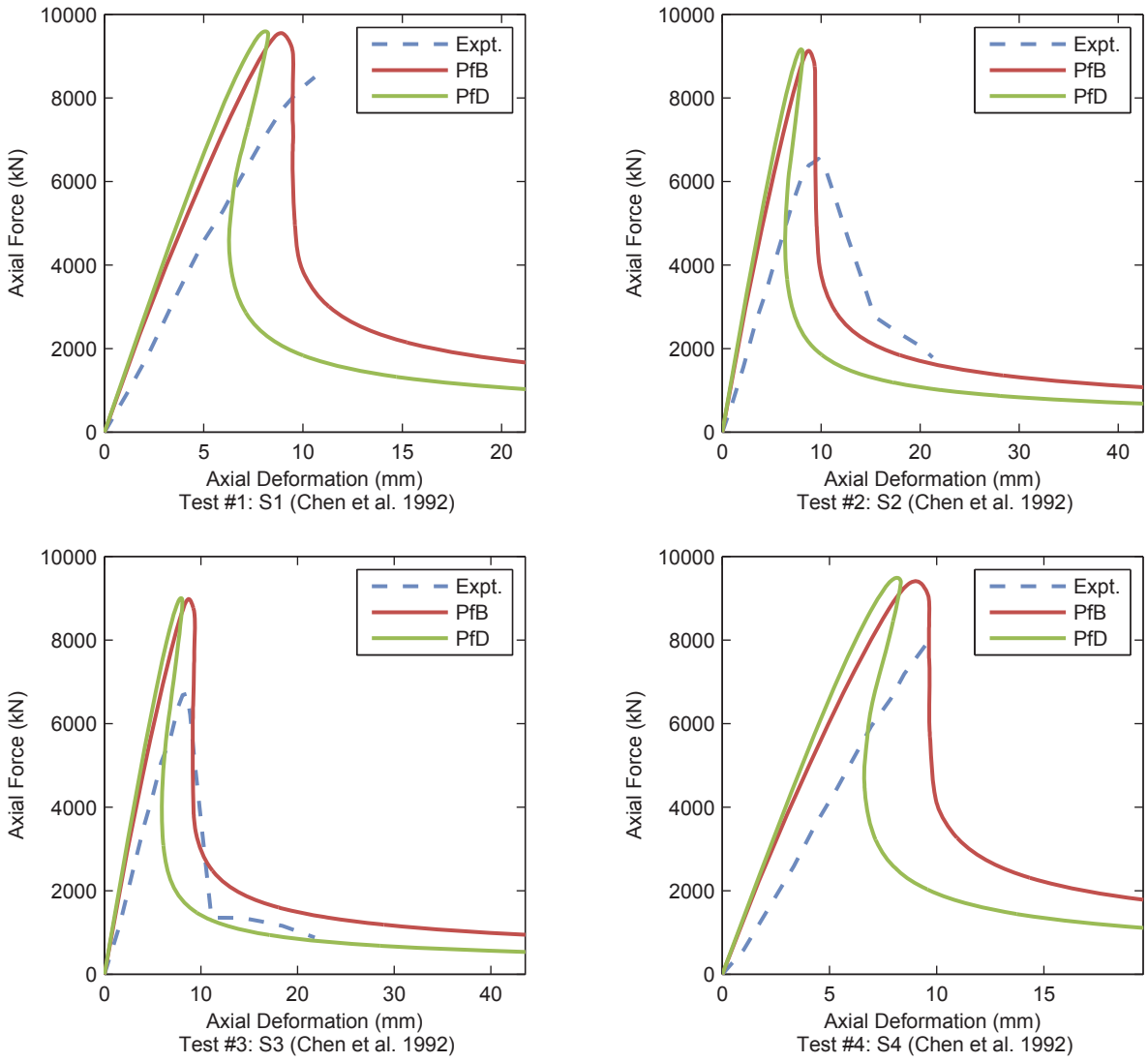

Figure 4.16. SRC Validation Results – Chen et al. 1992

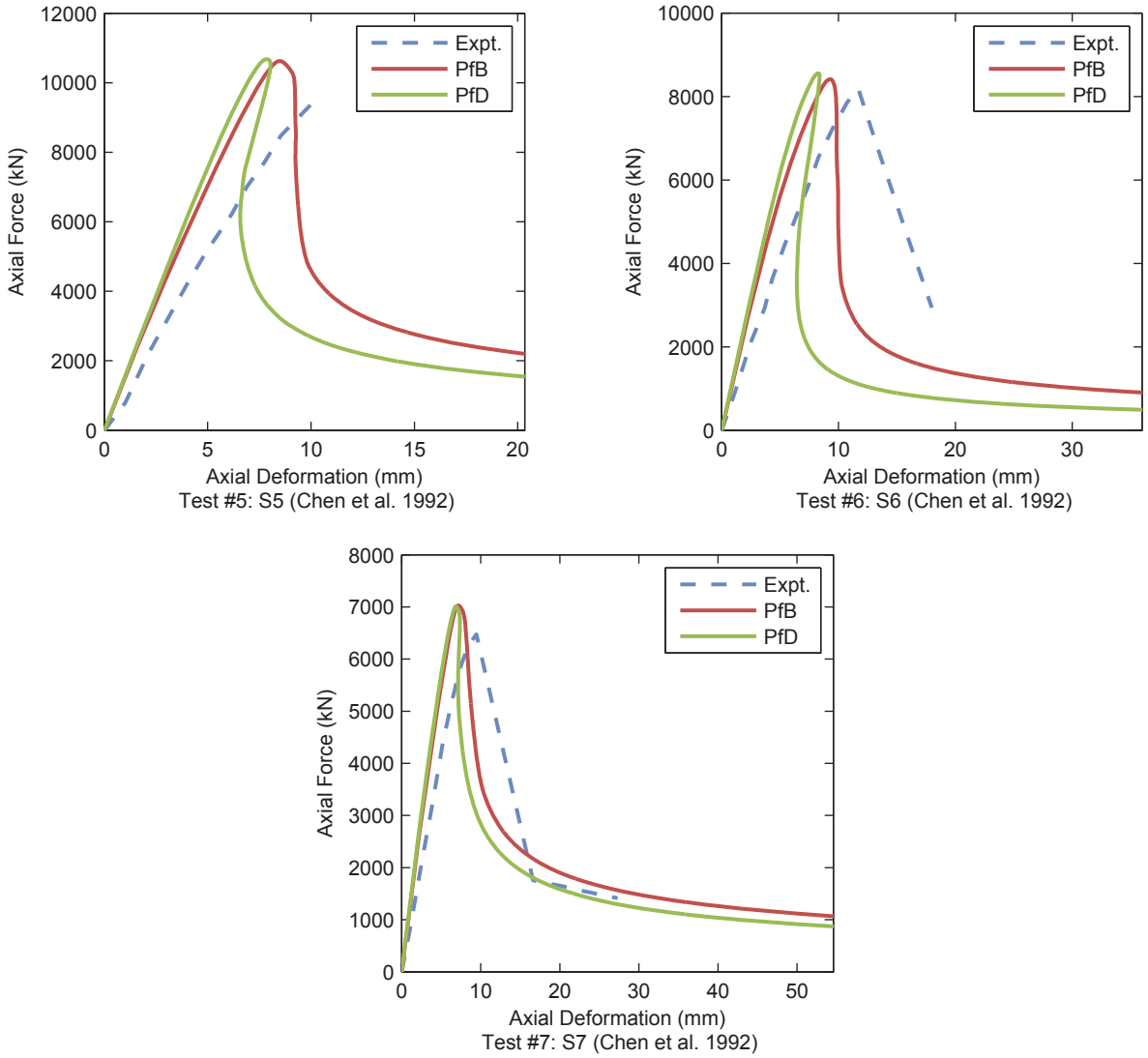

Figure 4.16. SRC Validation Results – Chen et al. 1992 (continued)

Table 4.46. Material and Geometric Properties – SRC Validation Set – Mirza et al. 1996

Test #	Author	Year	Specimen	H (mm)	B (mm)	f'_c (MPa)	Steel Section	F_y (MPa)	Reinforcement Configuration	F_{yr} (MPa)	Shear Span (mm)	Bending Span (mm)	e (mm)
1	Mirza et al.	1996	RHB-1	240	240	27.2	HE 100A	293	2x-2y	565	1,500	1,000	39.6
2	Mirza et al.	1996	RHB-2	240	240	27.2	HE 100A	293	2x-2y	565	1,500	1,000	65.8
3	Mirza et al.	1996	RHB-3	240	240	27.7	HE 100A	293	2x-2y	565	1,500	1,000	105.6
4	Mirza et al.	1996	RHB-4	240	240	25.8	HE 100A	311	2x-2y	634	1,500	1,000	200.2
5	Mirza et al.	1996	RHB-4A	240	240	25.1	HE 100A	293	2x-2y	565	1,500	1,000	370.8
6	Mirza et al.	1996	RHB-5	240	240	28.6	HE 100A	293	2x-2y	565	1,500	1,000	633.6
7	Mirza et al.	1996	RNHB-1	240	240	27.5	HE 100A	311	2x-2y	634	1,500	1,000	49.2
8	Mirza et al.	1996	RNHB-2	240	240	27.5	HE 100A	311	2x-2y	634	1,500	1,000	57.6
9	Mirza et al.	1996	RNHB-3	240	240	26.7	HE 100A	293	2x-2y	565	1,500	1,000	105.8
10	Mirza et al.	1996	RNHB-4	240	240	27.2	HE 100A	293	2x-2y	565	1,500	1,000	209.0
11	Mirza et al.	1996	RNHB-5	240	240	28.1	HE 100A	293	2x-2y	565	1,500	1,000	629.8
12	Mirza et al.	1996	RHNB-1	240	240	27.5	HE 100A	311	2x-2y	634	1,500	1,000	41.8
13	Mirza et al.	1996	RHNB-2	240	240	27.5	HE 100A	311	2x-2y	634	1,500	1,000	59.3
14	Mirza et al.	1996	RHNB-3	240	240	25.8	HE 100A	311	2x-2y	634	1,500	1,000	98.4
15	Mirza et al.	1996	RHNB-4	240	240	25.8	HE 100A	311	2x-2y	634	1,500	1,000	205.9
16	Mirza et al.	1996	RHNB-5	240	240	25.8	HE 100A	311	2x-2y	634	1,500	1,000	620.2

Table 4.47. Comparison Metrics – SRC Validation Set – Mirza et al. 1996 – Proposed for Behavior

Test #	Initial Tangent (kN/mm)			Peak Load (kN)			Deformation at Peak Load (mm)			Area Under Curve (kN-mm)		
	Expt.	Model	Error	Expt.	Model	Error	Expt.	Model	Error	Expt.	Model	Error
1	2.4	2.8	14.15%	22.8	24.9	9.15%	31.01	24.39	-21.38%	679	760	11.86%
2	1.6	2.9	77.99%	22.1	30.0	36.09%	51.67	40.33	-21.96%	1,134	1,591	40.24%
3	2.3	2.6	15.30%	34.3	32.5	-5.00%	31.89	31.89	-1.88E-07	712	691	-2.93%
4	1.1	1.6	50.16%	40.2	37.3	-7.22%	62.98	50.07	-20.50%	2,018	2,037	0.91%
5	1.2	1.5	18.67%	36.2	36.3	0.31%	45.51	44.08	-3.13%	1,643	1,738	5.76%
6	1.3	1.4	9.15%	37.8	37.6	-0.37%	51.51	48.73	-5.41%	1,508	1,599	6.05%
7	3.7	2.9	-22.32%	33.4	29.3	-12.46%	40.66	35.37	-12.99%	1,266	1,189	-6.06%
8	2.1	2.9	34.70%	31.1	31.3	0.46%	36.76	40.33	9.72%	1,082	1,156	6.82%
9	2.4	2.3	-2.62%	35.6	37.3	4.85%	45.05	45.22	0.37%	1,681	1,790	6.45%
10	1.7	1.7	-1.35%	47.4	39.7	-16.20%	57.45	43.63	-24.06%	2,467	2,165	-12.25%
11	1.5	1.5	1.18%	43.7	39.9	-8.67%	53.17	61.20	15.10%	2,172	2,108	-2.94%
12	3.1	2.8	-8.08%	27.2	27.3	0.17%	30.75	30.32	-1.42%	951	999	5.05%
13	2.3	2.9	26.61%	29.4	31.6	7.62%	39.92	41.55	4.08%	1,103	1,259	14.12%
14	1.8	2.4	33.98%	35.8	36.9	3.07%	51.55	48.92	-5.10%	1,498	1,623	8.31%
15	1.5	1.7	12.47%	39.6	40.6	2.72%	53.77	46.94	-12.70%	2,056	2,212	7.58%
16	1.4	1.5	3.82%	40.1	41.1	2.60%	54.20	58.80	8.48%	1,939	2,052	5.80%
Mean			16.49%			1.07%			-5.68%			5.92%
Standard Deviation			24.39%			11.67%			12.19%			11.39%
Median			13.31%			0.38%			-4.12%			5.92%

Table 4.48. Comparison Metrics – SRC Validation Set – Mirza et al. 1996 – Proposed for Design

Test #	Initial Tangent (kN/mm)			Peak Load (kN)			Deformation at Peak Load (mm)			Area Under Curve (kN-mm)		
	Expt.	Model	Error	Expt.	Model	Error	Expt.	Model	Error	Expt.	Model	Error
1	2.4	2.8	17.18%	22.8	25.0	9.84%	31.01	22.89	-26.21%	679	703	3.48%
2	1.6	2.3	42.19%	22.1	29.6	33.98%	51.67	34.20	-33.81%	1,134	1,042	-8.11%
3	2.3	1.8	-21.32%	34.3	32.6	-4.83%	31.89	31.89	-1.88E-07	712	671	-5.83%
4	1.1	1.4	30.15%	40.2	36.7	-8.77%	62.98	49.08	-22.07%	2,018	1,838	-8.92%
5	1.2	1.2	1.59%	36.2	36.2	-0.15%	45.51	43.32	-4.81%	1,643	1,025	-37.59%
6	1.3	1.2	-6.78%	37.8	37.5	-0.65%	51.51	44.51	-13.60%	1,508	1,540	2.13%
7	3.7	2.7	-25.11%	33.4	29.1	-12.91%	40.66	30.67	-24.55%	1,266	1,143	-9.75%
8	2.1	2.6	19.59%	31.1	30.9	-0.85%	36.76	35.07	-4.58%	1,082	1,141	5.50%
9	2.4	1.9	-21.91%	35.6	36.8	3.35%	45.05	43.49	-3.47%	1,681	1,647	-2.04%
10	1.7	1.5	-13.88%	47.4	39.6	-16.47%	57.45	42.15	-26.64%	2,467	1,315	-46.72%
11	1.5	1.3	-12.77%	43.7	39.5	-9.49%	53.17	47.83	-10.04%	2,172	2,049	-5.65%
12	3.1	2.9	-5.63%	27.2	27.3	0.32%	30.75	26.83	-12.75%	951	978	2.82%
13	2.3	2.5	10.63%	29.4	31.2	6.08%	39.92	35.94	-9.98%	1,103	1,224	10.95%
14	1.8	1.9	5.48%	35.8	36.1	0.80%	51.55	47.89	-7.11%	1,498	1,547	3.23%
15	1.5	1.5	-0.75%	39.6	40.3	1.81%	53.77	45.72	-14.96%	2,056	1,434	-30.27%
16	1.4	1.3	-9.57%	40.1	40.8	1.68%	54.20	47.40	-12.55%	1,939	1,790	-7.70%
Mean			0.57%			0.23%			-14.19%			-8.40%
Standard Deviation			19.32%			11.36%			9.80%			16.20%
Median			-3.19%			0.08%			-12.65%			-5.74%

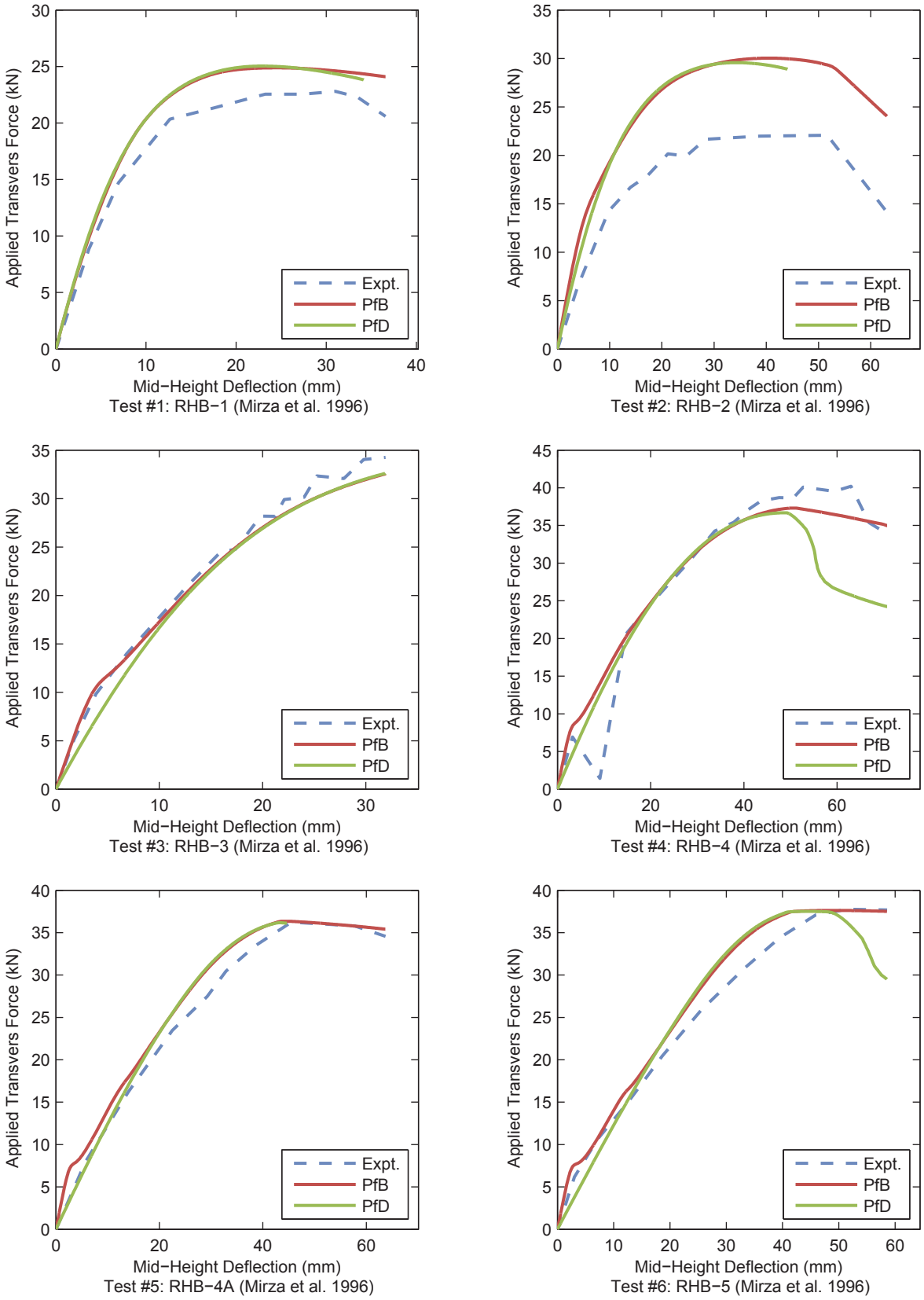

Figure 4.17. SRC Validation Results – Mirza et al. 1996

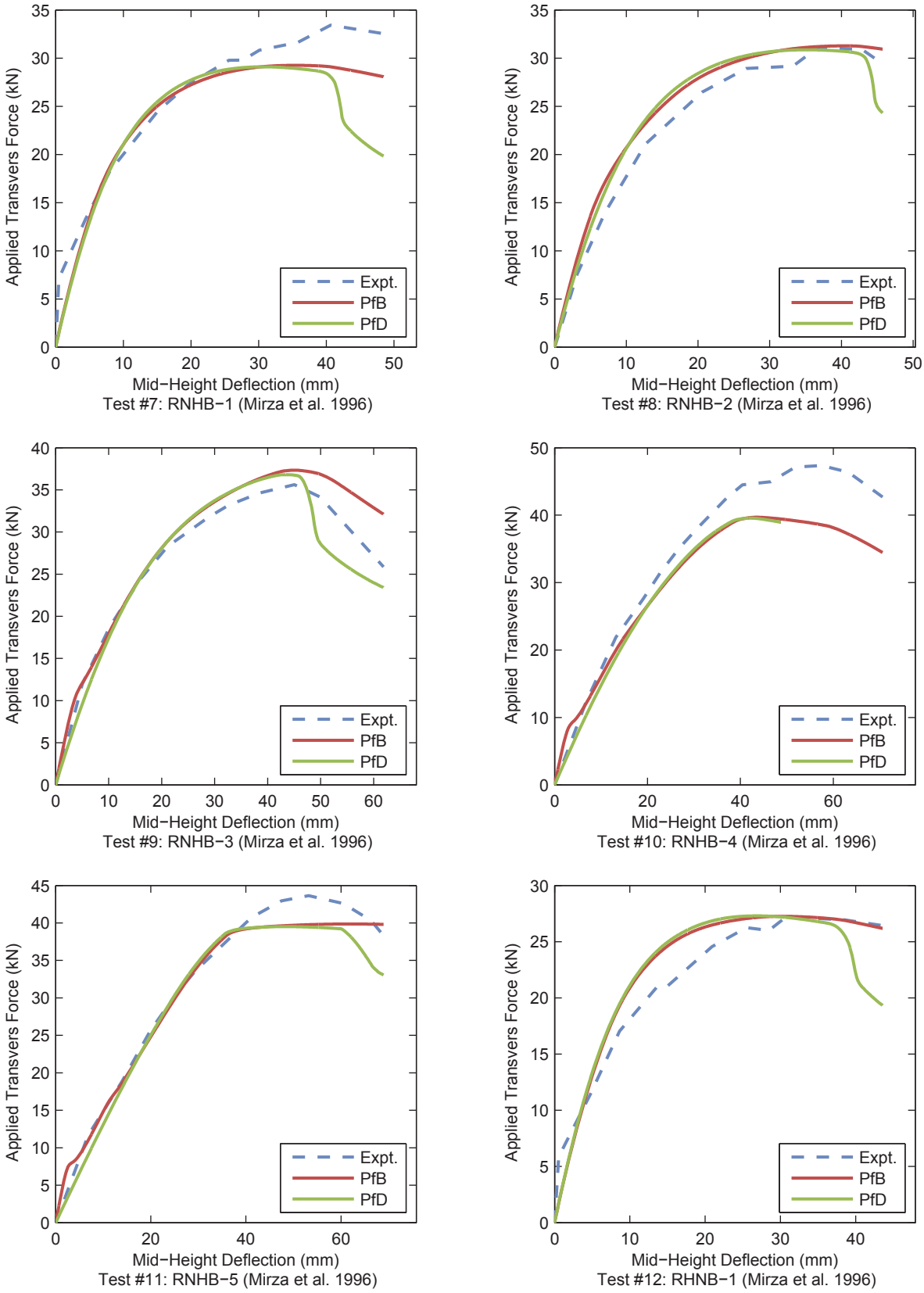

Figure 4.17. SRC Validation Results – Mirza et al. 1996 (continued)

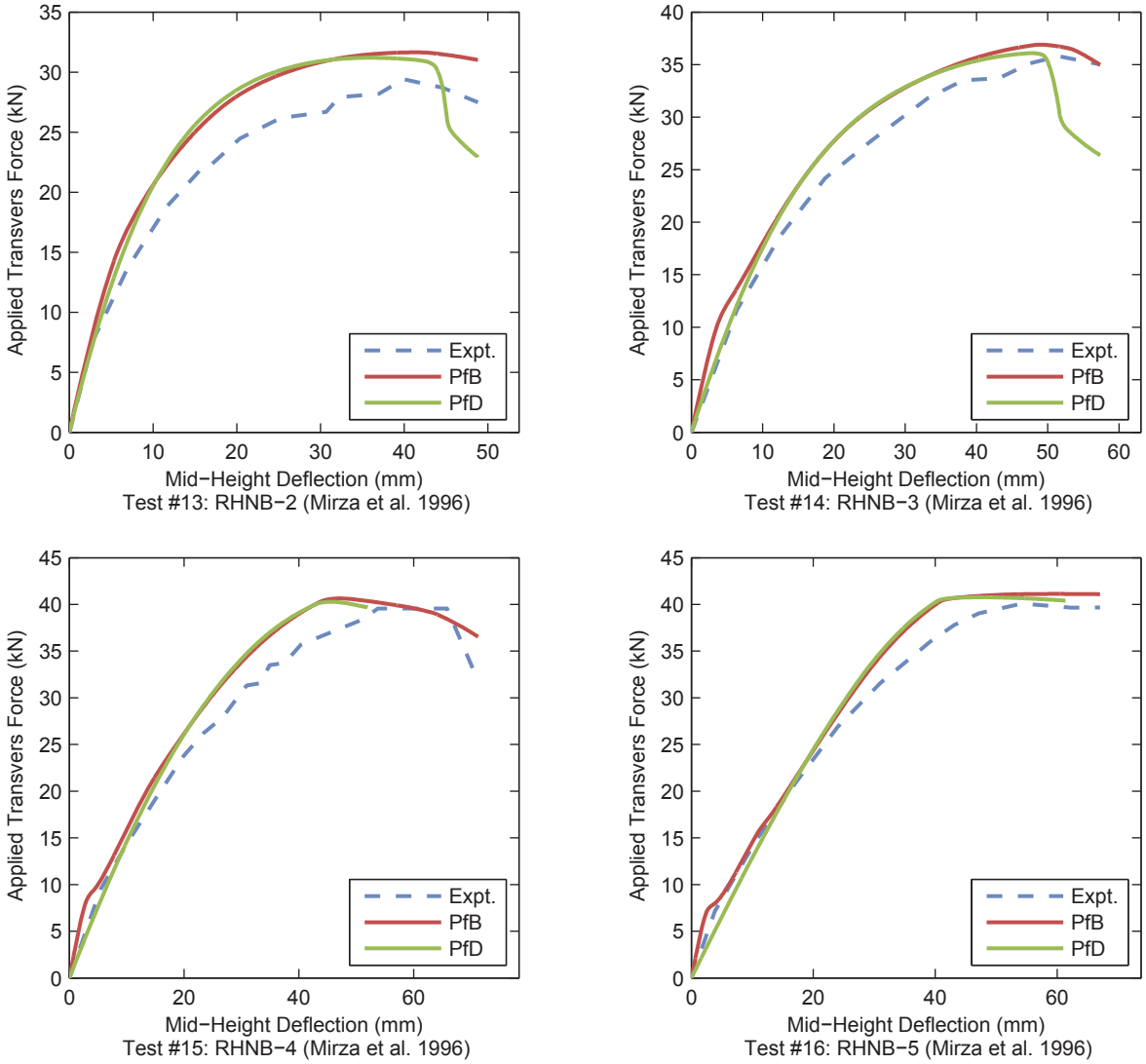

Figure 4.17. SRC Validation Results – Mirza et al. 1996 (continued)

4.6.2 Cyclic Validation Results – Ricles and Paboojian 1994

A set of carefully controlled and well documented non-proportionally loaded cyclic SRC beam-columns tests was performed by Ricles and Paboojian (1993, 1994). The specimens were subjected to a constant axial load and cyclically increasing horizontal displacements which induced strong axis bending in the column. The loading was the similar to that reported by Varma (2000) and was modeled the same way (Section 4.5.3). Material and geometric properties of the specimens are given in Table 4.49, results are shown in Figure 4.18.

The following observations are made regarding the validation results:

- A generally good correlation is seen between the computational and experimental results.
- The approximate bond-slip model employed in these analyses captures the average strain-penetration behavior well, as seen in the stiffness after some yielding has occurred. However, the inclusion of the rotational spring results in an underprediction of the initial stiffness in some of the tests. A more advanced bond-slip model would be necessary to alleviate these inaccuracies.
- Strength degradation in the last several cycles is seen in some of the experiments, which is not captured by the analyses.

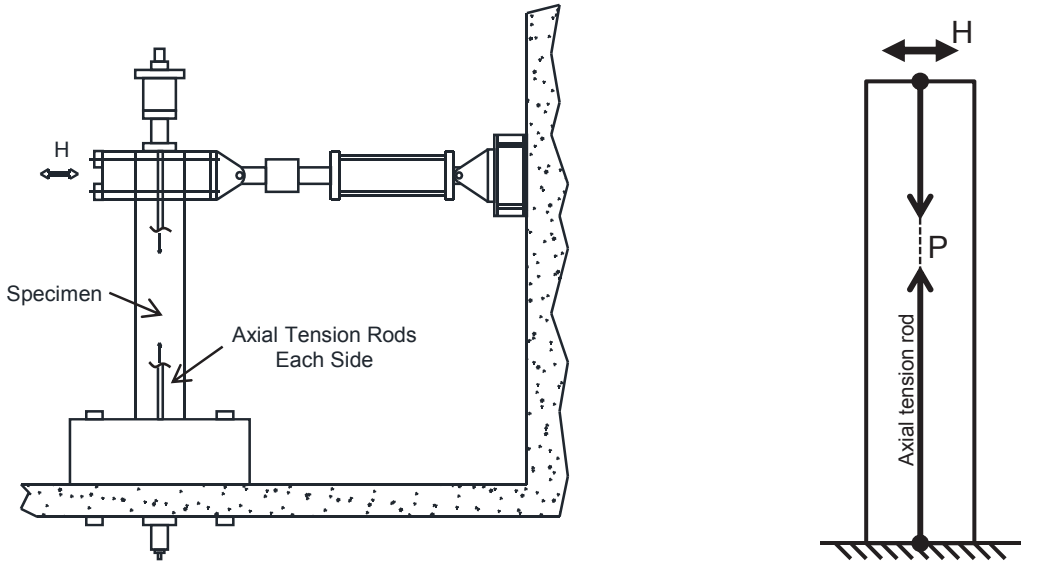

(a) Detailed Schematic [after Ricles and Paboojian (1994)] (b) Simple Schematic

Figure 4.18. Experiment Setup – Ricles and Paboojian 1994

Table 4.49. Material and Geometric Properties – Ricles and Paboojian 1994

Specimen	H (mm)	B (mm)	f'_c (MPa)	Steel Section	F_y (MPa)	Reinforcement Configuration	F_{yr} (MPa)	L (mm)	L/H	P (kN)	P/P_o
2	406	406	34.5	W8x40	372	2x-2y	434	2,489	6.1	1,490	0.19
3	406	406	31.0	W8x40	372	4x-4y	434	1,930	4.8	1,490	0.17
4	406	406	31.1	W8x40	372	2x-2y	448	1,930	4.8	1,490	0.19
5	406	406	34.5	W8x40	372	4x-4y	434	1,930	4.8	1,490	0.16
6	406	406	35.8	W8x40	372	2x-2y	448	1,930	4.8	1,490	0.17
7	406	406	62.9	W8x40	372	4x-4y	434	1,930	4.8	1,490	0.11
8	406	406	62.9	W8x40	372	4x-4y	434	1,930	4.8	1,490	0.11

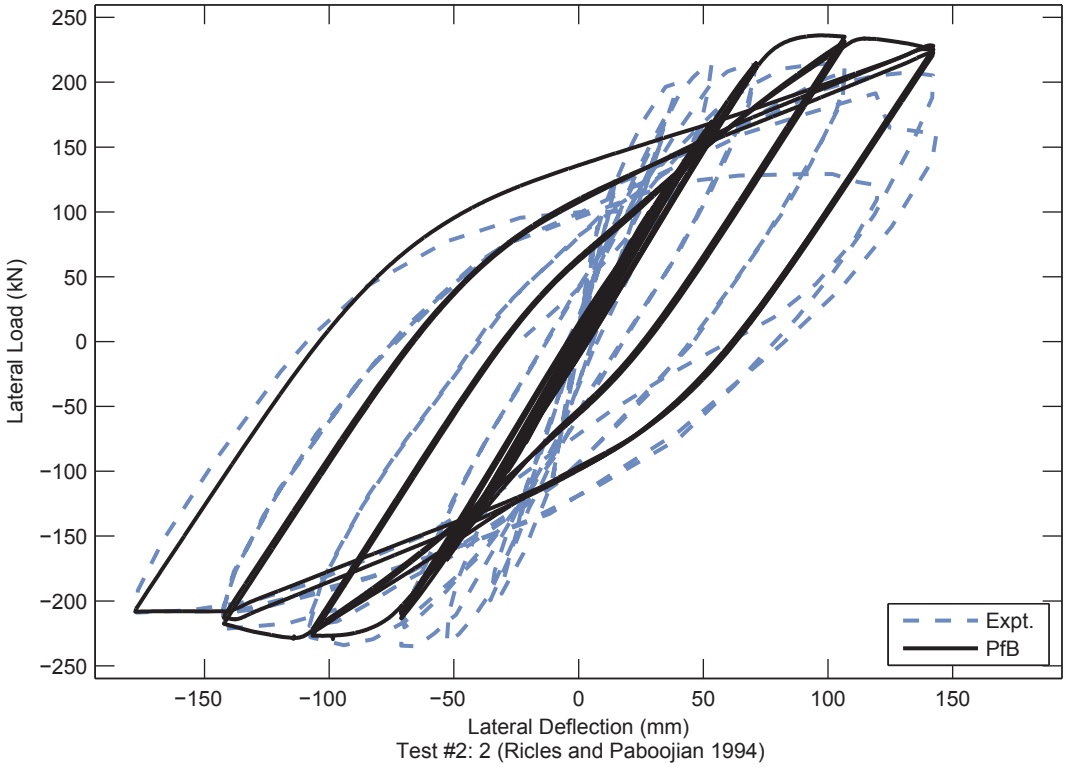

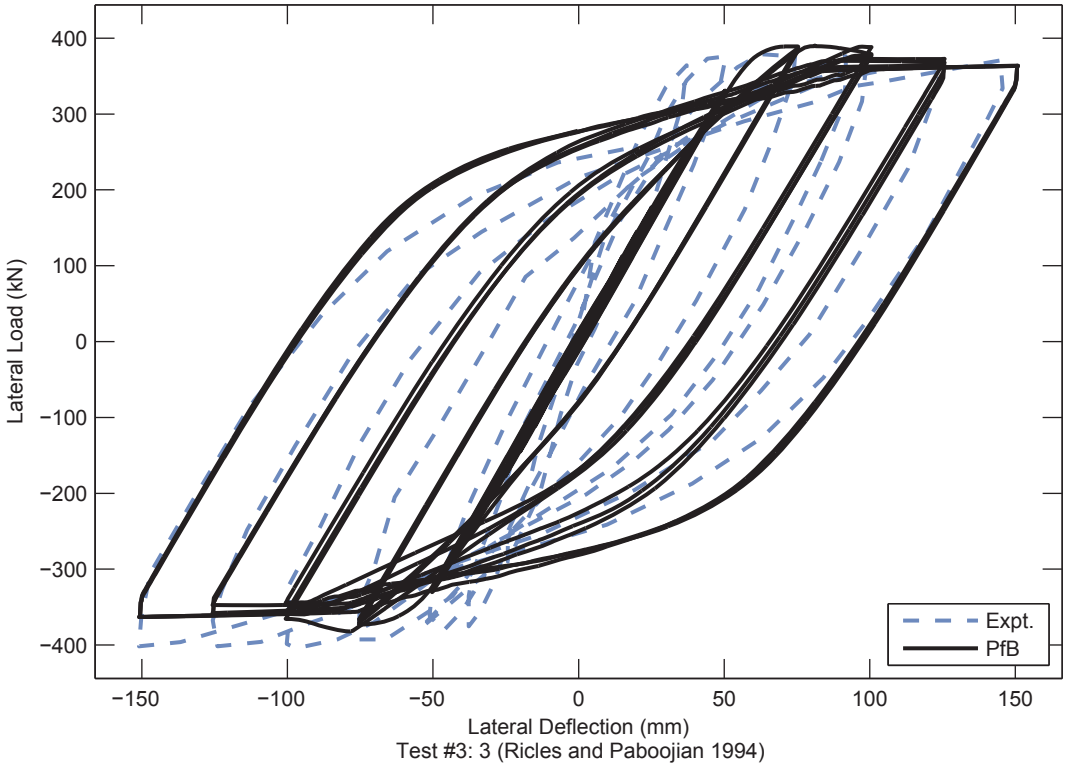

Figure 4.19. SRC Validation Results – Ricles and Paboojian 1994

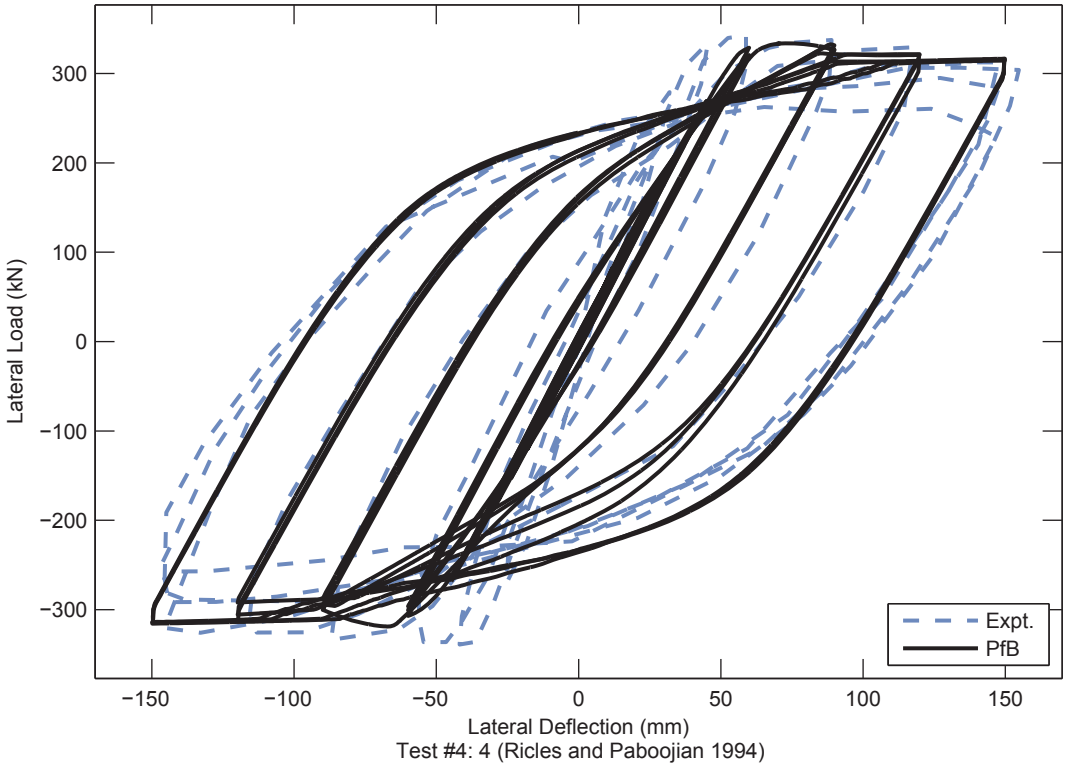

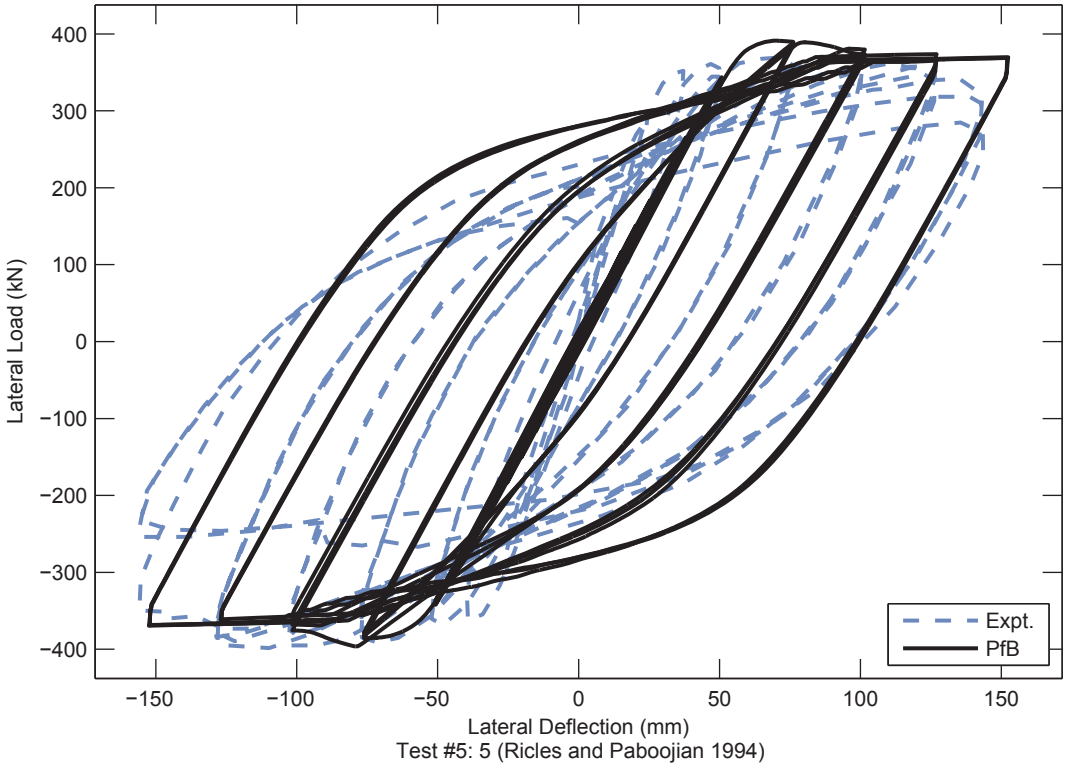

Figure 4.19. SRC Validation Results – Ricles and Paboojian 1994 (Continued)

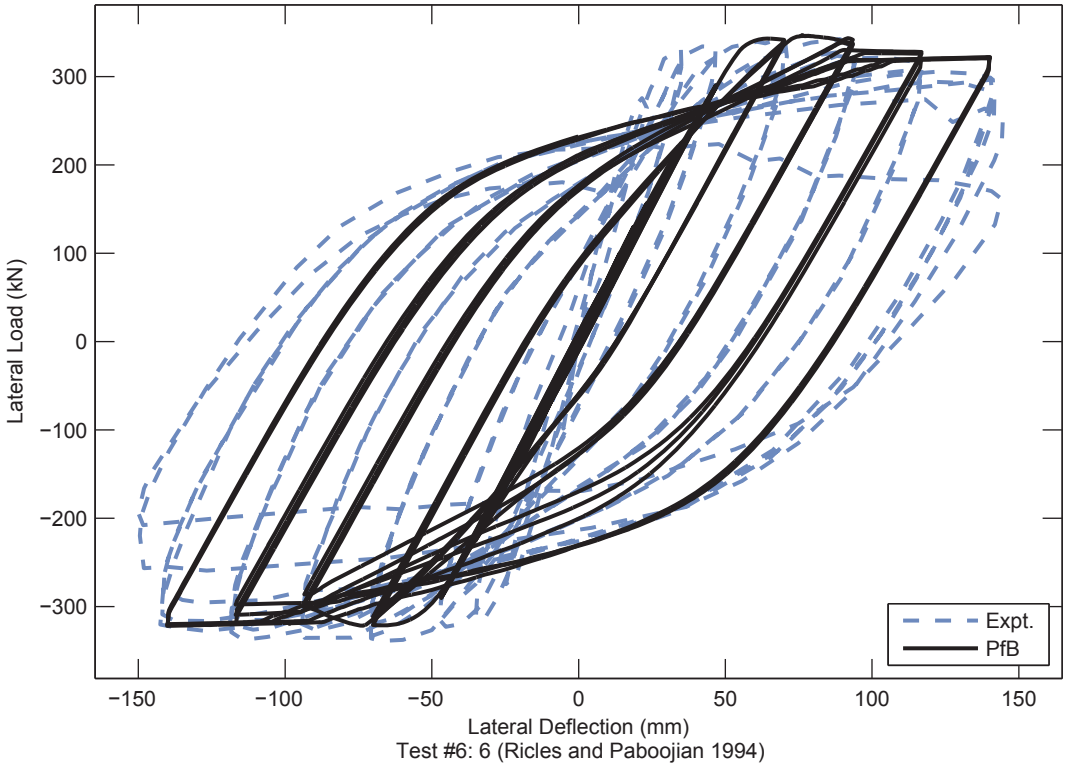

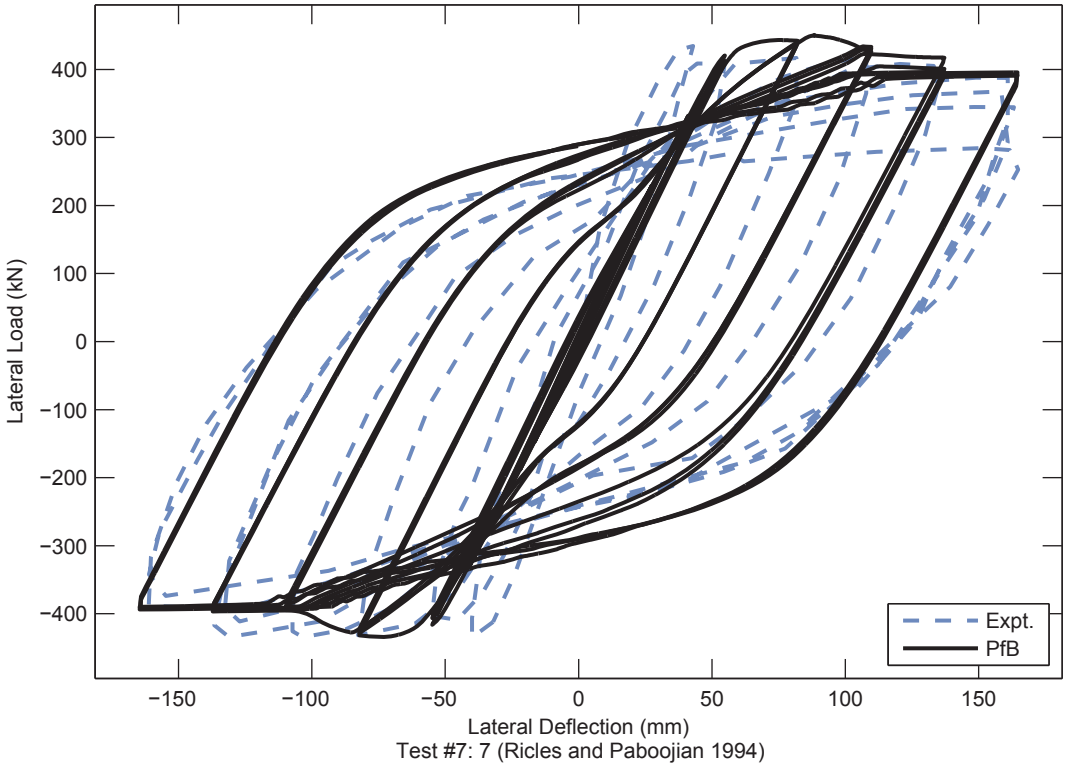

Figure 4.19. SRC Validation Results – Ricles and Paboojian 1994 (Continued)

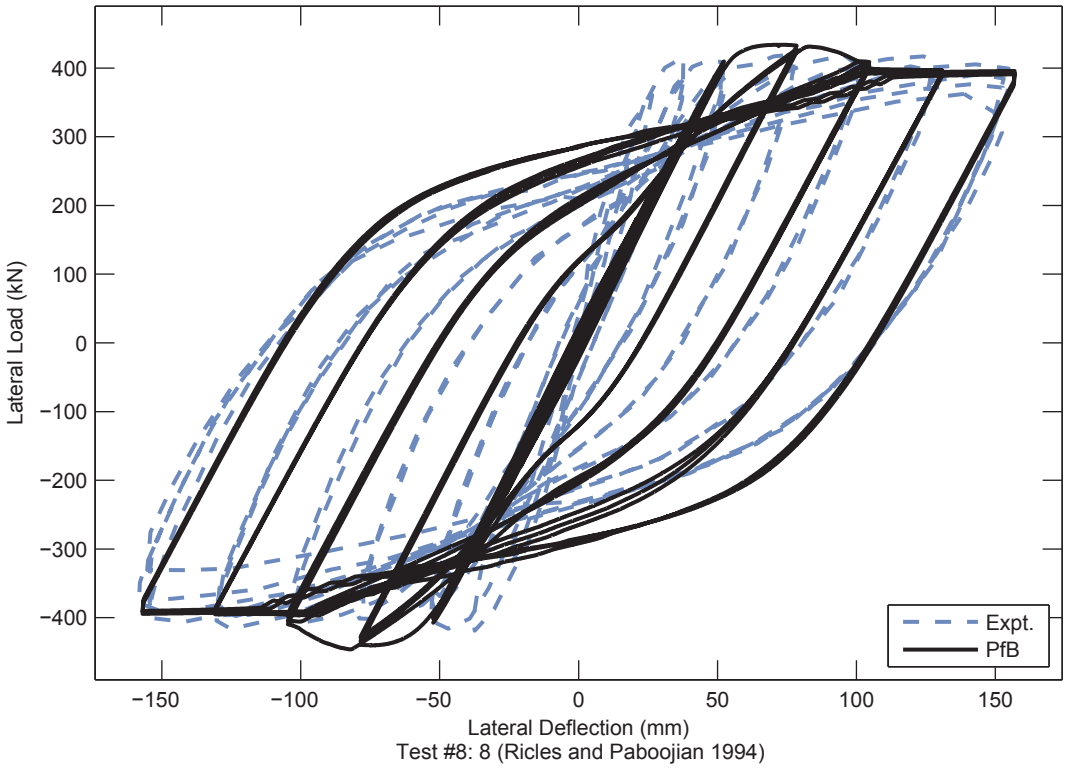

Figure 4.19. SRC Validation Results – Ricles and Paboojian 1994 (Continued)

4.7 Wide Flange Steel Beams

4.7.1 Monotonic Validation Results – Three Point Bending

The monotonic validation of the wide flange beam model includes only three-point bending experiments (Lukey and Adams 1969; Green 2000). Measured material and geometric properties are given in Table 4.50; error statistics for the PfB model are given in Table 4.51. Analysis results from the proposed for behavior model are shown along with results from the same model but with the local buckling neglected.

The following observations are made regarding the validation results:

- As expected, the model without local buckling does not show any degradation
- The model performs very well with median errors for all of the metrics less than 5%.
- Both the initiation of local buckling and post-peak softening slope are captured well by the model.

Table 4.50. Material and Geometric Properties – WF Validation Set – BM

Test #	Author	Year	Specimen	Type of Loading	d (mm)	b_f (mm)	t_f (mm)	t_w (mm)	F_y (MPa)	Shear Span (mm)
1	Lukey & Adams	1969	A-1	Three Point Bending	250	203	11	7.65	285	1,740
2	Lukey & Adams	1969	A-2	Three Point Bending	250	176	11	7.65	285	1,473
3	Lukey & Adams	1969	B-1	Three Point Bending	200	103	5	4.45	373	777
4	Lukey & Adams	1969	B-2	Three Point Bending	200	74	5	4.45	373	518
5	Lukey & Adams	1969	B-3	Three Point Bending	200	86	5	4.45	373	627
6	Lukey & Adams	1969	B-4	Three Point Bending	200	94	5	4.45	373	699
7	Lukey & Adams	1969	B-5	Three Point Bending	200	97	5	4.45	373	724
8	Lukey & Adams	1969	C-1	Three Point Bending	250	102	5	4.60	373	686
9	Lukey & Adams	1969	C-2	Three Point Bending	250	74	5	4.60	373	480
10	Lukey & Adams	1969	C-3	Three Point Bending	250	86	5	4.60	373	584
11	Lukey & Adams	1969	C-4	Three Point Bending	250	93	5	4.60	373	648
12	Lukey & Adams	1969	C-5	Three Point Bending	250	90	5	4.60	373	620
13	Green	2000	3	Three Point Bending	305	152	13	9.91	561	1,372
14	Green	2000	4	Three Point Bending	531	152	13	9.86	607	1,372
15	Green	2000	4A	Three Point Bending	533	152	13	9.83	607	1,372
16	Green	2000	5	Three Point Bending	532	152	13	9.81	331	1,372
17	Green	2000	6	Three Point Bending	302	228	13	10.30	607	1,372

Table 4.51. Comparison Metrics – WF Validation Set – BM – Proposed for Behavior

Test #	Initial Tangent (kN-m)			Peak Moment (kN-m)			Deformation at Peak Load (rad)			Area Under Curve (kN-m)		
	Expt.	Model	Error	Expt.	Model	Error	Expt.	Model	Error	Expt.	Model	Error
1	15948	16259	1.95%	245.9	218.8	-11.01%	0.067	0.060	-10.80%	26.64	24.36	-8.55%
2	15704	16893	7.57%	223.6	203.8	-8.83%	0.070	0.084	19.33%	24.86	23.81	-4.21%
3	7868	6601	-16.11%	61.1	59.6	-2.51%	0.021	0.025	21.36%	1.73	1.69	-2.21%
4	7594	7679	1.12%	50.2	51.4	2.33%	0.029	0.032	9.25%	2.82	2.93	4.01%
5	7707	7122	-7.59%	54.5	55.0	0.77%	0.033	0.029	-12.74%	3.17	3.33	5.27%
6	6359	6849	7.70%	54.4	57.2	5.08%	0.025	0.027	11.73%	3.56	3.90	9.48%
7	7302	6763	-7.38%	55.1	58.0	5.19%	0.019	0.027	43.06%	3.72	4.10	10.36%
8	13931	12477	-10.44%	82.3	79.3	-3.71%	0.018	0.018	1.16%	2.60	2.61	0.11%
9	11053	14112	27.67%	75.3	69.6	-7.63%	0.030	0.021	-31.31%	3.59	3.39	-5.63%
10	13818	12915	-6.54%	77.1	73.9	-4.12%	0.020	0.020	-2.86%	3.30	3.29	-0.23%
11	12225	12393	1.37%	78.3	76.6	-2.26%	0.017	0.019	12.70%	2.66	2.78	4.29%
12	12787	12589	-1.55%	77.4	75.3	-2.70%	0.022	0.019	-13.23%	4.20	4.23	0.67%
13	32360	30760	-4.95%	514.4	481.0	-6.48%	0.055	0.046	-17.00%	58.63	55.29	-5.70%
14	167224	112630	-32.65%	1,076.8	1,091.0	1.32%	0.013	0.024	90.28%	20.69	20.23	-2.20%
15	105700	113294	7.18%	1,098.6	1,092.1	-0.60%	0.021	0.024	10.47%	45.49	47.39	4.19%
16	132805	112949	-14.95%	653.5	654.8	0.20%	0.031	0.026	-17.14%	36.61	36.66	0.13%
17	43155	42798	-0.83%	724.6	692.1	-4.49%	0.038	0.038	1.19%	50.91	51.02	0.21%
Mean			-2.85%			-2.32%			6.79%			0.59%
Standard Deviation			12.85%			4.60%			28.03%			5.22%
Median			-1.55%			-2.51%			1.19%			0.13%

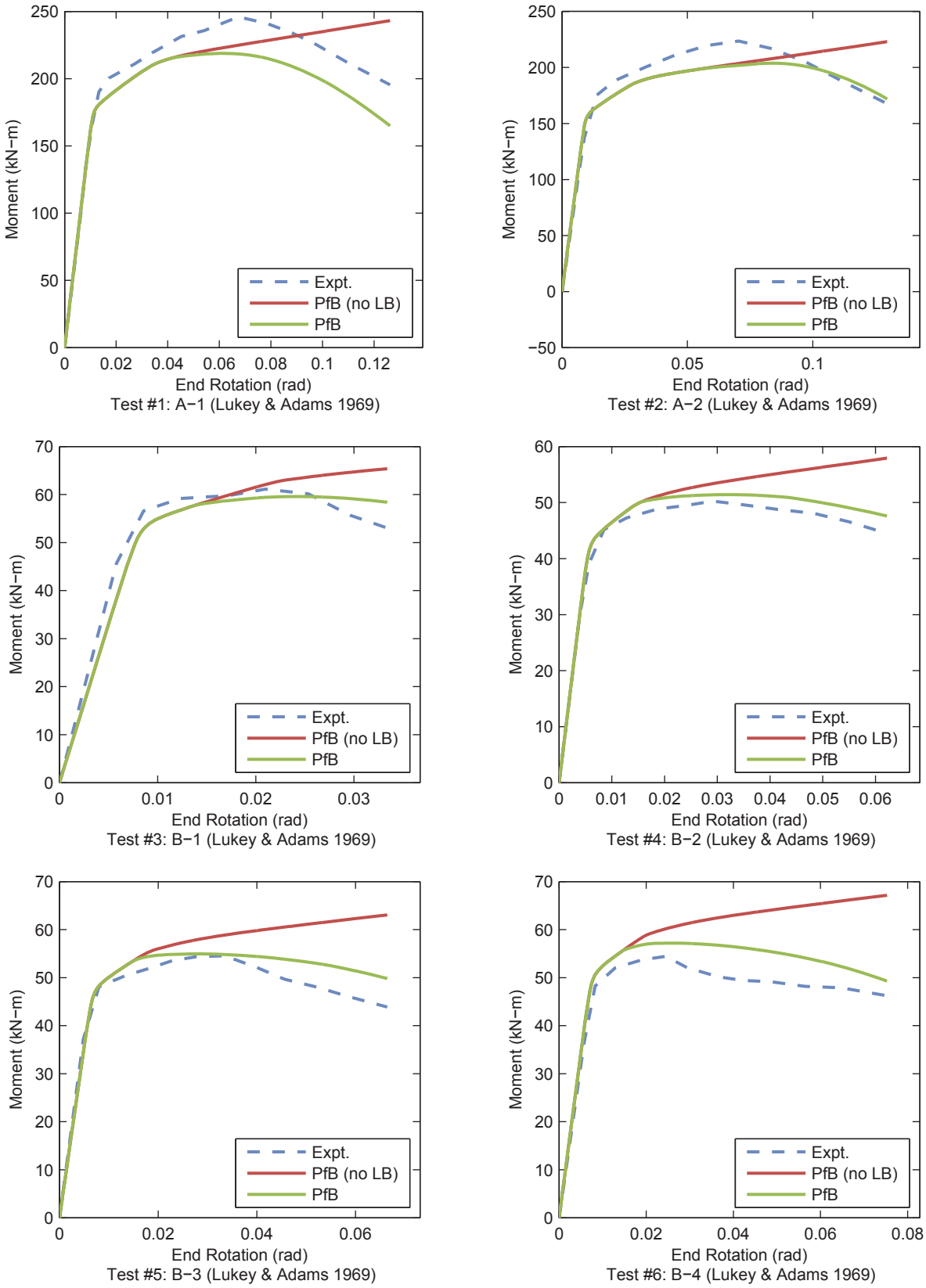

Figure 4.20. WF Validation Results – BM

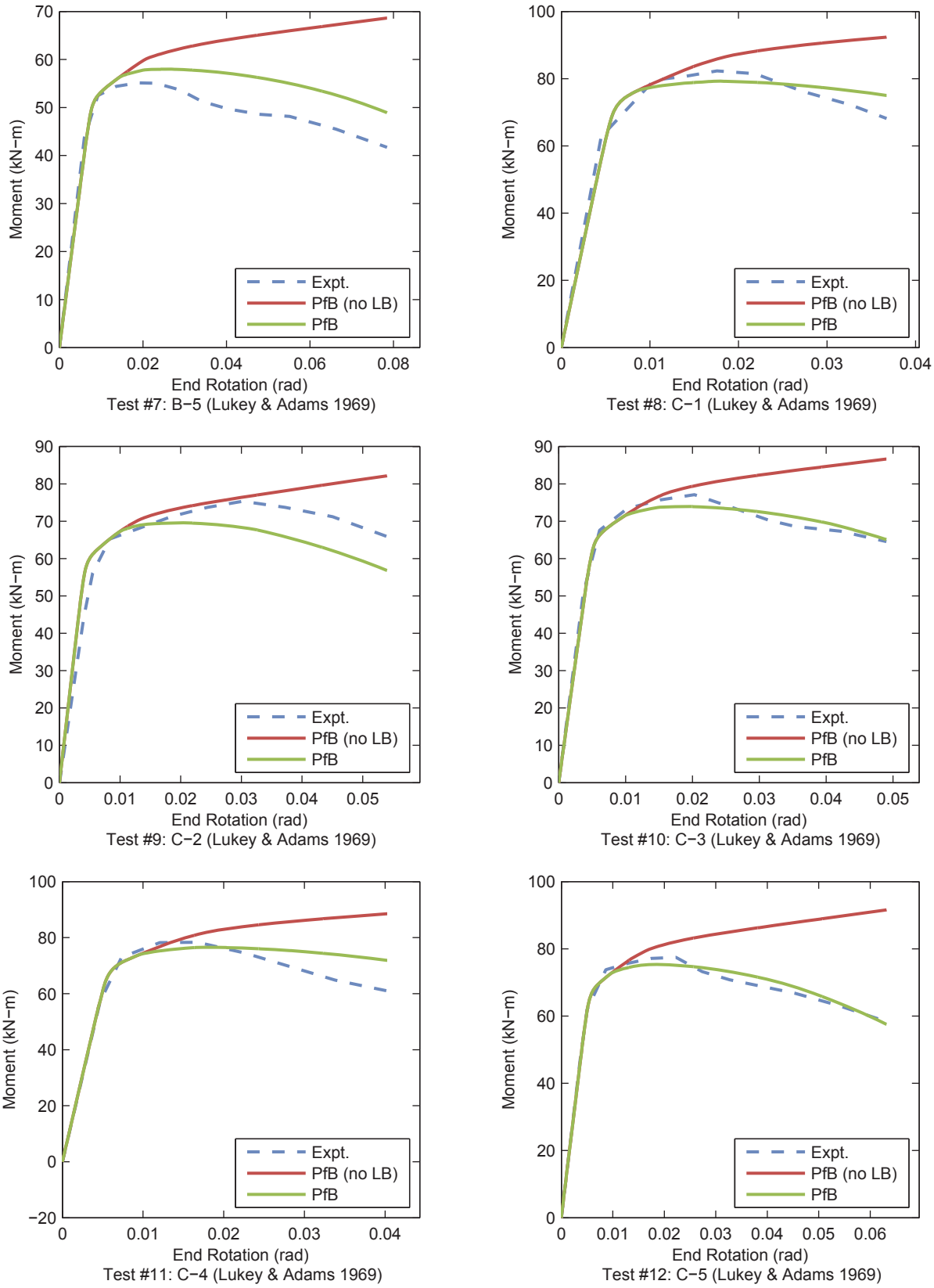

Figure 4.20. WF Validation Results – BM (continued)

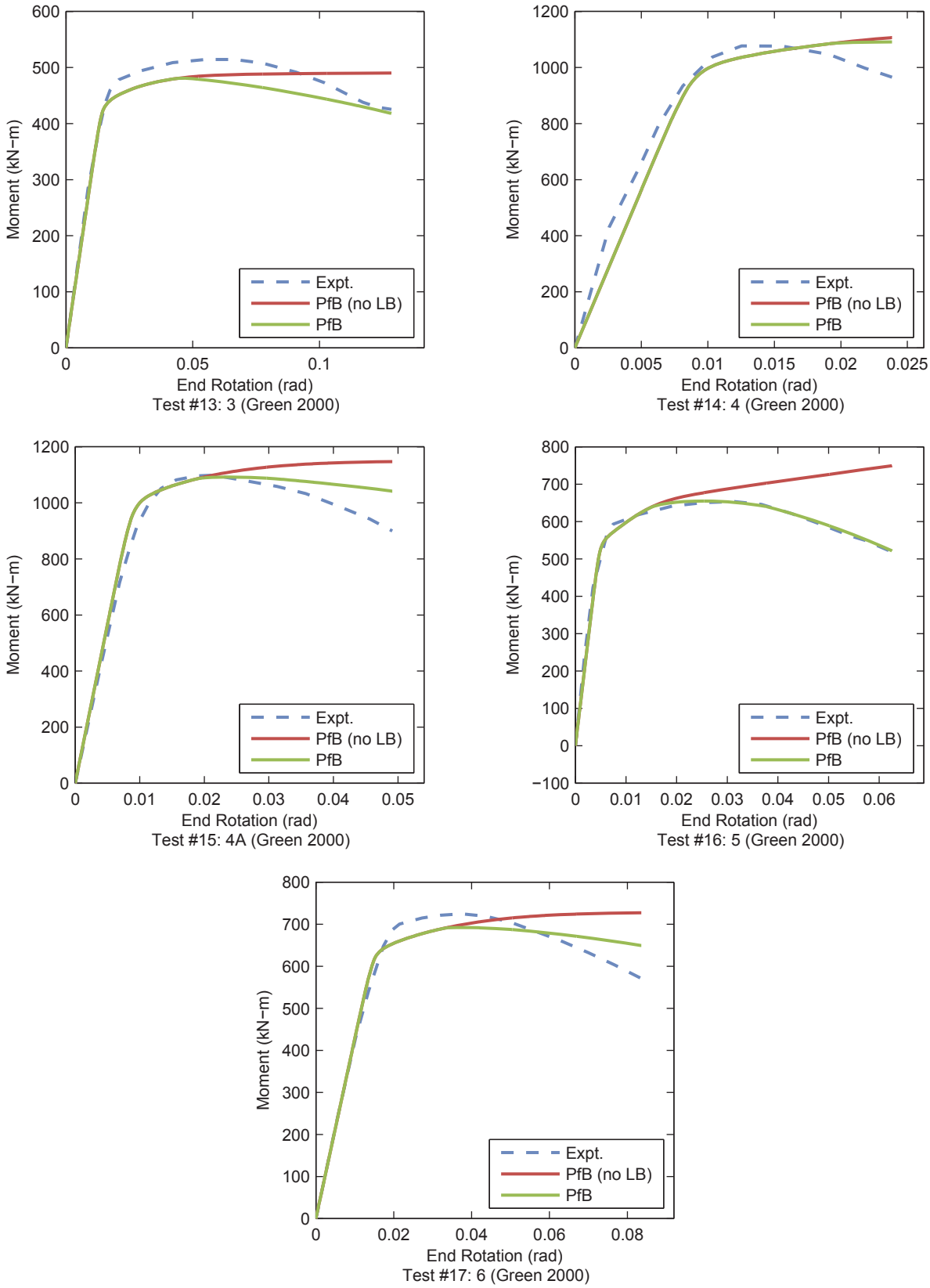

Figure 4.20. WF Validation Results – BM (continued)

4.7.2 Cyclic Validation Results – Ricles, Peng, and Lu 2004

A set of sub-assemblage tests consisting of RCFT columns and wide flange steel beams was performed by Ricles, Peng, and Lu (2004). The specimens were subjected to a constant axial load and cyclically increasing horizontal displacements applied at the top of the column. The axial load was applied in a manner similar to that reported by Varma (2000) and was modeled the same way (Section 4.5.3). Only the weak beam specimens were examined in this study, additionally the length of the elastic portion of the beam in the connection region was adjusted to include the length of the connection plus one half of the plastic hinge length to obtain better correspondence to the peak strength observed in the tests. Material and geometric properties of the specimens are given in Table 4.52, results are shown in Figure 4.22.

A generally good correlation is seen between the computational and experimental results. The initial stiffness, peak strength, and unloading stiffness are captured well by the model. Degradation due to flange and web local buckling is captured although differences between the computational and experimental results are observed.

Table 4.52. Material and Geometric Properties – Ricles, Peng, and Lu 2004

Specimen			Beam Data						Column Data		
name	height (mm)	length (mm)	d (mm)	b_f (mm)	t_f (mm)	t_w (mm)	F_y (MPa)	L_{conn} (mm)	H (mm)	H (mm)	F_y (MPa)
5	6096	3556	603	179	15	10.92	264	406	406	406.4	352
6	6096	3556	603	179	15	10.92	230	406	406	406.4	352
7	6096	3556	603	179	15	10.92	230	406	406	406.4	352

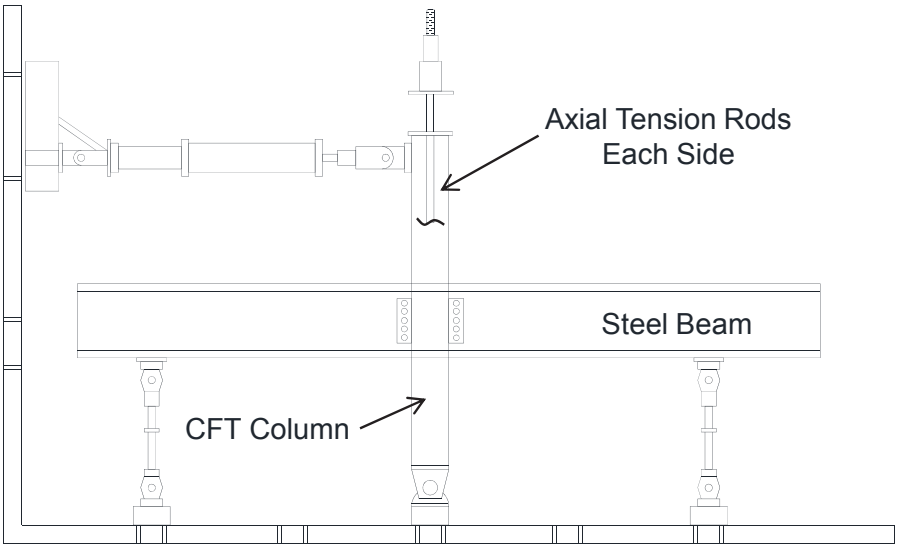

(a) Detailed Schematic [after Ricles, Peng, and Lu (2004)]

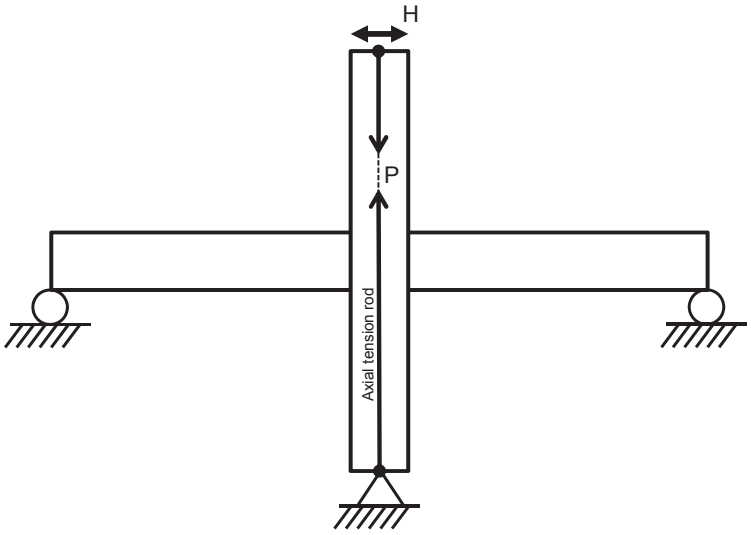

(b) Simple Schematic

Figure 4.21. Experiment Setup – Ricles, Peng, and Lu 2004

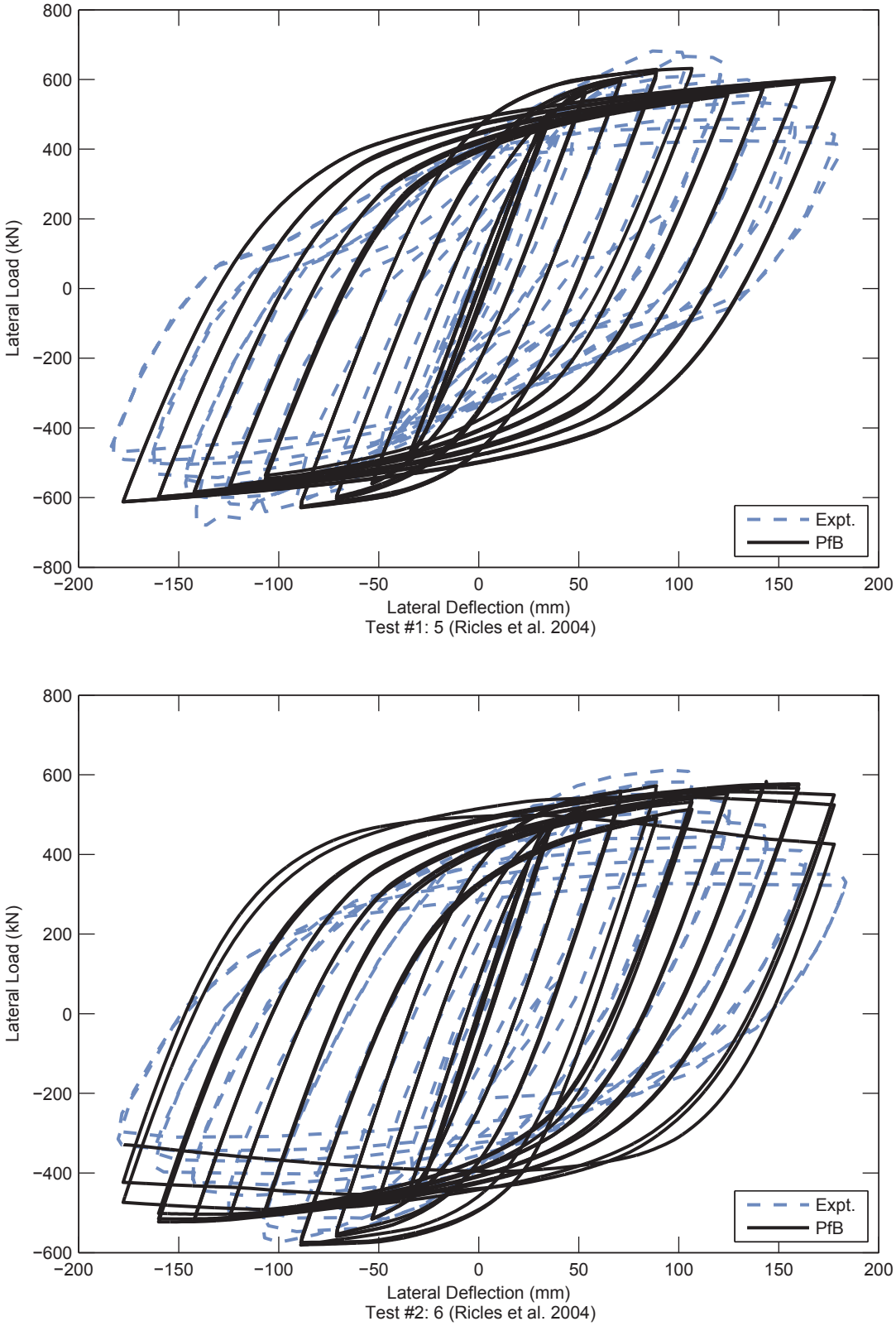

Figure 4.22. WF Validation Results – Ricles, Peng, Lu 2004

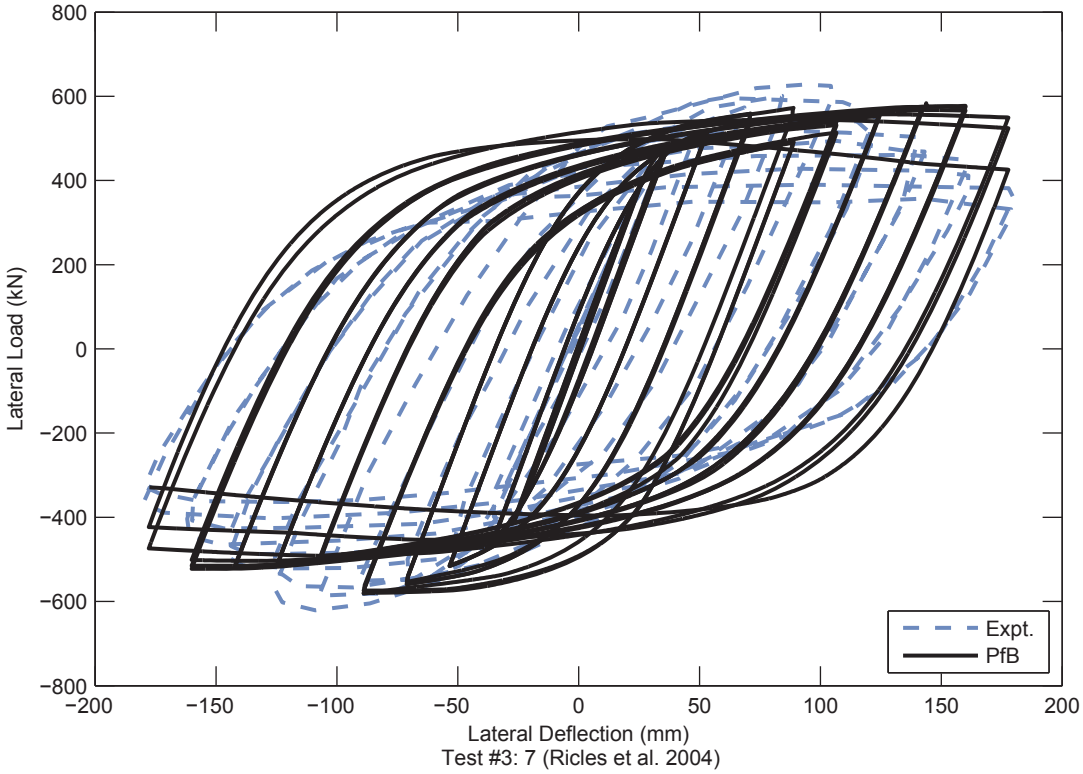

Figure 4.22. WF Validation Results – Ricles, Peng, Lu 2004 (Continued)

4.7.3 Cyclic Validation Results – Engelhardt and Sabol 1994

Engelhardt and Sabol (1994) performed a series of cyclic tests on steel moment frame sub-assemblages with wide flange columns and beams. The study focused on connection behavior but for some of the specimens the column, panel zone, and connection were strong and the inelastic behavior occurred primarily in the beams. The beams were all the same size (W36×150) and similar material properties so only one test is shown (F_y = 46.9 ksi, F_u = 66.9 ksi).

The experiment set up is as shown in Figure 4.23. The column was modeled with the wide flange model with no local buckling, the connection region was modeled as described in Chapter 3 with an elastic panel zone response (Equation 4.2) (ATC 2010):

$$K_{e,pz} = 0.95 d t_w G_s \tag{4.2}$$

Results are shown in Figure 4.24. The peak strength is captured well by the model, but the cyclic degradation is underpredicted.

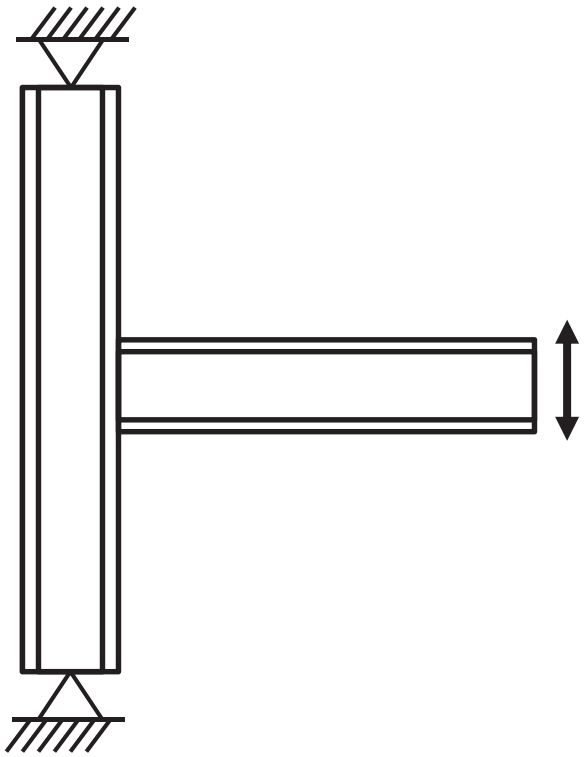

Figure 4.23. Experiment Setup – Engelhardt and Sabol 1994

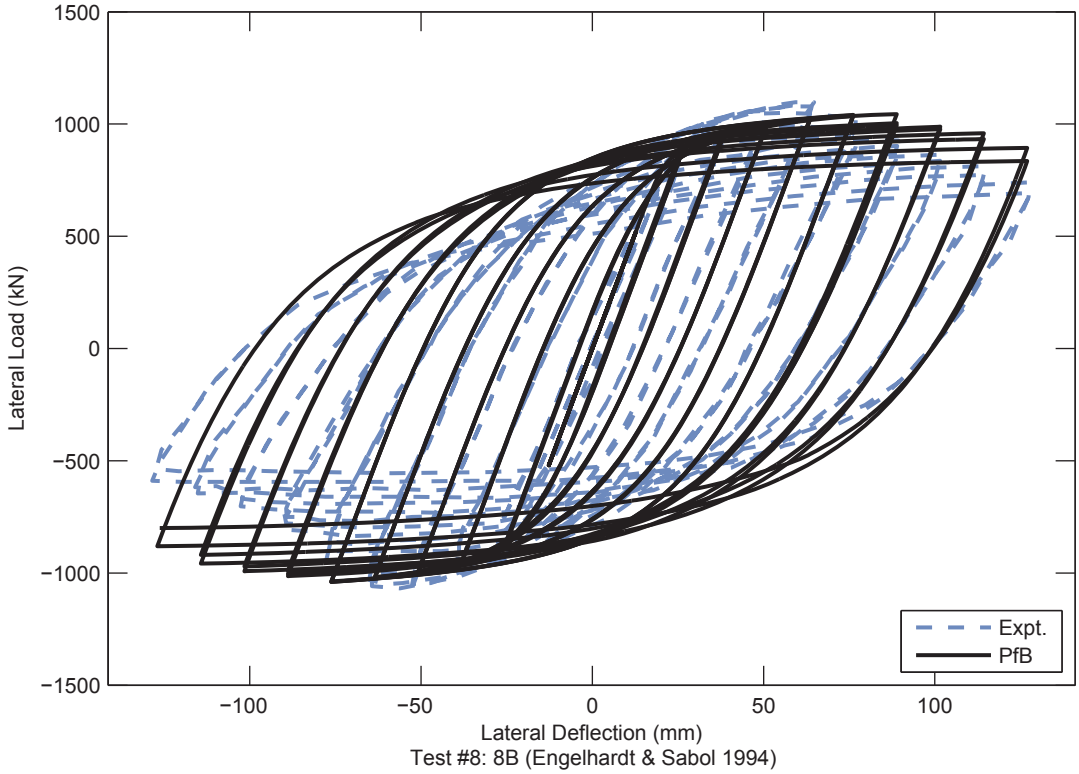

Figure 4.24. WF Validation Results – Engelhardt and Sabol 1994

4.8 Wide Flange and Rectangular Hollow Structural Steel Braces

4.8.1 Cyclic Validation Results

Experiments have been performed to assess the cyclic behavior of steel braces (Popov and Black 1981; Shaback 2001). Pinned ends were assumed. An initial imperfection equal to $L/1000$ was applied. Analyses were performed using four elements along the length, each with three integration points. The analyses were performed in two-dimensions and the nominal fiber size was $1/30^{th}$ of the section depth. Material and geometric properties of the specimens are given in Table 4.53, results are shown in Figure 4.25.

Table 4.53. Material and Geometric Properties – Cyclic Brace

Test #	Author	Year	Specimen	H (mm)	B (mm)	t (mm)	H/t	F_y (MPa)	L (mm)	L/H
1	Popov and Black	1981	Strut 17	102	102	5.91	17.2	407	2,765	27.2
2	Shaback	2001	1B	127	127	7.44	17.1	421	3,350	26.4
3	Shaback	2001	2A	152	152	7.44	20.4	442	3,950	26.0
4	Shaback	2001	2B	152	152	8.84	17.2	442	3,950	26.0
5	Shaback	2001	3A	127	127	5.95	21.3	461	4,350	34.3
6	Shaback	2001	3B	127	127	7.44	17.1	421	4,350	34.3
7	Shaback	2001	3C	127	127	8.84	14.4	461	4,350	34.3
8	Shaback	2001	4A	152	152	7.44	20.4	442	4,850	31.9
9	Shaback	2001	4B	152	152	8.84	17.2	442	4,850	31.9

The following observations are made regarding the validation results:

- The strength of the test by Popov and Black (1981) was captured well, but the strength of the tests by Shaback (2001) were underpredicted. This is likely due to the end conditions. Popov and Black used physical pinned boundary conditions while Shaback used gusset plate connections. The additional restraint provided by the gusset plate increased the strength.
- In the analyses, the braces initially deflect in the same direction as the initial imperfections. However, for some specimens (3A and 3C) after some loading, the brace snaps through and deflects in the opposite direction. This is not seen in the experiments and appears to have little effect on the axial response.

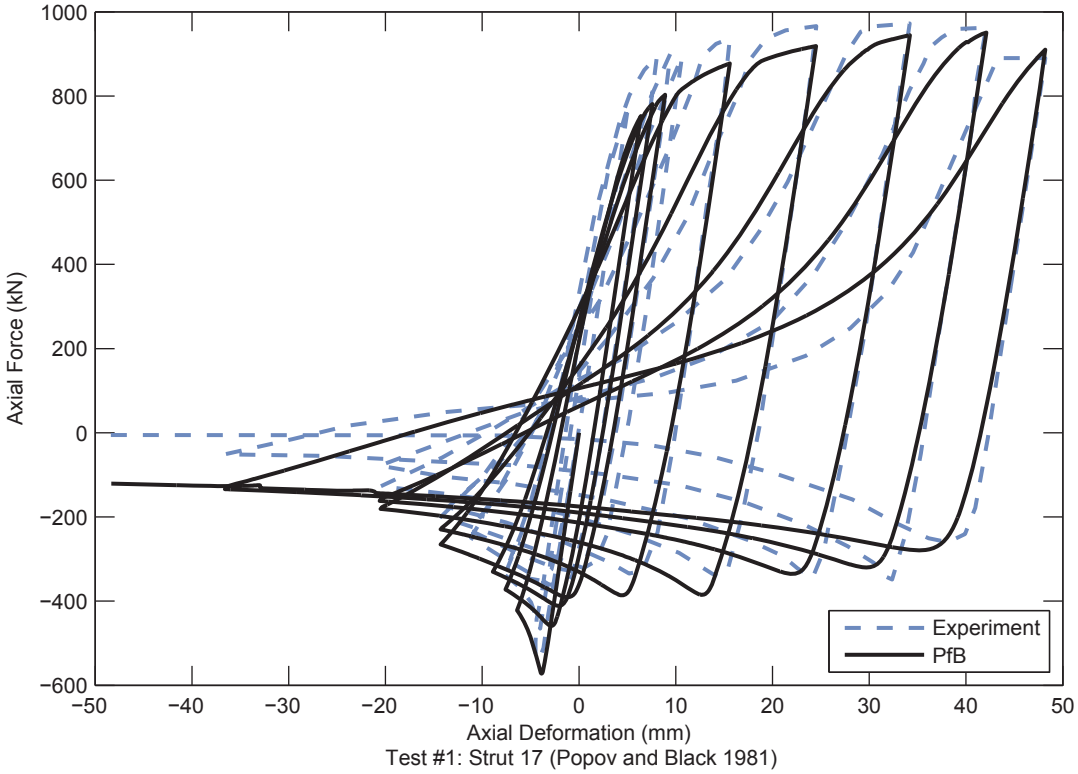

Figure 4.25. Rect. HSS Validation Results – Cyclic Brace

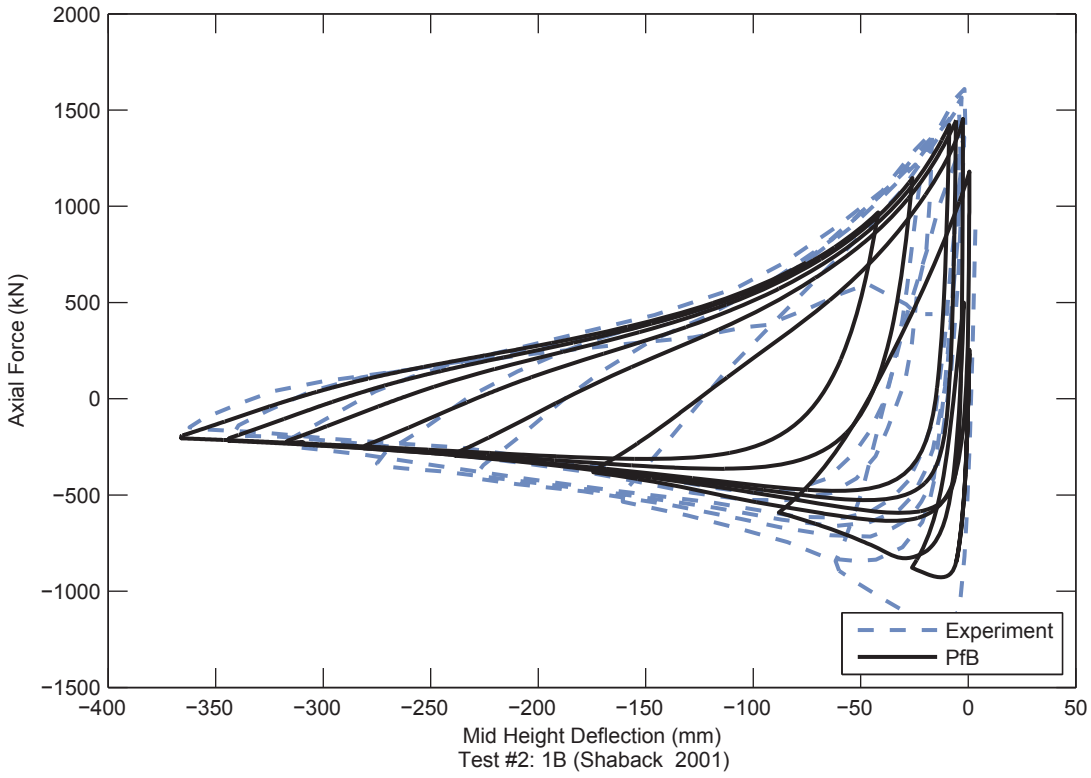

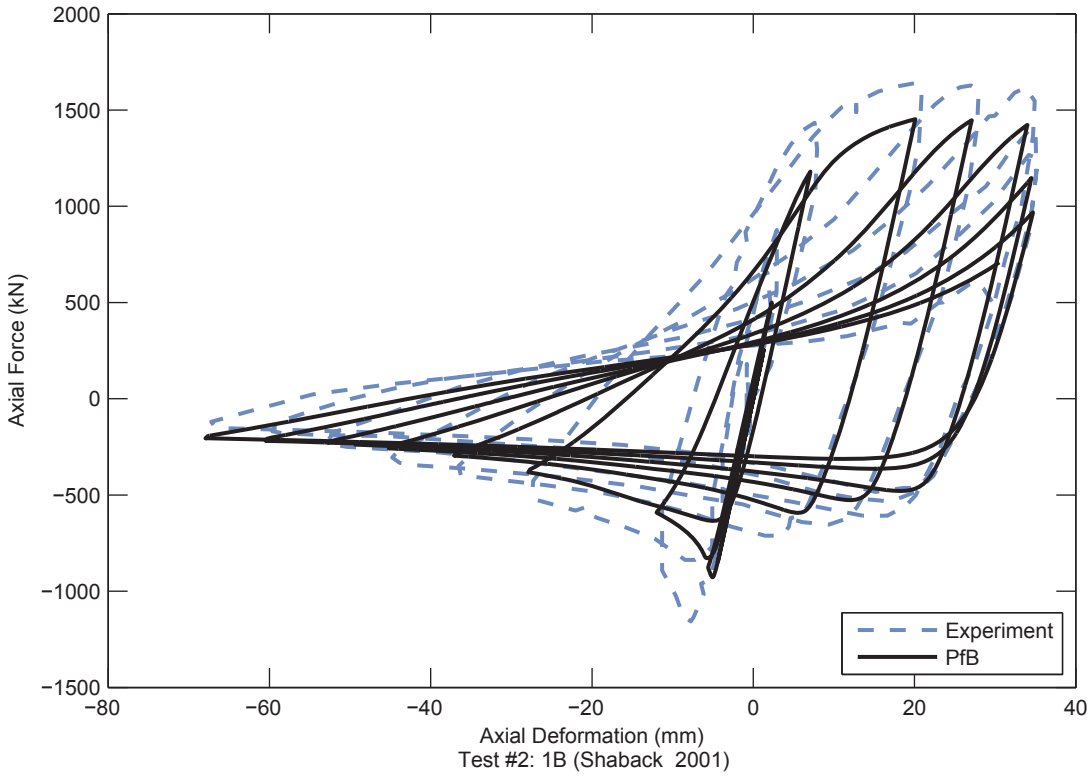

Figure 4.25. Rect. HSS Validation Results – Cyclic Brace (Continued)

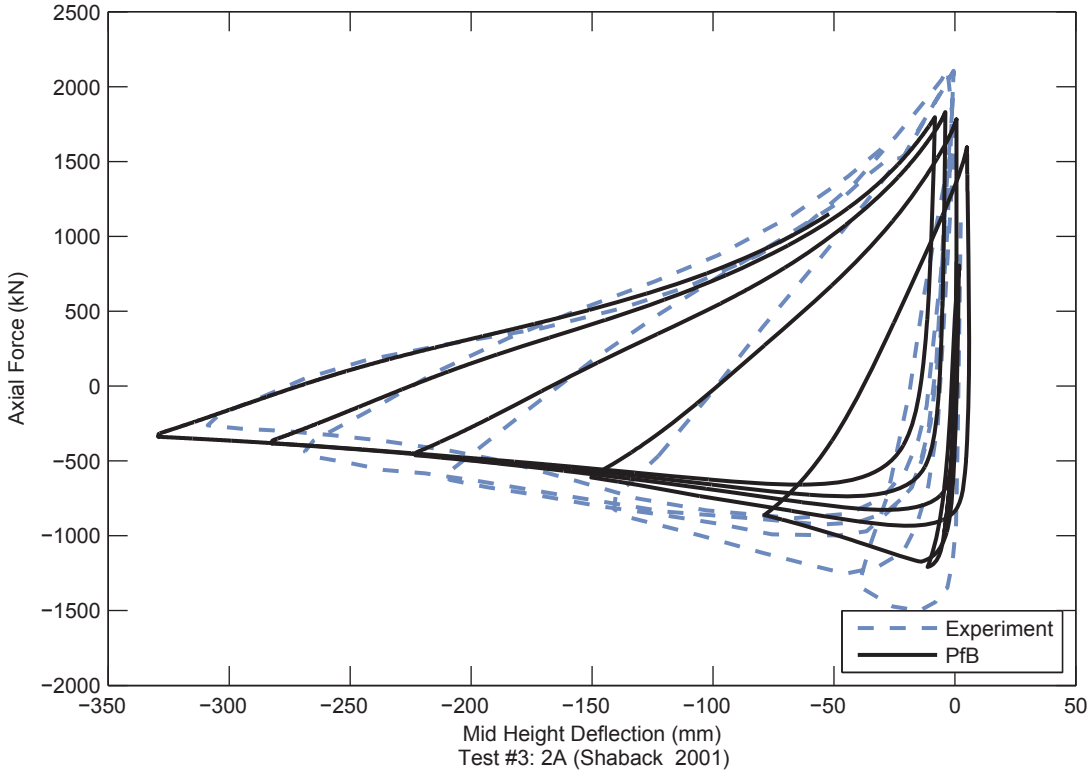

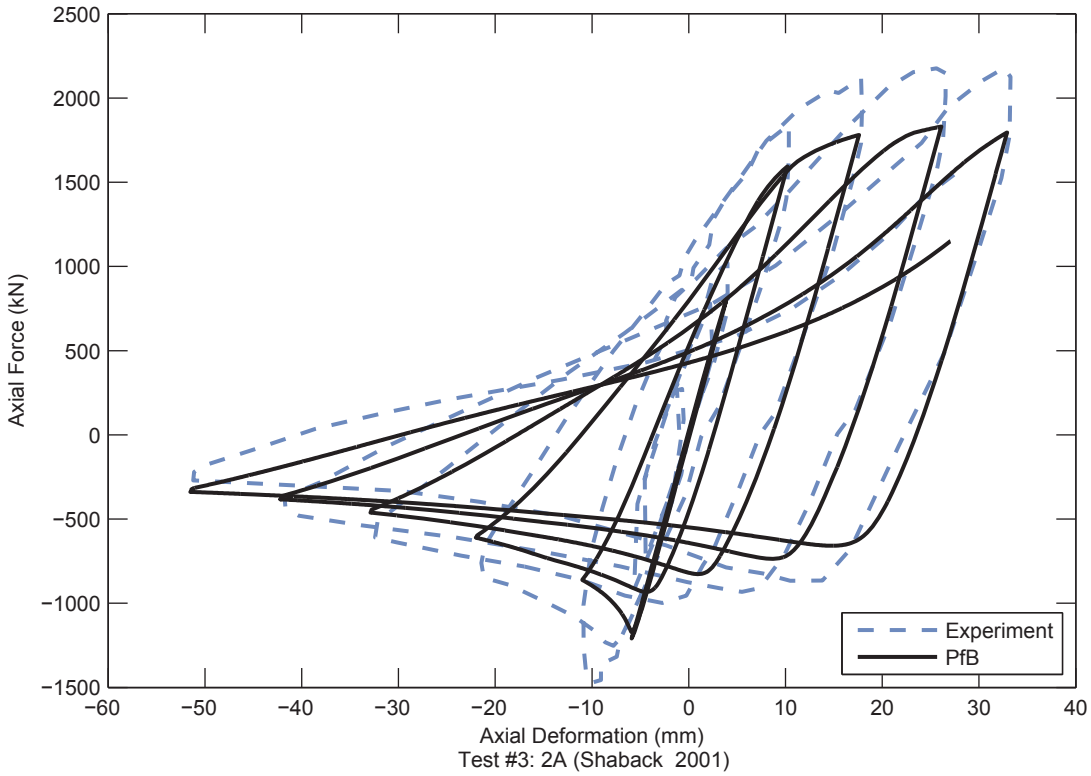

Figure 4.25. Rect. HSS Validation Results – Cyclic Brace (Continued)

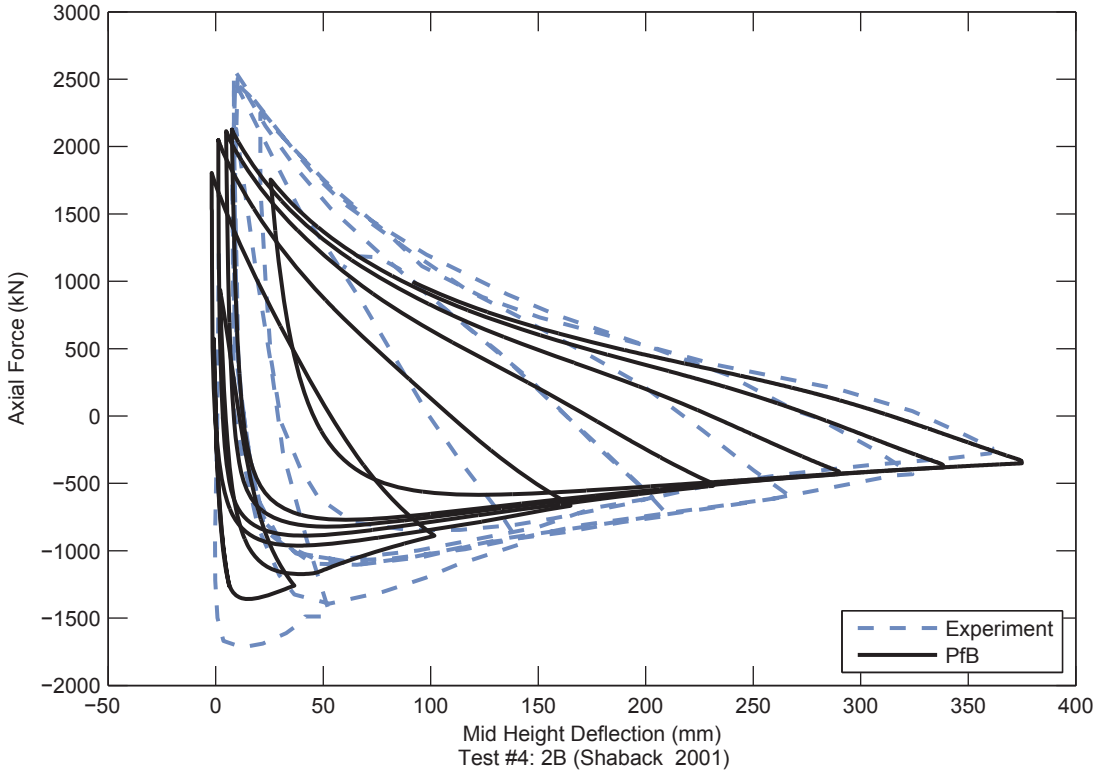

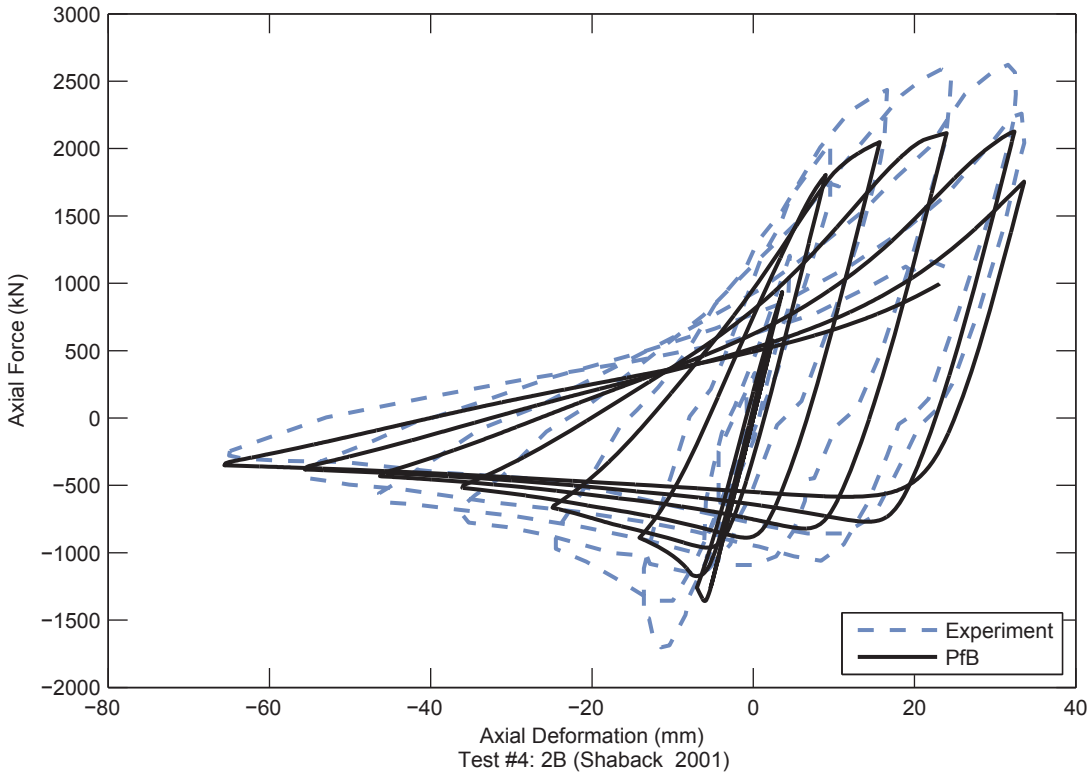

Figure 4.25. Rect. HSS Validation Results – Cyclic Brace (Continued)

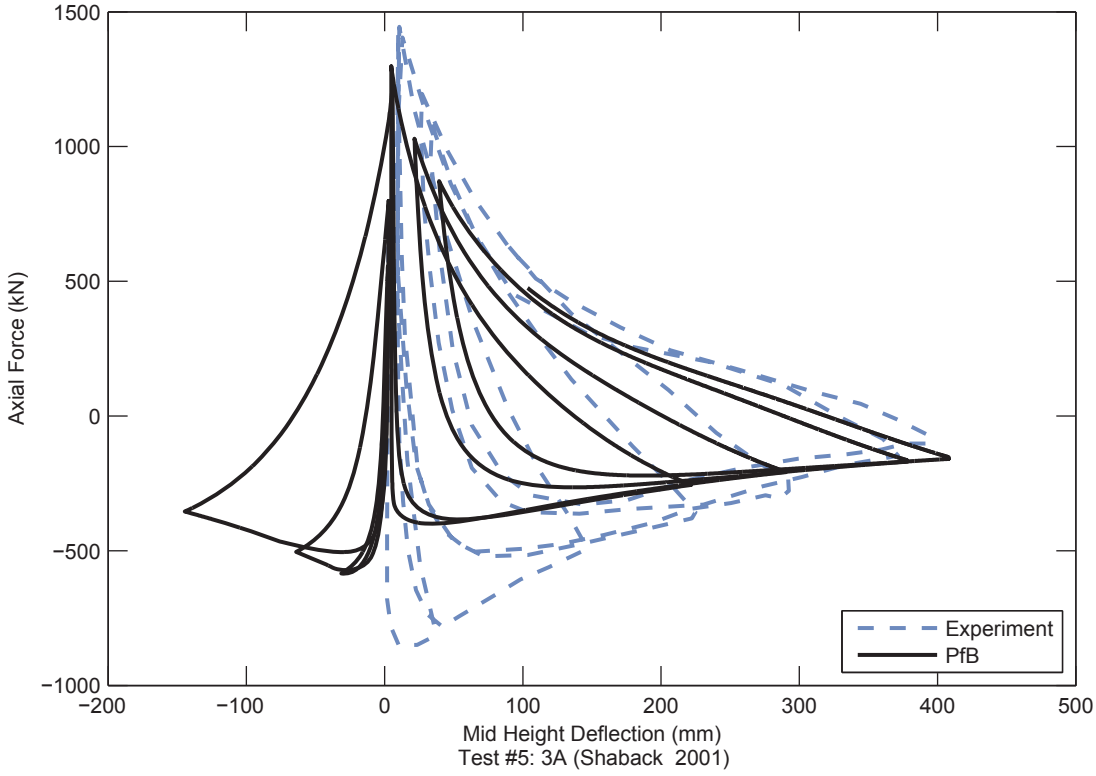

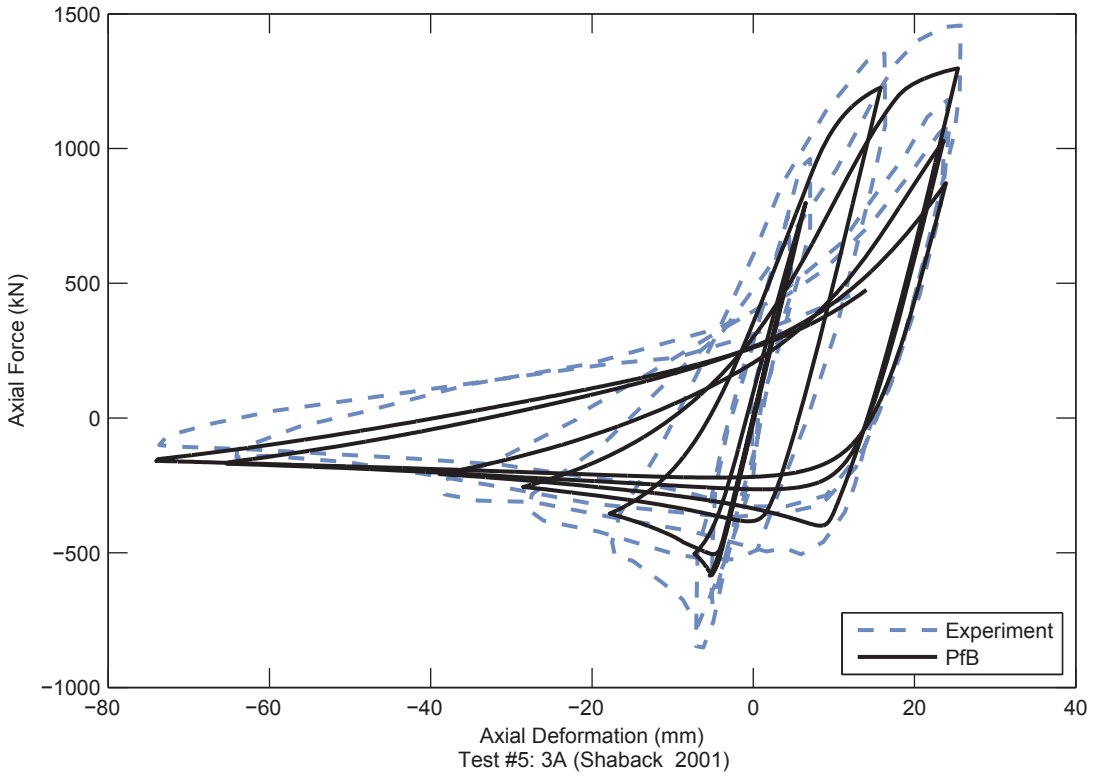

Figure 4.25. Rect. HSS Validation Results – Cyclic Brace (Continued)

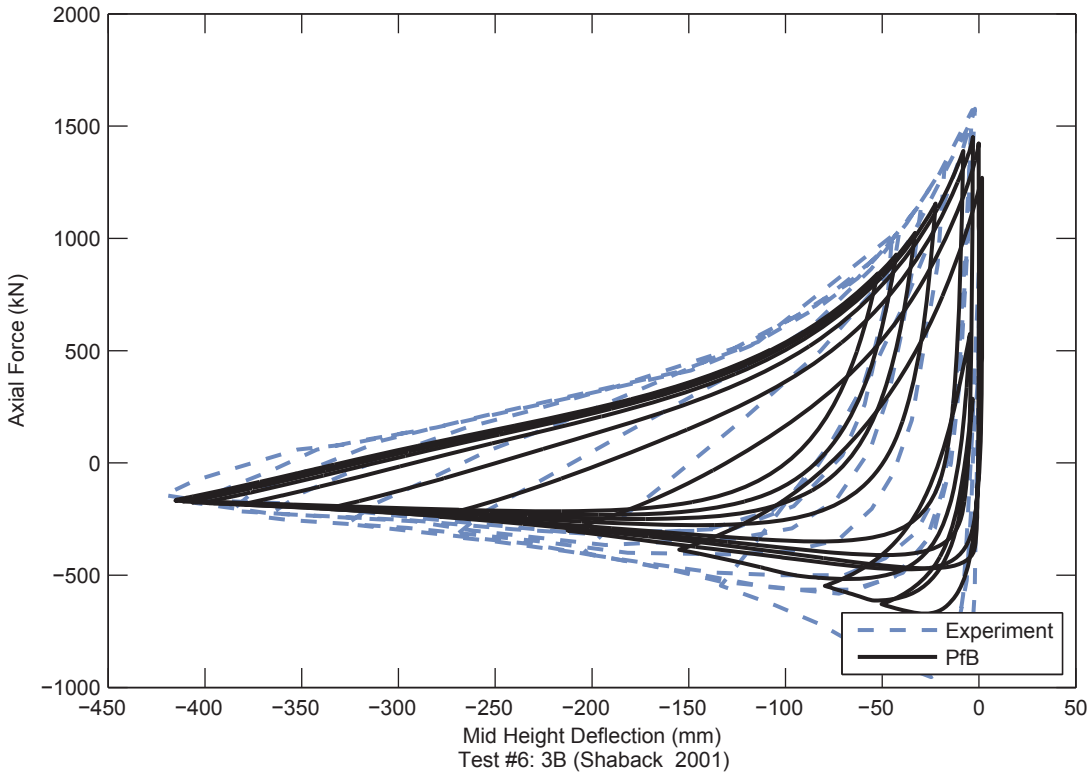

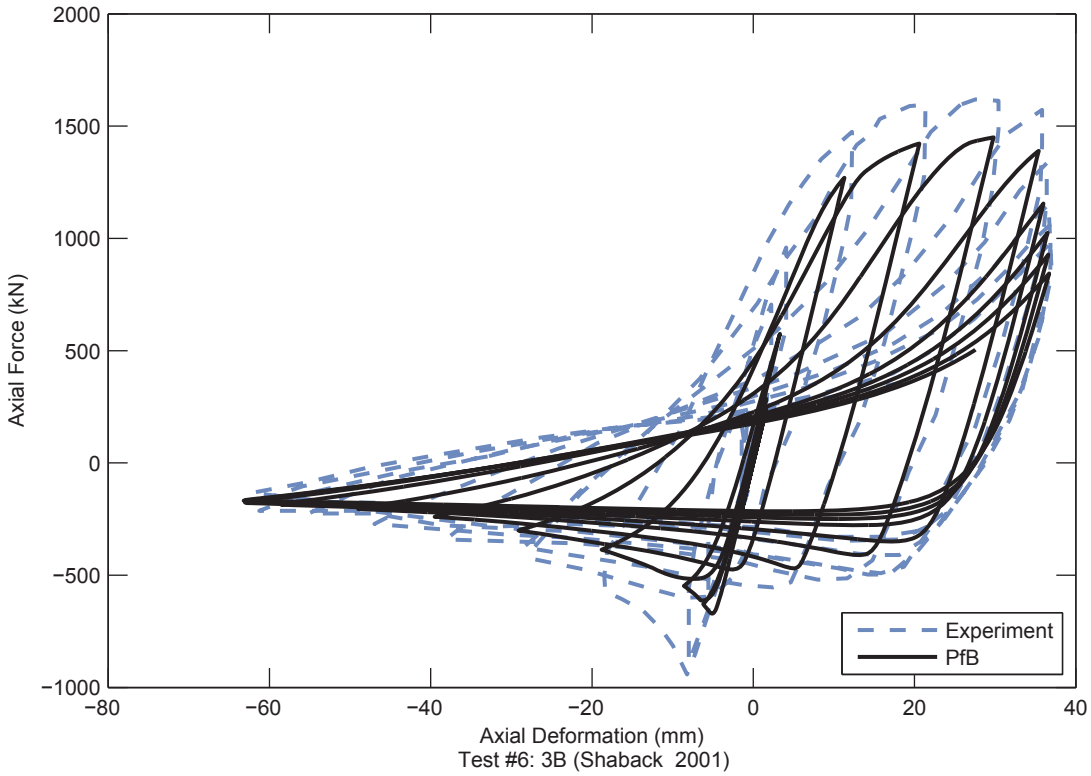

Figure 4.25. Rect. HSS Validation Results – Cyclic Brace (Continued)

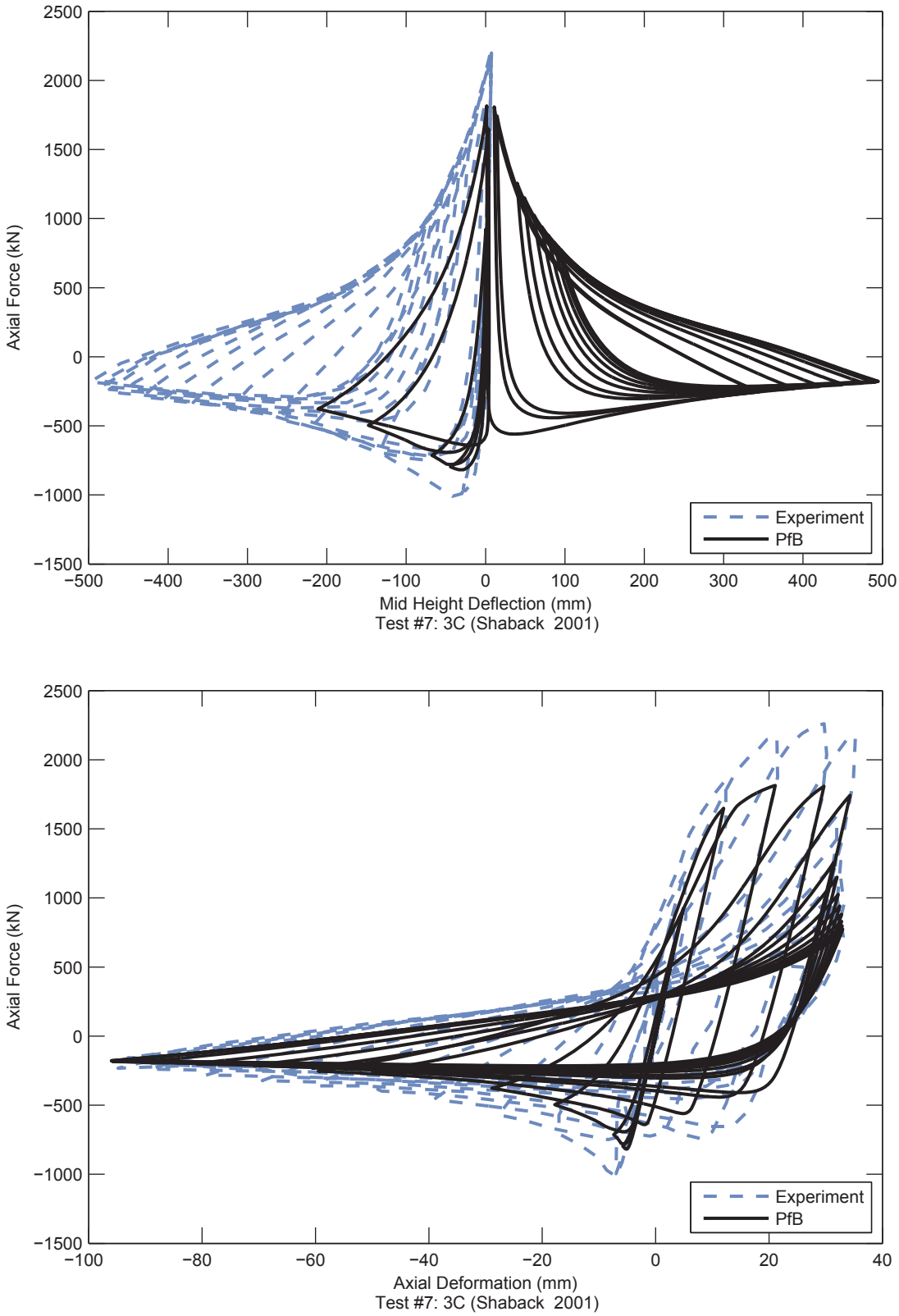

Figure 4.25. Rect. HSS Validation Results – Cyclic Brace (Continued)

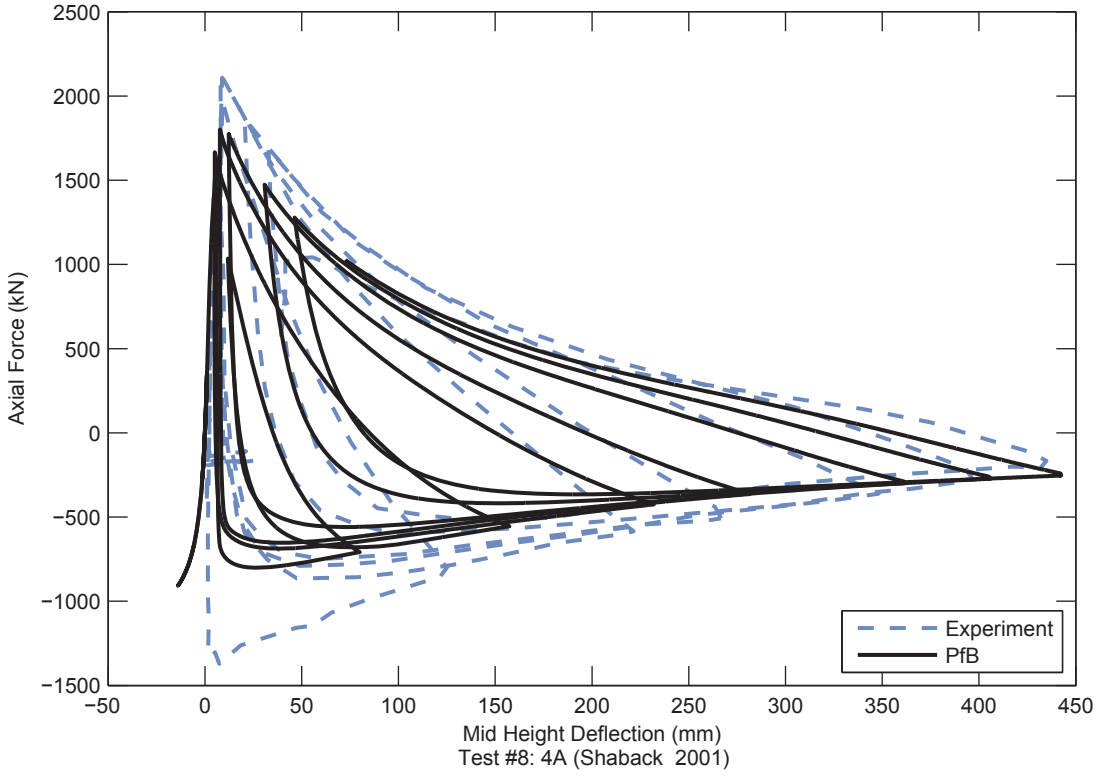

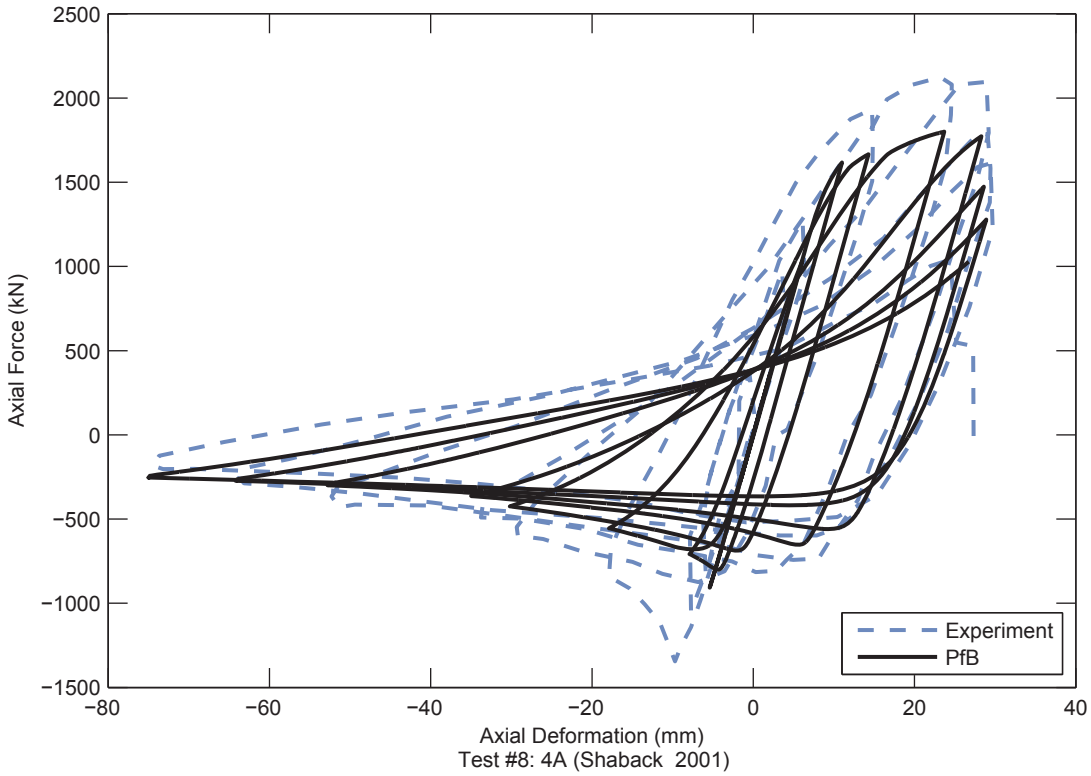

Figure 4.25. Rect. HSS Validation Results – Cyclic Brace (Continued)

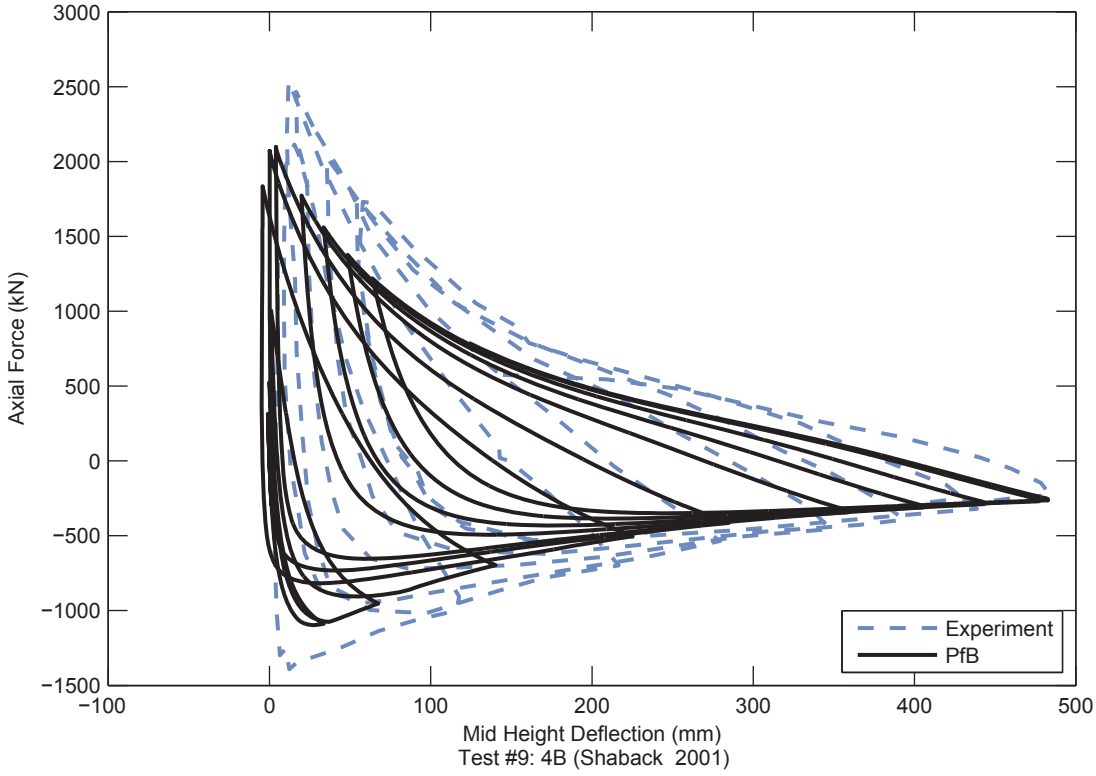

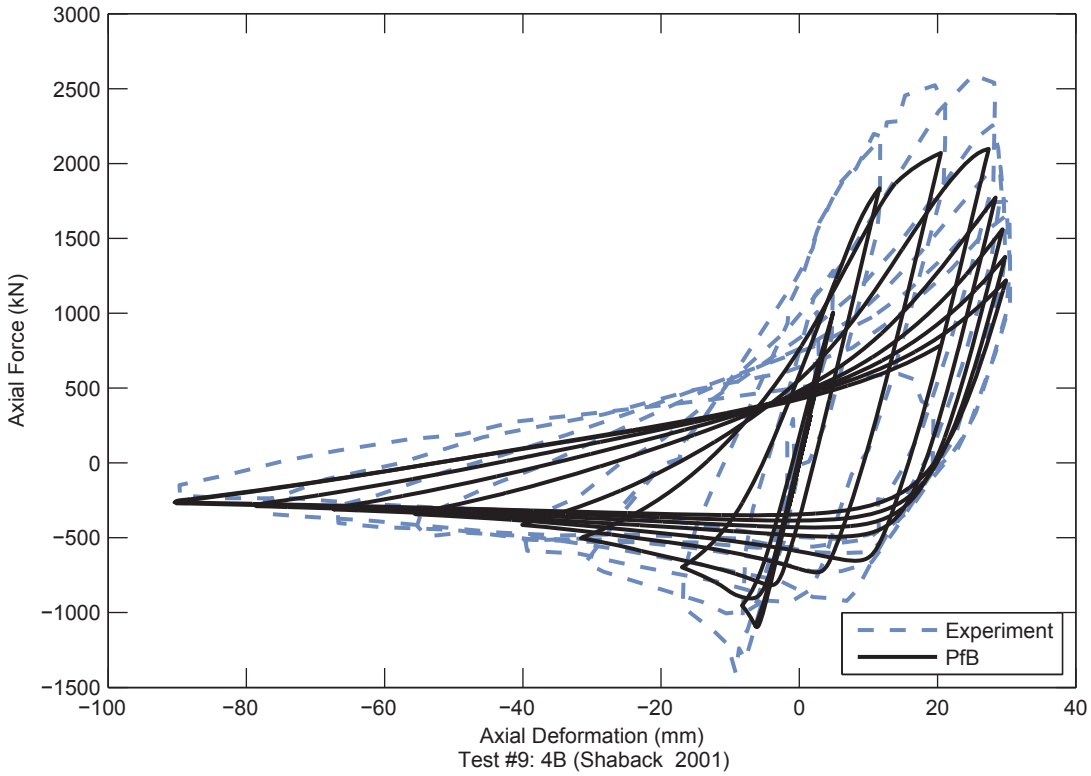

Figure 4.25. Rect. HSS Validation Results – Cyclic Brace (Continued)

Chapter 5

NATURAL BOND BEHAVIOR OF CFT COLUMNS

5.1 Introduction

Composite braced or unbraced frame structures that use concrete-filled steel tube (CFT) columns provide superior performance when subjected to non-seismic and seismic lateral loading. This has led to a continued increase in the use of these members in the primary lateral-resistance systems of structures. Steel tubes serve as the formwork for concrete placement, potentially expediting construction and reducing cost (Bridge and Webb 1993). In addition, the composite action of the steel tube and concrete core can effectively delay the buckling of steel tubes and significantly increase the ductility of the concrete core. To ensure these beneficial effects, it is important to have a comprehensive understanding of the composite action between the constituent materials, particularly in critical connection regions where load is transferred to the CFT column from girders or braces. If the steel tube cannot effectively transfer the axial forces to the concrete, the resulting localized stresses may lead to premature yielding or local buckling of the steel tube. Therefore, the bond transfer mechanisms need to be accurately assessed and incorporated into the design. Transfer of stress through natural bond, without the use of steel stud anchors or bearing mechanism, is often the most economical connection detail; however, efforts to characterize the bond strength are hindered by varying experimental results, even among like specimens (Roeder et al. 1999).

The design provisions for load transfer in CFTs through direct bond in the AISC *Specification for Structural Steel Buildings* (AISC 2010) are based predominantly on the results of push-out and push-off tests. Using only this data, there is little quantitative evidence to support the effective transfer area since these experimental configurations do not share the same loading and boundary conditions as typical composite columns. Thus, further investigation into bond behavior is important to ascertain a more accurate prediction on the bond strength of CFTs in the design provisions. In this work, a new formula for nominal bond strength is proposed. Nominal bond strength, longitudinal bond transfer length, circumferential bond transfer width, and resistance and safety factors are examined separately.

5.2 Existing Design Provisions

The nominal bond strength of rectangular (RCFT) and circular concrete filled-steel tubes (CCFT) prescribed in the AISC *Specification* (AISC 2010) is given as:

(a) For RCFT:

$$R_n = B^2 C_{in} F_{in} \tag{5.1}$$

(b) For CCFT:

$$R_n = 0.25\pi D^2 C_{in} F_{in} \tag{5.2}$$

where,

C_{in} = 2 if the CFT extends to one side of the point of force transfer
= 4 if the CFT extends to both sides of the point of force transfer
R_n = nominal bond strength, kips
F_{in} = nominal bond stress = 60 psi
B = overall width of rectangular steel section along face transferring load, in.
D = outside diameter of the round steel section, in.

This formula can be seen as the product of three values: the nominal bond stress, Fin; the circumferential bond transfer width, B for RCFT and $0.25\pi D$ for CCFT; and the longitudinal bond transfer length, BC_{in} for RCFT and DC_{in} for CCFT. The nominal bond stress, F_{in}, is taken as 60 psi (0.4 MPa). This value is seen as a reasonable lower bound of bond stresses observed in experimental results, mostly consisting of push-out tests (AISC 2010). The bond length is dependent on the value of C_{in}, which is equal to 2 if CFT extends to only one side of the point of force transfer (e.g., the top or bottom story) and 4 if the CFT extends both sides. The bond width is computed assuming only the face to which load is applied for RCFT or one-quarter of the perimeter for CCFT is active in transferring stress. The resistance factor, ϕ, is given as 0.45 and safety factor, Ω, is given as 3.33 based on an examination of push-off test results from Morishita et al. (1979a; b).

The European model building code (CEN 2004) also provides provisions relating to transfer strength by direct bond. A differentiation is made in the bond stress based on the shape of the steel tube; 60 psi (0.40 MPa) for RCFT and 80 psi (0.55 MPa) for CCFT. The bond transfer length is limited to the lesser of twice the minimum transverse dimension of the column or one-third the column length. No mention is given to the bond transfer width, so it may be assumed that the full perimeter is engaged in the load transfer. It is noted that for a RCFT column with two girders framing in, the nominal bond strength, as calculated by the AISC *Specification* and Eurocode, is the same.

Tomii (1985) highlights a design procedure from the Japanese code in which a lower bond strength and larger bond transfer area are used. For long-term loading, the bond strength is 14 psi (0.10 MPa) for RCFT and 21 psi (0.15 MPa) for CCFT. The bond length is taken as the distance from the mid-height of the upper column to the mid-height of the lower column and the bond width is taken as the full perimeter of the steel-concrete interface.

Other procedures have been proposed to characterize bond strength for design. Roeder et al. (1999) examined results from push-out tests on CCFTs and found a correlation between bond strength and the cross sectional dimensions of the tube. A linear equation was proposed to describe the bond stress as a function of the D/t ratio. The linear equation implied that no reliable bond stress could be obtained for CCFTs with a D/t ratio of greater than 80. Two checks are proposed using this bond stress. First, at the ultimate load level the bond stress is applied around the entire perimeter and along a length equal to the lesser of length of the column or 3.5 times the diameter of the steel tube. Second, noting evidence of cyclic deterioration of bond strength, at the serviceability level the bond strength is computed using a triangular stress distribution over a length of one-half the tube diameter.

Variation in the bond stress based on tube dimensions was also observed for RCFTs by Parsley et al. (2000). A formula for bond strength was proposed as a linear function of the slenderness parameter t/H^2.

5.3 Experimental Studies

Experimental studies on bond behavior of CFT members have most frequently been conducted through the use of push-out tests (Virdi and Dowling 1980; Shakir-Khalil 1993a; b; Roeder et al. 1999; Parsley et al. 2000; Xu et al. 2009; Aly et al. 2010; Yin and Lu 2010), push-off tests (Morishita et al. 1979a; b; Tomii et al. 1980a; b), or connection tests (Dunberry et al. 1987; Shakir-Khalil 1993c; d, 1994a; b; Shakir-Khalil and Al-Rawdan 1995). Each of these types of tests has advantages and disadvantages in the assessment of the natural bond strength of CFTs. The boundary conditions of push-out tests (Figure 5.1b and Figure 5.1c) induce constant bond stress at the ultimate limit state and thus provide little information as to the distribution of bond stress over the length along the column. However, in push-off and connections tests, where the bond stress is not constant, it is difficult to accurately estimate the magnitude of stress. In typical push-out and push-off tests, the specimen bears directly on a rigid support at the base (Figure 5.1b), excluding the beneficial effects that a shear connection provides. Push-out tests where force is applied to the concrete core and resisted by shear tabs attached to the steel tube (Figure 5.1c) and connection tests (Figure 5.2) include these beneficial effects and thus provide the closest analogs to typical shear connections (or other connection types that feature eccentric introduction of force into the CFT) used in practice (Figure 5.1d).

5.3.1 CFT Push-Out Tests without Shear Tabs

Critical bond stresses from push-out test results are computed by dividing the peak load attained during the test by the entire area of the steel-concrete interface. The resistance observed in these tests has been generally attributed to three primary mechanisms: adhesion, friction, and wedging (Parsley et al. 2000; Johansson 2003). Adhesion, provided by the chemical bond between the concrete and steel, is a brittle mechanism and only active at most during the early stages of load. It may not be active at all depending on the relative amplitudes of radial enlargement of the steel tube caused by the wet concrete, shrinkage of the concrete, and the roughness of the steel tube (Roeder et al. 1999). Friction is the product of the roughness of the steel-concrete interface and the contact pressure existing at the interface. Wedging occurs as the motion of the concrete core is resisted by geometric irregularities in the steel tube.

Bond stresses obtained from push-out tests are highly variable and found to range over two orders of magnitude. However, some noticeable trends have been identified (Roeder et al. 1999; Parsley et al. 2000). The bond stress for CCFTs is larger than for RCFTs. Tube dimensions have an effect on the results, with lower bond stress obtained for larger and more slender tubes. The surface preparation of the interior of the steel tube and the shrinkage/expansive potential of the concrete have also been shown to have an influence on the bond stress. Concrete and steel material strengths, however, appear to have no consistent effect on the bond stress. Eccentric loading of the column has also been shown to have a beneficial effect on the bond stress. This increase is so significant that it has been suggested that bond need not be checked in the presence of significant bending moments in the column (Roeder et al. 2009). This paper does not specifically address the effect of eccentrically loaded columns, rather concentrating on the worst-case concentric loading.

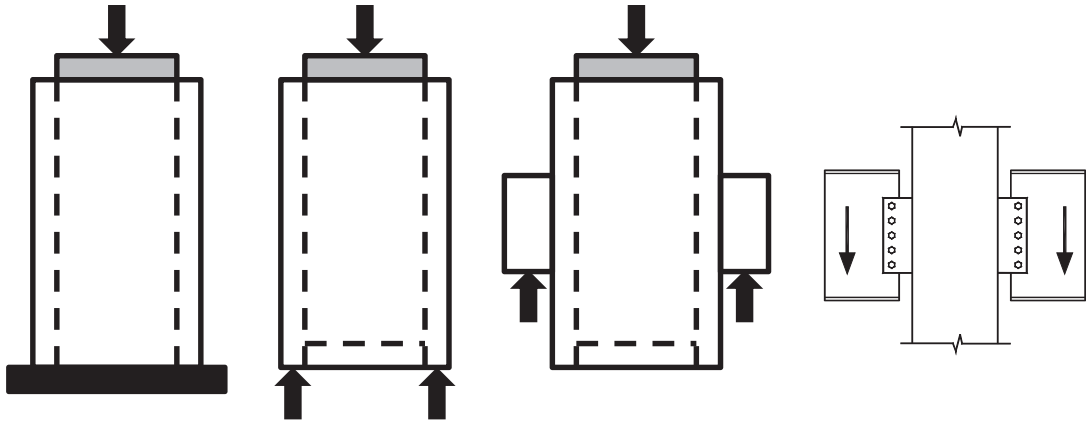

(a) Push-off test | (b) Push-out test without shear tabs | (c) Push-out test with shear tabs | (d) Typical CFT connection

Figure 5.1. Typical CFT Test Configurations to Assess Bond Behavior

Details of push-out tests without shear tabs reported in the literature are presented in Table 5.1 for RCFTs and

Table 5.2 for CCFTs. Where reported, measured material and geometric properties are listed, otherwise nominal properties are listed. All specimens from each reference were included with the exception of those with shear tabs, those with mechanical shear connecters, those where the steel-concrete interface was manipulated by machining or applying a lubricant, those where the load was applied eccentrically, or those with expansive concrete. Specimens that were loaded cyclically were included in the table since they represent loading conditions that typical connections may experience and they did not significantly skew the results of the analysis. Specimens that were loaded cyclically were: X1c and X1d (Shakir-Khalil 1993a); II-4 (Roeder et al. 1999); and A2, B2, C2, D2, E2, F2, and G2 (Aly et al. 2010).

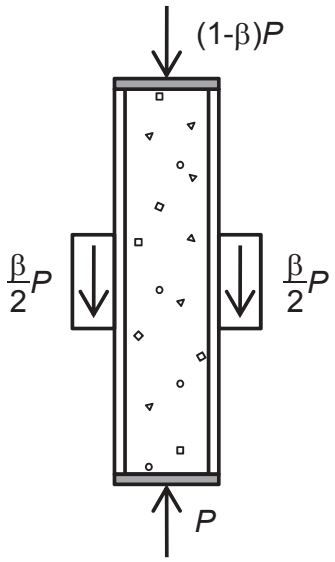

Figure 5.2. CFT Connection Test Schematic

Table 5.1. RCFT Push-Out Tests without Shear Tabs

Reference	Specimen	L (in)	H (in)	B (in)	t (in)	H/t	F_y (ksi)	f'_c (ksi)	$P_{applied}$ (kips)	F_{in} (psi)
Shakir-Khalil 1993a	X1a	15.5	4.72	3.15	0.197	24.0	Mild Steel	5.6	42.4	192.8
	X1b	15.6	4.72	3.15	0.197	24.0	Grade 43	5.6	31.0	140.4
	X1c	15.6	4.72	3.15	0.197	24.0	-	5.6	23.1	104.9
	X1d	15.6	4.72	3.15	0.197	24.0	-	5.6	25.7	115.8
	Y1a	8.0	5.91	5.91	0.197	30.0	-	5.9	15.2	86.1
	Y1b	8.0	5.91	5.91	0.197	30.0	-	5.9	15.0	84.6
	Y2a	15.7	5.91	5.91	0.197	30.0	-	5.9	17.2	49.9
	Y2b	15.6	5.91	5.91	0.197	30.0	-	5.9	16.7	48.4
	Y3a	23.6	5.91	5.91	0.197	30.0	-	5.9	27.7	53.1
	Y3b	23.6	5.91	5.91	0.197	30.0	-	5.9	32.9	63.2
Shakir-Khalil 1993b	A1a	15.7	5.91	5.91	0.197	30.0	Mild Steel	5.2	10.2	29.3
	A1b	15.7	5.91	5.91	0.197	30.0	Grade 43	5.2	10.3	29.8
	G1	15.7	5.91	5.91	0.197	30.0	-	5.7	21.1	60.9
Parsley et al. 2000	CFT4	48.0	8.00	8.00	0.229	34.9	48	6.6	61.0	42.1
	CFT3	48.0	8.00	8.00	0.228	35.1	48	6.6	56.0	38.7
	CFT7	60.0	10.00	10.00	0.234	42.7	48	5.9	61.0	26.7
	CFT1	60.0	10.00	10.00	0.234	42.7	48	5.9	57.0	24.9

Table 5.2. CCFT Push-Out Tests without Shear Tabs

Reference	Specimen	L (in)	D (in)	t (in)	D/t	F_y (ksi)	f'_c (ksi)	$P_{applied}$ (kips)	F_{in} (psi)
Virdi and Dowling 1980	MA 1	13.5	6.09	0.250	24.3	Mild Steel	3.7	Not Given	312.7
	MA 4	13.5	6.11	0.250	24.5	-	5.2	-	323.3
	MA 6	13.5	6.09	0.250	24.4	-	3.7	-	387.7
	MA 9	13.5	6.10	0.250	24.4	-	4.4	-	378.9
	MA 2	13.5	6.11	0.250	24.5	-	5.2	-	301.2
	MA 7	13.5	6.09	0.250	24.4	-	5.2	-	398.4
	MA 8	13.5	6.09	0.250	24.4	-	5.2	-	340.8
	MA 10	13.5	6.10	0.250	24.4	-	5.4	-	399.0
	MA 3	13.5	6.11	0.250	24.4	-	5.8	-	430.9
	MA 5	13.5	6.09	0.250	24.3	-	5.8	-	324.8
	CS14	13.5	6.13	0.250	24.5	-	3.2	-	281.7
	CS21	13.5	6.10	0.250	24.4	-	3.2	-	272.5
	CS28	13.5	6.12	0.250	24.5	-	3.2	-	188.9
	CS19	13.5	6.11	0.250	24.4	-	4.0	-	324.2
	CS22	13.5	6.12	0.250	24.5	-	4.0	-	200.6
	CS25	13.5	6.15	0.250	24.6	-	4.0	-	306.4
	CS13	13.5	6.15	0.250	24.6	-	4.1	-	208.1
	CS24	13.5	6.14	0.250	24.5	-	4.1	-	226.2
	CS27	13.5	6.16	0.250	24.6	-	4.1	-	268.8
	CS12	13.5	6.16	0.250	24.7	-	4.4	-	256.4
	CS18	13.5	6.11	0.250	24.4	-	4.4	-	274.1
	CS26	13.5	6.15	0.250	24.6	-	4.4	-	232.1
	CS11	13.5	6.15	0.250	24.6	-	5.3	-	276.5
	CS16	13.5	6.13	0.250	24.5	-	5.3	-	271.6
	CS20	13.5	6.15	0.250	24.6	-	5.3	-	305.8
	CS15	13.5	6.12	0.250	24.5	-	6.1	-	339.6
	CS17	13.5	6.16	0.250	24.6	-	6.1	-	219.5
	CS23	13.5	6.16	0.250	24.6	-	6.1	-	223.1
	LN41	5.9	5.92	0.375	15.8	-	5.8	-	285.1
	LN42	5.9	5.89	0.375	15.7	-	5.8	-	318.0
	LN43	5.9	5.88	0.375	15.7	-	5.8	-	311.4
	LN29	8.8	5.85	0.375	15.6	-	5.8	-	237.0
	LN30	8.8	5.85	0.375	15.6	-	5.8	-	281.2
	LN31	8.8	5.86	0.375	15.6	-	5.8	-	294.6
	LN32	11.8	5.85	0.375	15.6	-	5.8	-	304.5
	LN33	11.8	5.90	0.375	15.7	-	5.8	-	327.2
	LN34	11.8	5.94	0.375	15.8	-	5.8	-	343.6
	LN35	14.7	5.87	0.375	15.6	-	5.8	-	356.6
	LN36	14.7	5.93	0.375	15.8	-	5.8	-	370.9
	LN37	14.7	5.93	0.375	15.8	-	5.8	-	344.4
	LN38	17.6	5.87	0.375	15.7	-	5.8	-	421.3

Table 5.2. CCFT Push-Out Tests without Shear Tabs (Continued)

Reference	Specimen	L (in)	D (in)	t (in)	D/t	F_y (ksi)	f'_c (ksi)	$P_{applied}$ (kips)	F_{in} (psi)
Virdi and Dowling 1980	LN39	17.6	5.89	0.375	15.7	Mild Steel	5.8	Not Given	408.3
	LN40	17.6	5.90	0.375	15.7	-	5.8	-	395.3
	SZ50	18.3	5.87	0.381	15.4	-	6.7	-	350.3
	SZ51	18.3	5.91	0.383	15.4	-	6.7	-	259.6
	SZ52	18.3	5.88	0.379	15.5	-	6.7	-	344.6
	SZ53	18.3	6.16	0.257	24.0	-	6.7	-	159.2
	SZ54	18.3	6.15	0.258	23.8	-	6.7	-	187.8
	SZ55	18.3	6.17	0.261	23.7	-	6.7	-	146.8
	SZ56	18.3	6.26	0.226	27.7	-	6.7	-	213.1
	SZ57	18.3	6.21	0.224	27.7	-	6.7	-	181.1
	SZ58	18.3	6.25	0.221	28.3	-	6.7	-	209.7
	SZ59	18.3	8.15	0.256	31.8	-	6.7	-	275.6
	SZ60	18.3	8.18	0.261	31.3	-	6.7	-	282.0
	SZ61	18.3	8.14	0.268	30.4	-	6.7	-	255.5
	SZ62	18.3	9.12	0.289	31.5	-	6.7	-	90.9
	SZ63	18.3	9.11	0.289	31.5	-	6.7	-	75.4
	SZ64	18.3	9.13	0.283	32.3	-	6.7	-	84.2
	SZ65	18.3	12.04	0.376	32.0	-	6.7	-	291.8
	SZ66	18.3	12.02	0.377	31.9	-	6.7	-	288.7
	SZ67	18.3	12.05	0.375	32.1	-	6.7	-	290.4
	CC70	13.5	5.90	0.383	15.4	-	4.5	-	381.7
	CC71	13.5	5.86	0.391	15.0	-	4.5	-	370.5
	CC72	13.5	5.86	0.389	15.1	-	4.5	-	359.9
	CC73	13.5	5.88	0.385	15.3	-	5.4	-	293.4
	CC74	13.5	5.86	0.382	15.3	-	5.4	-	306.6
	CC75	13.5	5.90	0.382	15.4	-	5.4	-	310.8
	CC76	13.5	5.92	0.386	15.3	-	5.1	-	308.3
	CC77	13.5	5.86	0.386	15.2	-	5.1	-	329.9
	CC78	13.5	5.88	0.384	15.3	-	5.1	-	310.1
	CC79	13.5	5.92	0.381	15.5	-	5.1	-	268.0
	CC80	13.5	5.91	0.381	15.5	-	5.1	-	320.9
	CC81	13.5	5.89	0.378	15.6	-	5.1	-	216.7
	CC82	13.5	5.86	0.381	15.4	-	5.1	-	260.8
	CC83	13.5	5.84	0.382	15.3	-	5.1	-	223.6
	CC84	13.5	5.86	0.382	15.3	-	5.1	-	217.6
	CC85	13.5	5.86	0.382	15.4	-	5.1	-	168.5
	CC86	13.5	5.90	0.381	15.5	-	5.1	-	213.8
	CC87	13.5	5.89	0.397	14.8	-	5.1	-	241.2
	RD91	13.5	6.12	0.267	22.9	-	6.7	-	285.6
	RD92	13.5	6.08	0.285	21.3	-	6.7	-	312.8
	RD93	13.5	6.10	0.274	22.3	-	6.7	-	362.2

Table 5.2. CCFT Push-Out Tests without Shear Tabs (Continued)

Reference	Specimen	L (in)	D (in)	t (in)	D/t	F_y (ksi)	f'_c (ksi)	$P_{applied}$ (kips)	F_{in} (psi)
Shakir-Khalil 1993a	Y4a	8.0	6.63	0.197	33.7	Mild Steel	6.1	19.9	128.1
	Y4b	8.0	6.63	0.197	33.7	Grade 43	6.1	21.1	134.9
	Y5a	15.7	6.63	0.197	33.7	-	6.1	35.2	114.3
	Y5b	15.7	6.63	0.197	33.7	-	6.1	35.8	116.2
	Y6a	23.6	6.63	0.197	33.7	-	6.1	48.4	104.6
	Y6b	23.6	6.63	0.197	33.7	-	6.1	43.7	94.6
Shakir-Khalil 1993b	B1a	15.7	6.63	0.197	33.7	Mild Steel	5.6	19.5	63.2
	B1b	15.9	6.63	0.197	33.7	Grade 43	5.6	21.5	69.1
	H1	15.9	6.63	0.197	33.7	-	5.7	42.0	135.3
Roeder et al. 1999	I-1	29.8	10.81	0.530	20.4	Not Given	4.2	1.4	1.5
	I-3	41.9	14.00	0.280	50.0	-	4.0	8.1	4.6
	I-4	41.9	14.00	0.280	50.0	-	4.0	9.6	5.4
	I-5	69.9	14.00	0.280	50.0	-	5.4	55.7	18.9
	I-6	69.9	14.00	0.280	50.0	-	4.1	18.6	6.3
	I-7	75.9	24.00	0.220	109.0	-	4.2	43.2	7.7
	II-1	31.9	10.81	0.530	20.4	-	6.8	109.3	112.0
	II-2	31.9	10.81	0.530	20.4	-	6.8	111.2	113.9
	II-3	31.9	10.81	0.530	20.4	-	6.8	109.8	112.4
	II-4	58.9	10.81	0.530	20.4	-	6.4	83.5	46.3
	II-5	41.9	14.00	0.280	50.0	-	6.9	70.9	40.1
	II-6	41.9	14.00	0.280	50.0	-	6.9	90.8	51.4
	II-7	69.9	14.00	0.280	50.0	-	6.4	74.6	25.3
	II-8	69.9	14.00	0.280	50.0	-	6.4	79.9	27.1
	II-9	75.9	24.00	0.220	109.0	-	6.5	117.6	21.0
	II-10	75.9	24.00	0.220	109.0	-	6.8	143.0	25.5
	II-11	75.9	24.00	0.220	109.0	-	6.7	74.7	13.3
	II-12	75.9	24.00	0.220	109.0	-	6.7	74.8	13.3
Xu et al. 2009	SI-o	19.7	6.12	0.108	56.5	Not Given	6.8	31.8	87.0
	SII-o	19.7	6.18	0.138	44.9	-	6.8	34.4	94.3
	SIII-o	19.7	6.26	0.177	35.3	-	6.8	35.5	97.2
Aly et al. 2010	A1	15.7	4.50	0.126	35.7	50.8	10.3	30.6	145.5
	B1	15.7	4.50	0.126	35.7	50.8	5.9	36.0	171.1
	C1	15.7	4.50	0.126	35.7	50.8	10.0	27.9	132.6
	D1	15.7	4.50	0.126	35.7	50.8	9.3	36.0	171.1
	E1	15.7	4.50	0.126	35.7	50.8	5.9	38.0	180.8
	F1	15.7	4.50	0.126	35.7	50.8	11.7	18.7	88.8
	G1	15.7	4.50	0.126	35.7	50.8	10.2	31.2	148.7
	A2	15.7	4.50	0.126	35.7	50.8	10.7	Not Given	117.5
	B2	15.7	4.50	0.126	35.7	50.8	7.0	-	120.4
	C2	15.7	4.50	0.126	35.7	50.8	10.0	-	92.8
	D2	15.7	4.50	0.126	35.7	50.8	10.2	-	134.9
	E2	15.7	4.50	0.126	35.7	50.8	5.9	-	137.8
	F2	15.7	4.50	0.126	35.7	50.8	13.2	-	50.8
	G2	15.7	4.50	0.126	35.7	50.8	10.2	-	101.5

5.3.2 CFT Push-Out Tests with Shear Tabs

Assessing bond stress based on the results of typical push-out and push-off tests neglects beneficial effects that occur in typical beam-to-column connections due to the rotation of the shear tabs (or similar eccentricities that may occur for introduction of force between a girder and the steel tube in the connection topology) (Johansson 2003). The rotation of the shear tab during loading results in pinching of the concrete core where the shear tab rotates inward and constriction of the steel tube where the shear tab rotates outward (Figure 5.3). Both cases result in increased contact pressure between the steel and concrete and thus greater frictional resistance to slip.

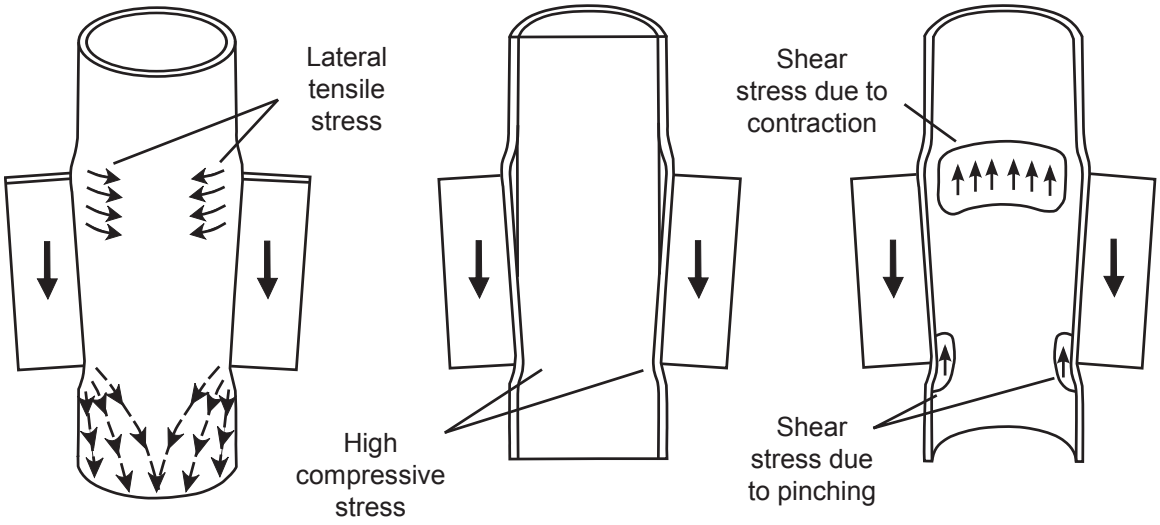

Figure 5.3. Increased Contact Force with Shear Tab Rotation [adapted from Johansson, (2003)]

Table 5.3. RCFT Push-Out Tests with Shear Tabs

Reference	Specimen	L (in)	H (in)	B (in)	t (in)	H/t	F_y (ksi)	f'_c (ksi)	$P_{applied}$ (kips)	F_{in} (psi)
Shakir-Khalil 1993b	C1a	15.6	5.91	5.91	0.197	30.0	Mild Steel	5.8	38.1	110.5
	C1b	15.6	5.91	5.91	0.197	30.0	Grade 43	5.8	51.5	149.5
	C2a	15.7	5.91	5.91	0.197	30.0	-	5.8	51.5	148.4
	C2b	15.7	5.91	5.91	0.197	30.0	-	5.8	53.1	153.3
	E1a	15.7	7.87	7.87	0.248	31.7	-	6.2	37.5	81.0
	E1b	15.7	7.87	7.87	0.248	31.7	-	6.2	18.0	38.7
	G2	15.8	5.91	5.91	0.197	30.0	-	5.7	44.7	128.2
	G3	15.9	5.91	5.91	0.197	30.0	-	5.7	47.0	133.7
	G4	15.8	5.91	5.91	0.197	30.0	-	5.7	23.4	67.0
Parsley et al. 2000	CFT2	48.0	8.00	8.00	0.228	35.1	48	6.6	98.0	67.7
	CFT5	48.0	8.00	8.00	0.228	35.1	48	6.6	101.0	69.7
	CFT8	58.5	10.00	10.00	0.232	43.1	48	5.9	67.0	30.0
	CFT6	58.5	10.00	10.00	0.234	42.7	48	5.9	70.0	31.4

Push-out tests where load was applied to the steel tube through shear tabs have been reported in the literature (Shakir-Khalil 1993b; Parsley et al. 2000). Details of these experiments

are presented in Table 5.3 for RCFTs and Table 5.4 for CCFTs. Where reported, measured material and geometric properties are listed, otherwise nominal properties are listed.

Table 5.4. CCFT Push-Out Tests with Shear Tabs

Reference	Specimen	L (in)	D (in)	t (in)	D/t	F_y (ksi)	f'_c (ksi)	$P_{applied}$ (kips)	F_{in} (psi)
Shakir-Khalil 1993b	D1a	15.7	6.63	0.197	33.7	Mild Steel	5.8	186.6	605.2
	D1b	15.7	6.63	0.197	33.7	Grade 43	5.8	182.1	593.5
	F1a	15.8	6.63	0.197	33.7	-	5.4	212.9	688.7
	F1b	15.6	6.63	0.197	33.7	-	5.9	218.3	715.1
	H2	15.8	6.63	0.197	33.7	-	5.7	172.0	556.4
	H3	15.9	6.63	0.197	33.7	-	5.7	167.0	537.7
	H4	15.7	6.63	0.197	33.7	-	5.7	60.5	196.1

The failure mode of the all of the RCFT specimens was slip. A typical load-slip relationship shows a high initial stiffness up to the peak load. Many specimens showed a sharp decrease in strength following the peak load, while others maintained a load near the peak load. Two specimens (G2 and G3) displayed a steadily increasing load following a reduction in stiffness near the peak load of other similar specimens. In all cases, $P_{applied}$ was taken as the peak load attained during the test. The average bond stress, F_{in}, for the full set of RCFT tests is 93 psi. The average bond stress for specimens where the shear tabs were located near mid-height of the column is 118 psi while it is 53 psi for specimens with shear tabs near the column ends.

Only some of the CCFT specimens failed due to slip. Specimens D1a, D1b, F1a, and F1b (Shakir-Khalil 1993b), achieved higher than expected strengths and the shear tabs failed prior to slip. In an analysis of one of these specimens, Johansson (2003) identified the rotation of the shear tabs and the increased contact forces to be the cause of the unexpectedly high bond strength. The failure mode of specimens H2 and H3 was slip, however, no peak load was observed, as the load was seen to steadily increase. One specimen, H4, failed through slip and displayed a peak load. Again, in all cases, $P_{applied}$ was taken as the peak load attained during the test. The bond stress for CCFTs is much larger than for RCFTs, with an average applied bond stress, F_{in}, of 556 psi. However, this value is unreasonably high for design purposes, since it was achieved only for a few similarly proportioned tests and may not be indicative of expected behavior for the variety of configurations expected in practice.

5.3.3 Nominal Bond Stress

Push-out tests, whether with or without shear tabs, provide a direct means of assessing the bond stress. Trends in the push-out test results that have been identified include the dependence of the bond stress on factors not typically known at the time of design (e.g., the condition of the steel-concrete surface and the shrinkage/expansive potential of the concrete). For a bond stress formula intended for design, these factors should thus be included in an average sense rather than explicitly. Among the strongest trends identified is the dependence of the bond stress on tube dimensions. Roeder et al. (1999) proposed a formula for bond stress of CCFTs based on the D/t ratio. Parsley et al. (2000) proposed a formula for bond stress of RCFTs based on t/H^2. The ratio t/H^2 was selected based on a mechanistic analysis; it is proportional to the radial stiffness of cylindrical thin-walled pressure vessels.

It is noted that there is insufficient experimental evidence to determine which of the two transverse dimensions of an RCFT cross sections, i.e., the width or the height, should be used for determining bond stress since most of the RCFT push-out tests (Table 5.1 and Table 5.3) had square sections. The height, defined here as the longer transverse dimension, was selected as the conservative choice, but further investigation is appropriate for sections with a high aspect ratio (H/B).

The results of push-out tests are plotted in Figure 5.4 against both of these parameters. All push-out tests from Table 5.1 through Table 5.4 were included. The bond stress is typically higher for push-out tests with shear tabs, showing the beneficial effects rotation of the shear tab has on bond stress. As seen in Figure 5.4, there is significant variation in the bond stress, indicating that the constant values used in current design methodologies are insufficient, especially for thin tubes and large cross sections where the bond stress may be overestimated.

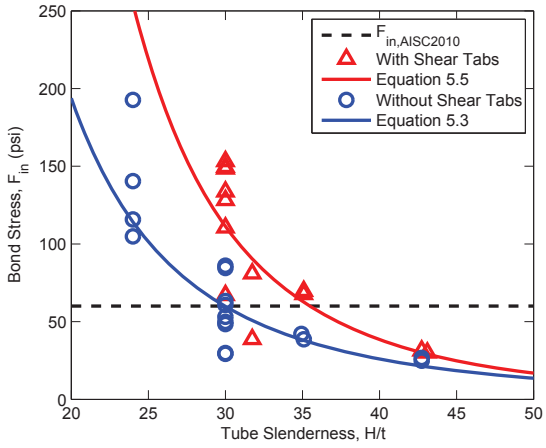

(a) Bond stress of RCFT as a function of H/t

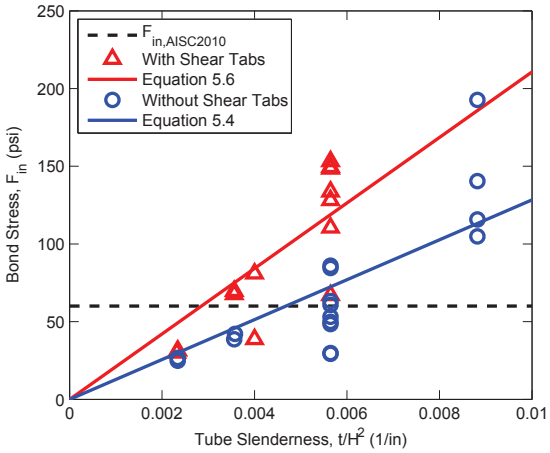

(b) Bond stress of RCFT as a function of t/H^2

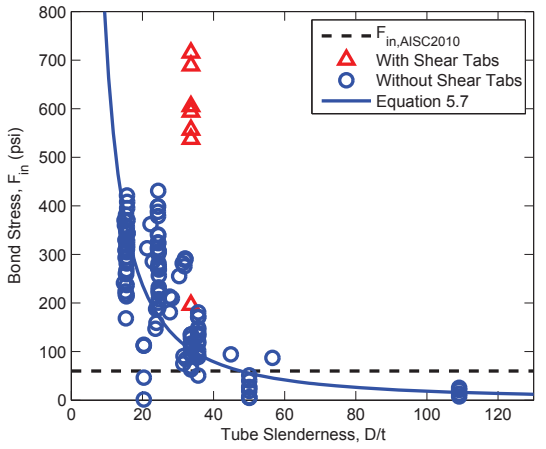

(c) Bond stress of CCFT as a function of D/t

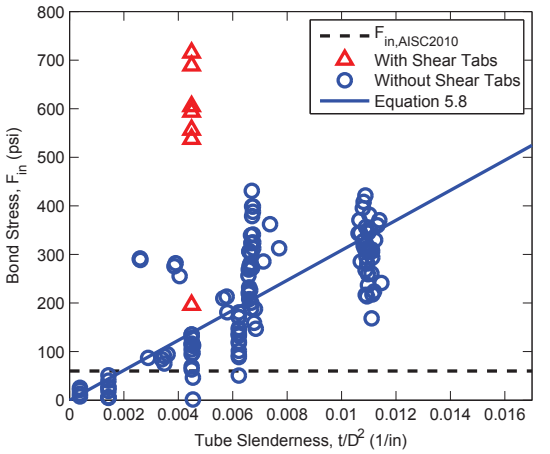

(d) Bond stress of CCFT as a function of t/D^2

Figure 5.4. Bond Stress for CFT as a Function of Tube Slenderness

To obtain a design formula, a least squares curve fit can be made to this data. The forms of the equations chosen were selected to provide a good fit to the available data, have reasonable bounds, and produce non-negative bond stress values. The results of the regression analysis are as follows:

RCFT push-out tests without shear tabs:

$$F_{in} = 1.15 \times 10^{6} \left(H / t \right)^{-2.90} \quad R^2 = 0.69 \tag{5.3}$$

$$F_{in} = 12800 \left(t / H^2 \right) \quad R^2 = 0.62 \tag{5.4}$$

RCFT push-out tests with shear tabs:

$$F_{in} = 3.23 \times 10^{7} \left(H / t \right)^{-3.70} \quad R^2 = 0.61 \tag{5.5}$$

$$F_{in} = 21100 \left(t / H^2 \right) \quad R^2 = 0.66 \tag{5.6}$$

CCFT push-out tests without shear tabs:

$$F_{in} = 27900 \left(D / t \right)^{-1.59} \quad R^2 = 0.32 \tag{5.7}$$

$$F_{in} = 30900 \left(t / D^2 \right) \quad R^2 = 0.50 \tag{5.8}$$

where,

F_{in} is in psi and t, H, and D are in inches.

A curve fit was not performed for CCFT push-out tests with shear tabs since all the available tests had nearly the same size tube. The two different functions for each case represent the two different parameters (e.g., H/t and t/H^2) chosen to represent the tube dimensions. In addition to accuracy, quantified by the R^2 value associated with each formula, the formulas can be judged by their usability. Based on these criteria, the formulas based on t/D^2 and t/H^2 are recommended for design. Furthermore, the formulas computed with the data from the push-out tests without shear tabs are recommended for design since they provide a lower bound for the behavior expected in typical shear connections and allow for the greatest consistency between tube shapes. Thus Equation 5.4 is recommended for the nominal bond stress of RCFTs and Equation 5.8 is recommended for CCFTs. Both of these formulas have no upper bound on the bond stress, though one could be implemented based on the results of the stockiest tubes for each shape (i.e., 100-200 psi for RCFTs and 200-400 psi for CCFTs).

5.3.4 CFT Connection Tests

Push-out tests have explicit boundary conditions and paths for load transfer and thus are well-suited for an assessment of bond stress; however, they provide little evidence of the bond length or bond width of typical connections. Column connection tests which are instrumented to

measure load transfer such as those conducted by Dunberry et al. (1987), Shakir-Khalil (1993c; d, 1994a; b), and Shakir-Khalil and Al-Rawdan (1995) provide a means to quantify the area over which a nominal bond stress acts in typical connections. A schematic of the test specimens and loading is presented in Figure 5.2. Shear tabs are welded to the outside of the steel tubes to transfer the eccentric shears through the interfaces. Load is applied at both column ends and at the shear connections, in a ratio described by β.

The experimental strength of all of these specimens was near the squash load, indicating that limit states other than cross sectional strength, including slip, either did not have a significant effect on the strength or did not occur. In the tests performed by Dunberry et al. (1987) local buckling was a typical failure mode. The local buckling occurred near the connection for some specimens, indicating that the loading conditions possibly had an influence on the strength, and away from the connection for other specimens. A strain incompatibility was observed in the connection region, which extended approximately three tube widths below the connection and one to two tube widths above the connection. The concrete load steadily rose in this region indicating a load was transferred along its length, although the rise was steepest in the bottom half of the connection, indicating that pinching due to rotation of the shear tabs played a significant role in transferring the load. The tests performed by Shakir-Khalil (1993c; d, 1994a; b) and Shakir-Khalil and Al-Rawdan (1995) displayed somewhat similar behavior. The typical failure mode was overall collapse of the column without indication of a detrimental effect on the strength from slip. The observed transfer length was shorter than that observed by Dunberry et al. (1987), as strains equalized within a tube width above and below the connection.

Additional details of the experiments are shown in Table 5.5 for RCFTs and in Table 5.6 for CCFTs. Where reported, measured material and geometric properties are listed, otherwise nominal properties are listed. The tabulated applied load, $P_{applied}$, is the total load applied to the steel tube in the connection region. This load is not necessarily indicative of the slip strength since many of the specimens failed away from the connection region or the strength was not reached due to test rig limitations. Nonetheless, these specimens were included in the table, as they provide a lower bound on the slip strength. The portion of the applied load that is transferred to the concrete core, $V'_{applied}$, is computed using Equation 5.9, which assumes secant stiffnesses based on the material strengths. Equation 5.9 is equivalent to provisions in the AISC *Specification* (AISC 2010) that specify how much load is transferred to the concrete since all of the specimens have compact members.

$$V'_{applied} = P_{applied}\left(1 - \frac{A_s F_y}{A_s F_y + C_2 A_c f'_c}\right) \tag{5.9}$$

where,

C_2 = 0.85 for RCFT and 0.95 for CCFT

The nominal bond strength based on current design provisions (AISC 2010) is tabulated for each of the specimens and is used and along with $V'_{applied}$ to compute the test-to-predicted ratio (Table 5.5 and Table 5.6). The current design provisions are seen to be very conservative for these specimens, with test-to-predicted ratios ranging from 1.2 to 5.1 for RCFTs and 1.8 to 4.2 for CCFTs, especially when noting that these ratios are a lower bound because few specimens exhibited a failure mode that included slip.

5.3.5 Effective Bond Transfer Length

The transfer length, the length along the column where significant bond stresses occur, varies with material and geometric properties of the CFT and increases with applied load. The length used in the bond strength formula must address two types of slip limit states. The first is slip along the entire length of the column, where, depending on the boundary conditions, a push-out type failure could occur. The second is slip occurring locally, near the point of load application. This type of slip failure is enabled by the formation of a plastic mechanism in either the steel tube or concrete core, allowing the relative motion. Other more localized failure modes that include slip (e.g., failure of one face of a CFT column where load is framing in) should be addressed in connection design and are not discussed here.

The CFT connection tests provide some insight into an appropriate bond length. The transfer length at peak load, $L_{transfer}$, is computed for the CFT connections tests (Table 5.5 and Table 5.6) using Equation 5.10, where p is the entire perimeter of the steel-concrete interface and F_{in} is the critical bond stress, as computed using Equation 5.6 for RCFTs and Equation 5.8 for CCFTs.

$$L_{transfer} = \frac{V'_{applied}}{p\,F_{in}} \tag{5.10}$$

Use of the formula for bond stress from push-out tests without shear tabs for RCFT (Equation 5.4) would result in transfer lengths approximately twice as large and could be justified since Equation 5.4 is recommended for design. However, the formula for bond stress from push-out tests with shear tabs is used for RCFTs, as it is a more accurate assessment for these specimens. The tabulated transfer lengths are of approximately the same magnitude as the lengths over which slip occurred, as reported by the researchers.

In Table 5.5 and Table 5.6, the transfer length is seen to have a strong correlation with the ratio of load applied at the connection to total load, β (Figure 5.2). This is due to the fact that the specimens failed at loads near the cross section strength, thus the specimens with larger β values had larger transferred loads at failure because a larger portion of the load was applied at the connection. The other specimens, with lower β values, presumably could have achieved the similar transferred loads at failure had a greater portion of the load been applied at the connection. Accordingly, the transfer length in Table 5.5 and Table 5.6 should be considered a lower bound. The ratio of transfer length to tube width for specimens with a large proportion of the load applied at the connection ranges from 2.3 to 4.1 ($\beta \geq 0.4$; Table 5.5: Specimens A1, A2, A3, B2, C1, D1, D2, D3, and D4 by Dunberry et al. (1987); Table 5.6: Specimen A5 by Shakir-Khalil (1993c)). Based on this data, the current provisions for bond length for the case of load applied to the steel tube and the CFT extending to both sides of the point of force transfer (i.e., $C_{in} = 4$) (AISC 2010), appear to be appropriate and safe for design.

While the CFT connection tests provide valuable information, they are limited by a lack of variety in geometric and material properties and loading configurations and because most specimens did not exhibit a slip related failure. A mechanistic analysis allows exploration of the effective bond transfer length for the range of properties and configurations seen in practice. A suitable bond length would account for both slip limit states: slip along the entire length and localized slip accompanied with overstressing and formation of a plastic mechanism in the steel tube or concrete core.

Table 5.5. RCFT Connection Tests

Reference	Specimen	L (in)	$H=B$ (in)	t (in)	H/t	F_y (ksi)	f'_c (ksi)	β	$P_{applied}$ (kip)	$V'_{applied}$ (kip)	Number of Girders	$R_{n,AISC2010}$ (kip)	*test-to-predicted*	F_{in} (Eq 5.6) (psi)	$L_{transfer}$ (in)	$L_{transfer}/H$
Dunberry et al. 1987	A1	118.1	4.01	0.193	20.8	53.7	3.6	1.00	186.6	38.2	2	7.73	4.9	252.9	10.41	2.6
	A2	118.1	4.99	0.187	26.7	51.3	3.6	1.00	200.8	52.9	2	11.96	4.4	158.3	18.08	3.6
	A3	118.1	5.00	0.189	26.5	51.3	3.6	0.50	130.4	34.1	2	11.98	2.8	159.4	11.59	2.3
	A4	118.1	4.98	0.187	26.7	51.3	3.6	0.30	81.7	21.5	2	11.89	1.8	159.0	7.35	1.5
	B1	118.1	7.02	0.244	28.7	56.3	2.5	0.30	142.7	28.1	2	23.65	1.2	104.7	10.28	1.5
	B2	118.1	7.01	0.189	37.1	51.2	2.5	0.45	172.0	45.3	2	23.60	1.9	81.1	21.05	3.0
	B3	118.1	8.01	0.246	32.5	57.9	2.5	0.30	180.6	38.9	2	30.78	1.3	81.0	15.96	2.0
	C1	59.1	4.01	0.190	21.1	54.2	3.5	1.00	198.1	39.6	2	7.71	5.1	249.3	10.94	2.7
	D1	78.7	6.00	0.190	31.6	64.3	4.3	0.50	201.3	58.1	2	17.28	3.4	111.5	23.20	3.9
	D2	78.7	6.00	0.189	31.8	64.3	4.3	0.50	203.0	59.0	2	17.30	3.4	110.4	23.76	4.0
	D3	78.7	6.00	0.189	31.7	64.3	4.3	0.50	210.8	61.1	2	17.30	3.5	110.8	24.49	4.1
	D4	78.7	6.00	0.189	31.8	64.3	4.3	0.50	199.6	57.9	2	17.30	3.3	110.6	23.28	3.9
Shakir-Khalil 1993d,1994a,1994b	B1	110.2	5.91	0.197	30.0	47.6	5.6	0.20	59.5	23.9	2	16.74	1.4	119.1	9.10	1.5
	B3	110.2	5.91	0.197	30.0	49.3	5.5	0.29	87.0	34.1	2	16.74	2.0	119.1	12.97	2.2
	B5	110.2	5.91	0.197	30.0	47.6	5.9	0.20	57.2	23.9	2	16.74	1.4	119.1	9.08	1.5
	B7	110.2	5.91	0.197	30.0	47.4	5.7	0.29	79.0	32.4	2	16.74	1.9	119.1	12.34	2.1
	D1	110.2	7.87	0.248	31.7	47.4	6.6	0.20	133.5	61.2	2	29.76	2.1	84.4	24.55	3.1
	D2	110.2	7.87	0.248	31.7	60.2	6.5	0.20	130.7	52.2	2	29.76	1.8	84.4	20.96	2.7
	E1	110.2	5.91	0.197	30.0	53.3	6.5	0.20	71.9	29.7	2	16.74	1.8	119.1	11.32	1.9
	E2	110.2	5.91	0.197	30.0	53.5	6.2	0.29	105.6	42.4	2	16.74	2.5	119.1	16.13	2.7
	E3	110.2	5.91	0.197	30.0	53.5	5.7	0.20	68.5	25.9	2	16.74	1.5	119.1	9.88	1.7
	E4	110.2	5.91	0.197	30.0	53.3	5.3	0.29	96.3	34.8	2	16.74	2.1	119.1	13.27	2.2
	E5	110.2	5.91	0.197	30.0	53.3	5.1	0.20	72.1	25.6	2	16.74	1.5	119.1	9.74	1.6
	E6	110.2	5.91	0.197	30.0	52.9	5.5	0.29	97.1	36.4	2	16.74	2.2	119.1	13.86	2.3
	E7	110.2	5.91	0.197	30.0	53.3	5.9	0.20	68.7	26.8	2	16.74	1.6	119.1	10.20	1.7
	E8	110.2	5.91	0.197	30.0	52.9	5.7	0.29	98.3	37.5	2	16.74	2.2	119.1	14.27	2.4
Shakir-Khalil & Al-Rawdan 1995	F1	110.2	5.91	0.197	30.0	47.9	5.3	0.17	44.9	17.5	1	8.37	2.1	119.1	6.67	1.1
	F2	110.2	5.91	0.197	30.0	47.9	6.6	0.11	33.9	15.0	1	8.37	1.8	119.1	5.71	1.0
	F3	110.2	5.91	0.197	30.0	48.2	6.3	0.17	43.8	18.7	1	8.37	2.2	119.1	7.13	1.2
	F4	110.2	5.91	0.197	30.0	48.2	6.5	0.11	33.2	14.6	1	8.37	1.7	119.1	5.54	0.9

Table 5.6. CCFT Connection Tests

Reference	Specimen	L (in)	D (in)	t (in)	D/t	F_y (ksi)	f'_c (ksi)	β	$P_{applied}$ (kip)	$V'_{applied}$ (kip)	Number of Girders	$R_{n,AISC2010}$ (kip)	*test-to-predicted*	F_{in} (Eq 5.8) (psi)	$L_{transfer}$ (in)	$L_{transfer}/D$
Shakir-Khalil (1993c,1994a)	A1	110.2	6.63	0.197	33.7	46.4	6.2	0.20	61.9	30.5	2	16.55	1.8	138.5	11.23	1.7
	A2	110.2	6.63	0.197	33.7	46.8	6.5	0.20	57.7	29.0	2	16.55	1.8	138.5	10.69	1.6
	A5	110.2	6.63	0.197	33.7	46.8	6.5	0.40	138.6	69.4	2	16.55	4.2	138.5	25.60	3.9
	A6	110.2	6.63	0.197	33.7	46.1	6.5	0.29	91.3	46.4	2	16.55	2.8	138.5	17.10	2.6
	C1	110.2	8.63	0.248	34.8	44.2	5.7	0.20	100.7	49.6	2	28.05	1.8	103.0	18.86	2.2
	C2	110.2	8.63	0.248	34.8	43.9	7.3	0.20	110.3	61.4	2	28.05	2.2	103.0	23.33	2.7

The normalized length (L/H for RCFT or L/D for CCFT) of the CFT push-out tests examined in this work varied from 1 to 6. The CFT connections tests exhibited normalized transfer lengths within the same range. While no definite trends were identified in the CFT push-out test results between the normalized length and bond stress, the bond stress as derived from the push-out tests may not be active along the entire length for longer columns. Thus, utilizing the entire length of the column to assess bond strength (i.e., $L_{bond} = L$, extending from mid-height of the column above the connection to mid-height of the column below the connection) may be inappropriate even for the case of slip occurring along the entire length of the column.

For localized slip, the length of the column that slips is relatively small, but to enable this failure mode a plastic mechanism needs to develop in either the steel tube or concrete core depending on where the load is applied. The applied force required to develop the plastic mechanism assuming strengths consistent with current provisions (AISC 2010) is given in Equation 5.11a for the case of load applied to the steel tube and the CFT extending to both sides of the point of force transfer, Equation 5.11b for the case of load applied to the steel tube and the CFT extending to only the compressive side of the point of force transfer, and Equation 5.11c for the case of load applied to the concrete core regardless of which sides the CFT extends.

$$P_{applied} = A_s F_{cr} + A_s F_y \tag{5.11a}$$

$$P_{applied} = A_s F_{cr} \tag{5.11b}$$

$$P_{applied} = C_2 A_c f'_c \tag{5.11c}$$

where,

F_{cr} is the critical compressive stress of the steel tube ($F_{cr} \leq F_y$) (AISC 2010)

Note that when load is applied to the steel tube and the CFT extends to both sides, the compressive strength on one side and the tensile strength on the other side need to be met simultaneously to form a plastic mechanism. Thus, depending on the proportioning of the section, this limit state may be precluded by the cross section strength of the composite column.

To determine an appropriate value for the bond length when a localized overstressing failure controls, the transfer length is computed when the applied load is equal to the limit (Equation 5.11). The transfer length is computed using Equation 5.12a for the case of load applied to the steel tube and Equation 5.12b for the case of load applied to the concrete core. These equations are as given in the AISC *Specification* (AISC 2010) with the exception that F_{cr} is used instead of F_y to determine the portion of the load supported by the steel tube. This change was necessary to yield realistic results for slender tubes. Note that $F_{cr} = F_y$ in the controlling cases presented below, thus this deviation from the AISC *Specification* has no effect on the proposed recommendations.

$$P_{applied}\left(1-\frac{A_s F_{cr}}{P_{no}}\right)=pF_{in}L_{transfer} \tag{5.12a}$$

$$P_{applied}\left(\frac{A_s F_{cr}}{P_{no}}\right)=pF_{in}L_{transfer} \tag{5.12b}$$

where,

P_{no} is the nominal compressive strength of zero length CFT (AISC 2010)

The computed transfer length is normalized by the outside dimension of the steel tube (H for RCFT; D for CCFT) to be comparable with the parameter C_{in}. The minimum normalized transfer lengths for practical ranges of material parameters ($F_y \geq 36$ ksi, $E_s = 29{,}000$ ksi, $f'_c \geq 3$ ksi) and geometric parameters ($H \geq 4$ in., $H/B \leq 2$, $B/t \geq 10$, $H/t \leq 400$ for RCFT; $D \geq 4$ in., $10 \leq D/t \leq 400$ for CCFT) and only for cases where the plastic mechanism was not precluded by the cross section strength are presented in Table 5.7 for RCFTs and

Table 5.8 for CCFTs for the various configurations. Based on these results, an appropriate value for C_{in} in the bond strength equation is 4 for the case of load applied to the steel tube and the CFT extending to both sides of the point of force transfer and 2 otherwise. The value of 4 for the case of load applied to the steel tube and steel tube and the CFT extending to both sides of the point of force transfer is in agreement with results of the CFT connection tests described above; there is no experimental evidence for the other configurations. These recommendations regarding C_{in} represent a minor change from the current provisions where C_{in} = 4 when the CFT extends to both sides of the point of force transfer regardless of whether the load is applied to the steel or to the concrete. It is further recommended that in cases where the nominal bond length (C_{in} H for RCFTs; C_{in} D for CCFTs) of adjacent connection regions overlaps (e.g., columns with a low length-to-depth ratio or with beams framing in a staggered pattern), the bond length should be taken as a reduced value computed such that no overlap occurs.

Table 5.7. RCFT Minimum Transfer Lengths from Mechanistic Analysis

	Case	H (in)	B (in)	t (in)	H/t	F_y (ksi)	f'_c (ksi)	$L_{transfer}$ (in)	$L_{transfer}/H$
Square CFT	Load On Steel, Column Extends Both Sides	4.00	4.00	0.067	59.5	36.0	3.0	45.78	11.45
	Load On Steel, Column Extends Below Only	4.00	4.00	0.132	30.3	36.0	3.0	18.12	4.53
	Load On Concrete	4.00	4.00	0.132	30.3	36.0	3.0	18.12	4.53
RCFT	Load On Steel, Column Extends Both Sides	4.00	4.00	0.067	59.5	36.0	3.0	45.78	11.45
	Load On Steel, Column Extends Below Only	7.16	4.00	0.400	17.9	36.0	3.0	23.12	3.23
	Load On Concrete	7.16	4.00	0.400	17.9	36.0	3.0	23.12	3.23

Table 5.8. CCFT Minimum Transfer Lengths from Mechanistic Analysis

Case	D (in)	t (in)	D/t	F_y (ksi)	f'_c (ksi)	$L_{transfer}$ (in)	$L_{transfer}/D$
Load On Steel, Column Extends Both Sides	4.00	0.075	53.5	36.0	3.0	19.00	4.75
Load On Steel, Column Extends Below Only	4.00	0.104	38.4	36.0	3.0	7.92	1.98
Load On Concrete	4.00	0.104	38.4	36.0	3.0	7.92	1.98

An alternative form of the bond length could include the height of the shear tab. This form would have the advantage of being more consistent with the definition of the load transfer region used for detailing shear connectors in composite columns (AISC 2010). If such a form was chosen, the value of C_{in} would need to be adjusted accordingly.

5.3.6 Effective Bond Transfer Width

Current design provisions in the AISC *Specification* allow only a portion of the perimeter of the steel-concrete interface to be used when computing the transfer strength (AISC 2010). This is unique among the existing and proposed design provisions examined in this paper (Tomii 1985; Roeder et al. 1999; Parsley et al. 2000; CEN 2004). Based on observations of friction marks on tested and disassembled push-out specimens, Shakir-Khalil (1993a) noted that for CCFTs the entire perimeter is engaged in bond transfer whereas for RCFTs only the corner regions participate. There is limited evidence regarding the portion of the width that is active when various numbers of girders frame into either a CCFT or a RCFT column since the majority of test have been completed with two girders. The CFT connection tests conducted by Shakir-Khalil and Al-Rawdan (1995) with only one girder framing in had experienced lower transfer loads than the other specimens (Table 5.5), but it is important to note that the specimen did not suffer a bond failure and would likely have resisted higher transfer loads if the specimen were designed to mitigate non-slip related failure. The experimental bond stress for push-out tests, including those with shear tabs, is computed assuming the full perimeter is engaged in slip. All of the push-out tests with shear tabs in Table 5.3 and Table 5.4 have two girders framing on opposite sides. This implies that, for columns with at least two girders framing in on opposite sides, the bond stress can be achieved for the entire perimeter. For the cases of edge and corner columns where one girder or two girders on adjacent sides frame in, it is unclear whether or not the entire perimeter is engaged. However, these configurations will induce bending moments into the columns, thus increasing the bond strength. Thus, using the entire perimeter for corner columns is likely justified and is proposed for use in this work.

5.4 Proposed Design Formula

Based on the preceding analyses of critical bond stress, longitudinal bond transfer length, and circumferential bond transfer width, the formula for nominal bond strength is proposed as:

(a) For RCFT:

$$R_n = 2\left(B+H\right)L_{bond}F_{in} \tag{5.13a}$$

$$L_{bond} = C_{in} H \tag{5.13b}$$

$$F_{in} = 12.8\left(t/H^2\right) \leq 0.1 \tag{5.13c}$$

(b) For CCFT:

$$R_n = \pi D L_{bond} F_{in} \tag{5.14a}$$

$$L_{bond} = C_{in} D \tag{5.14b}$$

$$F_{in} = 30.9\left(t/D^2\right) \leq 0.2 \tag{5.14c}$$

where,

R_n = nominal bond strength, kips
F_{in} = nominal bond stress, ksi
t = design wall thickness of steel section, in.
B = overall width of rectangular steel section ($B \leq H$), in.
H = overall height of rectangular steel section ($H \geq B$), in.
D = outside diameter of round steel section, in.
L_{bond} = length of the bond region (the bond region of adjacent connections shall not overlap)
C_{in} = 4 if load is applied to the steel tube and the CFT extends to both sides of the point of force transfer
= 2 otherwise

For simplicity in design, the perimeter of the steel-concrete interface is approximated using the outside dimensions of the steel tube (i.e., $p = 2(B+H)$ for RCFT and $p = \pi D$ for CCFT). The error introduced from this simplification is small in comparison to the scatter in the results.

An upper bound is placed on the bond stress based on the bond stress observed in experimental results of the stockiest tubes for each shape. For very large cross sections and thin steel tubes, the bond stress approaches zero, essentially requiring an alternate force transfer mechanism when significant loads are applied.

The proposed formula differs from the current formula (AISC 2010) in the bond strength, bond length, and bond width. In the proposed equation the bond width is the entire perimeter of the interface, regardless of the number of girders framing in. The resulting strength should be compared against the force transfer demand from all girders framing in, as opposed to checking each girder individually as implied by the current design formula (AISC 2010).

The proposed formula for bond stress is based on geometric properties of the tube only. It is noted that concrete quality (e.g., the shrinkage/expansive potential) also affects the bond stress. This was not included in the proposed formula since the concrete quality is not typically known at the time of design. However, higher and more reliable bond strengths could be obtained if there were requirements placed on the quality of the concrete (Roeder et al. 1999).

To compute a resistance factor for load and resistance factor design, the recommendations of Ravindra and Galambos (1978) are used. The proposed formula for the resistance factor (Equation 5.15) depends on the desired reliability index, β_o; coefficient of variation of the resistance, V_R; and the mean test-to-predicted ratio, R_m/R_n.

$$\phi = \frac{R_m}{R_n} e^{(-0.55\beta_o V_R)} \tag{5.15}$$

Unfortunately, no suitable set of tests exist to compute reliable statistics on the resistance or test-to-predicted ratio for the bond strength. The CFT connection tests results have unnaturally high variation because the peak applied loads do not always reflect bond failures (i.e., other failure modes govern the peak strength). An approximate result can be obtained by computing the resistance factor for the bond stress. The nominal bond stress given by Equations 5.13b and 5.14b is compared to the experimentally observed bond stress for the specimens in Table 5.1 and Table 5.2. The resulting mean and coefficient of variation of the test-to-predicted ratio are presented in Table 5.9. In this case, only uncertainty from the bond stress will be included. Assuming a reliability index of 3.0, as is recommended for members (Ravindra and Galambos 1978), the resistance factor is computed as 0.50 for RCFT and 0.56 for CCFT. A value of 0.50 is recommended for both shapes. The corresponding safety factor for allowable stress design is computed as 3.00 ($\Omega = 1.5/\phi$). These values are near the current values ($\phi = 0.45$; $\Omega = 3.33$) listed in AISC *Specification* (2010).

Table 5.9. Computation of Resistance and Safety Factors

Type	Number of Experiments	R_m/R_n	V_R	ϕ	Ω
RCFT	17	0.94	0.39	0.50	3.02
CCFT	126	1.27	0.50	0.56	2.70

5.5 Distribution of Bond Stress along Column Height

The current (AISC 2010) and the proposed design equations assume that the bond stress is uniform over a given height of the column. However, distribution of bond stress is known to vary both along the perimeter of the interface and along the height of the columns. This complex three-dimensional behavior is most accurately analyzed using detailed continuum finite element models (Roeder et al. 1999; Johansson 2003). One-dimensional analysis, assuming constant behavior around the perimeter of the interface, complements the more detailed analyses and provides a valuable link between the complex three-dimensional behavior and simple design equations. The derivation presented here is essentially a simple case of the bond model developed by Hajjar et al. (1998), applicable only to concentrically loaded columns with negligible geometric nonlinearity. This section thus assesses the nonlinear distribution of bond stress using one-dimensional analysis and justifies the use of a uniform bond stress in design calculations.

The distribution of bond stress along the height of the column depends on the response of the steel tube, the concrete core, as well as the interface between the two. A differential

equation can be formed to describe the slip behavior by assessing equilibrium on an infinitesimal length of a CFT column. A free-body diagram of the CFT segment is shown in Figure 5.5. Equilibrium can be assessed for the steel and concrete components (Equation 5.16).

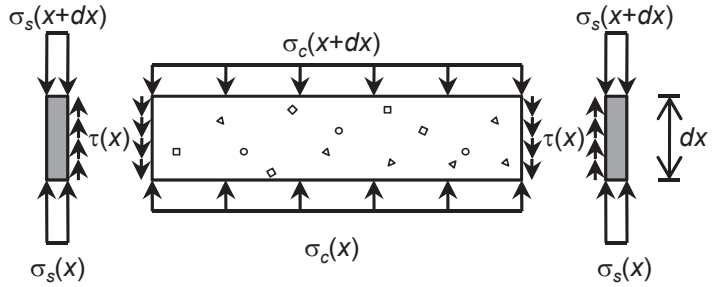

Figure 5.5. Free Body Diagram of CFT Section

$$\Sigma F_{concrete} = A_c\sigma_c(x) - A_c\sigma_c(x+dx) - p\,dx\,\tau(x) = 0 \tag{5.16a}$$

$$\Sigma F_{steel} = A_s\sigma_s(x) - A_s\sigma_s(x+dx) + p\,dx\,\tau(x) = 0 \tag{5.16b}$$

where,

A_s = cross sectional area of the steel tube,
A_c = cross sectional area of the concrete core,
p = perimeter of the steel-concrete interface,
x = variable defined by the length along the CFT,
dx = length of the segment of CFT analyzed (Figure 5.5),
$\sigma_s(x)$ = longitudinal stress in the steel tube,
$\sigma_c(x)$ = longitudinal stress in the concrete core,
$\tau(x)$ = bond stress.

Dividing both sides of Equation 5.16 by dx and taking the limit as dx approaches zero yields Equation 5.17

$$p\,\tau(x) = A_s\sigma_s'(x) = -A_c\sigma_c'(x) \tag{5.17}$$

where,

$'$ indicates derivative with respect to x

An analytical solution can be achieved if elastic behavior is assumed. The steel and concrete stresses are linear functions of strain, whereas the bond stress is a function of slip (Equation 5.18a). The first derivative of the steel and concrete relations (Equation 5.18b) and the second derivative of the slip relation (Equation 5.18c) are also computed.

$$\sigma_s(x) = E_s\varepsilon_s(x) \quad \sigma_c(x) = E_c\varepsilon_c(x) \quad \tau(x) = \kappa s(x) \tag{5.18a}$$

$$\sigma_s'(x) = E_s \varepsilon_s'(x) \quad \sigma_c'(x) = E_c \varepsilon_c'(x) \tag{5.18b}$$

$$\tau''(x) = \kappa s''(x) \tag{5.18c}$$

where,

E_s = elastic modulus of the steel tube,
E_c = elastic modulus of the concrete core,
$s(x)$ = slip,
κ = elastic stiffness of the bond-slip relation.

Substituting the relations of Equation 5.18b into Equation 5.17 and solving for the derivative of strain yields Equation 5.19

$$\varepsilon_c'(x) = -\frac{p}{E_c A_c}\tau(x) \tag{5.19a}$$

$$\varepsilon_s'(x) = \frac{p}{E_s A_s}\tau(x) \tag{5.19b}$$

Slip is defined as the difference between the displacement of the steel tube and the concrete core (Equation 5.20a), consistent with the direction of bond stress shown in Figure 5.5. Computing the first and second derivatives of slip yields Equations 5.20b and 5.20c.

$$s(x) = d_s(x) - d_c(x) \tag{5.20a}$$

$$s'(x) = d_s'(x) - d_c'(x) = \varepsilon_s(x) - \varepsilon_c(x) \tag{5.20b}$$

$$s''(x) = \varepsilon_s'(x) - \varepsilon_c'(x) \tag{5.20c}$$

Substituting Equations 5.18c, 5.19a, and 5.19b into Equation 5.20c yields a differential equation that characterizes bond stress along the length of a column assuming elastic behavior (Equation 5.21).

$$\tau''(x) = \left(\frac{p\kappa}{E_c A_c} + \frac{p\kappa}{E_s A_s} \right) \tau(x) = C^2 \tau(x) \tag{5.21}$$

where,

$$C = \sqrt{\frac{p\kappa}{E_c A_c} + \frac{p\kappa}{E_s A_s}}$$

The general solution of this differential equation is Equation 5.22.

$$\tau(x) = C_1 e^{Cx} + C_2 e^{-Cx} \tag{5.22}$$

where,

C_1 and C_2 = constants that depend on boundary conditions

The specific solution depends on the boundary conditions of the column. One representative case, one side of a shear connection where the peak bond stress is just reached and the column is of sufficient length to completely transfer the load, will be examined further. The boundary conditions for this case can be described by Equation 5.23.

$$\tau(0) = F_{in} \quad \tau(\infty) = 0 \tag{5.23}$$

Solving for the constants, the distribution of the bond stress is described by Equation 5.24. The equation indicates that the bond stress exponentially decays away from the point of load applications. The force transfer between materials persists along the full length of the column, although after a relatively short distance the bond stress is negligibly small. This behavior has been noted previously in analyses performed by Roeder et al. (1999).

$$\tau(x) = F_{in} e^{-Cx} \tag{5.24}$$

The load transferred can be computed by integrating along the length of the column and is found to be pF_{in}/C.

Examining the elastic behavior gives insight into the distribution of bond stress; however, nonlinearity in the steel tube, concrete core, and bond behavior is expected at the ultimate limit state. A material nonlinear analysis was conducted using existing structural analysis formulations noting that the governing differential equations can be modeled with two strands of linked truss elements. The steel tube and concrete core are modeled with truss elements and the interface is modeled with zero length springs located at the nodes. This configuration is shown schematically in Figure 5.6. Typically 200 elements along the length of the column were used in the analyses; the large number of elements provided for smooth results along the length of the column. When elastic materials are used, the analytical results (Equation 5.24) are captured exactly by this computational model. Suitable uniaxial material models have been developed in previous studies for RCFT and CCFT as described in Chapter 3. An elastic-perfectly plastic model is used to describe the load-slip relationship with peak stress computed by Equation 5.13b for RCFT and Equation 5.14b for CCFT and the initial stiffness taken as 66 kip/in^3, based on recommendations by Hajjar et al. (1998).

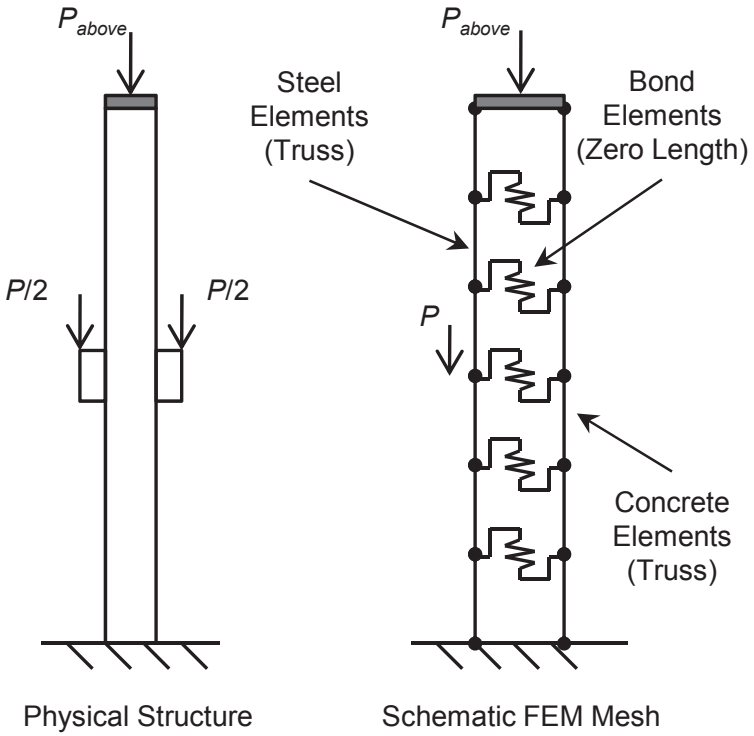

Figure 5.6. Schematic of FEM Mesh

Analyses were performed on column segments representing half the story height above and below a simple connection. Slip was constrained to be zero at the top and bottom of the column segment so that the introduction of load at the connection could be investigated without any influence of slip elsewhere in the column. The columns were subjected to a load applied at the top representing load in the column from upper stories and a load applied at the connection (mid-height of the segment) equal to the nominal bond strength (Equation 5.13a for RCFTs and Equation 5.14a for CCFTs). Results include the distribution of slip, bond stress, and axial load in the steel tube and concrete core along the height of the column. Sample results from one analysis are shown in Figure 5.7 for a 10 ft. long segment of a CCFT column constructed from an HSS 7.500×0.250 (F_y = 42 ksi, t_{design} = 0.233 in, F_{in} = 128 psi) and normal strength concrete (f'_c = 4 ksi). A load of 74.2 kips ($0.2P_{no}$) was applied at the top and a load of 213.2 kips was applied at the connection.

The horizontal dashed lines denote the nominal bond length ($C_{in}D$) in which the bond stress is assumed active in the design formulation. The nonlinear analysis confirms that the majority of the force transfer occurs in this region, although not all, with some slip extending both above and below this region. The distribution of slip is not symmetric about the connection, with the equilibrium achieved in a shorter length below the connection than above. This is due to the gradual decrease in stiffness of the steel tube and concrete core as loads are increased. The variation in stiffness with loading is also seen in the load sharing in the equilibrium regions. Above the connection the steel carries 52% of the axial load, while below the connection the steel carries 60% of the axial load. The percentage below the connection is in agreement with the AISC *Specification* (Equation 5.9) but since the percentage above is lower, the transferred load is slightly underpredicted. The magnitude of slip at the nominal bond strength is rather small (on

the order of one hundredth of an inch), confirming that natural bond strength should not be superimposed with other force transfer mechanisms which may not develop their full strength at these low levels of deformation.

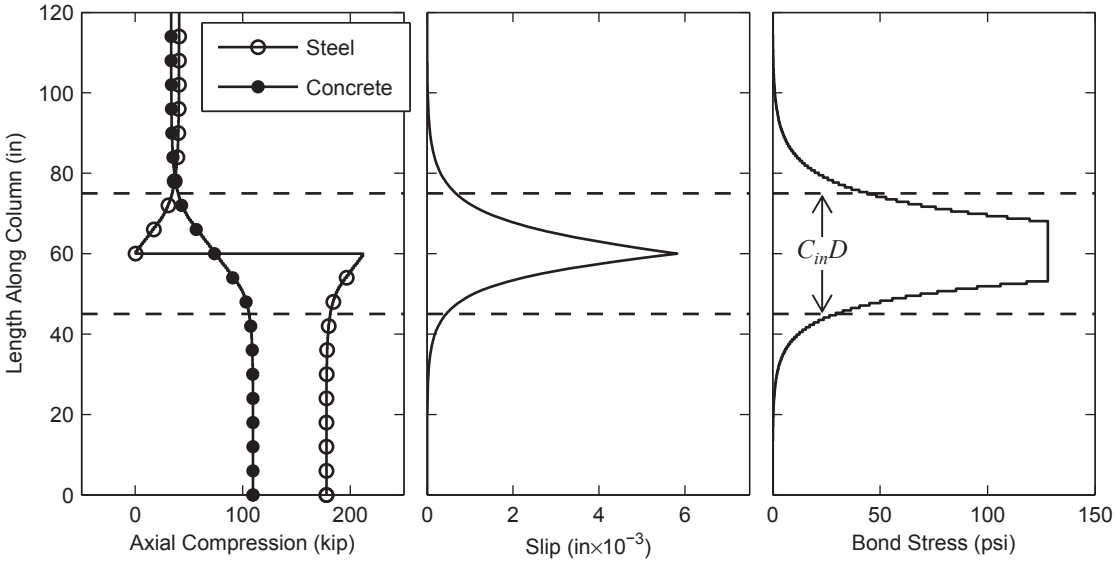

Figure 5.7. Sample Results of Nonlinear Bond Analysis

5.6 Conclusions

Current design provisions for the natural bond strength are overly simple and are found to be conservative for the cases examined. A new formula for nominal bond strength of CFT structures is proposed in this paper. The critical bond stress, given as a function of tube dimensions, is derived from results of push-out test and varies between RCFT and CCFT. The effective bond transfer area is determined based on an examination of experimental observations and results from specially instrumented connection tests. The resistance factor, ϕ, is computed as 0.50 and the safety factor, Ω, is computed as 3.00, based on the bond stress formula. Using a one-dimensional model the behavior of the connection region of a column was examined. The distribution of bond stress and the load deformation response at the joint both indicate that the proposed design formula is safe.

Finally, it is noted that since the proposed formula is based on experimental results that do not generally exhibit a bond slip failure, there is a degree of conservatism in the design recommendations. Thus, future experimental and analytical research is warranted to explore the behavior of CFT columns subjected large transfer forces.

STABILITY ANALYSIS AND DESIGN OF COMPOSITE STRUCTURES

6.1 Introduction

The Direct Analysis method provides a straightforward and accurate way of addressing frame in-plane stability considerations (White et al. 2006). In this method, required strengths are determined with a second-order elastic analysis where members are modeled with a reduced rigidity and initial imperfections are either directly modeled or represented with notional lateral loads. The method allows for the computation of available strength based on the unsupported length of the column, eliminating the need to compute an effective length factor. The validity of this approach has been established through comparisons between fully nonlinear analyses and elastic analyses (Surovek-Maleck and White 2004a; b; Deierlein 2003; Martinez-Garcia 2002). However, to date, no appropriate reduced elastic rigidity values have been developed nor has the methodology in general been thoroughly validated for composite members.

Among the challenges to validation of the Direct Analysis method for composite members is the lack of guidance on the value of elastic flexural rigidity (*EI*) that should be used for analysis of composite members. An estimation of the flexural rigidity is necessary for first- and second-order static and dynamic analyses, as well as eigenvalue analyses. When used for this purpose the flexural rigidity is denoted as $EI_{elastic}$. Such a value could be used: 1) in conjunction with Direct Analysis rigidity reductions to perform strength checks; 2) to compute deflections used in story drift checks; 3) to compute fundamental periods and mode shapes (including for response spectrum analysis); and 4) as the elastic component of a concentrated plasticity beam-column element.

The elastic flexural rigidity is also used in the determination of the elastic critical buckling load when computing axial compressive strength. When used for this purpose the flexural rigidity is denoted as EI_{eff}. The AISC *Specification* (2010b) provides expressions for EI_{eff} for steel reinforced concrete (SRC) columns (Equation 6.1) for concrete-filled steel tube (CFT) columns (Equation 6.3) based on an examination of experimental research (Leon et al. 2007).

$$EI_{eff} = E_s I_s + 0.5 E_s I_{sr} + C_1 E_c I_c \qquad \text{(SRC)} \tag{6.1}$$

$$C_1 = 0.1 + 2\left(\frac{A_s}{A_c + A_s}\right) \leq 0.3 \tag{6.2}$$

$$EI_{eff} = E_s I_s + E_s I_{sr} + C_3 E_c I_c \qquad \text{(CFT)} \tag{6.3}$$

$$C_3 = 0.6 + 2\left(\frac{A_s}{A_c + A_s}\right) \leq 0.9 \tag{6.4}$$

Since concrete experiences nonlinearity a relatively low load levels, one value or expression for the elastic rigidity is generally insufficient. For example, EI_{eff} should be representative of axial dominant behavior near incipient buckling whereas it may be more appropriate for $EI_{elastic}$ used to determine story drift to be representative of combined axial and bending behavior at lower load levels. This is in contrast to structural steel where $EI_{eff} = EI_{elastic} = E_sI_s$ is widely considered safe and accurate for nearly all of these purposes as they relate to common design procedures.

In order to address these current needs in design, a large parametric study has been conducted. The study focuses on two related aspects of stability design. First is the development of an effective elastic rigidity, $EI_{elastic}$, for use in frame analyses with composite beam-columns. Second is the development and validation of Direct Analysis recommendations for stability design of composite systems. This chapter describes the parametric study and main results; a comprehensive reporting of all key results is presented in Appendix A.

6.2 Benchmark Frames

The parametric study described in this work generally consists of comparisons between results from fully nonlinear analyses and elastic analyses on a set of benchmark frames. In order to ensure broad applicability of the recommendations, the benchmark frames are selected to cover a wide range of material and geometric properties. Similar studies for structural steel (Kanchanalai 1977; Surovek-Maleck and White 2004a; b) have used a set of small non-redundant frames and a W8×31 section in both strong and weak axis. For this work, this set of frames was expanded and a variety of composite cross sections were selected. In the parametric study, a complete matrix is laid out whereby each cross section is used within each benchmark frame to provide a comprehensive set of results.

6.2.1 Sections

The cross sections chosen for investigation in this work are segregated into four groups 1) Circular CFT (CCFT), 2) Rectangular CFT (RCFT), 3) SRC subjected to strong axis bending, and 4) SRC subjected to weak axis bending. Within these groups, sections were selected to span practical ranges of concrete strength, steel ratio, and for the SRC sections, reinforcing ratio (only CFTs without longitudinal reinforcing bars are analyzed in this work). Other section properties (e.g., steel yield stress, aspect ratio) were taken as typical values. Steel yield strengths were selected as F_y = 50 ksi for W shapes, F_y = 42 ksi for round HSS shapes, F_y = 46 ksi for rectangular HSS shapes, and F_{yr} = 60 ksi for reinforcing bars. Three concrete strengths were selected: 4, 8, and 16 ksi.

There is no prescribed upper limit of steel ratio for composite sections; however, practical considerations and the dimensions commonly produced steel shapes impose an upper limit of approximately 25% for CFT and 12% for SRC. The AISC *Specification* (2010b) sets a lower limit of steel ratio for composite sections as 1%. However, maximum permitted width-to-thickness ratios provide a stricter limit for CFT members. For the selected steel strengths, the width-to-thickness limits (Equation 6.5) correspond to steel ratio limits of 1.86% for CCFT and

3.16% for RCFT. For SRC members, the AISC *Specification* (2010b) prescribes a minimum reinforcing ratio of 0.4% and no maximum. The ACI *Code* prescribes a maximum reinforcing ratio of 8%.

$$\frac{D}{t} \le \frac{0.31E_s}{F_y} \qquad \text{(CCFT)}$$
$$\frac{h}{t} \le 5.00\sqrt{\frac{E_s}{F_y}} \qquad \text{(RCFT)} \tag{6.5}$$

Noting these limitations 5 round HSS shapes were selected for the CCFT sections, 5 rectangular HSS shapes were selected for the RCFT sections, and outside dimensions of 28 in. × 28 in., 4 wide-flange shapes, and 3 reinforcing configurations were selected for the SRC sections (Table 6.1). Altogether, 5 (steel shapes) × 3 (concrete strengths) = 15 total sections were selected each for RCFTs and CCFTs and 4 (steel shapes) × 3 (reinforcing configurations) × 3 (concrete strengths) = 36 total sections were selected each for strong and weak axis bending of SRCs.

Table 6.1. Selected steel shapes and reinforcing configurations

Index	Steel Shape	ρ_s
A	HSS 7.000×0.500	24.82%
B	HSS 10.000×0.500	17.70%
C	HSS 12.750×0.375	10.65%
D	HSS 16.000×0.250	5.72%
E	HSS 24.000×0.125*	1.93%

* Not in the AISC *Steel Construction Manual* (2011)

(a) CCFT

Index	Steel Shape	ρ_s
A	HSS 6×6×1/2	27.63%
B	HSS 9×9×1/2	19.06%
C	HSS 8×8×1/4	11.13%
D	HSS 9×9×1/8	5.05%
E	HSS 14×14×1/8*	3.27%

* Not in the AISC *Steel Construction Manual*

(b) RCFT

Index	Steel Shape	ρ_s
A	W14×311	11.66%
B	W14×233	8.74%
C	W12×120	4.49%
D	W8×31	1.16%

(c) SRC (steel shapes)

Index	Reinforcing	ρ_{sr}
A	20 #11	3.98%
B	12 #10	1.94%
C	4 #8	0.40%

(d) SRC (reinforcing configurations)

The naming convention of the sections consists of three components separated by dashes. The components are section type (i.e., CCFT, RCFT, SRCs, or SRCw), section shape and reinforcing (using the indices listed in Table 6.1), and concrete strength. For example, CCFT-A-4 denotes a CCFT constructed with a HSS 7.000×0.500 and f'_c = 4 ksi concrete; and SRCw-CB-16 denotes a SRC bent in the weak axis constructed with a W12×120, 12 #10 reinforcing bars, and f'_c = 16 ksi concrete. Scale drawings of the sections are shown in Figure 6.1.

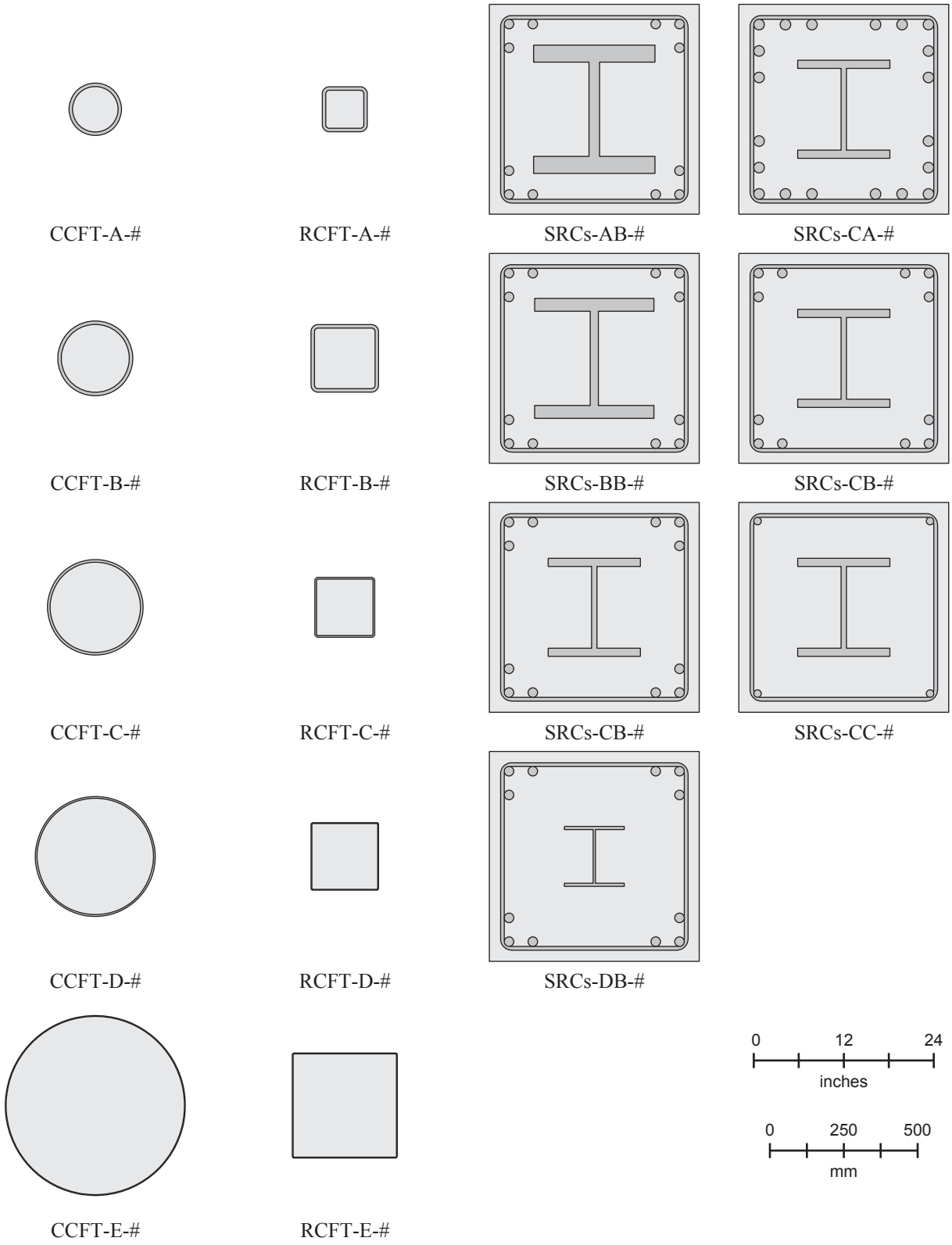

Figure 6.1. Scale Drawings of Sections

6.2.2 Frames

A set of 23 small non-redundant frames were described and used in previous stability studies on structural steel members (Kanchanalai 1977; Surovek-Maleck and White 2004a; b). The set includes both sidesway inhibited and sidesway uninhibited frames, a range of slenderness, end constraints, and leaning column loads. The set of frames was expanded and the frame parameters were generalized for use with composite sections in this study. The frames are shown schematically in Figure 6.2. The sidesway uninhibited frame is defined by a slenderness value, λ_{oe1g}, pair of end restraint parameters, $G_{g,top}$ and $G_{g,bot}$, and leaning column load ratio, γ. The sidesway inhibited frame is defined by a slenderness value, λ_{oe1g}, and end moment ratio, β. The values of these parameters selected for the frames are described in Table 6.2, a total of 84 frames are selected. The "*g*" in the end restraint parameters and slenderness value denotes that these values are defined with respect to gross section properties.

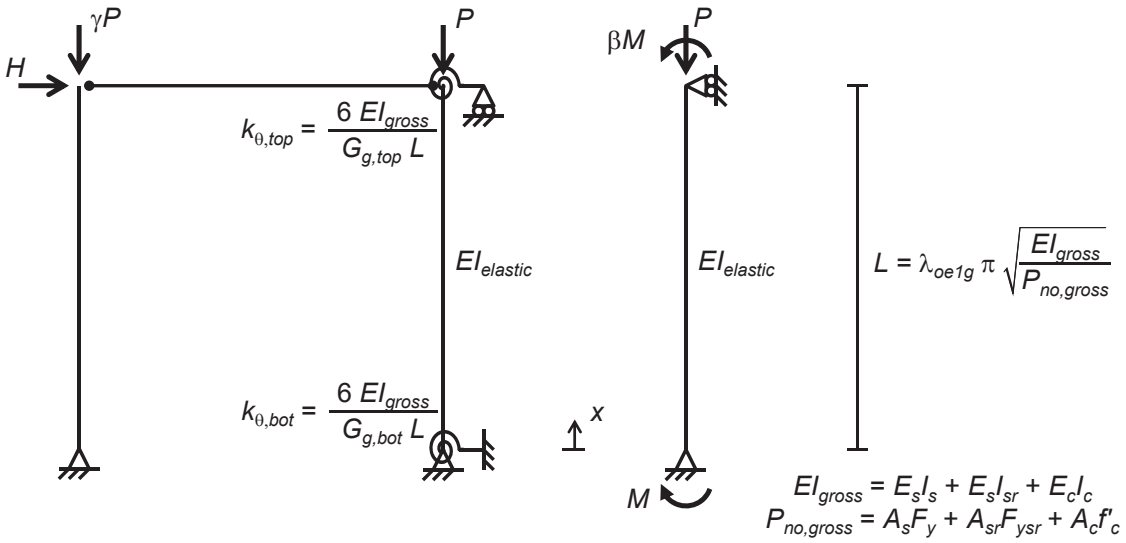

Figure 6.2. Schematic of the benchmark frames

Table 6.2. Benchmark frame variations

Frame	Slenderness	End Restraint	Leaning Column Load Ratio	End Moment Ratio	Number of Frames
Sidesway Uninhibited	4 values λ_{oe1g} = {0.22, 0.45, 0.67, 0.90}	4 value pairs (Table 6.3)	4 values γ = {0, 1, 2, 3}	n/a	64 (= 4 × 4 × 4)
Sidesway Inhibited	4 values λ_{oe1g} = {0.45, 0.90, 1.35, 1.90}	n/a	n/a	5 values β = {–1.0, –0.5, 0.0, 0.5, 1.0}	20 (= 4 × 5)

Table 6.3. End Restraint Value Pairs

Pair	$G_{g,top}$	$G_{g,bot}$
A	0	0
B	1 or 3*	1 or 3*
C	0	∞
D	1 or 3*	∞

*3 when $\gamma = 0$; 1 otherwise

The naming convention of the frames consists of components separated by dashes. For the sidesway uninhibited frames, the components are end restraint (using the indices listed in Table 6.3), slenderness and leaning column load ratio. For example, UC-45-g2 denotes a sidesway uninhibited frame with end restraint pair C ($G_{g,top} = 0$, $G_{g,bot} = \infty$), slenderness $\lambda_{oe1g} = 0.45$, and leaning column load ratio $\gamma = 2$. For the sidesway inhibited frames, the components are slenderness and end moment ratio (where the numbers 1 through 5 represent $\beta = -1.0$ through $\beta = 1.0$ in increments of 0.5). For example, I-135-b4 denotes a sidesway inhibited frame with slenderness $\lambda_{oe1g} = 1.35$ and end moment ratio $\beta = 0.5$.

6.2.3 Second-Order Elastic Analysis of Benchmark Frames

The second-order elastic results described in this work were obtained from the solution of the governing differential equation (Equation 6.6) using the appropriate boundary conditions (Table 6.4). Closed form solutions were obtained for displacement and moment along the length of column using a computer algebra system. This approach is computationally quick and accurate for moderate displacements; however, axial deformations are neglected. Where necessary, the effective length factor, *K,* for the benchmark frames was computed using the same differential equation.

$$v''''(x) + \frac{P}{EI_{elastic}} v''(x) = 0 \tag{6.6}$$

Table 6.4. Boundary conditions for the benchmark frames

Boundary Condition	Sidesway Uninhibited	Sidesway Inhibited
1	$v(0) = 0$	$v(0) = 0$
2	$-EI_{elastic} v''(0) = -k_{\theta bot} v'(0)$	$-EI_{elastic} v''(0) = M$
3	$-EI_{elastic} v'''(L) - Pv'(L) = H + \frac{\gamma P}{L} v(L)$	$v(L) = 0$
4	$-EI_{elastic} v''(L) = k_{\theta top} v'(L)$	$-EI_{elastic} v''(L) = \beta M$

6.3 Fully Nonlinear Analysis of Benchmark Frames

In order to provide results against which the proposed elastic design methodologies may be evaluated, the fully nonlinear analysis formulation introduced in Chapter 3 using the

"Proposed for Design" model is used to perform analyses on the benchmark frames. Key aspects of the model are summarized here.

6.3.1 Mixed Beam Finite Element Formulation

The mixed beam finite element formulation is implemented in the OpenSees framework (McKenna et al. 2000). It is a Total Lagrangian formulation assuming small strains and moderate rotations in the corotational frame and coupled with an accurate geometric transformation. With multiple elements along the length of a column, large displacement and rotation behavior is captured accurately.

The "Proposed for Design" constitutive relations were developed to better correspond to assumptions common in the development of design recommendations (e.g., neglecting steel hardening and concrete tension strength). Local buckling of the steel tube and other steel components was also neglected. This simplification allows for the investigation of the full range of steel ratios without the complexity of modeling local buckling, and is consistent with the validations conducted when developing Direct Analysis for steel structures (Surovek-Maleck and White 2004a; b). It is thus assumed that when combined with existing local buckling provisions in the AISC *Specification* (2010b), the proposed design provisions are applicable to composite members with non-compact or slender sections.

As in the prior work on the Direct Analysis method (Surovek-Maleck and White 2004b) wide-flange shapes are modeled with elastic-perfectly plastic constitutive relations (Figure 6.3c) and the Lehigh residual stress pattern (Galambos and Ketter 1959) (Figure 6.3a). Reinforcing steel was assumed to have negligible residual stress and was also modeled with an elastic-perfectly plastic constitutive relation. Residual stresses in cold formed steel tubes vary through thickness. To allow a reasonable fiber discretization of the CFT sections, residual stresses are included implicitly in the constitutive relation. A multilinear constitutive relation (Figure 6.3b) was used in which the stiffness decreases at 75% of the yield stress and again at 87.5% of the yield stress to approximate the gradual transition into plasticity observed in cold-formed steel (Abdel-Rahman and Sivakumaran 1997). In addition, the yield stress in the corner region of the rectangular members is increased to account for the additional work hardening in that region (Abdel-Rahman and Sivakumaran 1997).

The Popovics concrete model (Figure 6.3d) was selected and the modulus of elasticity of concrete is given by Equation 6.7; this is equivalent to expression in the ACI *Code* (2011) for normalweight concrete and to the expression in the AISC *Specification* (2010b) for w_c = 148.1 lbs/ft^3.

$$E_c\left[\text{ksi}\right] = 1802\sqrt{f'_c\left[\text{ksi}\right]} \tag{6.7}$$

All frame analyses were performed with six elements along the length of the member, each with three integration points. Since the analyses were two-dimensional, strips were used for the fiber section; the nominal height of the strips was 1/30th of the section depth (e.g., for a CCFT section, approximately 30 steel and 30 concrete strips of near equal height were used).

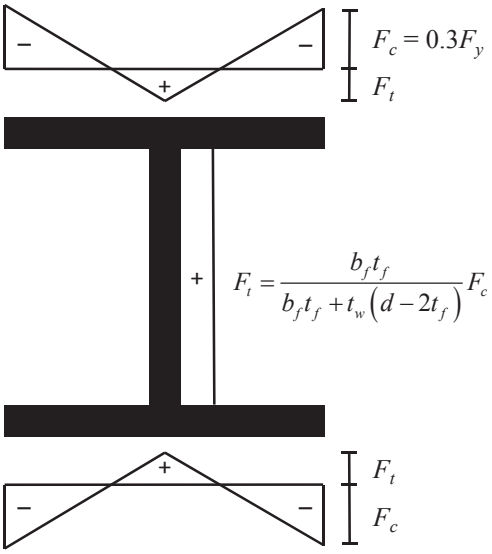

(a) Lehigh residual stress pattern

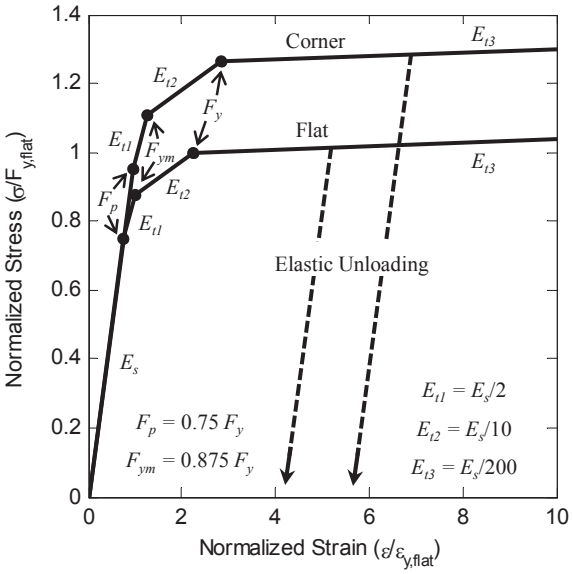

(b) Abdel-Rahman and Sivakumaran cold formed steel model

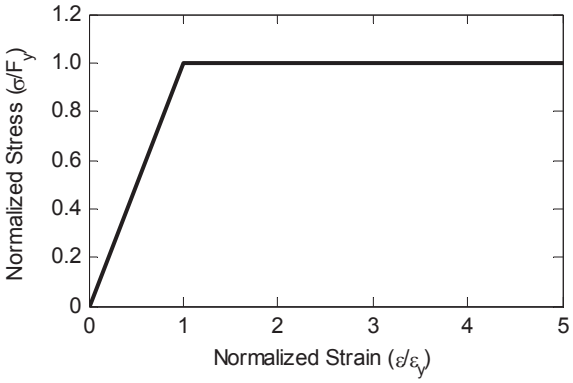

(c) Elastic-perfectly plastic model

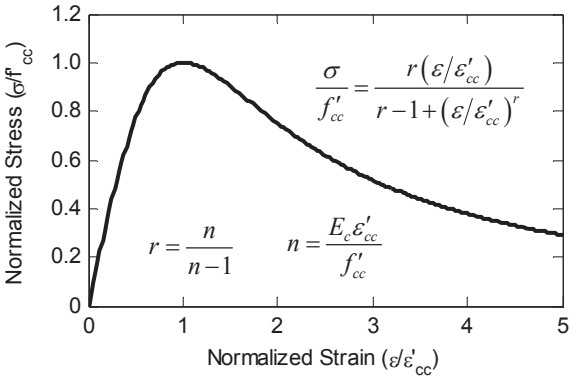

(d) Popovics concrete model

Figure 6.3. Steel and Concrete Constitutive Relations

6.3.2 Initial Geometric Imperfections

Nominal geometric imperfections equal to the fabrication and erection tolerations in the AISC *Code of Standard Practice* (AISC 2010a) were modeled explicitly. An out-of-plumbness of $L/500$ was included for the sidesway uninhibited frames and a half sine wave out-of-straightness with maximum amplitude of $L/1000$ was included for all frames. The initial out-of-plumbness and initial out-of-straightness were applied in the same direction (Figure 6.5a) as this produced the greatest destabilizing effect for these frames.

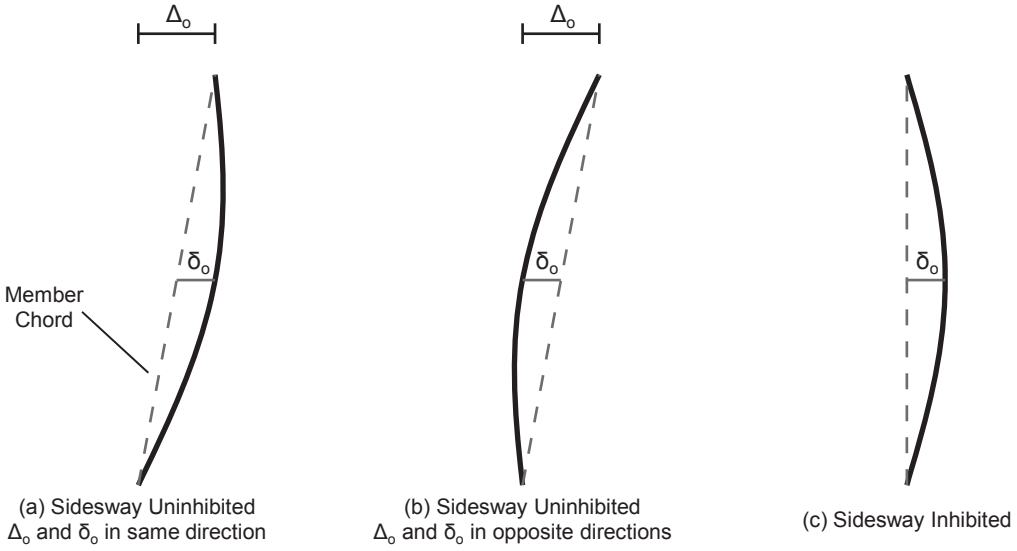

Figure 6.4. Initial Geometric Imperfections

6.3.3 Axial Compression-Bending Moment Interaction Diagrams

Through a series of fully nonlinear analyses, axial compression-bending moment interaction diagrams for each section and frame were constructed. One analysis was performed with axial load only to obtain the critical axial load, then a series analyses applying a constant axial load and increasing lateral load were performed. For the case of zero applied axial load, a cross section analysis was performed in lieu of the frame analysis. In each analysis, the limit point was identified as when the lowest eigenvalue reached zero; in cases where this did not occur, the limit point was defined as when the maximum longitudinal strain within any section in the member reached 0.05. At the limit point, both the applied loads and internal forces were recorded allowing for the construction of the first-order applied load interaction diagram and the second-order internal force interaction diagram, respectively. A sample of the results for two RCFT sections [RCFT-B-4 (ρ_s = 19.06%, f'_c = 4 ksi) and RCFT-E-4 (ρ_s = 3.27%, f'_c = 4 ksi)] and one frame [UA-67-g1 (sidesway uninhibited, fixed-fixed, K=1, λ_{oeg} = 0.67, leaning column load ratio = 1)] is shown in Figure 6.5. These two sections and one frame were selected primarily to illustrate the methodology. While the results from these sections and frame are typical and show variation between members with high and low steel ratios, they are not comprehensively representative of the wide range of material and geometric properties explored in this study. Detailed results, showing the behavior of each section, are presented in Appendix A.

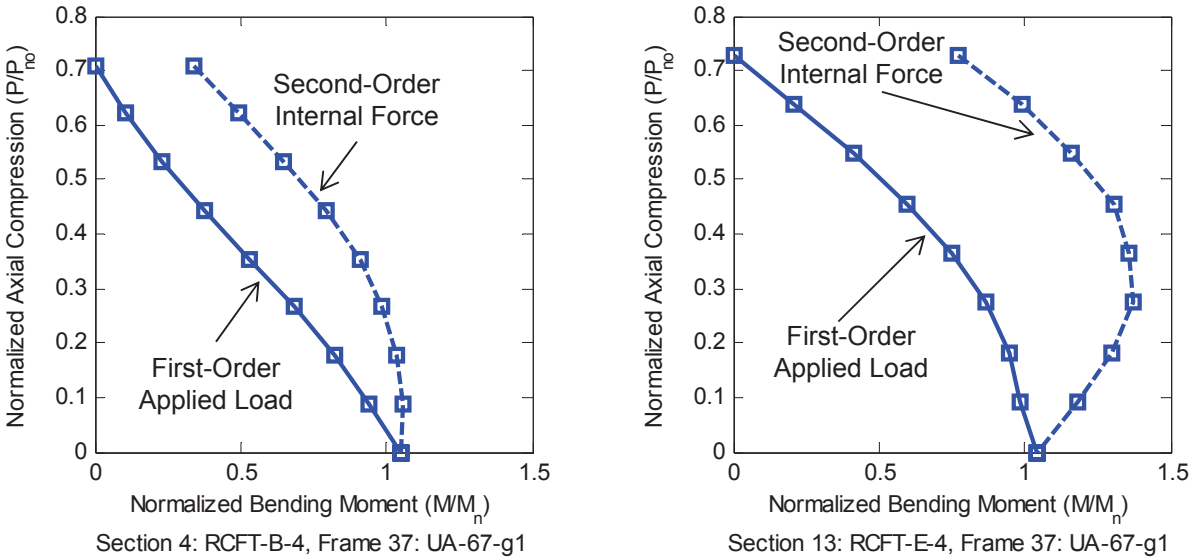

Figure 6.5. Example Results: Fully Nonlinear Applied Load and Internal Force Interaction Diagrams

6.4 Flexural Rigidity for Elastic Analyses

Because inelastic response in the concrete initiates at low load levels, an appropriate flexural rigidity for elastic analysis should be taken as a secant value. In order to assess the elastic flexural rigidity, $EI_{elastic}$, a parametric study was performed recording peak deformations from inelastic analyses and determining the value of $EI_{elastic}$ that, when used in an elastic analysis, would result in the same peak deformations. One value of $EI_{elastic}$ was determined for each frame and section and for different pairs of applied axial load and moment.

The pairs of applied axial load and moment were selected to be evenly spaced within the applied load interaction computed as described above. Secondary fully nonlinear analyses were performed to obtain the target peak deformations. The secondary fully nonlinear analyses differ from the fully nonlinear analyses described previously in that no initial geometric imperfections were included and tension strength was included in the concrete constitutive relation, since for this study the average behavior rather than lower bound behavior is of interest. For each load pair, $EI_{elastic}$ was determined through an iterative process such that the peak deformation from the elastic analysis was equal to the target peak deformation. A sample of the results for the sections and frame shown previously is shown in Figure 6.6 (similar plots for the same frame and all sections are presented in Appendix A). Each of the points represents one applied axial load and moment pair, the color corresponds to the value of $EI_{elastic}$ that was obtained as described above, normalized with respect to the gross flexural rigidity.

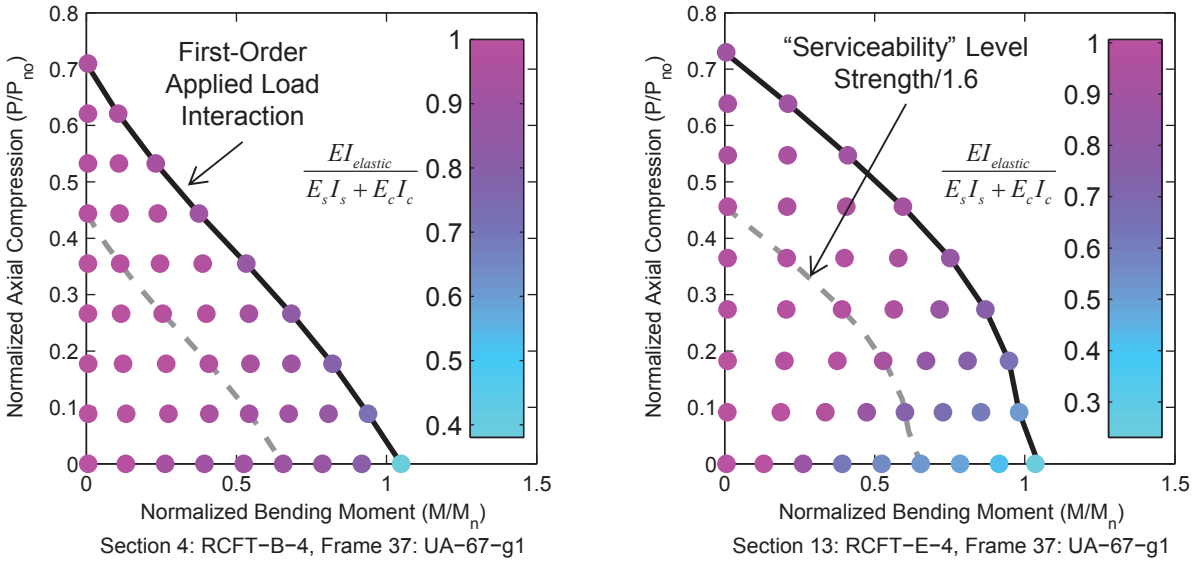

Figure 6.6. Example Results: $EI_{elastic}$

Figure 4 shows that the flexural rigidity varies with load level. At low loading, the gross flexural rigidity is a good estimate of the elastic rigidity ($EI_{elastic} \approx EI_{gross}$). As the load increases, the elastic rigidity decreases, with greater decreases for moment dominate loading and lesser decreases for axial dominant loading.

A linear regression analysis was performed on the data obtained in this study at or below the serviceability load level (as defined in Figure 6.6) to build expressions for $EI_{elastic}$. The strongest variations in $EI_{elastic}$ and thus the most accurate expressions depend on the loading. The resulting expressions are given in Equations 6.8 and 6.9 for SRCs and in Equations 6.10 and 6.11 for CFTs. The coefficients of determination from the linear regreassion are given in Table 6.5. Similar, load-dependent formulas have been developed for the flexural rigidity of reinforced concrete members (Khuntia and Ghosh 2004). Unfortunately, when $EI_{elastic}$ depends on the loading, the elastic analysis becomes iterative, making this type of formula cumbersome for design. More practical alternatives are discussed later in the context of the Direct Analysis method.

$$EI_{elastic} = E_sI_s + E_sI_{sr} + C_4E_cI_c \qquad \text{(SRC)} \tag{6.8}$$

$$C_4 = 1.21 - 1.01\frac{M}{M_n}\left(1 - 2.99\frac{P}{P_{no}}\right) \le 1.00 \qquad \text{(Strong Axis)} \tag{6.9a}$$

$$C_4 = 1.20 - 1.03\frac{M}{M_n}\left(1 - 3.00\frac{P}{P_{no}}\right) \le 1.00 \qquad \text{(Weak Axis)} \tag{6.9b}$$

$$EI_{elastic} = E_sI_s + C_5E_cI_c \qquad \text{(CFT)} \tag{6.10}$$

$$C_5 = 0.99 - 0.73\frac{M}{M_n}\left(1 - 3.47\frac{P}{P_{no}}\right) \le 1.00 \qquad \text{(CCFT)} \tag{6.11a}$$

$$C_5 = 1.01 - 0.90\frac{M}{M_n}\left(1 - 3.39\frac{P}{P_{no}}\right) \le 1.00 \qquad \text{(RCFT)} \tag{6.11b}$$

Table 6.5. Coefficients of Determination

Section Type	Coefficient of Determination
CCFT	0.55
RCFT	0.71
SRC (strong axis)	0.54
SRC (weak axis)	0.52

6.5 Nominal Axial Strength of Composite Columns

In the AISC *Specification* (2010b), the same column curve is used to predict the nominal axial compressive strength for both structural steel and composite columns (Equation 6.12), where the slenderness, λ_{oe}, is given by Equation 6.13, the effective rigidity, EI_{eff}, is given by Equation 6.1 for SRCs and by Equation 6.3 for CFTs, and the nominal zero-length compressive strength, P_{no}, is given by Equation 6.14 for SRCs and by Equation 6.15 for CFTs ($C_2 = 0.85$ for RCFTs and $C_2 = 0.95$ for CCFTs), noting that in this study local buckling is neglected and only CFTs without longitudinal reinforcement are investigated.

$$\frac{P_n}{P_{no}} = \begin{cases} 0.658^{\lambda_{oe}^2} & \text{for } \lambda_{oe} \le 1.5 \\ 0.877/\lambda_{oe}^2 & \text{for } \lambda_{oe} > 1.5 \end{cases} \tag{6.12}$$

$$\lambda_{oe} = \frac{KL}{\pi}\sqrt{\frac{P_{no}}{EI_{eff}}} \tag{6.13}$$

$$P_{no} = F_y A_s + F_{ysr} A_{sr} + 0.85 f_c' A_c \qquad \text{(SRC)} \tag{6.14}$$

$$P_{no} = F_y A_s + C_2 f_c' A_c \qquad \text{(CFT)} \tag{6.15}$$

The critical axial load obtained from the fully nonlinear analyses, $P_{n,analysis}$, for each frame and section is compared to the design strength in Figure 6.7. For CFTs, the design axial strength is generally accurate. In the low and intermediate slenderness range (λ_{oe}<2), the axial compressive strength of concrete dominant sections (low values of ρ_s) tends to be underpredicted. However, the strength tends to be overpredicted for these sections in the high

slenderness range (λ_{oe}>2) by as much as 15%. For CCFTs, the strength steel dominant sections in the intermediate slenderness range (0.5<λ_{oe}<2) is underpredicted by as much as 15%.

For SRCs, the design axial strength is inaccurate, underpredicting the strength by a significant margin, especially for concrete dominant sections. Based on these results, a new expression for the effective rigidity of SRC columns is presented (Equation 6.16-6.17). An alternative expression where $C_1 = 0.75$ for all sections was found to be accurate for axially loaded columns but is not recommended because it performed poorly when used to compute beam-column strength due to the concavity of the applied load interaction diagrams as described later. A comparison between the critical axial load obtained from the fully nonlinear analyses and the strength computed using the proposed expression is shown in Figure 6.8.

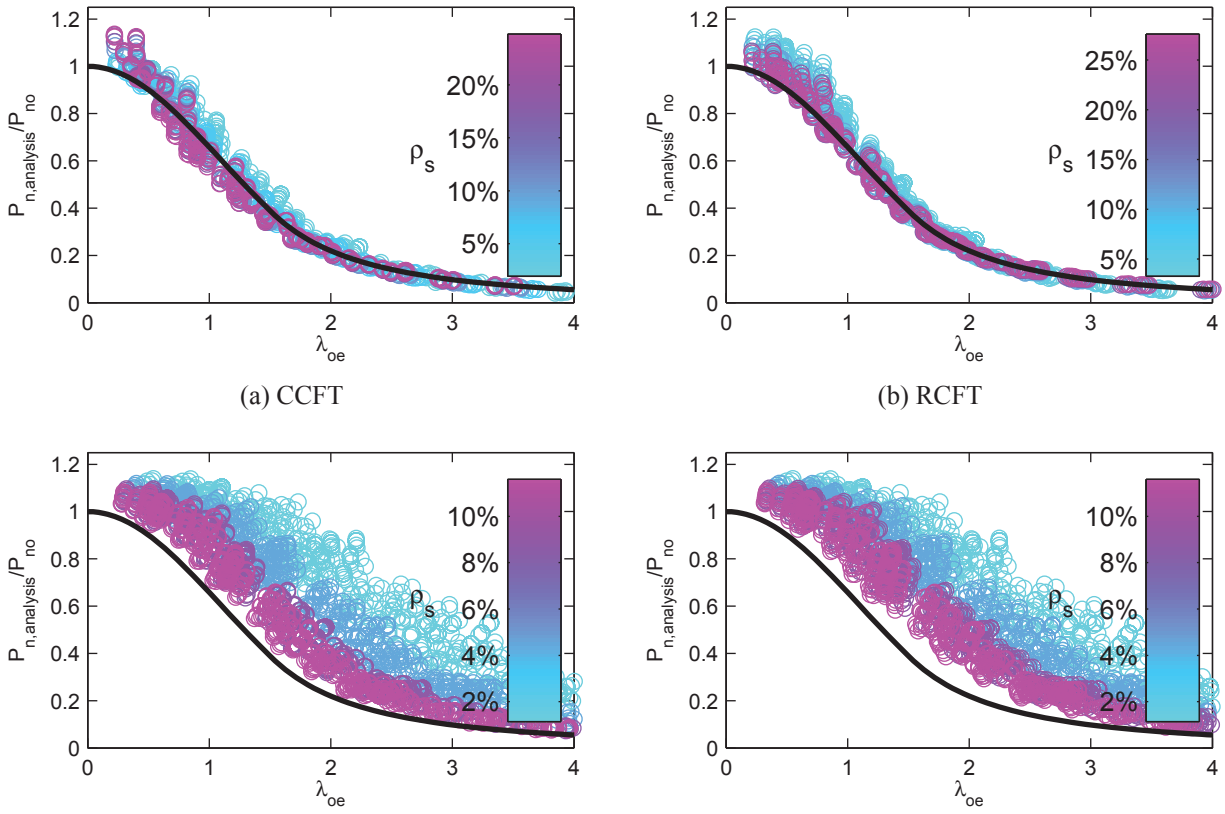

(a) CCFT (b) RCFT

(c) SRC (strong axis) (d) SRC (weak axis)

Figure 6.7. Comparison of Axial Strength: AISC (2010b)

$$EI_{eff,proposed} = E_s I_s + E_s I_{sr} + C_{1,proposed} E_c I_c \qquad \text{(SRC)} \tag{6.16}$$

$$C_{1,proposed} = 0.3 + 3\frac{A_s + A_{sr}}{A_g} \le 0.7 \tag{6.17}$$

The values of EI_{eff} computed with the proposed equation (Equation 6.16) will be larger than those computed with the existing equation (Equation 6.1), resulting in larger axial compressive strengths as seen in Figure 6.8a and b compared to Figure 6.7c and d. In order to

verify the accuracy of this new formula, a comparison is made with concentrically loaded SRC columns experiments. Axial compressive strengths of a representative subset (Anslijn and Janss 1974; Chen et al. 1992; Han and Kim 1995; Han et al. 1992; Roderick and Loke 1975) of the database used in the original calibration of C_1 (Leon et al. 2007) were computed using the proposed formulas (Equations 6.12-6.14 and 6.16-6.17) and compared against the experimental axial compressive strengths in Figure 6.9. For this set of 52 columns (which fail predominantly about the weak axis), the section depths range from 6.3 in. to 14 in., concrete strengths range from 2.9 ksi to 9.5 ksi, measured steel yield strengths range from 39 ksi to 73 ksi, and the length-to-depth ratios range from 3.1 to 17.8; see Leon et al. (2007) for the geometric, material, and boundary condition details of these experiments. The computed axial strength compares well for a majority of the tests, although some fall below the column curve. The current resistance factor and safety factors (ϕ_c = 0.75 and Ω_c = 2.00) were found to be suitable and somewhat conservative with the proposed formulas following the recommendations by Ravindra and Galambos (1978) and a reliability index of 3.0.

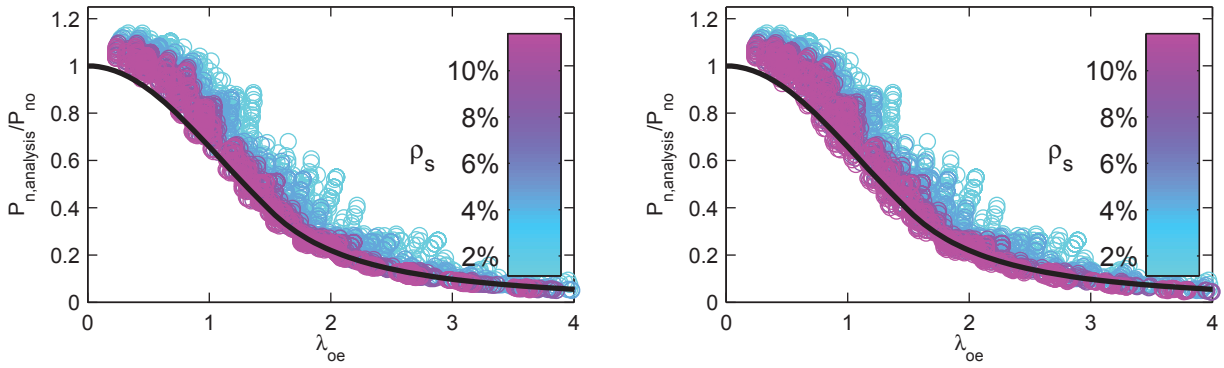

(a) SRC (strong axis) (b) SRC (weak axis)

Figure 6.8. Comparison of Axial Strength: Proposed

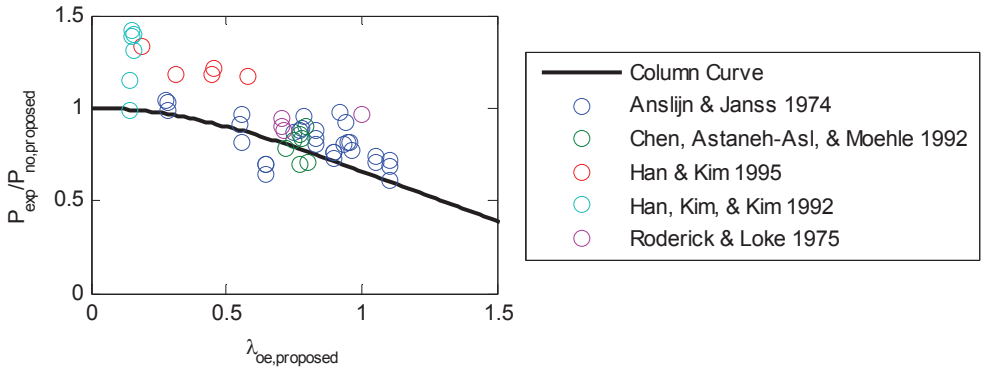

Figure 6.9. Comparison of Experimental Axial Strength: Proposed

Alternative expressions for EI_{eff} where the concrete contribution ratio is held at a constant value (Equation 6.3 with $C_3 = 0.9$ for CFT and Equation 6.16 with $C_{1,proposed} = 0.7$ for SRC) were found to result in acceptably good predictions of the axial strength (Figure 6.10). These expressions are simpler, however, they are not recommended for use in design since the underestimation of axial strength for concrete dominant sections can help reduce unconservative errors in the beam-column design methodology. An example is shown in Figure 6.11 (which was generated in the same manner as Figure 6.16 described later). For this frame and section pair, the axial strength from the analysis is shown to drop quickly with small bending moments (solid blue line), the design strength (solid green line) cannot reflect this concavity but remains safe because of the underprediction of the axial strength.

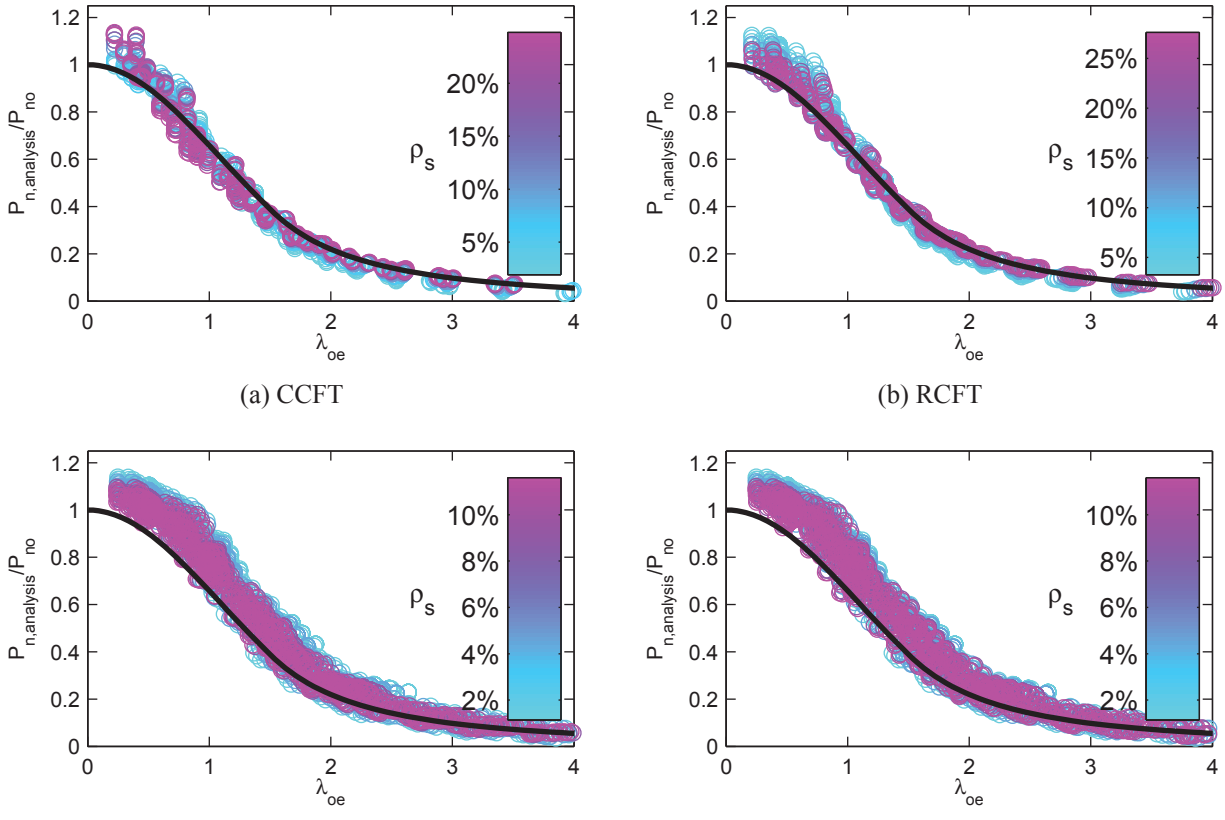

(a) CCFT

(b) RCFT

(c) SRC (strong axis)

(d) SRC (weak axis)

Figure 6.10. Comparison of Axial Strength: Constant Concrete Contribution

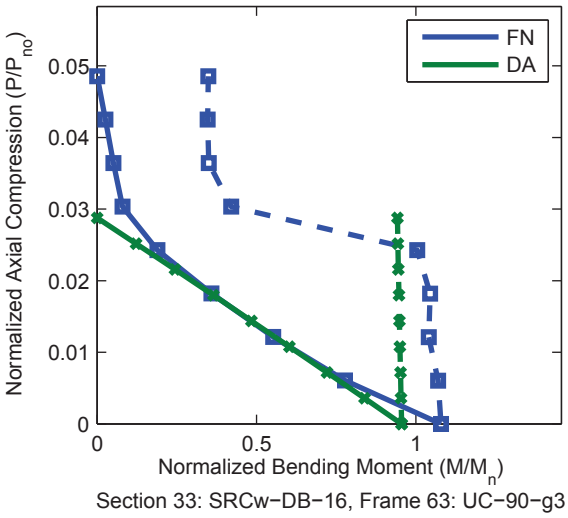

Figure 6.11. Example Interaction Diagrams

6.6 Nominal Flexural Strength of Composite Sections

The AISC *Specification* (2010b) allows for the flexural strength of composite columns to be computed by the plastic stress distribution method. In this method, the steel components are assumed to have reached a stress of F_y in either tension or compression and the concrete components are assumed to have reached a stress of $0.85f'_c$ in compression (or $0.95\,f'_c$ for CCFT to account for confinement).

The flexural strength obtained from the fully nonlinear analyses, $M_{n,analysis}$, for each section is compared to the design strength obtained from the AISC *Specification* (2010b) in Figure 6.12. For CFTs and SRCs in strong axis bending, the design strength is either accurate or conservative. For SRCs in weak axis bending, the design strength is unconservative for some sections, particularly steel dominant sections, overpredicting the strength by as much as 8%. This unconservative error is observed again in the evaluation of the beam-column design methodology (Section 6.7.3) and warrants further investigation and possible changes to the methodology for determining the nominal flexural strength.

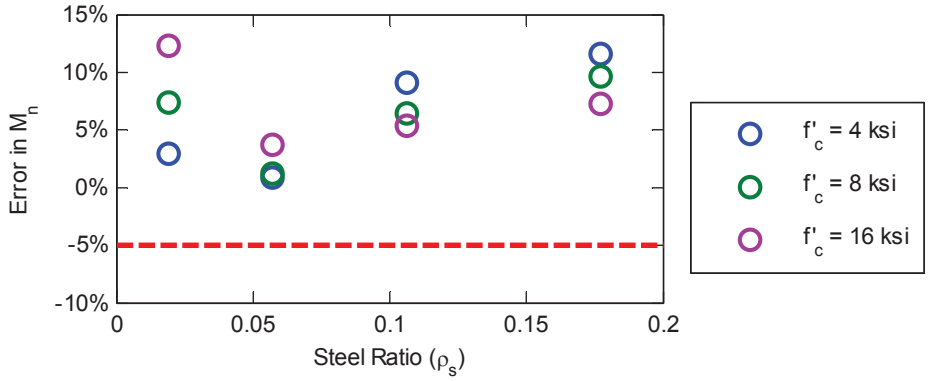

(a) CCFT

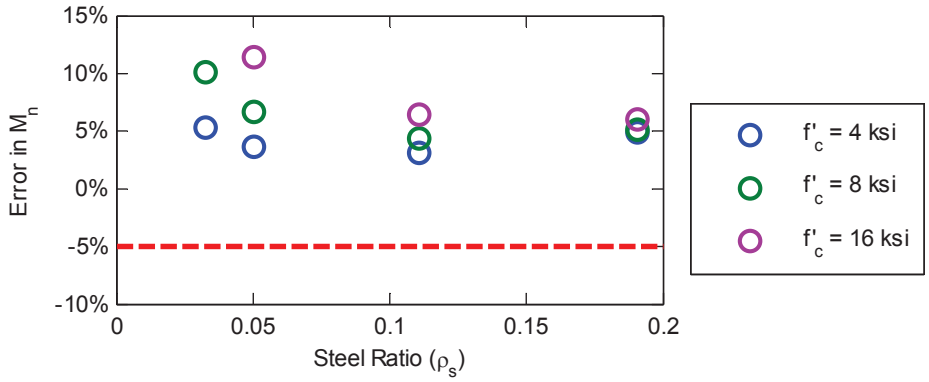

(b) RCFT

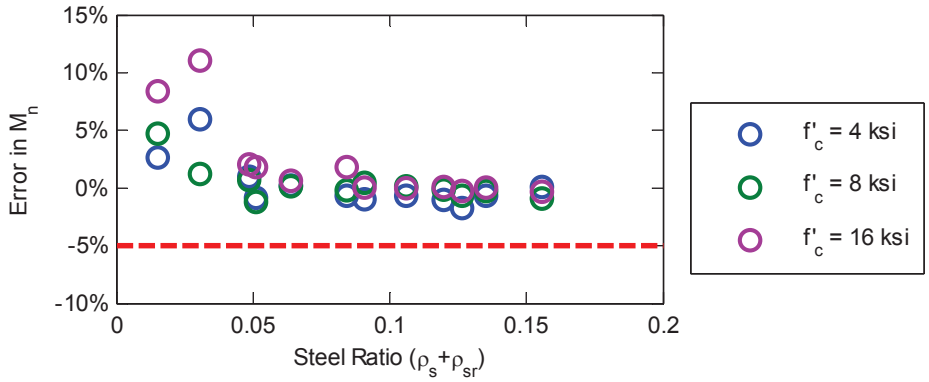

(c) SRC (strong axis)

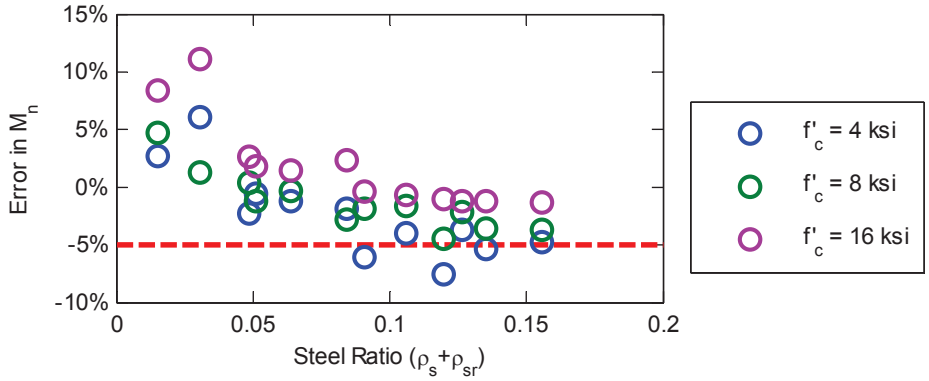

(d) SRC (weak axis)

Figure 6.12. Comparison of Nominal Flexural Strength of Composite Sections

6.7 Direct Analysis Method

Cross section strength curves for composite members are quite convex, especially for concrete dominant members. Beam-column strength curves are much less convex (and often concave) due to the fact that material nonlinearity (primarily concrete cracking but also concrete crushing and steel yielding) initiates at low load levels and severely reduces flexural rigidity. This effect is greater for more slender columns since the second-order effects are greater but also because the ratio of bending moment to axial load is greater, a condition which leads to greater reductions in effective slenderness (as seen in Section 4). An example of this variation with slenderness is shown in Figure 6.13 and Figure 6.14 where a series of interaction diagrams constructed with the fully nonlinear analyses are plotted. These figures correspond to section RCFT-E-4 (ρ_s = 3.27%, f'_c = 4 ksi) and a cantilever column with different lengths (i.e., sidesway uninhibited, fixed-free, K=2, leaning column load ratio = 0). Similar plots for all sections are presented in Appendix A.

For design methodologies in which the effective slenderness of the member is computed, it is possible for this variation to be accounted for directly in the shape of the design interaction diagram. For the Direct Analysis method, the effective slenderness is never computed, as the unsupported length of the member is used instead. Thus, unless the concave shape is accounted for otherwise, the strength of members with high effective length factors will be overestimated. Rigidity reductions that depend on both axial load and bending moment could potentially help account for the shape, but would be cumbersome in design. The proposed design methodology presented below accounts for these effects with modifications to the design interaction curve and is shown to be safe and accurate for all beam-columns with practical effective length factors (K<3). For beam-columns with large effective length factors, the unconservative error can sometimes exceed 5%, particularly for concrete dominant sections.

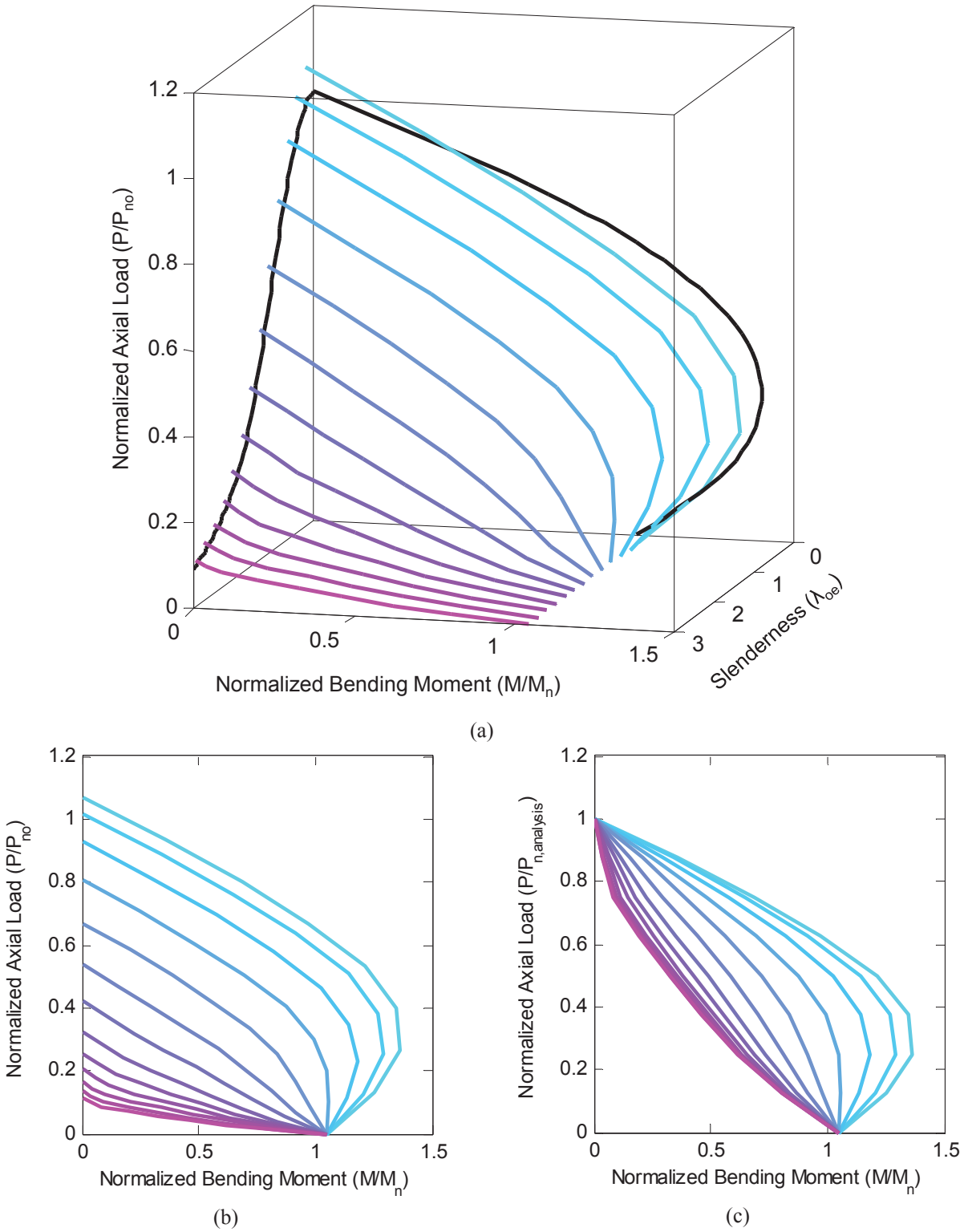

Figure 6.13. Variation of First-Order Interaction Strength with Slenderness

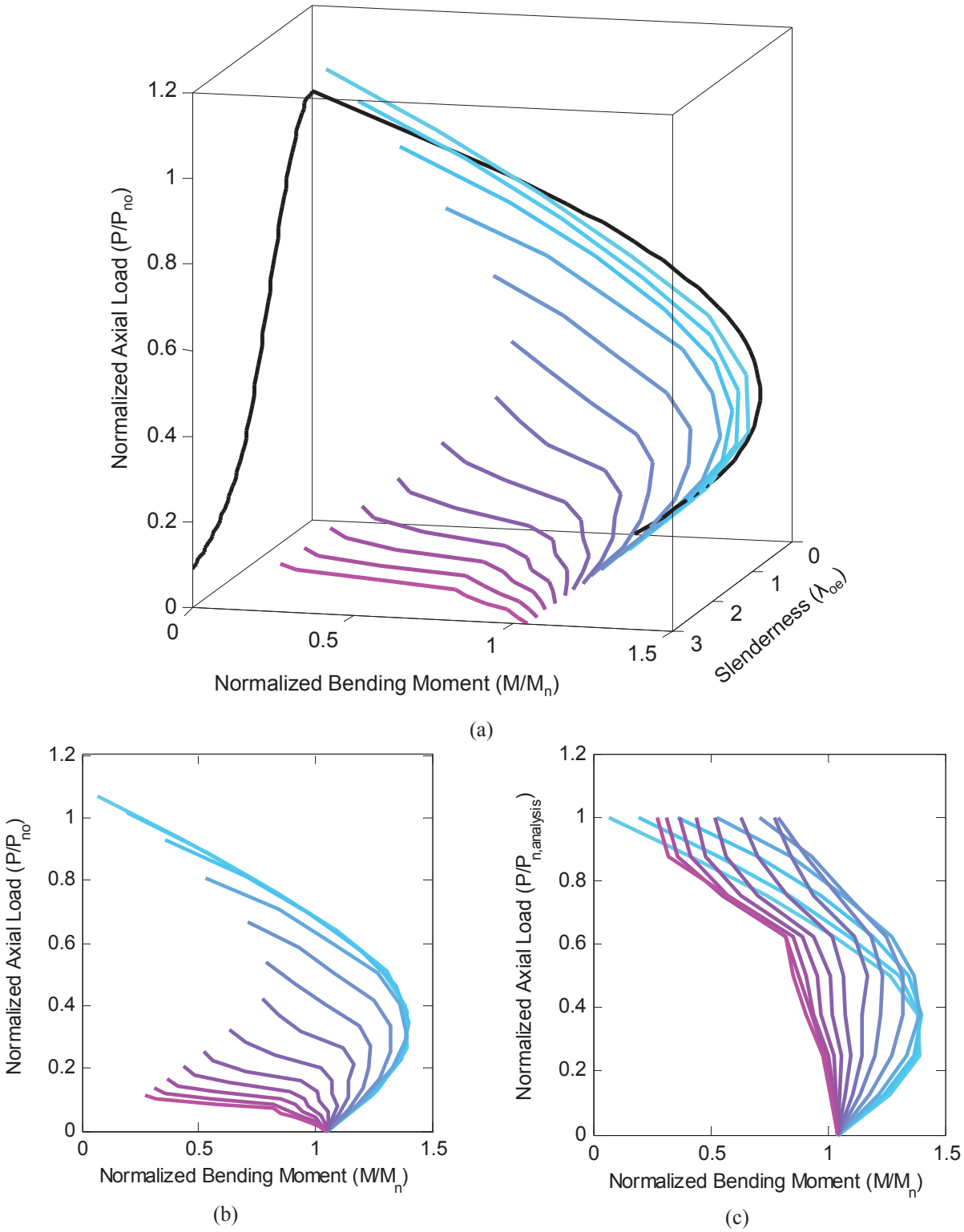

Figure 6.14. Variation of Second-Order Interaction Strength with Slenderness

6.7.1 Calculation of Required Strength

As prescribed in the Direct Analysis method, internal forces must be determined using a second-order elastic analysis with reduced elastic rigidity and consideration of initial imperfections. The reduced rigidity, EI_{DA}, for structural steel members is described by Equation 6.18 where τ_b depends on the required axial strength, P_r (Equation 6.19).

$$EI_{DA} = 0.8\tau_b EI_{elastic} \tag{6.18}$$

$$\tau_b = \begin{cases} 1.0 & \text{for } P_r/P_{no} \le 0.5 \\ 4\left(P_r/P_{no}\right)\left(1 - P_r/P_{no}\right) & \text{for } P_r/P_{no} > 0.5 \end{cases} \tag{6.19}$$

For simplicity in design and compatibility with the existing Direct Analysis procedure for steel members, it is beneficial to maintain the $0.8\tau_b$ factor and have differences in rigidity between steel and composite members manifest only in $EI_{elastic}$. There are several important considerations in the determination of an appropriate value of $EI_{elasitc}$. Even at loading levels below typical service load levels (e.g., those identified in Figure 4), this rigidity must account for the cracking and initial damage that accrues in the member at under combined axial load and bending moment. Additional load-based terms (beyond τ_b) in the expression for EI_{DA} (e.g., as seen in Equations 6.8-6.11 for a possible variation on $EI_{elastic}$) would be cumbersome and thus load-independent expressions roughly representative of $EI_{elastic}$ for members with high-moment low-axial service loads were selected. It is also important that the ratio of EI_{eff} to EI_{DA} is approximately equal to $0.877\phi_c$ (where ϕ_c is the resistance factor for axial compression (AISC 2010b)) for slender members in certain configurations so that the axial strength is not overestimated when performing the Direct Analysis method (Surovek-Maleck and White 2004a). A proposed expression for $EI_{elastic}$ for use with the Direct Analysis method is given by Equation 6.20 for SRCs and Equation 6.21 for CFTs. The factors C_1 and C_3 are the same as those in computation of EI_{eff} and are given in Equation 6.17 and 6.4 respectively. The validity of this expression for use in the Direct Analysis method is confirmed though the comparisons presented later in this section. It is likely that this expression is also valid for other purposes (e.g., those described in Section 1) but comprehensive studies have not been performed to confirm such a wide applicability.

$$EI_{elastic} = E_s I_s + E_s I_{sr} + 0.75 C_1 E_c I_c \qquad \text{(SRC)} \tag{6.20}$$

$$EI_{elastic} = E_s I_s + 0.75 C_3 E_c I_c \qquad \text{(CFT)} \tag{6.21}$$

Initial imperfections can either be directly modeled (as was done in the fully nonlinear analyses) or represented with notional loads. For these comparisons the notional load approach was used in the design methodology, applying an additional lateral load of 0.2% of the vertical load in each analysis. The AISC *Specification* (AISC 2010b sec. C2.2b(4)) allows the notional load to be taken as a minimum load when the ratio of maximum second-order drift to maximum first-order drift is less than or equal to 1.7. However, for this study the notional load was additive for all analyses.

6.7.2 Calculation of Available Strength

The commentary of the AISC *Specification* (2010b) describes a method of determining the design interaction curve based on the plastic stress distribution method. Three specific points on the section interaction diagram are computed: Point A, the pure axial strength; Point B, the pure bending strength; and Point C, a point with combined loading where the moment is equal to the pure bending strength. The axial strength of each of these points is then reduced by a factor $\chi = P_n/P_{no}$ to obtain the beam-column interaction diagram (Figure 6.15a). For the Direct Analysis method, P_n is computed using K=1.

The commentary methodology performs well for short and moderate length columns; however, it becomes less accurate for slender and concrete dominant columns, where the applied load interaction curve is noticeably concave as seen in Figure 6.13. Proposed modifications to this methodology are illustrated in Figure 6.15b. The same section strength is used as the basis, but points C and B are moved inward by factors that depend on the slenderness. The factor α_c (Equation 6.22) ranges from P_C/P_A for stocky columns, resulting in the same axial load for point C as in the existing method, and 0.2 for slender columns, resulting in an interaction diagram equivalent to that for structural steel columns (AISC 2010b). The factor α_B (Equation 6.23) is not meant to represent a physical reduction in the flexural strength but rather it is a practical option for accounting for the low axial strength of slender columns under large bending loads where the rigidity is severely reduced due to concrete cracking.

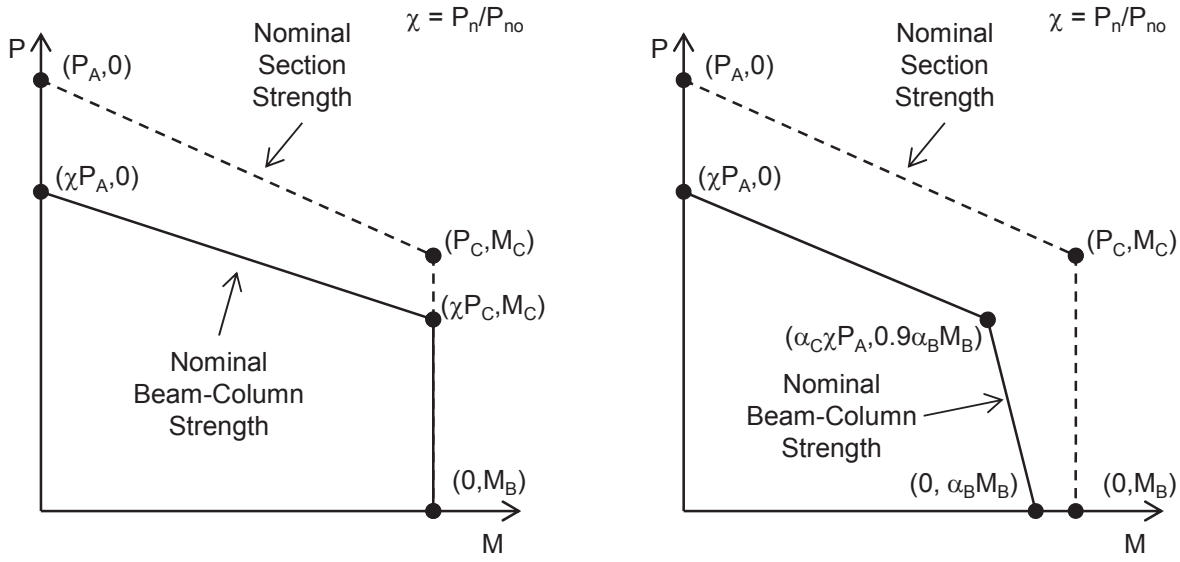

(a) AISC 2010 (b) Proposed

Figure 6.15. Computation of the Design Strength Interaction

$$\alpha_C = \begin{cases} P_C/P_A & \text{for } \lambda_{oe} \le 0.5 \\ P_C/P_A - \left(P_C/P_A - 0.2\right)\left(\lambda_{oe} - 0.5\right) & \text{for } 0.5 < \lambda_{oe} \le 1.5 \\ 0.2 & \text{for } \lambda_{oe} > 1.5 \end{cases} \tag{6.22}$$

$$\alpha_B = \begin{cases} 1 & \text{for } \lambda_{oe} \le 1 \\ 1 - 0.2\left(\lambda_{oe} - 1\right) & \text{for } 1 < \lambda_{oe} \le 2 \\ 0.8 & \text{for } \lambda_{oe} > 2 \end{cases} \tag{6.23}$$

6.7.3 Evaluation of the Proposed Design Methodology

To evaluate the validity of the proposed beam-column design methodology, interaction diagrams based on the proposed recommendations are constructed. Sample results for two RCFT sections and one frame are shown in Figure 6.16 along with the interaction diagrams from the fully nonlinear analyses (blue lines) as described in Section 6.3.3. The second-order internal force interaction diagram (green dashed lines) is constructed directly from the design equations (Figure 6.15b). The first-order applied load interaction diagram (green solid lines) is constructed by determining the applied loads that, when applied in a second-order elastic analysis with stiffness reduction (Equations 6.18-6.21) and notional load, result in peak internal forces that lay on the internal force interaction diagram. The comparisons are performed at the nominal strength level and thus neither resistance factors nor safety factors were used in the computation of the interaction diagrams. Similar plots showing a range of behavior for all sections are presented in Appendix A.

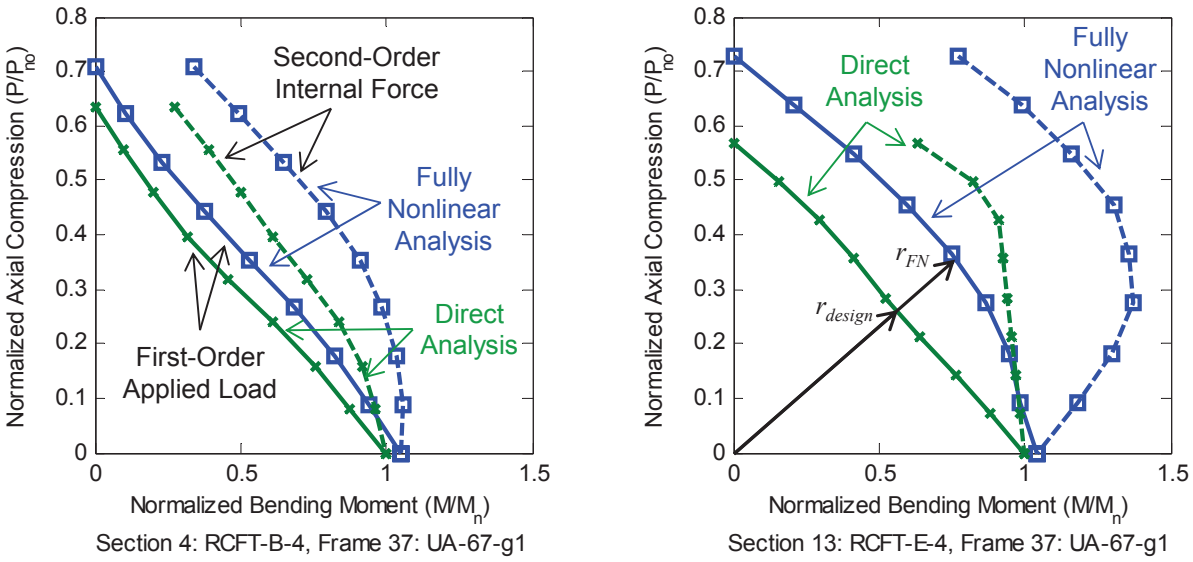

Figure 6.16. Example Results: Fully Nonlinear and Design Applied Load and Internal Force Interaction Diagrams

Error is computed between the fully nonlinear analysis interaction diagrams and the Direct Analysis interaction diagrams using a radial measure (Equation 6.24), where r_{FN} is the distance from the origin to the interaction diagram constructed from the fully nonlinear analyses and r_{design} is the distance along the same line to the interaction diagram constructed from the

design methodology. For the first-order applied load interaction diagram unconservative error is negative (e.g., when the green curve lies outside the blue curve in Figure 6.16).

$$\varepsilon = \frac{r_{FN} - r_{design}}{r_{FN}} \tag{6.24}$$

Using the radial error, interaction diagrams for different pairs of sections and frames can be compared. An example of this is shown in Figure 6.17 where the design applied load interaction diagrams for the two RCFT sections shown previously and all 84 frames are compared. The black line (a circle with a radius of one) represents the applied load interaction diagram from the fully nonlinear analyses. The colored lines were constructed by computing the error (Equation 6.24) for a sweep of angles and for the same angles plotting points with a distance of 1 – ε from the origin. The colors correspond to the effective length factor of the frame. A colored line outside the black line represents unconservative error and 5% unconservative error is noted by the red dashed line. Similar plots for all sections are presented in Appendix A.

In Figure 6.17, the effect of the effective length factor on the accuracy of the design methodology for these particular cross sections can be seen. Frames with low effective length factors (cyan lines) tend to be more conservative while frames with high effective length factors (magenta lines) tend to be less conservative. For the more concrete dominant section (Figure 6.17b) the frames with high effective length factors are sometimes greater than 5% unconservative. In the Direct Analyses, the effective length factor is never computed and thus it is difficult to properly account for these extreme cases without being unduly conservative in more common cases.

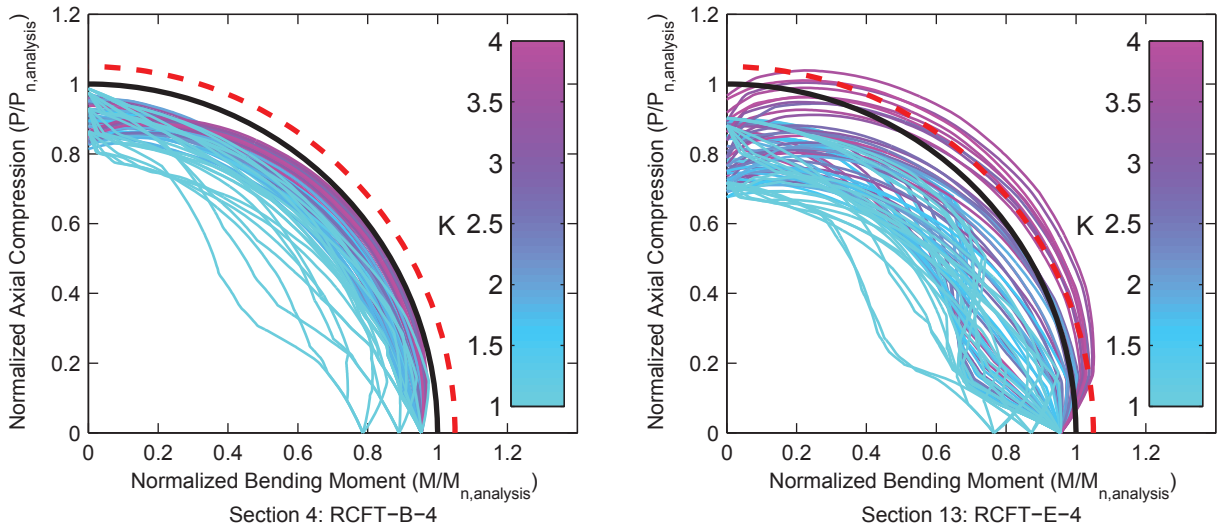

Figure 6.17. Example Results: Normalized Fully Nonlinear and Design Applied Load Interaction Diagrams

Histograms for each section type showing the relative frequency of the radial error from the first-order applied load interaction diagrams from all sections and frames and through a sweep of angles are shown in Figure 6.18 (conservative is shown as positive). A total of 84

(frames) × 15 (sections) = 1,260 sets of interaction diagrams are generated each for RCFTs and CCFTs, and 84 (frames) × 36 (sections) = 3,024 sets of interaction diagrams are generated each for strong and weak axis bending of SRCs. The median error (shown as a vertical dashed line in Figure 6.18) and the worst unconservative error for each of the section types are listed in Table 6.6.

Table 6.6. Summary Error Statistics

Section Type	Median Error	Worst Unconservative Error
CCFT	10.8%	–28.9%
RCFT	12.1%	–18.3%
SRC (strong axis)	17.4%	–23.6%
SRC (weak axis)	15.1%	–27.0%

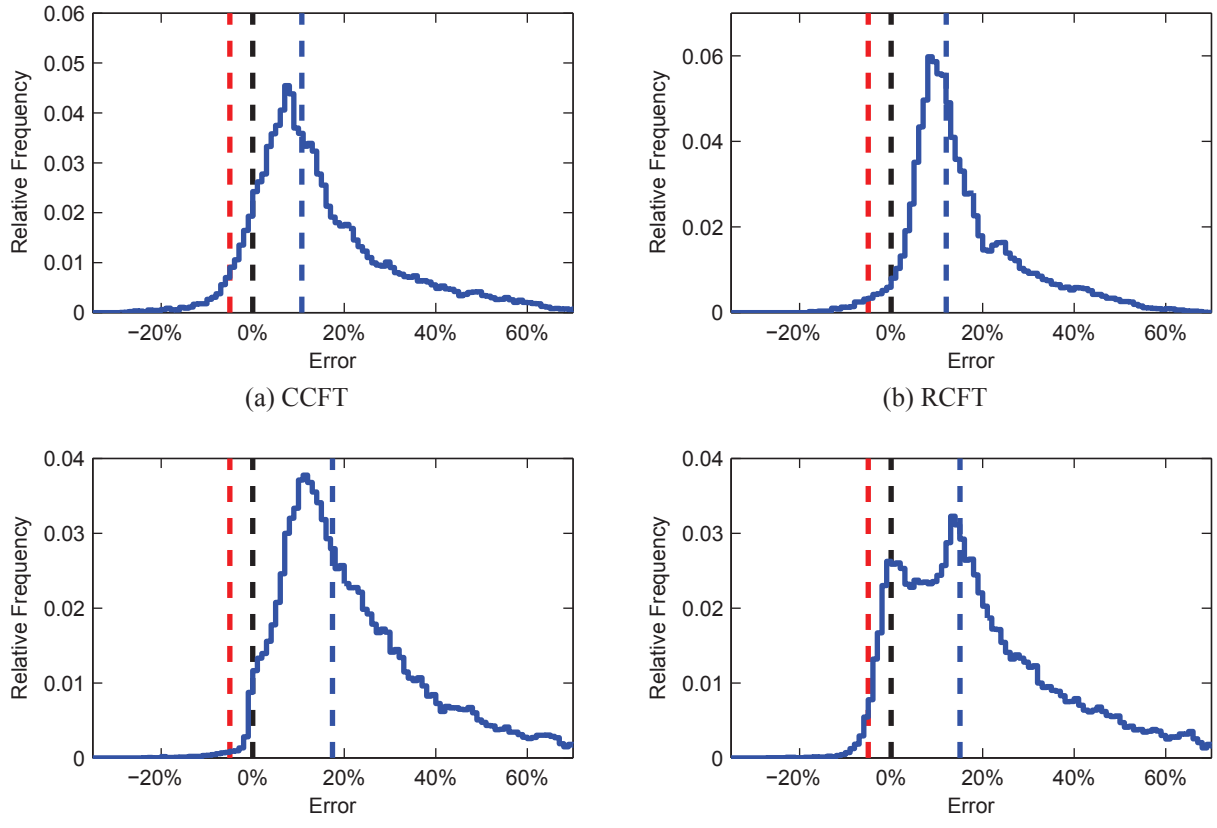

(a) CCFT (b) RCFT

(c) SRC (strong axis) (d) SRC (weak axis)

Figure 6.18. Summary Error Statistics

A maximum of 5% unconservative error is desired (ASCE 1997). The proposed design methodology achieves this for most cases. Exceptions are:

- Members with high effective length factors (e.g., an effective length factor, *K*, greater than approximately 3). An example of this error is shown in Figure 6.19.

- Steel dominant CCFT members where the axial compressive strength, P_n, is overpredicted by the design equations, as shown in Figure 6.7a.
- Steel dominant weak axis SRC members where the flexural strength, M_n, is overpredicted by the design equations, as shown in Figure 6.12b

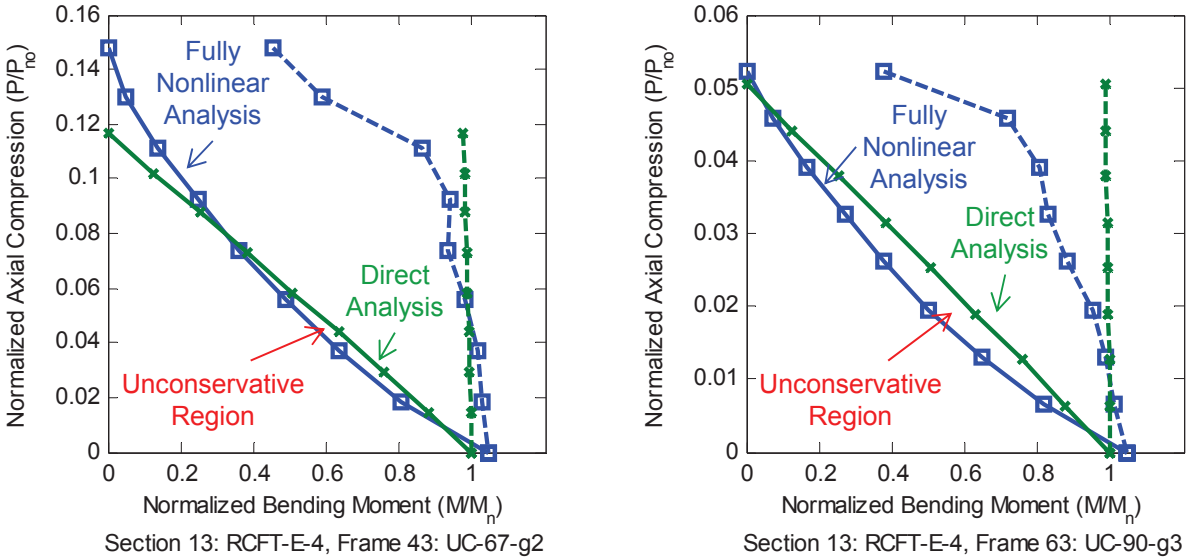

Figure 6.19. Example Results: Unconservative Error for High Effective Length Factor Cases

6.8 Alternative Methods of Design

The AISC *Specification* (2010b) allows variations on the Direct Analysis method as well as alternative methods of design including the effective length method. These methods are investigated in this study by treating each variation as a separate design methodology and evaluating them as described previously against the fully nonlinear solutions (Section 6.7.3).

The alternative methods of design investigated in this work are summarized in Table 6.7. The Direct Analysis method evaluated previously in Section 6.7 is denoted as "Method A". Two additional methods are investigated.

Table 6.7. Description of Alternative Methods of Design

Method Index	$EI_{elastic}$	Stiffness Reduction	Imperfections/ Notional Loads	Interaction Diagram	K
A	Proposed (Equations 6.20 and 6.21)	$0.8\tau_b$	$N_i = 0.002Y_i$ (Additive)	Proposed (Figure 6.15b)	1.0
B	Proposed (Equations 6.20 and 6.21)	0.8	$N_i = 0.003Y_i$ (Additive)	Proposed (Figure 6.15b)	1.0
C	Proposed (Equations 6.20 and 6.21)	None	$N_i = 0.002Y_i$ (Minimum)	Proposed (Figure 6.15b)	K

Use of the τ_b factor (Equation 6.19) in elastic analyses is somewhat cumbersome. The AISC *Specification* recognizes this and allows it to be taken as unity for all cases (i.e., $EI_{DA} = 0.8EI_{elastic}$) if an additional notional load of 0.001 of the gravity load is applied (AISC 2010b). This variation is denoted as "Method B" (Table 6.7). For the vast majority of composite frame and section pairs studied in this work, this methodology does not result in a maximum unconservative error greater than that obtained for "Method A", indicating that it is safe. The few cases in which the maximum unconservative error is larger than that of "Method A" are CFTs of intermediate slenderness in the high axial load range. Detailed results, including interaction diagrams, for these cases are given in Appendix A.

The effective length method was the primary method of design in the AISC *Specification* prior the Direct Analysis method, and is still allowed as an option to the engineer for cases where the ratio of maximum second-order drift to maximum first-order drift is less than or equal to 1.5. The effective length method ("Method C", Table 6.7) differs from the Direct Analysis method in that no stiffness reduction is used, notional loads are minimum lateral loads rather than additive lateral loads and the compressive strength is based on the effective length, *KL*. For the vast majority of composite frame and section pairs studied in this work, this methodology does not result in a maximum unconservative error greater than that obtained for "Method A", indicating that it is safe. The few cases in which the maximum unconservative error is larger than that of "Method A" and exceed the 5% unconservative limit are sidesway inhibited CFTs of intermediate to high slenderness. It is noted that in this comparison, all frame and sections pairs were included without regard to the drift limit on the effective length method described above. Detailed results, including interaction diagrams, for these cases are given in Appendix A.

6.9 Aspects of Design Not Directly Addressed in this Study

6.9.1 Elastic Rigidities Other than *EI*

Only flexural deformations were considered in the elastic analyses performed in this study, thus only the flexural rigidity, *EI*, was directly addressed. However, in the general case other rigidities contribute to the stability of the structure and their values should be carefully selected.

In the ACI *Code* (ACI 2011), the axial rigidity, *EA*, for reinforced concrete columns is taken as E_cA_g. Similarly, Schiller, Hajjar, and Gourley (1994) recommend using the gross section properties when determining *EA* for RCFT members (i.e., $EA = E_sA_s + E_cA_c$). Based on these existing recommendations, $EA_{elastic}$ should be taken as the gross section properties (Equation 6.25). For the Direct Analysis method, that rigidity should be reduced by a factor of 0.8 (Equation 6.26).

$$EA_{elastic} = E_s A_s + E_c A_c + E_s A_{sr} \tag{6.25}$$

$$EA_{DA} = 0.8EA_{elastic} \tag{6.26}$$

The torsional rigidity, *GJ*, is necessary for three-dimensional analyses. For CCFT and RCFT members, project collaborators (Perea 2010) developed recommended expressions for the torsional rigidity based on the full scale slender beam-column tests described in Chapter 2. For SRC members, no suitable expressions for *GJ* have been found in the literature, so it is

recommended to use the torsional rigidity of either the steel or concrete sections alone. For the Direct Analysis method, the rigidity should be reduced by a factor of 0.8.

The shear rigidity, *GA*, is necessary when shear deformations are included in the elastic model (i.e. Timoshenko beam theory). Tomii and Sakino (1979) performed experiments on RCFT members and recommended an expression for *GA*. For CCFT and SRC members, no suitable expressions for *GA* have been found in the literature, so it is recommended to use the shear rigidity of either the steel or concrete sections alone. For the Direct Analysis method, the rigidity should be reduced by a factor of 0.8.

6.9.2 Suitability of $EI_{elastic}$ for General Use

In this study, expressions for $EI_{elastic}$ were developed and recommended for design. A range of uses for $EI_{elastic}$ are noted in Section 6.1, but these expressions (Equation 6.20 for SRCs and Equation 6.21 for CFTs) were only explicitly validated for use in the execution of strength checks. However, the expressions may still be appropriate for the other uses.

The recommended expressions for $EI_{elastic}$ represent a practical lower bound on the elastic stiffness. This can be seen by comparing the recommended expressions for $EI_{elastic}$ (Equation 6.20 for SRCs and Equation 6.21 for CFTs) the more detailed expressions for $EI_{elastic}$ that depend on the loading level (Equations 6.8 and 6.9 for SRCs and Equations 6.10 and 6.11 for CFTs). The recommended and more detailed expressions result in the same value along lines in axial load-bending moment space as shown in Figure 6.20. The black dashed lines in Figure 6.20 are intended to schematically represent the current simplified A-C-B strength interaction diagram as described in the commentary of the AISC *Specification* (2010b); the ratio of axial compression at point A and point C was selected arbitrarily. The recommended expressions underestimate $EI_{elastic}$ with respect to the more detailed expressions in only a small region of the interaction diagram with high bending moments and low axial loads.

Being a practical lower bound, the recommended expressions can be considered conservative for the assessment of quantities such as drift. Nonetheless, a more detailed study is warranted to examine the accuracy the recommended expression for $EI_{elastic}$ for other uses in design.

6.9.3 Long-Term Effects Due to Creep and Shrinkage

The contribution of creep and shrinkage to structural instability was not addressed in this study. The ACI *Code* (ACI 2011) combines and addresses these effects with the use of beta factors when determining the elastic rigidities. A similar approach could be taken for composite columns, applying the beta factor to the concrete contribution to the elastic rigidities. However, a more detailed study is warranted to examine long-term effects.

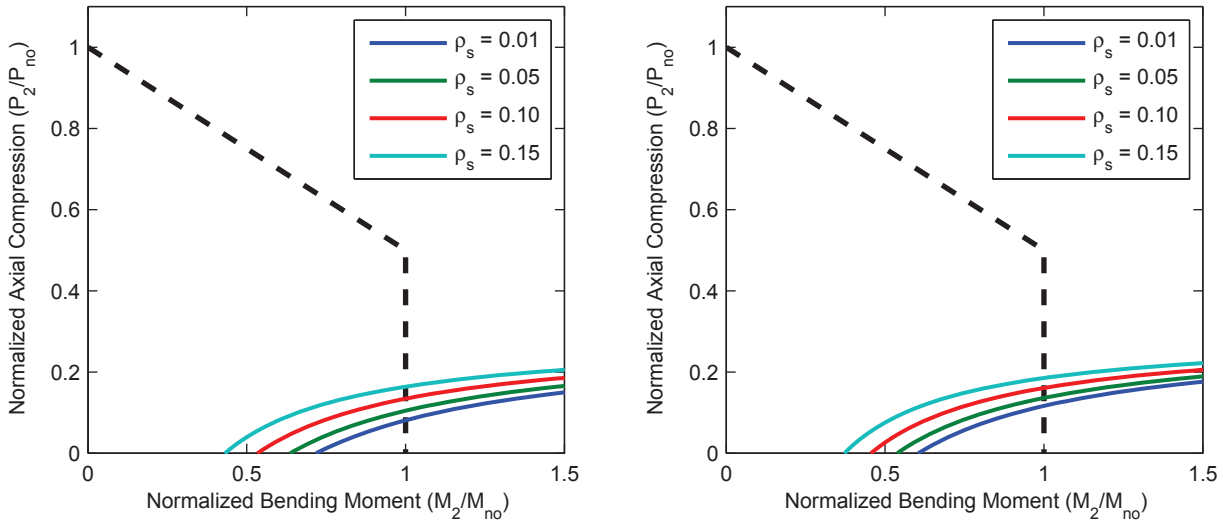

(a) CCFT

(b) RCFT

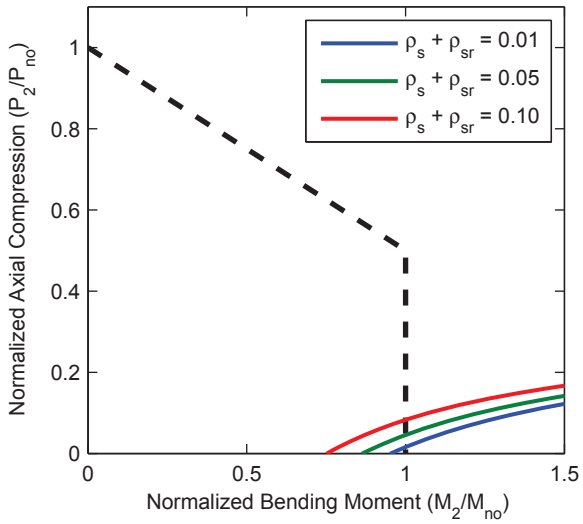

(c) SRC (strong axis)

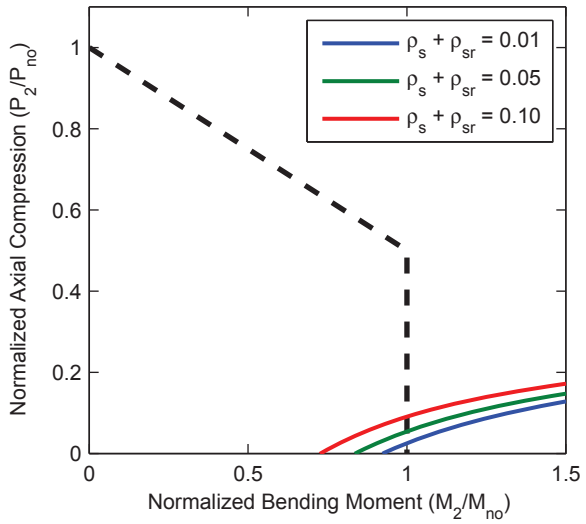

(d) SRC (weak axis)

Figure 6.20. Comparison of Expressions for $EI_{elastic}$

6.9.4 Biaxial Bending

Biaxial bending was not specifically included in this study, but recommendations can be made by extrapolating current design provisions. The strength of composite members subjected to flexure and axial compression may be evaluated by Equation 6.27.

When $P_r \geq \alpha_c \chi P_A$

$$\frac{P_r}{\chi P_A} + \frac{1-\alpha_C}{0.9}\left(\frac{M_{rx}}{\alpha_B M_{Bx}} + \frac{M_{ry}}{\alpha_B M_{By}}\right) \leq 1.0 \qquad (6.27a)$$

When $P_r < \alpha_c \chi P_A$

$$\frac{0.1P_r}{\alpha_C \chi P_A} + \left(\frac{M_{rx}}{\alpha_B M_{Bx}} + \frac{M_{ry}}{\alpha_B M_{By}} \right) \leq 1.0 \tag{6.27b}$$

where,

P_r = required axial strength
M_{rx} = required flexural strength in the strong axis
M_{Bx} = available flexural strength at point B in the strong axis
M_{ry} = required flexural strength in the weak axis
M_{By} = available flexural strength at point B in the weak axis

The parameters χ, α_C and α_B should be computed for both the strong and weak axes and the minimum of each should be used.

These recommendation imply a diamond shaped M_x-M_y interaction curve at any given axial load, this is conservative when compared to the results of the slender beam-column tests conducted by project collaborators (Perea 2010) which indicate that the shape is more convex.

6.10 Conclusions

This chapter presents the results of a large parametric study undertaken to assess the in-plane stability behavior of steel-concrete composite members, evaluate current design provisions, and develop and validate new design recommendations. This research has developed new elastic flexural rigidities for elastic analysis of composite members; new effective flexural rigidities for calculating the axial compressive strength of SRC members; and new recommendations for the construction of the interaction diagram for composite members.

The new recommendations provide a smooth transition between steel-concrete composite design and structural steel design for increasingly steel dominant members. Ideally, a smooth transition would also exist between steel-concrete composite design and reinforced concrete design for increasingly concrete dominant members; however, the different assumptions and simplifications employed by the AISC *Specification* (2010b) and ACI Code (2011) make such continuity challenging.

The proposed beam-column design methodology is safe and accurate for the vast majority of common cases of composite member behavior, although further research is recommended to continue to investigate the axial compressive strength of steel dominant CCFTs, the weak axis flexural strength of steel dominant SRCs, and members with very high effective length factors, so as to improve the recommendations. Detailed results, including representative figures for each section, are presented in Appendix A.

Chapter 7

EXPERIMENTAL EVALUATION AND EVOLUTION OF BEAM-COLUMN INTERACTION STRENGTH

A series of full-scale slender concrete-filled steel tube beam-column tests have been conducted at the NEES MAST Laboratory at the University of Minnesota (Figure 7.1), led by project collaborators (Perea 2010). These tests were introduced in Chapter 2; this chapter contains comparative computational results using the mixed formulation and detailed data interpretation focusing on the beam-column interaction strength.

Figure 7.1. Specimen 2C12-18-5 in the MAST Laboratory

7.1 Full-Scale Slender Concrete-Filled Steel Tube Beam-Column Tests

The specimens consisted of one CFT column with base plates welded on either end. Eighteen specimens were tested with variations in length, concrete strength, tube shape, tube size, bending axis. A text matrix showing measured material and geometric properties as well as measured out-of-plumbness is given in Table 7.1. The bases of the specimens were bolted to the strong floor, providing a rigid constraint. The tops of the specimens were bolted to the crosshead which, for the specimens and loading discussed in this chapter, was controlled so as to approximate a free boundary condition.

The loading protocol for each specimen is divided into several load cases. In the first load case, LC1, the specimens were subjected to concentric axial loading; cycles were performed in displacement control up the peak strength or load capacity of the actuators. In the second load case, LC2, the specimens were subjected to constant axial compression plus uniaxial flexure imposed by controlling the top in a prescribed displacement pattern. The third load case, LC3, is the same as LC2 but the prescribed displacement pattern imposed biaxial flexure on the beam-column. The biaxial load patterns used are shown schematically in Figure 7.2. Additional load cases were performed but are not described in this work. Details of the loading protocol for each specimen, including number of cycles for LC1 and axial load levels for LC2 and LC3 are given in Table 7.2.

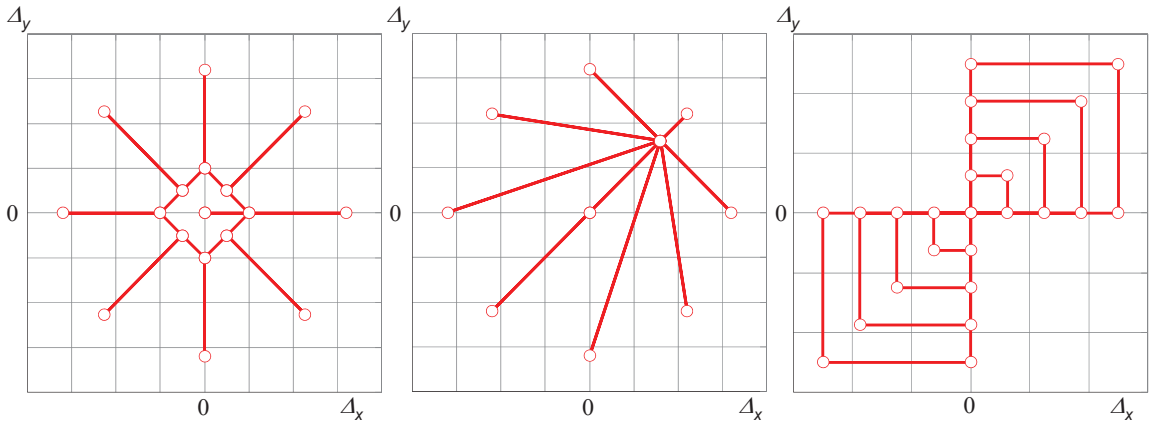

Figure 7.2. Displacement Patterns Used in Load Case 3

A variety of instruments were used to record the behavior of the specimens (Perea 2010). Of primary importance to these studies were the three-dimensional forces, moments, displacements, and rotations recorded at the top of the column. From these measurements, the three-dimensional forces and moments at the base are be computed by the principles of statics (Equation 7.1).

$$\begin{aligned} \mathbf{F}_{\text{base}} &= -\mathbf{F}_{\text{top}} \\ \mathbf{M}_{\text{base}} &= -\mathbf{M}_{\text{top}} - \mathbf{r} \times \mathbf{F}_{\text{top}} \end{aligned} \tag{7.1}$$

where,

$$\mathbf{F_{base}} = \begin{bmatrix} F_{x,base} & F_{y,base} & F_{z,base} \end{bmatrix}$$
$$\mathbf{F_{top}} = \begin{bmatrix} F_{x,top} & F_{y,top} & F_{z,top} \end{bmatrix}$$
$$\mathbf{M_{base}} = \begin{bmatrix} M_{x,base} & M_{y,base} & M_{z,base} \end{bmatrix}$$
$$\mathbf{M_{top}} = \begin{bmatrix} M_{x,top} & M_{y,top} & M_{z,top} \end{bmatrix}$$
$$\mathbf{r} = \begin{bmatrix} D_{x,top} & D_{y,top} & L + D_{z,top} \end{bmatrix}$$

$\times$ represents the cross product

In LC1 and LC2, the specimen was loaded uniaxially, but for the CCFT specimens, not necessarily along one of the coordinate axes. In these cases, a uniaxial response is obtained by projecting the biaxial response on a plane in the direction of motion (Equation 7.2) .

$$D_{x'} = \cos(\alpha) D_x + \sin(\alpha) D_y \tag{7.2a}$$

$$F_{x'} = \cos(\alpha) F_x + \sin(\alpha) F_y \tag{7.2b}$$

$$M_{x'} = \cos(\alpha - \tfrac{\pi}{2}) M_x + \sin(\alpha - \tfrac{\pi}{2}) M_y \tag{7.2c}$$

where,

α = Angle of the direction of motion (Table 7.2)

Table 7.1. Material and Geometric Properties of the Slender Beam-Column Specimens

Specimen	D or H (in)	B (in)	t (in)	D/t or H/t	f'_c (ksi)	F_y (ksi)	F_u (ksi)	L (in)	Δ_{ox} (in)	Δ_{oy} (in)
1-C5-18-5	5.563	---	0.124	44.9	5.5	55.6	70.7	216.5	0.00	0.00
2-C12-18-5	12.75	---	0.233	54.7	5.6	48.9	64.7	216.5	0.75	-0.32
3-C20-18-5	20	---	0.233	85.8	5.8	47.6	68.3	217.5	0.40	-0.87
4-Rw-18-5	20	12	0.291	68.7	5.9	53.0	72.8	218.0	1.34	0.00
5-Rs-18-5	20	12	0.291	68.7	5.9	53.0	72.8	218.0	-0.08	0.45
6-C12-18-12	12.75	---	0.233	54.7	13.2	48.9	64.7	216.5	0.36	-0.24
7-C20-18-12	20	---	0.233	85.8	13.2	47.6	68.3	217.9	-0.30	-0.47
8-Rw-18-12	20	12	0.291	68.7	13.3	53.0	72.8	218.6	1.81	-0.63
9-Rs-18-12	20	12	0.291	68.7	13.3	53.0	72.8	218.6	0.82	-0.24
10-C12-26-5	12.75	---	0.233	54.7	7.9	48.6	68.1	313.0	0.79	-0.63
11-C20-26-5	20	---	0.233	85.8	8.1	44.3	69.2	314.8	0.59	-2.12
12-Rw-26-5	20	12	0.291	68.7	8.2	58.9	77.4	313.3	0.63	0.00
13-Rs-26-5	20	12	0.291	68.7	8.3	55.5	73.2	313.8	0.68	0.00
14-C12-26-12	12.75	---	0.233	54.7	11.6	55.5	66.8	313.5	0.12	-0.66
15-C20-26-12	20	---	0.233	85.8	11.6	42.5	65.8	314.0	0.24	1.62
16-Rw-26-12	20	12	0.291	68.7	11.7	55.2	73.4	313.3	-0.60	0.00
17-Rs-26-12	20	12	0.291	68.7	11.7	55.1	71.9	313.5	1.68	0.00
18-C5-26-12	5.563	---	0.124	44.9	11.7	55.6	70.7	312.6	0.00	0.00

Table 7.2. Loading Data from the Slender Beam-Column Specimens

Specimen	*Load Case 1*		*Load Case 2*				*Load Case 3*		
	Number of Cycles	Direction of Motion (rad)	Axial Load 2a (kips)	2b (kips)	2c (kips)	Direction of Motion (rad)	Axial Load 3a (kips)	3a (kips)	3c (kips)
2-C12-18-5	2	-0.70	300	200	100	0	250	150	
3-C20-18-5	3	-1.38	1000	500		-1.28	1250	750	250
4-Rw-18-5	2	0	600	300		0	750	450	150
5-Rs-18-5	2	0	1000	500		0	750	250	
6-C12-18-12	2	1.27	300	150		1.29	375	225	75
7-C20-18-12	2	1.11	1000	500		1.11	1250		
8-Rw-18-12	2	0	600	300		0	800		
9-Rs-18-12	2	0	1200	400		0	800		
10-C12-26-5	1	-0.39	200	100		-0.87	150	50	
11-C20-26-5	2	-1.38	600	300		-1.31	450	150	
12-Rw-26-5	1	0	400	200		0	300	500	
13-Rs-26-5	2	0	400	800		0	300	500	
14-C12-26-12	1	1.47	100	200		0.78	150		
15-C20-26-12	2	1.01	400	800		0.78	200	600	
16-Rw-26-12	1	0	200	400		0	300	500	
17-Rs-26-12	1	0	400	800		0	200	600	

7.2 Comparison of Experimental and Computational Results

A comparison of experimental and computational results serves to validate both the experiments and the analytical model. Analyses were performed using the mixed finite element formulation of load cases LC1, LC2, and LC3 for all specimens with the exception of 1C5-18-5 and 18C5-26-12 (which were held in a different configuration than the others).

The specimens were analyzed using the "Proposed for Behavior" model (described in Chapter 3) with two elements along the length, each with three integration points. This mesh density was selected because for cases where the specimen exhibits hardening behavior little accuracy will be gained with additional elements or integration points and for cases where the specimen exhibits softening behavior additional elements or integration points would result in less accurate results because of localization. With this mesh density, the integration weight for the section located at the specimen base corresponds to 8.3% of the specimen length. This value is somewhat less than the plastic hinge length indicated by cross section analysis (Chapter 3). A dense fiber discretization was used, with nominal size of the fibers equal to $1/30^{th}$ of the width of the section in each direction. The specimens were modeled as perfectly straight but out-of-plumb by the measured amount (Table 7.1). The base was fully fixed against translation and rotation for the entirety of the loading. The top was controlled to replicate the loading from the experiment.

The analysis of the first load case, consisting of concentric loading, was completed in displacement control, up to the displacements experienced experimentally by the specimen. Or, for the specimens which reached actuator load limits, the analyses were conducted in load control up to the applied axial load. To ensure that the direction of motion in the analysis was the same as that of the specimen, a stiff spring was introduced perpendicular to the observed direction of motion. This spring was removed upon completion of the first load case. The later load cases, including both uniaxial cyclic and biaxial cyclic loading, used the same control as in the experiment: the horizontal DOFs were under displacement control while the vertical DOF was under force control.

Observations of the experimental data indicate that non-negligible friction existed in the crosshead. The crosshead friction is most clearly evident at the reversals in LC2, where a very stiff response is seen, resulting in a jump in transverse load of approximately 8.9 kN (2 kips). To account for this friction, zero length springs were added at the top of the column in the transverse (X and Y) directions as shown schematically in Figure 7.3. The constitutive model associated with the zero length springs was elastic-perfectly plastic with a yield force of 4.45 kN (1 kip, half of the value in transverse load observed in friction-related response in the experimental data). The stiffness of the elastic portion was selected such that the transition from positive to negative yielding occurred at a displacement less than the displacement step size used in the analysis, thus minimizing the influence of the spring on the nonlinear solution. Also, these springs were not used in the first load case. While friction in the crosshead is presumed to still be significant in the first load case, it is not modeled since the zero length springs described above, which are appropriate for the later load cases, lead to inappropriate results for the first load case, and a more accurate model is not readily attainable. For the first load case, the control of the specimen in the transverse directions was different as compared to the remainder of each experiment (i.e., for the first load case, the transverse directions were in force control rather than displacement control). These forces were controlled to be zero, and thus the spring force provided an artificial constraint that inappropriately dominated the results. Other than not being present in the first

load case of each specimen, the springs modeling crosshead friction were included throughout the loading history and for all specimens.

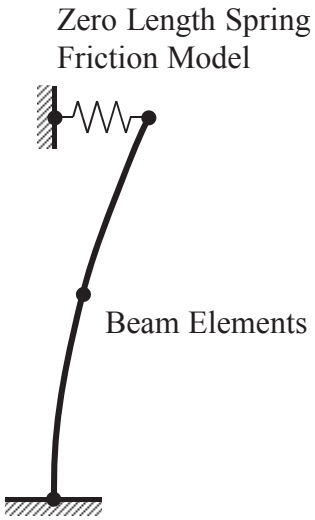

Figure 7.3. Schematic Representation of Friction Model

Experimental and analytical results are presented in Figure 7.4 through Figure 7.19 for specimens 2C12-18-5 through 17Rs-26-12. The main results (e.g., load, deformation, and moment) values for each load case are shown as separate plots. The following observations are made regarding the comparison between the experimental and analytical results:

- An overall excellent correlation is seen between the experimental and analytical results.
- Some specimens (4Rw-18-5, 10C12-26-5, 12Rw-26-5, 14C12-26-12, and 16Rw-26-12) exhibited a much greater strength in the experiment as compared to the analysis. These high loads have been noted elsewhere (Perea et al. 2012) and are likely due to friction in the crosshead.
- The experimental results of LC1 exhibit much greater hysteresis than the analysis results. This is likely due to friction in the crosshead.
- The analytical results of LC2 and LC3 for some specimens (4Rw-18-5, 5Rs-18-5, 9Rs-18-12, 12Rw-26-5, 13Rs-26-5) show earlier peaks and fuller hysteresis than the experimental results. The cause of these discrepancies is not known, but they could be related to discrepancies in the level of damage of the specimen at the time of the load case, because often later results compare well. Also, the elastic stiffness is typically captured well.
- For other specimens (10C12-26-5, 14C12-26-12, and 16Rw-26-12) the experimental and computational results of LC2 and LC3 also do not compare well, however, the magnitude of the force at the top is small (~2 kips) and differences could be due to limitations in the control of the experiments.

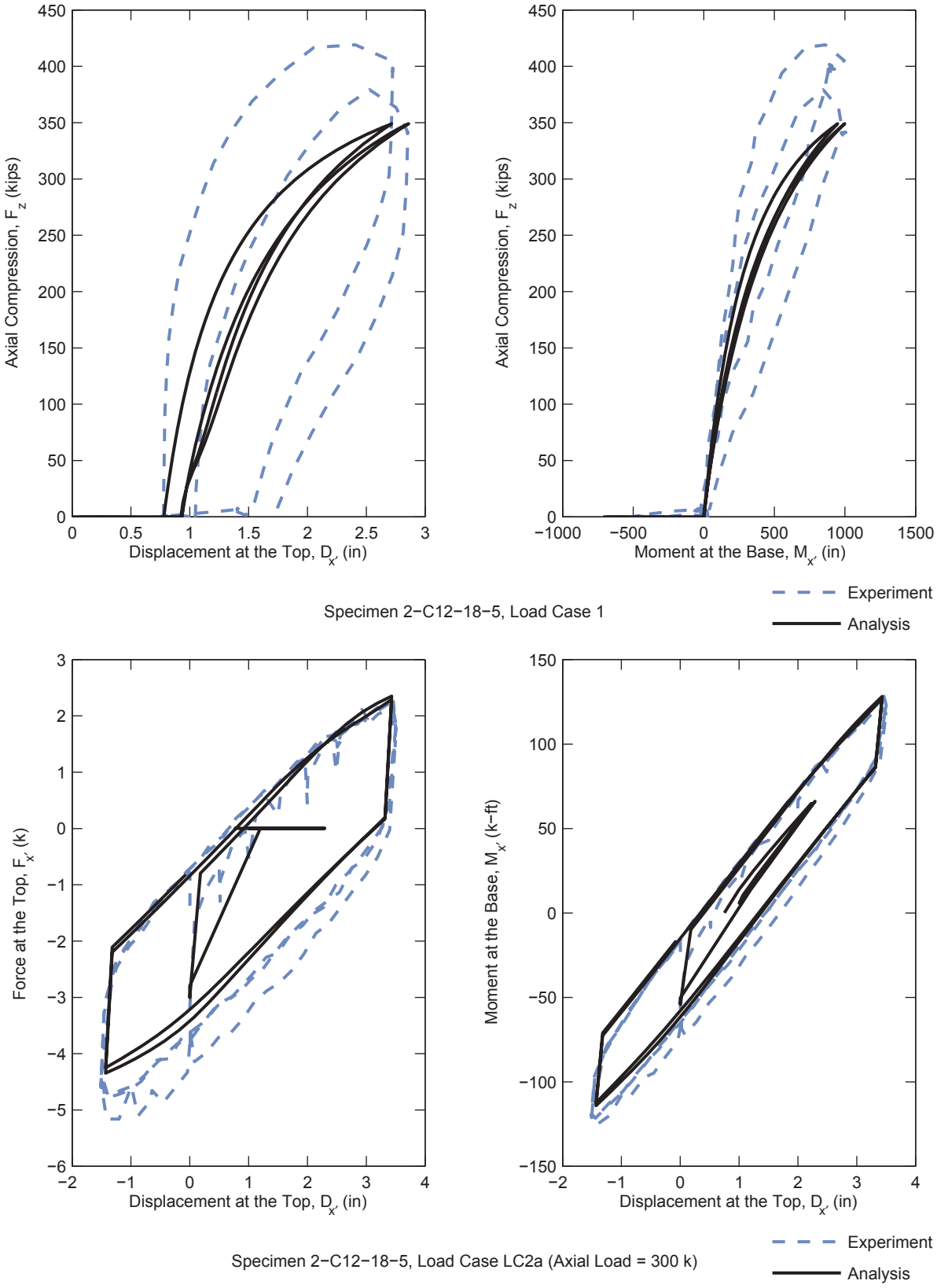

Figure 7.4. Comparison Results – Specimen 2C12-18-5

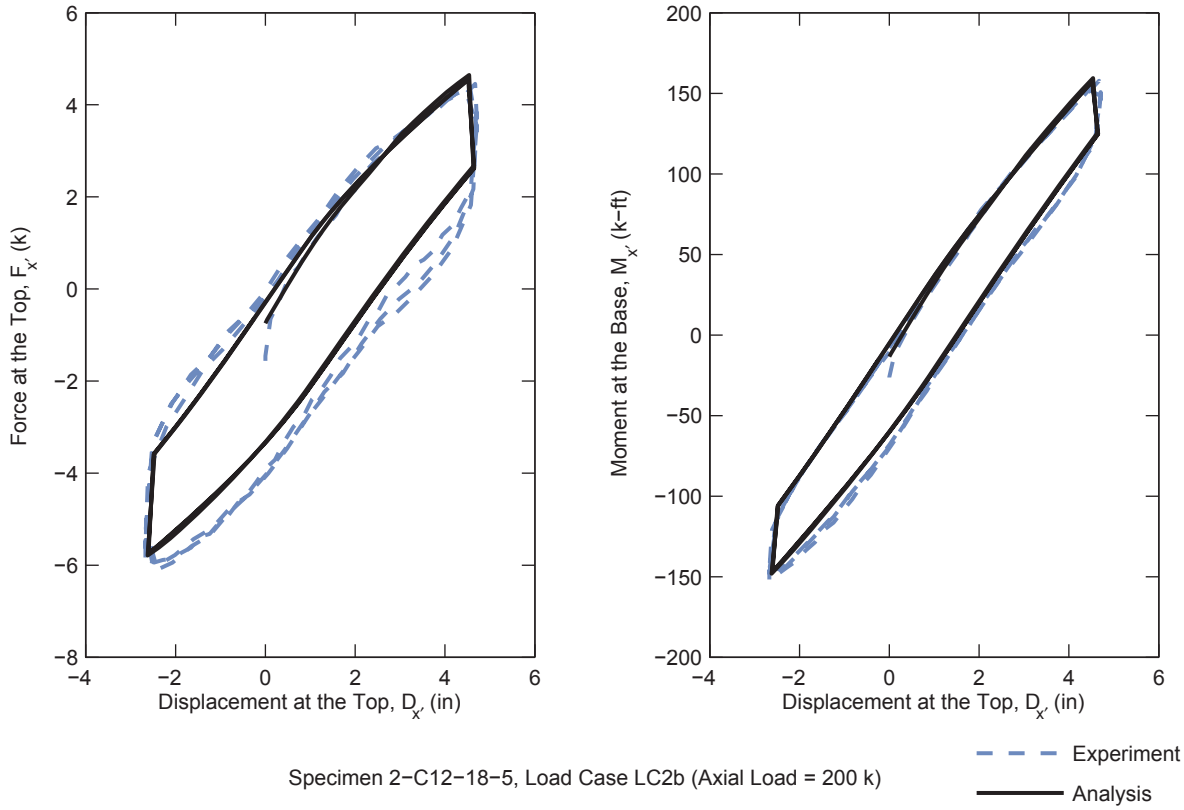

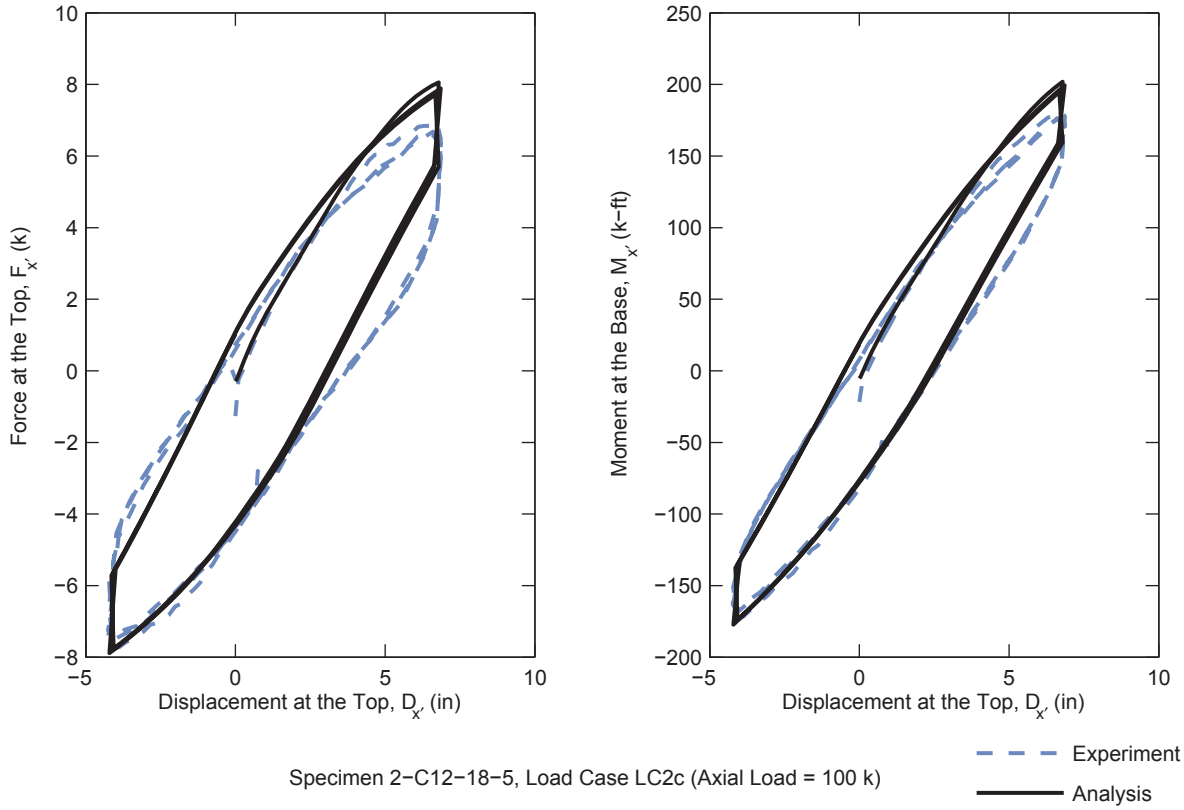

Figure 7.4. Comparison Results – Specimen 2C12-18-5 (continued)

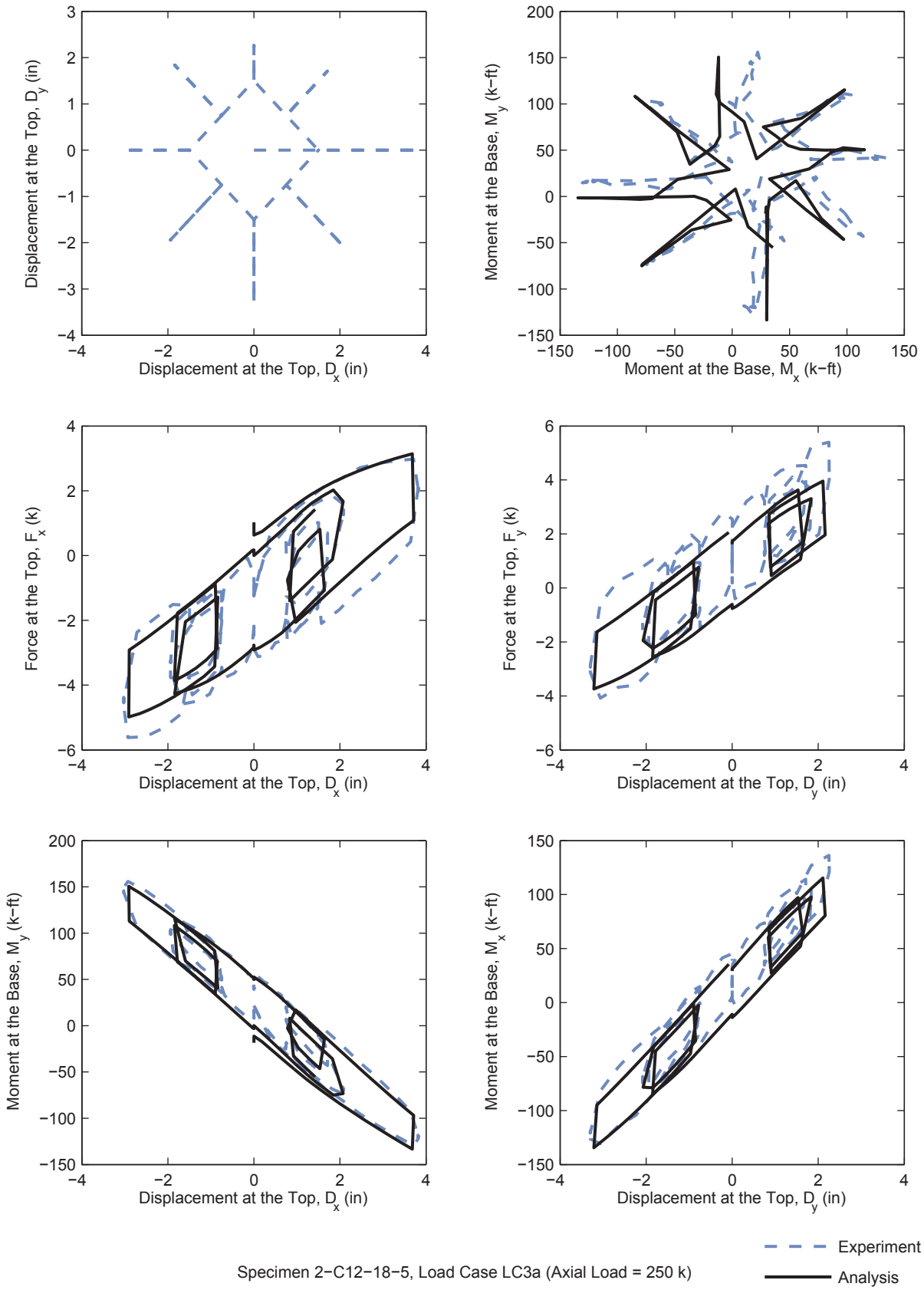

Figure 7.4. Comparison Results – Specimen 2C12-18-5 (continued)

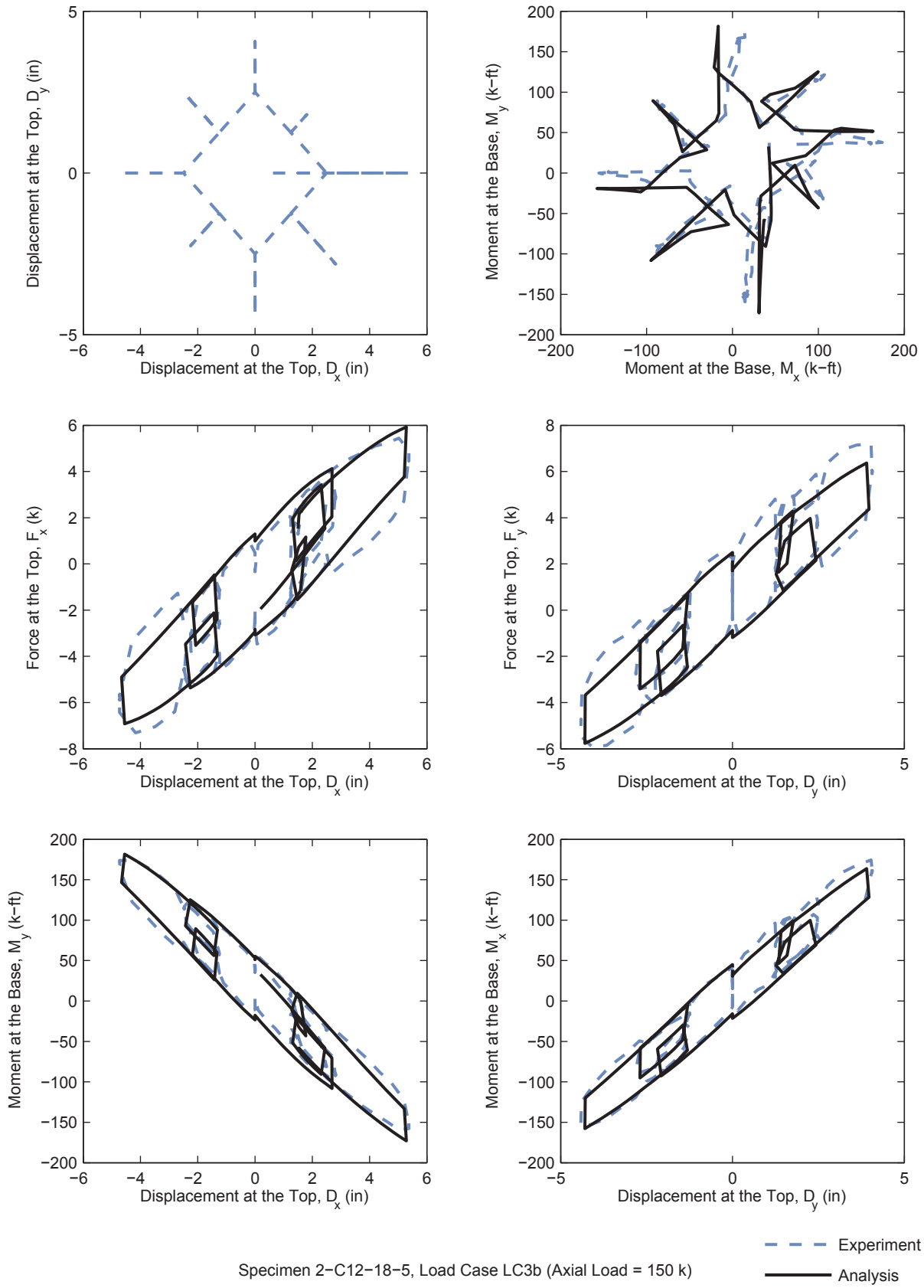

Figure 7.4. Comparison Results – Specimen 2C12-18-5 (continued)

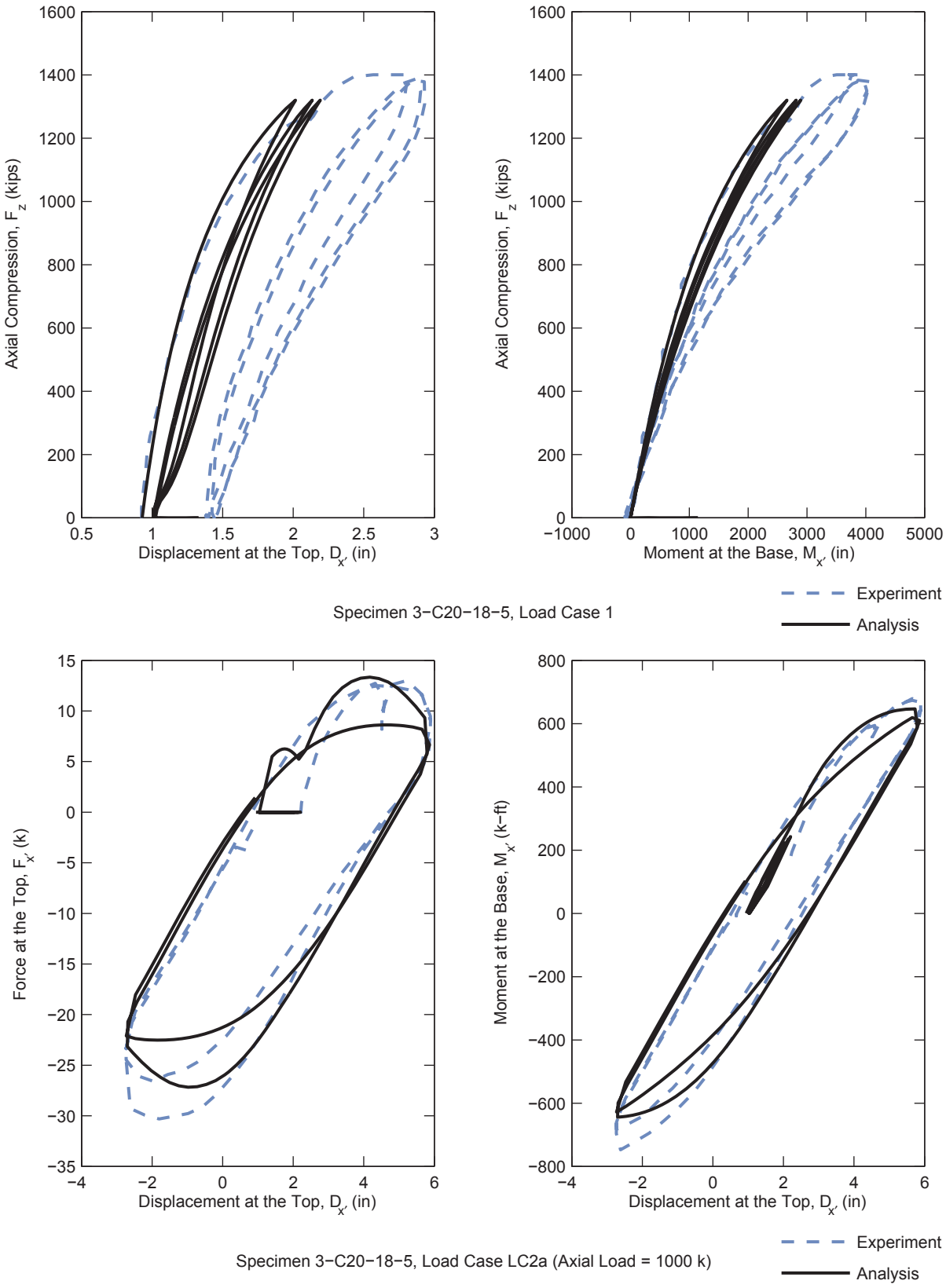

Figure 7.5. Comparison Results – Specimen 3C20-18-5

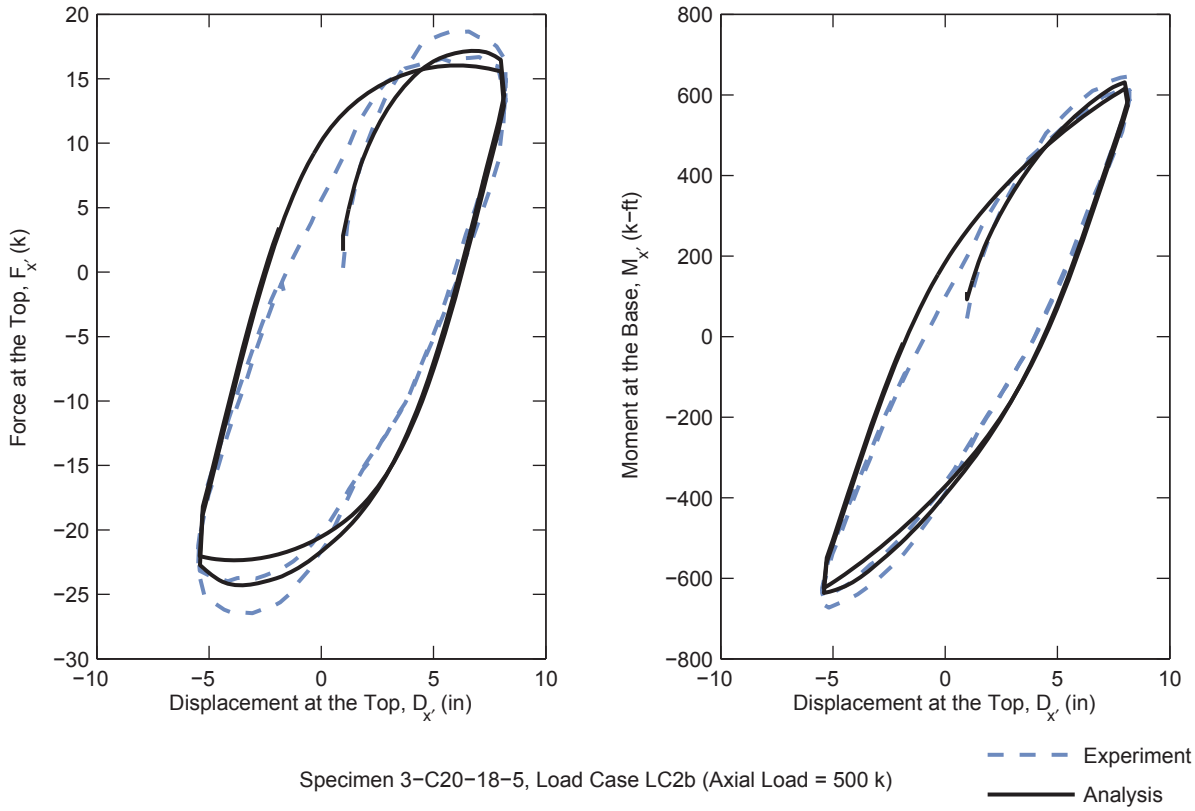

Figure 7.5. Comparison Results – Specimen 3C20-18-5 (continued)

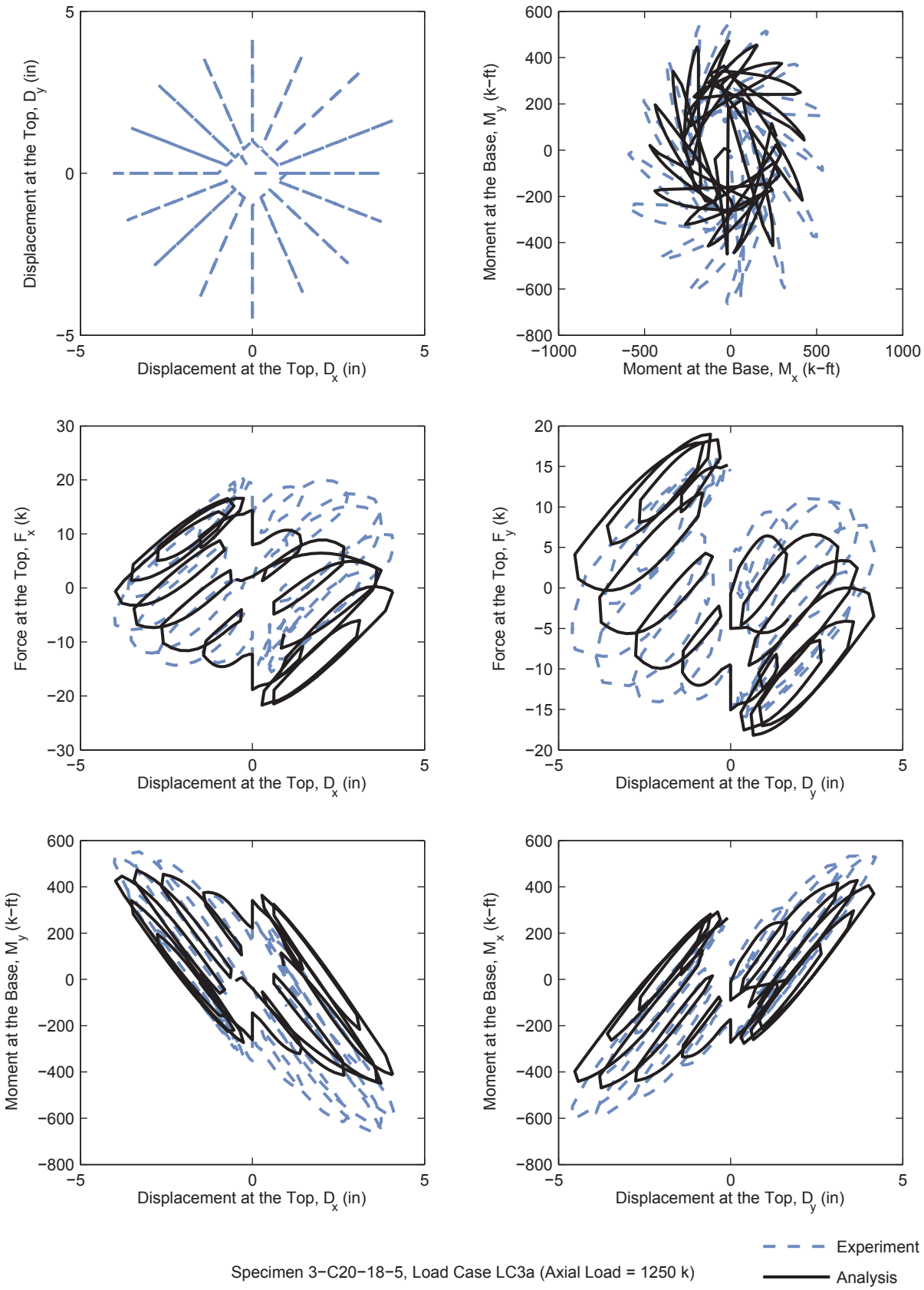

Figure 7.5. Comparison Results – Specimen 3C20-18-5 (continued)

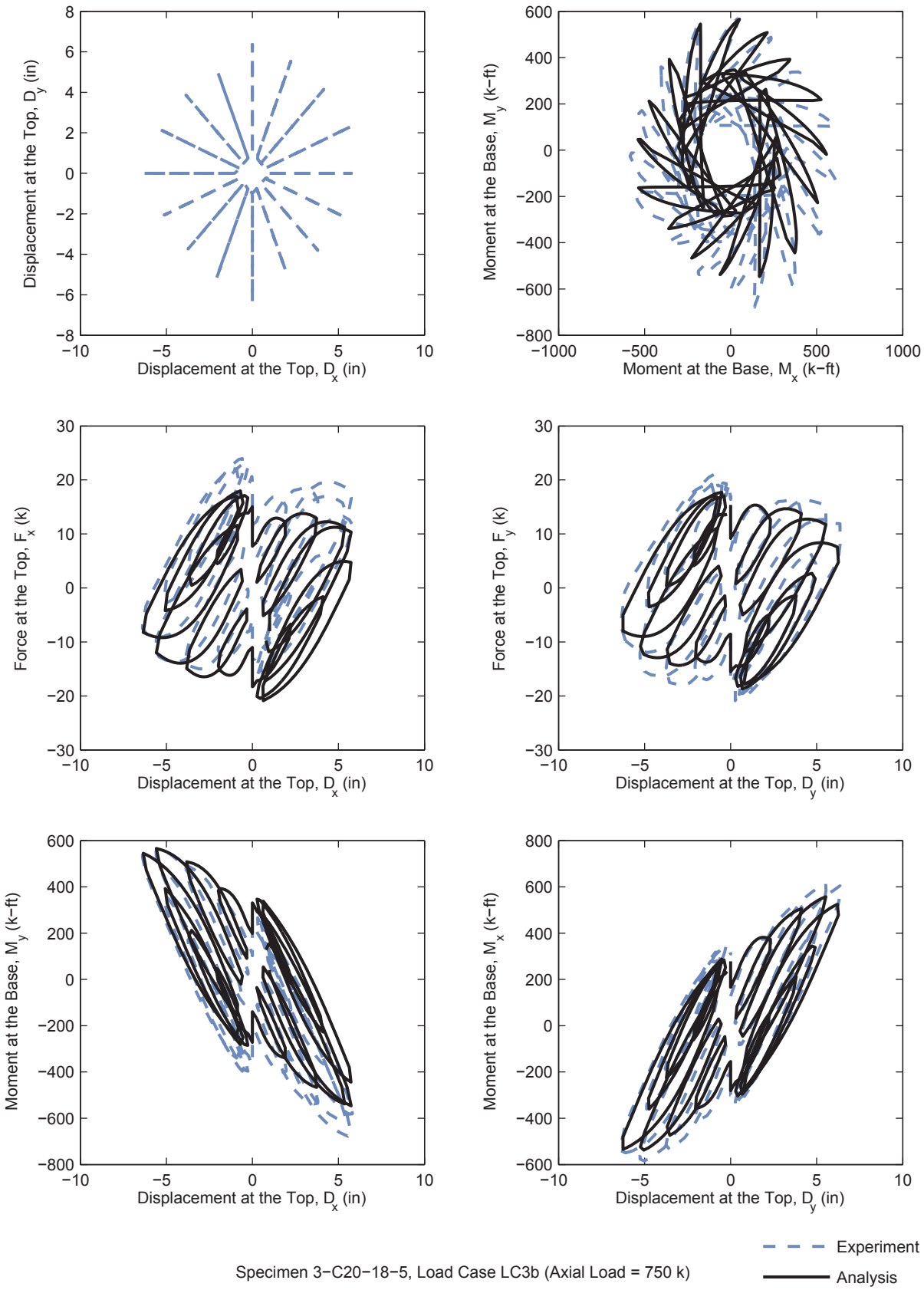

Figure 7.5. Comparison Results – Specimen 3C20-18-5 (continued)

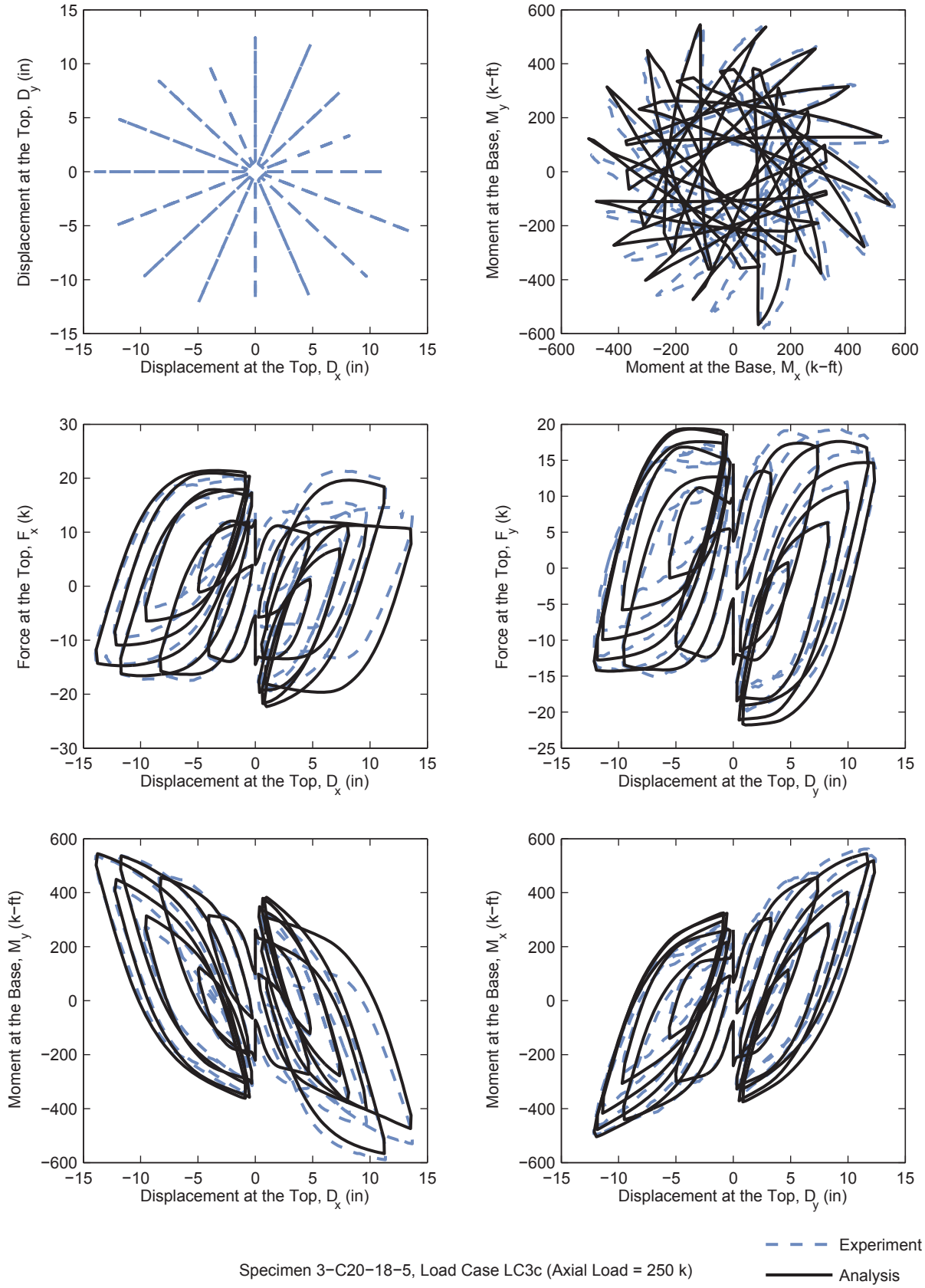

Figure 7.5. Comparison Results – Specimen 3C20-18-5 (continued)

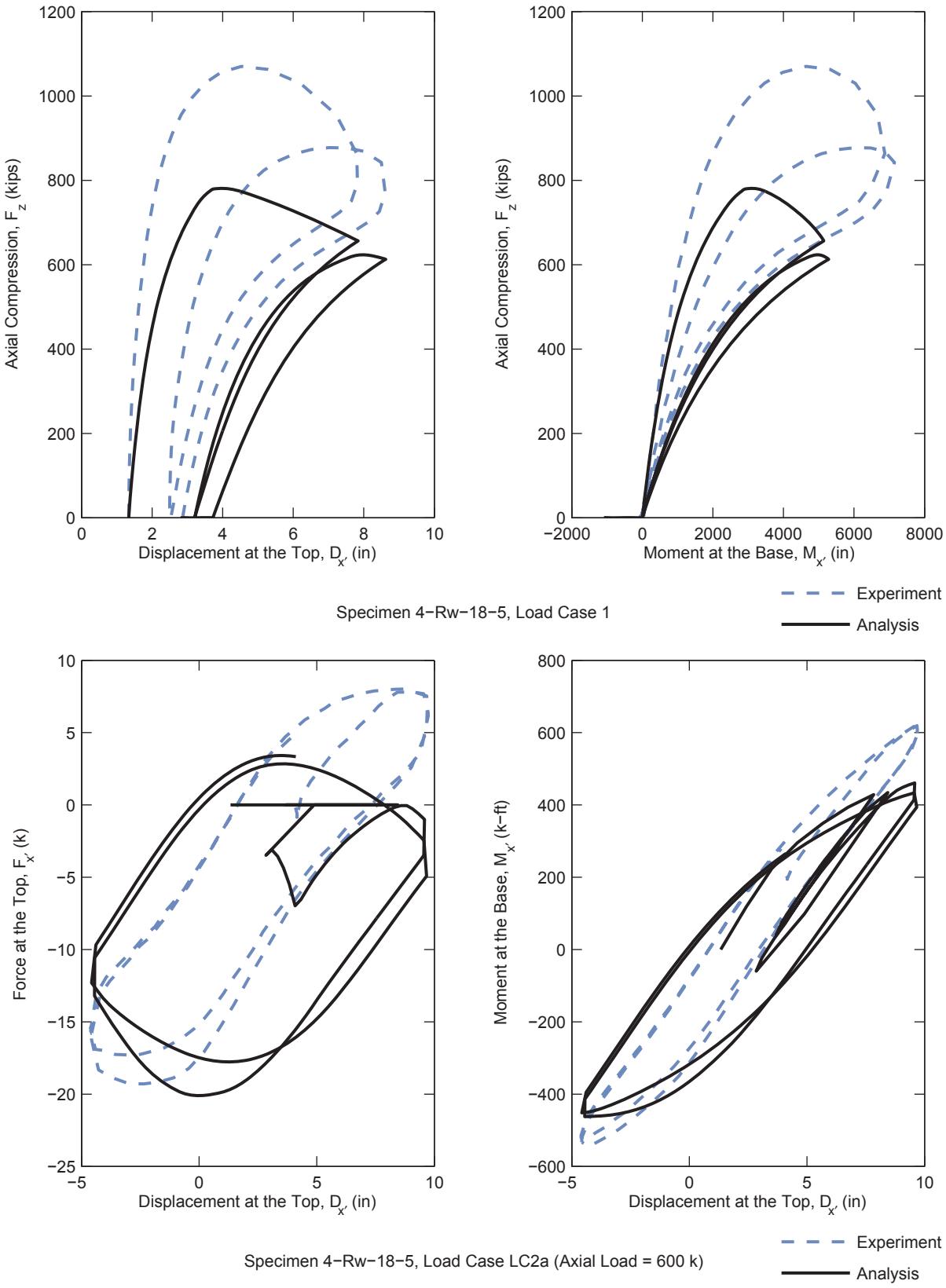

Figure 7.6. Comparison Results – Specimen 4Rw-18-5

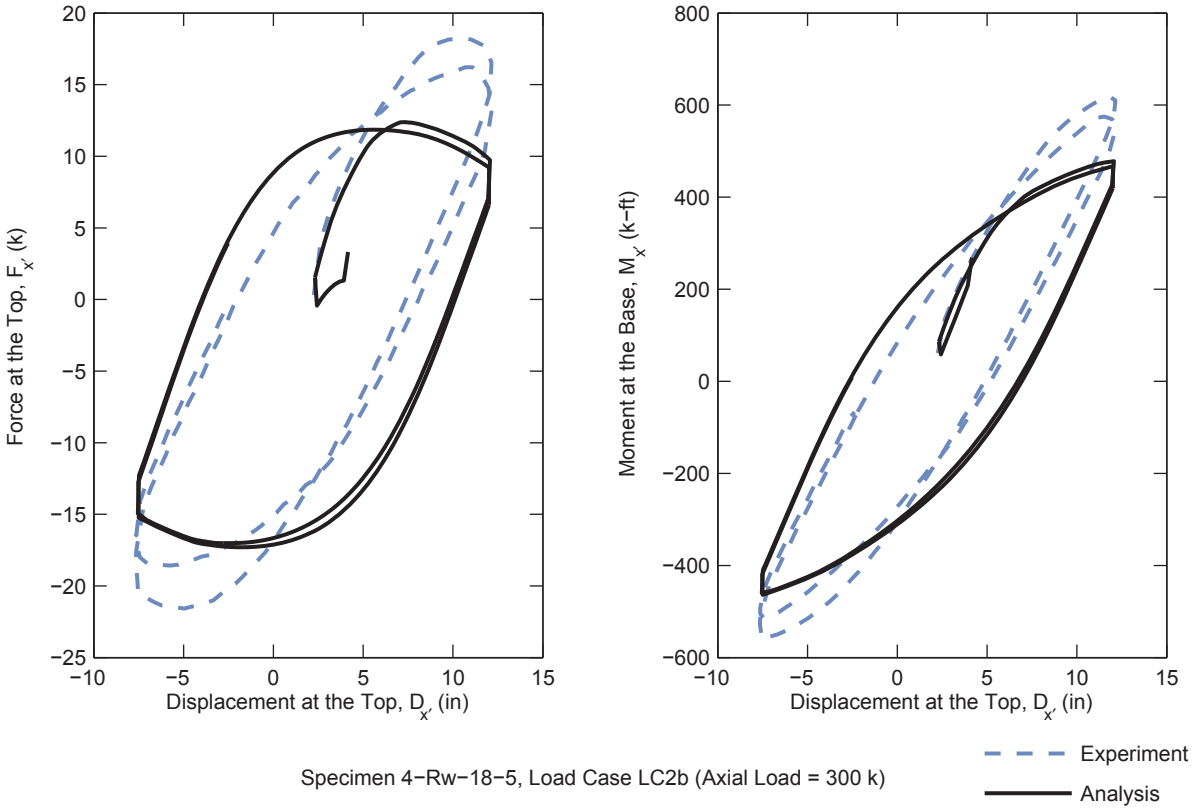

Figure 7.6. Comparison Results – Specimen 4Rw-18-5 (continued)

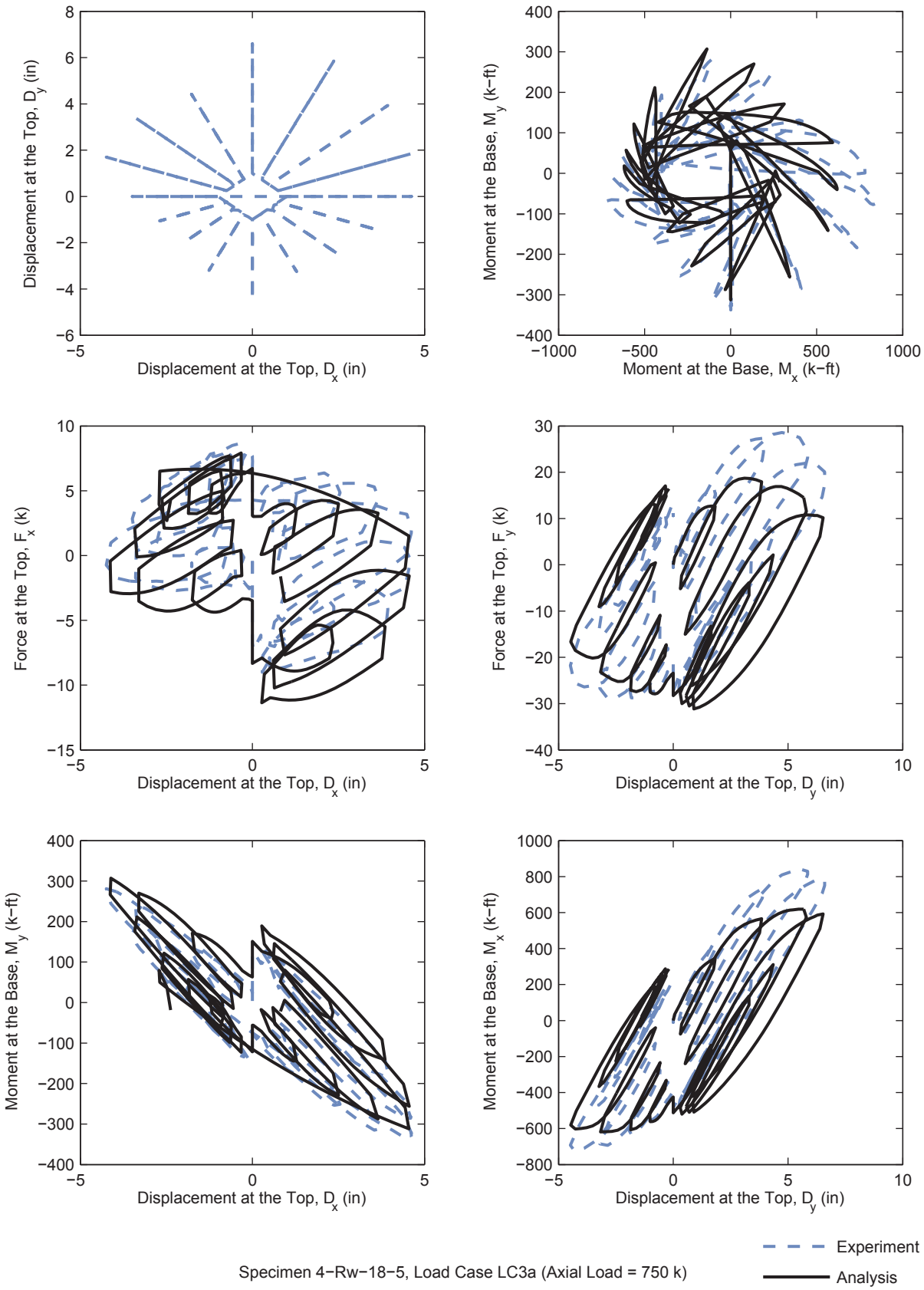

Figure 7.6. Comparison Results – Specimen 4Rw-18-5 (continued)

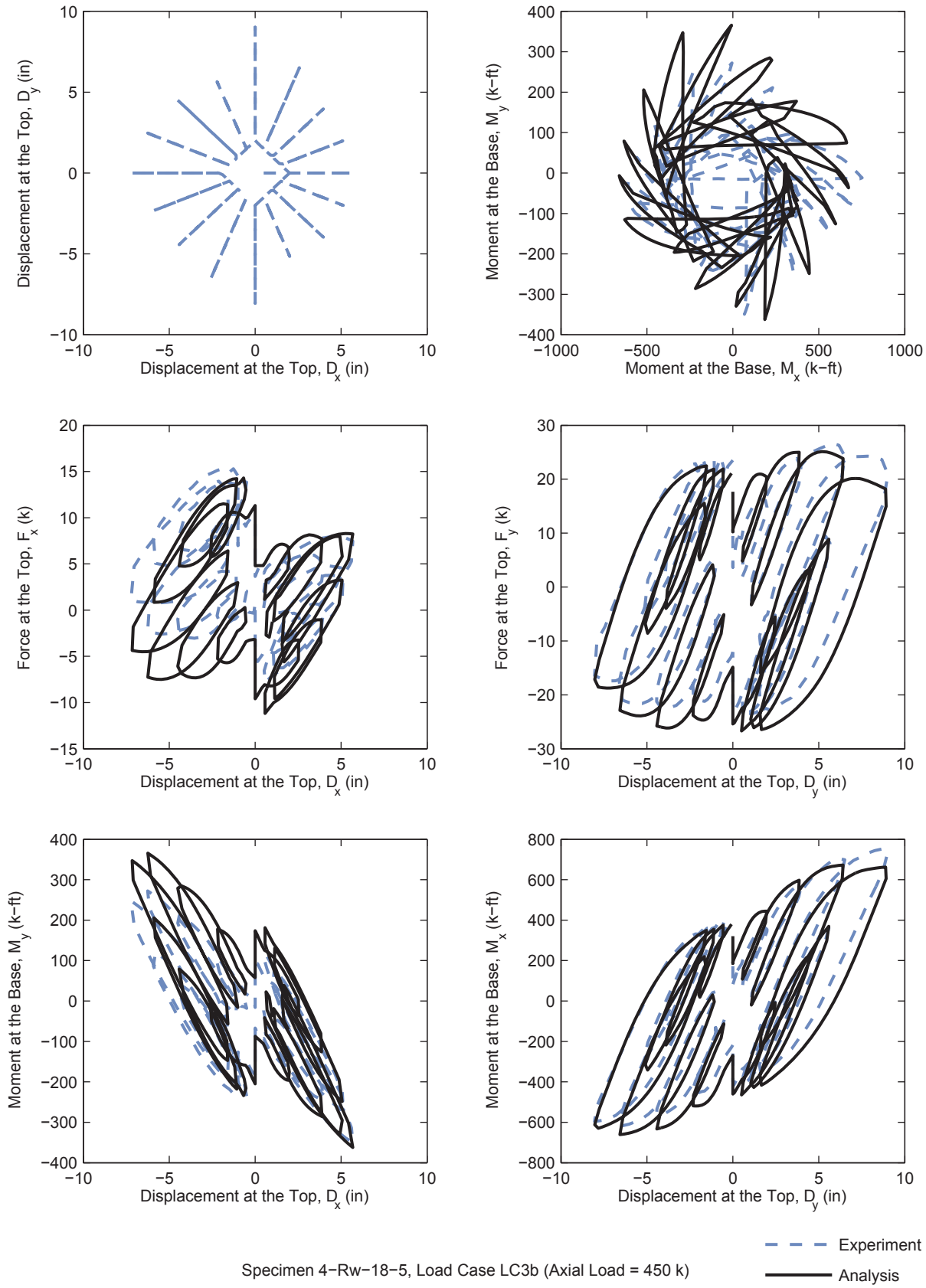

Figure 7.6. Comparison Results – Specimen 4Rw-18-5 (continued)

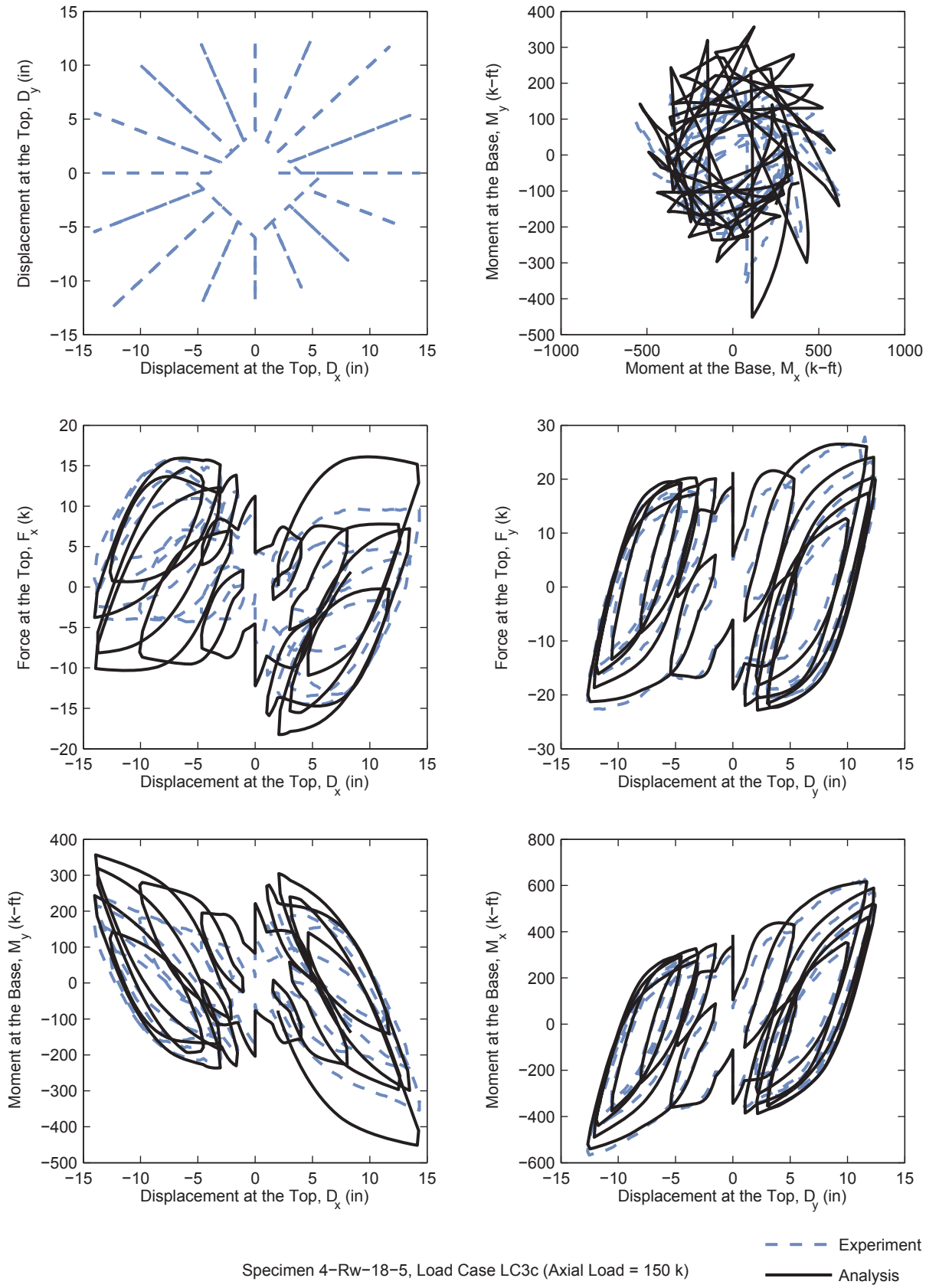

Figure 7.6. Comparison Results – Specimen 4Rw-18-5 (continued)

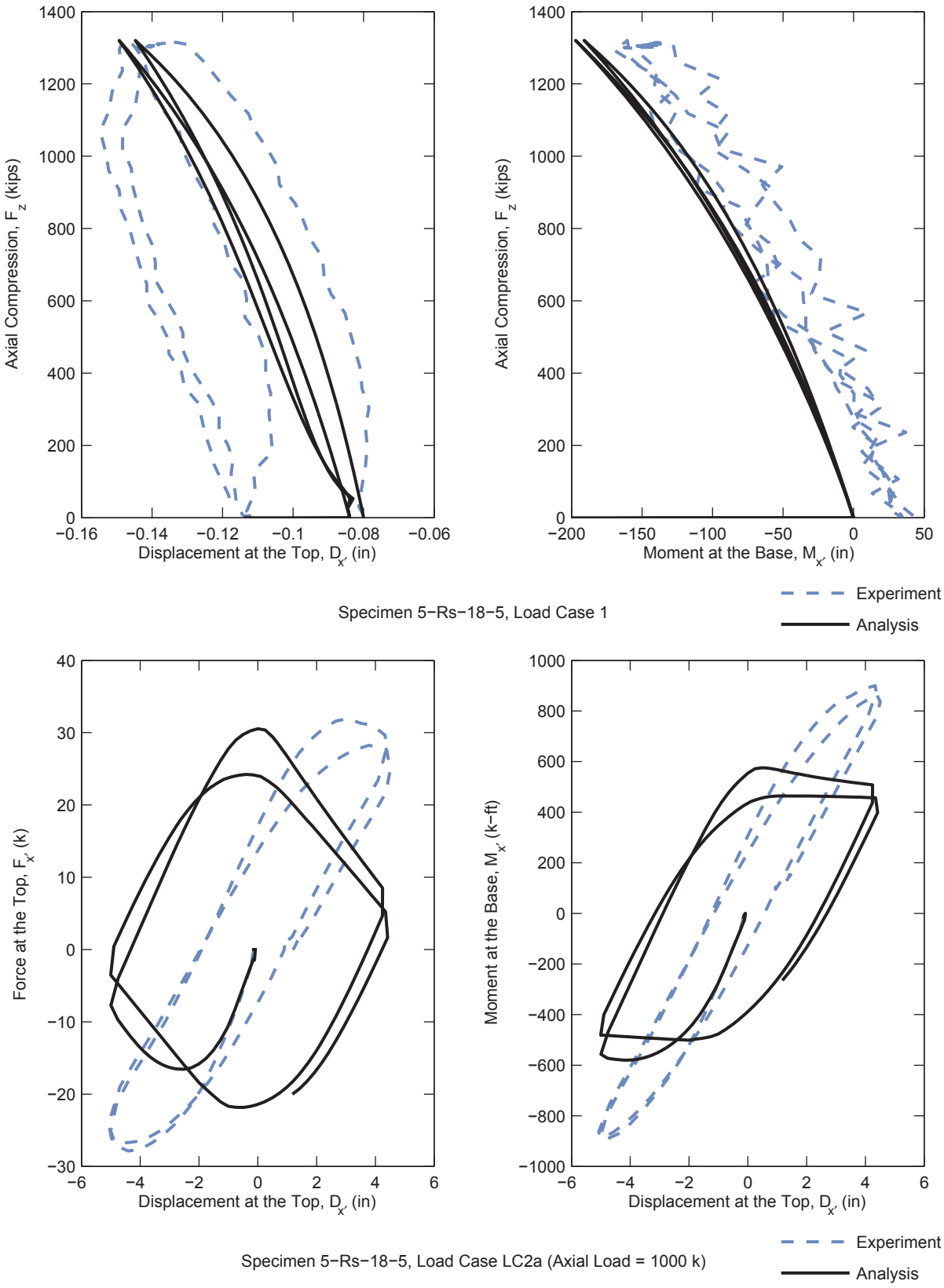

Figure 7.7. Comparison Results – Specimen 5Rs-18-5

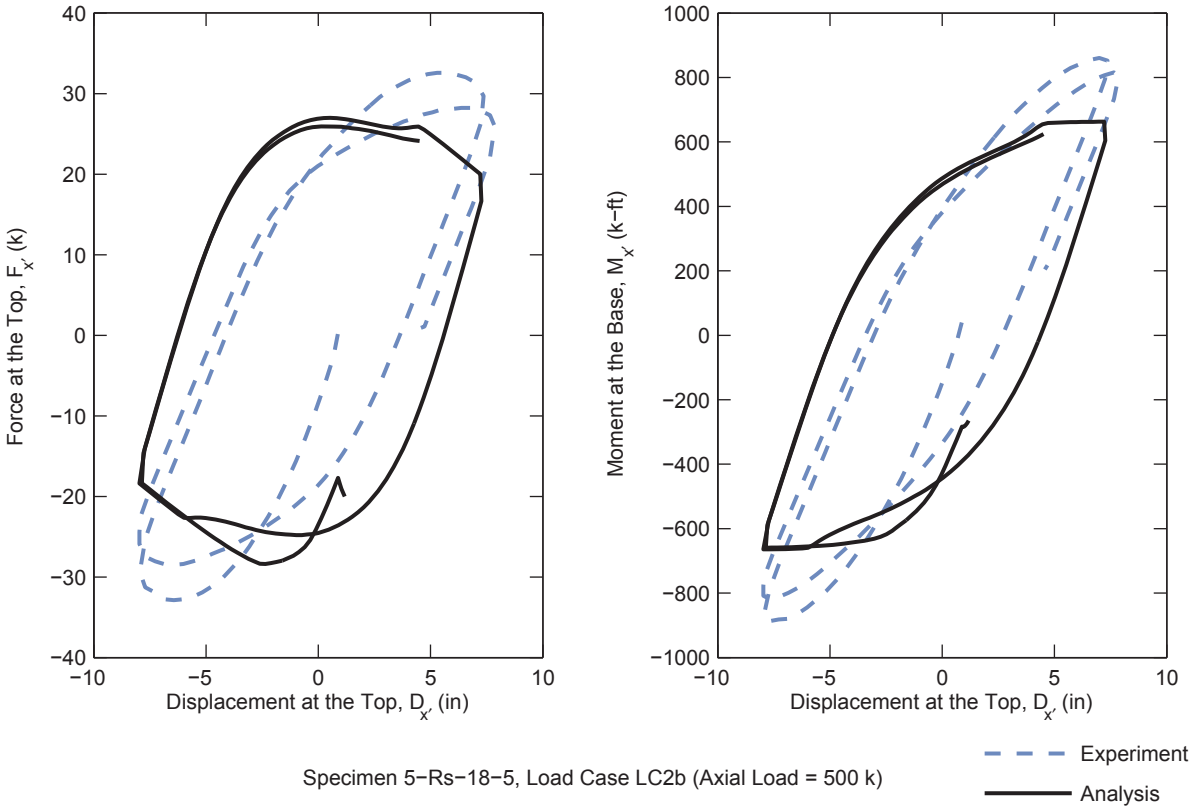

Figure 7.7. Comparison Results – Specimen 5Rs-18-5 (continued)

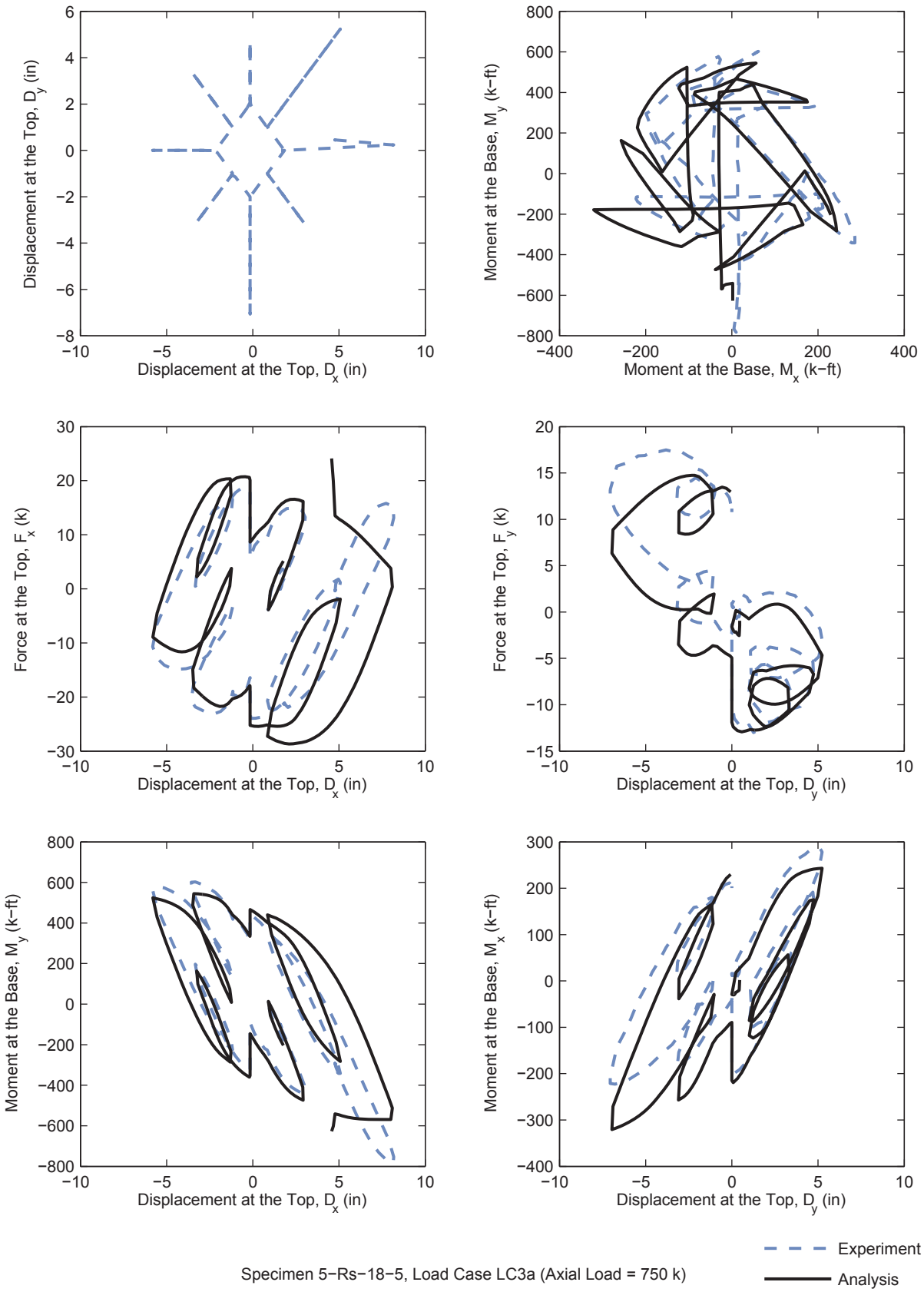

Figure 7.7. Comparison Results – Specimen 5Rs-18-5 (continued)

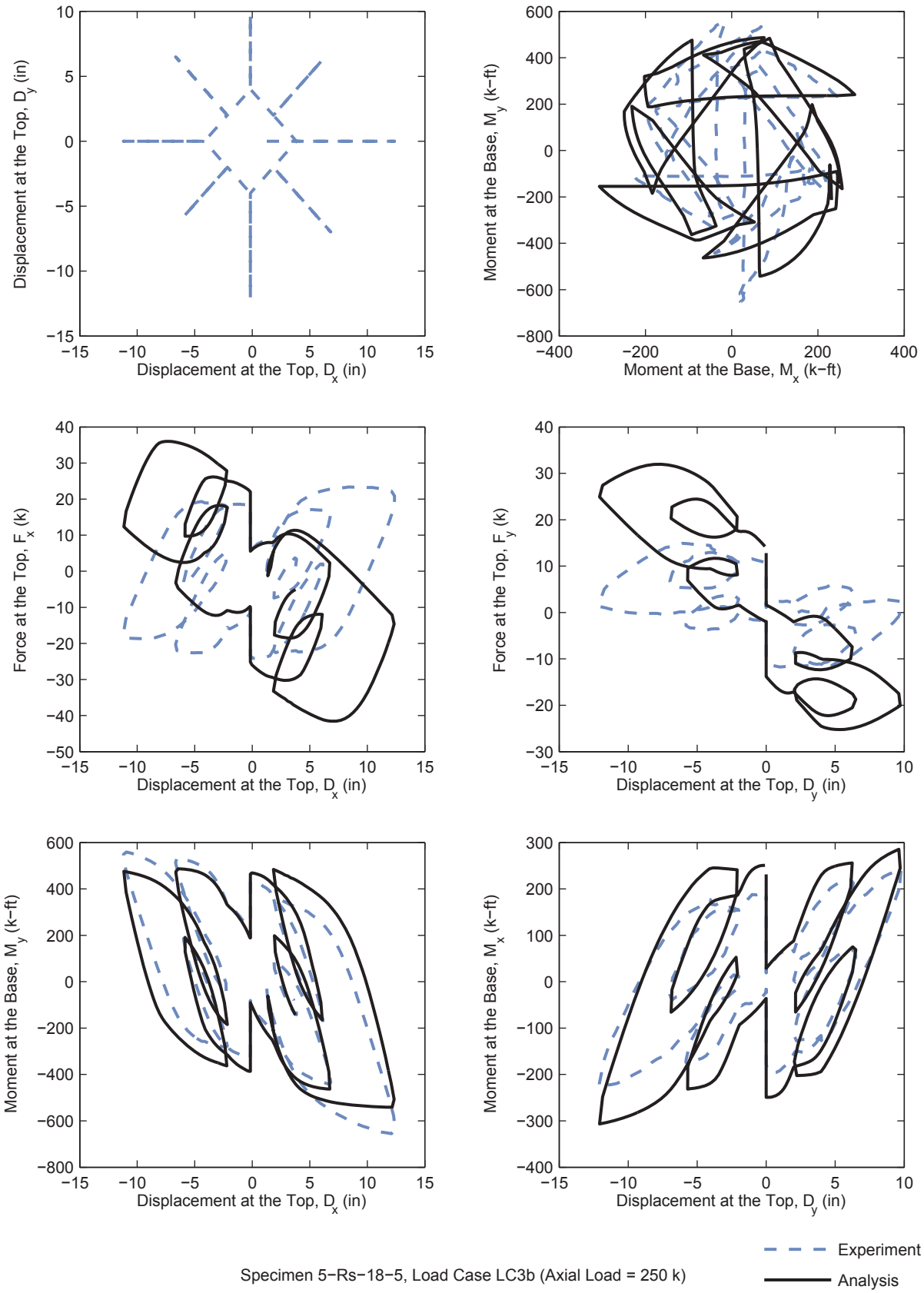

Figure 7.7. Comparison Results – Specimen 5Rs-18-5 (continued)

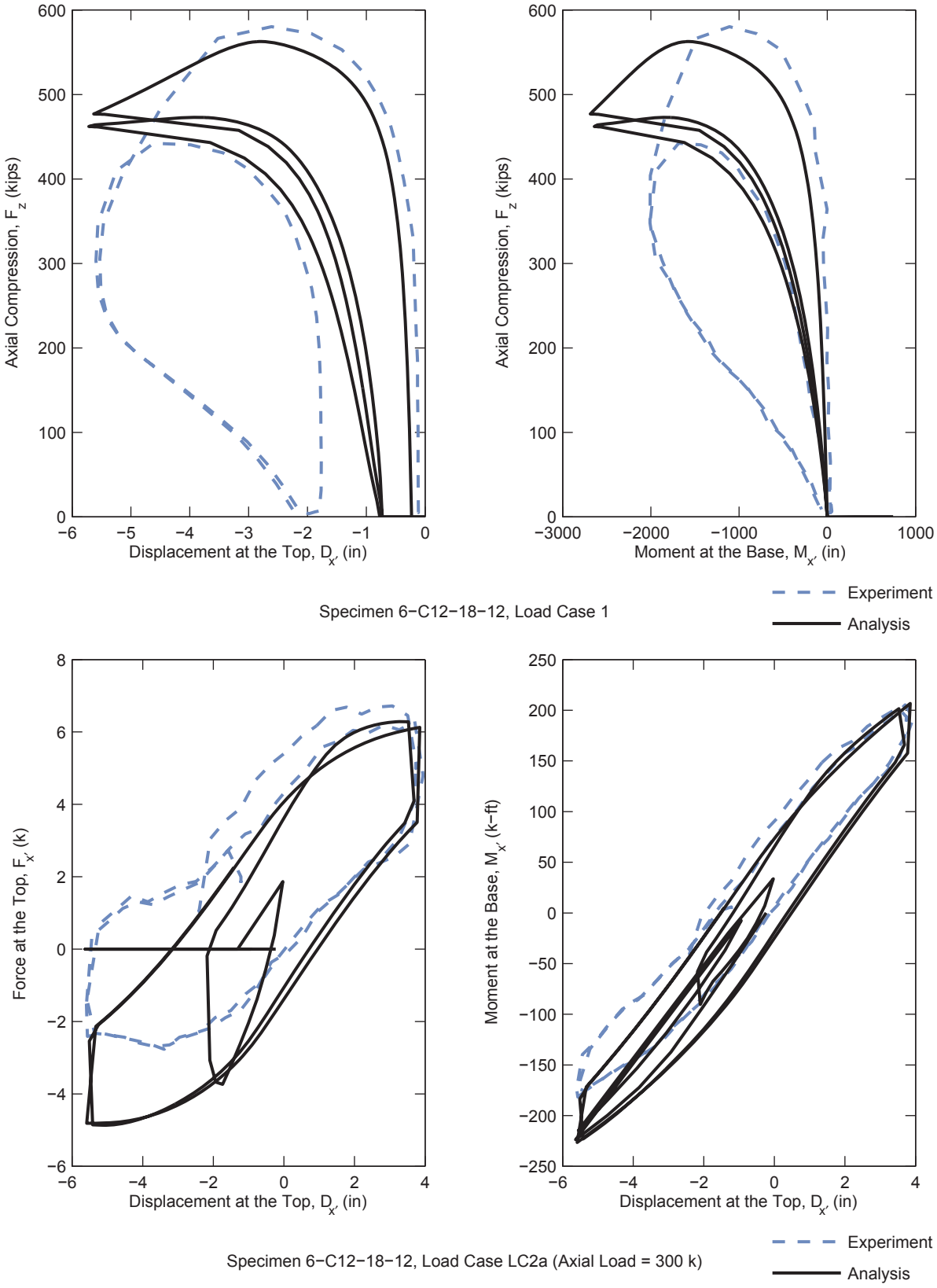

Figure 7.8. Comparison Results – Specimen 6C12-18-12

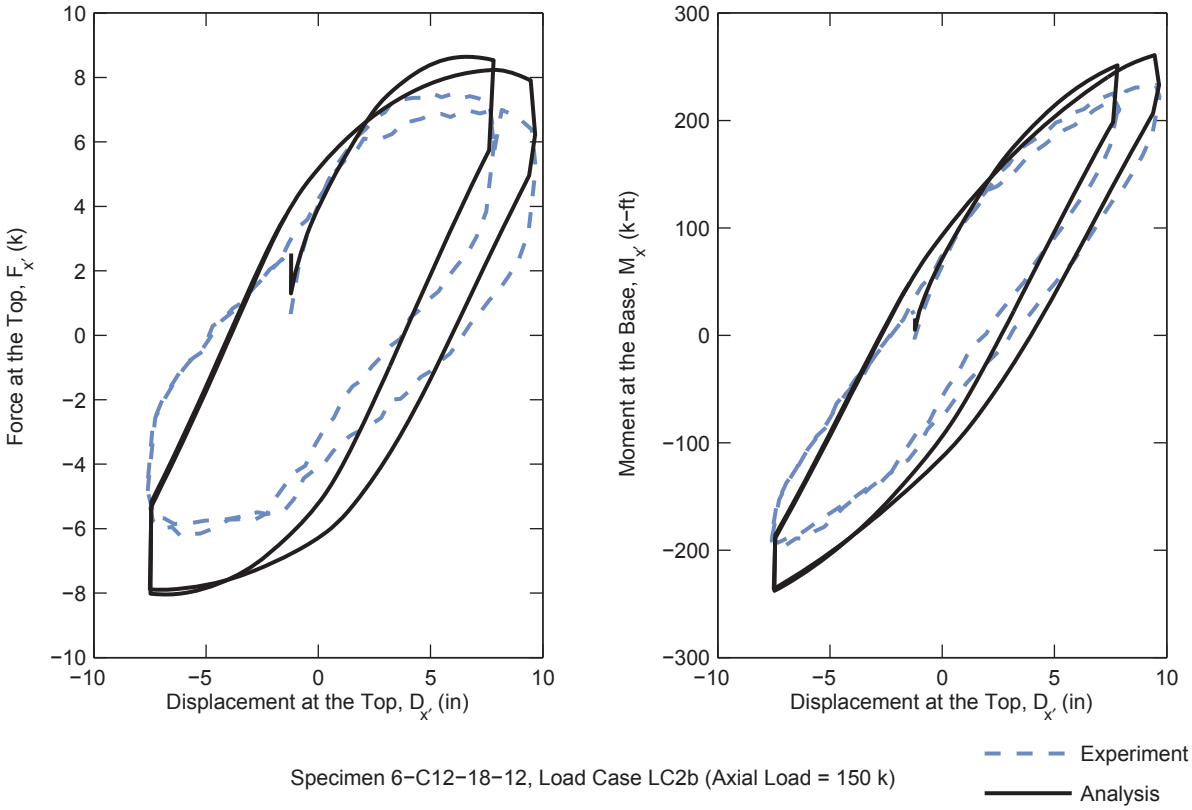

Figure 7.8. Comparison Results – Specimen 6C12-18-12 (continued)

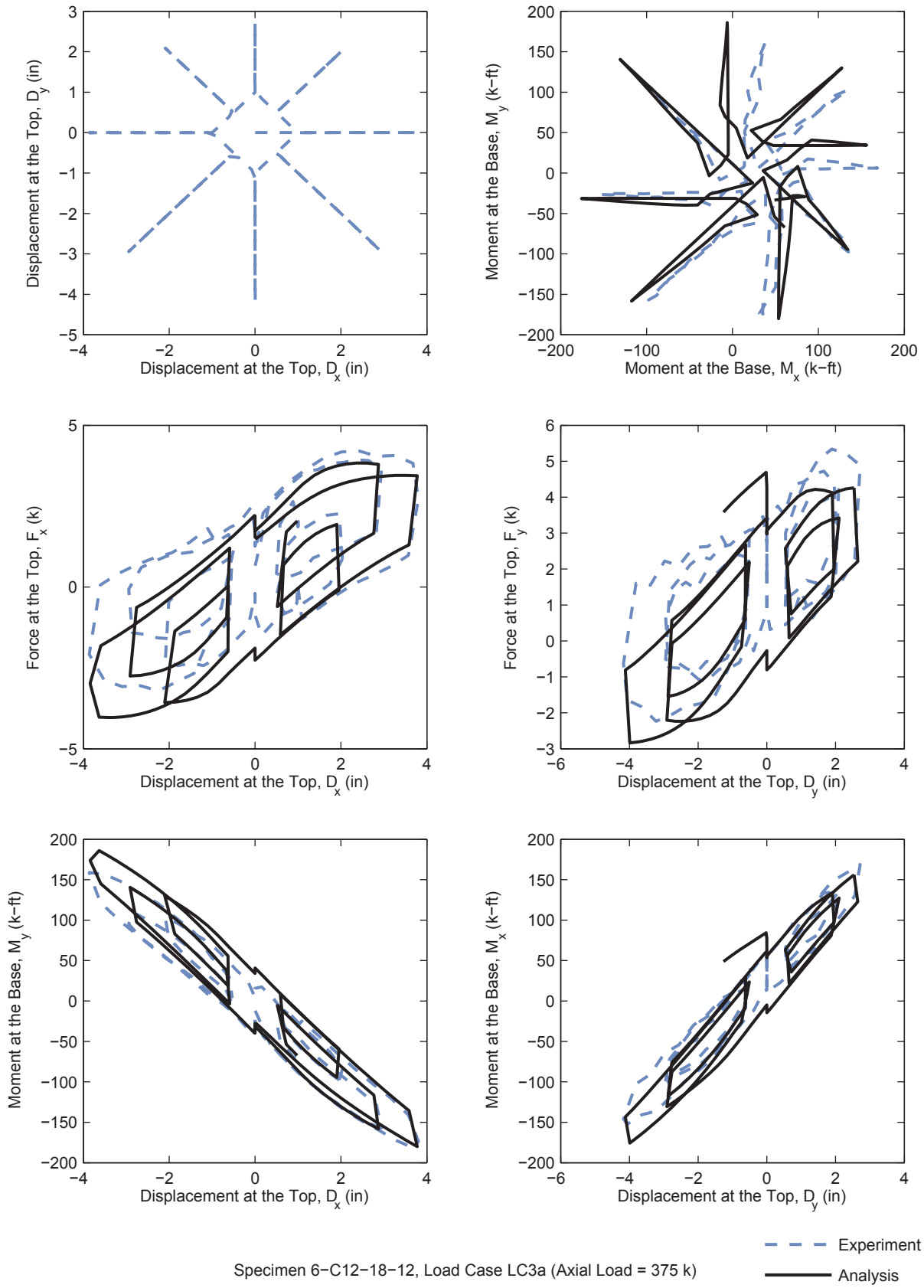

Figure 7.8. Comparison Results – Specimen 6C12-18-12 (continued)

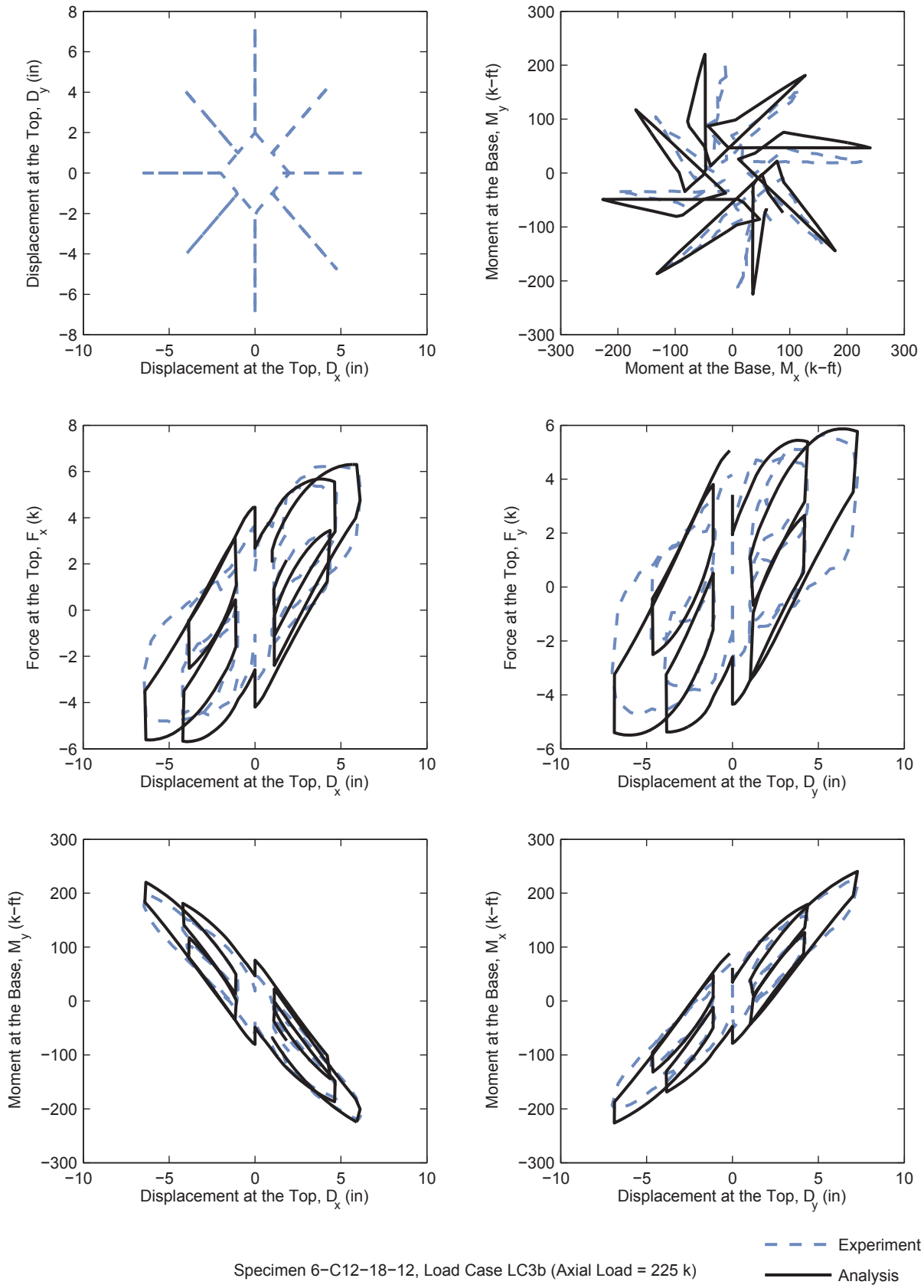

Figure 7.8. Comparison Results – Specimen 6C12-18-12 (continued)

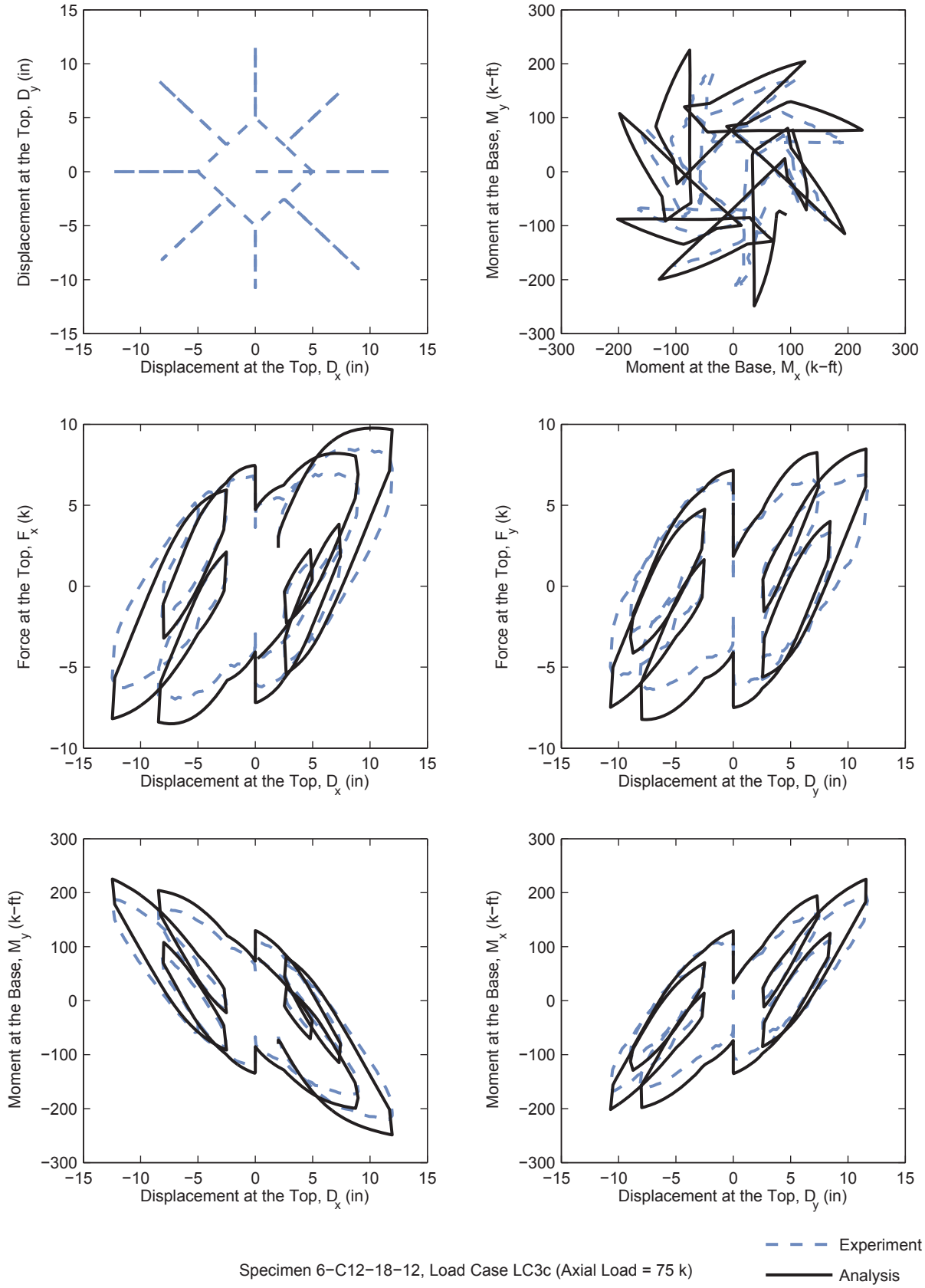

Figure 7.8. Comparison Results – Specimen 6C12-18-12 (continued)

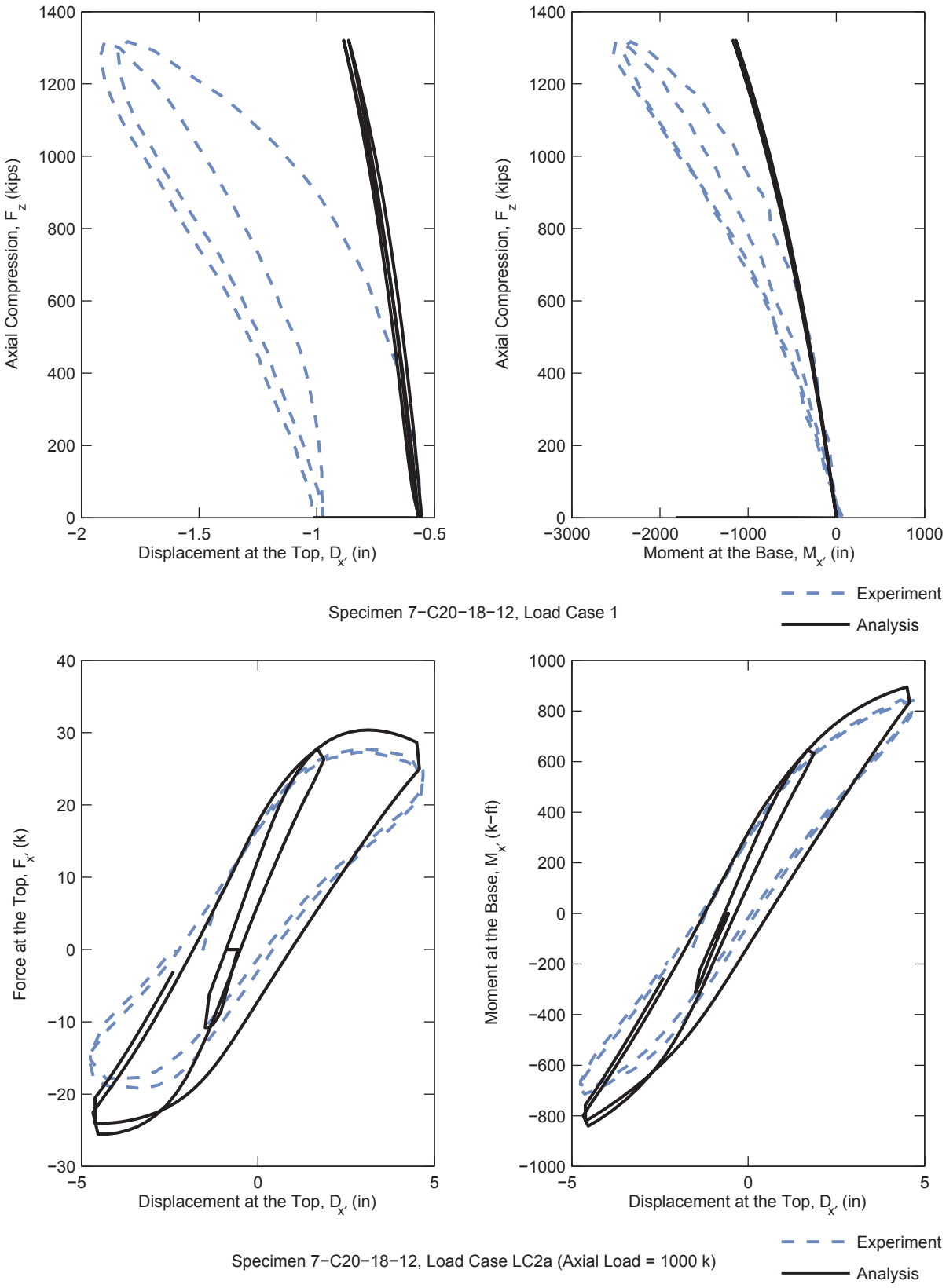

Figure 7.9. Comparison Results – Specimen 7C20-18-12

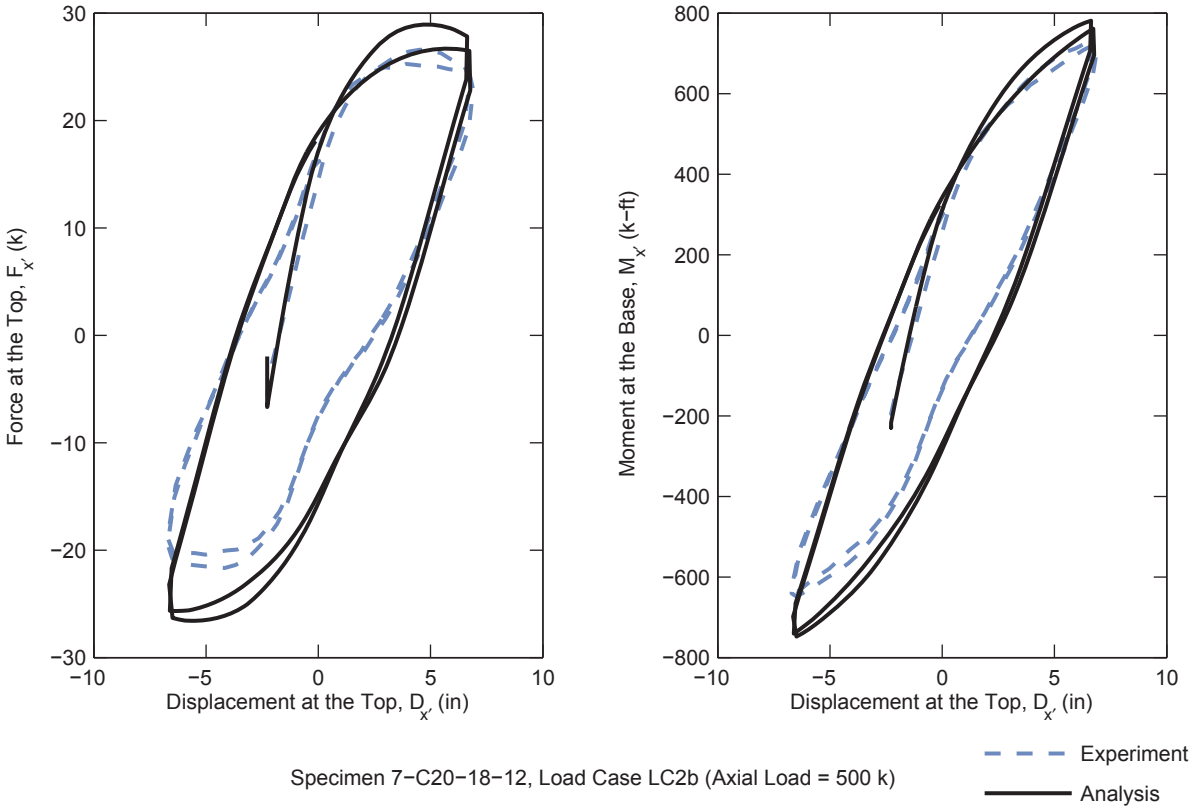

Figure 7.9. Comparison Results – Specimen 7C20-18-12 (continued)

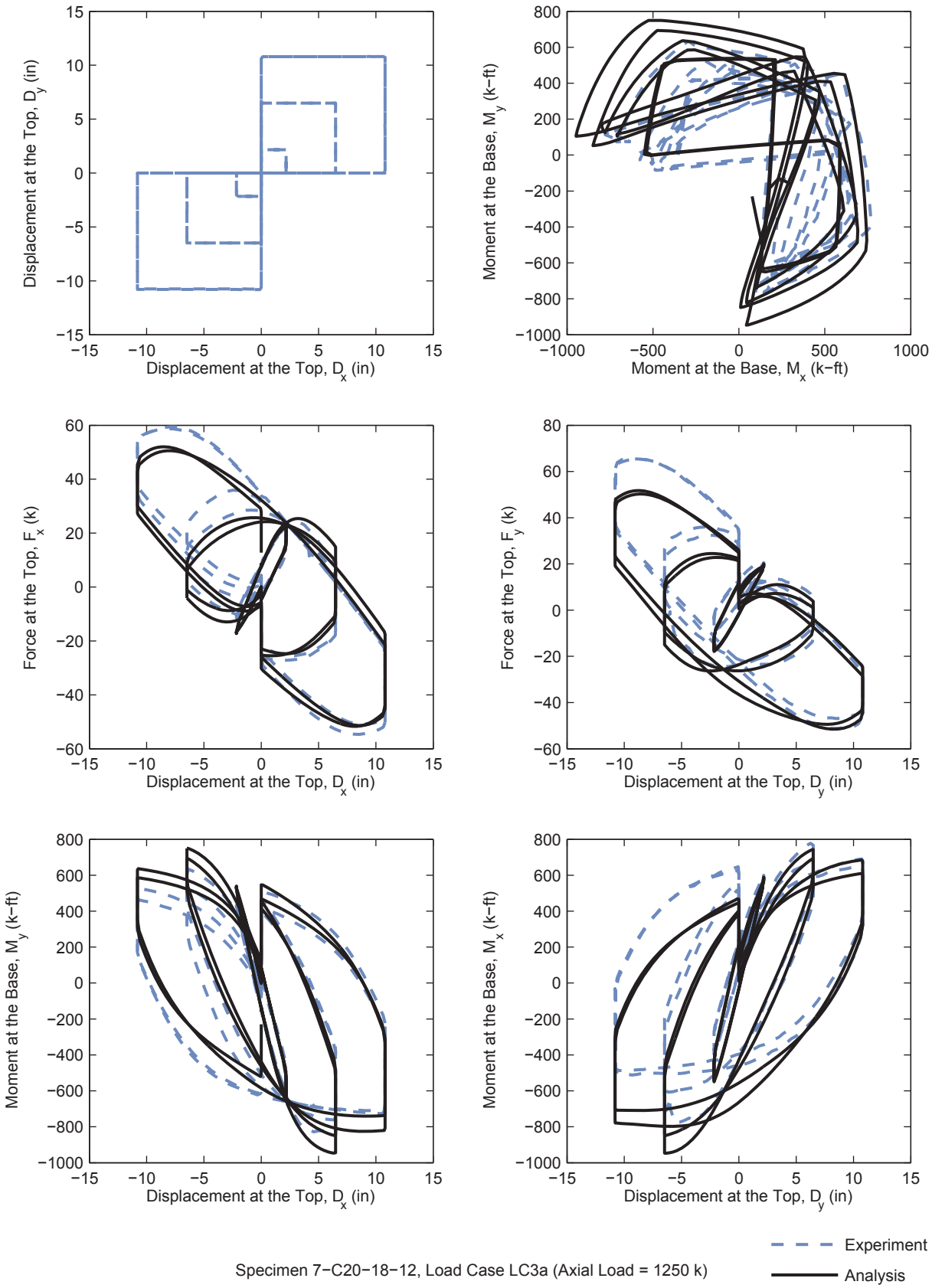

Figure 7.9. Comparison Results – Specimen 7C20-18-12 (continued)

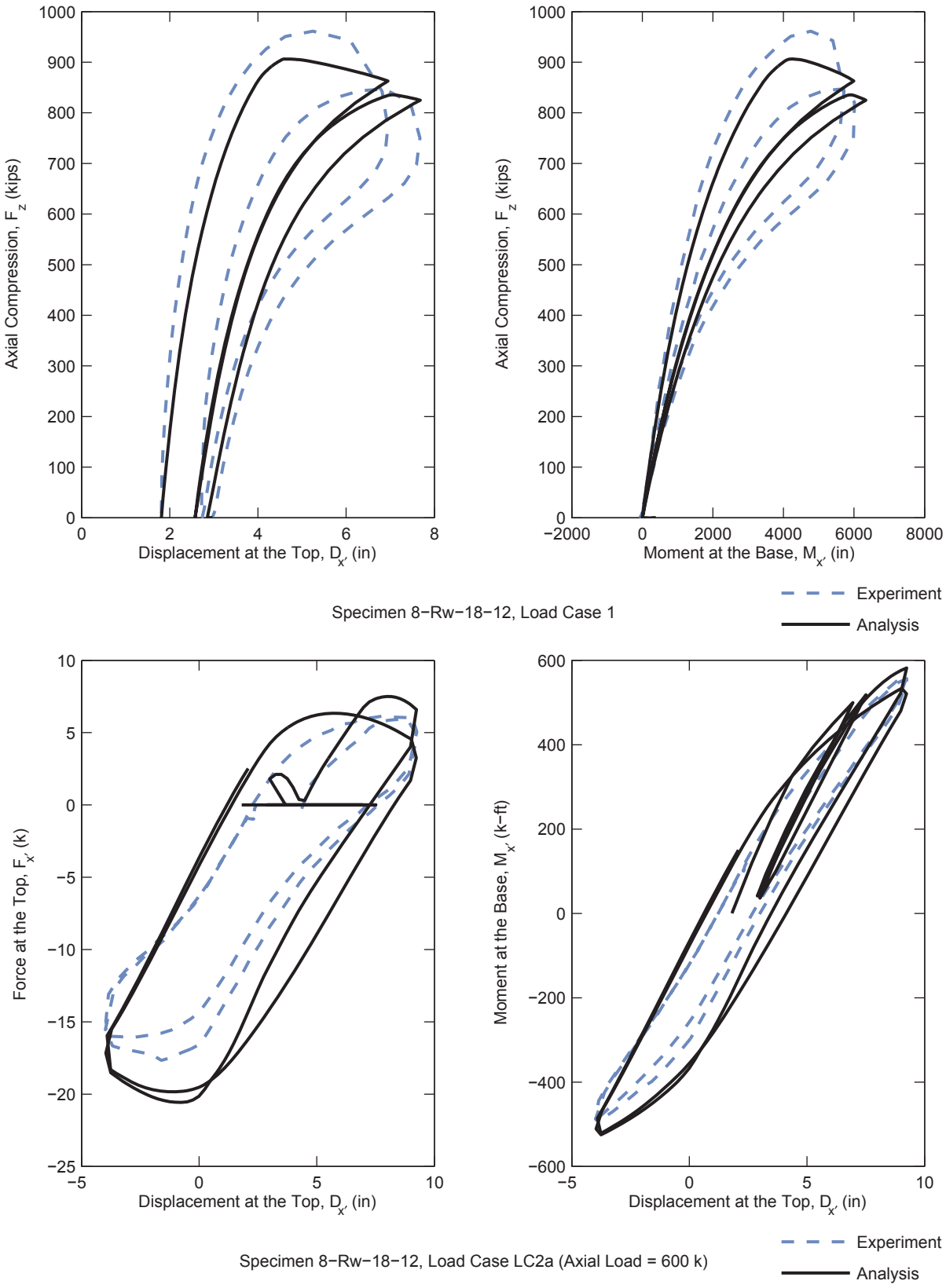

Figure 7.10. Comparison Results – Specimen 8Rw-18-12

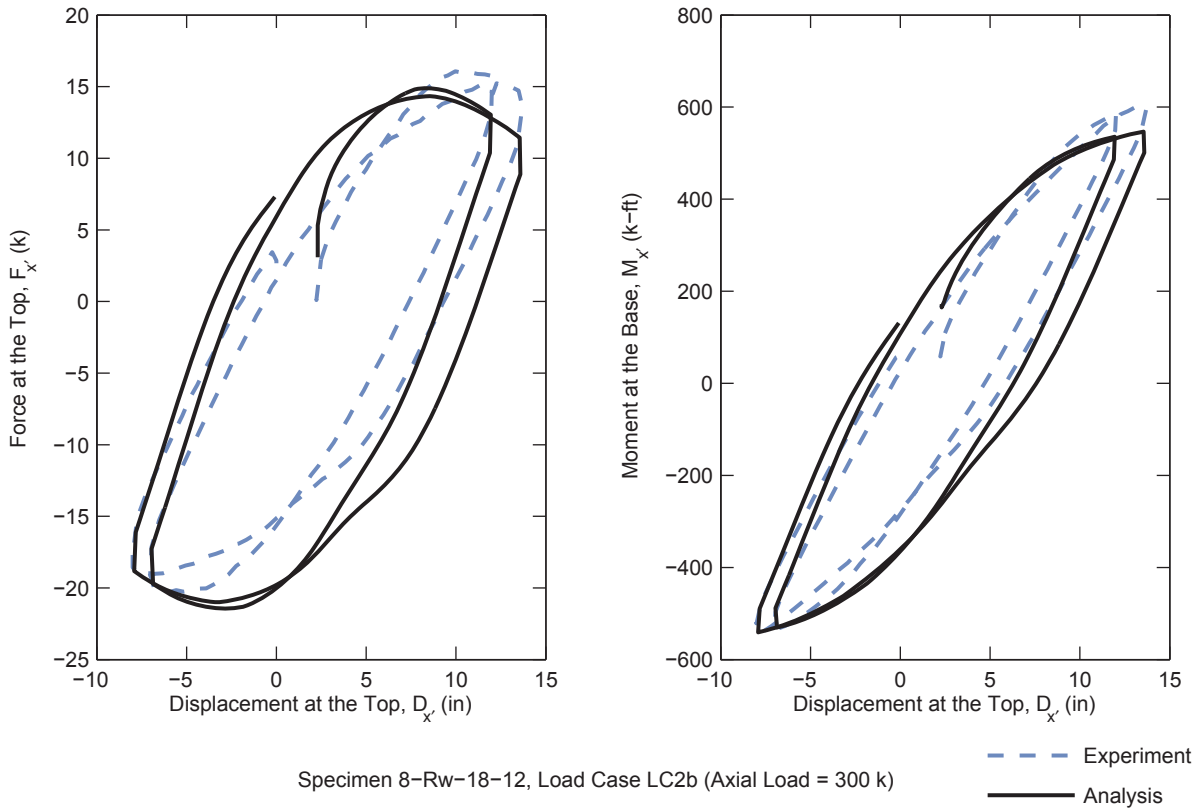

Figure 7.10. Comparison Results – Specimen 8Rw-18-12 (continued)

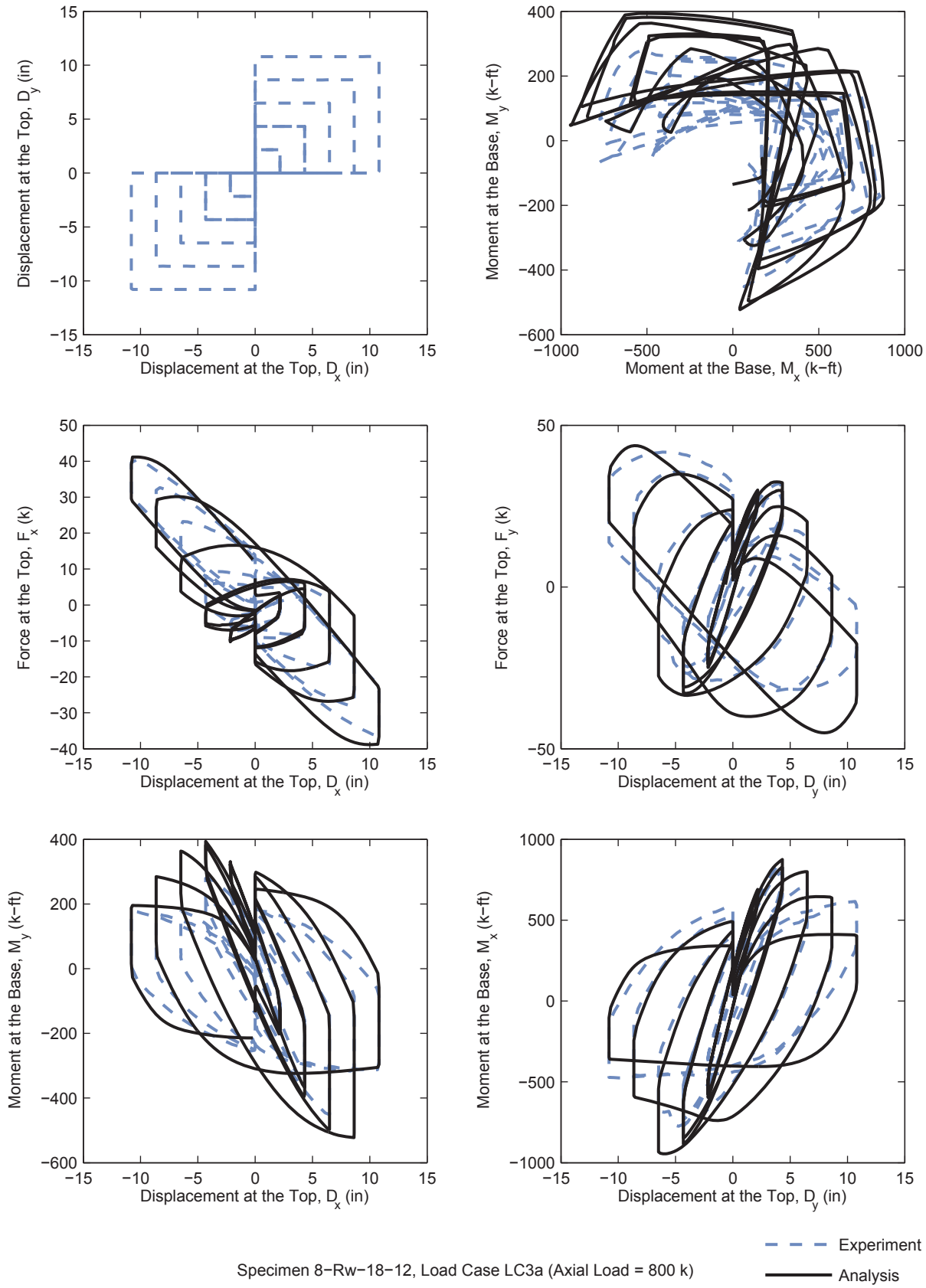

Figure 7.10. Comparison Results – Specimen 8Rw-18-12 (continued)

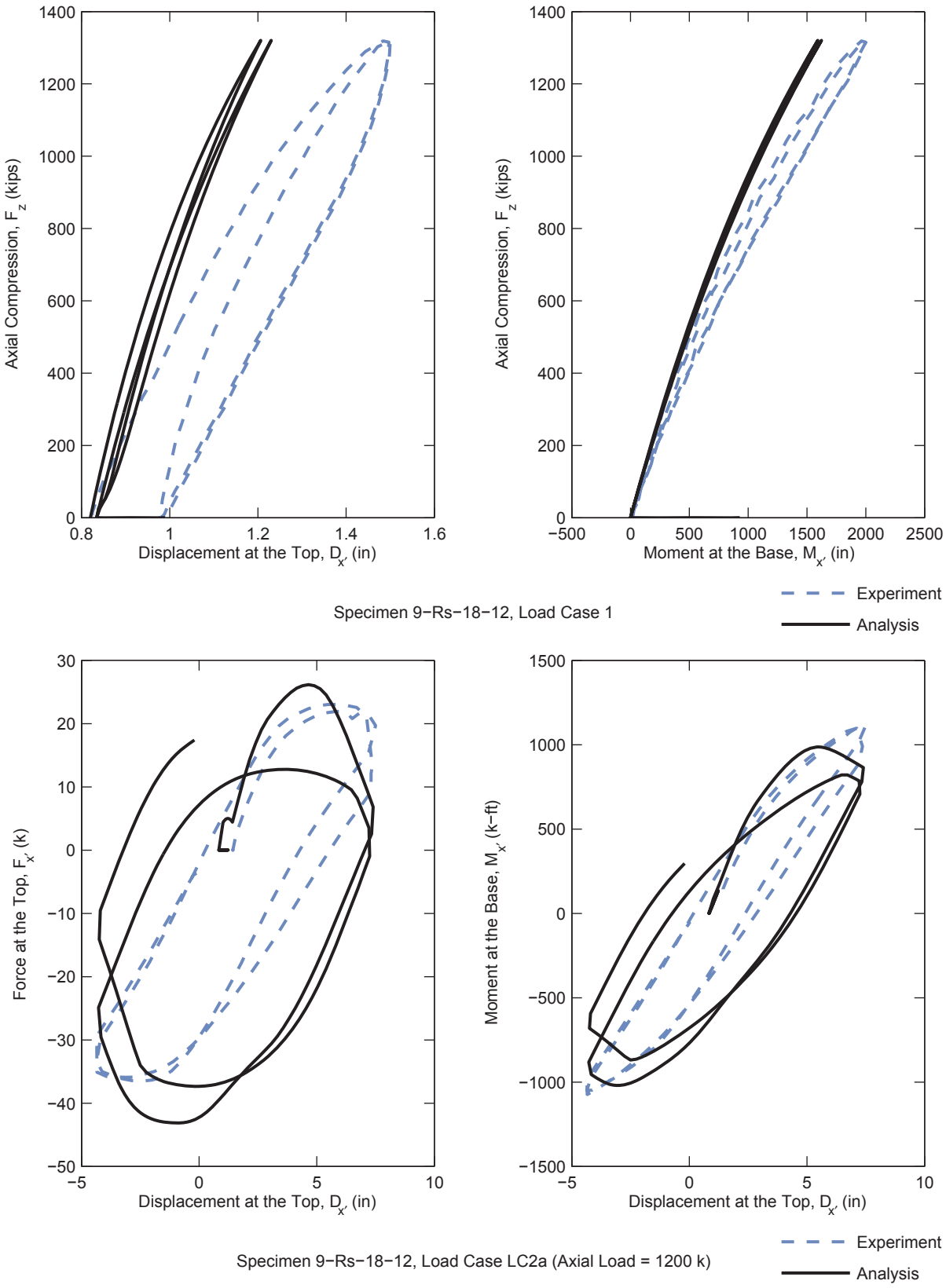

Figure 7.11. Comparison Results – Specimen 9Rs-18-12

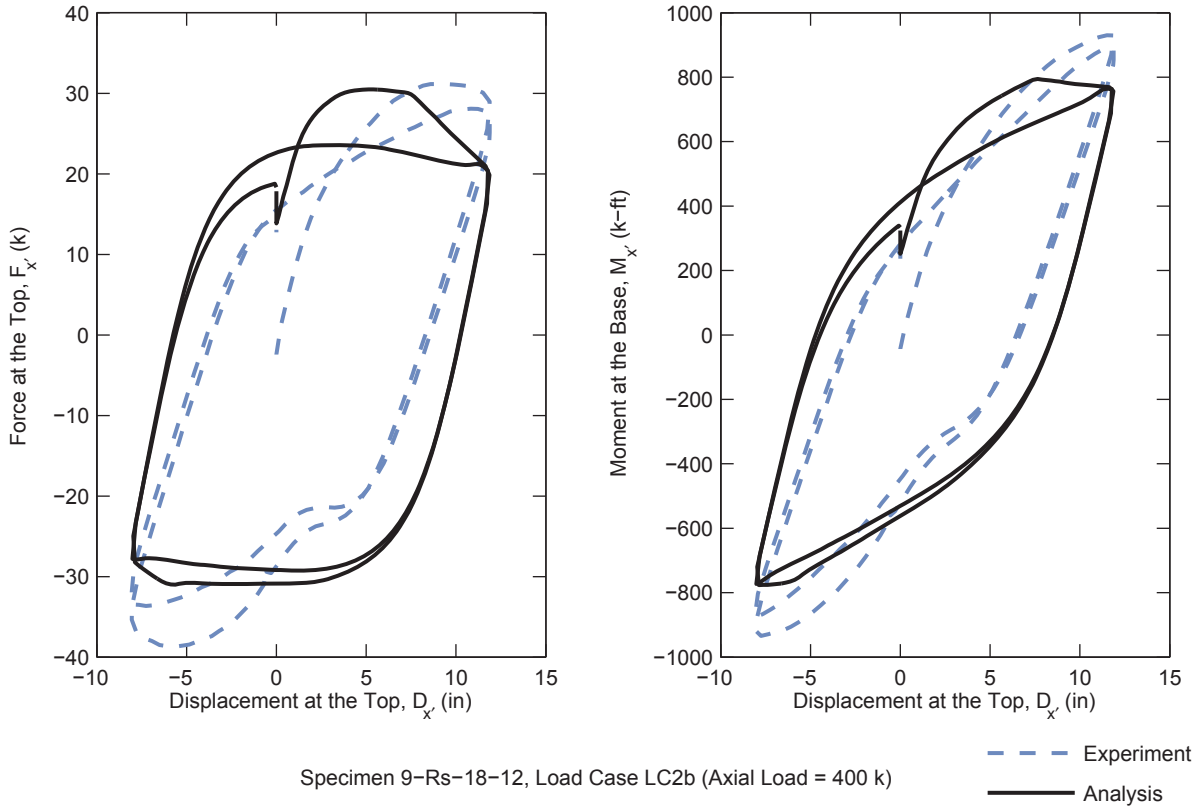

Figure 7.11. Comparison Results – Specimen 9Rs-18-12 (continued)

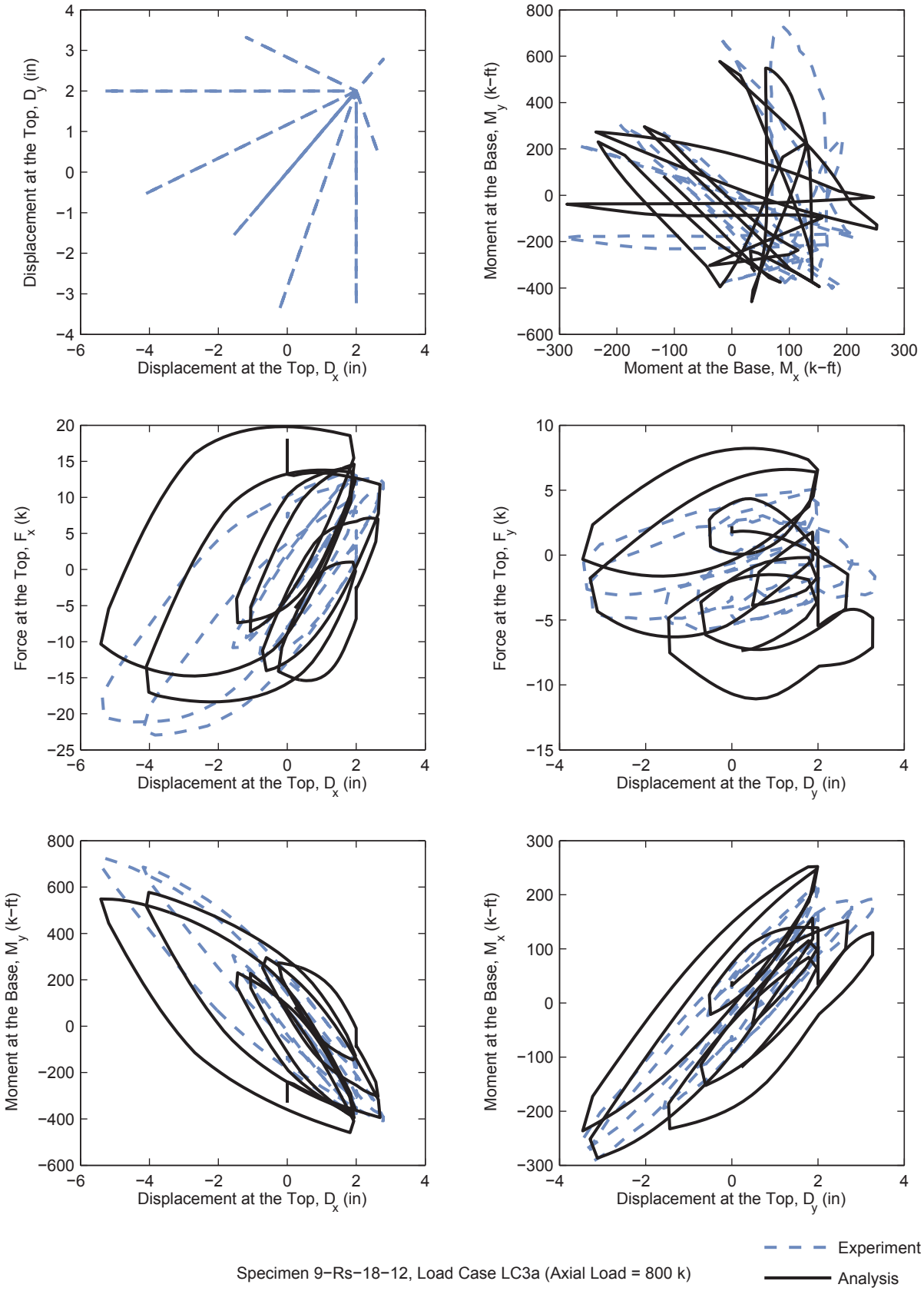

Figure 7.11. Comparison Results – Specimen 9Rs-18-12 (continued)

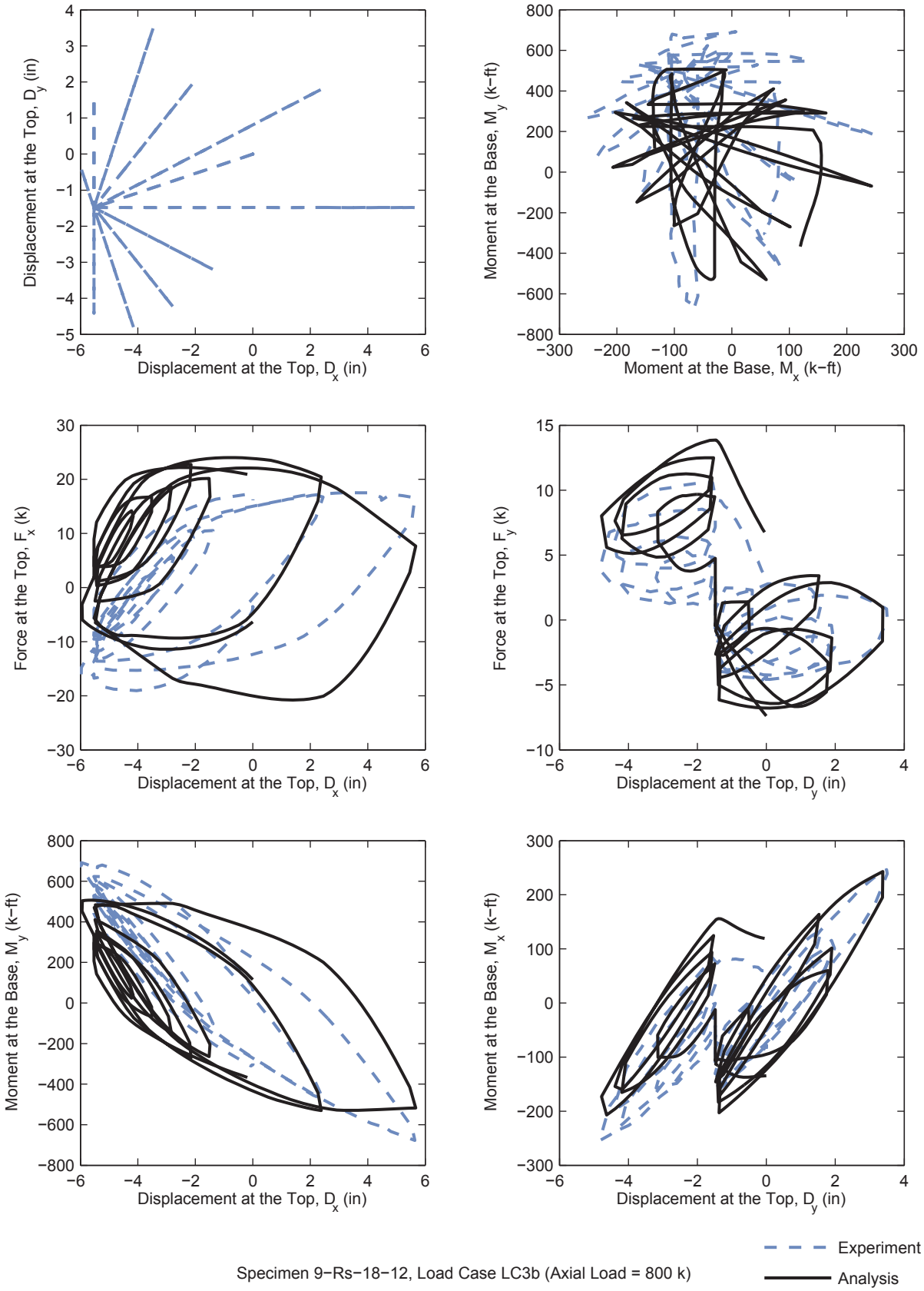

Figure 7.11. Comparison Results – Specimen 9Rs-18-12 (continued)

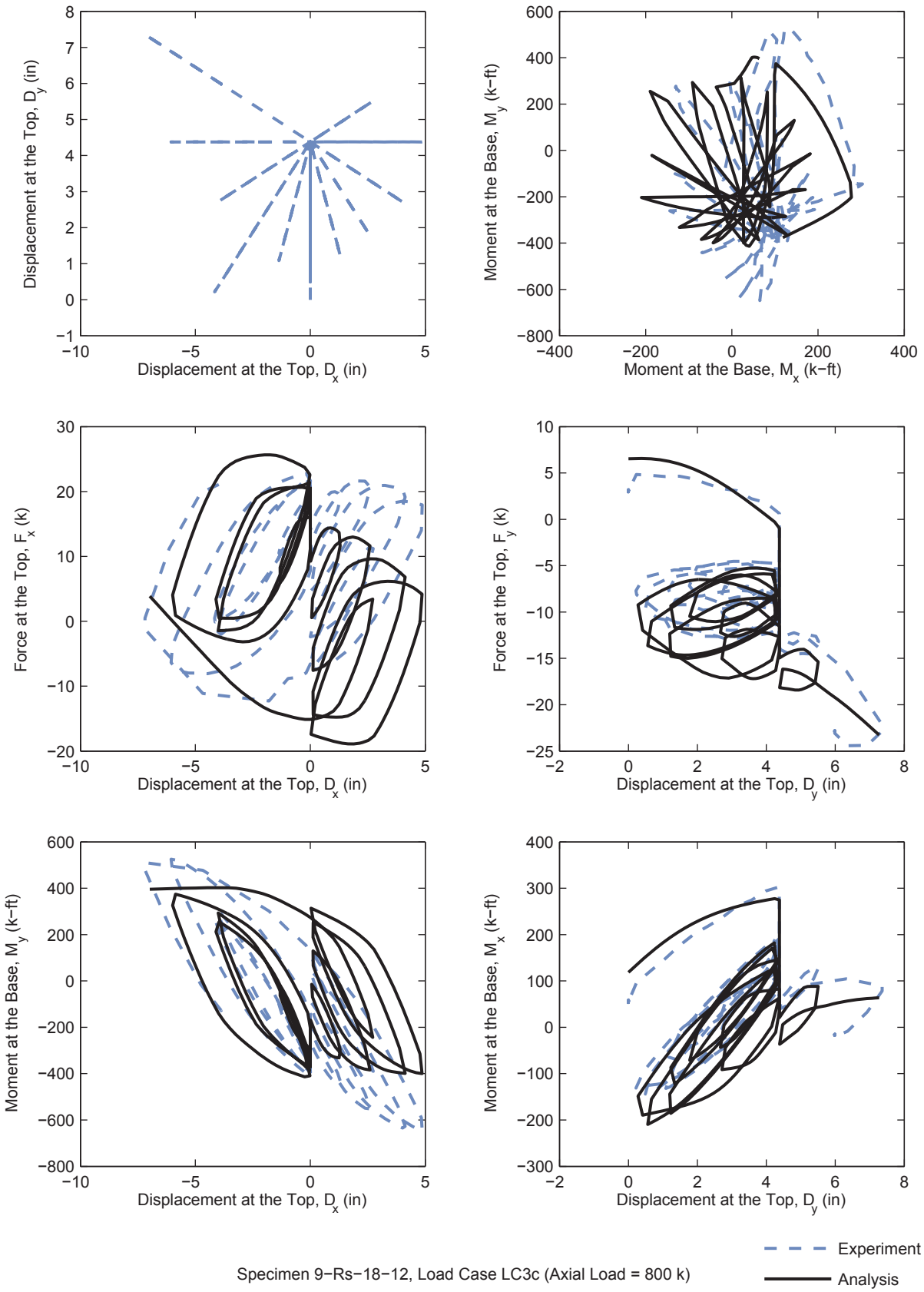

Figure 7.11. Comparison Results – Specimen 9Rs-18-12 (continued)

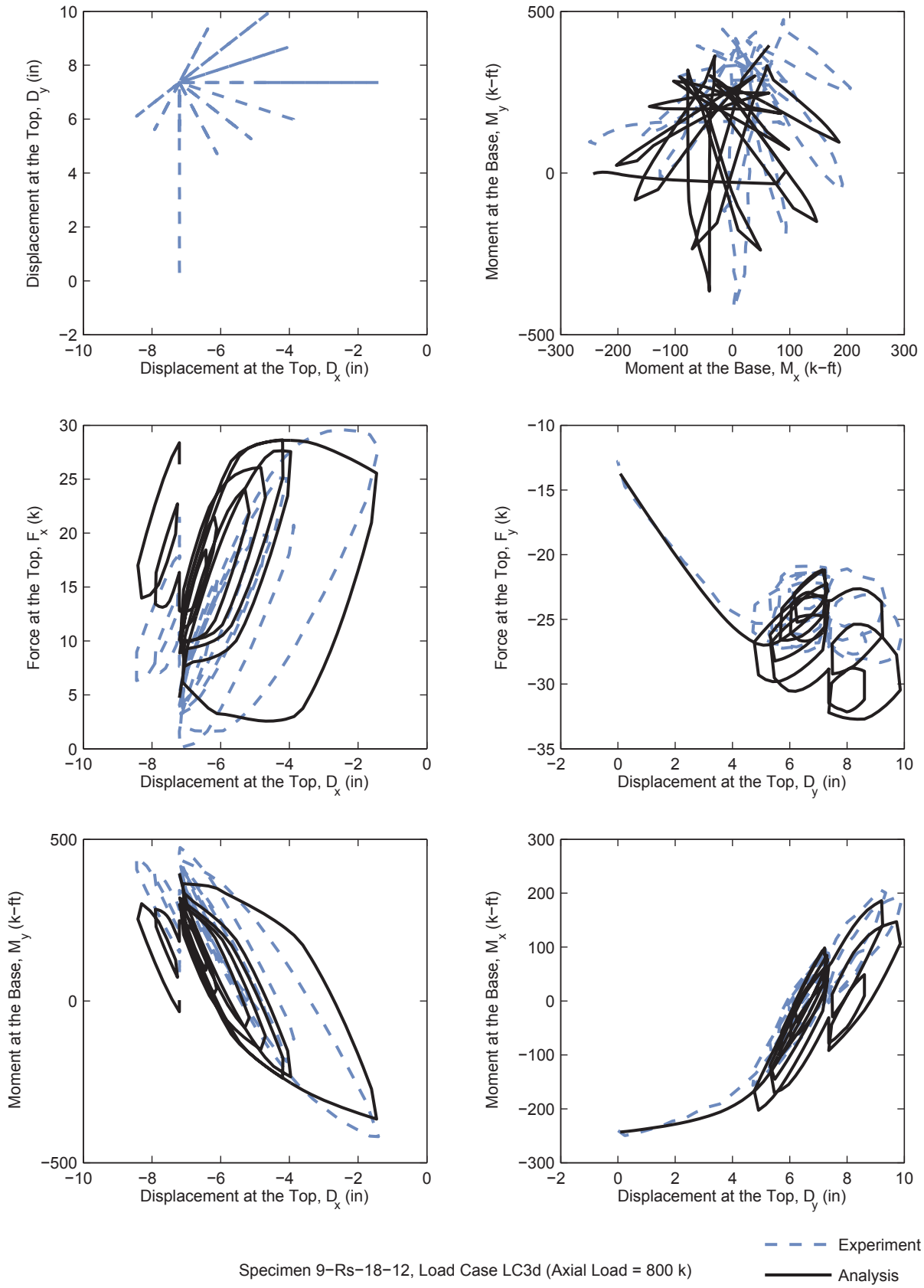

Figure 7.11. Comparison Results – Specimen 9Rs-18-12 (continued)

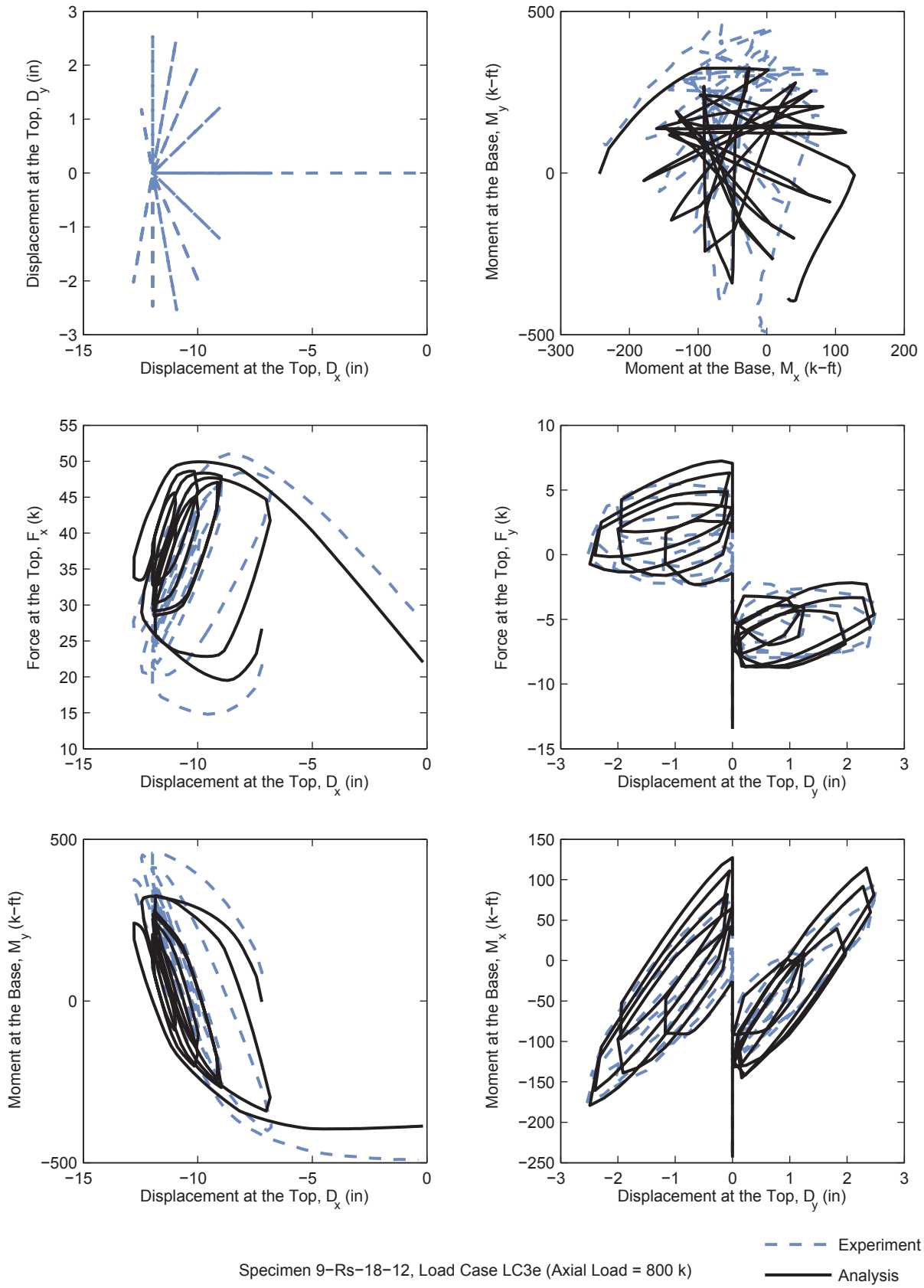

Figure 7.11. Comparison Results – Specimen 9Rs-18-12 (continued)

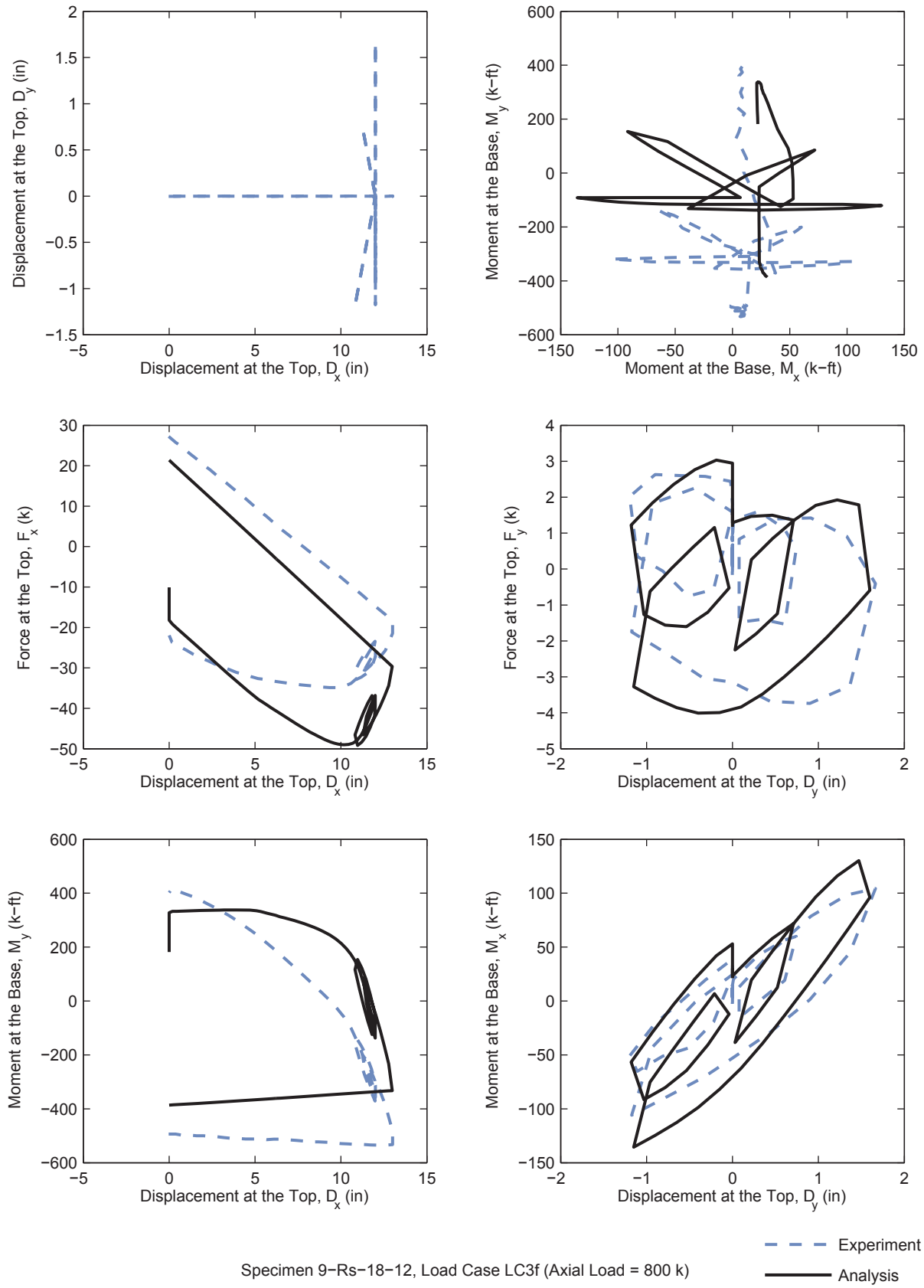

Figure 7.11. Comparison Results – Specimen 9Rs-18-12 (continued)

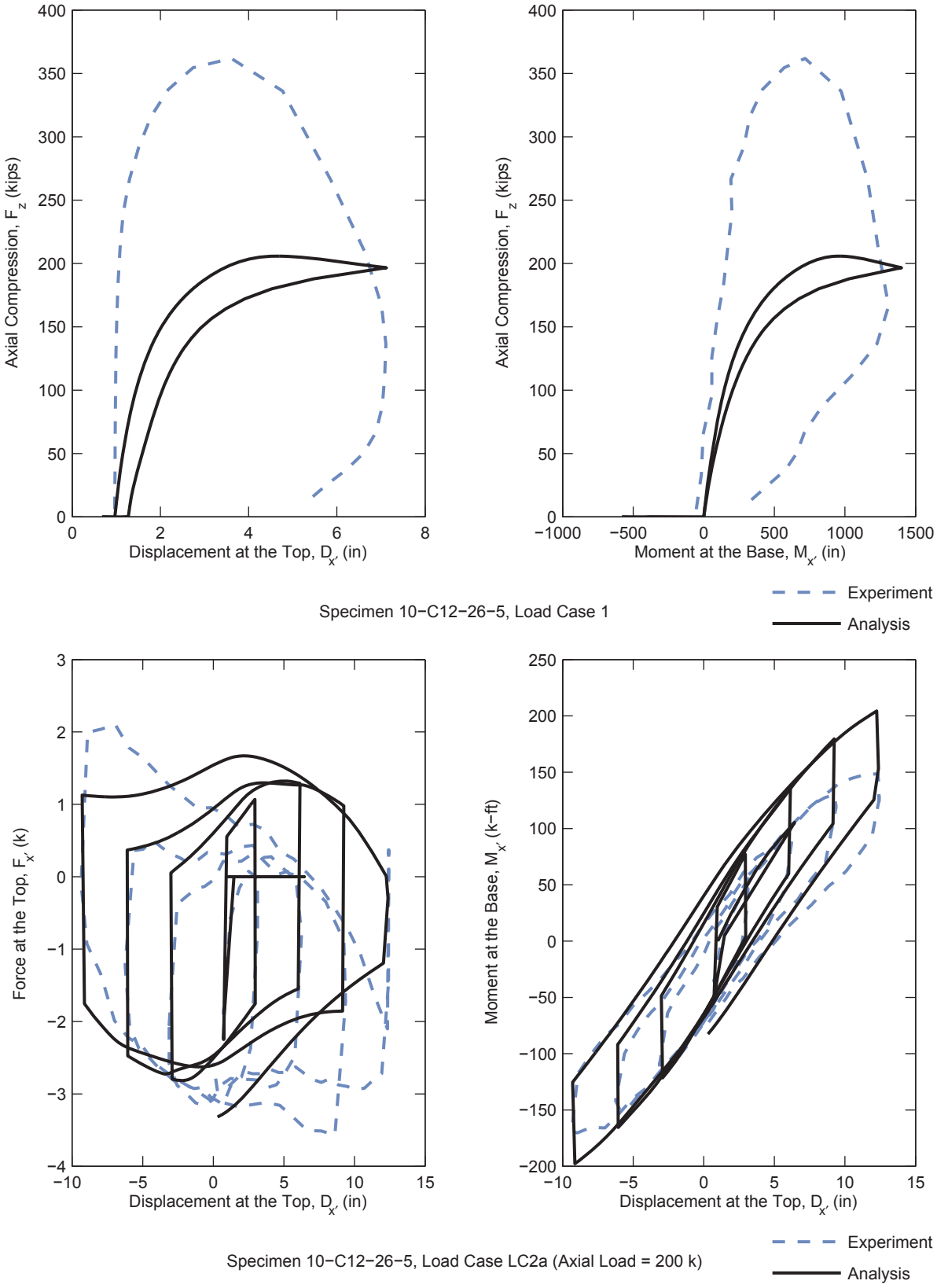

Figure 7.12. Comparison Results – Specimen 10C12-26-5

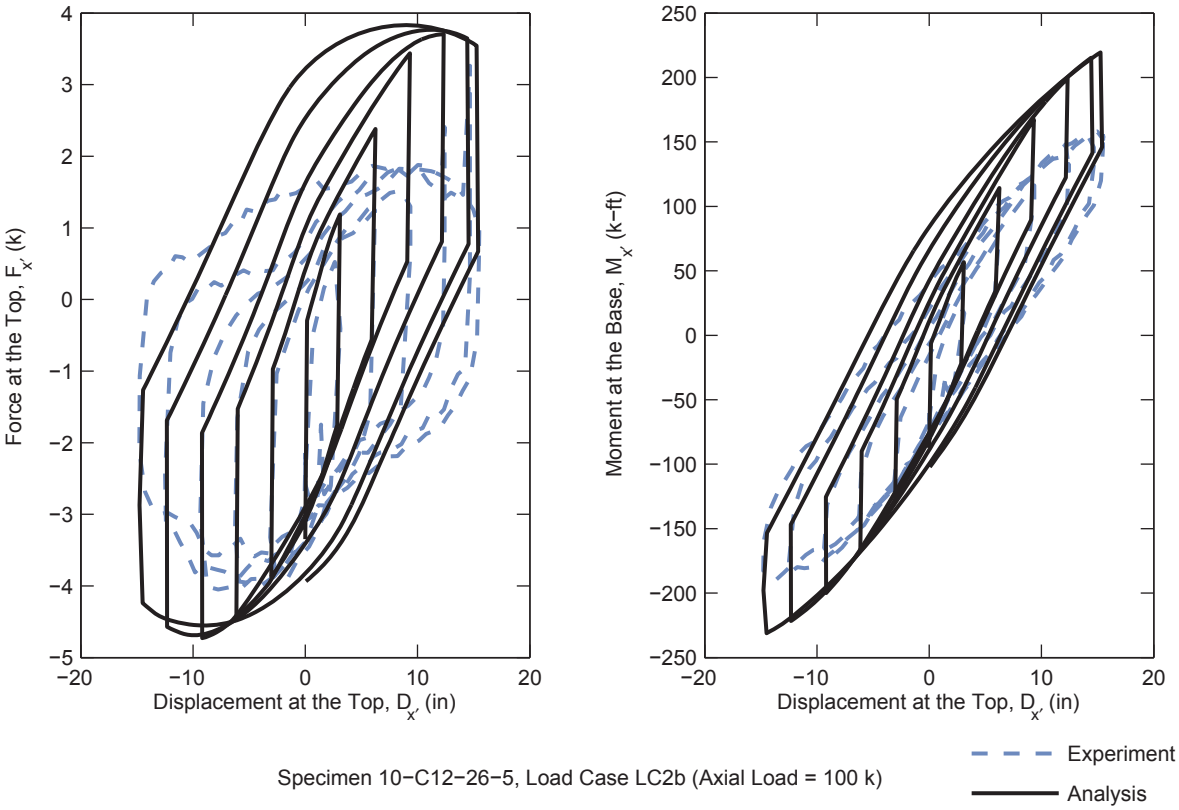

Figure 7.12. Comparison Results – Specimen 10C12-26-5 (continued)

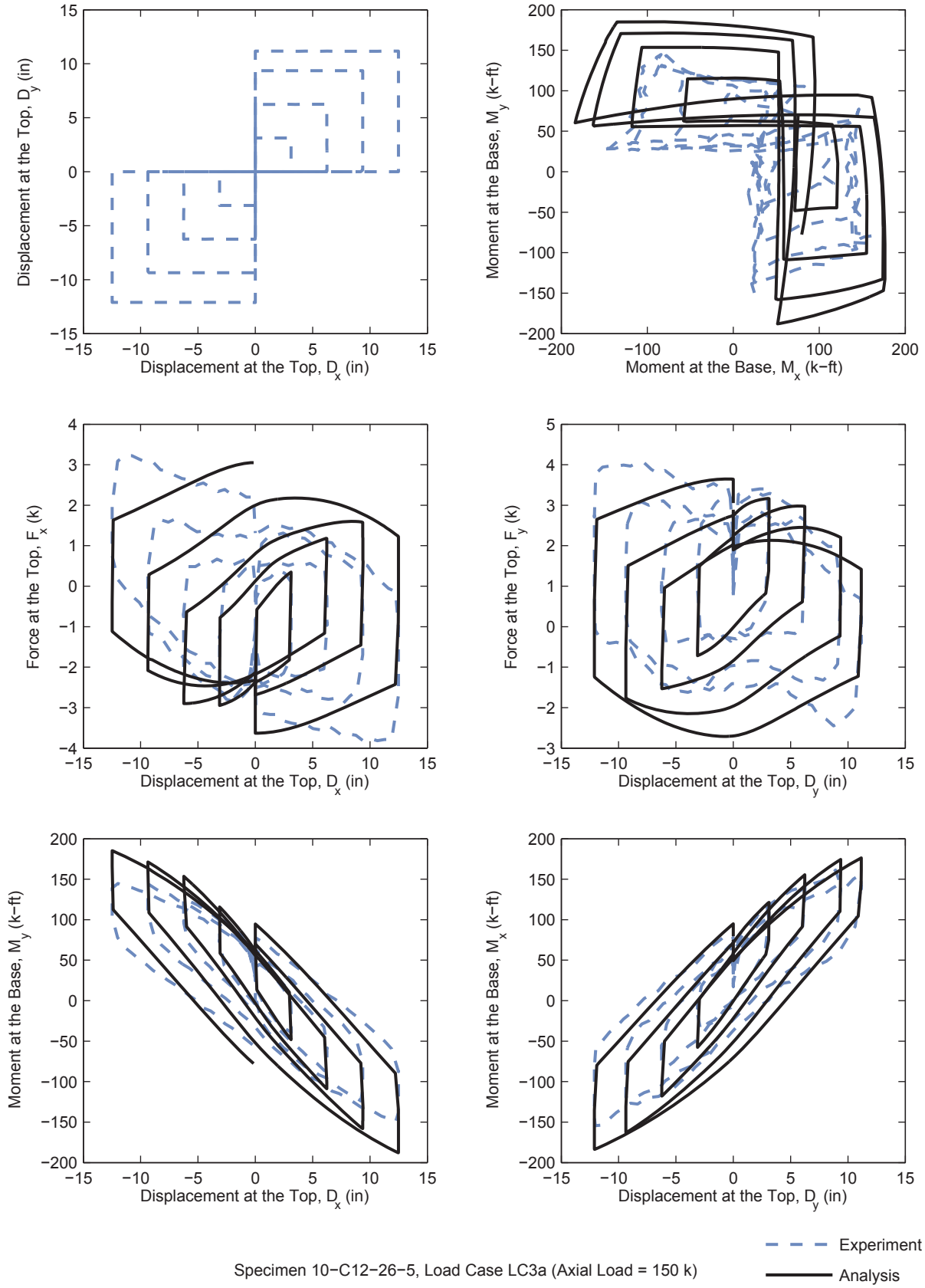

Figure 7.12. Comparison Results – Specimen 10C12-26-5 (continued)

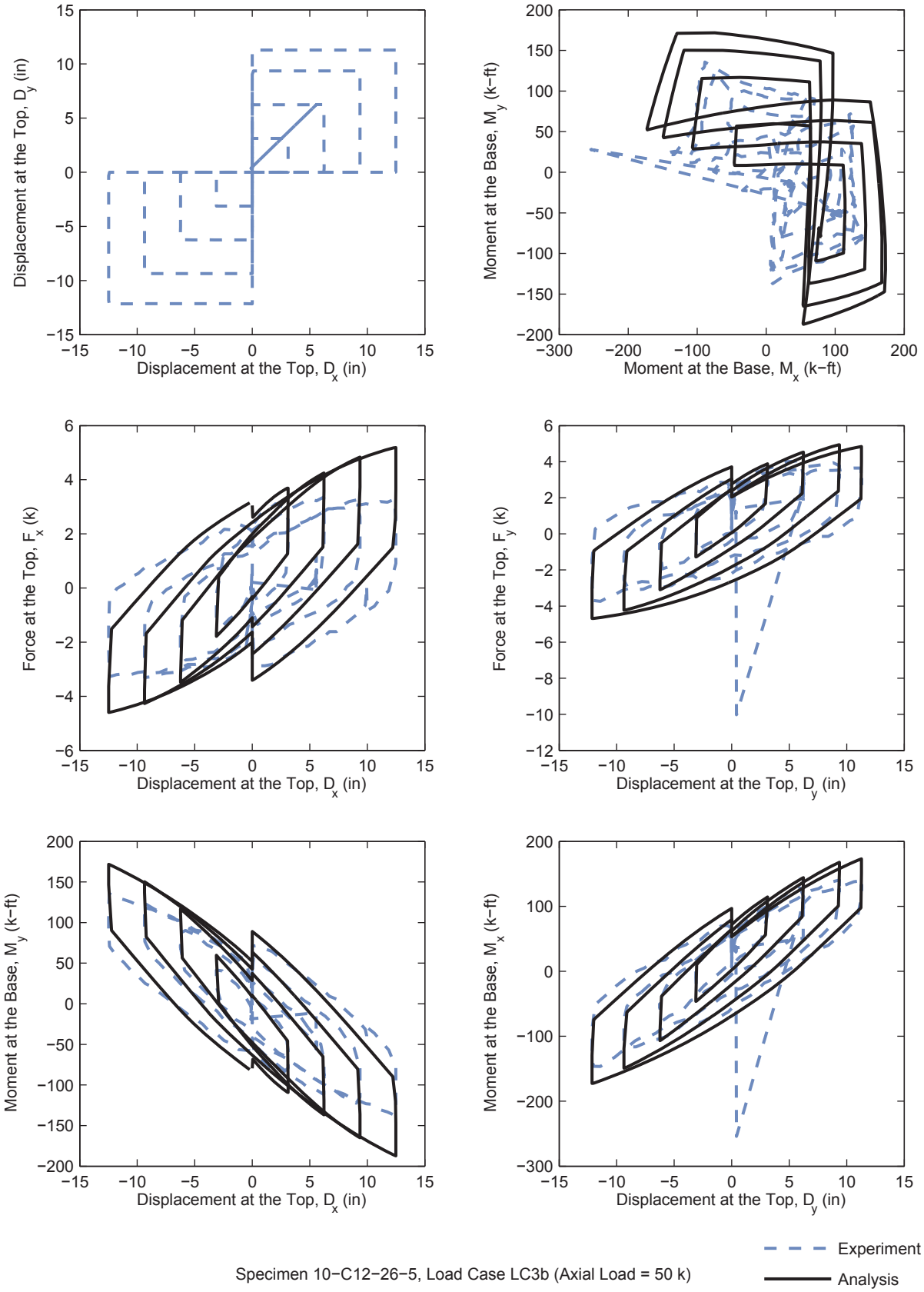

Figure 7.12. Comparison Results – Specimen 10C12-26-5 (continued)

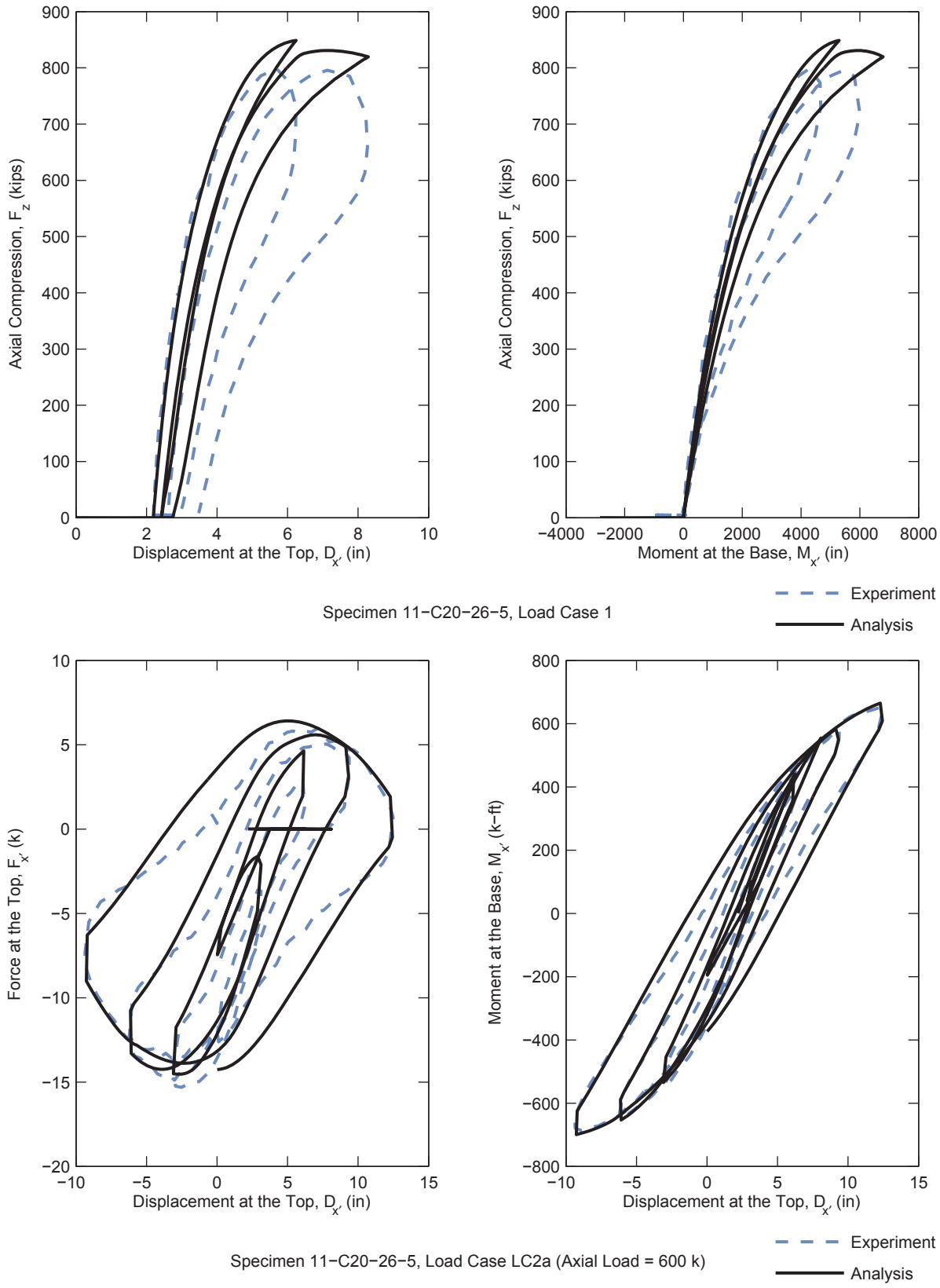

Figure 7.13. Comparison Results – Specimen 11C20-26-5

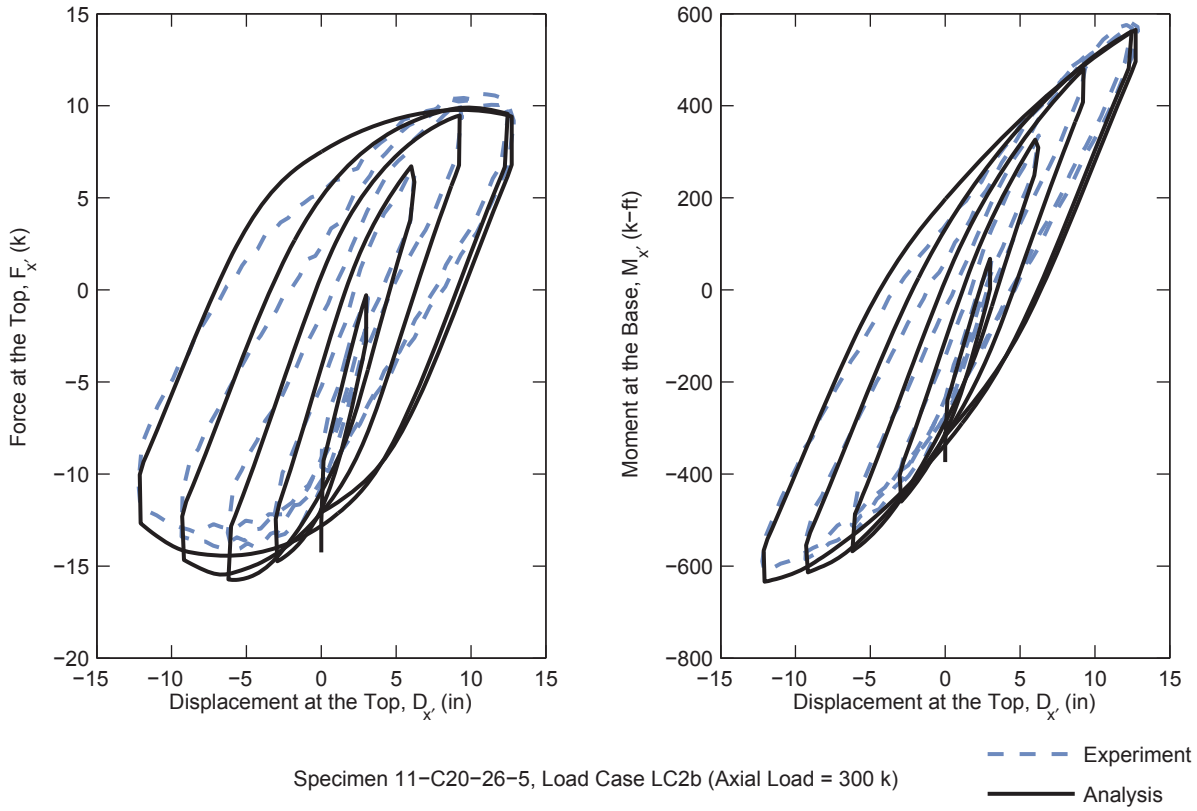

Figure 7.13. Comparison Results – Specimen 11C20-26-5 (continued)

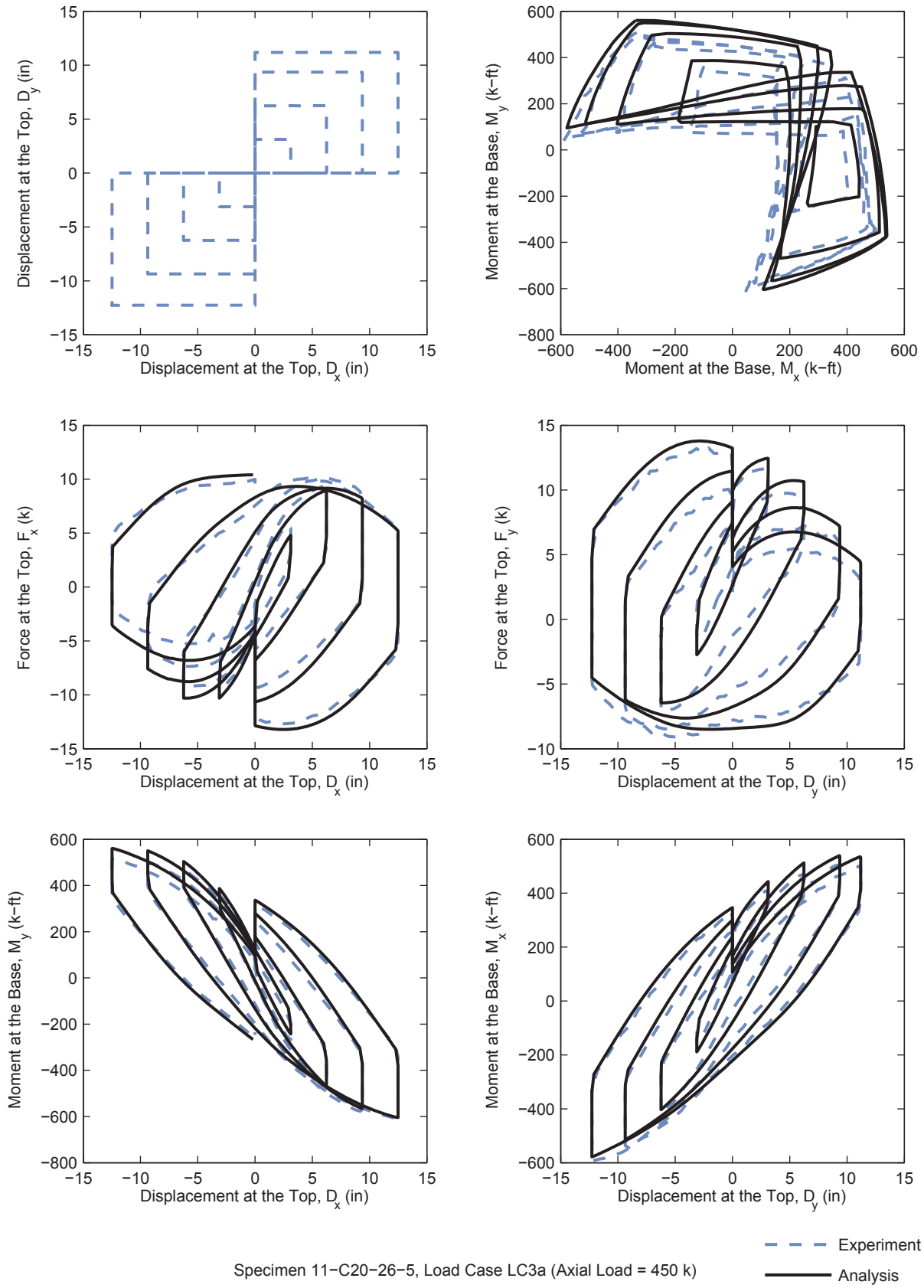

Figure 7.13. Comparison Results – Specimen 11C20-26-5 (continued)

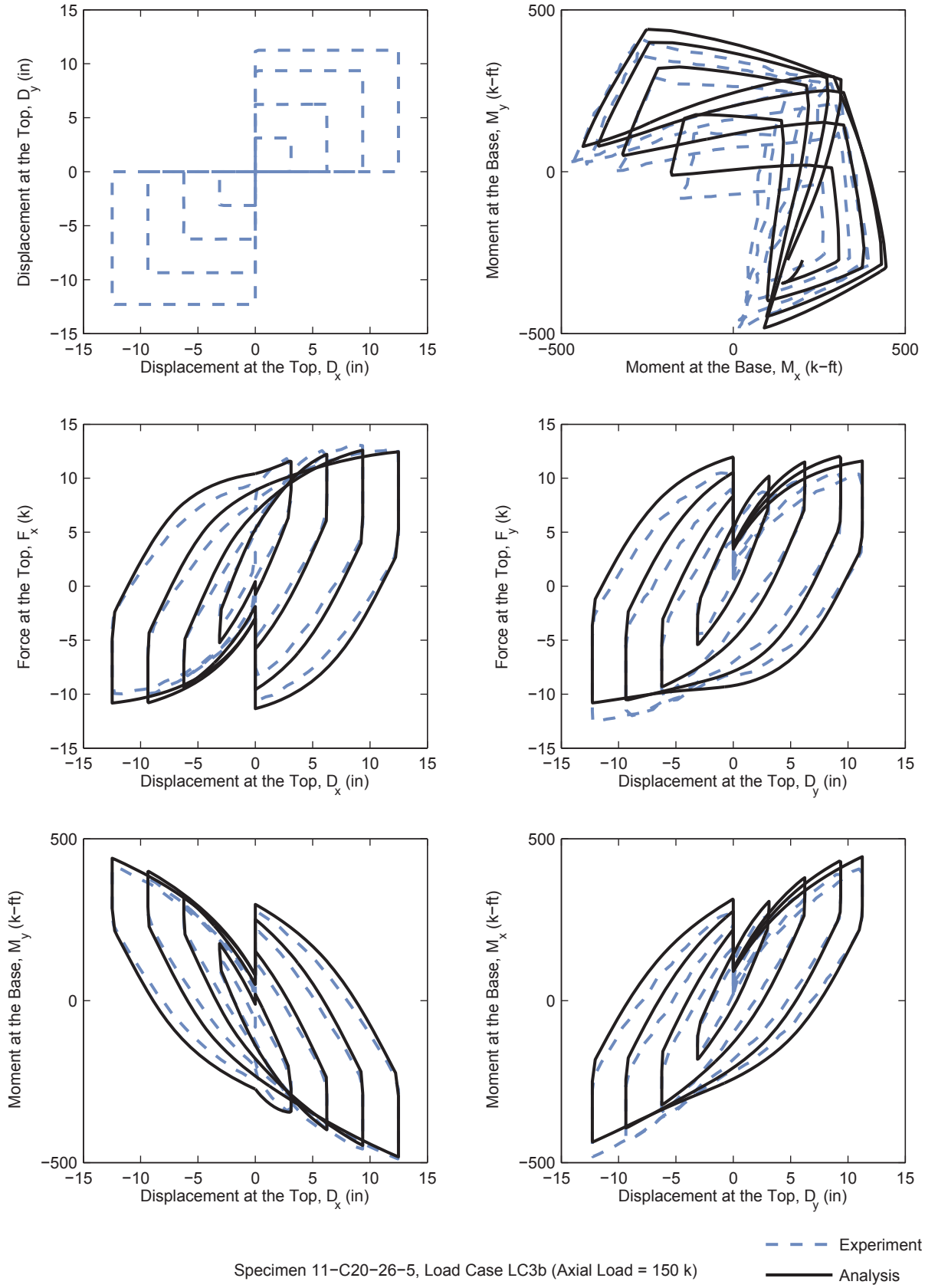

Figure 7.13. Comparison Results – Specimen 11C20-26-5 (continued)

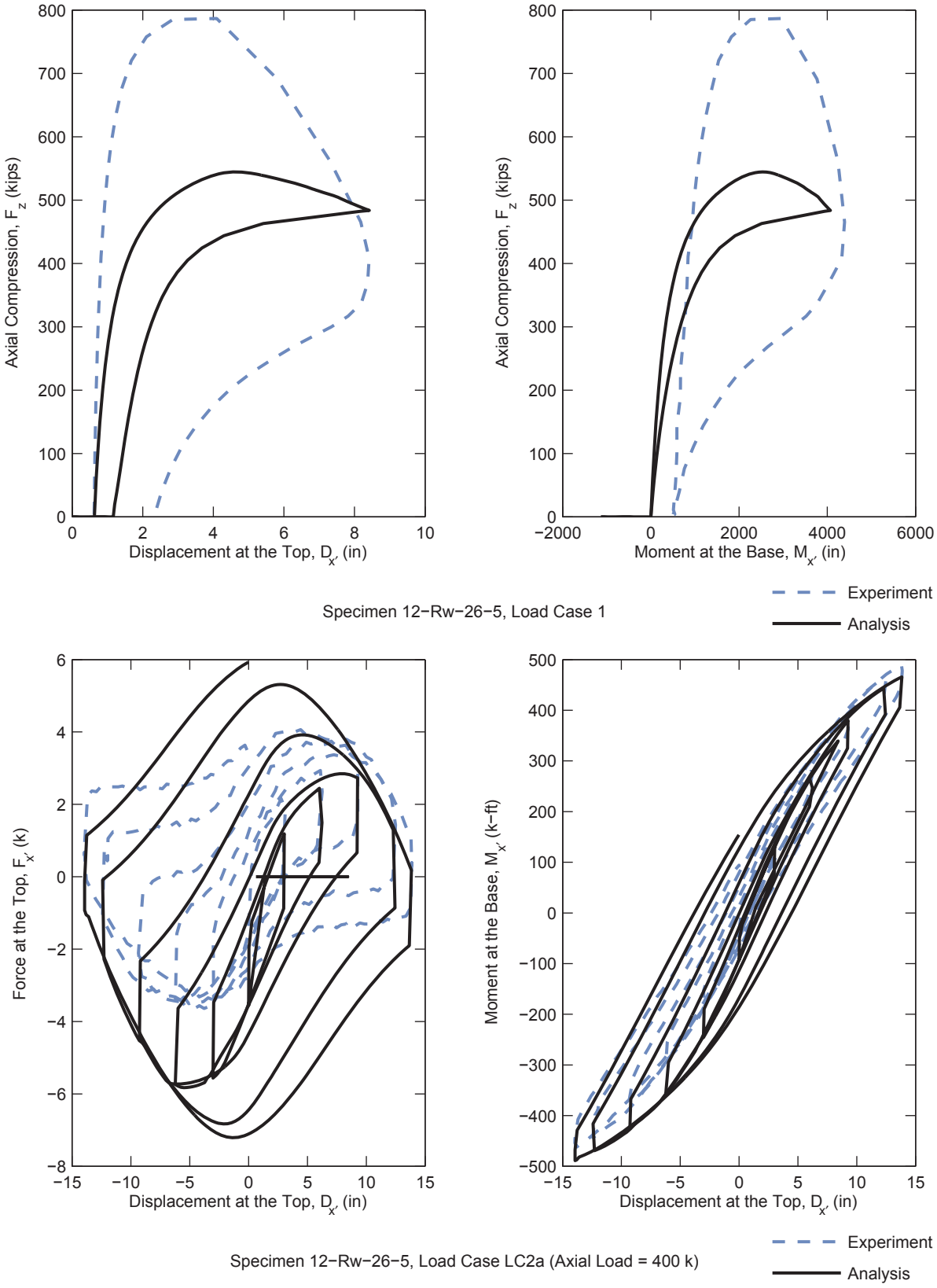

Figure 7.14. Comparison Results – Specimen 12Rw-26-5

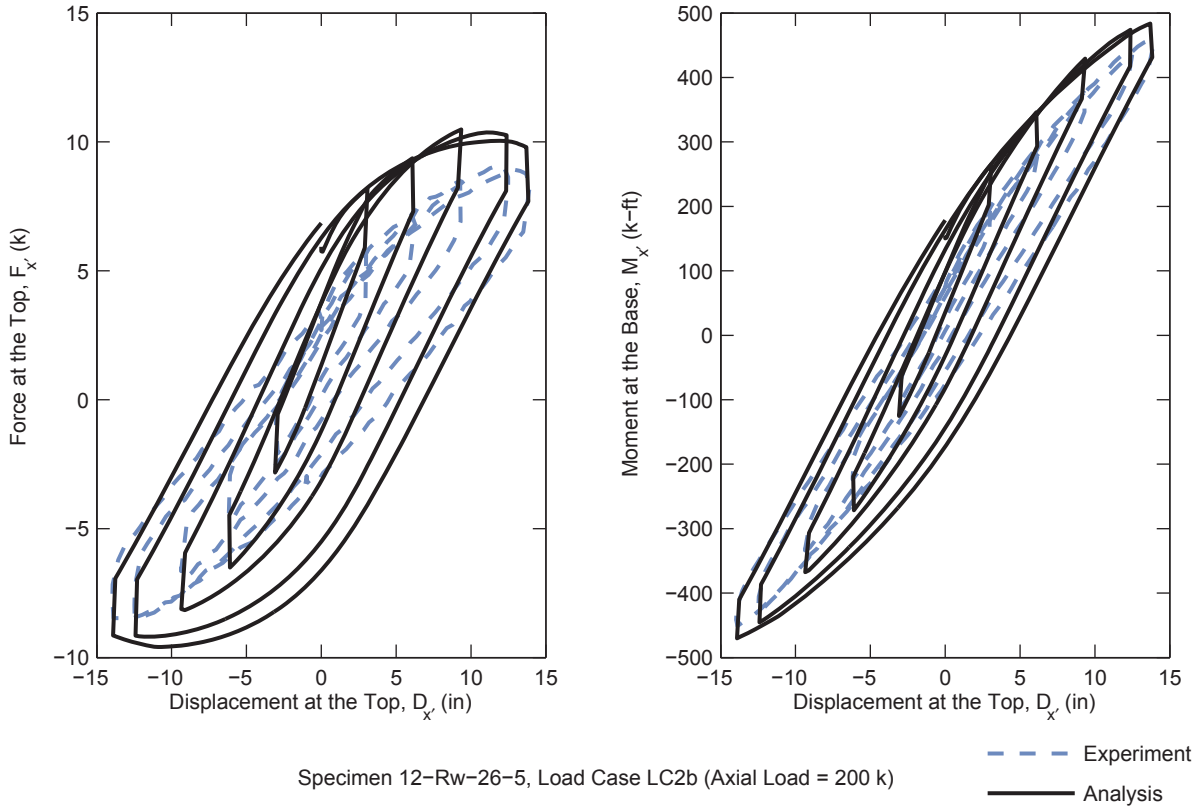

Figure 7.14. Comparison Results – Specimen 12Rw-26-5 (continued)

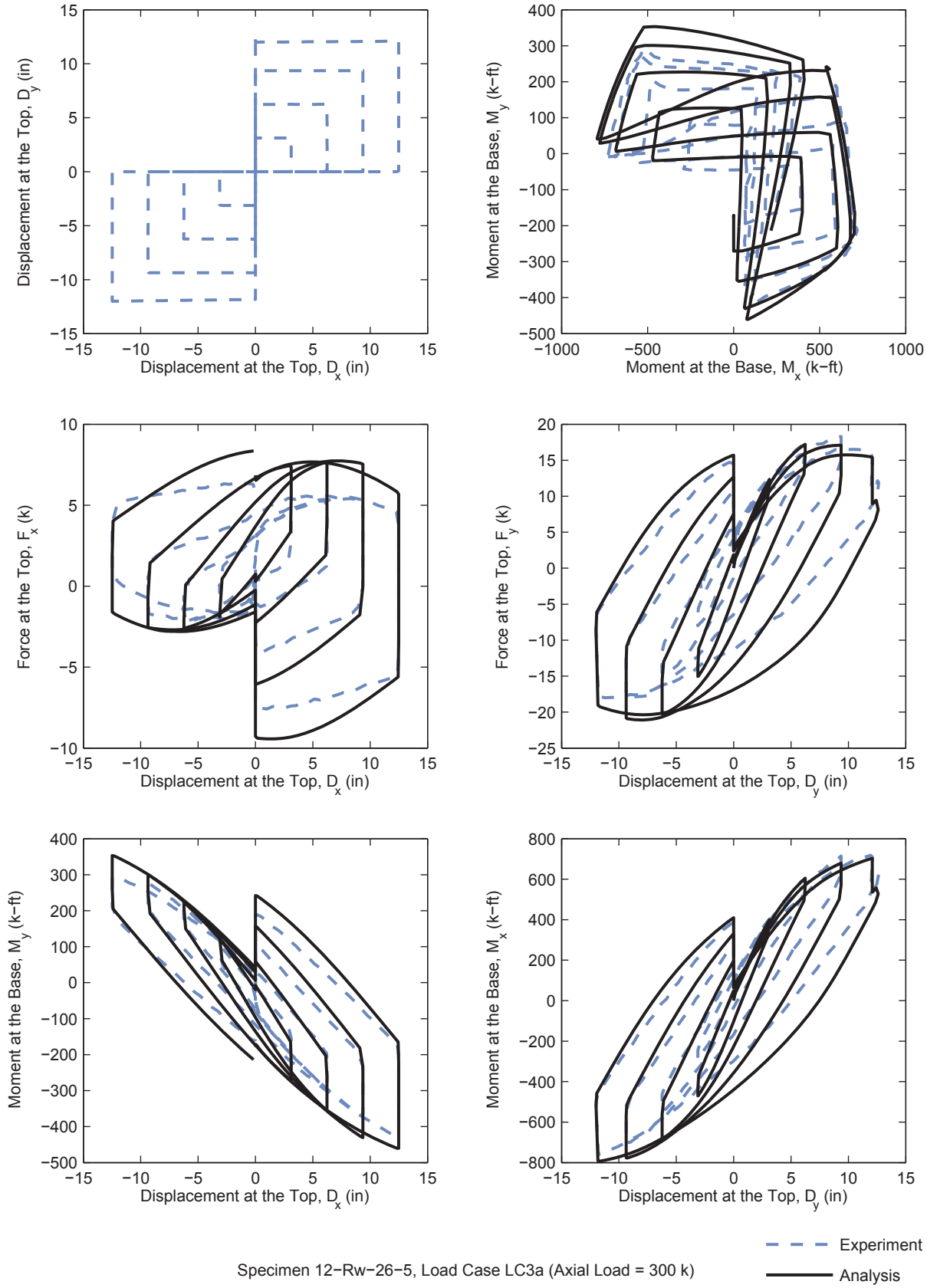

Figure 7.14. Comparison Results – Specimen 12Rw-26-5 (continued)

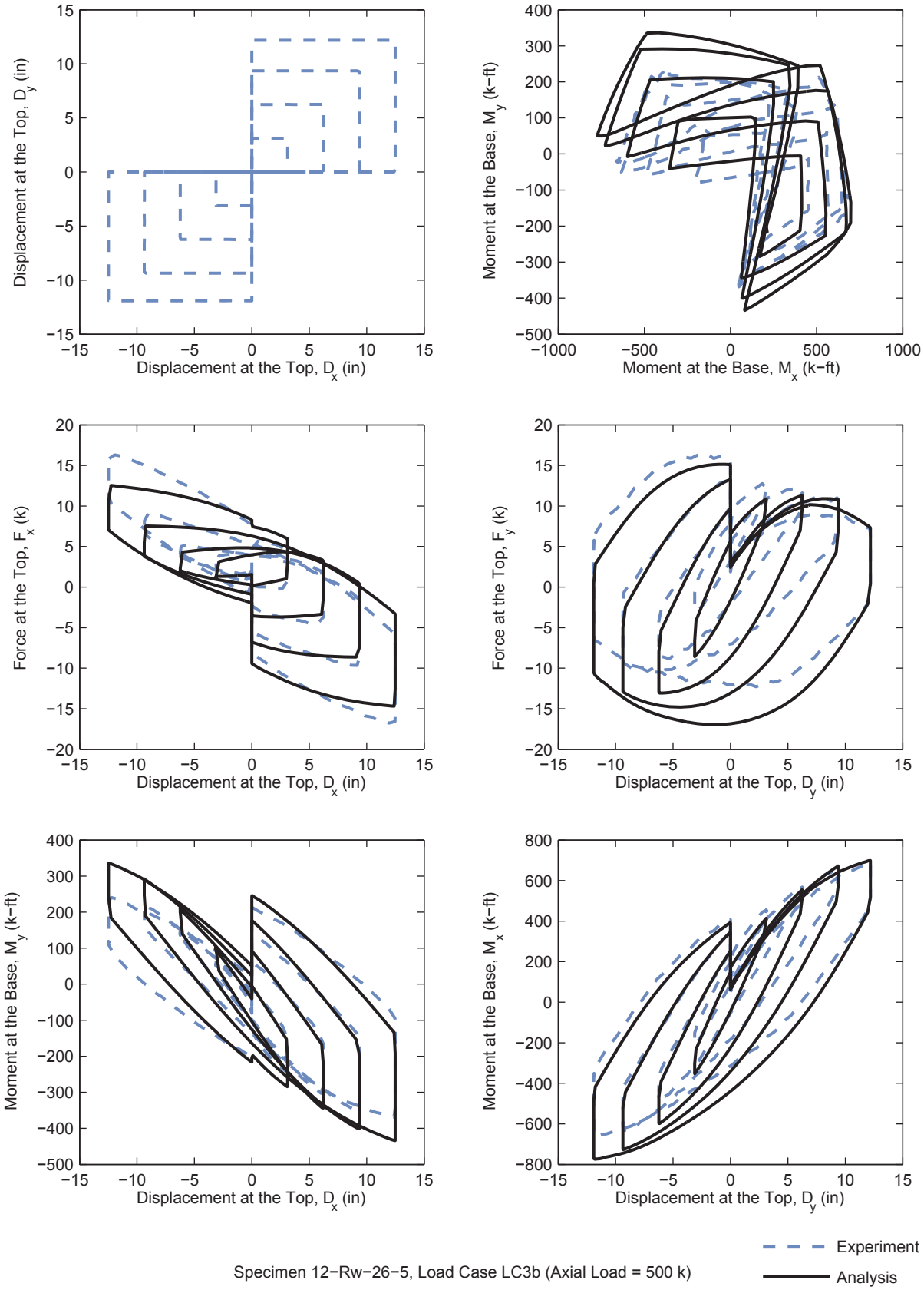

Figure 7.14. Comparison Results – Specimen 12Rw-26-5 (continued)

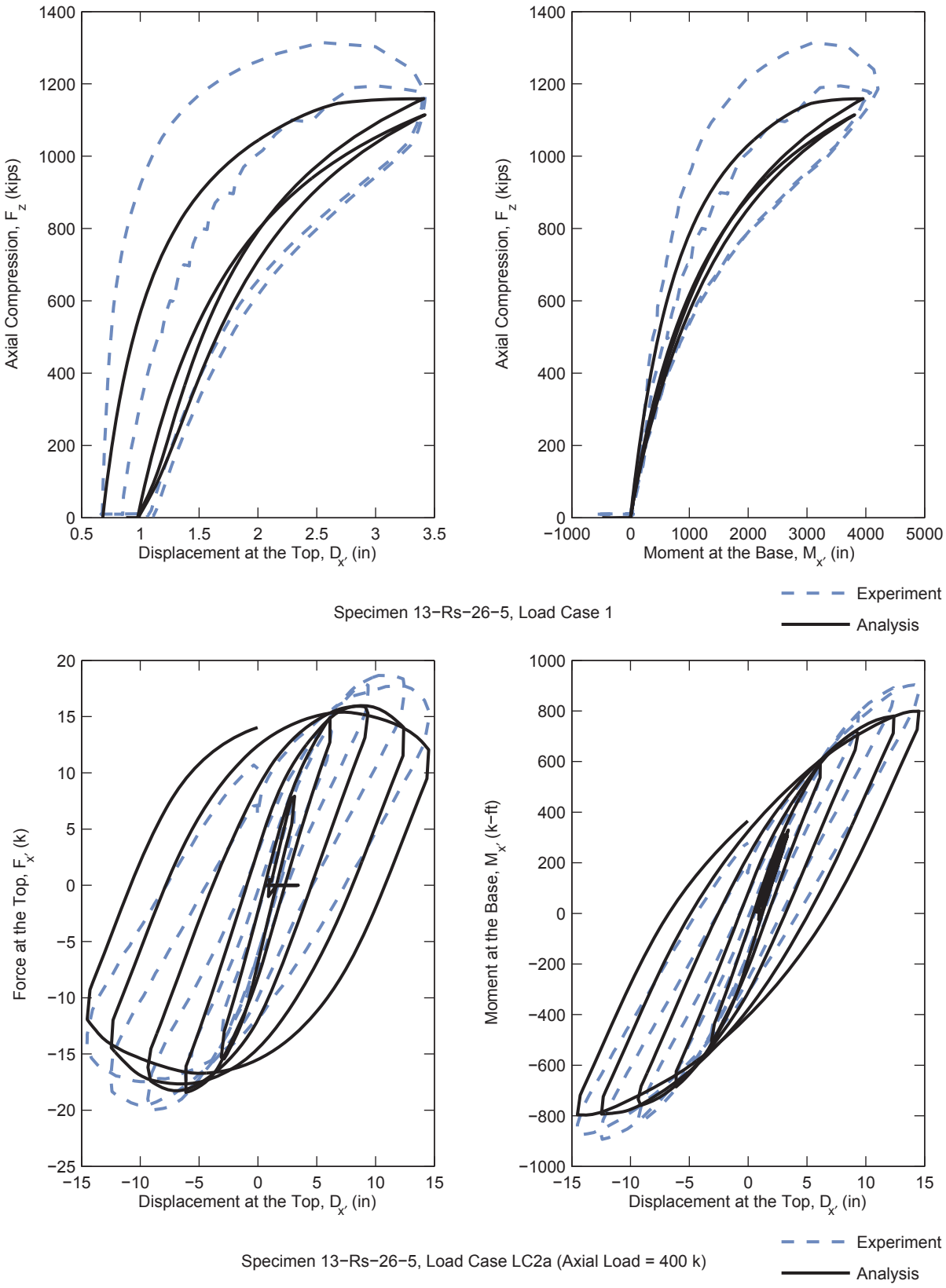

Figure 7.15. Comparison Results – Specimen 13Rs-26-5

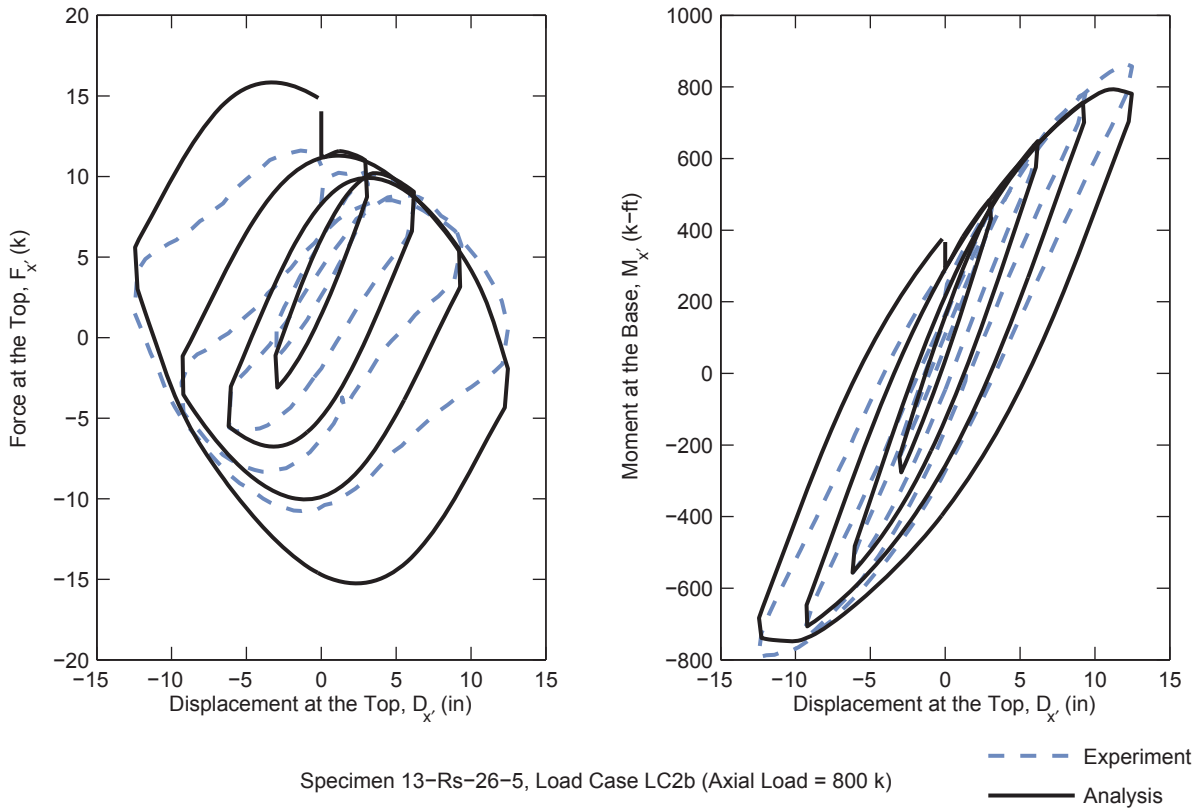

Figure 7.15. Comparison Results – Specimen 13Rs-26-5 (continued)

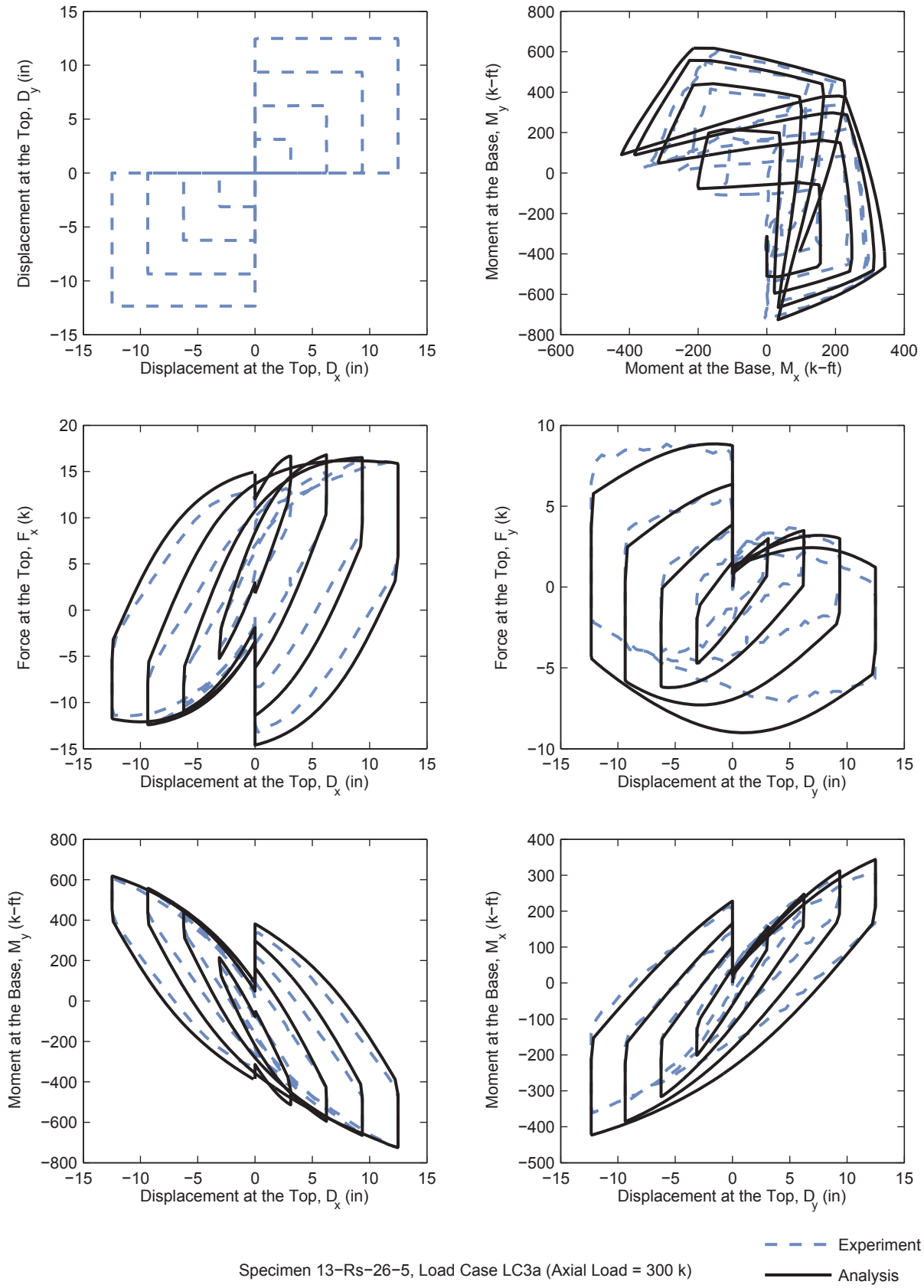

Figure 7.15. Comparison Results – Specimen 13Rs-26-5 (continued)

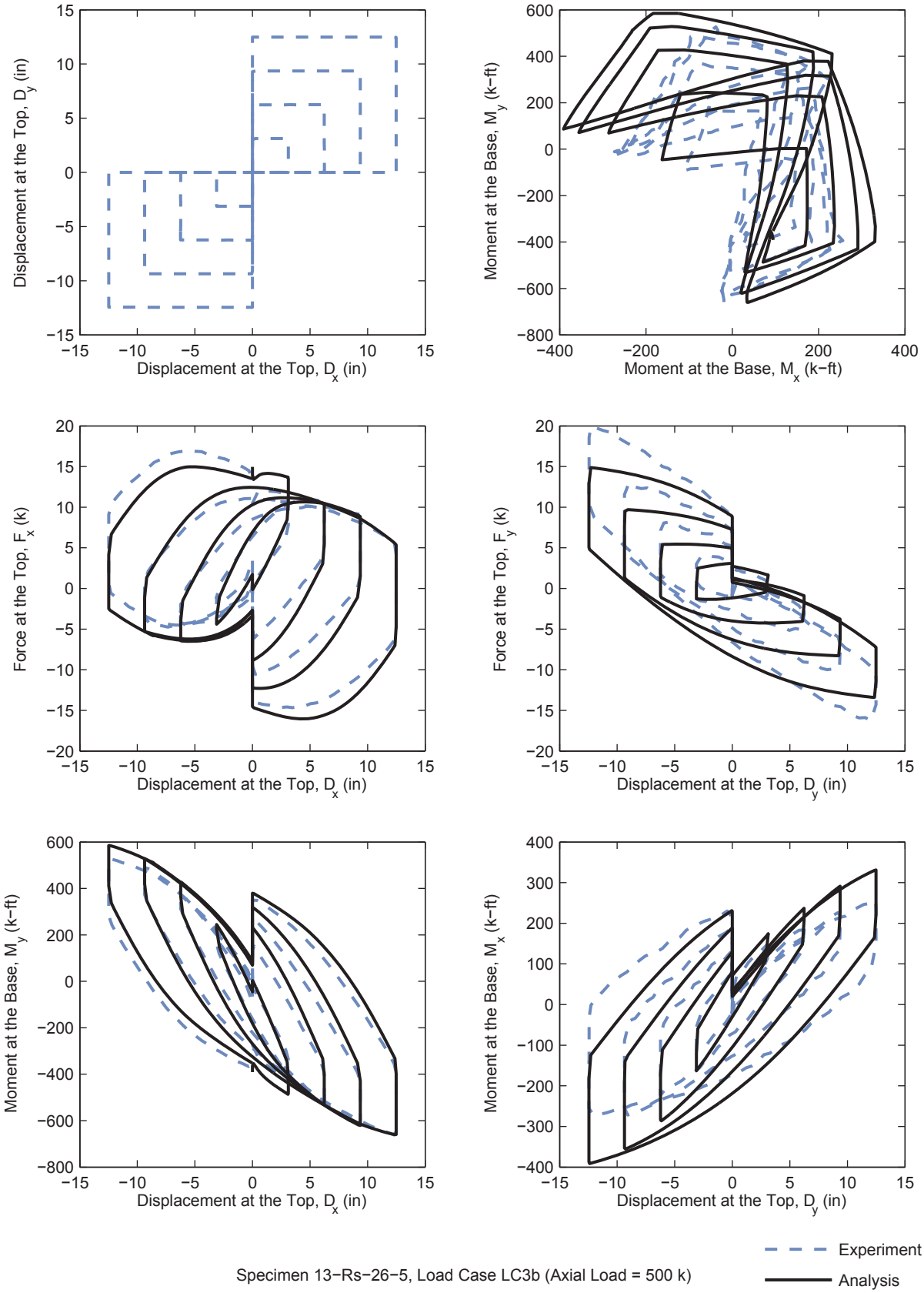

Figure 7.15. Comparison Results – Specimen 13Rs-26-5 (continued)

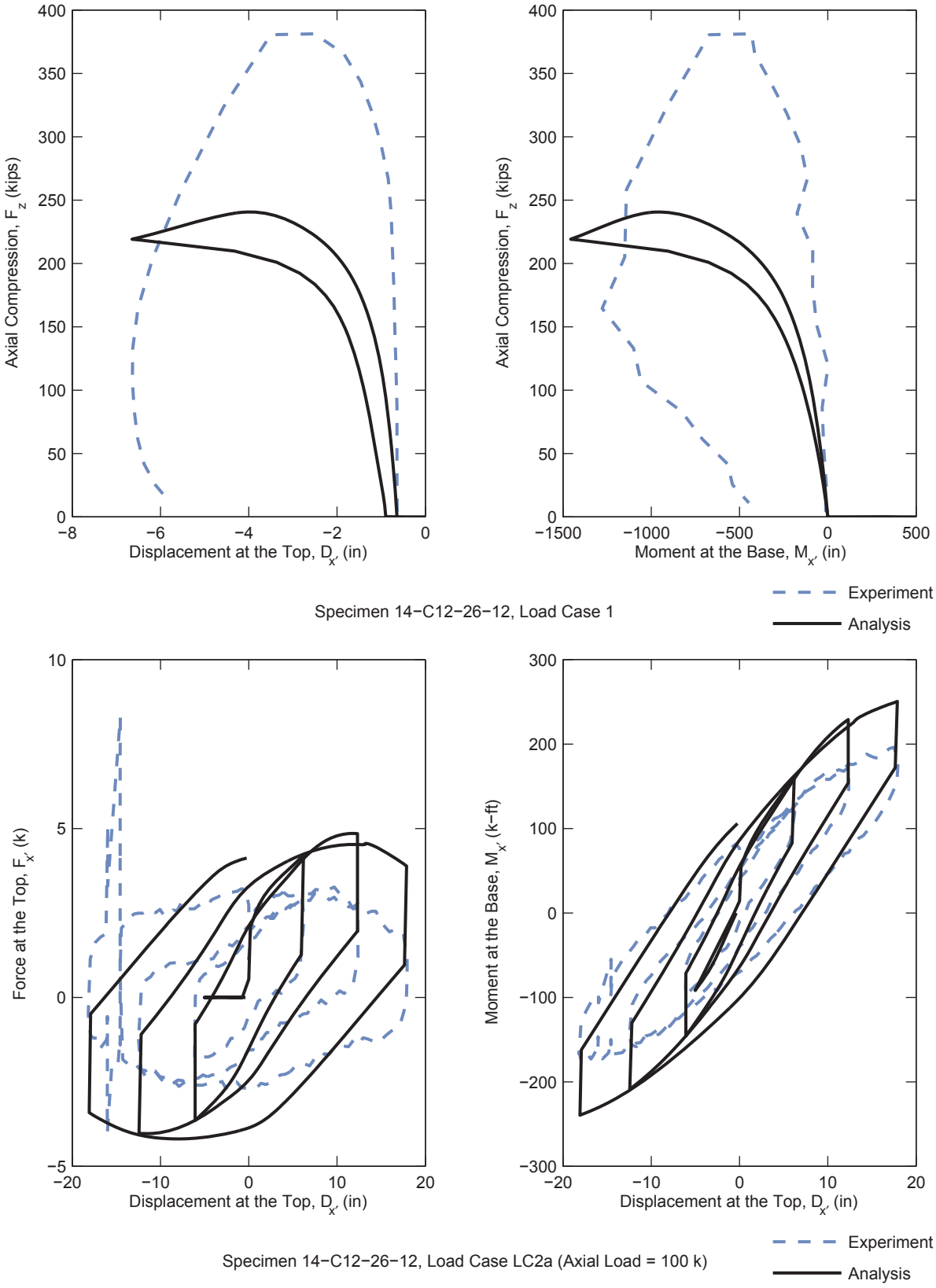

Figure 7.16. Comparison Results – Specimen 14C12-26-12

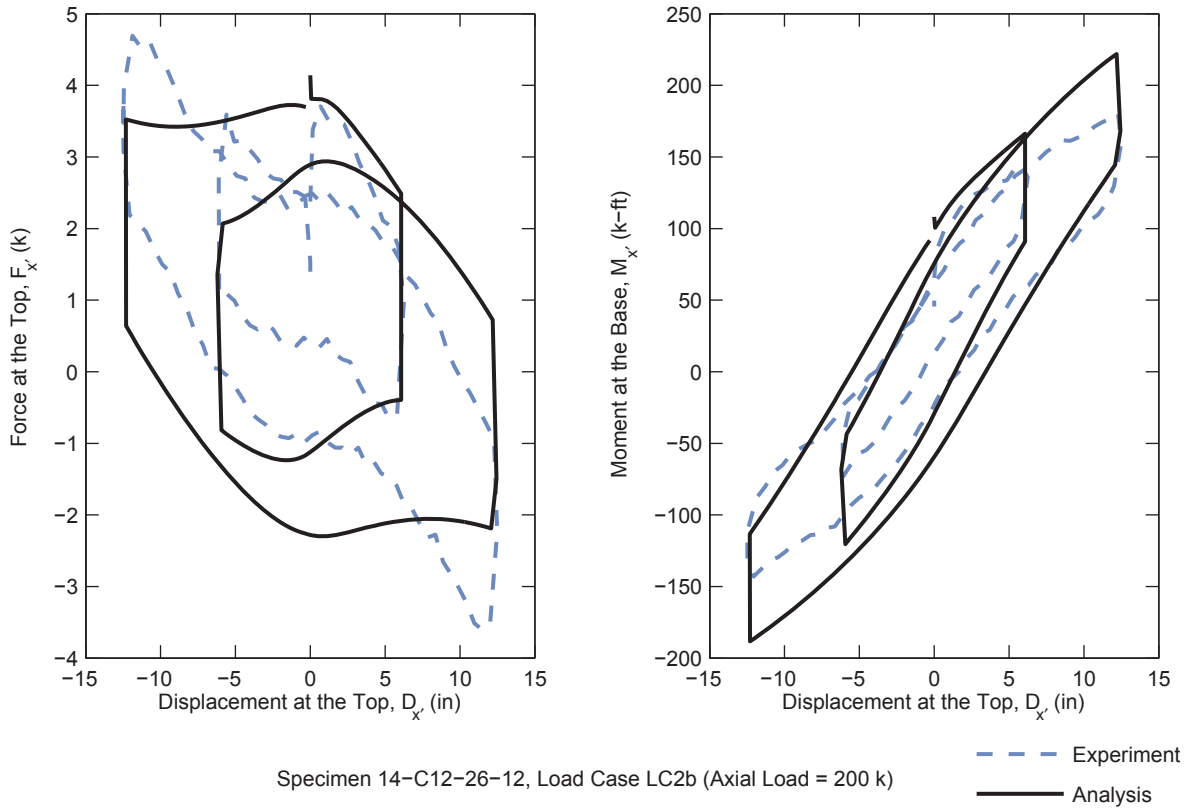

Figure 7.16. Comparison Results – Specimen 14C12-26-12 (continued)

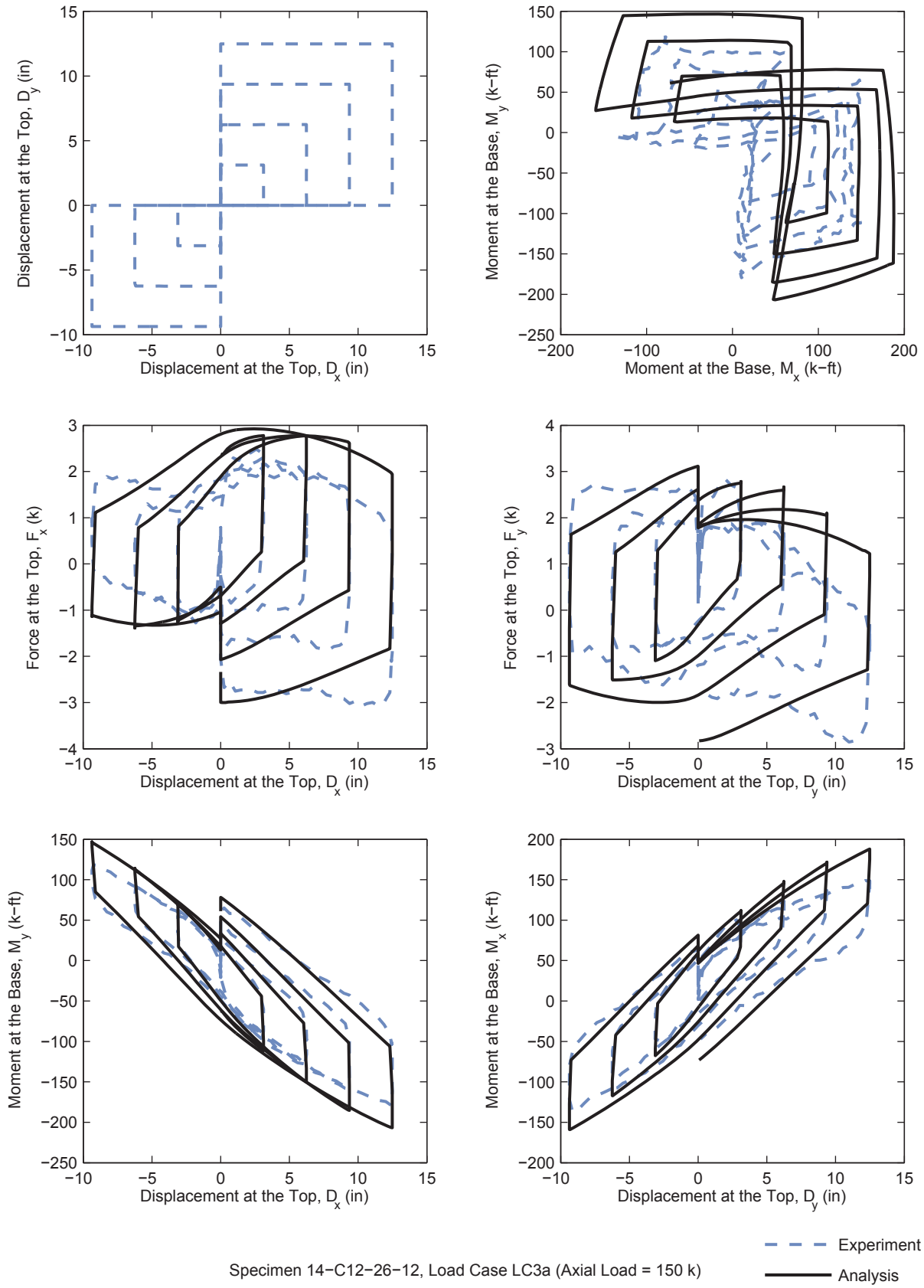

Figure 7.16. Comparison Results – Specimen 14C12-26-12 (continued)

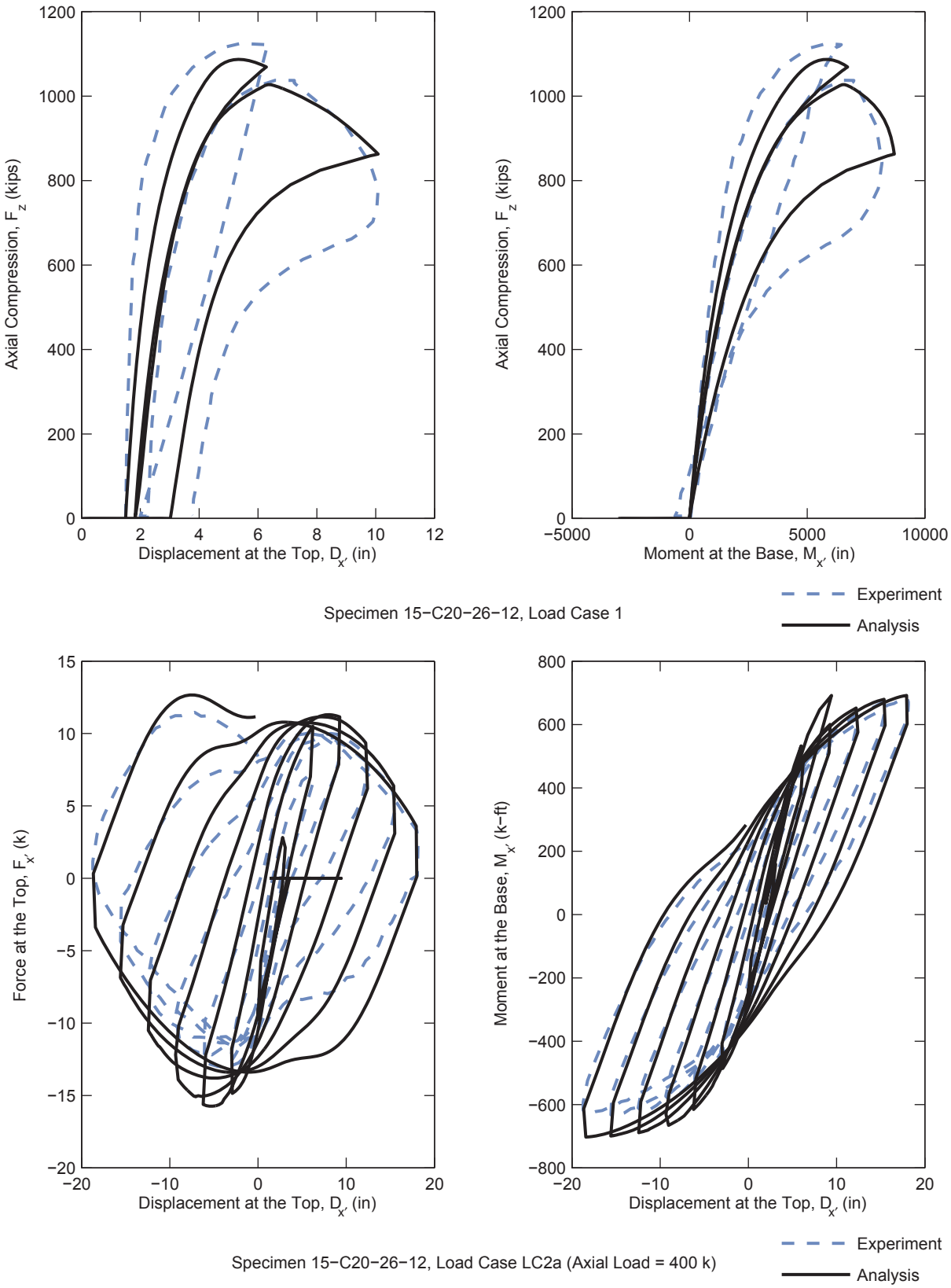

Figure 7.17. Comparison Results – Specimen 15C20-26-12

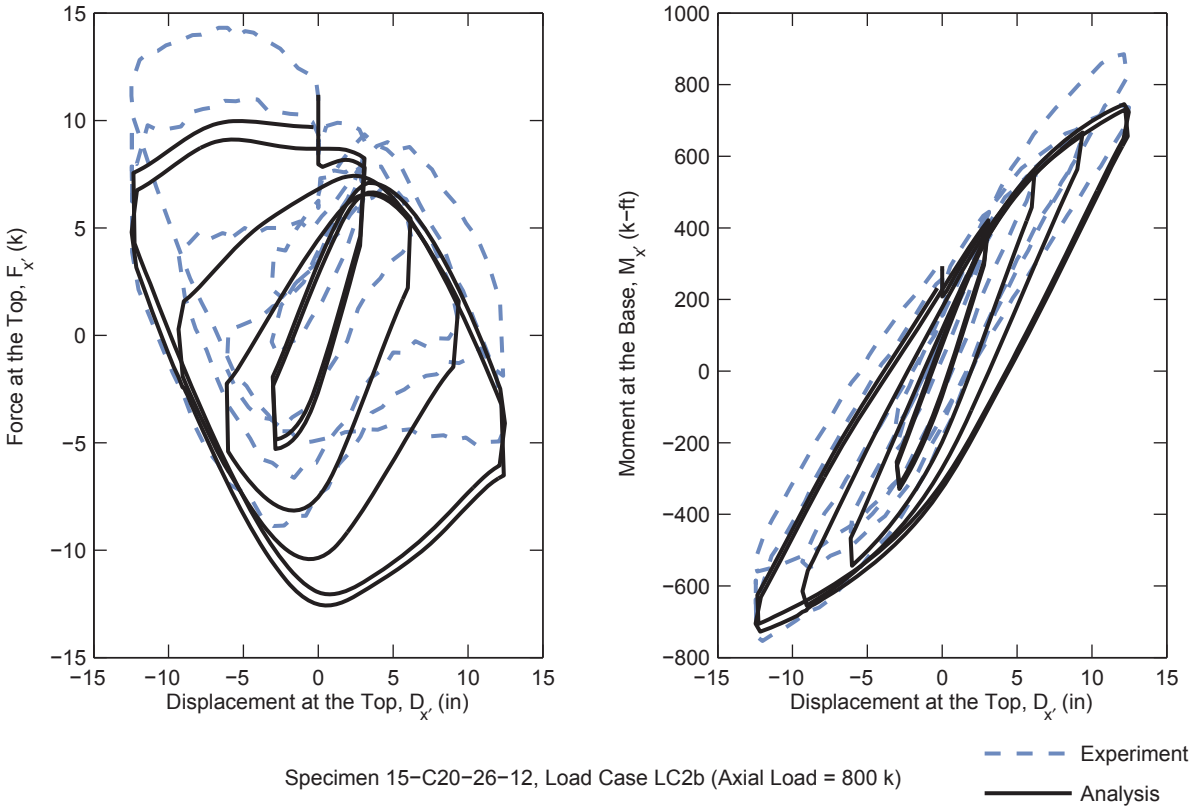

Figure 7.17. Comparison Results – Specimen 15C20-26-12 (continued)

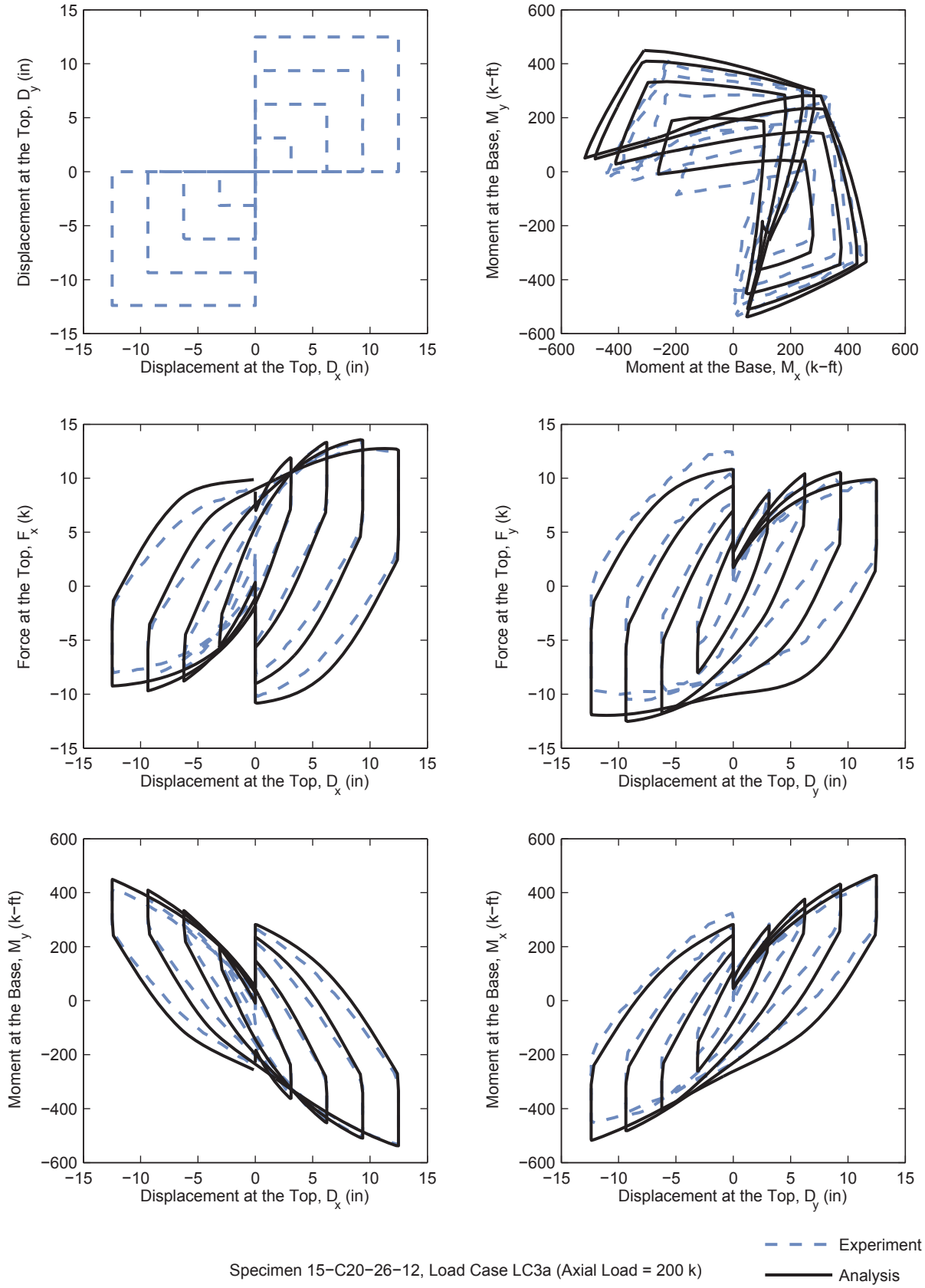

Figure 7.17. Comparison Results – Specimen 15C20-26-12 (continued)

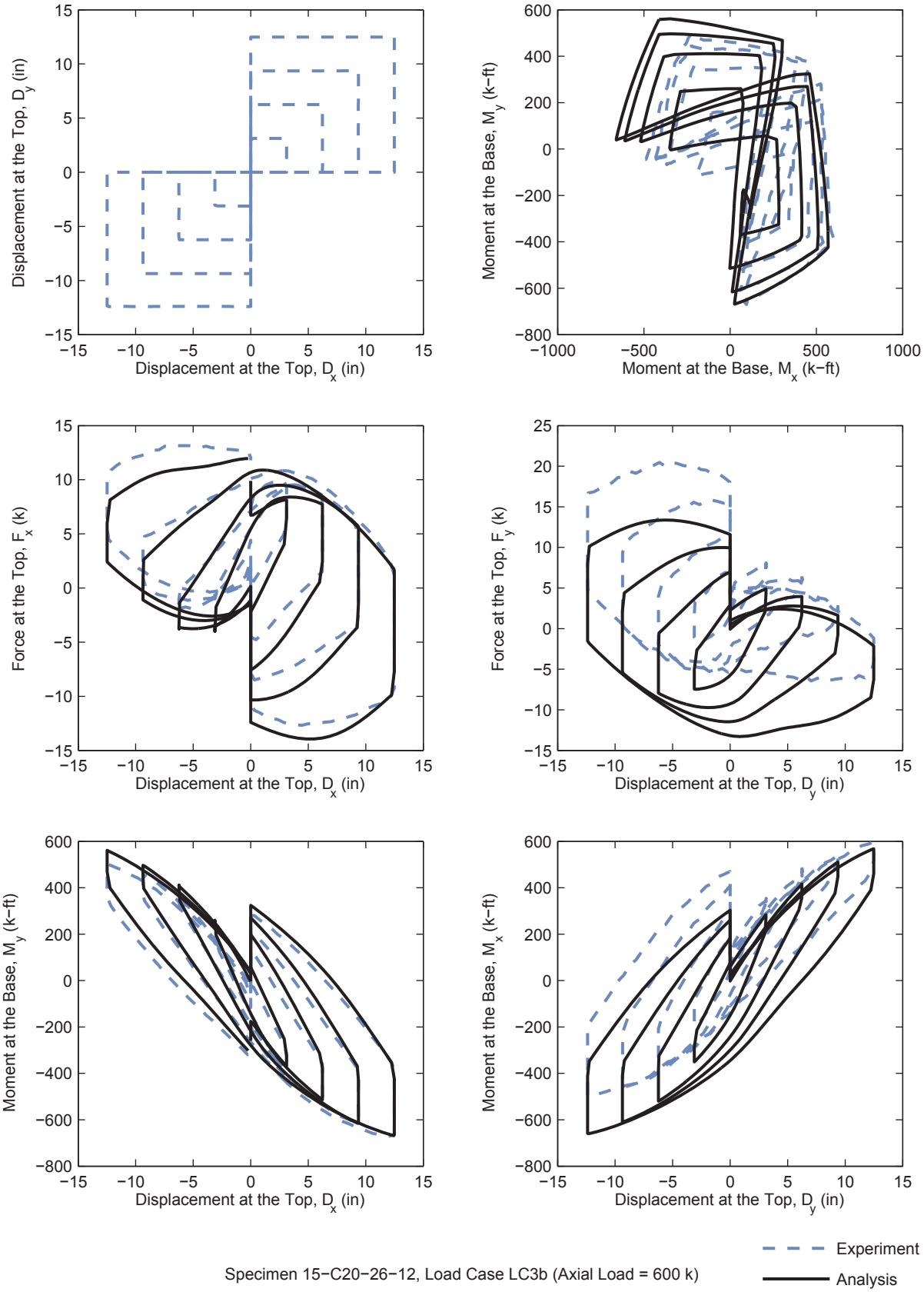

Figure 7.17. Comparison Results – Specimen 15C20-26-12 (continued)

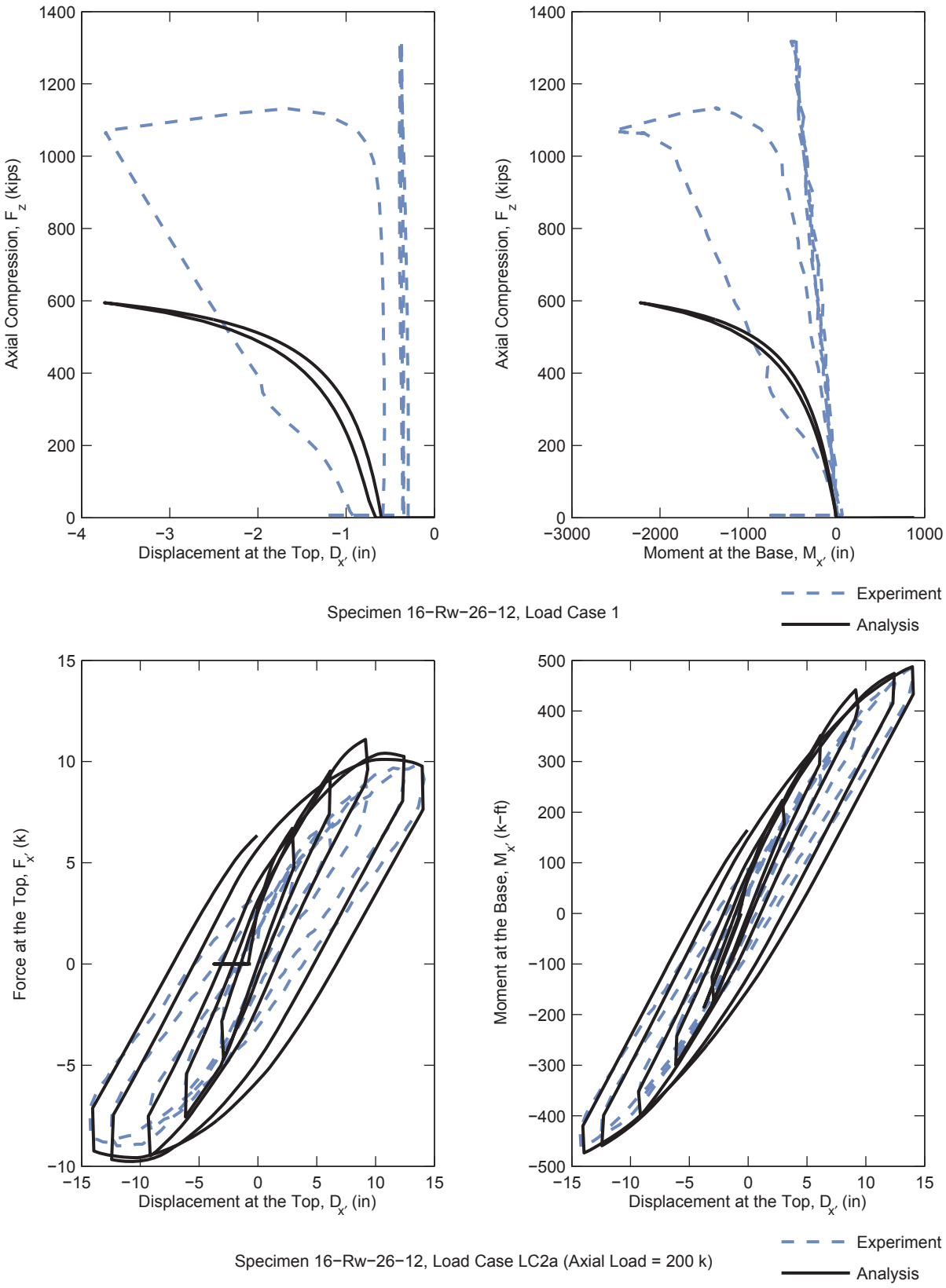

Figure 7.18. Comparison Results – Specimen 16Rw-26-12

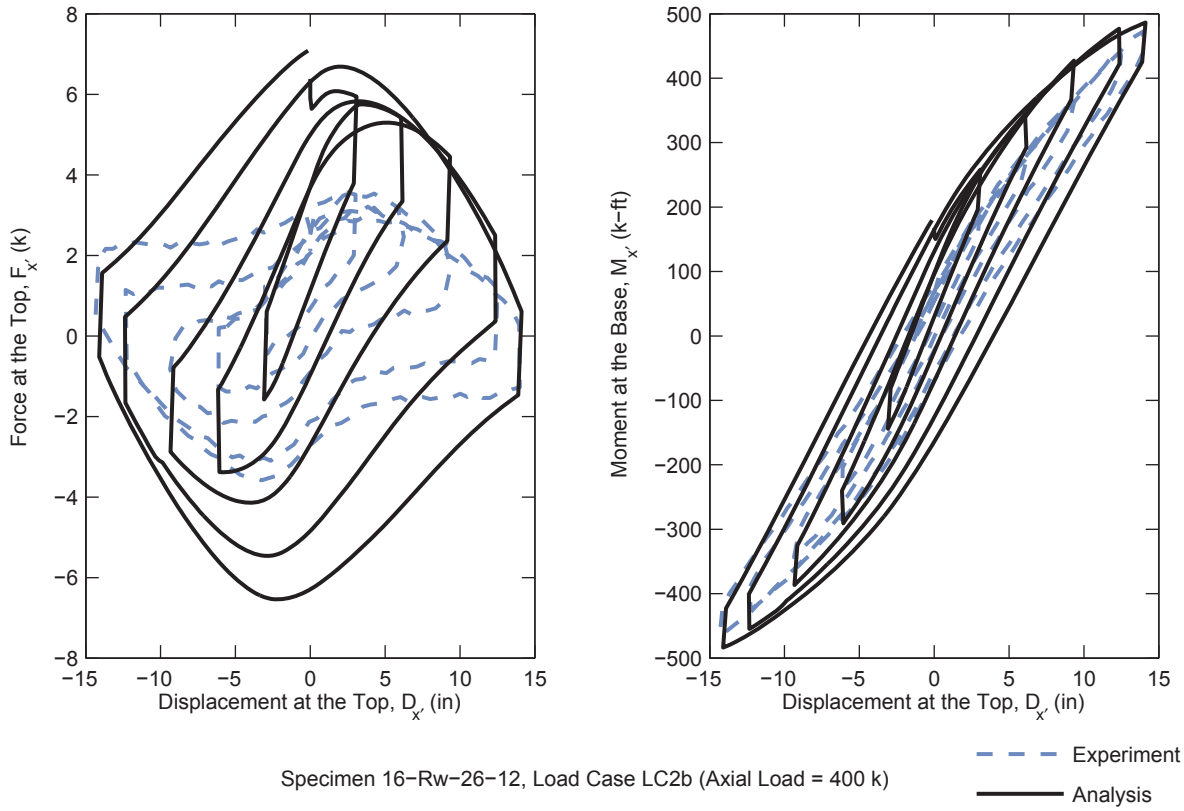

Figure 7.18. Comparison Results – Specimen 16Rw-26-12 (continued)

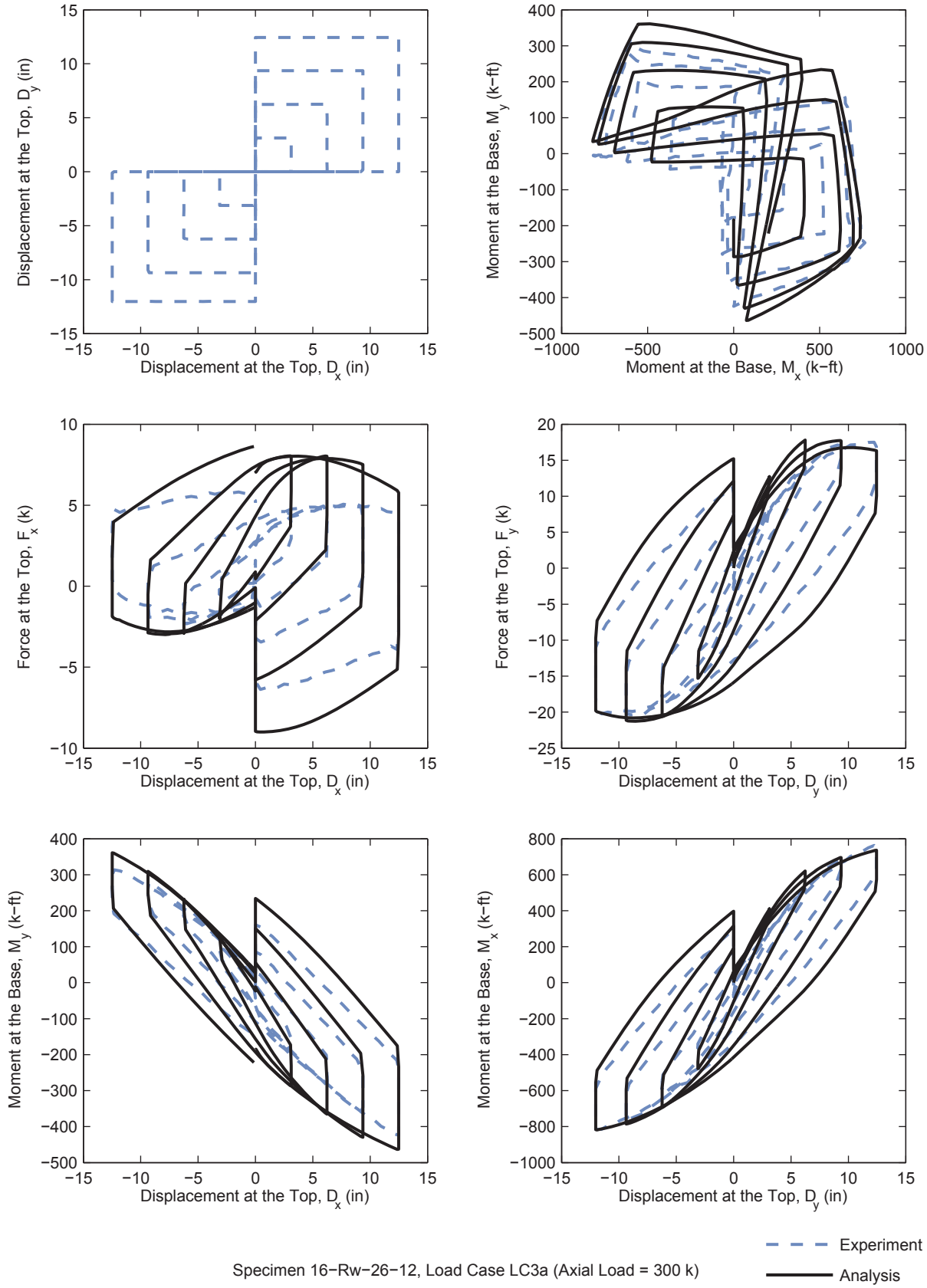

Figure 7.18. Comparison Results – Specimen 16Rw-26-12 (continued)

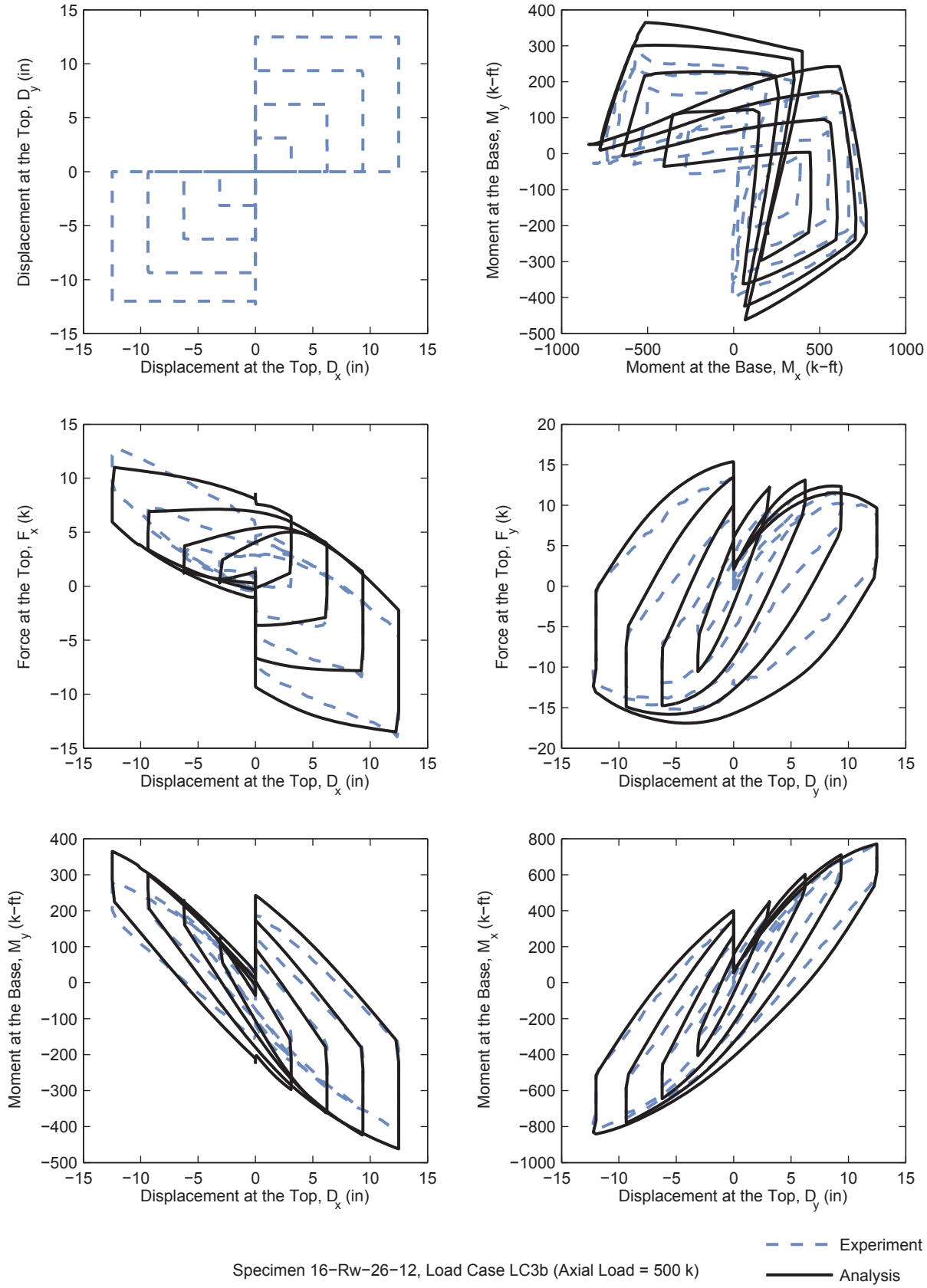

Figure 7.18. Comparison Results – Specimen 16Rw-26-12 (continued)

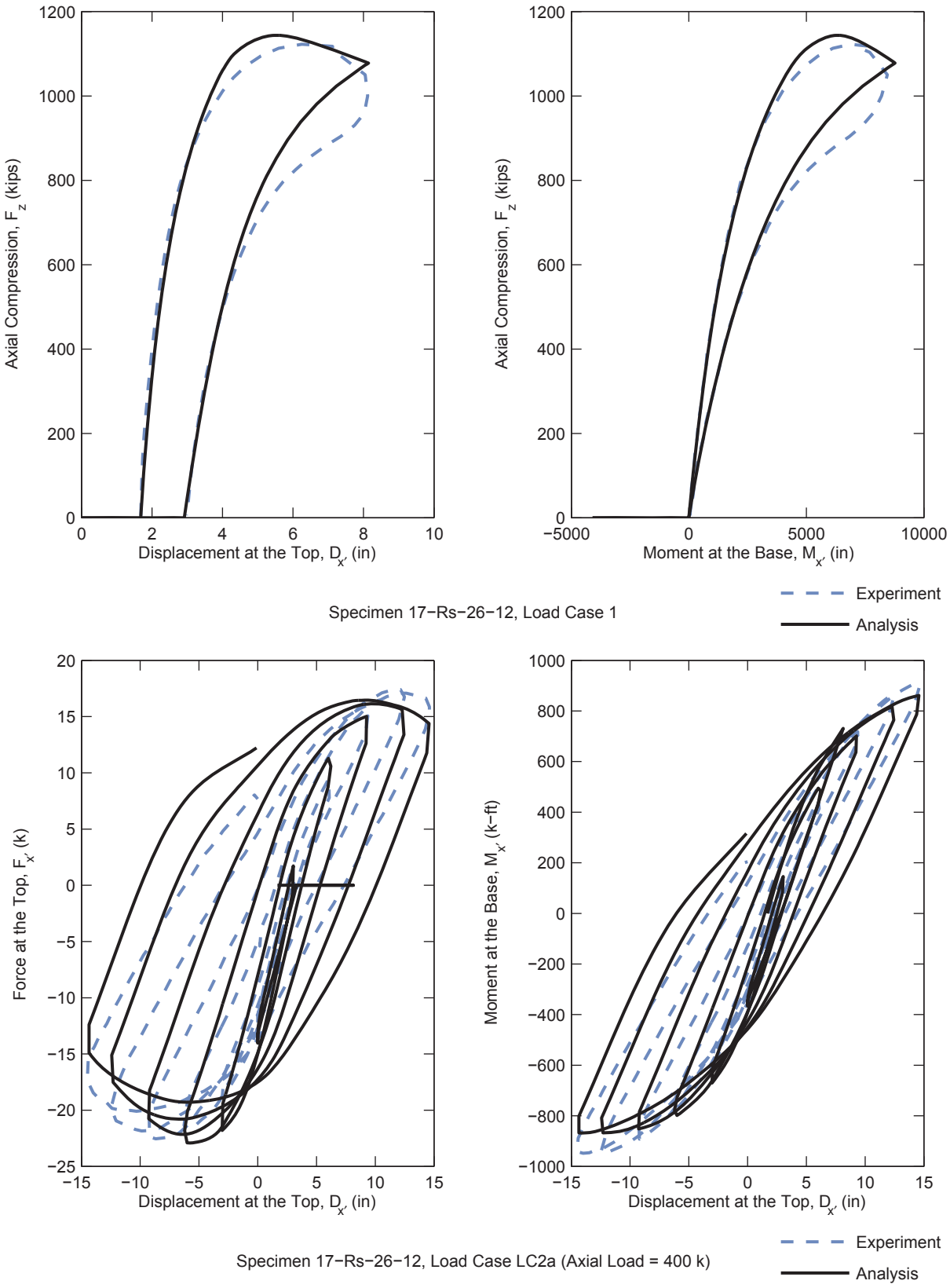

Figure 7.19. Comparison Results – Specimen 17Rs-26-12

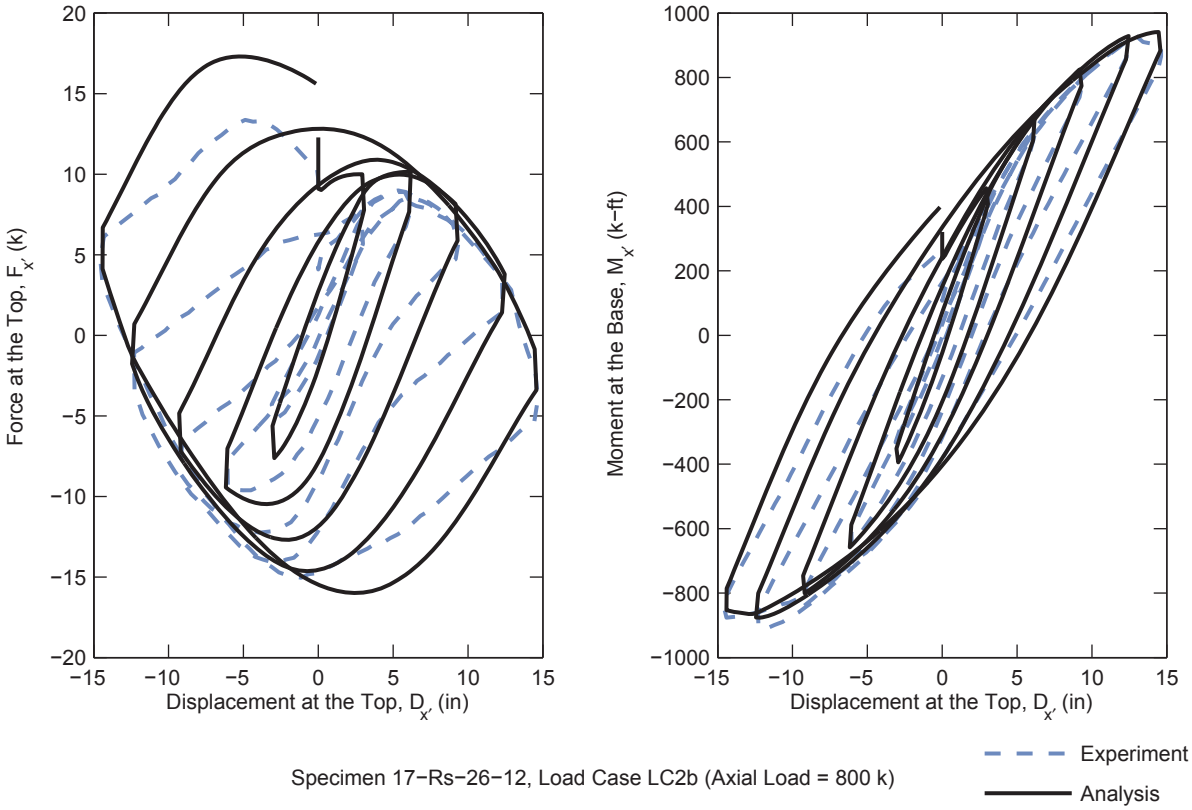

Figure 7.19. Comparison Results – Specimen 17Rs-26-12 (continued)

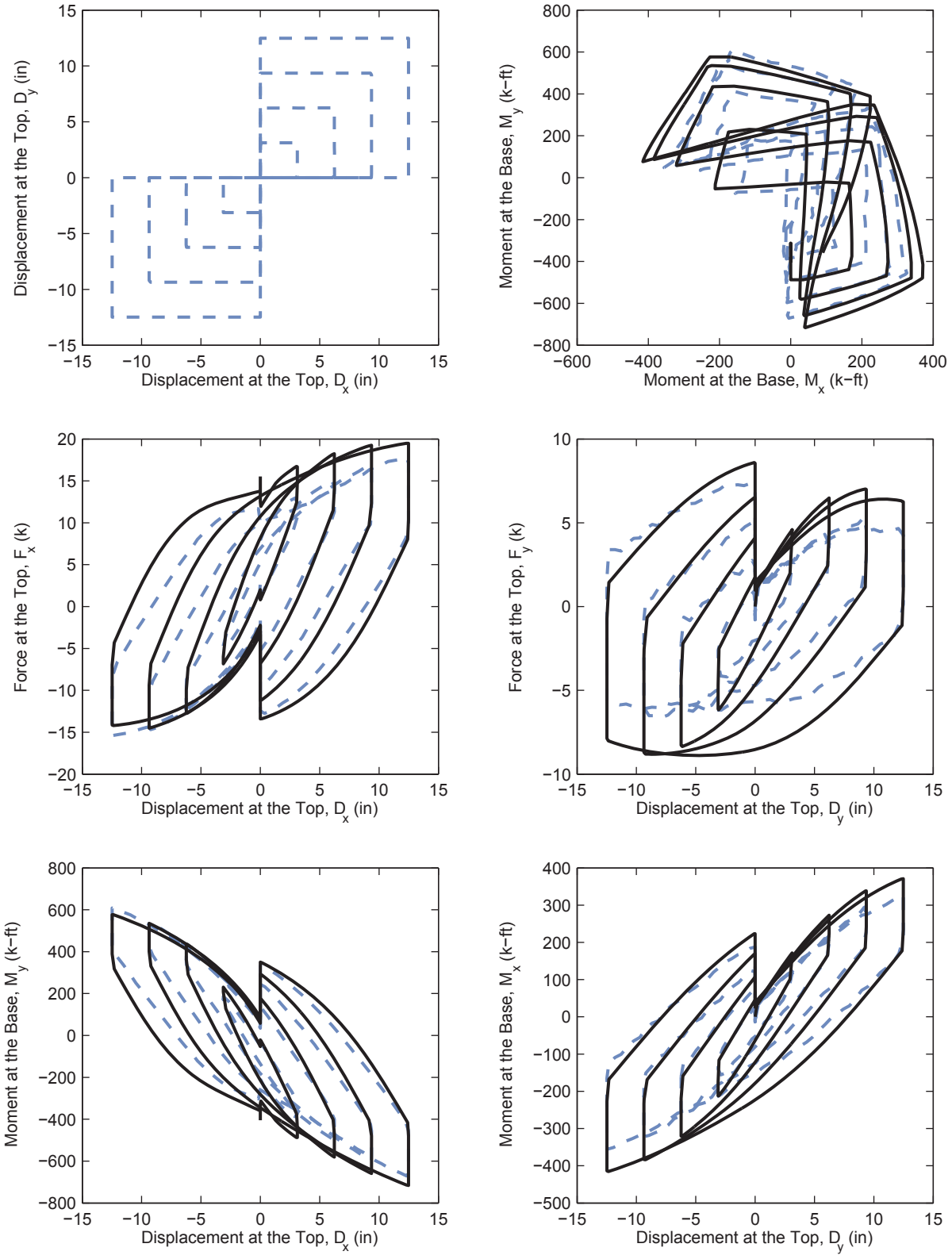

Figure 7.19. Comparison Results – Specimen 17Rs-26-12 (continued)

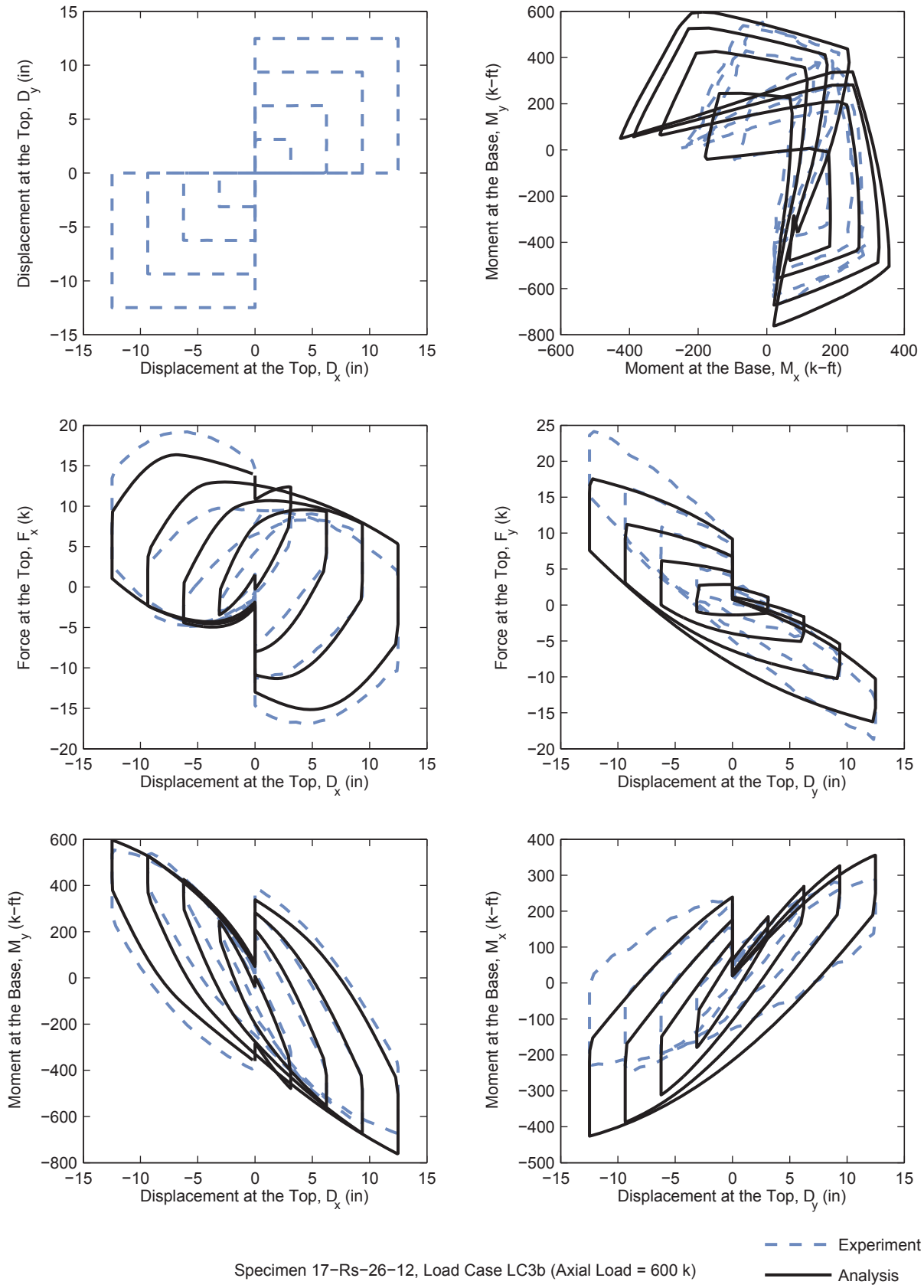

Figure 7.19. Comparison Results – Specimen 17Rs-26-12 (continued)

7.3 Experimental Evaluation of the Beam-Column Interaction Strength

Identifying the strength limit point is an important aspect of the data reduction. Simply taking the maximum second-order moment would be inaccurate since the highest second-order moments occurred when the beam-column was being held in an unstable configuration by the crosshead. For this reason, the limit point is identified as when a zero slope is observed in lateral force-deformation response. This point also corresponds to the peak first-order moment as shown in Figure 7.20.

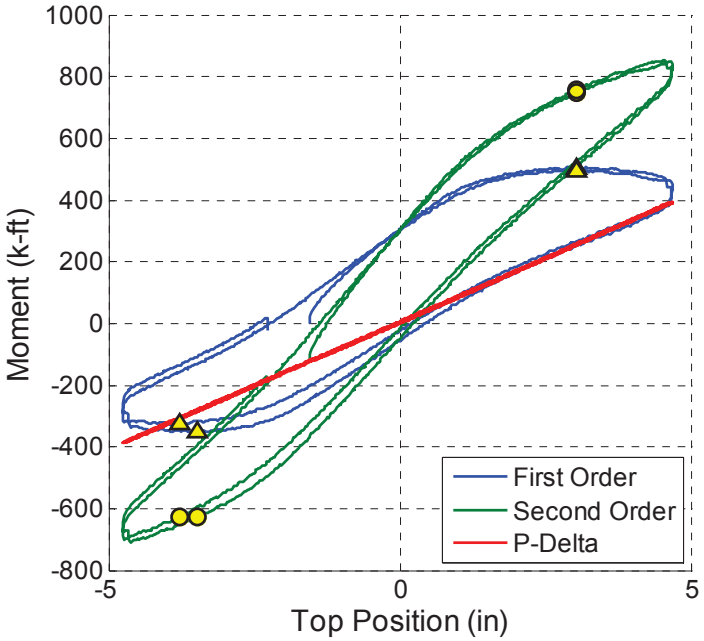

Figure 7.20. Identification of the Limit Point by First-Order Moment

7.4 Experimental Validation of the Proposed Beam-Column Design Methodology

The proposed beam-column design methodology developed in Chapter 6 was primarily validated against computational results. Validation against experimental results is also important. The specimens presented here are well suited for this purpose because they are slender, they were subjected a wide range of loading from axial dominant to moment dominant, and the instrumentation allowed for accurate measurements of first and second-order loads.

Validation results are shown in Figure 7.21 though Figure 7.36 and were constructed as follows:

- Experimental limit points from LC1 and LC2 were identified. Second-order moments are shown in the figures as blue triangles while first-order moments are shown as red circles.
- A series of fully nonlinear analyses was performed to construct interaction diagrams as described in Chapter 6 using the "Proposed for Design" model. These results are shown in the top plot of the figures. The black dashed line represents the second-order internal force interaction diagram and the black continuous line represents the first-order applied load interaction diagram. The grey continuous line is the first-order applied load interaction diagram from a secondary series of fully nonlinear analyses identical to the first except with measured out-of-plumbness in lieu of nominal out-of-plumbness
- Interaction diagrams constructed from current design provisions are shown in the middle plot of the figures. The black dashed line is the interaction diagram computed using the plastic stress distribution method (A-C-B) and assuming $K = 1$ in accordance with the Direct Analysis method (AISC 2010). The black continuous line is obtained from elastic analyses as the applied loads which result in internal forces on the interaction diagram. The flexural rigidity of the member in the elastic analyses was taken as $0.8\tau_b EI_{eff}$, where $0.8\tau_b$ is the Direct Analysis stiffness reduction and EI_{eff} is the effective flexural rigidity given in Chapter I of the AISC *Specification* for determining the axial compressive strength. A notional load was also included in the analyses. The grey continuous line was obtained using the same method as for the black continuous line but with a notional load representative of the measured out-of-plumbness.
- Interaction diagrams constructed from the proposed design provisions are shown in the bottom plot of the figures. The lines were constructed in the same manner as for the current design provisions, except the proposed strength interaction curve and proposed elastic flexural rigidity developed in Chapter 6 were used.

When the first-order experimental limit points (red circles) are outside the first-order design interaction curves (black or grey continuous lines), the specimens are exhibiting greater than predicted strength and the design methodology can be considered conservative and safe. This is the case for most of the recorded limit points. Some of the recorded limits points, however, fall within the design interaction curves indicating that the design methodology is overpredicting the strength and is unconservative for these cases. It is noted that some of the experimental limit points (especially those from LC2) were obtained after the specimen had undergone cyclic loading, potentially affecting the results.

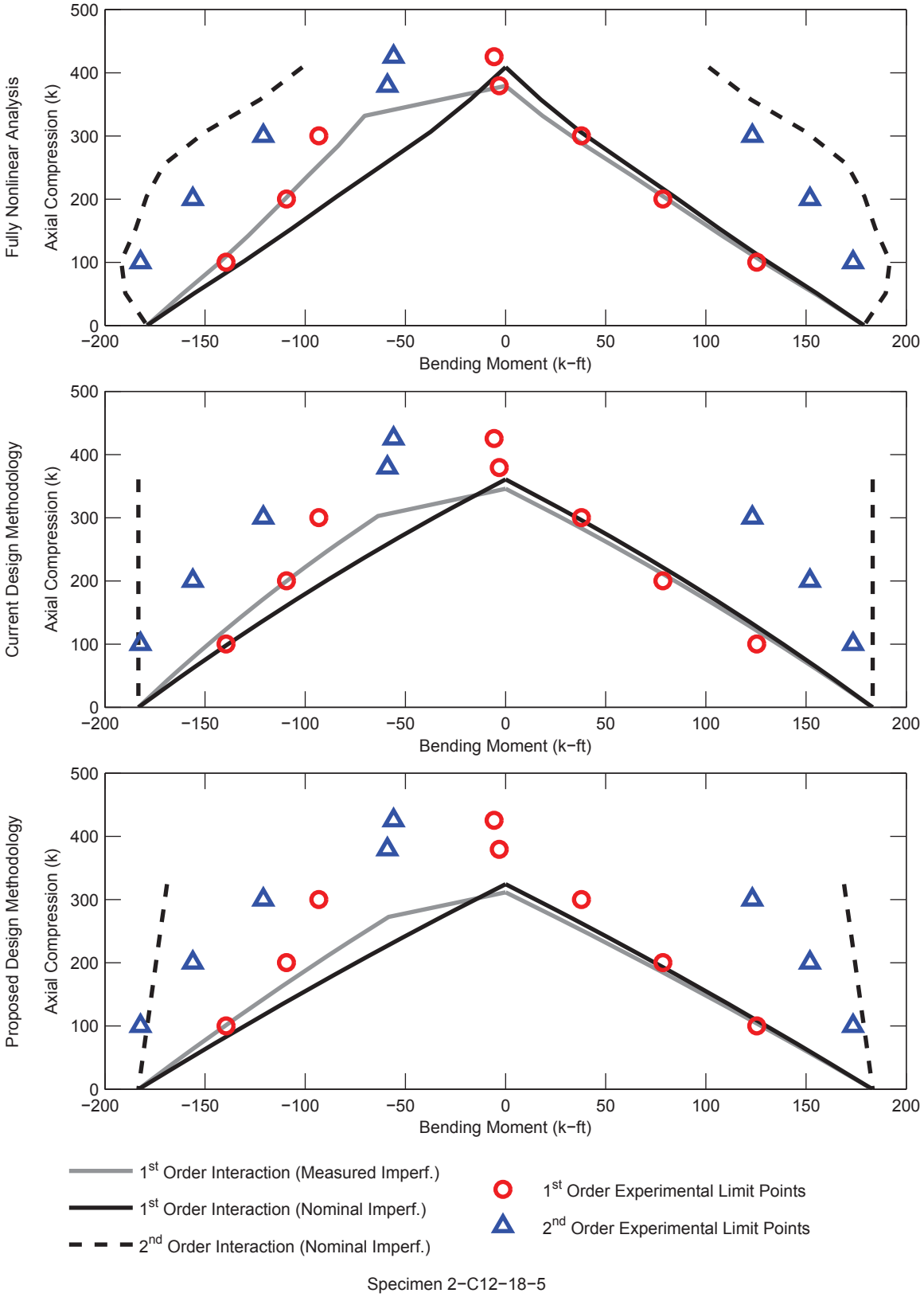

Figure 7.21 Interaction Diagrams – Specimen 2-C12-18-5

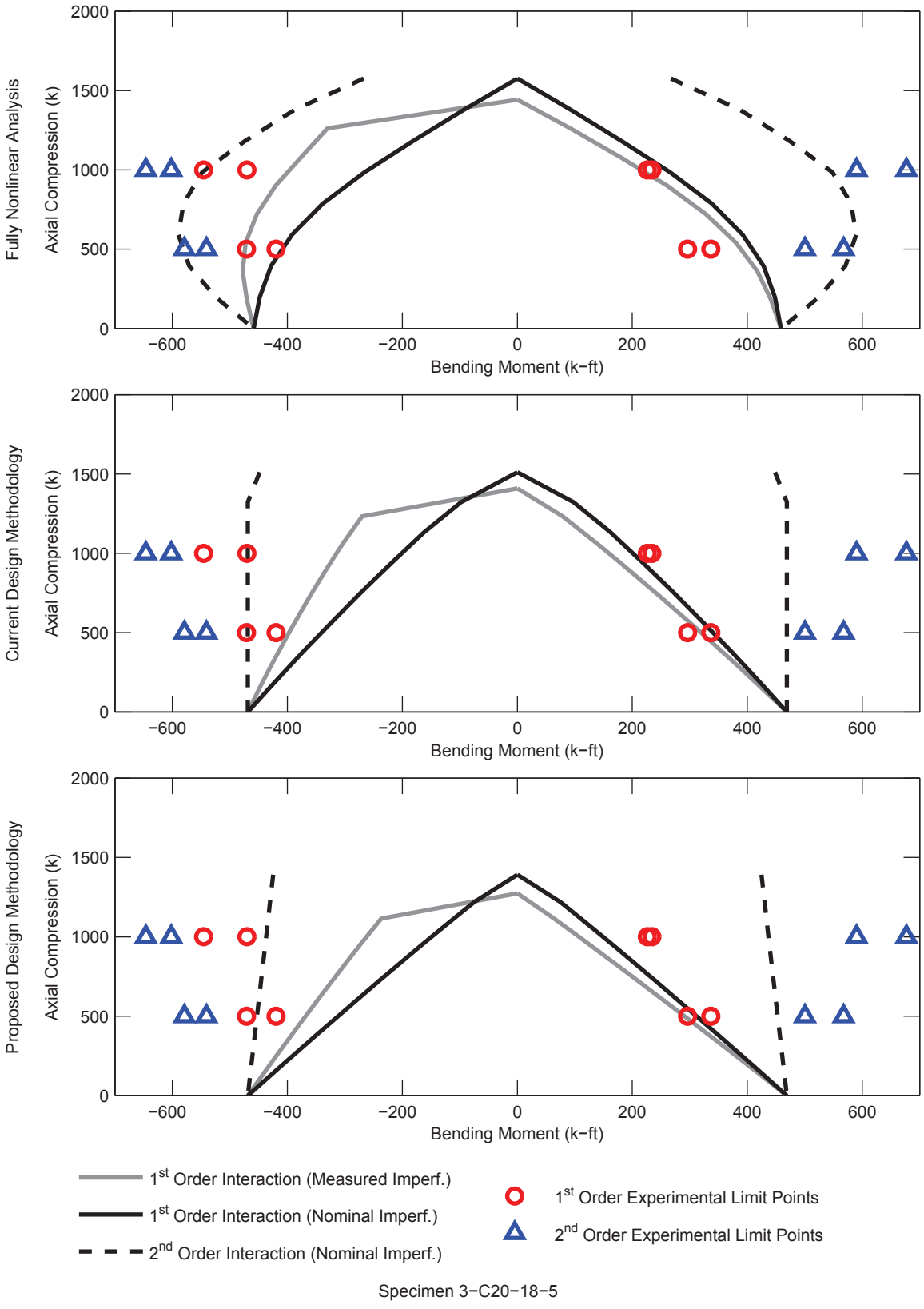

Figure 7.22 Interaction Diagrams – Specimen 3-C20-18-5

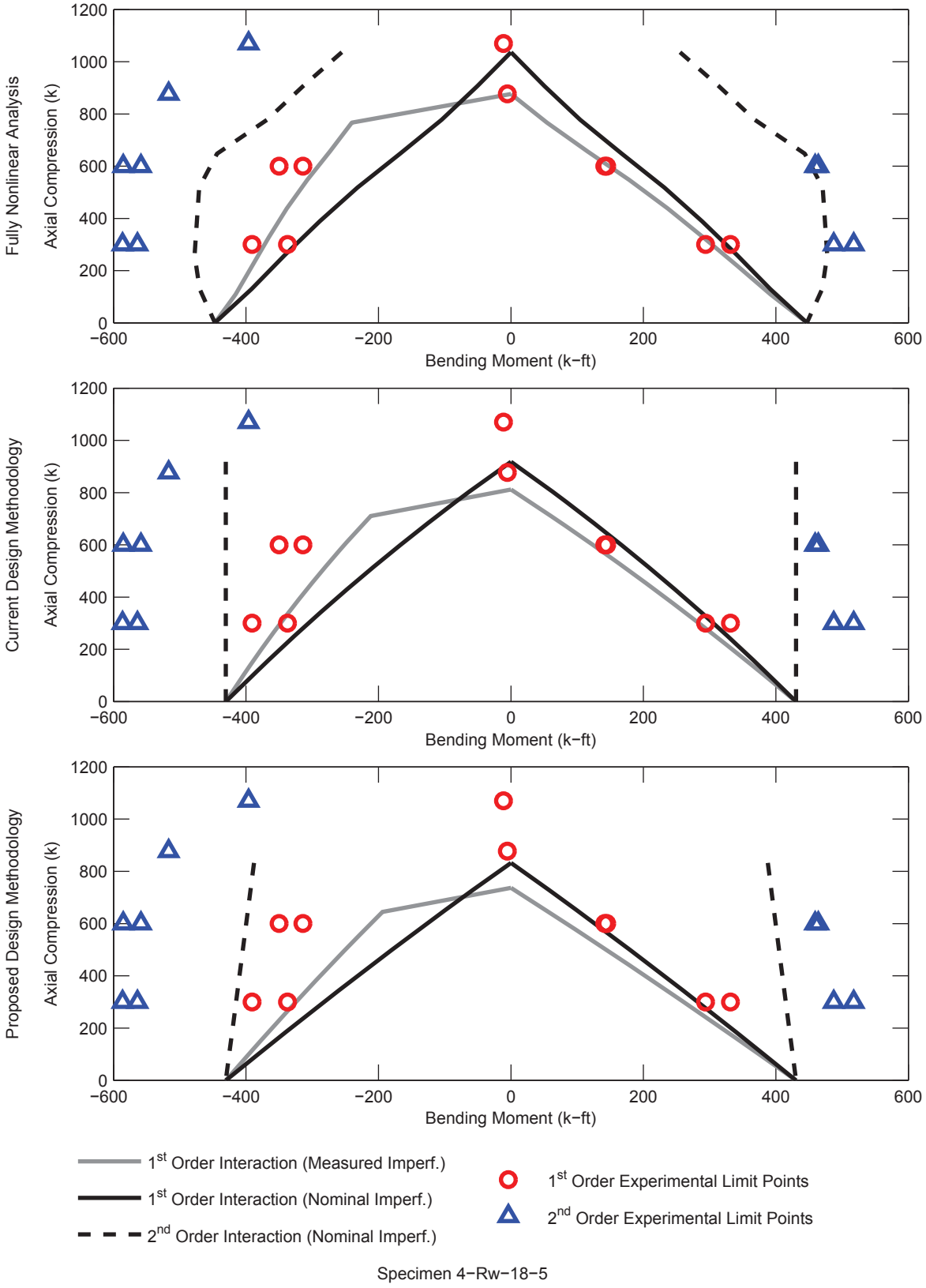

Figure 7.23 Interaction Diagrams – Specimen 4-Rw-18-5

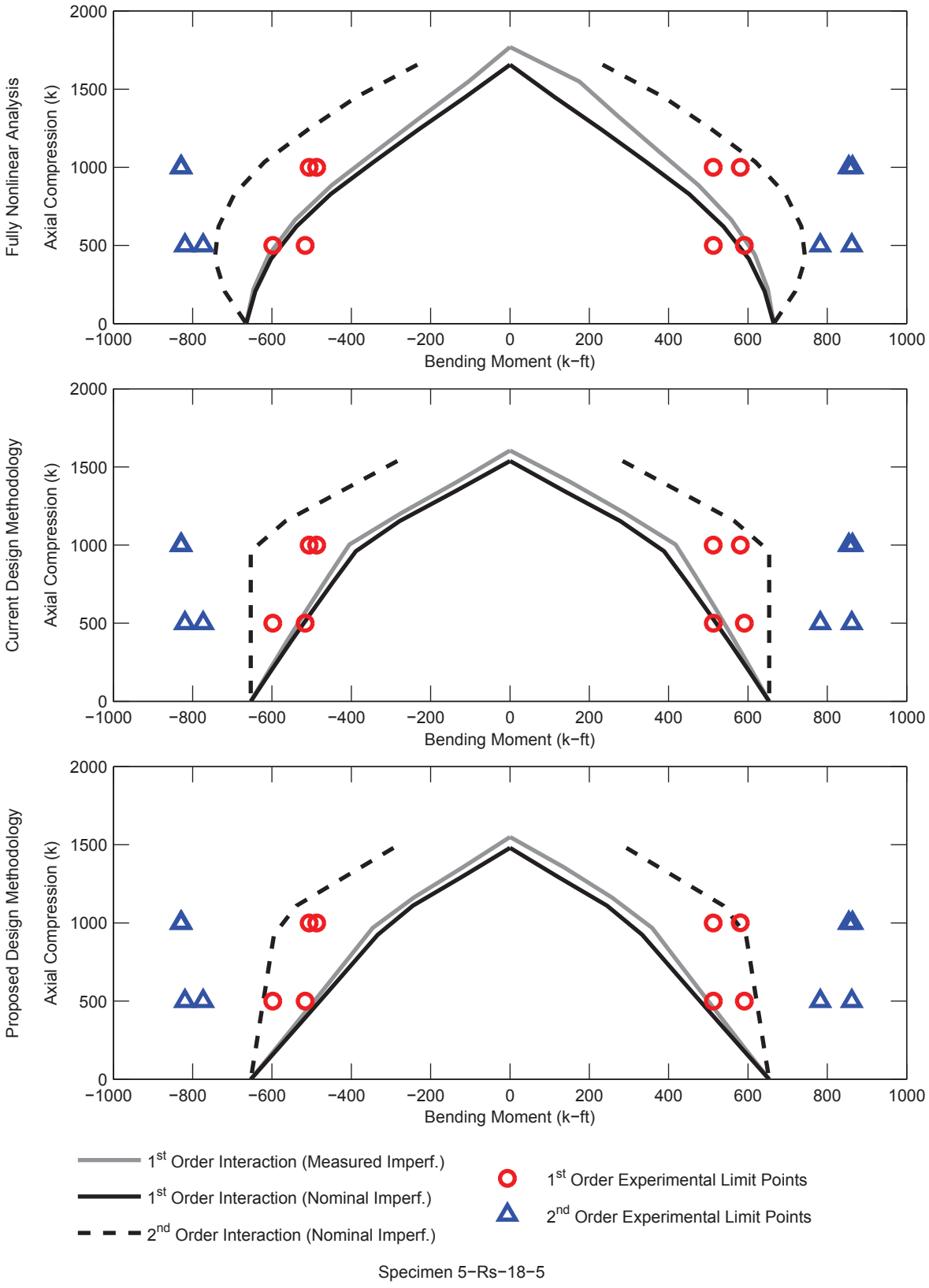

Figure 7.24 Interaction Diagrams – Specimen 5-Rs-18-5

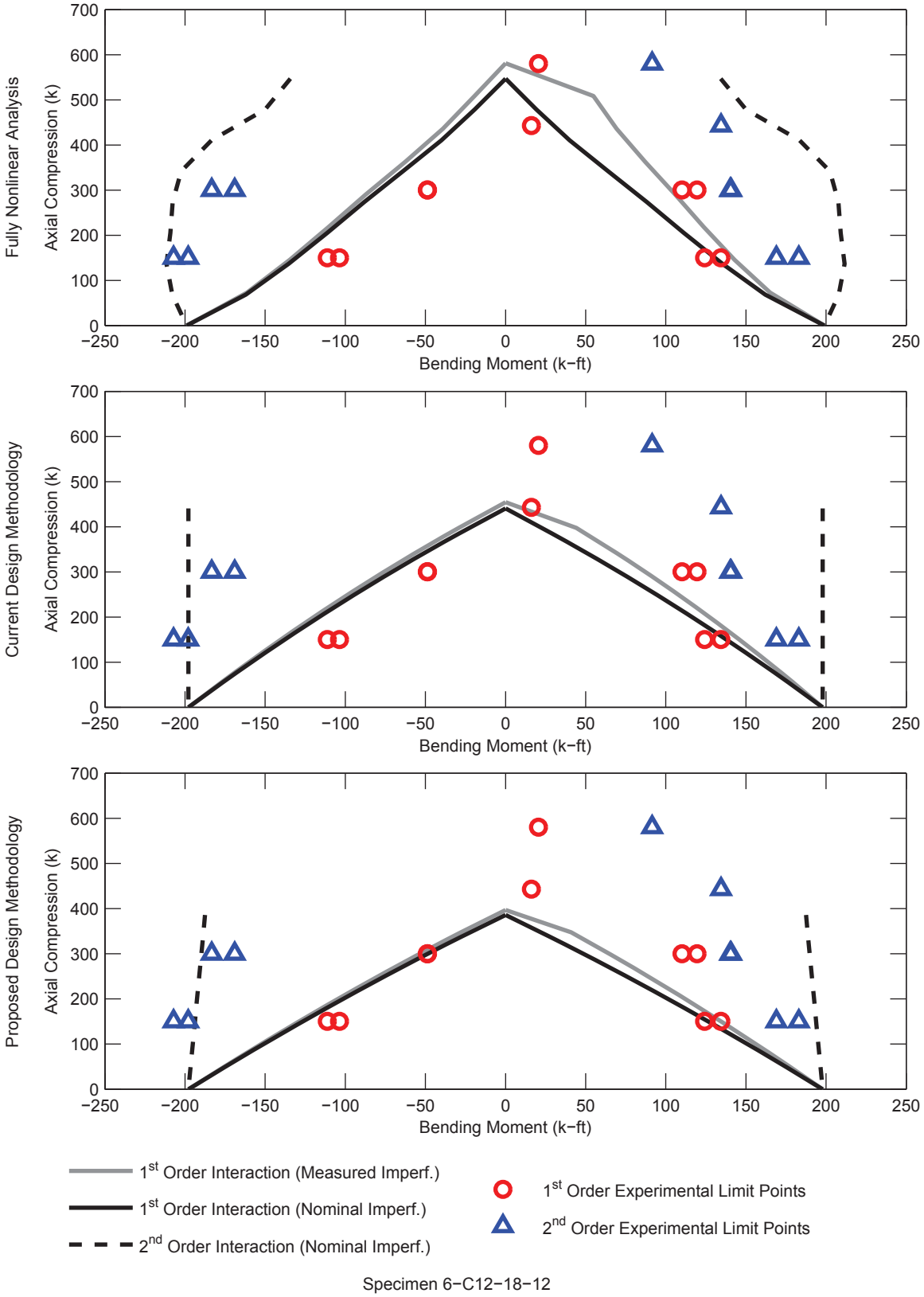

Figure 7.25 Interaction Diagrams – Specimen 6-C12-18-12

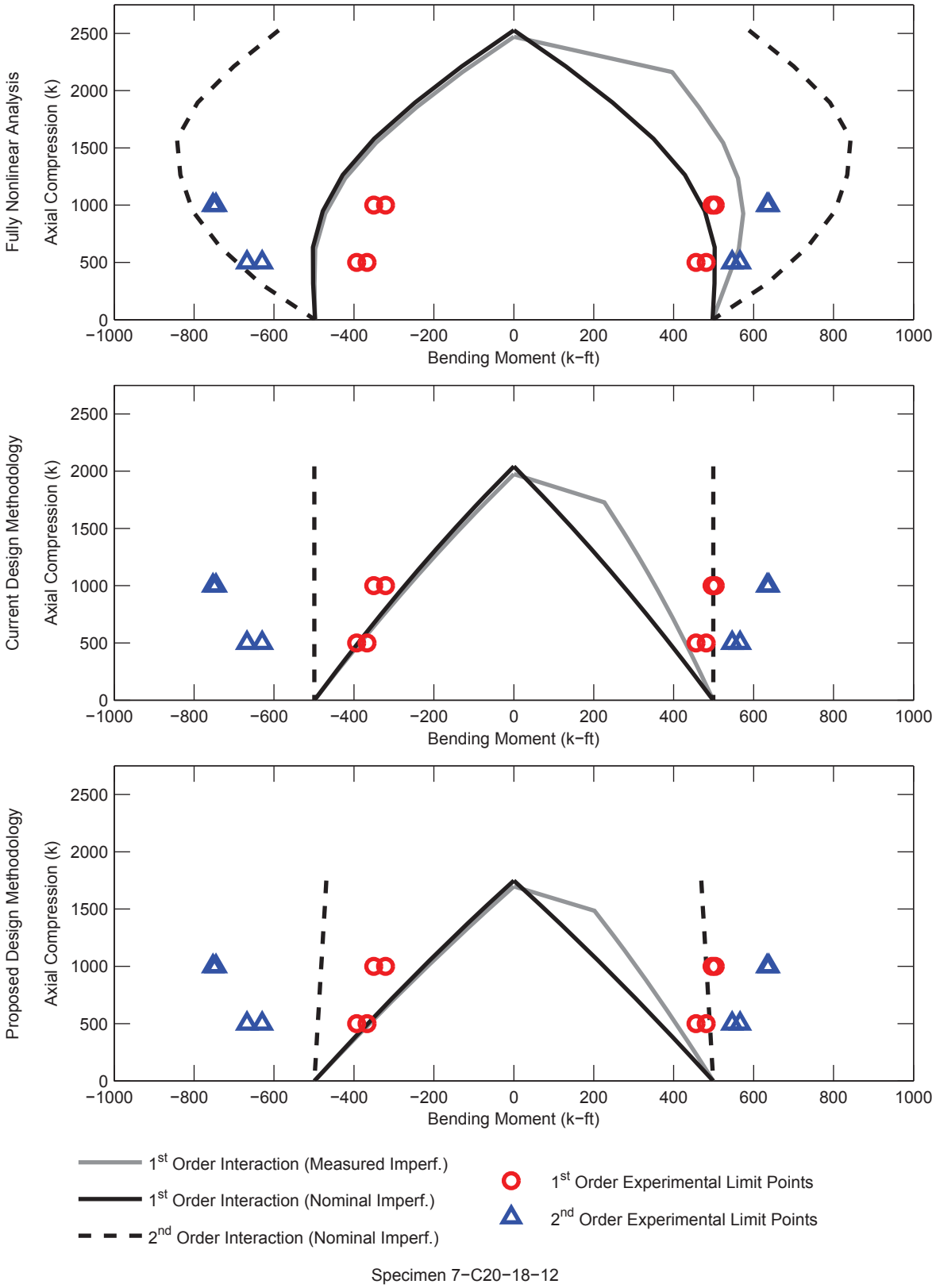

Figure 7.26 Interaction Diagrams – Specimen 7-C20-18-12

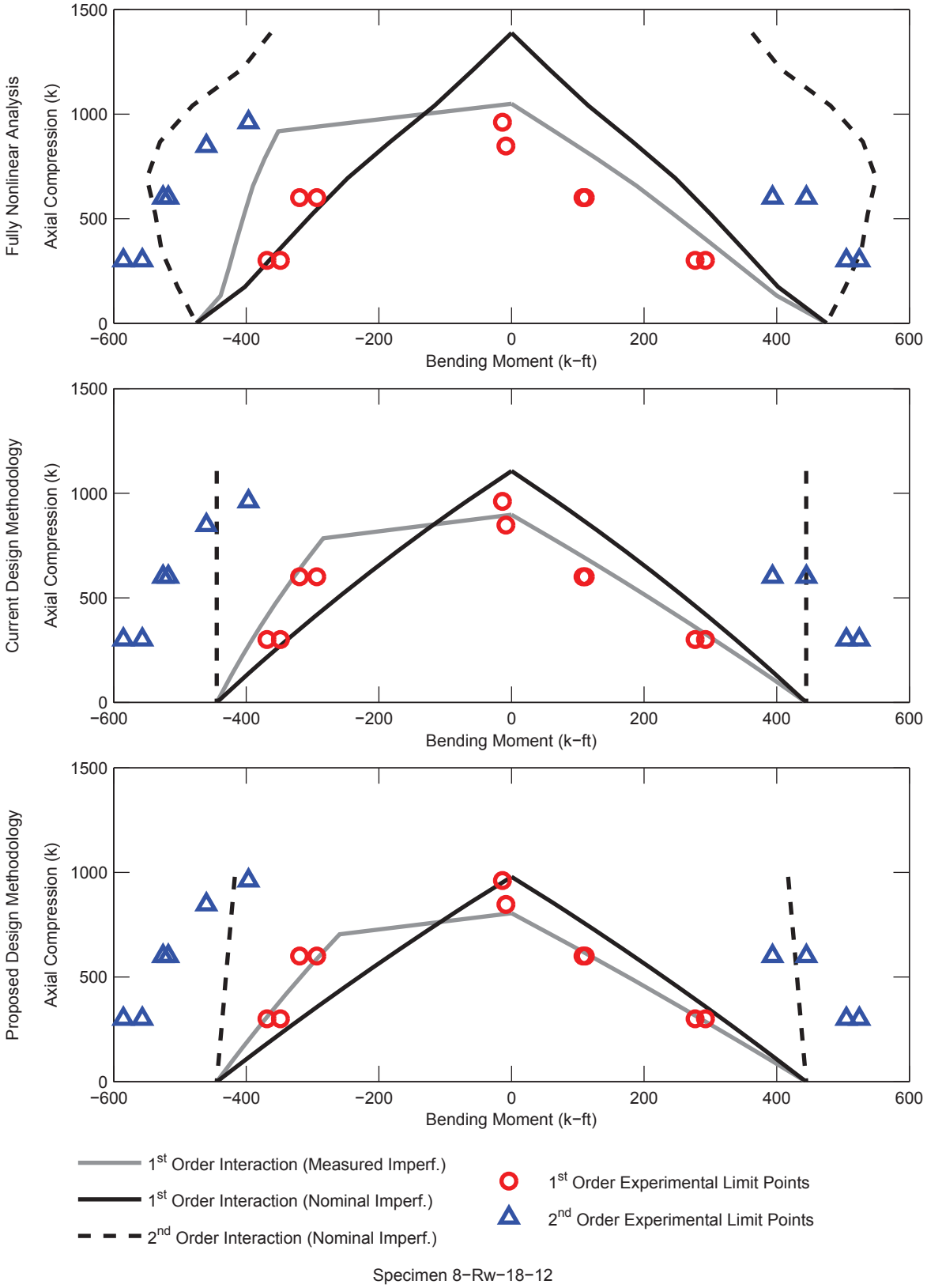

Figure 7.27 Interaction Diagrams – Specimen 8-Rw-18-12

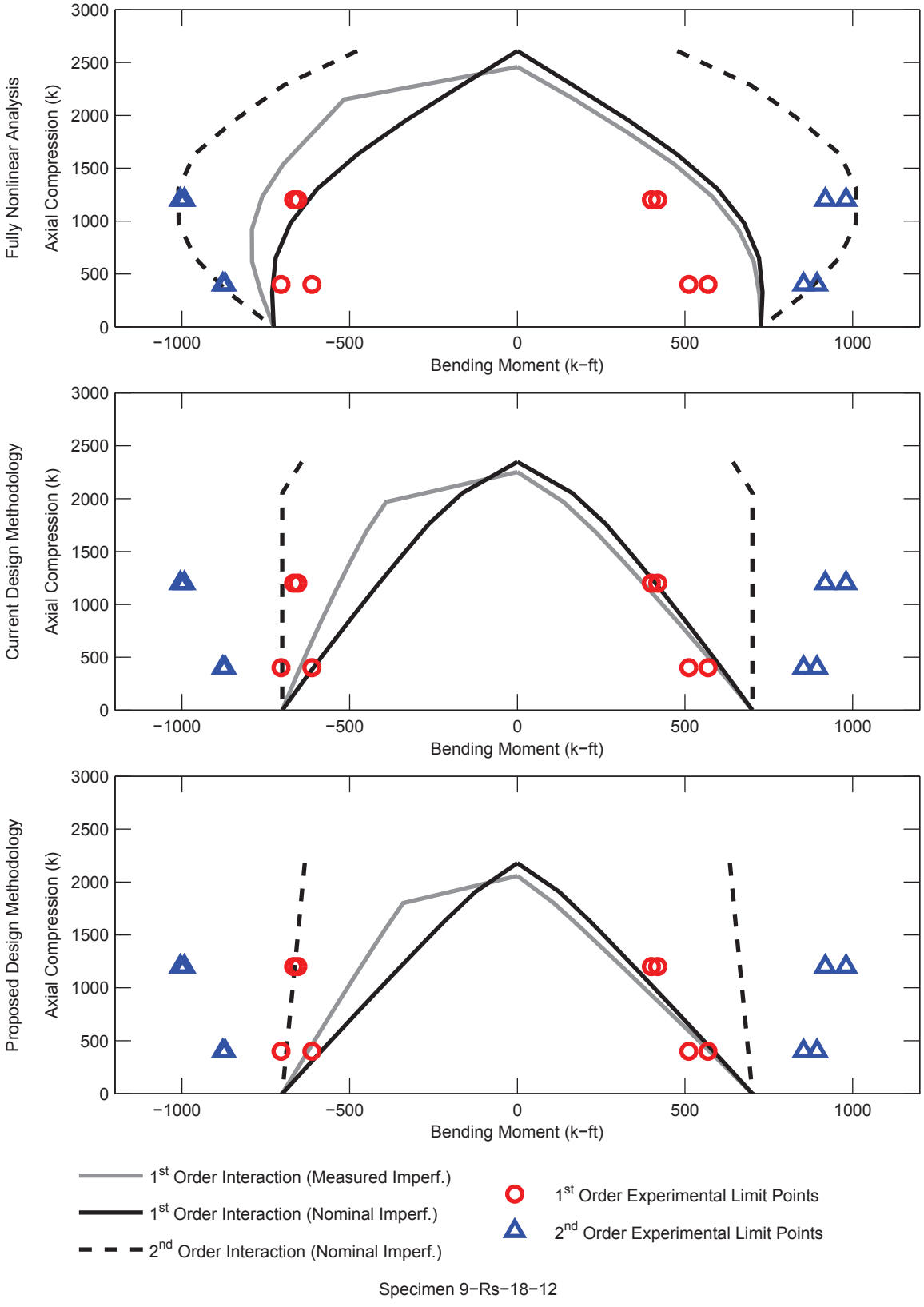

Figure 7.28 Interaction Diagrams – Specimen 9-Rs-18-12

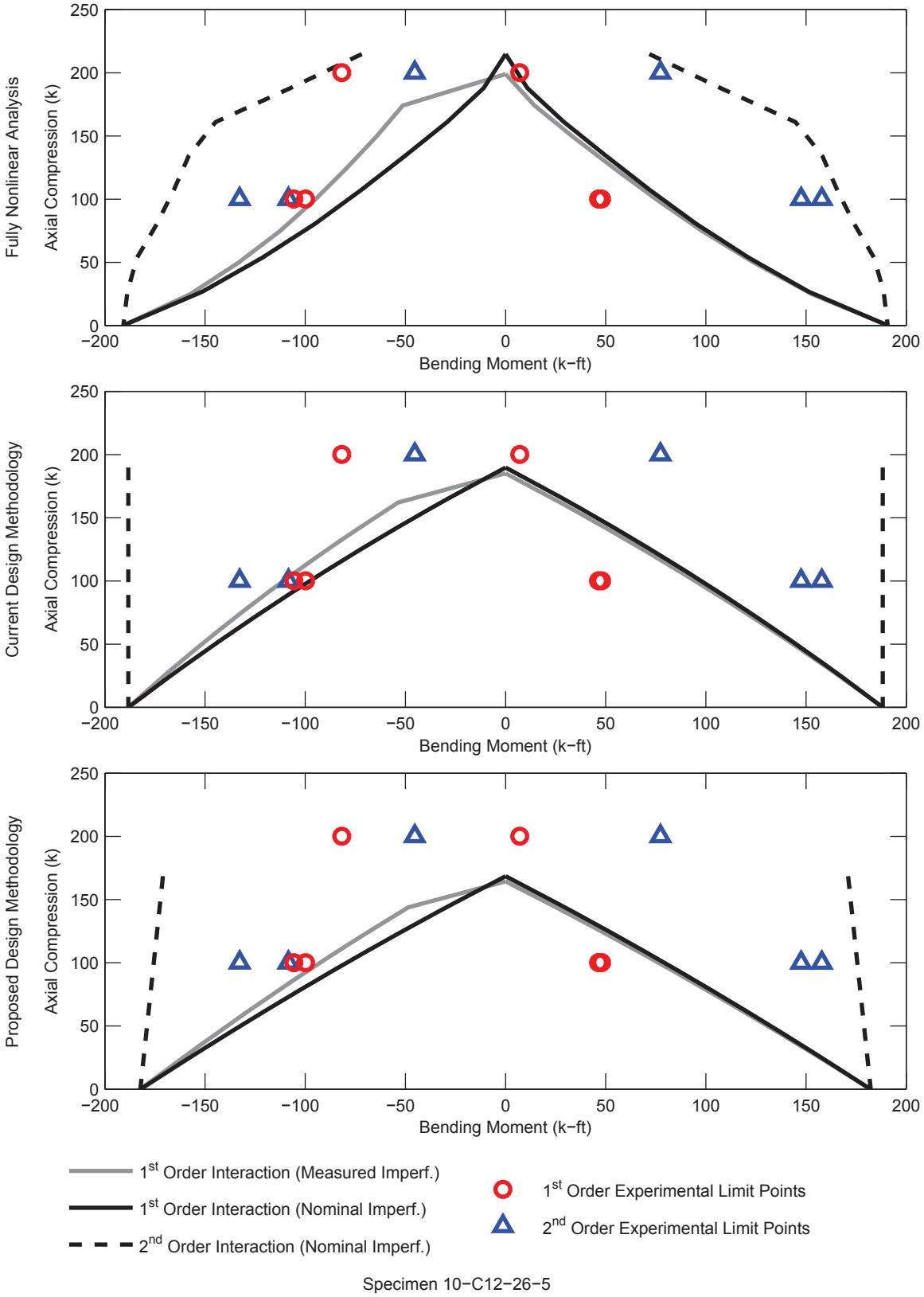

Figure 7.29 Interaction Diagrams – Specimen 10-C12-26-5

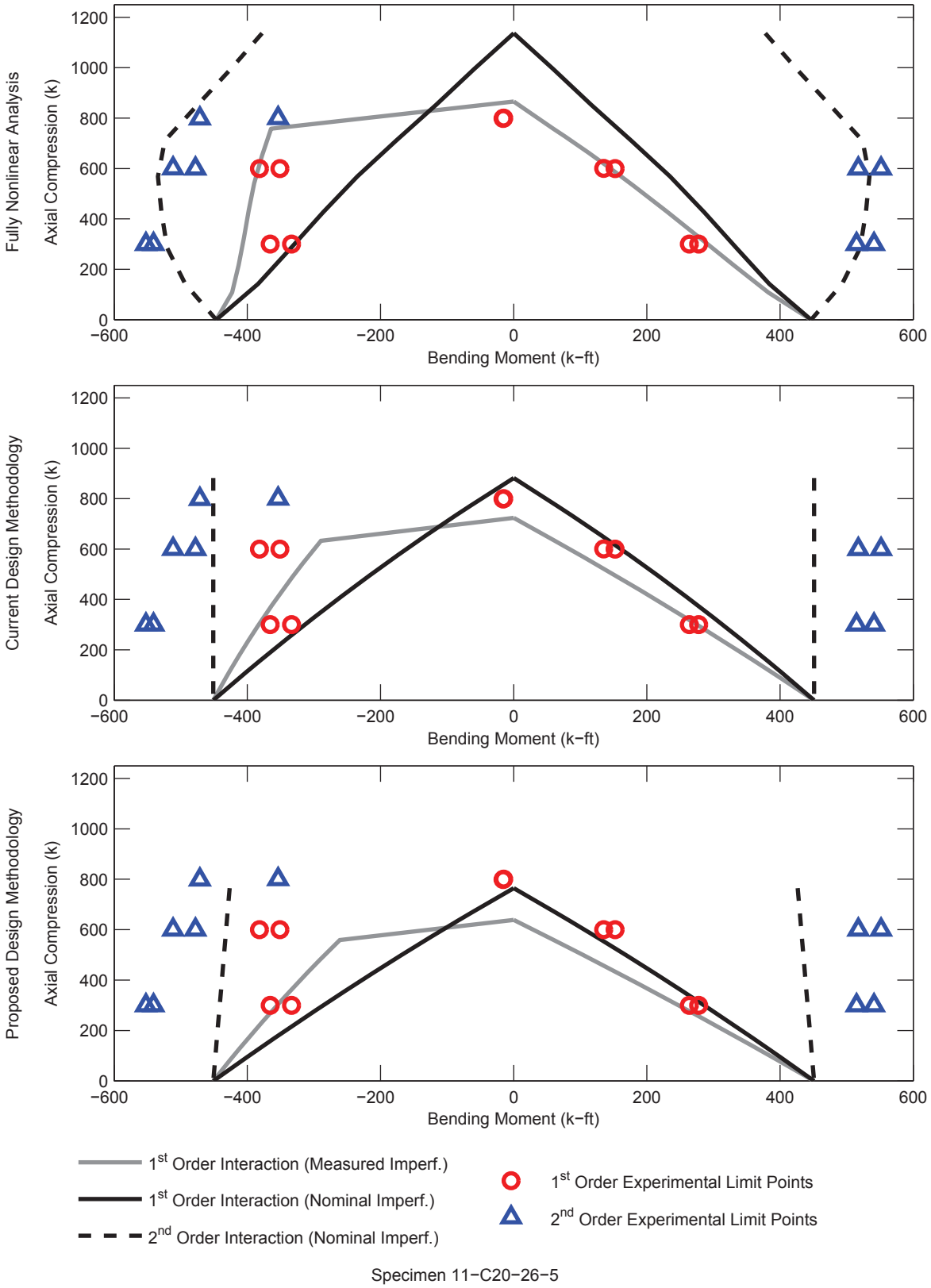

Figure 7.30 Interaction Diagrams – Specimen 11-C20-26-5

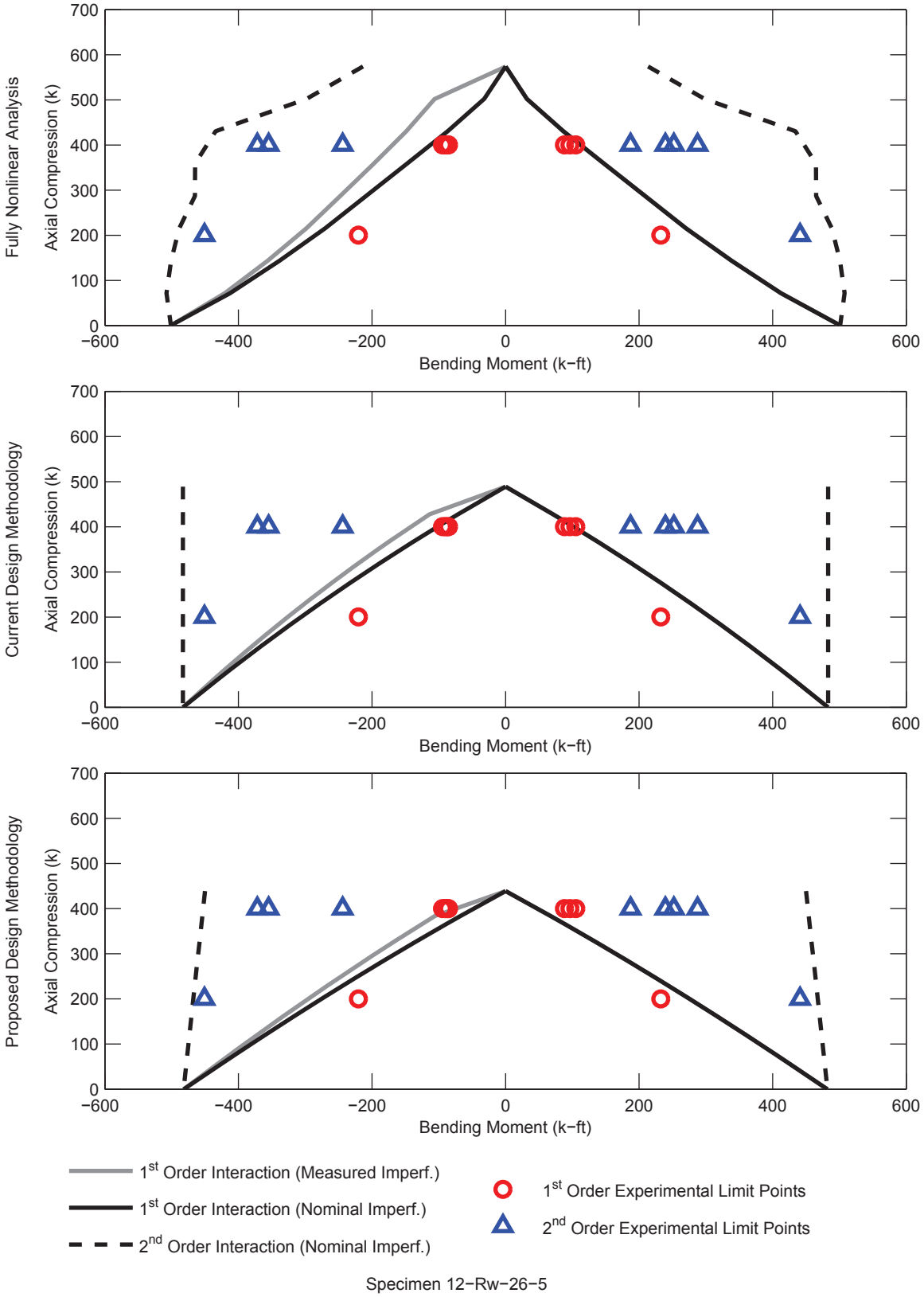

Figure 7.31 Interaction Diagrams – Specimen 12-Rw-26-5

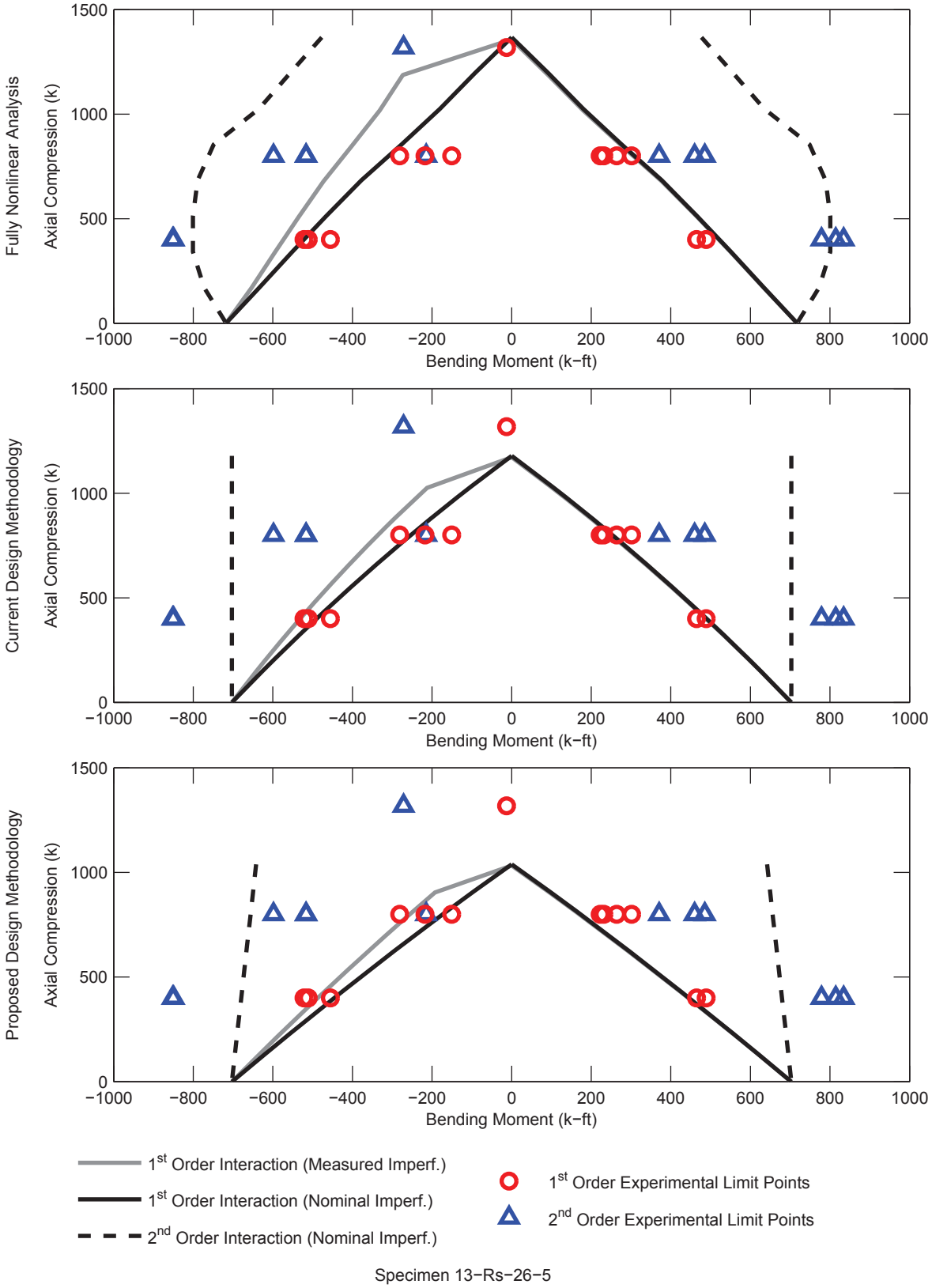

Figure 7.32 Interaction Diagrams – Specimen 13-Rs-26-5

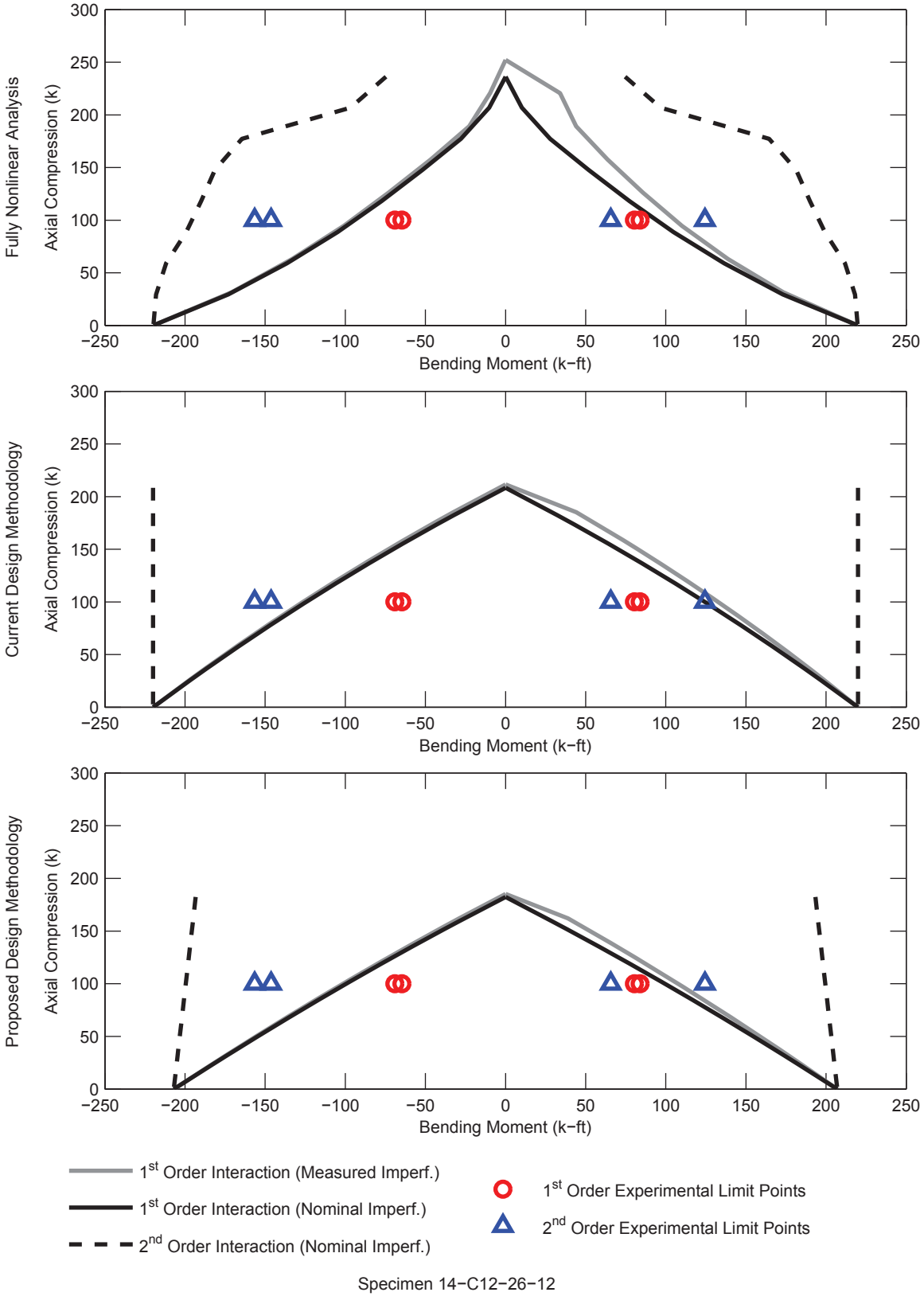

Figure 7.33 Interaction Diagrams – Specimen 14-C12-26-12

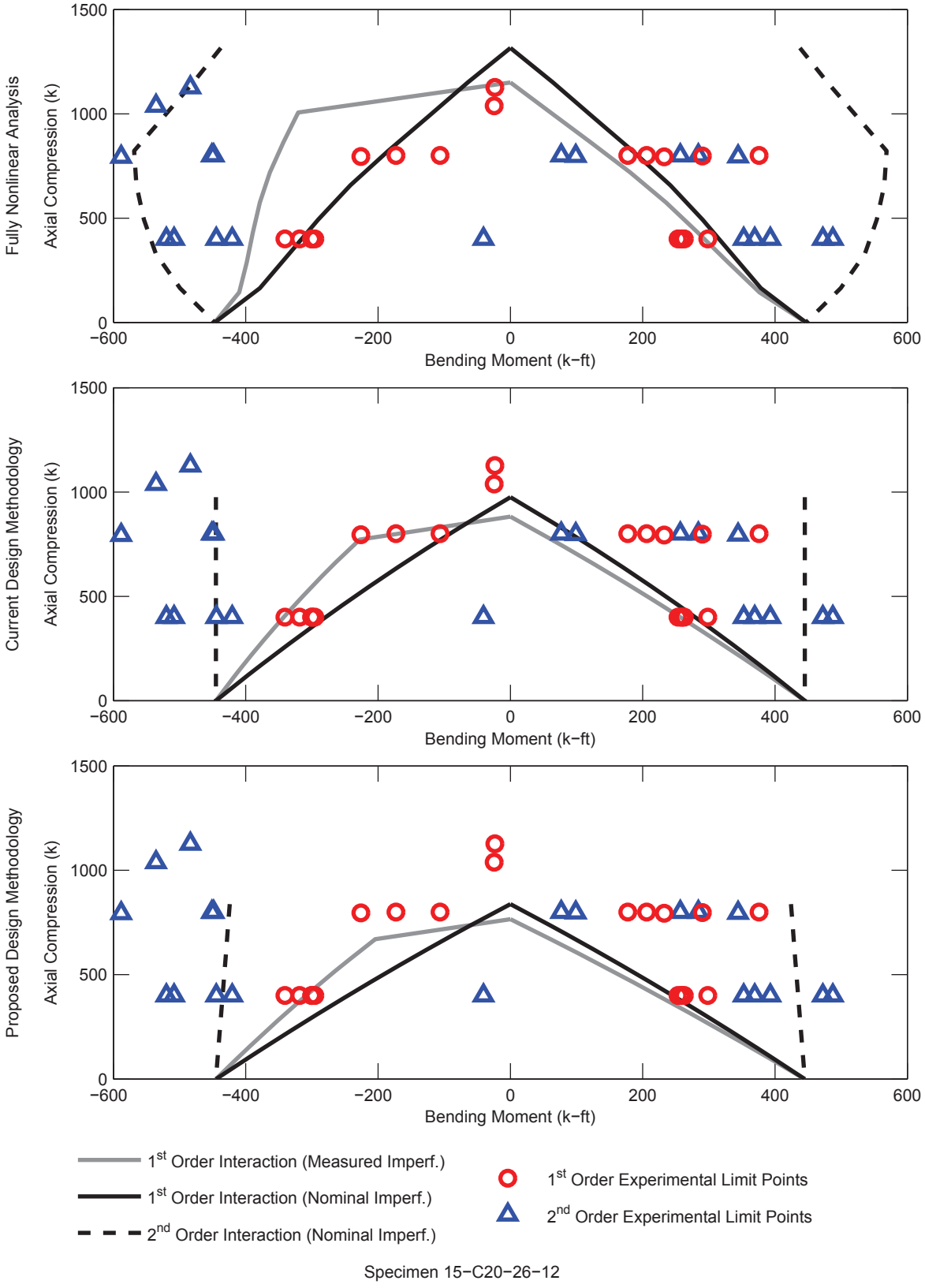

Figure 7.34 Interaction Diagrams – Specimen 15-C20-26-12

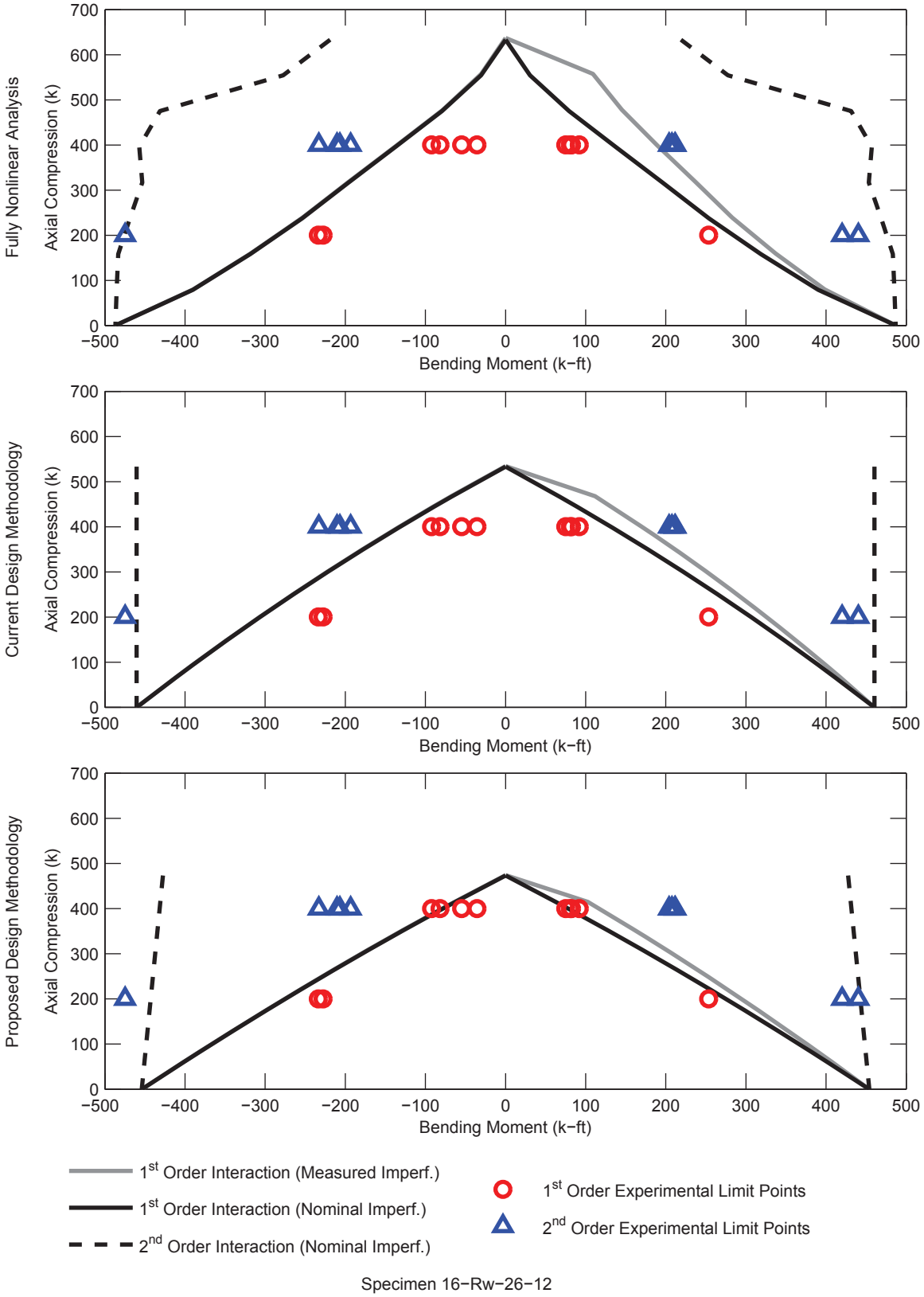

Figure 7.35 Interaction Diagrams – Specimen 16-Rw-26-12

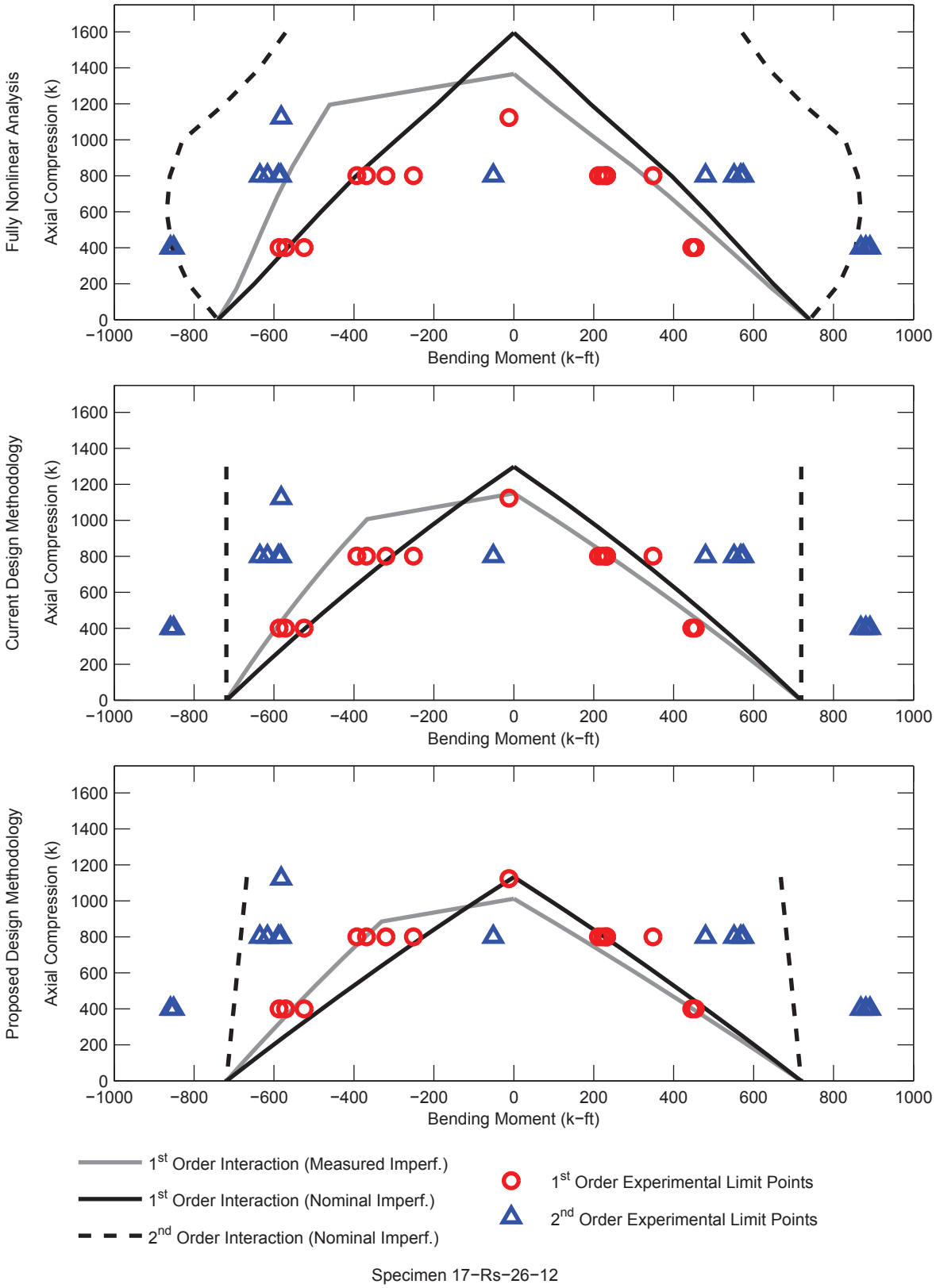

Figure 7.36 Interaction Diagrams – Specimen 17-Rs-26-12

7.5 Cyclic Evolution of Beam-Column Interaction Strength

The strength of a structural member does not remain constant, but rather evolves as damage accumulates and the state of the member changes under loading. This behavior is well known at the material level and is captured in constitutive relations where the loading and boundary surfaces are updated, for example in the steel plasticity model used in this work (Shen et al. 1995). Evolution in strength has been observed at the cross section level as well. Hajjar (2003) documented changes in the position, size, and shape of the loading and bounding surfaces of steel wide-flange cross sections subjected to monotonic plastic excursions. Specimen 9-Rs-18-12 was unique among the specimens because it was subjected to a series of probes and subprobes in LC3 chosen to explore the evolution of strength at the beam-column level. Specifically, to document the change in size, shape, and location of the interaction strength limit surfaces.

7.5.1 Experimental Results

After the completion of LC1 and LC2, Specimen 9-Rs-18-12 was moved to zero displacement and a compressive axial load of 3,560 kN (800 kips) was applied and held constant for the remainder of the test. A probe was completed by increasing the lateral displacements with a fixed ratio of X to Y displacement until a desired displacement, generally past the limit surface, was reached. From this position a series of subprobes were completed by increasing the displacements in a different fixed ratio of X to Y displacement until the critical flexural strength was reached, at which point the lateral displacements were reversed to the termination point of the main probe. The process was then repeated for several additional X/Y displacement combinations. Assuming that relatively little damage is sustained during the motion of the subprobes, this scan about the termination point of the probe determines the limit surface of the beam-column at that state. The process was repeated several times, with LC3a thorough LC3f representing six distinct probe/subprobe sets. The lateral displacement history from these load cases is seen in Figure 7.37a.

Where possible, a limit point was identified for each subprobe as described earlier (Section 7.3). These points are shown in Figure 7.37a as black dots. Connecting the limit points from the various subprobes creates experimental interaction surfaces in lateral displacement space. Using the same limit points, corresponding experimental interaction surfaces can be created in moment space (Figure 7.37b). These represent a slice of the three-dimensional (P-$M_{x,base}$-$M_{y,base}$) interaction surface for the applied axial load.

From Figure 7.37 it can be seen that the position, shape, and size of the limit surface evolve throughout the loading history. The shape of the interaction surfaces is approximate; however, an oblong trend is seen, with larger Y bending moments corresponding to the strong axis of the specimen and smaller X moments corresponding to the weak axis of the specimen. By comparing the relative locations of the load cases in Figure 7.37, the position of the interaction surfaces appears to be affected by the position of the termination point of the probe. Also, it can be seen that the size of the interaction surfaces decreases as the loading progresses. However, as the load cases progressed the distance between the termination point of the probe to the center location became greater, so it is unclear whether it is damage from cyclic loading or another factor that is diminishing the size of the interaction surface. The inelastic buckling limit state which defines these interaction surfaces is affected by a combination of material and geometric nonlinearity. As such, a wide variety of factors will influence the behavior, including material

strengths and section properties at the section level, to beam-column length and out-of-plumbness at the member level.

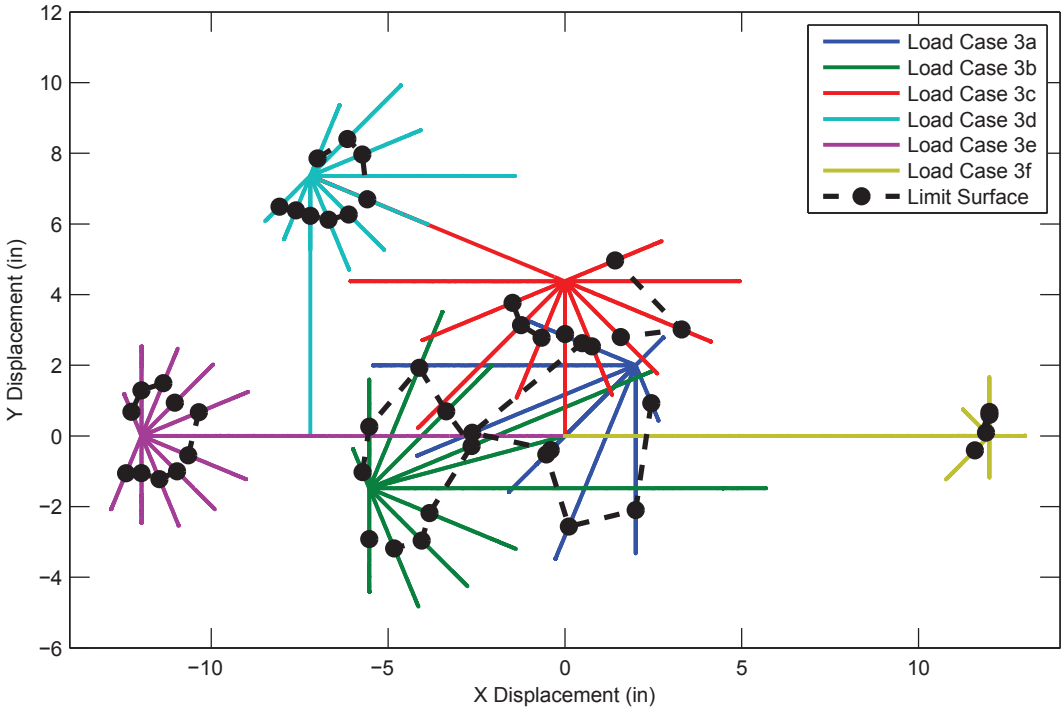

(a) Displacement Space

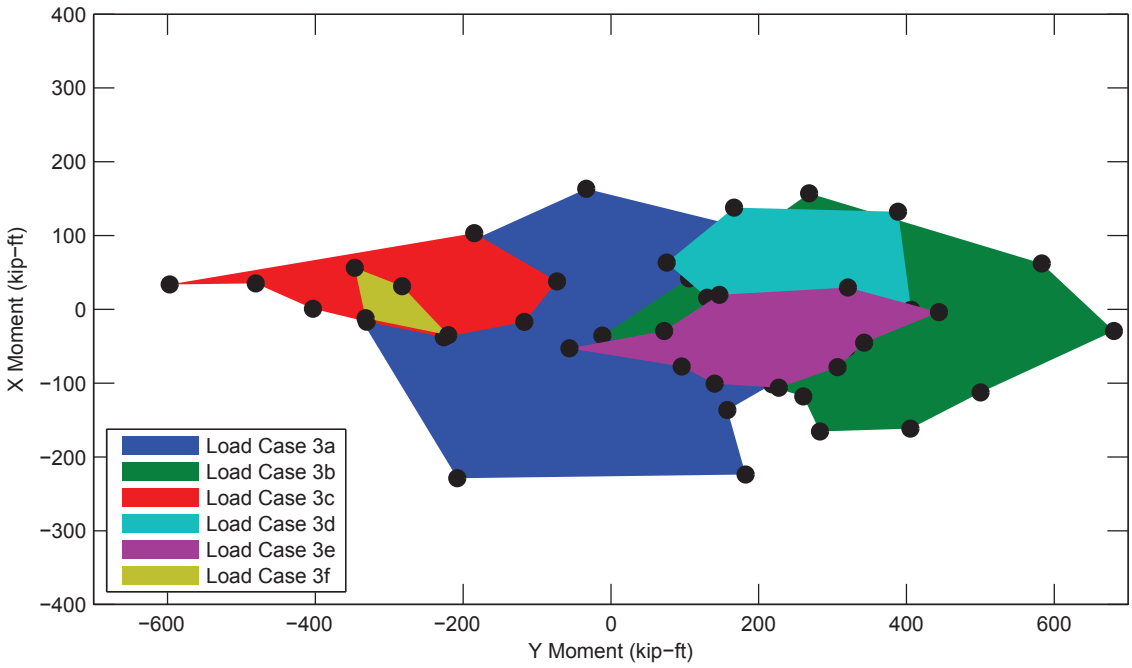

(b) Moment Space

Figure 7.37. Experimental Limit Surfaces, Specimen 9-Rs-18-12

7.5.2 Computational Study

The full loading history of Specimen 9-Rs-18-12 was analyzed with the mixed finite element model (Section 7.2). A generally good correlation is seen between the experimental and computational results (Figure 7.11). In this section, a small parametric study is described that further explores and documents the evolution on the limit surface. Specimen 9Rs-18-12 is analyzed using the "Proposed for Behavior" model (Chapter 3), but subjected to a simpler loading protocol than was used in the experiments. This loading protocol retains the key features of the probe/subprobe loading and it significantly easier to perform and interpret. The analyses were performed in two dimensions with bending about the strong axis. The loading includes several steps, for the analyses shown here they are:

- An axial compressive load of 800 kips is applied.
- The specimen is subjected to one initial full cycle of displacement with amplitude of 4 inches. This cycle is performed to introduce cracking and some initial damage to the specimen as was done in LC1 and LC2 in the experiment.
- The main probe loading is performed, moving the top of the specimen in displacement control to a specified positive displacement.
- The subprobe loading is performed, moving the top of the specimen in displacement control in the opposite direction of the main probe until a limit point is reached (the lowest eigenvalue of the system reaching zero).

Several separate analyses were performed with main probe loading distances ranging from 0 to 15 inches. The displacement pattern of the analyses is shown in Figure 7.38 where the different colored lines represent the separate analyses differentiated by specified main probe loading distance. The circular marker indicates the limit point observed in the sub-probe. The applied force at the top and the bending moment at the base were also recorded and shown in figure.

Of particular interest are two points during the loading: first, the reversal at the end of the main probe and second, the limit point in the sub-probe. These two points define the limit surface of the beam-column. Observing the displacements and moments at these two points for different main probe distances shows the change in the limit surface with main probe loading. This progression of the limit surface is shown in displacement space and moment space in Figure 7.38 where the horizontal distance between the two black lines represents the size of the limit surface for the state defined by the main probe loading distance (vertical axis). For main probe distances of up to approximately 10 inches, the displacement and moment at the limit point in the reversal do not vary significantly. For probe distances of greater than 10 inches, the limit point in the reversal occurs comparatively earlier. The reduction in the limit surface is not gradual, with relatively large changes in the limit surface occurring with relatively small changes in main probe loading. Examining the load deformation response, these changes correspond to the limit point being achieved under positive deflection, indicating that geometric nonlinear effects play a significant role in this behavior.

Comparable results were observed in the experiments. Figure 7.39 shows experimental results from Load Case LC2b of Specimen 17-Rs-26-12. The limit points are identified as red circles. For the first positive half cycles (i.e., moving in the positive direction) the limit points all occur at about the same deflection and force. However, for the final positive half cycle which had the largest deformation, the limit point occurred much earlier.

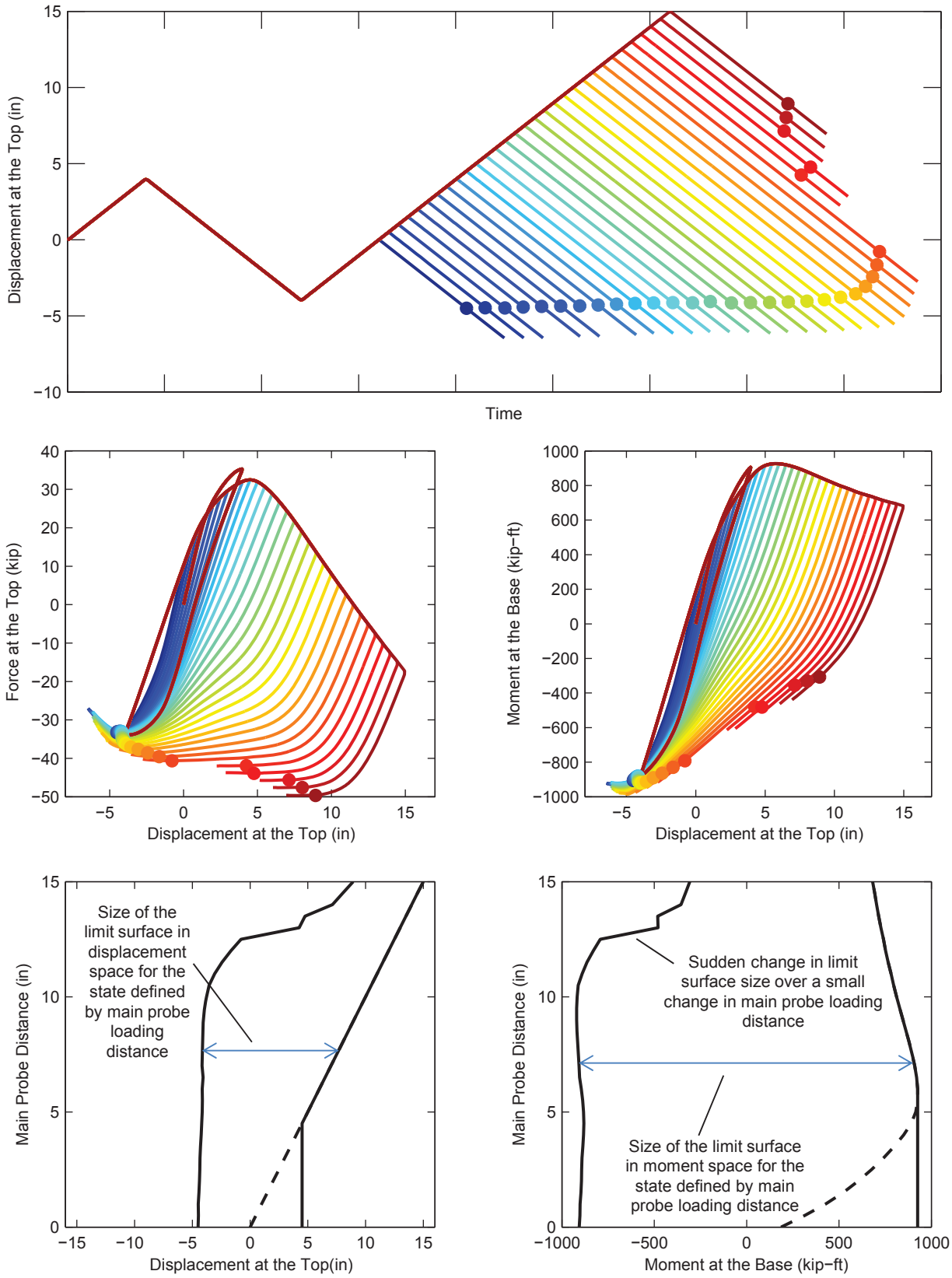

Figure 7.38. Beam-Column Probe Analysis Results

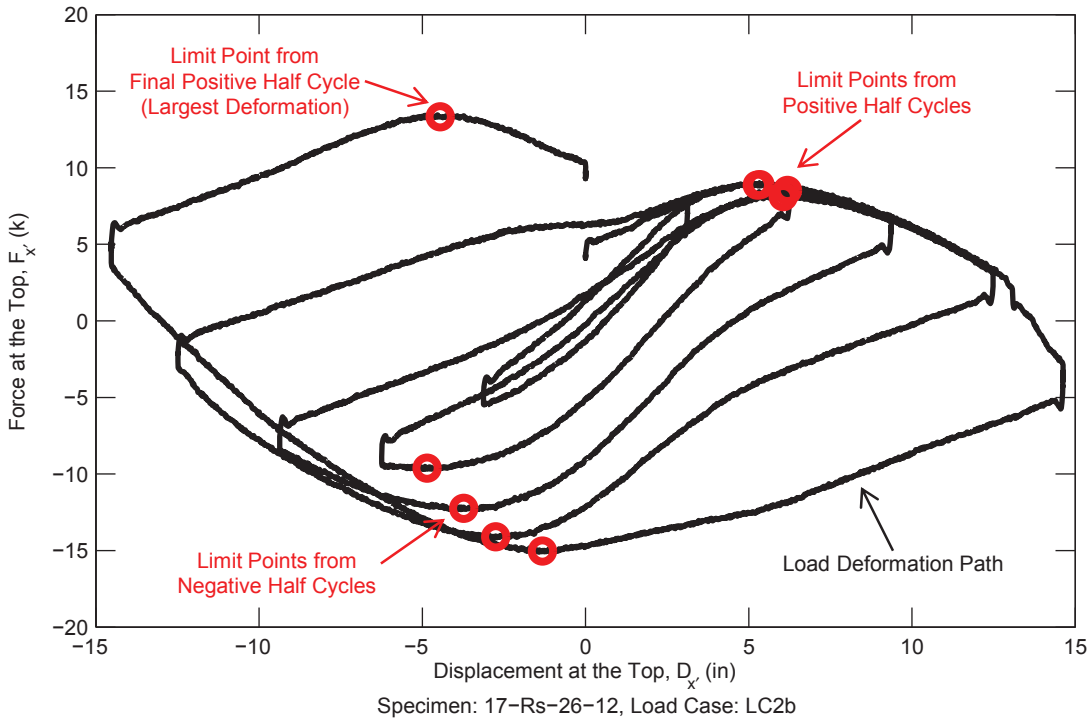

Figure 7.39. Experimental Results: Specimen 17-Rs-26-12, Load Case LC2b

Chapter 8

SEISMIC PERFORMANCE FACTORS FOR COMPOSITE FRAMES

8.1 Introduction

A key component of seismic design in the United States is the allowance for inelasticity in structural elements subjected to severe earthquake ground motions. However, static elastic analysis is prevalent for seismic design in current practice. Because of this, seismic performance factors have been developed. The factors are: the response modification factor, R, used in reducing seismic forces as determined through elastic methods; the displacement amplification factor, C_d, used in amplifying displacements as determined through elastic methods; and the system overstrength factor, Ω_o, used to estimate the actual strength as compared the to the design strength.

These three factors are tabulated for a variety of seismic force resisting systems in national codes (ASCE 2010; ICC 2012), however, they have been somewhat arbitrarily assigned. Many R factors were based largely on judgment and qualitative comparisons to the relatively few seismic force resisting systems that had known response capabilities (FEMA 2009). This is particularly true for composite moment and braced frames where the seismic performance factors were assigned based on comparisons to similar structural steel and reinforced concrete systems.

A methodology has been developed to provide a rational basis for determining seismic performance factors which provide equivalent safety against collapse for buildings with different seismic force resisting systems (FEMA 2009). Equivalent safety is provided through an acceptably low probability of structural collapse common to all systems. Structural collapse in the methodology is defined in the context of incremental dynamic analysis, in which nonlinear time history analyses are performed at increasing magnitudes of seismic loading until the structure achieves its peak strength or predefined displacement limits. In this approach, no explicit modeling of collapse is included. Statistical data is generated from the analyses for a set of archetype models and uncertainty is approximated based on the level of knowledge of the particular system and accuracy of the analysis.

This chapter presents a study to investigate the behavior of composite frames under seismic loading and to develop rational seismic performance factors following the methodology given in FEMA P-695 *Quantification of Building Seismic Performance Factors* (FEMA 2009).

8.2 Seismic Force Resisting Systems

Two separate seismic force resisting systems are analyzed in this study: composite special moment frames (C-SMF) and composite special concentrically braced frames (C-SCBF). The current seismic performance factors for these two systems are given in Table 8.1 (ASCE 2010).

Table 8.1. Current Seismic Performance Factors

System	Ω_o	R	C_d
C-SMF	3.0	8.0	5.5
C-SCBF	2.0	5.0	4.5

8.2.1 Composite Special Moment Frame, C-SMF

The requirements for composite special moment frames are described in the AISC *Seismic Specification* (AISC 2010c). C-SMFs utilize fully restrained connections and consist of either composite or reinforced concrete columns and either structural steel, concrete-encased composite, or composite beams. They are expected to provide significant inelastic deformation capacity through flexural yielding of the beams and limited yielding of the column panel zones. Columns are designed to be stronger than the fully yielded and strain-hardened beams, although flexural yielding in columns at the base is permitted.

8.2.2 Composite Special Concentrically Braced Frame, C-SCBF

The requirements for composite special concentrically braced frames are described in the AISC *Seismic Specification* (AISC 2010c). C-SCBFs consist of CFT or SRC composite columns, structural steel or composite beams, and structural steel or CFT braces. They are expected to provide significant inelastic deformation capacity primarily through brace buckling and yielding of the brace in tension.

8.3 Selection and Design of Archetype Frames

To perform the methodology, it is necessary to have a suite of frames (termed index archetypes) for which the analyses can be performed. Ideally that suite of frames is representative of the range of frames seen in practice. However, it is generally recognized within the methodology that a practical number of frames cannot fully represent the permissible range, thus simplifications must be made. The selected frames are described below.

The building layout is the same for each of the index archetype configurations: 3 bays by 5 bays with a bay width of either 20 ft or 30 ft (Figure 8.1). The buildings are 3 or 9 stories tall with a story height of 13 ft. For the moment frames the columns were either RCFTs or SRCs. For the braced frames the columns were CCFTs and the braces were either rectangular HSS or wide flange in a two-story X configuration (Figure 8.1b). A composite floor system was assumed for all configurations, although in the beams were designed and analyzed assuming bare steel.

Two levels of gravity load were selected: “high” which corresponded to warehouse live loading (250 psf) and the interior frame and “low” which corresponded to office live loading (65 psf) and the exterior frame. Two levels of seismic load were selected corresponding to the levels design earthquake associated with the maximum (D_{max}) and minimum (D_{min}) of seismic design category D.

The methodology prescribes that $C_d = R$ (FEMA 2009), which is contrary to current practice (ASCE 2010; ICC 2012) were C_d is typically less than R (Table 8.1). For deformation-controlled structures, such as moment frames, this change results in larger member sizes. In this study, most frames were designed assuming $C_d = R$, however, a subset of the moment frames

were duplicated and designed with the current value (C_d = 5.5) so as to compare to the current state of design practice.

In total, 60 frames were selected for this with variations of building height, column type, concrete strength, level of seismic load, level of gravity load, and bay width as summarized in Table 8.2 for C-SMFs Table 8.3 for C-SCBFs. The naming convention of the frames consists of three components separated by dashes. The components are column section type (i.e., CCFT, RCFT, or SRC), number of stories, and index identifier. The index identifier ranges from 1 to 16 and represents a specific combination of concrete strength, level of seismic load, level of gravity load, and bay width. For the frames designed with the current C_d, "-C_d" is appended to the frame name.

Selected material properties and highlights of the design process are presented in the remainder of this section. Full details of the design process and selected members for each frame are given in Appendix B.

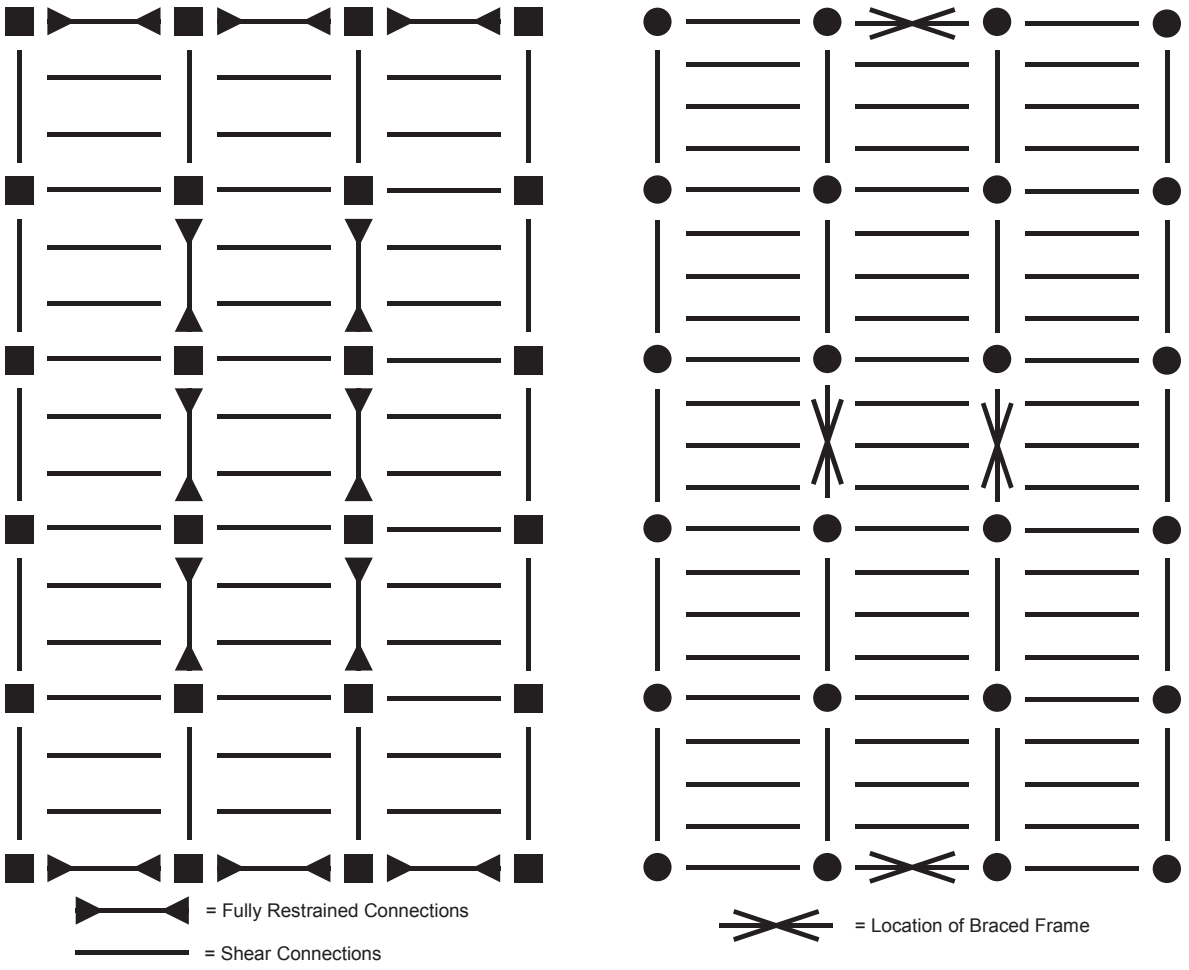

(a) C-SMF (b) C-SCBF

Figure 8.1. Building Layout

Table 8.2. Frame Information: C-SMFs

Frame #	Name	Number of Stories	Gravity Load	f'_c	Bay Width	SDC	$C_d = R$	T	Building V	Building W	C_s	Frame V
				ksi	*ft*			*s*	*kips*	*kips*		*kips*
1	RCFT-3-1	3	high	4	20	Dmax	yes	0.437	307.8	2,462	0.125	153.9
2	RCFT-3-2	3	high	12	20	Dmax	yes	0.437	307.8	2,462	0.125	153.9
3	RCFT-3-3	3	high	4	20	Dmin	yes	0.468	131.5	2,462	0.053	65.7
4	RCFT-3-4	3	high	12	20	Dmin	yes	0.468	131.5	2,462	0.053	65.7
5	RCFT-3-5	3	high	4	30	Dmax	yes	0.437	670.3	5,363	0.125	335.2
6	RCFT-3-6	3	high	12	30	Dmax	yes	0.437	670.3	5,363	0.125	335.2
7	RCFT-3-7	3	high	4	30	Dmin	yes	0.468	286.3	5,363	0.053	143.2
8	RCFT-3-8	3	high	12	30	Dmin	yes	0.468	286.3	5,363	0.053	143.2
9	RCFT-3-9	3	low	4	20	Dmax	yes	0.437	229.0	1,832	0.125	114.5
10	RCFT-3-10	3	low	12	20	Dmax	yes	0.437	229.0	1,832	0.125	114.5
11	RCFT-3-11	3	low	4	20	Dmin	yes	0.468	97.8	1,832	0.053	48.9
12	RCFT-3-12	3	low	12	20	Dmin	yes	0.468	97.8	1,832	0.053	48.9
13	RCFT-3-13	3	low	4	30	Dmax	yes	0.437	493.1	3,945	0.125	246.6
14	RCFT-3-14	3	low	12	30	Dmax	yes	0.437	493.1	3,945	0.125	246.6
15	RCFT-3-15	3	low	4	30	Dmin	yes	0.468	210.7	3,945	0.053	105.3
16	RCFT-3-16	3	low	12	30	Dmin	yes	0.468	210.7	3,945	0.053	105.3
17	RCFT-9-1	9	high	4	20	Dmax	yes	0.996	618.6	8,216	0.075	309.3
18	RCFT-9-3	9	high	4	20	Dmin	yes	1.067	192.5	8,216	0.023	96.2
19	RCFT-9-5	9	high	4	30	Dmax	yes	0.996	1,343.3	17,841	0.075	671.7
20	RCFT-9-7	9	high	4	30	Dmin	yes	1.067	417.9	17,841	0.023	209.0
21	RCFT-9-9	9	low	4	20	Dmax	yes	0.996	428.9	5,696	0.075	214.4
22	RCFT-9-11	9	low	4	20	Dmin	yes	1.067	133.4	5,696	0.023	66.7
23	RCFT-9-13	9	low	4	30	Dmax	yes	0.996	916.4	12,171	0.075	458.2
24	RCFT-9-15	9	low	4	30	Dmin	yes	1.067	285.1	12,171	0.023	142.6
25	SRC-3-1	3	high	4	20	Dmax	yes	0.437	307.8	2,462	0.125	153.9
26	SRC-3-2	3	high	12	20	Dmax	yes	0.437	307.8	2,462	0.125	153.9
27	SRC-3-3	3	high	4	20	Dmin	yes	0.468	131.5	2,462	0.053	65.7
28	SRC-3-4	3	high	12	20	Dmin	yes	0.468	131.5	2,462	0.053	65.7
29	SRC-3-9	3	low	4	20	Dmax	yes	0.437	229.0	1,832	0.125	114.5
30	SRC-3-10	3	low	12	20	Dmax	yes	0.437	229.0	1,832	0.125	114.5
31	SRC-3-11	3	low	4	20	Dmin	yes	0.468	97.8	1,832	0.053	48.9
32	SRC-3-12	3	low	12	20	Dmin	yes	0.468	97.8	1,832	0.053	48.9
33	RCFT-3-1-Cd	3	high	4	20	Dmax	no	0.437	307.8	2,462	0.125	153.9
34	RCFT-3-3-Cd	3	high	4	20	Dmin	no	0.468	131.5	2,462	0.053	65.7
35	RCFT-3-9-Cd	3	low	4	20	Dmax	no	0.437	229.0	1,832	0.125	114.5
36	RCFT-3-11-Cd	3	low	4	20	Dmin	no	0.468	97.8	1,832	0.053	48.9

Table 8.3. Frame Information: C-SCBFs

Frame #	Name	Number of Stories	Gravity Load	f'_c	Bay Width	SDC	$C_d = R$	T	Building V	Building W	C_s	Frame V
				ksi	*ft*			*s*	*kips*	*kips*		*kips*
1	CCFT-3-1	3	high	4	20	Dmax	yes	0.437	492.4	2,462	0.200	246.2
2	CCFT-3-2	3	high	12	20	Dmax	yes	0.437	492.4	2,462	0.200	246.2
3	CCFT-3-3	3	high	4	20	Dmin	yes	0.468	210.3	2,462	0.085	105.2
4	CCFT-3-4	3	high	12	20	Dmin	yes	0.468	210.3	2,462	0.085	105.2
5	CCFT-3-5	3	high	4	30	Dmax	yes	0.437	1,072.5	5,363	0.200	536.3
6	CCFT-3-6	3	high	12	30	Dmax	yes	0.437	1,072.5	5,363	0.200	536.3
7	CCFT-3-7	3	high	4	30	Dmin	yes	0.468	458.2	5,363	0.085	229.1
8	CCFT-3-8	3	high	12	30	Dmin	yes	0.468	458.2	5,363	0.085	229.1
9	CCFT-3-9	3	low	4	20	Dmax	yes	0.437	366.4	1,832	0.200	183.2
10	CCFT-3-10	3	low	12	20	Dmax	yes	0.437	366.4	1,832	0.200	183.2
11	CCFT-3-11	3	low	4	20	Dmin	yes	0.468	156.5	1,832	0.085	78.3
12	CCFT-3-12	3	low	12	20	Dmin	yes	0.468	156.5	1,832	0.085	78.3
13	CCFT-3-13	3	low	4	30	Dmax	yes	0.437	789.0	3,945	0.200	394.5
14	CCFT-3-14	3	low	12	30	Dmax	yes	0.437	789.0	3,945	0.200	394.5
15	CCFT-3-15	3	low	4	30	Dmin	yes	0.468	337.0	3,945	0.085	168.5
16	CCFT-3-16	3	low	12	30	Dmin	yes	0.468	337.0	3,945	0.085	168.5
17	CCFT-9-1	9	high	4	20	Dmax	yes	0.996	989.8	8,216	0.120	494.9
18	CCFT-9-3	9	high	4	20	Dmin	yes	1.067	307.9	8,216	0.037	154.0
19	CCFT-9-5	9	high	4	30	Dmax	yes	0.996	2,149.3	17,841	0.120	1074.7
20	CCFT-9-7	9	high	4	30	Dmin	yes	1.067	668.7	17,841	0.037	334.3
21	CCFT-9-9	9	low	4	20	Dmax	yes	0.996	686.2	5,696	0.120	343.1
22	CCFT-9-11	9	low	4	20	Dmin	yes	1.067	213.5	5,696	0.037	106.7
23	CCFT-9-13	9	low	4	30	Dmax	yes	0.996	1,466.3	12,171	0.120	733.1
24	CCFT-9-15	9	low	4	30	Dmin	yes	1.067	456.2	12,171	0.037	228.1

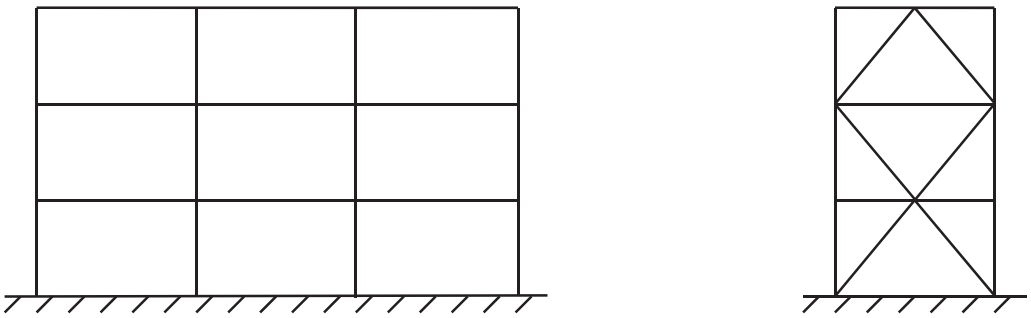

(a) C-SMF (b) C-SCBF

Figure 8.2. Elevation View of Three Story Frames

8.3.1 Material Strengths

Two sets of material strengths are used in this study as summarized in Table 8.4. The first is the nominal strength which is used in the design of the archetypes. The second is the expected strengths which are used in the analyses of the archetypes. The nominal strengths are selected as typical material properties. The expected strengths for the steel materials are defined as described in Section A3.2 of the AISC *Seismic Specification* (AISC 2010c). For lack of a more appropriate definition, the expected strengths for the concrete materials are defined as the required average

compressive strength when data are not available to establish a sample standard deviation as described in Section 5.3.2.2 of the ACI *Code* (ACI 2011).

Table 8.4. Nominal and Expected Material Strengths

Material	Nominal Strength (Used for Design)	Expected Strength (Used for Analysis)	Notes
Circular HSS (ASTM A500 Gr. B)	F_y = 42 ksi F_u = 58 ksi	F_y = 58.8 ksi F_u = 75.4 ksi	R_y = 1.4 R_t = 1.3
Rectangular HSS (ASTM A500 Gr. B)	F_y = 46 ksi F_u = 58 ksi	F_y = 64.4 ksi F_u = 75.4 ksi	R_y = 1.4 R_t = 1.3
Wide Flange (ASTM A992)	F_y = 50 ksi F_u = 65 ksi	F_y = 55.0 ksi F_u = 71.5 ksi	R_y = 1.1 R_t = 1.1
Reinforcement (ASTM A615)	F_{yr} = 60 ksi F_u = 90 ksi	F_{yr} = 75.0 ksi F_u = 112.5 ksi	R_y = 1.25 R_t = 1.25
Plate (ASTM A572 Gr. 50)	F_y = 50 ksi F_u = 65 ksi	F_y = 55.0 ksi F_u = 78.0 ksi	R_y = 1.1 R_t = 1.2
4 ksi Concrete	f'_c = 4 ksi	f'_c = 5.2 ksi	
12 ksi Concrete	f'_c = 12 ksi	f'_c = 13.9 ksi	

8.3.2 Seismic Design

The equivalent lateral force method (ASCE 2010) was used for the seismic design. The level of seismic loading is defined in terms of the seismic design category. The frames in this study were designed for seismic design category D at either the maximum (D_{max}) or minimum (D_{min}). Mapped values of the spectral acceleration, which define design base shear for these levels of seismicity, are given in Table 8.5.

Table 8.5. Mapped Values of Spectral Acceleration by Seismic Design Category

SDC	S_S (g)	F_a	S_{MS} (g)	S_{DS} (g)	S_1 (g)	F_v	S_{M1} (g)	S_{D1} (g)
D_{max}	1.5	1.0	1.5	1.0	0.60	1.5	0.90	0.60
D_{min}/C_{max}	0.55	1.36	0.75	0.50	0.132	2.28	0.30	0.20
D_{min}/C_{max}	0.33	1.53	0.50	0.33	0.083	2.4	0.20	0.133
B_{min}	0.156	1.6	0.25	0.167	0.042	2.4	0.10	0.067

8.3.3 Fundamental Period

The fundamental period of the building, T, is used to determine the design base shear and to define the ground motion spectral intensity for proper scaling and evaluation of the nonlinear response history analyses. It is defined by Equation 8.1.

$$T = C_u T_a = C_u C_t h_n^{\,x} \geq 0.25\,\text{s} \tag{8.1}$$

where,

T = Fundamental period in seconds
C_u = A coefficient based on S_{D1} (Table 12.8-1 (ASCE 2010))
C_t = A coefficient based on the SFRS, equal to 0.02 for the frames studied in this study (Table 12.8-2 (ASCE 2010))
h_n = Structural height in feet
x = A factor based on the SFRS, equal to 0.75 for the frames studied in this study (Table 12.8-2 (ASCE 2010))

8.3.4 Effective Seismic Weight

The effective seismic weight of the building is determined in accordance with Section 12.7.2 of ASCE 7 (ASCE 2010). The effective seismic weight, W, is the sum of the following:

- 100% of the dead load
- 25% of the warehouse floor live load (which is deemed storage)
- 15.4% of the office floor live load (equivalent to 10 psf for partitions)

Live load reduction was not included when determining the seismic weight. All other loading, including roof live loading, does not contribute to the seismic weight.

8.3.5 Seismic Base Shear

The seismic base shear, V, is defined as the product of the effective seismic weight, W, and the seismic coefficient, C_s (Equation 8.2). The seismic coefficient is given by Equation 8.3 based on the fundamental period.

$$V = C_s W \tag{8.2}$$

$$C_s = \begin{cases} \dfrac{S_{DS}}{R} \geq 0.01 & T \leq T_s \\ \dfrac{S_{D1}}{TR} \geq 0.044 S_{DS} \geq 0.01 & T > T_s \end{cases} \tag{8.3}$$

$$T_s = \frac{S_{D1}}{S_{DS}} \tag{8.4}$$

The buildings are symmetric and accidental torsion is neglected, thus the seismic load for each frame is equal to 50% of the seismic load for the building. The accidental torsion is neglected in the design because the nonlinear analyses are performed in two dimensions not including any torsional effects.

8.4 Nonlinear Analysis Model

Analyses are performed using the distributed plasticity mixed beam finite element formulation described in Chapter 3. Additional details of the model specific to the frames are presented in this section. Details of the analyses are presented in later sections.

Each model consisted of beam and zero length element representing the seismic force resisting frame and nonlinear truss elements representing the destabilizing effect of the remainder of the building that is tributary to the frame.

The analyses were performed in two-dimensions. The mesh density was selected such that the model was refined enough to obtain accurate results, but not so dense as to introduce the ill-effects of localization. The nominal length of the column elements was one-third of the story height. The nominal length of the girder elements was one-third of the bay width for the C-SMFs and one-fourth of the bay width for the C-SCBFs corresponding to the beam spacing (Figure 8.1). The actual length of the elements depended on the modeling of the connection region. The constitutive relations used for the braces do not include softening so there was no potential for localization and eight elements were used along the length of each brace. Three integration points were used for all beam elements. Nominal size of the strips in the fiber discretization was $1/20^{th}$ of the section depth, with the number of fibers in each component defined based on this fixed ratio and rounded up to the nearest integer.

The braces in the C-SCBFs are assumed to be physically oriented such that weak axis buckling is out-of-plane of the frame. However, in the model the brace is oriented such that weak axis buckling is in-plane to allow for the use of a two-dimensional model. Correspondingly, the moment releases at the brace ends represent the relatively weak out-of-plane rotational strength of the gusset plate.

As prescribed in the methodology (FEMA 2009), prior to application of the lateral load, gravity load equal to 105% of the dead load plus 25% of the live load and roof live load (1.05 D + 0.25 L + 0.25L_r) was applied and held constant for the remainder of the analysis. All gravity loads were applied as nodal loads based on tributary areas. This load case is contrasted against the load cases used in the design in Table 8.6.

Table 8.6. Gravity Load and Mass in Design and Analysis

	Design	Analysis
Gravity Load	1.4 D 1.2 D + 1.6 L + 0.5L_r 1.2 D + 0.5 L + 1.6L_r etc., including live load reduction Section 2.3 (ASCE 2010)	1.05 D + 0.25 L + 0.25 L_r Equation 6-1 (FEMA 2009)
Mass	D + 25% storage live load + 10 psf for partitions Section 12.7.2 (ASCE 2010)	Same as for design

The methodology (FEMA 2009) does not explicitly define the mass to be used in the analyses. Thus, mass was assigned to the structure based on the effective seismic weight computed for design (Section 8.3.4) as described in Table 8.6. For nodes with gravity load, the

two translational DOFs were assigned equal masses equivalent to the dead load plus a percentage of the live load (Section 8.3.4 and Table 8.6). Additionally, for numerical stability, a minimum nominal mass was assigned to all degrees-of-freedom. The value of the minimum nominal mass was 1×10^{-6} kip·s^2/in for the translational DOFs and 1×10^{-6} kip·in·s^2 for the rotational DOFs.

Additional modeling details specific to this study are:

- An additional elastic stiffness of EA = 300 and EI = 3000 was added to each brace section for numerical stability (e.g., in the event of significant yielding along the full length of the member).
- Rayleigh damping was used, defined as 2.5% in the 1st and 3rd modes based on recommendations from the methodology (FEMA 2009).

The model accurately captures member plasticity, local buckling, global buckling, and panel zone behavior as demonstrated through validation studies presented in Chapter 4. However, some aspects of behavior and failure modes have not been modeled.

- Fracture is not included in the model. While fracture is expected during structural collapse, this study is not explicitly modeling collapse. Fracture is not anticipated to control the behavior of well-designed C-SMF, where ductile yielding of the beams in flexure is expected to dominate the response, or C-SCBF, where ductile yielding of the braces and buckling of the braces is expected to dominate the response.
- Connection regions are modeled as described in Chapter 3. Failure or degradation of the connecting elements is not included in these models. Experimental testing has shown that with proper design and detailing the connecting elements inelasticity can be confined to the member.
- In the design of the frames it was assumed that the beams were provided with lateral bracing sufficient to ensure the full plastic moment capacity could be achieved. Correspondingly, lateral torsional buckling was not included in the model

8.5 Static Pushover Analyses

Static pushover analyses were performed on each frame. Lateral loads were applied at each story in fixed ratios described by Equation 8.4 based on the story mass and the mode shape of the structure. Thus, an eigenvalue analysis was performed prior to the application of lateral load (but after gravity load was applied). The loading was conducted in displacement control until at least a 20% drop in strength after the peak (V_{80}) was observed.

$$F_x = \lambda \frac{m_x \phi_{1,x}}{\sum_i^N m_i \phi_{1,i}} \tag{8.4}$$

where,

F_x = lateral load applied at story x
λ = load factor
m_x = mass as story x

$\phi_{1,x}$ = ordinate of the fundamental mode at story x

8.5.1 Analysis Results

Key results from these analyses are tabulated in Table 8.7 for C-SMFs and in Table 8.8 for C-SCBFs. These results include:

- The fundamental period from the model, T_1
- The maximum base shear capacity, V_{max}
- The overstrength factor, $\Omega = V_{max}/V$
- The ultimate roof displacement (the displacement at V_{80}), δ_u
- The effective yield roof drift displacement, $\delta_{u,eff}$, Equation 8.4 (FEMA 2009)
- The period-based ductility, $\mu_T = \delta_u / \delta_{u,eff}$ (where the ultimate roof displacement was unable to be determined from the analyses, the largest achieved displacement was used in lieu of δ_u)

$$\delta_{y,eff} = C_o \frac{V_{max}}{W}\left(\frac{g}{4\pi^2}\right)\left(\max(T, T_1)\right)^2 \tag{8.4}$$

$$C_o = \phi_{1,r} \frac{\sum_1^N m_x \phi_{1,x}}{\sum_1^N m_x \phi_{1,x}^2} \tag{8.4}$$

Detailed results for each frame are shown in Appendix C illustrating the overall behavior of the frames as well as the distribution of inelasticity within the frames as the loading progresses. These results include 1) the base shear vs. roof drift response; 2) distribution of applied lateral loads; and 3) story drift ratios at V, V_{max}, and V_{80}.

For the C-SMFs, an initially linear response is observed followed by gradual stiffness reduction up to the peak lateral capacity of the frame then near linear post peak degradation until the analysis was stopped after at least a 20% drop in capacity was observed. For the 3 story frames an even distribution of deformation is seen among the stories with the exception of the roof story of some frames where lower deformations were observed at the V_{80} level. For the 9 story frames, the distribution of deformation was even among the stories at the design base shear level, however, at the maximum base shear and after a 20% drop in capacity, the deformation was concentrated in ranges of 4 to 6 stories forming a multi-story mechanism (Krishnan and Muto 2012). The story groups where the inelasticity was concentrated were either located at the top, middle, or bottom of the structure. No fundamental behavioral differences were observed between the frames with RCFT columns and those with SRC columns owing to the fact that flexural yielding of the beams controlled the response.

For the C-SCBFs, the response was initially linear, however, in contrast to the C-SMFs, sharp changes in stiffness including drops in capacity were observed in the response corresponding to yielding and buckling of the individual braces. These jumps are exacerbated by the fact that only one bay of bracing was modeled; had multiple bays been included with slightly different loading or material properties, the response would likely have been smoother. Also in

contrast to the C-SMFs, for the 3 story frames the deformation was often concentrated into one story. The 9 story frames showed a similar response to the C-SMFs in that multi-story mechanisms were developed where the deformation was concentrated in 4 to 6 consecutive stories.

Further discussion of the observed overstrength from these analyses is presented in Section 0.

Table 8.7. Static Pushover Analysis Results: C-SMFs

Frame #	Name	T *s*	T_1 *s*	V *kips*	V_{max} *kips*	Ω	$\delta_{y,eff}$ *in*	δ_u *in*	μ_T
1	RCFT-3-1	0.437	0.638	153.9	879.3	5.71	4.0	50.8	12.75
2	RCFT-3-2	0.437	0.622	153.9	885.7	5.76	3.8	49.9	12.97
3	RCFT-3-3	0.468	0.997	65.7	416.7	6.34	4.4	38.5	8.71
4	RCFT-3-4	0.468	0.985	65.7	417.6	6.35	4.3	37.7	8.73
5	RCFT-3-5	0.437	0.633	335.2	1842.8	5.50	3.8	61.3	16.27
6	RCFT-3-6	0.437	0.632	335.2	1777.8	5.30	3.6	59.1	16.29
7	RCFT-3-7	0.468	0.789	143.2	1291.6	9.02	4.0	49.2	12.20
8	RCFT-3-8	0.468	0.774	143.2	1289.8	9.01	3.9	45.2	11.65
9	RCFT-3-9	0.437	0.671	114.5	707.0	6.18	4.5	51.1	11.38
10	RCFT-3-10	0.437	0.678	114.5	670.0	5.85	4.3	58.9	13.56
11	RCFT-3-11	0.468	0.972	48.9	367.6	7.52	4.8	49.4	10.33
12	RCFT-3-12	0.468	0.946	48.9	373.3	7.63	4.6	53.3	11.56
13	RCFT-3-13	0.437	0.685	246.6	1438.2	5.83	4.4	74.9	17.02
14	RCFT-3-14	0.437	0.690	246.6	1342.1	5.44	4.2	67.9	16.25
15	RCFT-3-15	0.468	1.058	105.3	707.2	6.71	5.2	63.3	12.24
16	RCFT-3-16	0.468	1.064	105.3	695.8	6.61	5.1	53.5	10.40
17	RCFT-9-1	0.996	1.278	309.3	1656.4	5.36	9.5	44.4	4.65
18	RCFT-9-3	1.067	1.924	96.2	865.1	8.99	11.2	65.6	5.88
19	RCFT-9-5	0.996	1.278	671.7	3506.1	5.22	9.2	66.7	7.22
20	RCFT-9-7	1.067	1.682	209.0	2260.1	10.82	10.1	89.0	8.83
21	RCFT-9-9	0.996	1.349	214.4	1190.9	5.55	10.6	51.9	4.89
22	RCFT-9-11	1.067	2.430	66.7	429.6	6.44	12.4	49.2	3.96
23	RCFT-9-13	0.996	1.328	458.2	2501.5	5.46	10.1	85.1	8.42
24	RCFT-9-15	1.067	2.436	142.6	925.6	6.49	12.5	52.0	4.15
25	SRC-3-1	0.437	0.864	153.9	1028.4	6.68	8.1	40.8	5.05
26	SRC-3-2	0.437	0.802	153.9	1011.1	6.57	6.9	50.2	7.27
27	SRC-3-3	0.468	1.243	65.7	495.2	7.53	8.1	45.4	5.62
28	SRC-3-4	0.468	1.184	65.7	482.1	7.33	7.2	38.9	5.42
29	SRC-3-9	0.437	0.867	114.5	785.9	6.86	8.1	44.7	5.51
30	SRC-3-10	0.437	0.827	114.5	802.4	7.01	7.6	34.1	4.51
31	SRC-3-11	0.468	1.275	48.9	397.3	8.12	8.8	32.8	3.72
32	SRC-3-12	0.468	1.215	48.9	404.1	8.26	8.2	25.4	3.10
33	RCFT-3-1-Cd	0.437	0.799	153.9	642.9	4.18	4.5	54.4	11.98
34	RCFT-3-3-Cd	0.468	1.049	65.7	374.1	5.69	4.5	46.3	10.19
35	RCFT-3-9-Cd	0.437	0.806	114.5	499.9	4.37	4.6	52.6	11.50
36	RCFT-3-11-Cd	0.468	1.239	48.9	260.5	5.33	5.6	42.3	7.51

Table 8.8. Static Pushover Analysis Results: C-SCBFs

Frame #	Name	T *s*	T_1 *s*	V *kips*	V_{max} *kips*	Ω	$\delta_{v.eff}$ *in*	δ_u *in*	μ_T
1	CCFT-3-1	0.437	0.413	246.2	519.6	2.11	1.1	18.6	16.94
2	CCFT-3-2	0.437	0.410	246.2	519.5	2.11	1.1	15.0	13.65
3	CCFT-3-3	0.468	0.503	105.2	360.9	3.43	1.0	4.2	4.18
4	CCFT-3-4	0.468	0.515	105.2	305.6	2.91	0.9	15.9	17.97
5	CCFT-3-5	0.437	0.419	536.3	1090.7	2.03	1.1	16.1	15.18
6	CCFT-3-6	0.437	0.426	536.3	1092.9	2.04	1.0	13.2	12.53
7	CCFT-3-7	0.468	0.536	229.1	574.5	2.51	0.8	20.3	25.34
8	CCFT-3-8	0.468	0.535	229.1	571.1	2.49	0.8	19.5	24.63
9	CCFT-3-9	0.437	0.459	183.2	319.2	1.74	0.9	18.5	19.70
10	CCFT-3-10	0.437	0.458	183.2	310.3	1.69	0.9	18.9	20.89
11	CCFT-3-11	0.468	0.551	78.3	185.7	2.37	0.8	12.8	16.04
12	CCFT-3-12	0.468	0.565	78.3	181.8	2.32	0.8	15.8	19.60
13	CCFT-3-13	0.437	0.449	394.5	732.2	1.86	1.0	15.1	15.61
14	CCFT-3-14	0.437	0.444	394.5	729.3	1.85	0.9	12.1	12.82
15	CCFT-3-15	0.468	0.568	168.5	379.3	2.25	0.8	11.8	14.90
16	CCFT-3-16	0.468	0.590	168.5	400.9	2.38	0.9	13.1	14.48
17	CCFT-9-1	0.996	1.063	494.9	1007.2	2.04	4.1	32.8	7.94
18	CCFT-9-3	1.067	1.510	154.0	411.0	2.67	3.3	27.6	8.33
19	CCFT-9-5	0.996	1.058	1074.7	1956.7	1.82	3.6	49.3	13.65
20	CCFT-9-7	1.067	1.438	334.3	905.2	2.71	3.0	27.1	9.02
21	CCFT-9-9	0.996	1.094	343.1	573.6	1.67	3.5	34.7	9.91
22	CCFT-9-11	1.067	1.704	106.7	228.3	2.14	3.3	15.9	4.80
23	CCFT-9-13	0.996	1.092	733.1	1208.8	1.65	3.4	44.0	13.10
24	CCFT-9-15	1.067	1.591	228.1	519.9	2.28	3.1	---	7.40

8.6 Dynamic Response History Analyses

In the methodology, collapse is assessed in the context of incremental dynamic analyses (IDA) (Vamvatsikos and Cornell 2002). Dynamic response history analyses are performed, subjecting each frame to a suite of ground motions scaled at different intensities.

8.6.1 Ground Motions

The set of 22 earthquake records described in the methodology (FEMA 2009) was used for this study. Details of the records are given in Table 8.9. Each record has a pair of horizontal components, both of which were utilized, giving a total of 44 ground motions. Details of the ground motions are given in Table 8.10.

Three layers of ground motion scaling were employed as described in Equation 8.4.

$$\ddot{x}_{g,scaled}(t) = NF \cdot SF_1 \cdot SF_2 \cdot \ddot{x}_{g,recorded}(t) \tag{8.4}$$

where,

$\ddot{x}_{g,recorded}(t)$ = recorded ground motion

$\ddot{x}_{g,scaled}(t)$ = scaled ground motion used in the analyses

NF = normalization factor, Equation 8.4
SF_1 = scaling factor 1, Equation 8.4
SF_2 = scaling factor 2

The first layer of ground motion scaling is normalization by peak ground velocity to remove unwarranted variation between records due to differences in event magnitude, distance to source, source type, and site conditions. One normalization factor was computed for each record (pair of components) by Equation 8.4 with values given in Table 8.9.

$$NF_i = \frac{\text{median}\left(\text{PGV}_{\text{PEER},i}\right)}{\text{PGV}_{\text{PEER},i}} \tag{8.4}$$

where,

PGV_{PEER} = peak ground velocity of the ground motion from the PEER database (PEER 2006)

The second layer of ground motion scaling was to adjust the geometric mean of the 5% damped spectral intensity at the fundamental period ($\hat{S}_{NRT}$) to be equal to the intensity of the maximum considered earthquake (S_{MT}, Equation 8.5). One scaling factor, SF_1, was computed for each frame by Equation 8.4. Values of $\hat{S}_{NRT}$ and SF_1 are given in Table 8.11 based on the fundamental period.

$$SF_1 = \frac{S_{MT}}{\hat{S}_{NRT}} \tag{8.4}$$

$$S_{MT} = \begin{cases} S_{MS} & T \le T_s \\ S_{M1}/T & T > T_s \end{cases} \tag{8.5}$$

The third layer of ground motion scaling was to obtain ground motions of different intensities for the response history analyses. This scaling factor, SF_2, varied among the analyses.

Table 8.9. Earthquake Record Data

ID #	Earthquake			Recording Station		PEER Database		Normalization Factor
	Name	Year	Magnitude	Name	Owner	Record Number	PGV *(cm/s)*	
1	Northridge	1994	6.69	Beverly Hills - Mulhol	USC	953	54.22	0.694
2	Northridge	1994	6.69	Canyon Country-WLC	USC	960	43.33	0.869
3	Duzce, Turkey	1999	7.14	Bolu	ERD	1602	59.68	0.631
4	Hector Mine	1999	7.13	Hector	SCSN	1787	34.21	1.101
5	Imperial Valley	1979	6.53	Delta	UNAMUCSD	169	29.75	1.266
6	Imperial Valley	1979	6.53	El Centro Array #11	USGS	174	38.41	0.980
7	Kobe, Japan	1995	6.9	Nishi-Akashi	CUE	1111	35.73	1.054
8	Kobe, Japan	1995	6.9	Shin-Osaka	CUE	1116	32.82	1.147
9	Kocaeli, Turkey	1999	7.51	Duzce	ERD	1158	55.32	0.681
10	Kocaeli, Turkey	1999	7.51	Arcelik	KOERI	1148	28.45	1.323
11	Landers	1992	7.28	Yermo Fire Station	CDMG	900	36.89	1.021
12	Landers	1992	7.28	Coolwater	SCE	848	34.64	1.087
13	Loma Prieta	1989	6.93	Capitola	CDMG	752	34.51	1.091
14	Loma Prieta	1989	6.93	Gilroy Array #3	CDMG	767	43.11	0.873
15	Manjil, Iran	1990	7.37	Abbar	BHRC	1633	43.78	0.860
16	Superstition Hills	1987	6.54	El Centro Imp. Co.	CDMG	721	45.16	0.834
17	Superstition Hills	1987	6.54	Poe Road (temp)	USGS	725	30.88	1.219
18	Cape Mendocino	1992	7.01	Rio Dell Overpass	CDMG	829	47.95	0.785
19	Chi-Chi, Taiwan	1999	7.62	CHY101	CWB	1244	87.47	0.430
20	Chi-Chi, Taiwan	1999	7.62	TCU045	CWB	1485	38.89	0.968
21	San Fernando	1971	6.61	LA - Hollywood Stor	CDMG	68	18.15	2.074
22	Friuli, Italy	1976	6.5	Tolmezzo	--	125	25.06	1.502
						Median:	37.65	

Table 8.10. Earthquake Ground Motion Data

ID #	PEER Component Name	Recorded PGA (g)	Recorded PGV (cm/s)	Normalization Factor	Normalized PGA (g)	Normalized PGV (cm/s)	Record Length (s)	dt (s)
01a	NORTHR/MUL009	0.416	58.95	0.694	0.289	40.93	30.0	0.01
01b	NORTHR/MUL279	0.516	62.77	0.694	0.359	43.59	30.0	0.01
02a	NORTHR/LOS000	0.410	42.98	0.869	0.356	37.35	20.0	0.01
02b	NORTHR/LOS270	0.482	44.92	0.869	0.419	39.03	20.0	0.01
03a	DUZCE/BOL000	0.728	56.44	0.631	0.459	35.60	55.9	0.01
03b	DUZCE/BOL090	0.822	62.09	0.631	0.519	39.17	55.9	0.01
04a	HECTOR/HEC000	0.266	28.55	1.101	0.292	31.43	45.3	0.01
04b	HECTOR/HEC090	0.337	41.74	1.101	0.371	45.94	45.3	0.01
05a	IMPVALL/H-DLT262	0.238	26.00	1.266	0.301	32.90	99.9	0.01
05b	IMPVALL/H-DLT352	0.351	33.00	1.266	0.444	41.76	99.9	0.01
06a	IMPVALL/H-E11140	0.364	34.43	0.980	0.357	33.75	39.0	0.005
06b	IMPVALL/H-E11230	0.380	42.14	0.980	0.372	41.30	39.0	0.005
07a	KOBE/NIS000	0.509	37.29	1.054	0.537	39.29	41.0	0.01
07b	KOBE/NIS090	0.503	36.62	1.054	0.530	38.59	41.0	0.01
08a	KOBE/SHI000	0.243	37.79	1.147	0.279	43.35	41.0	0.01
08b	KOBE/SHI090	0.212	27.89	1.147	0.243	32.00	41.0	0.01
09a	KOCAELI/DZC180	0.312	58.84	0.681	0.212	40.05	27.2	0.005
09b	KOCAELI/DZC270	0.358	46.39	0.681	0.244	31.58	27.2	0.005
10a	KOCAELI/ARC000	0.219	17.69	1.323	0.290	23.41	30.0	0.005
10b	KOCAELI/ARC090	0.150	39.56	1.323	0.198	52.36	30.0	0.005
11a	LANDERS/YER270	0.245	51.41	1.021	0.250	52.47	44.0	0.02
11b	LANDERS/YER360	0.152	29.71	1.021	0.155	30.33	44.0	0.02
12a	LANDERS/CLW-LN	0.283	25.64	1.087	0.307	27.87	28.0	0.0025
12b	LANDERS/CLW-TR	0.417	42.34	1.087	0.453	46.02	28.0	0.0025
13a	LOMAP/CAP000	0.529	35.01	1.091	0.577	38.19	40.0	0.005
13b	LOMAP/CAP090	0.443	29.21	1.091	0.484	31.87	40.0	0.005
14a	LOMAP/G03000	0.555	35.68	0.873	0.485	31.16	39.9	0.005
14b	LOMAP/G03090	0.367	44.66	0.873	0.321	39.00	39.9	0.005
15a	MANJIL/ABBAR--L	0.515	42.47	0.860	0.443	36.52	53.5	0.02
15b	MANJIL/ABBAR--T	0.496	52.09	0.860	0.427	44.80	46.0	0.02
16a	SUPERST/B-ICC000	0.358	46.35	0.834	0.298	38.64	40.0	0.005
16b	SUPERST/B-ICC090	0.258	40.86	0.834	0.215	34.07	40.0	0.005
17a	SUPERST/B-POE270	0.446	35.72	1.219	0.544	43.54	22.3	0.01
17b	SUPERST/B-POE360	0.300	32.78	1.219	0.366	39.97	22.3	0.01
18a	CAPEMEND/RIO270	0.385	43.81	0.785	0.303	34.40	36.0	0.02
18b	CAPEMEND/RIO360	0.549	41.88	0.785	0.431	32.89	36.0	0.02
19a	CHICHI/CHY101-E	0.353	70.63	0.430	0.152	30.40	90.0	0.005
19b	CHICHI/CHY101-N	0.440	115.00	0.430	0.189	49.50	90.0	0.005
20a	CHICHI/TCU045-E	0.474	36.69	0.968	0.459	35.52	90.0	0.005
20b	CHICHI/TCU045-N	0.512	39.06	0.968	0.496	37.82	90.0	0.005
21a	SFERN/PEL090	0.210	18.87	2.074	0.435	39.15	28.0	0.01
21b	SFERN/PEL180	0.174	14.85	2.074	0.361	30.80	28.0	0.01
22a	FRIULI/A-TMZ000	0.351	22.03	1.502	0.528	33.10	36.3	0.005
22b	FRIULI/A-TMZ270	0.315	30.79	1.502	0.473	46.26	36.3	0.005

Table 8.11. Geometric Mean of the Spectral Acceleration of the Normalized Record Set, $\hat{S}_{NRT}$, and Scaling Factor, SF_1

Period (T)	$\hat{S}_{NRT}$	Scaling Factor (SF_1)			
		SDC D_{max}	SDC D_{min}/C_{max}	SDC C_{min}/B_{max}	SDC B_{min}
s	*g*				
0.25	0.785	1.91	0.96	0.64	0.32
0.30	0.781	1.92	0.96	0.64	0.32
0.35	0.767	1.96	0.98	0.65	0.33
0.40	0.754	1.99	0.99	0.66	0.33
0.45	0.755	1.99	0.88	0.59	0.29
0.5	0.742	2.02	0.81	0.54	0.27
0.6	0.607	2.47	0.82	0.55	0.27
0.7	0.541	2.38	0.79	0.53	0.26
0.8	0.453	2.48	0.83	0.55	0.28
0.9	0.402	2.48	0.83	0.55	0.28
1.0	0.350	2.57	0.86	0.57	0.29
1.2	0.303	2.47	0.82	0.55	0.27
1.4	0.258	2.49	0.83	0.55	0.28
1.6	0.210	2.68	0.89	0.59	0.30
1.8	0.169	2.95	0.98	0.66	0.33
2.0	0.149	3.02	1.01	0.67	0.34
2.2	0.134	3.06	1.02	0.68	0.34
2.4	0.119	3.15	1.05	0.70	0.35
2.6	0.106	3.25	1.08	0.72	0.36
2.8	0.092	3.51	1.17	0.78	0.39
3.0	0.081	3.72	1.24	0.83	0.41
3.5	0.063	4.07	1.36	0.90	0.45
4.0	0.053	4.26	1.42	0.95	0.47
4.5	0.046	4.31	1.44	0.96	0.48
5.0	0.041	4.40	1.47	0.98	0.49

8.6.2 Analysis Results

Explicit modeling of the collapse of structures is a challenging task and the subject of current research (Bažant and Verdure 2007; Khandelwal et al. 2009; McAllister et al. 2012; Szyniszewski and Krauthammer 2012). The FEMA (2009) methodology has avoided the need to explicitly model collapse by defining collapse in the context of incremental dynamic analyses. In incremental dynamic analyses, a frame is analyzed under different ground motions and at different intensities. The resulting curve shows a response value (typically peak story drift) versus an intensity measure. Typical results would show an initially high slope, gradually transitioning to a low slope; however, in practice a wide variety of behavior is seen.

Determination of "collapse" is necessary for the methodology and thus approximate definitions are adopted. In this work, collapse is defined when a prescribed maximum story drift of 10% is observed in the incremental dynamic analysis results. This is an approximate method since collapse is not associated with any particular drift limit (Krawinkler et al. 2003); however, some justification of the 10% limit exists. Generally, little hardening response is seen incremental dynamic analysis results beyond 10% drift. Also, the nonlinear models were not validated for deformations beyond this range (Chapter 4) and nonlinear effects that are not being modeled directly in this work, such as fracture, lateral torsion buckling, or connection degradation may occur at these higher drift levels.

Key results from the dynamic response history analyses are tabulated in Table 8.12 for C-SMFs and in Table 8.13 for C-SCBFs. These results include:

- The specific scale factor, SF_1, used in the analyses
- The median collapse intensity, $\hat{S}_{CT}$, determined as the intensity, S_T, at which half of the ground motions cause maximum story drifts of greater than 10%
- The collapse margin ratio, $CMR = \hat{S}_{CT}/S_{MT}$
- Additional results used in the performance evaluation describe later (Section 8.7.3)

Detailed results for each frame are shown in Appendix C, including full incremental dynamic analysis curves that illustrate the overall behavior of the frames under the different ground motions and distributions of maximum story drift ratios at the maximum considered earthquake intensity (i.e., $S_T = S_{MT}$).

For both the C-SMFs and C-SCBFs, the majority of incremental dynamic analysis curves exhibit the typical response with an initial relatively high slope followed by a relatively low slope at higher intensities. The initial slope of the curves for each frame varies, owing to inherent differences between the 44 ground motions. In general, at the maximum considered earthquake intensity (i.e., $S_T = S_{MT}$), the distribution of story drifts is relatively uniform along the height of the building. An exception is the 9 story C-SCBFs where often the top story exhibits deformations several times greater than that of the other stories.

Further discussion of the results of these analyses with regard to the response modification factor and deflection amplification factor is presented in Section 0.

Table 8.12. Dynamic Response History Analysis Results: C-SMFs

Frame #	Name	T *s*	SF_1	S_{MT} *g*	$\hat{S}_{CT}$ *g*	CMR	μ_T	SSF	ACMR	β_{total}	$ACMR_{20\%}$	Pass/ Fail
1	RCFT-3-1	0.437	1.987	1.500	5.720	3.813	12.75	1.330	5.071	0.525	1.556	Pass
2	RCFT-3-2	0.437	1.987	1.500	5.588	3.725	12.97	1.330	4.955	0.525	1.556	Pass
3	RCFT-3-3	0.468	0.854	0.641	3.784	5.905	8.71	1.140	6.731	0.525	1.556	Pass
4	RCFT-3-4	0.468	0.854	0.641	3.879	6.054	8.73	1.140	6.902	0.525	1.556	Pass
5	RCFT-3-5	0.437	1.987	1.500	6.147	4.098	16.27	1.330	5.451	0.525	1.556	Pass
6	RCFT-3-6	0.437	1.987	1.500	5.549	3.699	16.29	1.330	4.920	0.525	1.556	Pass
7	RCFT-3-7	0.468	0.854	0.641	5.181	8.086	12.20	1.140	9.218	0.525	1.556	Pass
8	RCFT-3-8	0.468	0.854	0.641	5.167	8.064	11.65	1.140	9.193	0.525	1.556	Pass
9	RCFT-3-9	0.437	1.987	1.500	6.009	4.006	11.38	1.330	5.328	0.525	1.556	Pass
10	RCFT-3-10	0.437	1.987	1.500	5.989	3.992	13.56	1.330	5.310	0.525	1.556	Pass
11	RCFT-3-11	0.468	0.854	0.641	4.247	6.628	10.33	1.140	7.556	0.525	1.556	Pass
12	RCFT-3-12	0.468	0.854	0.641	4.325	6.750	11.56	1.140	7.694	0.525	1.556	Pass
13	RCFT-3-13	0.437	1.987	1.500	6.262	4.174	17.02	1.330	5.552	0.525	1.556	Pass
14	RCFT-3-14	0.437	1.987	1.500	6.065	4.043	16.25	1.330	5.377	0.525	1.556	Pass
15	RCFT-3-15	0.468	0.854	0.641	3.953	6.169	12.24	1.140	7.032	0.525	1.556	Pass
16	RCFT-3-16	0.468	0.854	0.641	4.286	6.689	10.40	1.140	7.625	0.525	1.556	Pass
17	RCFT-9-1	0.996	2.567	0.904	2.259	2.500	4.65	1.335	3.338	0.525	1.556	Pass
18	RCFT-9-3	1.067	0.841	0.281	1.724	6.132	5.88	1.221	7.485	0.525	1.556	Pass
19	RCFT-9-5	0.996	2.567	0.904	2.580	2.855	7.22	1.432	4.088	0.525	1.556	Pass
20	RCFT-9-7	1.067	0.841	0.281	2.113	7.518	8.83	1.263	9.499	0.525	1.556	Pass
21	RCFT-9-9	0.996	2.567	0.904	2.294	2.539	4.89	1.345	3.415	0.525	1.556	Pass
22	RCFT-9-11	1.067	0.841	0.281	1.853	6.591	3.96	1.175	7.747	0.525	1.556	Pass
23	RCFT-9-13	0.996	2.567	0.904	2.685	2.971	8.42	1.459	4.336	0.525	1.556	Pass
24	RCFT-9-15	1.067	0.841	0.281	1.461	5.197	4.15	1.180	6.134	0.525	1.556	Pass
25	SRC-3-1	0.437	1.987	1.500	4.619	3.079	5.05	1.252	3.854	0.525	1.556	Pass
26	SRC-3-2	0.437	1.987	1.500	5.031	3.354	7.27	1.312	4.400	0.525	1.556	Pass
27	SRC-3-3	0.468	0.854	0.641	3.682	5.746	5.62	1.114	6.403	0.525	1.556	Pass
28	SRC-3-4	0.468	0.854	0.641	3.786	5.909	5.42	1.111	6.566	0.525	1.556	Pass
29	SRC-3-9	0.437	1.987	1.500	4.948	3.298	5.51	1.265	4.173	0.525	1.556	Pass
30	SRC-3-10	0.437	1.987	1.500	4.695	3.130	4.51	1.235	3.867	0.525	1.556	Pass
31	SRC-3-11	0.468	0.854	0.641	4.002	6.246	3.72	1.087	6.791	0.525	1.556	Pass
32	SRC-3-12	0.468	0.854	0.641	3.566	5.566	3.10	1.081	6.016	0.525	1.556	Pass
33	RCFT-3-1-Cd	0.437	1.987	1.500	5.256	3.504	11.98	1.330	4.660	0.525	1.556	Pass
34	RCFT-3-3-Cd	0.468	0.854	0.641	3.722	5.809	10.19	1.140	6.623	0.525	1.556	Pass
35	RCFT-3-9-Cd	0.437	1.987	1.500	4.816	3.211	11.50	1.330	4.271	0.525	1.556	Pass
36	RCFT-3-11-Cd	0.468	0.854	0.641	3.748	5.850	7.51	1.135	6.640	0.525	1.556	Pass

Table 8.13. Dynamic Response History Analysis Results: C-SCBFs

Frame #	Name	T *s*	SF_1	S_{MT} *g*	$\hat{S}_{CT}$ *g*	CMR	μ_T	SSF	ACMR	β_{total}	$ACMR_{20\%}$	Pass/ Fail
1	CCFT-3-1	0.437	1.987	1.500	3.929	2.619	16.94	1.330	3.484	0.525	1.556	Pass
2	CCFT-3-2	0.437	1.987	1.500	3.758	2.505	13.65	1.330	3.332	0.525	1.556	Pass
3	CCFT-3-3	0.468	0.854	0.641	2.980	4.651	4.18	1.093	5.083	0.525	1.556	Pass
4	CCFT-3-4	0.468	0.854	0.641	2.838	4.429	17.97	1.140	5.049	0.525	1.556	Pass
5	CCFT-3-5	0.437	1.987	1.500	3.655	2.436	15.18	1.330	3.240	0.525	1.556	Pass
6	CCFT-3-6	0.437	1.987	1.500	3.750	2.500	12.53	1.330	3.325	0.525	1.556	Pass
7	CCFT-3-7	0.468	0.854	0.641	2.915	4.548	25.34	1.140	5.185	0.525	1.556	Pass
8	CCFT-3-8	0.468	0.854	0.641	2.877	4.490	24.63	1.140	5.119	0.525	1.556	Pass
9	CCFT-3-9	0.437	1.987	1.500	3.013	2.008	19.70	1.330	2.671	0.525	1.556	Pass
10	CCFT-3-10	0.437	1.987	1.500	2.845	1.897	20.89	1.330	2.523	0.525	1.556	Pass
11	CCFT-3-11	0.468	0.854	0.641	2.243	3.500	16.04	1.140	3.990	0.525	1.556	Pass
12	CCFT-3-12	0.468	0.854	0.641	2.232	3.483	19.60	1.140	3.971	0.525	1.556	Pass
13	CCFT-3-13	0.437	1.987	1.500	3.083	2.055	15.61	1.330	2.734	0.525	1.556	Pass
14	CCFT-3-14	0.437	1.987	1.500	3.034	2.023	12.82	1.330	2.691	0.525	1.556	Pass
15	CCFT-3-15	0.468	0.854	0.641	2.237	3.491	14.90	1.140	3.979	0.525	1.556	Pass
16	CCFT-3-16	0.468	0.854	0.641	1.841	2.874	14.48	1.140	3.276	0.525	1.556	Pass
17	CCFT-9-1	0.996	2.567	0.904	1.059	1.172	7.94	1.457	1.708	0.525	1.556	Pass
18	CCFT-9-3	1.067	0.841	0.281	1.258	4.476	8.33	1.263	5.655	0.525	1.556	Pass
19	CCFT-9-5	0.996	2.567	0.904	1.833	2.029	13.65	1.459	2.961	0.525	1.556	Pass
20	CCFT-9-7	1.067	0.841	0.281	1.129	4.018	9.02	1.263	5.076	0.525	1.556	Pass
21	CCFT-9-9	0.996	2.567	0.904	2.023	2.239	9.91	1.459	3.267	0.525	1.556	Pass
22	CCFT-9-11	1.067	0.841	0.281	0.843	3.000	4.80	1.195	3.586	0.525	1.556	Pass
23	CCFT-9-13	0.996	2.567	0.904	1.617	1.789	13.10	1.459	2.611	0.525	1.556	Pass
24	CCFT-9-15	1.067	0.841	0.281	0.875	3.114	7.40	1.251	3.897	0.525	1.556	Pass

8.7 Evaluation of Seismic Performance Factors

8.7.1 Performance Groups

For the purposes of evaluation, the methodology requires the archetype frames be categorized into performance groups based on the design gravity load level, design seismic load level, and period domain. The categorization is shown in Table 8.14 for C-SMFs and Table 8.15 for C-SCBFs. Select analysis results are shown along with mean results for each performance group in Table 8.16 for C-SMFs and Table 8.17 for C-SCBFs.

Table 8.14. Performance Groups: C-SMFs

Group Number	Design Load Level		Period Domain	Number of Frames	Archetype Frames
	Gravity	Seismic			
PG-1	High	SDC Dmax	Short	6	RCFT-3-1, RCFT-3-2, RCFT-3-5, RCFT-3-6, SRC-3-1, SRC-3-2
PG-2	High	SDC Dmax	Long	2	RCFT-9-1, RCFT-9-5
PG-3	High	SDC Dmin	Short	6	RCFT-3-3, RCFT-3-4, RCFT-3-7, RCFT-3-8, SRC-3-3, SRC-3-4
PG-4	High	SDC Dmin	Long	2	RCFT-9-3, RCFT-9-7
PG-5	Low	SDC Dmax	Short	6	RCFT-3-9, RCFT-3-10, RCFT-3-13, RCFT-3-14, SRC-3-9, SRC-3-10
PG-6	Low	SDC Dmax	Long	2	RCFT-9-9, RCFT-9-13
PG-7	Low	SDC Dmin	Short	6	RCFT-3-11, RCFT-3-12, RCFT-3-15, RCFT-3-16, SRC-3-11, SRC-3-12
PG-8	Low	SDC Dmin	Long	2	RCFT-9-11, RCFT-9-15

Table 8.15. Performance Groups: C-SCBFs

Group Number	Design Load Level		Period Domain	Number of Frames	Archetype Frames
	Gravity	Seismic			
PG-1	High	SDC Dmax	Short	4	CCFT-3-1, CCFT-3-2, CCFT-3-5, CCFT-3-6
PG-2	High	SDC Dmax	Long	2	CCFT-9-1, CCFT-9-5
PG-3	High	SDC Dmin	Short	4	CCFT-3-3, CCFT-3-4, CCFT-3-7, CCFT-3-8
PG-4	High	SDC Dmin	Long	2	CCFT-9-3, CCFT-9-7
PG-5	Low	SDC Dmax	Short	4	CCFT-3-9, CCFT-3-10, CCFT-3-13, CCFT-3-14
PG-6	Low	SDC Dmax	Long	2	CCFT-9-9, CCFT-9-13
PG-7	Low	SDC Dmin	Short	4	CCFT-3-11, CCFT-3-12, CCFT-3-15, CCFT-3-16
PG-8	Low	SDC Dmin	Long	2	CCFT-9-11, CCFT-9-15

Table 8.16. Performance Group Results: C-SMFs

Frame	Ω	μ_T	CMR	ACMR	$ACMR_{10\%}$	Pass/Fail
Performance Group: PG-1						
RCFT-3-1	5.71	12.75	3.81	5.07		
RCFT-3-2	5.76	12.97	3.73	4.95		
RCFT-3-5	5.50	16.27	4.10	5.45		
RCFT-3-6	5.30	16.29	3.70	4.92		
SRC-3-1	6.68	5.05	3.08	3.85		
SRC-3-2	6.57	7.27	3.35	4.40		
mean	5.92	11.77	3.63	4.77	1.96	Pass
Performance Group: PG-2						
RCFT-9-1	5.36	4.65	2.50	3.34		
RCFT-9-5	5.22	7.22	2.86	4.09		
mean	5.29	5.93	2.68	3.71	1.96	Pass
Performance Group: PG-3						
RCFT-3-3	6.34	8.71	5.90	6.73		
RCFT-3-4	6.35	8.73	6.05	6.90		
RCFT-3-7	9.02	12.20	8.09	9.22		
RCFT-3-8	9.01	11.65	8.06	9.19		
SRC-3-3	7.53	5.62	5.75	6.40		
SRC-3-4	7.33	5.42	5.91	6.57		
mean	7.60	8.72	6.63	7.50	1.96	Pass
Performance Group: PG-4						
RCFT-9-3	8.99	5.88	6.13	7.48		
RCFT-9-7	10.82	8.83	7.52	9.50		
mean	9.90	7.35	6.83	8.49	1.96	Pass
Performance Group: PG-5						
RCFT-3-9	6.18	11.38	4.01	5.33		
RCFT-3-10	5.85	13.56	3.99	5.31		
RCFT-3-13	5.83	17.02	4.17	5.55		
RCFT-3-14	5.44	16.25	4.04	5.38		
SRC-3-9	6.86	5.51	3.30	4.17		
SRC-3-10	7.01	4.51	3.13	3.87		
mean	6.20	11.37	3.77	4.93	1.96	Pass
Performance Group: PG-6						
RCFT-9-9	5.55	4.89	2.54	3.42		
RCFT-9-13	5.46	8.42	2.97	4.34		
mean	5.51	6.66	2.76	3.88	1.96	Pass
Performance Group: PG-7						
RCFT-3-11	7.52	10.33	6.63	7.56		
RCFT-3-12	7.63	11.56	6.75	7.69		
RCFT-3-15	6.71	12.24	6.17	7.03		
RCFT-3-16	6.61	10.40	6.69	7.62		
SRC-3-11	8.12	3.72	6.25	6.79		
SRC-3-12	8.26	3.10	5.57	6.02		
mean	7.48	8.56	6.34	7.12	1.96	Pass
Performance Group: PG-8						
RCFT-9-11	6.44	3.96	6.59	7.75		
RCFT-9-15	6.49	4.15	5.20	6.13		
mean	6.47	4.05	5.89	6.94	1.96	Pass

Table 8.17. Performance Group Results: C-SCBFs

Frame	Ω	μ_T	CMR	ACMR	$ACMR_{10\%}$	Pass/Fail
Performance Group: PG-1						
CCFT-3-1	2.11	16.94	2.62	3.48		
CCFT-3-2	2.11	13.65	2.51	3.33		
CCFT-3-5	2.03	15.18	2.44	3.24		
CCFT-3-6	2.04	12.53	2.50	3.33		
mean	2.07	14.57	2.52	3.35	1.96	Pass
Performance Group: PG-2						
CCFT-9-1	2.04	7.94	1.17	1.71		
CCFT-9-5	1.82	13.65	2.03	2.96		
mean	1.93	10.79	1.60	2.33	1.96	Pass
Performance Group: PG-3						
CCFT-3-3	3.43	4.18	4.65	5.08		
CCFT-3-4	2.91	17.97	4.43	5.05		
CCFT-3-7	2.51	25.34	4.55	5.19		
CCFT-3-8	2.49	24.63	4.49	5.12		
mean	2.83	18.03	4.53	5.11	1.96	Pass
Performance Group: PG-4						
CCFT-9-3	2.67	8.33	4.48	5.66		
CCFT-9-7	2.71	9.02	4.02	5.08		
mean	2.69	8.67	4.25	5.37	1.96	Pass
Performance Group: PG-5						
CCFT-3-9	1.74	19.70	2.01	2.67		
CCFT-3-10	1.69	20.89	1.90	2.52		
CCFT-3-13	1.86	15.61	2.06	2.73		
CCFT-3-14	1.85	12.82	2.02	2.69		
mean	1.79	17.26	2.00	2.65	1.96	Pass
Performance Group: PG-6						
CCFT-9-9	1.67	9.91	2.24	3.27		
CCFT-9-13	1.65	13.10	1.79	2.61		
mean	1.66	11.50	2.01	2.94	1.96	Pass
Performance Group: PG-7						
CCFT-3-11	2.37	16.04	3.50	3.99		
CCFT-3-12	2.32	19.60	3.48	3.97		
CCFT-3-15	2.25	14.90	3.49	3.98		
CCFT-3-16	2.38	14.48	2.87	3.28		
mean	2.33	16.25	3.34	3.80	1.96	Pass
Performance Group: PG-8						
CCFT-9-11	2.14	4.80	3.00	3.59		
CCFT-9-15	2.28	7.40	3.11	3.90		
mean	2.21	6.10	3.06	3.74	1.96	Pass

8.7.2 System Overstrength Factor, Ω_o

According to the methodology, the system overstrength factor, Ω_o, should not be taken as less than the largest average value of overstrength, Ω, from any performance group, however, upper limits of 1.5R and 3.0 are applied (FEMA 2009).

For the C-SMFs, the average overstrength for the performance groups ranges from 5.3 for PG-2 (high gravity load, SDC: D_{max}, long period) to 9.9 for PG-4 (high gravity load, SDC: D_{min}, long period). These values are quite high and reflect the displacement controlled design of these structures (Appendix B). Other studies on steel special moment frames (NIST 2010) have also shown high overstrength. Several factors have led to particularly high overstrength values seen in this study. The use of $C_d = R$ in the design of the frames reduced the allowable story drifts thus increasing member sizes. In the model, the plastic hinges were forced to a location 2d/3 away from the column face. This distance was the assumed length of the connection. Selection of this distance resulted in higher frame strengths as compared to shorter connections. Additionally, reduced beam section connections were not used for these structures; if they had been used, lower overstrength would have been observed. For the results shown, all of the performance groups exceed the practical upper limit of 3.0, so it is recommended that the systems overstrength factor remain unchanged from its current value ($\Omega_o = 3.0$).

For the C-SCBFs, the average overstrength for the performance groups ranges from 1.7 for PG-5 (high gravity load, SDC: D_{min}, short period) to 2.8 for PG-3 (low gravity load, SDC: D_{max}, short period). These results are in contrast to the C-SMFs where high overstrength was observed and reflect the strength controlled design of these structures (Appendix B). Other studies on steel special concentrically frames (NIST 2010) have shown similar overstrength results. In light of these results ($\Omega = 2.8$ for PG-3), an increase the system overstrength factor for C-SCBFs could be warranted, although the current value ($\Omega_o = 2.0$) is likely sufficient.

8.7.3 Response Modification Factor, R

According to the methodology, the response modification factor that was used to design the archetype frames is acceptable if the probability of collapse for maximum considered earthquake ground motions is approximately 20% or less for each index archetype and 10% or less on average for each performance group (FEMA 2009). To evaluate these conditions, adjusted collapse margin ratios are computed and compared against reference values (Equations 8.5a and 8.5b).

$$ACMR_i \geq ACMR_{20\%} \tag{8.5a}$$

$$\text{mean}\left(ACMR_i\right) \geq ACMR_{10\%} \tag{8.5b}$$

where,

$ACMR_i$ = adjusted collapse margin ratio for each index archetype, i

$ACMR_{20\%}$ = acceptable value of the adjusted collapse margin ratio for 20% collapse probability

$ACMR_{10\%}$ = acceptable value of the adjusted collapse margin ratio for 10% collapse probability

The adjusted collapse margin ratio is the product of the collapse margin ratio, *CMR*, as determined from the response history analyses and a spectral shape factor, *SSF*, given in FEMA P695 (2009). The spectral shape factor depends on the fundamental period, *T*, and period based ductility, μ_T, and accounts for the frequency content of the selected ground motion record set.

$$ACMR_i = SSF_i \; CMR_i \tag{8.6}$$

The acceptable values of the adjusted collapse margin ratio are derived from the lognormal distribution and depend on the desired collapse probability (10% or 20%) and a measure of the total system collapse uncertainty. Uncertainty in the system collapse assessment comes from a number of sources.

Uncertainty due to the variability between ground motions records is characterized by β_{RTR} [Equation 8.7 (FEMA 2009)]

$$\beta_{RTR} = 0.1 + 0.1\mu_T \leq 0.4 \tag{8.7}$$

Uncertainty in the design requirements, test data, and nonlinear modeling are characterized by qualitative quality ratings.

For both of systems, the design requirements have been well-vetted and provide extensive safeguards against unanticipated failure modes. The hierarchy of yielding and failure of components is well established. However, construction practices are comparatively less mature than for either structural steel or reinforced concrete structures. For these reasons, a quality rating of good (B) is given to the design requirements for both C-SMFs and C-SCBFs.

Numerous tests on composite members, connections, and frames have been conducted and reported in the literature. The tests span most of the important parameters which affect design requirements and the behavior is generally well understood. For these reasons, a quality rating of good (B) is given to the test data for both C-SMFs and C-SCBFs.

The nonlinear models directly simulate all predominate inelastic effects and have been extensively validated against experimental results. The sets of archetype frames provide a reasonably broad representation of the design space. However, fracture is not included in the modeling and the frames were assumed to be properly designed to preclude connection deterioration and lateral torsional buckling. For these reasons, a quality rating of good (B) is given to the nonlinear modeling for both C-SMFs and C-SCBFs.

The quality ratings are assigned lognormal standard deviation parameters (Table 8.18) and the total system collapse uncertainty is computed with Equation 8.8 then rounded to the nearest 0.025. The value depends on the period based ductility but is constant for $\mu_T \geq 3$, this value is given in Table 8.18.

$$\beta_{total} = \sqrt{\beta_{RTR}^2 + \beta_{DR}^2 + \beta_{TD}^2 + \beta_{MDL}^2} \tag{8.8}$$

Table 8.18. Quality Ratings

System	Quality of Design Requirements	Quality of Test Data	Quality of Nonlinear Modeling	Total System Collapse Uncertainty for $\mu_T \geq 3$
C-SMF	B (Good) $\beta_{DR} = 0.2$	B (Good) $\beta_{TD} = 0.2$	B (Good) $\beta_{MDL} = 0.2$	$\beta_{total} = 0.525$
C-SCBF	B (Good) $\beta_{DR} = 0.2$	B (Good) $\beta_{TD} = 0.2$	B (Good) $\beta_{MDL} = 0.2$	$\beta_{total} = 0.525$

Values of *SSF*, *ACMR*, β_{total}, $ACMR_{20\%}$, and a Pass/Fail evaluation for each frame are presented in Table 8.12 for C-SMFs and in Table 8.13 for C-SCBFs. Values of mean *ACMR*, $ACMR_{10\%}$, and a Pass/Fail evaluation for each performance group are presented in Table 8.16 for C-SMFs and Table 8.17 for C-SCBFs.

For the C-SMFs, all of the evaluations pass and thus the current response modification factor is deemed acceptable. In fact, all frames pass by a significant margin. Many of the IDA curves retain a significant positive slope even at the high levels of earthquake ground motion used in this study (up to 5-7 times MCE intensity). This is indicative of the excellent performance of C-SMFs subjected to earthquake ground motions. For the C-SCBFs, all of the evaluations pass and thus the current response modification factor is deemed acceptable. The margin of passing is not as great as for the C-SMFs, nonetheless, the C-SCBFs exhibit excellent performance. It should be noted that these results are only strictly applicable to well designed and detailed frames where connection deterioration will not occur and sufficient lateral bracing is provided.

8.7.4 Deflection Amplification Factor, C_d

According to the methodology, for systems with typical levels of damping, including the systems studied here, the deflection amplification factor, C_d, is equal to the response modification factor (FEMA 2009). For C-SCBFs this represents a minor change as the current difference between R and C_d is small and there structures are typically not displacement controlled. For C-SMFs this represents a significant change. Setting $C_d = R$ results in a 45% increase in C_d from the current value. Additionally, C_d plays a central role in the design of moment frames since they are often displacement-controlled.

In this study, four frames were designed with the current C_d value. These frames had smaller members than their counterparts designed with $C_d = R = 8.0$. Differences in performance were also noted. The average overstrength of the frames designed with the current C_d was 4.9 while it was 6.4 for their counterparts. The average adjusted collapse margin ratio of the frames designed with the current C_d was 5.5 while it was 6.2 for their counterparts. These results indicate that the frames designed with the current C_d value have acceptable performance and that setting $C_d = R$ for this system would serve to only in increase the overstrength.

All in all, further study is needed to determine the ramifications of setting $C_d = R$ and whether such a change is necessary. Further study should include the possibility of a corresponding increase in the deformation limits should $C_d = R$.

8.8 Conclusions

A study was conducted following recommendations in FEMA P695 (2009) to determine the seismic performance factors (i.e., R, C_d, and Ω_o) for composite special moment frames (C-SMF) and composite special concentrically braced frames (C-SCBF). A suite of 60 archetype frames was selected and designed according to current design specifications. Nonlinear static pushover analyses and dynamic response history analyses were performed on the frames to characterize the behavior and generate statistical data to be used in evaluation of the seismic performance factors. Both systems exhibited excellent seismic behavior and current seismic performance factors were found to be acceptable. In particular, it was noted that frames designed with the current deflection amplification factor, C_d, were found to be acceptable and thus a potential change to set $C_d = R$ should be studied further and perhaps accompanied by a corresponding change to the drift limits to such that future seismic drift requirements are equivalent to the current seismic drift requirements.

Chapter 9

CONCLUSIONS

Properly designed and detailed steel-concrete composite framing systems take advantage of the strengths of the constituent materials resulting in efficient structures that exhibit excellent performance. A wide range of synergistic effects are possible in steel-concrete composite members. Confinement provided by the steel will enhance the strength and ductility of the concrete. The concrete will delay or prevent local buckling of the steel. The steel can be designed to support construction loads, allowing the steel to be framed several floors above the concrete pouring. Despite the potential advantages, the use of composite systems in practice is limited compared to the traditional alternatives: structural steel and reinforced concrete. This is due, in part, because the behavior of composite members and frames is less understood and correspondingly gaps exist in the design provisions.

A consistent and transparent reasoning should be applied in the development of design provisions. Analysis and experimentation should serve as fundamental sources of knowledge on behavior, neither taking a primary role but rather each reinforcing the other, leading to better understanding. Inconsistencies from different experiments and different levels of analyses need to be acknowledged and reconciled. Then to ensure the design provisions are practical, judicious simplifications are necessary. The research described in this dissertation has followed this path, starting from the fundamentals of structural mechanics (equilibrium, kinematics, and constitutive relations), buttressed by experimental results, leading to characterization of behavior and finally distillation into practical design recommendations.

9.1 Modeling of Composite Members and Frames

A mixed finite element formulation was developed for the analysis of composite members and frames. Two- and three-dimensional mixed beam finite elements developed in prior work are used. The mixed formulation, meaning that both displacements and forces are taken as primary variables, was selected to achieve accurate results for both geometric and material nonlinearity. The element is derived in the corotational frame, with small strain and moderate rotation assumptions. When accompanied with an exact transformation between the corotational and global frames the element is capable of capturing large displacement and rotation behavior.

Material inelasticity is tracked with fiber cross sections located at integration points along the length of the element. Comprehensive uniaxial cyclic constitutive relations were developed for concrete and steel. These models account for the salient features of each material and the interaction between the two, including: cracking and confinement of the concrete and yielding and local buckling of the steel.

A rule-based approach is used for the cyclic behavior of the concrete. Either Popovics' equation or Tsai's equation is used for the monotonic backbone response. Mander's confinement model is used to determine the increase in compressive strength and ductility given confinement pressures. Tension is included and a comprehensive set of rules define any unloading/reloading path with a continuous smooth response.

A bounding surface plasticity formulation is used for the cyclic behavior of the steel. The model accounts for various effects including: reduction in size of the elastic range, combined kinematic and isotropic hardening, shifting of the bounding lines. Local buckling was incorporated into the uniaxial response. Under monotonic load local buckling is triggered by a strain limit, at which point the response from the plasticity formulation is overridden by a linear degradation curve followed by a constant residual stress. Under cyclic loading, a combined stress and strain limit triggers local buckling and degradation in the elastic range and plastic modulus for reloading back to tension is included.

Models for CFT and SRC beam-column cross sections were developed. The models take as input only material and geometric properties known at the time of design and define the fiber discretization and the specific parameters to be used in the steel and concrete uniaxial materials. Included in these models are assessments of the level of confinement in the concrete and susceptibility of steel to local buckling.

Secondary, simpler cross section models were also defined following assumptions common in the development of design recommendations. These models neglect concrete tension, utilize simpler relations for the post-peak response of concrete in compression, and use multi-linear constitutive relations for the steel.

Composite cross sections, particularly those under high axial load, can exhibit softening behavior, thus localization is a potential issue affecting the results of the finite element formulation. Efforts were taken in the analyses to select mesh densities such that the integration weight associated with the critical integration point was representative of the physical plastic hinge length. The plastic hinge length was assessed from cross section analyses based on the yield and ultimate moments.

Models were also developed for wide flange steel beams and wide flange or rectangular hollow structural steel braces. Flange and web local buckling was included in the beam model based on an assessment of three-point bending tests. Connection region models for moment frames and braced were defined based on prior research.

The formulation was validated against a wide range of monotonic and cyclic experiments, including short columns, beams, and proportionally and non-proportionally loaded beam-columns. Over 250 individual specimens were analyzed. Quantitative comparisons are made using various metrics computed from the resulting load deformation response. These metrics include initial stiffness, peak load, deformation at peak load, and area under the curve. The studies showed the strengths and weakness of the models. Over all it was shown that accurate results can be obtained under a variety of loading conditions.

9.2 Behavior of Composite Members and Frames

A series of experiments on full-scale CFT beam-columns has been completed by project collaborators. The tests explore several aspects of the behavior of composite columns, including the multi-dimensional interaction surface, biaxial cyclic seismic behavior, and evolution of damage. Comparative analyses were performed in this work based on the formulations developed herein and detailed data interpretation focusing on the beam-column interaction strength was conducted.

The specimens were modeled using the mixed finite element formulation and subjected to the same loading history as in the experiment. Detailed comparison of results was presented demonstrating the accuracy of the formulation.

Interaction strength limit points were identified in the experimental results. These points were used to further validate the proposed-beam column design methodology developed in this work. The limit points were compared against interaction diagrams developed from fully nonlinear analyses and from elastic design provisions. The results indicate that the proposed methodology is safe and accurate.

The experimental results of one specimen were examined in detail. The specimen was subjected to a series of probes and subprobes to determine experimental interaction surfaces. These surfaces were shown to evolve in size, position, and shape as the loading progressed. Corresponding computational results were presented, which showed a good correspondence with the experimental results, indicating that the finite element formulation is capable of predicting the complex behavior observed in CFT members.

9.3 Design of Composite Members and Frames

9.3.1 Natural Bond Behavior of CFTs

Available experimental results on load transfer by natural bond in CFTs were reviewed, including simple push-out and push-off test as well as connection tests. Trends in the data were identified, notably the variation of bond stress with the size of the steel tube and the beneficial effects of the rotation of the shear tab on the bond strength.

Existing design provisions were evaluated against the experimental results. Comparing to push-out tests, the prescribed bond stress was found to be overly simple and in the case of large and thin steel tubes unconservative. Comparing to connection tests, the bond strength was found to be conservative. Thus, a new formula for nominal bond strength of CFT connections was developed. The critical bond stress was derived from results of push-out test and is given as a function of tube dimensions. The effective bond transfer area was determined based on an examination of experimental observations and results from specially instrumented connection tests. The resistance factor was computed as 0.45 based on the bond stress formula.

The distribution of bond stress along the length of a column was derived analytically for the elastic case. For the nonlinear case, it was assessed using a one-dimensional linked truss model and uniaxial constitutive relations. The analyses confirm that the majority of the force transfer occurs within the region assumed in the design provisions. They also indicate that the distribution of slip is not symmetric about the connection, with equilibrium achieved in a shorter length below the connection than above

9.3.2 Stability Analysis and Design of Composite Frames

The Direct Analysis method provides a straightforward and accurate way of addressing frame in-plane stability considerations. However, no appropriate reduced elastic rigidity values have been developed nor has the methodology in general been thoroughly validated for composite members. To address these needs a large parametric study was conducted.

Sets of cross sections and frames were defined to be representative of the range of properties seen in design. Four groups of cross sections were defined 1) CCFT, 2) RCFT, 3) SRC subjected to strong axis bending, and 4) SRC subjected to weak axis bending. Within these groups of sections, properties were selected to range practical extremes of steel ratio, concrete strength, and for SRCs reinforcing ratio. The frames were either sidesway uninhibited with

variations of slenderness, end restraint, and leaning column ratio, or sidesway inhibited with variations of slenderness and end moment ratio.

Interaction diagrams were constructed through a series of nonlinear analyses for each frame and section pair. The pure axial strength and pure bending strength from the analyses were examined in detail. The current design provisions for the axial strength of SRC columns were found to be overly conservative and a new formula for the effective flexural rigidity was recommended.

Elastic rigidity was evaluated for specific frames as the *EI*, which, when used in a second-order elastic analysis, results in the same peak lateral deformation as recorded from a fully nonlinear analysis at the same applied loads. This elastic rigidity was shown to reduce with increased loading, with more severe reductions for moment dominant loading. Based on these results and other strength design considerations, new elastic flexural rigidities for elastic analysis of composite members were developed.

Design interaction curves were constructed based on the proposed Direct Analysis method. These curves were compared against those computed from the fully nonlinear analyses. Assessment of the error between the two sets of interaction diagrams indicated that the proposed design methodology is safe and accurate for the majority of practical design cases. However three cases that exceed the targeted error limit were noted: 1) members with very high effective length factors, 2) steel dominant CCFT members where the axial compressive strength is overpredicted by the design equations, and 3) steel dominant weak axis SRC members where the flexural strength is overpredicted by the design equations.

9.3.3 Seismic Performance Factors for Composite Frames

Seismic behavior of composite braced and moment frames was assessed in the context of FEMA P695 *Quantification of Building Seismic Performance Factors* (2009). A suite of 60 archetype frames was selected to be representative of the typical frames seen in practice. The frames included variations in column section type, number of stories, design gravity load, design seismic load, concrete strength, and bay width. Member sizes for the frames were selected according to current design specifications.

Nonlinear static pushover and dynamic response history analyses were performed on the frames using the mixed beam finite element formulation developed in this work. Connections were assumed to be strong; however, panel zone behavior for the moment frames and bond-slip behavior for SRC columns were included in the model.

The composite special moment frames exhibited excellent behavior. Significant ductility in the overall frame response and good distribution of deformations among stories was observed from the pushover results. Collapse was defined as when the peak story drift reached 10%. The probabilities of collapse determined from the results of the incremental dynamic analyses were found to be well within acceptable values indicating that the current response modification factor is adequate. The composite special concentrically braced frames also exhibited excellent behavior. Results of the pushover analyses typically showed significant ductility although, the overall frame response showed drops in capacity associated with buckling of individual braces and deformations were often concentrated into one story in the three story frames.

9.4 Further Research Needs

Additional research needs were identified throughout this work and are summarized here:

- There is a strong need for beam finite element formulations that comprehensively and accurately account for softening in the section response without placing restrictions on mesh density.
- The proposed formula for natural bond strength developed in Chapter 5 is based on experimental results that do not generally exhibit a bond slip failure. Experimental and analytical research to explore the behavior of CFT columns subjected large transfer forces would be helpful to understand the behavior, particularly the limit states
- An evaluation of the moment strength provisions for composite members in the AISC *Specification* (AISC 2010) is needed, particularly for steel dominant SRC sections in weak axis bending. The parametric studies presented in Chapter 6 indicated that the current provisions may overestimate the strength in some cases.
- The elastic stiffness recommendations developed in Chapter 6 were only explicitly shown to be acceptable for use in the Direct Analysis method for strength design. The accuracy of these recommendations should be assessed for determination of deformations and fundamental periods of vibration.
- The studies presented in Chapter 6 were two-dimensional dealing only explicitly with the in-plane behavior of composite frames. Further study on the three-dimensional behavior of composite frames to assess current design recommendations would be valuable.
- The contribution of creep and shrinkage to structural instability was not addressed in the s studies presented in Chapter 6. Such effects should be investigated.
- Further evaluation of the evolution of the beam-column limit surface is warranted. Of particular interest is an evaluation of the ability of simpler stress-resultant plasticity formulations to capture this behavior.
- The behavior of ordinary and intermediate composite moment and braced frames will be more dependent on the behavior of the columns than the special moment and braced frames investigated in Chapter 8. Ordinary and intermediate frames should be studied further and seismic performance factors should be developed.

REFERENCES

Abdel-Rahman, N., and Sivakumaran, K. S. (1997). "Material Properties Models for Analysis of Cold-Formed Steel Members." *Journal of Structural Engineering*, ASCE, 123(9), 1135–1143.

ACI. (2011). *Building Code Requirements for Structural Concrete and Commentary*. American Concrete Institute, Farmington Hills, MI.

Aho, M. F., and Leon, R. T. (1997). *A Database for Encased and Concrete-Filled Columns*. Report #97-01, School of Civil and Environmental Engineering, Georgia Institute of Technology, Atlanta, Georgia.

AISC. (1936). *Specification for the Design, Fabrication and Erection of Structural Steel for Buildings*. American Institute of Steel Construction, Chicago, Illinois.

AISC. (2005). *Specification for Structural Steel Buildings*. American Institute of Steel Construction, Chicago, Illinois.

AISC. (2010a). *Code of Standard Practice for Steel Buildings and Bridges*. American Institute of Steel Construction, Chicago, Illinois.

AISC. (2010b). *Specification for Structural Steel Buildings*. American Institute of Steel Construction, Chicago, Illinois.

AISC. (2010c). *Seismic Provisions for Structural Steel Buildings*. American Institute of Steel Construction, Chicago, Illinois.

AISC. (2011). *Steel Construction Manual, 14th Edition*. American Institute of Steel Construction, Chicago, Illinois.

Akiyama, M., Suzuki, M., and Frangopol, D. M. (2010). "Stress-Averaged Strain Model for Confined High-Strength Concrete." *ACI Structural Journal*, 107(2), 179–188.

Alemdar, B. N., and White, D. W. (2005). "Displacement, Flexibility, and Mixed Beam-Column Finite Element Formulations for Distributed Plasticity Analysis." *Journal of Structural Engineering*, ASCE, 131(12), 1811–1819.

Altoontash, A. (2004). "Simulation and Damage Models for Performance Assessment of Reinforced Concrete Beam-Column Joints." Ph.D. Dissertation, Stanford University, Palo Alto, California.

Aly, T., Elchalakani, M., Thayalan, P., and Patnaikuni, I. (2010). "Incremental Collapse Threshold for Pushout Resistance of Circular Concrete Filled Steel Tubular Columns." *Journal of Constructional Steel Research*, 66(1), 11–18.

Anslijn, R., and Janss, J. (1974). *Le Calcul des Charges Ultimes des Colonnes Métalliques Enrobées de Béton*. Rapport MT 89, C.R.I.F., Brussels, Belgium.

ASCE. (1997). *Effective Length and Notional Load Approaches for Assessing Frame Stability: Implications for American Steel Design*. American Society of Civil Engineers, Reston, Virginia.

ASCE. (2010). *Minimum Design Loads for Buildings and Other Structures*. American Society of Civil Engineers, Reston, Virginia.

Assi, I. M., Qudeimat, E. M., and Hunaiti, Y. M. (2003). "Ultimate Moment Capacity of Foamed and Lightweight Aggregate Concrete-Filled Steel Tubes." *Steel and Composite Structures*, 3(3), 199–212.

Ata Rafi, T. (2009). "Development of Archetype Structures for Concrete-Filled Steel Tube Braced and Unbraced Frames for Establishing Seismic System Factors." Undergraduate Thesis, Department of Civil and Environmental Engineering, University of Illinois at Urbana-Champaign, Urbana, Illinois.

ATC. (2010). *Modeling and Acceptance Criteria for Seismic Design and Analysis of Tall Buildings*. PEER/ATC 72-1, Applied Technology Council, Redwood City, California.

Attalla, M. R., Deierlein, G. G., and McGuire, W. (1994). "Spread of Plasticity: Quasi-Plastic-Hinge Approach." *Journal of Structural Engineering*, ASCE, 120(8), 2451–2473.

Aval, S. B. B., Saadeghvaziri, M. A., and Golafshani, A. A. (2002). "Comprehensive Composite Inelastic Fiber Element for Cyclic Analysis of Concrete-Filled Steel Tube Columns." *Journal of Engineering Mechanics*, 128, 428.

Bae, S., and Bayrak, O. (2008). "Plastic Hinge Length of Reinforced Concrete Columns." *ACI Structural Journal*, 105(3), 290–300.

Baker, W. F. (1987). "Design of Steel Buildings for Second Order Effects." *Materials and Member Behavior, Proceedings of the ASCE Structures Congress '87*, ASCE, Orlando, Florida, 534–554.

Bambach, M. R., Jama, H., Zhao, X. L., and Grzebieta, R. H. (2008). "Hollow and Concrete Filled Steel Hollow Sections under Transverse Impact Loads." *Engineering Structures*, 30(10), 2859–2870.

Bažant, Z. P., and Verdure, M. (2007). "Mechanics of Progressive Collapse: Learning from World Trade Center and Building Demolitions." *Journal of Engineering Mechanics*, 133(3), 308–319.

Bergmann, R. (1994). "Load introduction in composite columns filled with high strength concrete." *Tubular Structures VI, Proceedings of 6th International Symposium on Tubular Structures*, Melbourne, Australia, 373–380.

Bradford, M. A., Loh, H. Y., and Uy, B. (2002). "Slenderness Limits for Filled Circular Steel Tubes." *Journal of Constructional Steel Research*, 58(2), 243–252.

Bridge, R. Q. (1976). *Concrete Filled Steel Tubular Columns*. Research Report No. R283, School of Civil Engineering, University of Sydney, Sydney, Australia.

Bridge, R., and Webb, J. (1993). "Thin Walled Circular Concrete Filled Steel Tubular Columns." *Composite Construction in Steel and Concrete II*, American Society of Civil Engineers, Trout Lodge, Potosi, Missouri, USA, 634–649.

CEN. (2004). *Eurocode 4: Design of Composite Steel and Concrete Structures, EN1994-1-1*. European Committee for Standardization, Brussels, Belgium.

Chang, G. A., and Mander, J. B. (1994). *Seismic Energy Based Fatigue Damage Analysis of Bridge Columns: Part I - Evaluation of Seismic Capacity*. National Center for Earthquake Engineering Research, Department of Civil Engineering, State University of New York at Buffalo, Buffalo, New York.

Chen, C., Astaneh-Asl, A., and Moehle, J. P. (1992). "Behavior and Design of High Strength Composite Columns." *Structures Congress '92*, ASCE, San Antonio, Texas, 820–823.

Chen, C.-C., and Lin, N.-J. (2006). "Analytical Model for Predicting Axial Capacity and Behavior of Concrete Encased Steel Composite Stub Columns." *Journal of Constructional Steel Research*, 62(5), 424–433.

Choi, Y. H., Foutch, D. A., and LaFave, J. M. (2006). "New Approach to AISC P–M Interaction Curve for Square Concrete Filled Tube (CFT) Beam–Columns." *Engineering Structures*, 28(11), 1586–1598.

Choi, Y.-H., Kim, K. S., and Choi, S.-M. (2008). "Simplified P-M Interaction Curve for Square Steel Tube Filled with High-Strength Concrete." *Thin-Walled Structures*, 46(5), 506–515.

Coleman, J., and Spacone, E. (2001). "Localization Issues in Force-Based Frame Elements." *Journal of Structural Engineering*, ASCE, 127(11), 1257–1265.

CSA. (2009). *S16-09 - Design of Steel Structures*. Canadian Standards Association, Toronto, Ontario.

Deierlein, G. G. (2003). *Background and Illustrative Examples of Proposed Direct Analysis Method for Stability Design of Moment Frames*. Report to Task Committee 10, American Institute of Steel Construction, Chicago, Illinois.

Denavit, M. D., and Hajjar, J. F. (2010). *Nonlinear Seismic Analysis of Circular Concrete-Filled Steel Tube Members and Frames*. Newmark Structural Laboratory Report Series, Report No. NSEL-023, University of Illinois at Urbana-Champaign, Urbana, Illinois.

Denavit, M. D., and Hajjar, J. F. (2012). "Nonlinear Seismic Analysis of Circular Concrete-Filled Steel Tube Members and Frames." *Journal of Structural Engineering*, ASCE, 138(9), 1089–1098.

Denavit, M. D., Hajjar, J. F., and Leon, R. T. (2011). "Seismic Behavior of Steel Reinforced Concrete Beam-Columns and Frames." *Proceedings of the ASCE/SEI Structures Congress*, ASCE, Las Vegas, Nevada.

Dunberry, E., LeBlanc, D., and Redwood, R. G. (1987). "Cross-Section Strength of Concrete-Filled HSS Columns at Simple Beam Connections." *Canadian Journal of Civil Engineering*, 14(2), 408–417.

Elchalakani, M., Zhao, X. L., and Grzebieta, R. H. (2001). "Concrete-Filled Circular Steel Tubes Subjected to Pure Bending." *Journal of Constructional Steel Research*, 57(11), 1141–1168.

Elchalakani, M., and Zhao, X.-L. (2008). "Concrete-Filled Cold-Formed Circular Steel Tubes Subjected to Variable Amplitude Cyclic Pure Bending." *Engineering Structures*, 30(2), 287–299.

Elghazouli, A. Y., and Elnashai, A. S. (1993). "Performance of Composite Steel/Concrete Members under Earthquake Loading. Part II: Parametric Studies and Design Considerations." *Earthquake Engineering & Structural Dynamics*, 22(4), 347–368.

Elnashai, A. S., and Elghazouli, A. Y. (1993). "Performance of Composite Steel/Concrete Members under Earthquake Loading. Part I: Analytical Model." *Earthquake Engineering & Structural Dynamics*, 22(4), 315–345.

Elremaily, A., and Azizinamini, A. (2002). "Behavior and Strength of Circular Concrete-Filled Tube Columns." *Journal of Constructional Steel Research*, 58(12), 1567–1591.

El-Tawil, S., and Deierlein, G. G. (1999). "Strength and Ductility of Concrete Encased Composite Columns." *Journal of Structural Engineering*, ASCE, 125(9), 1009–1019.

El-Tawil, S., and Deierlein, G. G. (2001). "Nonlinear Analysis of Mixed Steel-Concrete Frames. I: Element Formulation." *Journal of Structural Engineering*, ASCE, 127(6), 647–655.

El-Tawil, S. M., and Deierlein, G. G. (1996). *Inelastic Dynamic Analysis of Mixed Steel-Concrete Space Frames*. School of Civil and Environmental Engineering, Cornell University, Ithaca, New York.

Elwood, K. J., and Eberhard, M. O. (2009). "Effective Stiffness of Reinforced Concrete Columns." *ACI Structural Journal*, 106(4), 476–484.

Engelhardt, M. D., and Sabol, T. A. (1994). *Testing of Welded Steel Moment Connections in Response to the Northridge Earthquake*. Progress Report to the AISC Advisory Subcommittee on Special Moment Resisting Frame Research, American Institute of Steel Construction, Chicago, Illinois.

FEMA. (2009). *Quantification of Building Seismic Performance Factors*. FEMA P695, Federal Emergency Management Agency, Washington, D.C.

La Fore, S., and Hajjar, J. F. (2005). *Design of Concrete-Filled Steel Tube Frames for Assessment under Seismic Loading*. Structural Engineering Report No. ST-05-1, Department of Civil Engineering, University of Minnesota, Minneapolis, Minnesota.

Fujikura, S., Bruneau, M., and Lopez-Garcia, D. (2008). "Experimental Investigation of Multihazard Resistant Bridge Piers Having Concrete-Filled Steel Tube under Blast Loading." *Journal of Bridge Engineering*, ASCE, 13(6), 586–594.

Fukumoto, T., and Morita, K. (2005). "Elastoplastic Behavior of Panel Zone in Steel Beam-to-Concrete Filled Steel Tube Column Moment Connections." *Journal of Structural Engineering*, ASCE, 131(12), 1841–1853.

Fukumoto, Y., and Kusama, H. (1985). "Local Instability Tests of Plate Elements under Cyclic Uniaxial Loading." *Journal of Structural Engineering*, ASCE, 111(5), 1051–1067.

Galambos, T. V. (2000). "Recent Research and Design Developments in Steel and Composite Steel–Concrete Structures in USA." *Journal of Constructional Steel Research*, 55(1–3), 289–303.

Galambos, T. V., and Ketter, R. L. (1959). "Columns under Combined Bending and Thrust." *Journal of Engineering Mechanics Division*, ASCE, 85(2), 135–152.

Gartner, S. M., and Hajjar, J. F. (2006). *Design and Evaluation of Rectangular Concrete Filled Tube (RCFT) Frames for Seismic Demand Assessment*. Structural Engineering Report No. ST-06-1, Department of Civil Engineering, University of Minnesota, Minneapolis, Minnesota.

Gho, W.-M., and Liu, D. (2004). "Flexural Behaviour of High-Strength Rectangular Concrete-Filled Steel Hollow Sections." *Journal of Constructional Steel Research*, 60(11), 1681–1696.

Giakoumelis, G., and Lam, D. (2004). "Axial Capacity of Circular Concrete-Filled Tube Columns." *Journal of Constructional Steel Research*, 60(7), 1049–1068.

Gioncu, V., and Mazzolani, F. (2001). *Ductility of Seismic-Resistant Steel Structures*. CRC Press.

Goode, C. D. (2008). "Composite Columns - 1819 Tests on Concrete-Filled Steel Tube Columns Compared with Eurocode 4." *The Structural Engineer*, 86(16), 33–38.

Gourley, B. C., and Hajjar, J. F. (1994). *Representation of Cross-Section Strength For Low and High Strength Rectangular Concrete-Filled Steel Tubes*. Structural Engineering Report No. ST-94-1, Department of Civil Engineering, University of Minnesota, Minneapolis, Minnesota.

Gourley, B. C., Tort, C., Denavit, M. D., Schiller, P. H., and Hajjar, J. F. (2008). *A Synopsis of Studies of the Monotonic and Cyclic Behavior of Concrete-Filled Steel Tube Members, Connections, and Frames*. Newmark Structural Laboratory Report NSEL-008, Department of Civil and Environmental Engineering, University of Illinois at Urbana-Champaign, Urbana, Illinois.

Grauers, M. (1993). "Composite Columns of Hollow Steel Sections Filled with High Strength Concrete." Ph.D. Dissertation, Chalmers University, Göteborg, Sweden.

Green, P. S. (2000). "The Inelastic Behavior of Flexural Members Fabricated from High Performance Steel." Ph.D. Dissertation, Lehigh University, Bethlehem, Pennsylvania.

Green, P. S., Sause, R., and Ricles, J. M. (2002). "Strength and Ductility of HPS Flexural Members." *Journal of Constructional Steel Research*, 58(5-8), 907–941.

Griffis, L. G. (1992). *Load and Resistance Factor Design of W-Shapes Encased in Concrete*. Design Guide 6, American Institute of Steel Construction, Chicago, Illinois.

Griffis, L. G. (2005). "Composite Design Provisions 2005 AISC Specification for Steel Buildings." *Proceedings of the 2005 Structures Congress*, ASCE, New York, New York.

Hajjar, J. F. (2003). "Evolution of Stress-Resultant Loading and Ultimate Strength Surfaces in Cyclic Plasticity of Steel Wide-Flange Cross-Sections." *Journal of Constructional Steel Research*, 59, 713–750.

Hajjar, J. F., and Gourley, B. C. (1996). "Representation of Concrete-Filled Steel Tube Cross-Section Strength." *Journal of Structural Engineering*, ASCE, 122(11), 1327–1336.

Hajjar, J. F., and Gourley, B. C. (1997). "A Cyclic Nonlinear Model for Concrete-Filled Tubes. I: Formulation." *Journal of Structural Engineering*, ASCE, 123(6), 736–744.

Hajjar, J. F., Molodan, A., and Schiller, P. H. (1998). "A Distributed Plasticity Model for Cyclic Analysis of Concrete-Filled Steel Tube Beam-Columns and Composite Frames." *Engineering Structures*, 20(4-6), 398–412.

Hajjar, J. F., Schiller, P. H., and Molodan, A. (1998). "A Distributed Plasticity Model for Concrete-Filled Steel Tube Beam-Columns with Interlayer Slip." *Engineering Structures*, 20(8), 663–676.

Han, D. J., and Kim, K. S. (1995). "A Study on the Strength and Hysteretic Characteristics of Steel Reinforced Concrete Columns." *Journal of the Architectural Institute of Korea*, 11(4), 183–190.

Han, D. J., Kim, P. J., and Kim, K. S. (1992). "The Influence of Hoop Bar on the Compressive Strength of Short Steel Reinforced Concrete Columns." *Journal of the Architectural Institute of Korea*, 12(1), 335–338.

Han, L. H., and Yang, Y. F. (2005). "Cyclic Performance of Concrete-Filled Steel CHS Columns under Flexural Loading." *Journal of Constructional Steel Research*, 61(4), 423–452.

Han, L. H., and Yao, G. H. (2004). "Experimental Behaviour of Thin-Walled Hollow Structural Steel (HSS) Columns Filled with Self-Consolidating Concrete (SCC)." *Thin-Walled Structures*, 42(9), 1357–1377.

Han, L.-H., Ren, Q.-X., and Li, W. (2010). "Tests on Inclined, Tapered and STS Concrete-Filled Steel Tubular (CFST) Stub Columns." *Journal of Constructional Steel Research*, 66(10), 1186–1195.

Han, L.-H., Yao, G.-H., and Zhao, X.-L. (2005). "Tests and Calculations for Hollow Structural Steel (HSS) Stub Columns Filled with Self-Consolidating Concrete (SCC)." *Journal of Constructional Steel Research*, 61(9), 1241–1269.

Hatzigeorgiou, G. D. (2008). "Numerical Model for the Behavior and Capacity of Circular CFT Columns, Part I: Theory." *Engineering Structures*, 30(6), 1573–1578.

Herrera, R. A., Ricles, J. M., and Sause, R. (2008). "Seismic Performance Evaluation of a Large-Scale Composite MRF Using Pseudodynamic Testing." *Journal of Structural Engineering*, ASCE, 134(2), 279–288.

Hjelmstad, K. D., and Taciroglu, E. (2003). "Mixed Variational Methods for Finite Element Analysis of Geometrically Non-Linear, Inelastic Bernoulli-Euler Beams." *Communications in Numerical Methods in Engineering*, 19(10), 809–832.

Hoshikuma, J., Kawashima, K., Nagaya, K., and Taylor, A. W. (1997). "Stress-Strain Model for Confined Reinforced Concrete in Bridge Piers." *Journal of Structural Engineering*, ASCE, 123(5), 624.

Hsiao, P.-C., Lehman, D. E., and Roeder, C. W. (2012). "Improved Analytical Model for Special Concentrically Braced Frames." *Journal of Constructional Steel Research*, 73, 80–94.

Hu, H. T., Huang, C., Wu, M., and Wu, Y. (2003). "Nonlinear Analysis of Axially Loaded Concrete-Filled Tube Columns with Confinement Effect." *Journal of Structural Engineering*, ASCE, 129(10), 1322–1329.

ICC. (2012). *2012 International Building Code*. International Code Council, Inc., Washington, D.C.

Ichinohe, Y., Matsutani, T., Nakajima, M., Ueda, H., and Takada, K. (1991). "Elasto-Plastic Behavior of Concrete Filled Steel Circular Columns." *Proceedings of the Third International Conference on Steel-Concrete Composite Structures*, Fukuoka, Japan.

Inai, E., Mukai, A., Kai, M., Tokinoya, H., Fukumoto, T., and Mori, K. (2004). "Behavior of Concrete-Filled Steel Tube Beam Columns." *Journal of Structural Engineering*, ASCE, 130(2), 189–202.

Johansson, M. (2003). "Composite Action in Connection Regions of Concrete-Filled Steel Tube Columns." *Steel & Composite Structures*, 3(1), 47–64.

Johansson, M., and Gylltoft, K. (2002). "Mechanical Behavior of Circular Steel–Concrete Composite Stub Columns." *Journal of Structural Engineering*, ASCE, 128(8), 1073–1081.

Juang, J.-L., and Hsu, H.-L. (2008). "Seismic Performance Assessment of Steel Reinforced Concrete Members Accounting for Double Pivot Stiffness Degradation." *Steel and Composite Structures*, 8(6), 441–455.

Kanatani, H., Tabuchi, M., Kamba, T., Hsiaolien, J., and Ishikawa, M. (1987). "A Study on Concrete Filled RHS Column to H-Beam Connections Fabricated with HT Bolts in Rigid Frames." *Composite Construction in Steel and Concrete*, ASCE, Henniker, New Hampshire, USA, 614–635.

Kanchanalai, T. (1977). *The Design and Behavior of Beam-Columns in Unbraced Steel Frames*. CESRL Report No. 77-2, Structures Research Laboratory, Department of Civil Engineering, The University of Texas at Austin, Austin, Texas.

Kawaguchi, J., Morino, S., Shirai, J., and Tatsuta, E. (1998). "Database and Structural Characteristics of CFT Beam-Columns." *Proceedings of Fifth Pacific Structural Steel Conference*, Seoul, Korea.

Kawaguchi, J., Morino, S., Sugimoto, T., and Shirai, J. (2002). "Experimental Study on Structural Characteristics of Portal Frames Consisting of Square CFT Columns." *Proceedings of the Composite Construction in Steel and Concrete IV Conference*, ASCE, Banff, Alberta, Canada, 725–733.

Kemp, A. R., and Dekker, N. W. (1991). "Available Rotation Capacity in Steel and Composite Beams." *The Structural Engineer*, 69(5), 88–97.

Kent, D. C., and Park, R. (1971). "Flexural Members with Confined Concrete." *Journal of the Structural Division*, 97(7), 1969—1990.

Khandelwal, K., El-Tawil, S., and Sadek, F. (2009). "Progressive Collapse Analysis of Seismically Designed Steel Braced Frames." *Journal of Constructional Steel Research*, 65(3), 699–708.

Khuntia, M., and Ghosh, S. K. (2004a). "Flexural Stiffness of Reinforced Concrete Columns and Beams: Analytical Approach." *ACI Structural Journal*, 101(3), 351–363.

Khuntia, M., and Ghosh, S. K. (2004b). "Flexural Stiffness of Reinforced Concrete Columns and Beams: Experimental Verification." *ACI Structural Journal*, 101(3), 364–374.

Kilpatrick, A. E., and Rangan, B. V. (1999). "Tests on High-Strength Concrete-Filled Steel Tubular Columns." *ACI Structural Journal*, 96(2), 268–274.

Kim, D. K. (2005). "A Database for Composite Columns." M.S. Thesis, School of Civil and Environmental Engineering, Georgia Institute of Technology, Atlanta, Georgia.

Kim, K. D., and Engelhardt, M. D. (2002). "Monotonic and Cyclic Loading Models for Panel Zones in Steel Moment Frames." *Journal of Constructional Steel Research*, 58(5–8), 605–635.

Kostic, S. M., and Filippou, F. C. (2012). "Section Discretization of Fiber Beam-Column Elements for Cyclic Inelastic Response." *Journal of Structural Engineering*, ASCE, 138(5), 592–601.

Krawinkler, H., Medina, R., and Alavi, B. (2003). "Seismic Drift and Ductility Demands and their Dependence on Ground Motions." *Engineering Structures*, 25(5), 637–653.

Krishnan, S., and Muto, M. (2012). "Mechanism of Collapse of Tall Steel Moment Frame Buildings under Earthquake Excitation." *Journal of Structural Engineering*, ASCE, 138(11), 1361–1387.

Kunnath, S. K., Heo, Y., and Mohle, J. F. (2009). "Nonlinear Uniaxial Material Model for Reinforcing Steel Bars." *Journal of Structural Engineering*, 135(4), 335–343.

Lay, M. G. (1965). "Flange Local Buckling in Wide-Flange Shapes." *Journal of the Structural Division*, ASCE, 91(6), 95–115.

LeMessurier, W. M. (1977). "A Practical Method of Second Order Analysis: Part 2—Rigid Frames." *Engineering Journal*, AISC, 14(2), 49–67.

Leon, R. T., and Hajjar, J. F. (2008). "Limit State Response of Composite Columns and Beam-Columns Part II: Application of Design Provisions for the 2005 AISC Specification." *Engineering Journal*, AISC, 45(1), 21–46.

Leon, R. T., Kim, D. K., and Hajjar, J. F. (2007). "Limit State Response of Composite Columns and Beam-Columns Part 1: Formulation of Design Provisions for the 2005 AISC Specification." *Engineering Journal*, AISC, 44(4), 341–358.

Liu, J., Zhou, X., and Zhang, S. (2008). "Seismic Behaviour of Square CFT Beam-Columns under Biaxial Bending Moment." *Journal of Constructional Steel Research*, 64(12), 1473–1482.

Lu, Y. Q., and Kennedy, D. J. L. (1994). "The Flexural Behaviour of Concrete-Filled Hollow Structural Sections." *Canadian Journal of Civil Engineering*, 21(1), 111–130.

Lukey, A. F., and Adams, P. F. (1969). "Rotation Capacity of Beams under Moment Gradient." *Journal of the Structural Division*, ASCE, 95(6), 1173–1188.

Lundberg, J. E., and Galambos, T. V. (1996). "Load and Resistance Factor Design of Composite Columns." *Structural Safety*, 18(2-3), 169–177.

MacGregor, J. G., and Hage, S. E. (1977). "Stability Analysis and Design of Concrete Frames." *Journal of the Structural Division, ASCE*, 103(10), 1953–1970.

Malley, J. O. (2010). "The AISC Seismic Provisions: Past, Present and Future." *Proceedings of the 2010 NASCC: The Steel Conference*, Orlando, Florida.

Mamaghani, I. H. P., Usami, T., and Mizuno, E. (1996). *Cyclic Elastoplastic Behavior of Steel Structures: Theory and Experiment*. Department of Civil Engineering, Nagoya University, Chikusa-ku, Nagoya, Japan.

Mander, J. B., Priestley, M. J. N., and Park, R. (1988). "Theoretical Stress-Strain Model for Confined Concrete." *Journal of Structural Engineering*, ASCE, 114(8), 1804—1826.

Marson, J., and Bruneau, M. (2004). "Cyclic Testing of Concrete-Filled Circular Steel Bridge Piers having Encased Fixed-Based Detail." *Journal of Bridge Engineering*, ASCE, 9(1), 14–23.

Martinez-Garcia, J. M. (2002). "Benchmark Studies to Evaluate New Provisions for Frame Stability Using Second-Order Analysis." M.S. Thesis, Department of Civil and Environmental Engineering, Bucknell University, Lewisburg, Pennsylvania.

Matsui, C., and Tsuda, K. (1996). "Strength And Behavior Of Slender Concrete Filled Steel Tubular Columns." *Proceedings of The Second International Symposium on Civil Infrastructure Systems*, P. T. Y. Chang, L. W. Lu, and L. Wei, eds., Hong Kong, China.

McAllister, T., MacNeill, R., Erbay, O., Sarawit, A., Zarghamee, M., Kirkpatrick, S., and Gross, J. (2012). "Analysis of Structural Response of WTC 7 to Fire and Sequential Failures Leading to Collapse." *Journal of Structural Engineering*, ASCE, 138(1), 109–117.

McKenna, F., Fenves, G. L., and Scott, M. H. (2000). *Open System for Earthquake Engineering Simulation*. Department of Civil and Environmental Engineering, University of California, Berkeley, Berkeley, California.

Mirza, S. A. (1989). "Parametric Study of Composite Column Strength Variability." *Journal of Constructional Steel Research*, 14(2), 121–137.

Mirza, S. A. (1990). "Flexural Stiffness of Rectangular Reinforced Concrete Columns." *ACI Structural Journal*, 87(4), 425–435.

Mirza, S. A., Hyttinen, V., and Hyttinen, E. (1996). "Physical Tests and Analyses of Composite Steel-Concrete Beam-Columns." *Journal of Structural Engineering*, ASCE, 122(11), 1317–1326.

Mirza, S. A., and Skrabek, B. W. (1992). "Statistical Analysis of Slender Composite Beam-Column Strength." *Journal of Structural Engineering*, 118(5), 1312–1332.

Morino, S., Matsui, C., and Watanabe, H. (1984). "Strength of Biaxially Loaded SRC Columns." Seattle, Washington.

Morishita, Y., Tomii, M., and Yoshimura, K. (1979a). "Experimental Studies on Bond Strength in Concrete Filled Circular Steel Tubular Columns Subjected to Axial Loads." *Transactions of Japan Concrete Institute*, 1, 351–358.

Morishita, Y., Tomii, M., and Yoshimura, K. (1979b). "Experimental Studies on Bond Strength in Concrete Filled Square and Octagonal Steel Tubular Columns Subjected to Axial Loads." *Transactions of Japan Concrete Institute*, 1, 359–366.

Mróz, Z. (1967). "On the Description of Anisotropic Workhardening." *Journal of the Mechanics and Physics of Solids*, 15(3), 163–175.

Muhummud, T. (2003). "Seismic Behavior and Design of Composite SMRFs with Concrete Filled Steel Tubular Columns and Steel Wide Flange Beams." Ph.D. Dissertation, Lehigh University, Bethlehem, Pennsylvania.

Nakahara, H., and Sakino, K. (1998). "Axial Compressive and Uniform Bending Tests of High Strength Concrete Filled Square Steel Tubular Columns." *Proceedings of 5th Pacific Structural Steel Conference*, Seoul, Korea, 943–948.

Nakahara, H., and Sakino, K. (2000). "Flexural Behavior of Concrete Filled Square Steel Tubular Beam-Columns." *12th World Conference on Earthquake Engineering*, Auckland, New Zealand.

Nishiyama, I., Morino, S., Sakino, K., Nakahara, H., Fujimoto, T., Mukai, A., Inai, E., Kai, M., Tokinoya, H., Fukumoto, T., Mori, K., Yoshioka, K., Mori, O., Yonezawa, K., Uchikoshi, M., and Hayashi, Y. (2002). *Summary of Research on Concrete-Filled Structural Steel Tube Columns System Carried Out Under The US-Japan Cooperative Research Program on Composite and Hybrid Structures*. BRI Research Paper, Building Research Institute, Japan.

NIST. (2010). *Evaluation of the FEMA P-695 Methodology for Quantification of Building Seismic Performance Factors*. National Institute of Standards and Technology, Gaithersburg, Maryland.

Nukala, P. K. V. V., and White, D. W. (2004). "A Mixed Finite Element for Three-Dimensional Nonlinear Analysis of Steel Frames." *Computer Methods in Applied Mechanics and Engineering*, 193(23-26), 2507–2545.

O'Shea, M. D., and Bridge, R. (1997a). *Tests on Circular Thin-Walled Steel Tubes Filled with Very High Strength Concrete*. Research Report No. R754, Department of Civil Engineering, The University of Sydney, Sydney, Australia.

O'Shea, M. D., and Bridge, R. (1997b). *Tests on Circular Thin-Walled Steel Tubes Filled with Medium and High Strength Concrete*. Research Report No. R755, Department of Civil Engineering, The University of Sydney, Sydney, Australia.

Ou, Z., Chen, B., Hsieh, K., Halling, M., and Barr, P. (2011). "Experimental and Analytical Investigation of Concrete Filled Steel Tubular Columns." *Journal of Structural Engineering*, ASCE, 137(6), 635–645.

Parsley, M. A., Yura, J. A., and Jirsa, J. O. (2000). "Push-Out Behavior of Rectangular Concrete-Filled Steel Tubes." *ACI SP-196 Composite and Hybrid Systems*, R. S. Aboutaha and J. M. Bracci, eds.

PEER. (2006). *PEER NGA Database*. Pacific Earthquake Engineering Research Center, University of California, Berkeley, California.

Perea, T. (2010). "Analytical and Experimental Study on Slender Concrete-Filled Steel Tube Columns and Beam-Columns." Ph.D. Dissertation, School of Civil and Environmental Engineering, Georgia Institute of Technology, Atlanta, Georgia.

Perea, T., Leon, R. T., Hajjar, J. F., and Denavit, M. D. (2012). "Full-Scale Tests of Slender Concrete-Filled Tubes: Axial Behavior." *Journal of Structural Engineering*, ASCE, (submitted for publication).

Popov, E. P., and Black, R. G. (1981). “Steel Struts under Severe Cyclic Loadings.” *Journal of the Structural Division*, ASCE, 107(9), 1857–1881.

Popovics, S. (1973). “A Numerical Approach to the Complete Stress-Strain Curve of Concrete.” *Cement and Concrete Research*, 3(5), 583–599.

Ravindra, M. K., and Galambos, T. V. (1978). “Load and Resistance Factor Design for Steel.” *Journal of the Structural Division*, ASCE, 104(9), 1337–1353.

Richart, F. E., Brandtzæg, A., and Brown, R. L. (1929). *The Failure of Plain and Spirally Reinforced Concrete in Compression*. University of Illinois Bulletin No. 190, University of Illinois at Urbana-Champaign, Urbana, Illinois.

Ricles, J. M., and Paboojian, S. D. (1994). “Seismic Performance of Steel-Encased Composite Columns.” *Journal of Structural Engineering*, ASCE, 120(8), 2474–2494.

Ricles, J. M., Peng, S. W., and Lu, L. W. (2004). “Seismic Behavior of Composite Concrete Filled Steel Tube Column-Wide Flange Beam Moment Connections.” *Journal of Structural Engineering*, 130, 223.

Ricles, J., and Paboojian, S. D. (1993). *Seismic Performance of Composite Beam-Columns*. ATLSS Report No. 93-01, ATLSS Engineering Research Center, Lehigh University, Bethlehem, Pennsylvania.

Roderick, J. W., and Loke, Y. O. (1975). “Pin-Ended Composite Columns Bent About the Minor Axis.” *Civil Engineering Transactions*, 17(2), 51–58.

Roeder, C. W., Cameron, B., and Brown, C. B. (1999). “Composite Action in Concrete Filled Tubes.” *Journal of Structural Engineering*, 125(5), 477–484.

Roeder, C. W., Lehman, D. E., and Bishop, E. (2010). “Strength and Stiffness of Circular Concrete-Filled Tubes.” *Journal of Structural Engineering*, ASCE, 136(12), 1545–1553.

Roeder, C. W., Lehman, D. E., and Thody, R. (2009). “Composite Action in CFT Components and Connections.” *Engineering Journal*, AISC, 46(4), 229–242.

Sakino, K., Nakahara, H., Morino, S., and Nishiyama, I. (2004). “Behavior of Centrally Loaded Concrete-Filled Steel-Tube Short Columns.” *Journal of Structural Engineering*, ASCE, 130(2), 180–188.

Sanz Picon, C. F. (1992). “Behavior of Composite Column Cross Sections under Biaxial Bending.” M.S. Thesis, Cornell University, Ithaca, New York.

Sawyer, H. A. (1961). “Post-Elastic Behavior of Wide-Flange Steel Beams.” *Journal of the Structural Division*, ASCE, 87(ST8), 43–71.

Schiller, P. H., Hajjar, J. F., and Gourley, B. C. (1994). *Expressions for the Elastic Rigidity of Rectangular Concrete-Filled Steel Tube Beam-Columns*. Structural Engineering Report No. ST-94-2, Department of Civil Engineering, University of Minnesota, Minneapolis, Minnesota.

Schneider, S. P. (1998). “Axially Loaded Concrete-Filled Steel Tubes.” *Journal of Structural Engineering*, ASCE, 124(10), 1125–1138.

Scott, M. H., and Fenves, G. L. (2006). “Plastic Hinge Integration Methods for Force-Based Beam--Column Elements.” *Journal of Structural Engineering*, ASCE, 132(2), 244–252.

Scott, M. H., Fenves, G. L., McKenna, F., and Filippou, F. C. (2008). "Software Patterns for Nonlinear Beam-Column Models." *Journal of Structural Engineering*, ASCE, 134(4), 562–571.

Scott, M. H., and Hamutcuoglu, O. M. (2008). "Numerically Consistent Regularization of Force-Based Frame Elements." *International Journal for Numerical Methods in Engineering*, 76(10), 1612–1631.

Sezen, H., and Moehle, J. P. (2003). "Bond-Slip Behavior of Reinforced Concrete Members." *Proceedings of FIB Symposium on Concrete Structures in Seismic Regions*, Athens, Greece.

Shaback, J. B. (2001). "Behaviour of square HSS braces with end connections under reversed cyclic axial loading." M.S. Thesis, University of Calgary, Calgary, Alberta.

Shakir-Khalil, H. (1993a). "Pushout Strength of Concrete-Filled Steel Hollow Sections." *The Structural Engineer*, 71(13), 230–233.

Shakir-Khalil, H. (1993b). "Resistance of Concrete-Filled Steel Tubes to Pushout Forces." *The Structural Engineer*, 71(13), 234–243.

Shakir-Khalil, H. (1993c). "Full-Scale Tests on Composite Connections." *Composite Construction in Steel and Concrete II*, American Society of Civil Engineers, Trout Lodge, Potosi, Missouri, USA, 634–649.

Shakir-Khalil, H. (1993d). "Connection of Steel Beams to Concrete-Filled Tubes." *International Symposium on Tubular Structures*, Nottingham, England, UK, 195–203.

Shakir-Khalil, H. (1994a). "Finplate Connections to Concrete-Filled Tubes." *4th International Conference on Steel-Concrete Composite Structures*, Istanbul, Turkey, 181–185.

Shakir-Khalil, H. (1994b). "Beam Connections to Concrete-Filled Tubes." *6th International Symposium on Tubular Structures*, Melbourne, Australia, 357–364.

Shakir-Khalil, H., and Al-Rawdan, A. (1995). "Behavior of Concrete-Filled Tubular Edge Columns." *3rd International Conference on Steel and Aluminum Structures*, Istanbul, Turkey, 515–522.

Shakir-Khalil, H., and Zeghiche, J. (1989). "Experimental Behaviour of Concrete-Filled Rolled Rectangular Hollow-Section Columns." *The Structural Engineer*, 67, 346–53.

Shams, M., and Saadeghvaziri, M. A. (1999). "Nonlinear Response of Concrete-Filled Steel Tubular Columns under Axial Loading." *ACI Structural Journal*, 96(6).

Sheikh, S. A., and Uzumeri, S. M. (1980). "Strength and Ductility of Tied Concrete Columns." *Journal of the Structural Division*, ASCE, 106(5), 1079–1102.

Shen, C., Mamaghani, I. H. P., Mizuno, E., and Usami, T. (1995). "Cyclic Behavior of Structural Steels. II: Theory." *Journal of Engineering Mechanics*, ASCE, 121(11), 1165–1172.

Smith, R. J., and Adams, P. F. (1968). *Experiments on Wide-Flange Beams under Moment Gradient*. Structural Engineering Report No. 13, Department of Civil Engineering, University of Alberta, Edmonton, Alberta.

De Souza, R. M. (2000). "Force-Based Finite Element for Large Displacement Inelastic Analysis of Frames." Ph.D. Dissertation, University of California, Berkeley, Berkeley, California.

SSRC, Task Group 20. (1979). "A Specification for the Design of Steel-Concrete Composite Columns." *Engineering Journal*, AISC, 16(4), 101–115.

Standards Australia. (1998). *AS 4100-1998 Steel Structures*. Standards Australia, Sydney, Australia.

Surovek-Maleck, A. E., and White, D. W. (2004a). "Alternative Approaches for Elastic Analysis and Design of Steel Frames. I: Overview." *Journal of Structural Engineering*, ASCE, 130(8), 1186–1196.

Surovek-Maleck, A. E., and White, D. W. (2004b). "Alternative Approaches for Elastic Analysis and Design of Steel Frames. II: Verification Studies." *Journal of Structural Engineering*, ASCE, 130(8), 1197–1205.

Susantha, K. A. S., Ge, H., and Usami, T. (2001). "Uniaxial Stress–Strain Relationship of Concrete Confined by Various Shaped Steel Tubes." *Engineering Structures*, 23(10), 1331–1347.

Szyniszewski, S., and Krauthammer, T. (2012). "Energy Flow in Progressive Collapse of Steel Framed Buildings." *Engineering Structures*, 42, 142–153.

Tikka, T. K., and Mirza, S. A. (2006a). "Nonlinear Equation for Flexural Stiffness of Slender Composite Columns in Major Axis Bending." *Journal of Structural Engineering*, ASCE, 132, 387–399.

Tikka, T. K., and Mirza, S. A. (2006b). "Nonlinear EI Equation for Slender Composite Columns Bending about the Minor Axis." *Journal of Structural Engineering*, 132, 1590.

Tomii, M. (1985). "Bond Check for Concrete-Filled Steel Tubular Columns." *Composite and Mixed Construction*, American Society of Civil Engineers, 195–204.

Tomii, M., and Sakino, K. (1979a). "Experimental Studies on the Ultimate Moment of Concrete Filled Square Steel Tubular Beam-Columns." *Transactions of the Architectural Institute of Japan*, 275, 55–65.

Tomii, M., and Sakino, K. (1979b). "Experimental Studies on Concrete Filled Square Steel Tubular Beam-Columns Subjected to Monotonic Shearing Force and Constant Axial Force." *Transactions of the Architectural Institute of Japan*, 281, 81–90.

Tomii, M., Yoshimura, K., and Morishita, Y. (1980a). "A Method of Improving Bond Strength between Steel Tube and Concrete Core Cast in Square and Octagonal Steel Tubular Columns." *Transactions of the Japan Concrete Institute*, 2, 327–334.

Tomii, M., Yoshimura, K., and Morishita, Y. (1980b). "A Method of Improving Bond Strength between Steel Tube and Concrete Core Cast in Circular Steel Tubular Columns." *Transactions of the Japan Concrete Institute*, 2, 319–326.

Tort, C., and Hajjar, J. F. (2007). *Reliability-Based Performance-Based Design of Rectangular Concrete-Filled Steel Tube (RCFT) Members and Frames*. Structural Engineering Report No. ST-07-1, Department of Civil Engineering, University of Minnesota, Minneapolis, Minnesota.

Tort, C., and Hajjar, J. F. (2010a). "Mixed Finite-Element Modeling of Rectangular Concrete-Filled Steel Tube Members and Frames under Static and Dynamic Loads." *Journal of Structural Engineering*, ASCE, 136(6), 654–664.

Tort, C., and Hajjar, J. F. (2010b). "Mixed Finite Element for Three-Dimensional Nonlinear Dynamic Analysis of Rectangular Concrete-Filled Steel Tube Beam-Columns." *Journal of Engineering Mechanics*, ASCE, 136(11), 1329–1339.

Tsai, K.-C., Hsiao, P.-C., Wang, K.-J., Weng, Y.-T., Lin, M.-L., Lin, K.-C., Chen, C.-H., Lai, J.-W., and Lin, S.-L. (2008). "Pseudo-Dynamic Tests of a Full-Scale CFT/BRB Frame - Part I: Specimen Design, Experiment and Analysis." *Earthquake Engineering & Structural Dynamics*, 37(7), 1081–1098.

Tsai, K.-C., and Popov, E. P. (1988). *Steel Beam-Column Joints in Seismic Moment Resisting Frames*. Report No. UCB/EERC-88/19, Earthquake Engineering Research Center, University of California, Berkeley, California.

Tsai, W. T. (1988). "Uniaxial Compressional Stress-Strain Relation of Concrete." *Journal of Structural Engineering*, ASCE, 114(9), 2133–2136.

Uriz, P., Filippou, F. C., and Mahin, S. A. (2008). "Model for Cyclic Inelastic Buckling of Steel Braces." *Journal of Structural Engineering*, ASCE, 134(4), 619–628.

Vamvatsikos, D., and Cornell, C. A. (2002). "Incremental Dynamic Analysis." *Earthquake Engineering & Structural Dynamics*, 31(3), 491–514.

Varma, A. H. (2000). "Seismic Behavior, Analysis, and Design of High Strength Square Concrete Filled Steel Tube (CFT) Columns." Ph.D. Dissertation, Lehigh University, Bethlehem, Pennsylvania.

Varma, A. H., Ricles, J. M., Sause, R., and Lu, L. W. (2002). "Seismic Behavior and Modeling of High-Strength Composite Concrete-Filled Steel Tube (CFT) Beam–Columns." *Journal of Constructional Steel Research*, 58(5-8), 725–758.

Virdi, K. S., and Dowling, P. J. (1973). "The Ultimate Strength of Composite Columns in Biaxial Bending." *Proceedings of the Institution of Civil Engineers*, 55(1), 251–272.

Virdi, K. S., and Dowling, P. J. (1980). "Bond Strength in Concrete Filled Steel Tubes." *IABSE Periodical*, 125–139.

Wang, Y. C. (1999). "Tests on Slender Composite Columns." *Journal of Constructional Steel Research*, 49(1), 25–41.

Wheeler, A., and Bridge, R. (2004). "The Behaviour of Circular Concrete-Filled Thin-Walled Steel Tubes in Flexure." *Proceedings of the 5th International Conference on Composite Construction in Steel and Concrete V*, R. T. Leon and J. Lange, eds., Berg-en-Dal, Mpumalanga, South Africa.

White, D. W., Surovek, A. E., Alemdar, B. N., Chang, C. J., Kim, Y. D., and Kuchenbecker, G. H. (2006). "Stability Analysis and Design of Steel Building Frames Using the 2005 AISC Specification." *Steel Structures*, 6, 71–91.

Xu, C., Chengkui, H., Decheng, J., and Yuancheng, S. (2009). "Push-Out Test of Pre-Stressing Concrete Filled Circular Steel Tube Columns by Means of Expansive Cement." *Construction and Building Materials*, 23(1), 491–497.

Yamamoto, T., Kawaguchi, J., and Morino, S. (2000). "Experimental Studies of Scale Effects on the Compressive Behavior of Short Concrete-Filled Steel Tube Columns." *Composite Construction in Steel and Concrete IV, Proceedings of the United Engineering Foundation Conference on Composite Construction in Steel and Concrete IV*, Banff, Alberta, Canada, 879–890.

Yang, Y. F., and Han, L. H. (2006). "Experimental Behaviour of Recycled Aggregate Concrete Filled Steel Tubular Columns." *Journal of Constructional Steel Research*, 62(12), 1310–1324.

Yang, Y. F., and Han, L. H. (2012). "Concrete Filled Steel Tube (CFST) Columns Subjected to Concentrically Partial Compression." *Thin-Walled Structures*, 50(1), 147–156.

Yin, X., and Lu, X. (2010). "Study on Push-Out Test and Bond Stress-Slip Relationship of Circular Concrete Filled Steel Tube." *Steel and Composite Structures*, 10(4), 317–329.

Yoshioka, K., Inai, E., Hukumoto, N., Kai, M., Murata, Y., Noguchi, T., Tanaka, Y., Tokinoya, H., and Mukai, A. (1995). "Compressive Tests on CFT Short Columns Part 1: Circular CFT Columns." *Proceedings of the Second Joint Technical Coordinating Committee (JTCC) on Composite and Hybird Structures*, Hawaii.

Yura, J. A. (1971). "The Effective Length of Columns in Unbraced Frames." *Engineering Journal*, AISC, 37–42.

Zhang, G. W., Xiao, Y., and Kunnath, S. (2009). "Low-Cycle Fatigue Damage of Circular Concrete-Filled-Tube Columns." *ACI Structural Journal*, 106(2), 151–159.

Zhao, J., and Sritharan, S. (2007). "Modeling of Strain Penetration Effects in Fiber-Based Analysis of Reinforced Concrete Structures." *ACI Structural Journal*, 104(2), 133–141.

Ziemian, R. D., and McGuire, W. (1992). "A Method for Incorporating Live Load Reduction Provisions in Frame Analysis." *Engineering Journal*, AISC, (First Quarter), 1–3.

DETAILED BENCHMARK STUDY RESULTS

This appendix presents detailed results from the parametric study described in Chapter 6.

A.1 Evaluation of the Proposed Design Methodology

For each cross section analyzed in the study, a set of six plots are shown. The plots are selected to illustrate the overall performance of the proposed beam-column design methodology, best and worst cases, as well as typical elastic stiffness results. The arrangement of the plots is the same for each figure and follows the layout described in Table A.1. The top left and bottom left plots in each figure correspond to one frame, UA-67-g1. These plots are intended to show the variation between the different sections, the frame was selected since because of its average properties (e.g., intermediate slenderness).

Table A.1. Layout of Section Results Figures

$EI_{elastic}$ results for frame UA-67-g1	Three dimensional (M-P-λ_{oe}) plot showing first-order applied load interaction diagrams from sidesway uninhibited frames with $\lambda_{oe} \leq 3$
Normalized interaction diagrams for the frame with the smallest mean absolute error and no unconservative error greater than 5% (the "best" frame)	Normalized interaction diagrams for the frame with the greatest unconservative error (the "worst" frame)
Normalized interaction diagrams for frame UA-67-g1	Error diagram showing all frames

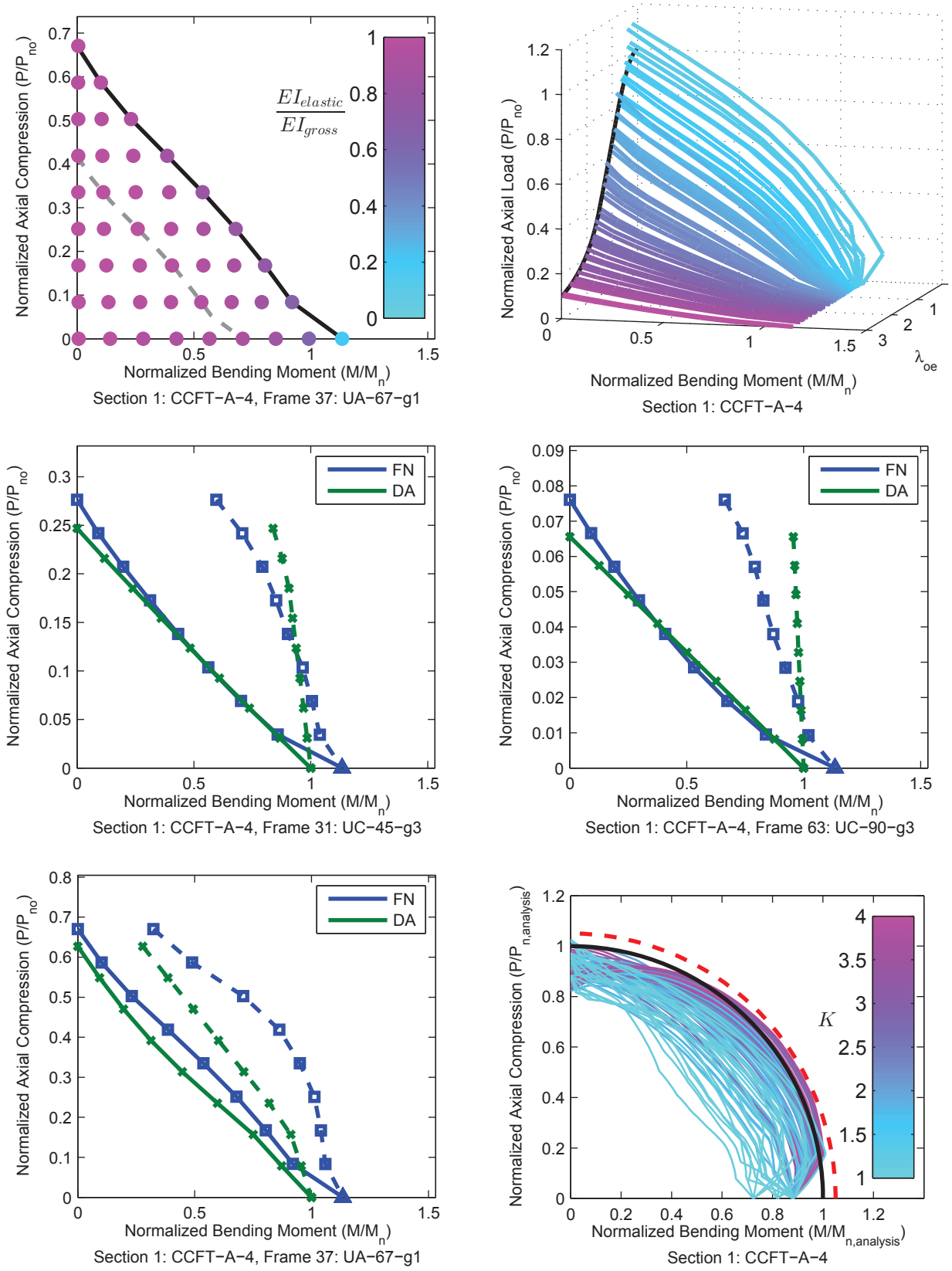

Figure A.1. Detailed Results for Section CCFT-A-4

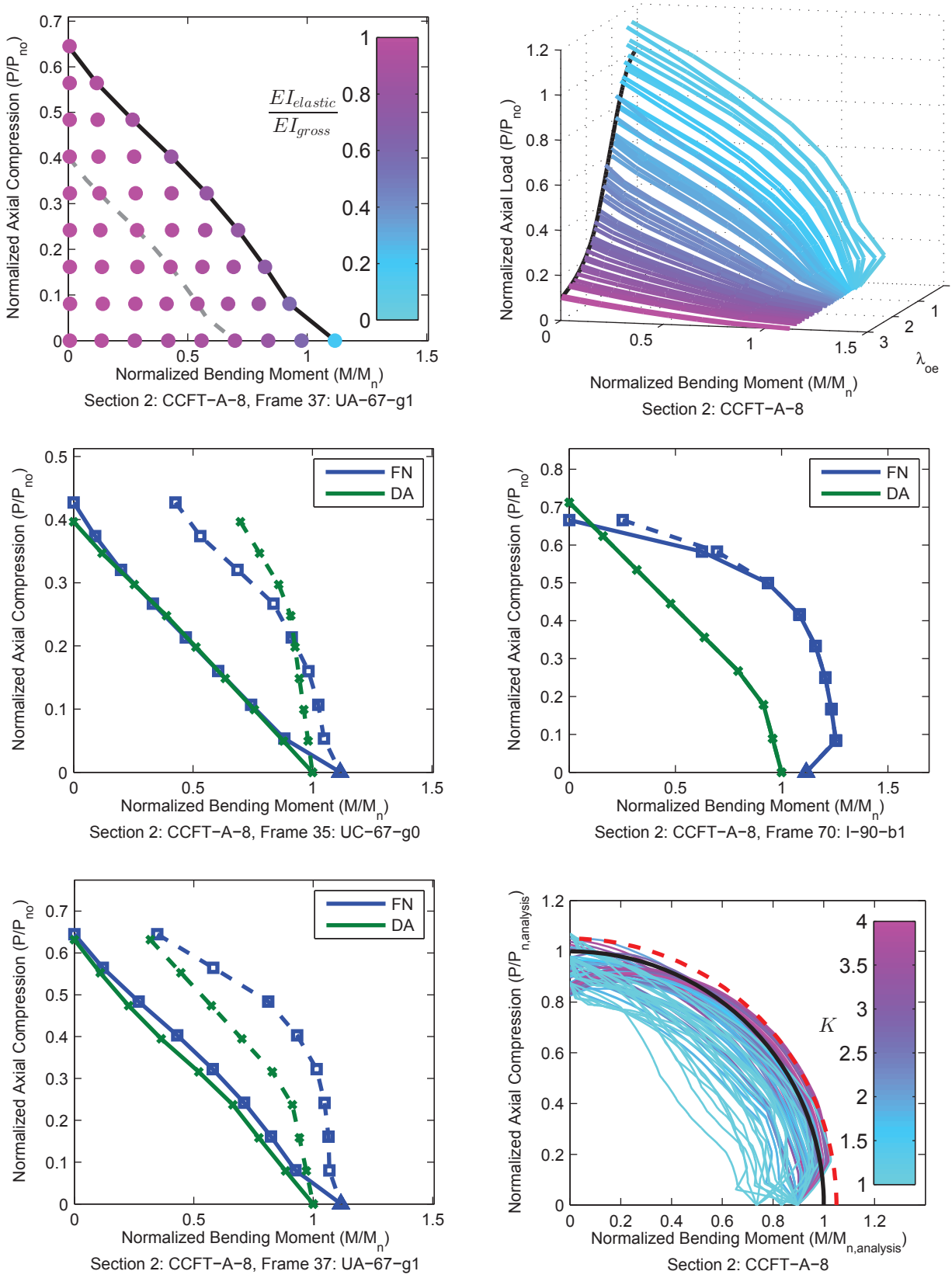

Figure A.2. Detailed Results for Section CCFT-A-8

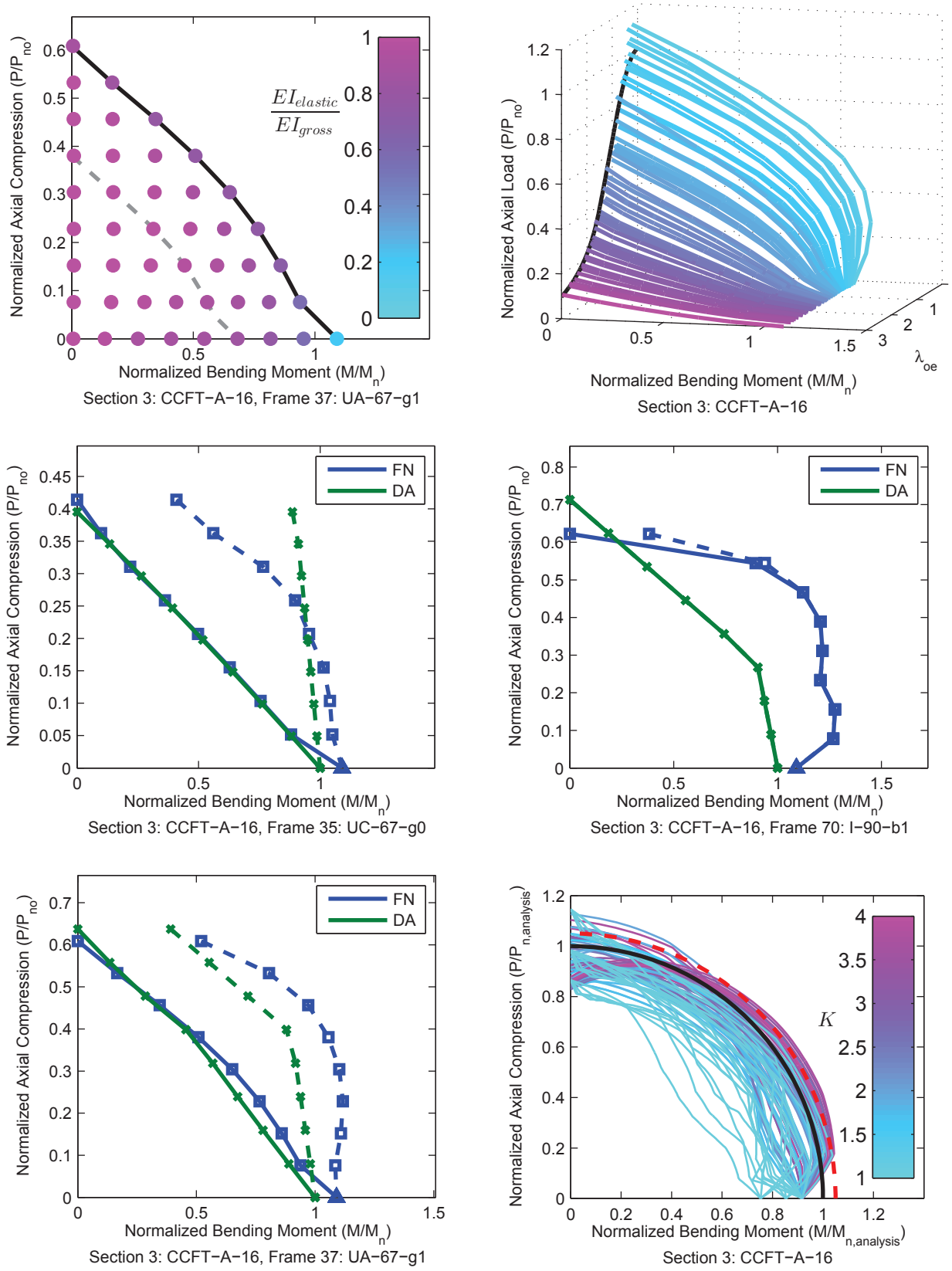

Figure A.3. Detailed Results for Section CCFT-A-16

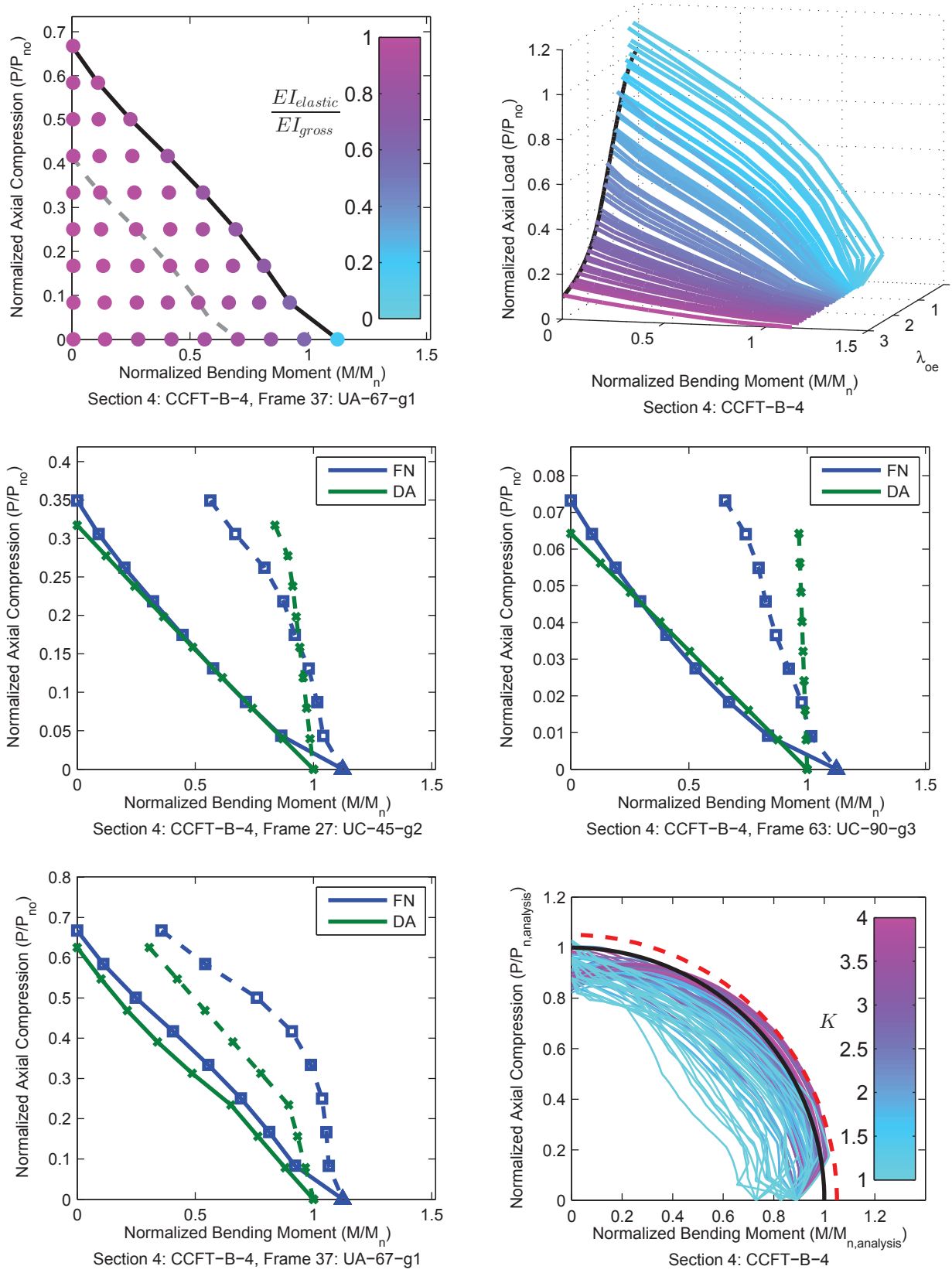

Figure A.4. Detailed Results for Section CCFT-B-4

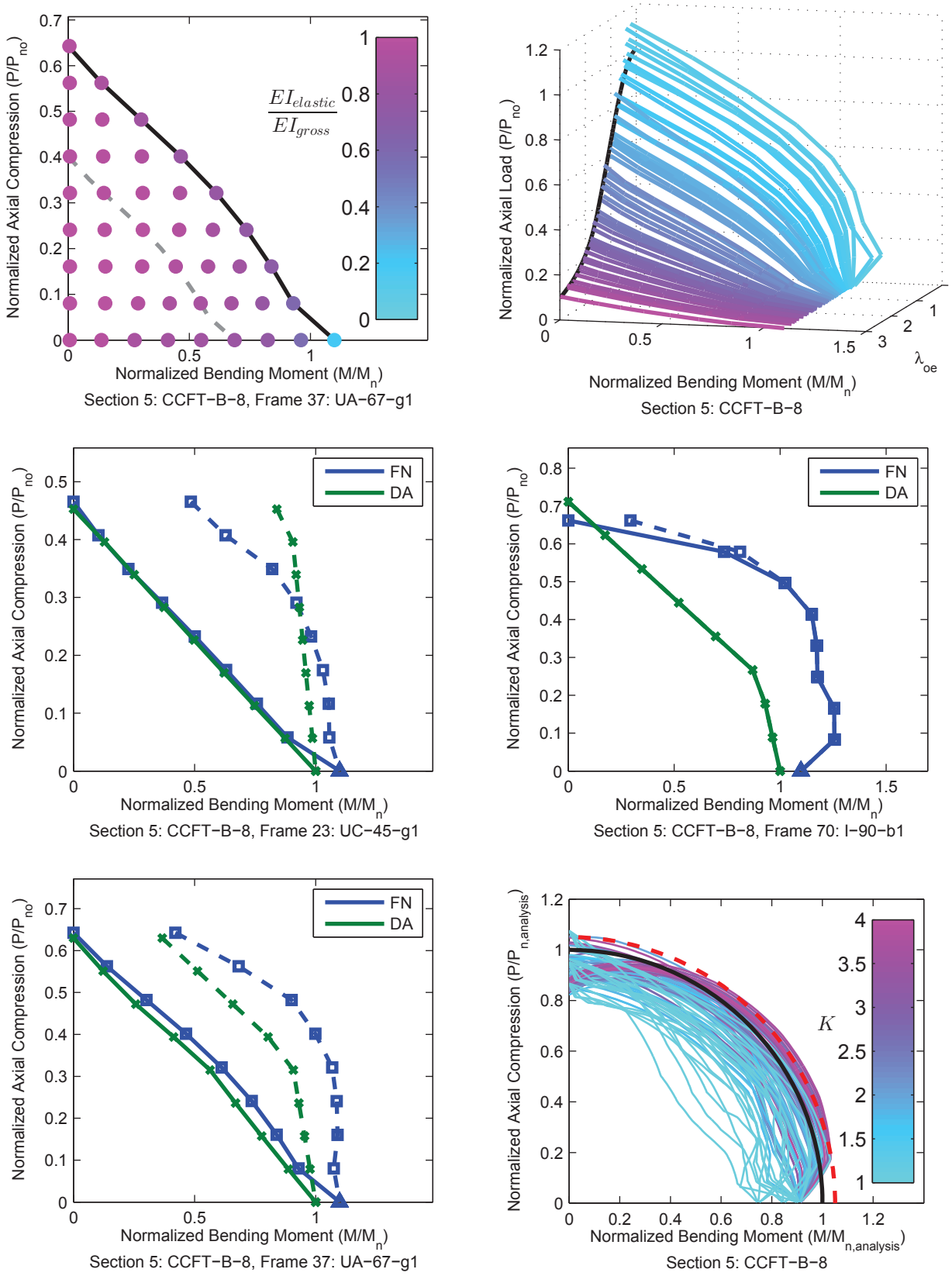

Figure A.5. Detailed Results for Section CCFT-B-8

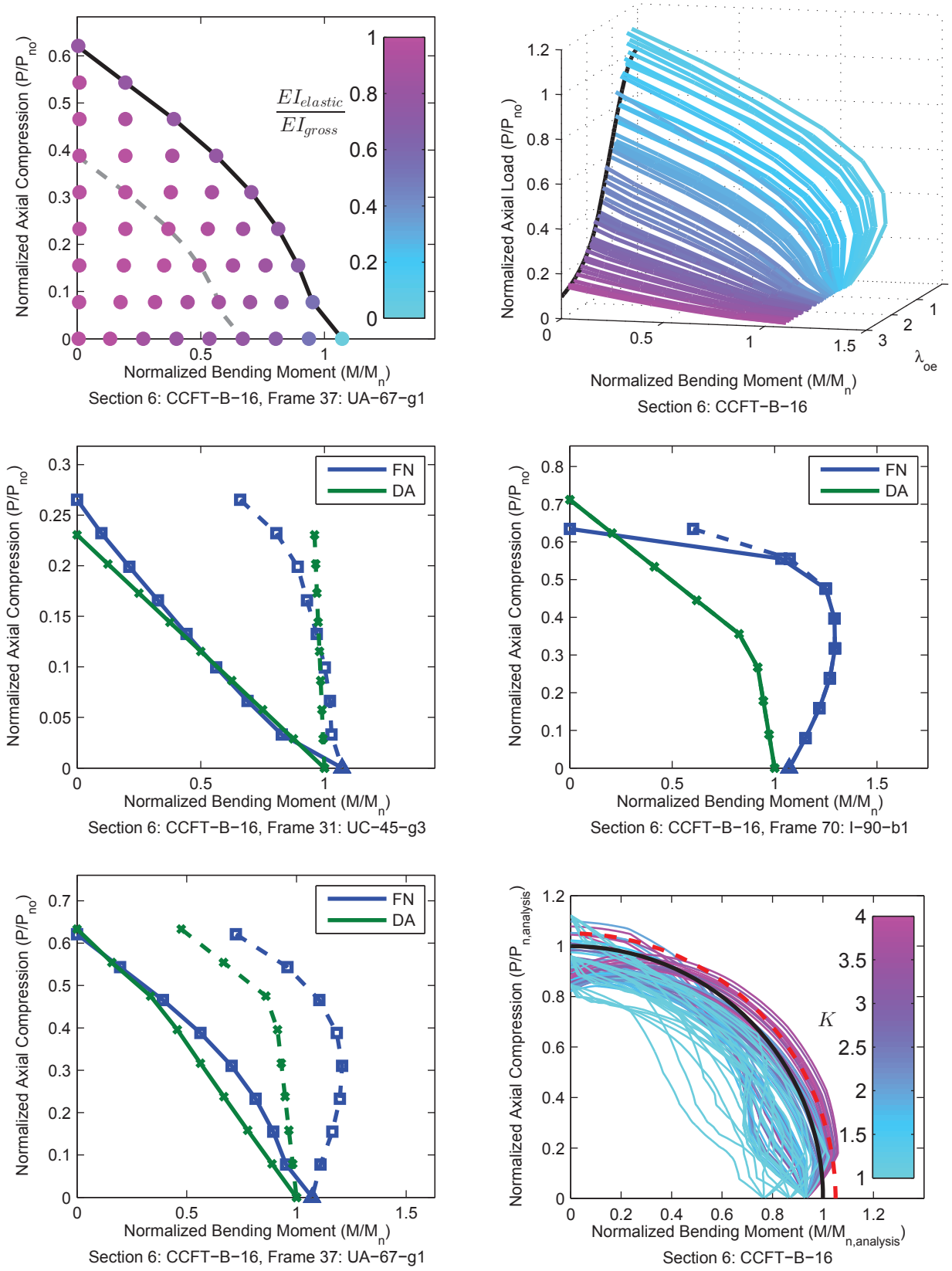

Figure A.6. Detailed Results for Section CCFT-B-16

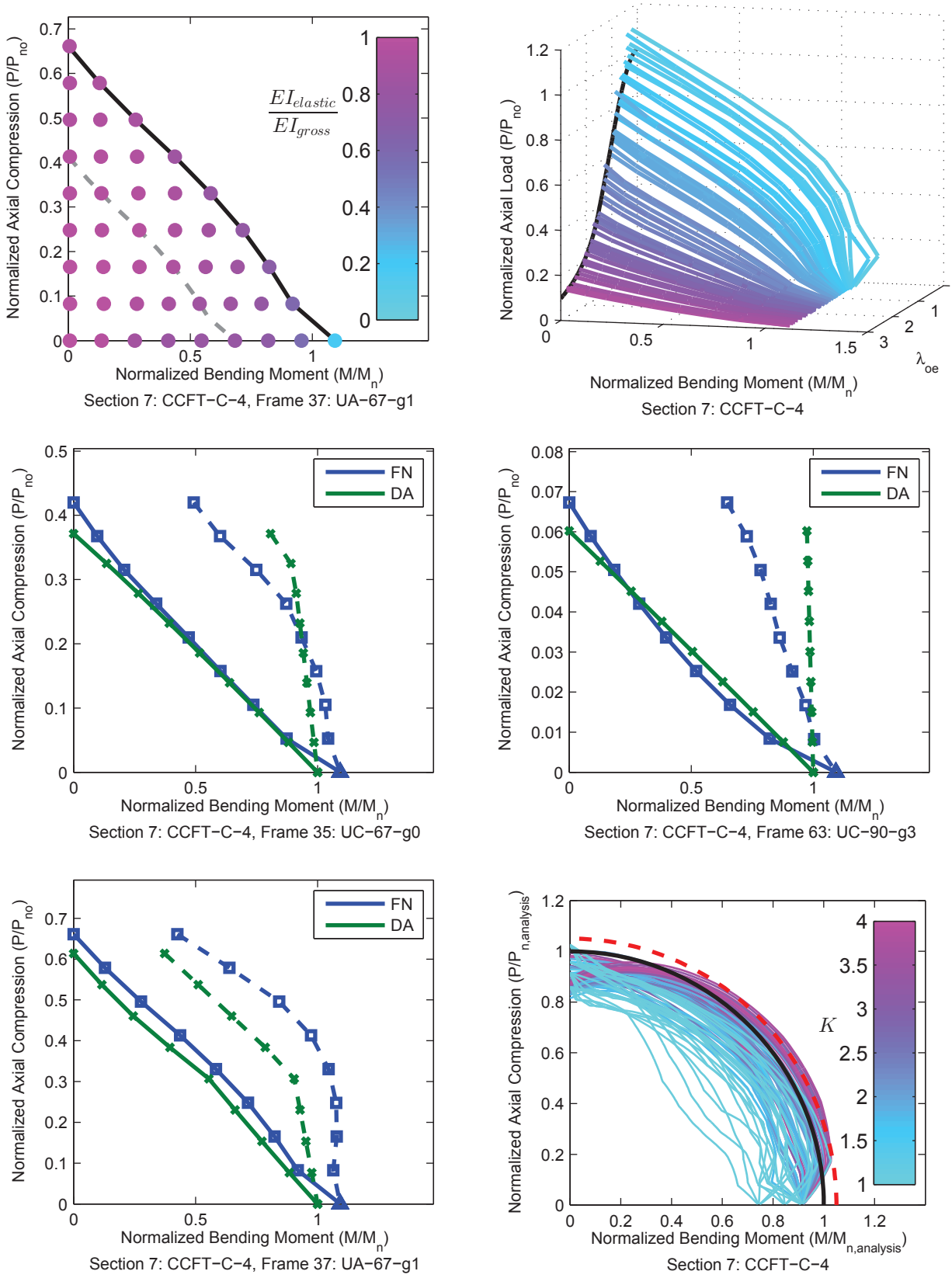

Figure A.7. Detailed Results for Section CCFT-C-4

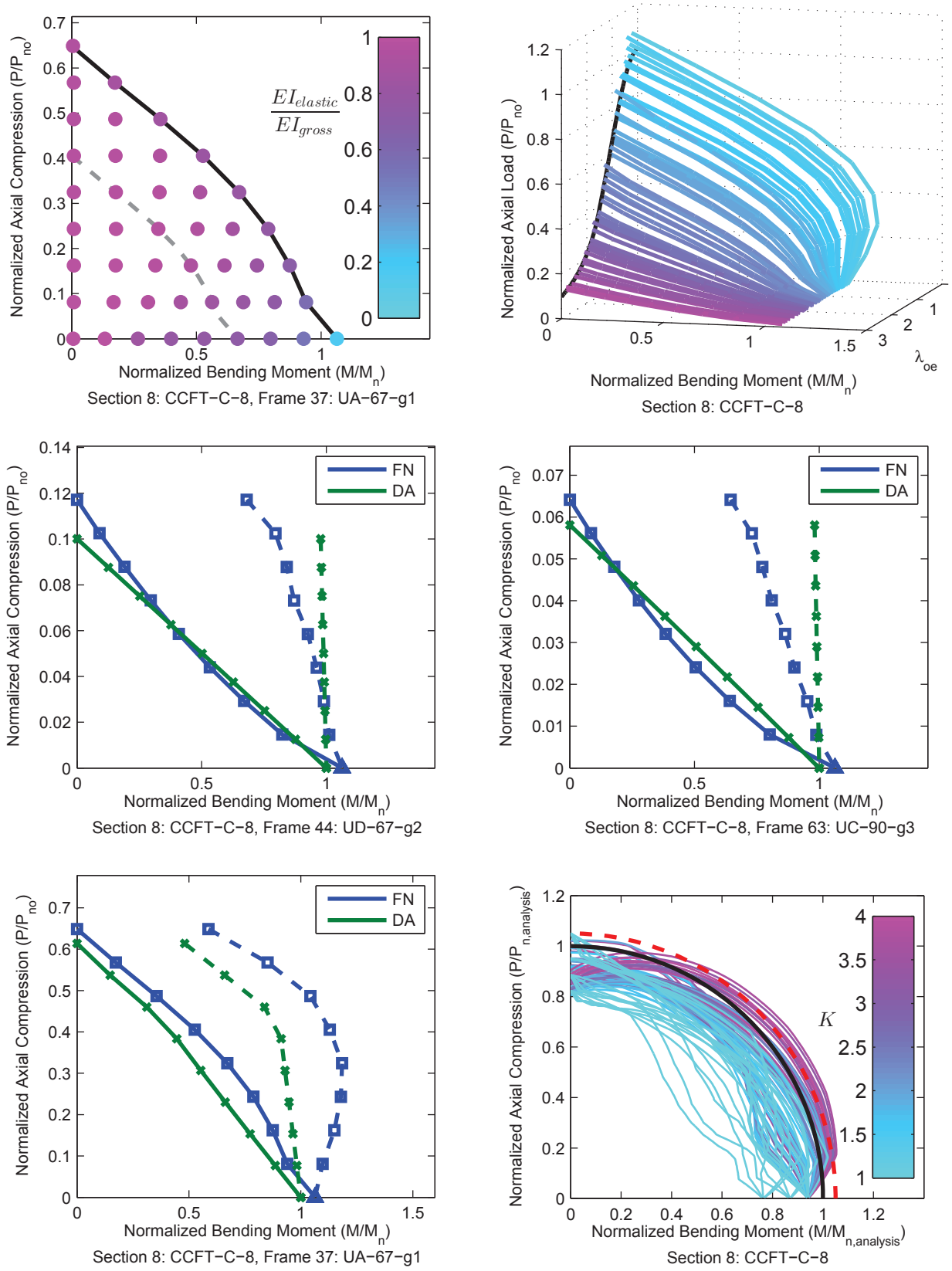

Figure A.8. Detailed Results for Section CCFT-C-8

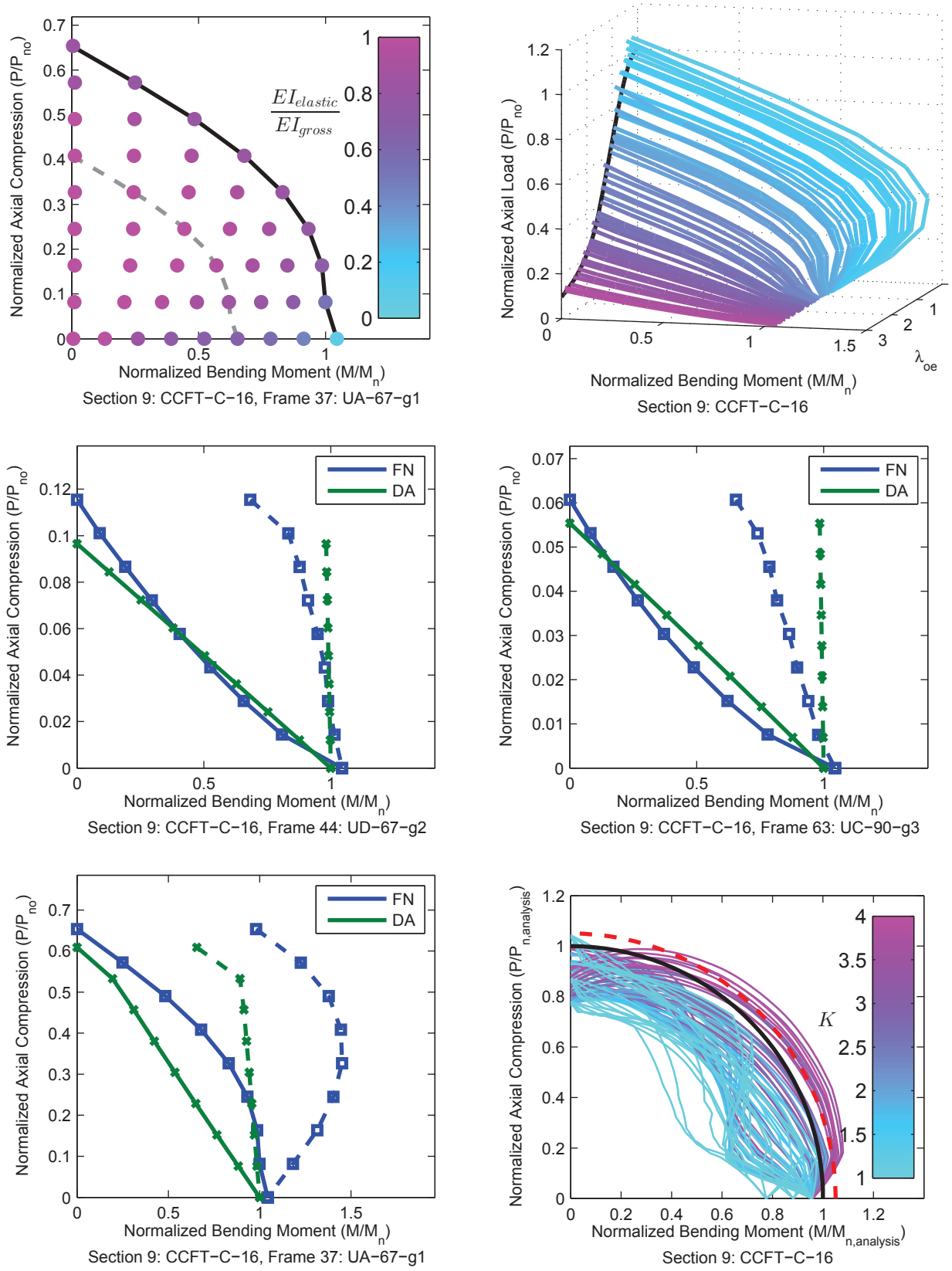

Figure A.9. Detailed Results for Section CCFT-C-16

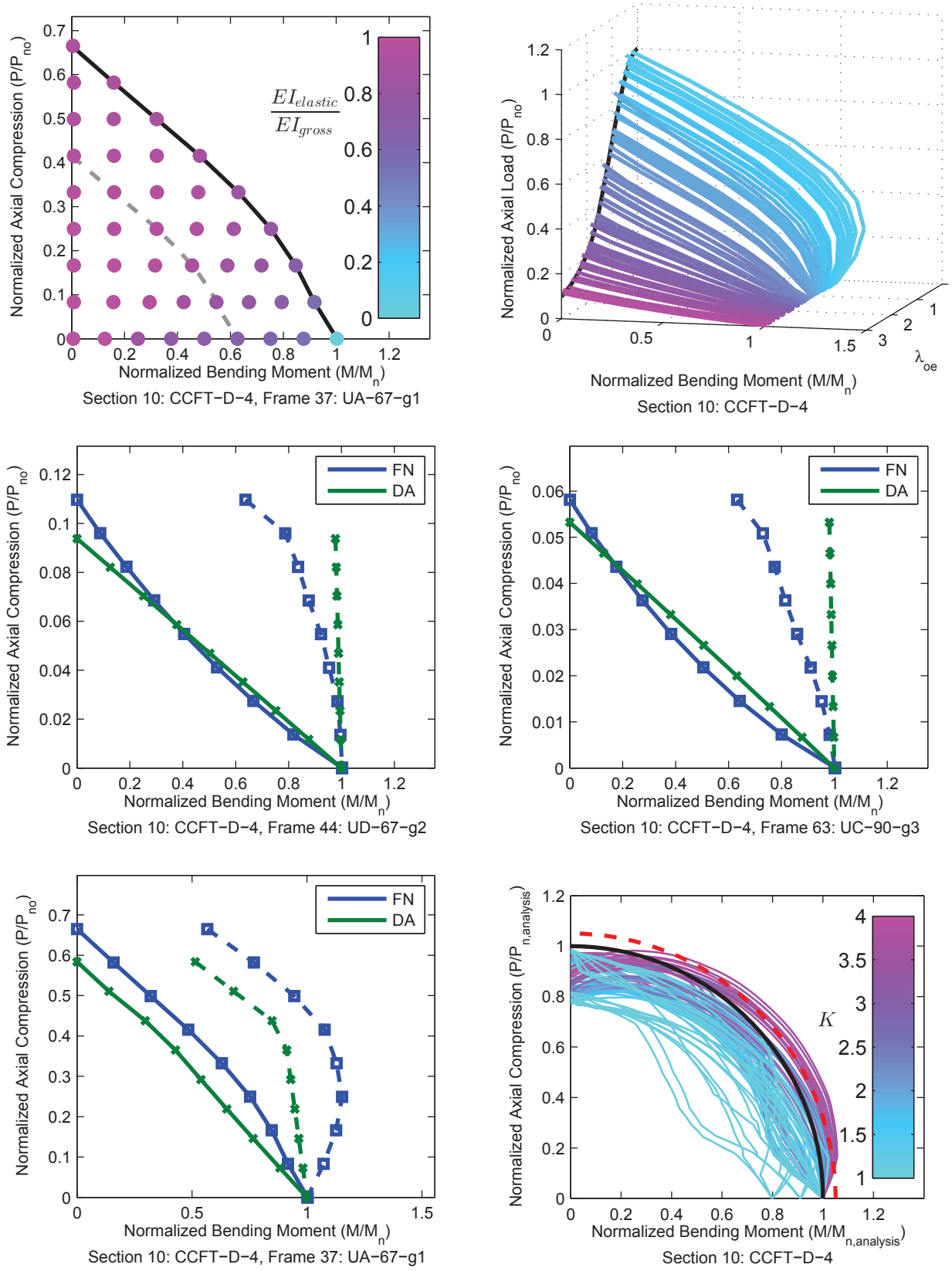

Figure A.10. Detailed Results for Section CCFT-D-4

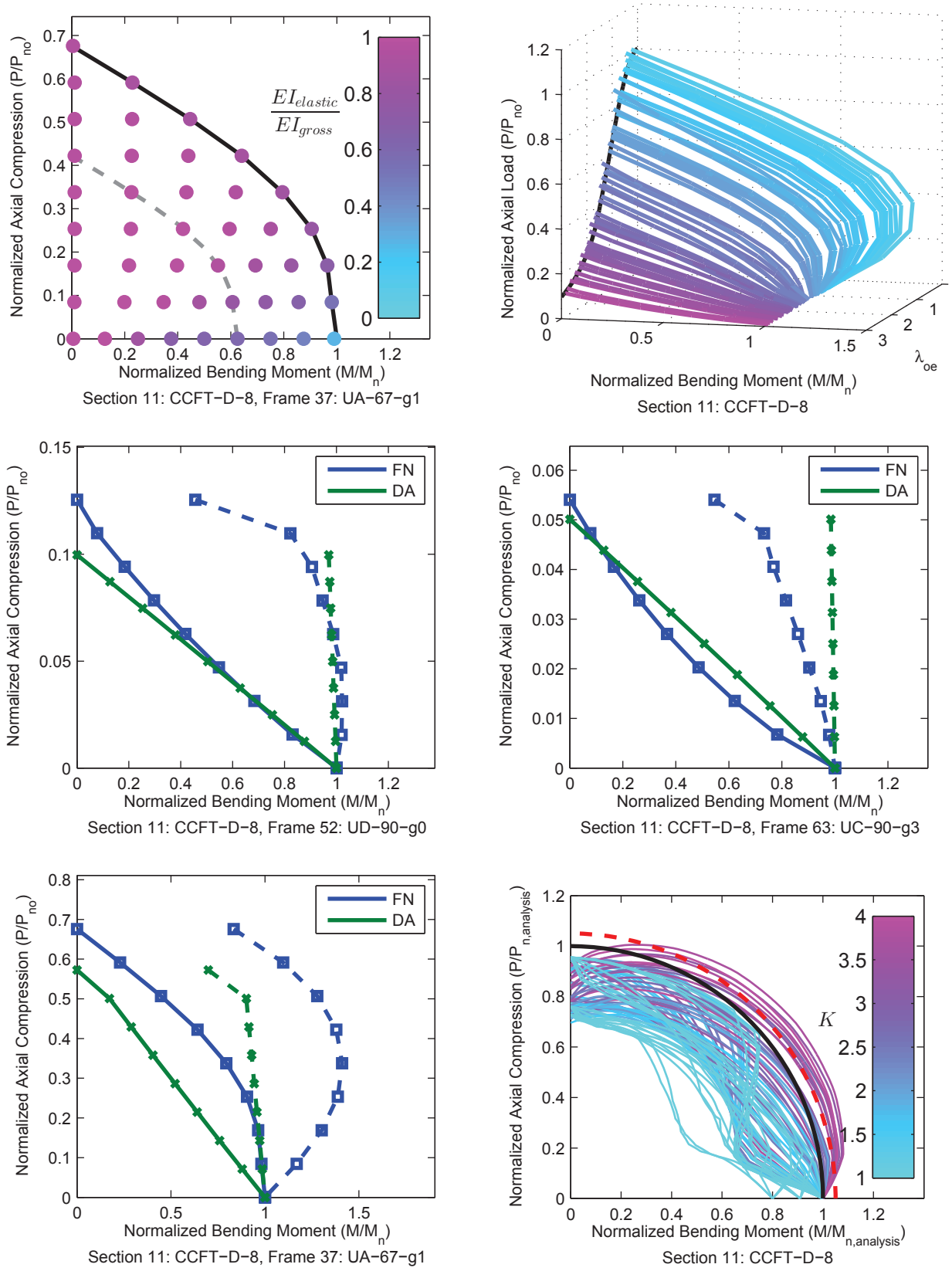

Figure A.11. Detailed Results for Section CCFT-D-8

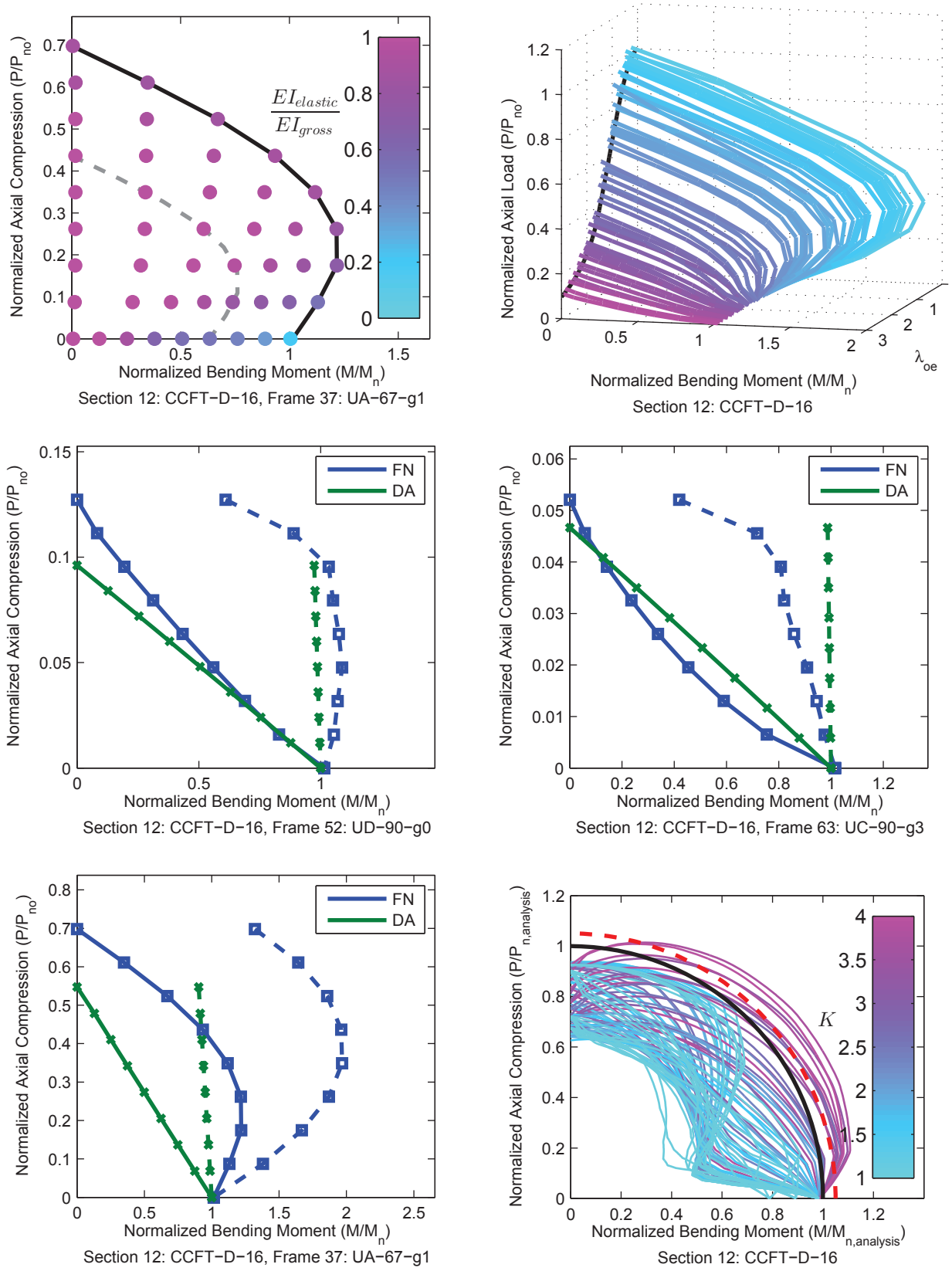

Figure A.12. Detailed Results for Section CCFT-D-16

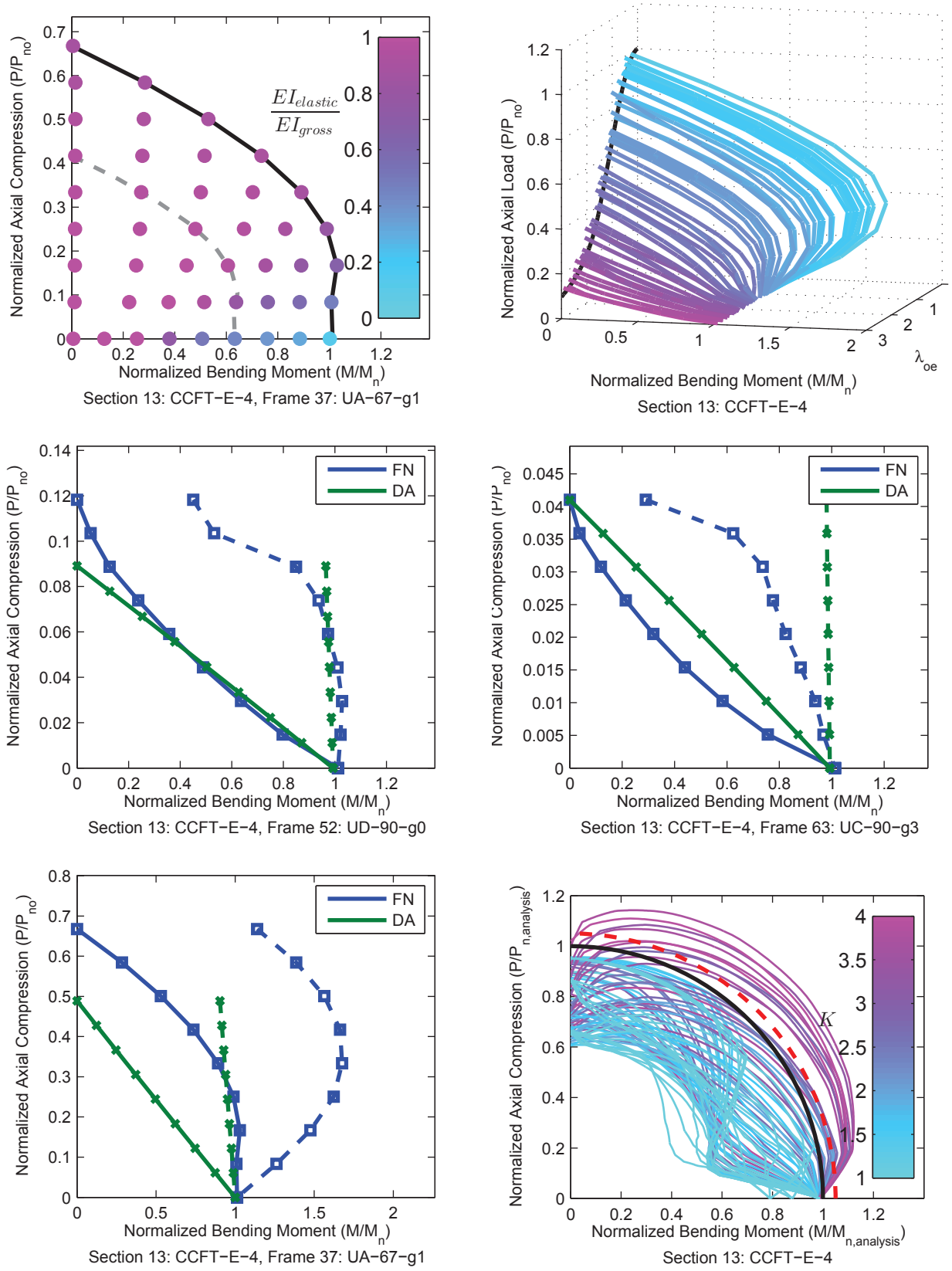

Figure A.13. Detailed Results for Section CCFT-E-4

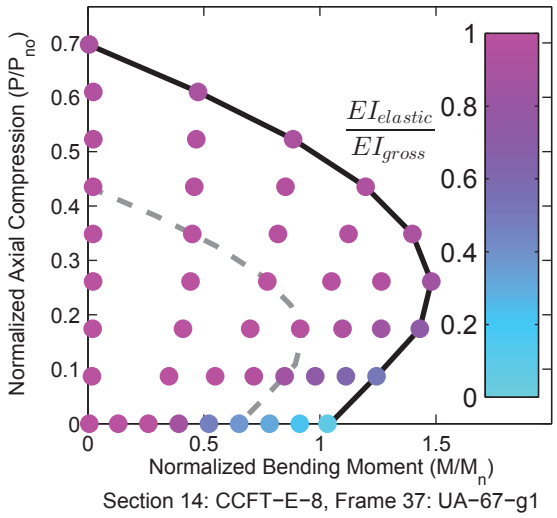

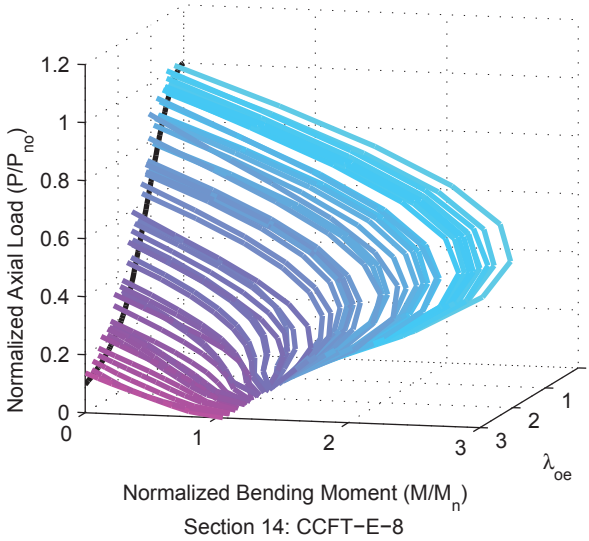

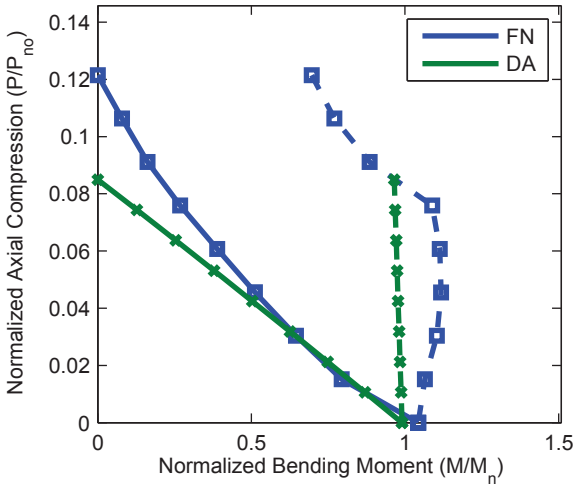

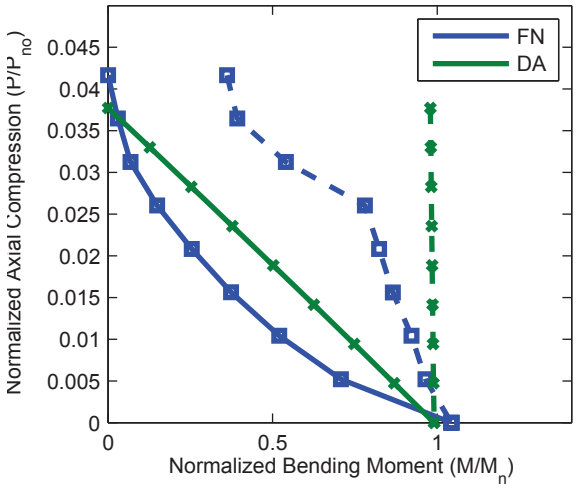

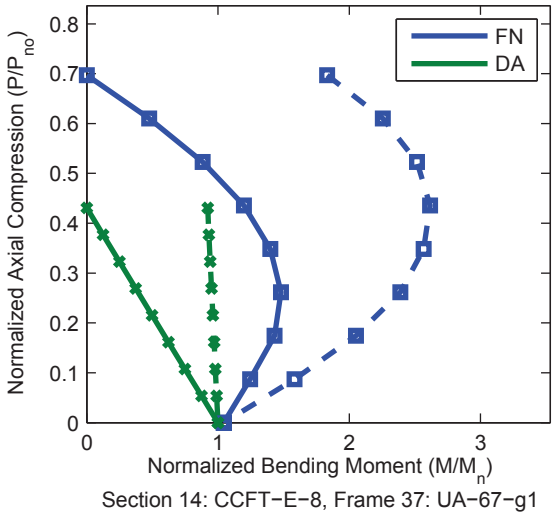

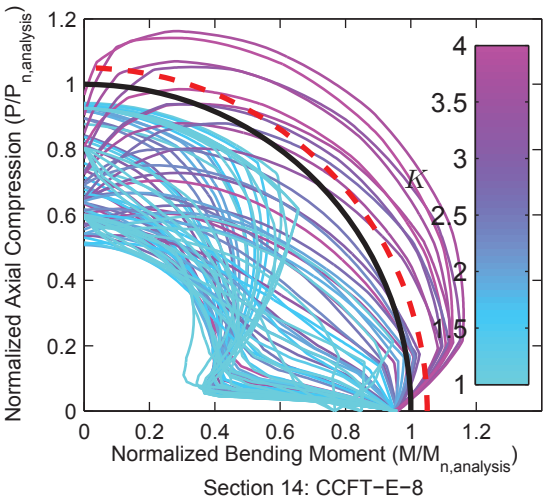

Figure A.14. Detailed Results for Section CCFT-E-8

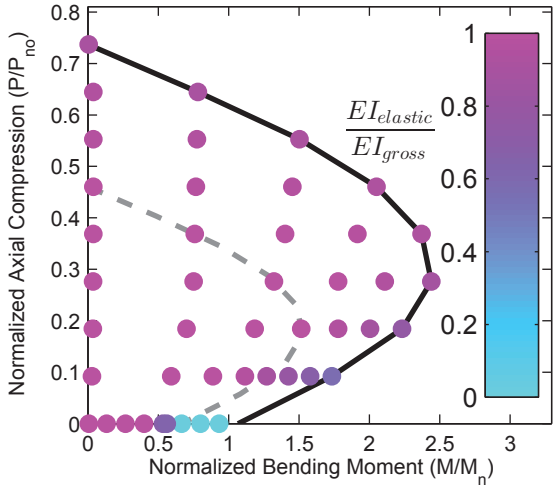

Section 15: CCFT−E−16, Frame 37: UA−67−g1

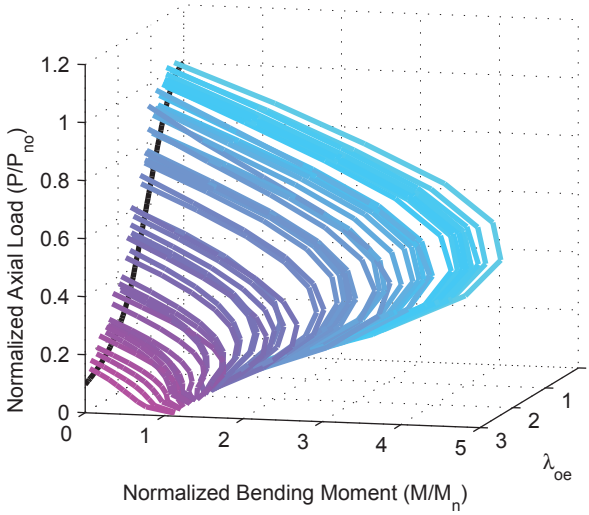

Section 15: CCFT−E−16

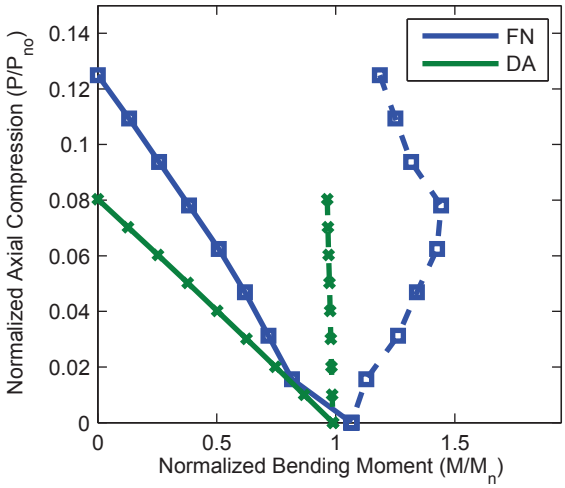

Section 15: CCFT−E−16, Frame 52: UD−90−g0

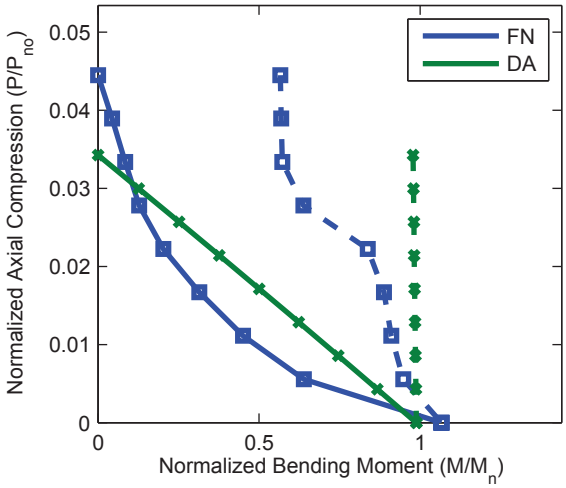

Section 15: CCFT−E−16, Frame 63: UC−90−g3

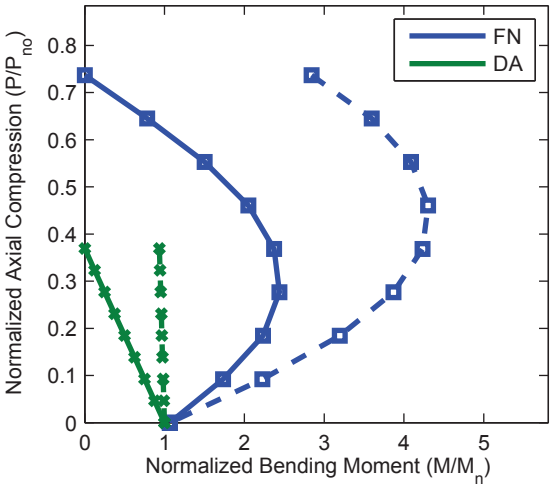

Section 15: CCFT−E−16, Frame 37: UA−67−g1

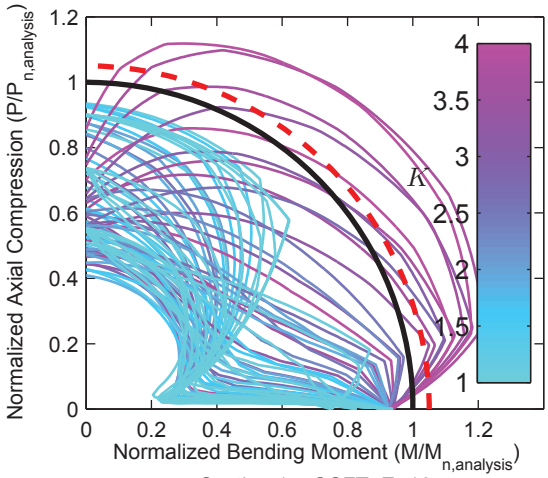

Section 15: CCFT−E−16

Figure A.15. Detailed Results for Section CCFT-E-16

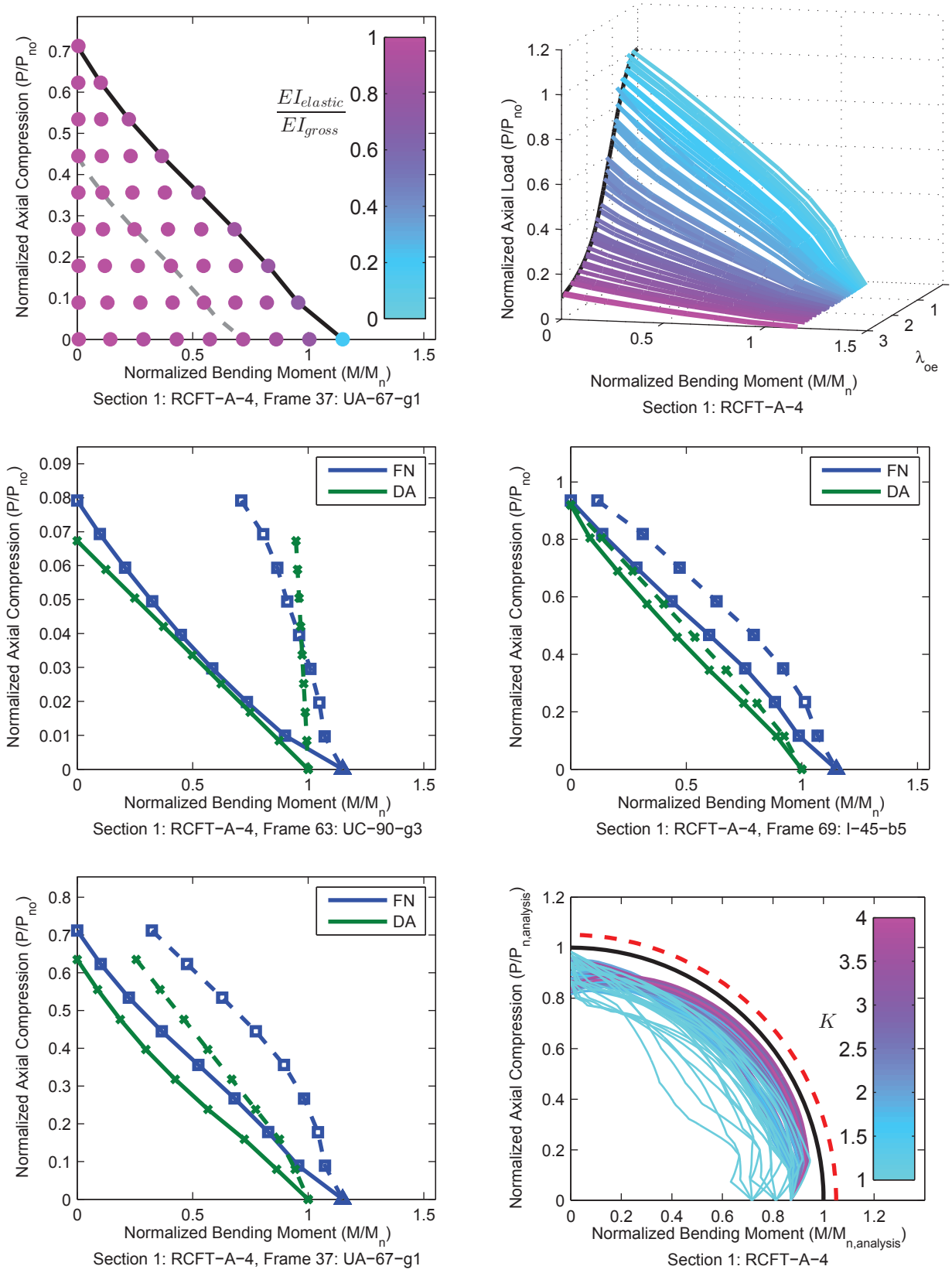

Figure A.16. Detailed Results for Section RCFT-A-4

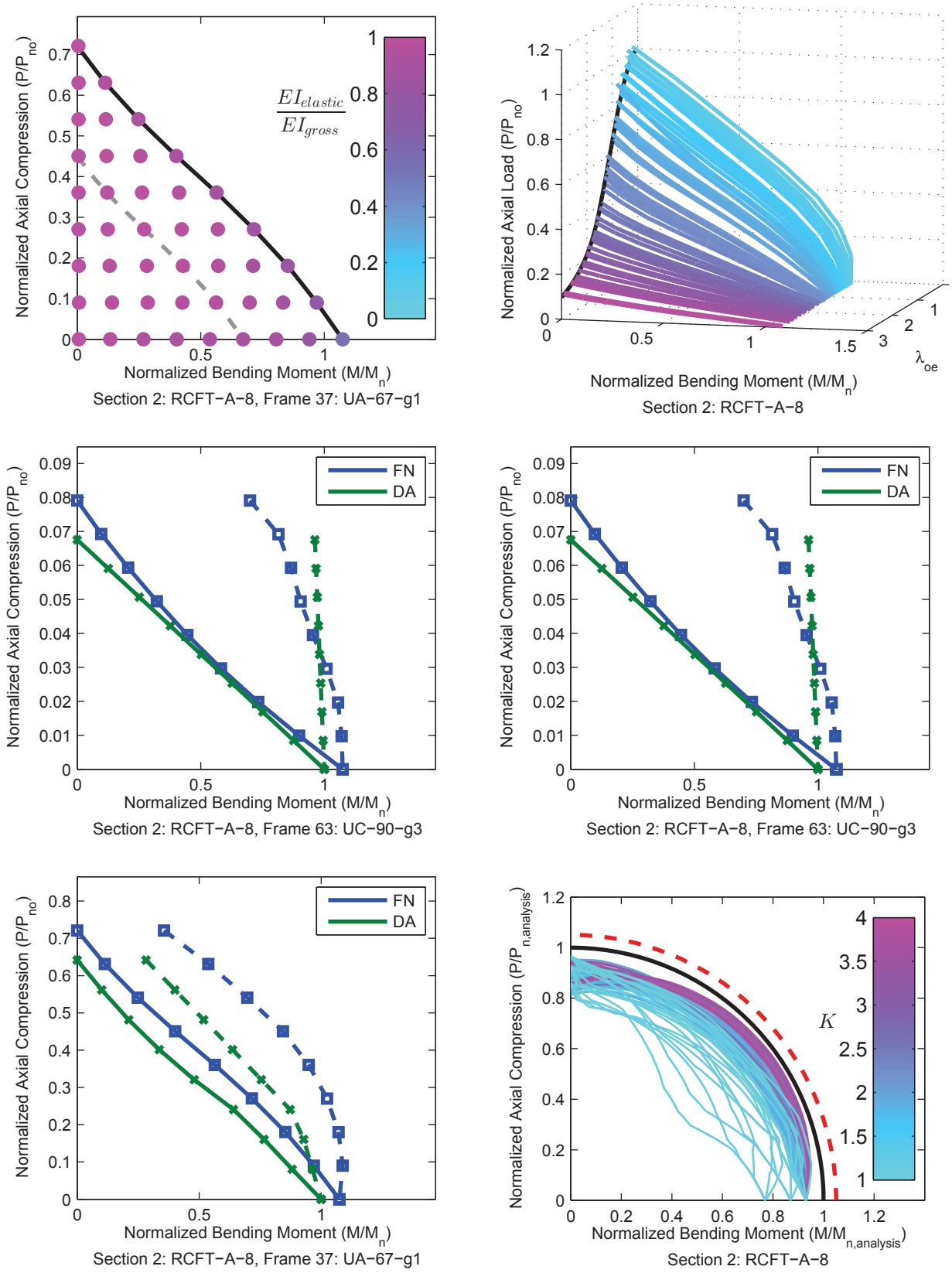

Figure A.17. Detailed Results for Section RCFT-A-8

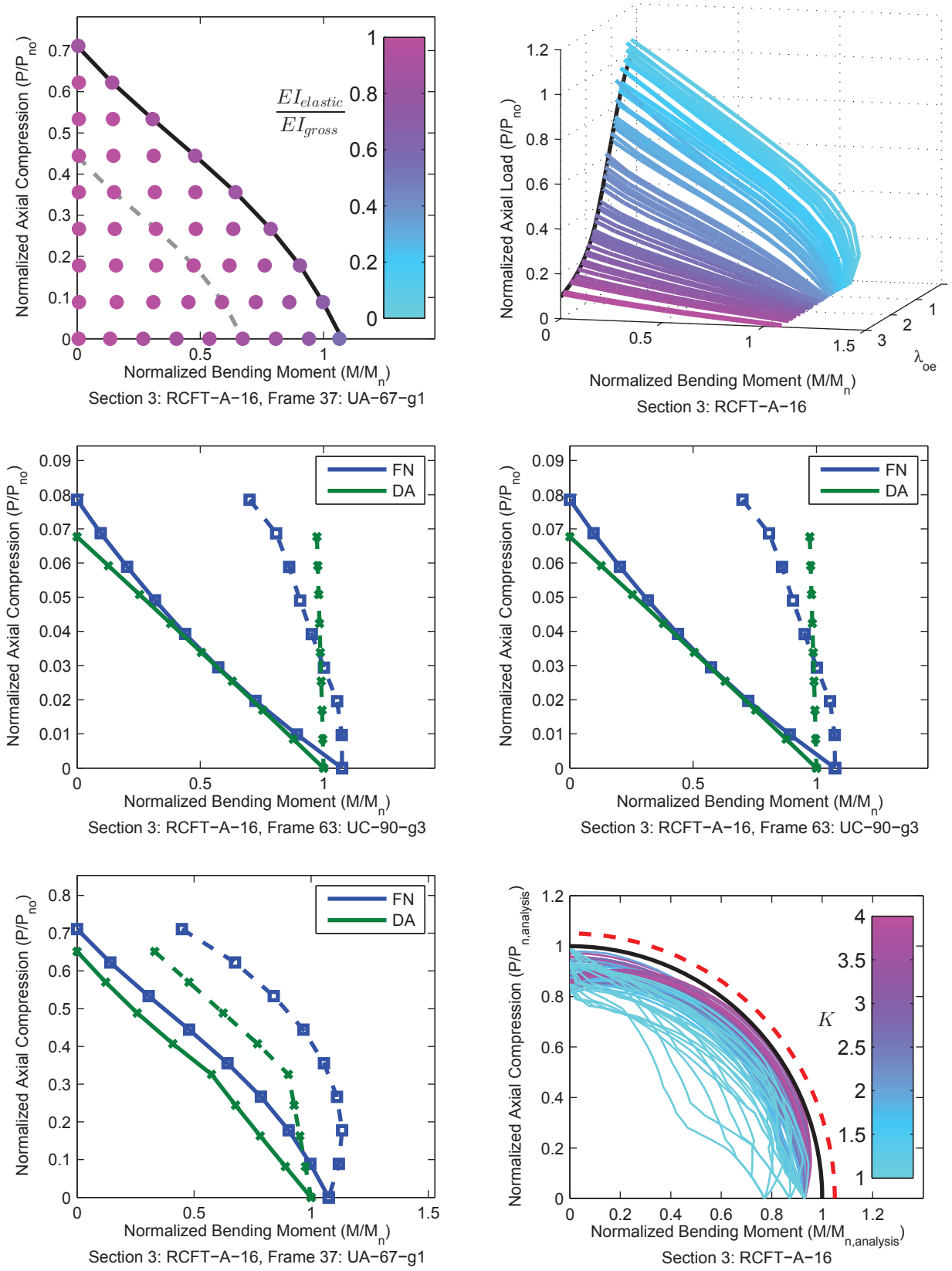

Figure A.18. Detailed Results for Section RCFT-A-16

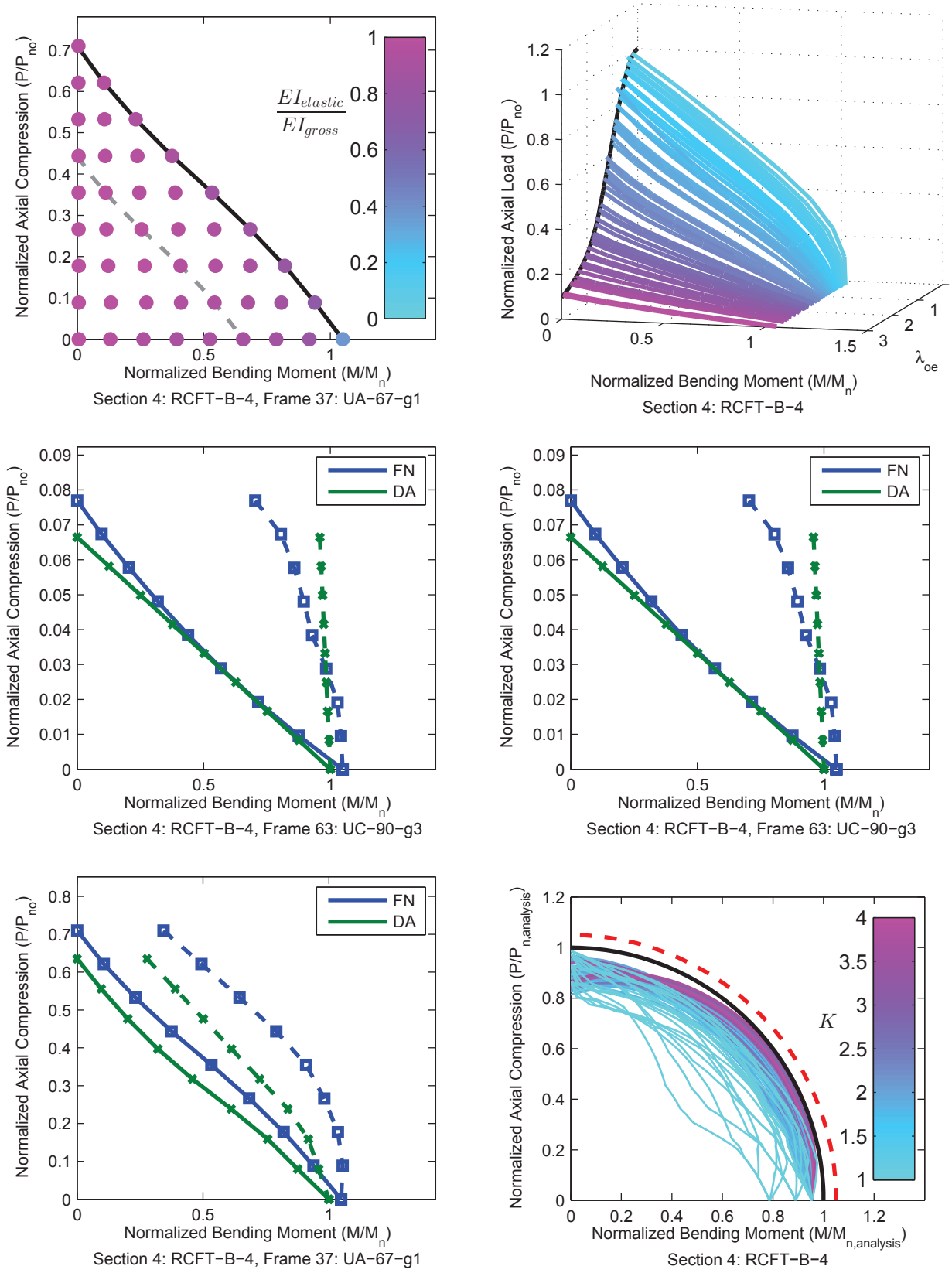

Figure A.19. Detailed Results for Section RCFT-B-4

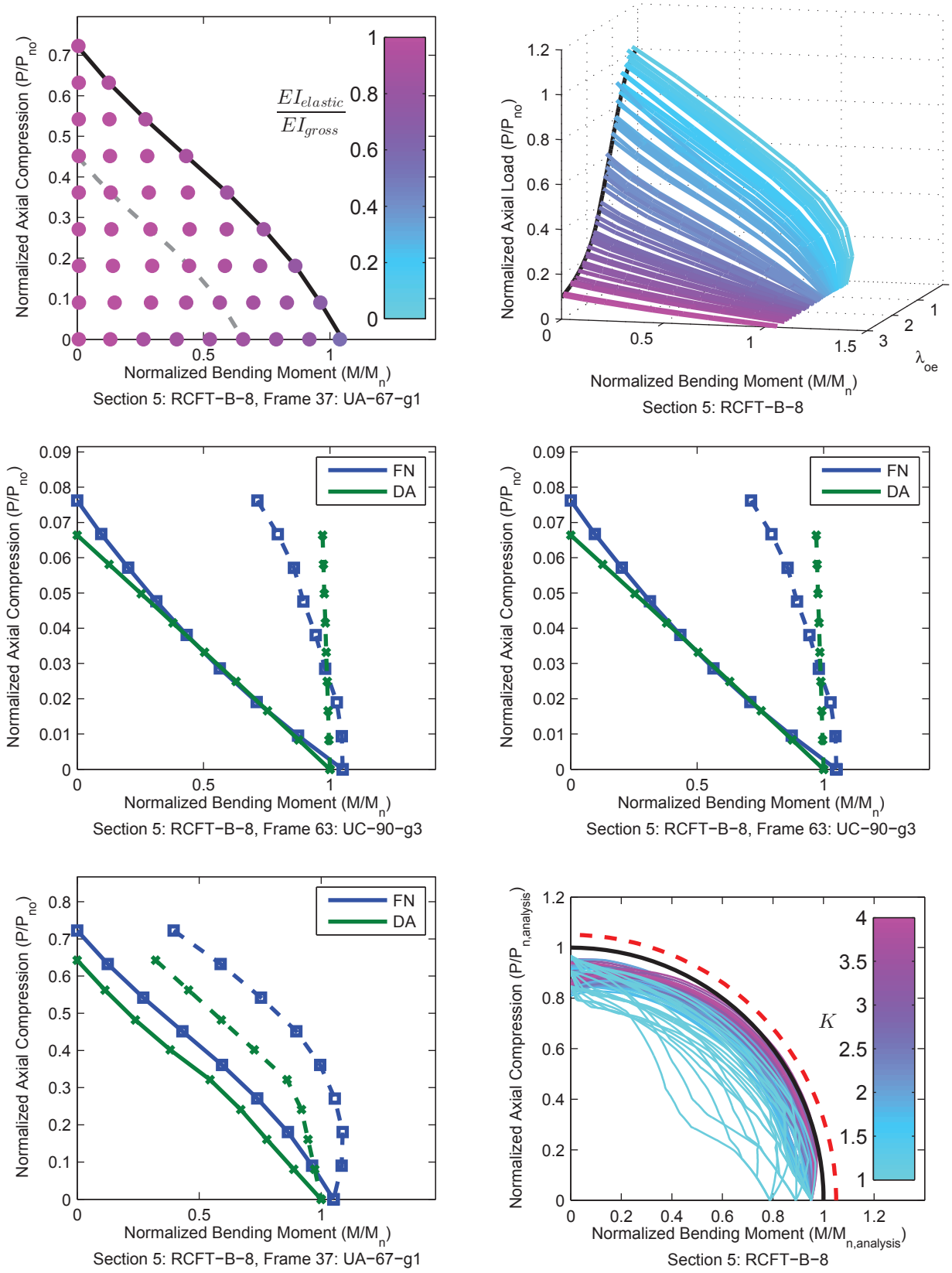

Figure A.20. Detailed Results for Section RCFT-B-8

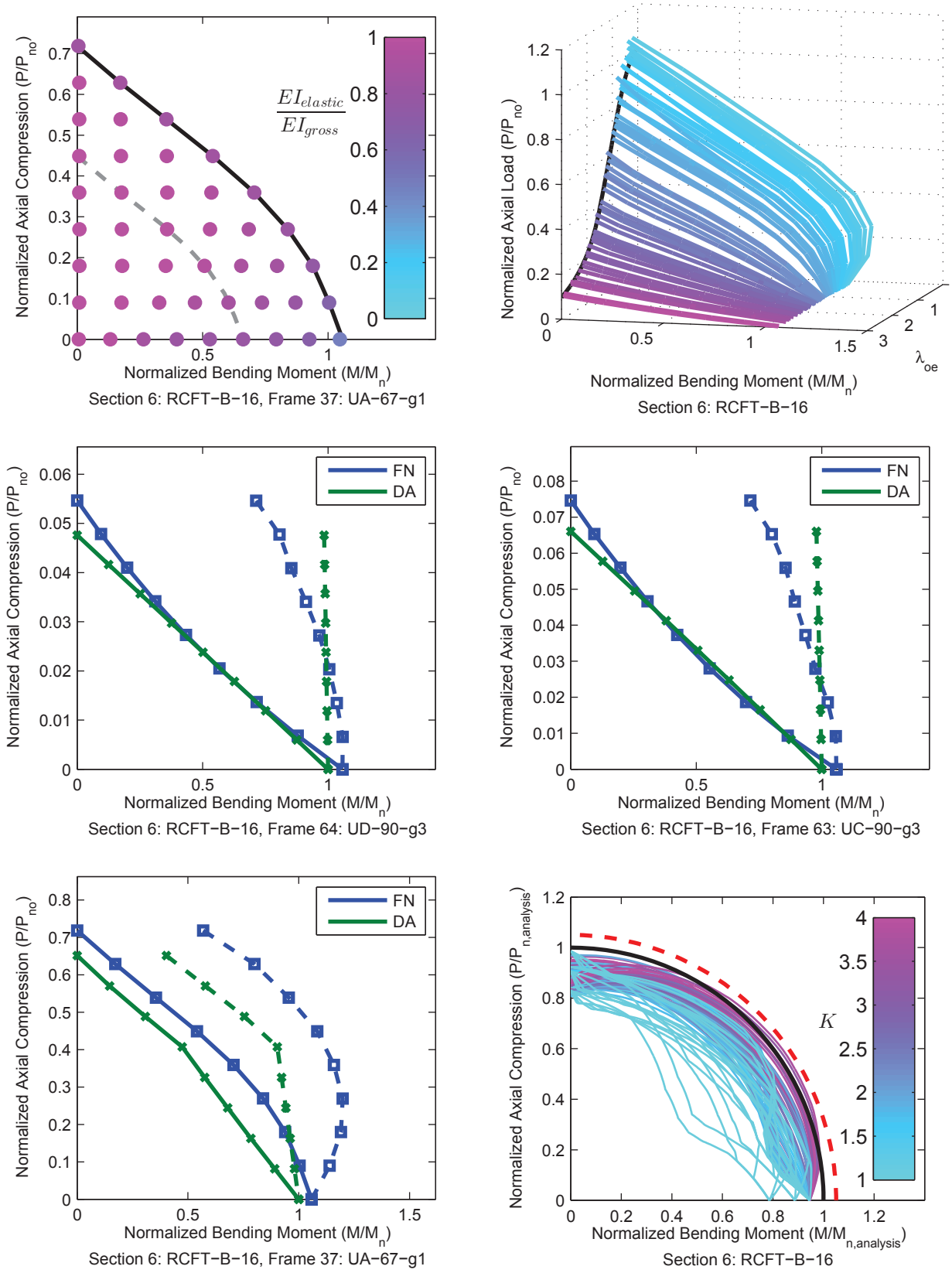

Figure A.21. Detailed Results for Section RCFT-B-16

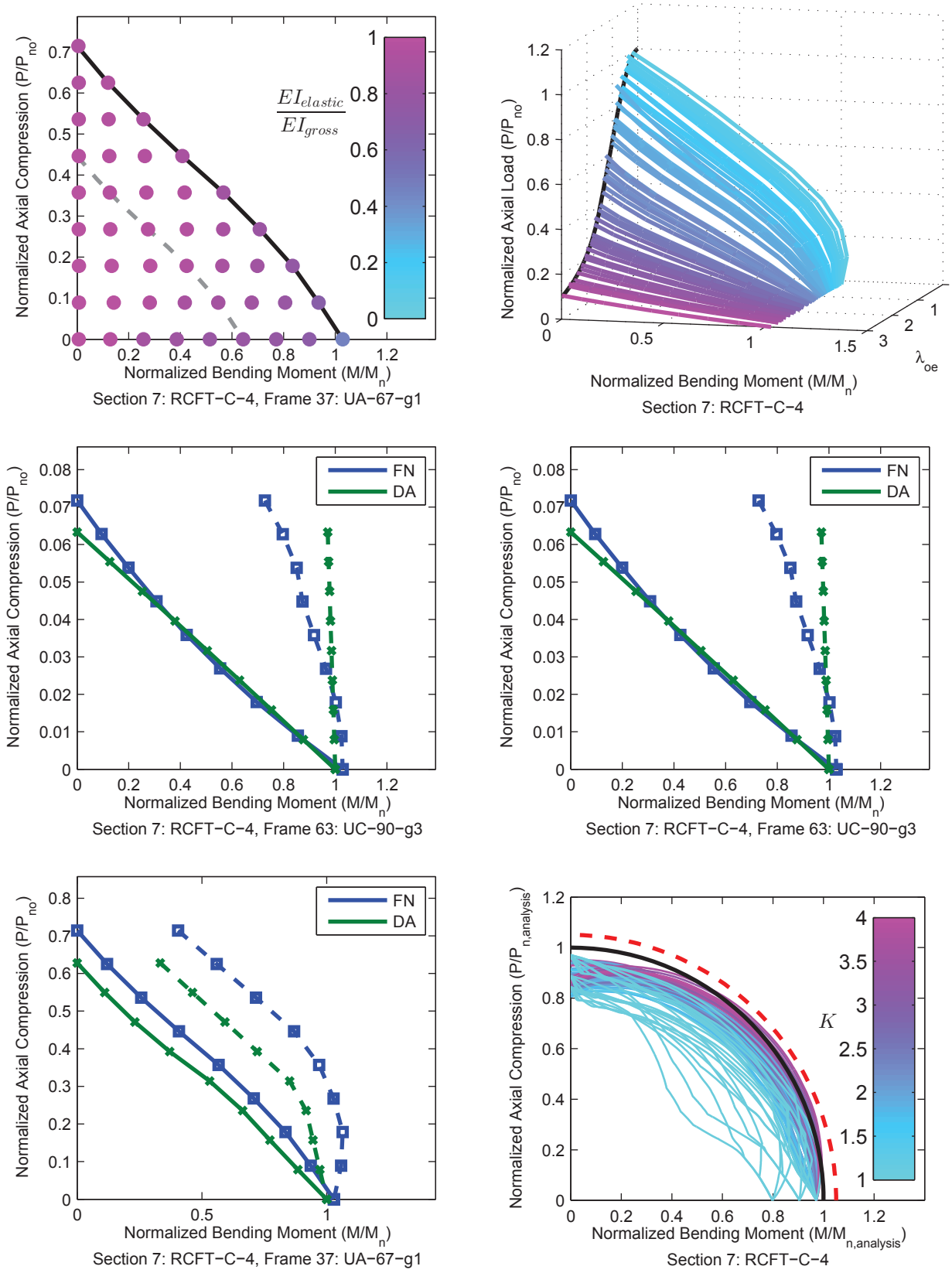

Figure A.22. Detailed Results for Section RCFT-C-4

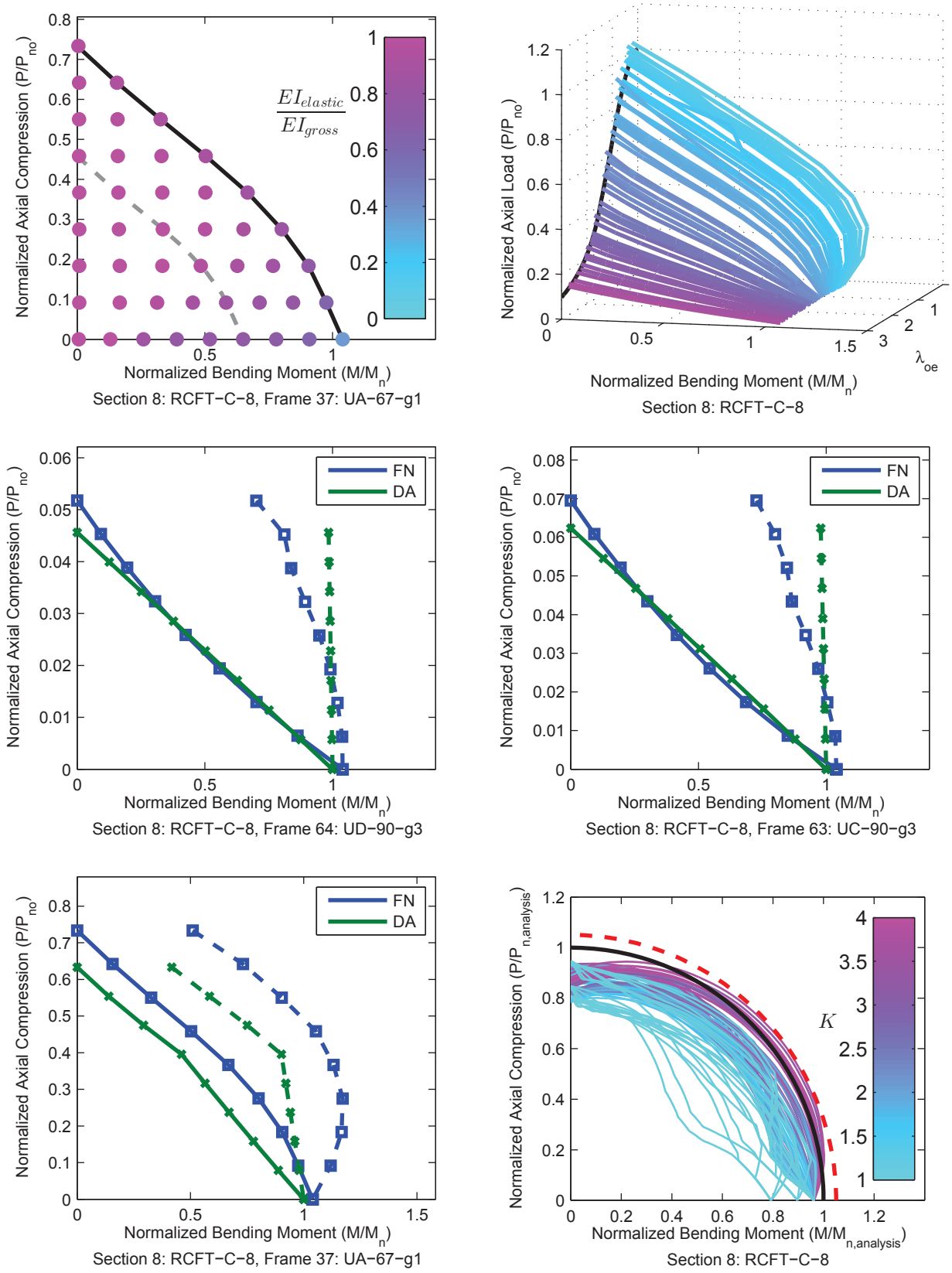

Figure A.23. Detailed Results for Section RCFT-C-8

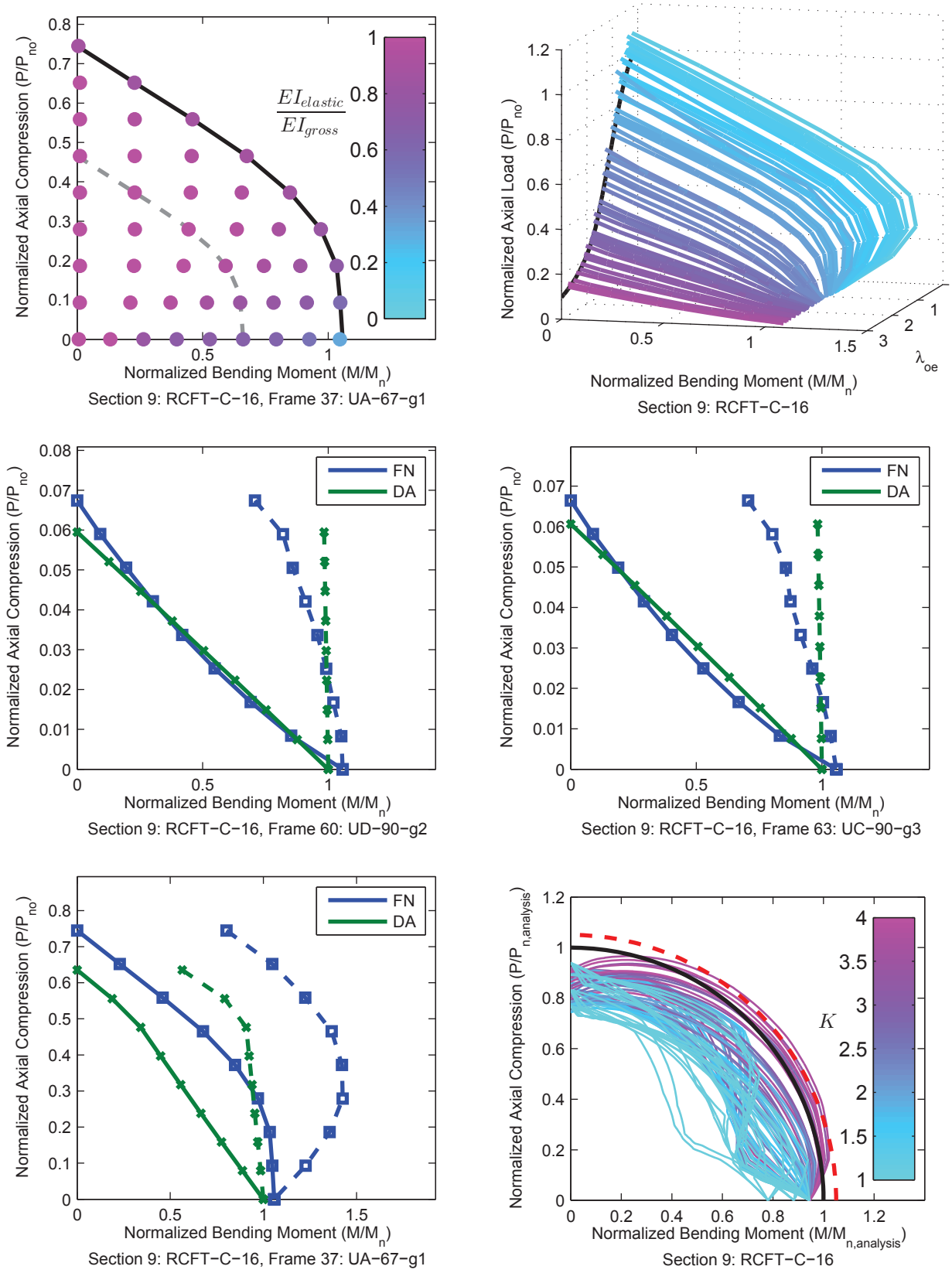

Figure A.24. Detailed Results for Section RCFT-C-16

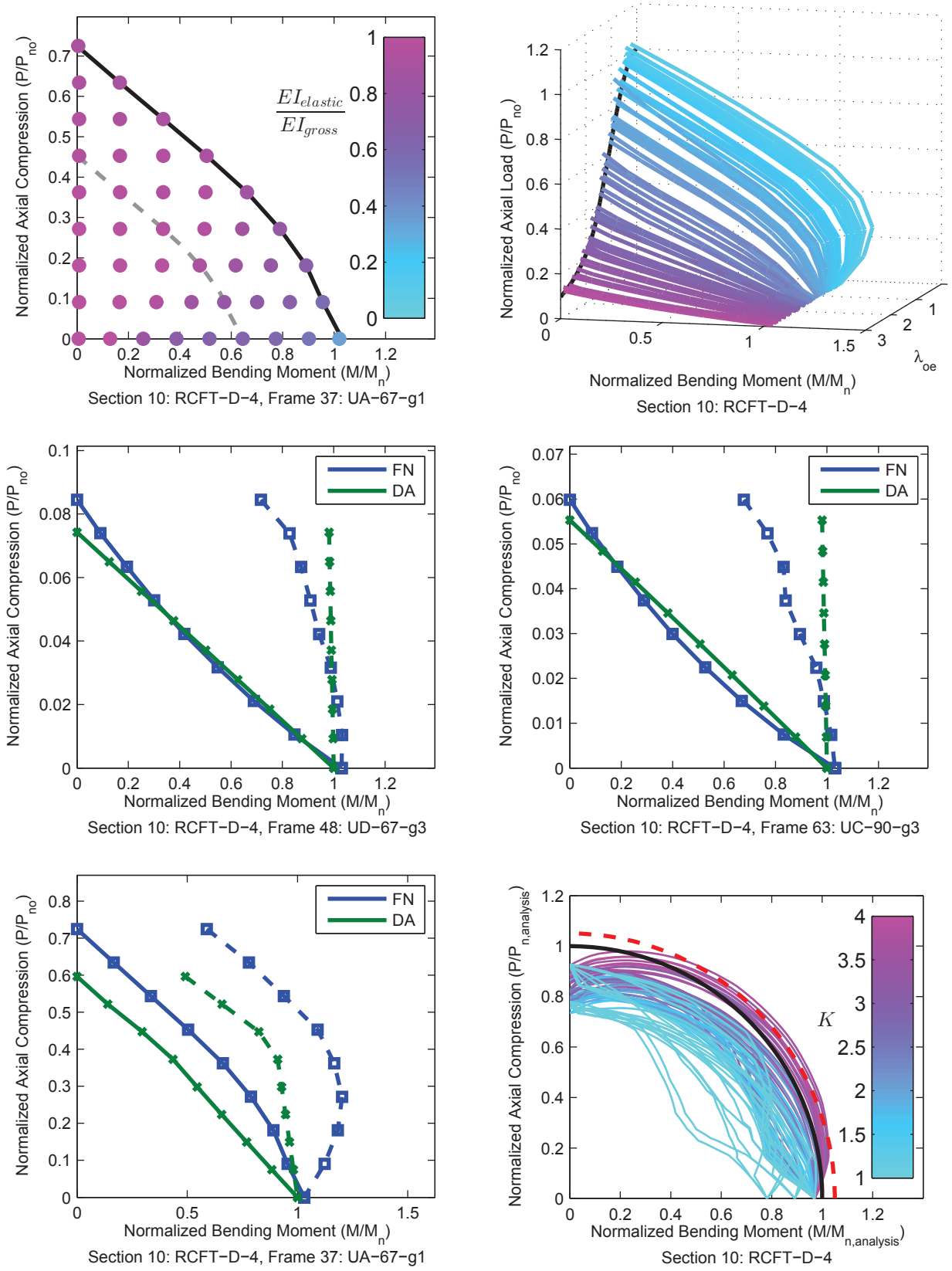

Figure A.25. Detailed Results for Section RCFT-D-4

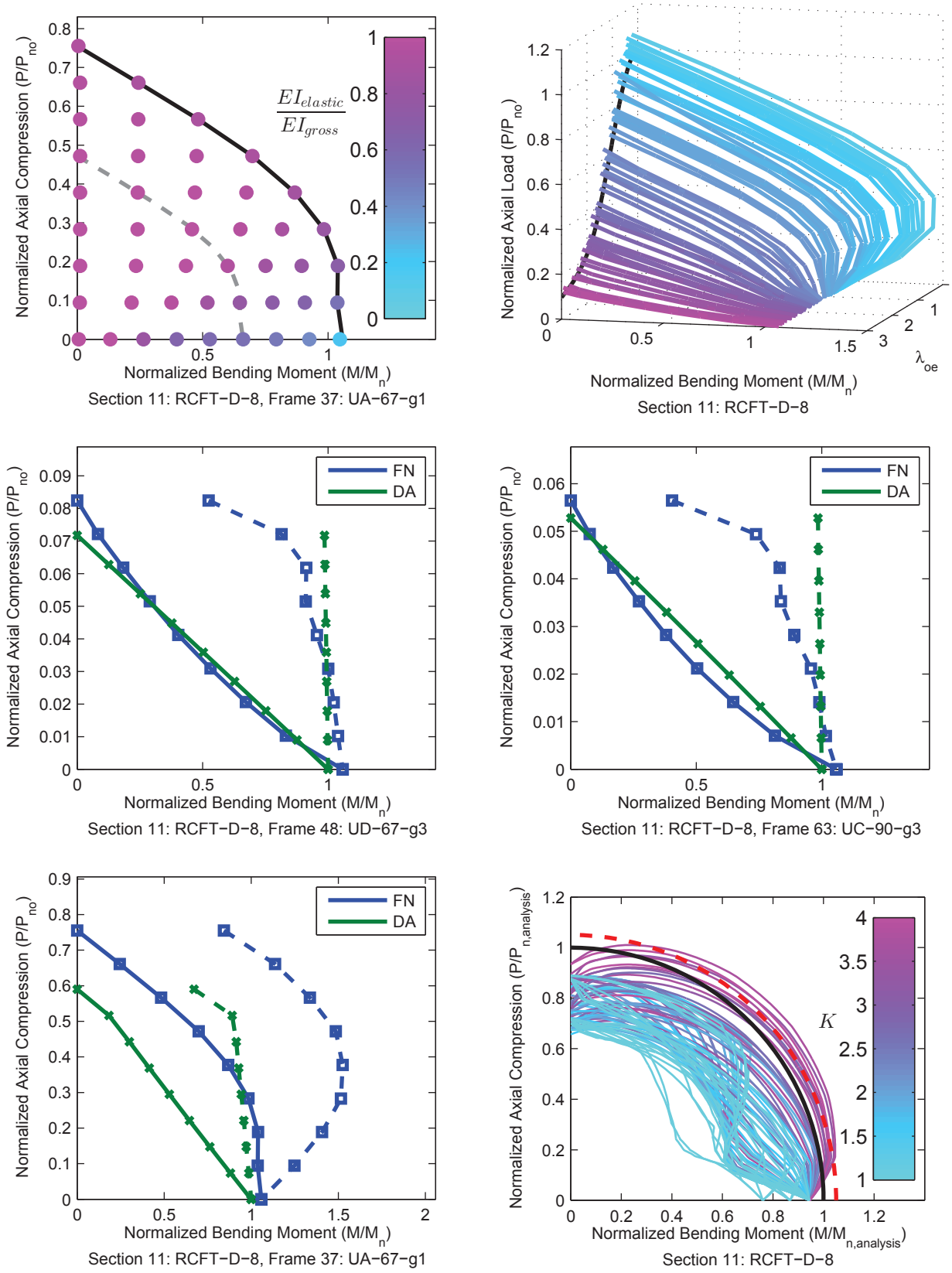

Figure A.26. Detailed Results for Section RCFT-D-8

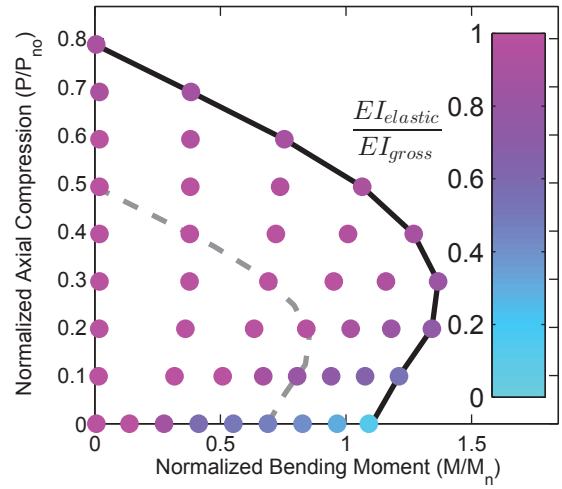

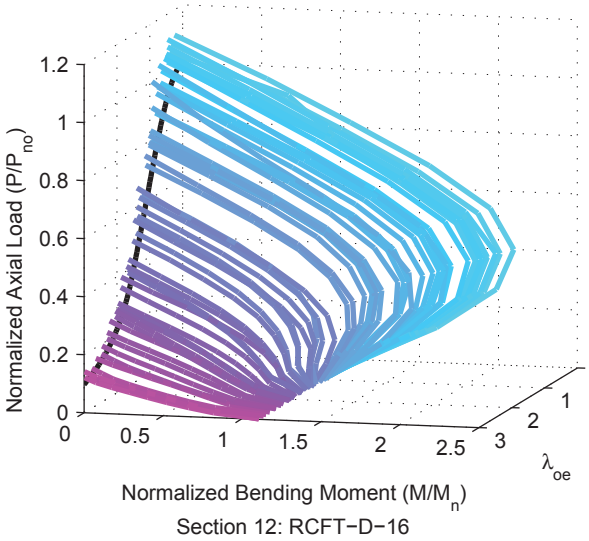

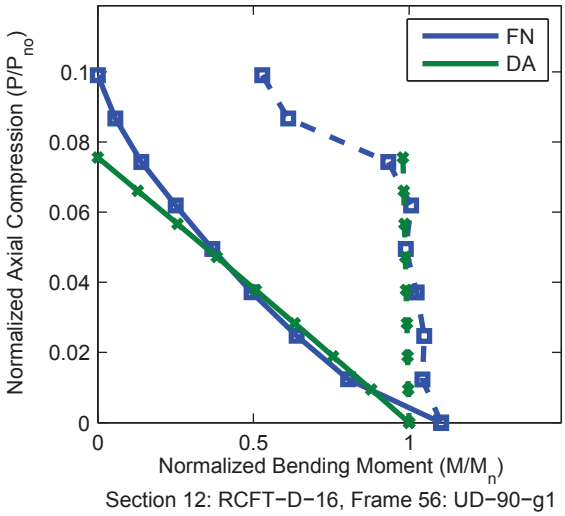

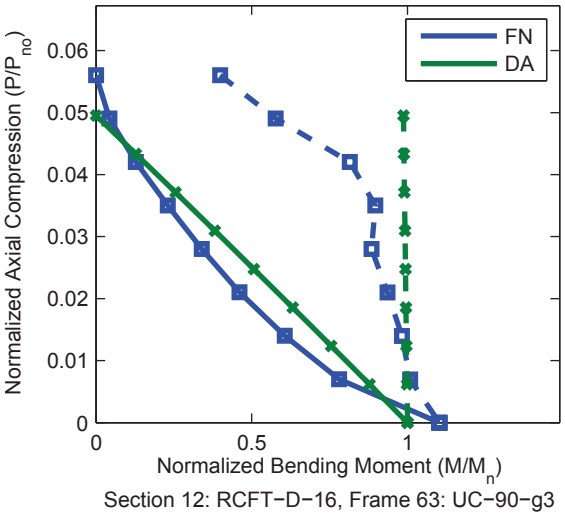

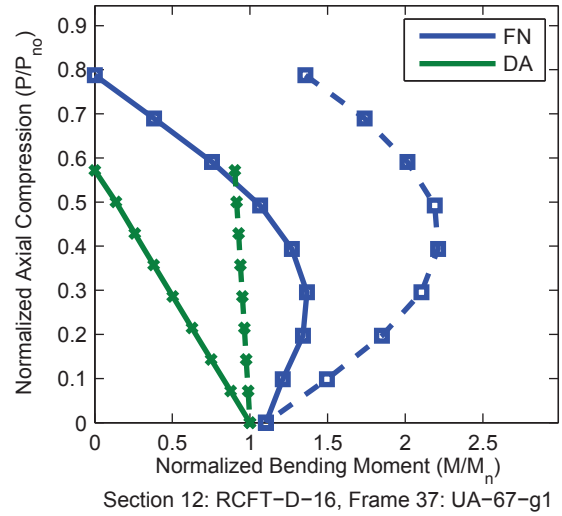

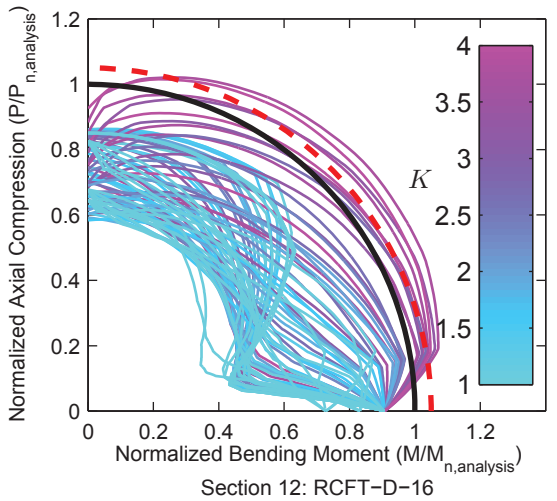

Figure A.27. Detailed Results for Section RCFT-D-16

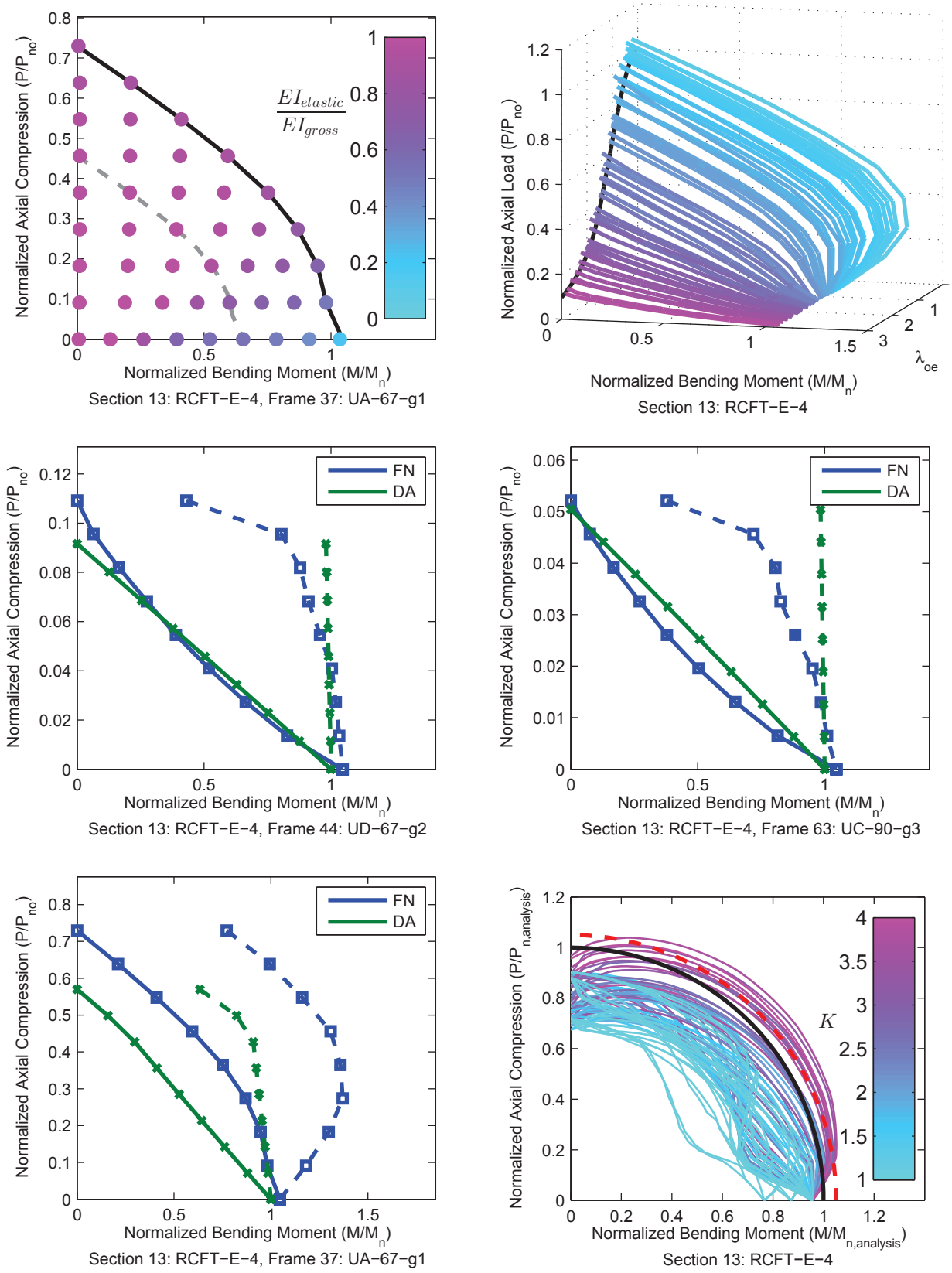

Figure A.28. Detailed Results for Section RCFT-E-4

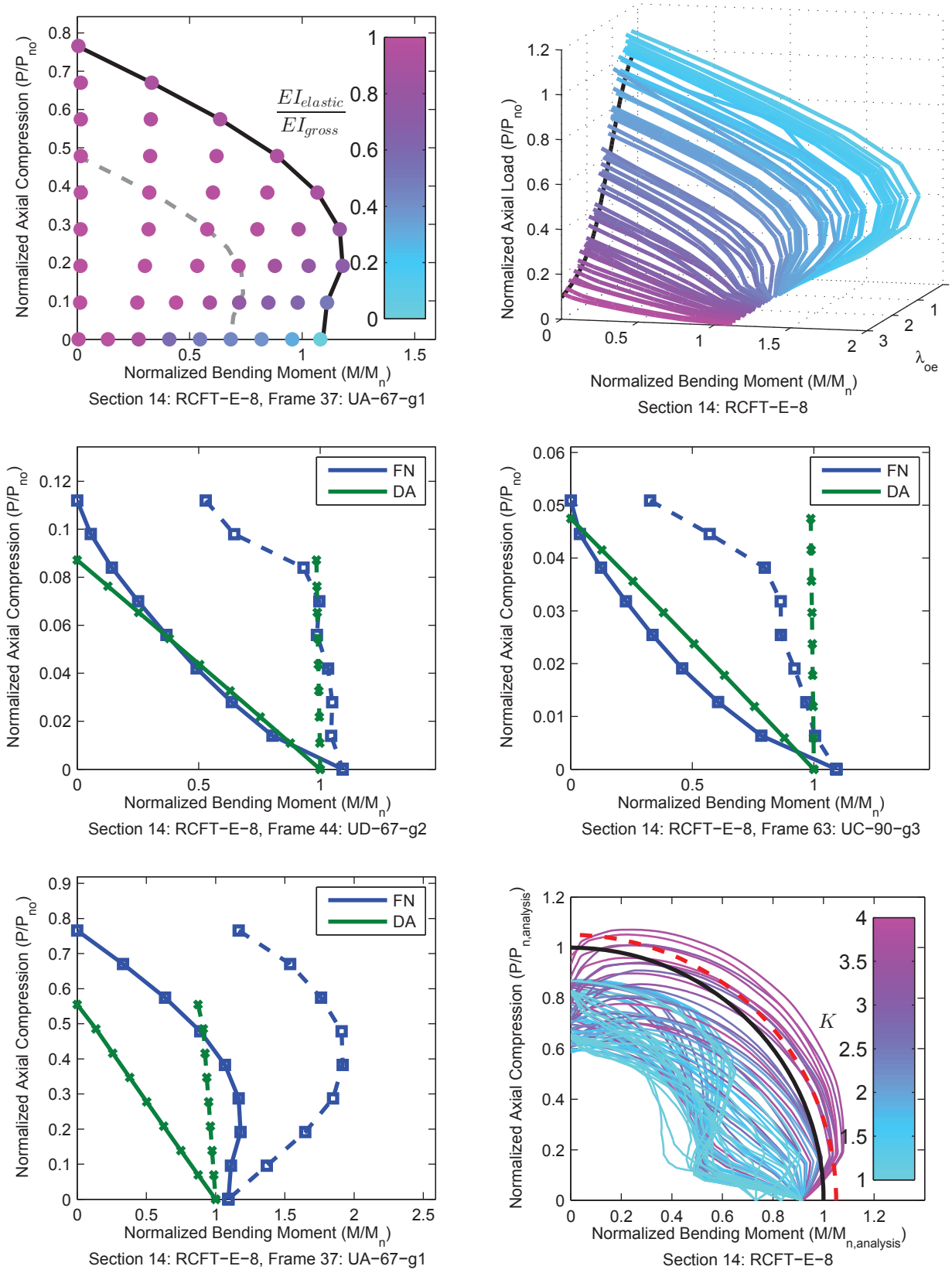

Figure A.29. Detailed Results for Section RCFT-E-8

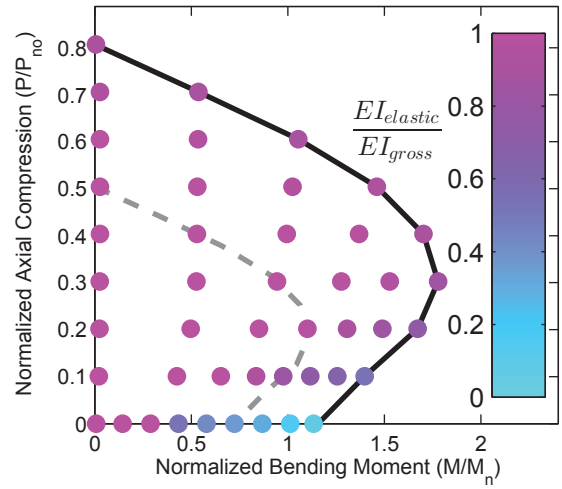

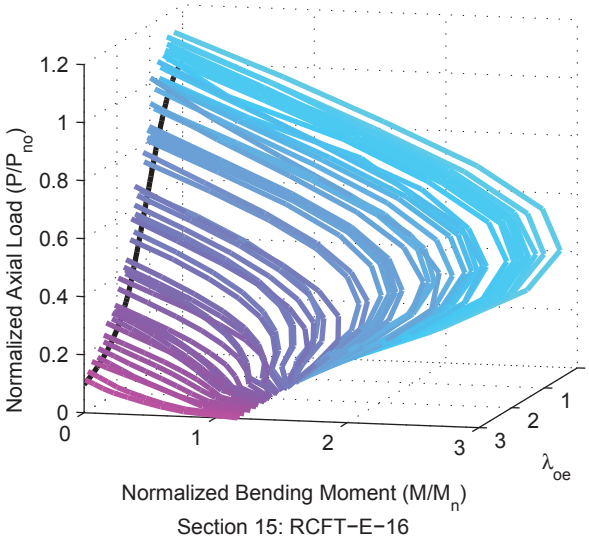

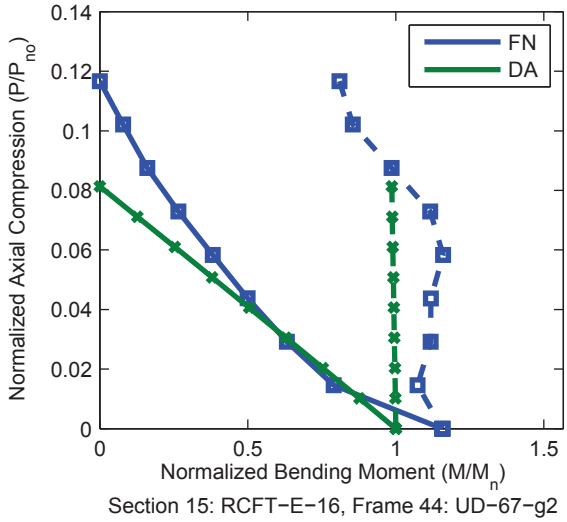

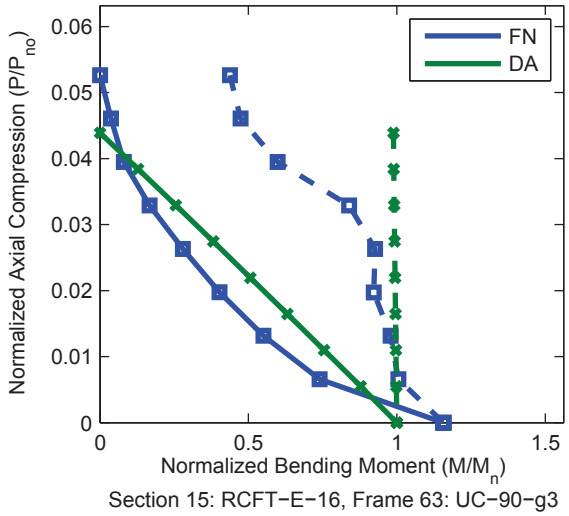

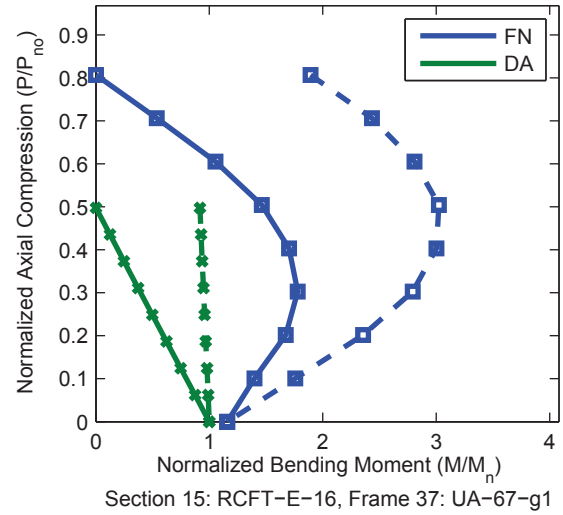

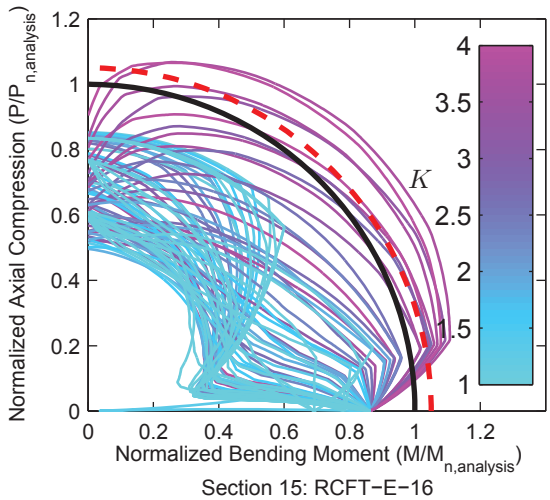

Figure A.30. Detailed Results for Section RCFT-E-16

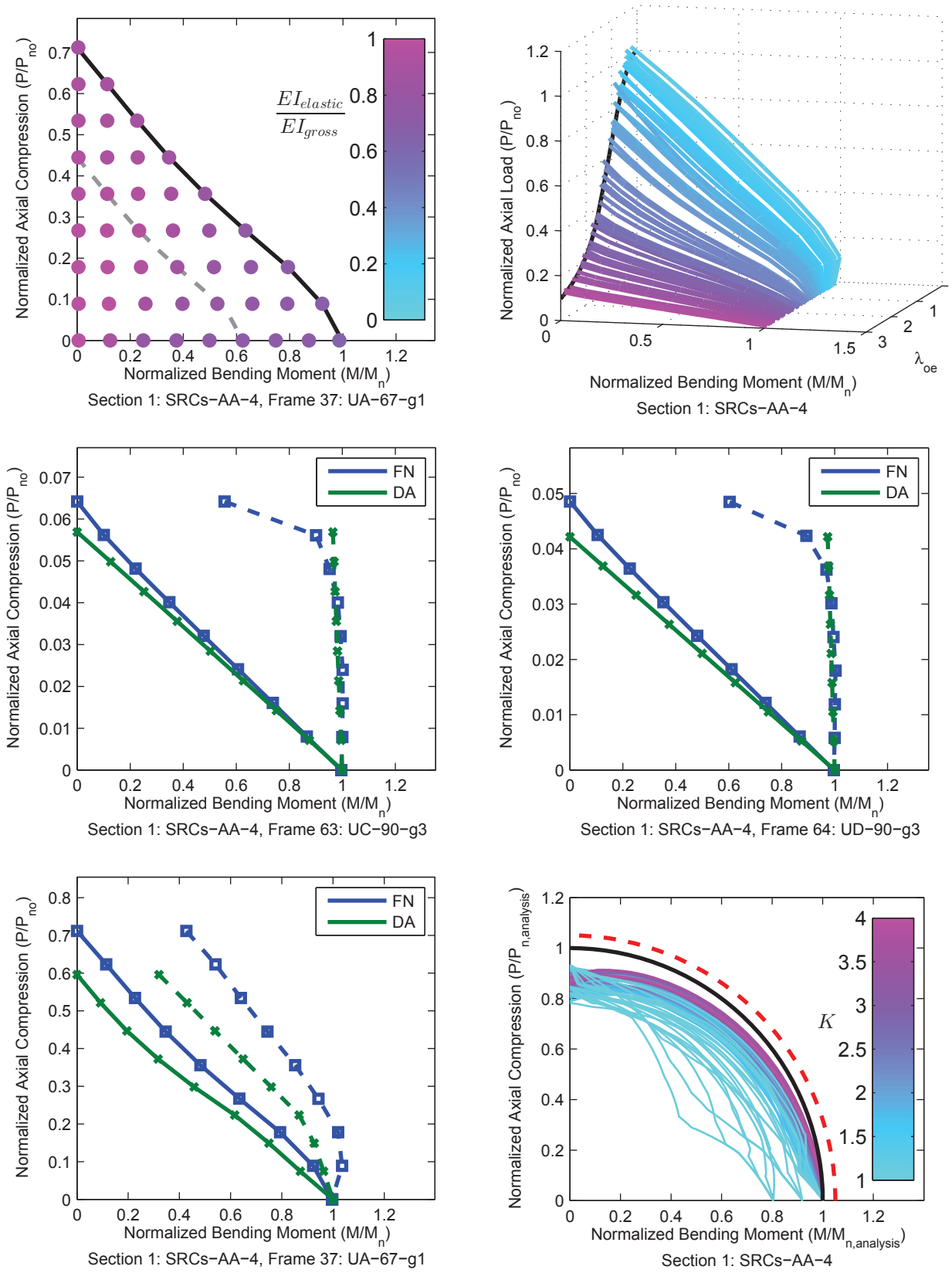

Figure A.31. Detailed Results for Section SRCs-AA-4

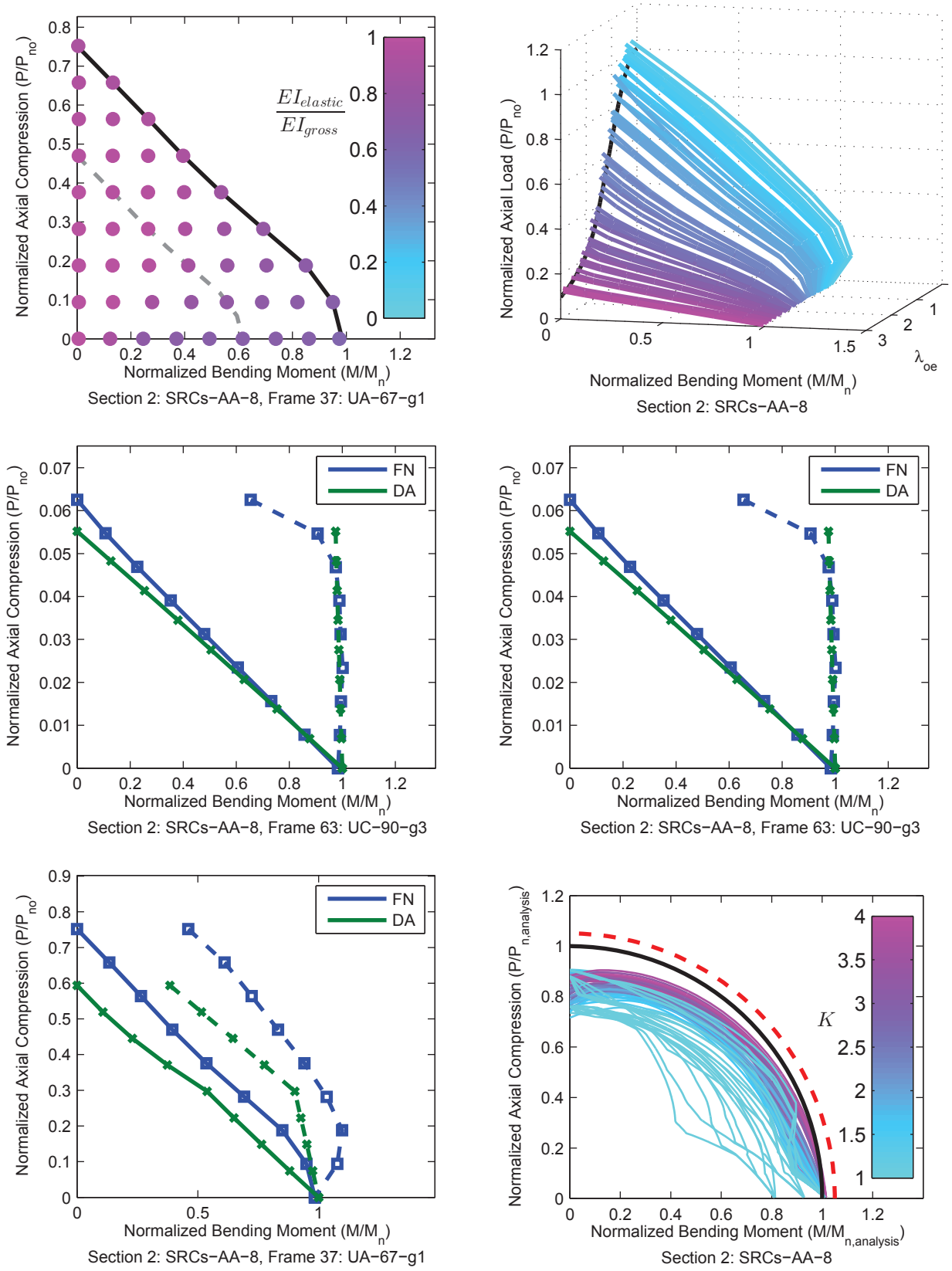

Figure A.32. Detailed Results for Section SRCs-AA-8

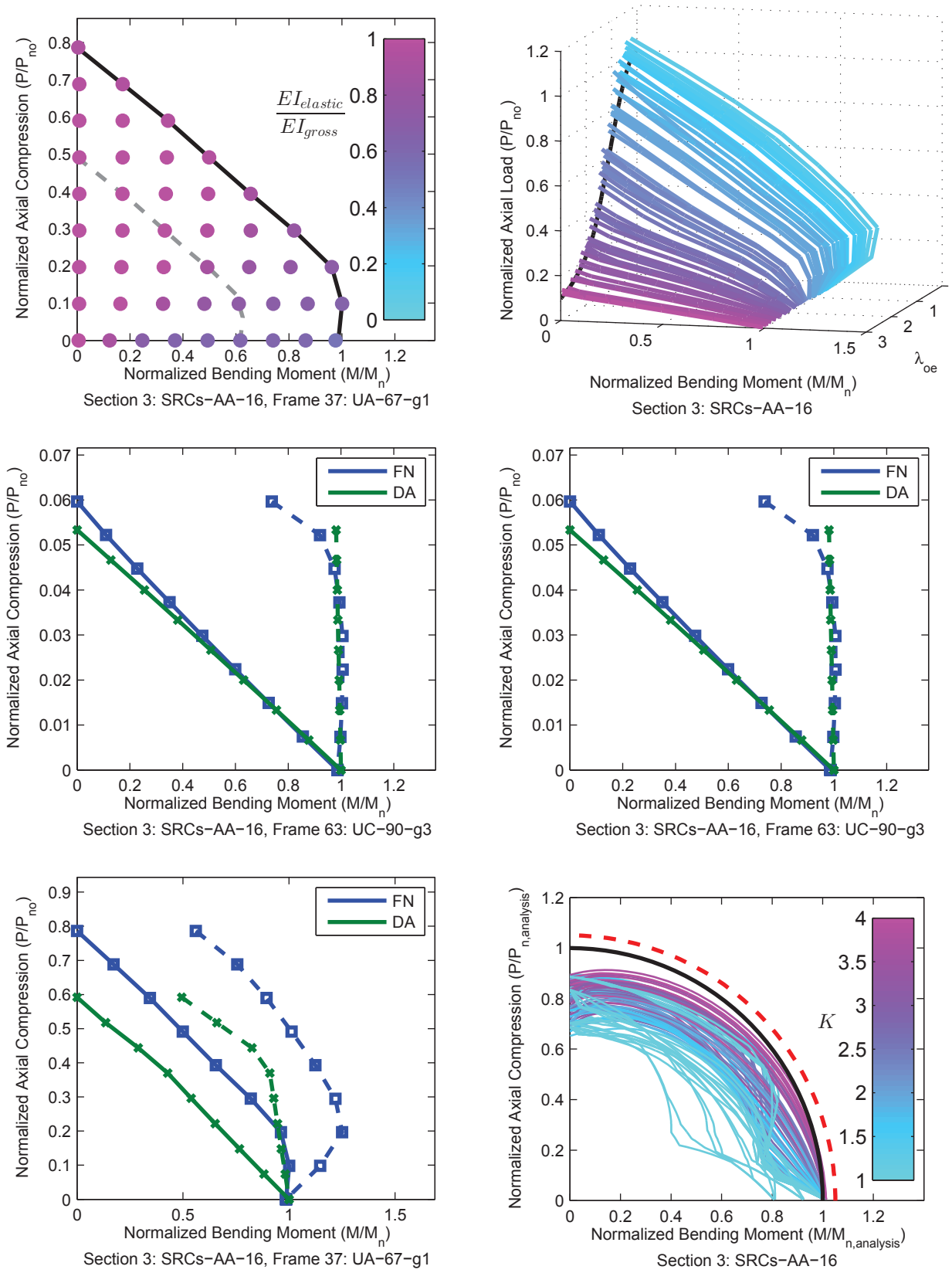

Figure A.33. Detailed Results for Section SRCs-AA-16

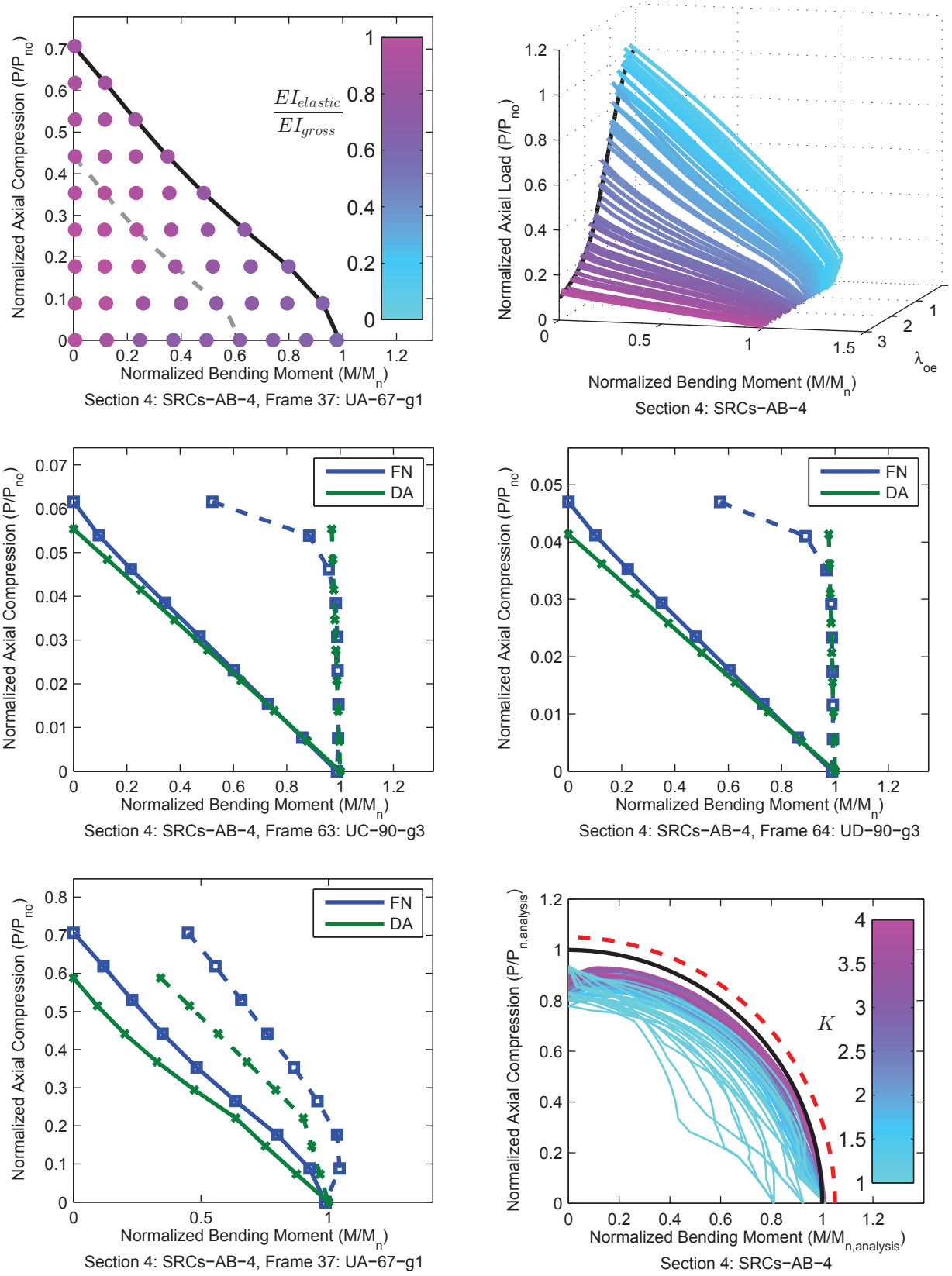

Figure A.34. Detailed Results for Section SRCs-AB-4

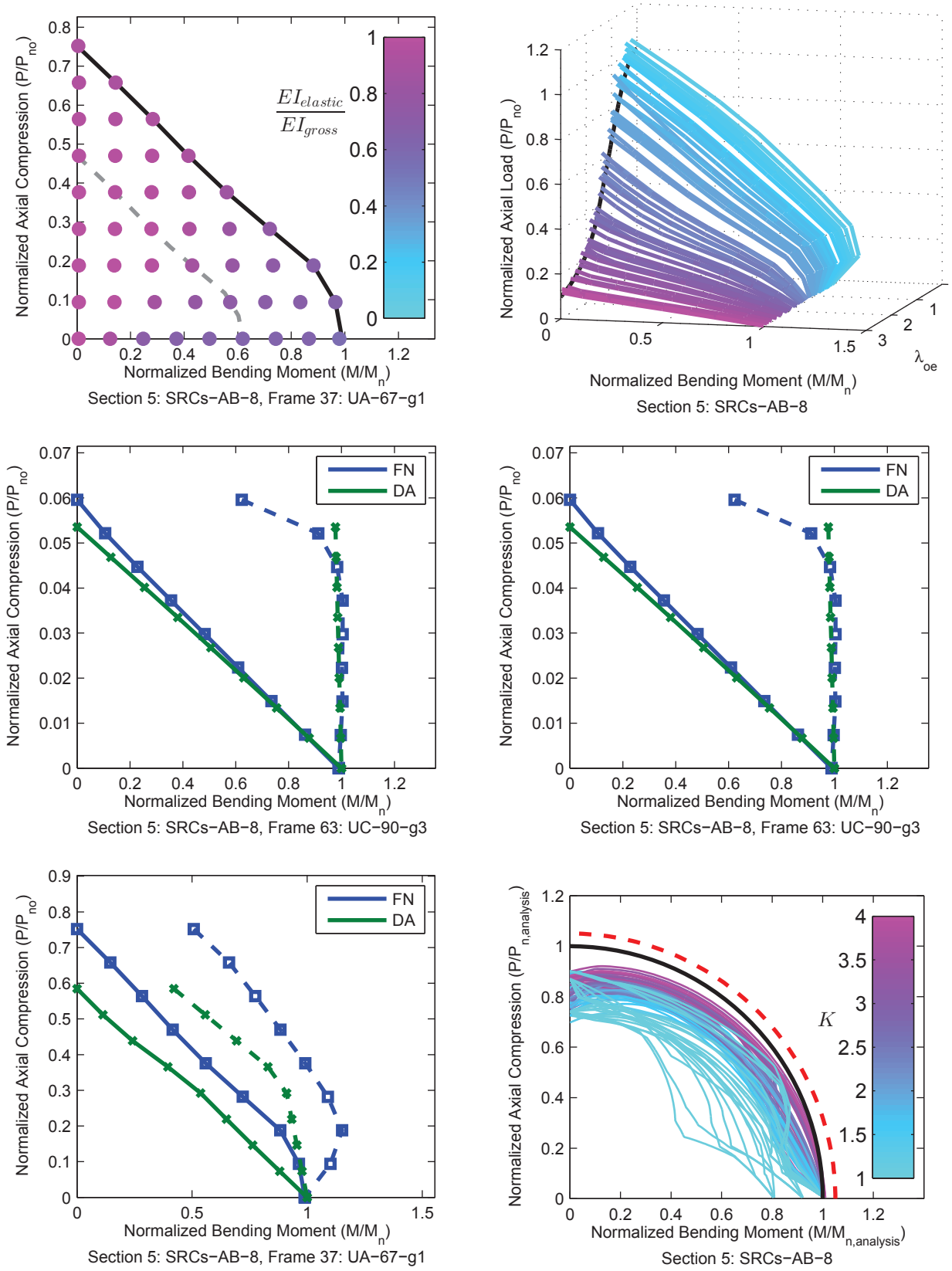

Figure A.35. Detailed Results for Section SRCs-AB-8

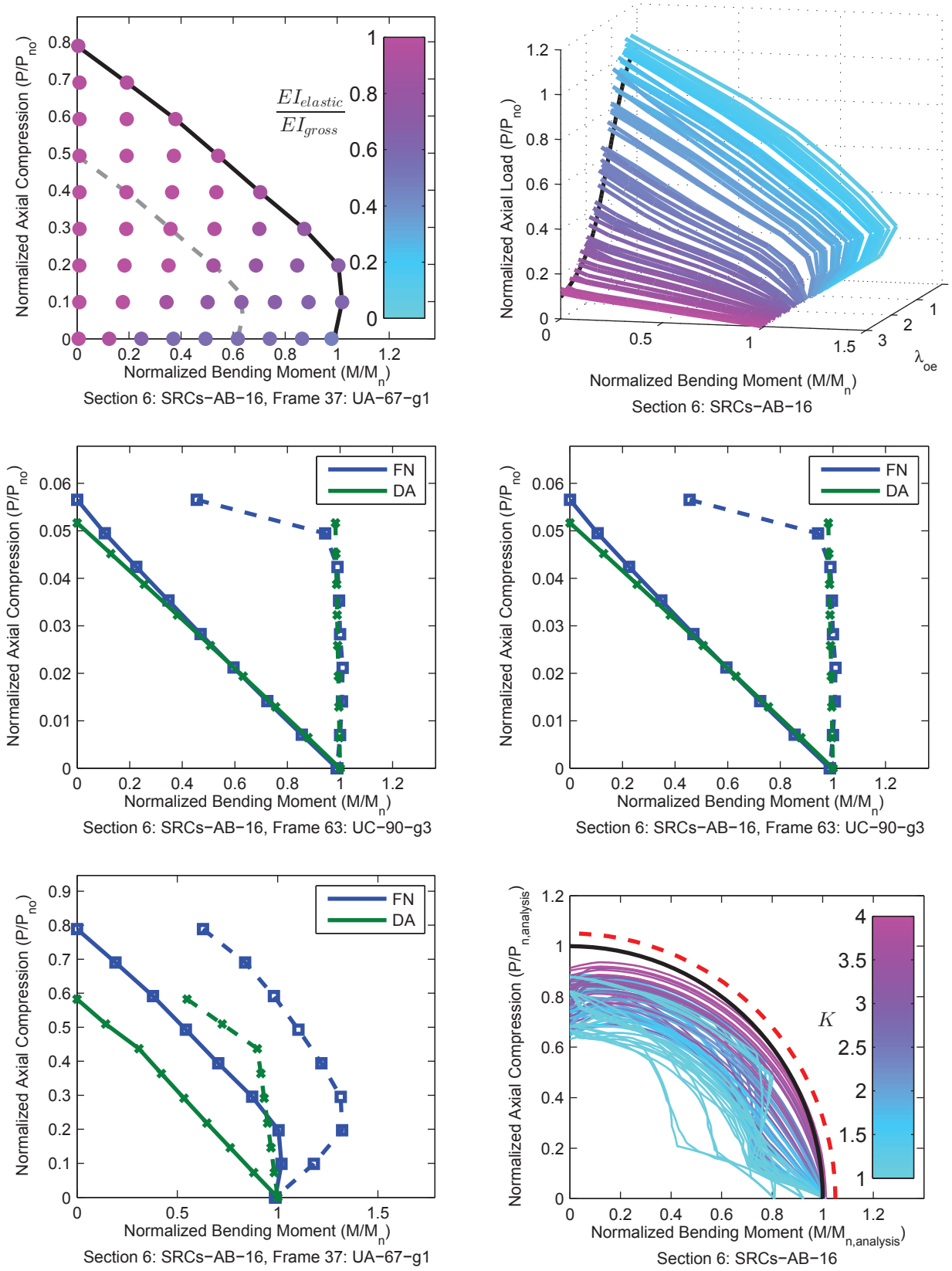

Figure A.36. Detailed Results for Section SRCs-AB-16

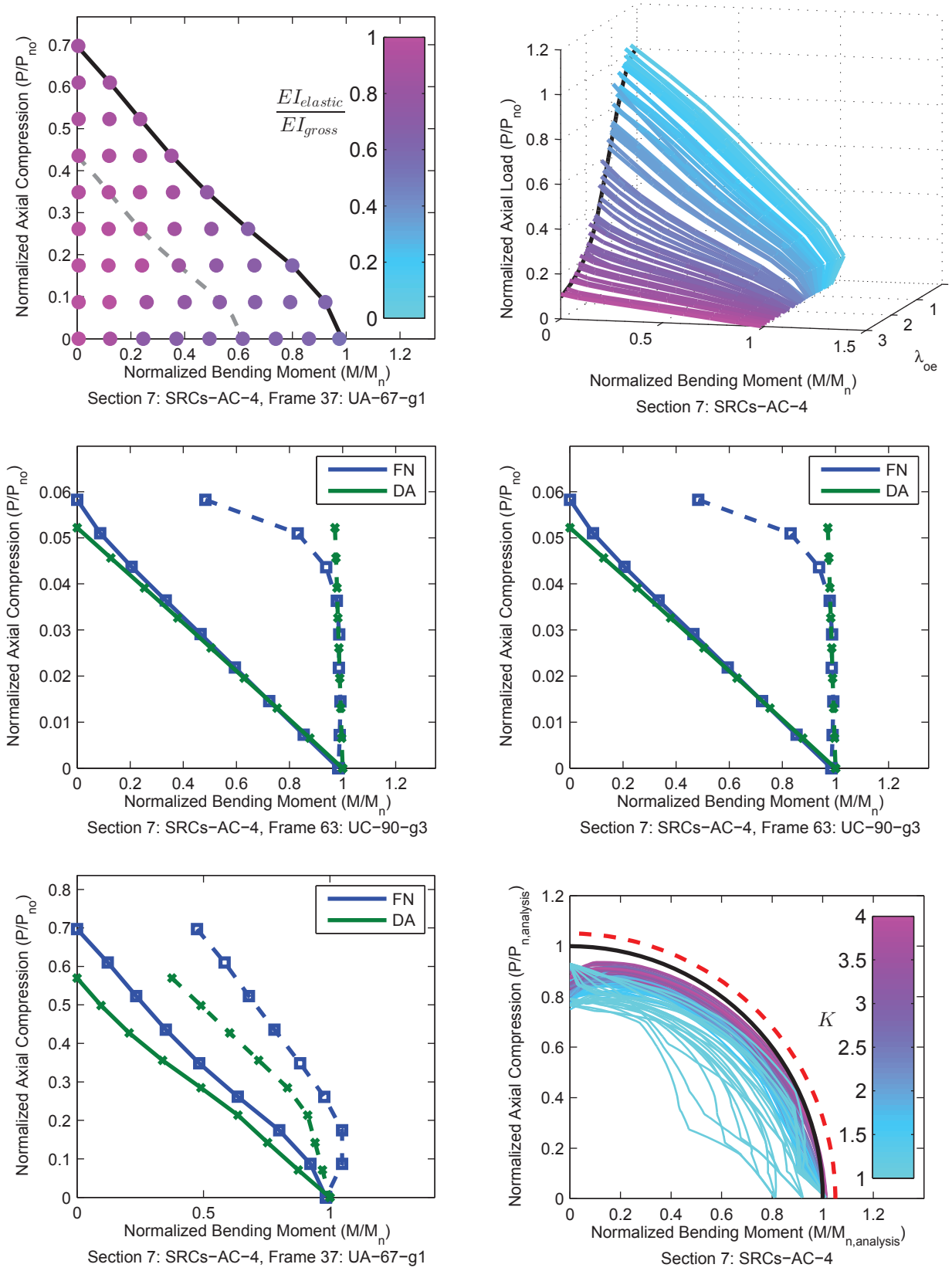

Figure A.37. Detailed Results for Section SRCs-AC-4

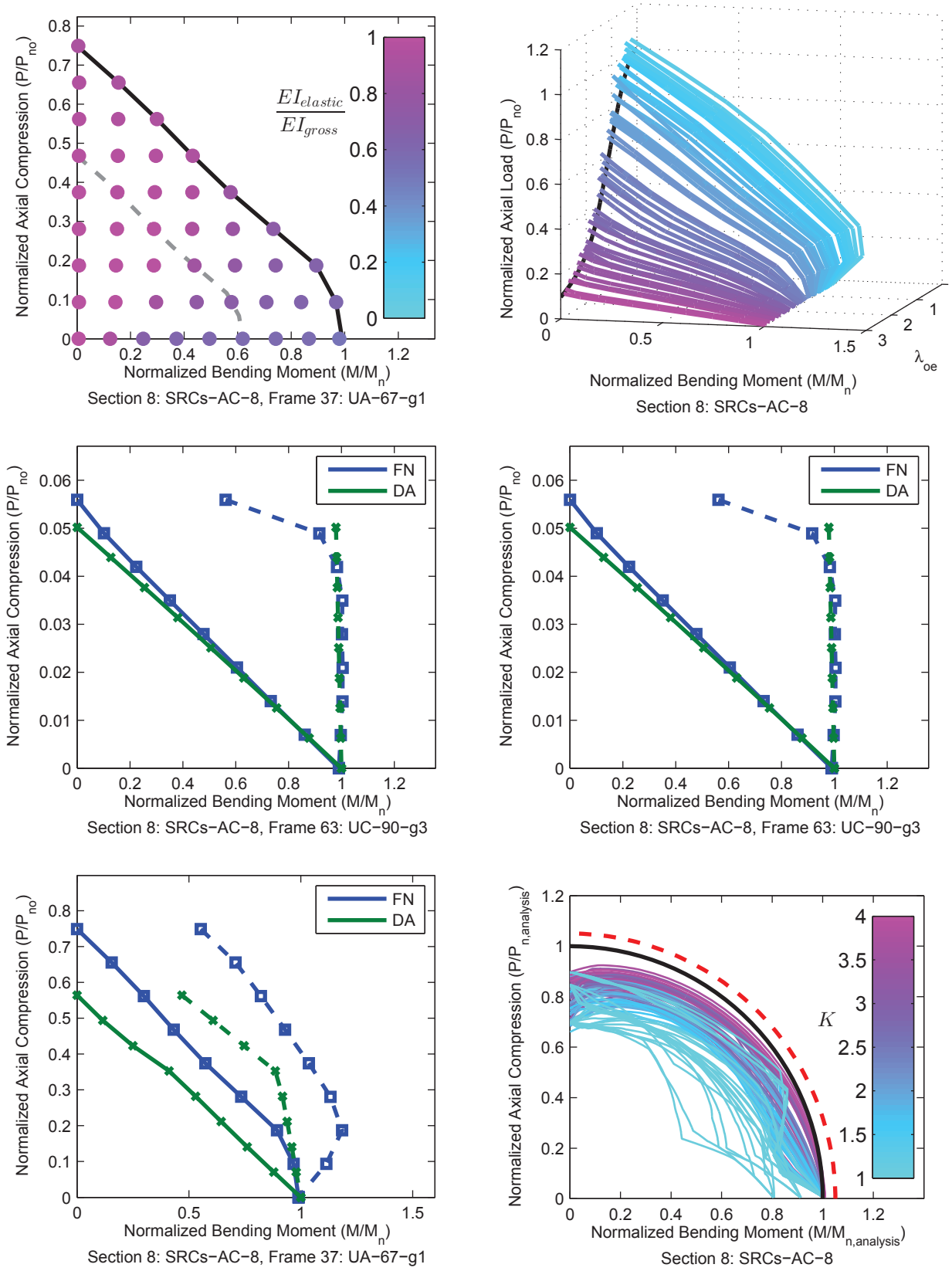

Figure A.38. Detailed Results for Section SRCs-AC-8

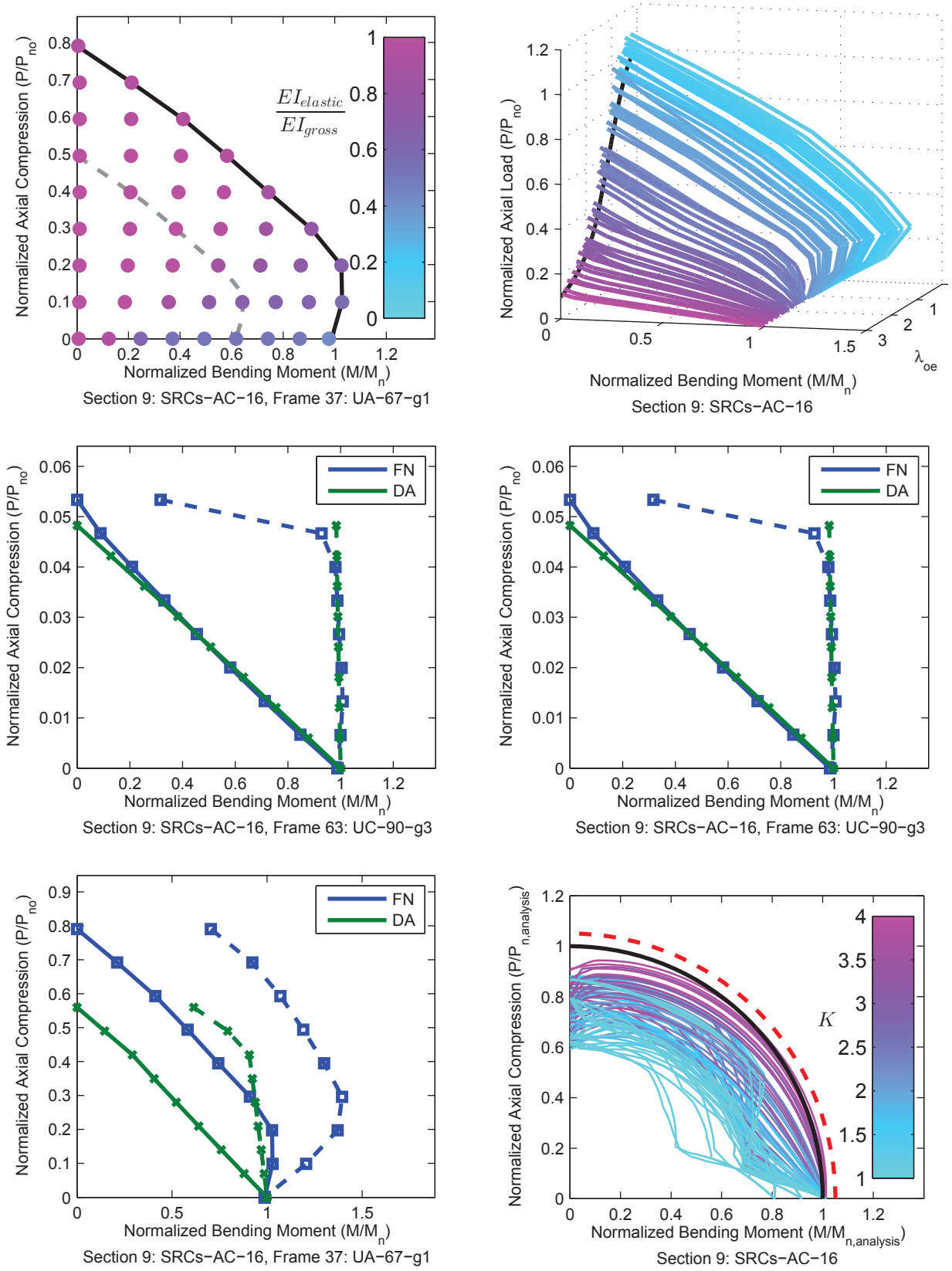

Figure A.39. Detailed Results for Section SRCs-AC-16

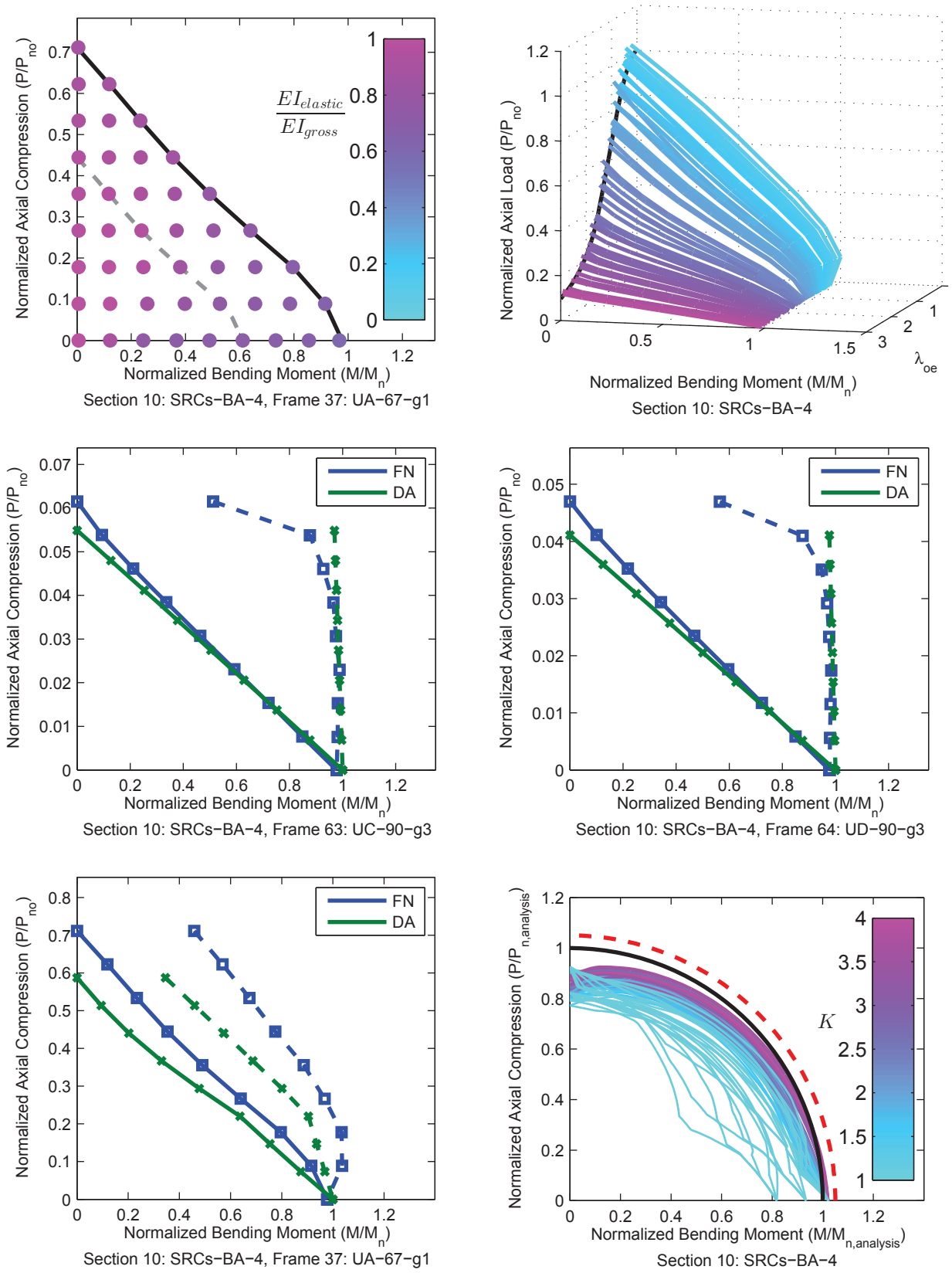

Figure A.40. Detailed Results for Section SRCs-BA-4

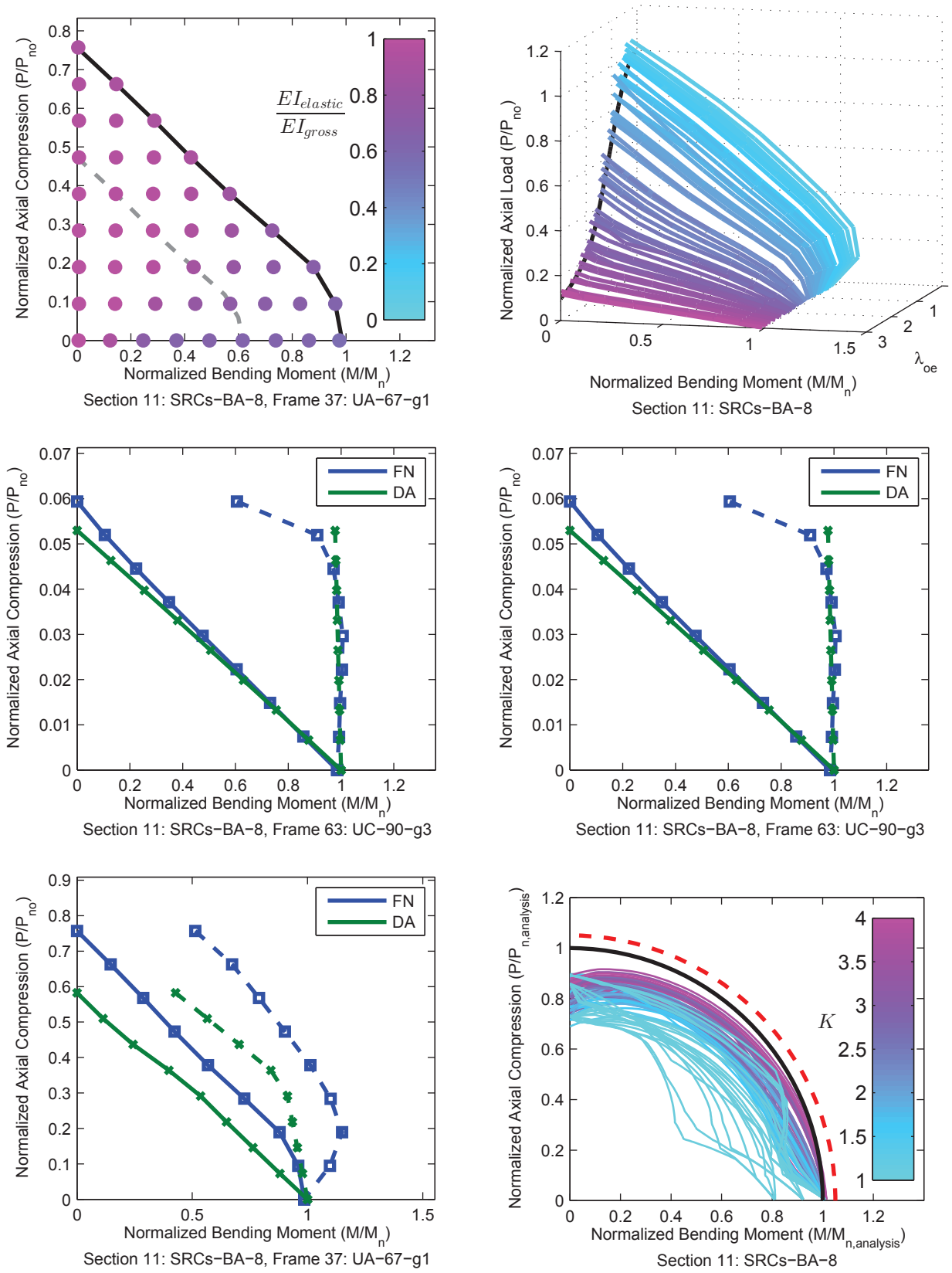

Figure A.41. Detailed Results for Section SRCs-BA-8

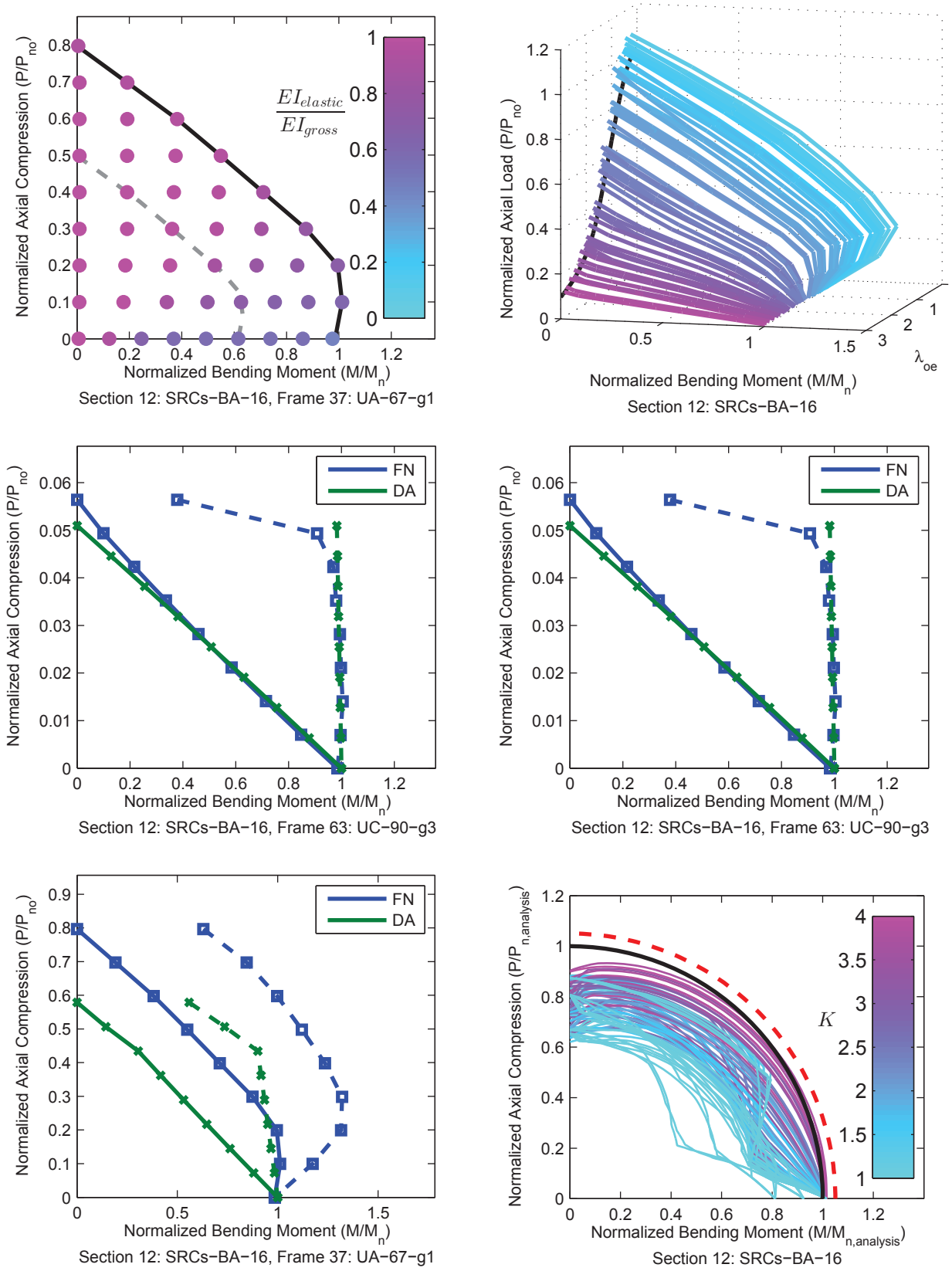

Figure A.42. Detailed Results for Section SRCs-BA-16

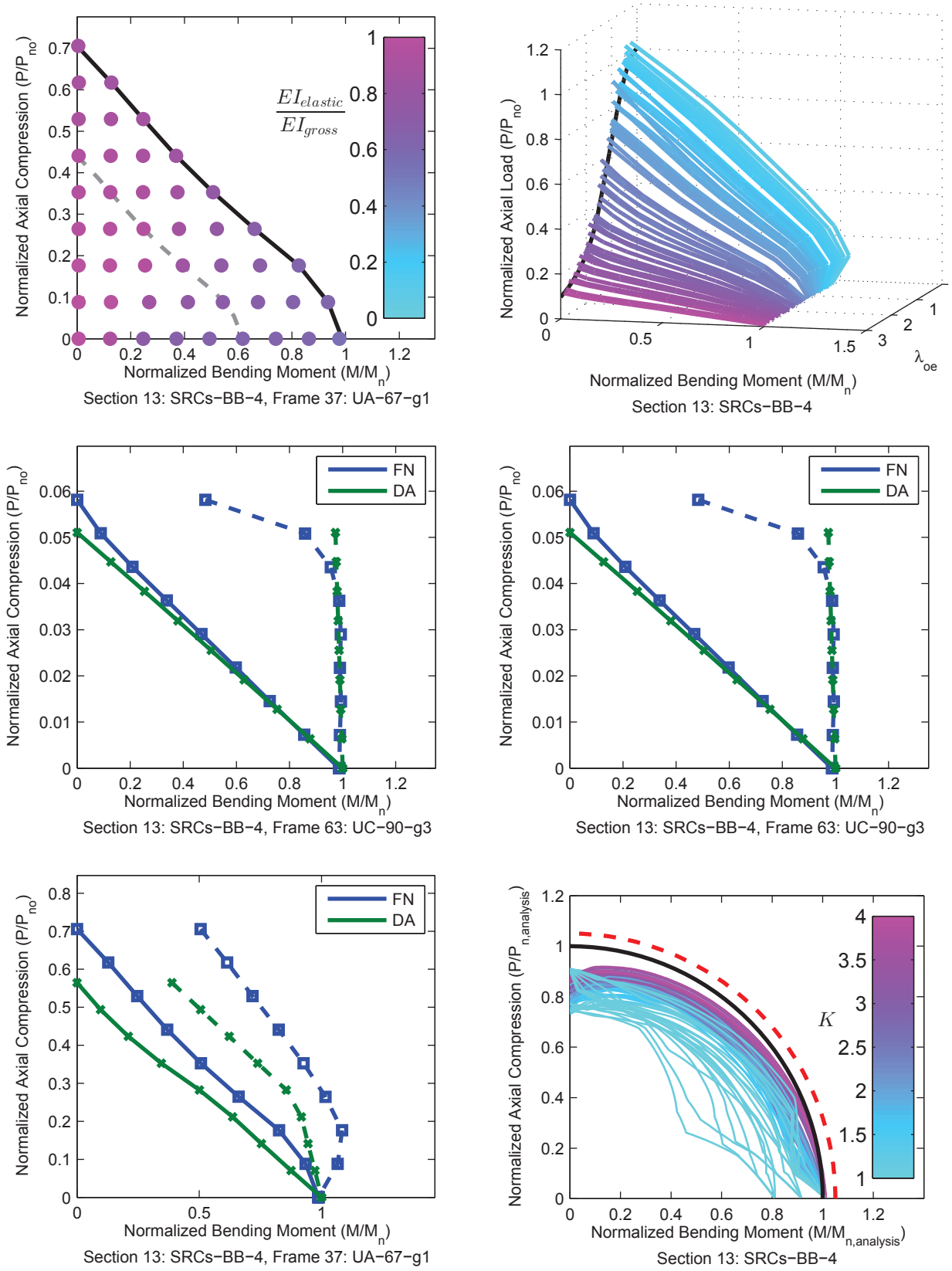

Figure A.43. Detailed Results for Section SRCs-BB-4

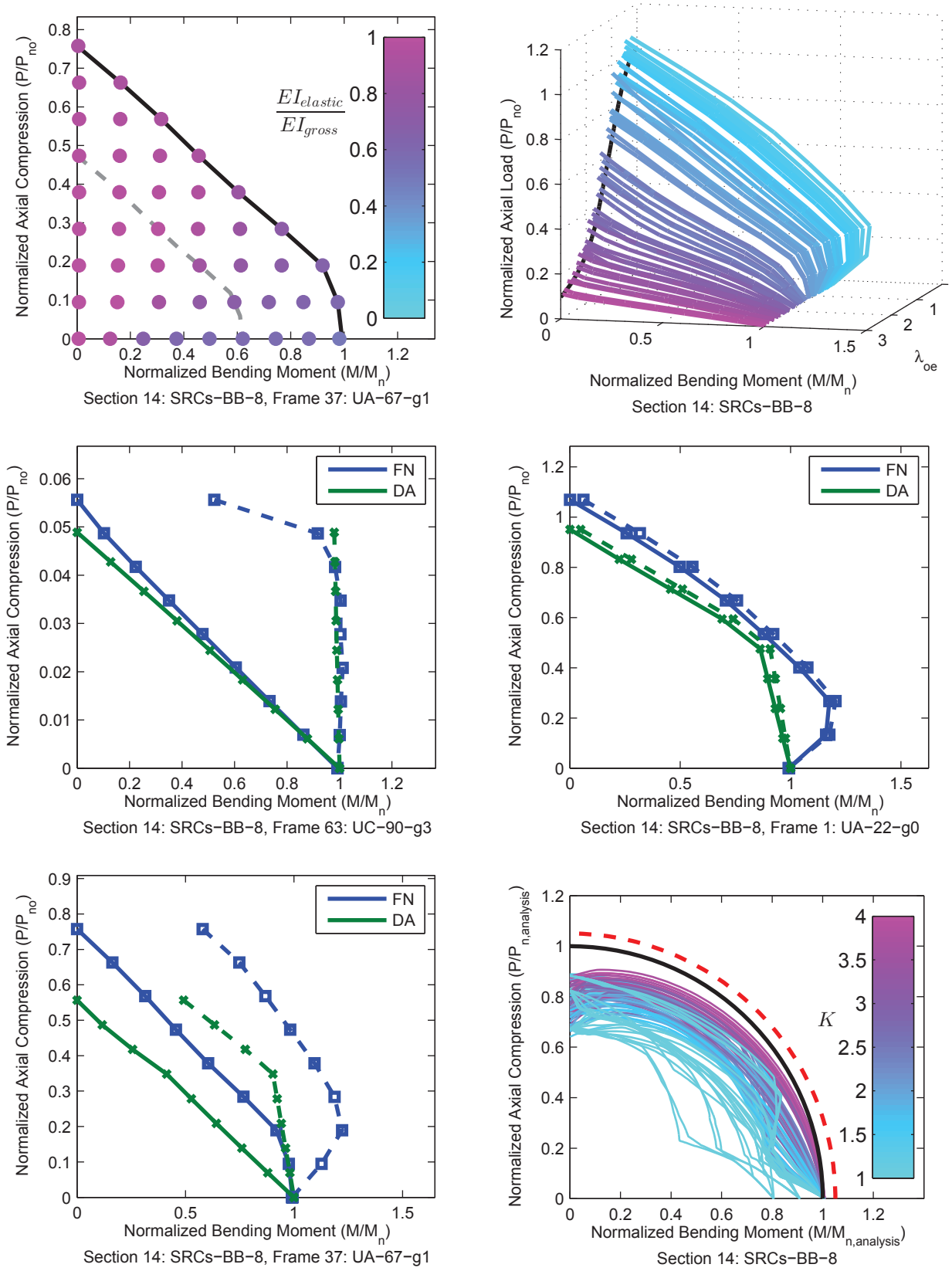

Figure A.44. Detailed Results for Section SRCs-BB-8

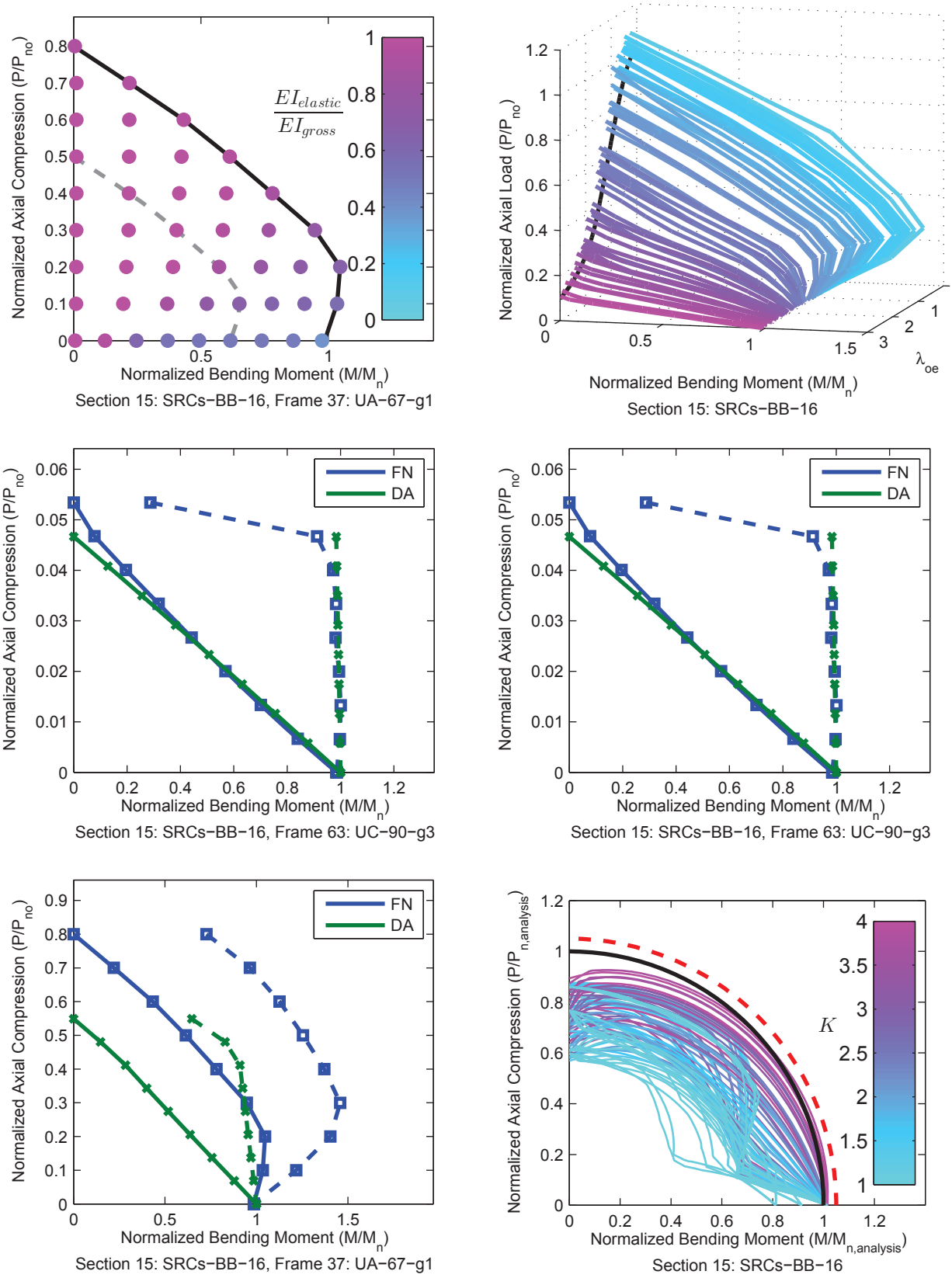

Figure A.45. Detailed Results for Section SRCs-BB-16

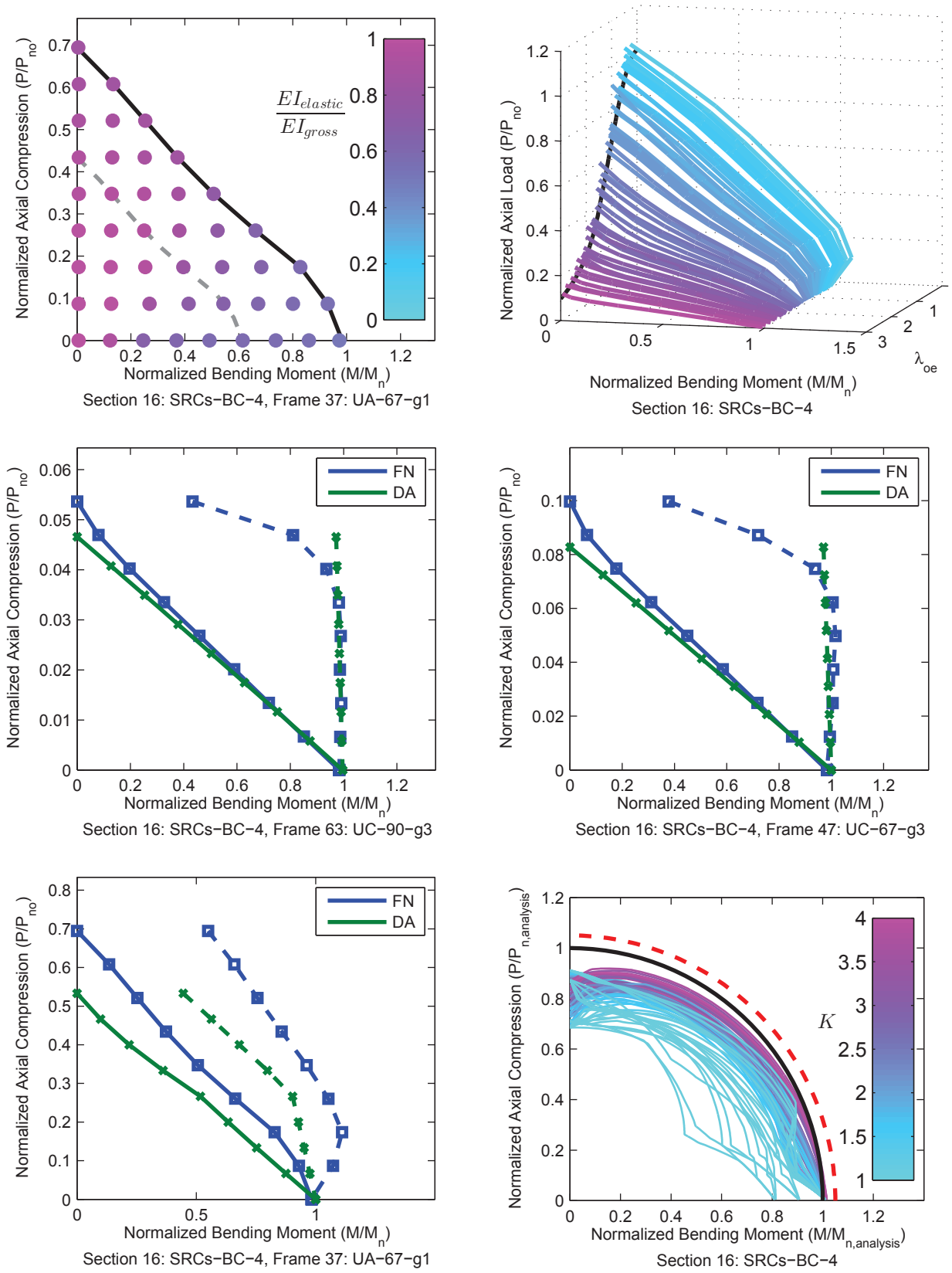

Figure A.46. Detailed Results for Section SRCs-BC-4

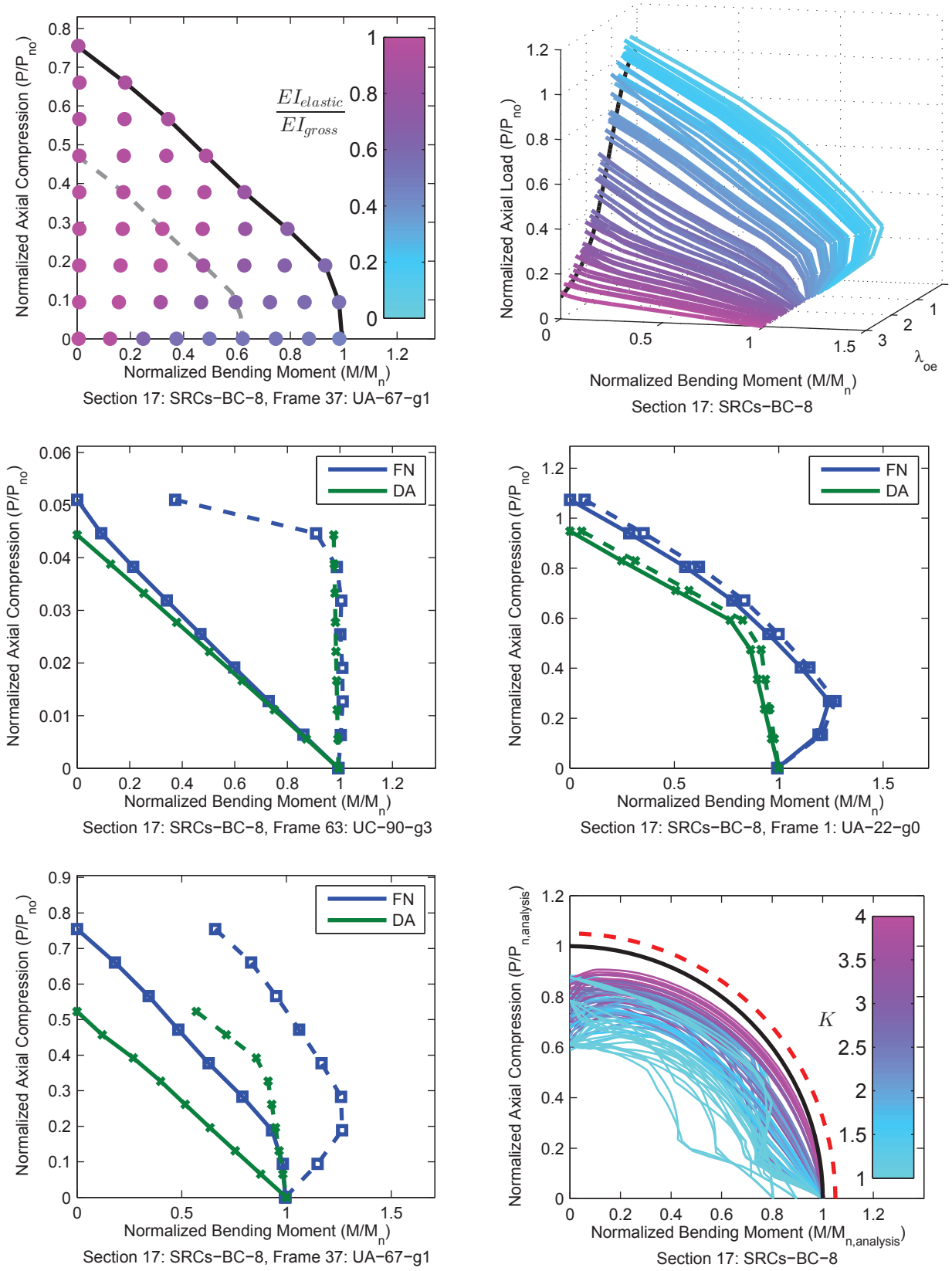

Figure A.47. Detailed Results for Section SRCs-BC-8

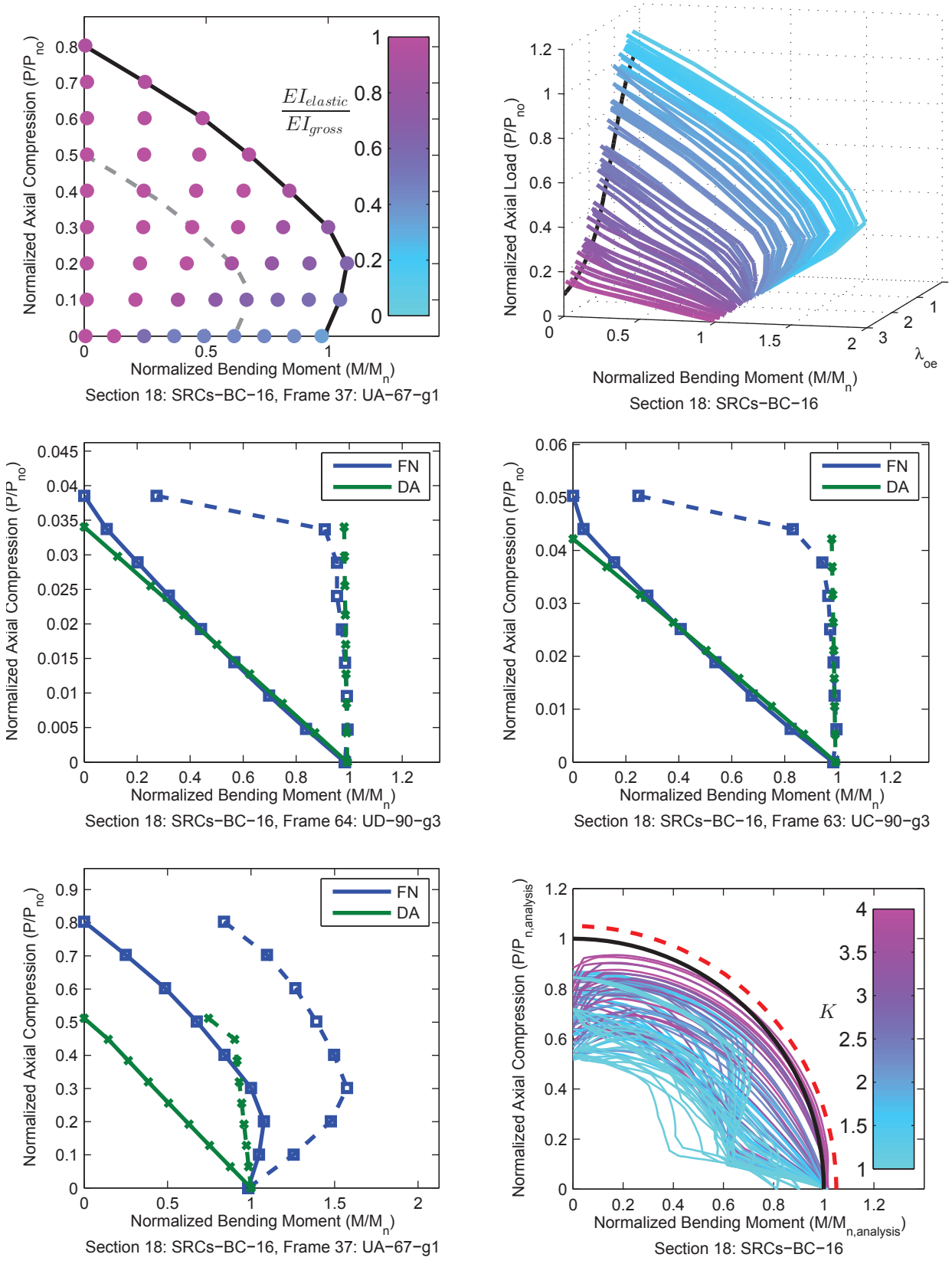

Figure A.48. Detailed Results for Section SRCs-BC-16

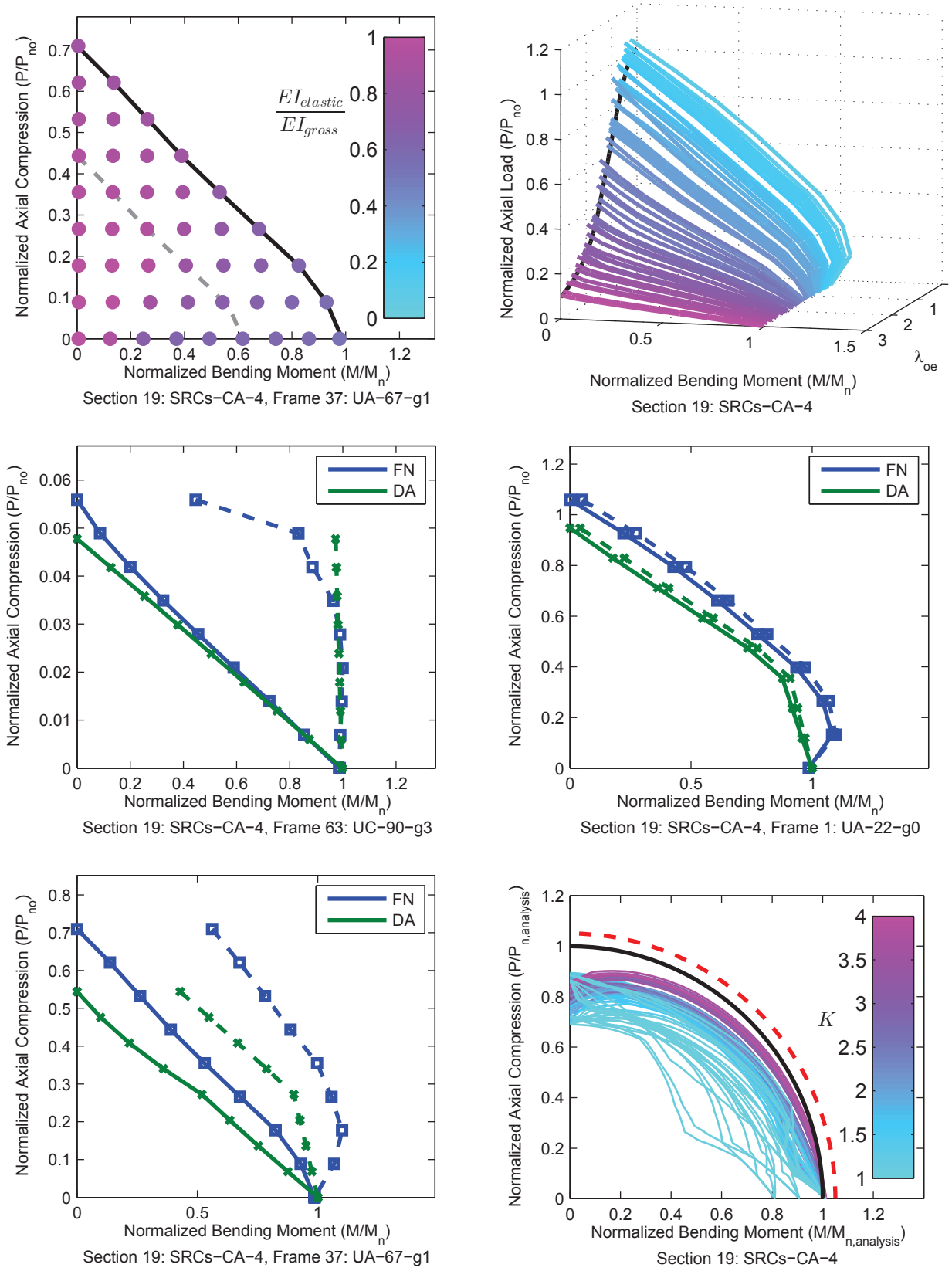

Figure A.49. Detailed Results for Section SRCs-CA-4

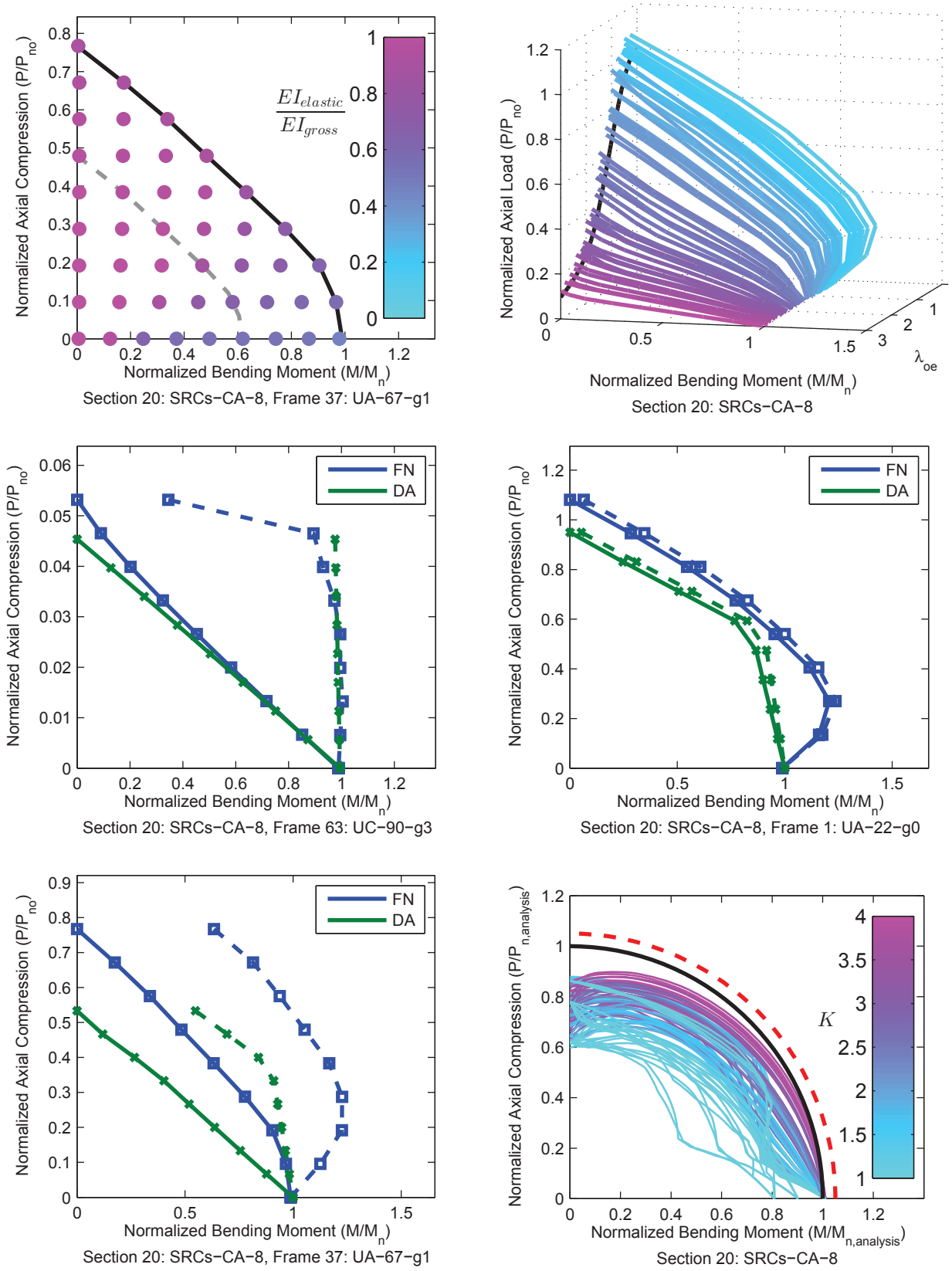

Figure A.50. Detailed Results for Section SRCs-CA-8

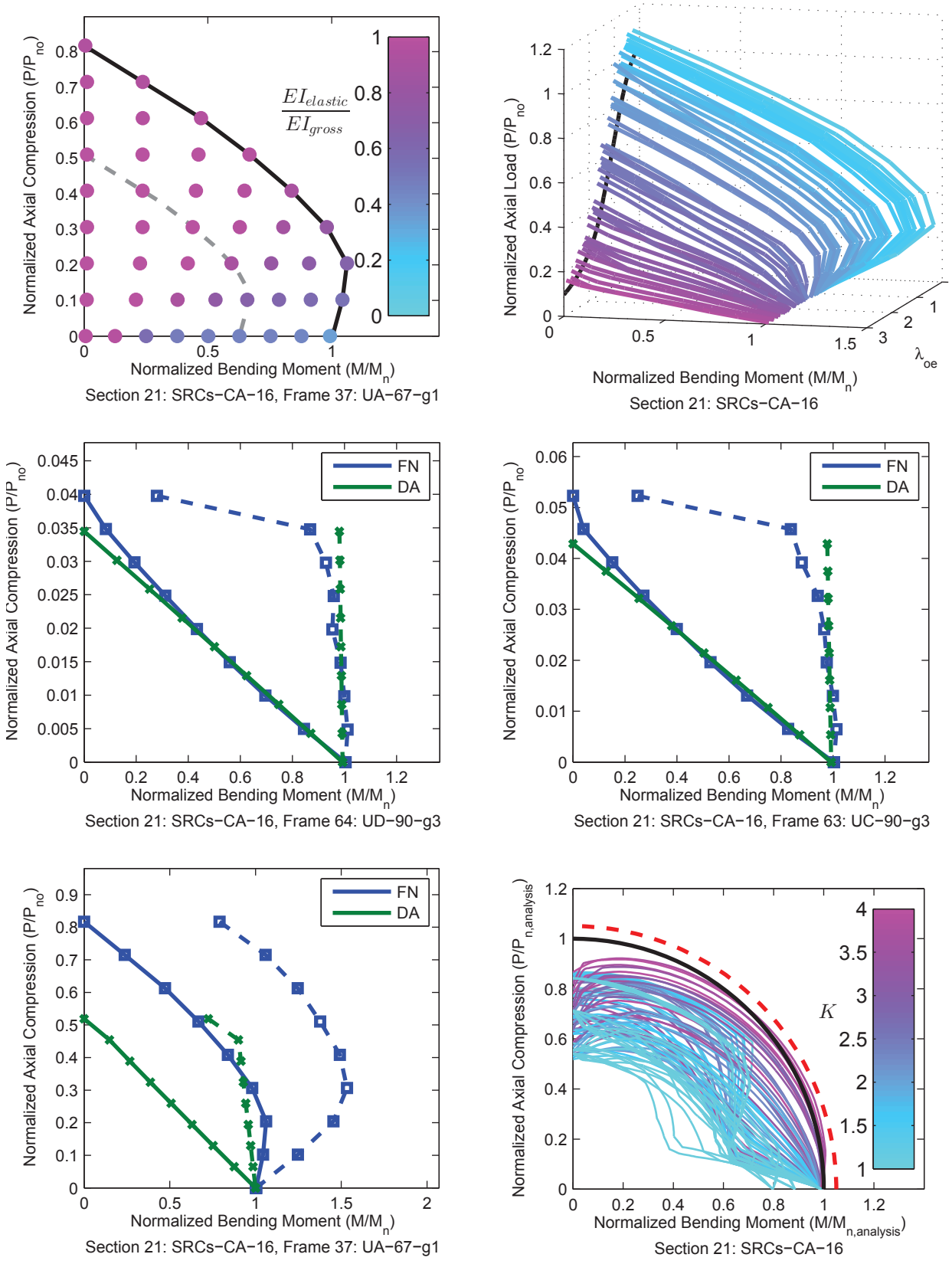

Figure A.51. Detailed Results for Section SRCs-CA-16

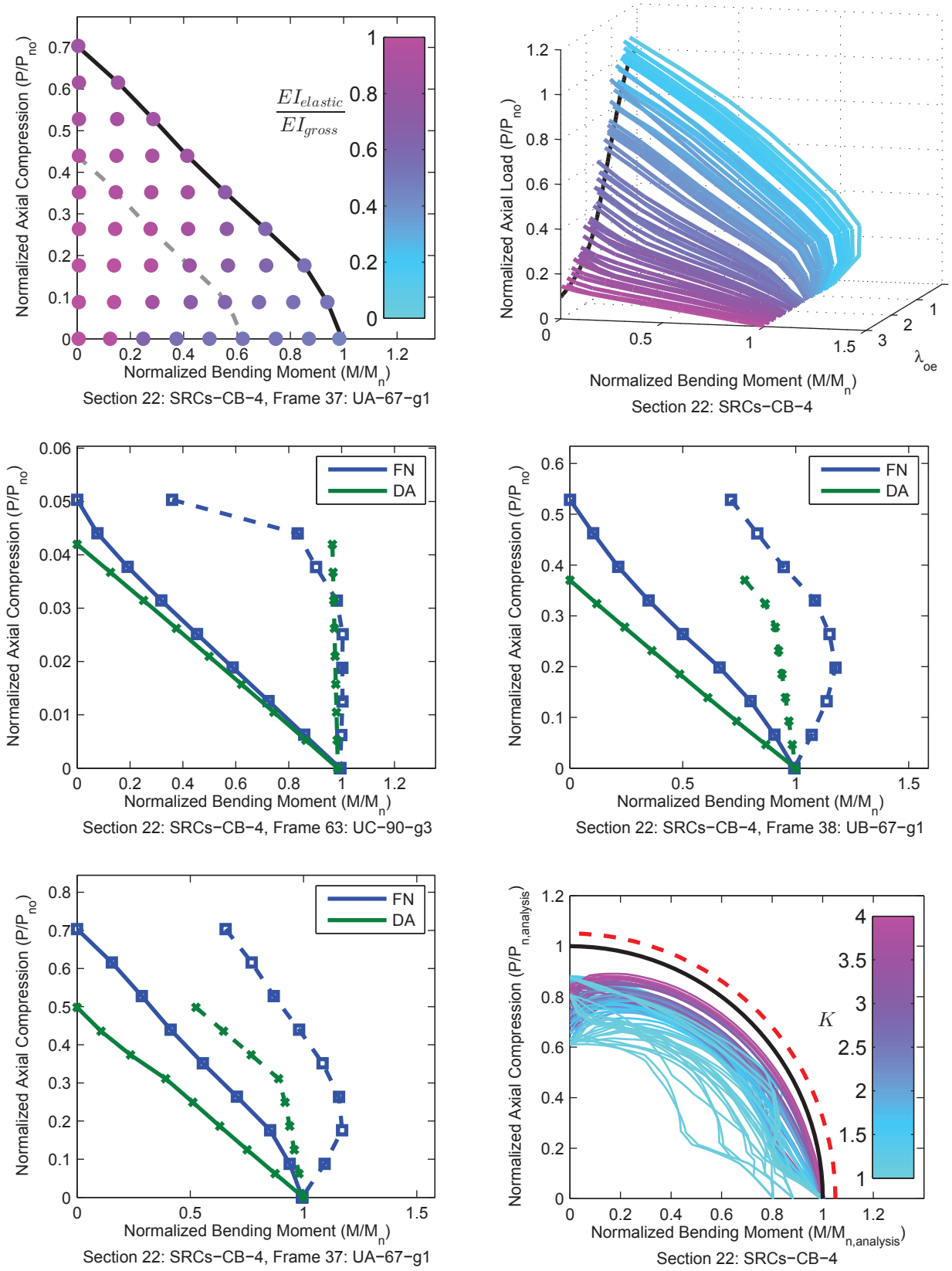

Figure A.52. Detailed Results for Section SRCs-CB-4

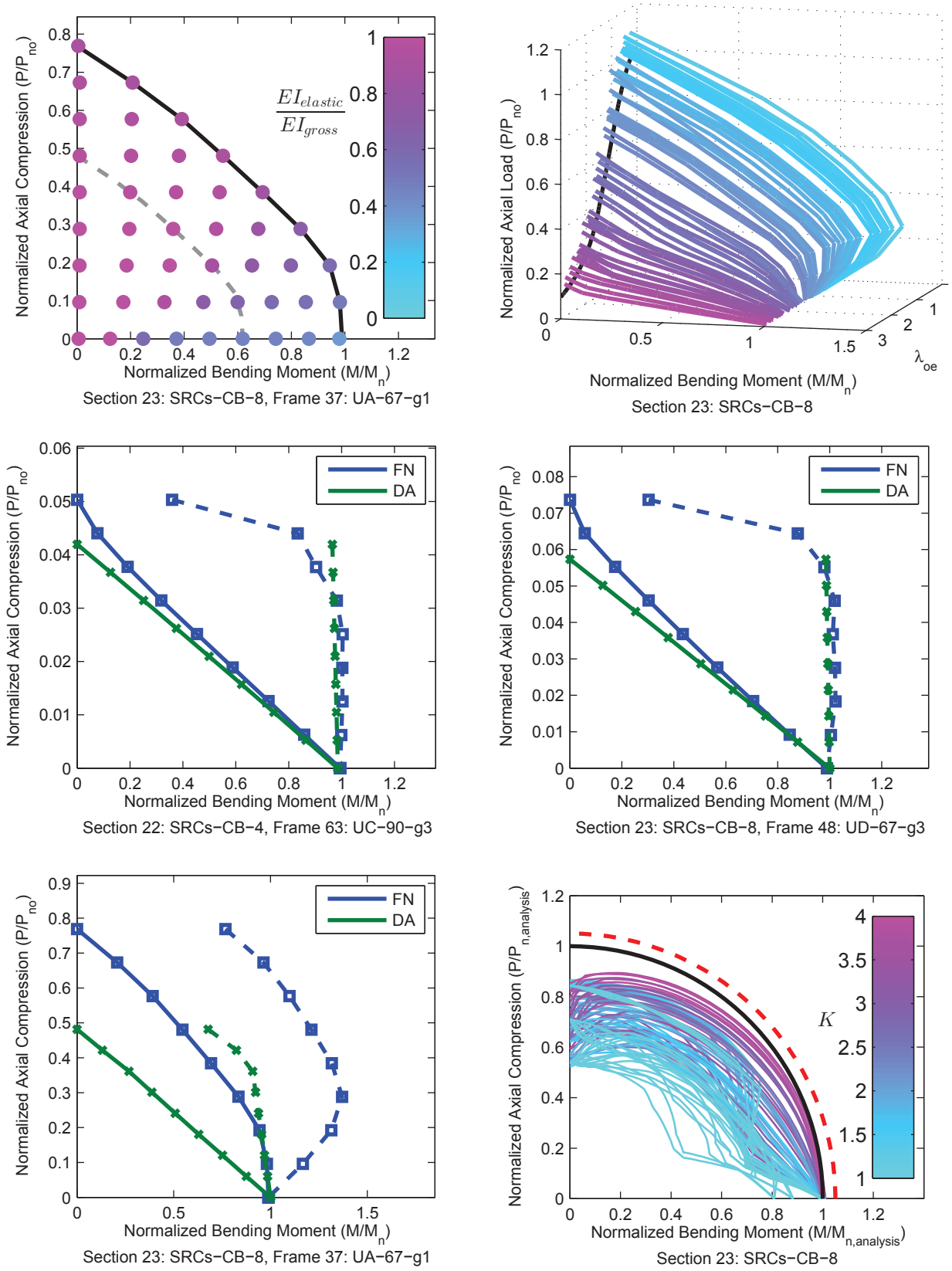

Figure A.53. Detailed Results for Section SRCs-CB-8

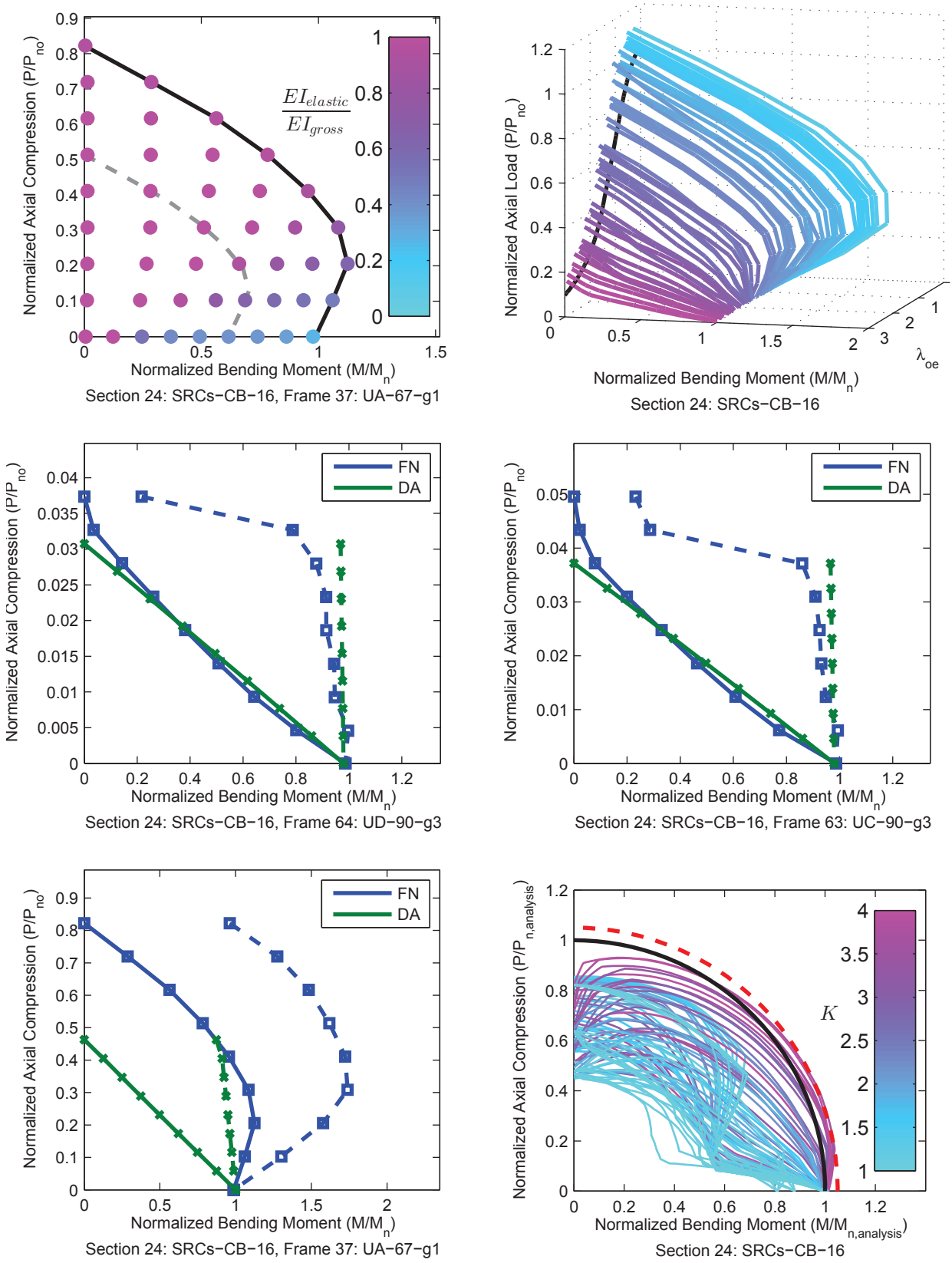

Figure A.54. Detailed Results for Section SRCs-CB-16

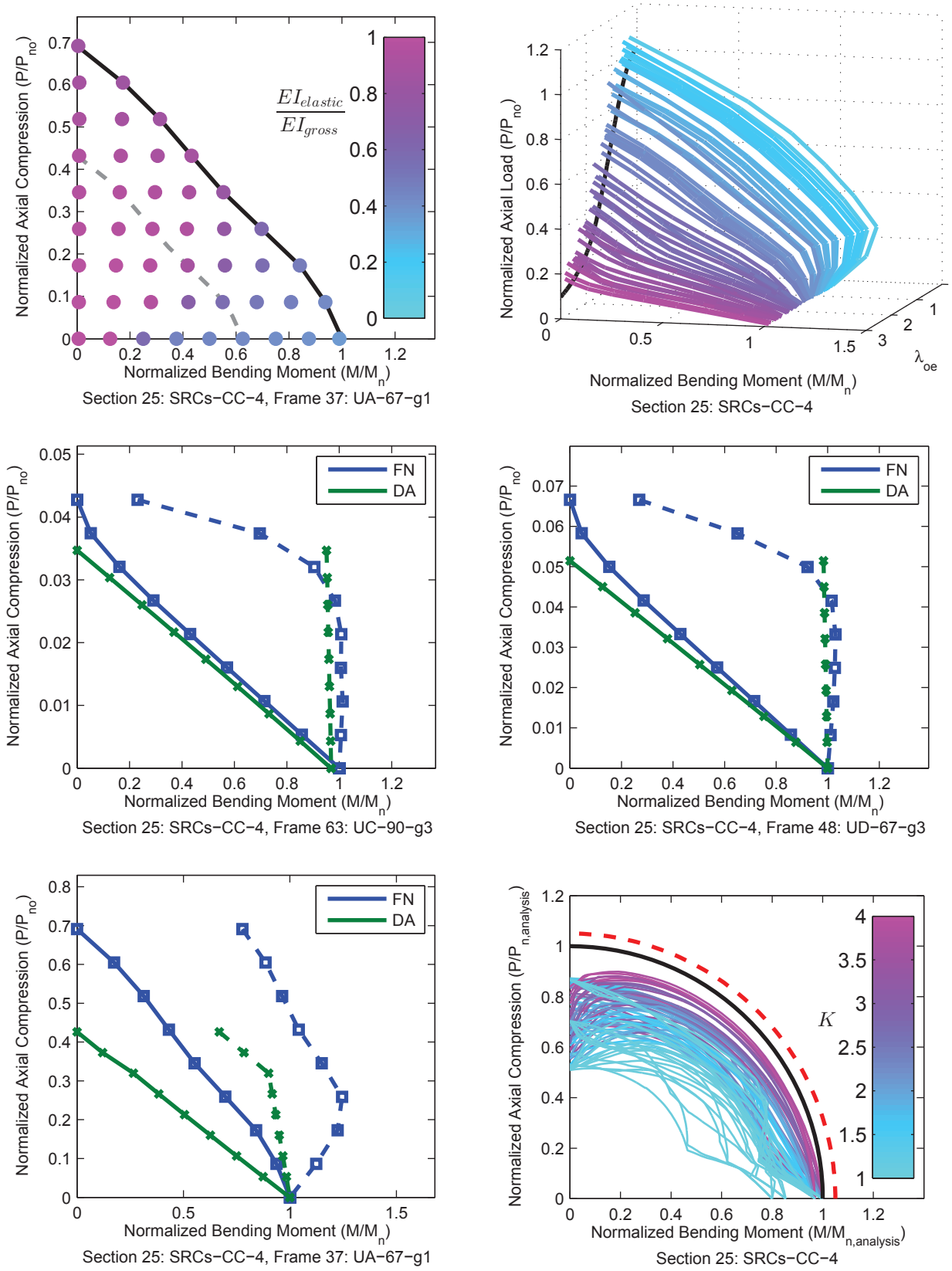

Figure A.55. Detailed Results for Section SRCs-CC-4

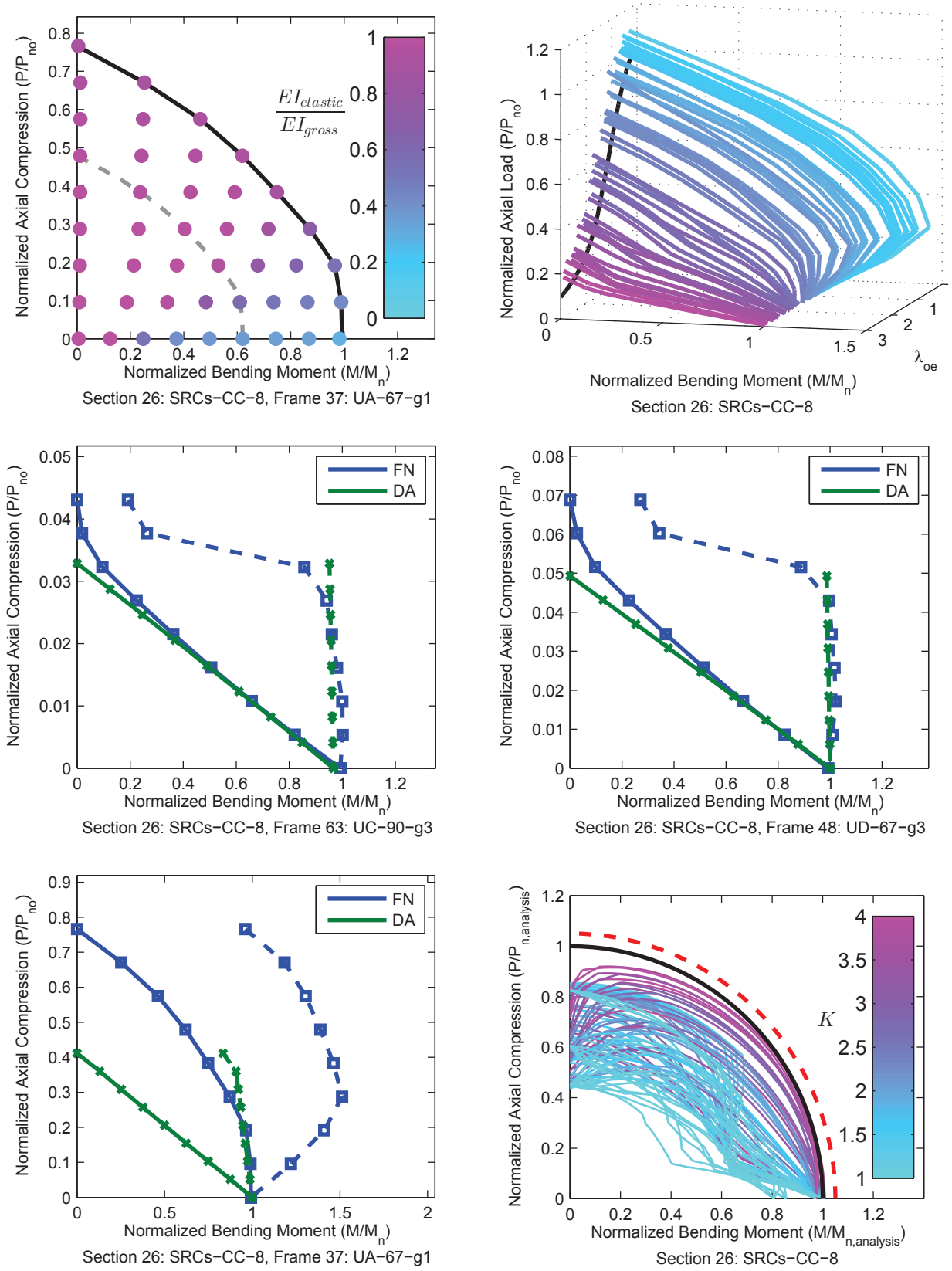

Figure A.56. Detailed Results for Section SRCs-CC-8

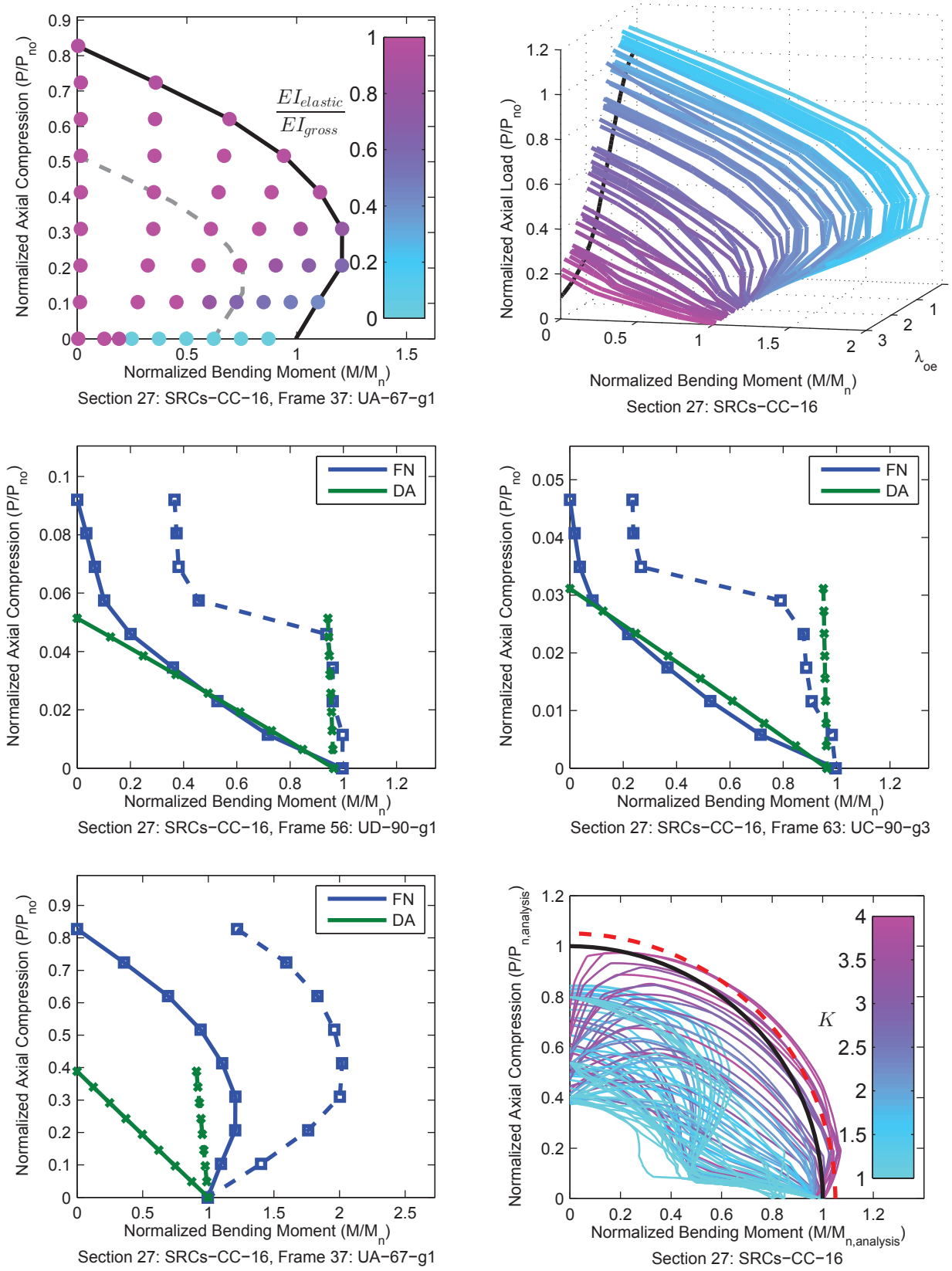

Figure A.57. Detailed Results for Section SRCs-CC-16

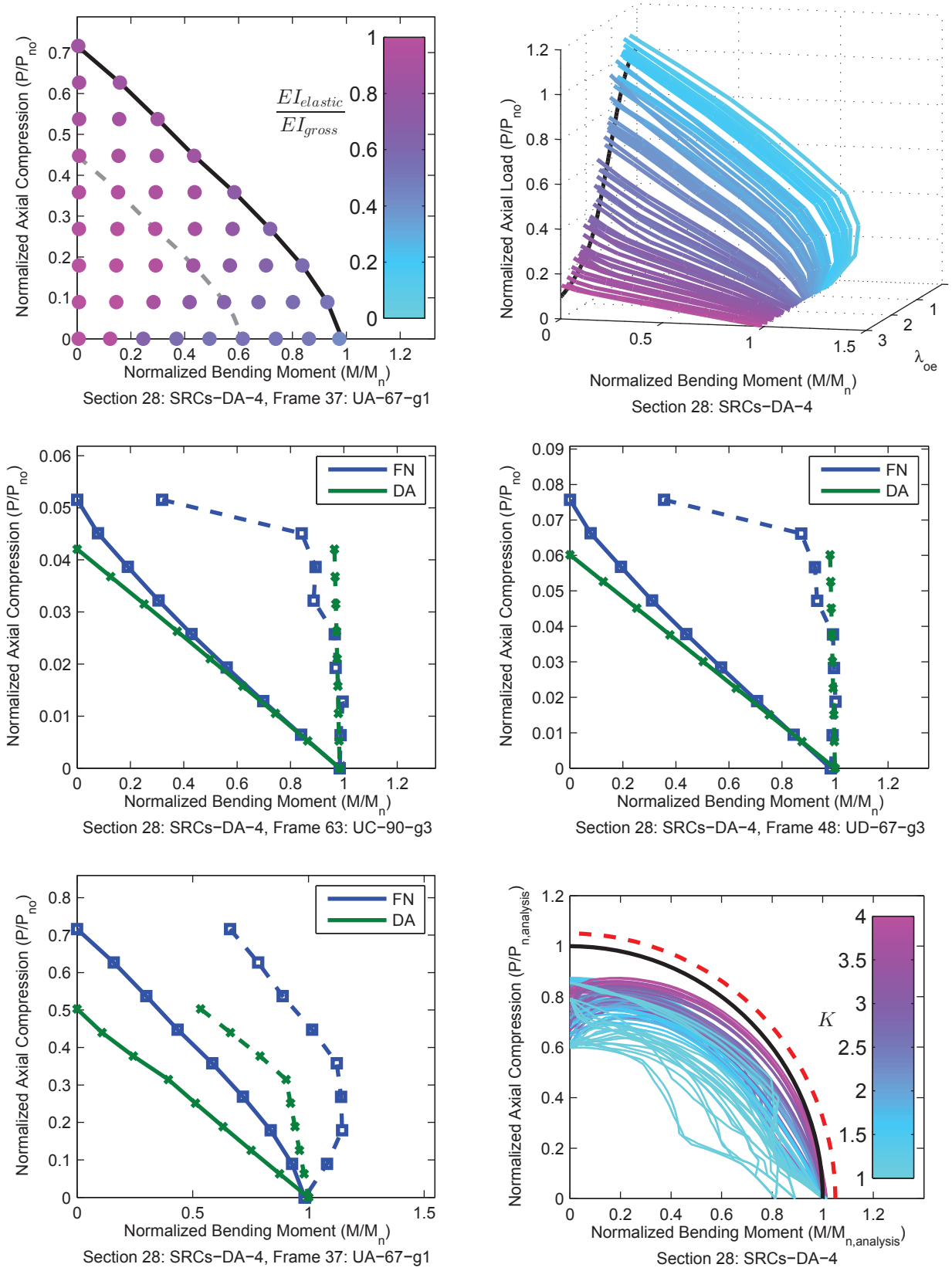

Figure A.58. Detailed Results for Section SRCs-DA-4

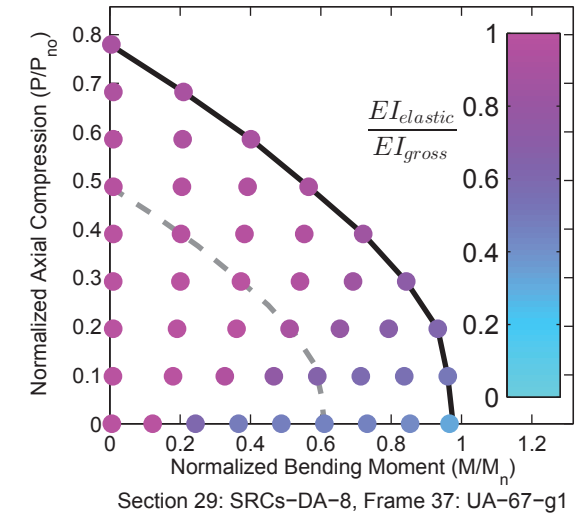

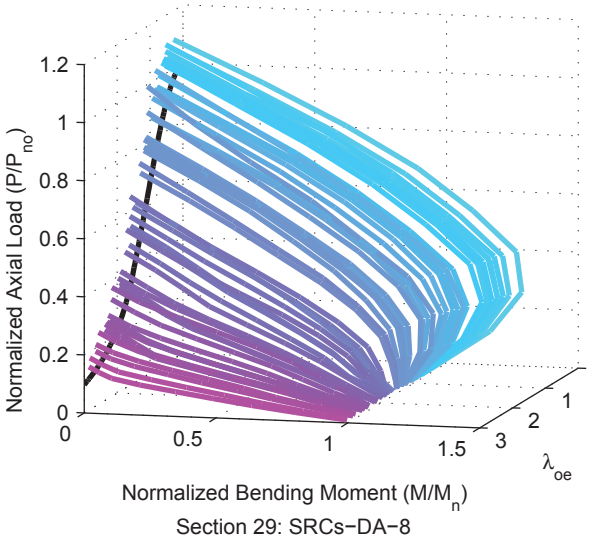

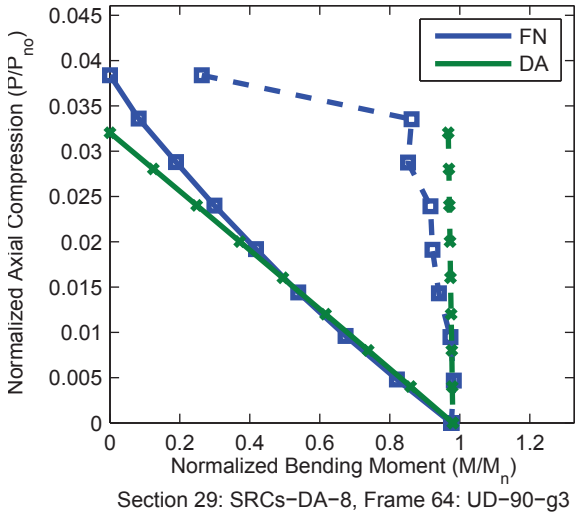

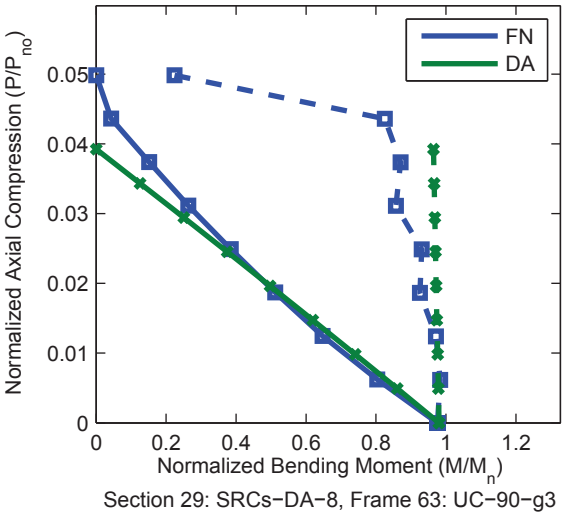

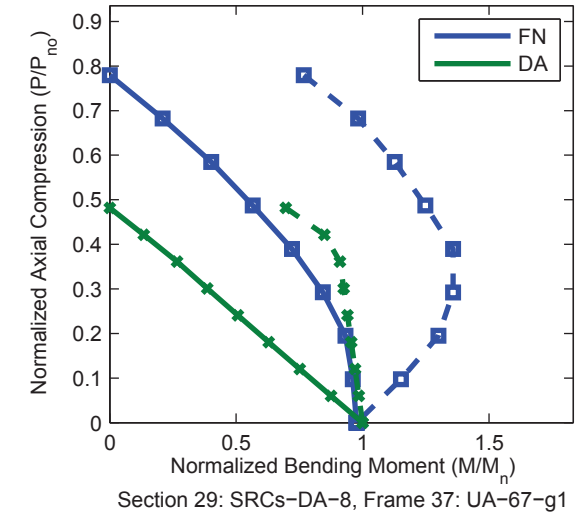

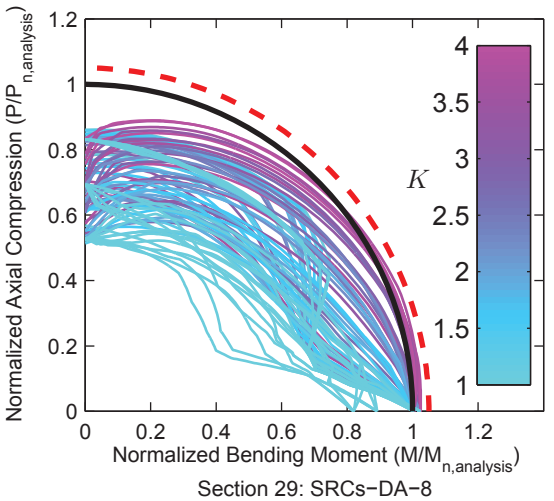

Figure A.59. Detailed Results for Section SRCs-DA-8

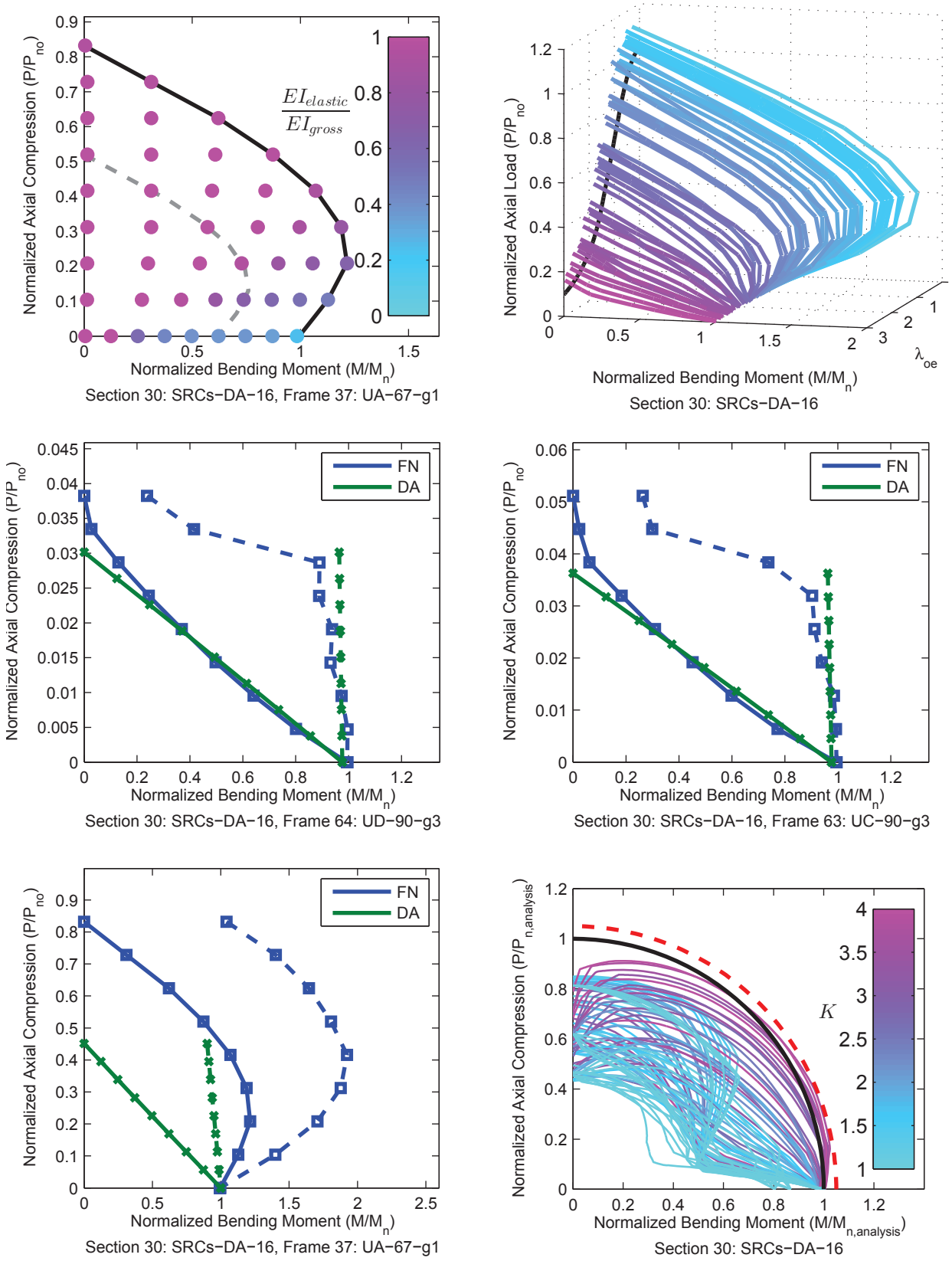

Figure A.60. Detailed Results for Section SRCs-DA-16

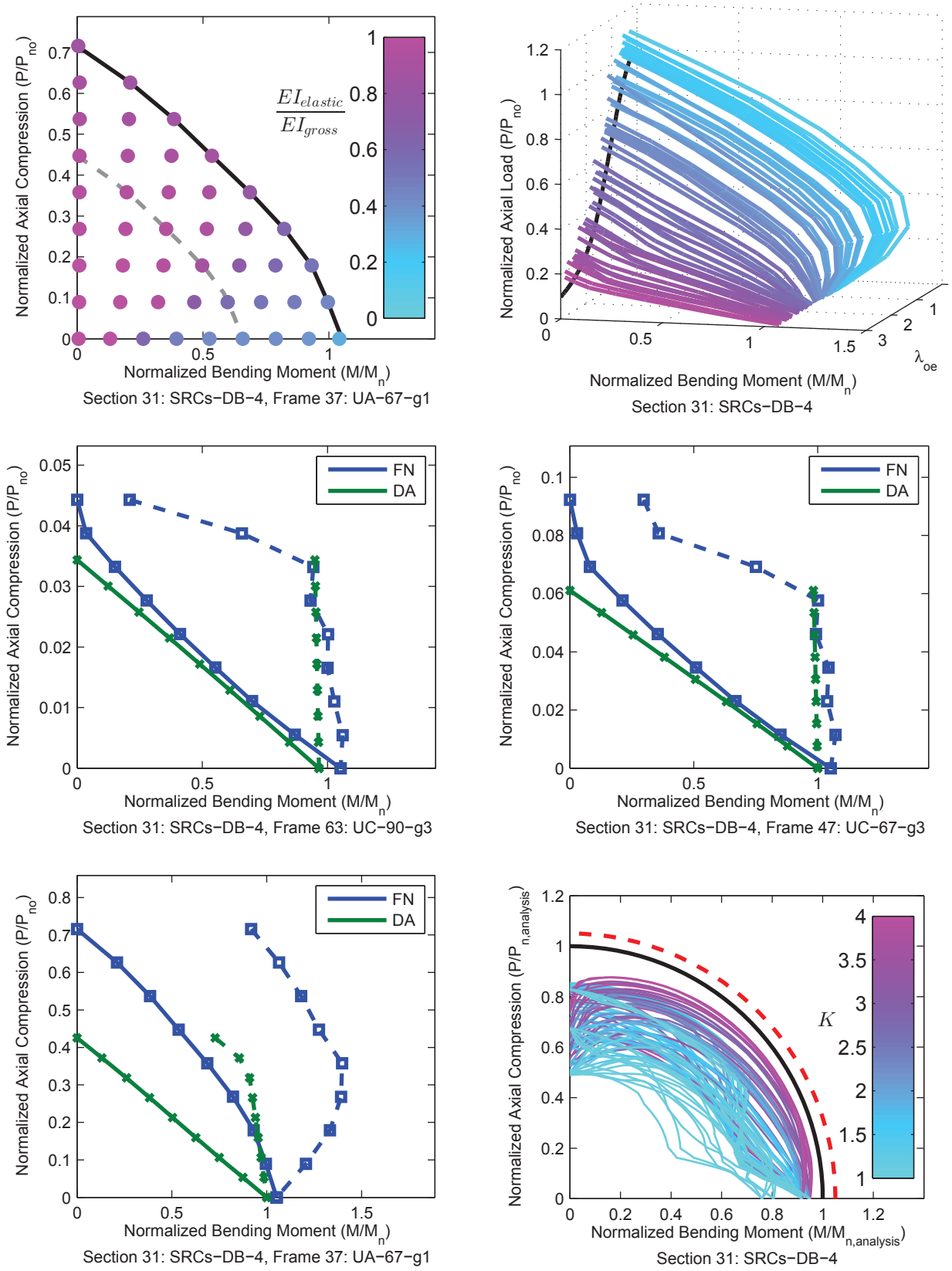

Figure A.61. Detailed Results for Section SRCs-DB-4

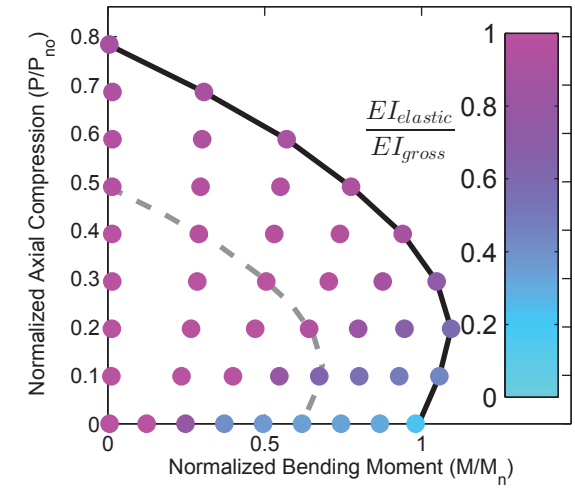

Section 32: SRCs−DB−8, Frame 37: UA−67−g1

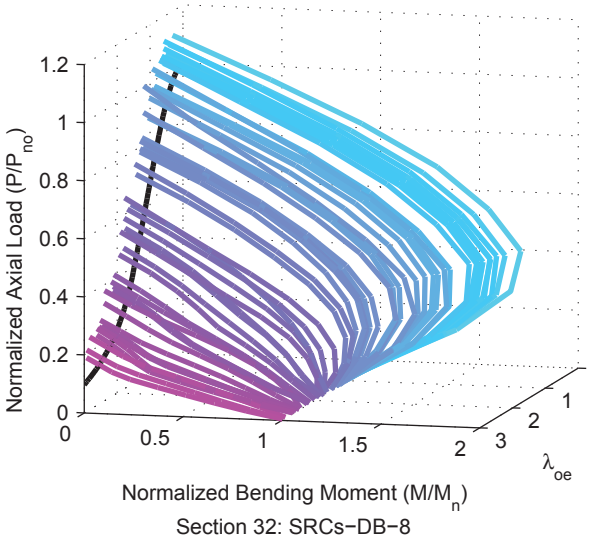

Section 32: SRCs−DB−8

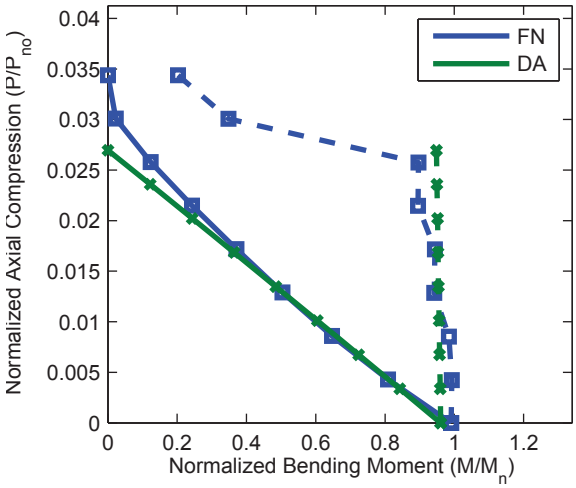

Section 32: SRCs−DB−8, Frame 64: UD−90−g3

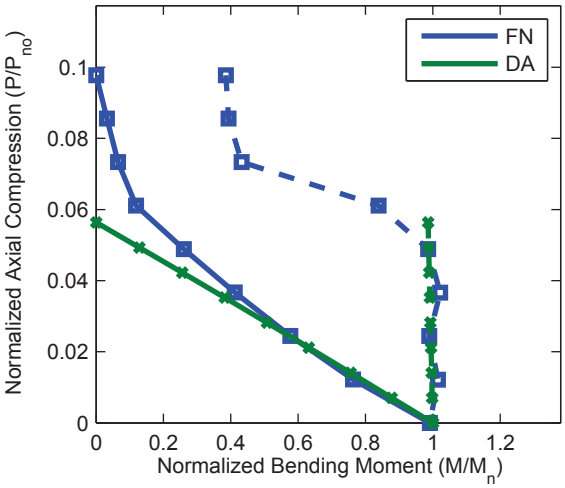

Section 32: SRCs−DB−8, Frame 47: UC−67−g3

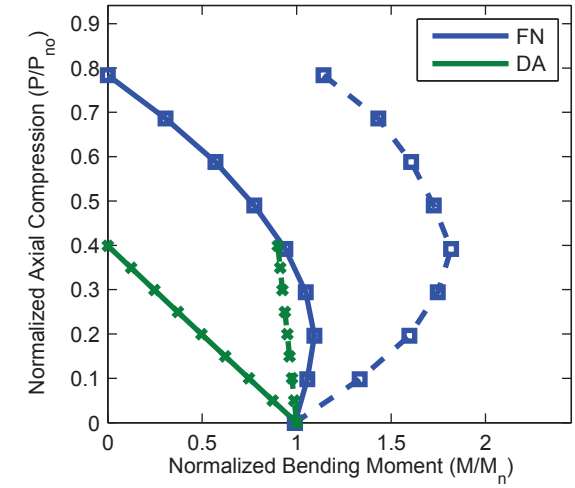

Section 32: SRCs−DB−8, Frame 37: UA−67−g1

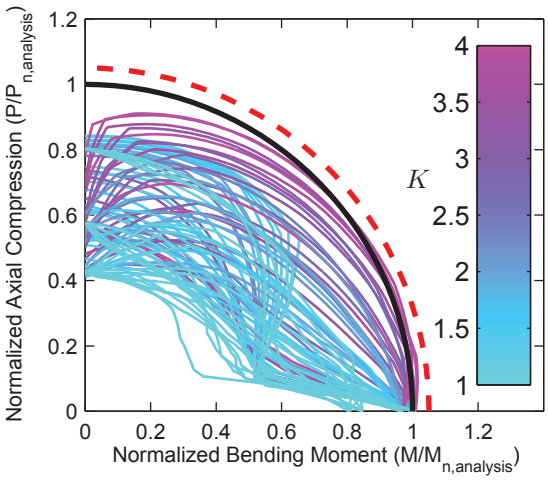

Section 32: SRCs−DB−8

Figure A.62. Detailed Results for Section SRCs-DB-8

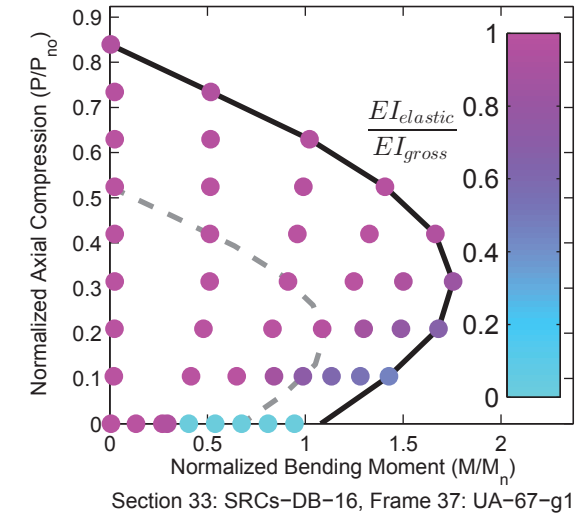

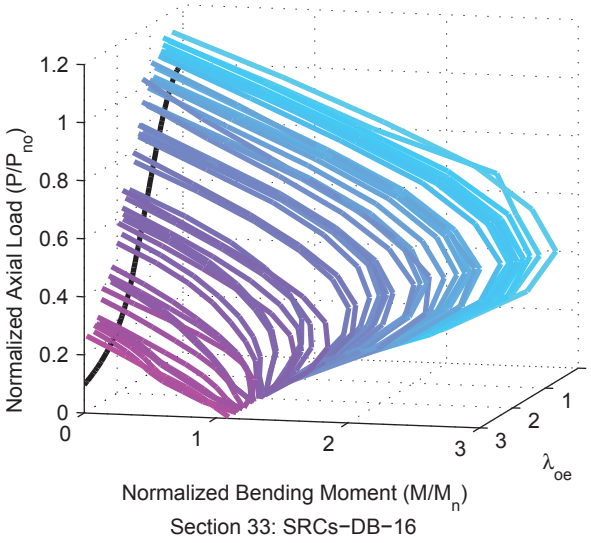

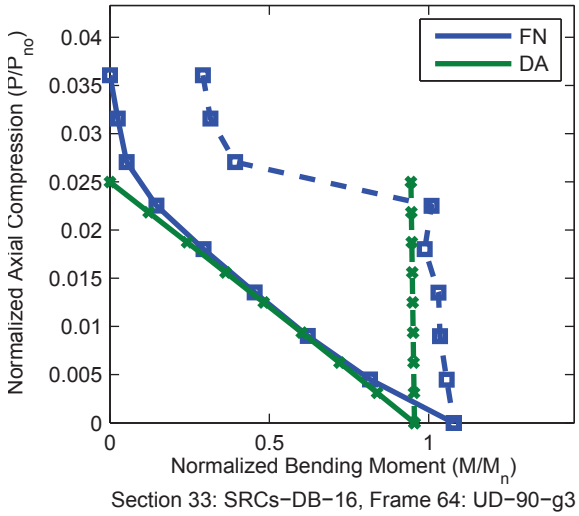

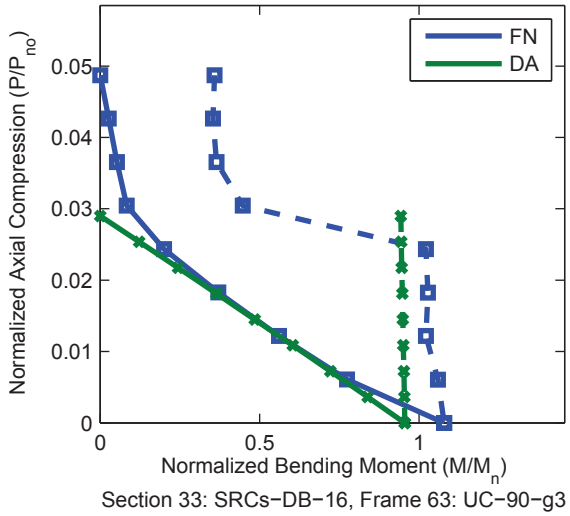

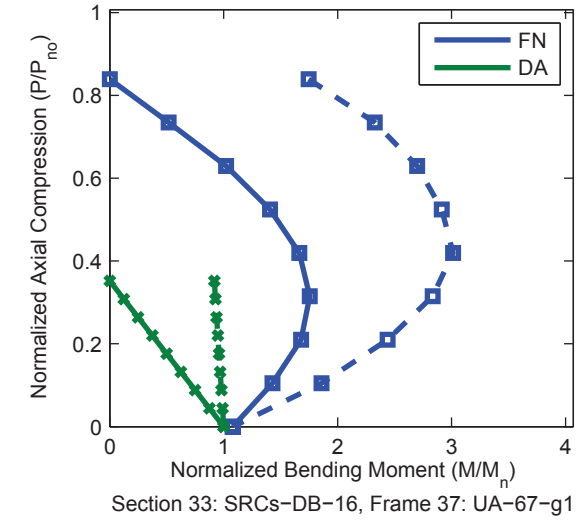

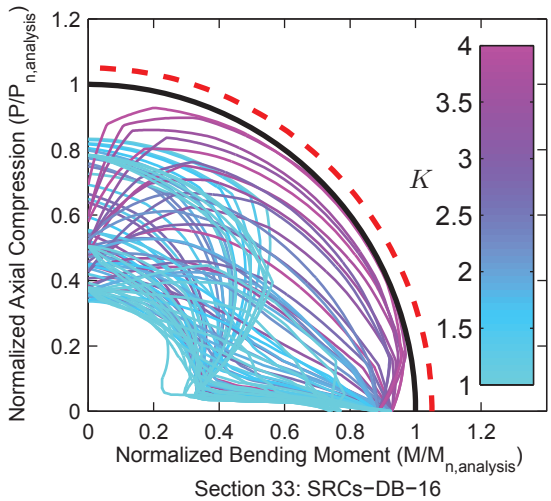

Figure A.63. Detailed Results for Section SRCs-DB-16

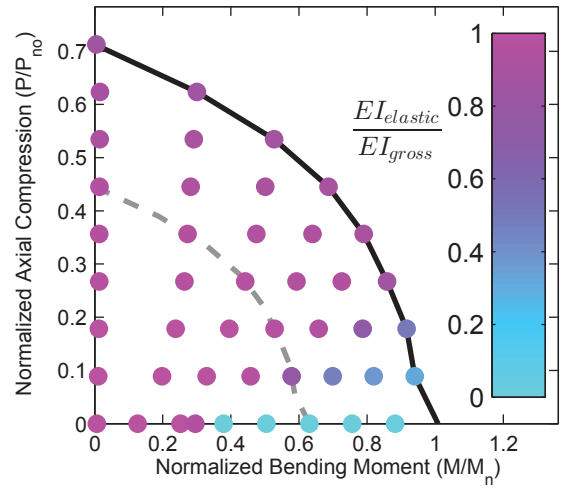

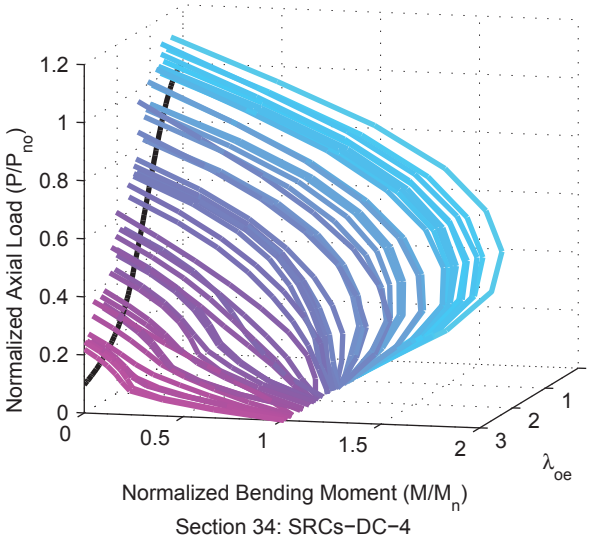

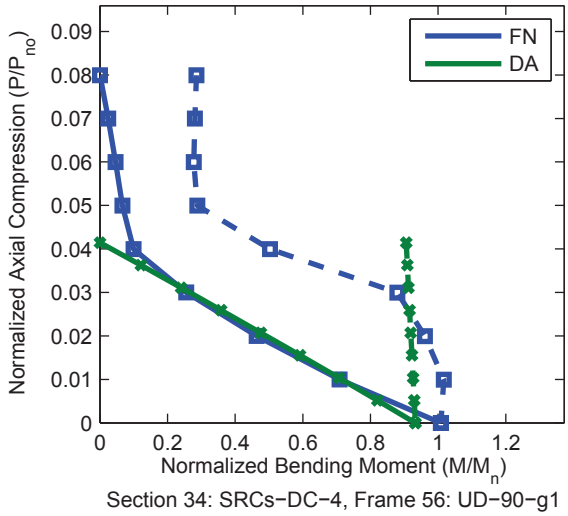

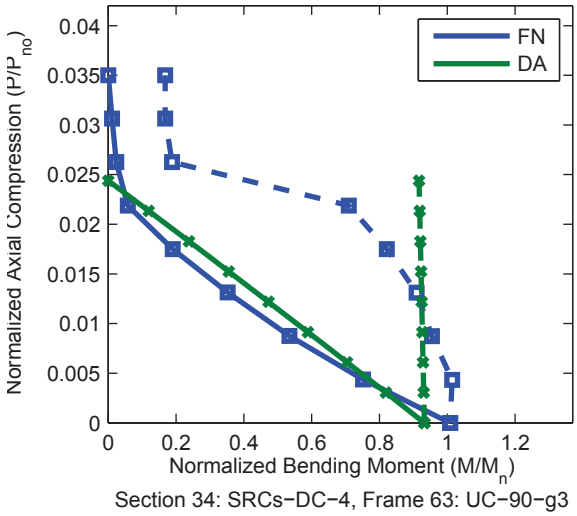

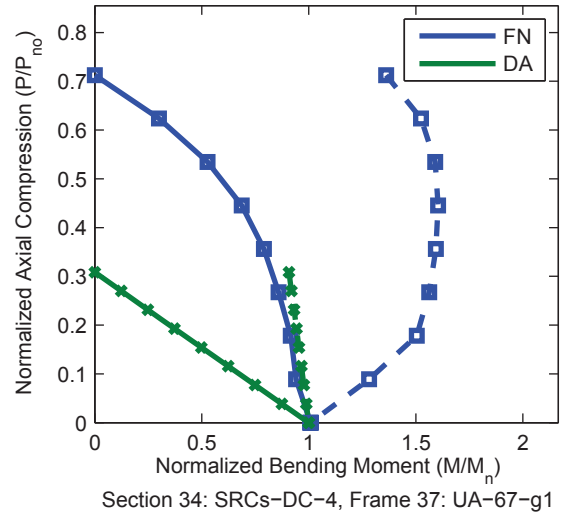

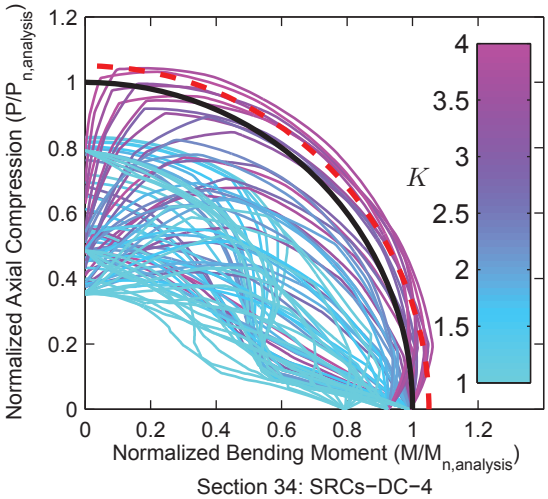

Figure A.64. Detailed Results for Section SRCs-DC-4

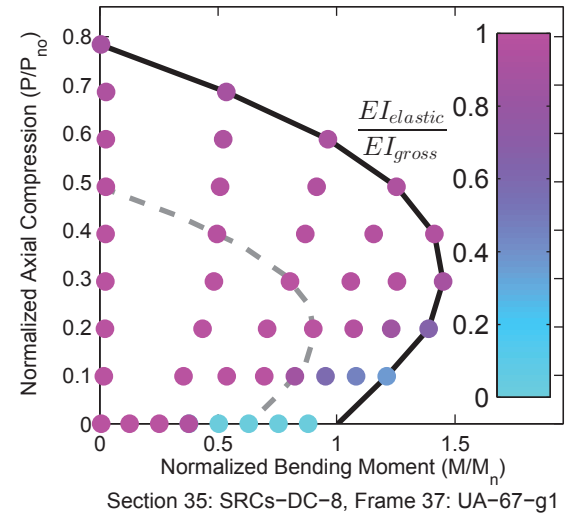

Section 35: SRCs-DC-8, Frame 37: UA-67-g1

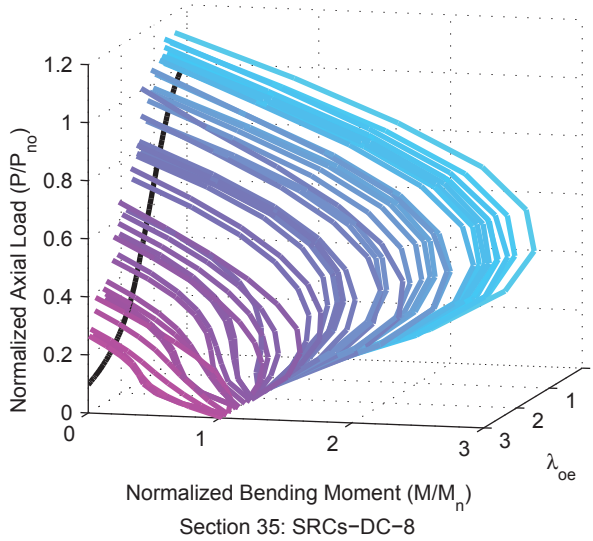

Section 35: SRCs-DC-8

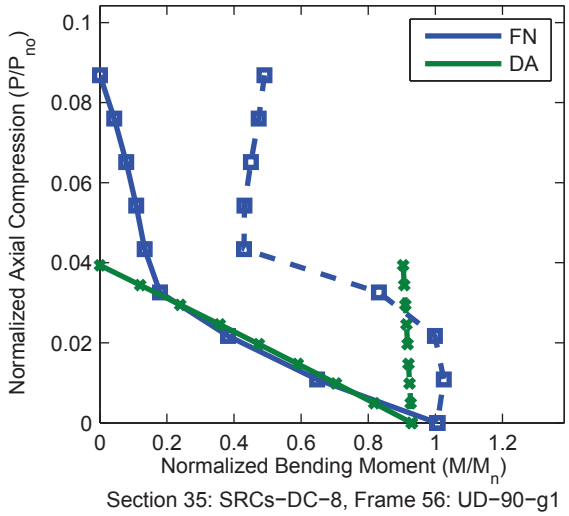

Section 35: SRCs-DC-8, Frame 56: UD-90-g1

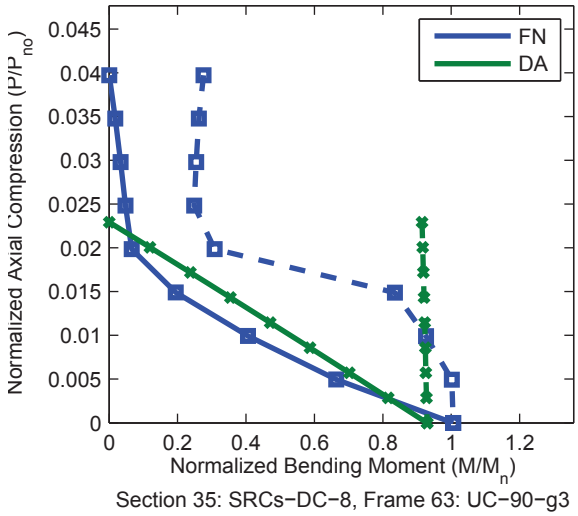

Section 35: SRCs-DC-8, Frame 63: UC-90-g3

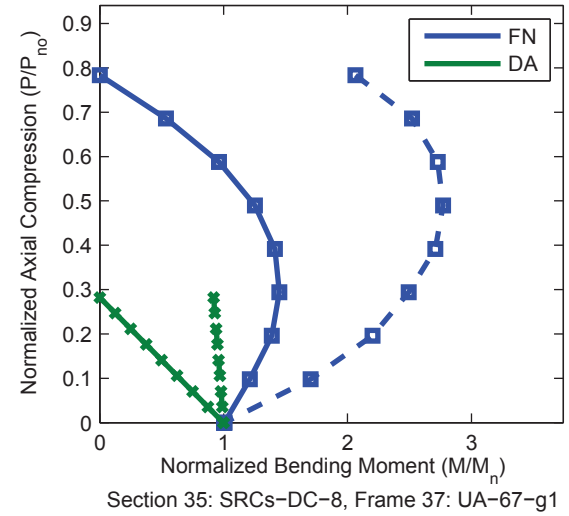

Section 35: SRCs-DC-8, Frame 37: UA-67-g1

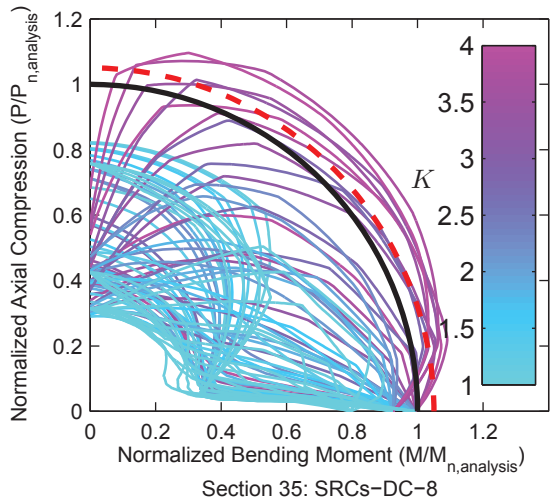

Section 35: SRCs-DC-8

Figure A.65. Detailed Results for Section SRCs-DC-8

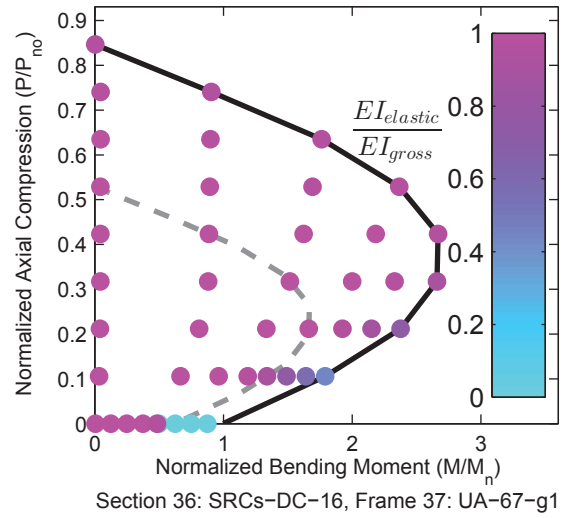

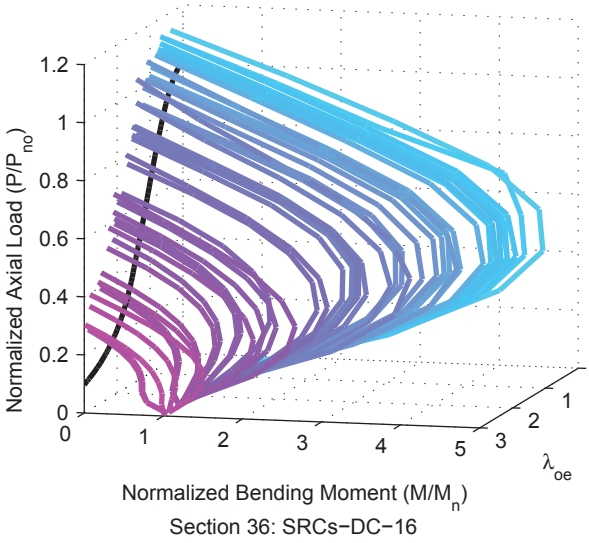

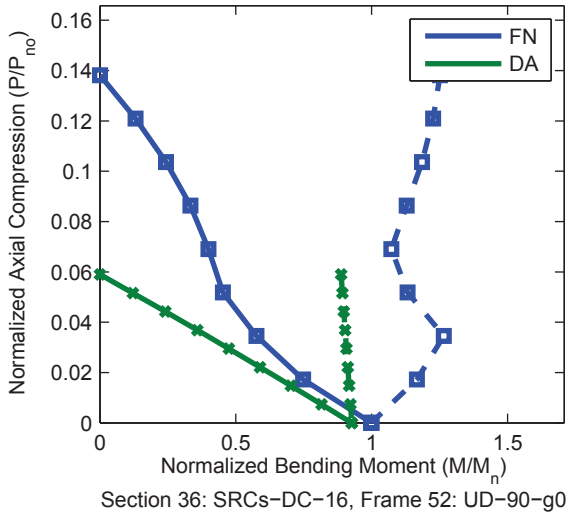

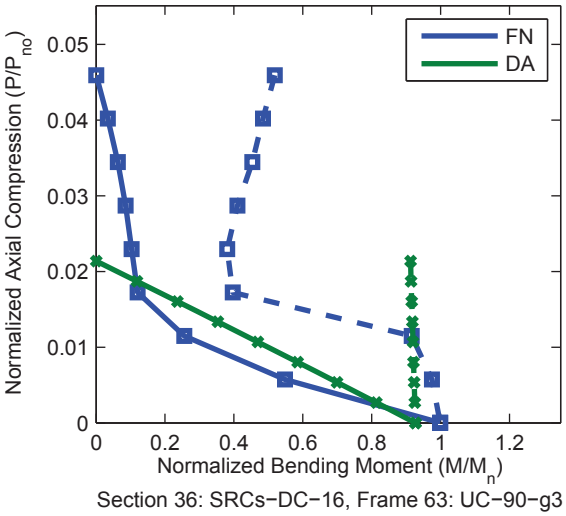

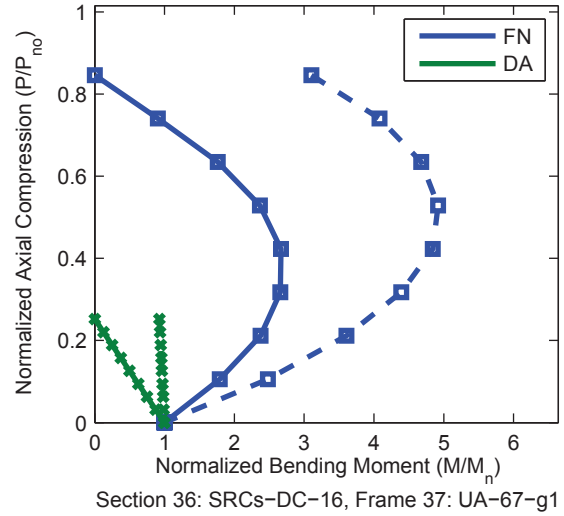

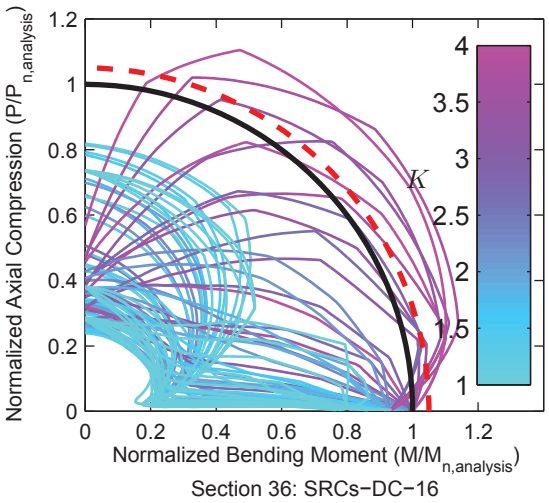

Figure A.66. Detailed Results for Section SRCs-DC-16

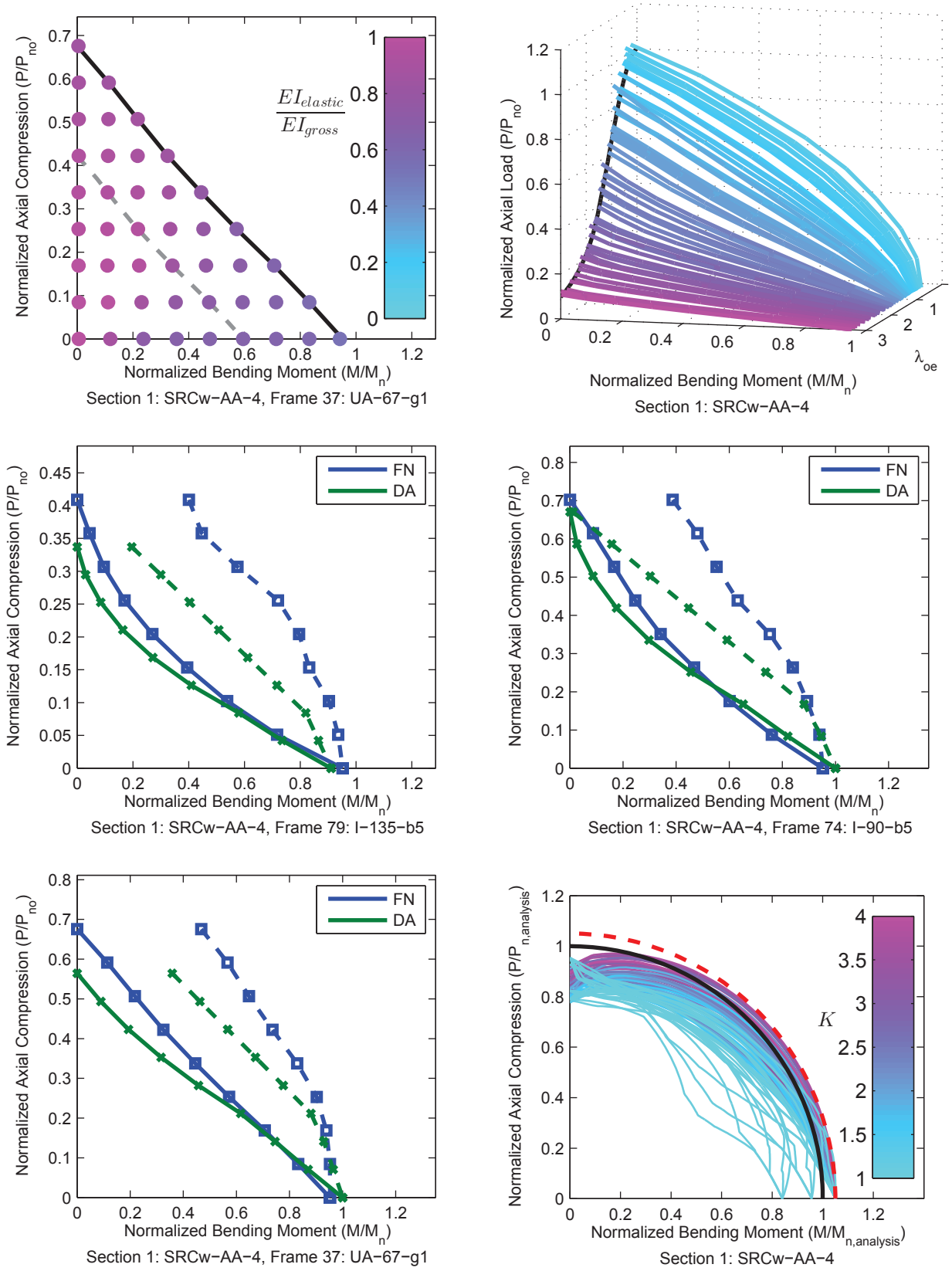

Figure A.67. Detailed Results for Section SRCw-AA-4

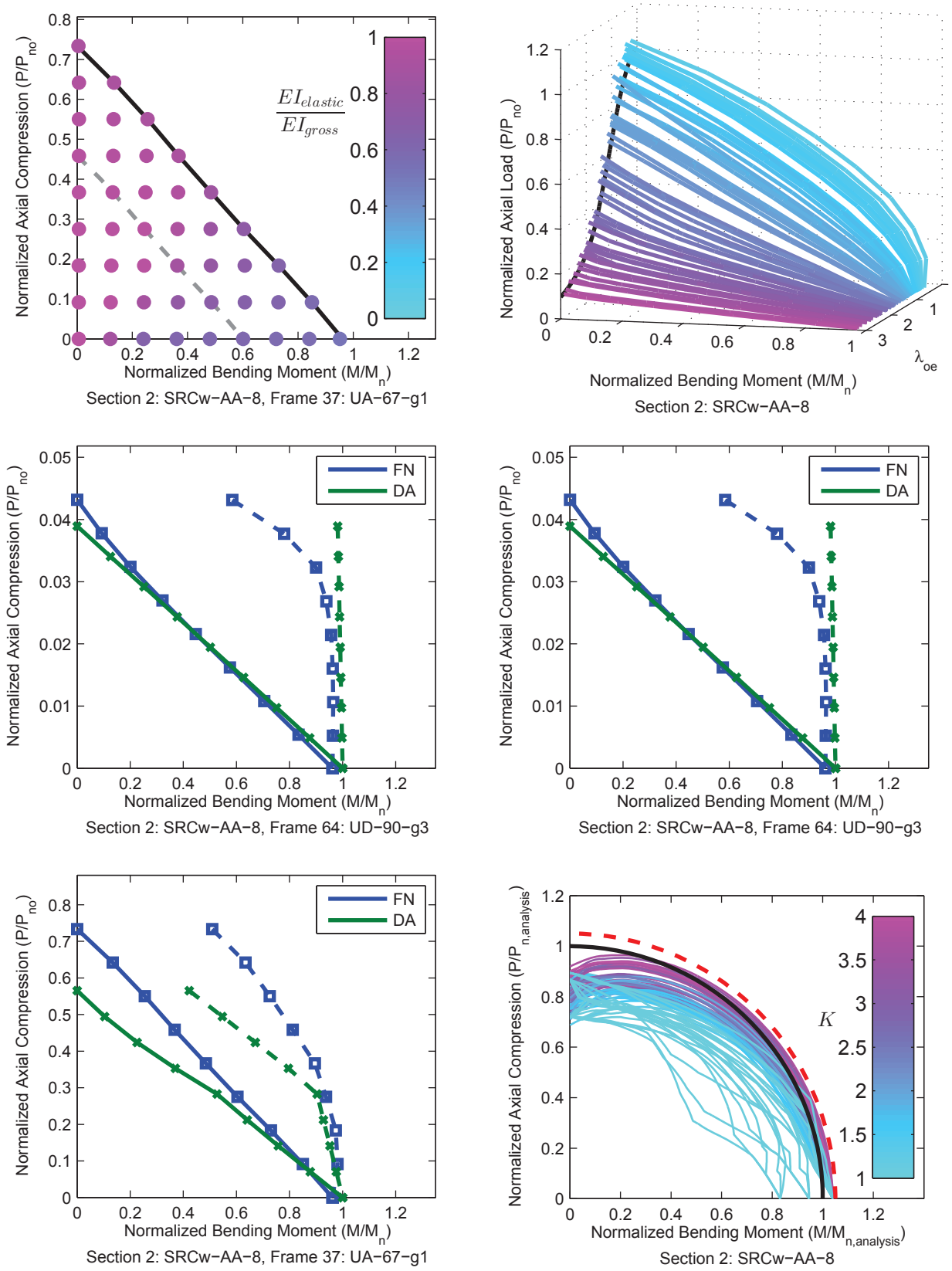

Figure A.68. Detailed Results for Section SRCw-AA-8

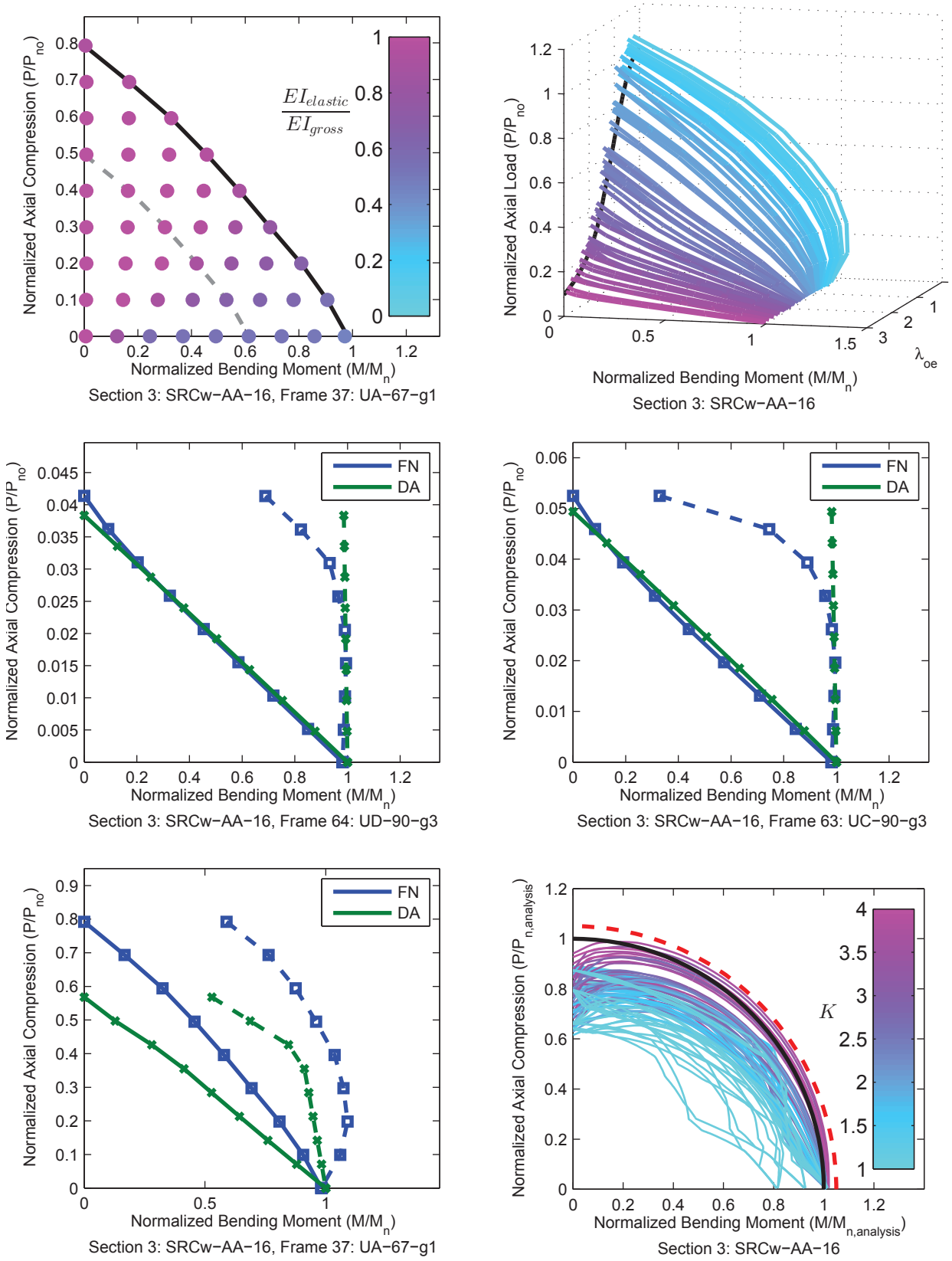

Figure A.69. Detailed Results for Section SRCw-AA-16

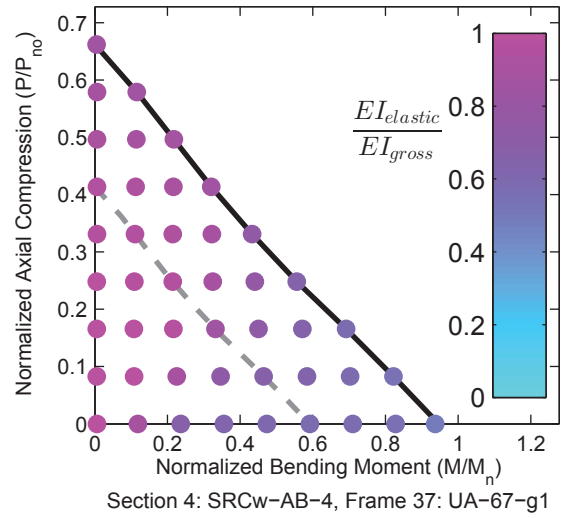

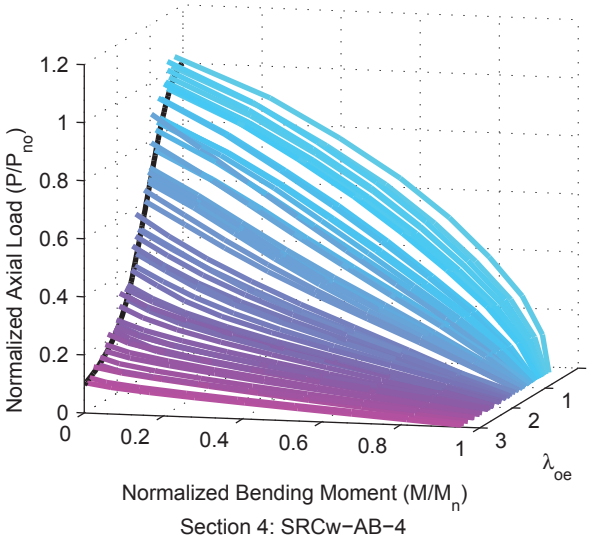

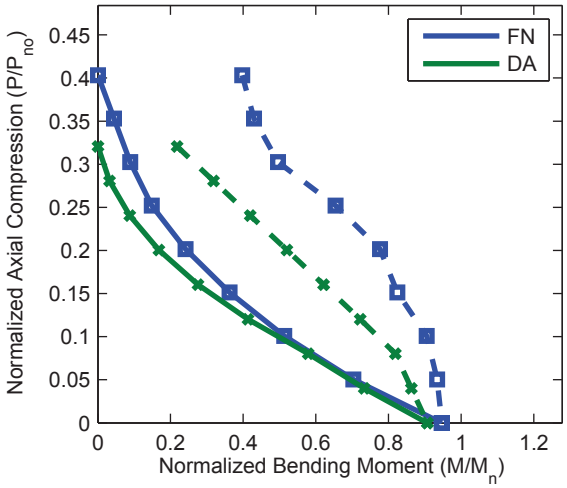

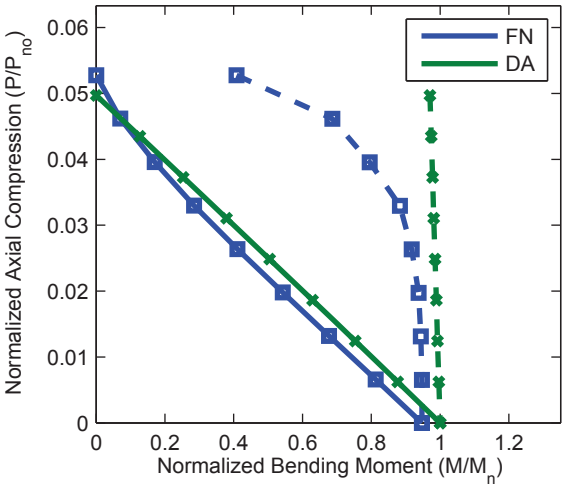

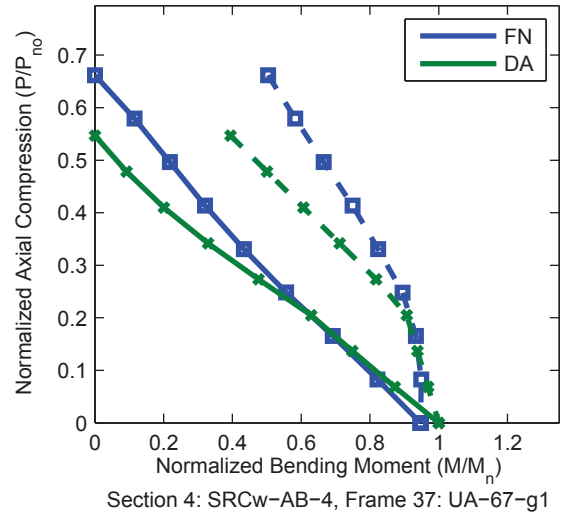

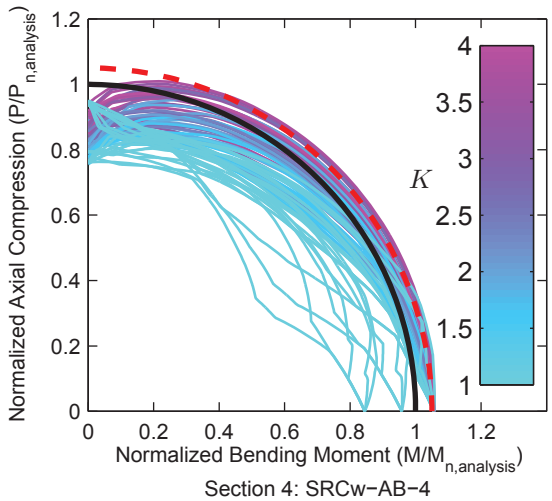

Figure A.70. Detailed Results for Section SRCw-AB-4

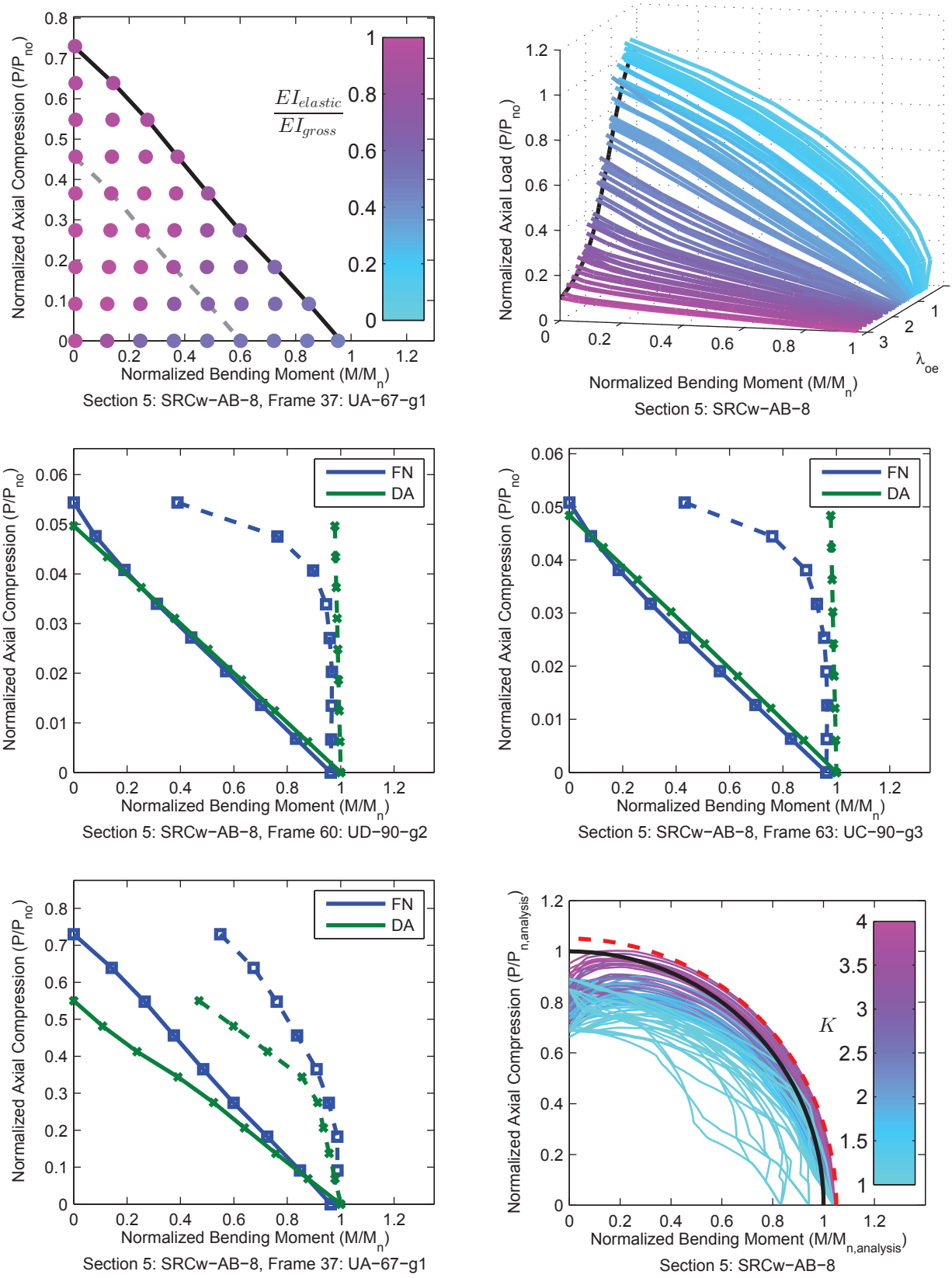

Figure A.71. Detailed Results for Section SRCw-AB-8

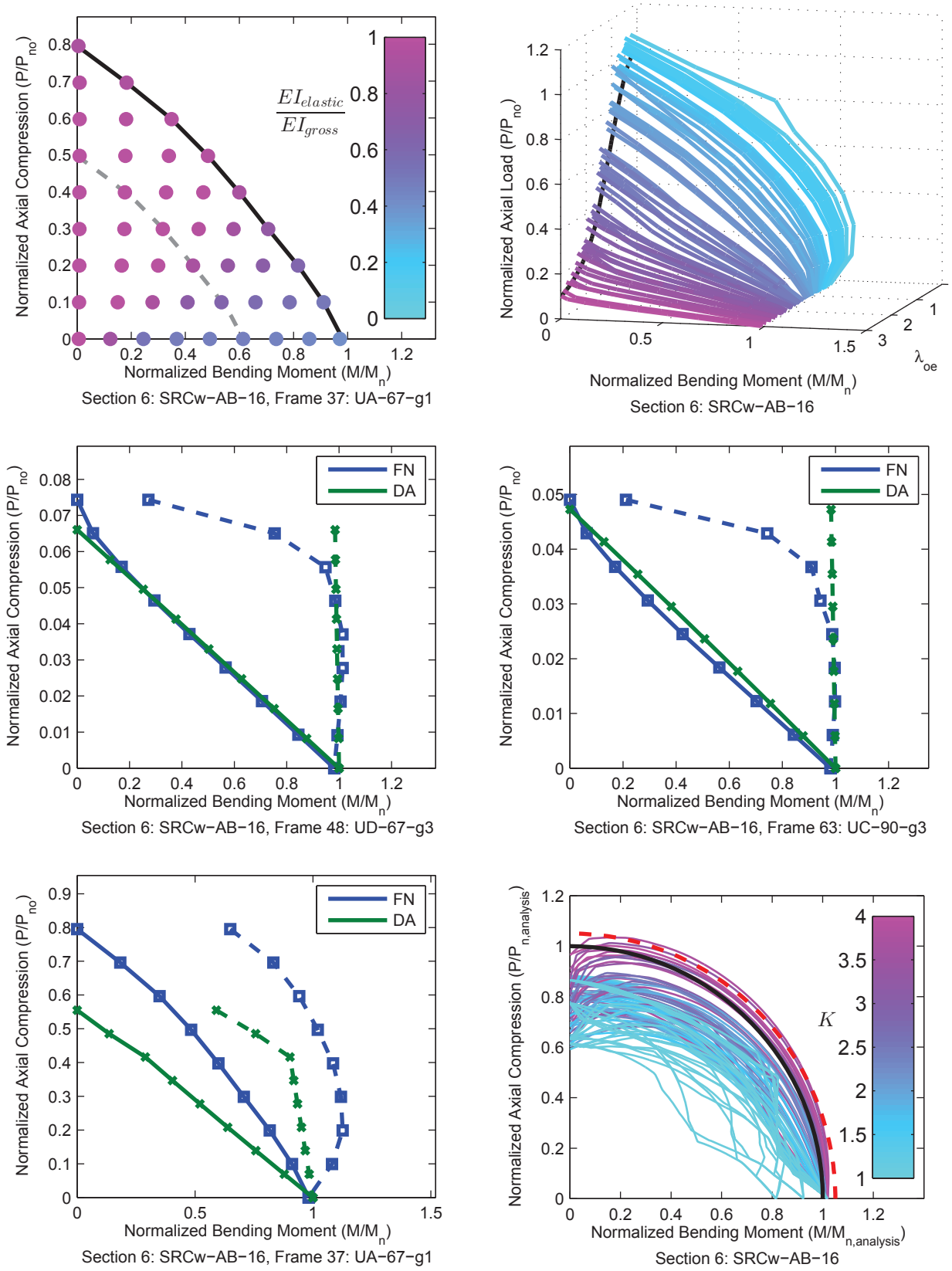

Figure A.72. Detailed Results for Section SRCw-AB-16

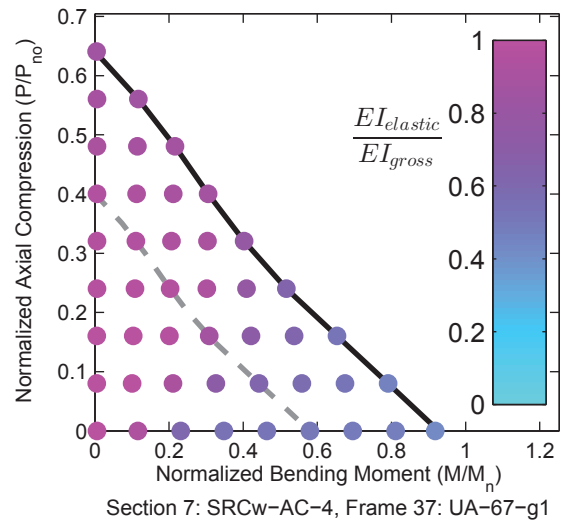

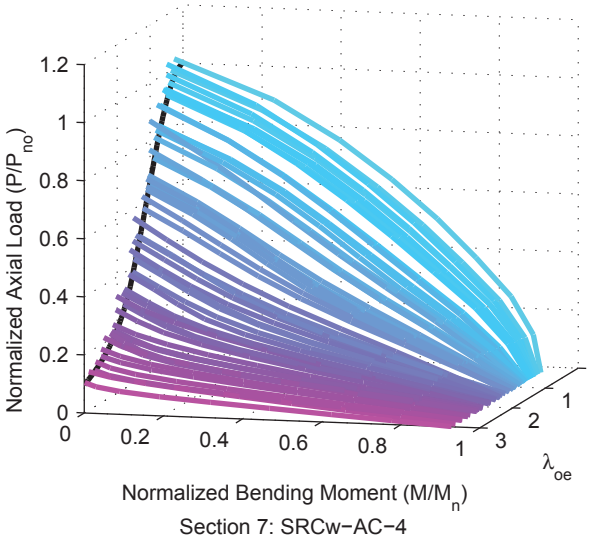

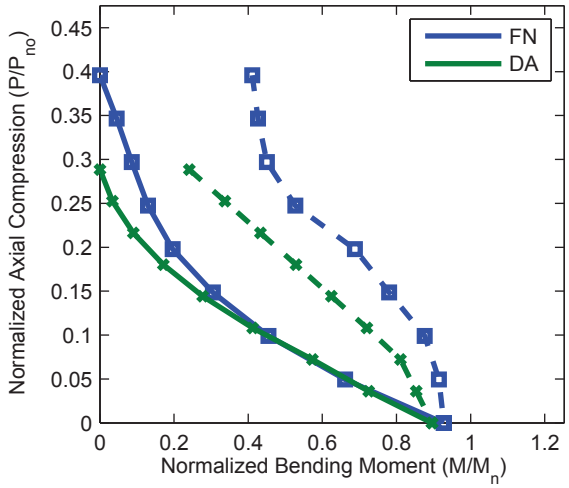

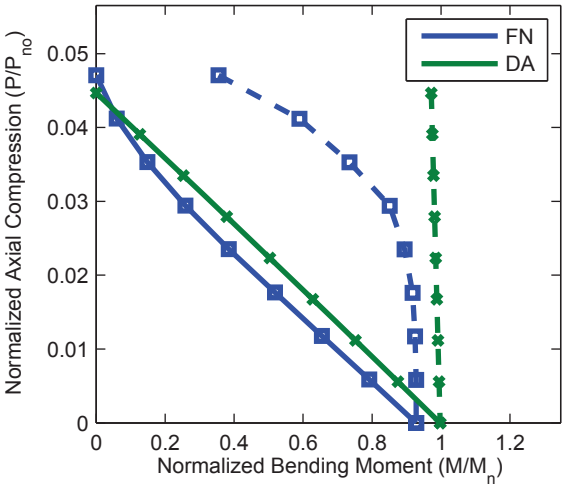

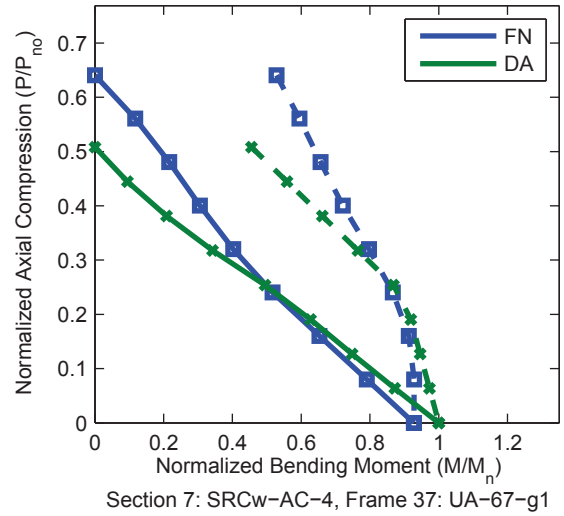

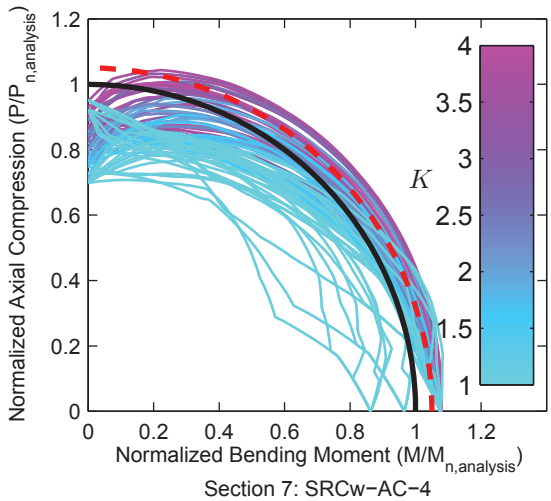

Figure A.73. Detailed Results for Section SRCw-AC-4

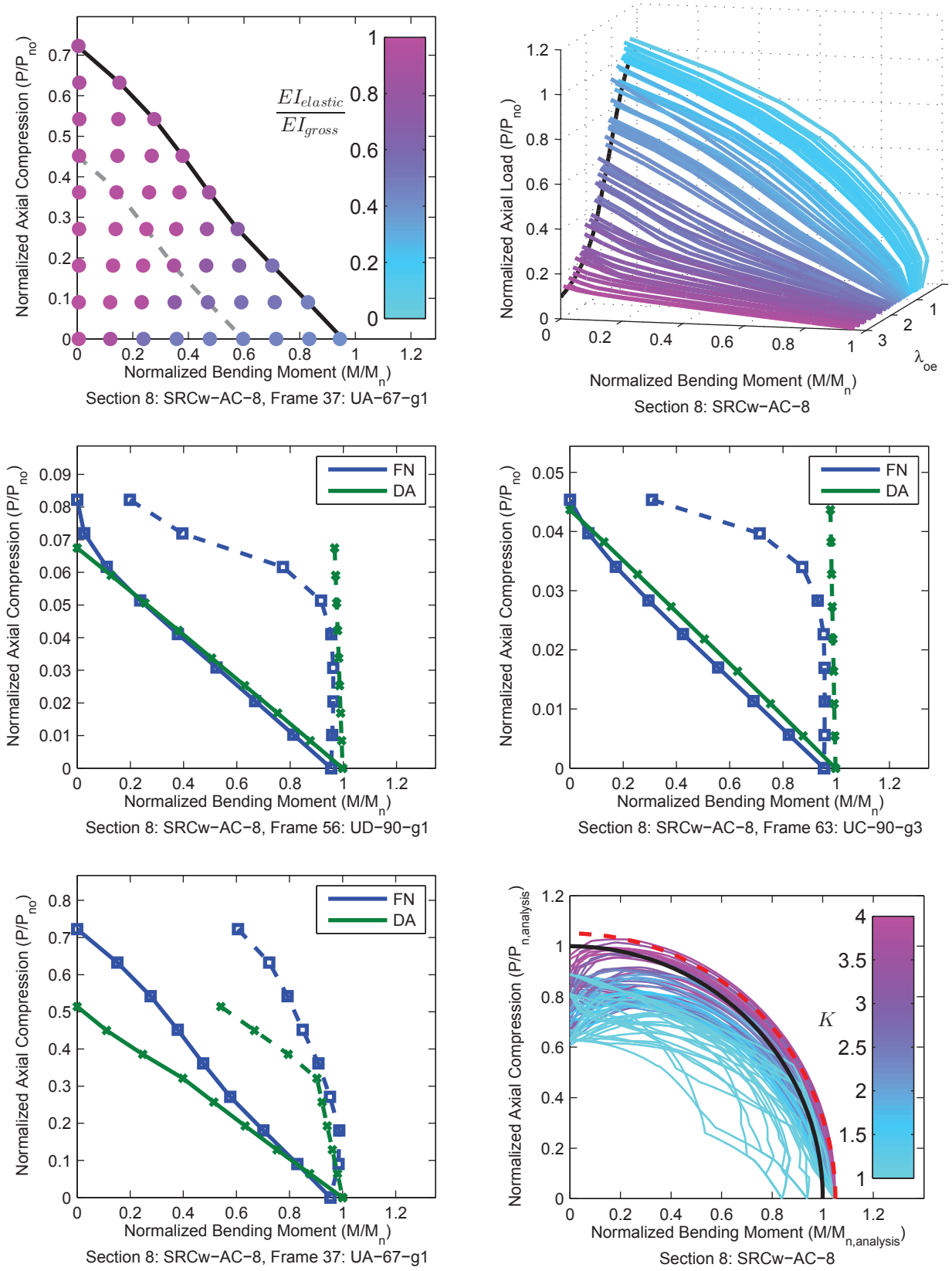

Figure A.74. Detailed Results for Section SRCw-AC-8

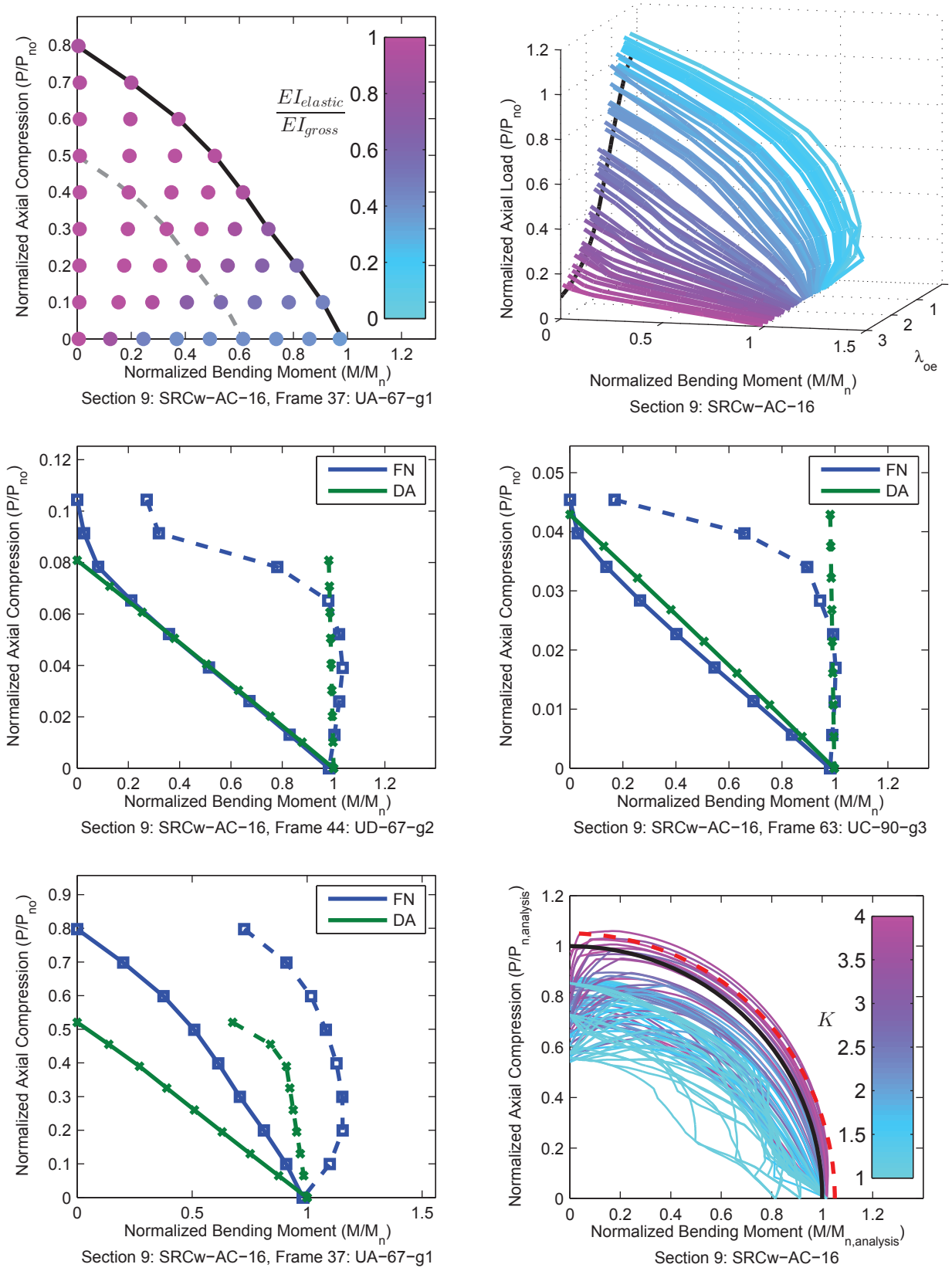

Figure A.75. Detailed Results for Section SRCw-AC-16

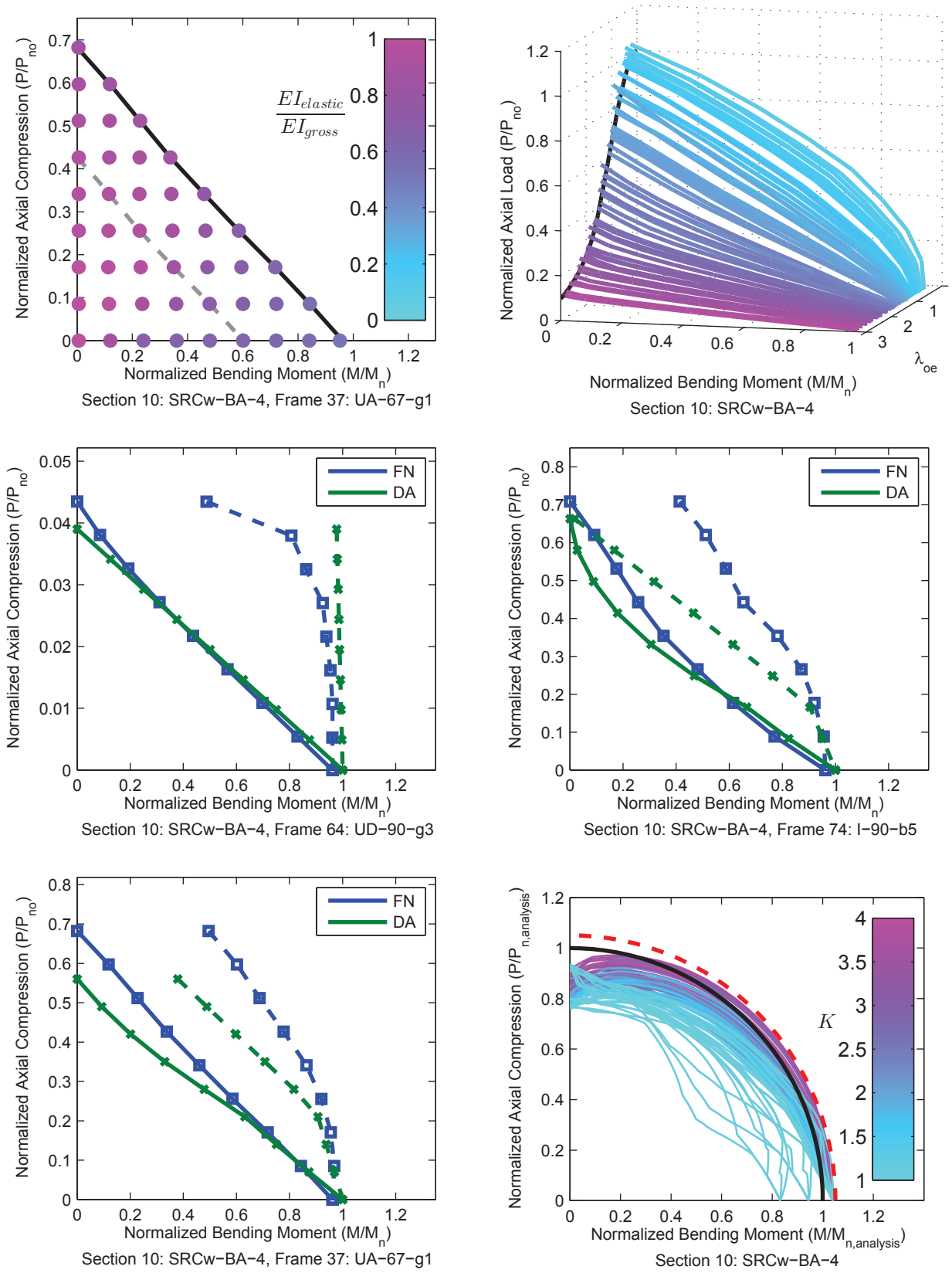

Figure A.76. Detailed Results for Section SRCw-BA-4

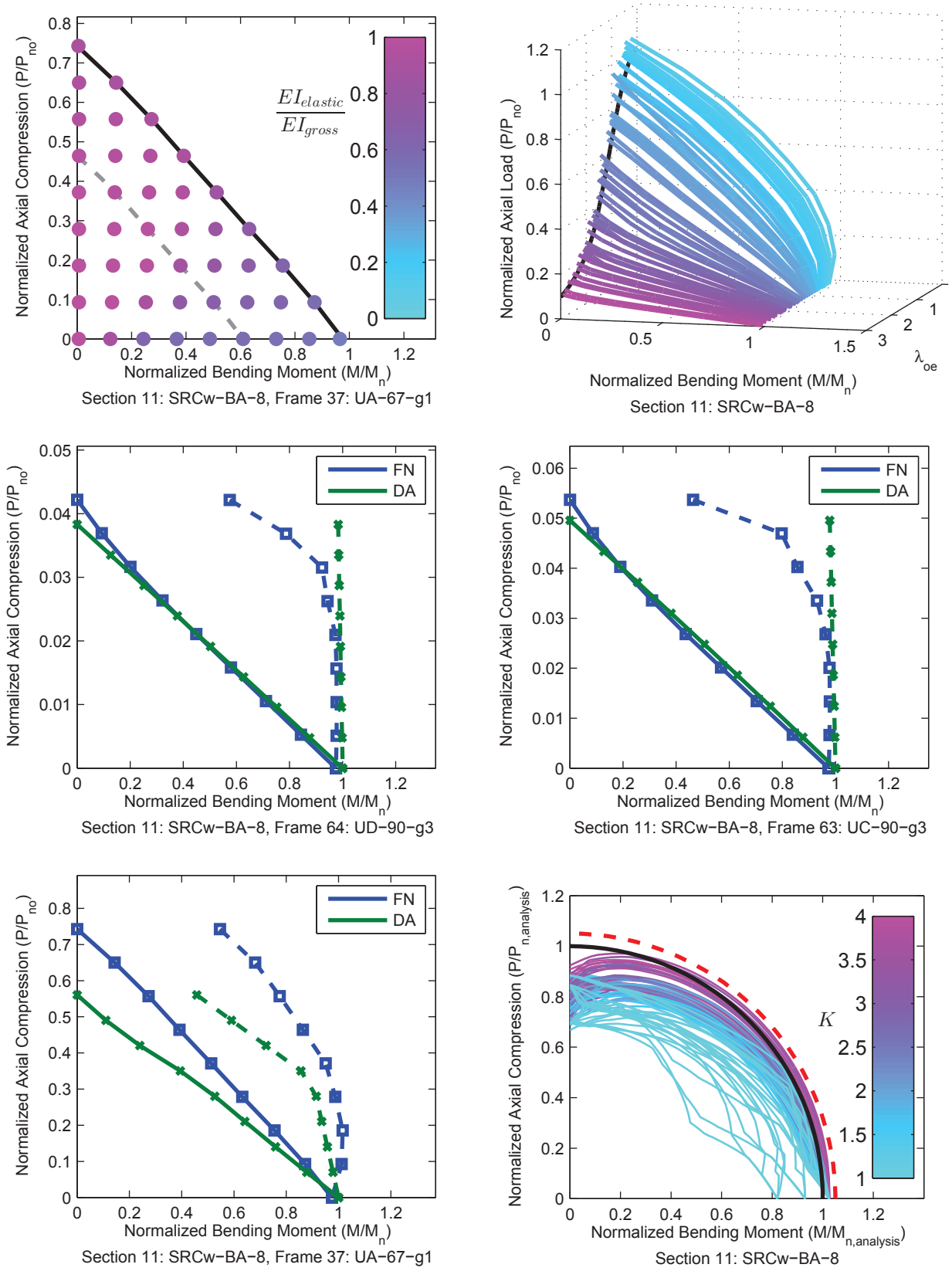

Figure A.77. Detailed Results for Section SRCw-BA-8

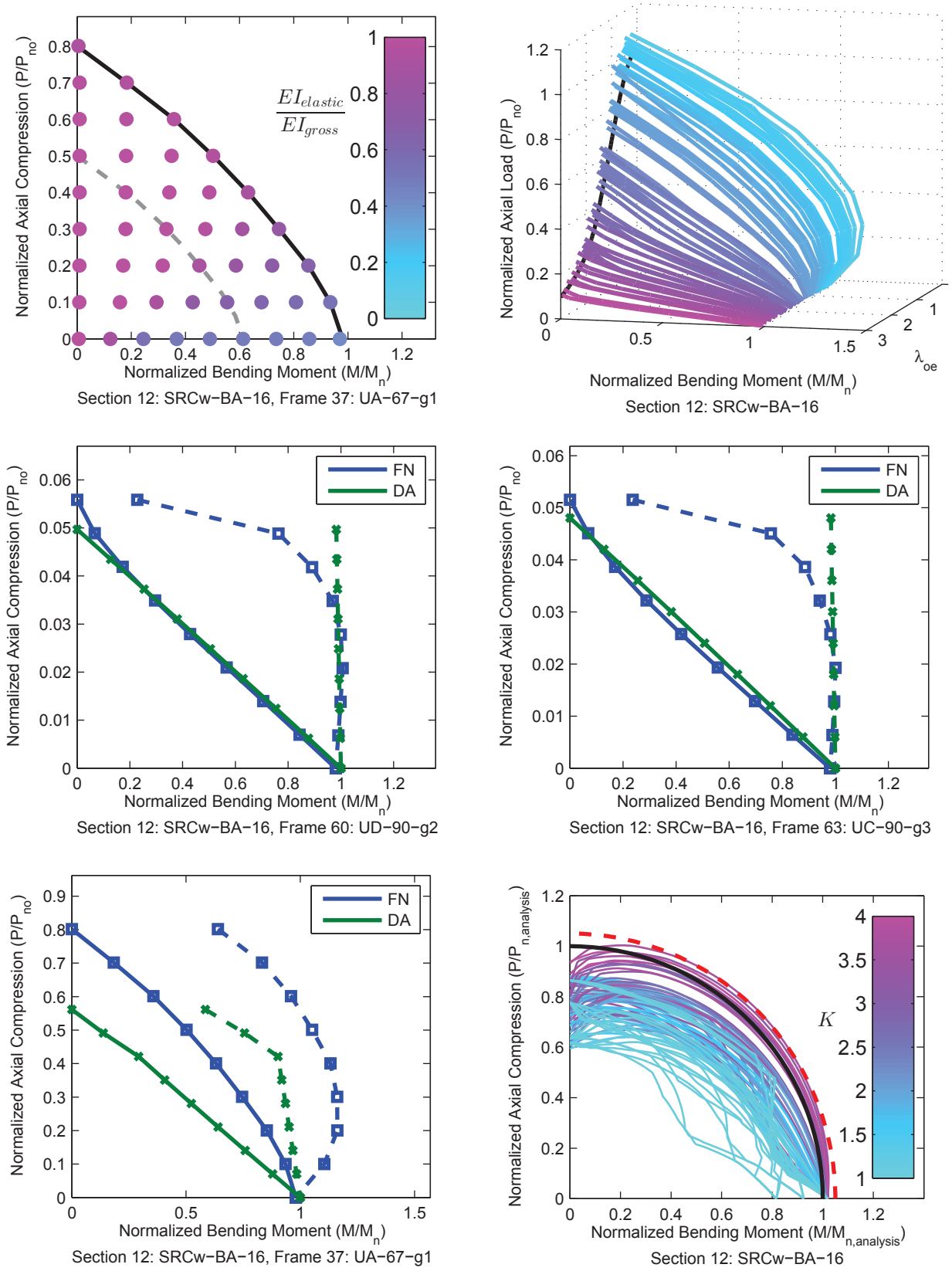

Figure A.78. Detailed Results for Section SRCw-BA-16

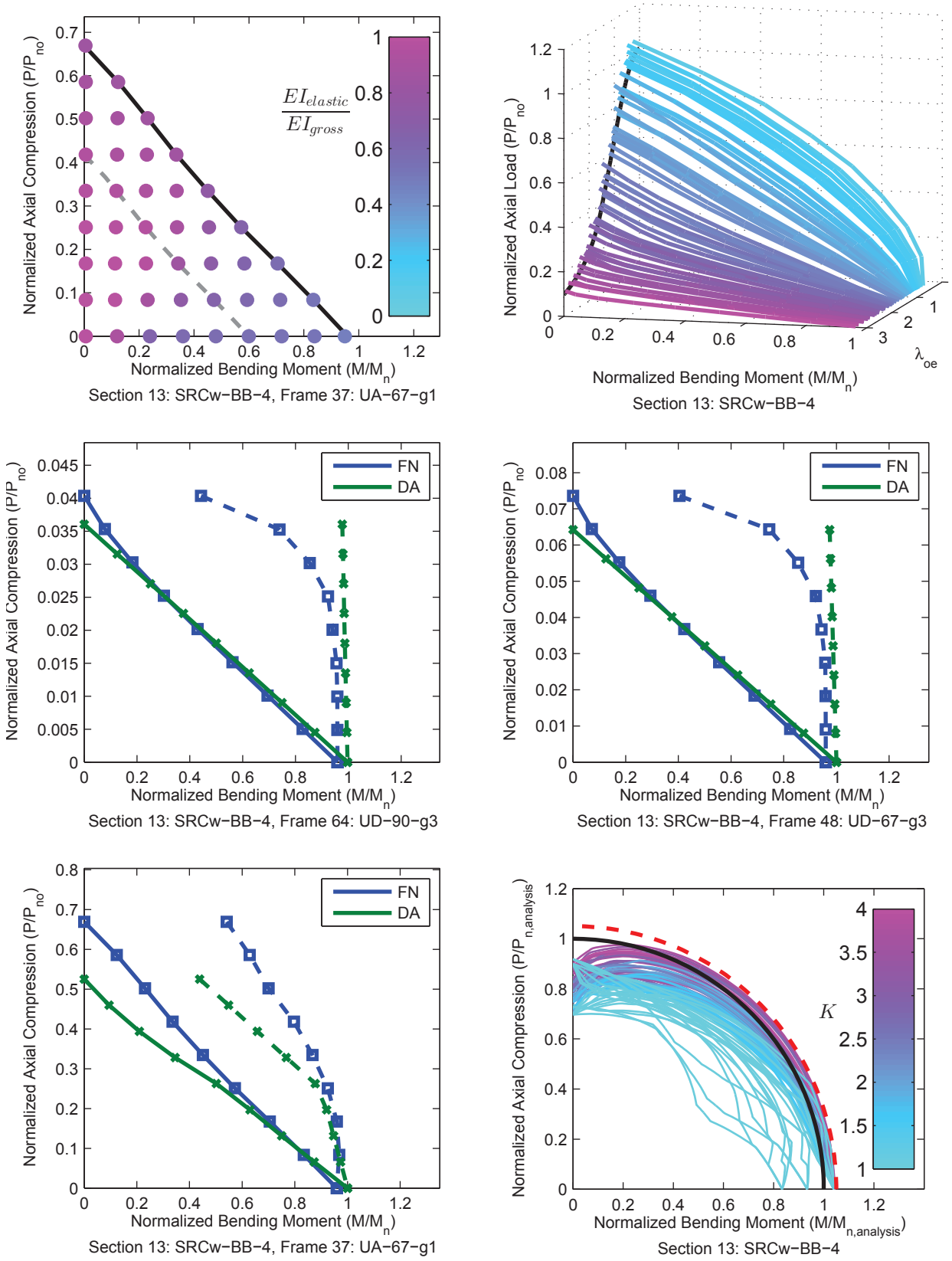

Figure A.79. Detailed Results for Section SRCw-BB-4

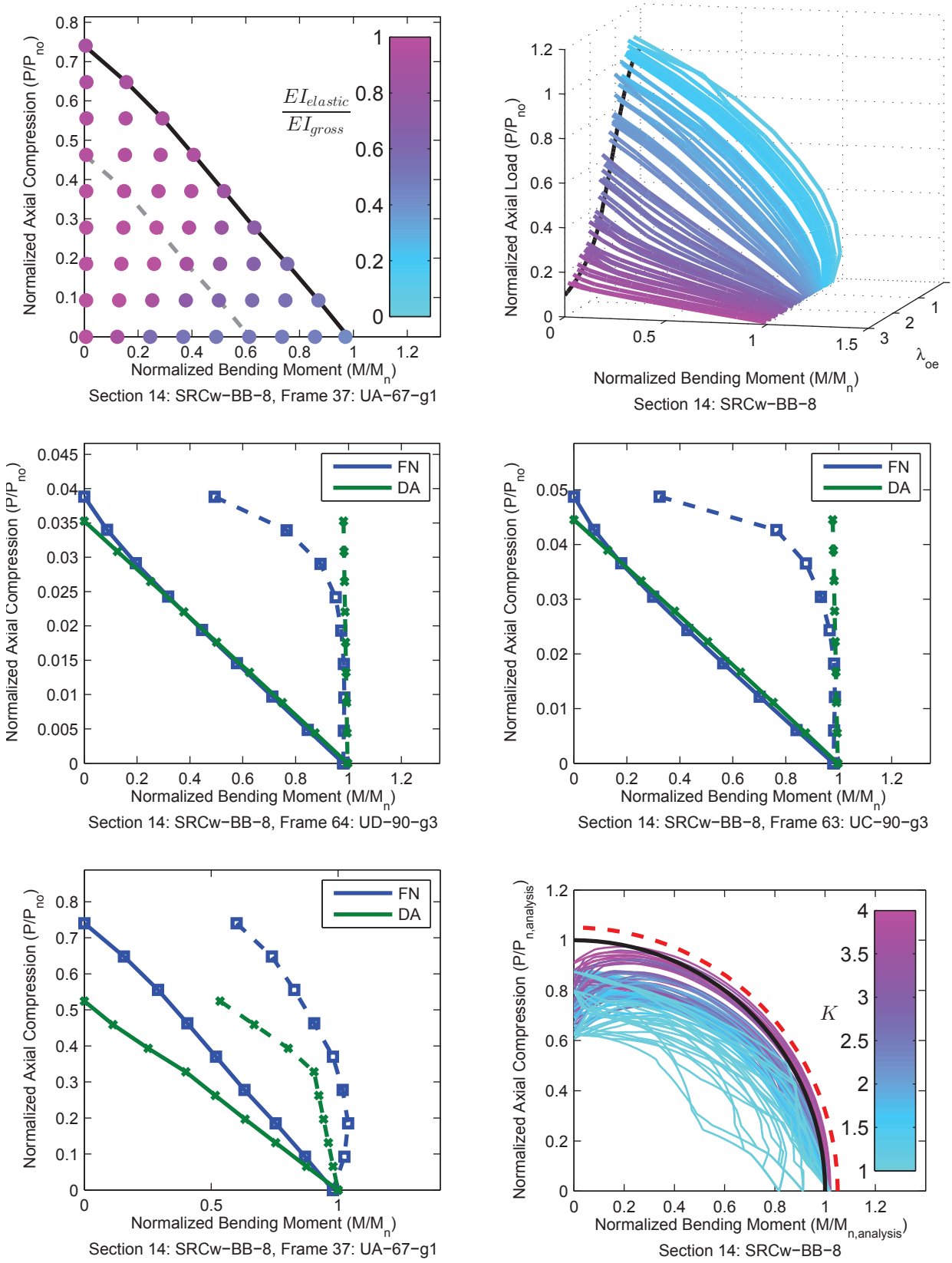

Figure A.80. Detailed Results for Section SRCw-BB-8

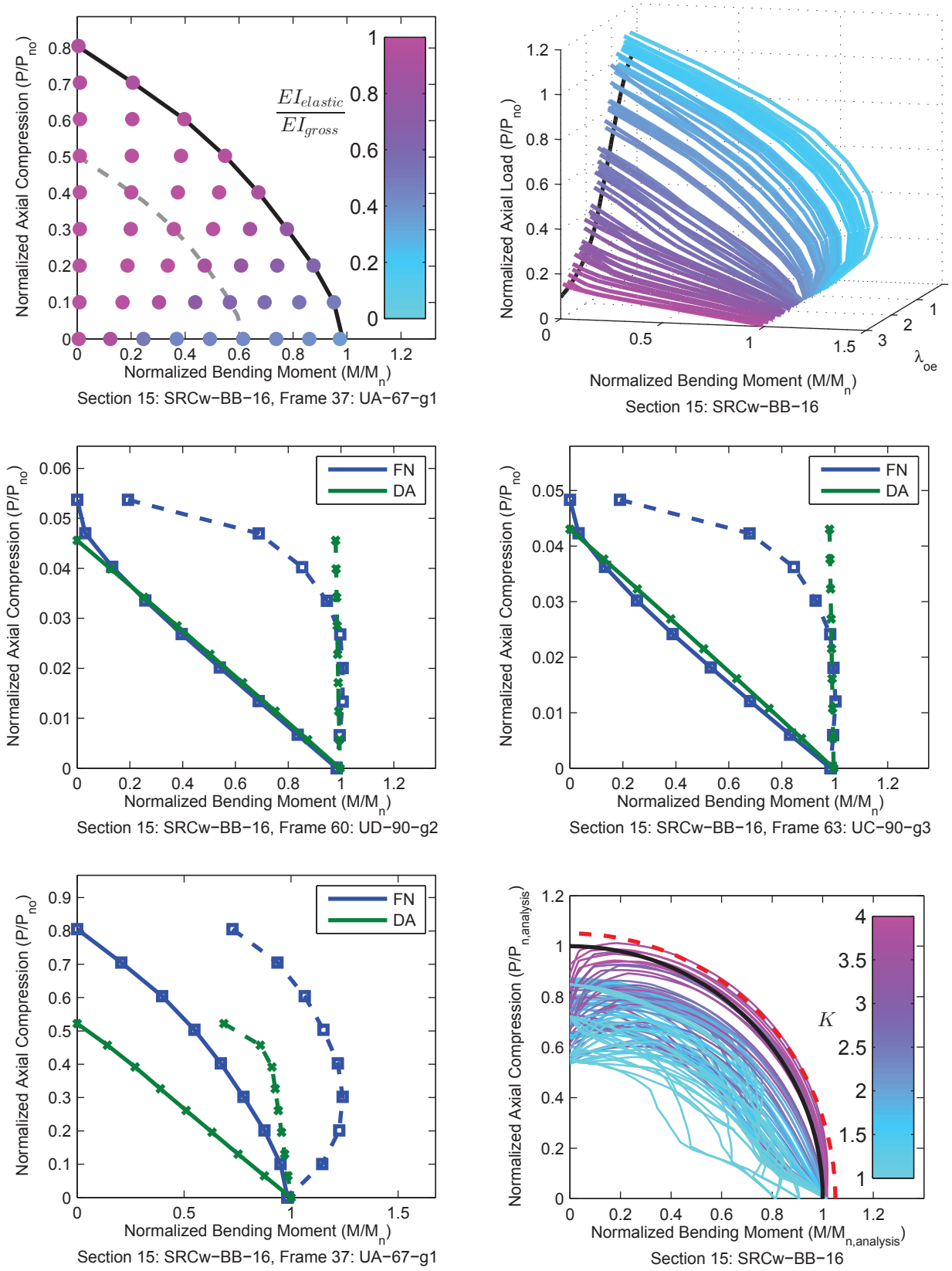

Figure A.81. Detailed Results for Section SRCw-BB-16

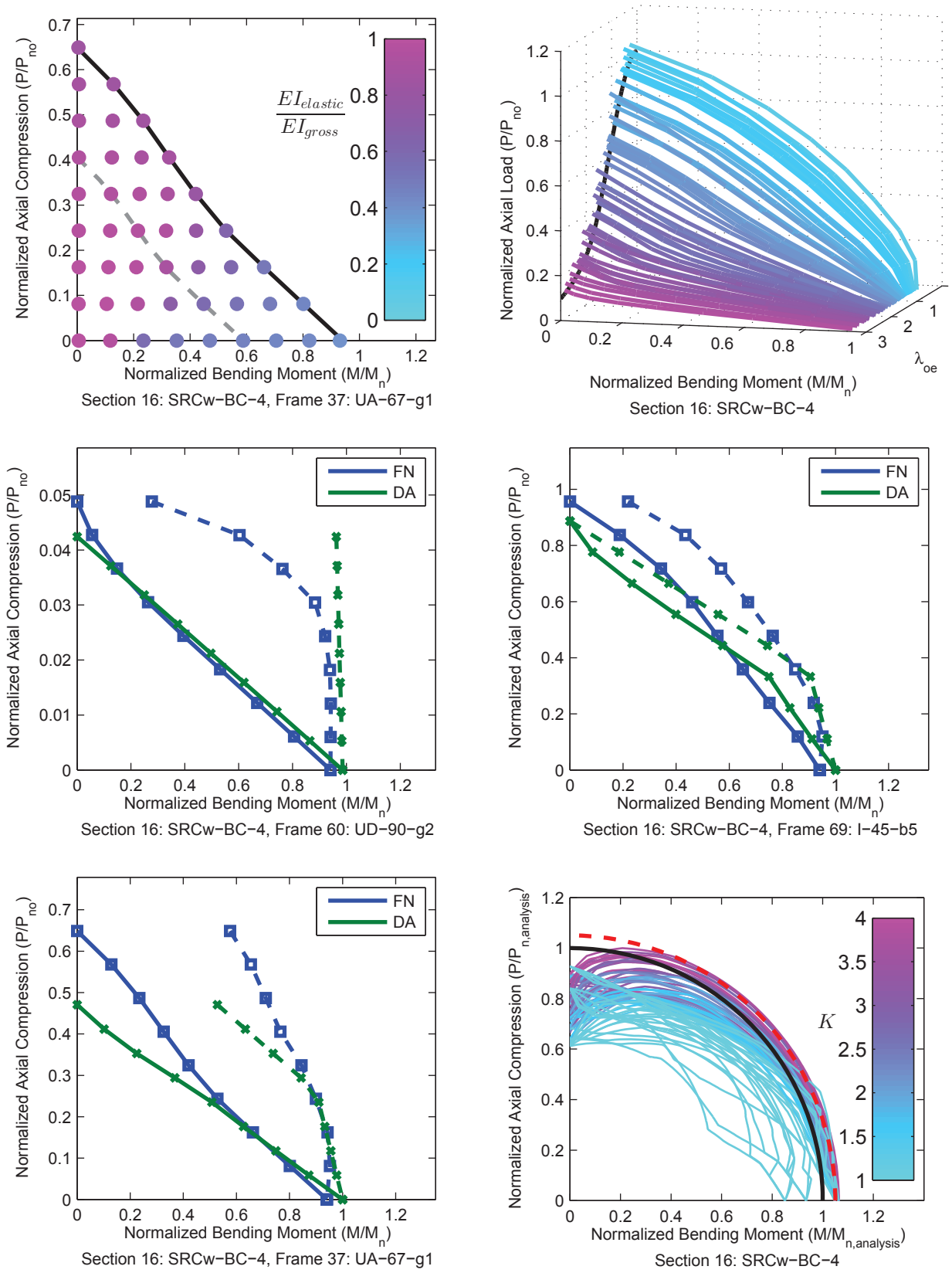

Figure A.82. Detailed Results for Section SRCw-BC-4

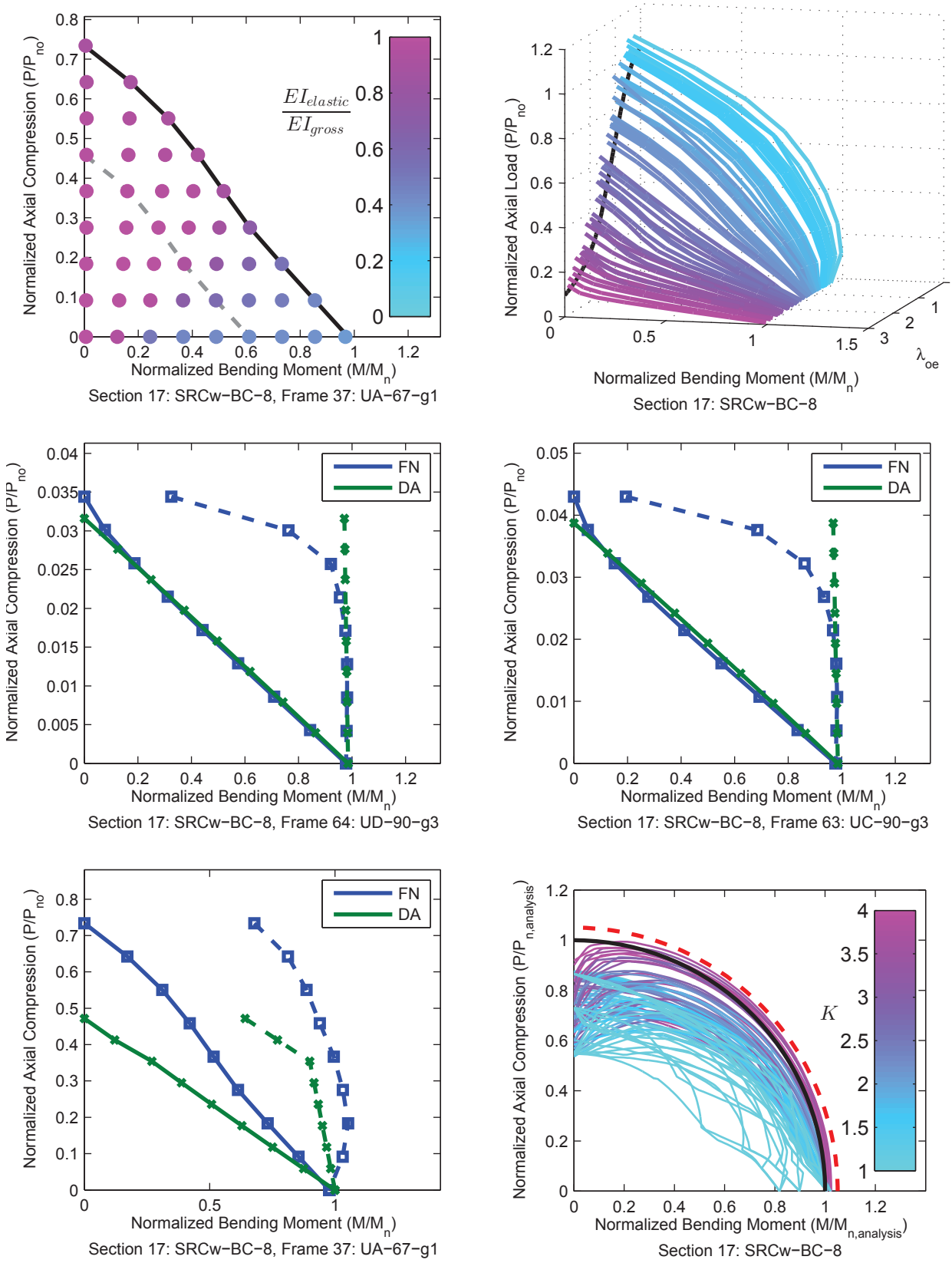

Figure A.83. Detailed Results for Section SRCw-BC-8

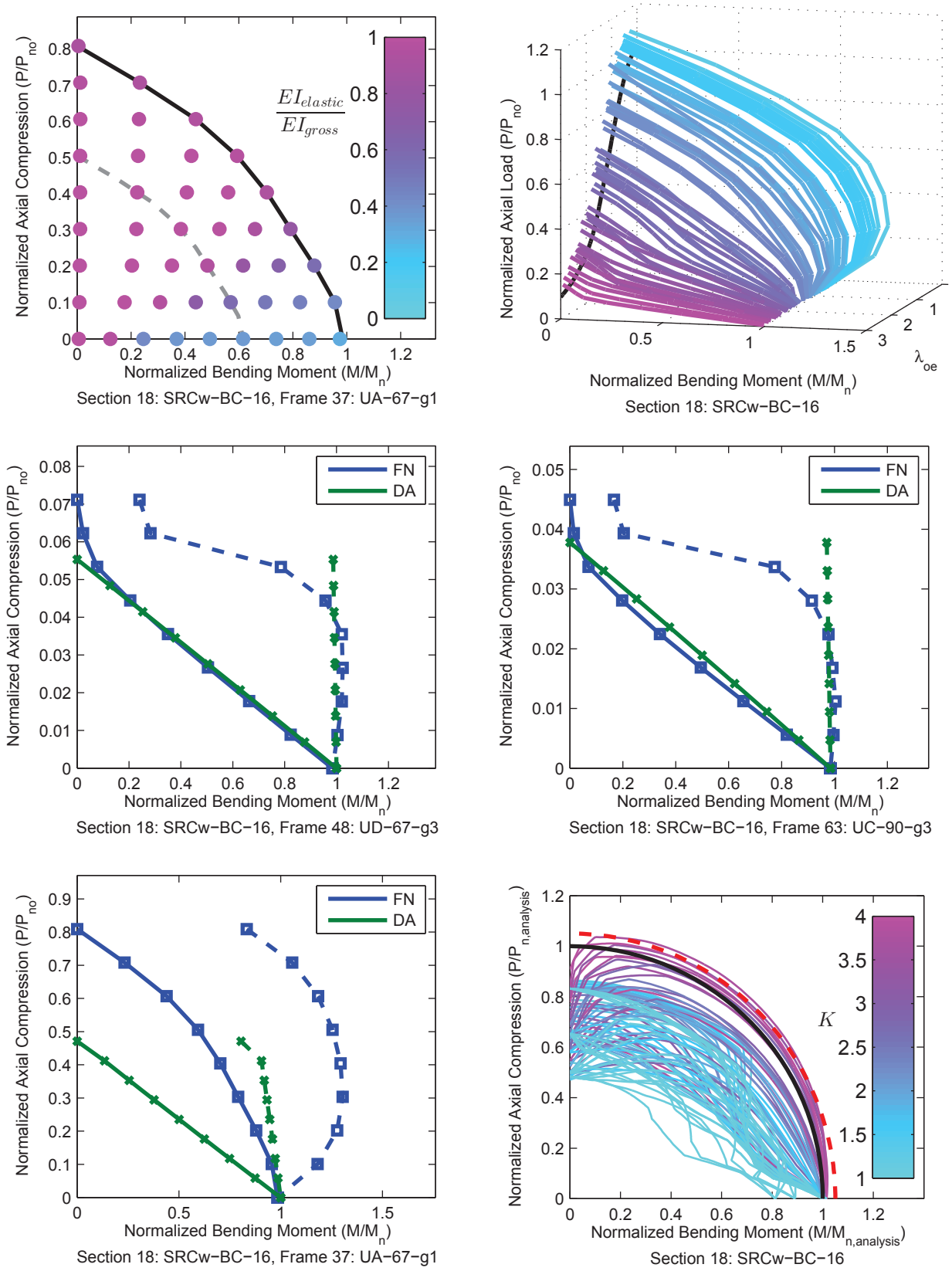

Figure A.84. Detailed Results for Section SRCw-BC-16

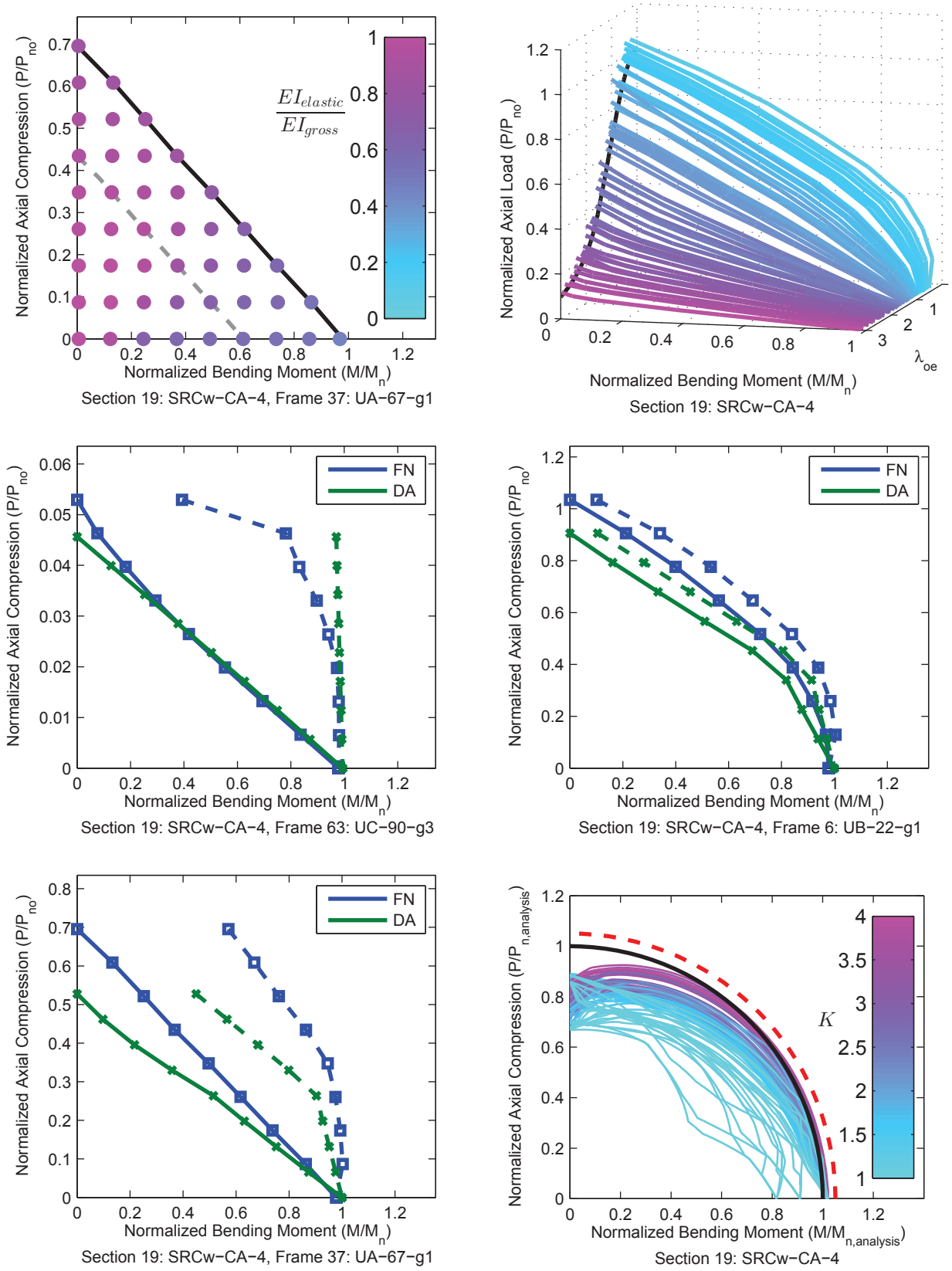

Figure A.85. Detailed Results for Section SRCw-CA-4

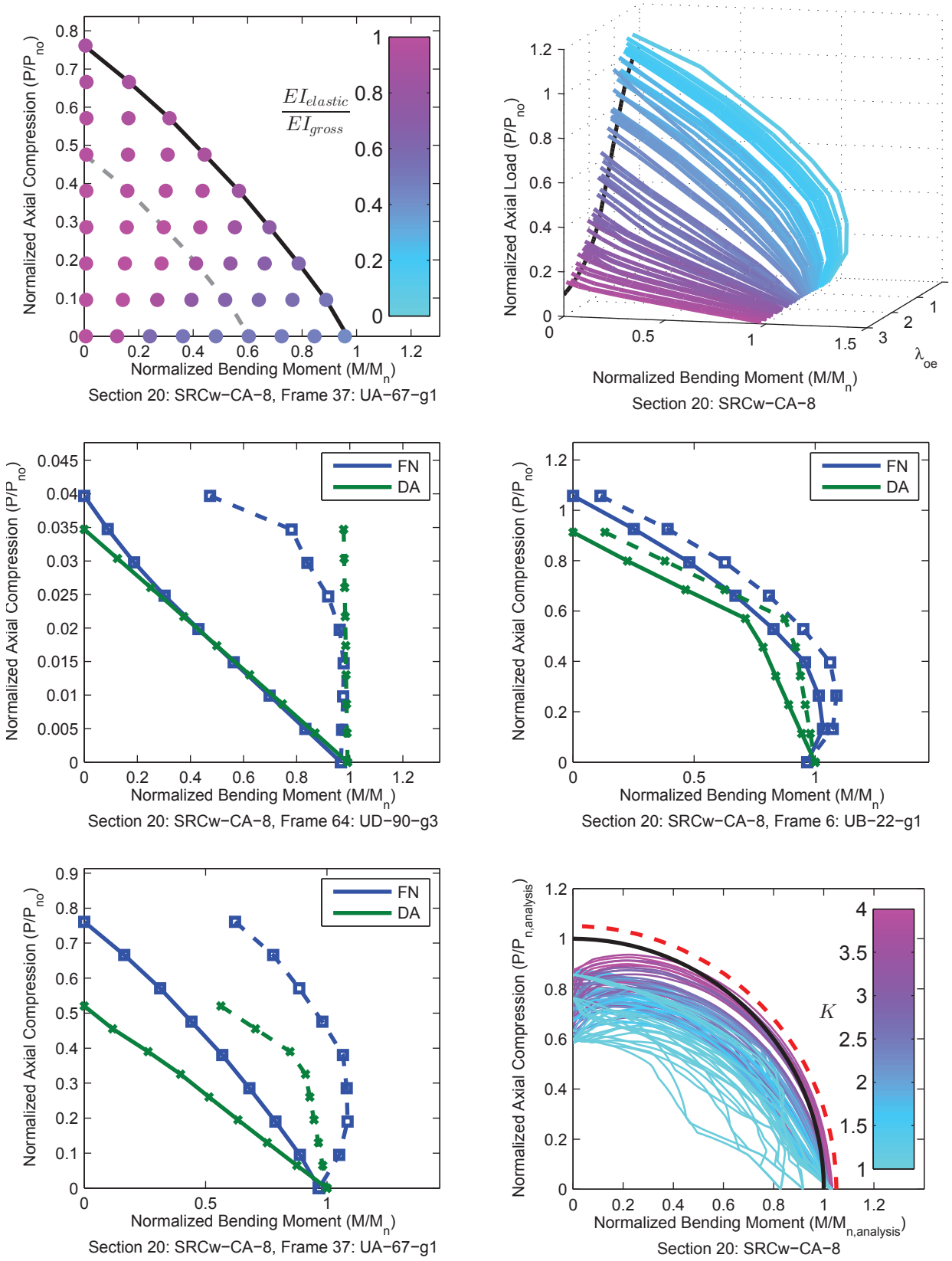

Figure A.86. Detailed Results for Section SRCw-CA-8

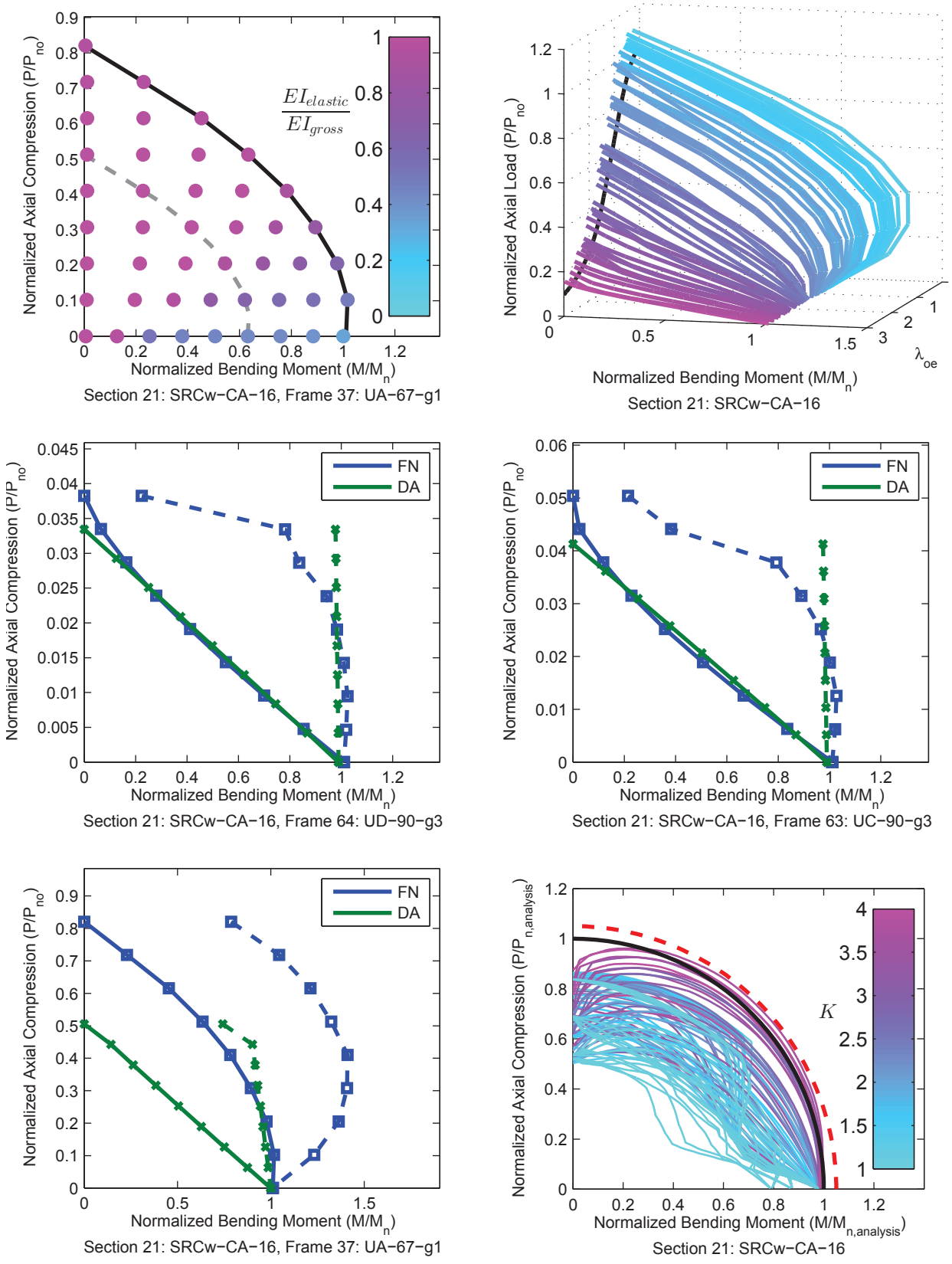

Figure A.87. Detailed Results for Section SRCw-CA-16

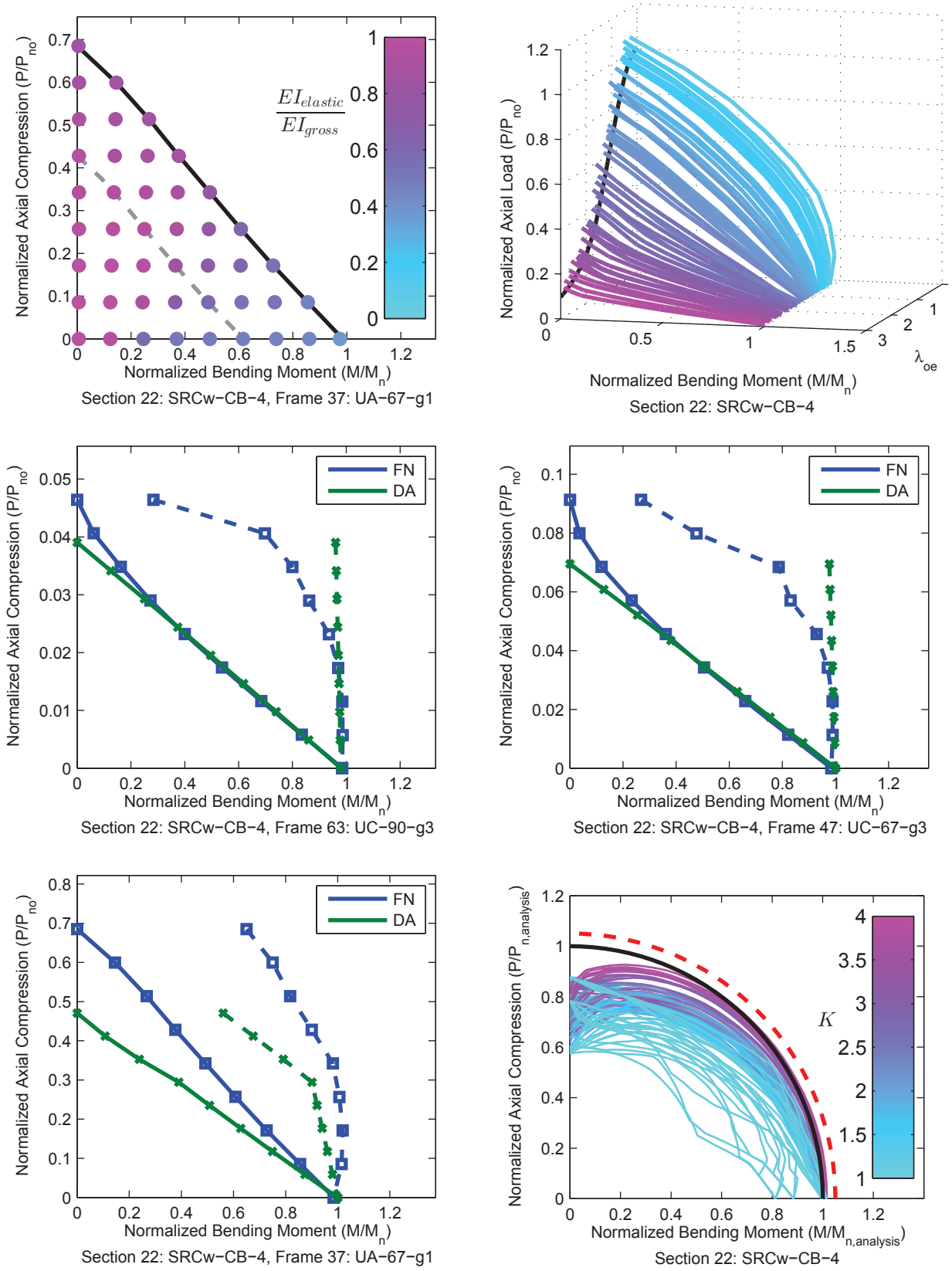

Figure A.88. Detailed Results for Section SRCw-CB-4

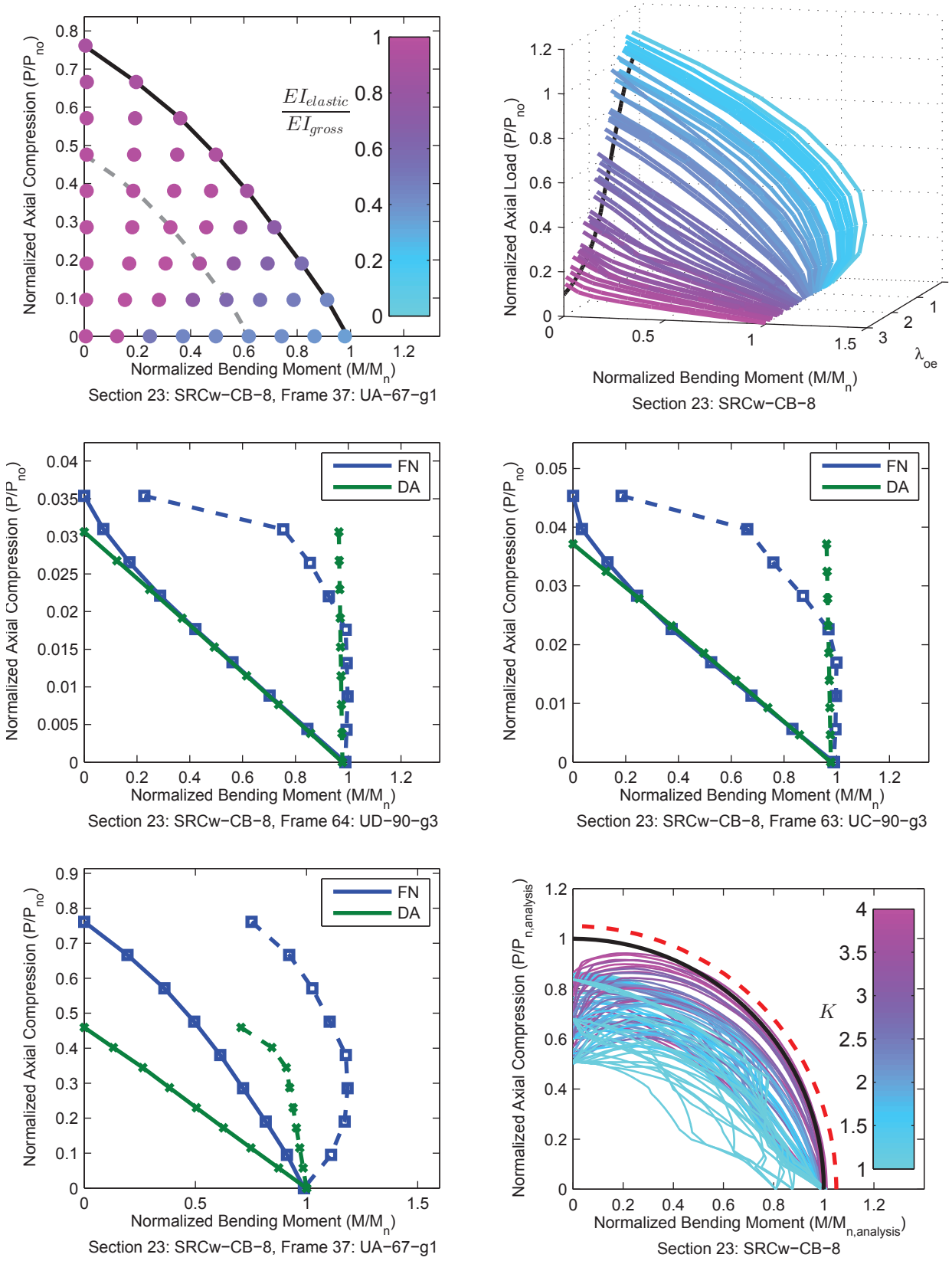

Figure A.89. Detailed Results for Section SRCw-CB-8

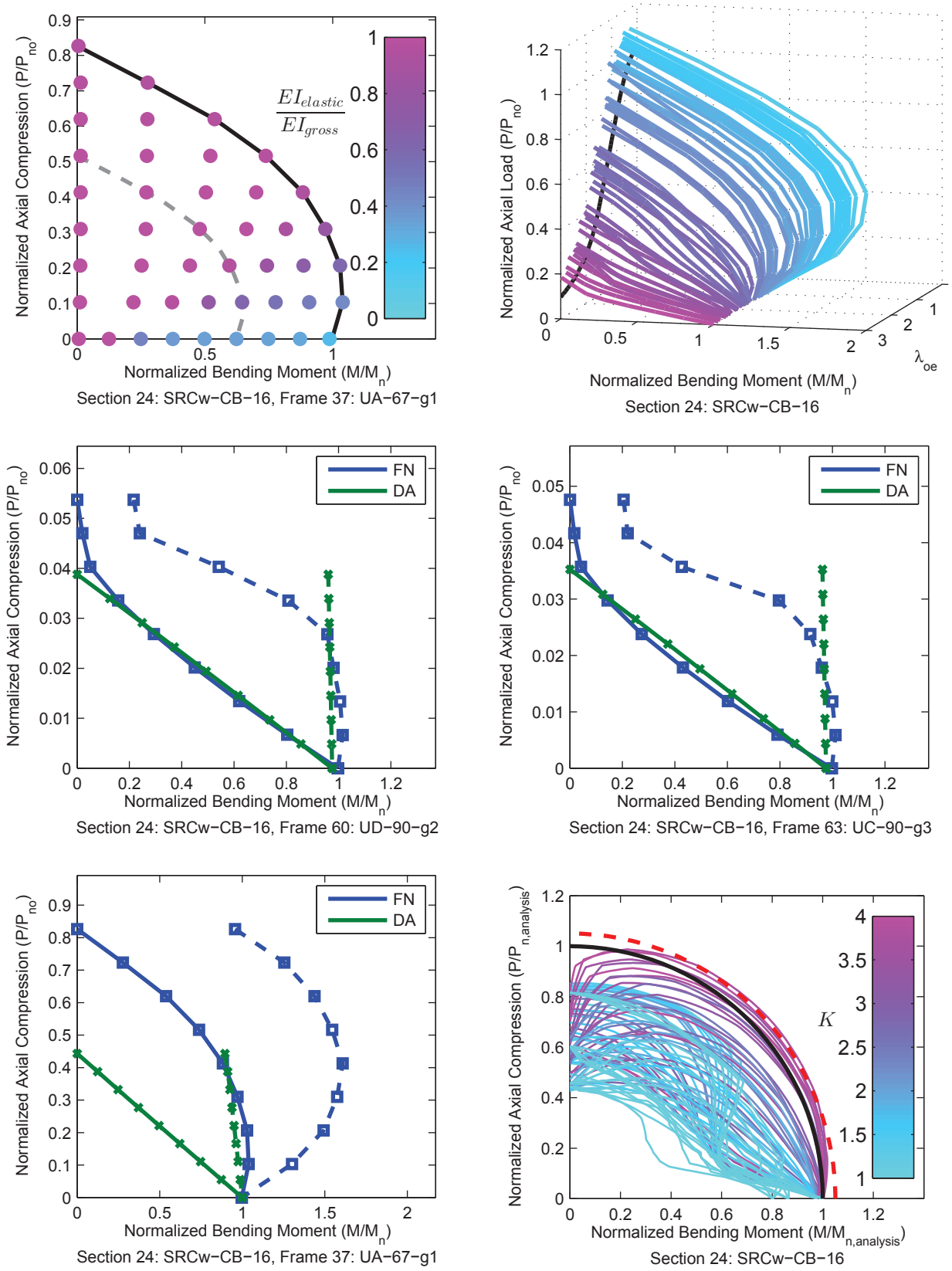

Figure A.90. Detailed Results for Section SRCw-CB-16

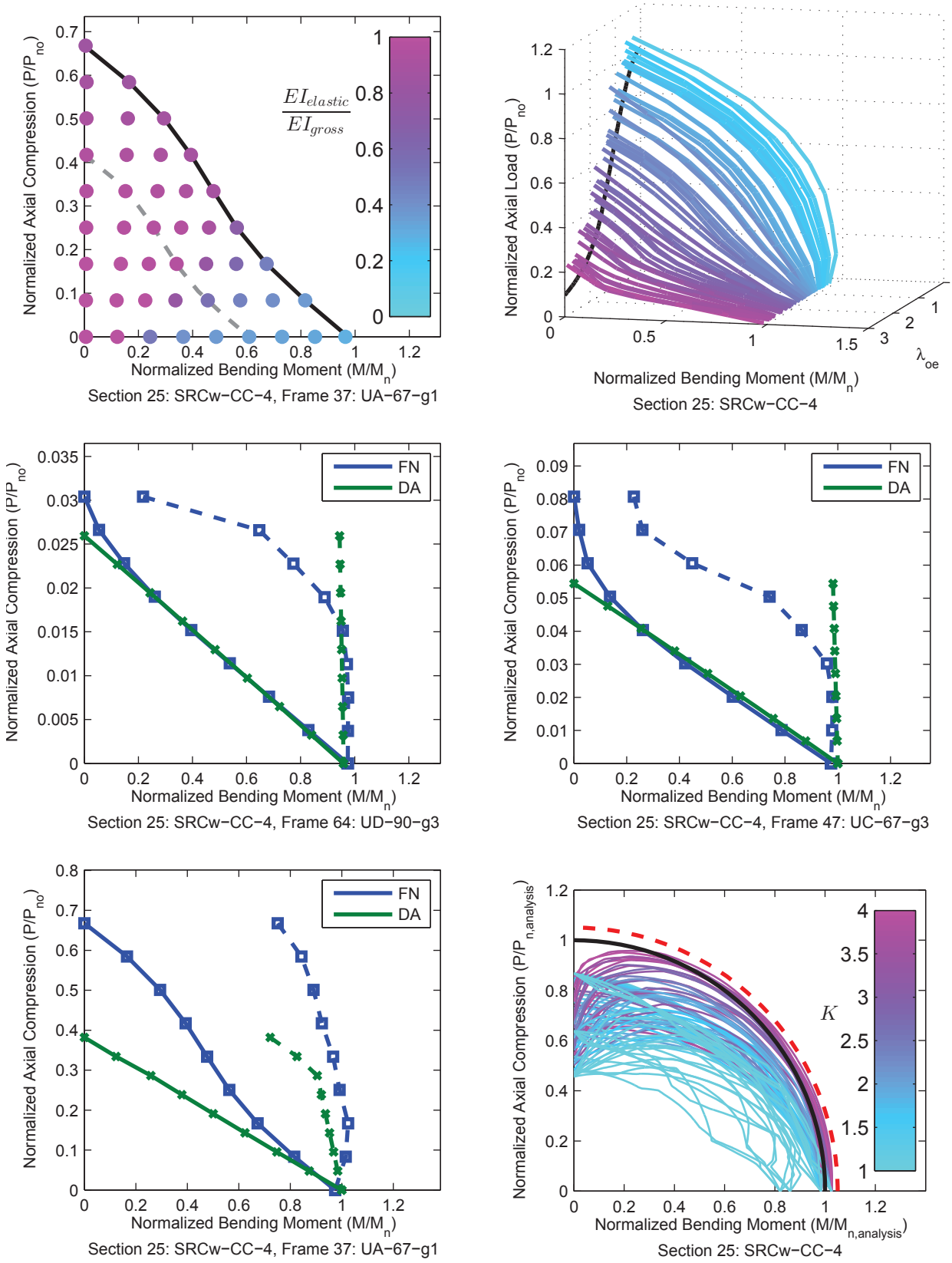

Figure A.91. Detailed Results for Section SRCw-CC-4

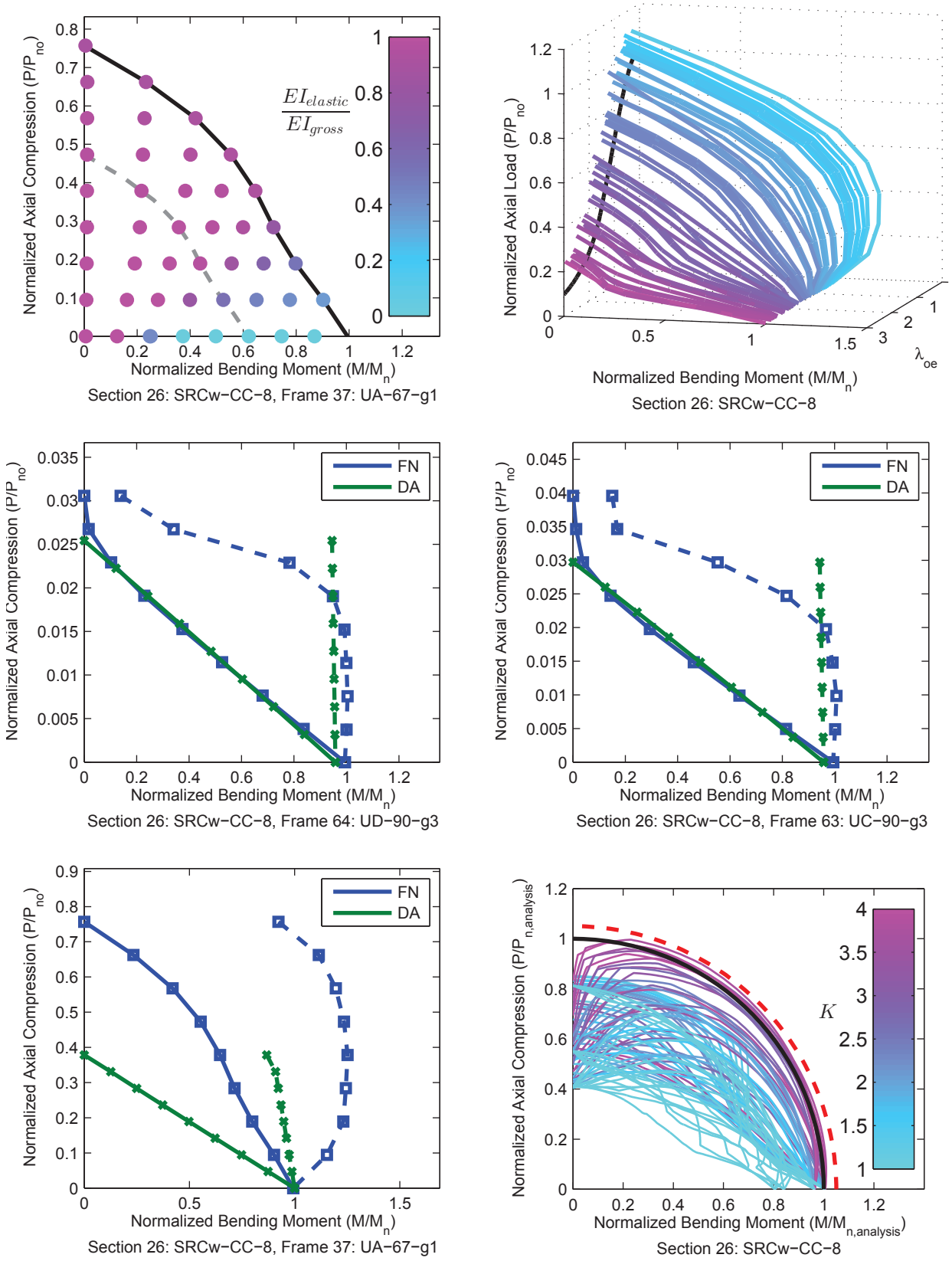

Figure A.92. Detailed Results for Section SRCw-CC-8

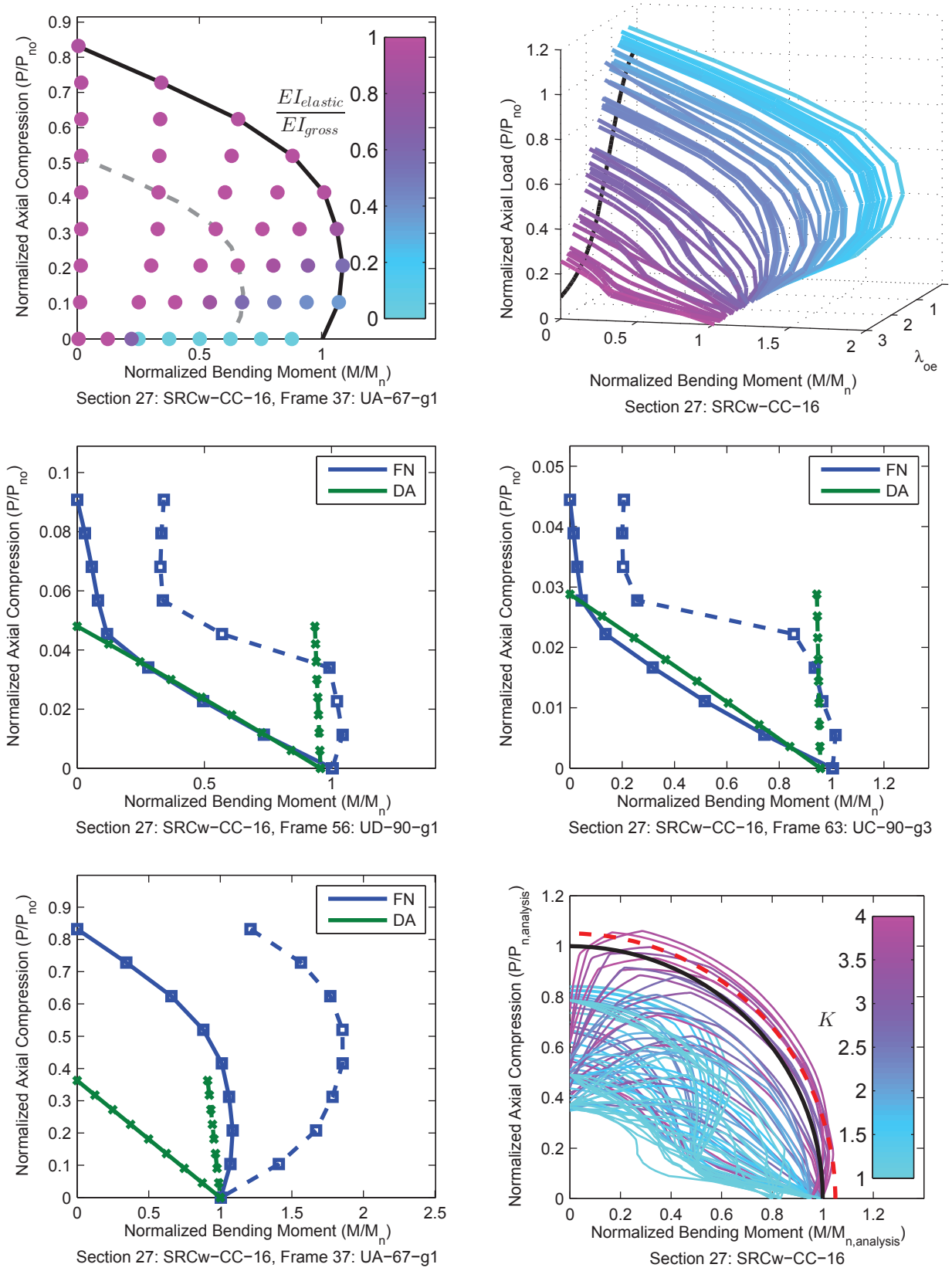

Figure A.93. Detailed Results for Section SRCw-CC-16

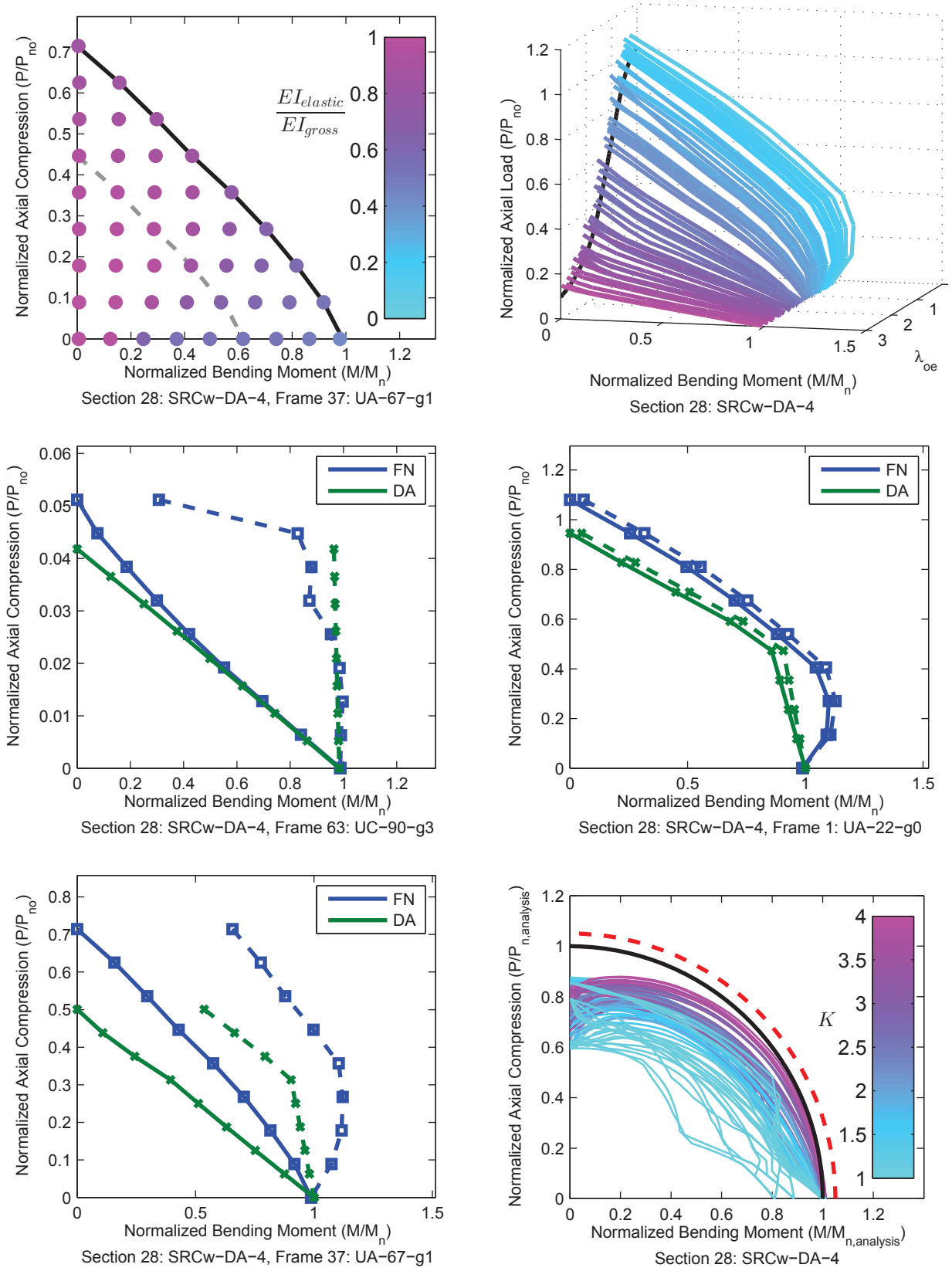

Figure A.94. Detailed Results for Section SRCw-DA-4

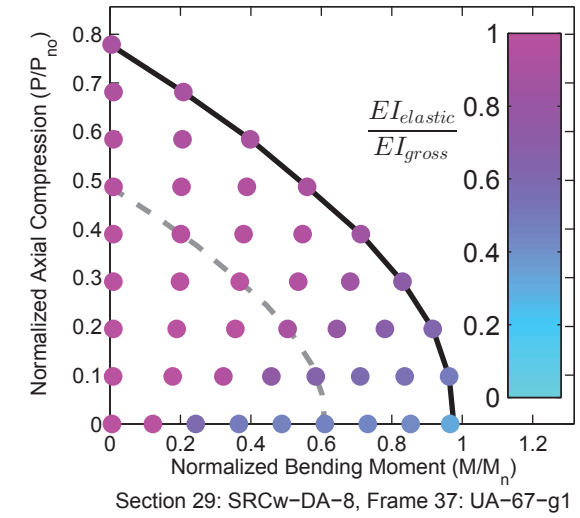

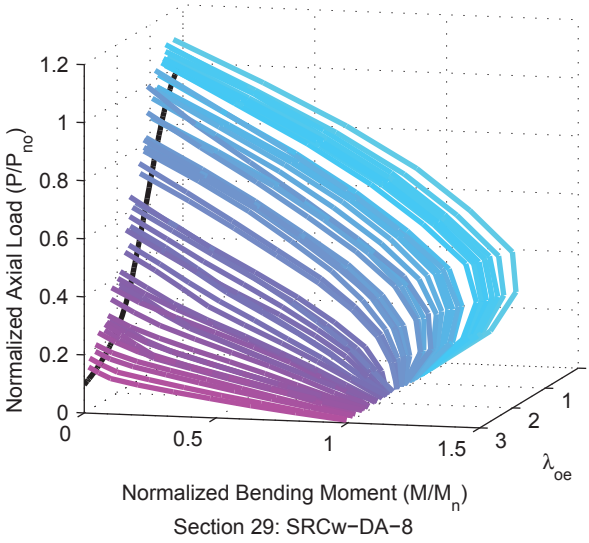

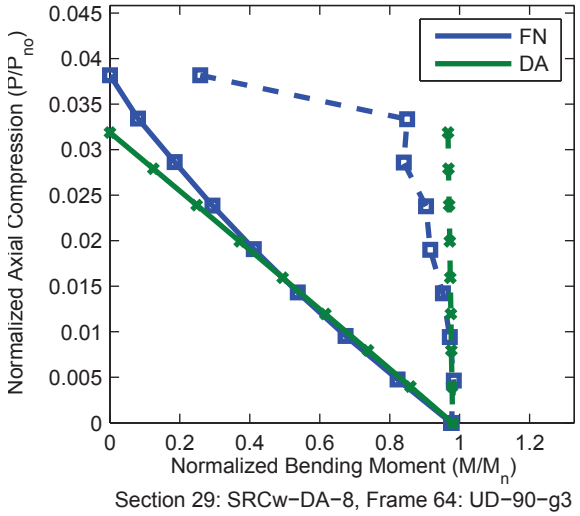

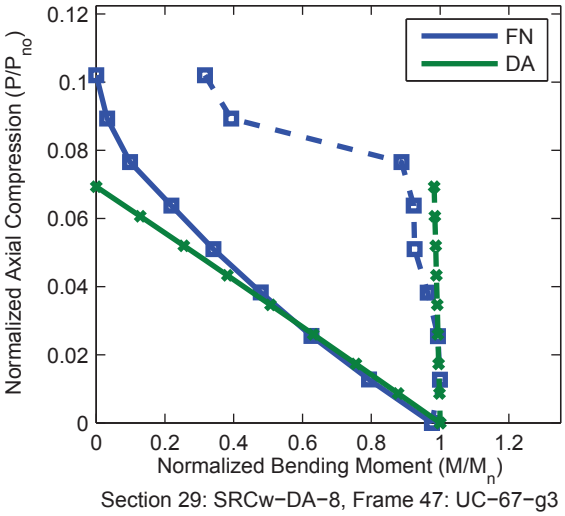

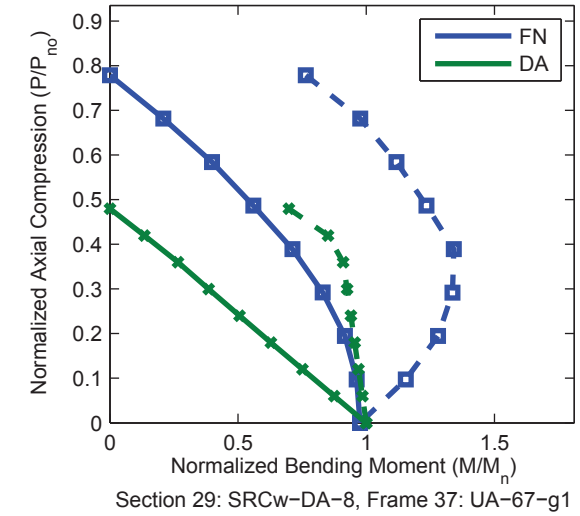

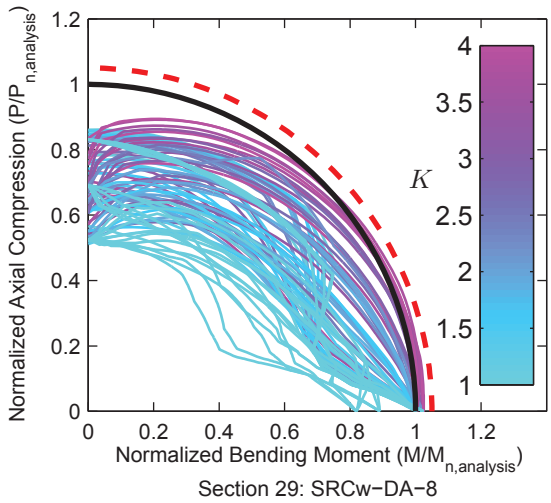

Figure A.95. Detailed Results for Section SRCw-DA-8

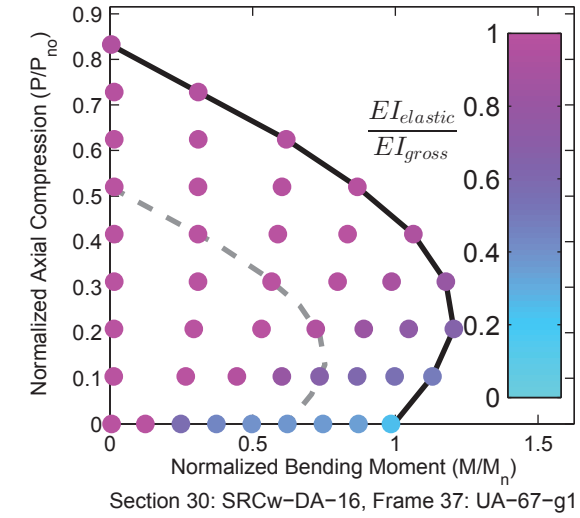

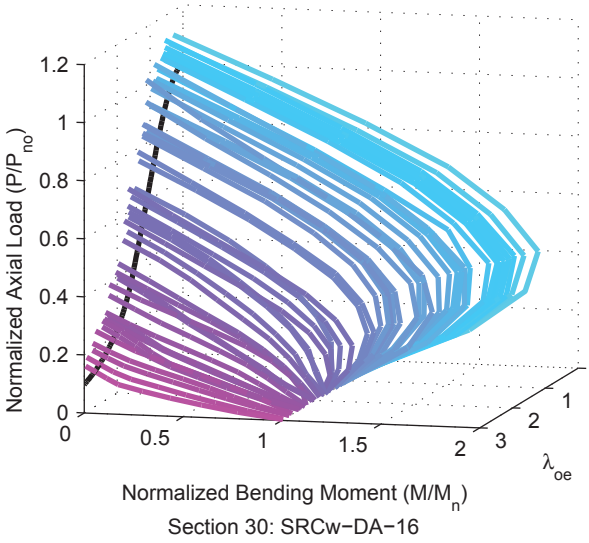

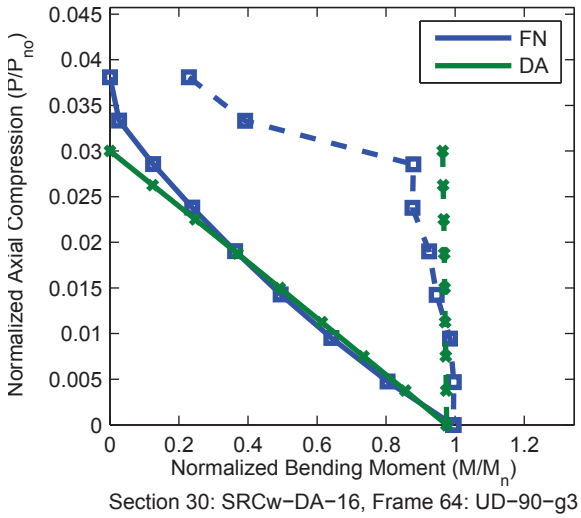

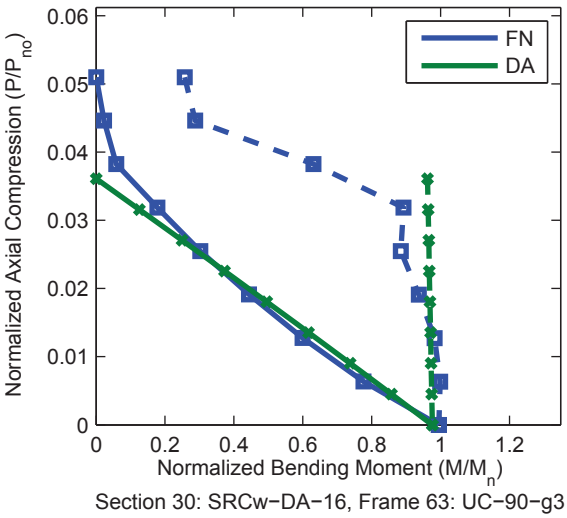

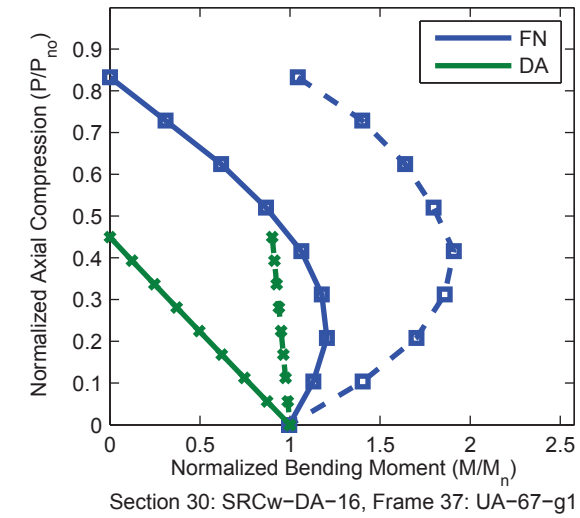

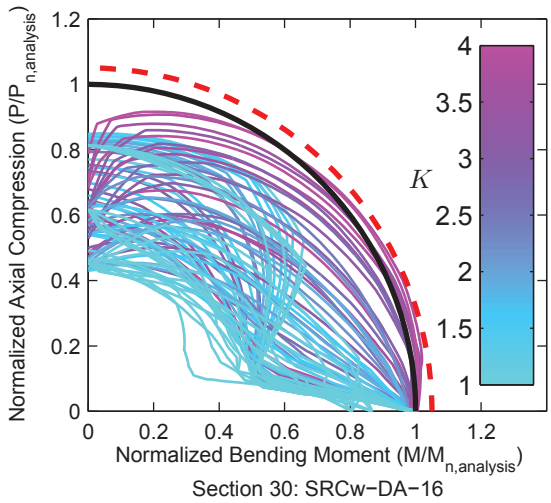

Figure A.96. Detailed Results for Section SRCw-DA-16

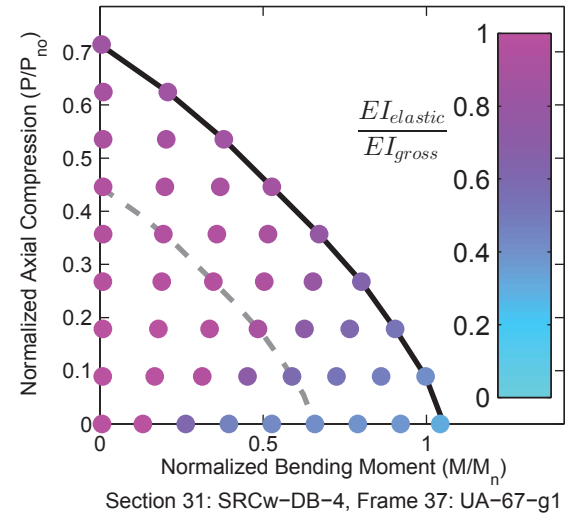

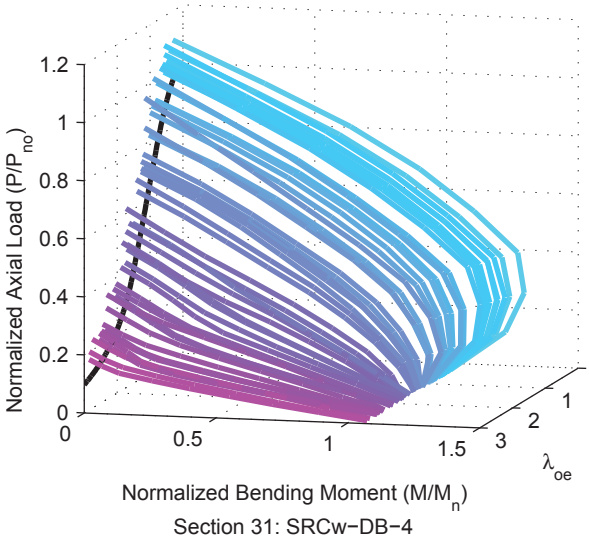

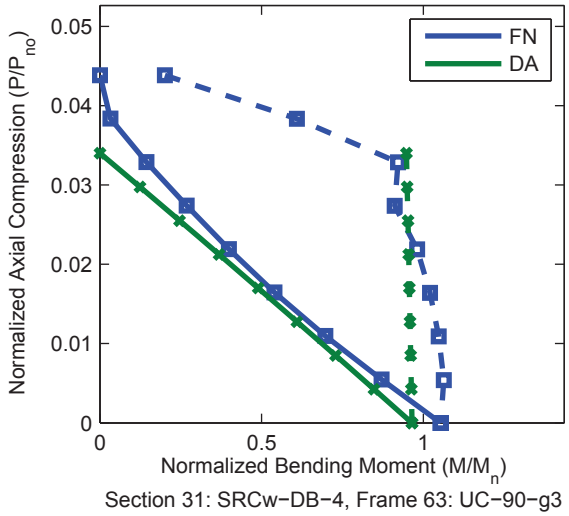

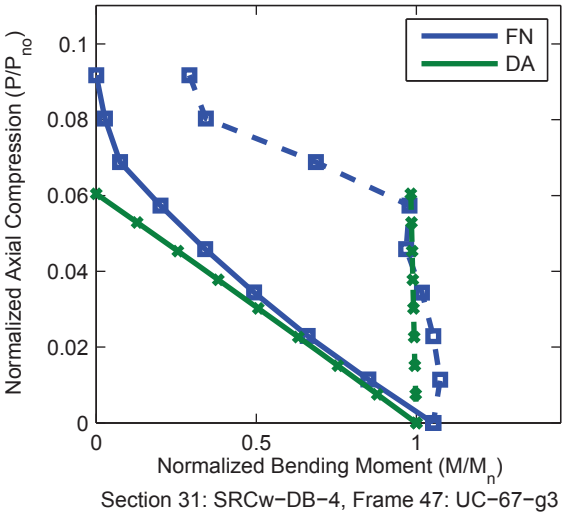

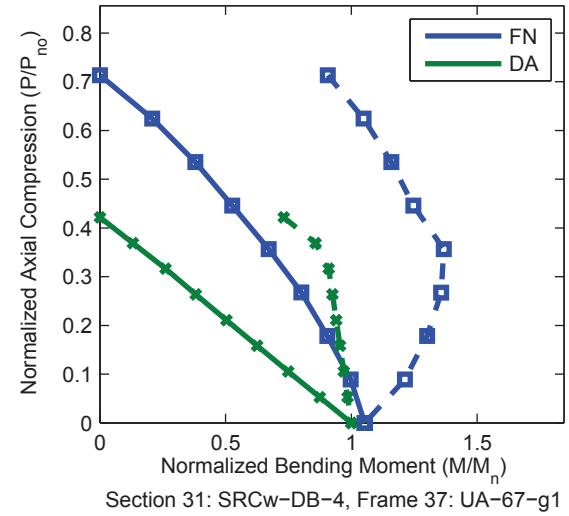

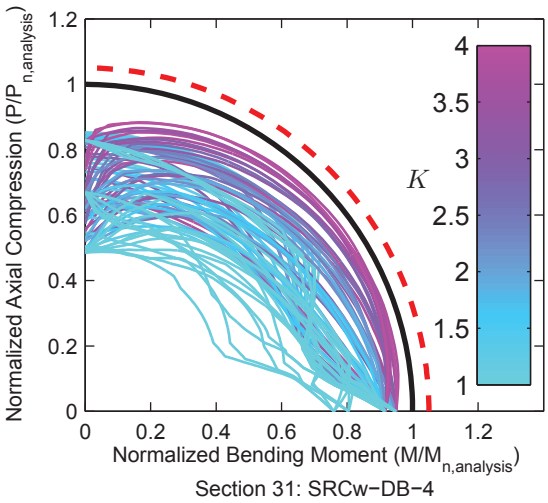

Figure A.97. Detailed Results for Section SRCw-DB-4

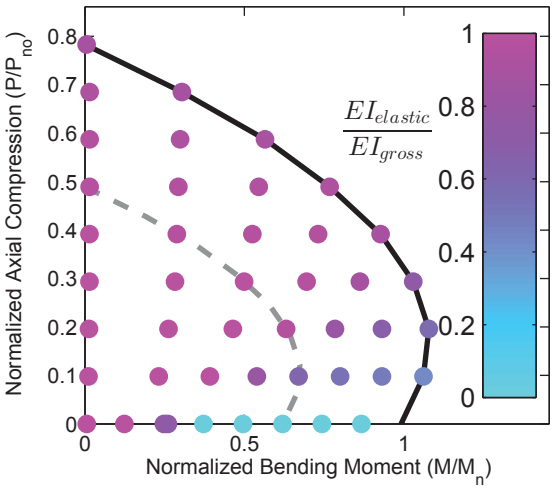

Section 32: SRCw−DB−8, Frame 37: UA−67−g1

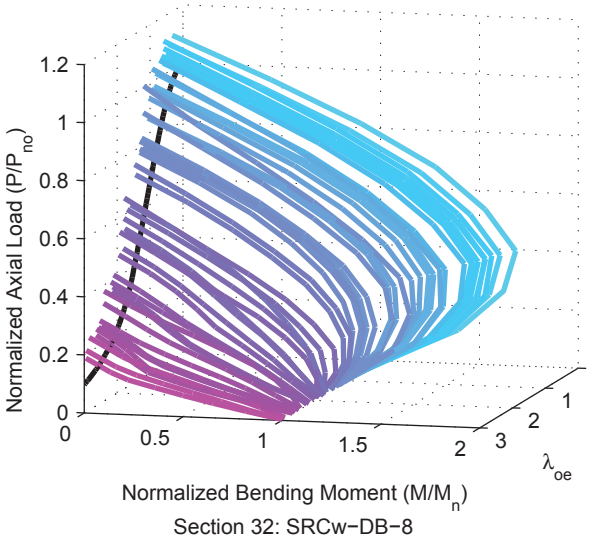

Section 32: SRCw−DB−8

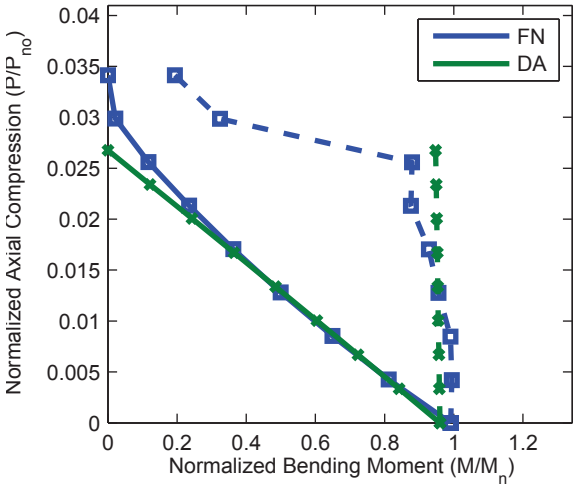

Section 32: SRCw−DB−8, Frame 64: UD−90−g3

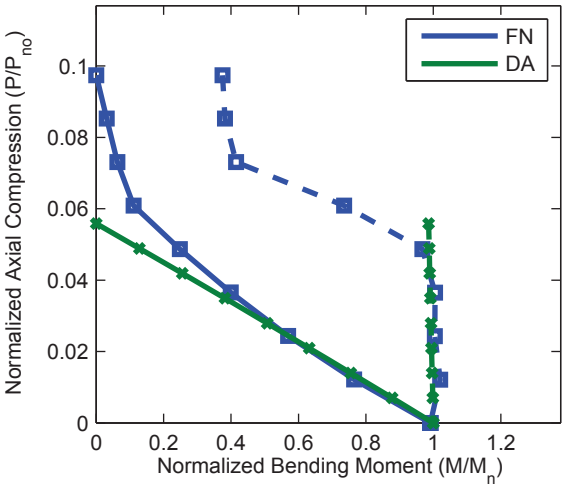

Section 32: SRCw−DB−8, Frame 47: UC−67−g3

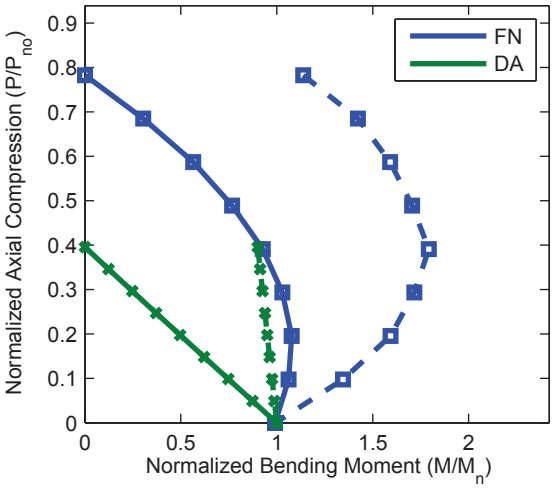

Section 32: SRCw−DB−8, Frame 37: UA−67−g1

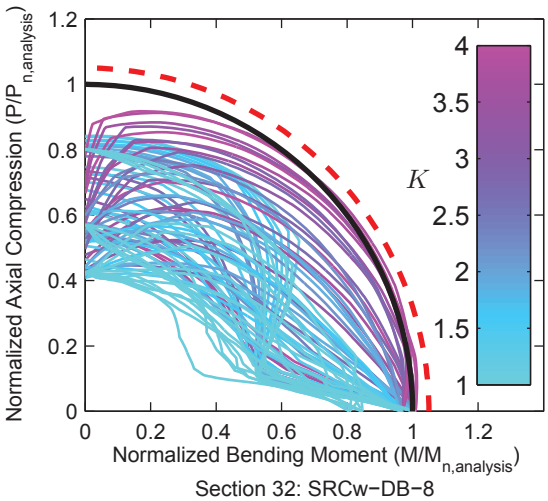

Section 32: SRCw−DB−8

Figure A.98. Detailed Results for Section SRCw-DB-8

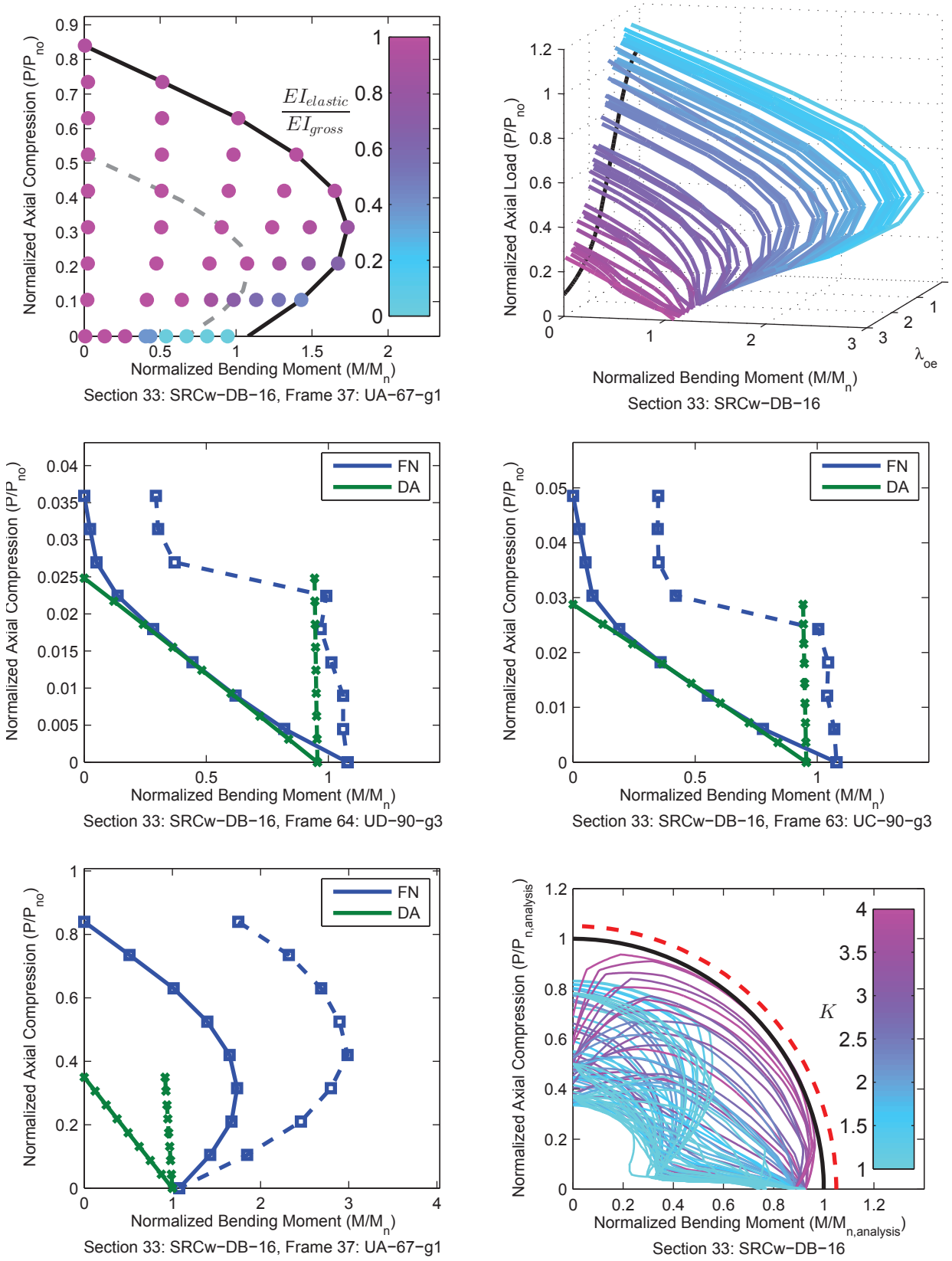

Figure A.99. Detailed Results for Section SRCw-DB-16

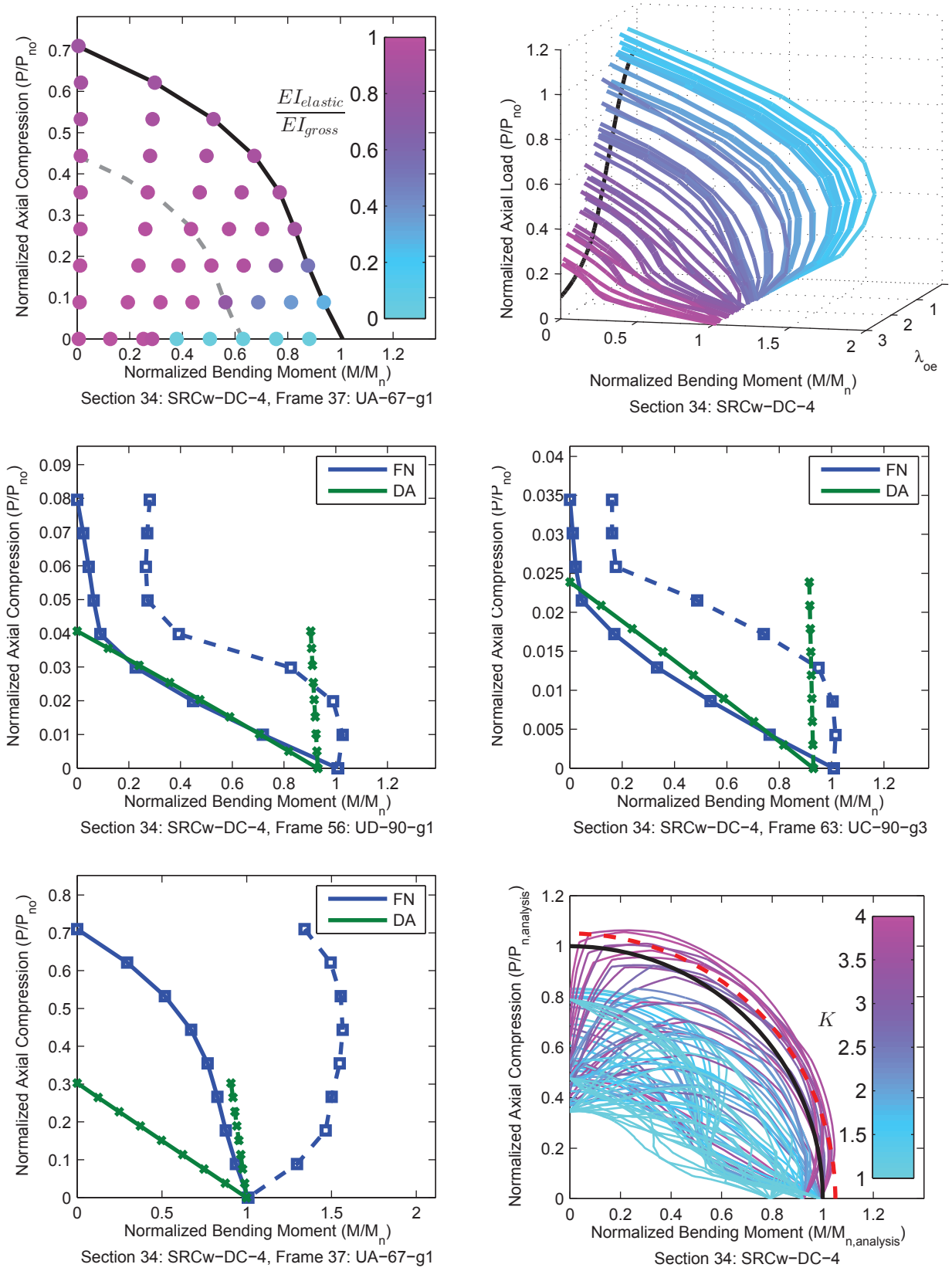

Figure A.100. Detailed Results for Section SRCw-DC-4

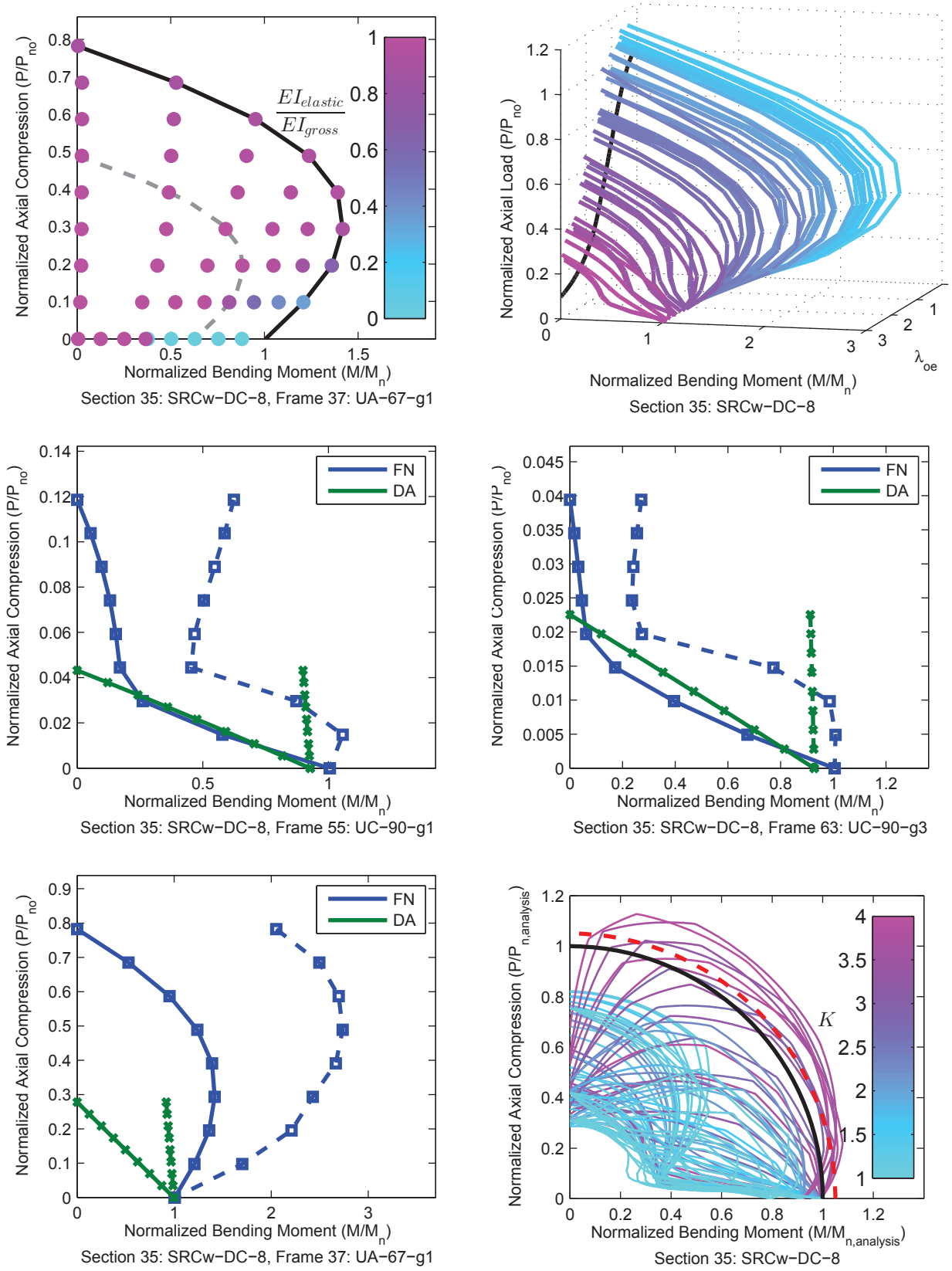

Figure A.101. Detailed Results for Section SRCw-DC-8

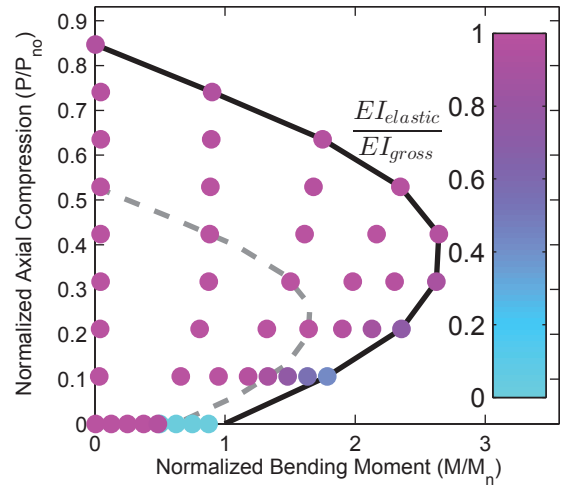

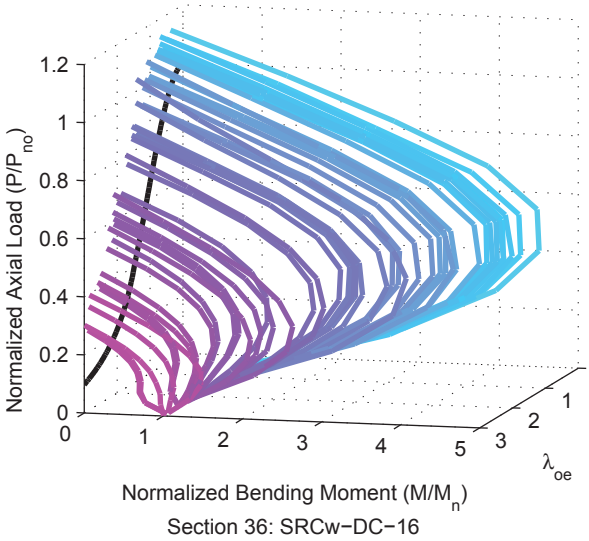

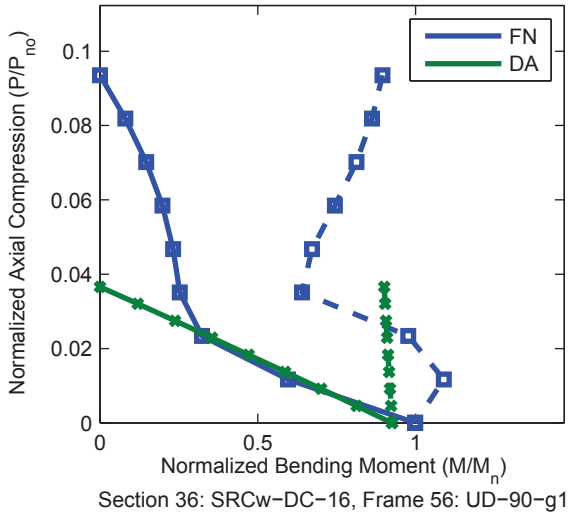

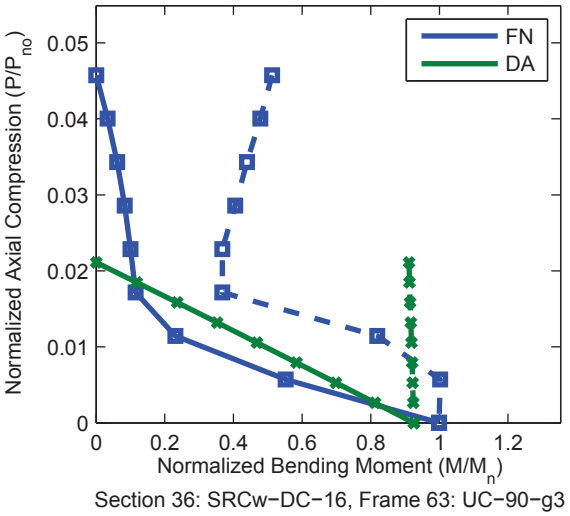

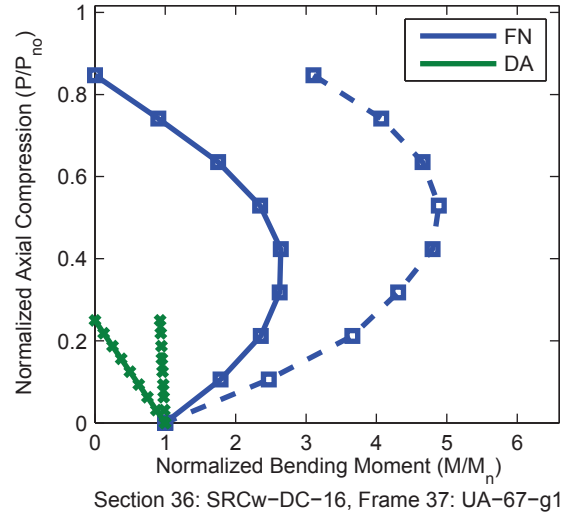

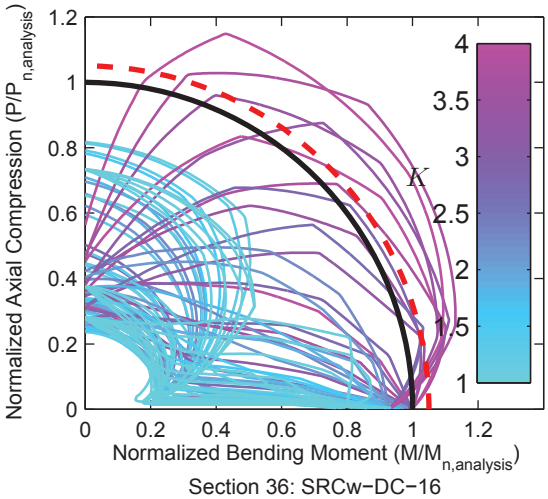

Figure A.102. Detailed Results for Section SRCw-DC-16

A.2 Alternative Methods of Design

For each alternative method of design analyzed in Chapter 6, all frame and section pairs where the maximum unconservative error was larger than that of Method A by more than 0.5% were identified and are presented here. Tabular listings of the frame and section pairs are given followed by figure with interaction diagrams that compare the fully nonlinear analyses, Method A, and the alternative method of design. Descriptions of the different methods are presented and details of the analyses are presented in Chapter 6.

A.2.1 Method B

Table A.2. Maximum Unconservative Error Results for Method B

Frame	Section	Maximum Unconservative Error	
		Method A	Method B
UC-45-g0	RCFT-A-16	0.00%	-0.85%
UC-45-g0	RCFT-B-16	0.00%	-0.53%
UC-22-g1	CCFT-A-8	-0.94%	-3.10%
UD-22-g1	CCFT-A-8	-1.08%	-2.61%
UC-45-g0	CCFT-A-8	-5.16%	-6.59%
UD-22-g0	CCFT-A-16	0.00%	-0.55%
UC-22-g1	CCFT-A-16	-3.26%	-6.65%
UD-22-g1	CCFT-A-16	-3.79%	-6.73%
UC-22-g2	CCFT-A-16	-7.72%	-9.53%
UC-45-g0	CCFT-A-16	-12.64%	-15.85%
UA-45-g1	CCFT-A-16	-0.18%	-0.83%
UC-22-g1	CCFT-C-16	0.00%	-1.45%
UD-22-g1	CCFT-C-16	0.00%	-1.34%
UC-22-g2	CCFT-C-16	0.00%	-2.93%
UC-45-g0	CCFT-C-16	-0.49%	-4.42%

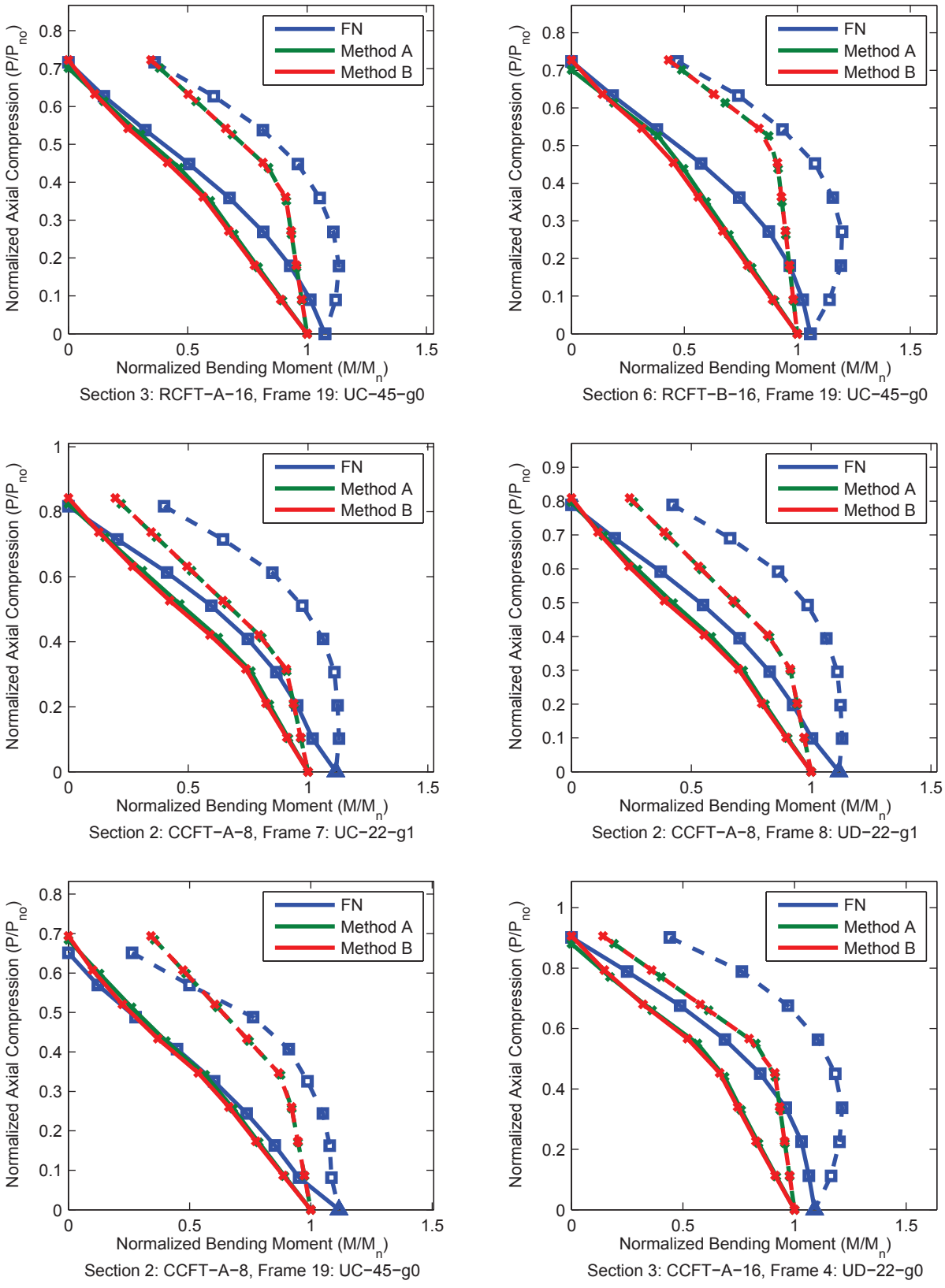

Figure A.103. Detailed Results for Method B

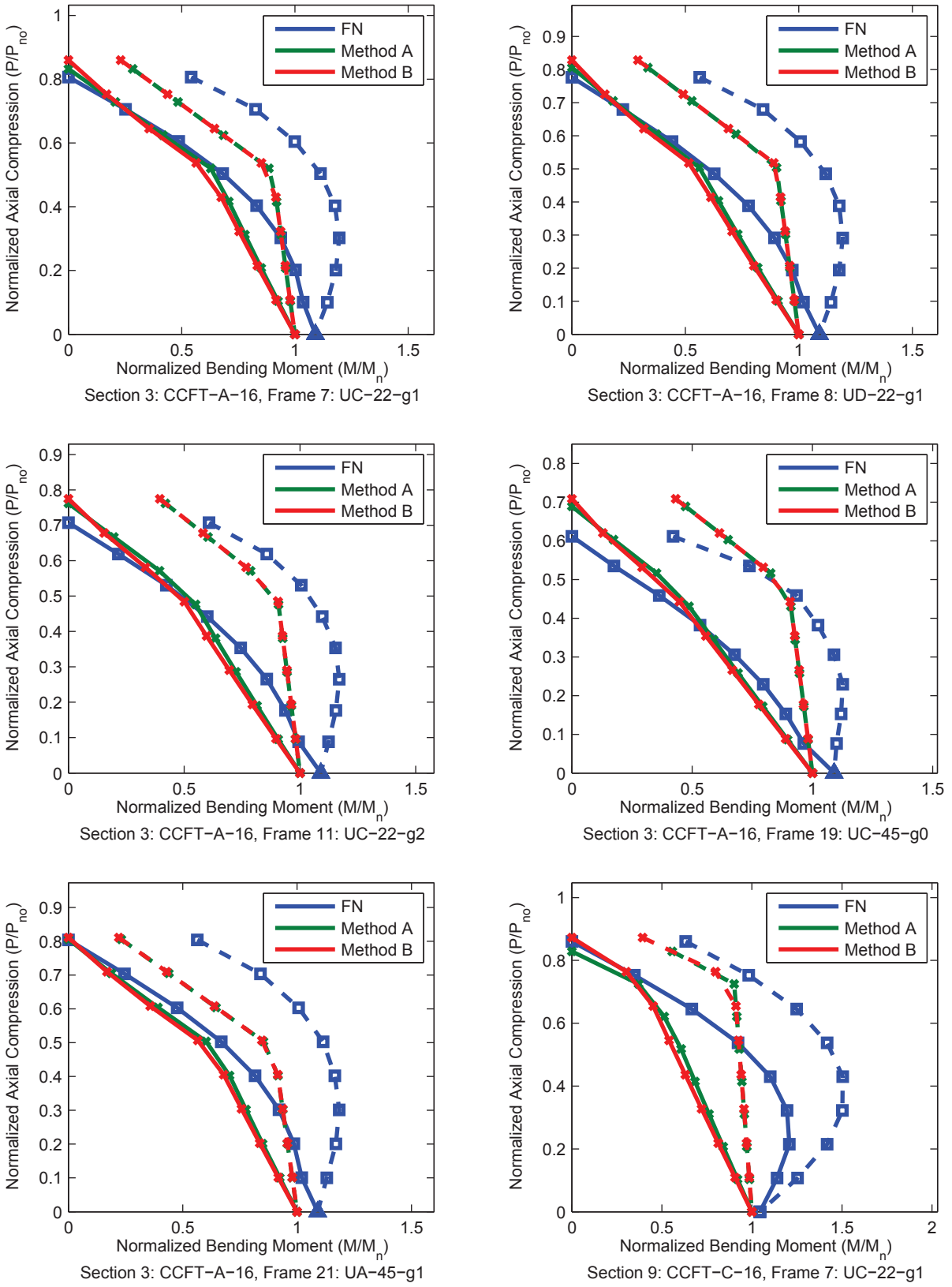

Figure A.103. Detailed Results for Method B (continued)

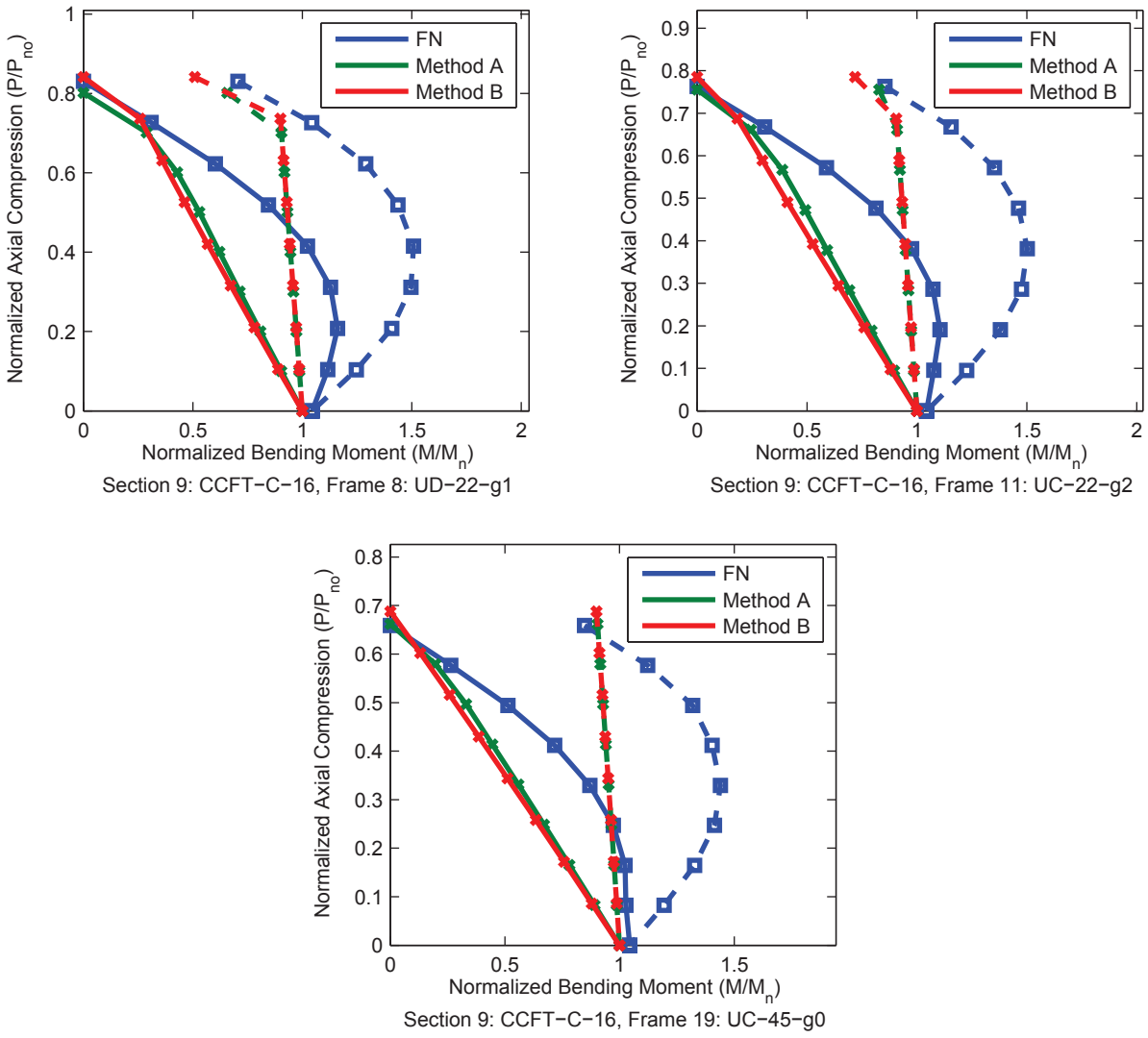

Figure A.103. Detailed Results for Method B (continued)

A.2.2 Method C

Table A.3. Maximum Unconservative Error Results for Method C

Frame	Section	Maximum Unconservative Error	
		Method A	Method C
I-135-b1	RCFT-A-4	0.00%	-2.49%
I-135-b2	RCFT-A-4	0.00%	-2.49%
I-135-b3	RCFT-A-4	0.00%	-2.49%
I-135-b4	RCFT-A-4	0.00%	-2.49%
I-135-b5	RCFT-A-4	0.00%	-2.49%
I-135-b1	RCFT-A-8	0.00%	-1.47%
I-135-b2	RCFT-A-8	0.00%	-1.47%
I-135-b3	RCFT-A-8	0.00%	-1.47%
I-135-b4	RCFT-A-8	0.00%	-1.47%
I-135-b5	RCFT-A-8	0.00%	-1.47%
I-135-b1	RCFT-A-16	0.00%	-2.55%
I-135-b2	RCFT-A-16	0.00%	-2.55%
I-135-b3	RCFT-A-16	0.00%	-2.55%
I-135-b4	RCFT-A-16	0.00%	-2.55%
I-135-b5	RCFT-A-16	0.00%	-2.55%
I-90-b5	RCFT-B-4	0.00%	-0.76%
I-135-b1	RCFT-B-4	0.00%	-2.93%
I-135-b2	RCFT-B-4	0.00%	-2.93%
I-135-b3	RCFT-B-4	0.00%	-2.93%
I-135-b4	RCFT-B-4	0.00%	-2.93%
I-135-b5	RCFT-B-4	0.00%	-2.93%
I-90-b5	RCFT-B-8	0.00%	-0.62%
I-135-b1	RCFT-B-8	0.00%	-1.38%
I-135-b2	RCFT-B-8	0.00%	-1.38%
I-135-b3	RCFT-B-8	0.00%	-1.38%
I-135-b4	RCFT-B-8	0.00%	-1.38%
I-135-b5	RCFT-B-8	0.00%	-1.38%
I-135-b1	RCFT-B-16	0.00%	-2.55%
I-135-b2	RCFT-B-16	0.00%	-2.55%
I-135-b3	RCFT-B-16	0.00%	-2.55%
I-135-b4	RCFT-B-16	0.00%	-2.55%
I-135-b5	RCFT-B-16	0.00%	-2.55%
I-90-b5	RCFT-C-4	-0.22%	-2.74%
I-135-b1	RCFT-C-4	0.00%	-1.31%
I-135-b2	RCFT-C-4	0.00%	-1.31%
I-135-b3	RCFT-C-4	0.00%	-1.31%
I-135-b4	RCFT-C-4	0.00%	-1.31%
I-135-b5	RCFT-C-4	0.00%	-1.31%
I-90-b5	RCFT-D-4	0.00%	-1.15%
I-90-b5	CCFT-A-4	-2.64%	-4.82%
I-135-b1	CCFT-A-4	0.00%	-5.65%
I-135-b2	CCFT-A-4	0.00%	-5.65%
I-135-b3	CCFT-A-4	0.00%	-5.65%
I-135-b4	CCFT-A-4	0.00%	-5.65%
I-135-b5	CCFT-A-4	0.00%	-5.65%
I-90-b5	CCFT-A-8	-6.98%	-8.03%
I-135-b1	CCFT-A-8	0.00%	-7.25%
I-135-b2	CCFT-A-8	0.00%	-7.25%
I-135-b3	CCFT-A-8	0.00%	-7.25%
I-135-b4	CCFT-A-8	0.00%	-7.25%
I-135-b5	CCFT-A-8	-0.96%	-7.25%
UA-67-g0	CCFT-A-16	0.00%	-0.91%
UA-90-g0	CCFT-A-16	0.00%	-2.74%
I-45-b5	CCFT-A-16	0.00%	-0.61%

Table A.3. Maximum Unconservative Error Results for Method C (continued)

Frame	Section	Maximum Unconservative Error	
		Method A	Method C
I-135-b1	CCFT-A-16	0.00%	-10.68%
I-135-b2	CCFT-A-16	0.00%	-10.68%
I-135-b3	CCFT-A-16	0.00%	-10.68%
I-135-b4	CCFT-A-16	0.00%	-10.68%
I-135-b5	CCFT-A-16	-2.38%	-10.68%
I-190-b1	CCFT-A-16	0.00%	-0.56%
I-190-b2	CCFT-A-16	0.00%	-0.56%
I-190-b3	CCFT-A-16	0.00%	-0.56%
I-190-b4	CCFT-A-16	0.00%	-0.56%
I-190-b5	CCFT-A-16	0.00%	-0.56%
I-90-b5	CCFT-B-4	-3.45%	-7.00%
I-135-b1	CCFT-B-4	0.00%	-6.52%
I-135-b2	CCFT-B-4	0.00%	-6.52%
I-135-b3	CCFT-B-4	0.00%	-6.52%
I-135-b4	CCFT-B-4	0.00%	-6.52%
I-135-b5	CCFT-B-4	-0.13%	-6.52%
I-190-b1	CCFT-B-4	0.00%	-1.30%
I-190-b2	CCFT-B-4	0.00%	-1.30%
I-190-b3	CCFT-B-4	0.00%	-1.30%
I-190-b4	CCFT-B-4	0.00%	-1.30%
I-190-b5	CCFT-B-4	0.00%	-1.30%
I-135-b1	CCFT-C-16	0.00%	-5.28%
I-135-b2	CCFT-C-16	0.00%	-5.28%
I-135-b3	CCFT-C-16	0.00%	-5.28%
I-135-b4	CCFT-C-16	0.00%	-5.28%
I-135-b5	CCFT-C-16	0.00%	-5.28%
UA-22-g1	CCFT-D-4	0.00%	-0.50%
UA-22-g2	CCFT-D-4	0.00%	-1.36%
UA-22-g3	CCFT-D-4	0.00%	-1.55%
I-45-b5	CCFT-D-4	-0.33%	-2.86%
I-90-b5	CCFT-D-4	-3.30%	-6.06%
I-135-b5	CCFT-D-4	0.00%	-3.12%
UA-22-g0	CCFT-D-8	0.00%	-1.53%
UA-22-g1	CCFT-D-8	0.00%	-1.13%
UA-22-g2	CCFT-D-8	0.00%	-0.71%
UA-22-g3	CCFT-D-8	0.00%	-1.39%
I-45-b4	CCFT-D-8	0.00%	-1.00%
I-45-b5	CCFT-D-8	0.00%	-2.36%
I-135-b5	CCFT-D-8	0.00%	-0.87%
UA-22-g0	CCFT-D-16	0.00%	-1.30%
UA-22-g1	CCFT-D-16	0.00%	-0.66%
UA-22-g2	CCFT-D-16	0.00%	-1.65%
UA-22-g3	CCFT-D-16	0.00%	-1.08%
UA-22-g0	CCFT-E-4	0.00%	-0.80%
UA-22-g1	CCFT-E-4	0.00%	-1.38%
UA-22-g2	CCFT-E-4	0.00%	-2.08%
UA-22-g3	CCFT-E-4	0.00%	-2.86%
I-190-b5	CCFT-E-4	0.00%	-2.66%
I-190-b5	CCFT-E-8	0.00%	-0.85%
I-90-b4	SRCw-AA-4	-5.05%	-6.05%
I-90-b5	SRCw-AA-4	-5.51%	-8.64%
I-135-b1	SRCw-AA-4	0.00%	-1.76%
I-135-b2	SRCw-AA-4	0.00%	-1.76%
I-135-b3	SRCw-AA-4	0.00%	-1.76%
I-135-b4	SRCw-AA-4	0.00%	-1.76%
I-135-b5	SRCw-AA-4	0.00%	-1.85%

Table A.3. Maximum Unconservative Error Results for Method C (continued)

Frame	Section	Maximum Unconservative Error	
		Method A	Method C
I-45-b5	SRCw-AA-8	-3.99%	-5.30%
I-90-b5	SRCw-AA-8	-3.99%	-5.76%
UA-45-g3	SRCw-AB-4	-5.61%	-6.39%
I-45-b5	SRCw-AB-4	-5.67%	-7.45%
I-90-b4	SRCw-AB-4	-5.61%	-9.27%
I-90-b5	SRCw-AB-4	-6.68%	-11.72%
I-135-b4	SRCw-AB-4	0.00%	-1.86%
I-135-b5	SRCw-AB-4	0.00%	-3.56%
UC-22-g2	SRCw-AC-4	-7.80%	-9.23%
UA-22-g3	SRCw-AC-4	-7.80%	-9.95%
UC-22-g3	SRCw-AC-4	-7.80%	-10.71%
UA-45-g2	SRCw-AC-4	-7.80%	-9.43%
UA-45-g3	SRCw-AC-4	-7.80%	-10.85%
UA-67-g1	SRCw-AC-4	-7.80%	-8.47%
I-45-b5	SRCw-AC-4	-9.45%	-11.47%
I-90-b4	SRCw-AC-4	-9.02%	-13.60%
I-90-b5	SRCw-AC-4	-10.02%	-15.84%
I-135-b4	SRCw-AC-4	0.00%	-4.85%
I-135-b5	SRCw-AC-4	-0.82%	-6.52%
UA-22-g0	SRCw-AC-8	-4.79%	-5.36%
UA-22-g1	SRCw-AC-8	-4.79%	-5.61%
UA-22-g2	SRCw-AC-8	-4.79%	-5.87%
UA-22-g3	SRCw-AC-8	-4.79%	-6.18%
I-45-b5	SRCw-AC-8	-4.79%	-6.63%
I-90-b4	SRCw-AC-8	-4.50%	-5.24%
I-90-b5	SRCw-AC-8	-4.50%	-7.06%
UD-90-g3	SRCw-AC-16	-4.98%	-5.51%
I-45-b5	SRCw-BA-4	-3.99%	-4.55%
I-90-b4	SRCw-BA-4	-3.99%	-5.94%
I-90-b5	SRCw-BA-4	-4.43%	-8.34%
UA-22-g3	SRCw-BA-8	-2.55%	-3.28%
I-90-b5	SRCw-BA-8	-2.55%	-3.59%
UA-22-g3	SRCw-BB-4	-4.27%	-4.80%
UA-45-g3	SRCw-BB-4	-4.27%	-5.00%
I-45-b5	SRCw-BB-4	-4.27%	-6.00%
I-90-b4	SRCw-BB-4	-3.97%	-6.24%
I-90-b5	SRCw-BB-4	-4.10%	-8.39%
I-90-b5	SRCw-BB-8	-1.64%	-2.35%
UA-22-g2	SRCw-BC-4	-6.32%	-7.05%
UA-22-g3	SRCw-BC-4	-6.32%	-7.69%
UC-22-g3	SRCw-BC-4	-6.32%	-7.53%
UA-45-g2	SRCw-BC-4	-6.32%	-6.84%
UA-45-g3	SRCw-BC-4	-6.32%	-7.69%
I-45-b5	SRCw-BC-4	-7.96%	-11.13%
I-90-b4	SRCw-BC-4	-4.82%	-9.17%
I-90-b5	SRCw-BC-4	-5.79%	-10.94%
I-135-b5	SRCw-BC-4	0.00%	-0.61%
I-90-b5	SRCw-BC-8	-0.80%	-1.43%
I-90-b5	SRCw-CA-4	-1.56%	-4.41%
I-90-b5	SRCw-CB-4	0.00%	-2.86%
I-90-b5	SRCw-CC-4	0.00%	-2.85%
UD-90-g3	SRCw-CC-16	-8.27%	-9.47%
UD-90-g3	SRCw-DC-8	-17.05%	-17.82%

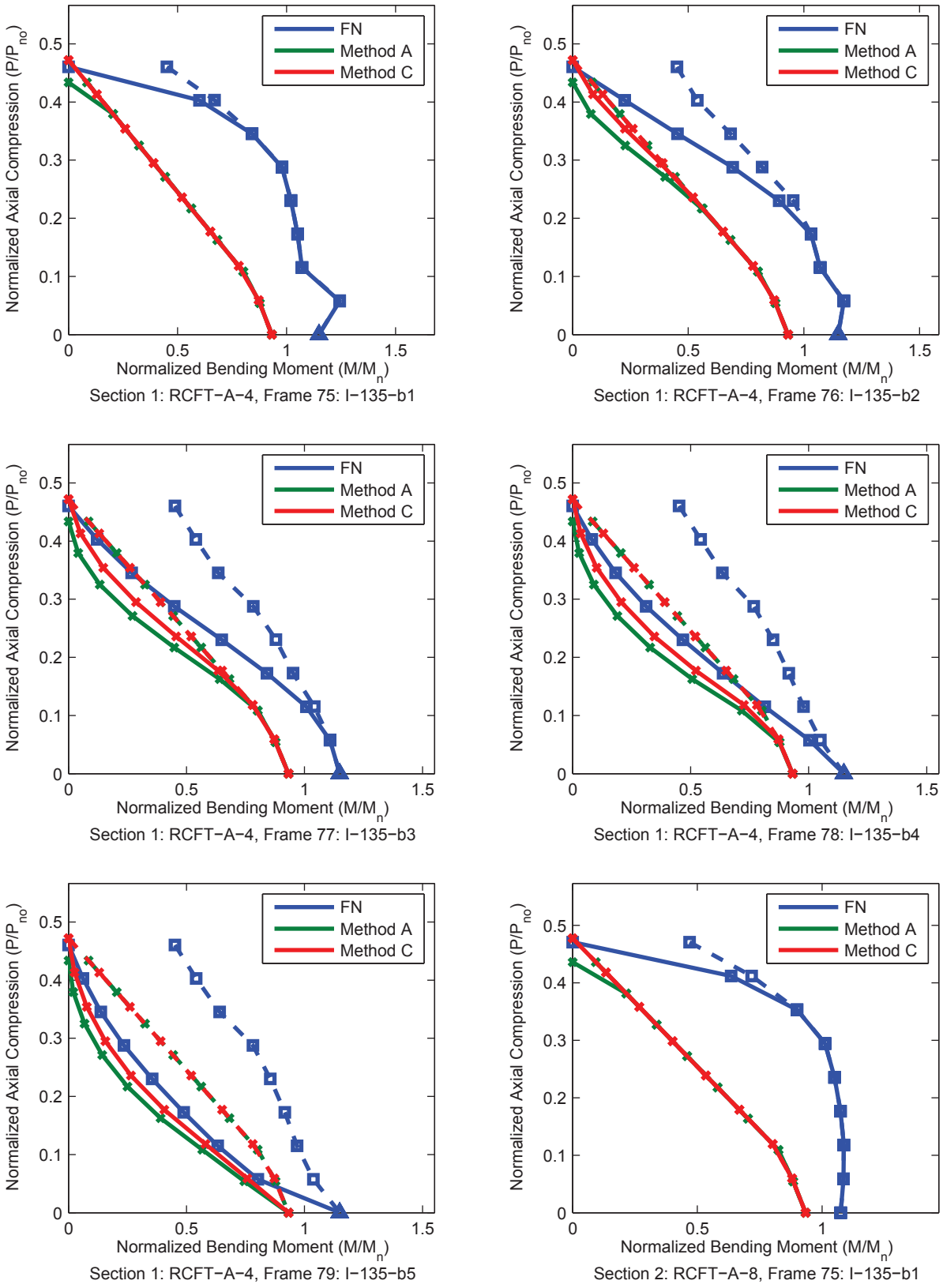

Figure A.104. Detailed Results for Method C

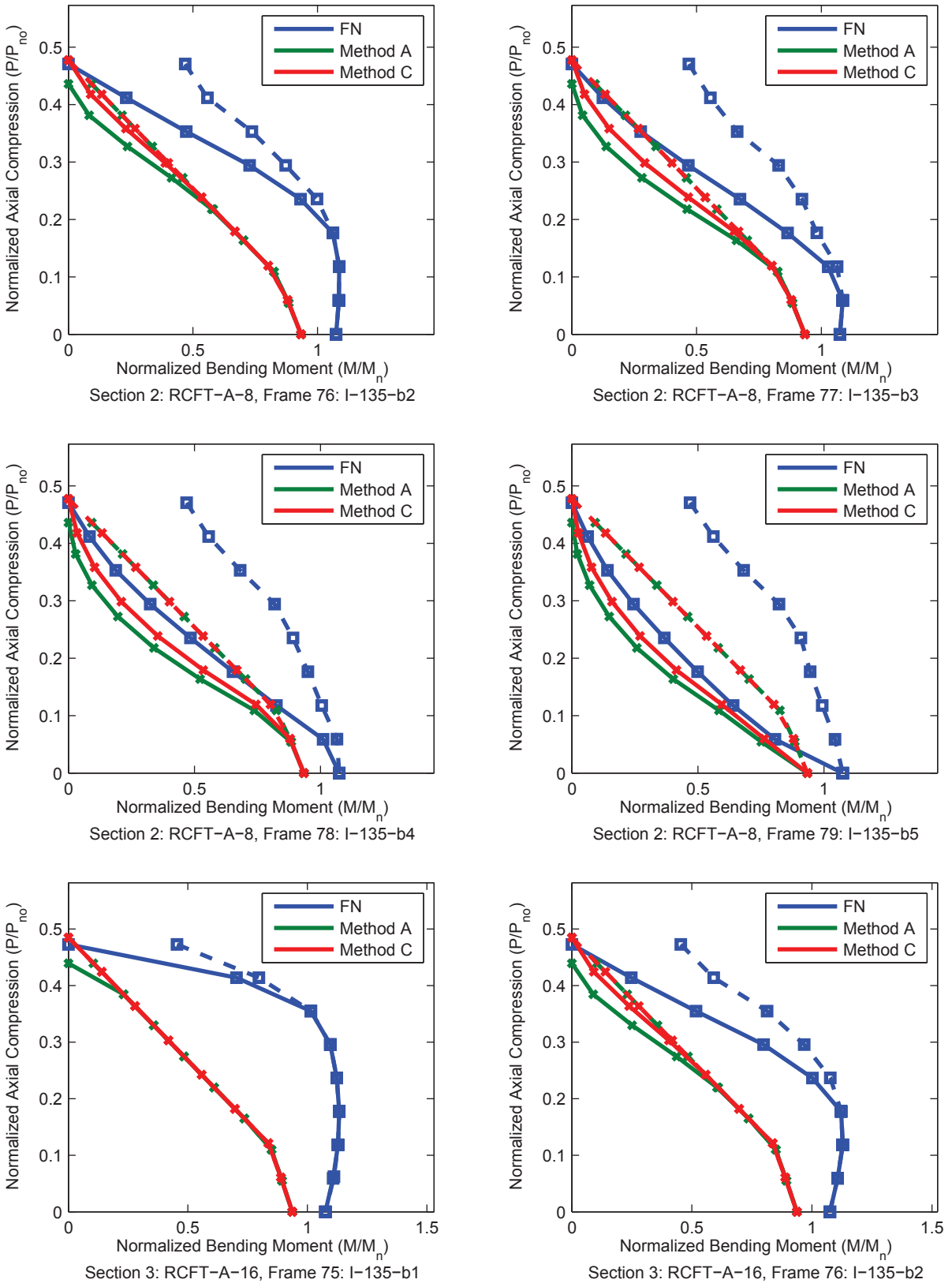

Figure A.104. Detailed Results for Method C (continued)

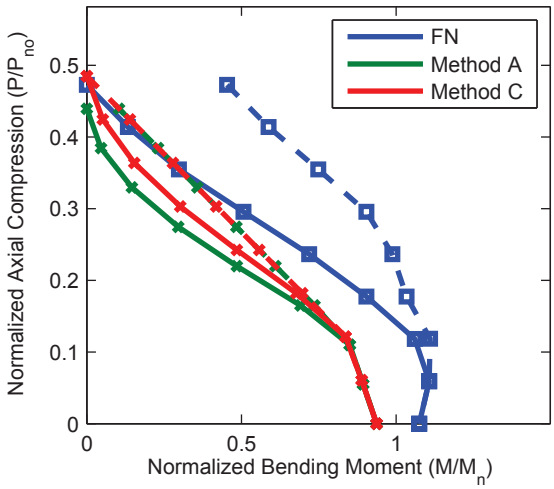

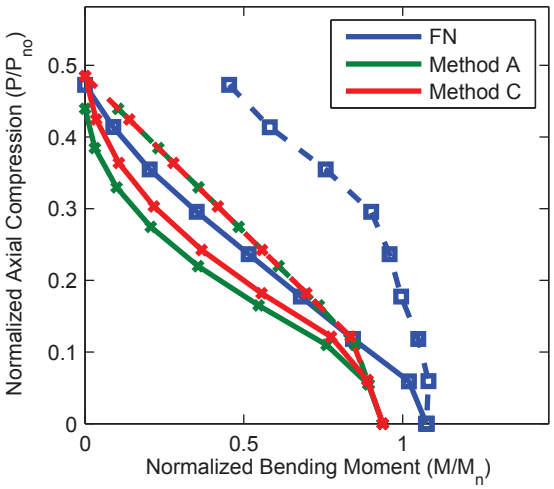

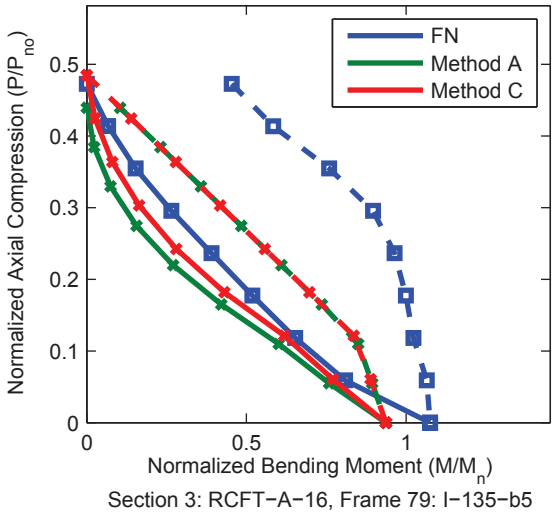

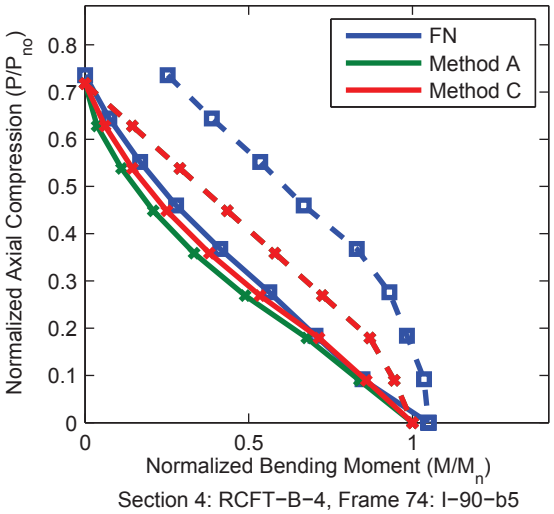

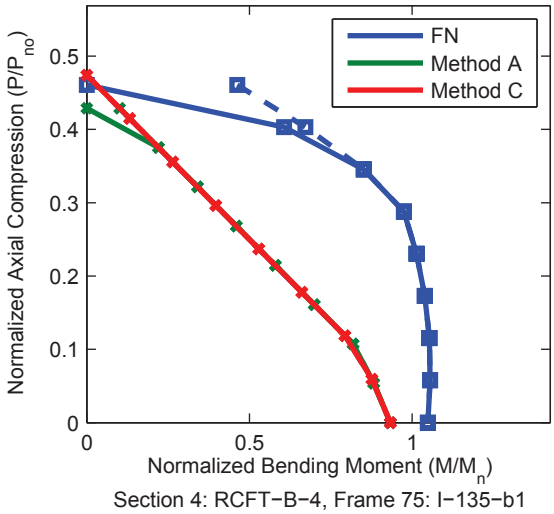

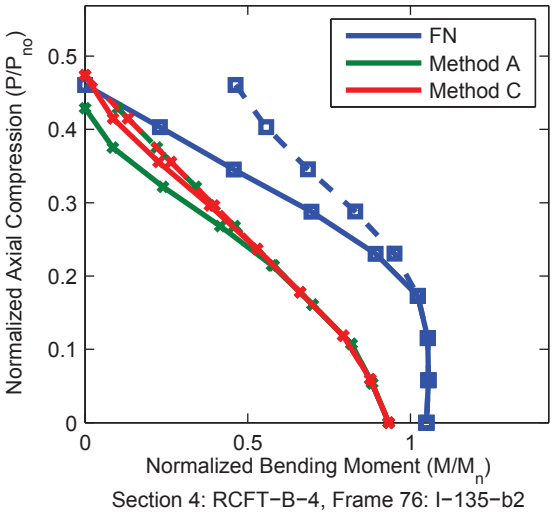

Figure A.104. Detailed Results for Method C (continued)

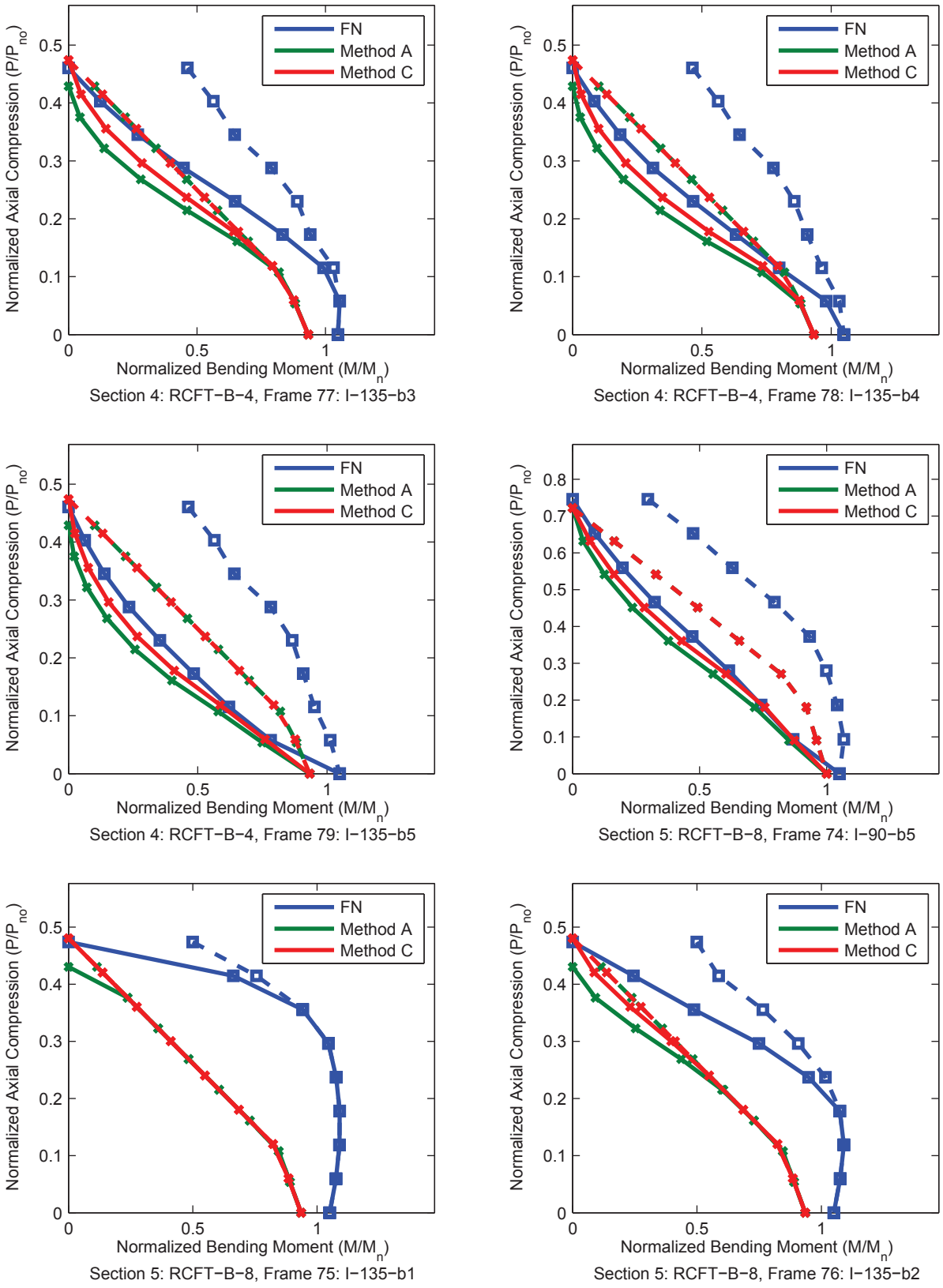

Figure A.104. Detailed Results for Method C (continued)

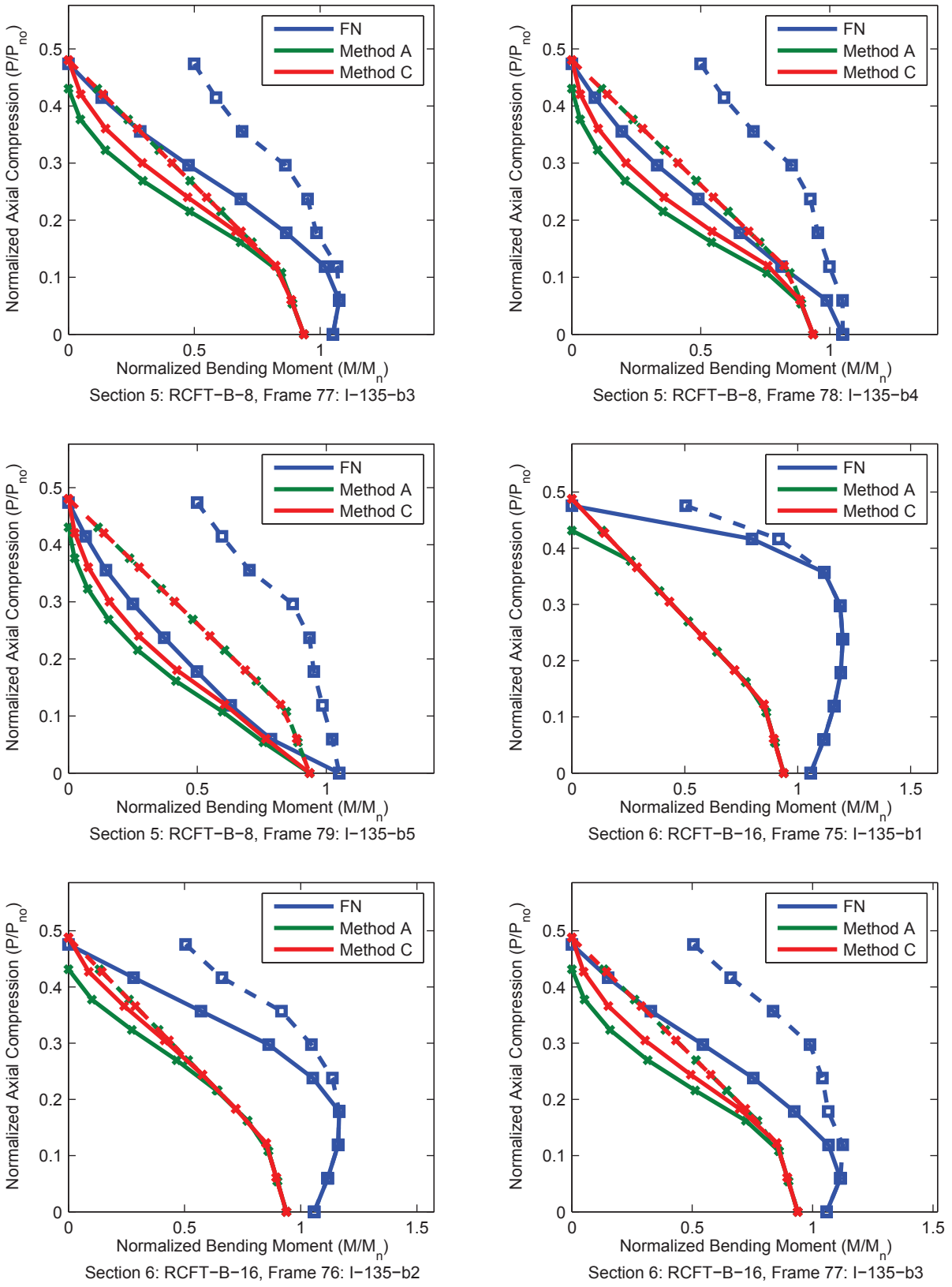

Figure A.104. Detailed Results for Method C (continued)

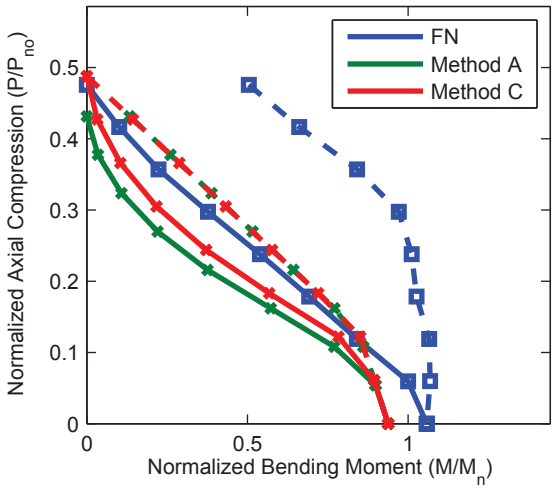

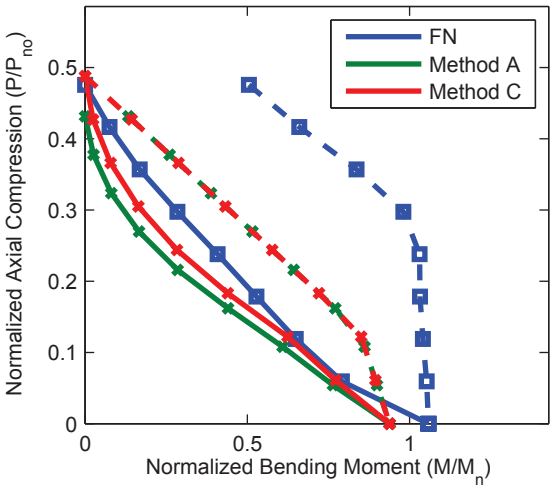

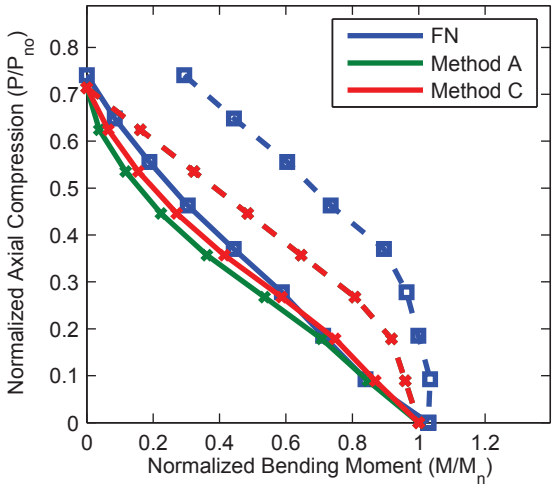

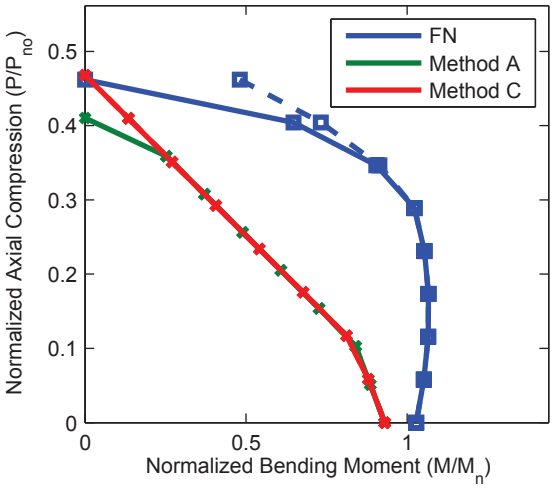

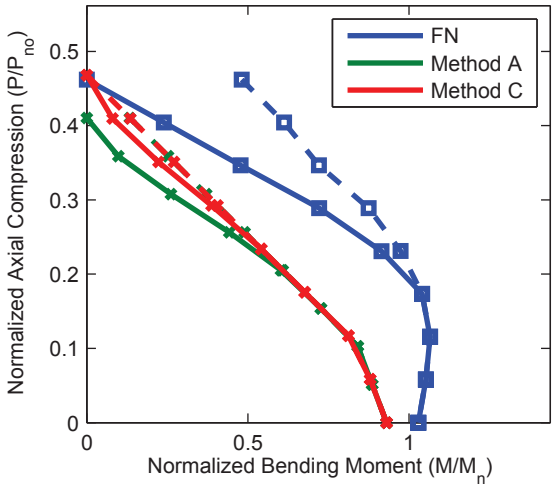

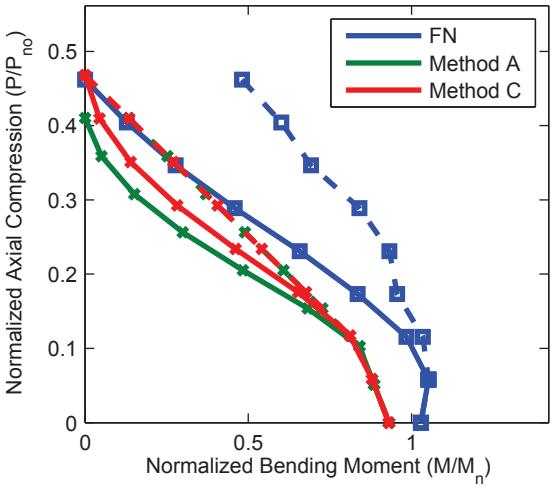

Figure A.104. Detailed Results for Method C (continued)

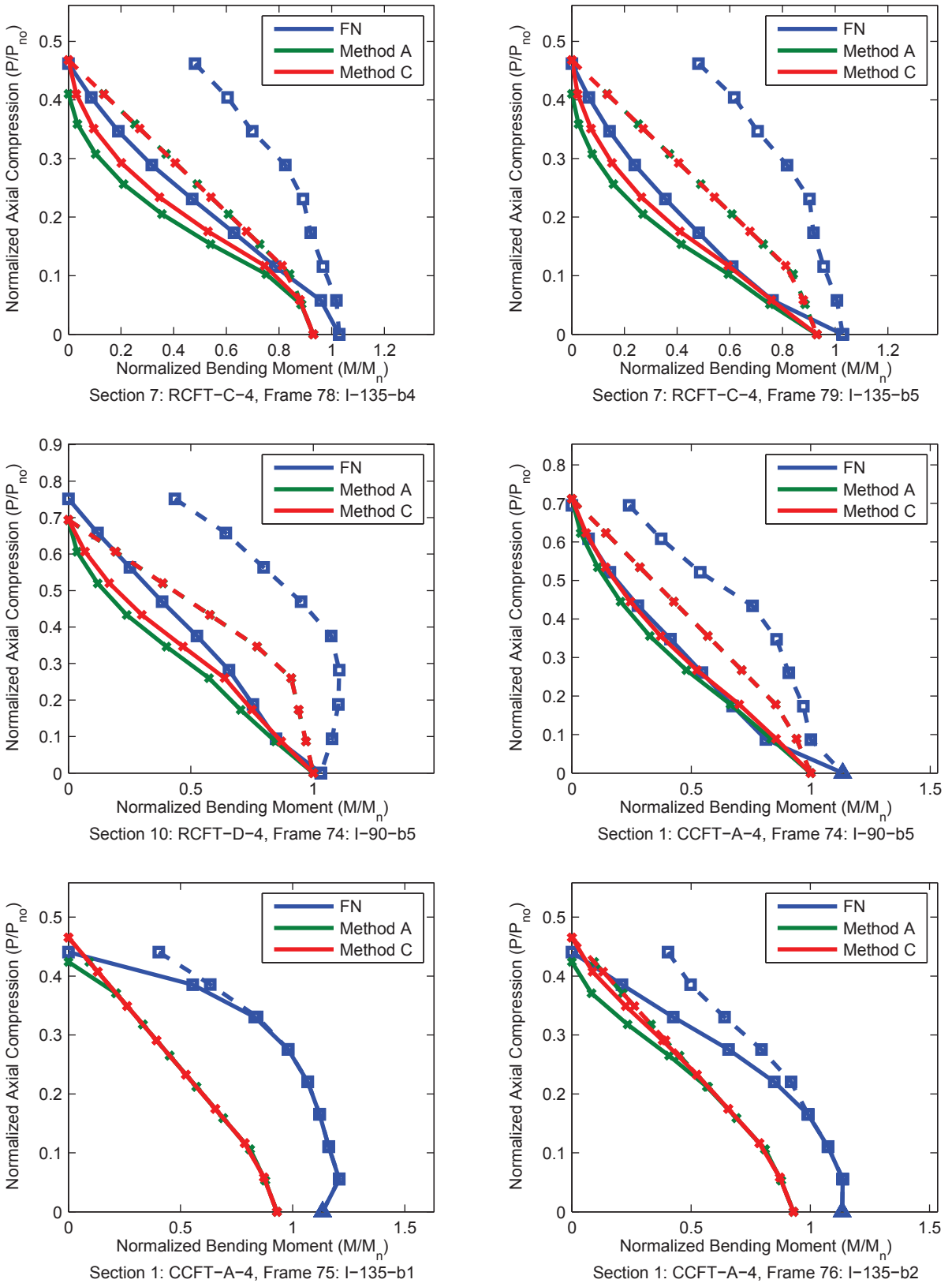

Figure A.104. Detailed Results for Method C (continued)

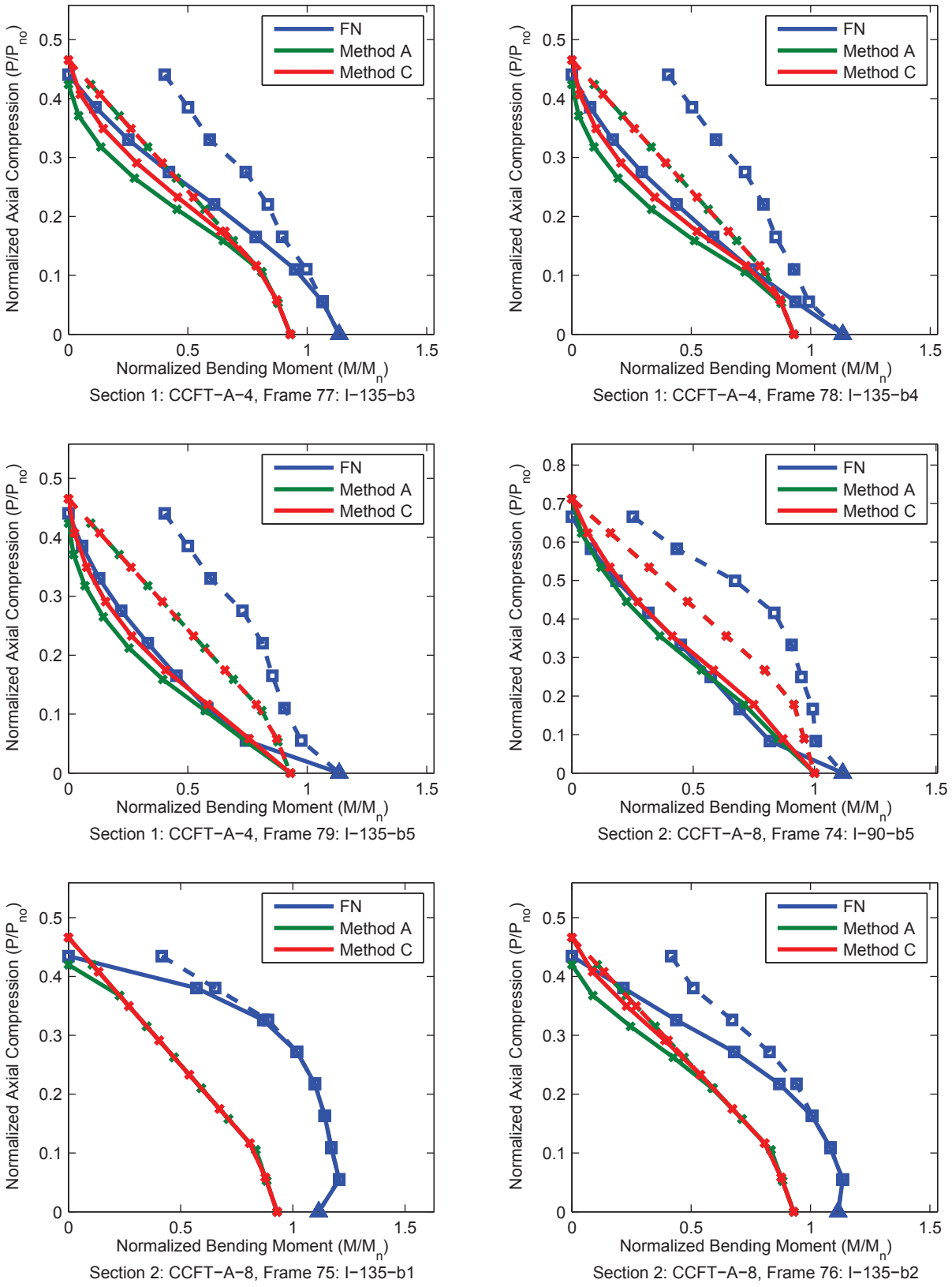

Figure A.104. Detailed Results for Method C (continued)

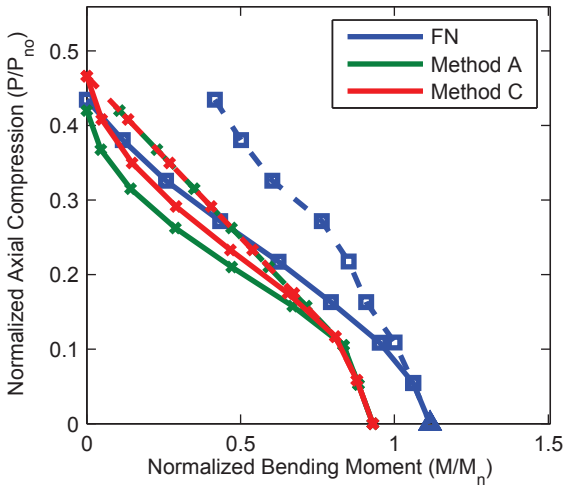

Section 2: CCFT−A−8, Frame 77: I−135−b3

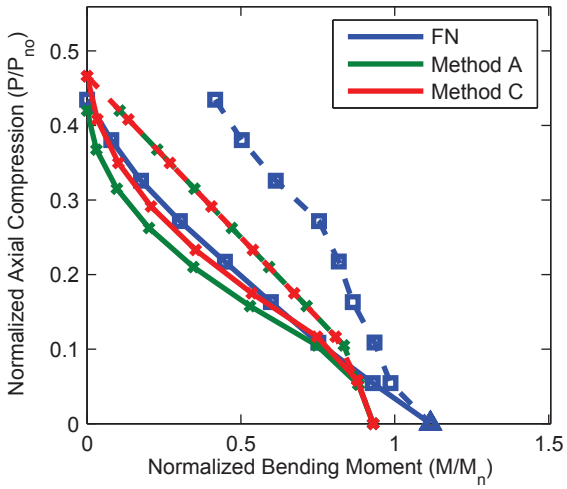

Section 2: CCFT−A−8, Frame 78: I−135−b4

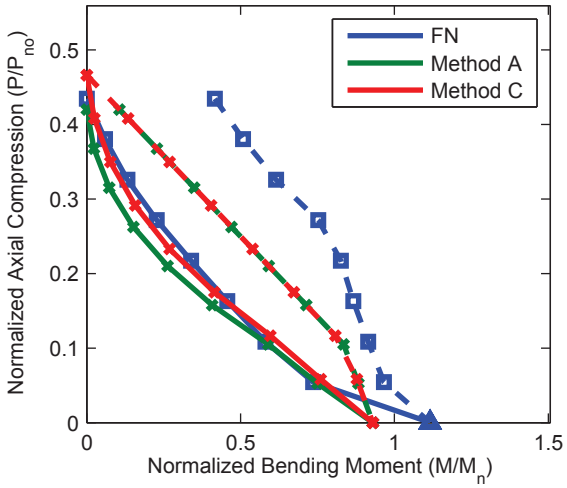

Section 2: CCFT−A−8, Frame 79: I−135−b5

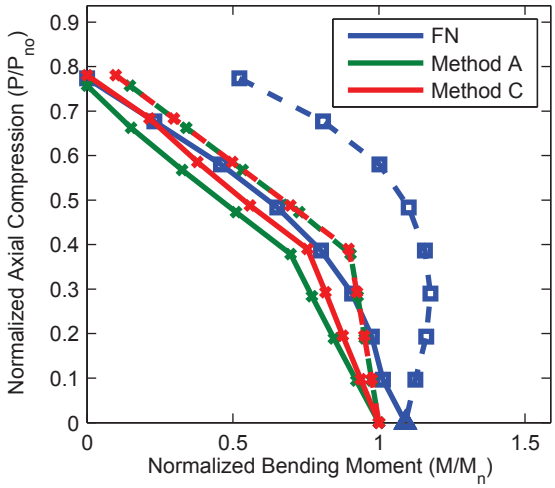

Section 3: CCFT−A−16, Frame 33: UA−67−g0

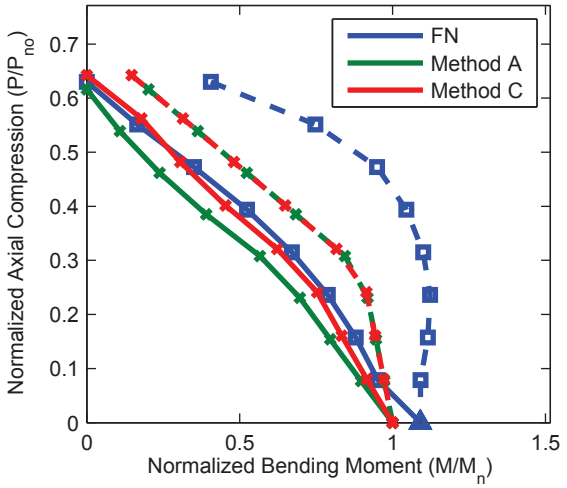

Section 3: CCFT−A−16, Frame 49: UA−90−g0

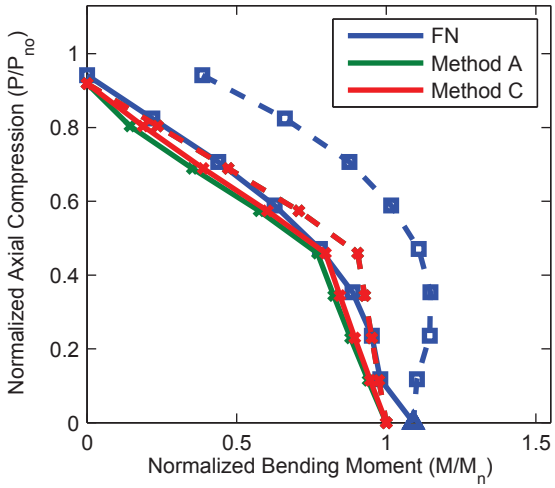

Section 3: CCFT−A−16, Frame 69: I−45−b5

Figure A.104. Detailed Results for Method C (continued)

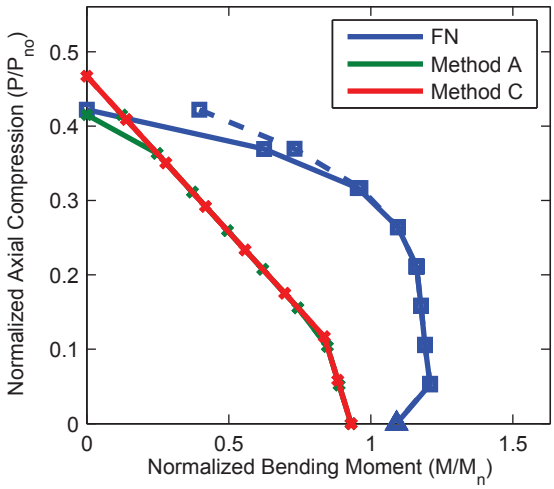

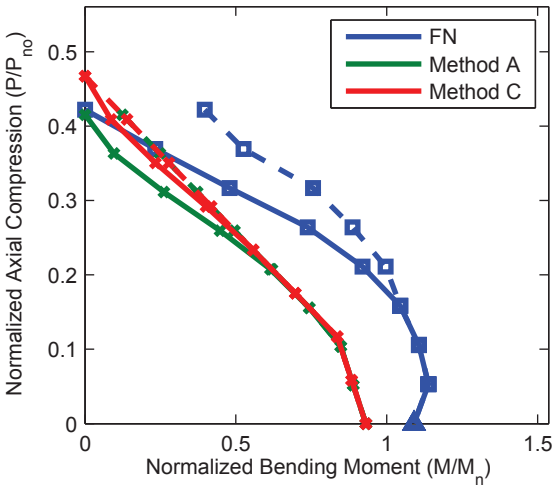

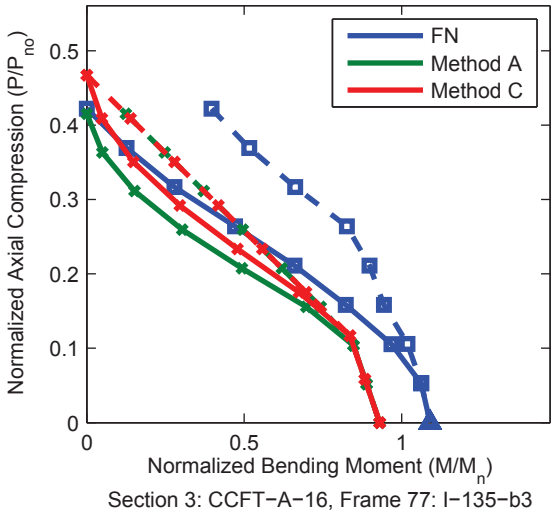

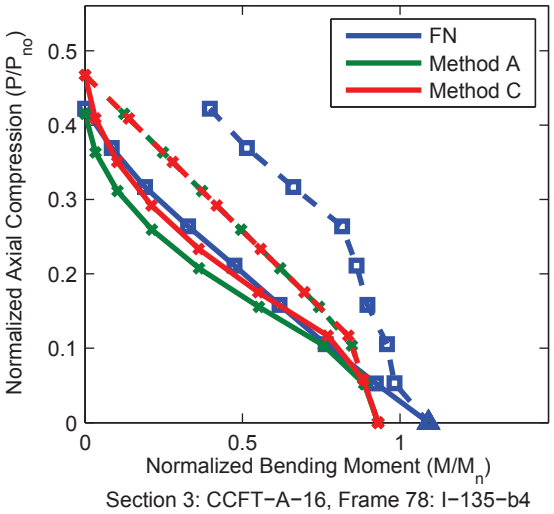

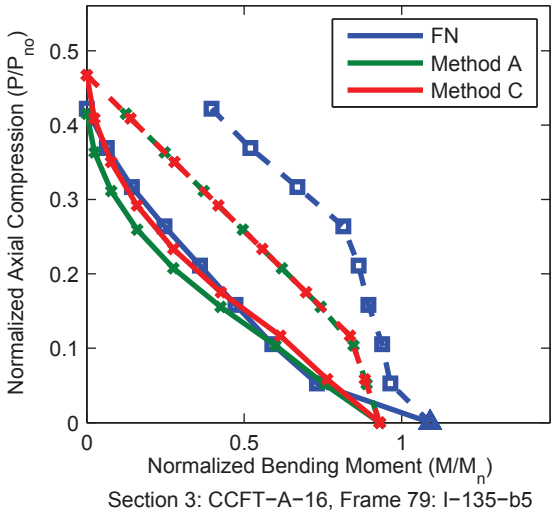

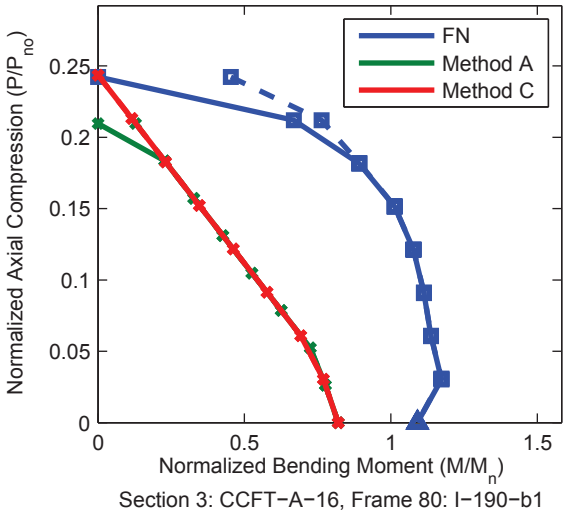

Figure A.104. Detailed Results for Method C (continued)

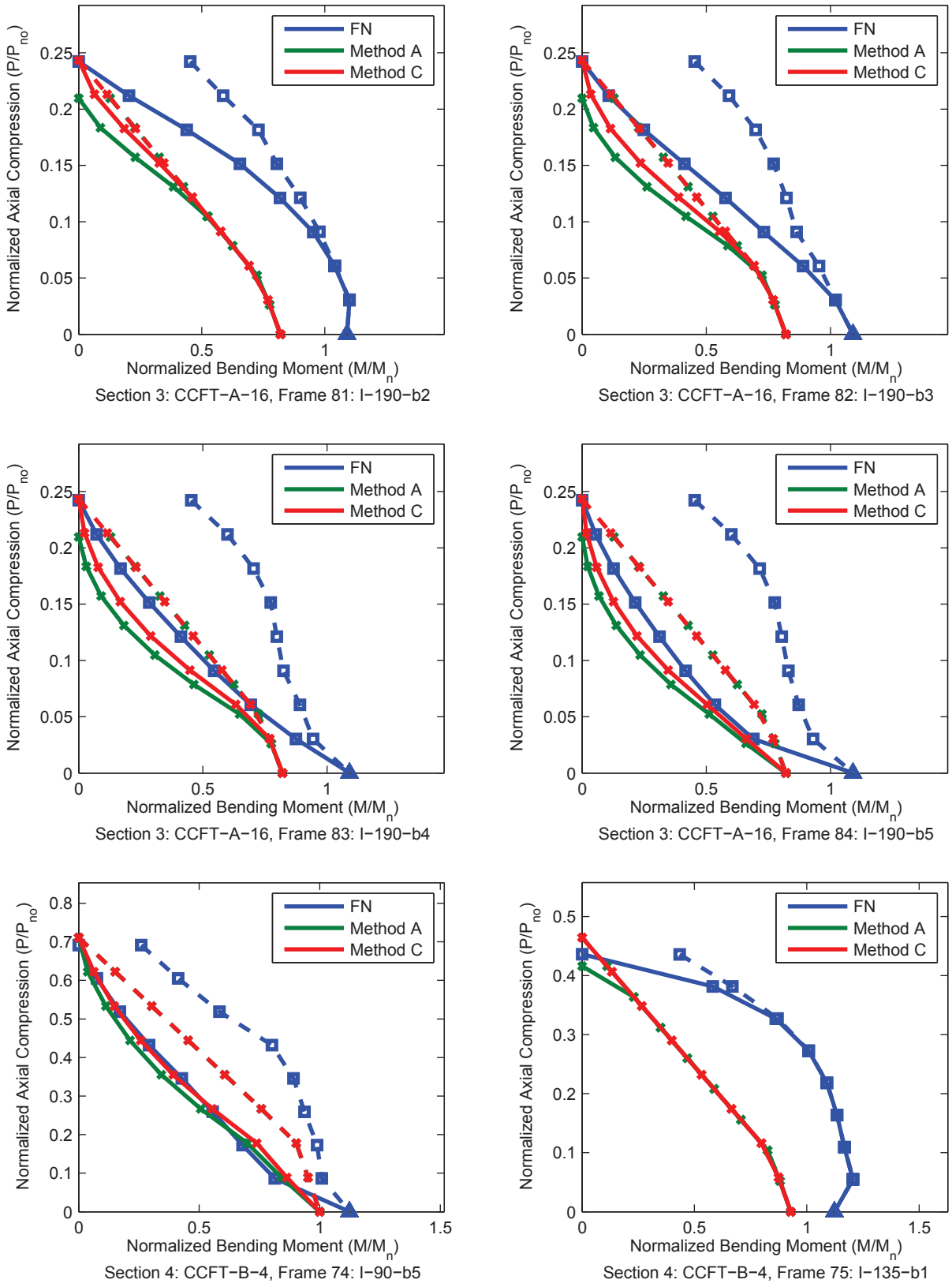

Figure A.104. Detailed Results for Method C (continued)

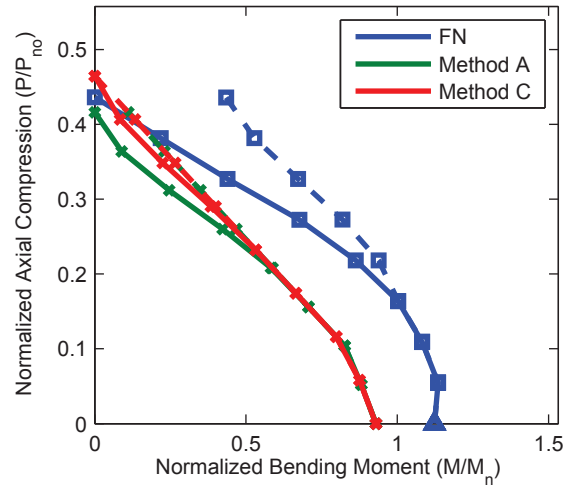

Section 4: CCFT−B−4, Frame 76: I−135−b2

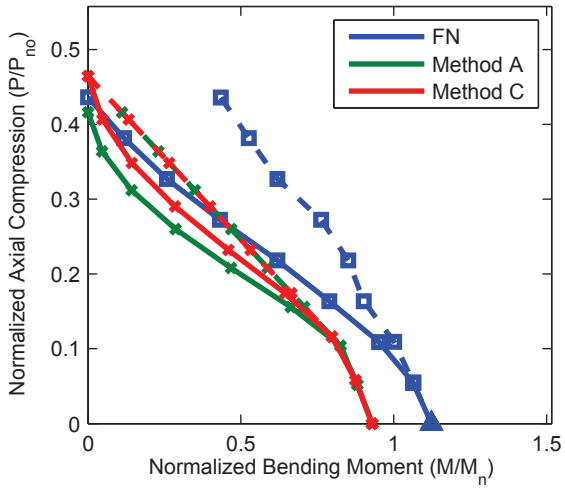

Section 4: CCFT−B−4, Frame 77: I−135−b3

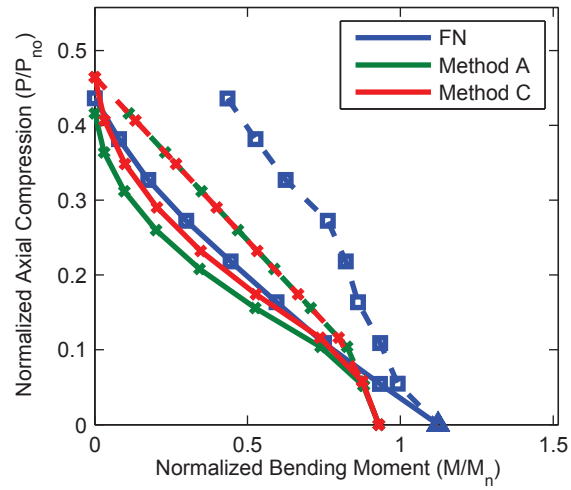

Section 4: CCFT−B−4, Frame 78: I−135−b4

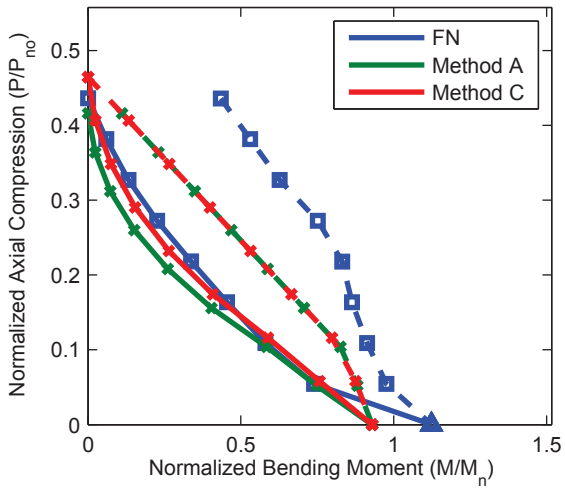

Section 4: CCFT−B−4, Frame 79: I−135−b5

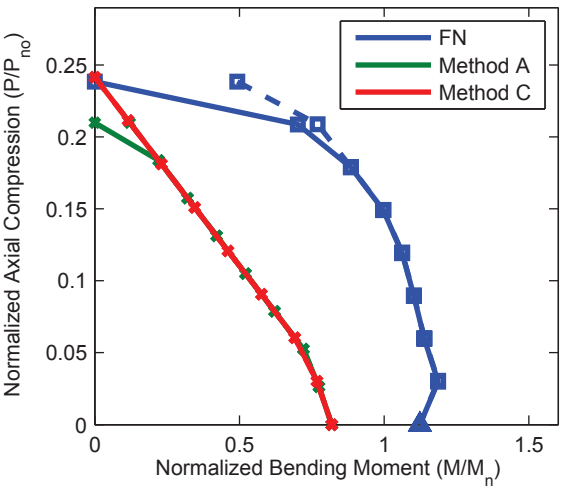

Section 4: CCFT−B−4, Frame 80: I−190−b1

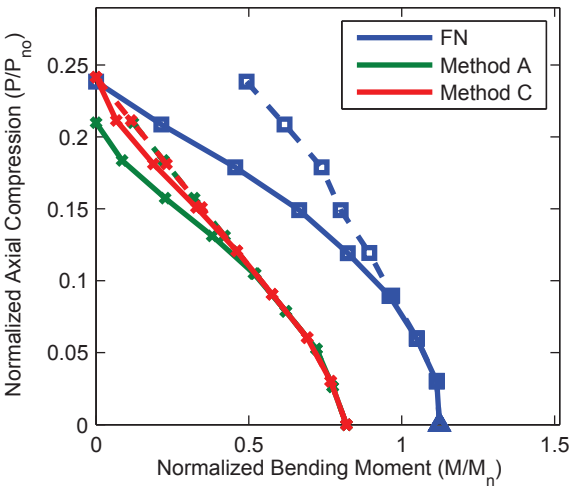

Section 4: CCFT−B−4, Frame 81: I−190−b2

Figure A.104. Detailed Results for Method C (continued)

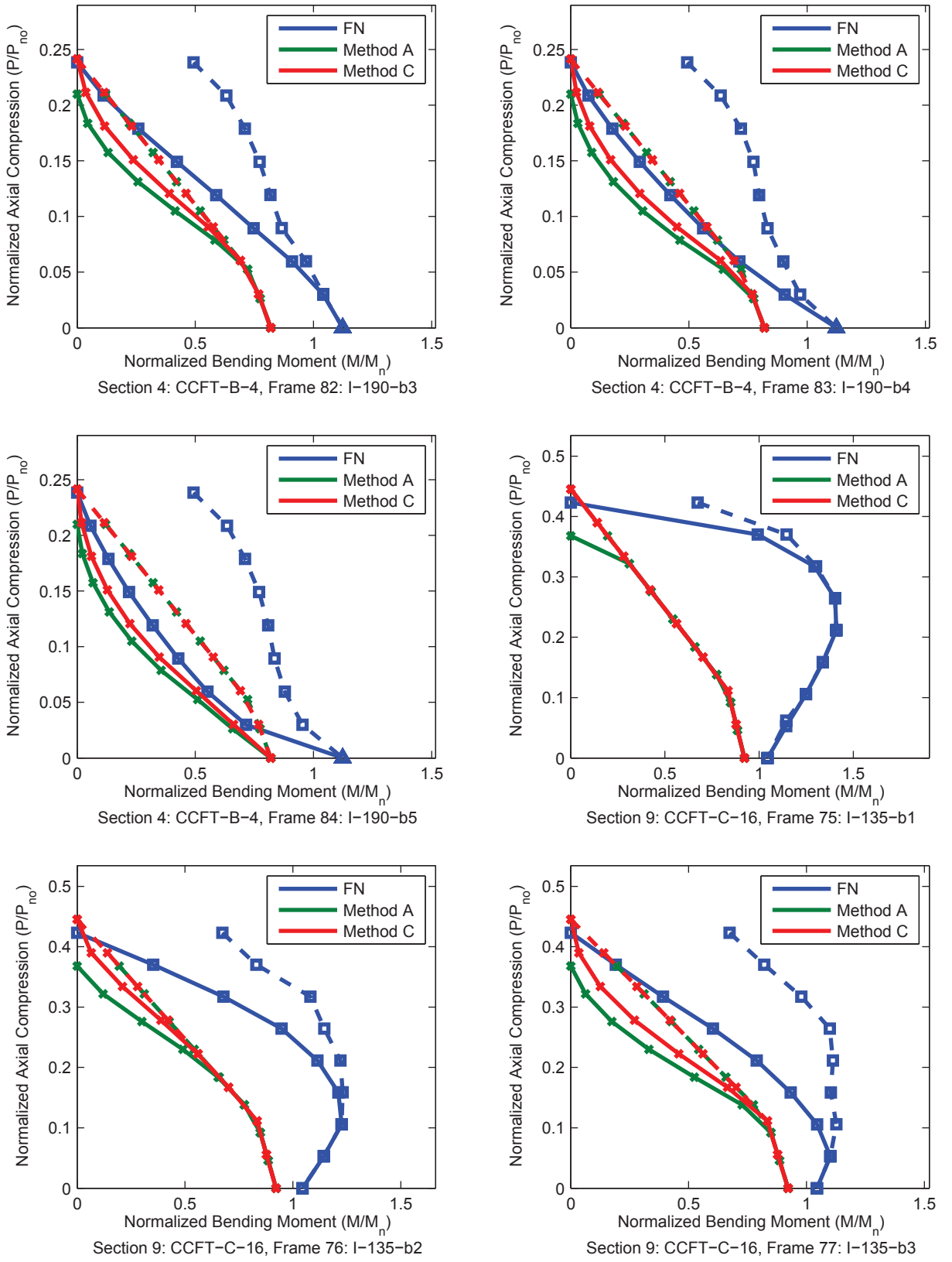

Figure A.104. Detailed Results for Method C (continued)

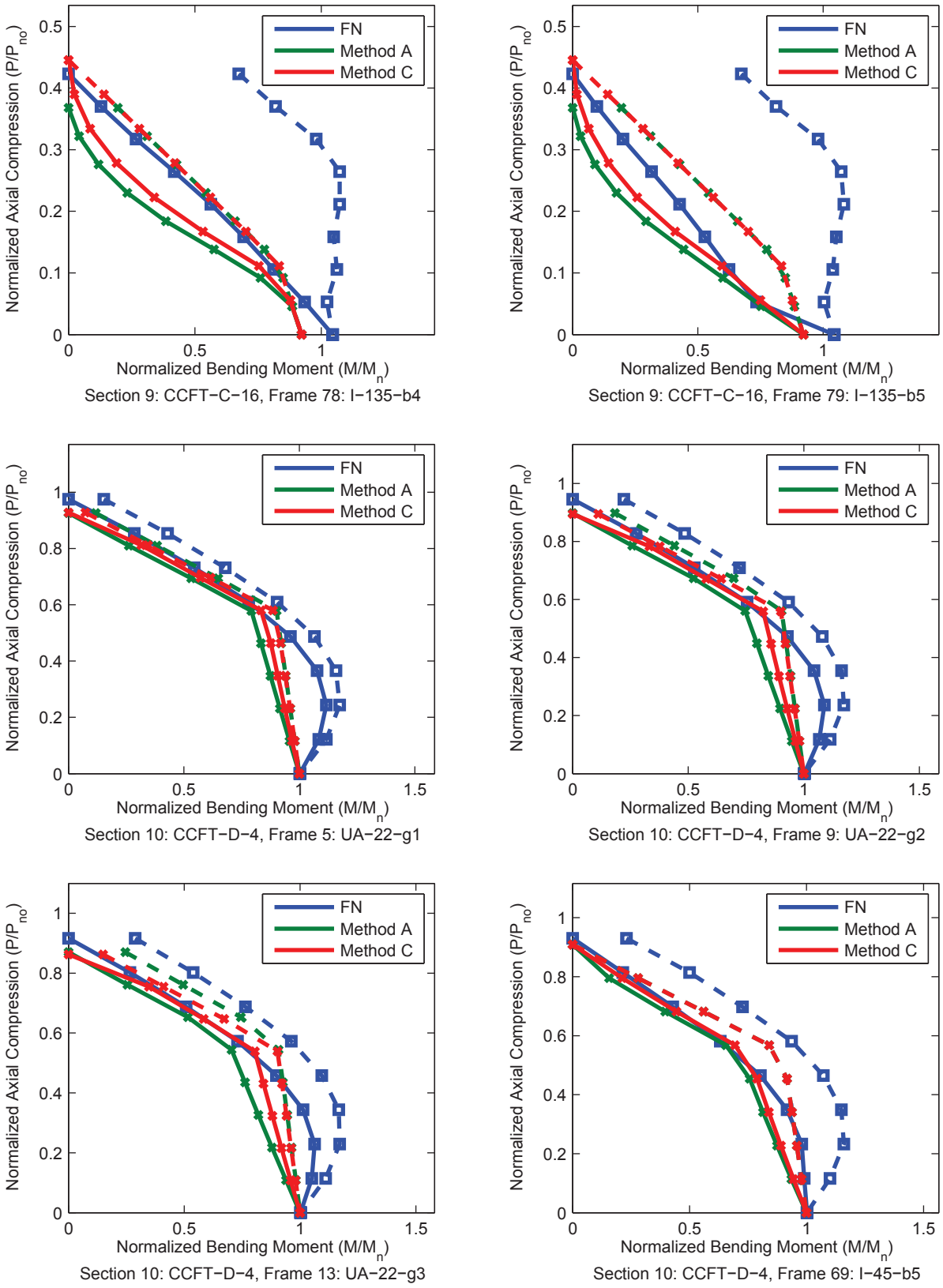

Figure A.104. Detailed Results for Method C (continued)

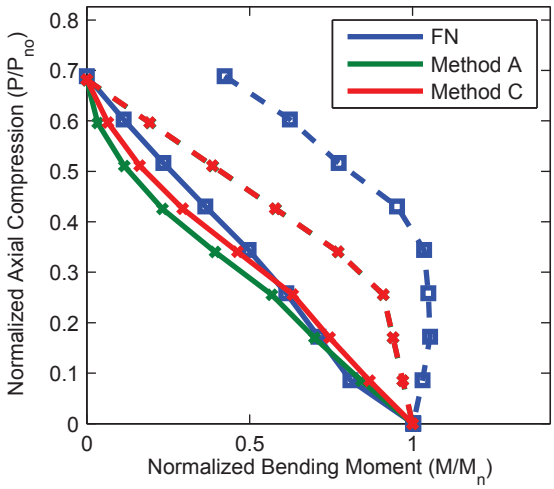

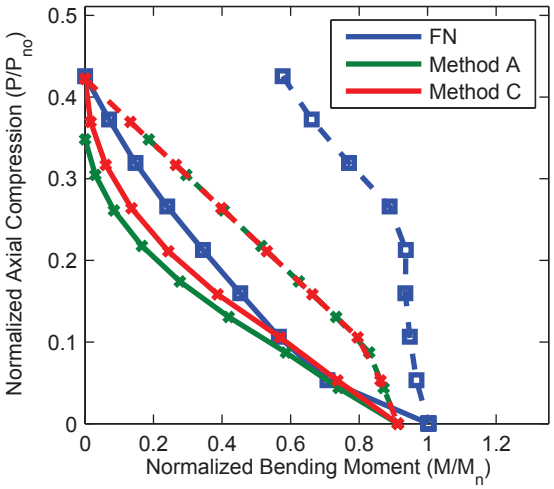

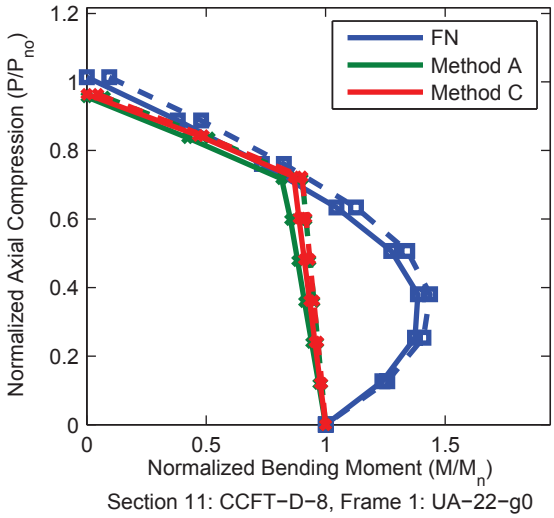

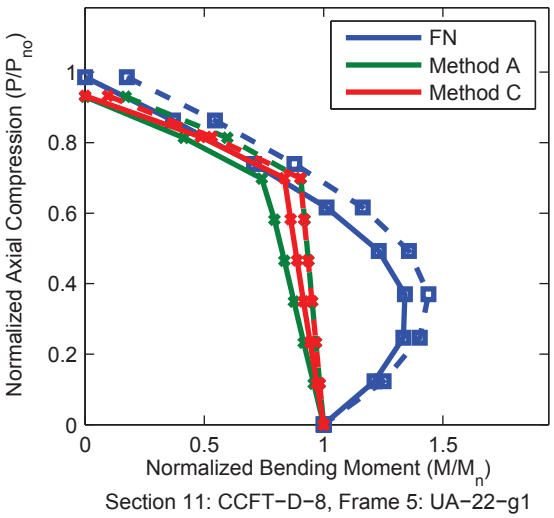

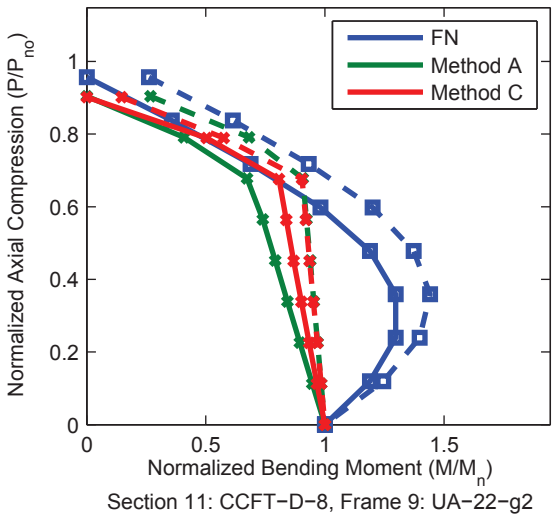

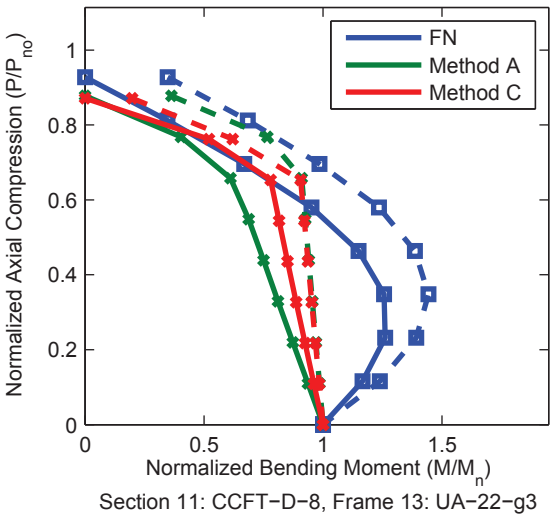

Figure A.104. Detailed Results for Method C (continued)

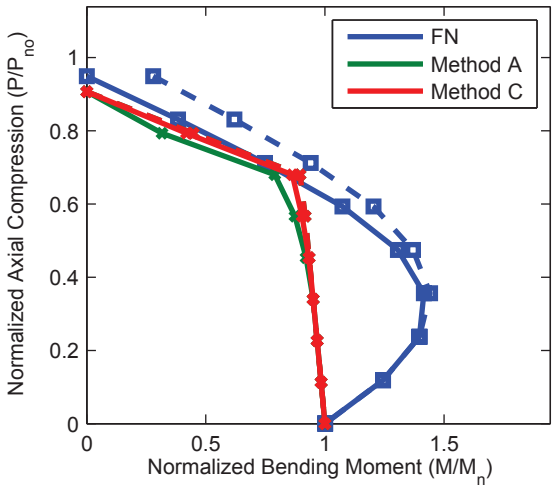

Section 11: CCFT−D−8, Frame 68: I−45−b4

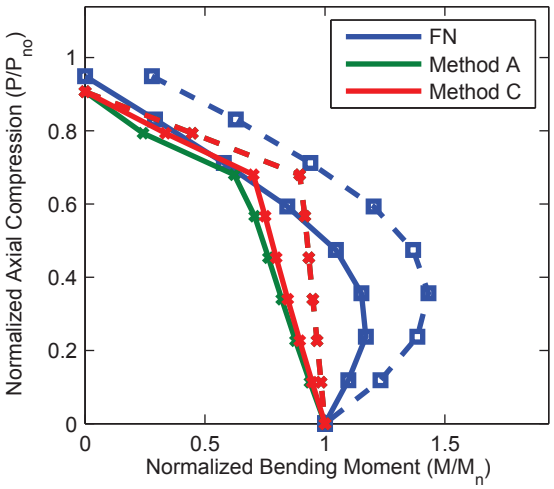

Section 11: CCFT−D−8, Frame 69: I−45−b5

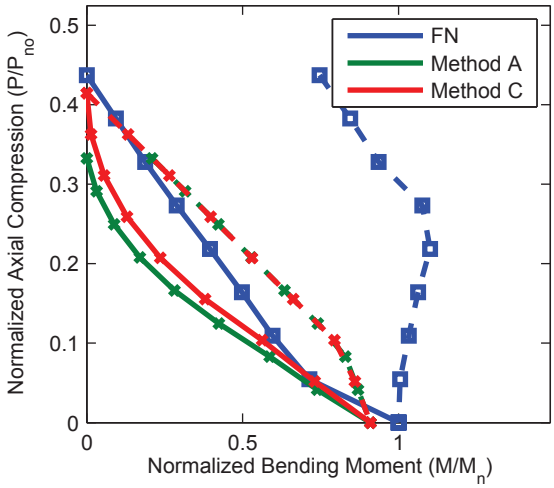

Section 11: CCFT−D−8, Frame 79: I−135−b5

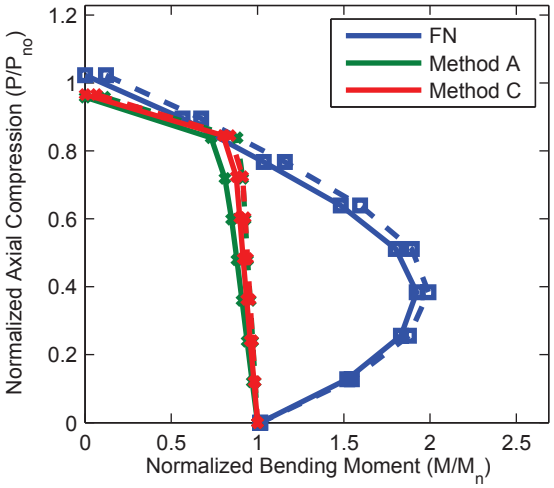

Section 12: CCFT−D−16, Frame 1: UA−22−g0

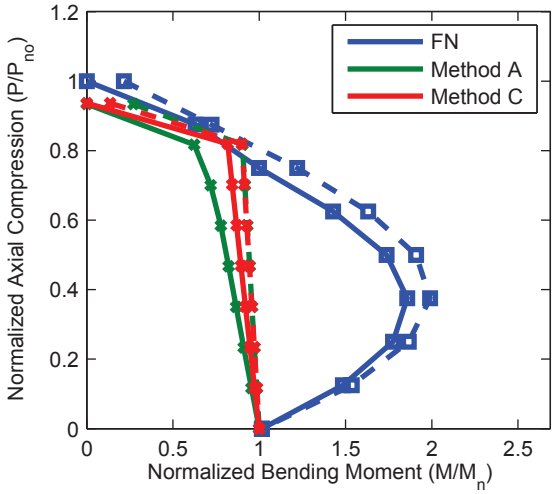

Section 12: CCFT−D−16, Frame 5: UA−22−g1

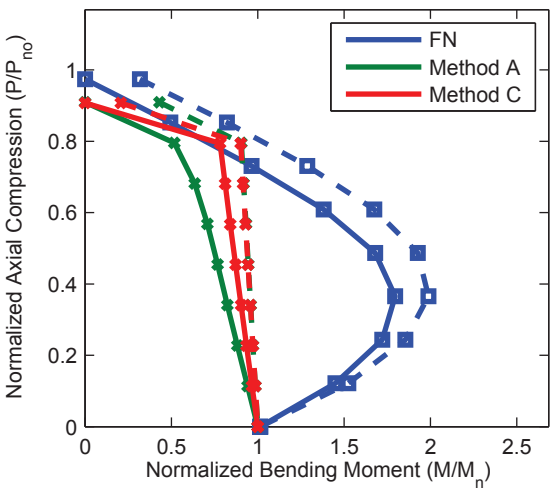

Section 12: CCFT−D−16, Frame 9: UA−22−g2

Figure A.104. Detailed Results for Method C (continued)

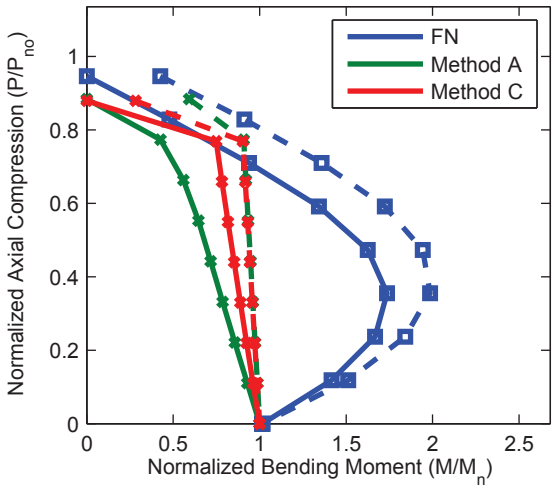

Section 12: CCFT−D−16, Frame 13: UA−22−g3

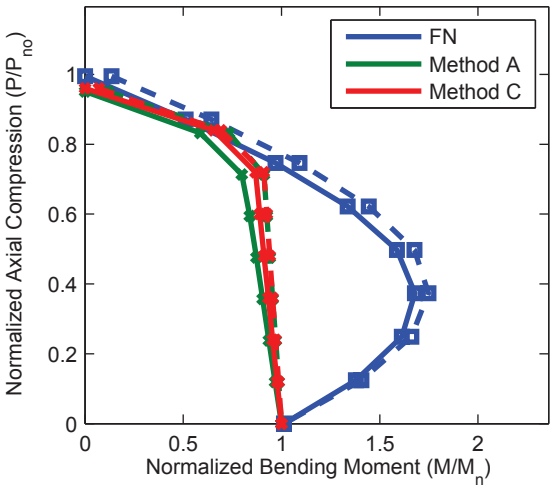

Section 13: CCFT−E−4, Frame 1: UA−22−g0

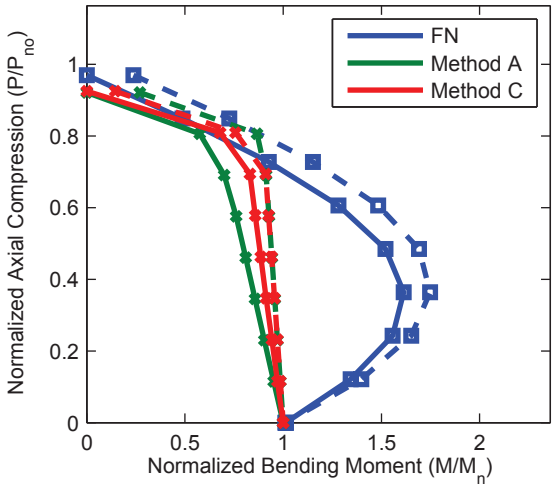

Section 13: CCFT−E−4, Frame 5: UA−22−g1

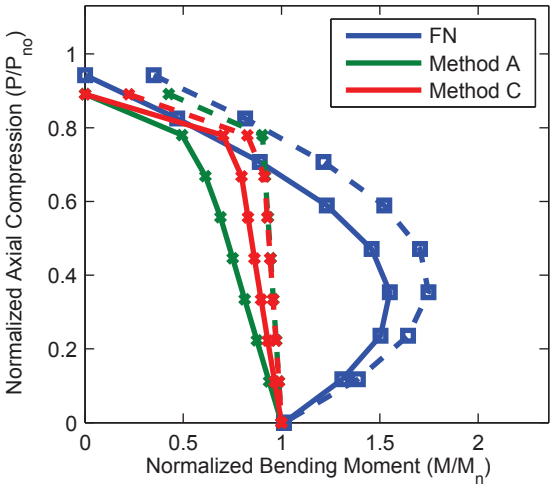

Section 13: CCFT−E−4, Frame 9: UA−22−g2

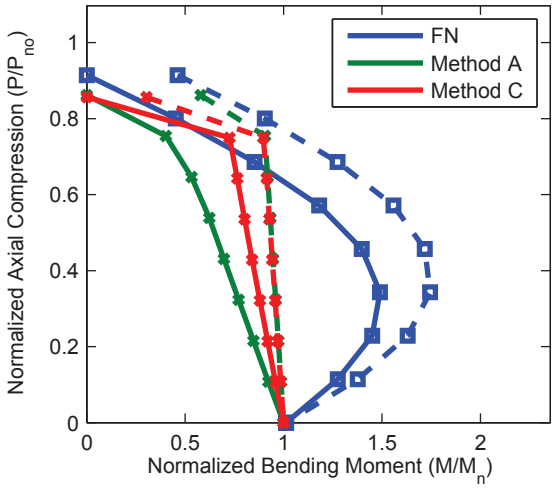

Section 13: CCFT−E−4, Frame 13: UA−22−g3

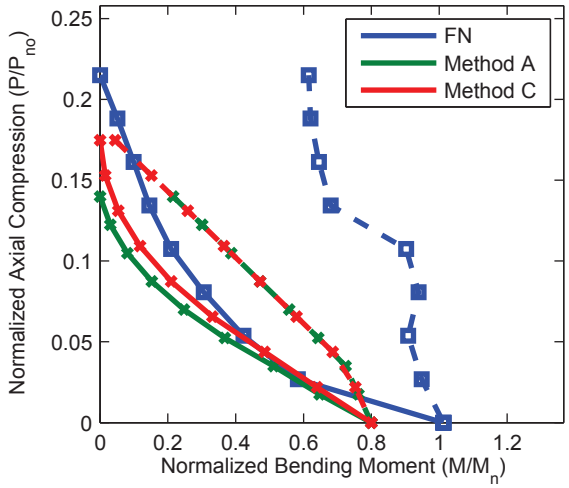

Section 13: CCFT−E−4, Frame 84: I−190−b5

Figure A.104. Detailed Results for Method C (continued)

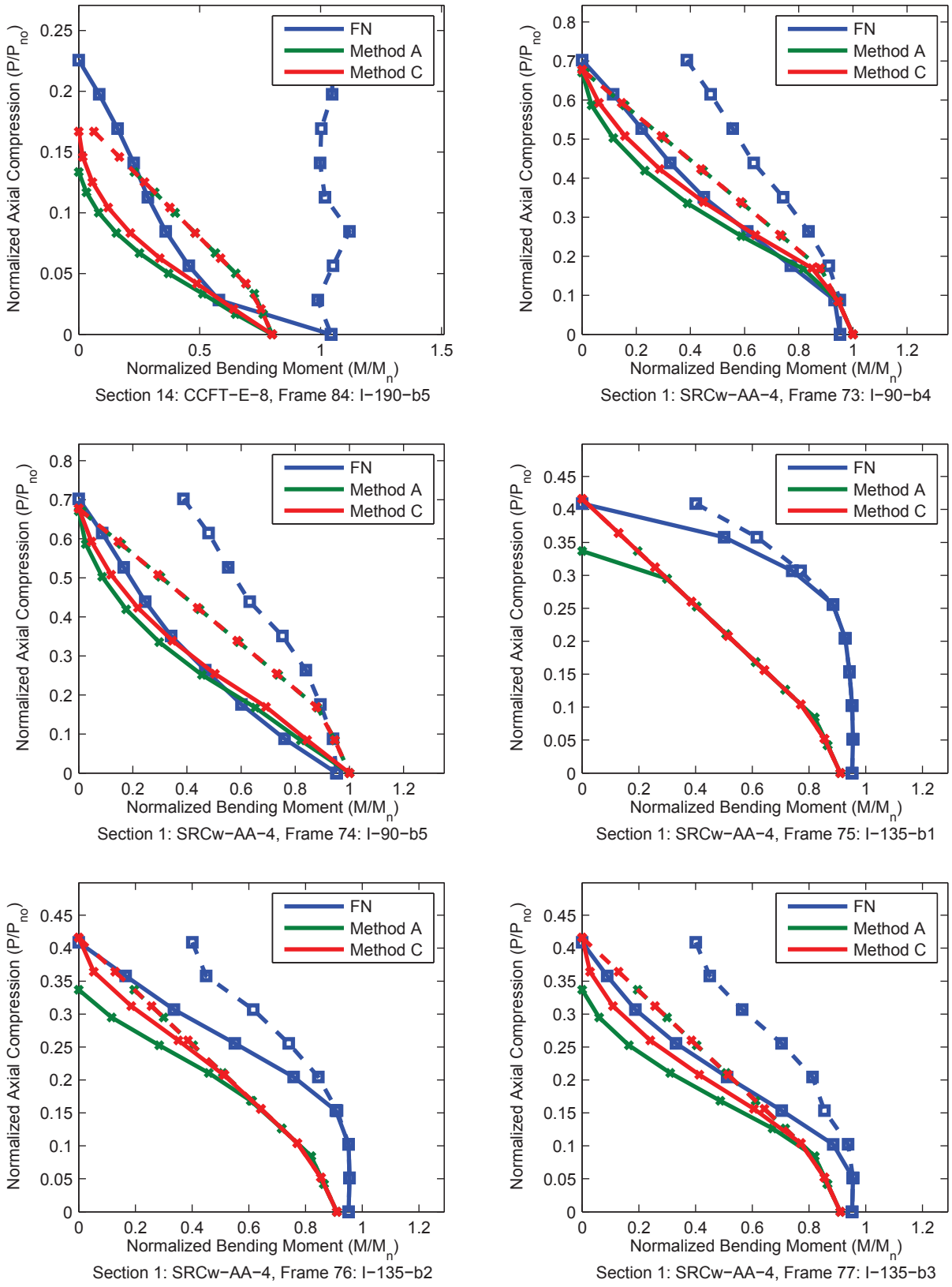

Figure A.104. Detailed Results for Method C (continued)

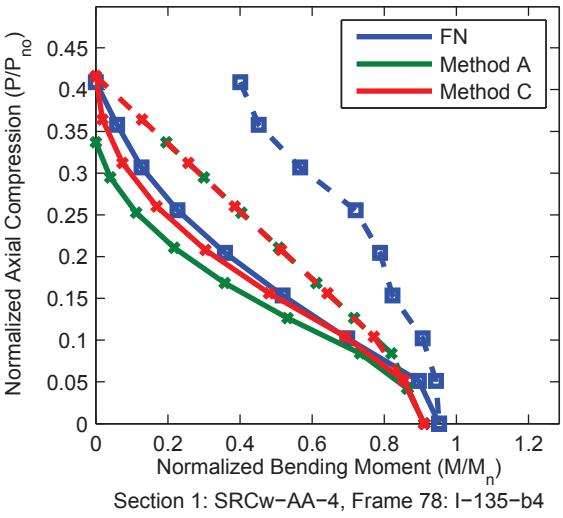

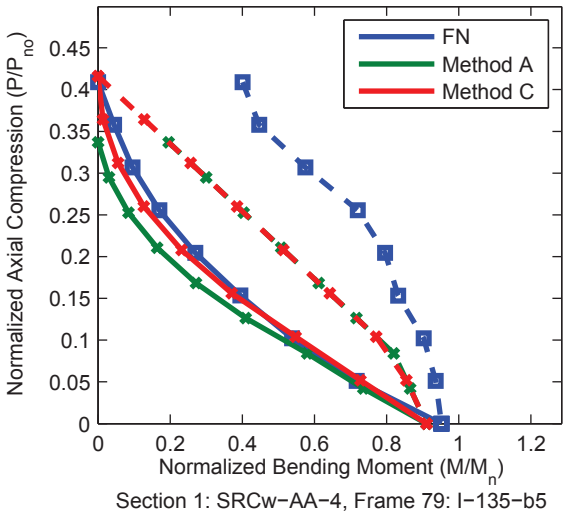

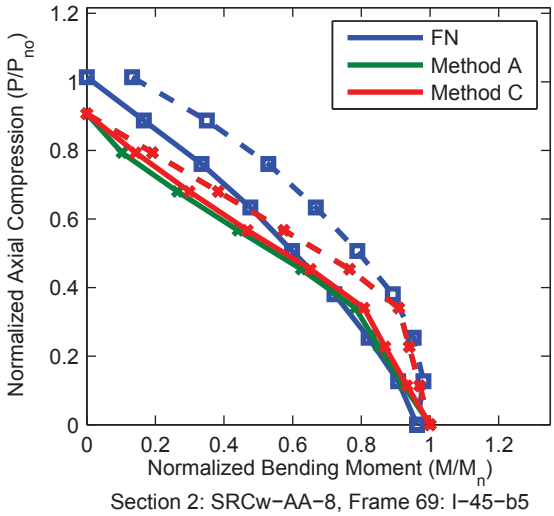

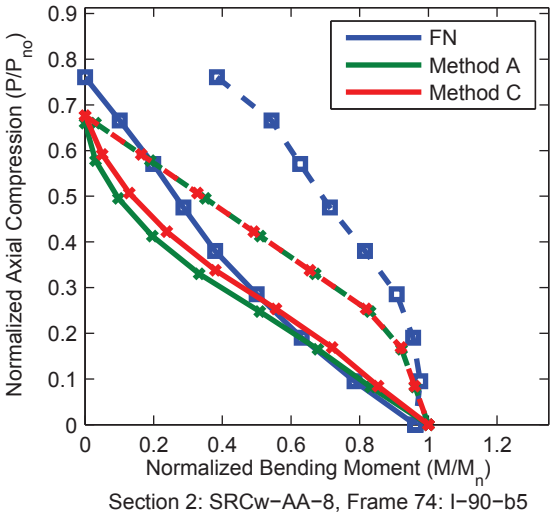

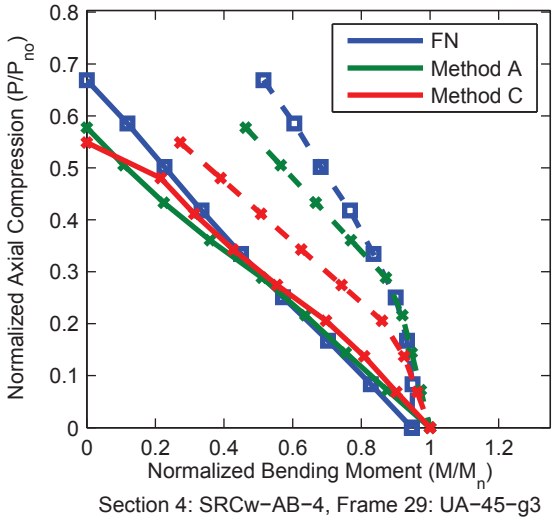

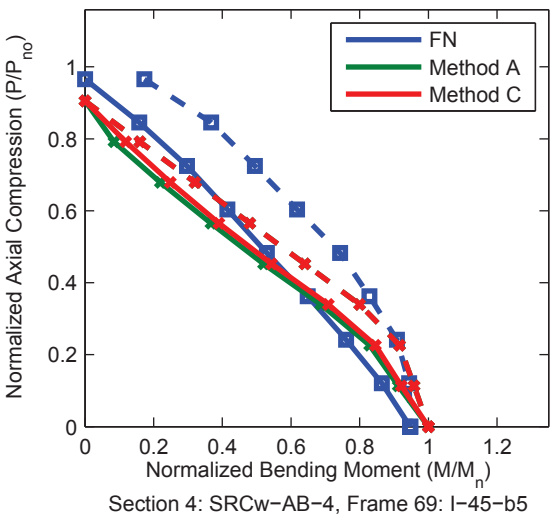

Figure A.104. Detailed Results for Method C (continued)

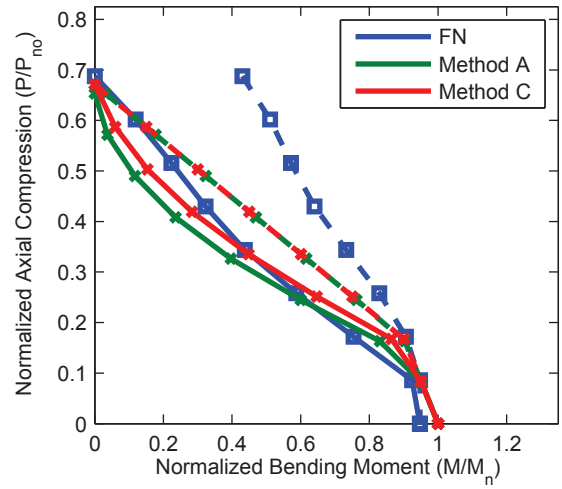

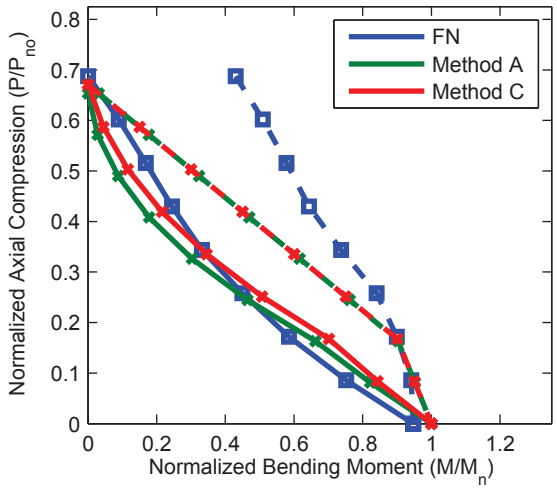

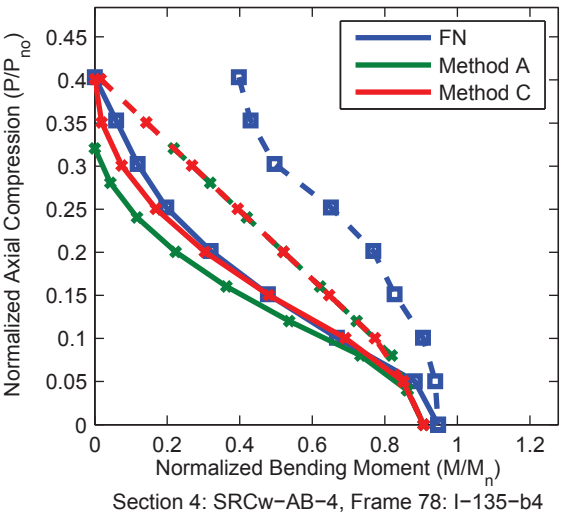

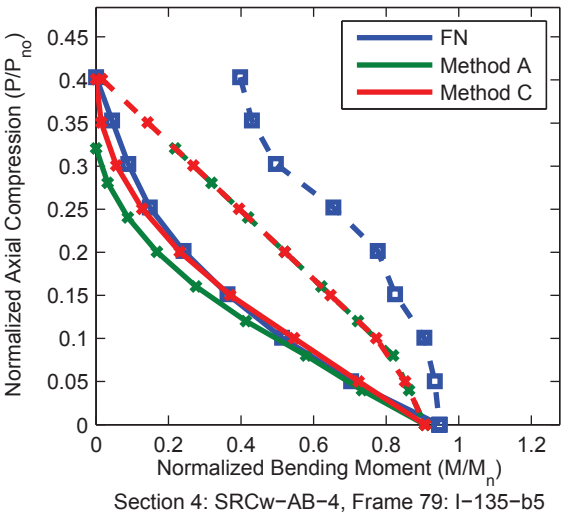

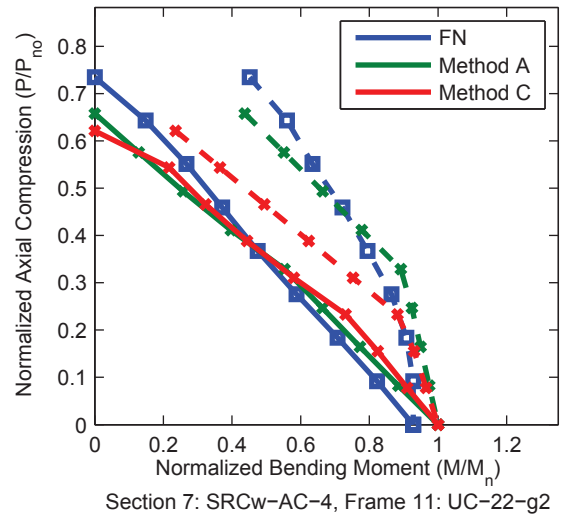

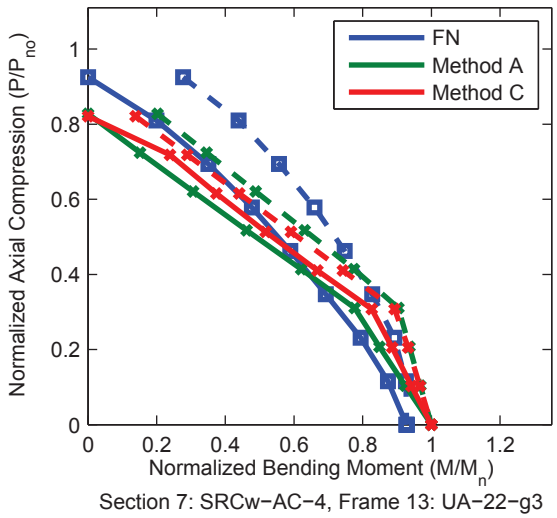

Figure A.104. Detailed Results for Method C (continued)

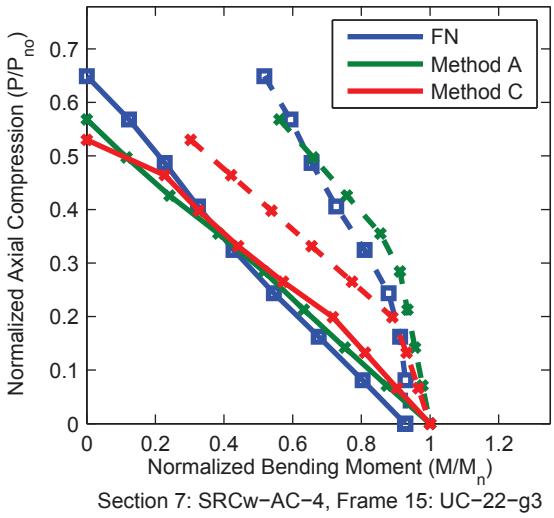

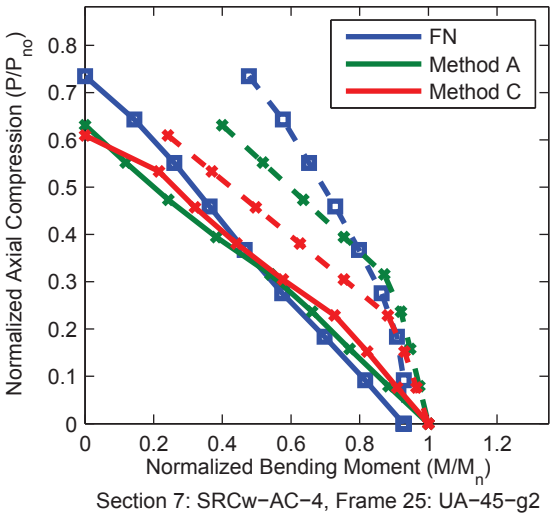

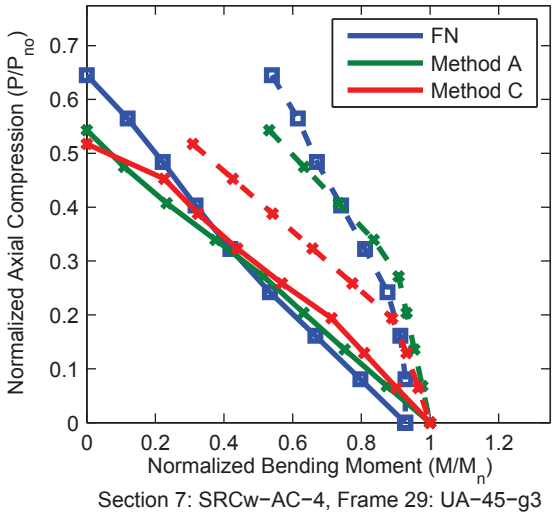

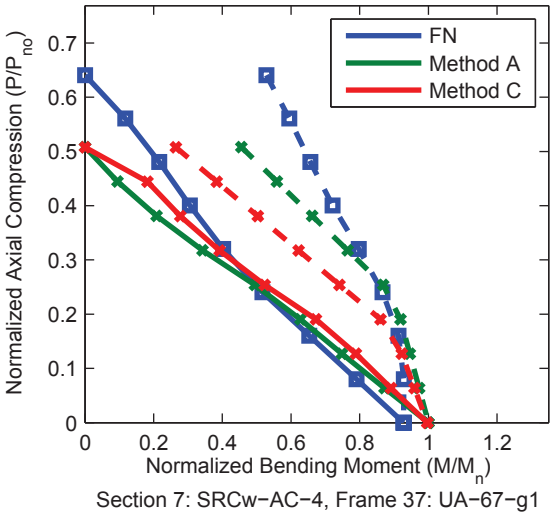

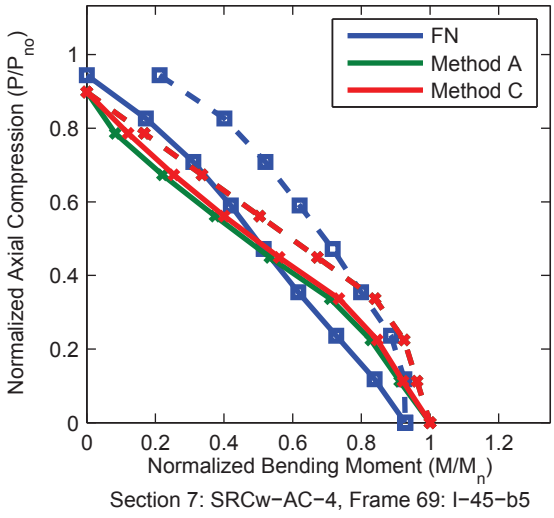

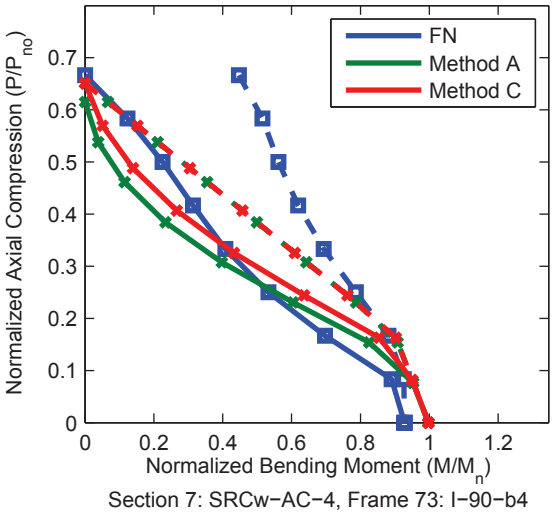

Figure A.104. Detailed Results for Method C (continued)

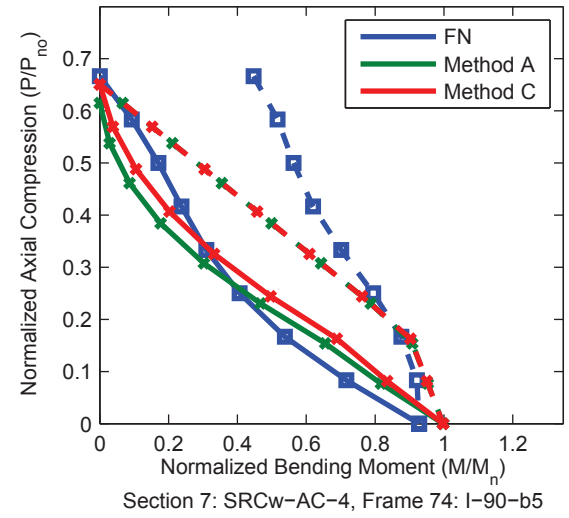

Section 7: SRCw−AC−4, Frame 74: I−90−b5

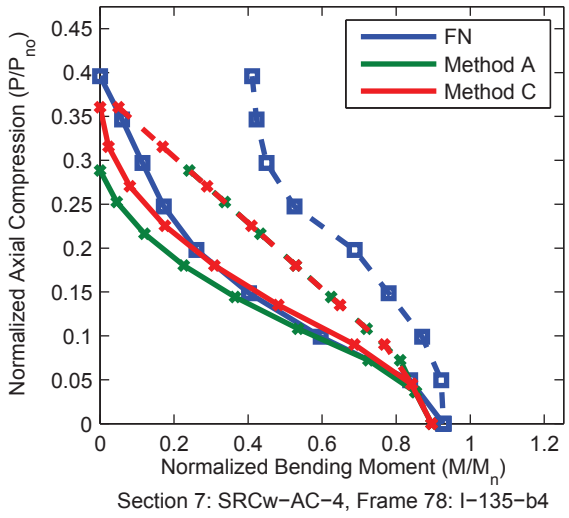

Section 7: SRCw−AC−4, Frame 78: I−135−b4

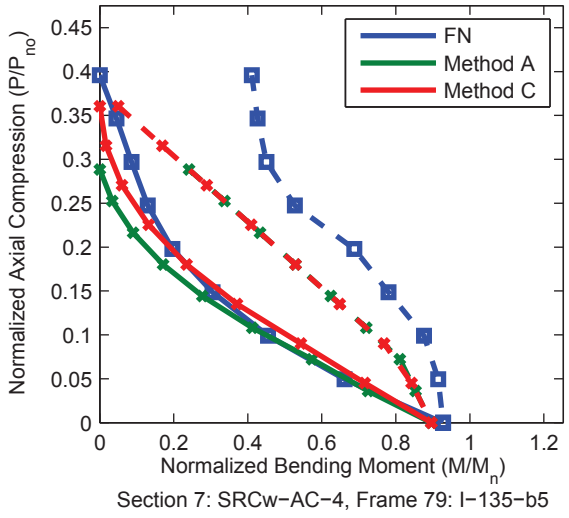

Section 7: SRCw−AC−4, Frame 79: I−135−b5

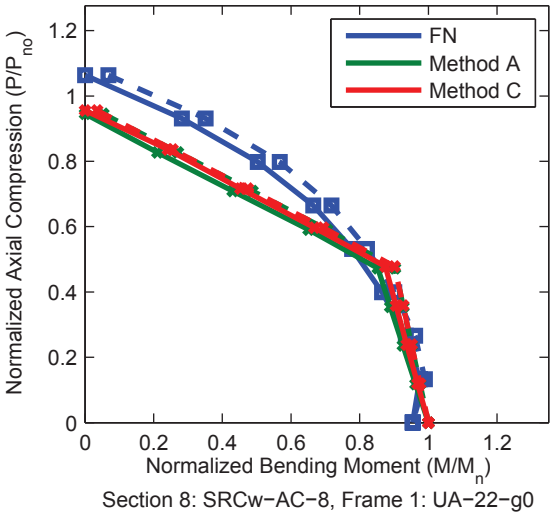

Section 8: SRCw−AC−8, Frame 1: UA−22−g0

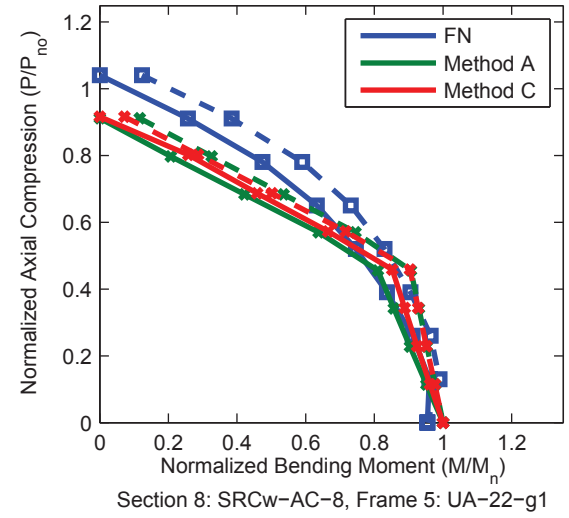

Section 8: SRCw−AC−8, Frame 5: UA−22−g1

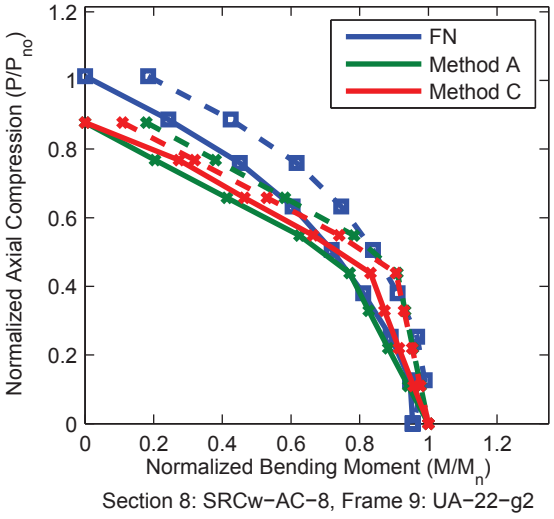

Section 8: SRCw−AC−8, Frame 9: UA−22−g2

Figure A.104. Detailed Results for Method C (continued)

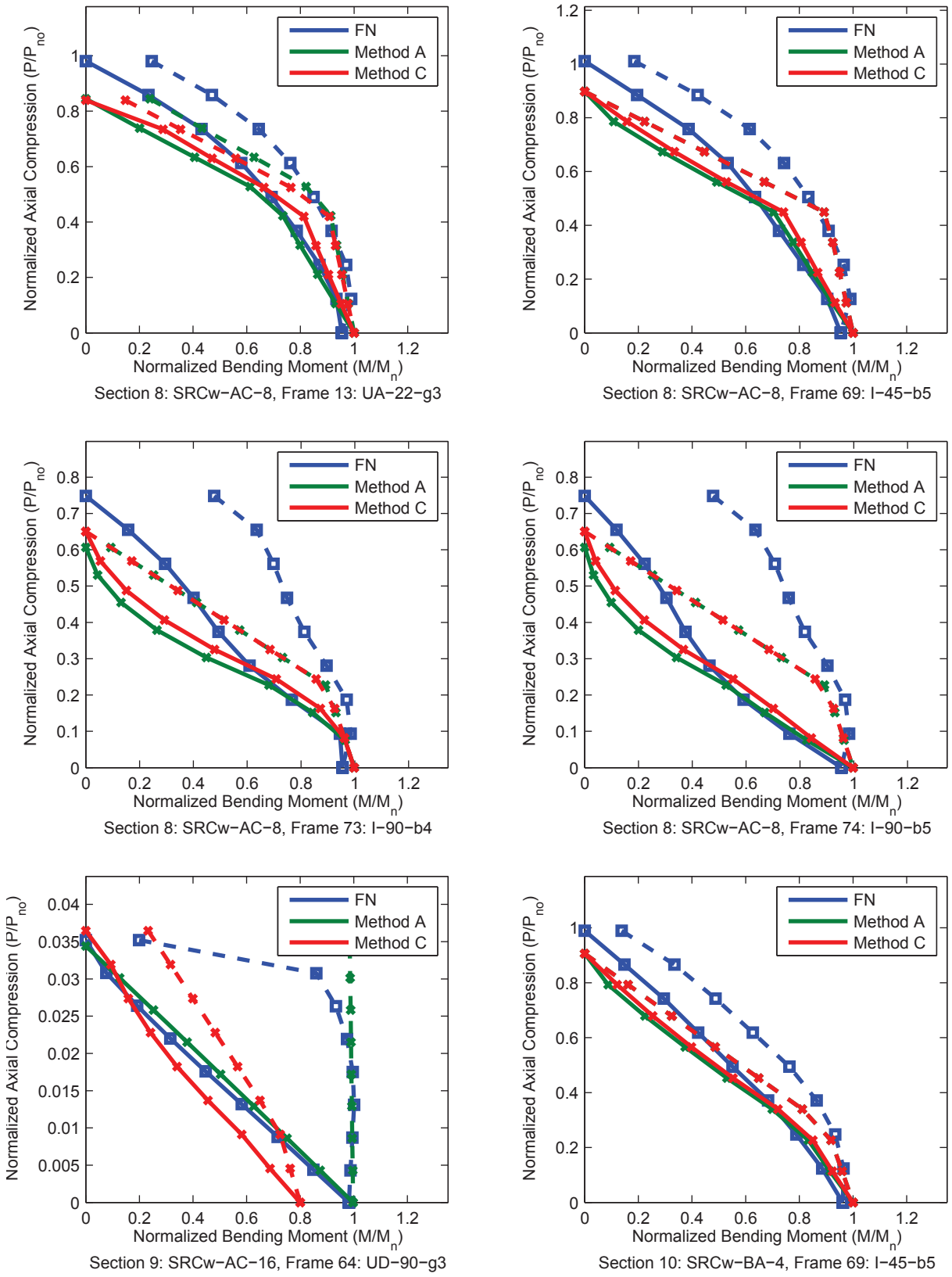

Figure A.104. Detailed Results for Method C (continued)

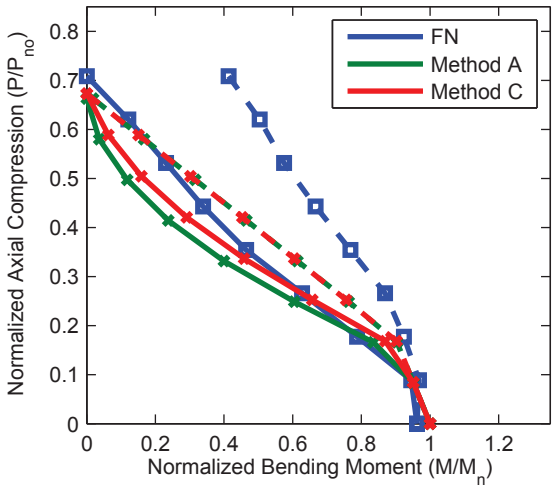

Section 10: SRCw−BA−4, Frame 73: I−90−b4

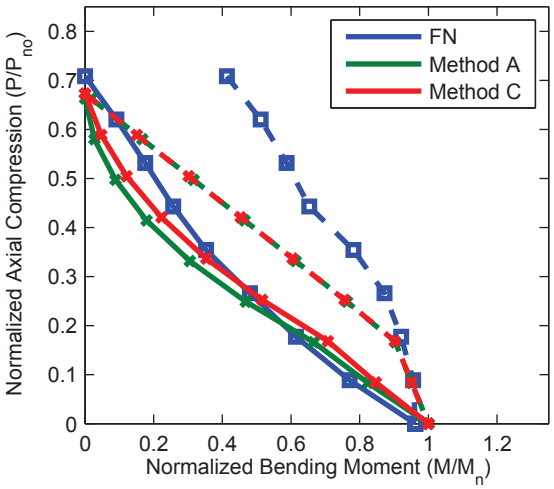

Section 10: SRCw−BA−4, Frame 74: I−90−b5

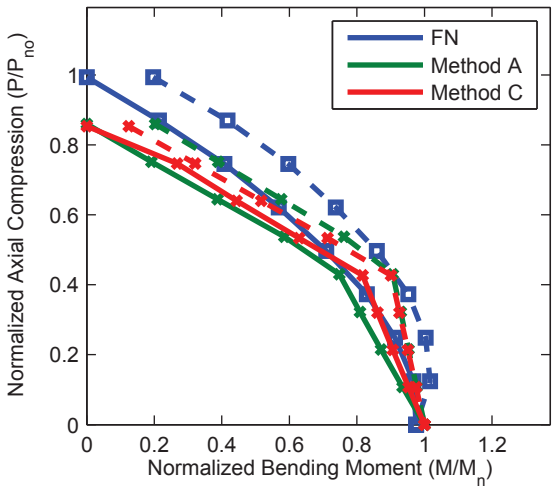

Section 11: SRCw−BA−8, Frame 13: UA−22−g3

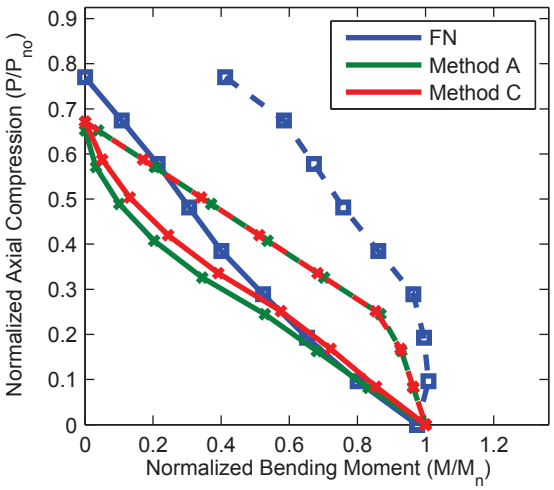

Section 11: SRCw−BA−8, Frame 74: I−90−b5

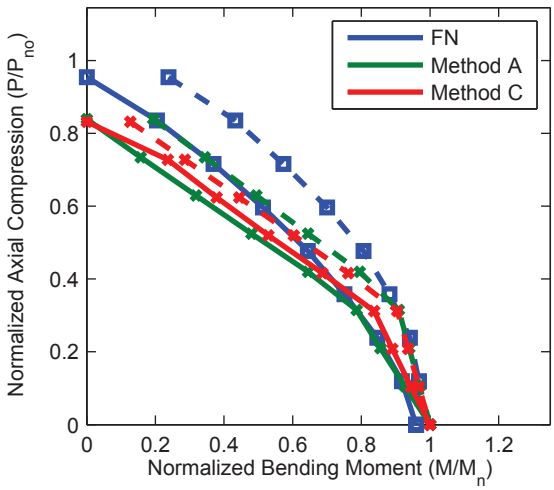

Section 13: SRCw−BB−4, Frame 13: UA−22−g3

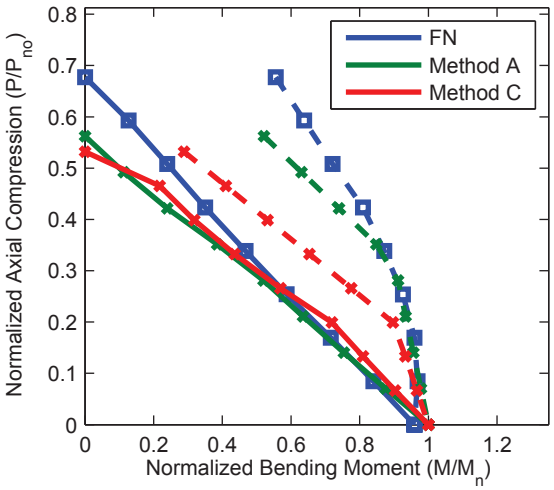

Section 13: SRCw−BB−4, Frame 29: UA−45−g3

Figure A.104. Detailed Results for Method C (continued)

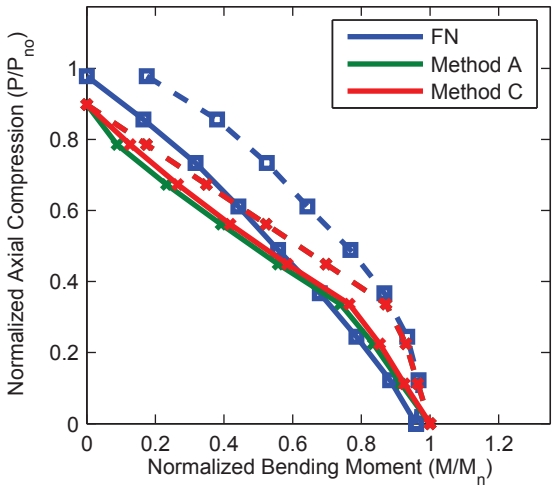

Section 13: SRCw−BB−4, Frame 69: I−45−b5

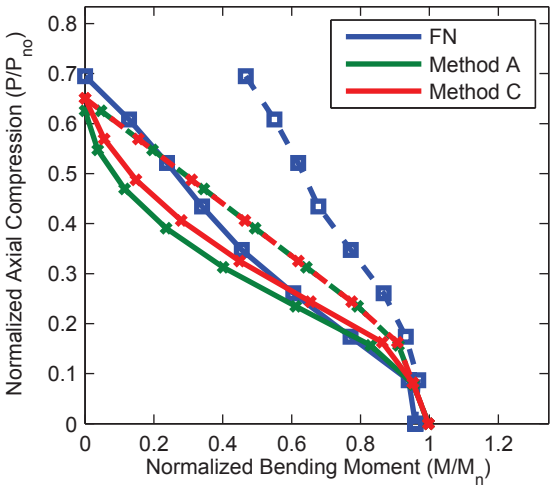

Section 13: SRCw−BB−4, Frame 73: I−90−b4

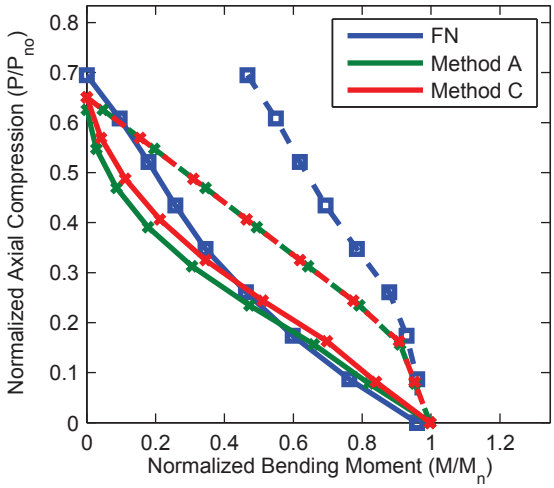

Section 13: SRCw−BB−4, Frame 74: I−90−b5

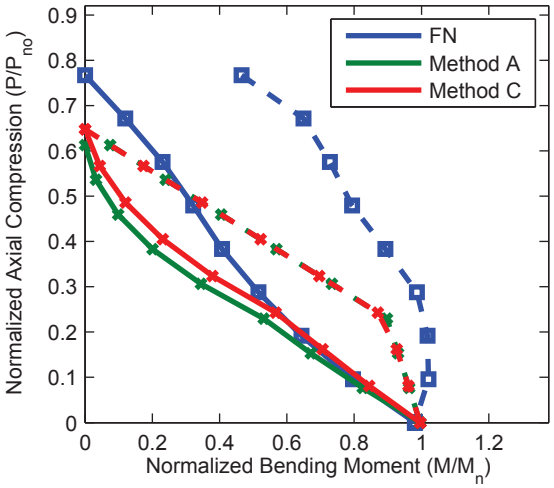

Section 14: SRCw−BB−8, Frame 74: I−90−b5

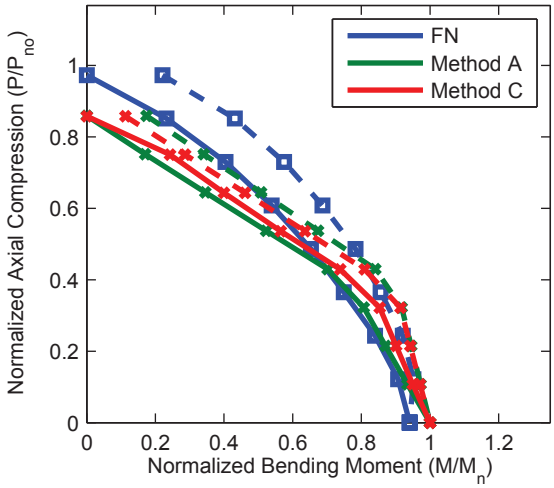

Section 16: SRCw−BC−4, Frame 9: UA−22−g2

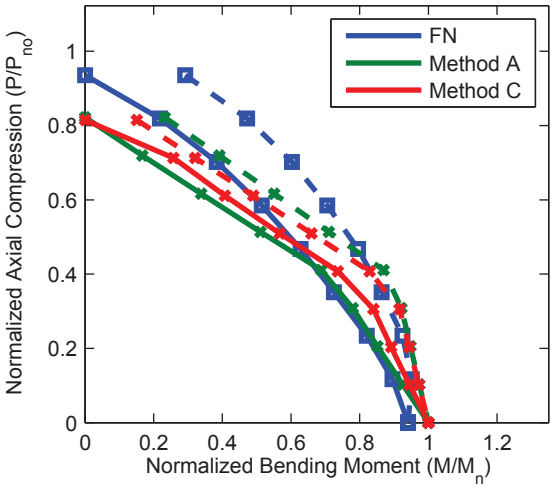

Section 16: SRCw−BC−4, Frame 13: UA−22−g3

Figure A.104. Detailed Results for Method C (continued)

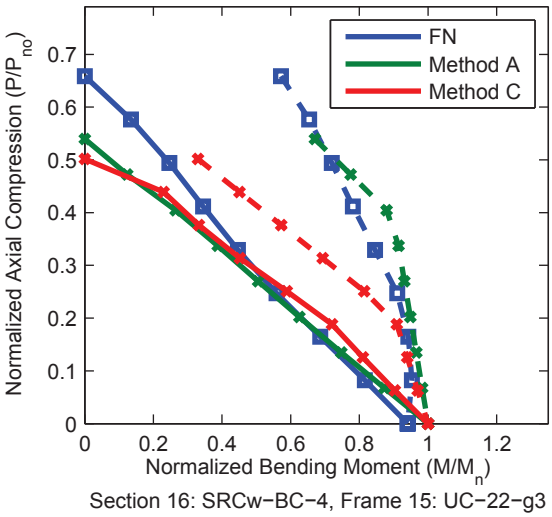

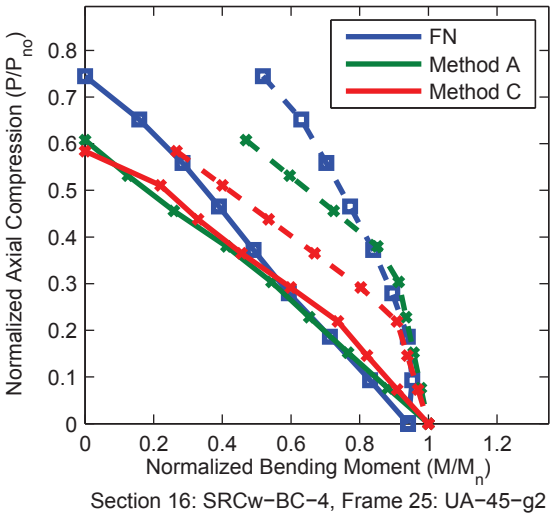

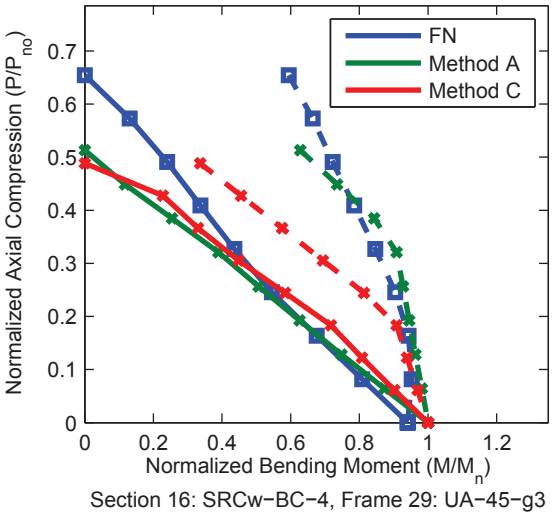

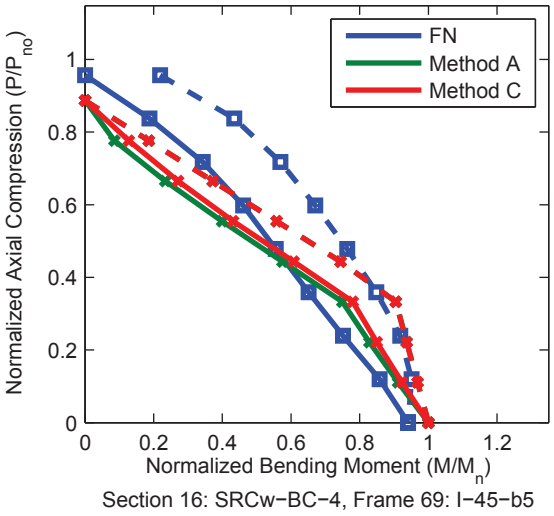

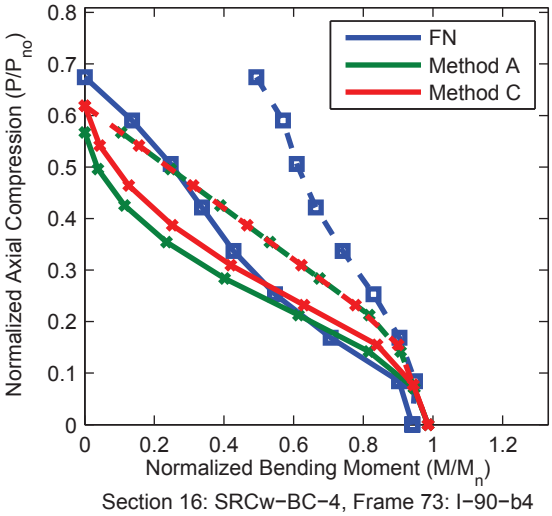

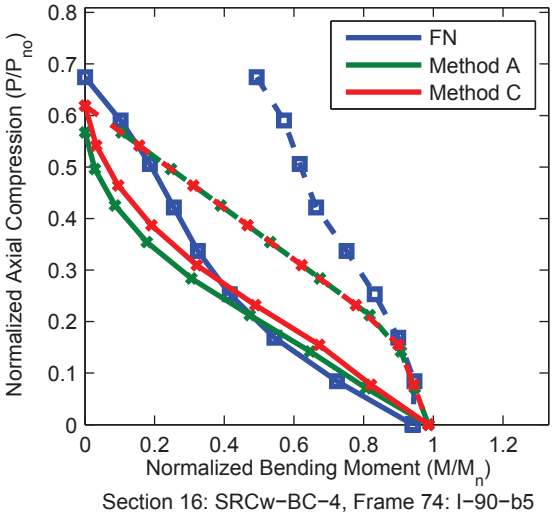

Figure A.104. Detailed Results for Method C (continued)

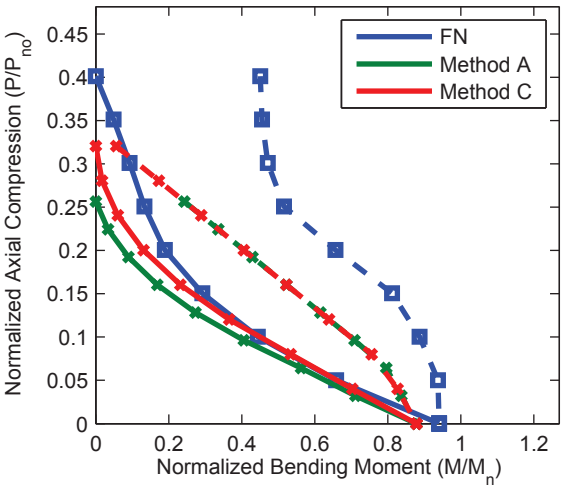

Section 16: SRCw−BC−4, Frame 79: I−135−b5

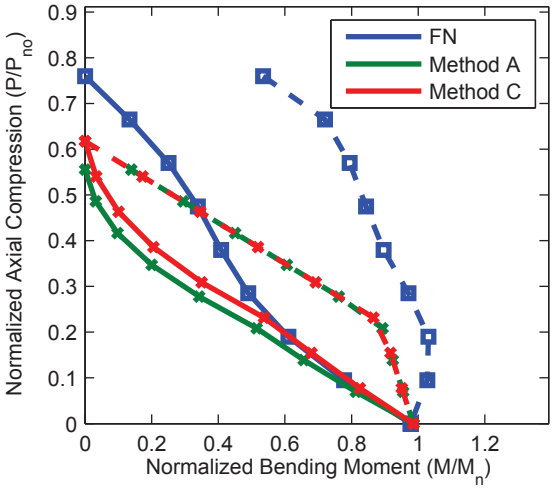

Section 17: SRCw−BC−8, Frame 74: I−90−b5

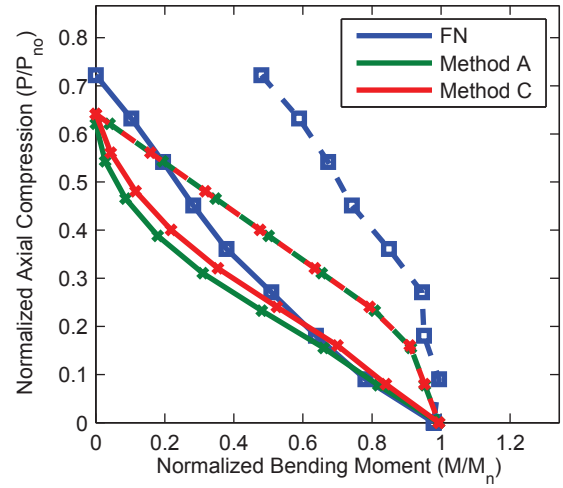

Section 19: SRCw−CA−4, Frame 74: I−90−b5

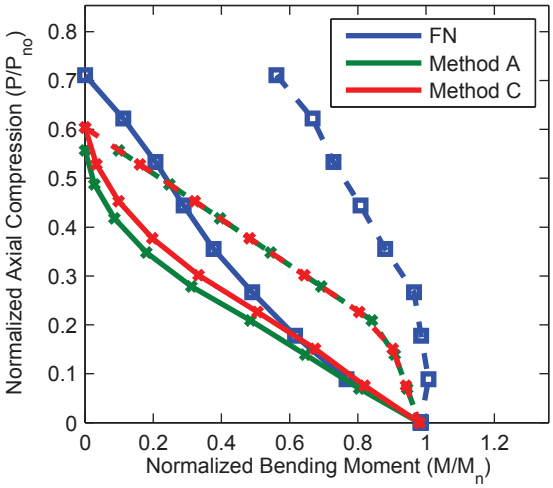

Section 22: SRCw−CB−4, Frame 74: I−90−b5

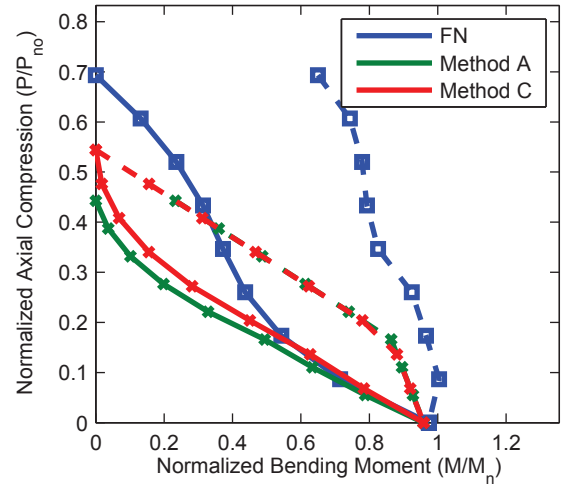

Section 25: SRCw−CC−4, Frame 74: I−90−b5

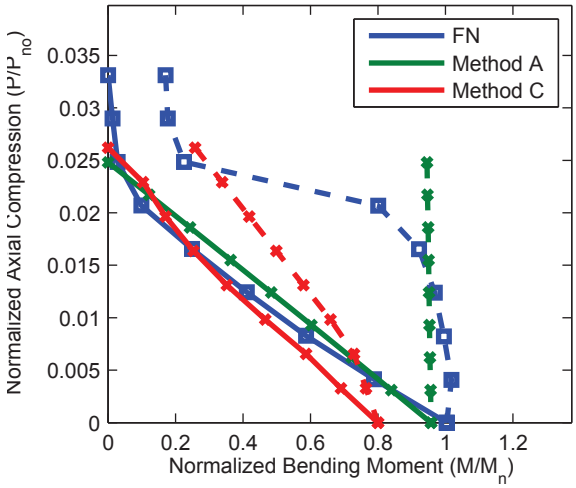

Section 27: SRCw−CC−16, Frame 64: UD−90−g3

Figure A.104. Detailed Results for Method C (continued)

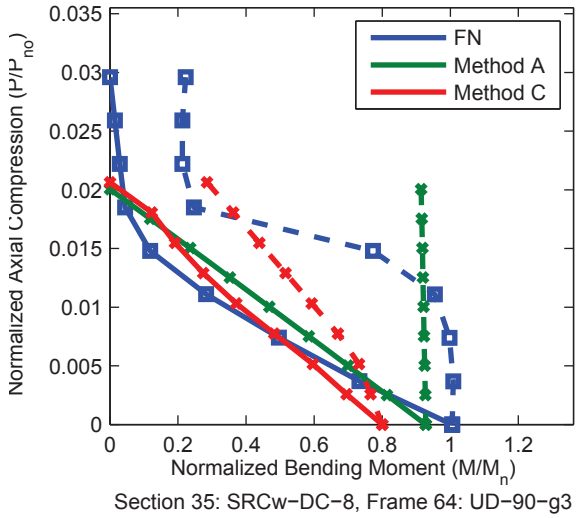

Figure A.104. Detailed Results for Method C (continued)

DESIGN OF ARCHETYPE FRAMES

The parametric studies performed in Chapter 8 require a suite of frames that are reasonably representative of the range of permissible configurations of two seismic force resisting systems: composite special moment frame (C-SMF) and composite special concentrically braced frame (C-SCBF). Selection of the suite of prototypical buildings, termed index archetype configurations, was discussed in the Chapter 8 while details of the design process and final designs, termed index archetype designs, are presented here. These designs build off of previous studies that have included the design of frames with concrete-filled steel tubes (La Fore and Hajjar 2005; Gartner and Hajjar 2006; Ata Rafi 2009).

Loads were determined for the entire structure and members were selected for the seismic force resisting systems. The frames were designed in accordance with the relevant design codes: *Minimum Design Loads for Buildings and Other Structures* (referred to as ASCE 7-10) (ASCE 2010), *The 2012 International Building Code* (referred to as IBC 2012) (ICC 2012), the AISC *Specification for Structural Steel Buildings* (referred to as the AISC *Specification* or AISC 360-10) (2010b) and the AISC *Seismic Provisions for Structural Steel Buildings* (referred to as the AISC *Seismic Specification* or AISC 341-10) (2010c). Additionally, the frames were designed to comply with requirements and recommendations in *Quantification of Building Seismic Performance Factors* (referred to as FEMA P695) (FEMA 2009).

B.1 Index Archetype Configurations

The building layout is the same for each of the index archetype configurations: 3 bays by 5 bays with a bay width of either 20 ft. or 30 ft. (Figure B.1). The buildings are 3 or 9 stories tall with a story height of 13 ft. All buildings have a 42 in. tall parapet on the roof that is not designed but included in the loading calculations.

The C-SMF index archetype configurations have two three-bay moment frames in both directions. The columns are composite (RCFT or SRC). The C-SCBF index archetype configurations have two one-bay braced frames in both directions. The columns are composite (CCFT) and the braces are steel (rectangular HSS or WF) in a “two story X” configuration (Figure B.2b). In both sets, the floor was assumed to consist of a composite deck, although the girders in the seismic force resisting system were designed as bare steel. It is assumed that the beams are provided with sufficient lateral bracing to achieve their full plastic moment strength. Column splices are assumed to occur at one-third the story height above the work point.

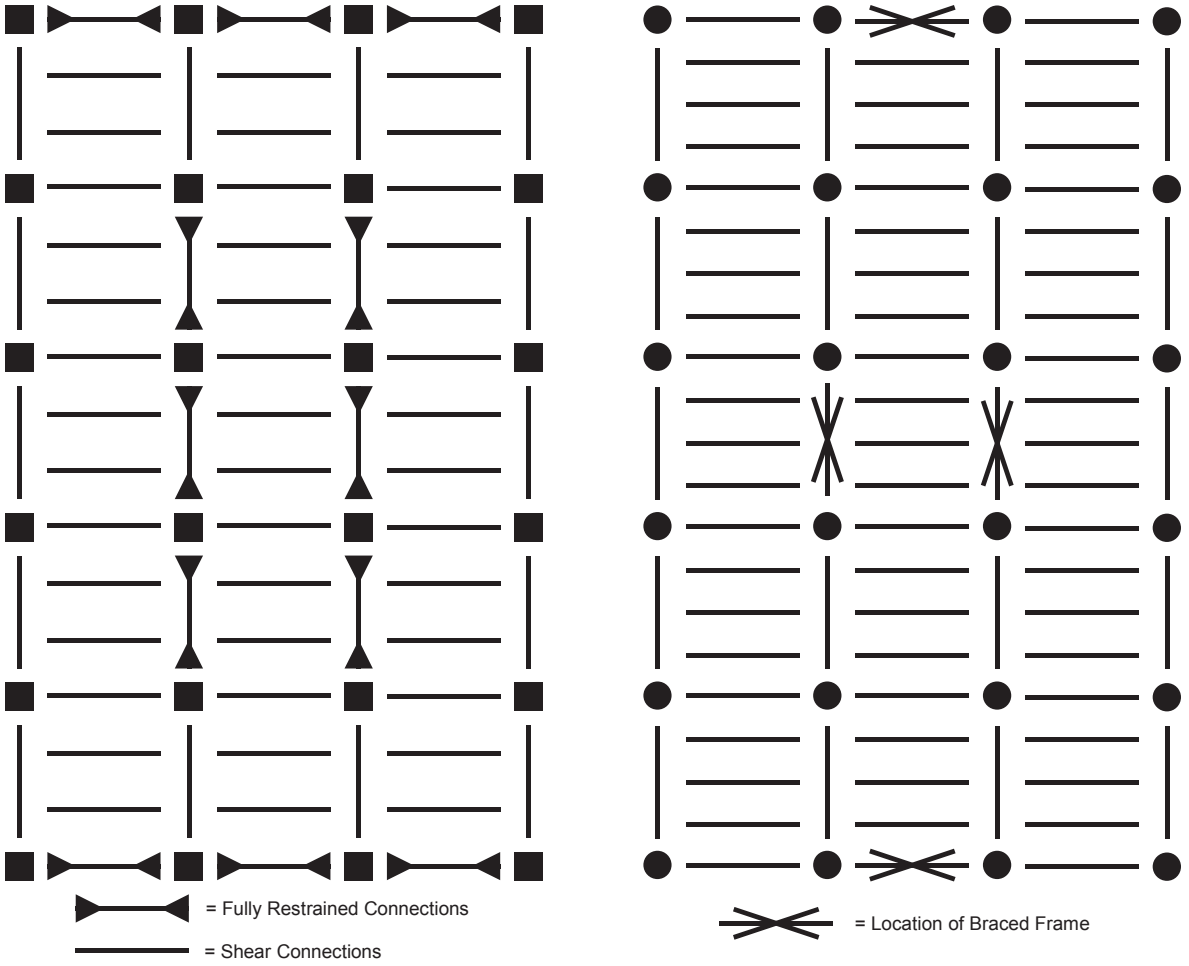

(a) C-SMF (b) C-SCBF

Figure B.1. Building Layout

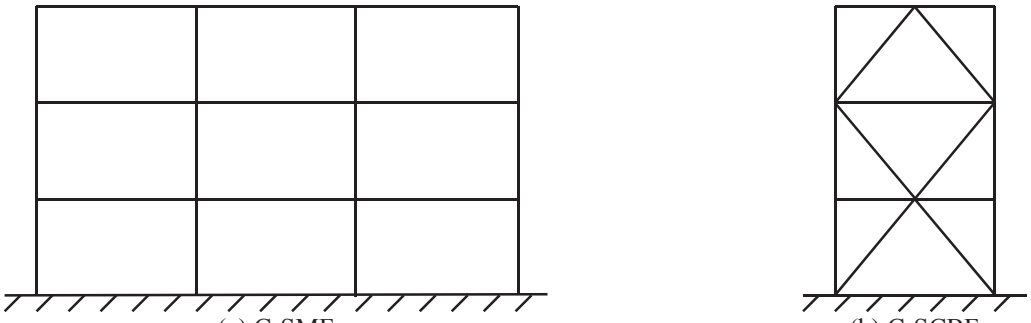

(a) C-SMF (b) C-SCBF

Figure B.2. Elevation View of Three Story Frames

B.2 Loads

Loading on the index archetype configurations includes gravity load (of which there are three cases: dead load, live load, and roof live load), live load reduction, seismic load, and wind load.

B.2.1 Gravity Load

The dead load was estimated using equivalent distributed loads. The dead load on horizontal surfaces (applied to the surface area of the floor or roof) is as described in Table B.1. The composite floor system includes the concrete plus the metal decking. The ceiling, fireproofing, mechanical and electrical loads for the floors and roof are from the story below. The dead load on vertical surfaces (applied to the surface area of the wall or parapet) was assumed to be 25 psf.

Table B.1. Breakdown of Dead Loading on Horizontal Surfaces

Description	Roof *(psf)*	Floor *(psf)*
Composite Floor System	50	50
Ceiling and Fireproofing	2	2
Flooring	---	1
Roofing	7	---
Mechanical and Electrical	7	7
Steel/Composite Framing	20	20
Total, Dead Load	**86**	**80**

The live load was determined in accordance with ASCE 7-10 (2010). Two different levels of gravity load were employed to represent the practical extremes. The lower gravity load corresponds to office occupancy (65 psf = 50 psf + 15 psf for partitions) and the higher gravity load corresponds to warehouse occupancy (250 psf). To further exacerbate the differences, the perimeter frame was designed and analyzed for the configurations with the office live load and interior frame was designed and analyzed for the configurations with the warehouse live load. Roof live load was assumed to be 20 psf for all index archetype configurations. Table B.2 summarizes the distributed gravity load for all surfaces.

Table B.2. Summary of Gravity Load

Applicable Area	Warehouse			Office		
	Dead *(psf)*	Live *(psf)*	Live Roof *(psf)*	Dead *(psf)*	Live *(psf)*	Live Roof *(psf)*
Floor	80	250	---	80	65	---
Wall	25	---	---	25	---	---
Roof	86	---	20	86	---	20
Parapet	25	---	---	25	---	---

B.2.2 Live Load Reduction

Live load reduction was computed and included in the design process following the recommendations of Ziemian and McGuire (1992). Upward loads are applied on the beams and at beam-to-column joints such that the effective live load on the beams and columns is equal to that computed using the applicable provisions from ASCE 7-10 (2010).

B.2.3 Earthquake Load

The level of seismic loading is selected for each index archetype configuration with respect to the seismic design categories (e.g., maximum of seismic design category D). The seismic base shear is computed as described in Chapter 8. The vertical distribution of seismic forces is as described by Equations B.1 and B.2 from Section 12.8.3 of ASCE 7-10 (2010).

$$F_x = C_{vx} V \tag{B.1}$$

$$C_{vx} = \frac{w_x h_x^k}{\sum_{i=1}^{n} w_i h_i^k} \tag{B.2}$$

where,

C_{vx} = vertical distribution factor
V = total seismic base shear
w_i and w_x = the portion of the total effective seismic weight of the structure (W) located at level i or x
h_i and h_x = the height from the base to level i or x
k = an exponent related to the structure period (Equation B.3).

$$k = \begin{cases} 1 & T \le 0.5 \\ 1 + 0.5(T - 0.5) & 0.5 < T < 2.5 \\ 2 & T \ge 2.5 \end{cases} \tag{B.3}$$

B.2.4 Wind and Snow Load

Wind and snow are assumed to be environmental effects that vary independently from the seismic loading (FEMA 2009), as such, minimum wind loads of 10 psf were applied to the structure and snow load was neglected in the design of the archetype frames.

B.3 Design Criteria

The various design criteria for the frames are summarized in Table B.3 with references to the applicable code provisions. Details of each of the checks are described below.

Table B.3. Summary of Design Criteria

Design Check	Reference	C-SMF						C-SCBF					
		System	RCFT Columns		SRC Columns		Beams	System	CCFT Columns		Beams		Braces
Member Strength (Axial Load, Bending Moment, Shear)	AISC 360-10		✓	Ch I	✓	Ch I	✓ Ch F		✓	Ch I	✓	Ch F	✓ Ch E
Seismic Story Drift Limit	ASCE 7-10	✓ 12.12.1						✓ 12.12.1					
Stability Coefficient	ASCE 7-10	✓ 12.8.7						✓ 12.8.7					
Moment Ratio	AISC 341-10	✓ G3.4a											
Brace Capacity Strength	AISC 341-10								✓	H2.3	✓	H2.3	
Moderately Ductile Section	AISC 341-10										✓	D1.1	
Highly Ductile Section	AISC 341-10		✓	D1.1	✓	D1.1	✓ D1.1		✓	D1.1			✓ D1.1
Live Load Deflection Limit	IBC 2012						✓ 1604.3.1				✓	1604.3.1	

B.3.1 Elastic Analysis Model

Elastic analyses of the frame are required for several of the design criteria. Two-dimensional analyses were utilized examining the building one direction at a time. The elastic model of the frame included only the lateral force resisting system and a leaning column representing the destabilizing effect of the gravity load applied on the remainder of the building. The elastic analyses were performed in OpenSees (McKenna et al. 2000) using elastic beam elements. Six elements were used along the length of each member.

For structural steel members, the gross section properties were used (i.e., $E = E_s$, $A = A_s$, $I = I_s$). For composite members, section properties were determined as described in Table B.4. Elastic section properties for composite members were developed in this work (Chapter 6), but the results were unavailable at the time of design. The section properties described in this section do not include reductions for the Direct Analysis method, which are described later.

Table B.4. Section Properties for Elastic Analyses

Parameter	Symbol	CFT	SRC
Modulus of Elasticity	E	$E = E_s$	$E = E_s$
Area	A	$A = EA_{eff} / E_s$ $EA_{eff} = E_s A_s + E_s A_{sr} + E_c A_c$	$A = EA_{eff} / E_s$ $EA_{eff} = E_s A_s + E_s A_{sr} + E_c A_c$
Moment of Inertia	I	$I = EI_{eff} / E_s$ $EI_{eff} = E_s I_s + C_3 E_c I_c$ $C_3 = 0.6 + 2\left(\frac{A_s}{A_c + A_s}\right) \le 0.9$	$I = EI_{eff} / E_s$ $EI_{eff} = E_s I_s + 0.5 E_s I_{sr} + C_1 E_c I_c$ $C_1 = 0.1 + 2\left(\frac{A_s}{A_c + A_s}\right) \le 0.3$

B.3.2 Member Strength

The member strength design check was performed using the Direct Analysis method (AISC 2010b). Second-order elastic analyses were performed to determine the required strengths. The elastic analyses employed a stiffness reduction of 0.80 and a horizontal notional load of 0.003 times the gravity load was applied to the buildings. The additional 0.001 was used so that the stiffness reduction factor, τ_b, could be taken as unity.

The eight load cases described in Table B.5 were used, where,

D = dead load
L = live load
L_r = roof live load
W = wind load
E = earthquake load

The load factor on the live load in LC3a, LC4 and LC5 is 0.5 for the office loading and 1.0 for the warehouse loading. Amplified seismic load for C-SCBF is handled in a separate design criteria (Section B.3.6).

Available strength was computed for each member in accordance with Chapters D through I of the AISC *Specification* (AISC 2010b) using and effective length factor equal to

unity. A tolerance of 3% was used in the interaction check so that small overstresses were acceptable.

Table B.5. Load Combinations Used in Design

Index	Load Combination
LC1	$1.4D$
LC2	$1.2D + 1.6L + 0.5L_r$
LC3a	$1.2D + 1.6L_r + (0.5 \text{ or } 1.0)L$
LC3b	$1.2D + 1.6L_r + 0.5W$
LC4	$1.2D + 1.0W + (0.5 \text{ or } 1.0)L + 0.5L_r$
LC5	$1.2D + 1.0E + (0.5 \text{ or } 1.0)L$
LC6	$0.9D + 1.0W$
LC7	$0.9D + 1.0E$

B.3.3 Seismic Story Drift Limit

Story drift limits as described by ASCE 7-10 (2010) were employed. Elastic analyses were performed with unreduced stiffnesses for load combinations LC5 and LC7 (Table B.5). The story drift was computed and compared to a limiting value (Equation B.4).

$$\Delta_{limit,x} = \frac{0.020 h_{sx}}{C_d} \tag{B.4}$$

where,

$\Delta_{limit,x}$ = story drift limit for level x
h_{sx} = story height below level x

B.3.4 Stability Coefficient

The stability coefficient as described by ASCE 7-10 (2010) is computed and checked against the maximum acceptable value. Elastic analyses were performed with unreduced stiffnesses for load combinations LC5 and LC7 (Table B.5). The stability coefficient was computed based on the story drift and column loads using Equation B.5.

$$\theta = \frac{P_x \Delta}{V_x h_{sx} C_d} \tag{B.5}$$

where,

θ = stability coefficient
P_x = total vertical design load at and above level x
Δ = design story drift occurring simultaneously with V_x

V_x = seismic shear force acting between levels x and $x - 1$
h_{sx} = story height below level x
C_d = deflection amplification factor
I_e in Equation 12.8-16 ASCE 7-10 (2010) has been taken as unity

The frames were designed such that the stability coefficient did not exceed the limiting value given by Equation B.6.

$$\theta_{\max} = \frac{0.5}{\beta C_d} \leq 0.25 \tag{B.6}$$

where,

θ_{max} = limiting value of the stability coefficient
β = ratio of shear demand to shear capacity for the story between levels x and $x - 1$, estimated based on interaction strength ratios from the member strength limit check (Section B.3.2)

B.3.5 Moment Ratio (Strong Column-Weak Beam)

The moment ratio requirements in the AISC *Seismic Specification* (AISC 2010c) for the C-SMFs are given by Equation B.7 and are enforced in the design.

$$\frac{\Sigma M^*_{pcc}}{\Sigma M^*_{p,exp}} > 1.0 \tag{B.7}$$

where,

ΣM^*_{pcc} = sum of the moments in the composite columns above and below the joint at the intersection of the beam and column centerlines
$\Sigma M^*_{p,exp} = \Sigma\left(1.1 M_{p,exp} + M_{uv}\right)$ = sum of the moments in the steel beams at the intersection of the beam and column centerlines
$M_{p,exp} = R_y M_p$ = expected flexural strength of the steel beam
M_{uv} = moment due to shear amplification from the location of the plastic hinge to the column centerline

Column splices are assumed to be located one-third of the story height above the work point. Accordingly, the section specified for the column in the story below the joint is used when computing the strength of the column above the joint.

B.3.6 Braced Frame Capacity Design

Member strength under load combinations that include the amplified seismic load are treated as a separate design criteria. Required strengths for the beams and columns are determined from special analyses where the elements representing the braces are removed and replaced with assumed self-equilibrating forces representing the brace capacity. Two cases of assumed forces are used. In the first, the braces are assumed to resist forces corresponding to their expected strength in compression or in tension. In the second, the braces in tension are assumed to resist forces corresponding to their expected strength and the braces in compression are assumed to resist their expected post-buckling strength. Expected brace strengths were determined in accordance with Section F2.3 of the AISC *Seismic Specification* (AISC 2010c). Fictitious lateral supports were applied at each story to prevent lateral instability in the analysis. The reactions at these supports are representative of the seismic loads necessary to achieve the assumed brace forces. Two cases of gravity loads, those from LC5 and LC7 (Table B.5), are applied, resulting in four separate analyses. Following the Direct Analysis method, a stiffness reduction of 0.8 was applied and available strengths were determined using an effective length factor equal to unity.

B.3.7 Ductility Limitations

The AISC *Seismic Specification* (AISC 2010c) places requirements on structural members to ensure the expected level of ductility can be achieved. These requirements are primarily width-to-thickness limitations as summarized in Table B.6. For the WF beams, the checks are performed assuming zero axial load.

Additional requirements exist for composite columns to be classified as highly ductile. For CFT columns, the nominal shear strength must be taken as that of the steel section alone. For SRC columns, the requirements are given in section D1.4b(2) of the AISC *Seismic Specification* (AISC 2010c) and pertain mostly to the steel reinforcing. In the design process, these limitations are enforced by not selecting members that do not satisfy the requirements.

B.3.8 Live Load Deflection Limitations

The international building code (ICC 2012) places requirements on member stiffness to limit deflections to acceptable values. The evaluation of these requirements is summarized in Table B.7. Three simple beam configurations were identified to be sufficiently representative of various beams and girders in the archetype frames. For each of the simple beam configurations, the maximum deflections based on linear elastic beam theory were determined and an expression for the required moment of inertia was computed based on the deflection limit of $L/360$, assumed to be applicable to all floor and roof beams. The required minimum moment of inertia was computed for the floor and roof beams for each frame based on the live load and roof live load respectively. Only members with a moment of inertia that satisfied the requirement were selected.

B.3.9 Other Design Checks

The panel zone shear strength was checked for the moment frames. It was determined that the strength was sufficient for all of the RCFT frames; however, doubler plates were necessary for some of the SRC frames.

The AISC *Specification* (AISC 2010b) includes material limitations for composite members. One of the limitations is that the concrete compressive strength may not exceed 10 ksi. This limitation is neglected for this study.

Table B.6. Width-to-Thickness Limitations

Member	Required Ductility	Limitation
CCFT Columns	Highly Ductile	$\frac{D}{t} \le 0.076\frac{E_s}{F_y}$
RCFT Columns	Highly Ductile	$\frac{H}{t} \le 1.4\sqrt{\frac{E_s}{F_y}}$
SRC Columns	Highly Ductile	none
WF Beams	Highly Ductile	$\frac{b_f}{2t_f} \le 0.30\sqrt{\frac{E_s}{F_y}}$ and $\frac{h}{t_w} \le 2.45\sqrt{\frac{E_s}{F_y}}$
WF Beams	Moderately Ductile	$\frac{b_f}{2t_f} \le 0.38\sqrt{\frac{E_s}{F_y}}$ and $\frac{h}{t_w} \le 3.76\sqrt{\frac{E_s}{F_y}}$
Rect. HSS Braces	Highly Ductile	$\frac{H}{t} \le 0.55\sqrt{\frac{E_s}{F_y}}$
WF Braces	Highly Ductile	$\frac{b_f}{2t_f} \le 0.30\sqrt{\frac{E_s}{F_y}}$ and $\frac{h}{t_w} \le 1.49\sqrt{\frac{E_s}{F_y}}$

Table B.7. Live Load Deflection Limitations

Member	Schematic	Maximum Deflection	Required Moment of Inertia
Beams in Exterior Frames	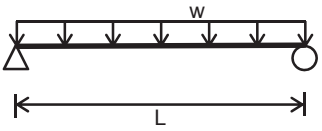	$\delta_{max} = \frac{5wL^4}{384EI}$	$I_{required} = \frac{75wL^3}{16E}$
Beams in Interior Moment Frames	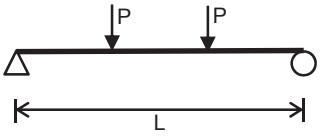	$\delta_{max} = \frac{23PL^3}{648EI}$	$I_{required} = \frac{115PL^2}{9E}$
Beams in Interior Braced Frames	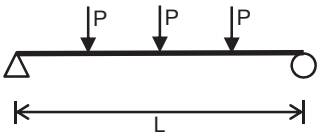	$\delta_{max} = \frac{19PL^3}{384EI}$	$I_{required} = \frac{285PL^2}{16E}$

B.3.10 Sizing Restrictions

With the exception of beams in C-SCBFs, members were selected such that sizes were not smaller than those of the stories above.

HSS braces were used where their strength was sufficient. In cases where the required strength exceeded the available strength of the largest suitable HSS brace, wide flange braces were used. Once a wide flange brace was used, all stories below used wide flange braces.

Often CFT columns with sizes that exceed those of the HSS shapes listed in the Steel Construction Manual were required. In these cases, HSS shapes were selected from available sections listed by manufactures. Only in rare cases were even greater sizes required. In these cases, sections were selected with outside dimensions in increments of 2 inches and thickness in increments of 1/4 inch.

B.4 Design Process and Observations

The design process consisted of selecting initial trial members then entering an iterative process of performing checks and resizing members as necessary until all criteria were satisfied and no members were significantly overdesigned. Different criteria controlled the design of the different frames as described below.

Observations from the design of the C-SMFs

- Typically, the story drift and moment ratio limitations controlled the design.
- For the 9 story frames with lower seismic load (SDC: D_{min}), the stability coefficient check controlled for some stories.
- Composite member strength was rarely limiting.
- The columns in the first story frame RCFT-9-5 (high gravity, high seismic, 30 ft bay width) were near the member strength limit.

Observations from the design of the C-SCBFs

- Typically, the braces were controlled by the member strength criteria and the beams and columns were controlled by the brace capacity strength criteria.
- The member strength criteria controlled for some of the beams and columns in some of the frames.
- Relatively small beams were needed for the stories where the braces framed into the beam-to-column joints. Relatively large beams were needed for the stories where the braces framed in the mid-span of the beam.

B.5 Final Designs

The following tables describe the final member sizes. Material properties are as given in Chapter 8.

Table B.8. Member Sizes for C-SMFs

Frame	Story	Exterior Column	Interior Column	Exterior Beam	Interior Beam
RCFT-3-1	3	RCFT14x8x5/8	RCFT20x12x5/8	W18x35	W18x35
	2	RCFT16x12x5/8	RCFT22x14x5/8	W24x76	W24x84
	1	RCFT16x12x5/8	RCFT22x18x5/8	W24x84	W27x94
RCFT-3-2	3	RCFT14x8x5/8	RCFT18x10x5/8	W18x35	W18x35
	2	RCFT16x8x5/8	RCFT22x14x5/8	W24x76	W24x84
	1	RCFT16x12x5/8	RCFT22x16x5/8	W24x84	W27x94
RCFT-3-3	3	RCFT14x8x1/2	RCFT18x10x5/8	W18x35	W18x35
	2	RCFT14x8x1/2	RCFT18x10x5/8	W21x50	W21x50
	1	RCFT14x8x1/2	RCFT18x10x5/8	W21x50	W21x50
RCFT-3-4	3	RCFT14x8x1/2	RCFT18x8x5/8	W18x35	W18x35
	2	RCFT14x8x1/2	RCFT18x8x5/8	W21x50	W21x50
	1	RCFT14x8x1/2	RCFT18x8x5/8	W21x50	W21x50
RCFT-3-5	3	RCFT20x14x5/8	RCFT26x20x3/4	W21x73	W21x73
	2	RCFT22x18x5/8	RCFT28x20x1	W33x130	W33x130
	1	RCFT22x18x5/8	RCFT28x20x1	W33x130	W33x141
RCFT-3-6	3	RCFT20x12x5/8	RCFT26x18x3/4	W21x73	W21x73
	2	RCFT22x14x5/8	RCFT26x22x3/4	W33x130	W33x130
	1	RCFT22x14x5/8	RCFT26x24x3/4	W33x130	W33x141
RCFT-3-7	3	RCFT20x12x5/8	RCFT26x16x3/4	W21x73	W21x73
	2	RCFT20x12x3/4	RCFT26x16x3/4	W30x108	W30x108
	1	RCFT20x12x3/4	RCFT26x16x3/4	W30x108	W30x108
RCFT-3-8	3	RCFT20x12x5/8	RCFT26x14x3/4	W21x73	W21x73
	2	RCFT20x12x5/8	RCFT26x14x3/4	W30x108	W30x108
	1	RCFT20x12x5/8	RCFT26x14x3/4	W30x108	W30x108
RCFT-3-9	3	RCFT12x12x5/8	RCFT18x12x5/8	W18x35	W18x35
	2	RCFT14x12x5/8	RCFT20x14x5/8	W24x76	W24x76
	1	RCFT14x12x5/8	RCFT20x14x5/8	W24x76	W24x76
RCFT-3-10	3	RCFT14x8x5/8	RCFT16x12x5/8	W18x35	W18x35
	2	RCFT16x8x5/8	RCFT20x12x5/8	W21x73	W24x76
	1	RCFT16x10x5/8	RCFT20x12x5/8	W21x73	W24x76
RCFT-3-11	3	RCFT12x12x1/2	RCFT16x12x5/8	W18x35	W18x35
	2	RCFT12x12x1/2	RCFT16x12x5/8	W21x44	W21x44
	1	RCFT12x12x1/2	RCFT16x12x5/8	W21x44	W21x44
RCFT-3-12	3	RCFT12x10x1/2	RCFT16x12x5/8	W18x35	W18x35
	2	RCFT12x10x1/2	RCFT16x12x5/8	W21x44	W21x44
	1	RCFT12x10x1/2	RCFT16x12x5/8	W21x44	W21x44
RCFT-3-13	3	RCFT18x14x5/8	RCFT24x18x3/4	W21x73	W21x73
	2	RCFT20x16x5/8	RCFT24x22x3/4	W30x124	W30x124
	1	RCFT20x16x5/8	RCFT24x22x3/4	W30x124	W30x124
RCFT-3-14	3	RCFT18x12x5/8	RCFT22x18x3/4	W24x62	W24x62
	2	RCFT20x12x5/8	RCFT24x20x3/4	W30x116	W30x116
	1	RCFT20x12x5/8	RCFT24x20x3/4	W30x116	W30x124
RCFT-3-15	3	RCFT12x12x5/8	RCFT18x14x3/4	W18x40	W21x44
	2	RCFT16x12x5/8	RCFT20x14x3/4	W24x84	W24x84
	1	RCFT16x12x5/8	RCFT20x14x3/4	W24x84	W24x84
RCFT-3-16	3	RCFT12x12x5/8	RCFT18x10x3/4	W18x40	W21x44
	2	RCFT14x12x5/8	RCFT20x12x3/4	W24x84	W24x84
	1	RCFT14x12x5/8	RCFT20x12x3/4	W24x84	W24x84

Table B.8. Member Sizes for C-SMFs (Continued)

Frame	Story	Exterior Column	Interior Column	Exterior Beam	Interior Beam
	9	RCFT12x10x3/4	RCFT14x14x1	W18x40	W18x40
	8	RCFT16x10x3/4	RCFT20x14x1	W21x73	W24x84
	7	RCFT18x12x3/4	RCFT24x14x1	W27x94	W27x102
	6	RCFT18x14x3/4	RCFT24x14x1	W30x108	W30x124
RCFT-9-1	5	RCFT22x14x3/4	RCFT26x16x1	W33x130	W33x130
	4	RCFT22x14x3/4	RCFT26x16x1	W33x130	W33x130
	3	RCFT22x14x3/4	RCFT28x16x1	W33x130	W33x141
	2	RCFT24x14x3/4	RCFT28x18x1	W33x130	W33x141
	1	RCFT24x14x3/4	RCFT28x18x1	W33x130	W33x141
	9	RCFT10x8x5/8	RCFT12x10x3/4	W14x26	W12x22
	8	RCFT14x8x5/8	RCFT16x12x3/4	W24x55	W24x55
	7	RCFT14x8x5/8	RCFT18x12x3/4	W24x62	W24x62
	6	RCFT14x10x5/8	RCFT18x14x3/4	W21x73	W21x73
RCFT-9-3	5	RCFT16x10x5/8	RCFT20x16x3/4	W24x76	W24x76
	4	RCFT18x12x5/8	RCFT22x16x3/4	W27x94	W27x94
	3	RCFT18x12x5/8	RCFT22x18x3/4	W27x94	W27x94
	2	RCFT20x12x5/8	RCFT22x22x3/4	W30x108	W30x108
	1	RCFT20x12x5/8	RCFT22x22x3/4	W30x108	W30x108
	9	RCFT18x16x3/4	RCFT24x20x1	W21x73	W24x76
	8	RCFT24x18x3/4	RCFT26x20x1	W30x124	W33x130
	7	RCFT24x20x3/4	RCFT28x24x1	W33x141	W40x149
	6	RCFT26x20x1	RCFT34x28x1	W40x211	W40x211
RCFT-9-5	5	RCFT26x20x1	RCFT34x28x1	W40x211	W40x211
	4	RCFT26x20x1	RCFT36x28x1-1/4	W40x215	W44x230
	3	RCFT26x22x1	RCFT36x28x1-1/4	W40x215	W44x230
	2	RCFT26x22x1	RCFT36x28x1-1/4	W44x230	W44x230
	1	RCFT26x22x1	RCFT36x28x1-1/4	W44x230	W44x230
	9	RCFT18x12x3/4	RCFT24x18x3/4	W24x62	W24x62
	8	RCFT20x12x3/4	RCFT26x18x3/4	W30x108	W30x108
	7	RCFT20x14x3/4	RCFT26x20x1	W30x116	W33x130
	6	RCFT20x16x3/4	RCFT26x24x1	W30x124	W33x141
RCFT-9-7	5	RCFT22x16x3/4	RCFT30x24x1	W33x141	W33x141
	4	RCFT22x18x1	RCFT30x24x1	W40x167	W40x167
	3	RCFT22x20x1	RCFT32x26x1	W40x167	W40x183
	2	RCFT24x20x1	RCFT32x26x1	W40x183	W40x211
	1	RCFT24x20x1	RCFT32x26x1	W40x183	W40x211

Table B.8. Member Sizes for C-SMFs (Continued)

Frame	Story	Exterior Column	Interior Column	Exterior Beam	Interior Beam
RCFT-9-9	9	RCFT12x8x3/4	RCFT14x14x3/4	W18x35	W18x35
	8	RCFT14x10x3/4	RCFT18x14x3/4	W24x76	W24x76
	7	RCFT14x10x3/4	RCFT22x14x1	W24x76	W27x94
	6	RCFT18x12x3/4	RCFT22x14x1	W24x84	W30x116
	5	RCFT18x12x3/4	RCFT24x14x1	W27x102	W30x116
	4	RCFT18x12x3/4	RCFT24x14x1	W30x108	W30x124
	3	RCFT18x14x3/4	RCFT24x16x1	W30x108	W30x124
	2	RCFT18x14x3/4	RCFT24x16x1	W30x108	W30x124
	1	RCFT18x14x3/4	RCFT24x16x1	W30x108	W30x124
RCFT-9-11	9	RCFT8x8x5/8	RCFT10x10x3/4	W12x22	W12x22
	8	RCFT10x8x5/8	RCFT12x10x3/4	W18x40	W18x40
	7	RCFT12x8x5/8	RCFT14x10x3/4	W21x50	W21x50
	6	RCFT12x8x5/8	RCFT16x12x3/4	W21x50	W24x55
	5	RCFT14x8x5/8	RCFT16x12x3/4	W24x55	W24x62
	4	RCFT14x10x5/8	RCFT18x14x3/4	W24x62	W24x62
	3	RCFT14x10x5/8	RCFT18x14x3/4	W24x62	W24x62
	2	RCFT14x10x5/8	RCFT18x14x3/4	W24x62	W24x62
	1	RCFT14x10x5/8	RCFT18x14x3/4	W24x62	W24x62
RCFT-9-13	9	RCFT16x12x3/4	RCFT22x14x1	W24x62	W24x62
	8	RCFT18x14x3/4	RCFT24x16x1	W30x116	W30x124
	7	RCFT20x14x3/4	RCFT28x18x1	W33x130	W40x167
	6	RCFT24x16x3/4	RCFT30x22x1	W33x141	W40x167
	5	RCFT24x16x3/4	RCFT32x26x1	W40x149	W40x183
	4	RCFT24x16x3/4	RCFT32x26x1	W40x149	W40x211
	3	RCFT24x20x3/4	RCFT32x26x1	W40x183	W40x211
	2	RCFT24x20x3/4	RCFT32x26x1	W40x183	W40x211
	1	RCFT24x20x3/4	RCFT32x26x1	W40x183	W40x211
RCFT-9-15	9	RCFT12x10x5/8	RCFT14x14x3/4	W18x35	W18x35
	8	RCFT12x12x5/8	RCFT18x14x3/4	W24x62	W24x76
	7	RCFT16x12x5/8	RCFT20x14x3/4	W24x84	W24x84
	6	RCFT18x12x3/4	RCFT22x16x3/4	W27x94	W27x94
	5	RCFT18x12x3/4	RCFT22x18x3/4	W27x102	W27x102
	4	RCFT18x12x3/4	RCFT22x18x1	W30x108	W30x108
	3	RCFT18x14x3/4	RCFT22x18x1	W30x108	W30x108
	2	RCFT18x14x3/4	RCFT22x20x1	W30x108	W30x108
	1	RCFT18x14x3/4	RCFT22x20x1	W30x108	W30x108

Table B.8. Member Sizes for C-SMFs (Continued)

Frame	Story	Exterior Column								Interior Column								Exterior Beam	Interior Beam
		H	B	WF Shape	$t_{doubler}$	long. reinf.		trans. reinf.		H	B	WF Shape	$t_{doubler}$	long. reinf.		trans. reinf.			
						size	config	size	s					size	config	size	s		
		in	*in*		*in*				*in*	*in*	*in*		*in*				*in*		
SRC-3-1	3	18	18	W8X48	0.00	#7	4x-4y	#4	4	24	22	W14X82	0.00	#9	4x-4y	#4	4	W18x35	W18x35
	2	20	20	W10X68	0.25	#8	4x-4y	#4	4	26	26	W16X100	0.50	#10	4x-4y	#4	4	W27x94	W27x94
	1	20	20	W10X68	0.25	#8	4x-4y	#4	4	26	26	W16X100	0.50	#10	4x-4y	#4	4	W27x94	W27x94
SRC-3-2	3	18	18	W8X58	0.00	#8	4x-4y	#5	2	20	20	W10X77	0.00	#8	4x-4y	#5	2	W18x40	W21x44
	2	18	18	W8X58	0.00	#8	4x-4y	#5	2	28	26	W16X100	0.00	#10	4x-4y	#6	2	W24x84	W27x94
	1	18	18	W8X58	0.00	#8	4x-4y	#5	2	28	26	W16X100	0.00	#10	4x-4y	#6	2	W24x84	W27x94
SRC-3-3	3	16	16	W6X25	0.00	#7	4x-4y	#4	4	18	18	W8x48	0.00	#8	4x-4y	#4	4	W14x26	W16x31
	2	18	18	W8X48	0.00	#7	4x-4y	#4	4	22	20	W10X77	0.50	#9	4x-4y	#4	4	W24x55	W24x55
	1	18	18	W8X48	0.00	#7	4x-4y	#4	4	22	20	W10X77	0.50	#9	4x-4y	#4	4	W24x55	W24x55
SRC-3-4	3	16	16	W6X25	0.00	#6	4x-4y	#5	2	18	18	W8X48	0.00	#7	4x-4y	#5	2	W14x26	W14x26
	2	18	18	W8X40	0.00	#6	4x-4y	#5	2	20	20	W10X68	0.00	#8	4x-4y	#5	2	W24x55	W24x55
	1	18	18	W8X40	0.00	#6	4x-4y	#5	2	20	20	W10X68	0.00	#8	4x-4y	#5	2	W24x55	W24x55
SRC-3-9	3	18	18	W8X48	0.00	#7	4x-4y	#4	4	24	22	W12X58	0.00	#8	4x-4y	#4	4	W18x40	W18x40
	2	18	18	W8X58	0.25	#8	4x-4y	#4	4	26	26	W16X89	0.25	#8	4x-4y	#4	4	W24x76	W24x84
	1	18	18	W8X58	0.25	#8	4x-4y	#4	4	26	26	W16X89	0.25	#8	4x-4y	#4	4	W24x76	W27x94
SRC-3-10	3	18	18	W8X31	0.00	#7	4x-4y	#5	2	22	22	W10X60	0.00	#8	4x-4y	#6	2	W18x35	W18x35
	2	18	18	W8X58	0.00	#7	4x-4y	#5	2	24	24	W12X87	0.00	#8	4x-4y	#6	2	W24x84	W27x94
	1	18	18	W8X58	0.00	#7	4x-4y	#5	2	24	24	W12X87	0.00	#8	4x-4y	#6	2	W24x84	W27x94
SRC-3-11	3	16	16	W6X15	0.00	#7	4x-4y	#4	4	18	18	W8x48	0.00	#8	4x-4y	#4	4	W14x26	W16x31
	2	16	16	W6X25	0.00	#7	4x-4y	#4	4	20	20	W10X68	0.50	#8	4x-4y	#4	4	W21x50	W24x62
	1	16	16	W6X25	0.00	#7	4x-4y	#4	4	20	20	W10X68	0.50	#8	4x-4y	#4	4	W21x50	W24x62
SRC-3-12	3	14	14	W5X19	0.00	#5	4x-4y	#5	2	18	18	W8X48	0.00	#5	4x-4y	#5	2	W14x26	W14x26
	2	16	16	W6X25	0.00	#7	4x-4y	#5	2	18	18	W8X67	0.00	#7	4x-4y	#5	2	W24x55	W24x55
	1	16	16	W6X25	0.00	#7	4x-4y	#5	2	18	18	W8X67	0.00	#7	4x-4y	#5	2	W24x55	W24x55

Table B.8. Member Sizes for C-SMFs (Continued)

Frame	Story	Exterior Column	Interior Column	Exterior Beam	Interior Beam
RCFT-3-1-Cd	3	RCFT12x8x5/8	RCFT16x12x5/8	W16x31	W16x31
	2	RCFT16x10x5/8	RCFT20x12x5/8	W21x73	W21x73
	1	RCFT16x10x5/8	RCFT20x12x5/8	W21x73	W21x73
RCFT-3-3-Cd	3	RCFT12x8x1/2	RCFT14x10x5/8	W14x26	W14x26
	2	RCFT14x8x1/2	RCFT18x10x5/8	W21x44	W21x44
	1	RCFT14x8x1/2	RCFT18x10x5/8	W21x50	W21x44
RCFT-3-9-Cd	3	RCFT10x10x5/8	RCFT16x10x5/8	W16x31	W16x31
	2	RCFT12x10x5/8	RCFT20x10x5/8	W24x55	W24x62
	1	RCFT12x10x5/8	RCFT20x10x5/8	W24x55	W24x62
RCFT-3-11-Cd	3	RCFT10x6x1/2	RCFT12x8x5/8	W12x22	W12x22
	2	RCFT10x8x1/2	RCFT14x10x5/8	W18x40	W21x44
	1	RCFT10x8x1/2	RCFT14x10x5/8	W18x40	W21x44

Table B.9. Member Sizes for C-SCBFs

Frame	Story	Column	Beam	Brace
CCFT-3-1	3	CCFT6.625x0.250	W30X99	HSS4x4x5/16
	2	CCFT16.000x0.375	W21X50	HSS5x5x3/8
	1	CCFT16.000x0.375	W30X90	HSS6x6x1/2
CCFT-3-2	3	CCFT5.563x0.258	W30X99	HSS4x4x5/16
	2	CCFT14.000x0.375	W21X50	HSS5x5x3/8
	1	CCFT14.000x0.375	W30X99	HSS6x6x1/2
CCFT-3-3	3	CCFT6.000x0.250	W30X90	HSS3-1/2x3-1/2x1/4
	2	CCFT14.000x0.375	W21X50	HSS3-1/2x3-1/2x3/8
	1	CCFT14.000x0.375	W24X76	HSS5x5x3/8
CCFT-3-4	3	CCFT5.500x0.258	W30X90	HSS3-1/2x3-1/2x1/4
	2	CCFT10.000x0.375	W21X50	HSS4x4x5/16
	1	CCFT10.000x0.375	W24X84	HSS5x5x3/8
CCFT-3-5	3	CCFT8.625x0.250	W40X167	HSS5-1/2x5-1/2x3/8
	2	CCFT20.000x0.500	W30X116	HSS7x7x1/2
	1	CCFT20.000x0.500	W40X183	HSS8x8x5/8
CCFT-3-6	3	CCFT6.625x0.250	W40X167	HSS5-1/2x5-1/2x3/8
	2	CCFT20.000x0.500	W30X116	HSS6x6x1/2
	1	CCFT20.000x0.500	W40X183	HSS8x8x5/8
CCFT-3-7	3	CCFT7.500x0.250	W40X149	HSS4-1/2x4-1/2x3/8
	2	CCFT22.000x0.500	W30X116	HSS4-1/2x4-1/2x3/8
	1	CCFT22.000x0.500	W40X167	HSS6x6x1/2
CCFT-3-8	3	CCFT6.625x0.250	W40X149	HSS4-1/2x4-1/2x3/8
	2	CCFT20.000x0.500	W30X116	HSS4-1/2x4-1/2x3/8
	1	CCFT20.000x0.500	W40X167	HSS6x6x1/2
CCFT-3-9	3	CCFT6.000x0.250	W30X90	HSS3-1/2x3-1/2x3/8
	2	CCFT10.750x0.375	W16X26	HSS4-1/2x4-1/2x5/16
	1	CCFT10.750x0.375	W21X44	HSS5x5x3/8
CCFT-3-10	3	CCFT5.500x0.258	W30X90	HSS3-1/2x3-1/2x3/8
	2	CCFT9.625x0.312	W16X26	HSS4-1/2x4-1/2x5/16
	1	CCFT9.625x0.312	W21X44	HSS5x5x3/8
CCFT-3-11	3	CCFT5.000x0.250	W24X68	HSS3x3x1/4
	2	CCFT10.000x0.250	W14X22	HSS3-1/2x3-1/2x5/16
	1	CCFT10.000x0.250	W16X31	HSS3-1/2x3-1/2x3/8
CCFT-3-12	3	CCFT5.000x0.188	W24X76	HSS3x3x1/4
	2	CCFT8.625x0.250	W12X19	HSS3-1/2x3-1/2x1/4
	1	CCFT8.625x0.250	W18X50	HSS3-1/2x3-1/2x3/8
CCFT-3-13	3	CCFT6.875x0.250	W40X149	HSS5x5x3/8
	2	CCFT14.000x0.375	W24X62	HSS6x6x1/2
	1	CCFT14.000x0.375	W24X62	HSS7x7x1/2
CCFT-3-14	3	CCFT6.000x0.250	W33X141	HSS5x5x3/8
	2	CCFT12.750x0.375	W24X62	HSS6x6x1/2
	1	CCFT12.750x0.375	W24X62	HSS7x7x1/2
CCFT-3-15	3	CCFT6.625x0.250	W30X116	HSS4x4x5/16
	2	CCFT12.750x0.375	W18X40	HSS4-1/2x4-1/2x3/8
	1	CCFT12.750x0.375	W24X68	HSS4-1/2x4-1/2x1/2
CCFT-3-16	3	CCFT5.500x0.258	W30X116	HSS4x4x5/16
	2	CCFT10.000x0.250	W21X44	HSS4-1/2x4-1/2x3/8
	1	CCFT10.000x0.250	W21X44	HSS5x5x3/8

Table B.9. Member Sizes for C-SCBFs (Continued)

Frame	Story	Column	Beam	Brace
CCFT-9-1	9	CCFT6.625x0.250	W30X90	HSS3-1/2x3-1/2x5/16
	8	CCFT16.000x0.375	W21X50	HSS5x5x3/8
	7	CCFT16.000x0.375	W30X108	HSS6x6x1/2
	6	CCFT24.000x0.625	W24X62	HSS6x6x1/2
	5	CCFT24.000x0.625	W30X108	HSS7x7x5/8
	4	CCFT34.000x0.750	W24X68	HSS7x7x5/8
	3	CCFT34.000x0.750	W24X55	HSS7x7x5/8
	2	CCFT40.000x0.875	W24X55	HSS7x7x5/8
	1	CCFT40.000x0.875	W27X84	HSS8x8x5/8
CCFT-9-3	9	CCFT6.625x0.250	W30X90	HSS3x3x5/16
	8	CCFT14.000x0.375	W21X50	HSS4x4x5/16
	7	CCFT14.000x0.375	W24X55	HSS4-1/2x4-1/2x5/16
	6	CCFT18.000x0.500	W21X50	HSS4-1/2x4-1/2x5/16
	5	CCFT18.000x0.500	W24X76	HSS5x5x3/8
	4	CCFT24.000x0.500	W21X50	HSS5x5x3/8
	3	CCFT24.000x0.500	W24x76	HSS5x5x1/2
	2	CCFT28.000x0.625	W21X50	HSS5x5x1/2
	1	CCFT28.000x0.625	W21X50	HSS5x5x1/2
CCFT-9-5	9	CCFT8.625x0.250	W36X160	HSS5x5x3/8
	8	CCFT22.000x0.500	W30X116	HSS6x6x1/2
	7	CCFT22.000x0.500	W40X183	HSS8x8x5/8
	6	CCFT30.000x0.625	W30X116	HSS8x8x5/8
	5	CCFT30.000x0.625	W40X149	W10x77
	4	CCFT38.000x0.875	W30X116	W10x77
	3	CCFT38.000x0.875	W40X183	W12x96
	2	CCFT42.000x1.125	W30X116	W12x96
	1	CCFT42.000x1.125	W30X116	W12x96
CCFT-9-7	9	CCFT7.500x0.250	W33X130	HSS4x4x5/16
	8	CCFT22.000x0.500	W30X116	HSS4x4x5/16
	7	CCFT22.000x0.500	W36X182	HSS6x6x1/2
	6	CCFT24.000x0.500	W30X116	HSS6x6x1/2
	5	CCFT26.000x0.625	W33X130	HSS7x7x1/2
	4	CCFT30.000x0.625	W30X116	HSS7x7x1/2
	3	CCFT32.000x0.750	W30x116	HSS7x7x1/2
	2	CCFT36.000x0.750	W30X116	HSS7x7x1/2
	1	CCFT36.000x0.750	W36X135	HSS7x7x5/8

Table B.9. Member Sizes for C-SCBFs (Continued)

Frame	Story	Column	Beam	Brace
CCFT-9-9	9	CCFT6.000x0.250	W27x84	HSS3-1/2x3-1/2x5/16
	8	CCFT12.750x0.375	W16x26	HSS4-1/2x4-1/2x5/16
	7	CCFT12.750x0.375	W24x62	HSS5x5x3/8
	6	CCFT20.000x0.500	W18x40	HSS5x5x1/2
	5	CCFT20.000x0.500	W21x50	HSS6x6x1/2
	4	CCFT28.000x0.625	W16x31	HSS6x6x1/2
	3	CCFT28.000x0.625	W21x44	HSS6x6x1/2
	2	CCFT36.000x0.750	W14x30	HSS6x6x1/2
	1	CCFT36.000x0.750	W14x30	HSS6x6x1/2
CCFT-9-11	9	CCFT5.500x0.258	W24x76	HSS3x3x1/4
	8	CCFT9.625x0.250	W14x22	HSS3x3x5/16
	7	CCFT10.000x0.250	W14x26	HSS3-1/2x3-1/2x5/16
	6	CCFT12.750x0.375	W14x22	HSS3-1/2x3-1/2x5/16
	5	CCFT12.750x0.375	W14x26	HSS4x4x5/16
	4	CCFT16.000x0.500	W14x22	HSS4x4x5/16
	3	CCFT16.000x0.500	W16x26	HSS4-1/2x4-1/2x5/16
	2	CCFT20.000x0.500	W14x22	HSS4-1/2x4-1/2x5/16
	1	CCFT20.000x0.500	W14x22	HSS4-1/2x4-1/2x5/16
CCFT-9-13	9	CCFT6.875x0.250	W36x135	HSS4-1/2x4-1/2x3/8
	8	CCFT16.000x0.375	W24x68	HSS6x6x1/2
	7	CCFT16.000x0.375	W24x68	HSS7x7x1/2
	6	CCFT24.000x0.625	W24x68	HSS7x7x5/8
	5	CCFT24.000x0.625	W24x76	HSS7x7x5/8
	4	CCFT32.000x0.750	W24x62	HSS7x7x5/8
	3	CCFT32.000x0.750	W27x84	HSS8x8x5/8
	2	CCFT38.000x0.875	W24x62	HSS8x8x5/8
	1	CCFT38.000x0.875	W27x84	HSS9x9x5/8
CCFT-9-15	9	CCFT6.625x0.250	W30x99	HSS3-1/2x3-1/2x1/4
	8	CCFT10.750x0.375	W14x34	HSS4x4x5/16
	7	CCFT12.750x0.375	W24x62	HSS4-1/2x4-1/2x3/8
	6	CCFT16.000x0.375	W21x44	HSS5x5x3/8
	5	CCFT18.000x0.375	W24x76	HSS5x5x1/2
	4	CCFT22.000x0.500	W21x50	HSS5x5x1/2
	3	CCFT22.000x0.500	W21x50	HSS5x5x1/2
	2	CCFT24.000x0.625	W21x50	HSS5x5x1/2
	1	CCFT24.000x0.625	W21x68	HSS6x6x1/2

DETAILED ARCHETYPE STUDY RESULTS

This appendix presents detailed results from the study described in Chapter 8 showing the seismic behavior of each frame.

C.1 Static Pushover Analysis Results

Results of the static pushover analyses for each frame are shown in the following figures. The results include:

- The base shear vs. roof drift response, showing the overall response of each frame
- The distribution of lateral loads applied at each story in the analysis.
- Story drift ratios at the design base shear, V, the maximum base shear, V_{max}, and after a 20% in shear strength, V_{80}, showing the distribution of inelasticity within each frame.

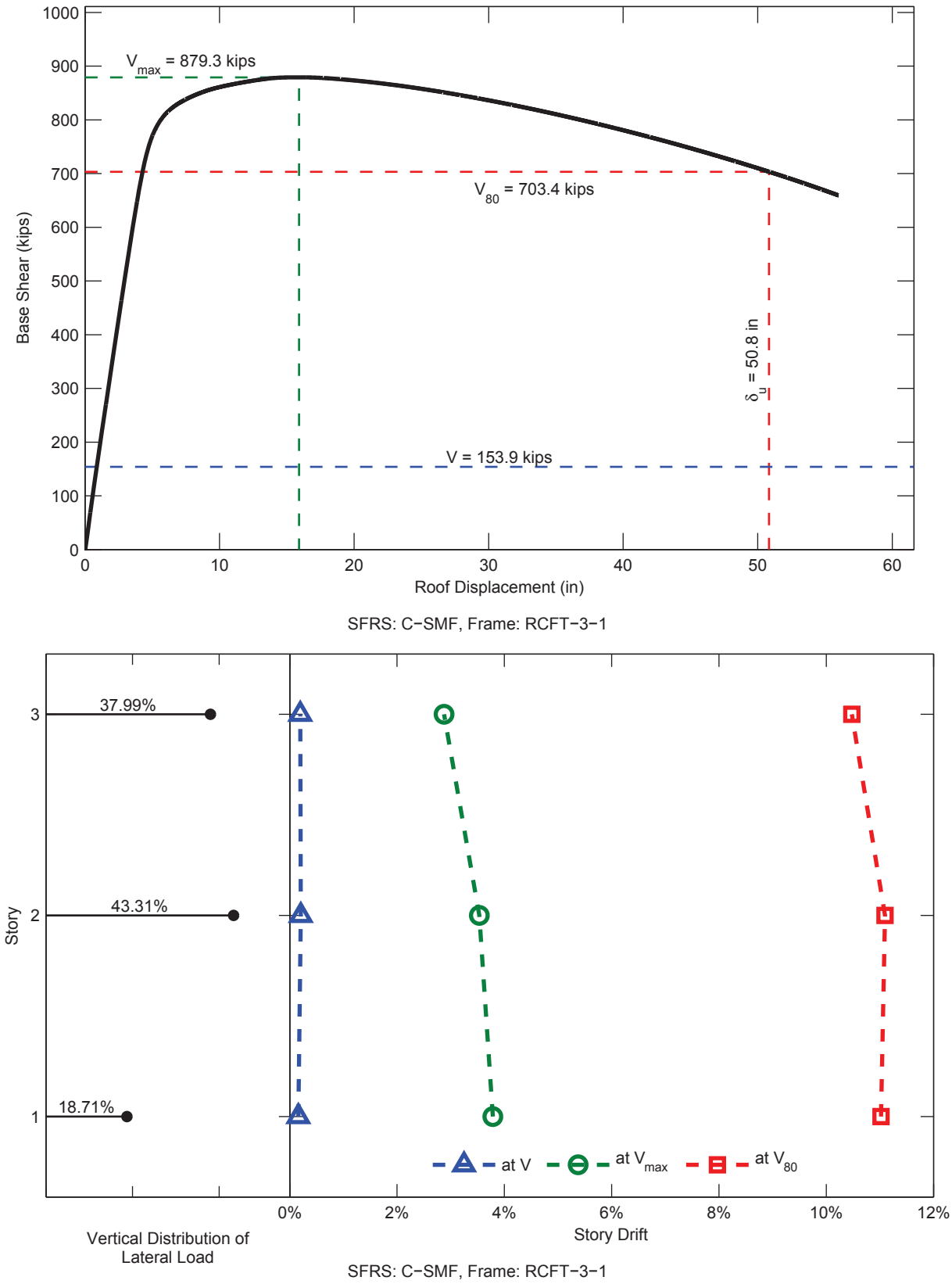

Figure C.1. Static Pushover Analysis Results: Frame RCFT-3-1

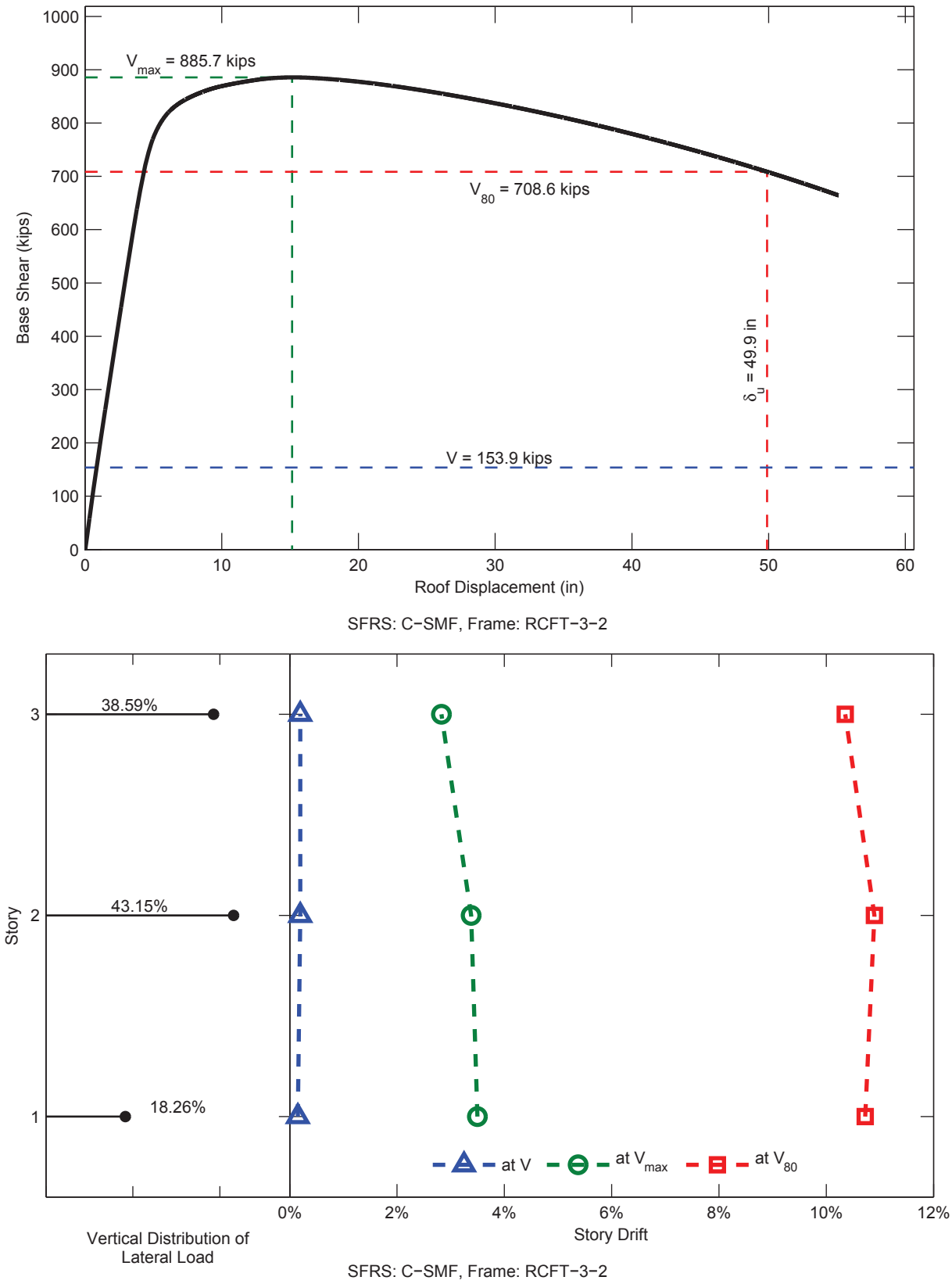

Figure C.2. Static Pushover Analysis Results: Frame RCFT-3-2

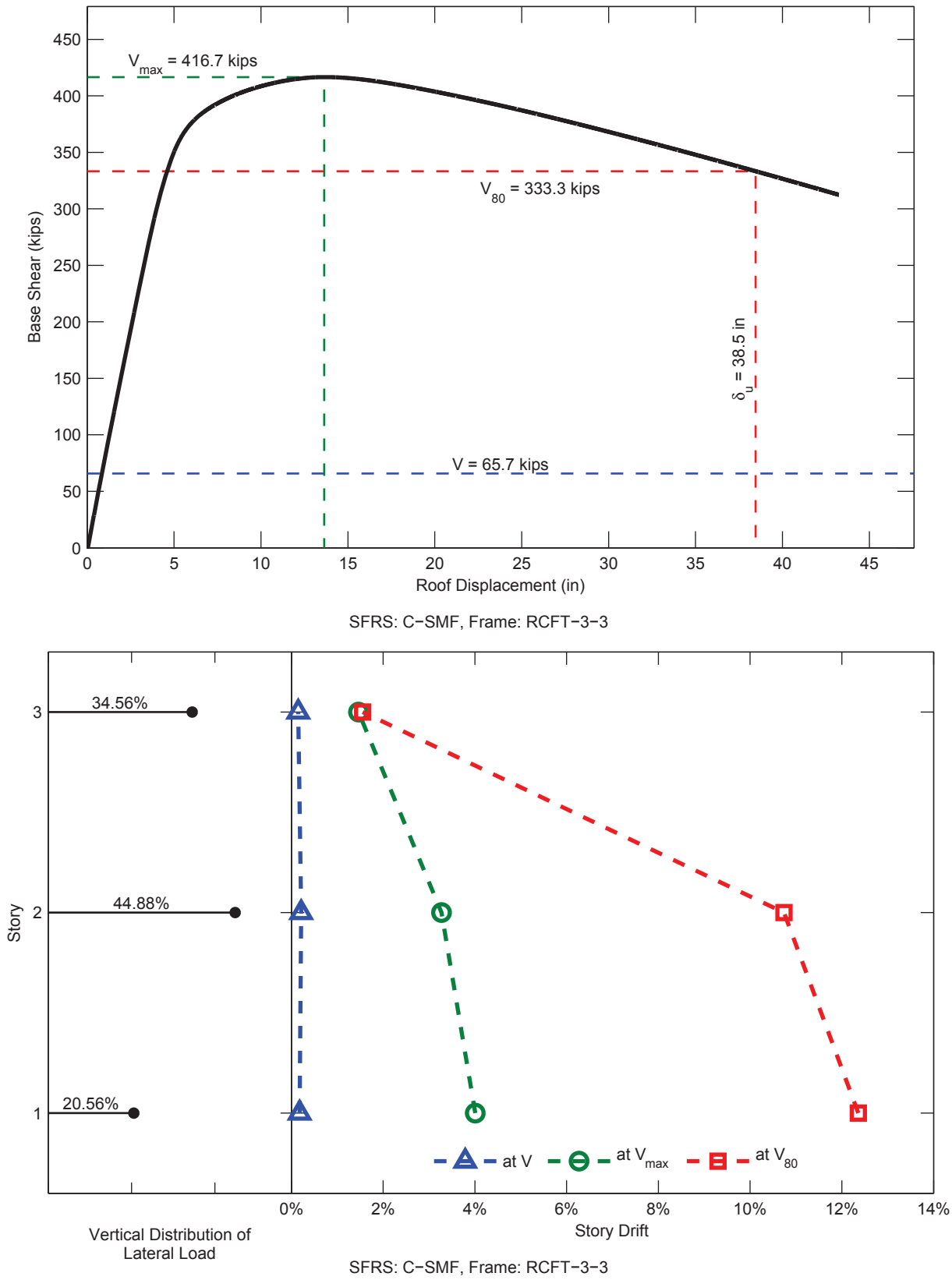

Figure C.3. Static Pushover Analysis Results: Frame RCFT-3-3

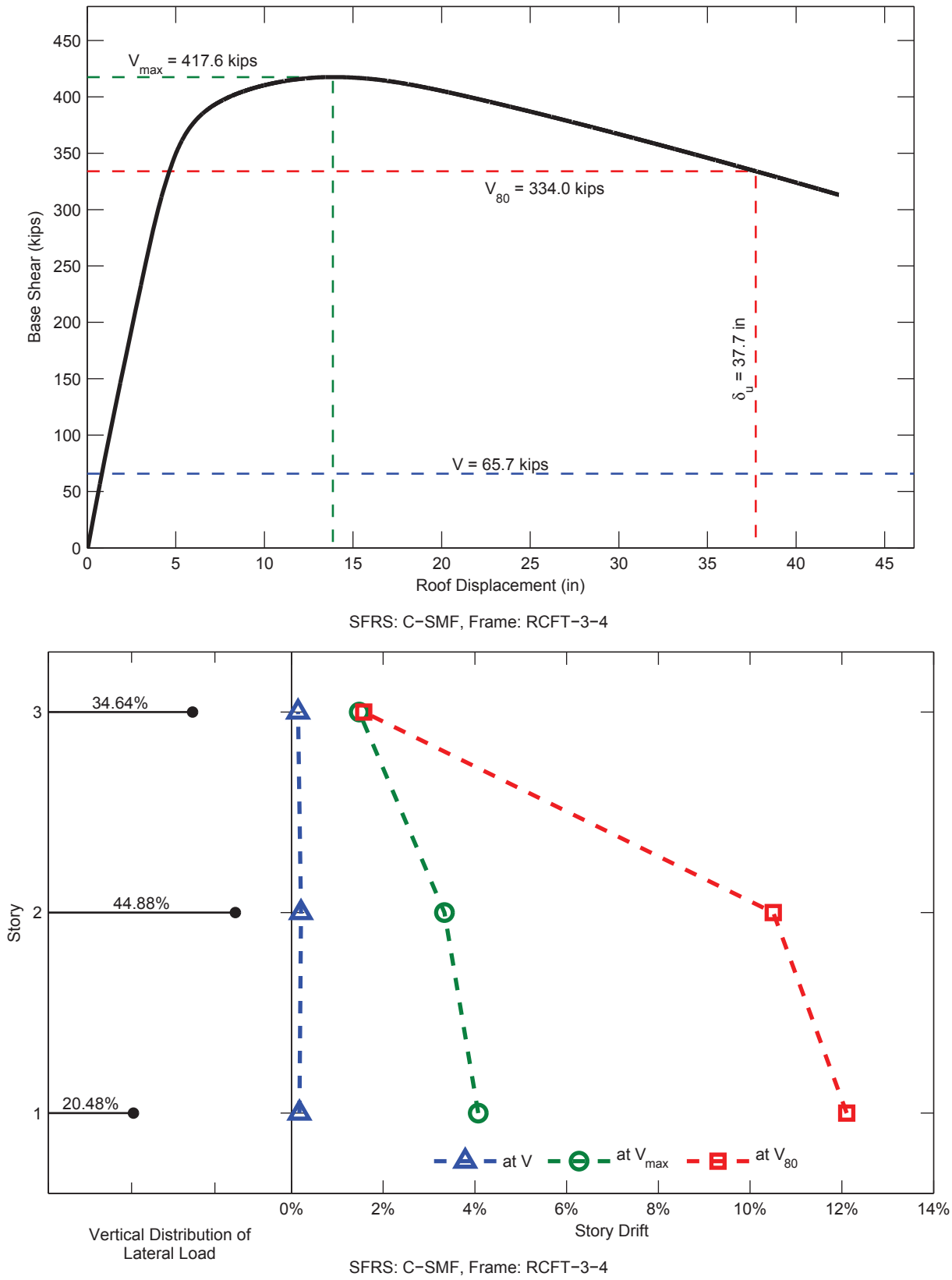

Figure C.4. Static Pushover Analysis Results: Frame RCFT-3-4

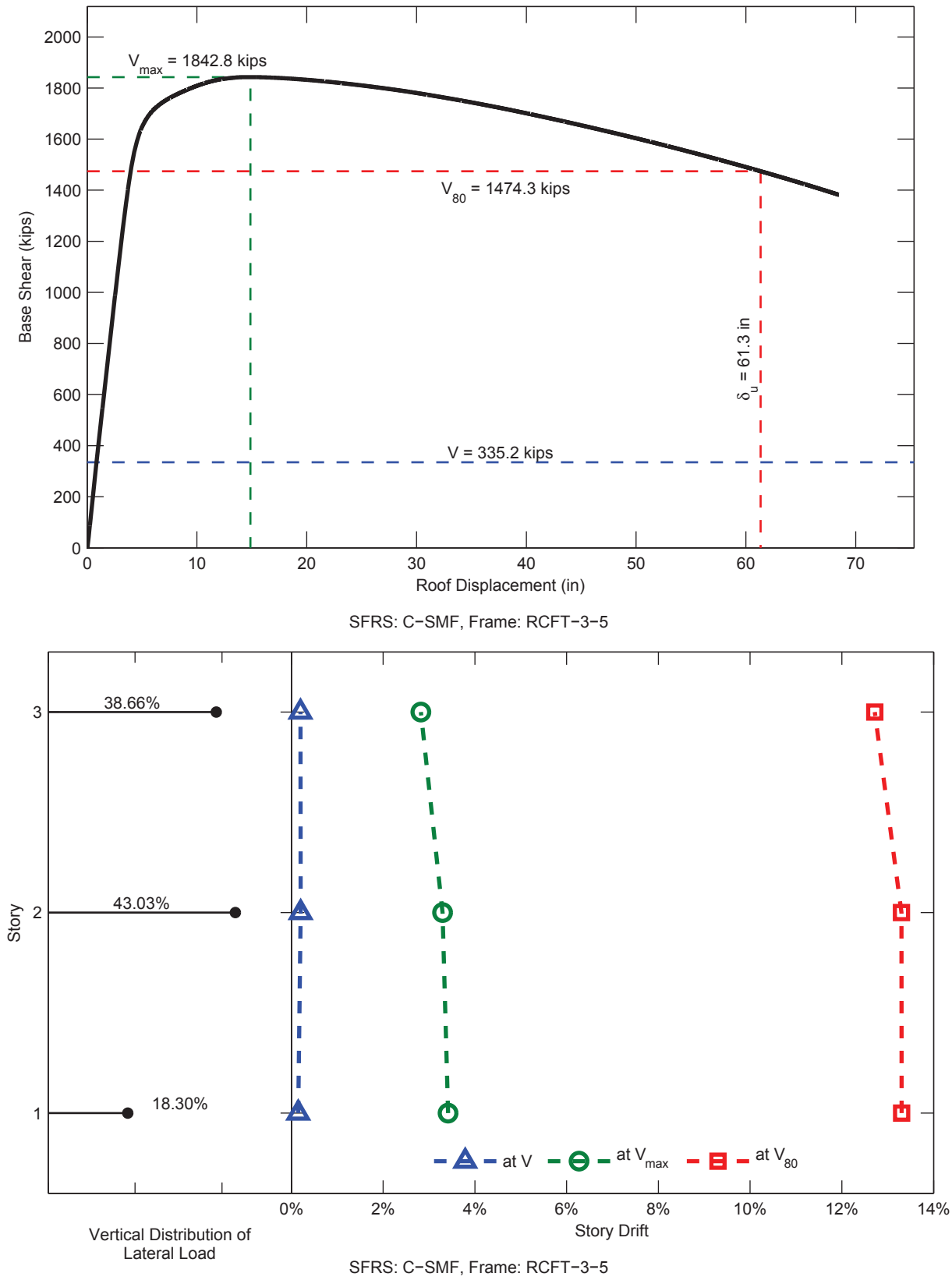

Figure C.5. Static Pushover Analysis Results: Frame RCFT-3-5

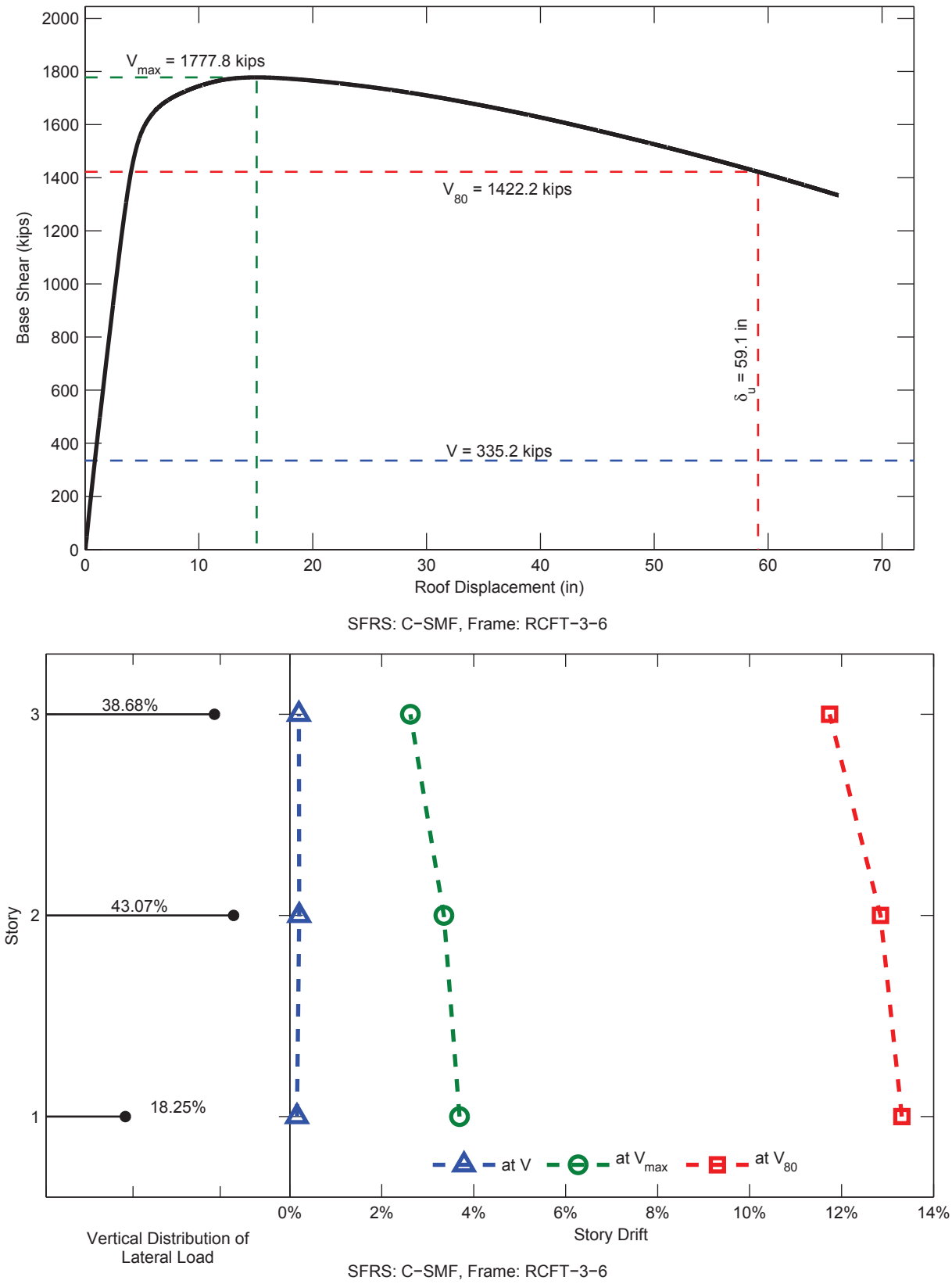

Figure C.6. Static Pushover Analysis Results: Frame RCFT-3-6

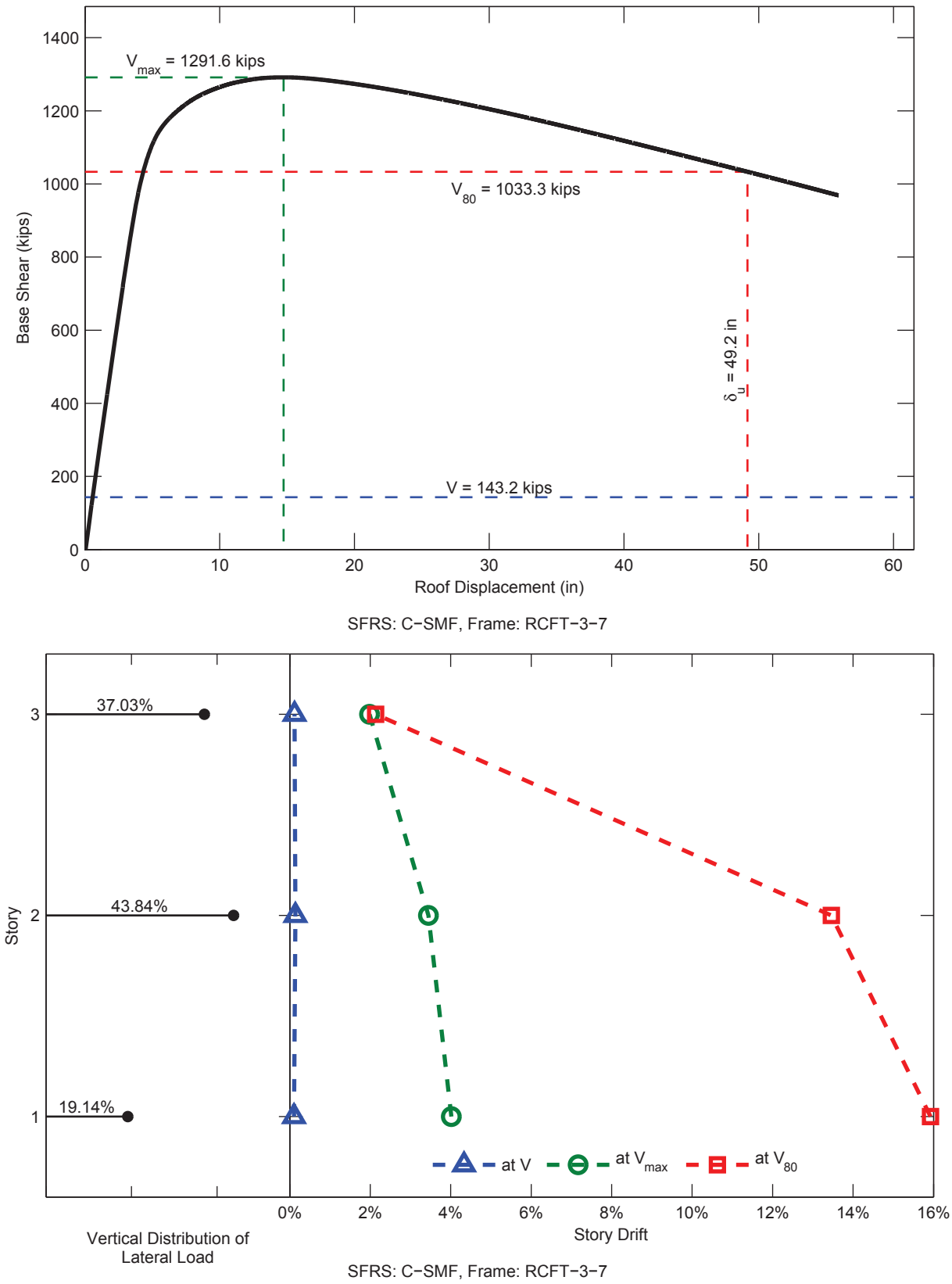

Figure C.7. Static Pushover Analysis Results: Frame RCFT-3-7

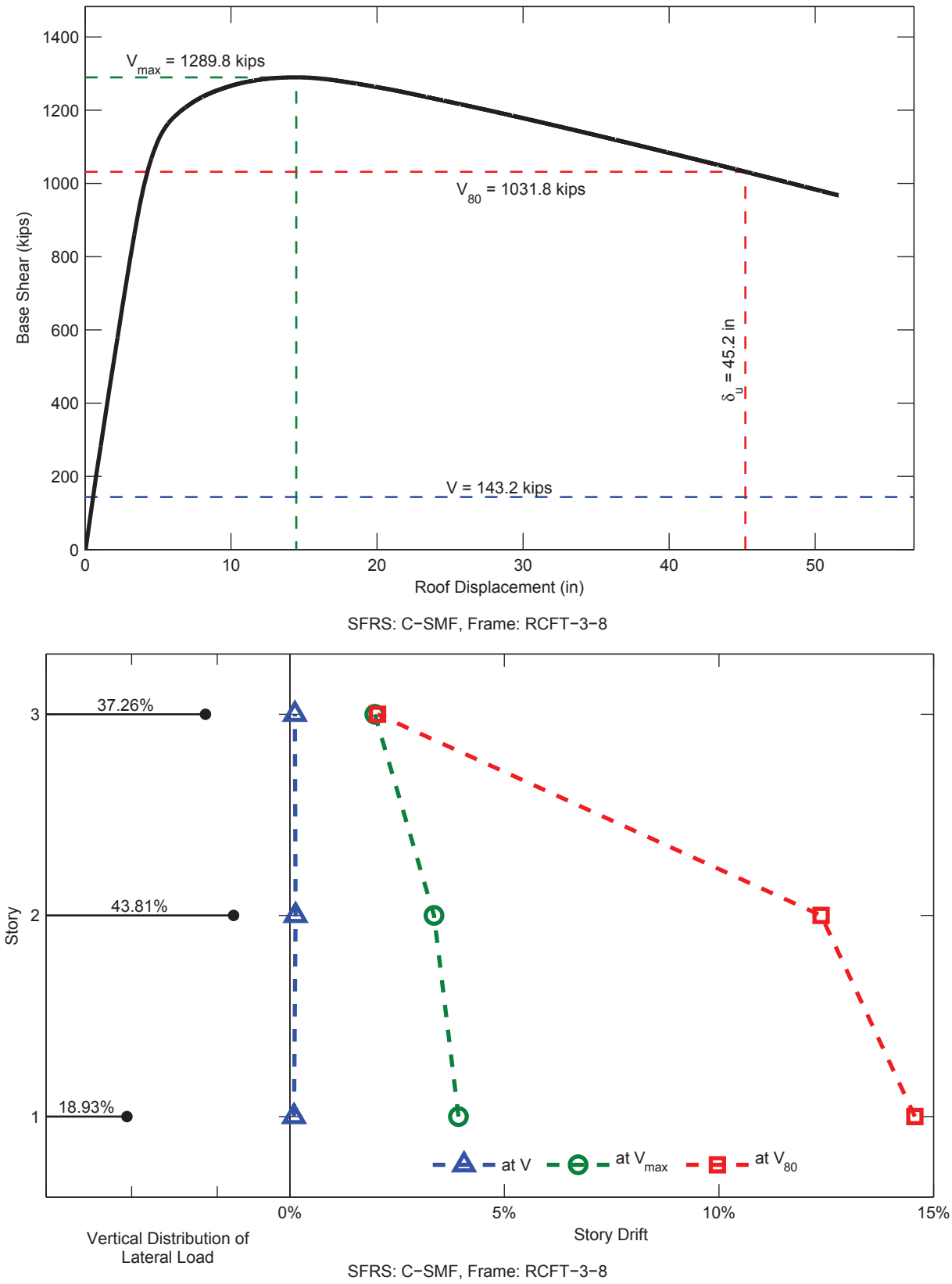

Figure C.8. Static Pushover Analysis Results: Frame RCFT-3-8

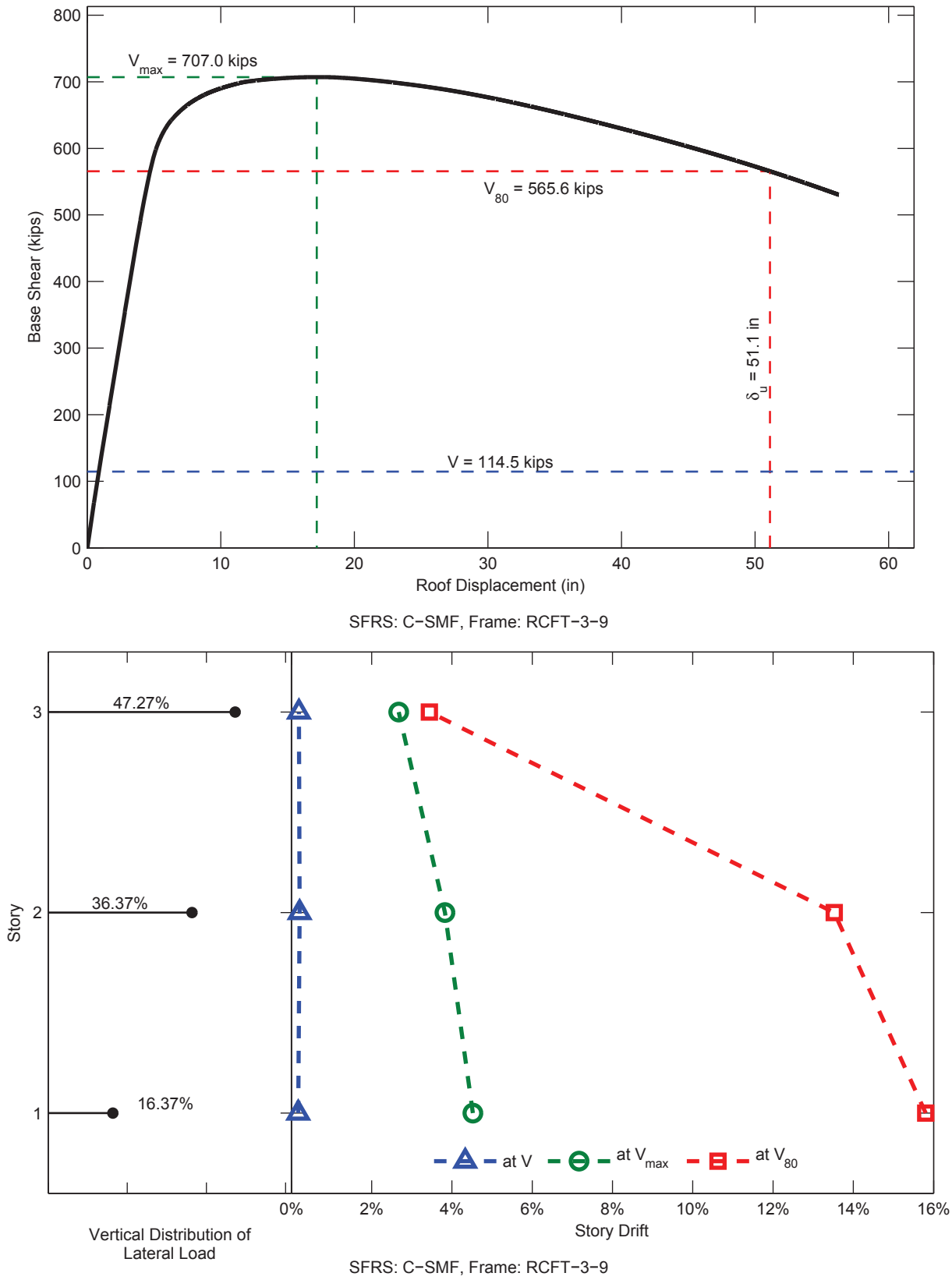

Figure C.9. Static Pushover Analysis Results: Frame RCFT-3-9

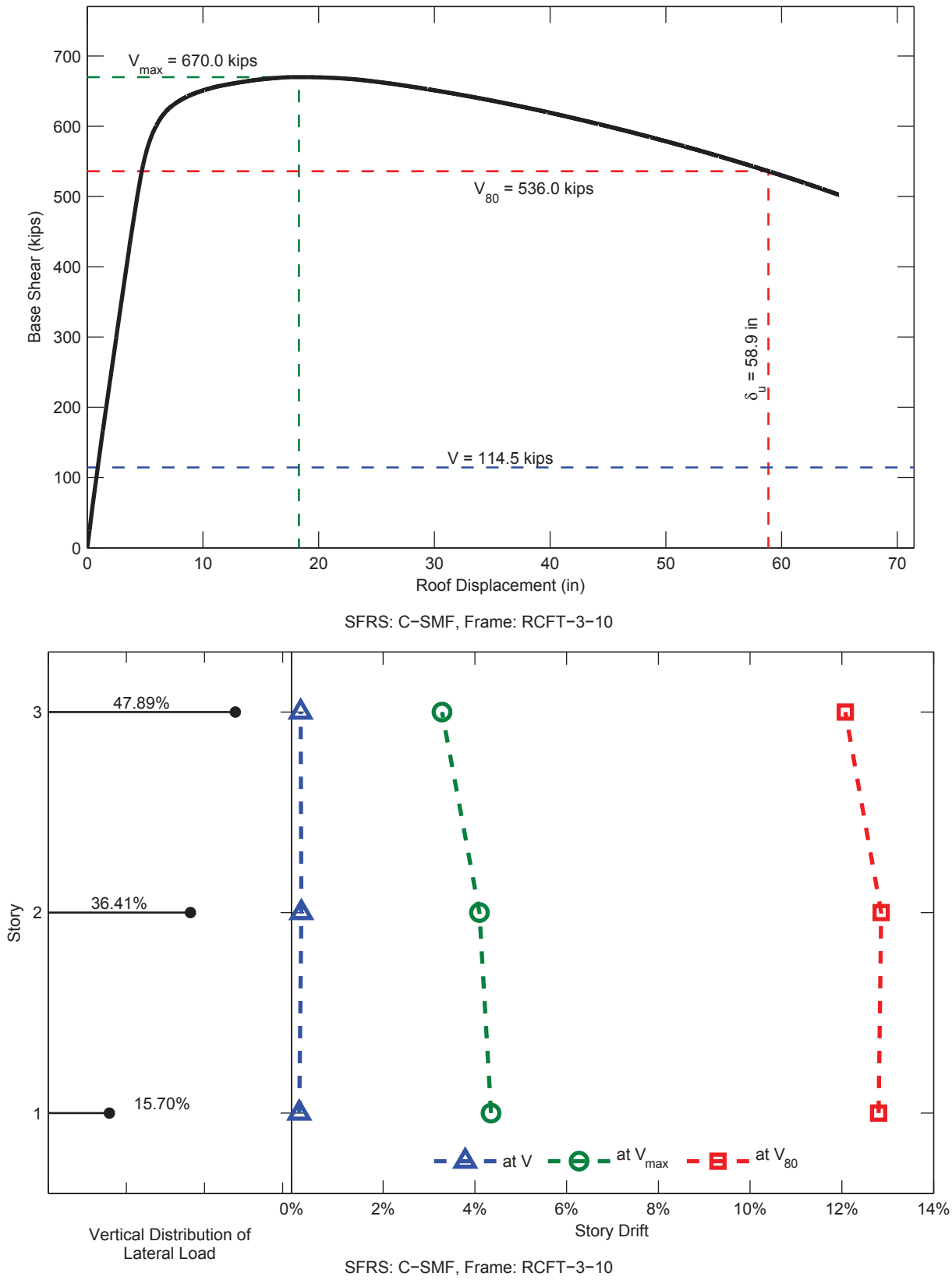

Figure C.10. Static Pushover Analysis Results: Frame RCFT-3-10

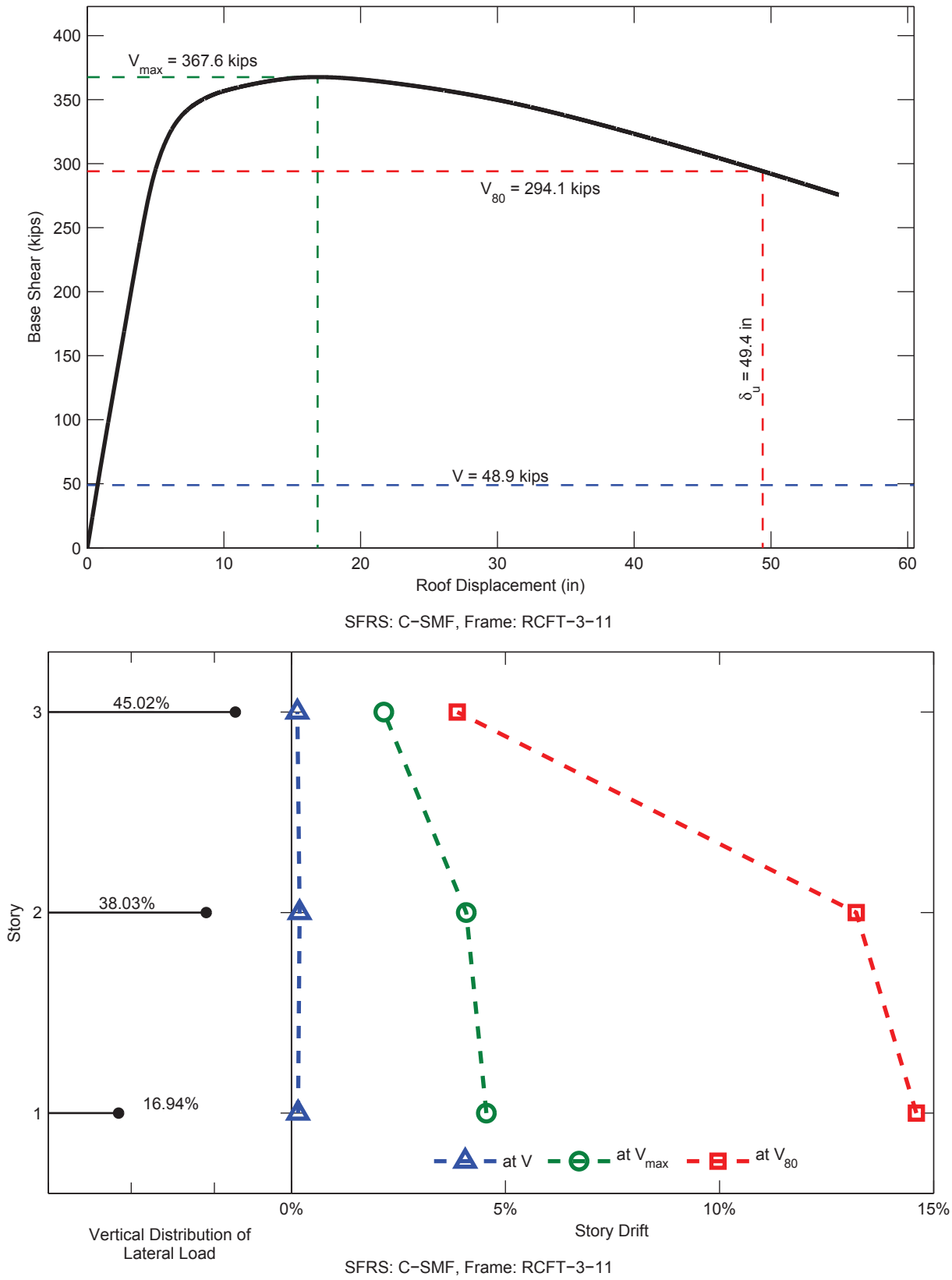

Figure C.11. Static Pushover Analysis Results: Frame RCFT-3-11

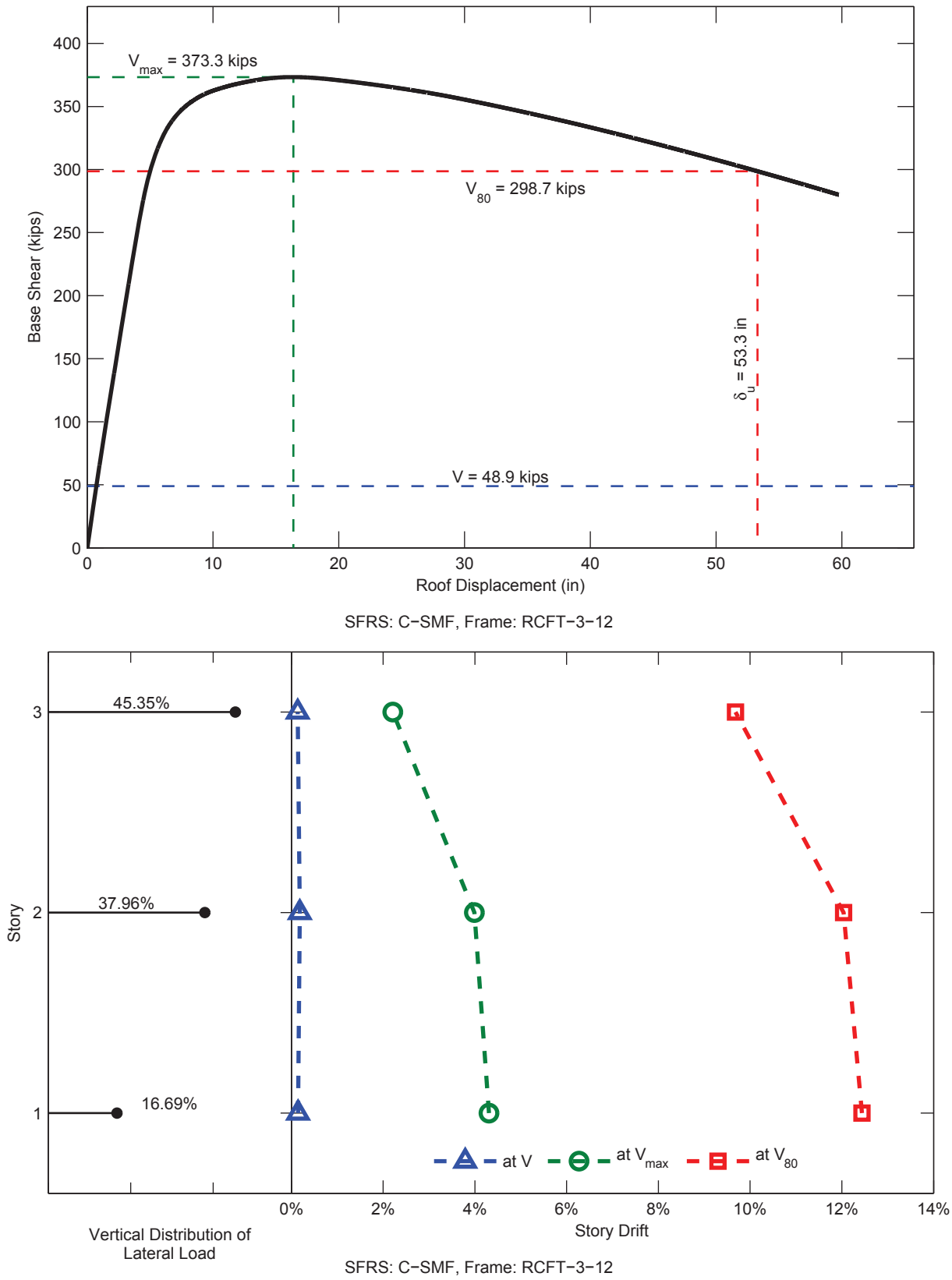

Figure C.12. Static Pushover Analysis Results: Frame RCFT-3-12

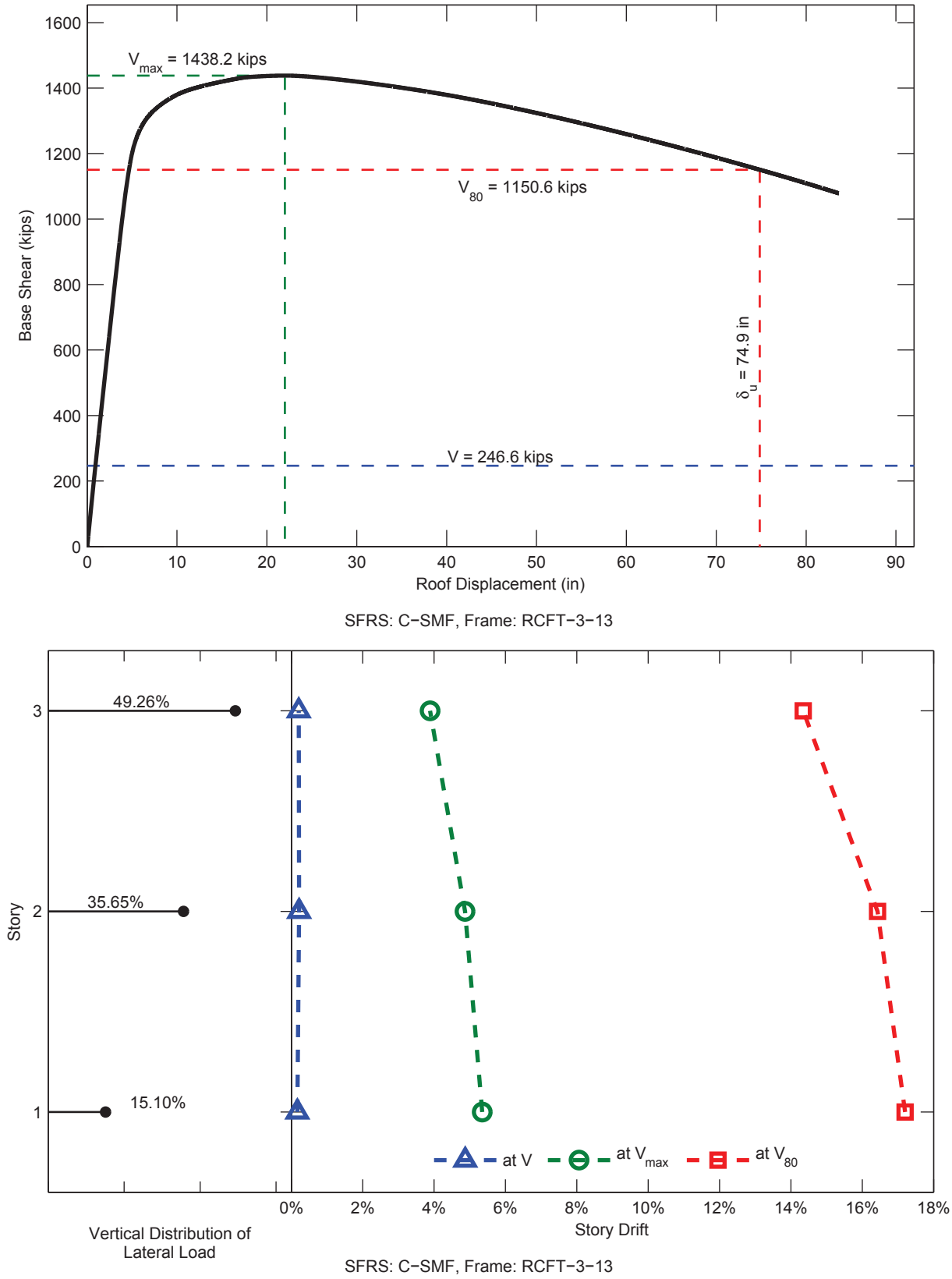

Figure C.13. Static Pushover Analysis Results: Frame RCFT-3-13

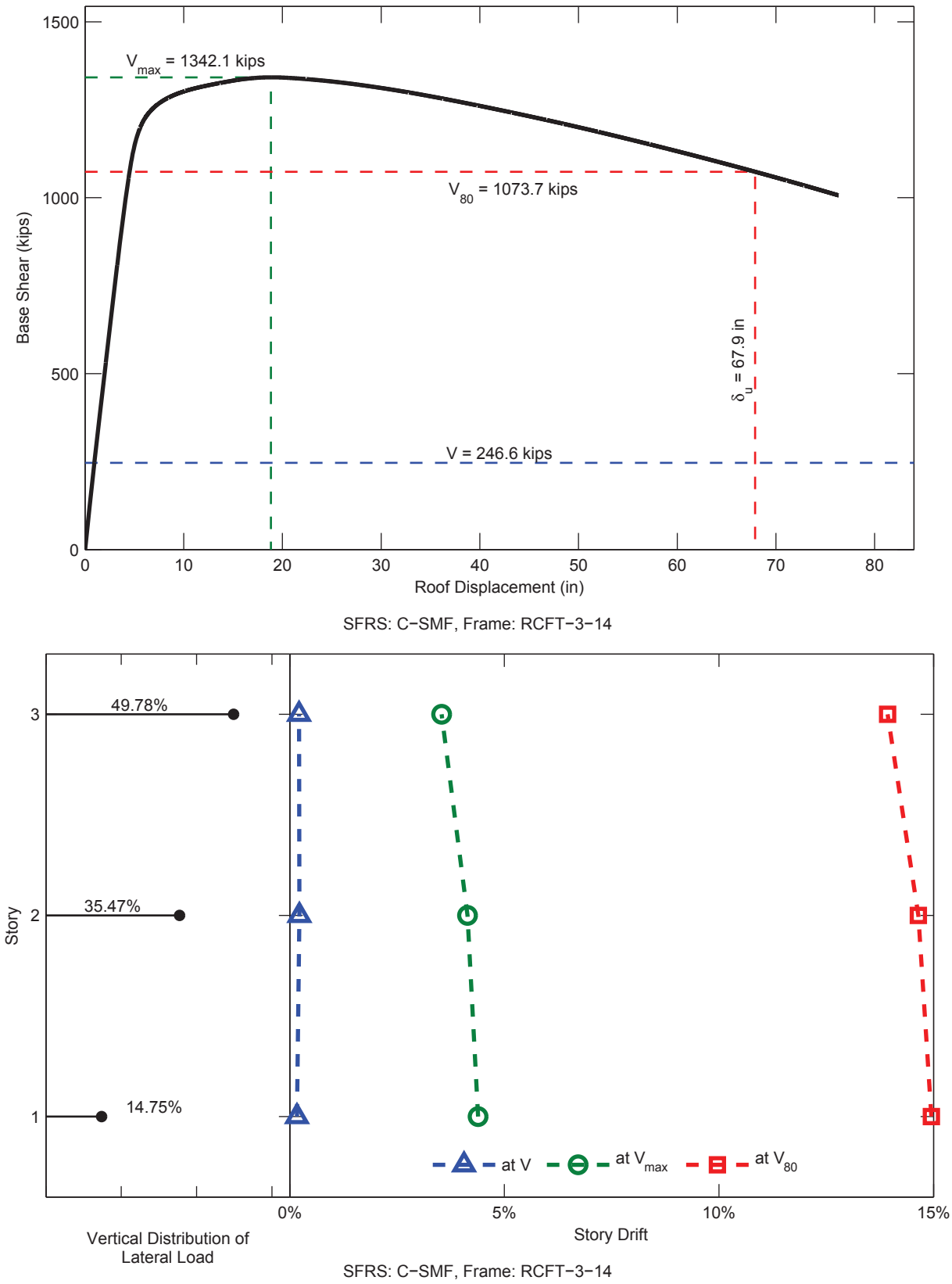

Figure C.14. Static Pushover Analysis Results: Frame RCFT-3-14

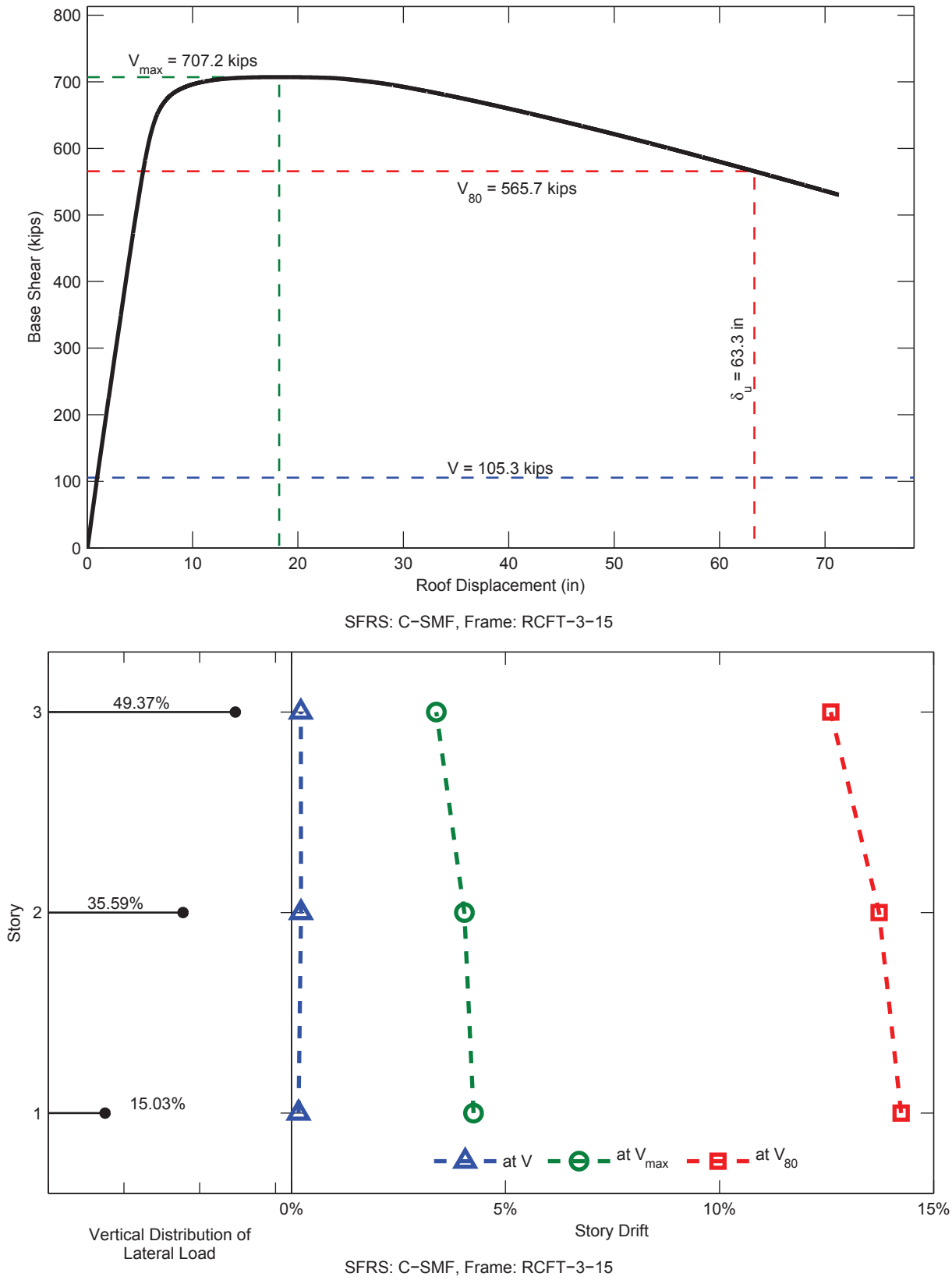

Figure C.15. Static Pushover Analysis Results: Frame RCFT-3-15

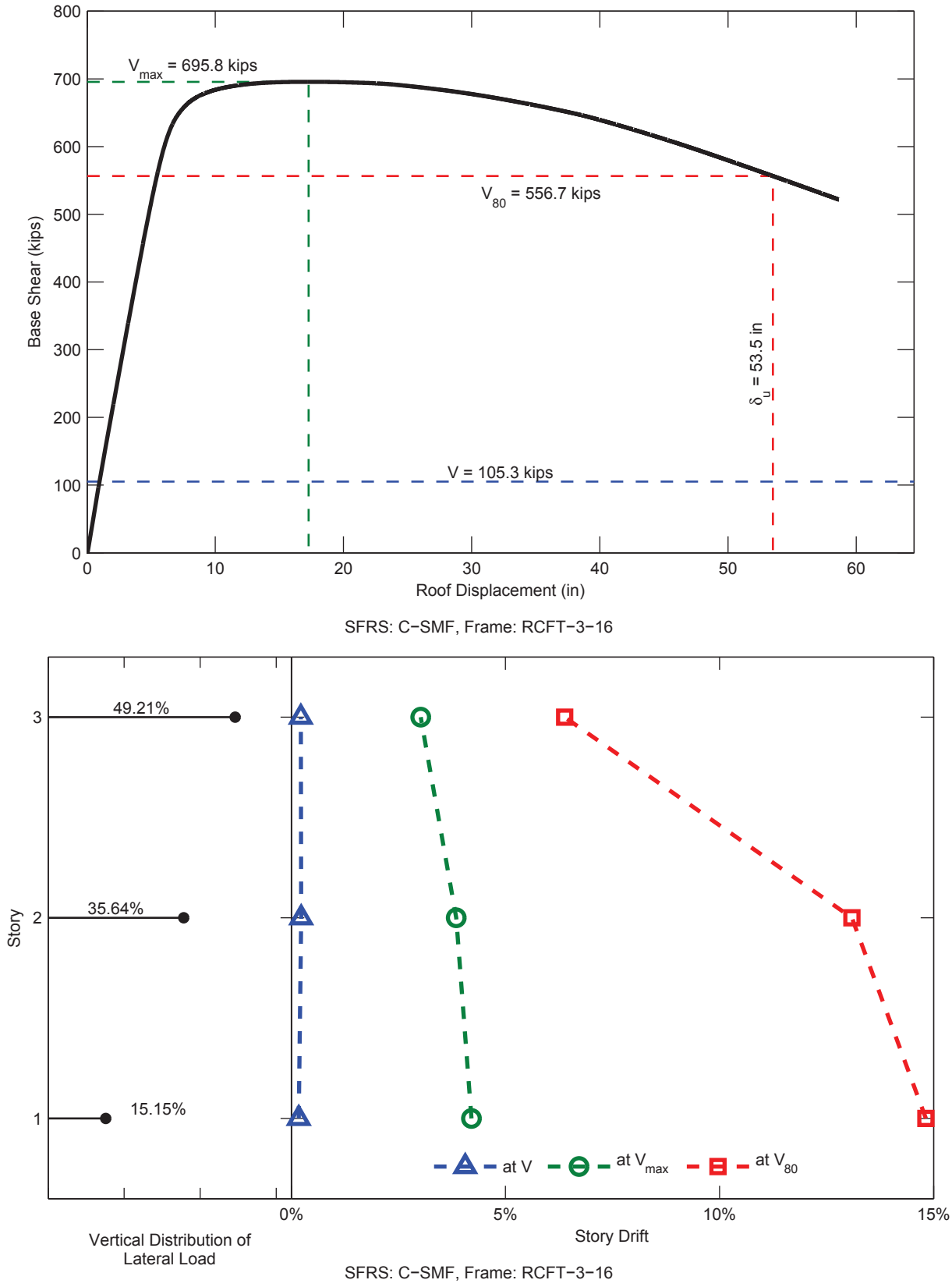

Figure C.16. Static Pushover Analysis Results: Frame RCFT-3-16

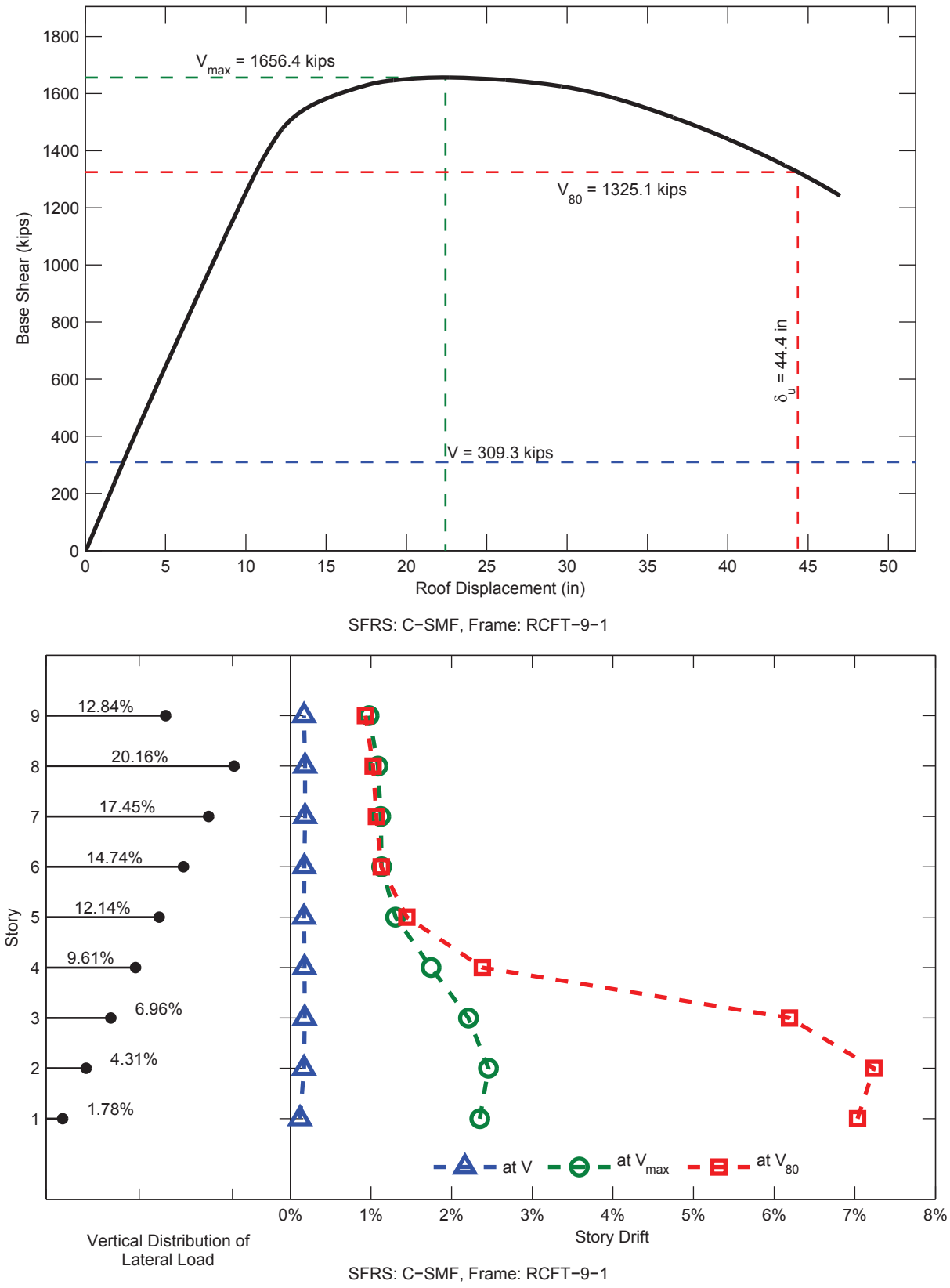

Figure C.17. Static Pushover Analysis Results: Frame RCFT-9-1

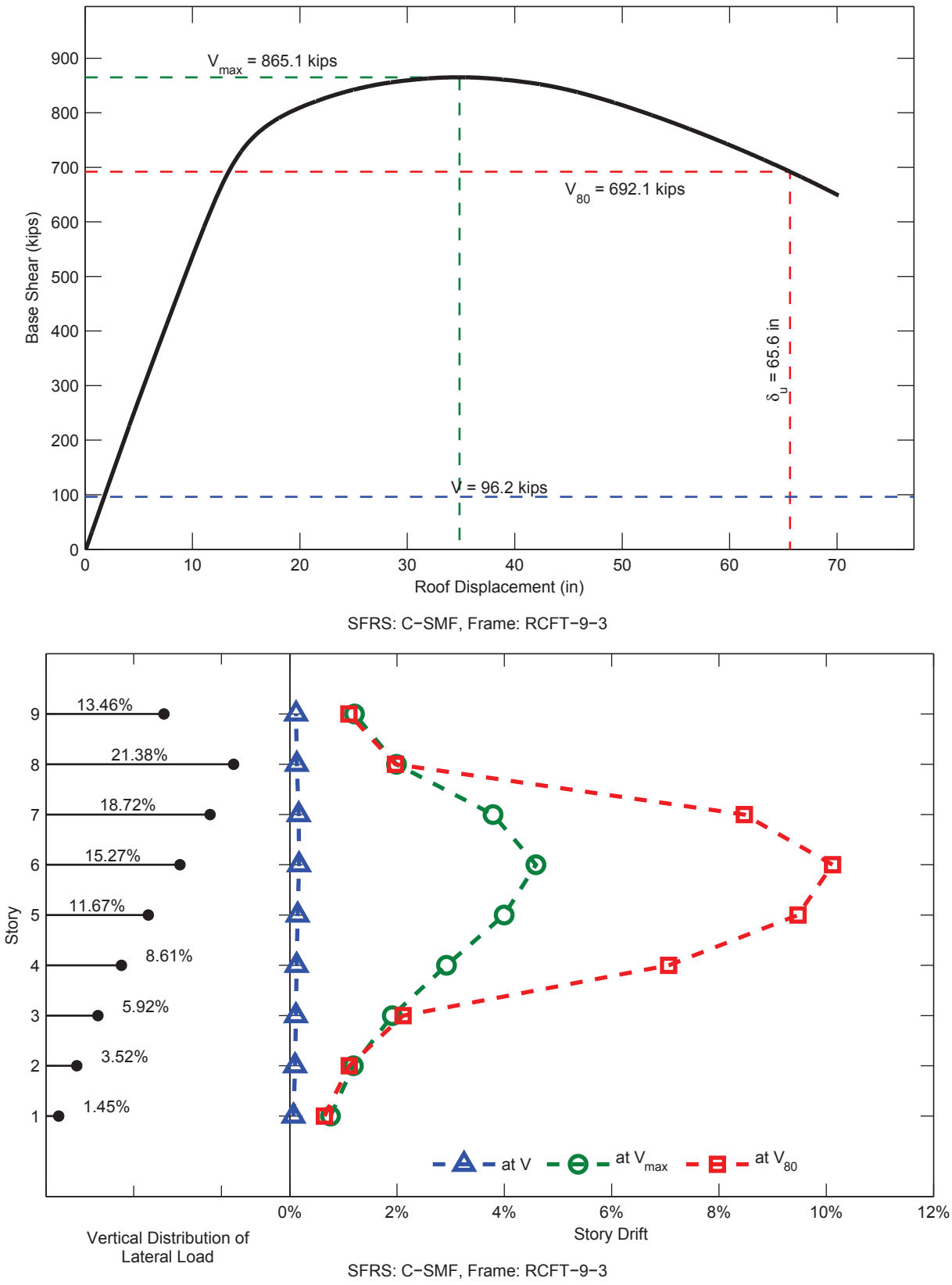

Figure C.18. Static Pushover Analysis Results: Frame RCFT-9-3

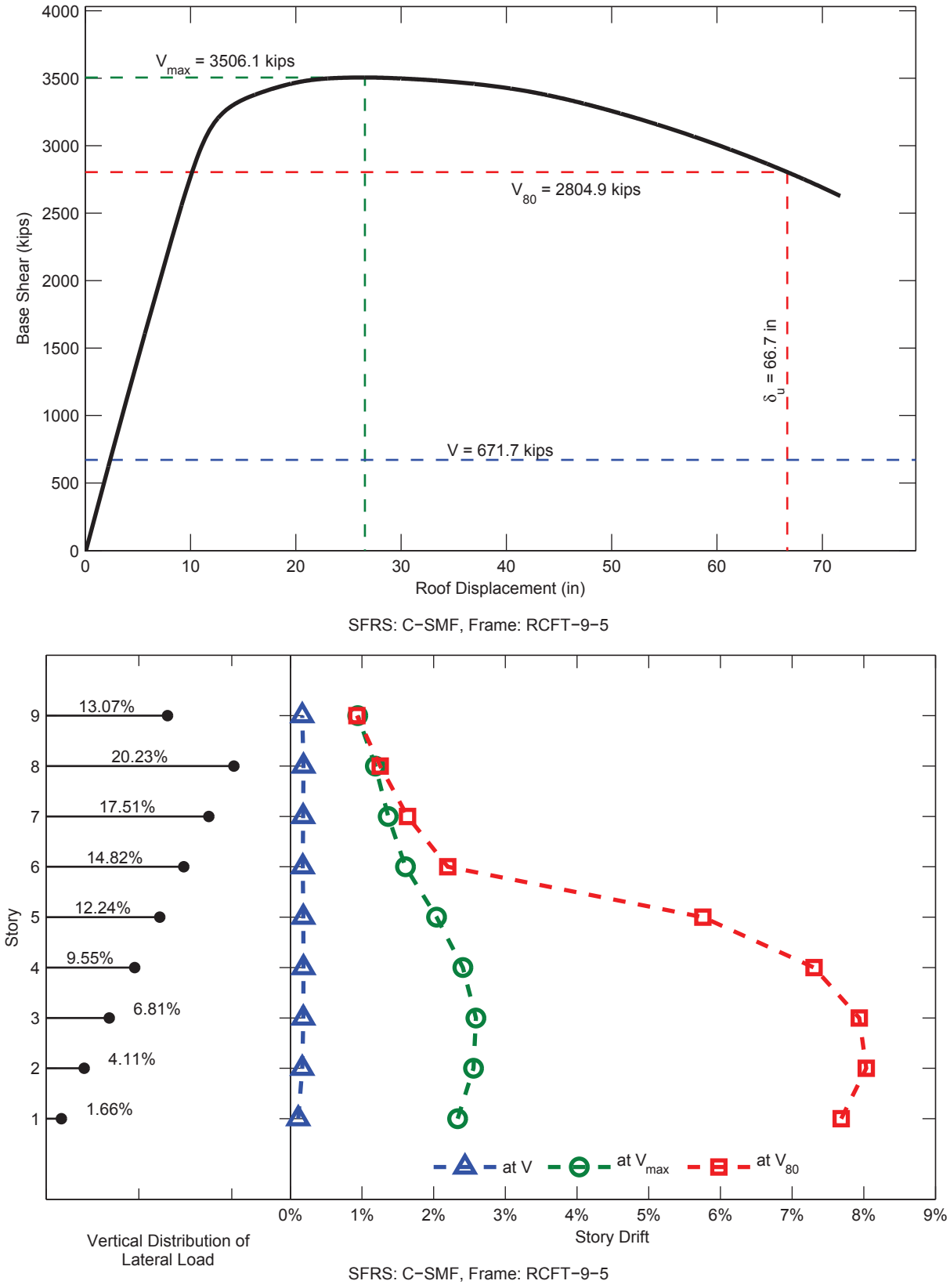

Figure C.19. Static Pushover Analysis Results: Frame RCFT-9-5

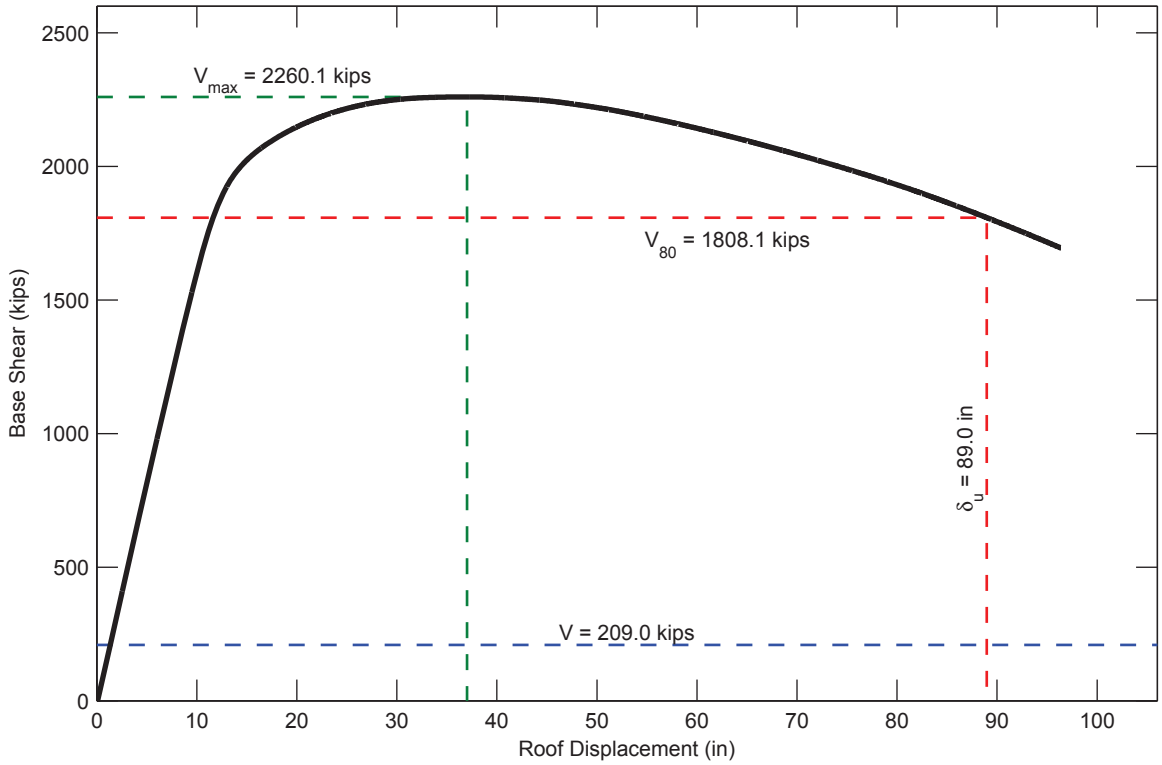

SFRS: C−SMF, Frame: RCFT−9−7

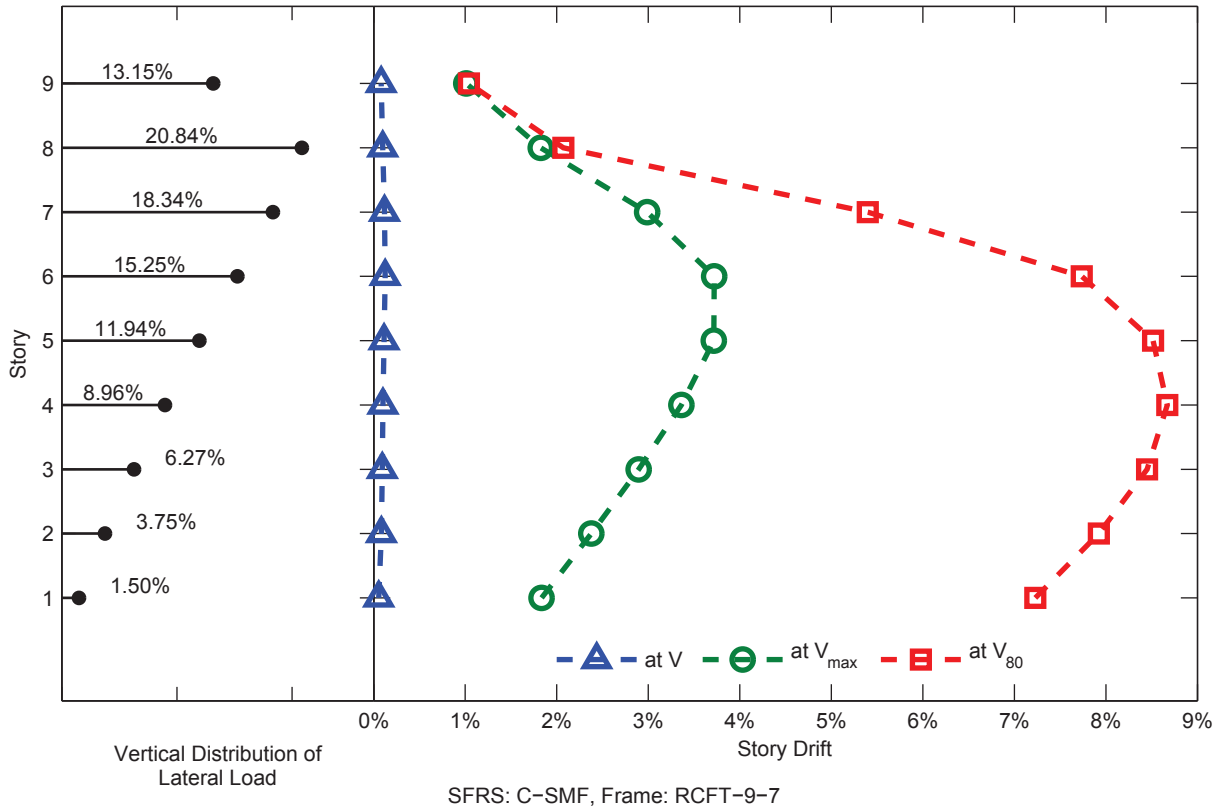

SFRS: C−SMF, Frame: RCFT−9−7

Figure C.20. Static Pushover Analysis Results: Frame RCFT-9-7

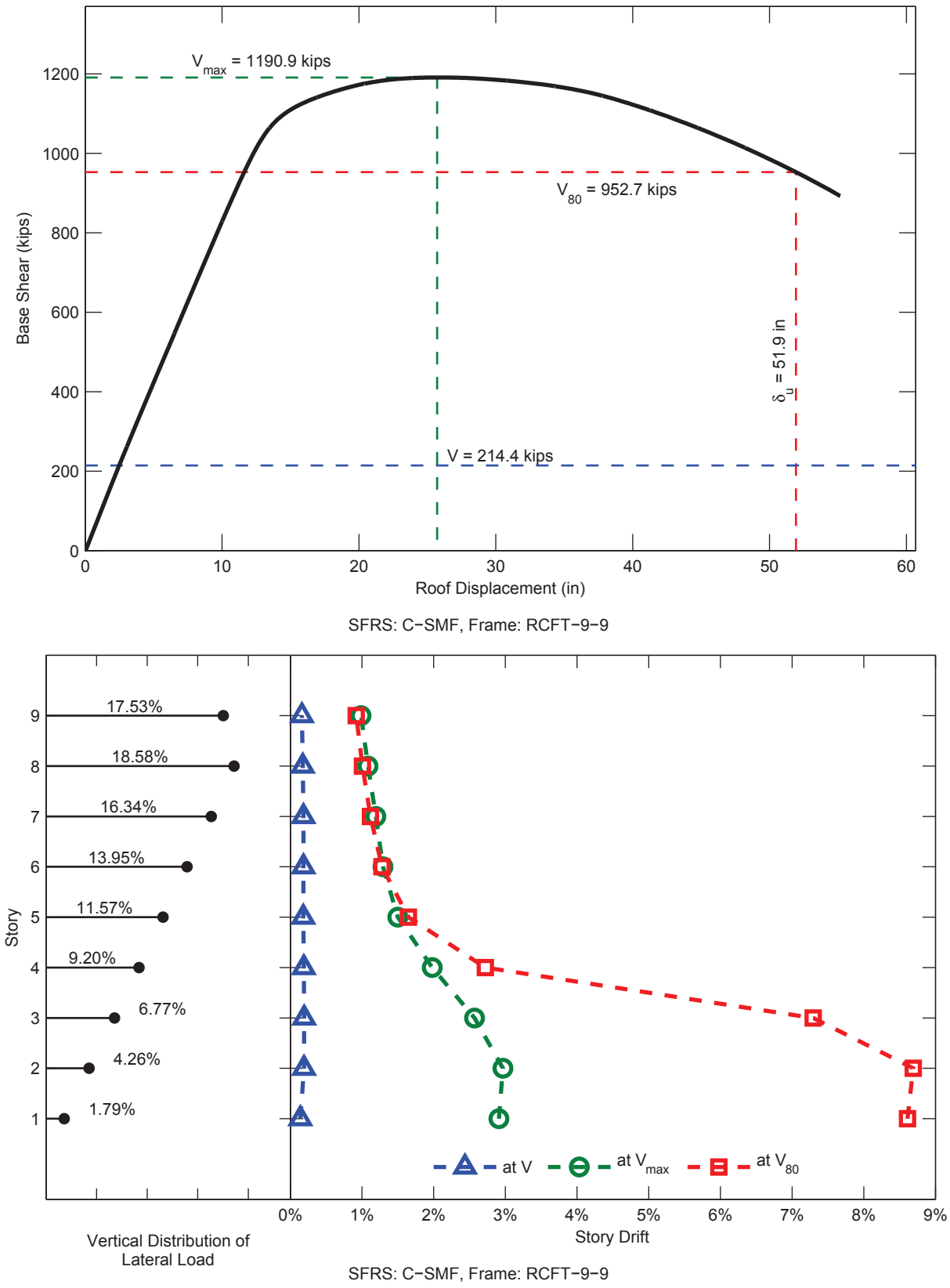

Figure C.21. Static Pushover Analysis Results: Frame RCFT-9-9

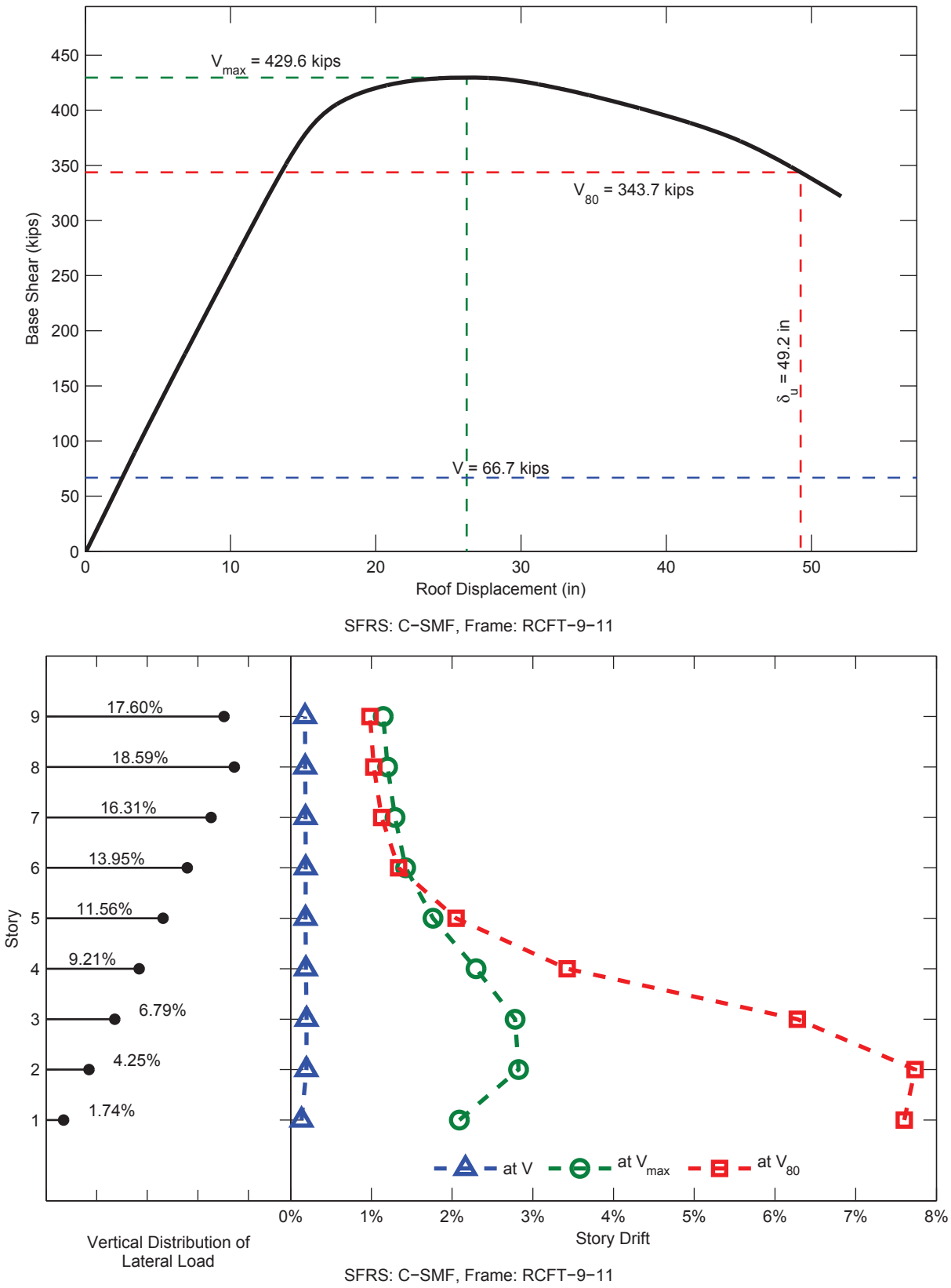

Figure C.22. Static Pushover Analysis Results: Frame RCFT-9-11

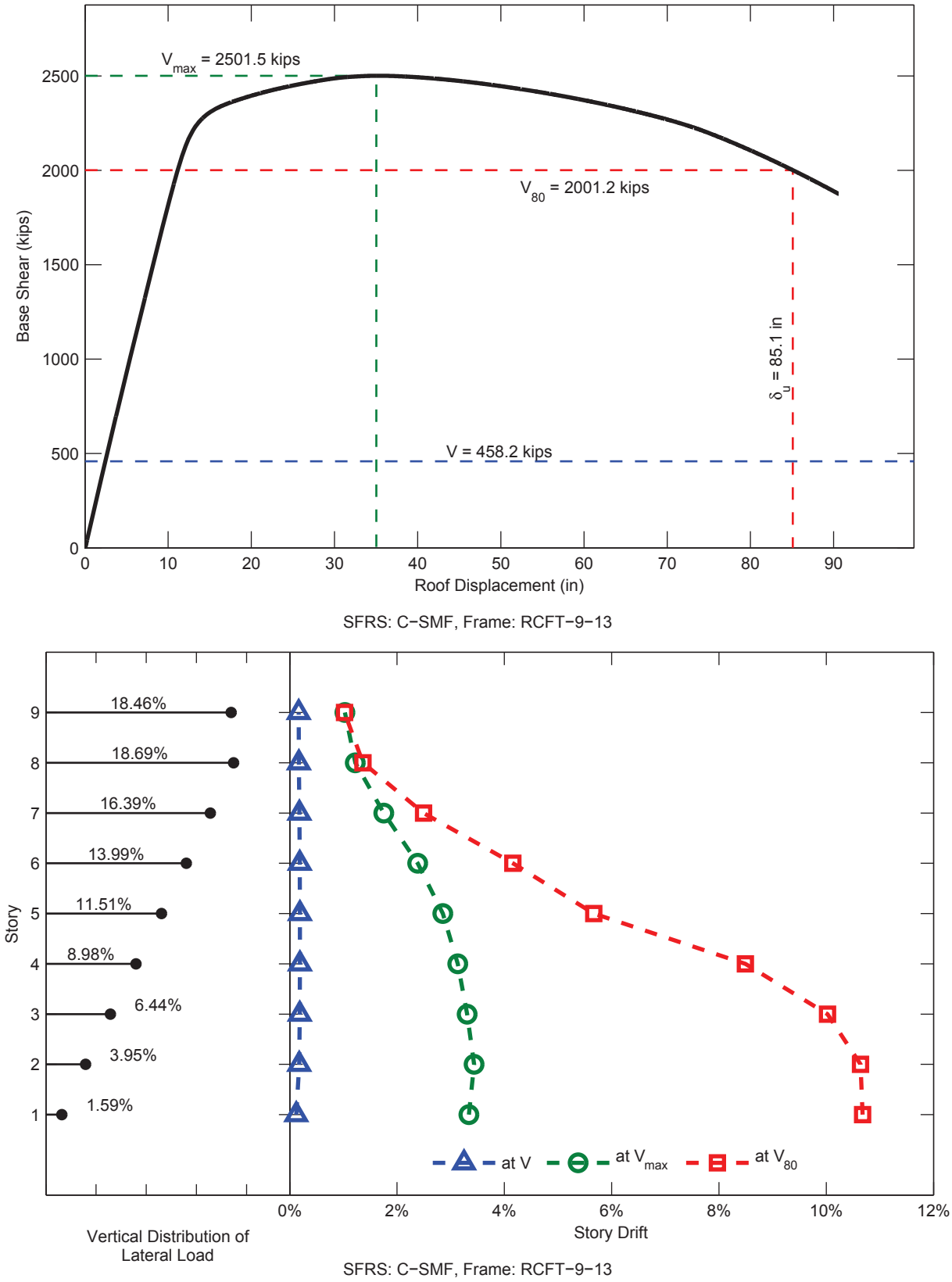

Figure C.23. Static Pushover Analysis Results: Frame RCFT-9-13

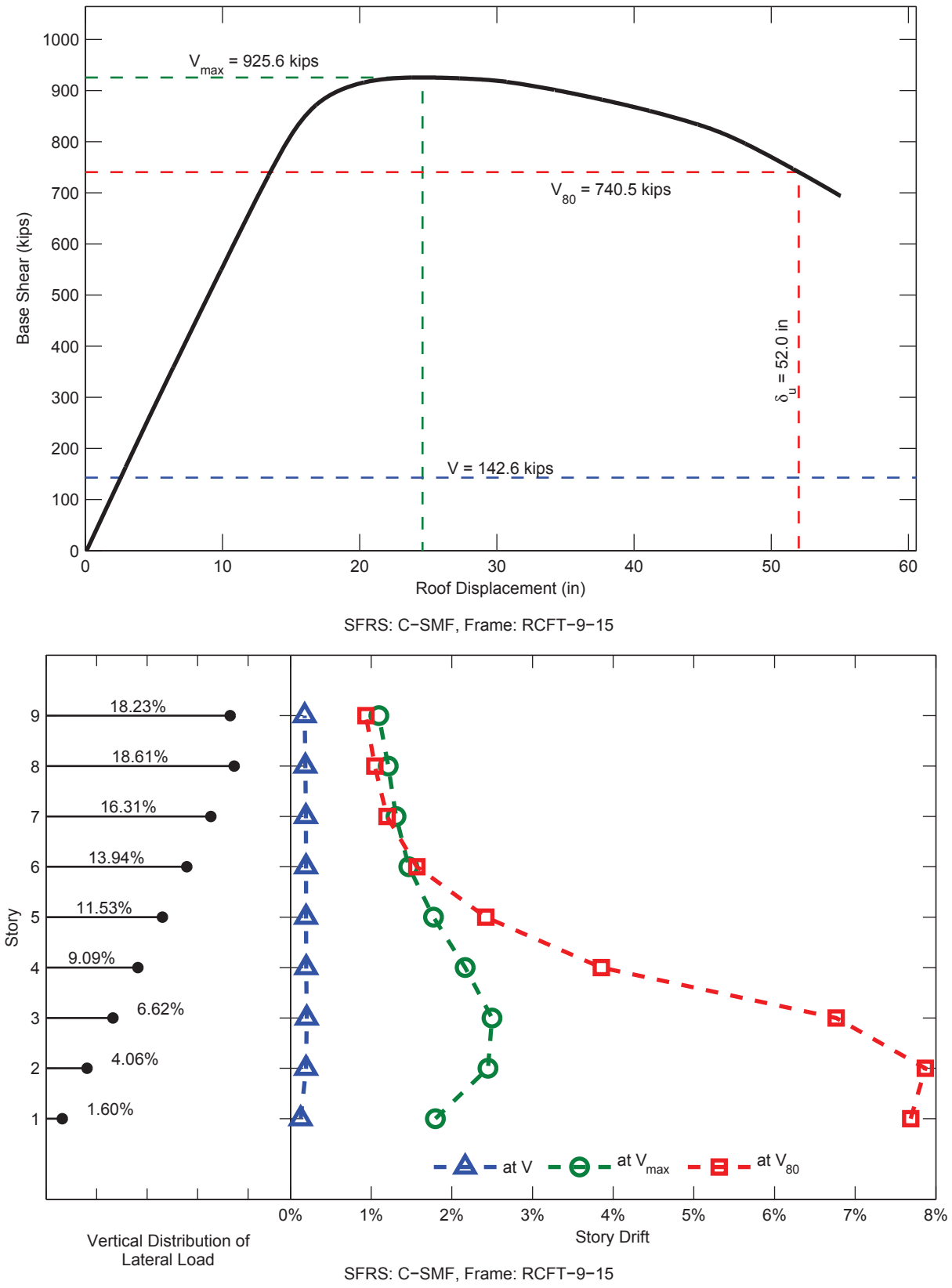

Figure C.24. Static Pushover Analysis Results: Frame RCFT-9-15

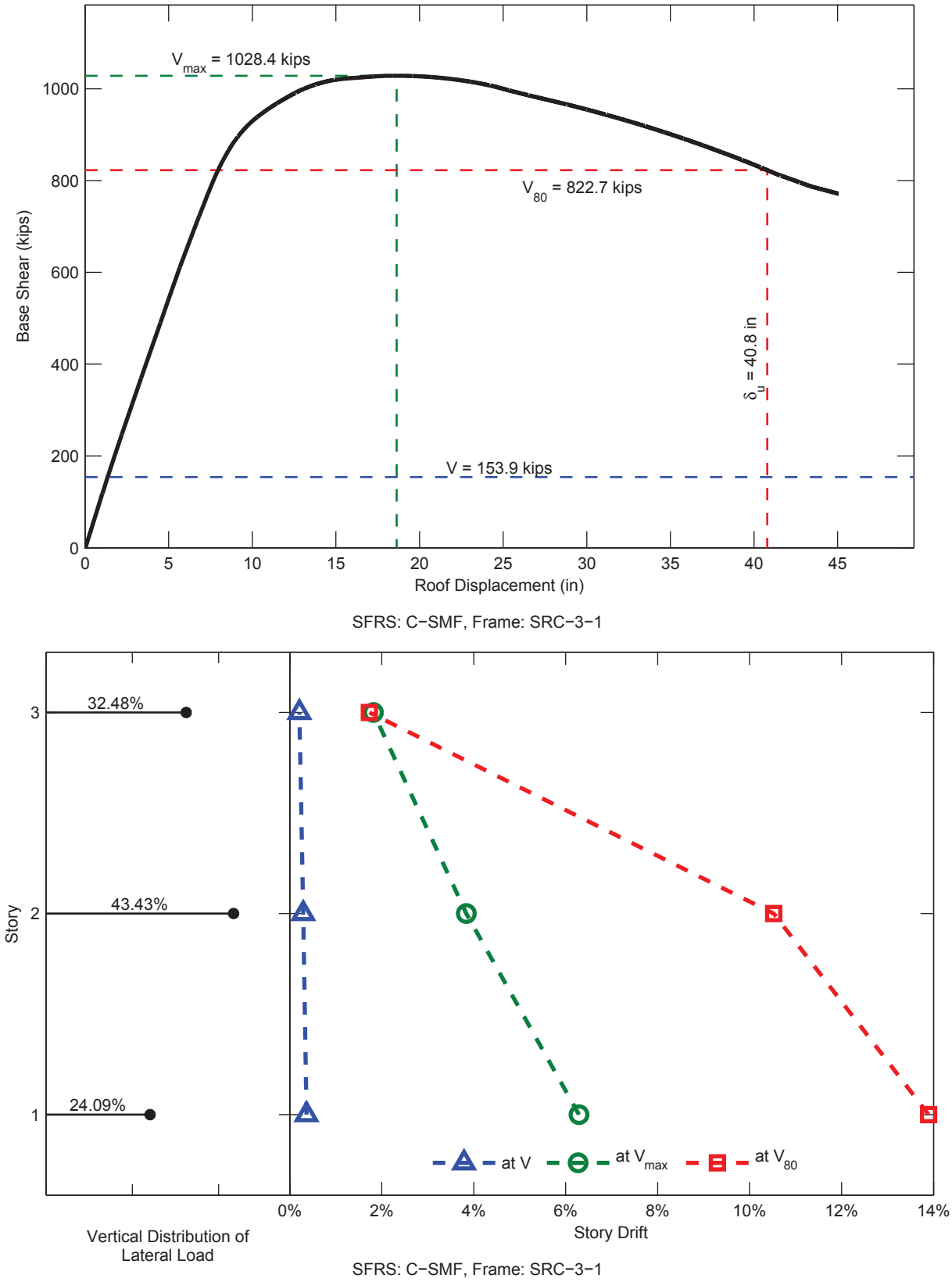

Figure C.25. Static Pushover Analysis Results: Frame SRC-3-1

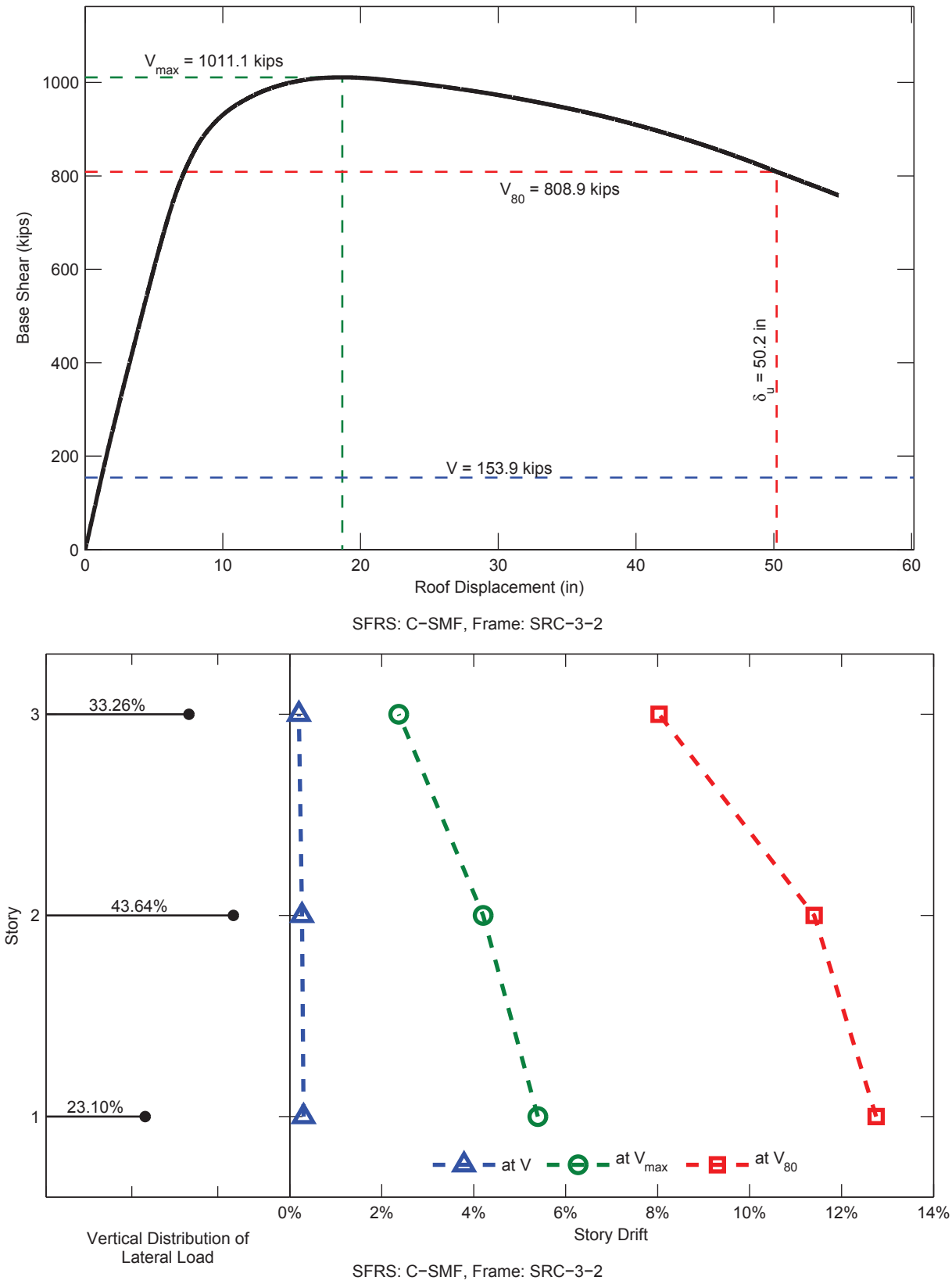

Figure C.26. Static Pushover Analysis Results: Frame SRC-3-2

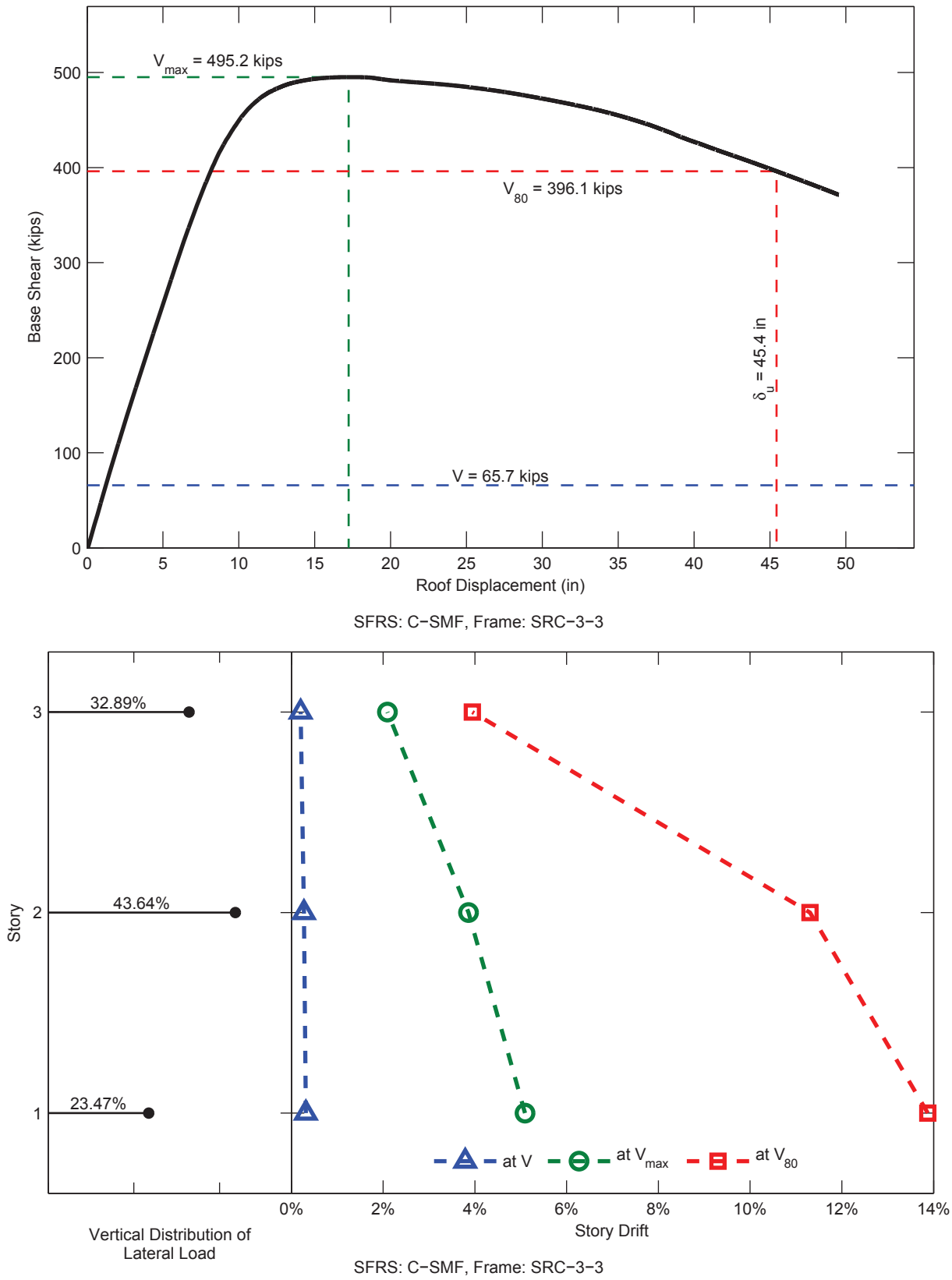

Figure C.27. Static Pushover Analysis Results: Frame SRC-3-3

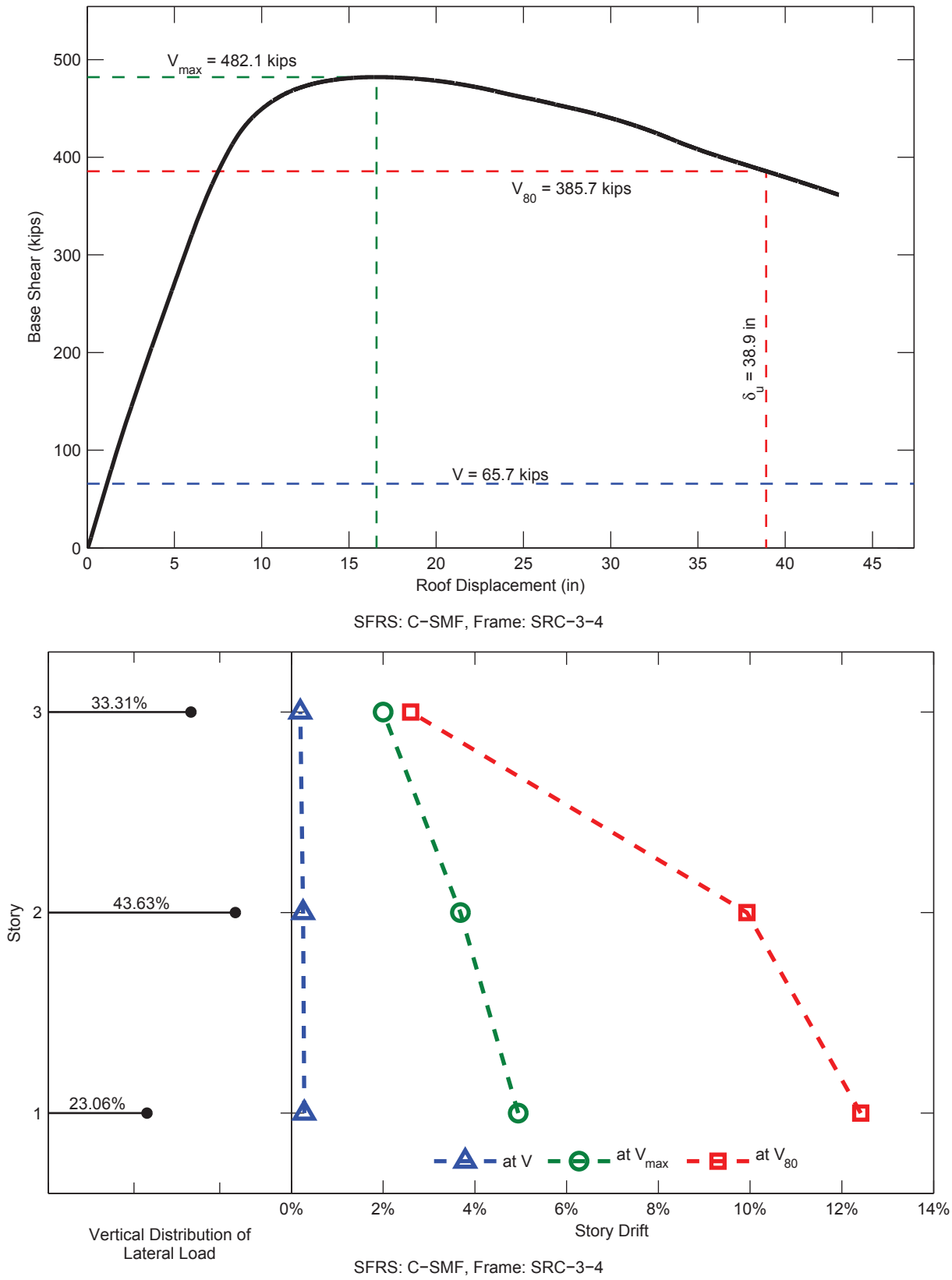

Figure C.28. Static Pushover Analysis Results: Frame SRC-3-4

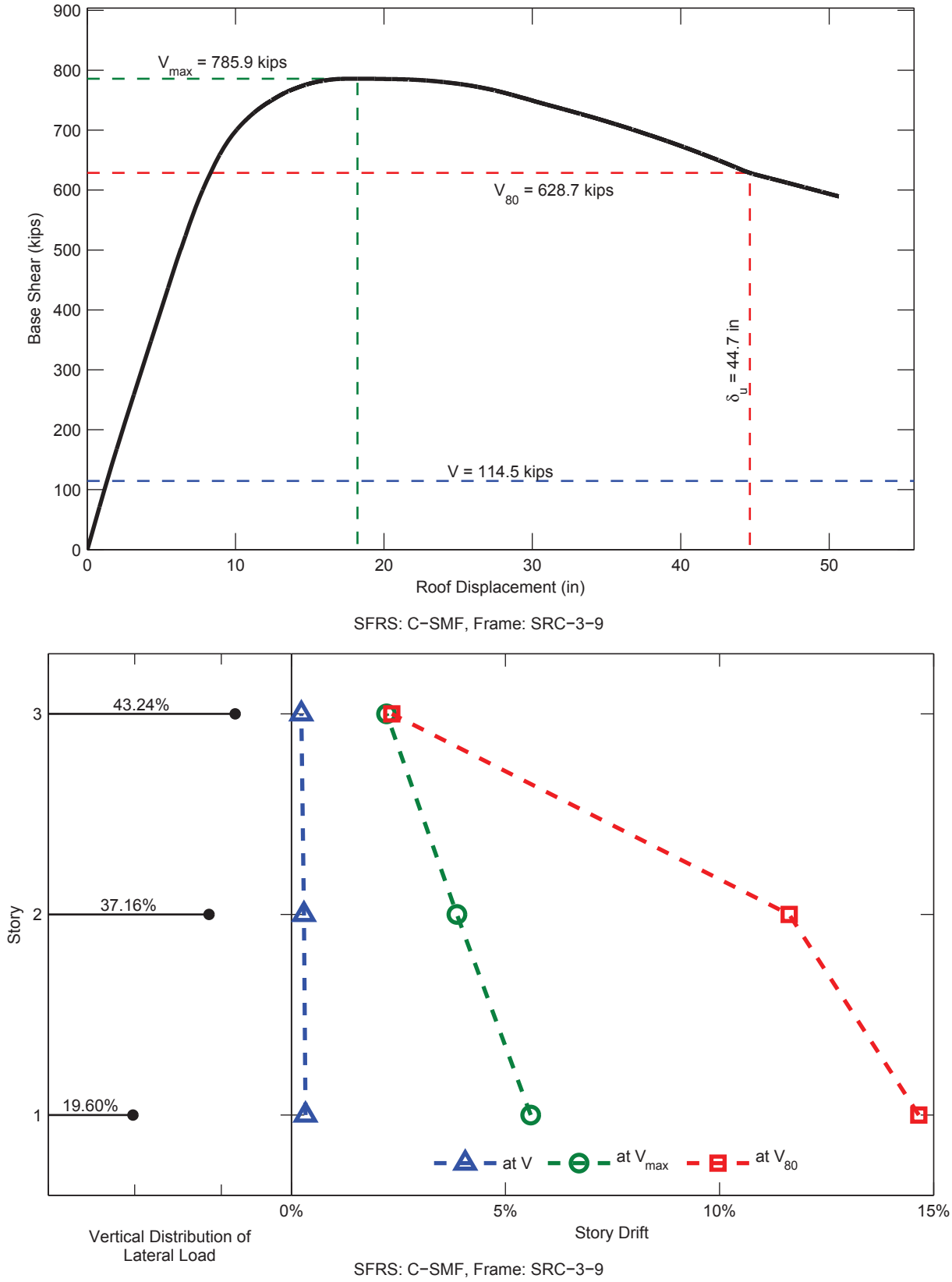

Figure C.29. Static Pushover Analysis Results: Frame SRC-3-9

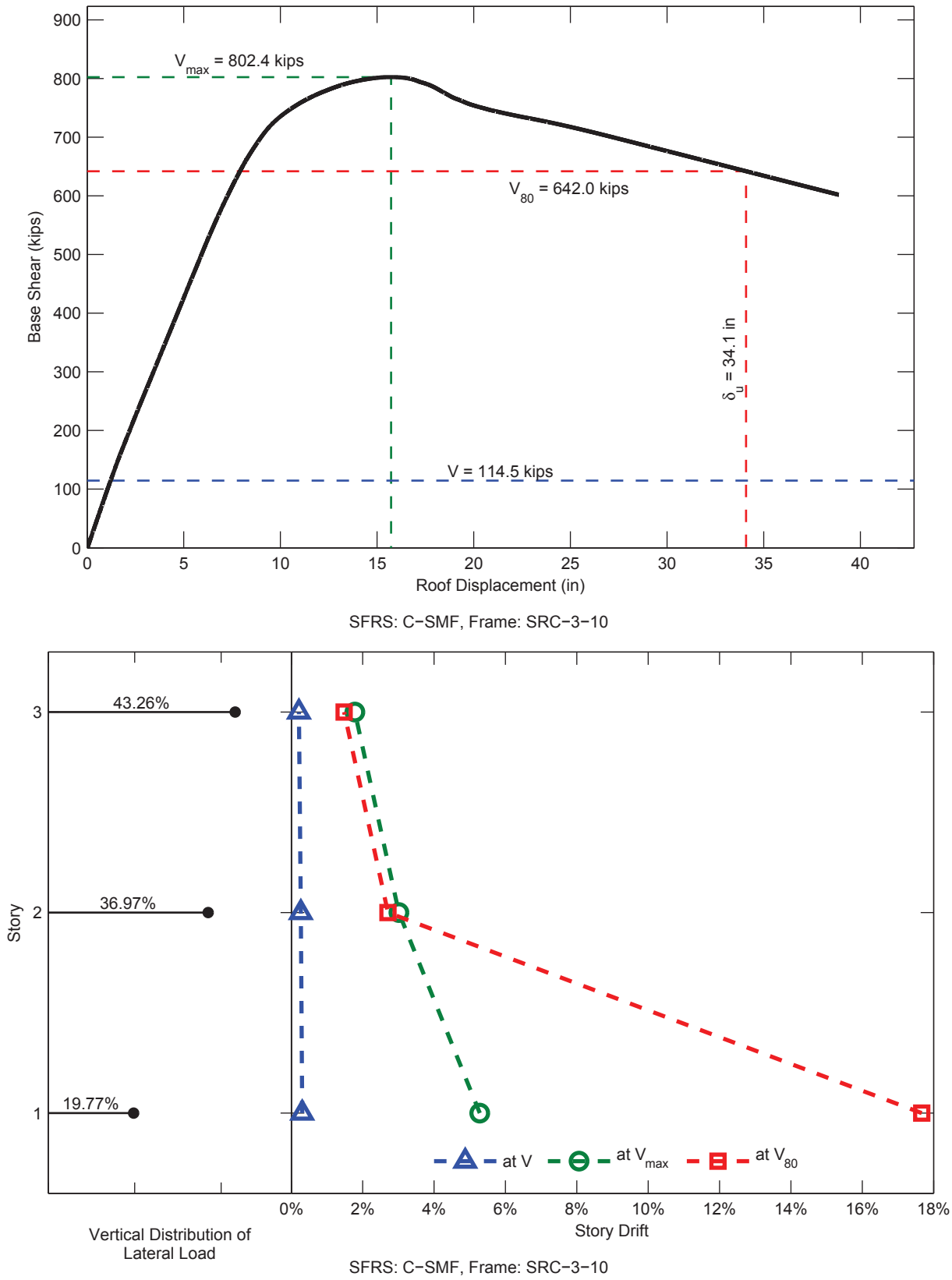

Figure C.30. Static Pushover Analysis Results: Frame SRC-3-10

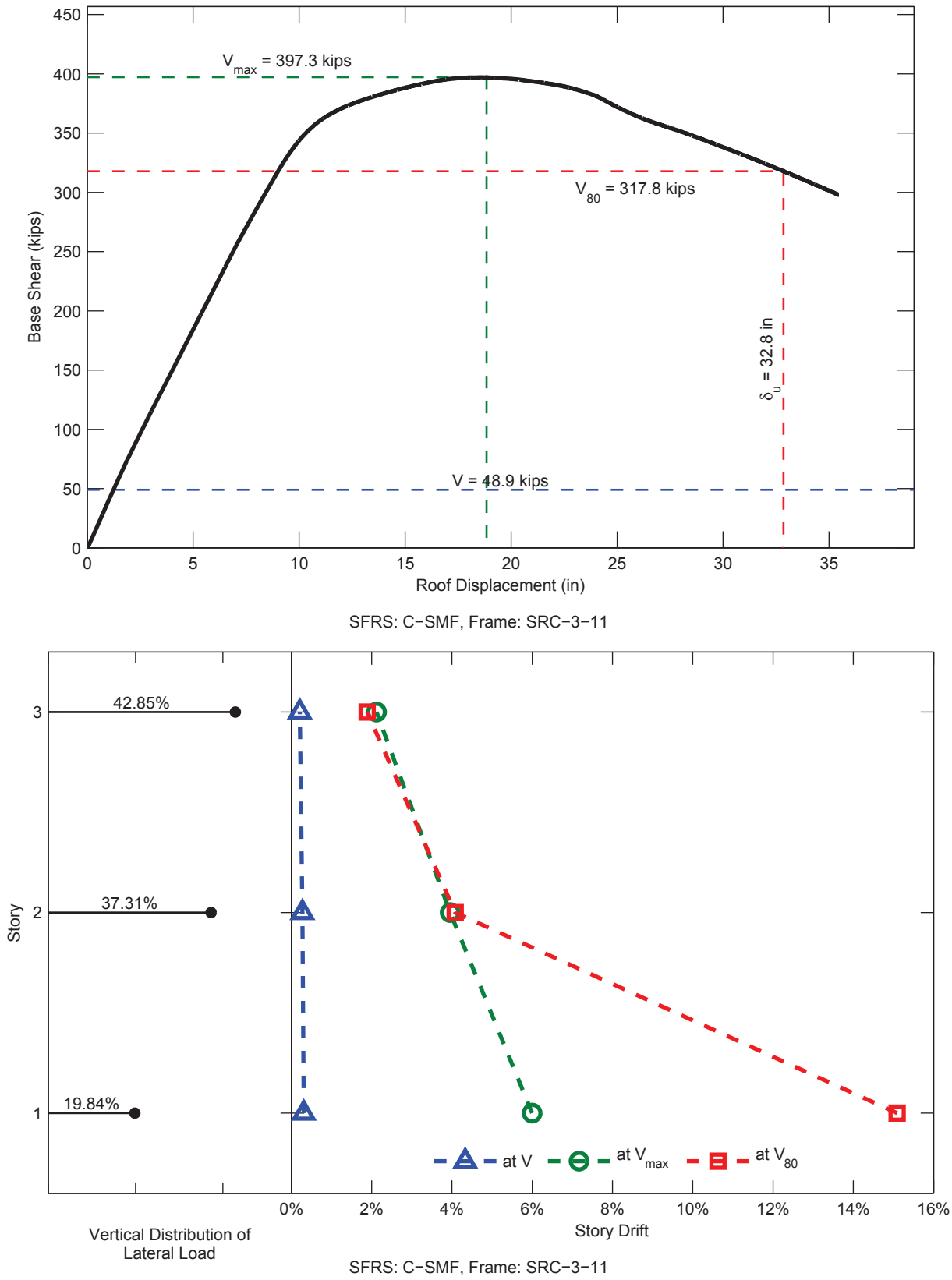

Figure C.31. Static Pushover Analysis Results: Frame SRC-3-11

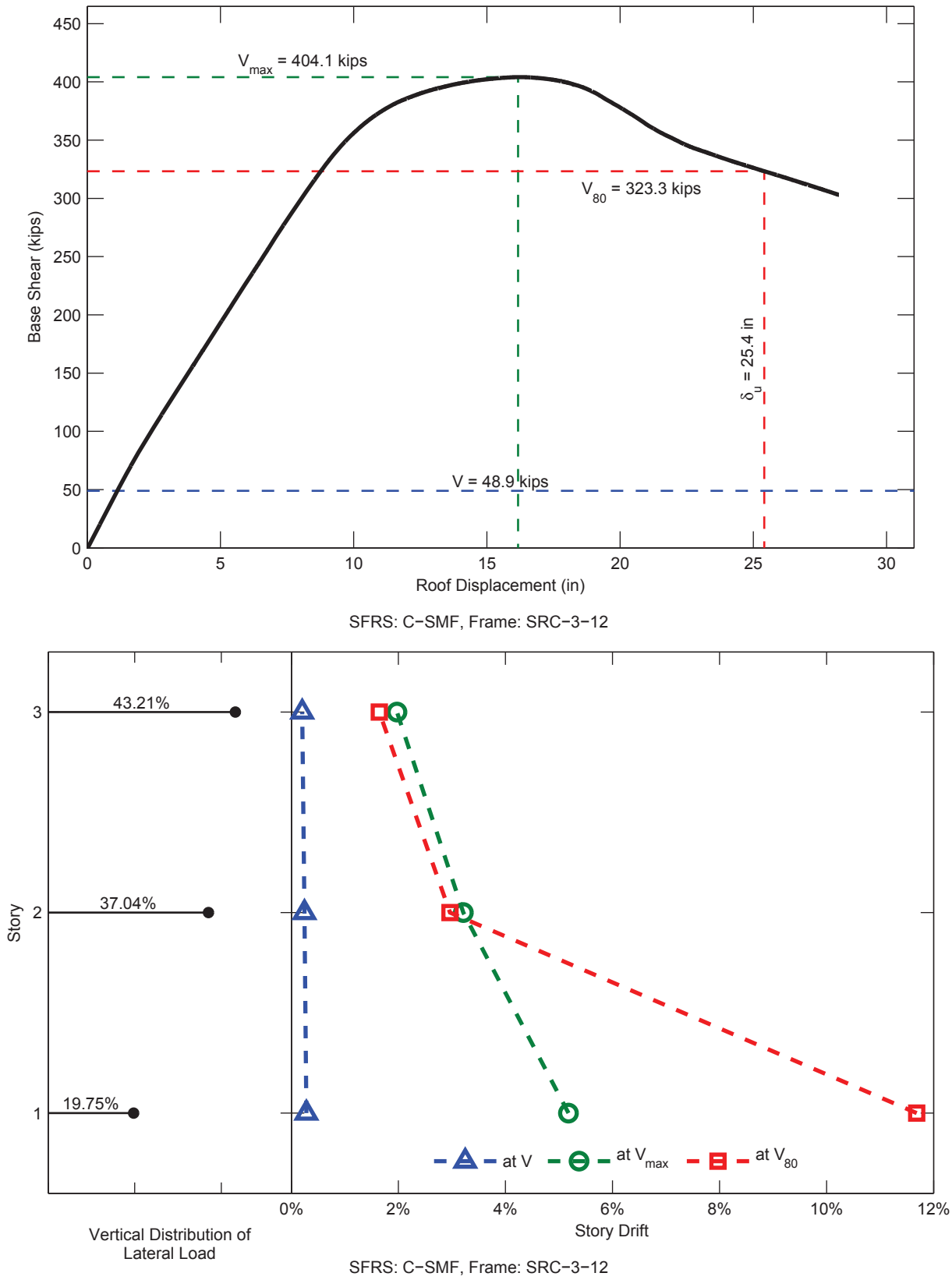

Figure C.32. Static Pushover Analysis Results: Frame SRC-3-12

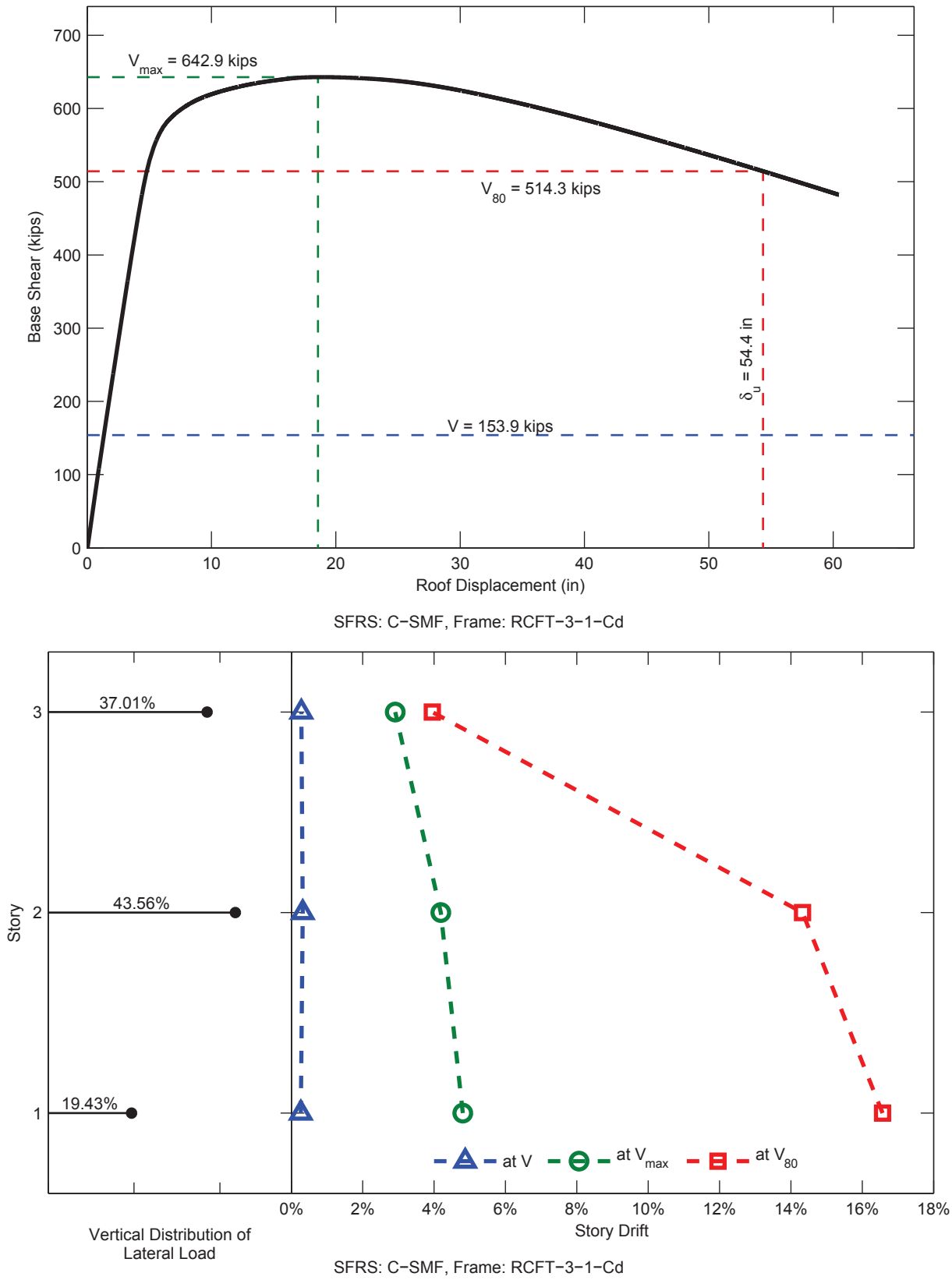

Figure C.33. Static Pushover Analysis Results: Frame RCFT-3-1-Cd

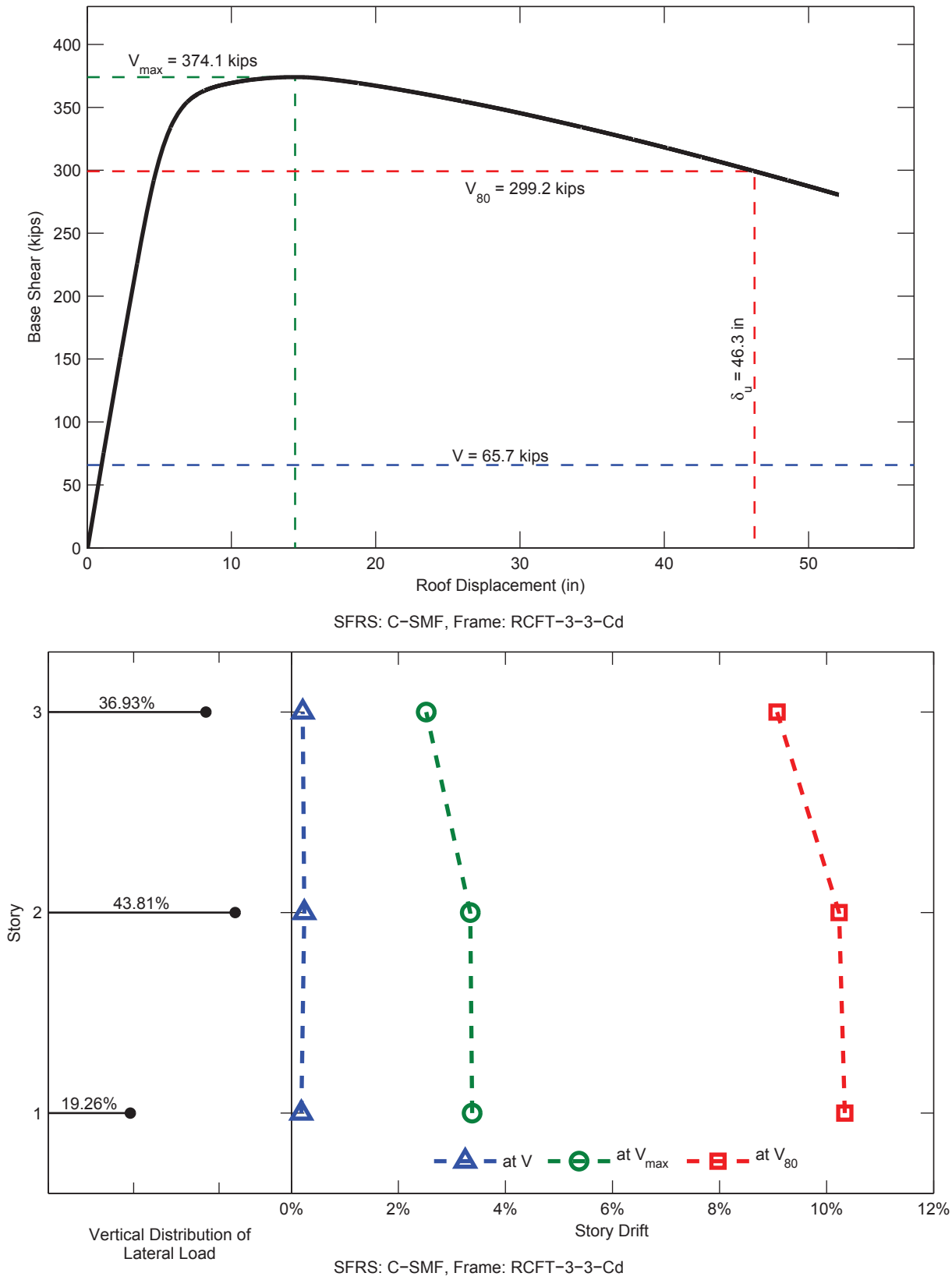

Figure C.34. Static Pushover Analysis Results: Frame RCFT-3-3-Cd

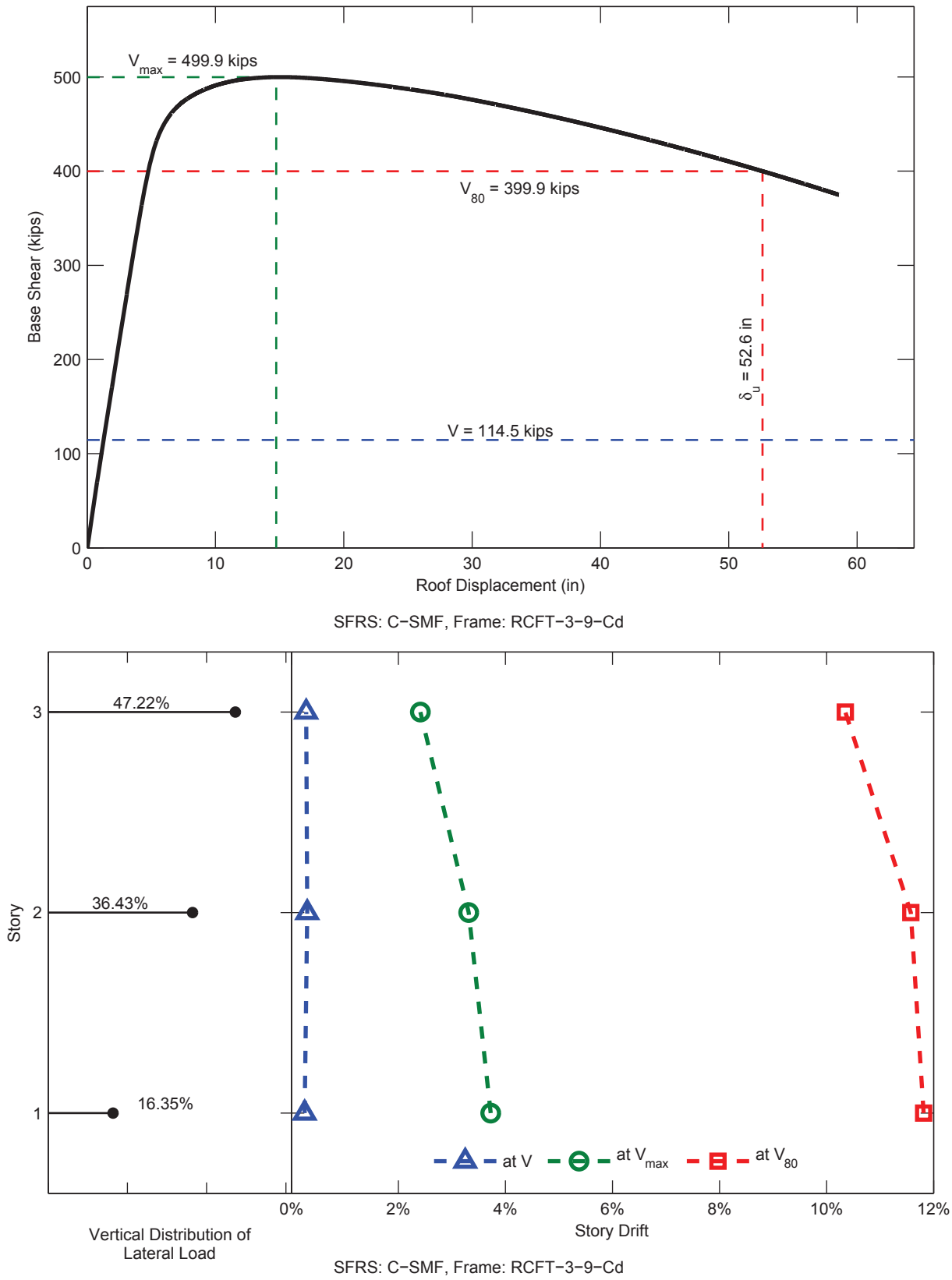

Figure C.35. Static Pushover Analysis Results: Frame RCFT-3-9-Cd

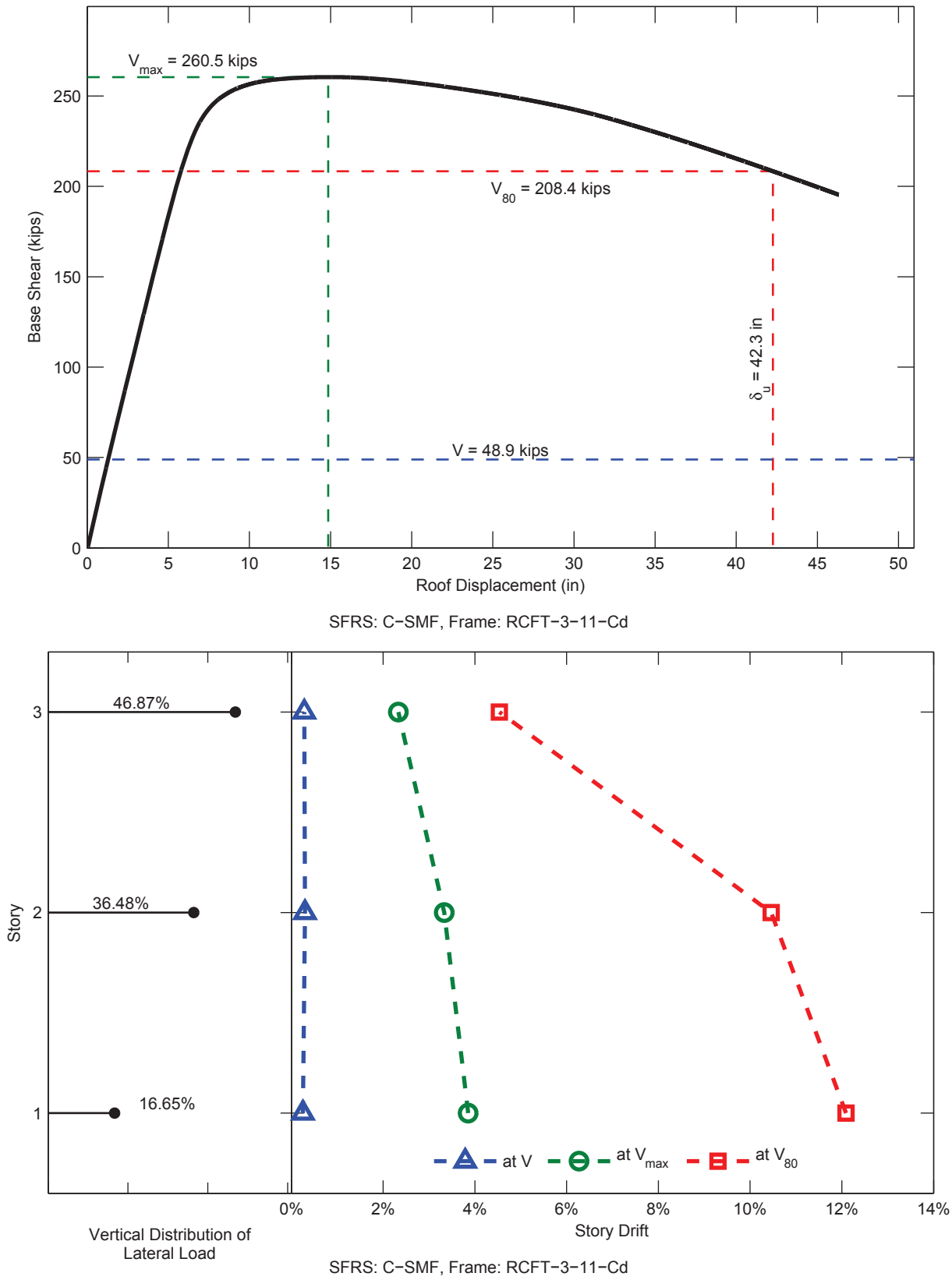

Figure C.36. Static Pushover Analysis Results: Frame RCFT-3-11-Cd

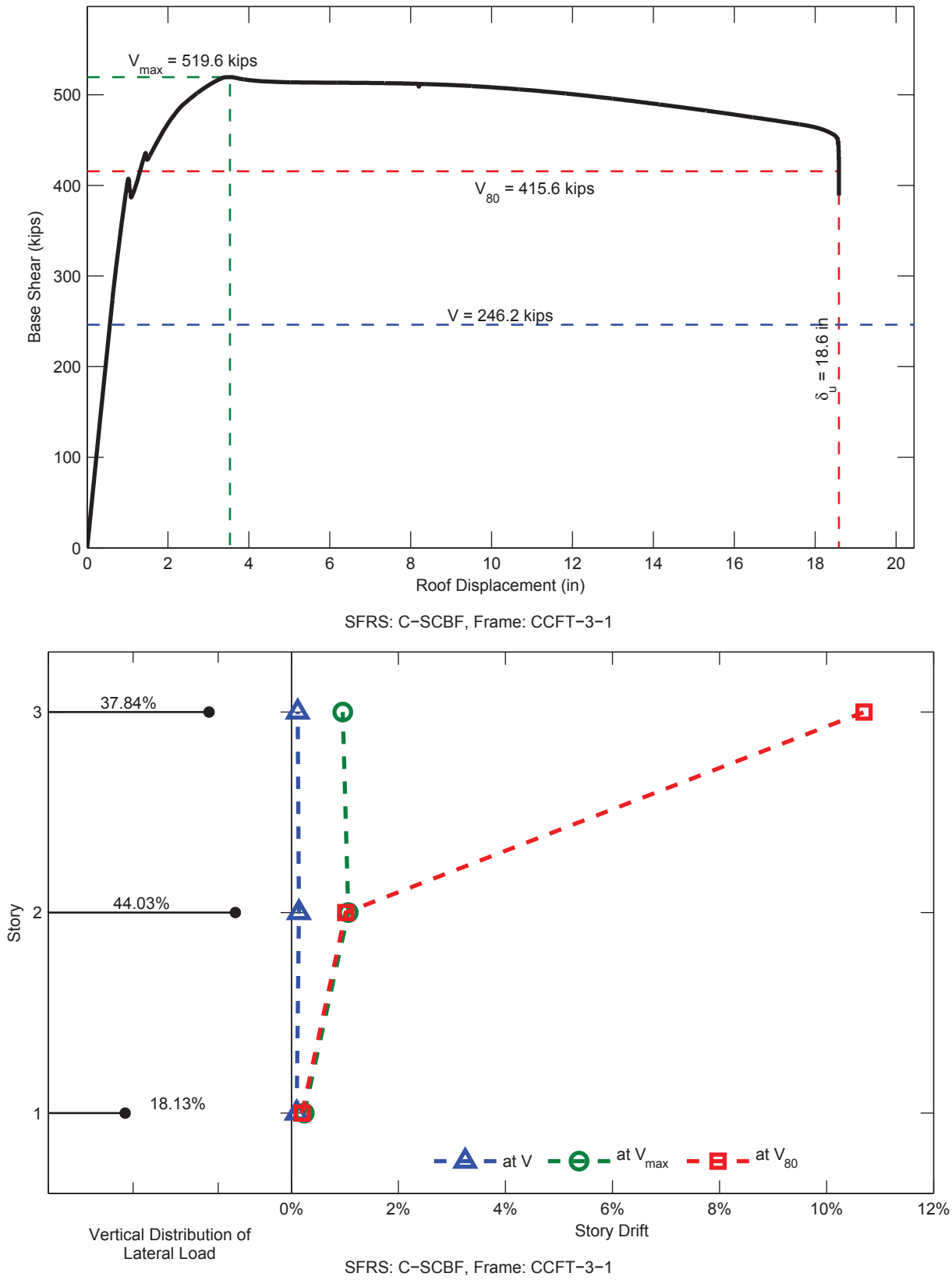

Figure C.37. Static Pushover Analysis Results: Frame CCFT-3-1

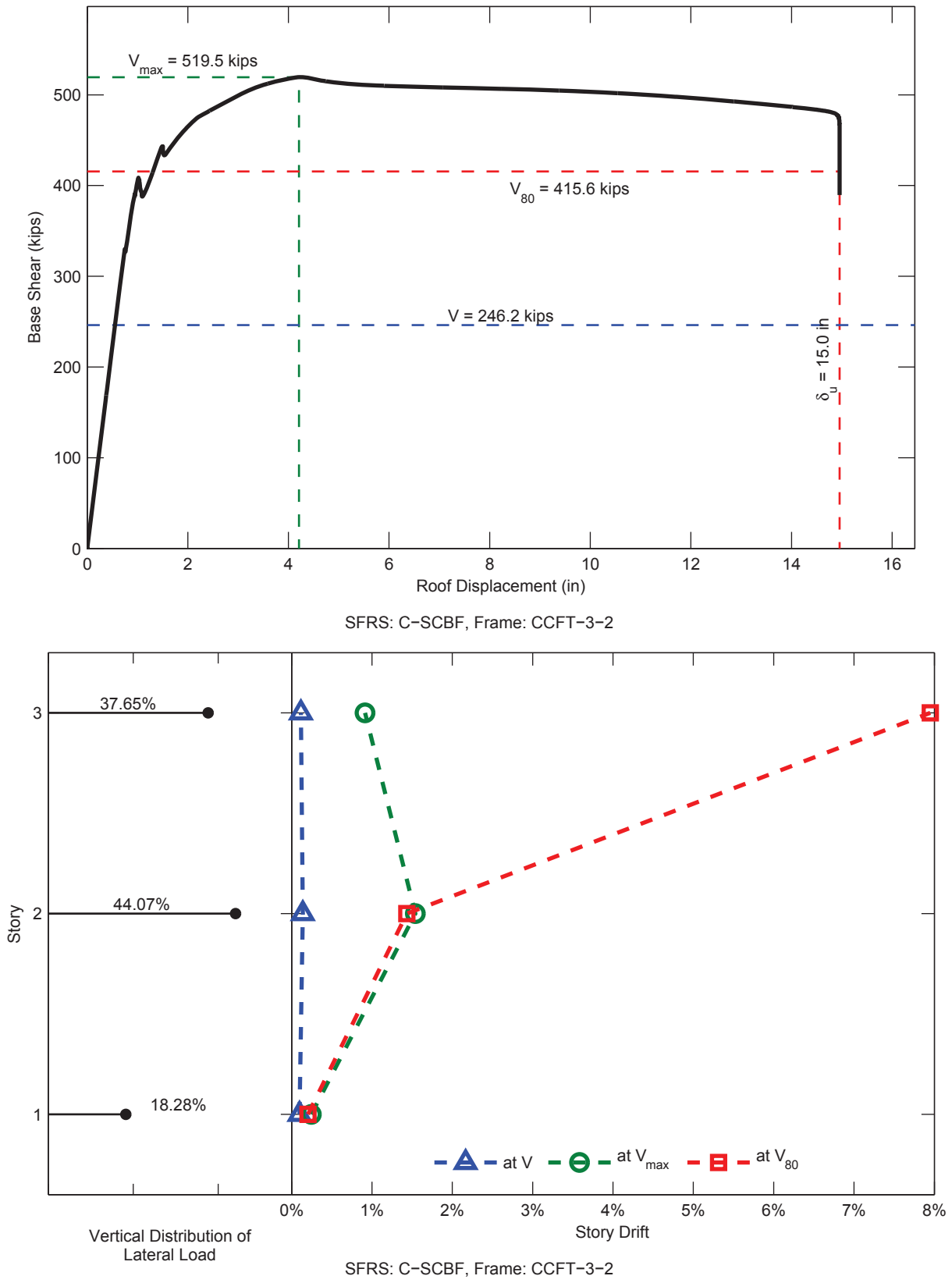

Figure C.38. Static Pushover Analysis Results: Frame CCFT-3-2

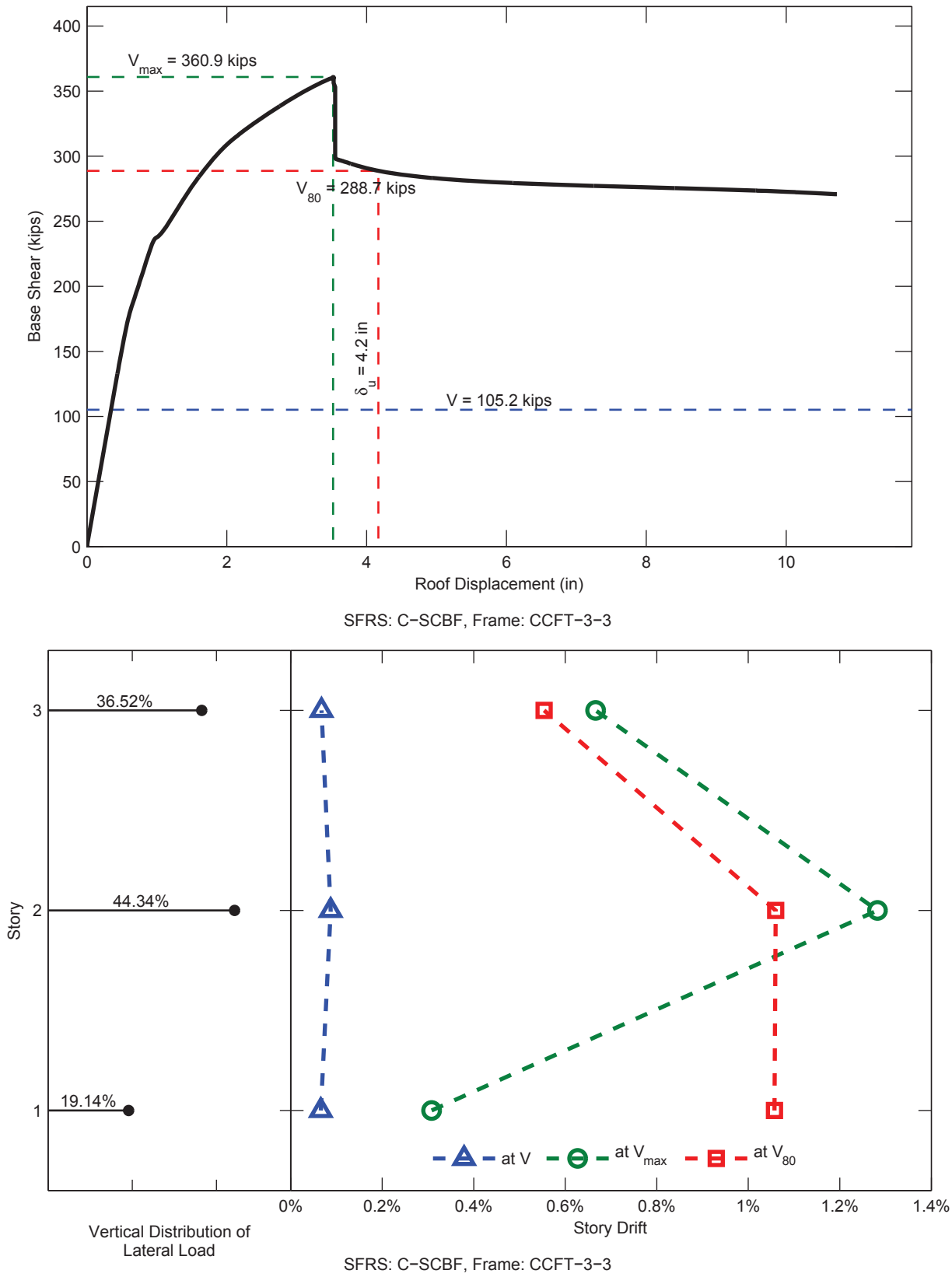

Figure C.39. Static Pushover Analysis Results: Frame CCFT-3-3

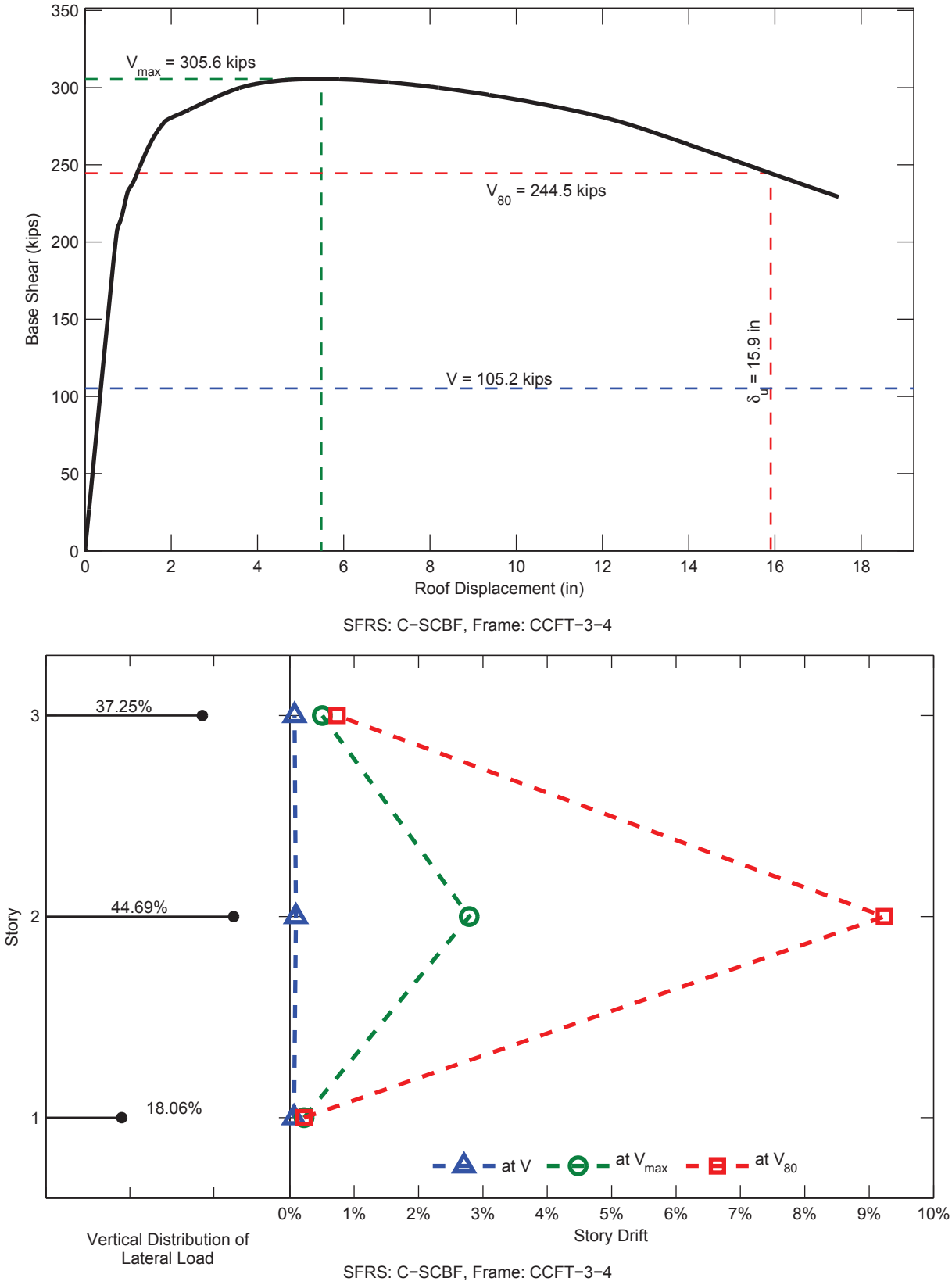

Figure C.40. Static Pushover Analysis Results: Frame CCFT-3-4

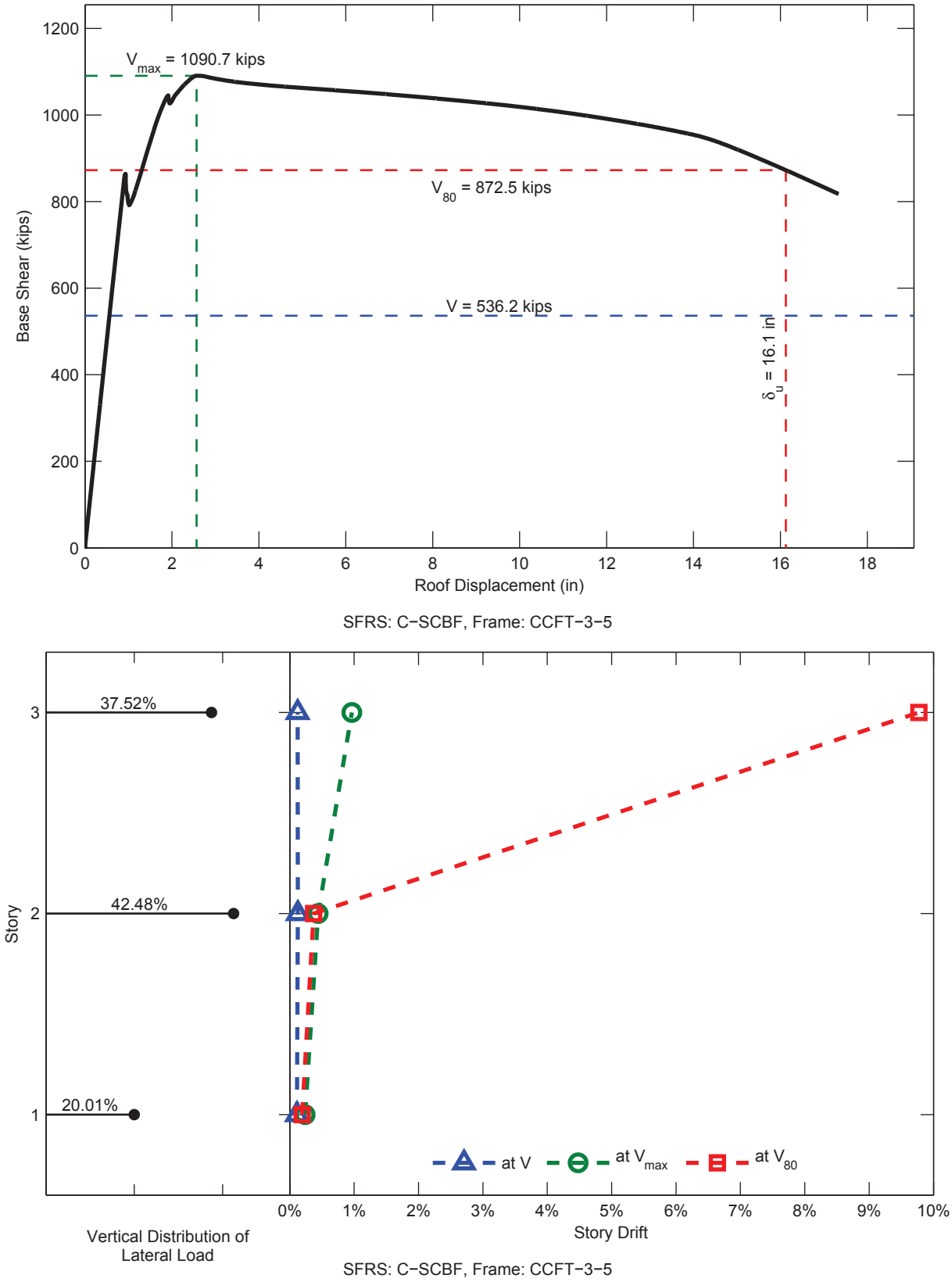

Figure C.41. Static Pushover Analysis Results: Frame CCFT-3-5

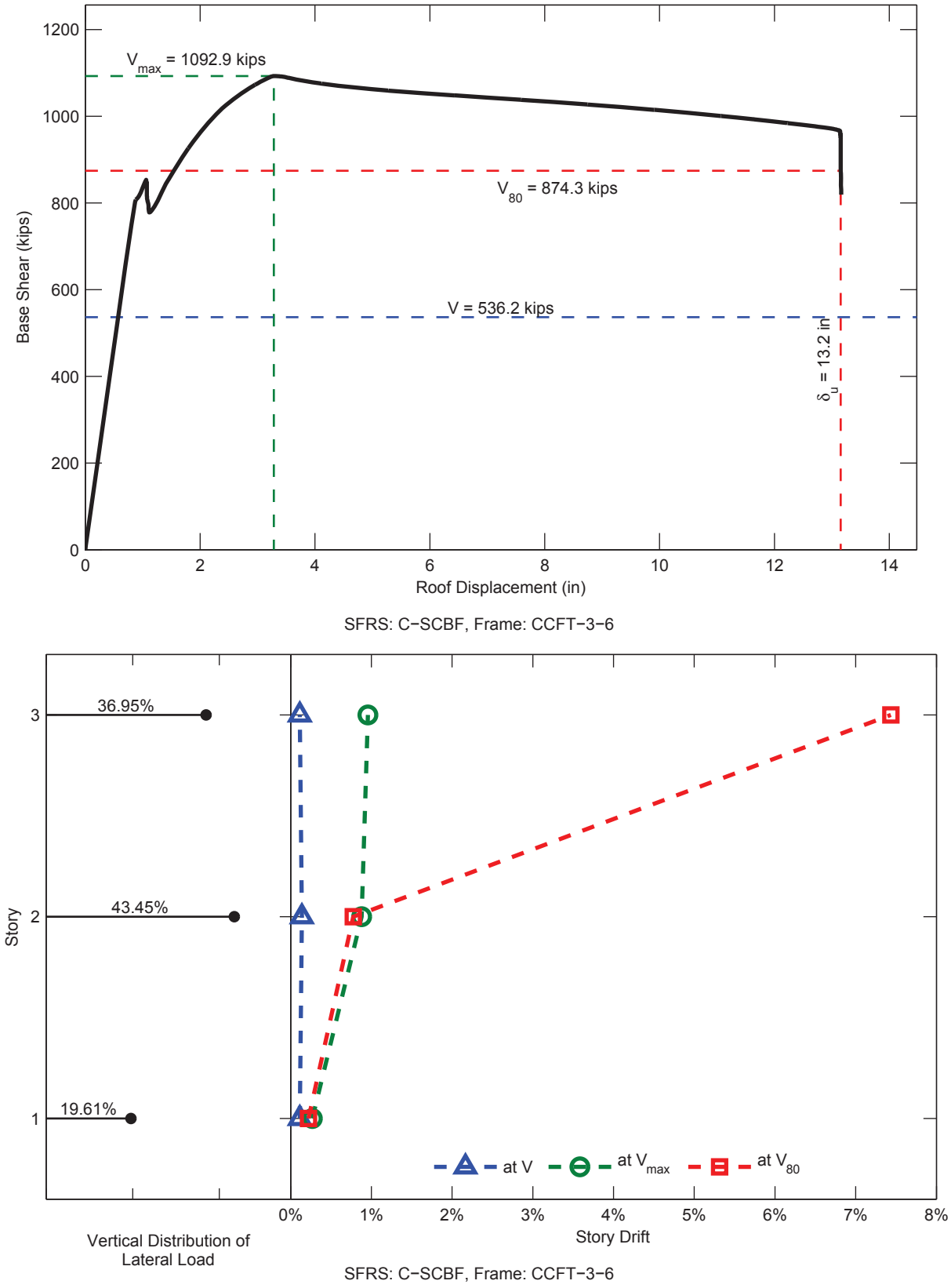

Figure C.42. Static Pushover Analysis Results: Frame CCFT-3-6

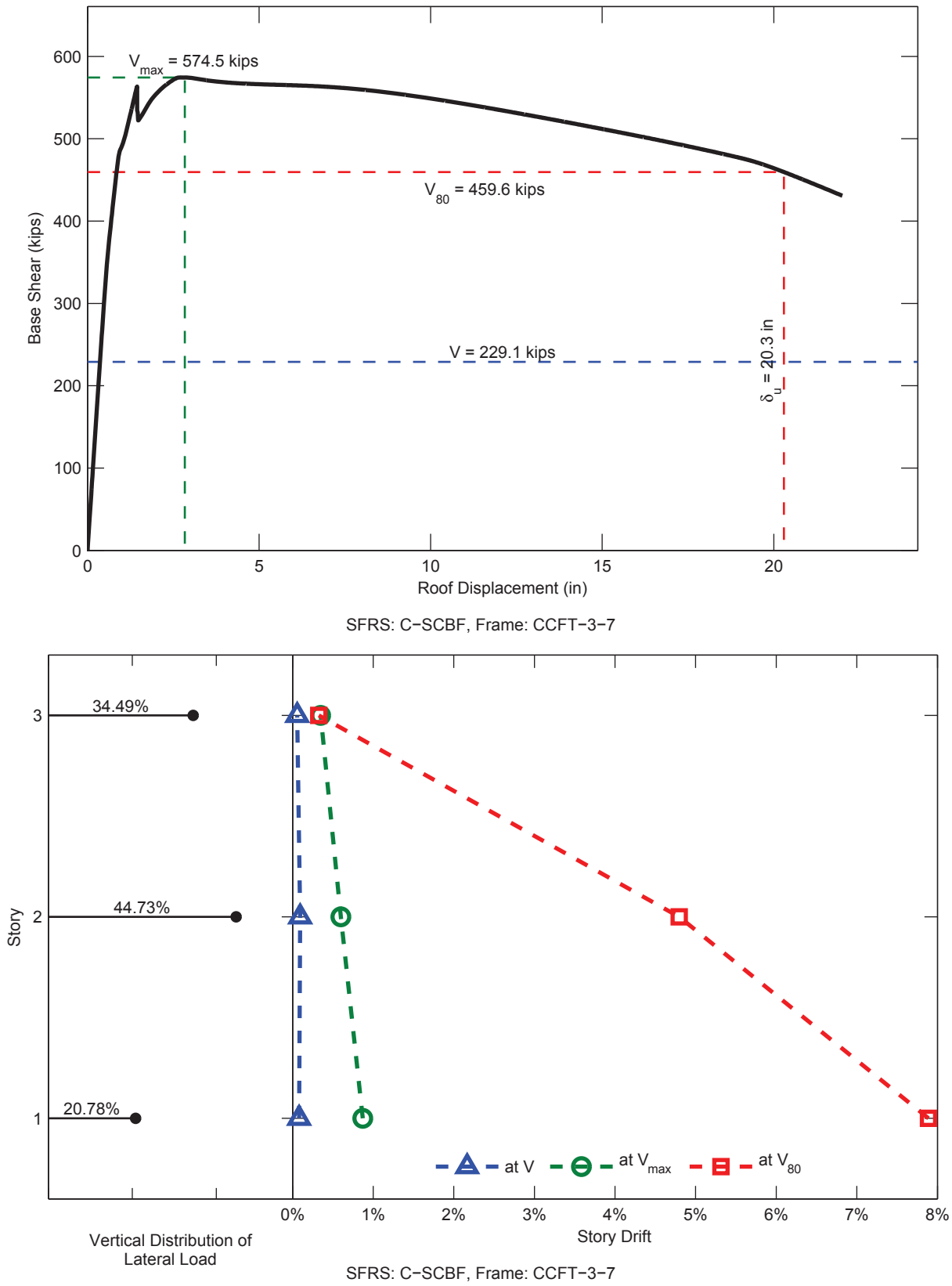

Figure C.43. Static Pushover Analysis Results: Frame CCFT-3-7

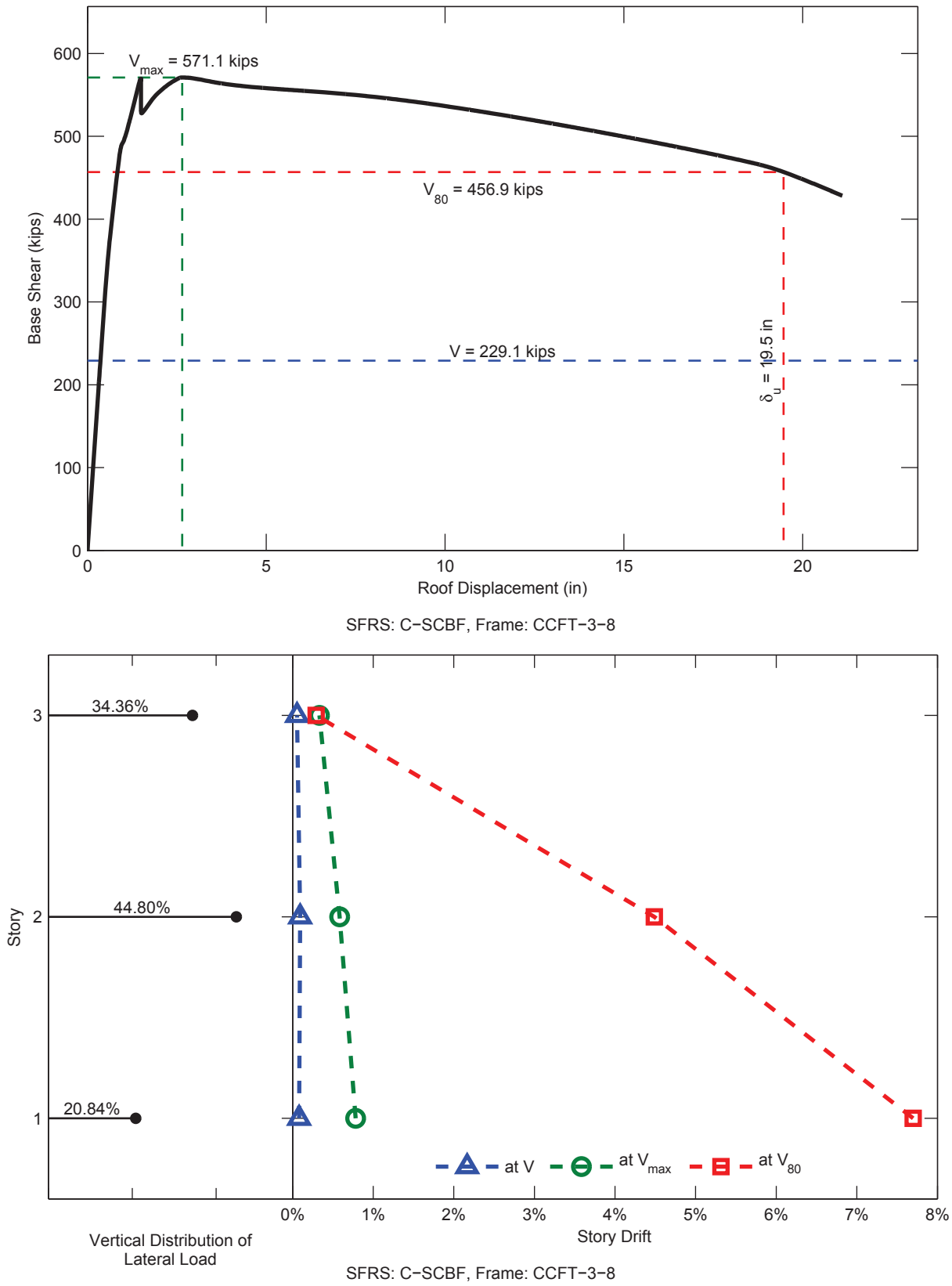

Figure C.44. Static Pushover Analysis Results: Frame CCFT-3-8

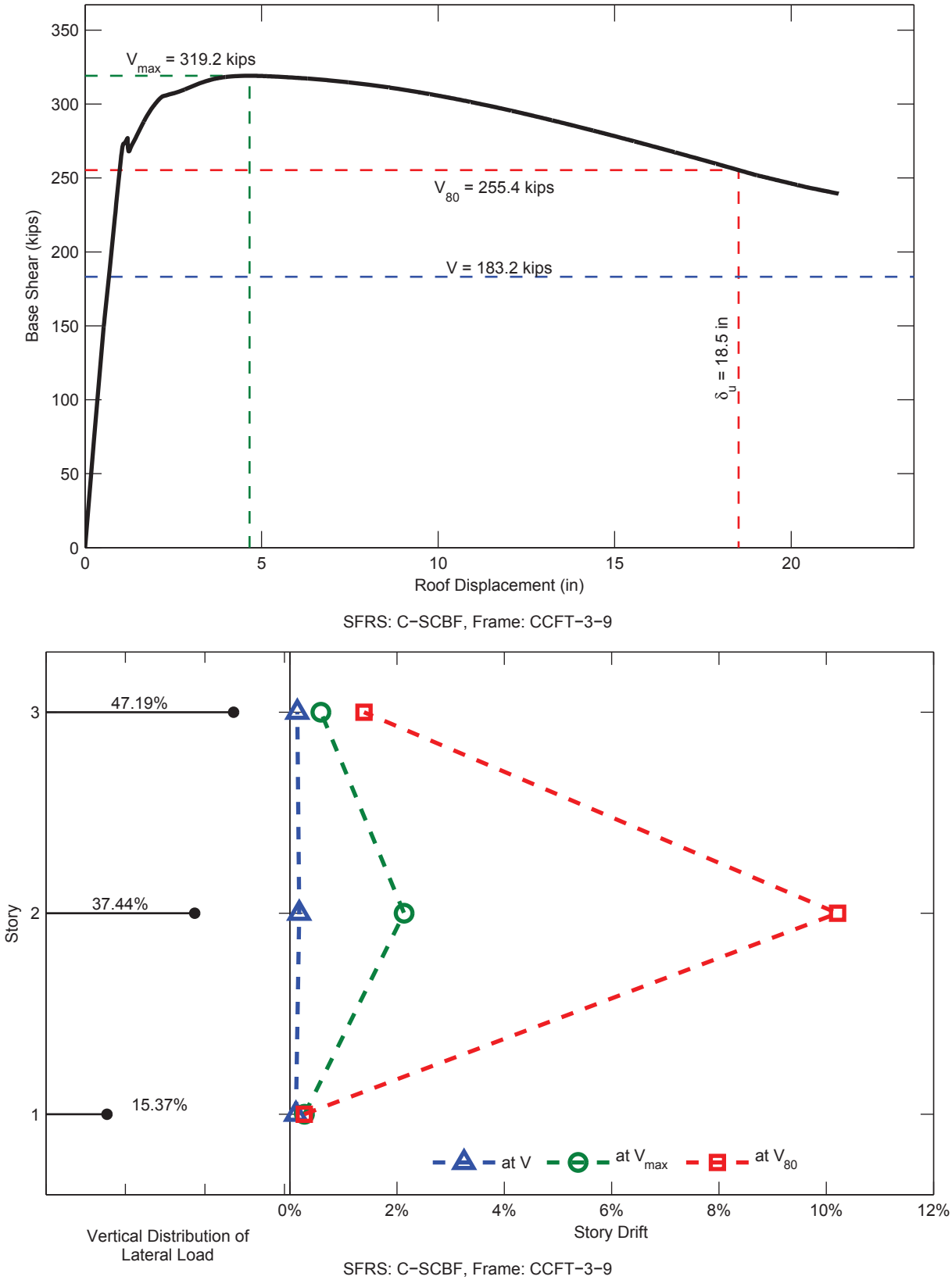

Figure C.45. Static Pushover Analysis Results: Frame CCFT-3-9

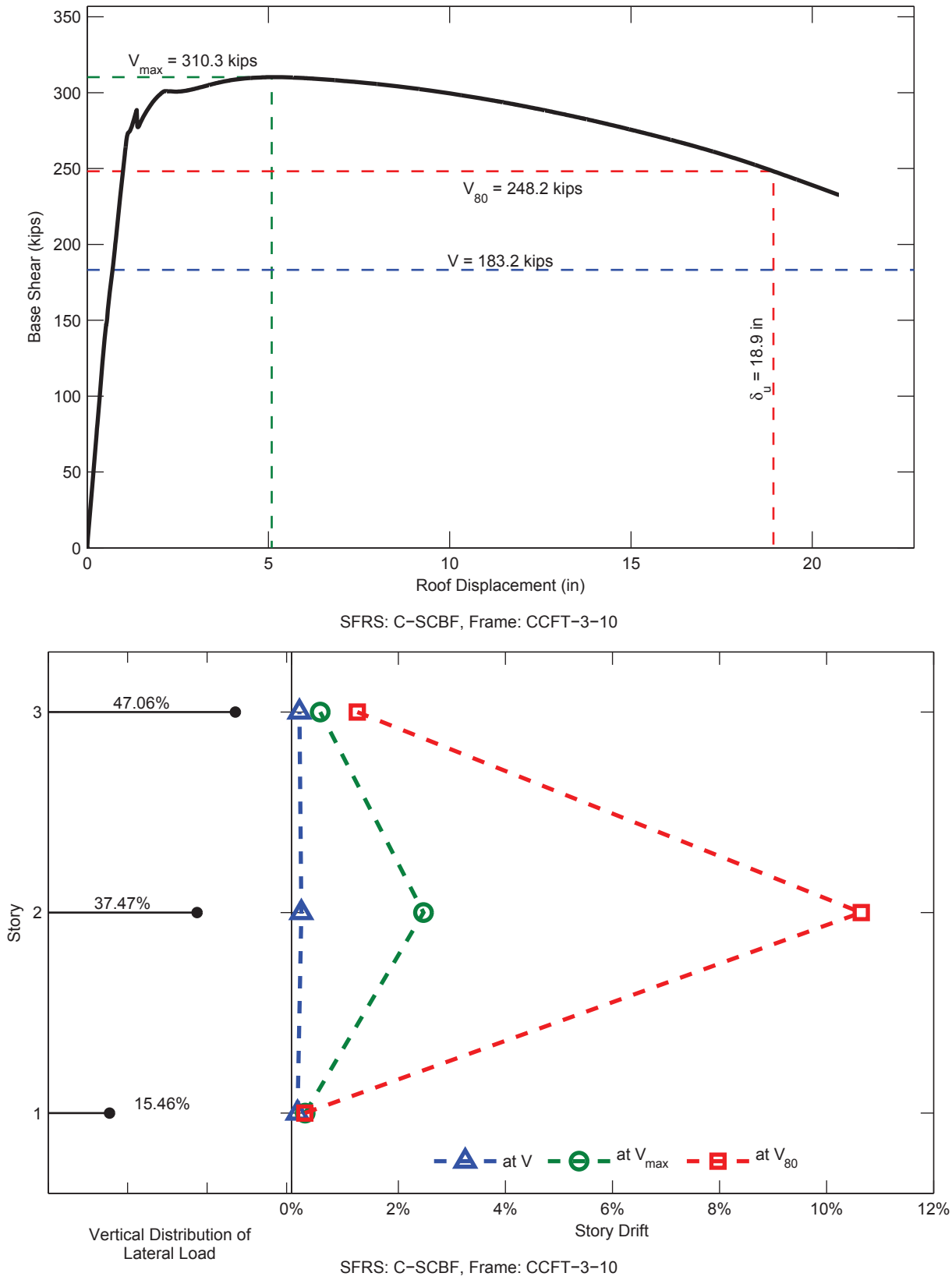

Figure C.46. Static Pushover Analysis Results: Frame CCFT-3-10

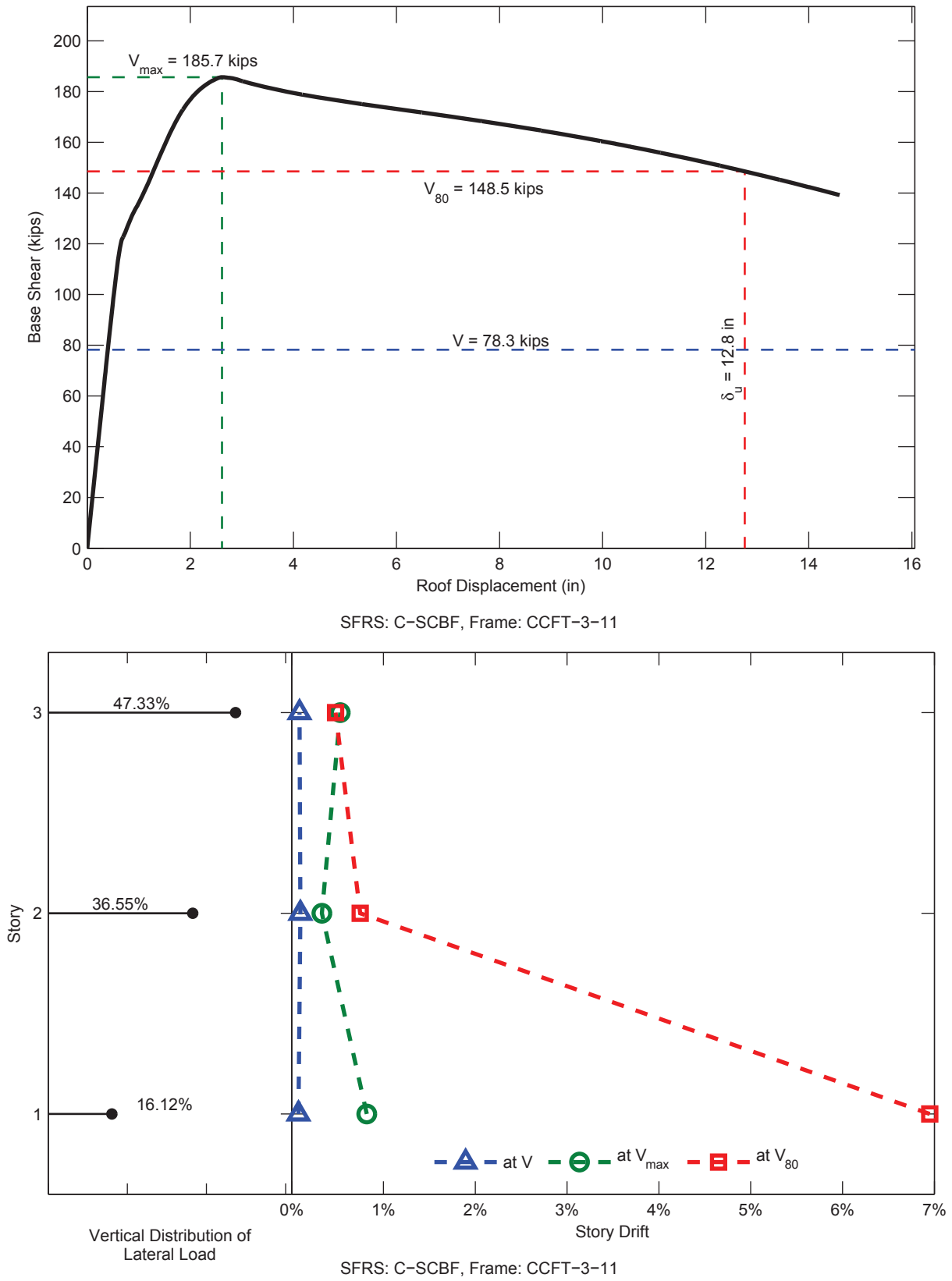

Figure C.47. Static Pushover Analysis Results: Frame CCFT-3-11

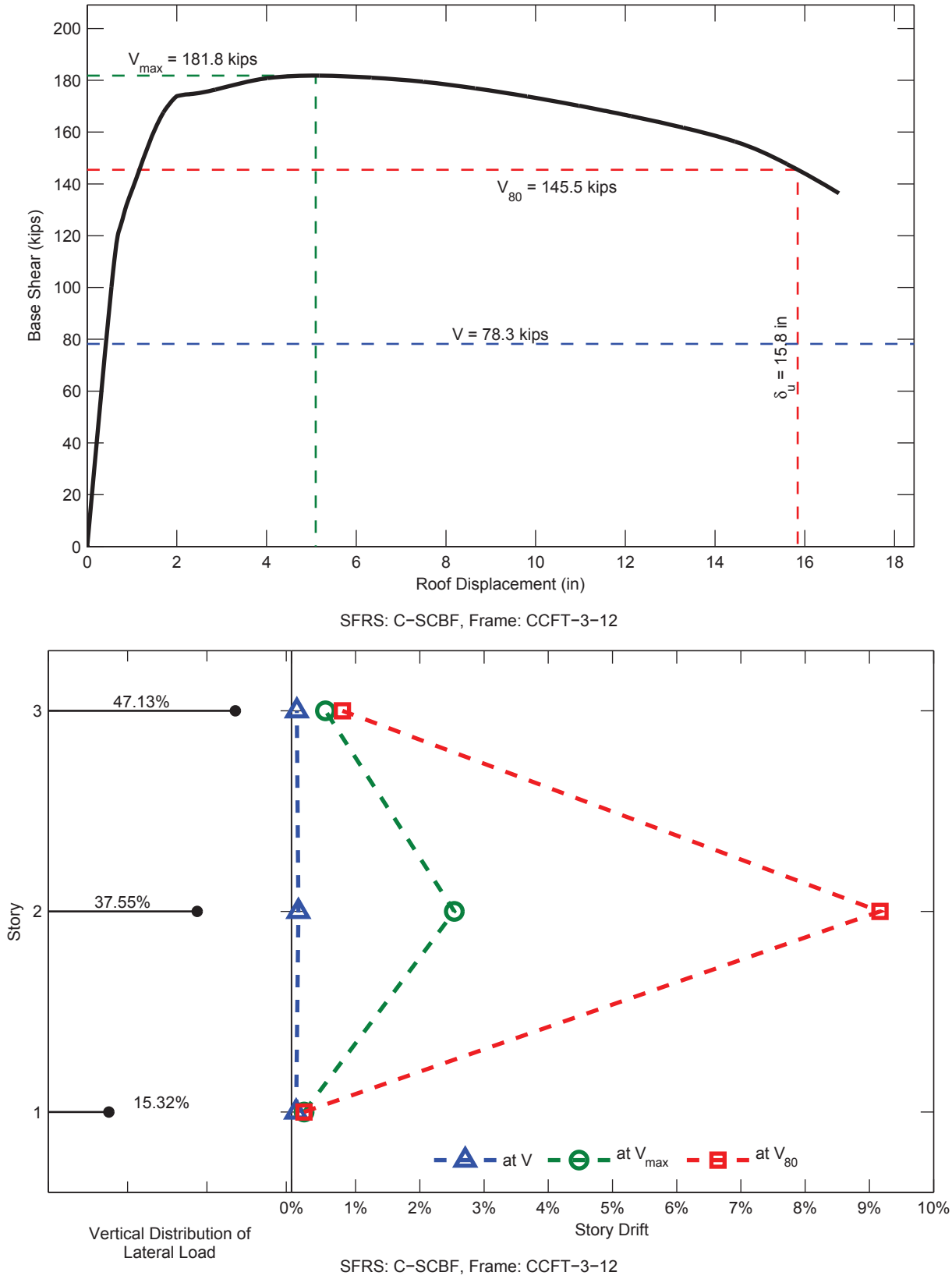

Figure C.48. Static Pushover Analysis Results: Frame CCFT-3-12

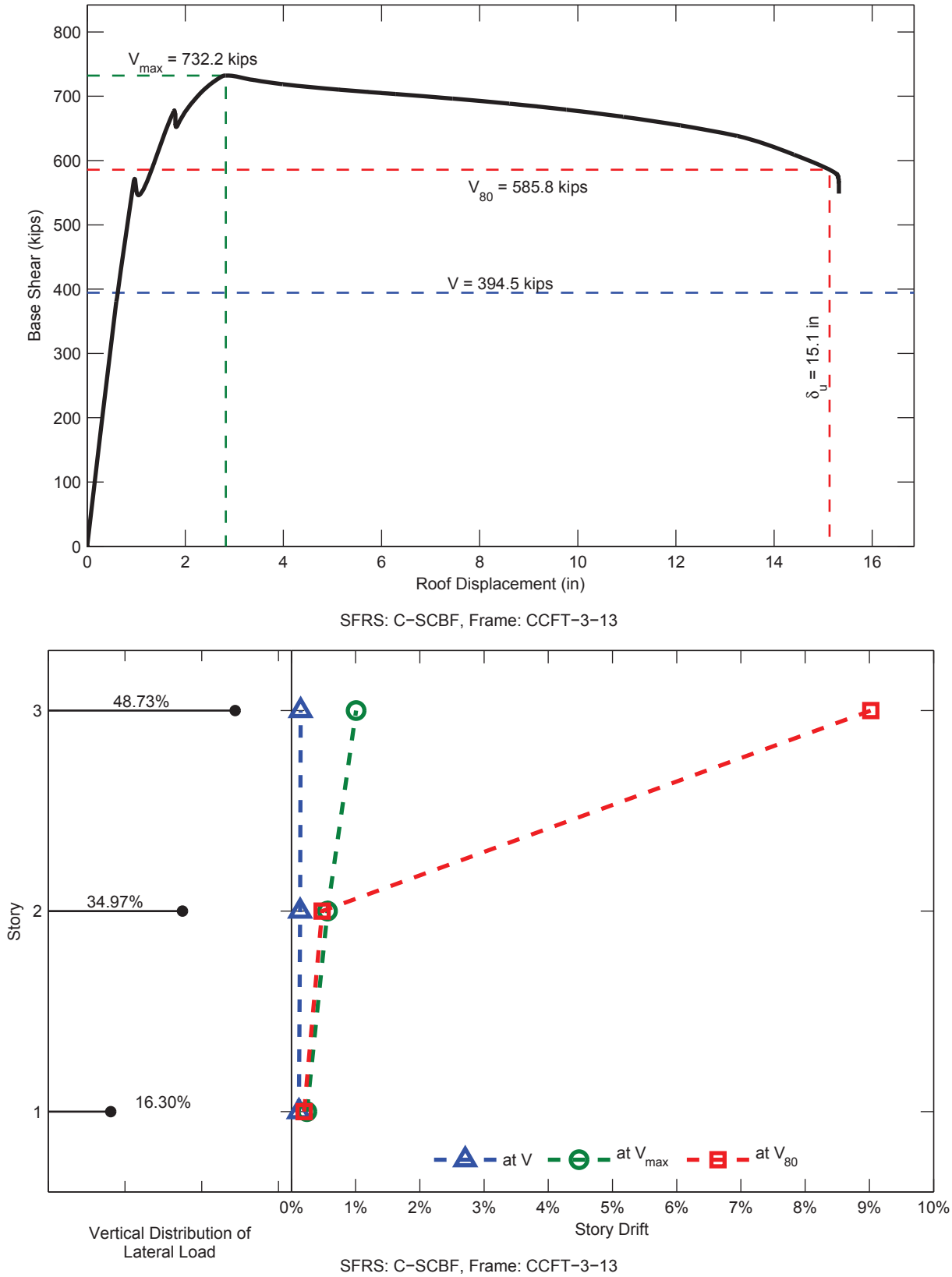

Figure C.49. Static Pushover Analysis Results: Frame CCFT-3-13

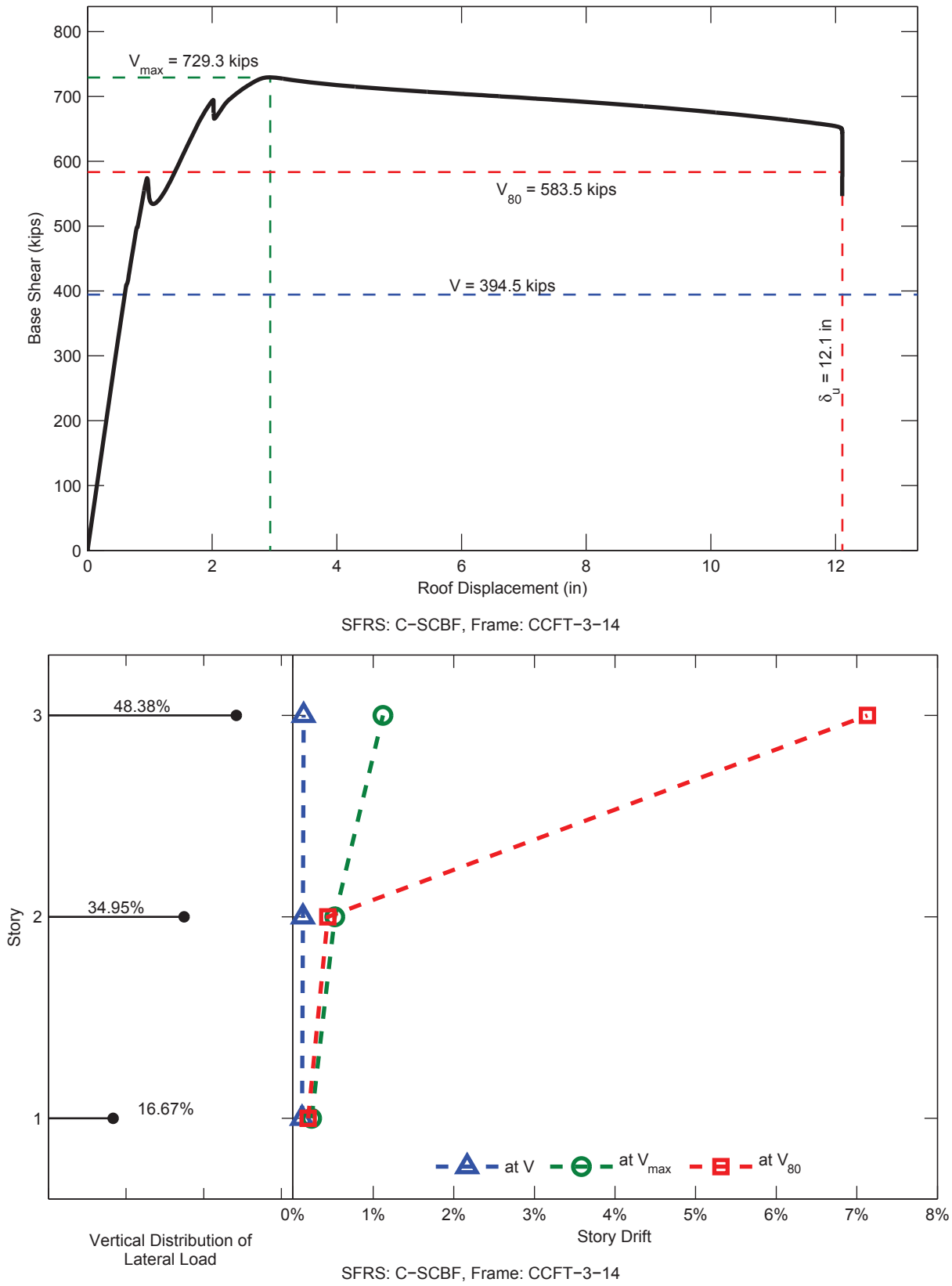

Figure C.50. Static Pushover Analysis Results: Frame CCFT-3-14

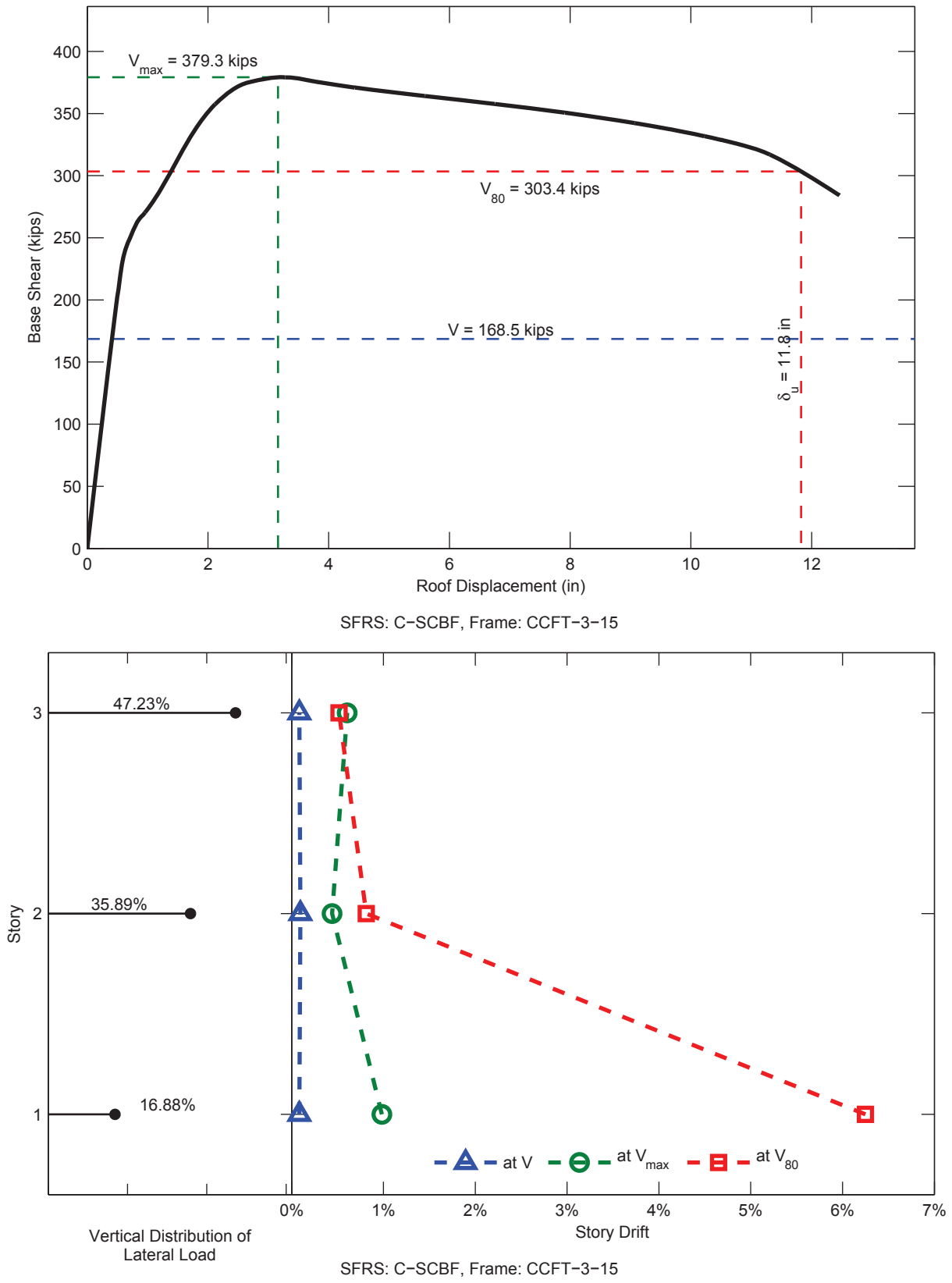

Figure C.51. Static Pushover Analysis Results: Frame CCFT-3-15

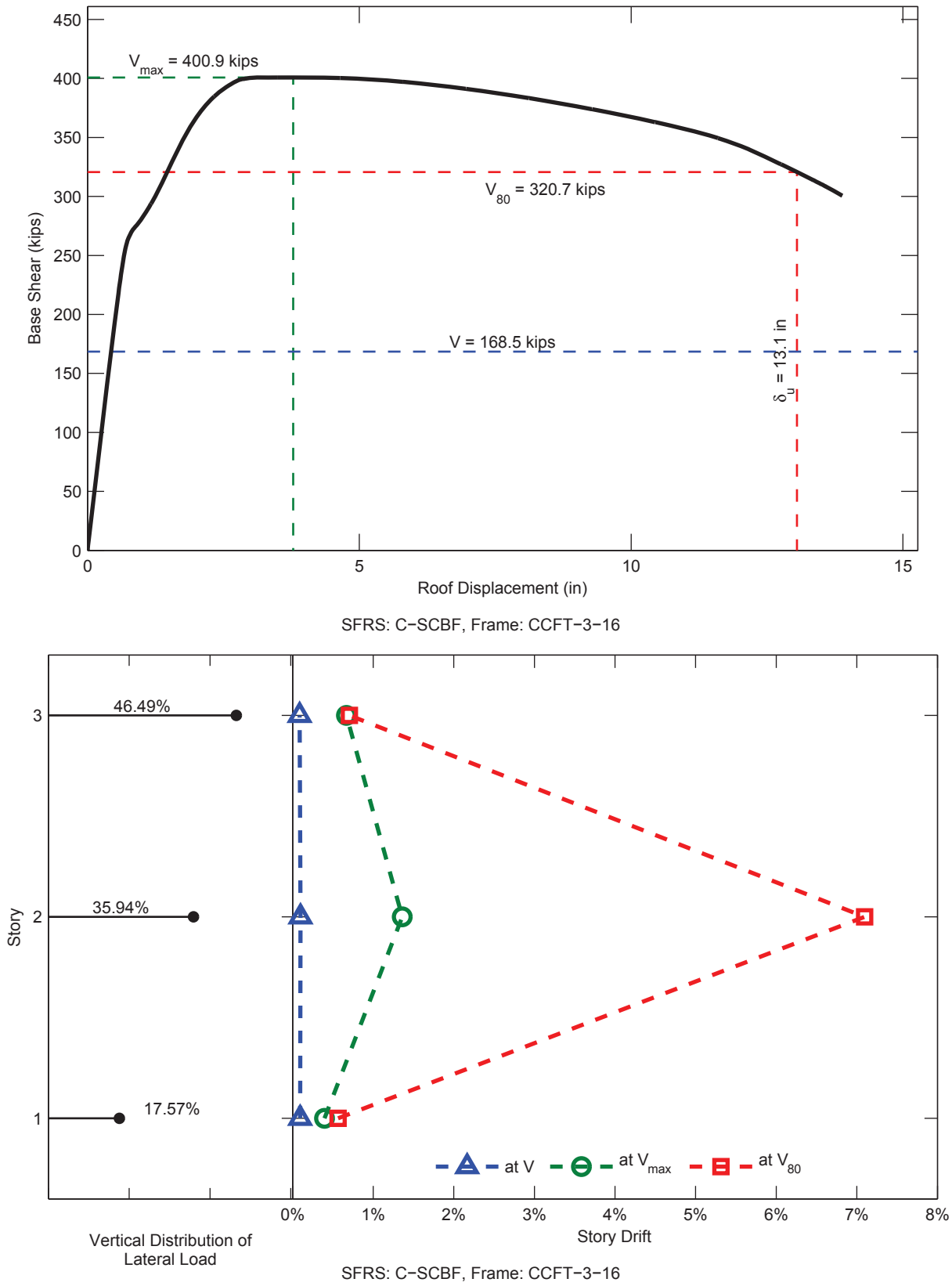

Figure C.52. Static Pushover Analysis Results: Frame CCFT-3-16

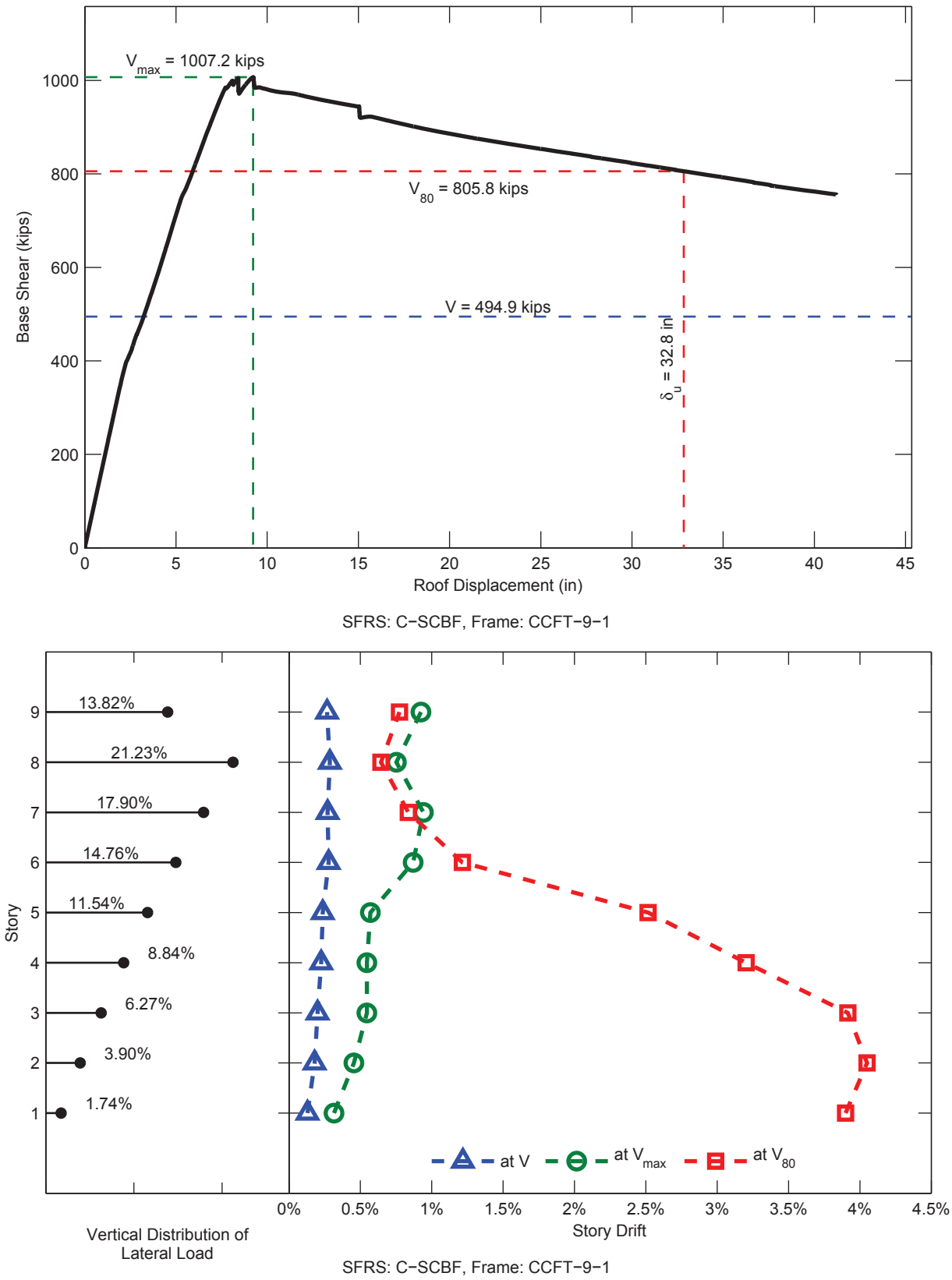

Figure C.53. Static Pushover Analysis Results: Frame CCFT-9-1

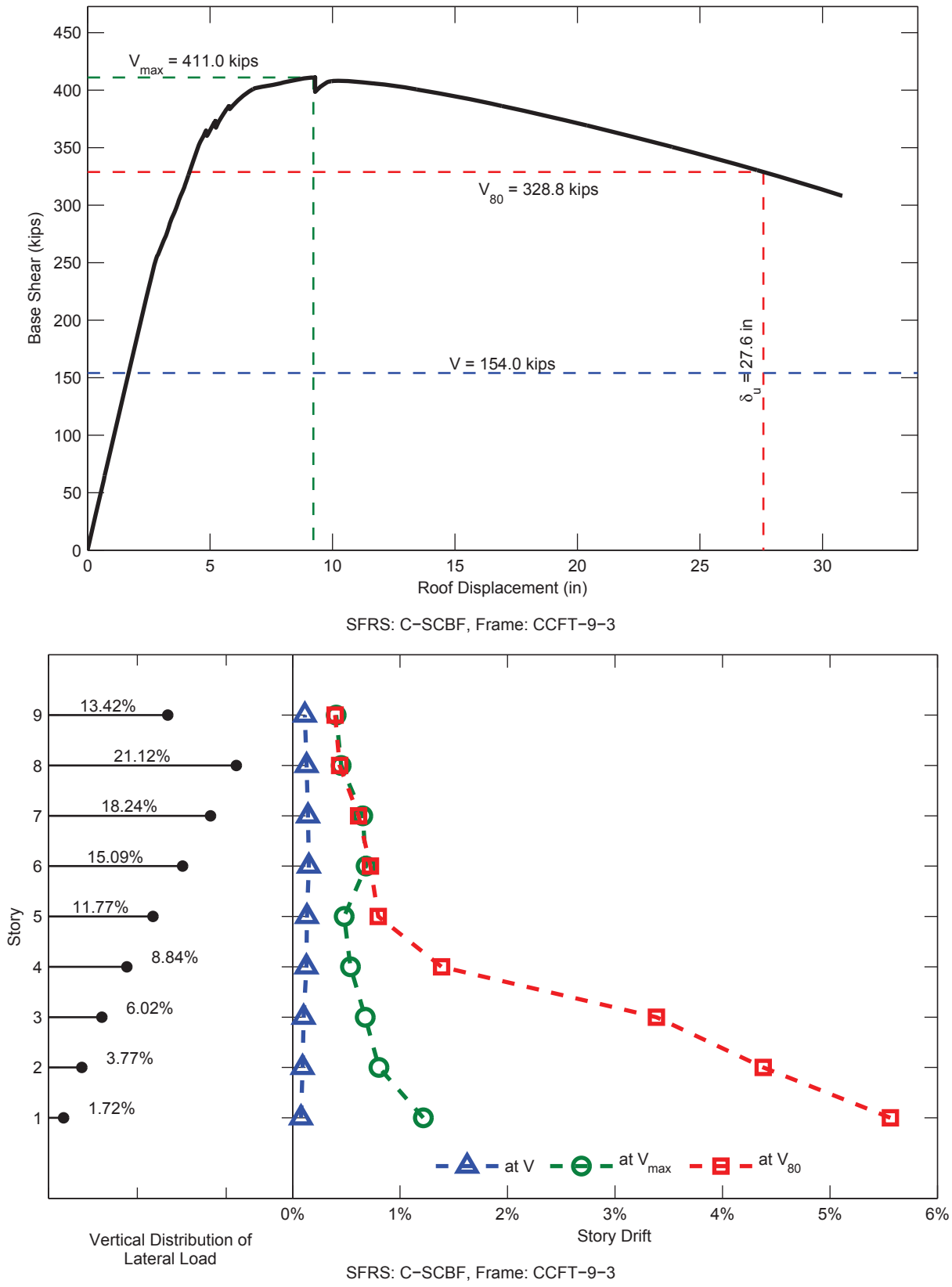

Figure C.54. Static Pushover Analysis Results: Frame CCFT-9-3

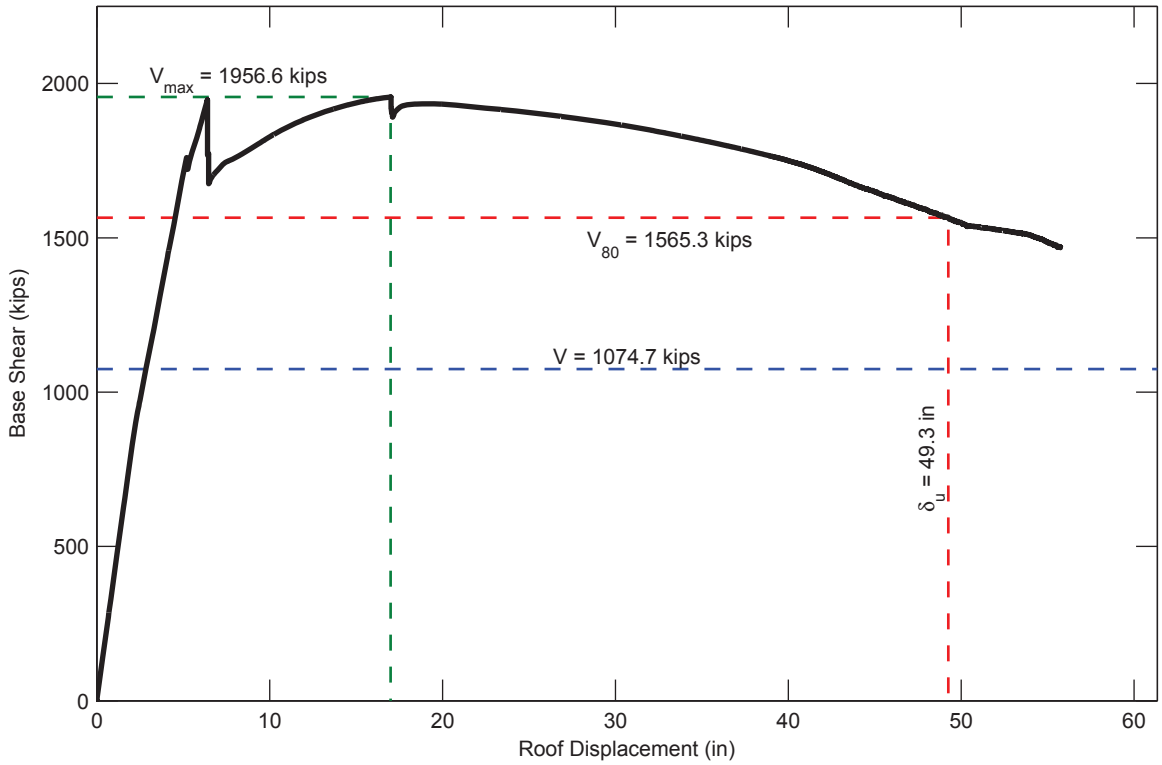

SFRS: C−SCBF, Frame: CCFT−9−5

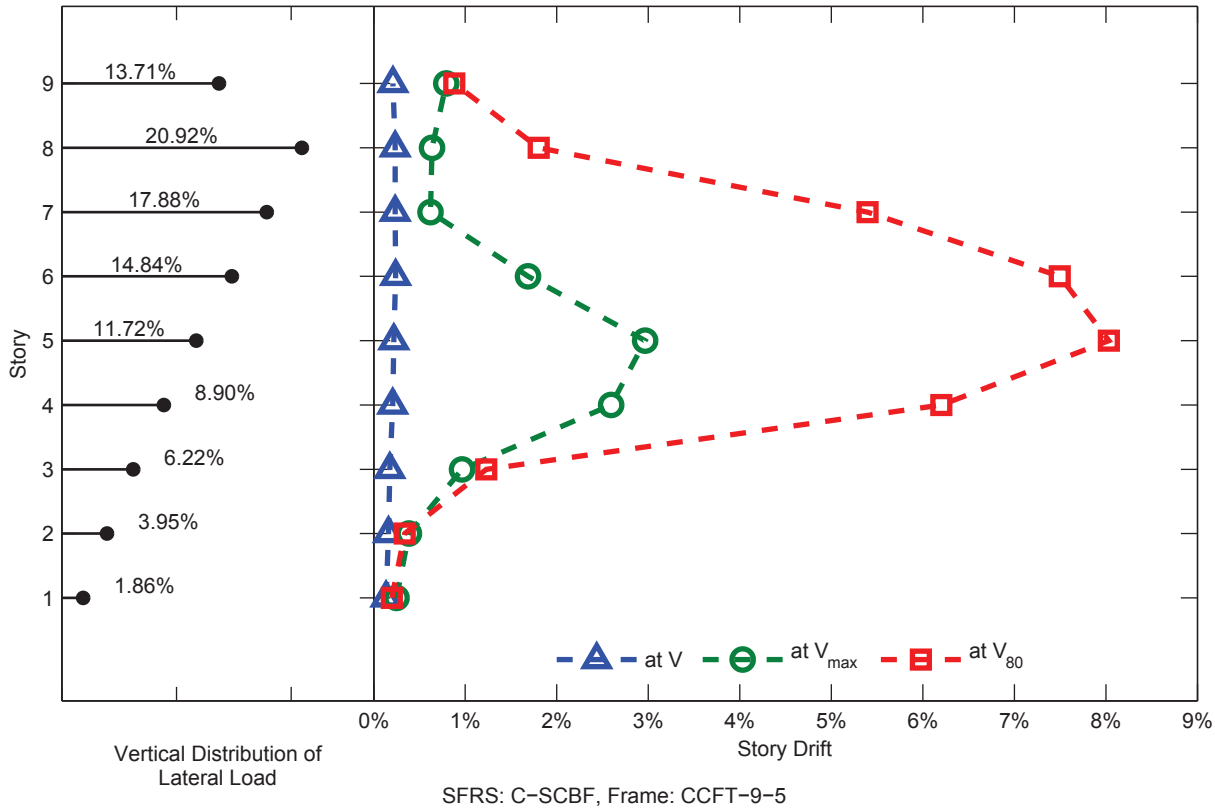

SFRS: C−SCBF, Frame: CCFT−9−5

Figure C.55. Static Pushover Analysis Results: Frame CCFT-9-5

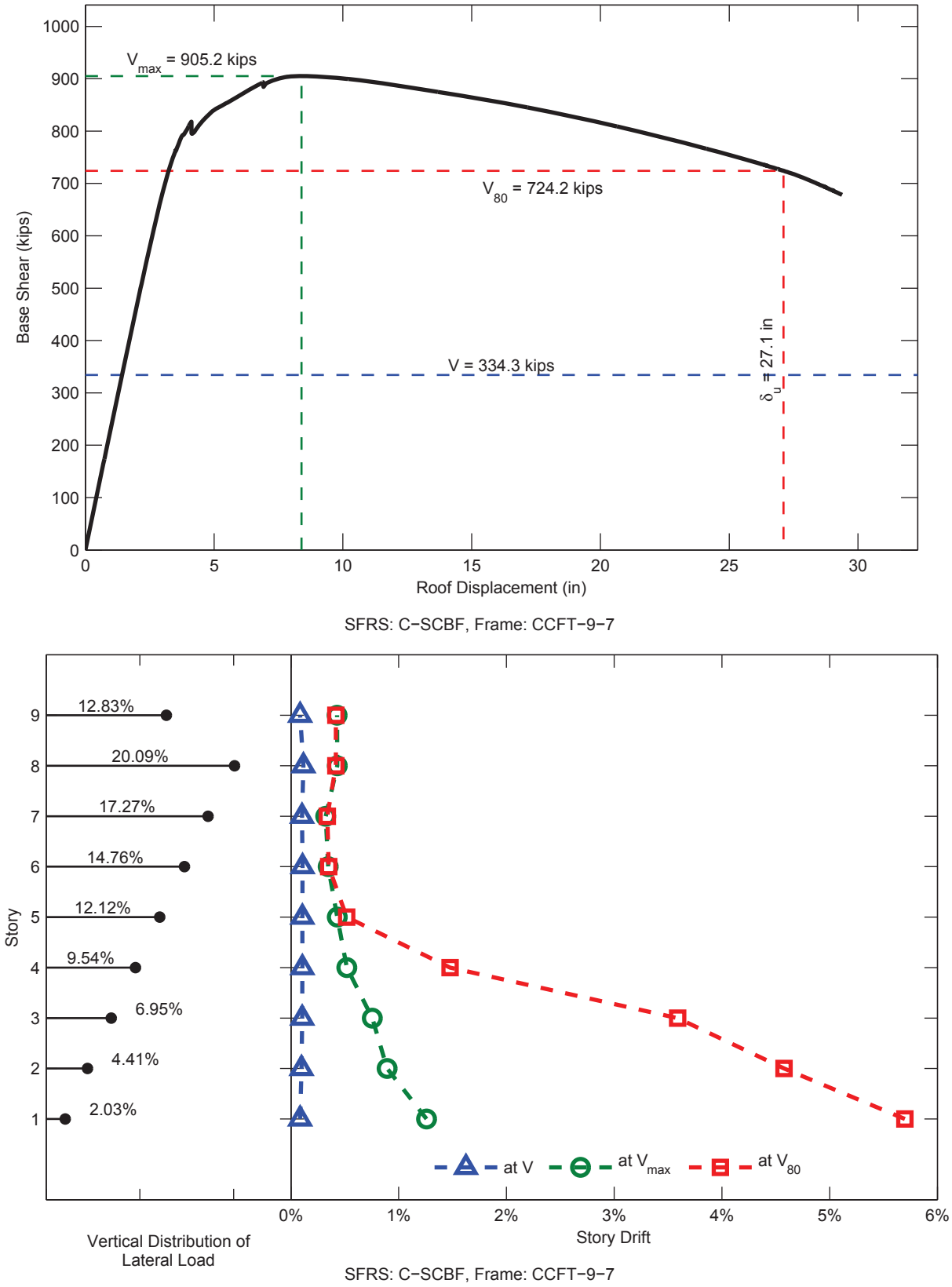

Figure C.56. Static Pushover Analysis Results: Frame CCFT-9-7

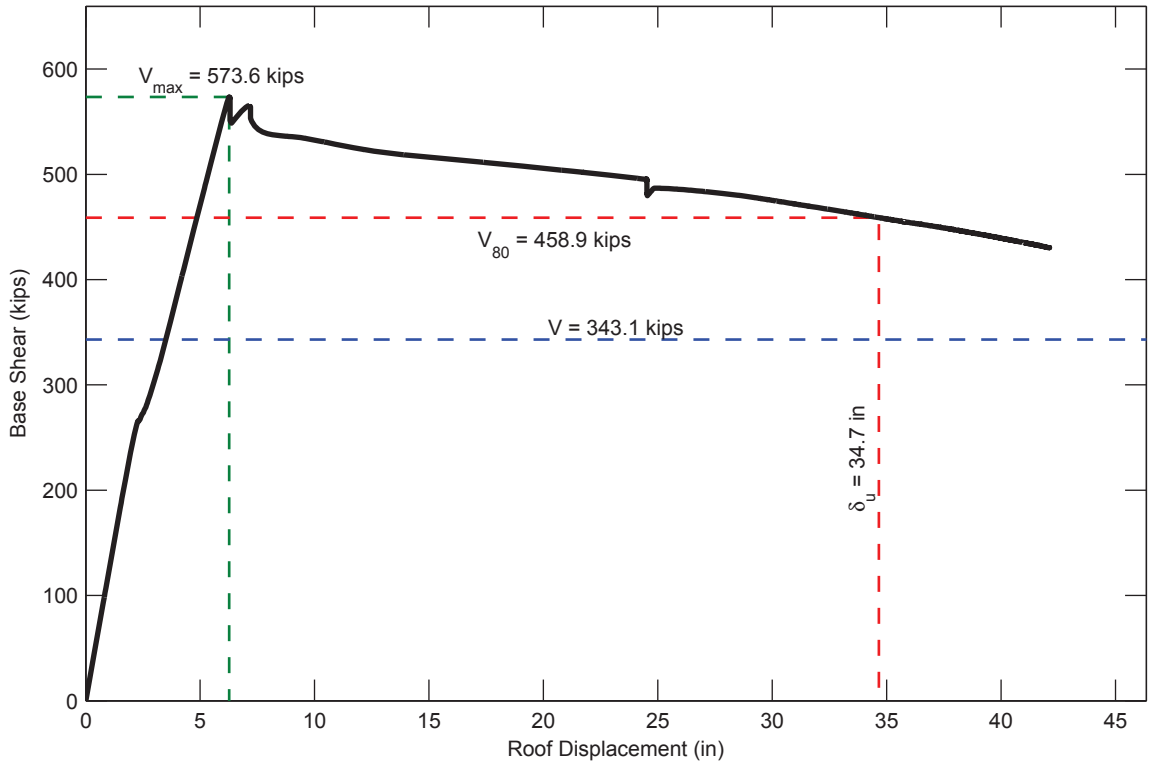

SFRS: C−SCBF, Frame: CCFT−9−9

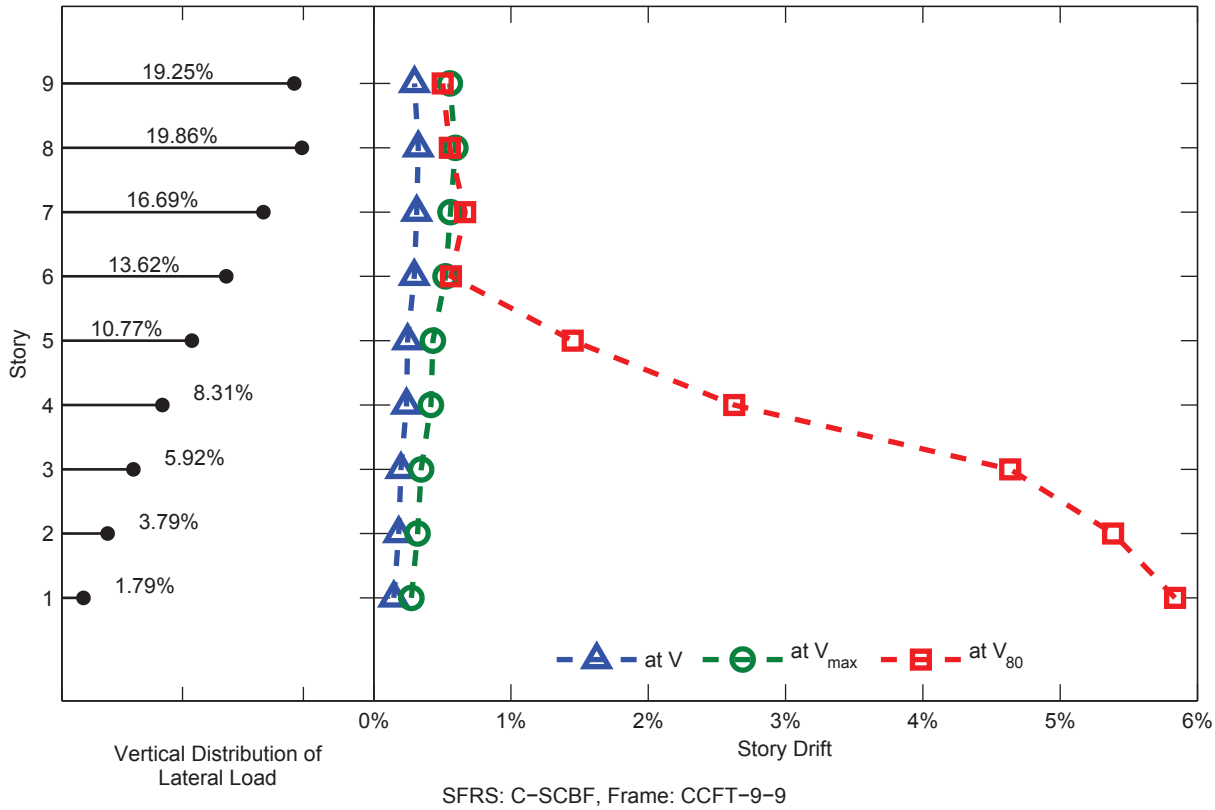

SFRS: C−SCBF, Frame: CCFT−9−9

Figure C.57. Static Pushover Analysis Results: Frame CCFT-9-9

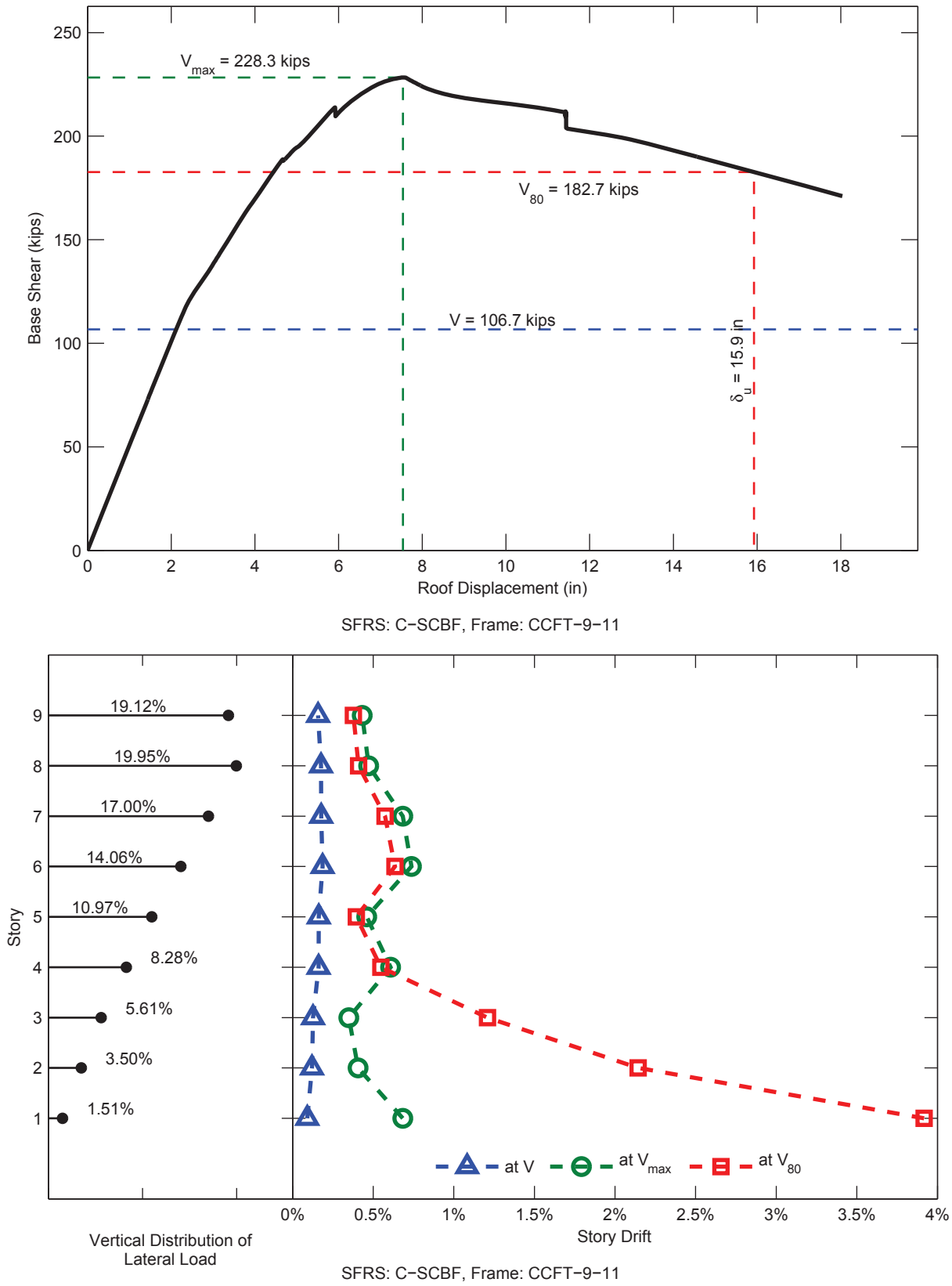

Figure C.58. Static Pushover Analysis Results: Frame CCFT-9-11

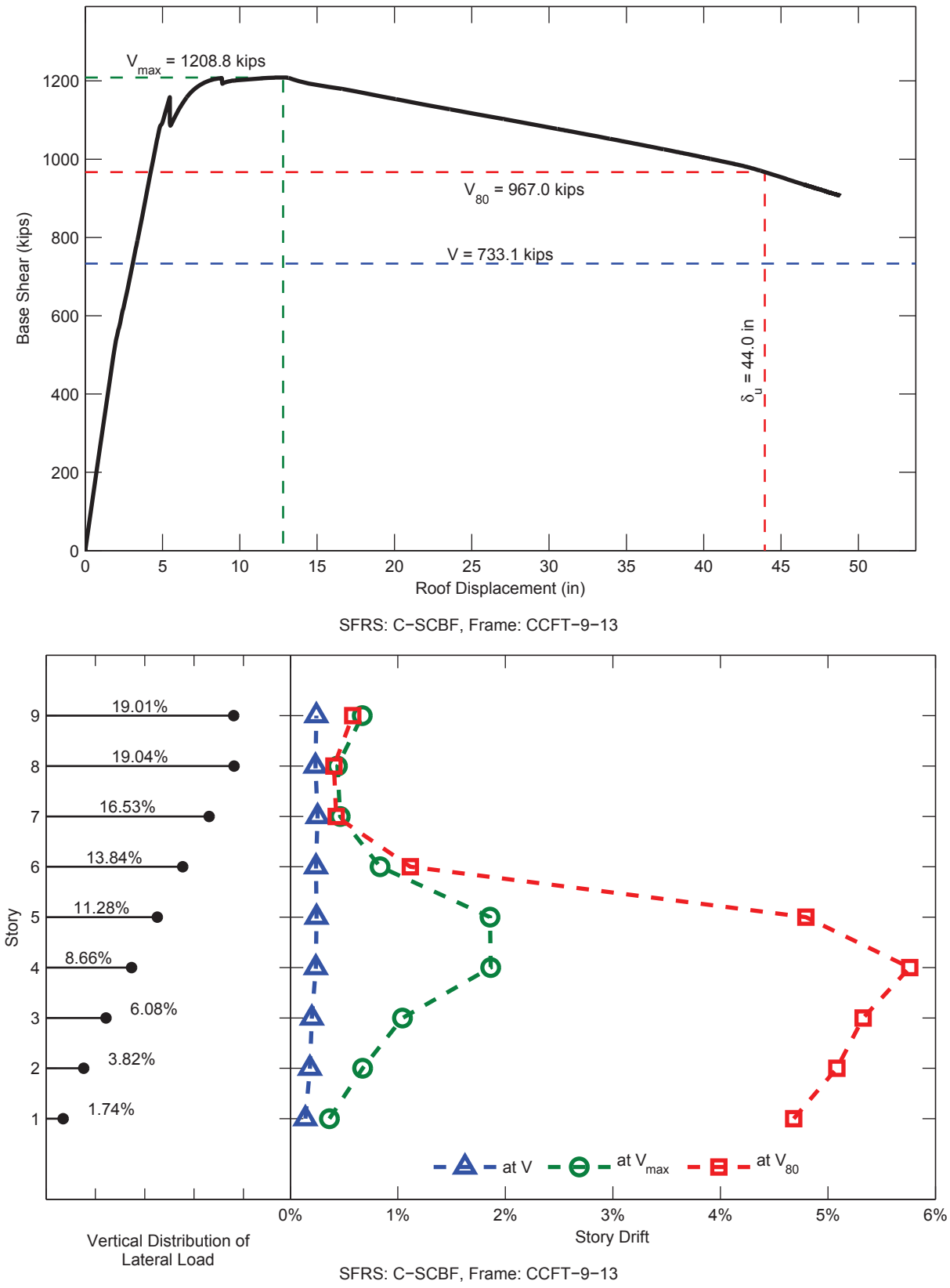

Figure C.59. Static Pushover Analysis Results: Frame CCFT-9-13

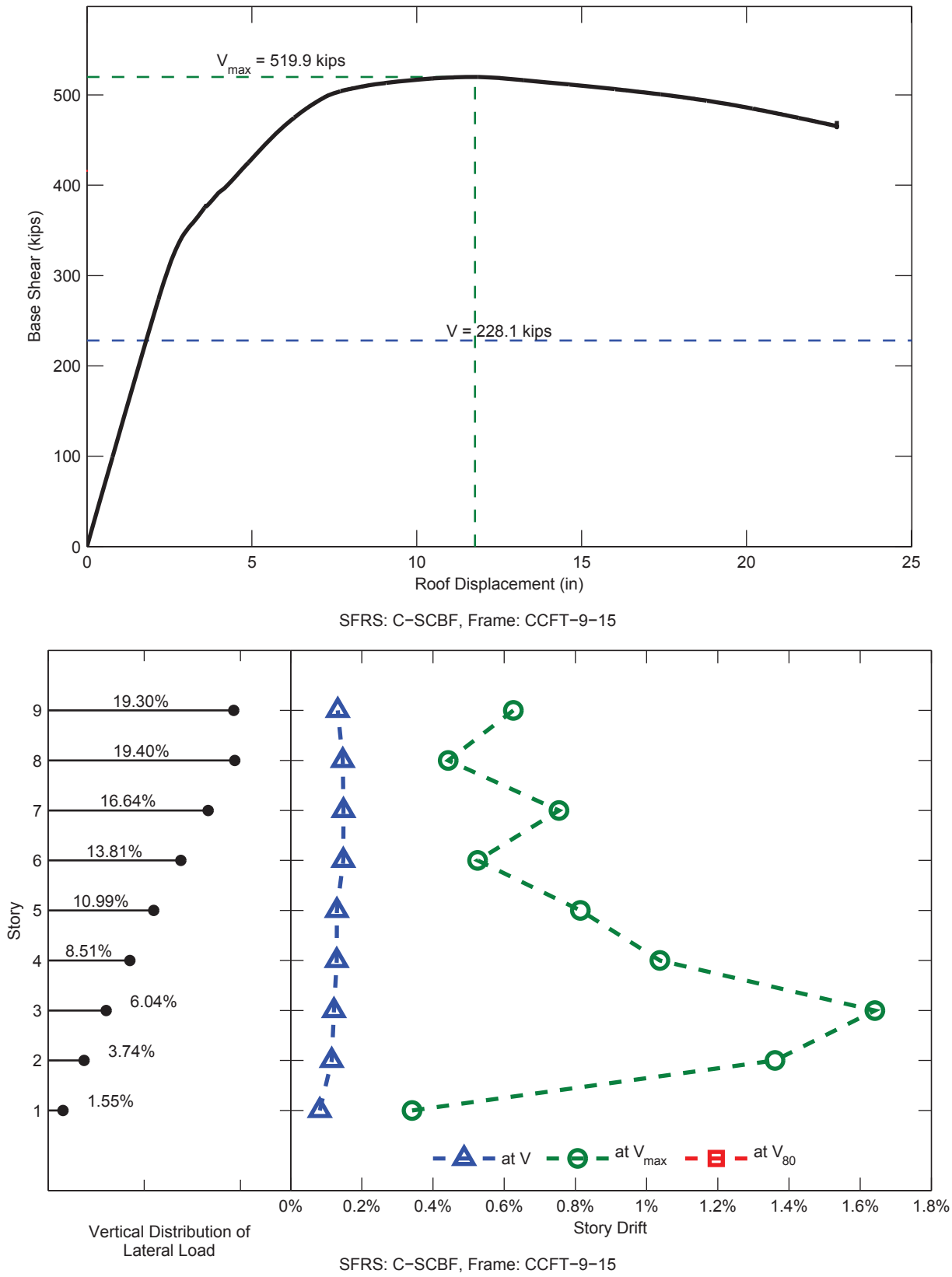

Figure C.60. Static Pushover Analysis Results: Frame CCFT-9-15

C.2 Dynamic Response History Analysis Results

Results of the dynamic response history analyses for each frame are shown in the following figures. The results include:

- Incremental dynamic analysis curves, showing peak story drift ratios obtained from individual time history analyses for different ground motions (each line) and different scale factors (each point).
- Identification of the median collapse intensity, $\hat{S}_{CT}$, computed as described in Chapter 8 as the intensity, S_T, at which half of the ground motions cause peak story drift ratios of 5%.
- Identification of the maximum considered earthquake intensity, S_{MT}, computed as described in Chapter 8 and used as the basis for determining the collapse margin ratio, CMR = $\hat{S}_{CT}/S_{MT}$.
- Maximum story drift ratios for each ground motion scaled to the maximum considered earthquake intensity (i.e. $SF_2 = 1.0$).
- The median and 84th percentile of the maximum story drifts ratios, showing the distribution of inelasticity within each frame.

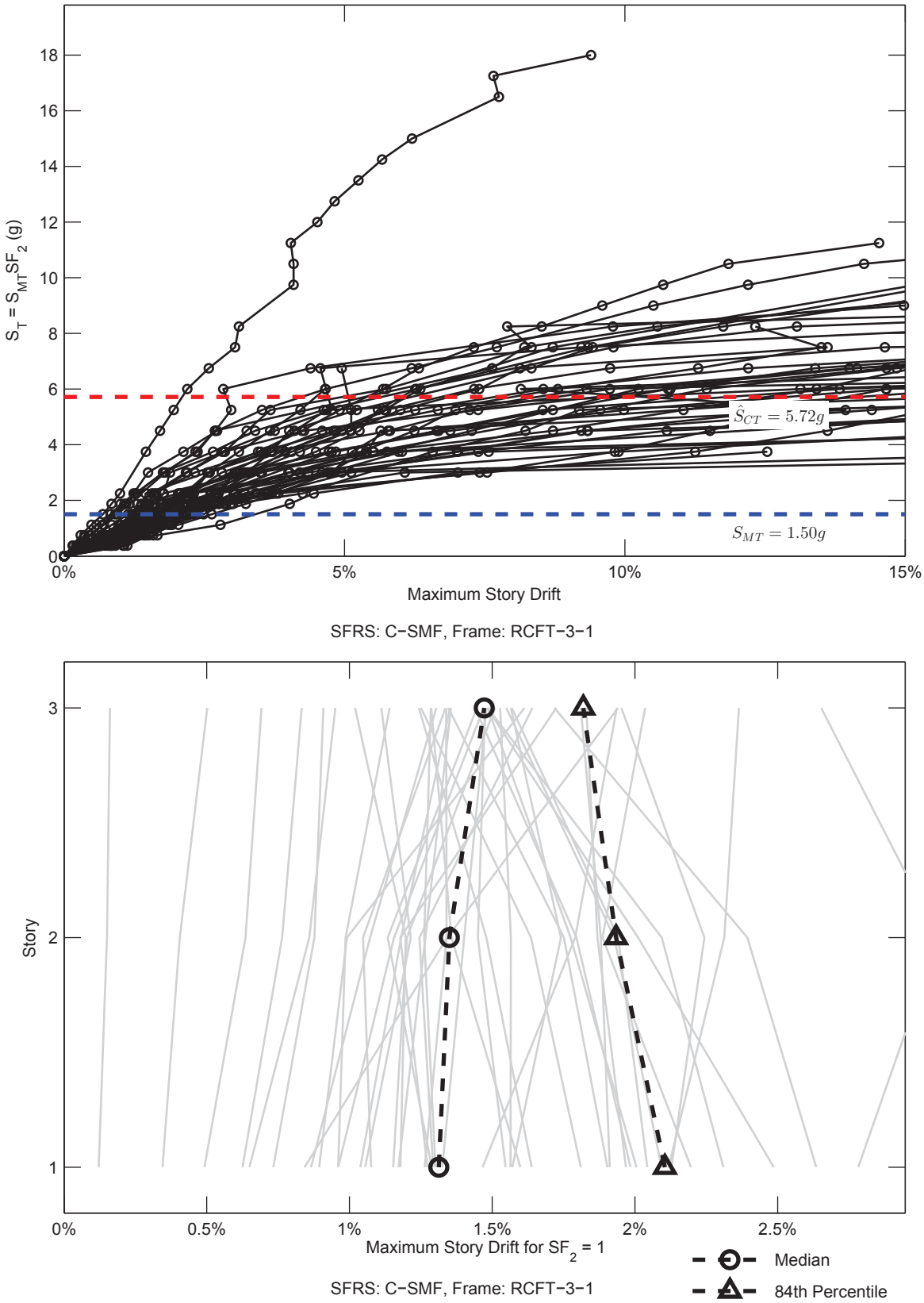

Figure C.61. Dynamic Response History Analysis Results: Frame RCFT-3-1

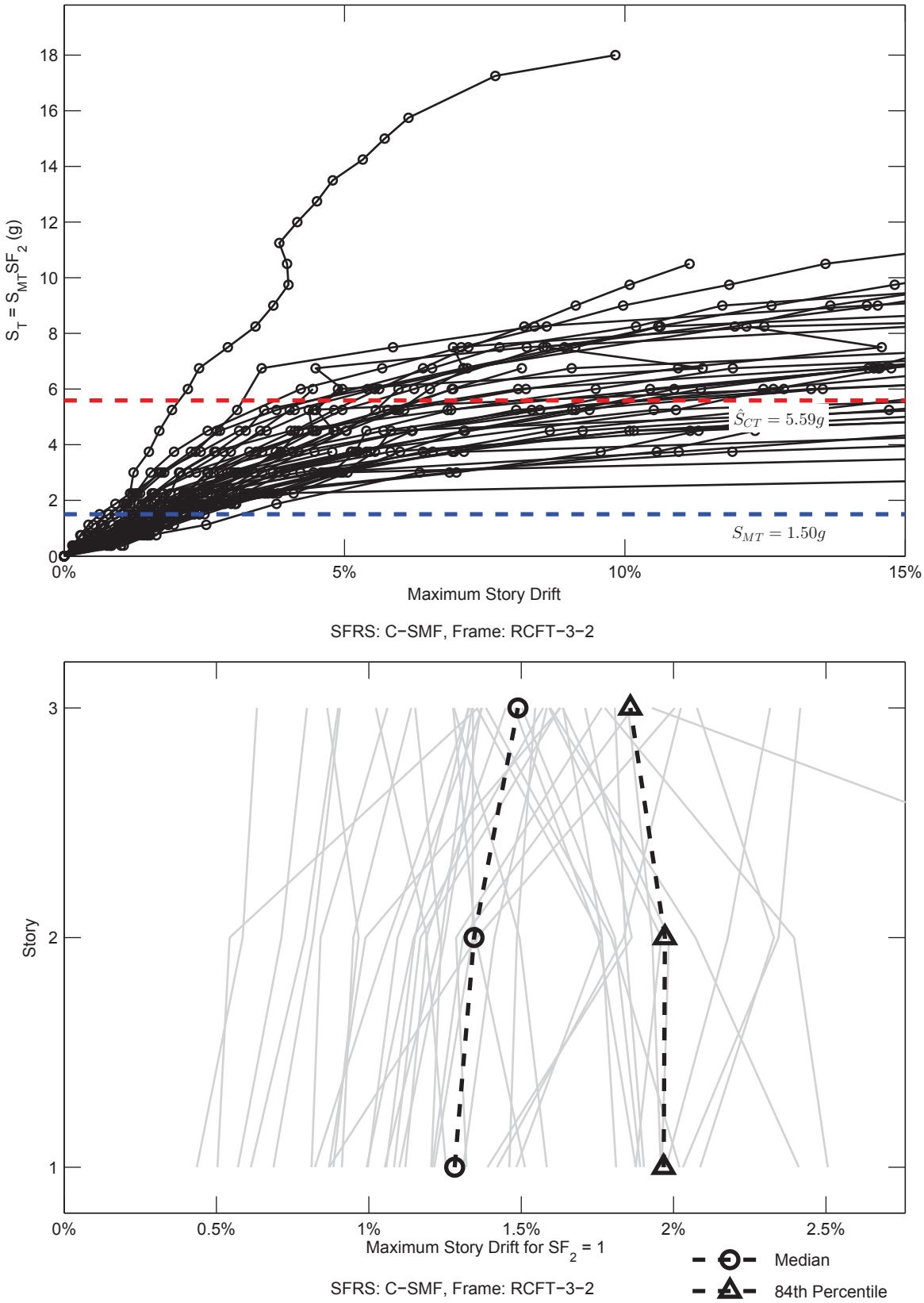

Figure C.62. Dynamic Response History Analysis Results: Frame RCFT-3-2

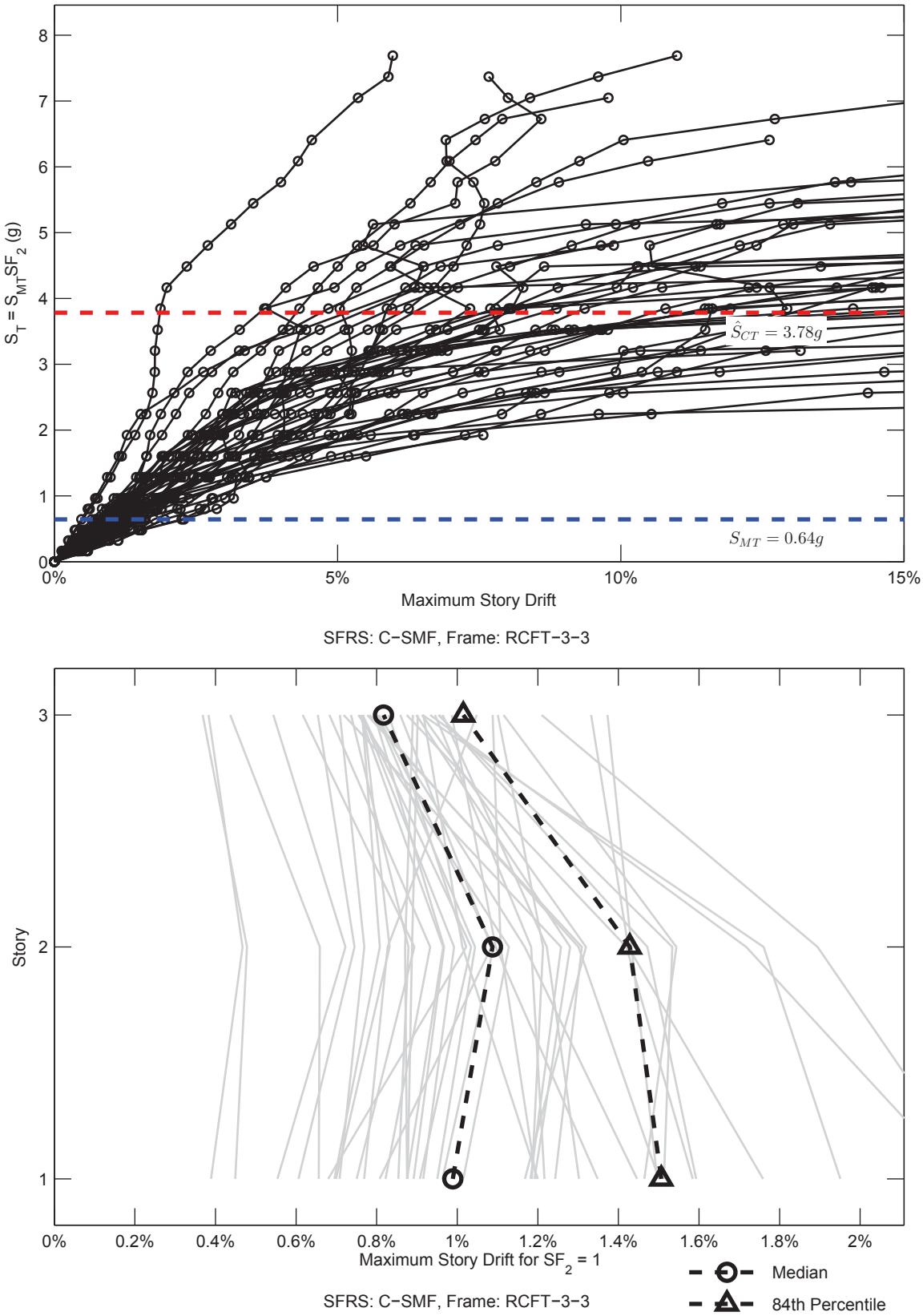

Figure C.63. Dynamic Response History Analysis Results: Frame RCFT-3-3

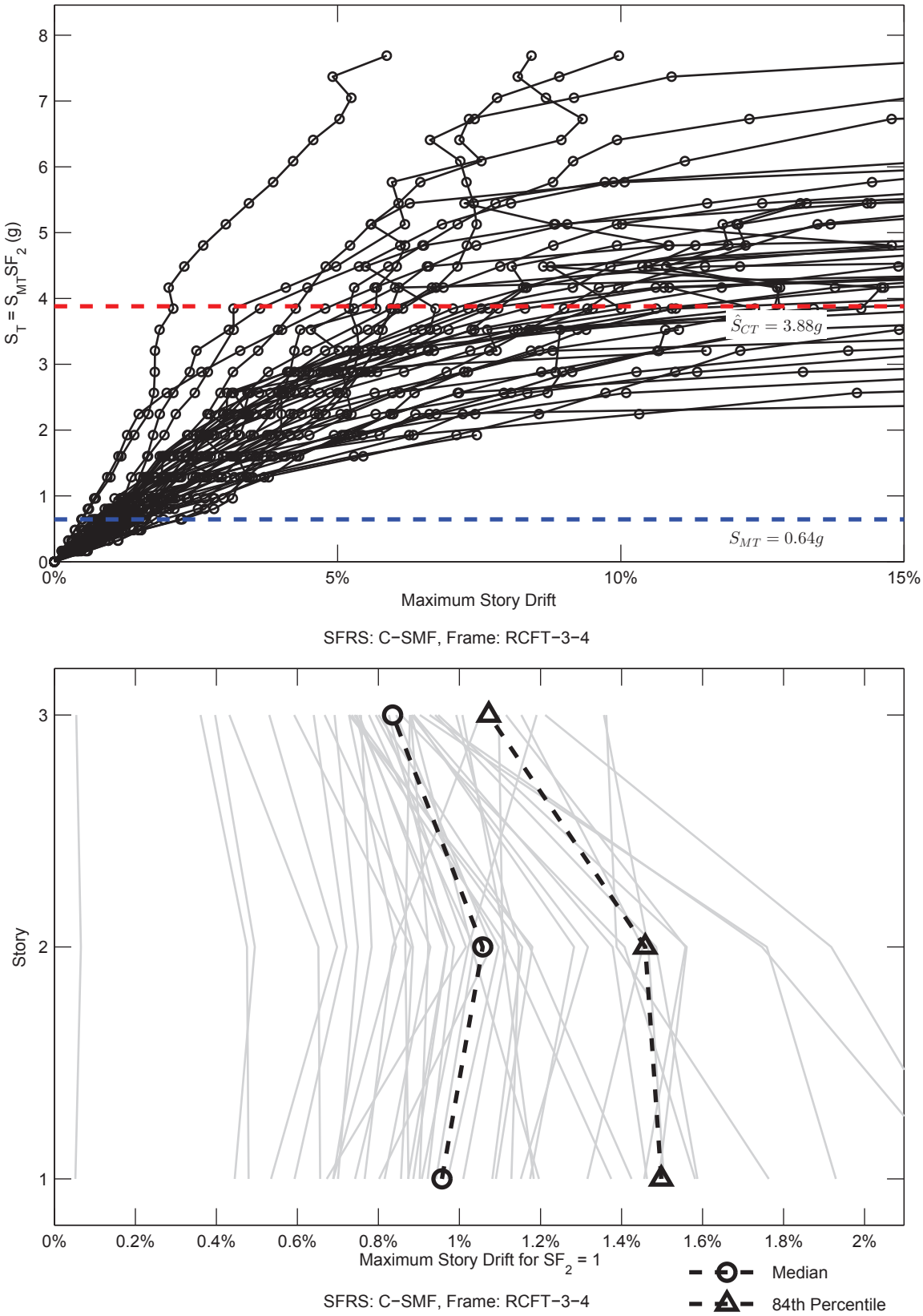

Figure C.64. Dynamic Response History Analysis Results: Frame RCFT-3-4

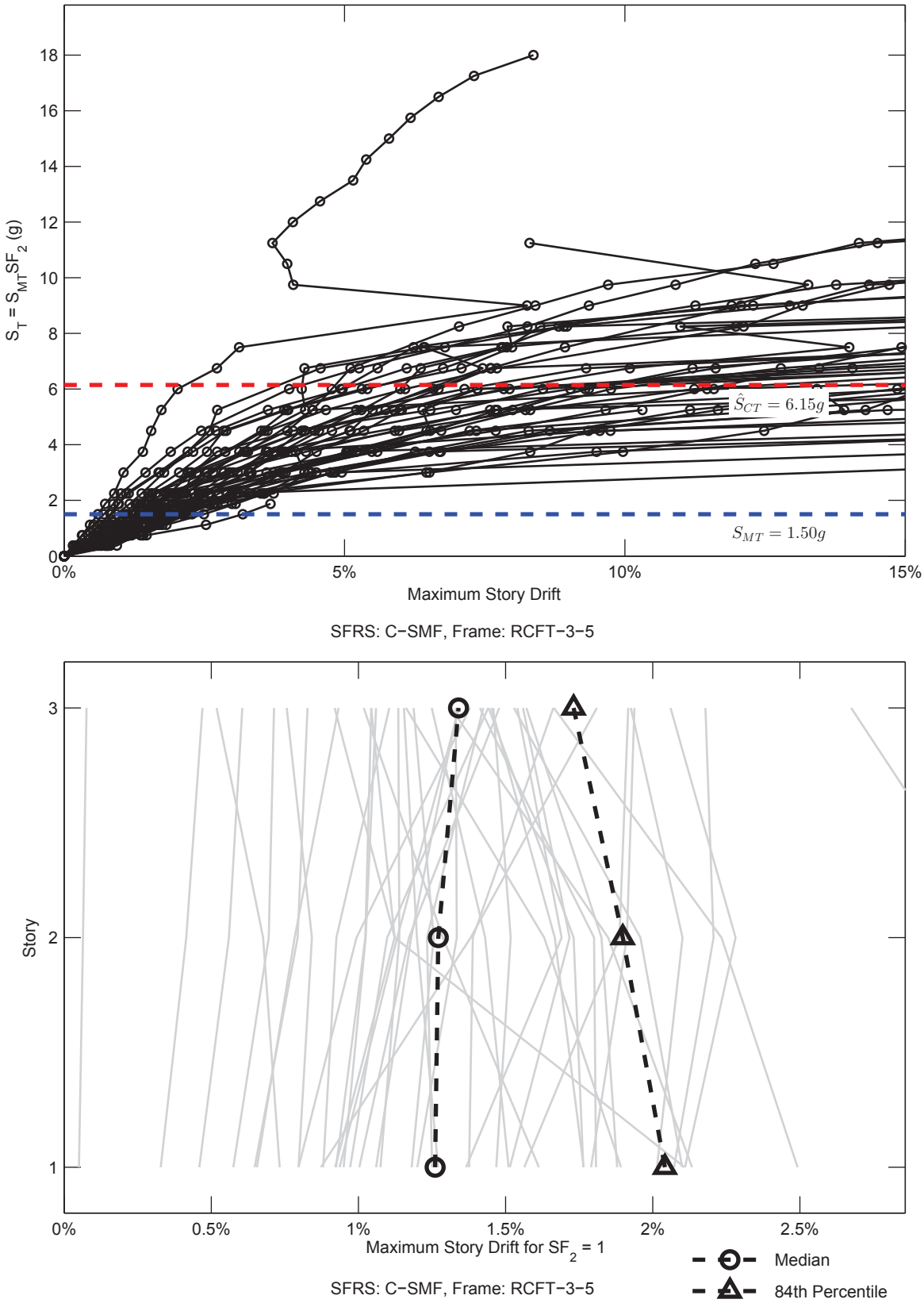

Figure C.65. Dynamic Response History Analysis Results: Frame RCFT-3-5

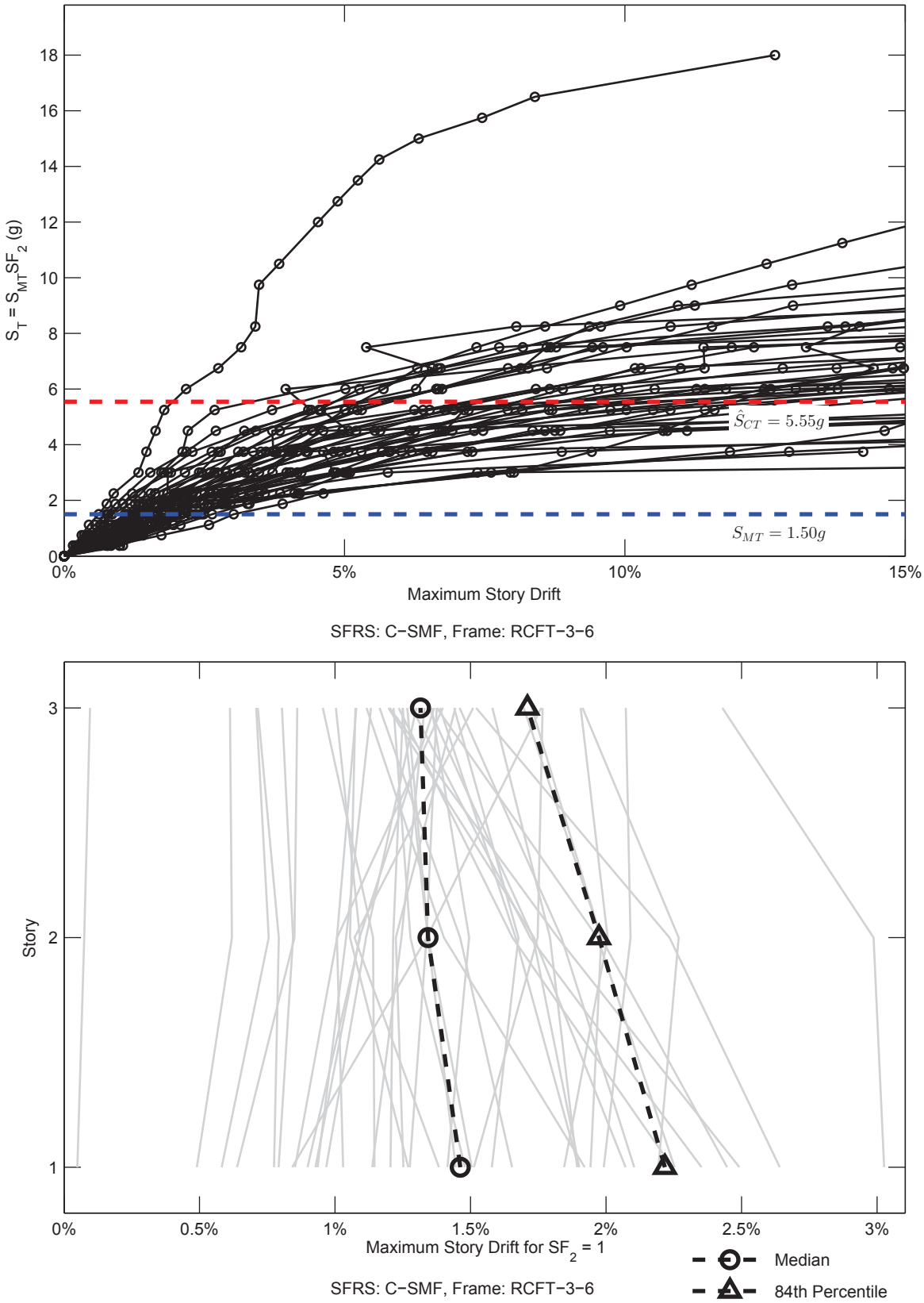

Figure C.66. Dynamic Response History Analysis Results: Frame RCFT-3-6

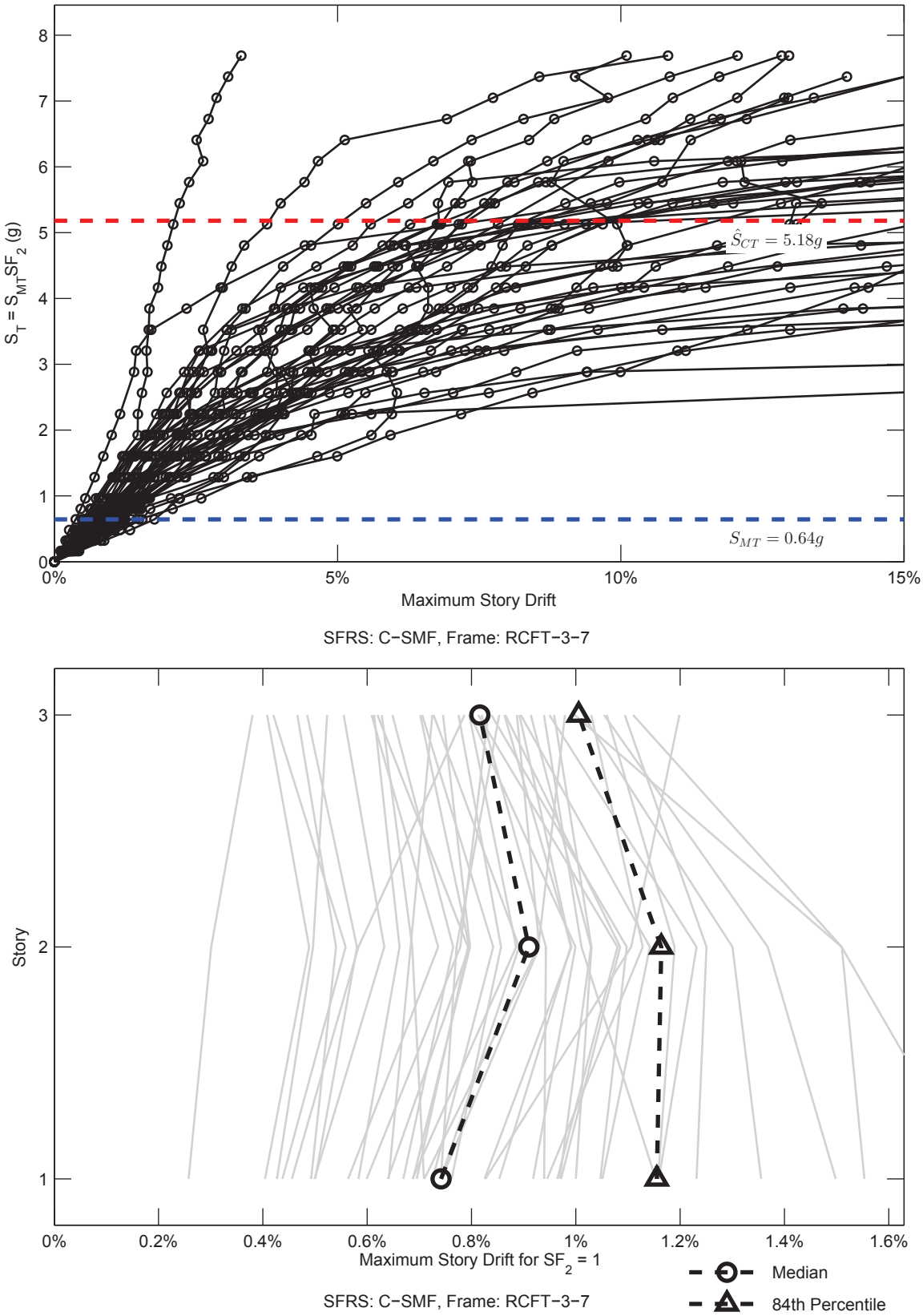

Figure C.67. Dynamic Response History Analysis Results: Frame RCFT-3-7

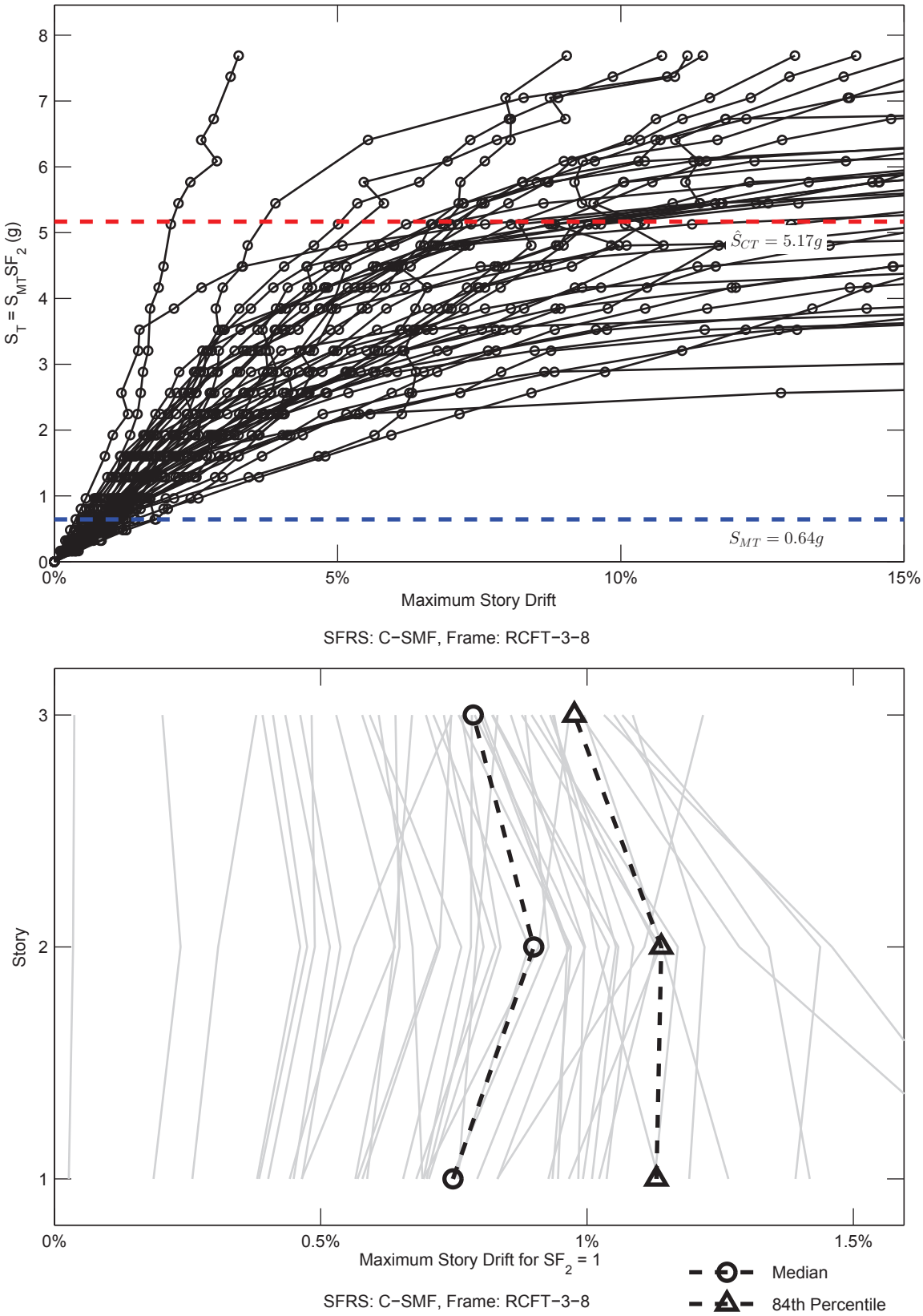

Figure C.68. Dynamic Response History Analysis Results: Frame RCFT-3-8

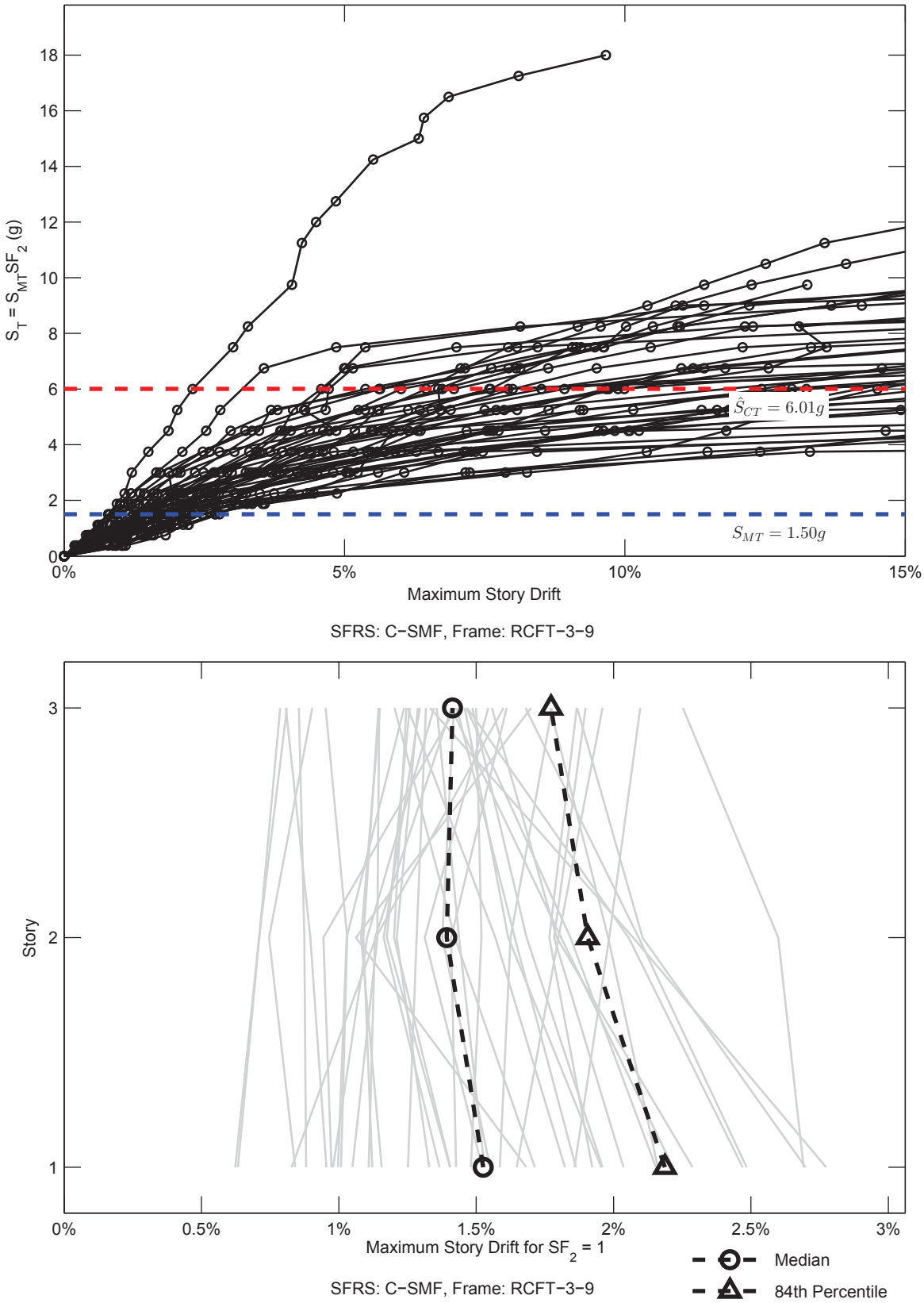

Figure C.69. Dynamic Response History Analysis Results: Frame RCFT-3-9

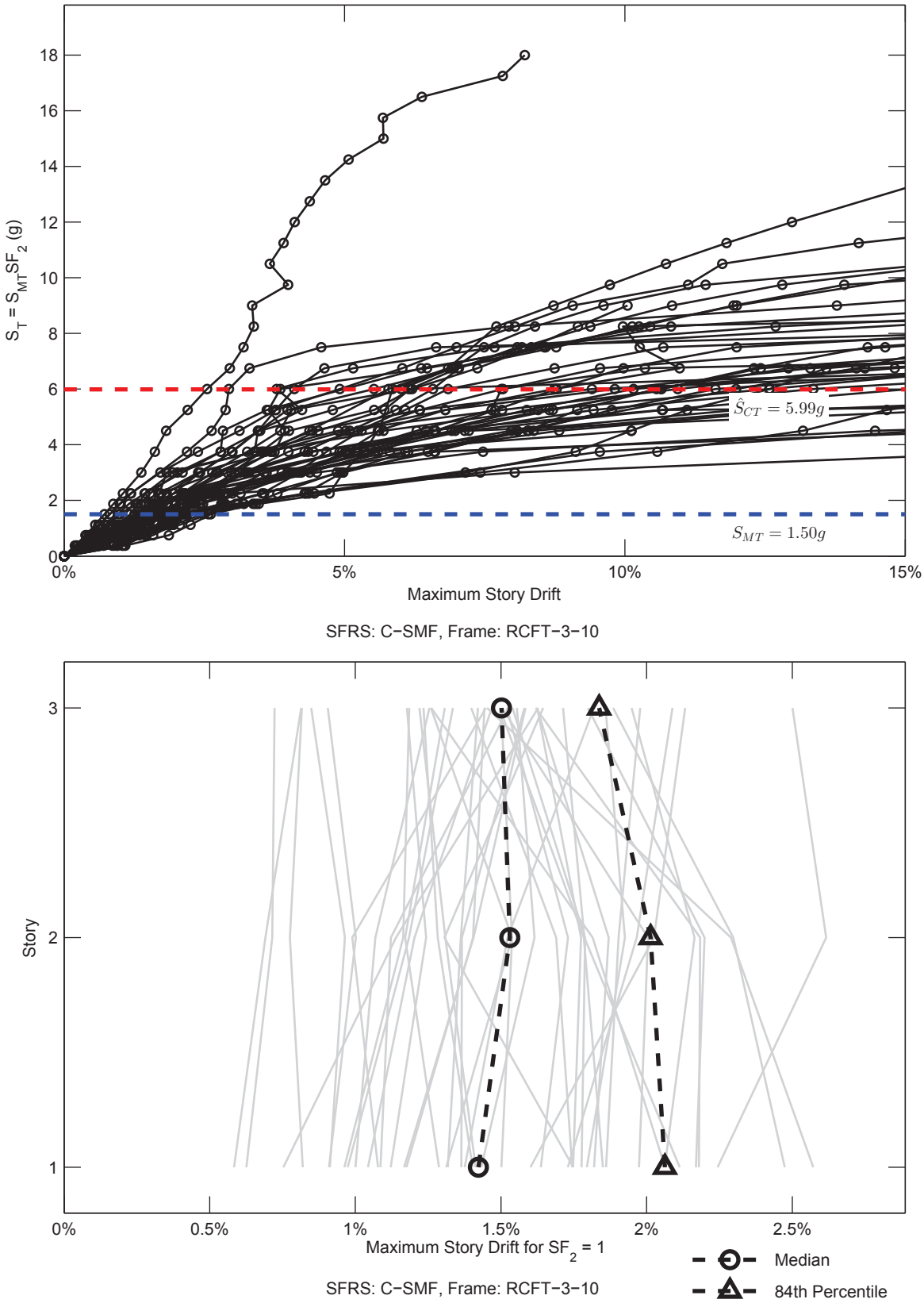

Figure C.70. Dynamic Response History Analysis Results: Frame RCFT-3-10

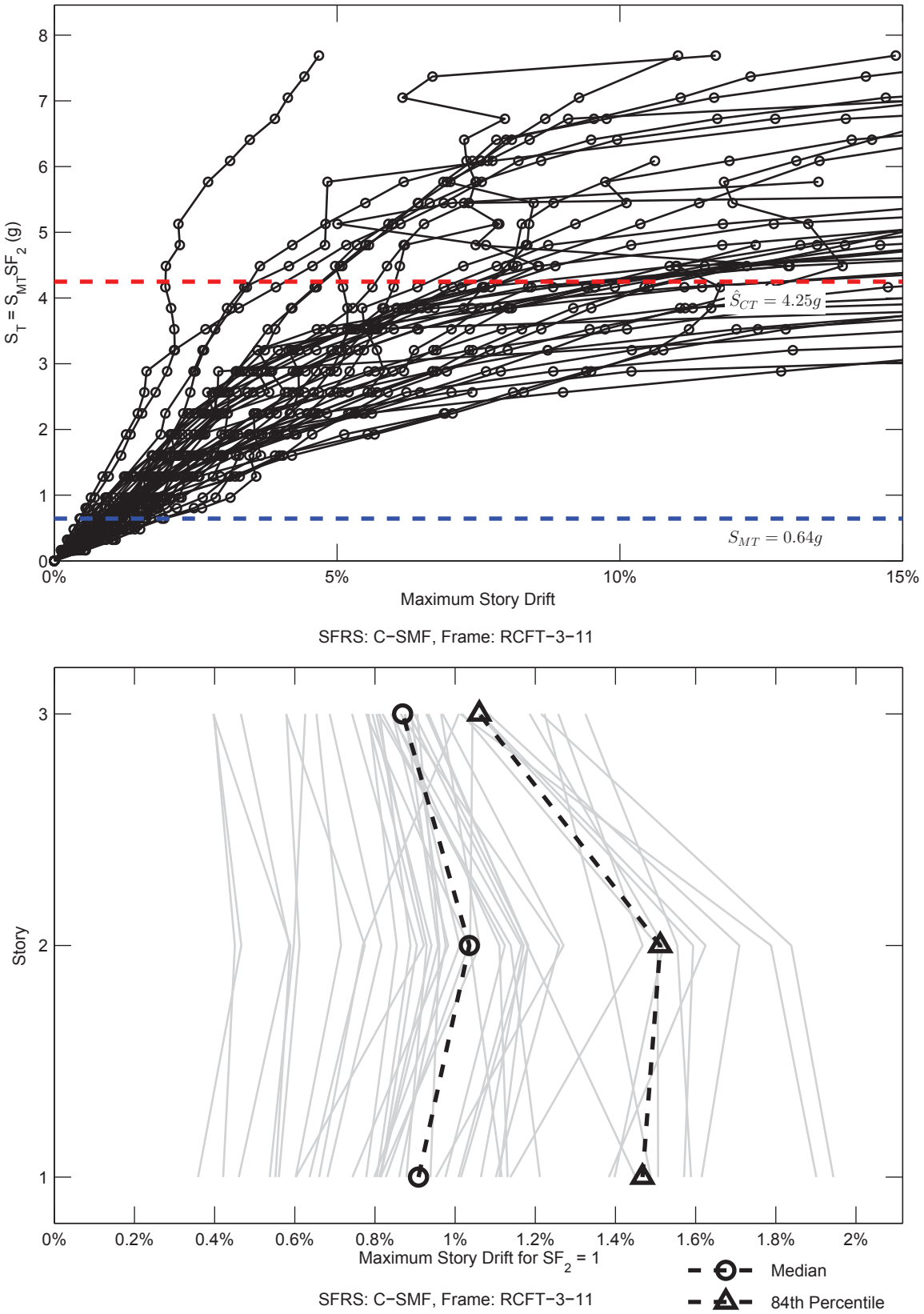

Figure C.71. Dynamic Response History Analysis Results: Frame RCFT-3-11

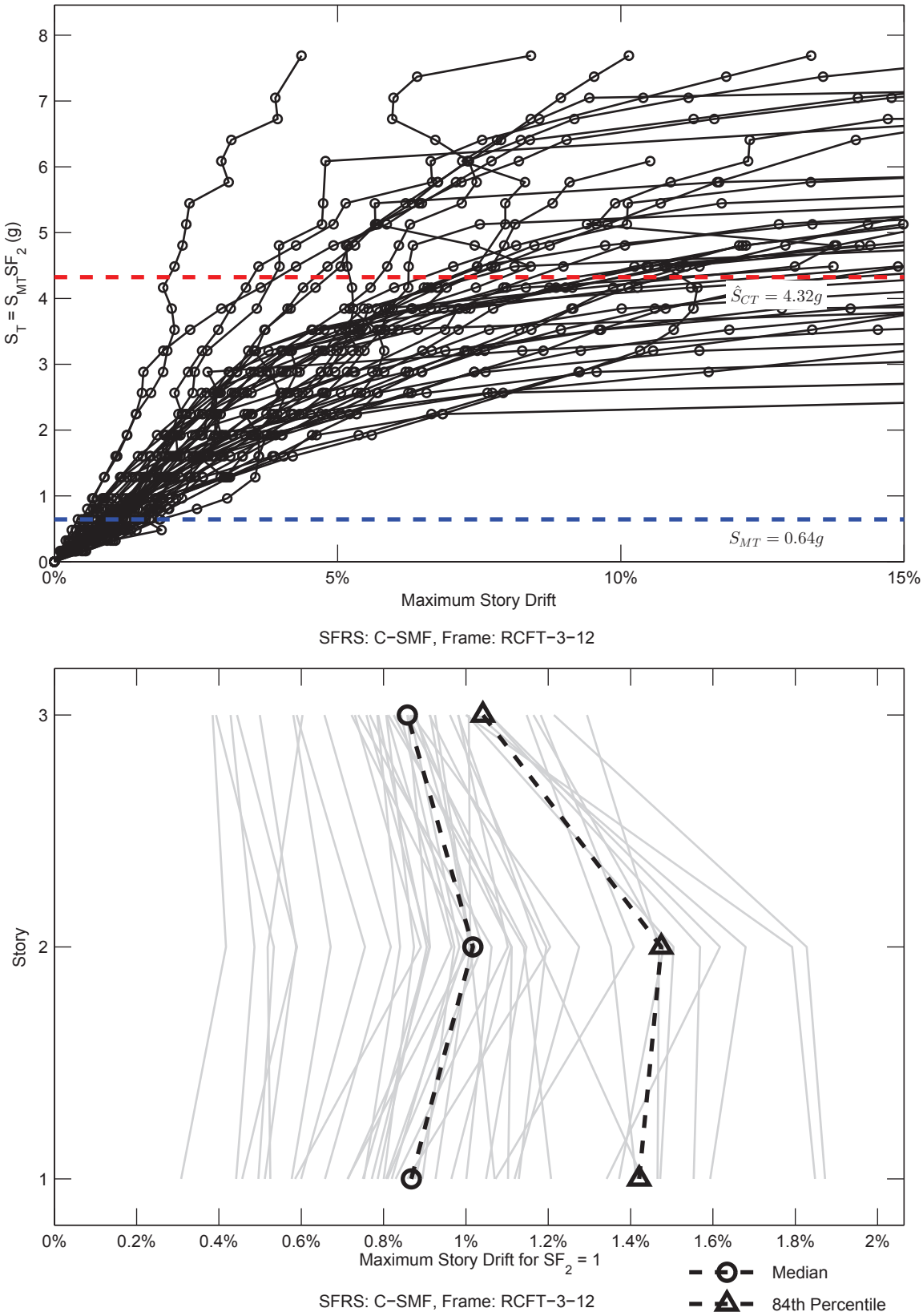

Figure C.72. Dynamic Response History Analysis Results: Frame RCFT-3-12

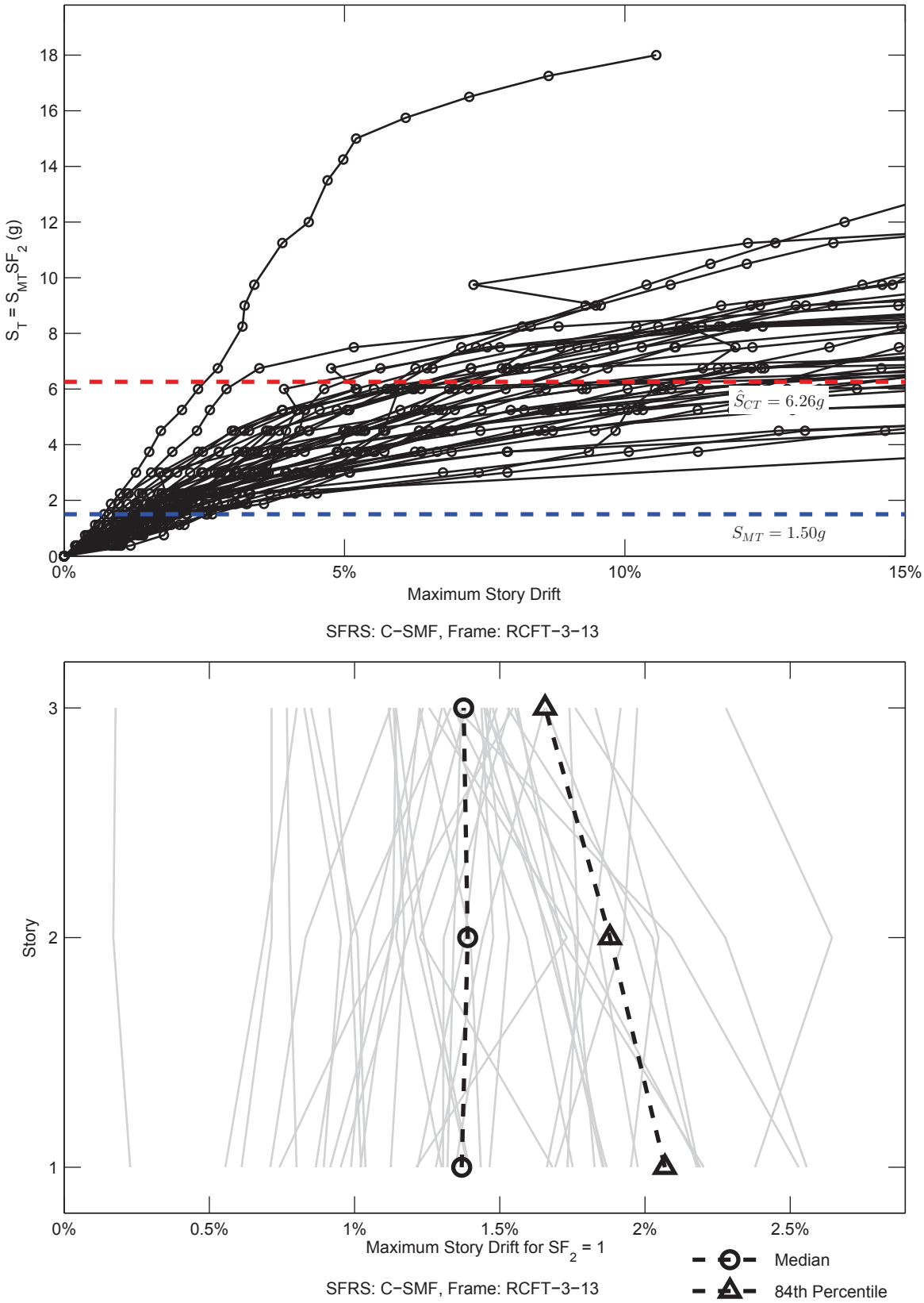

Figure C.73. Dynamic Response History Analysis Results: Frame RCFT-3-13

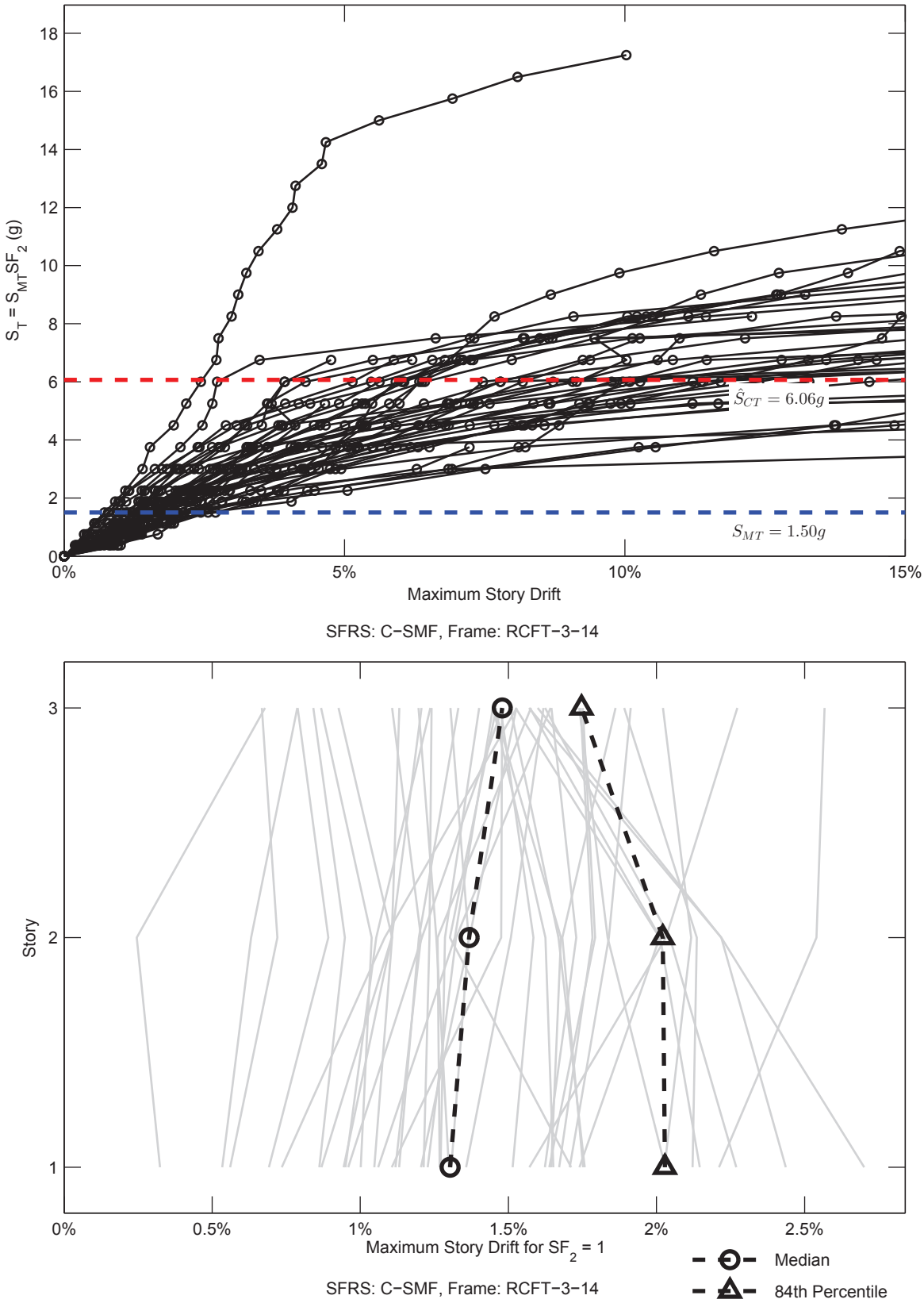

Figure C.74. Dynamic Response History Analysis Results: Frame RCFT-3-14

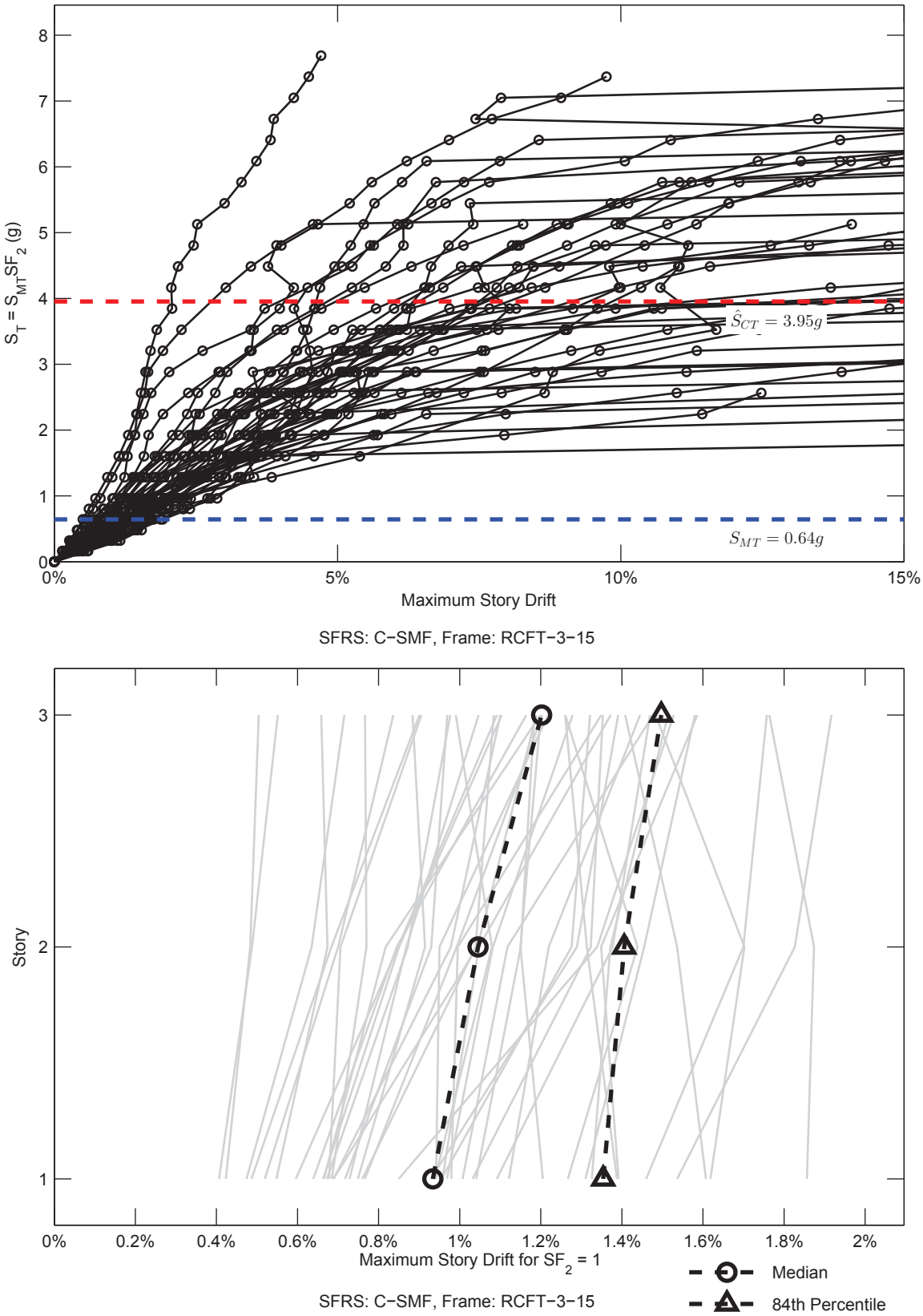

Figure C.75. Dynamic Response History Analysis Results: Frame RCFT-3-15

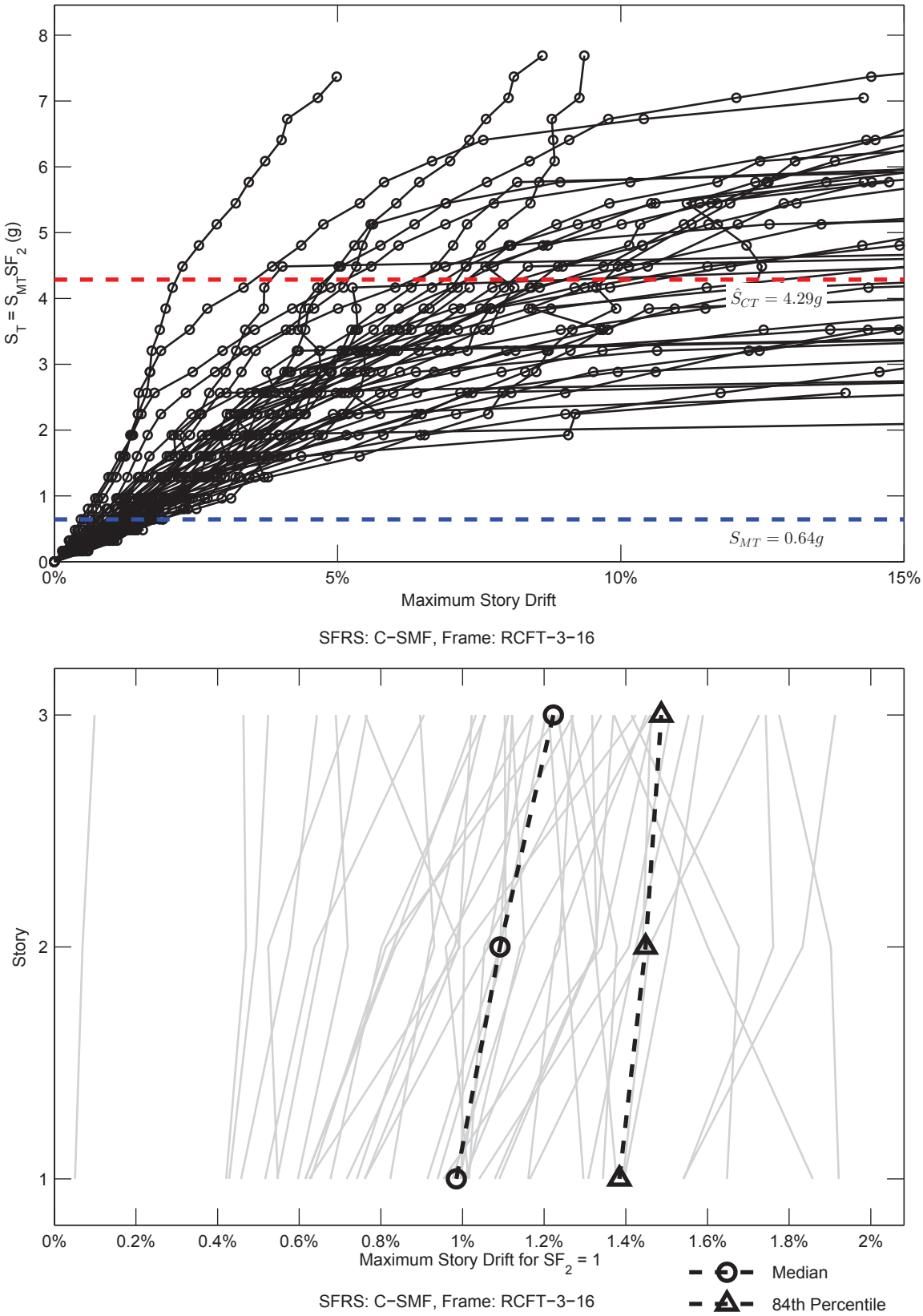

Figure C.76. Dynamic Response History Analysis Results: Frame RCFT-3-16

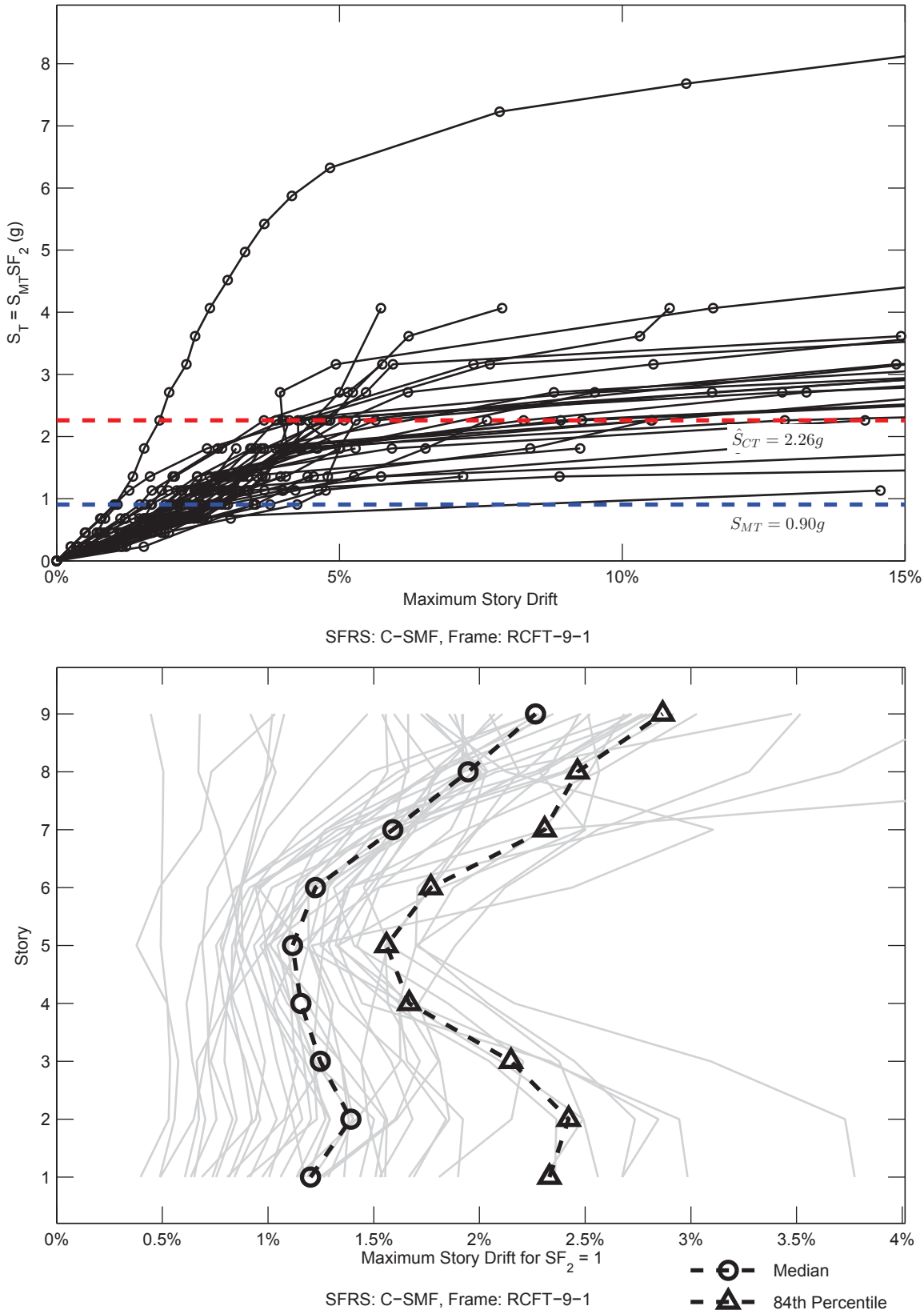

Figure C.77. Dynamic Response History Analysis Results: Frame RCFT-9-1

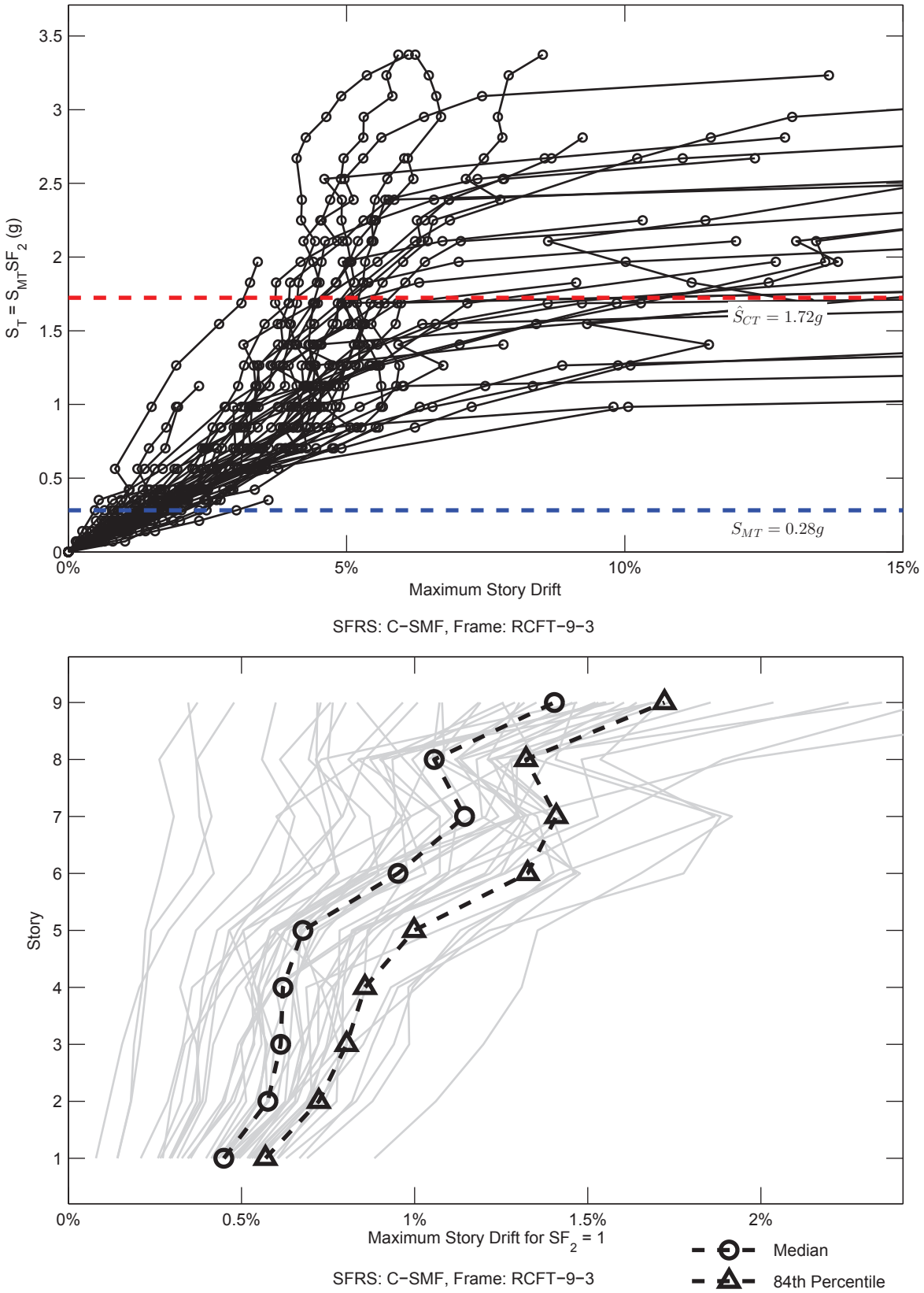

Figure C.78. Dynamic Response History Analysis Results: Frame RCFT-9-3

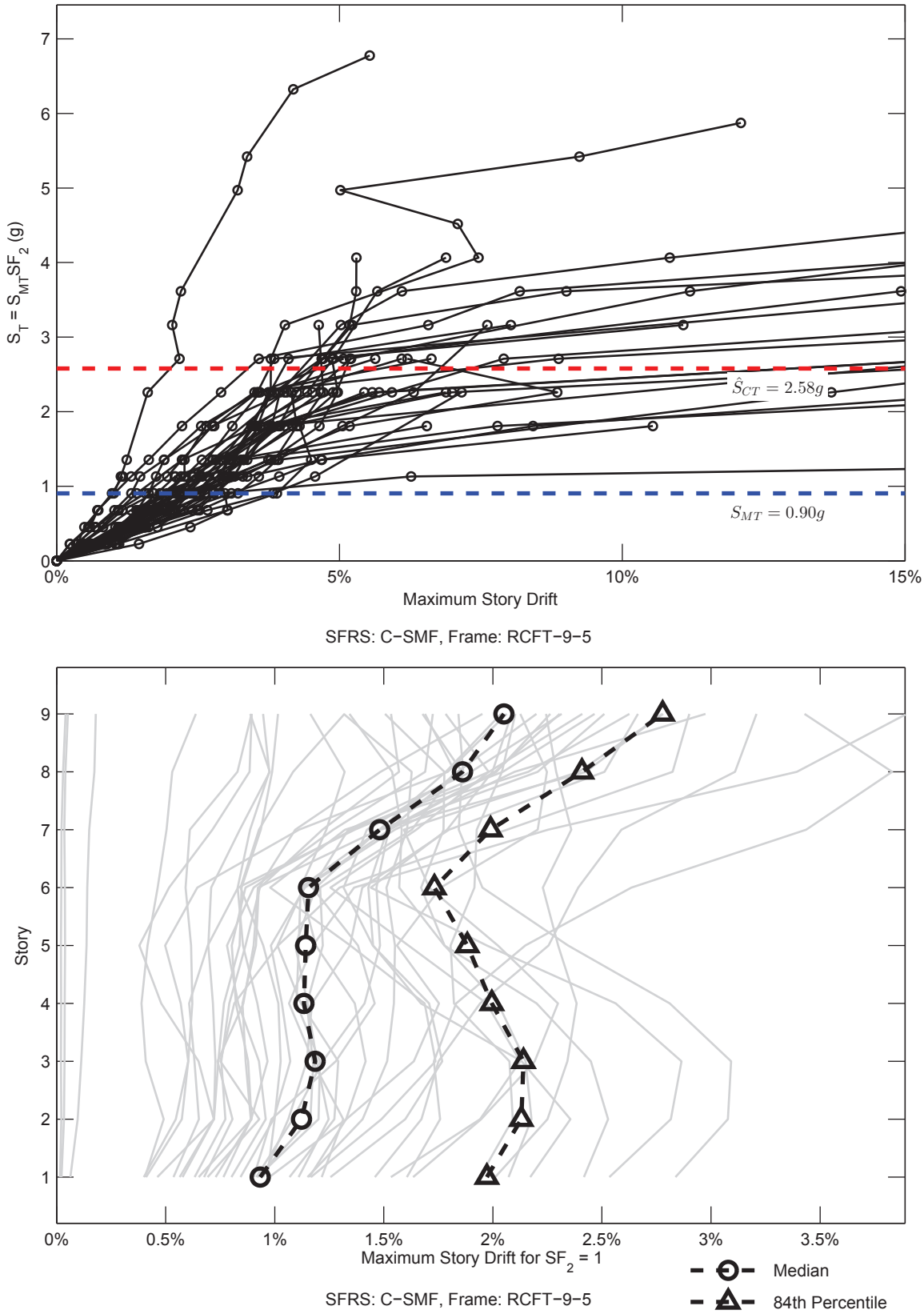

Figure C.79. Dynamic Response History Analysis Results: Frame RCFT-9-5

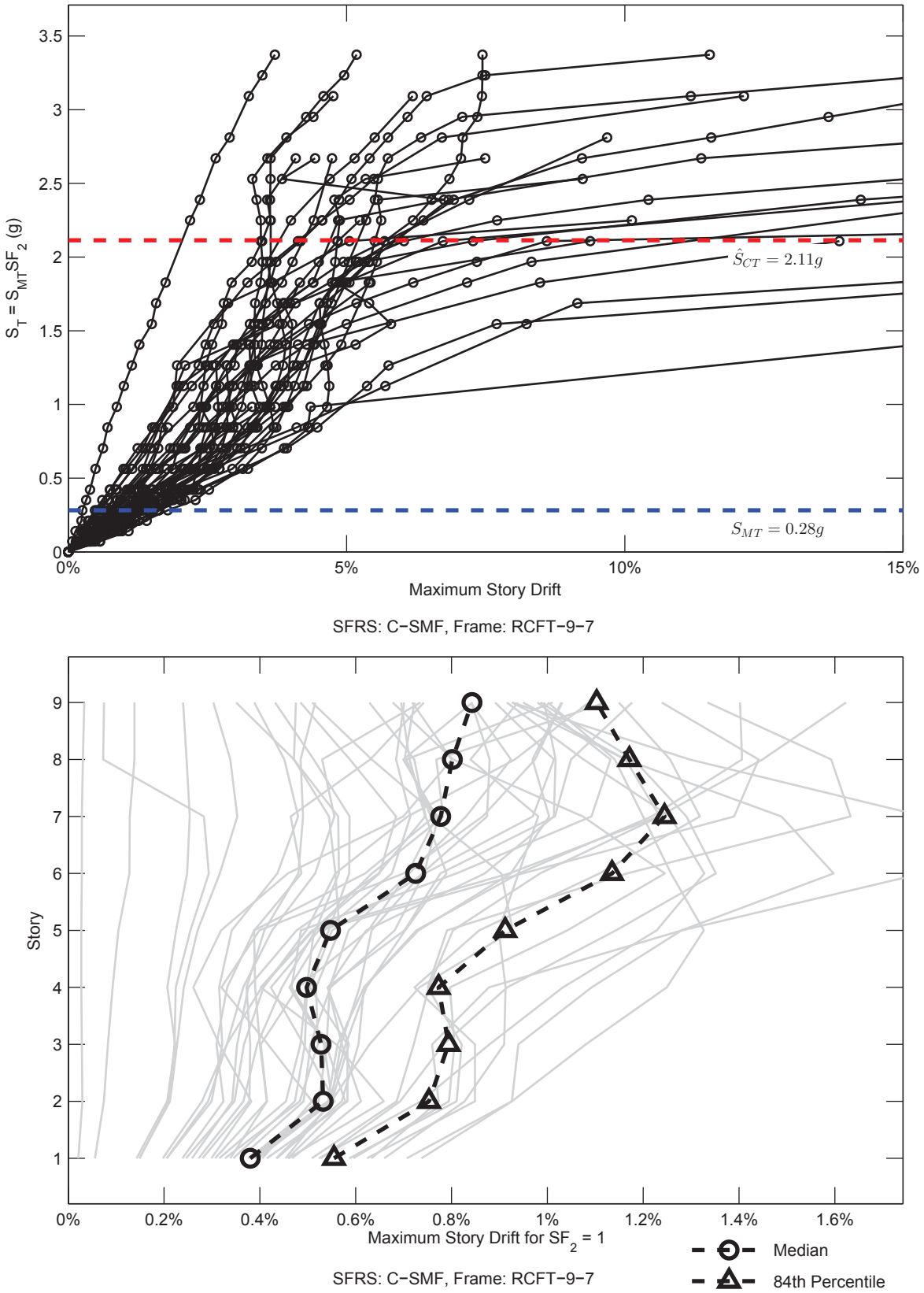

Figure C.80. Dynamic Response History Analysis Results: Frame RCFT-9-7

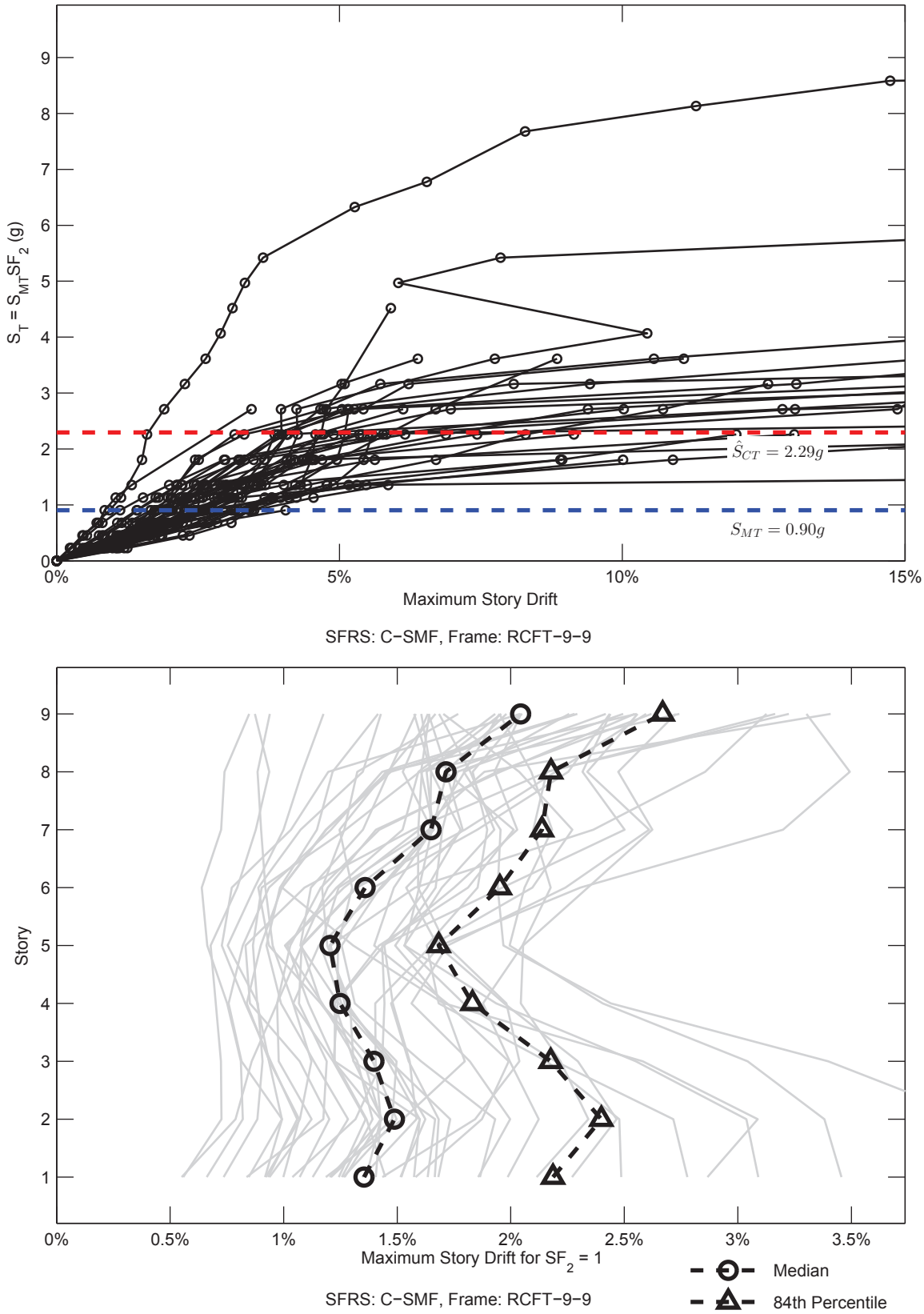

Figure C.81. Dynamic Response History Analysis Results: Frame RCFT-9-9

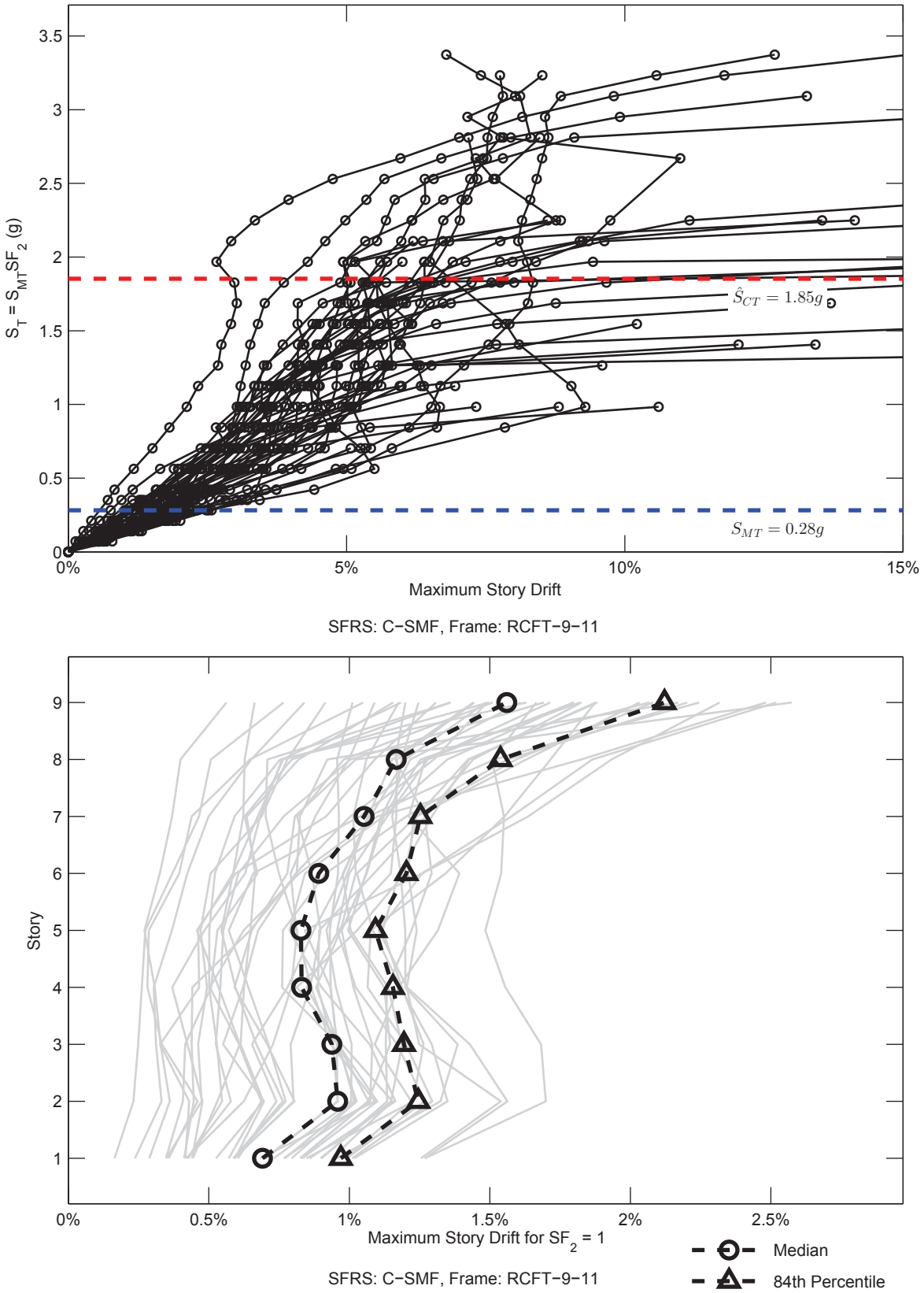

Figure C.82. Dynamic Response History Analysis Results: Frame RCFT-9-11

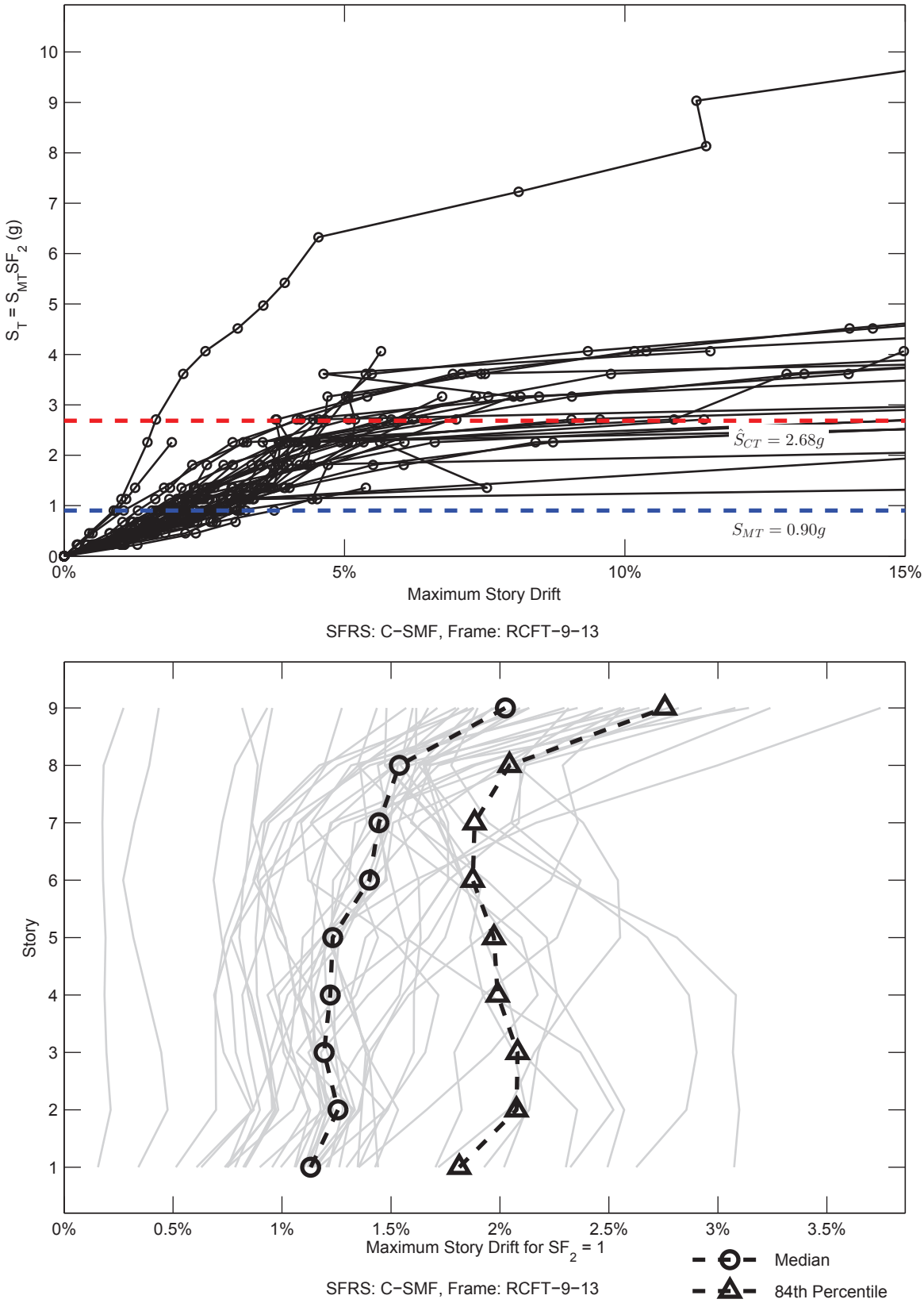

Figure C.83. Dynamic Response History Analysis Results: Frame RCFT-9-13

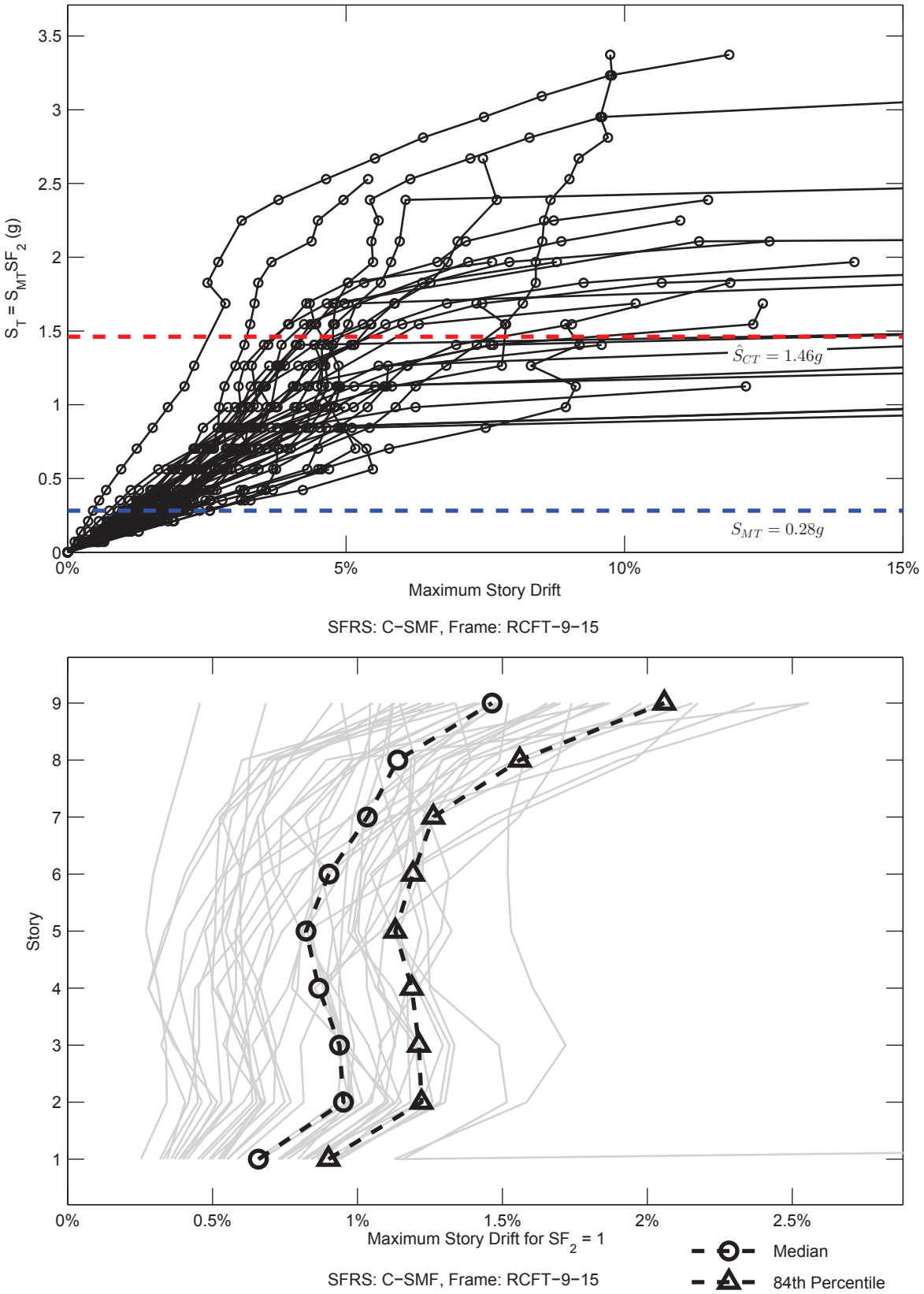

Figure C.84. Dynamic Response History Analysis Results: Frame RCFT-9-15

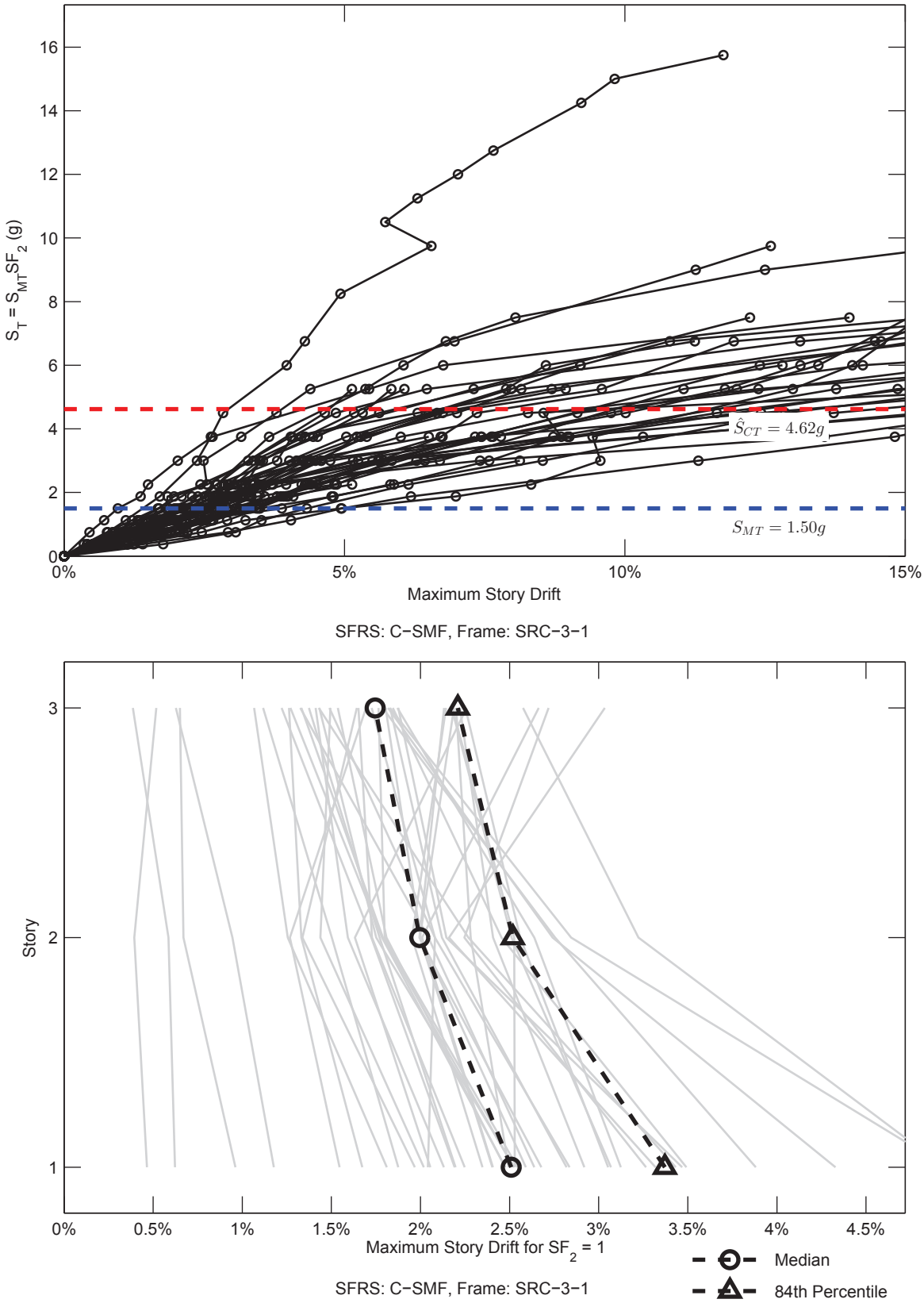

Figure C.85. Dynamic Response History Analysis Results: Frame SRC-3-1

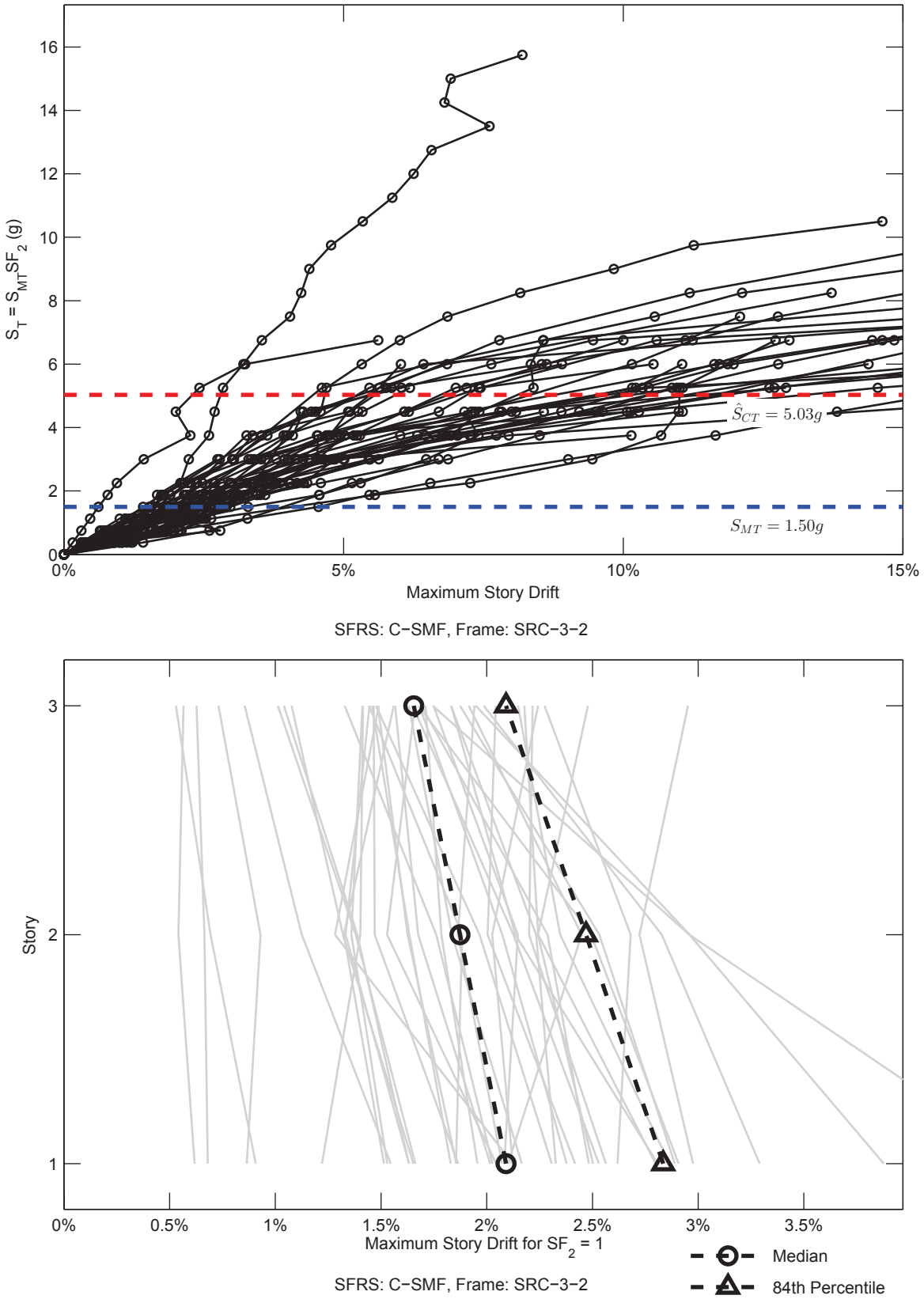

Figure C.86. Dynamic Response History Analysis Results: Frame SRC-3-2

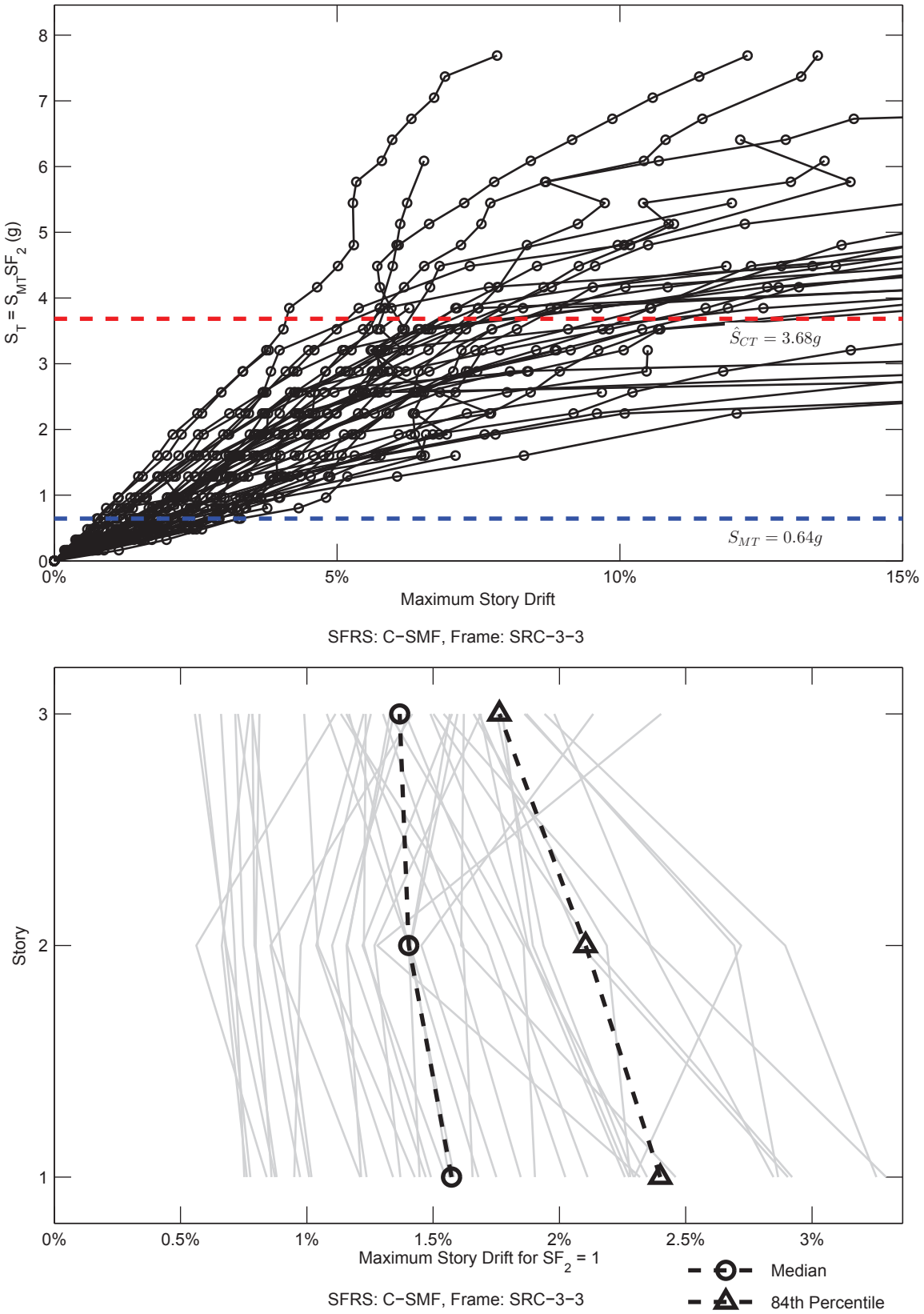

Figure C.87. Dynamic Response History Analysis Results: Frame SRC-3-3

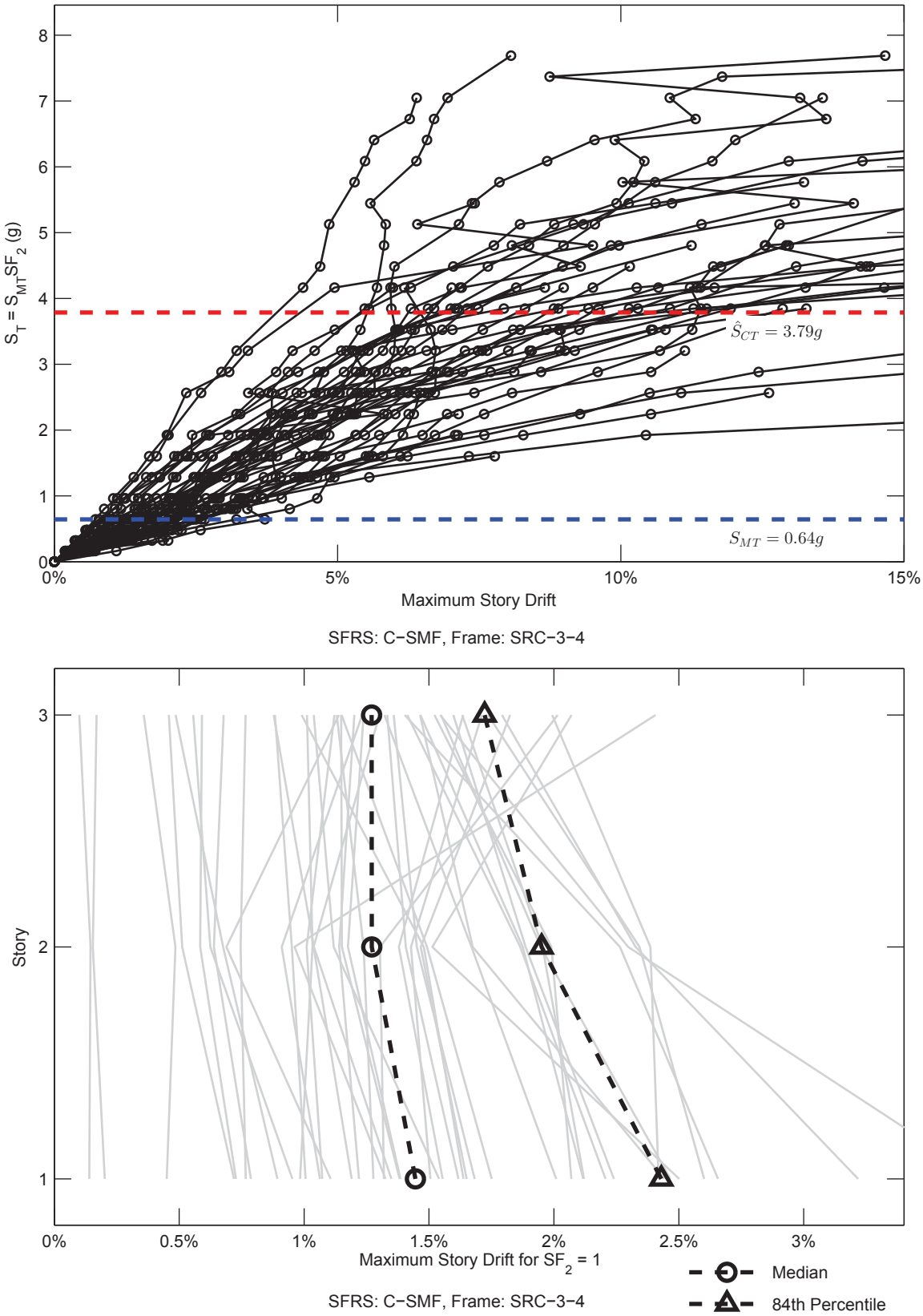

Figure C.88. Dynamic Response History Analysis Results: Frame SRC-3-4

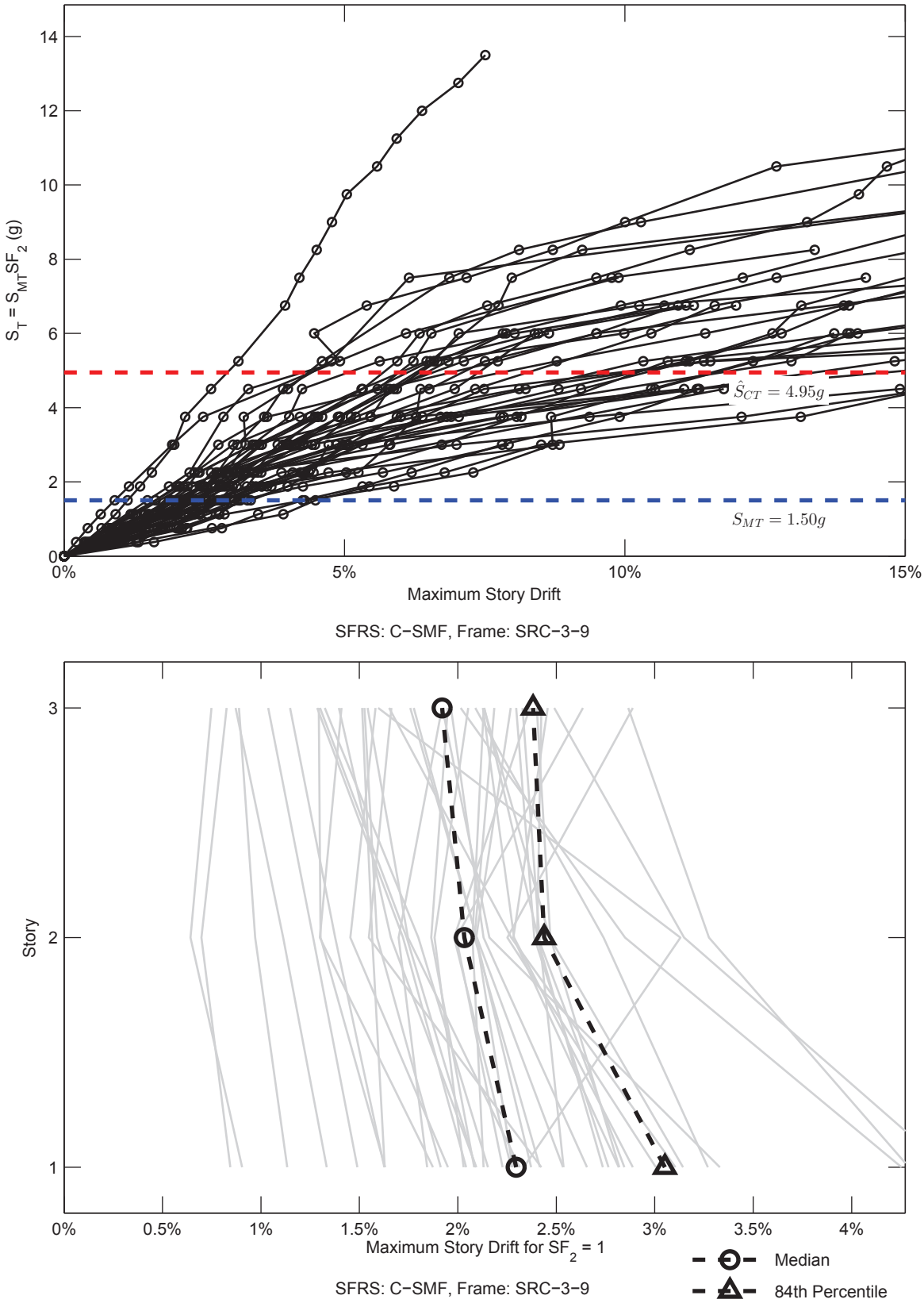

Figure C.89. Dynamic Response History Analysis Results: Frame SRC-3-9

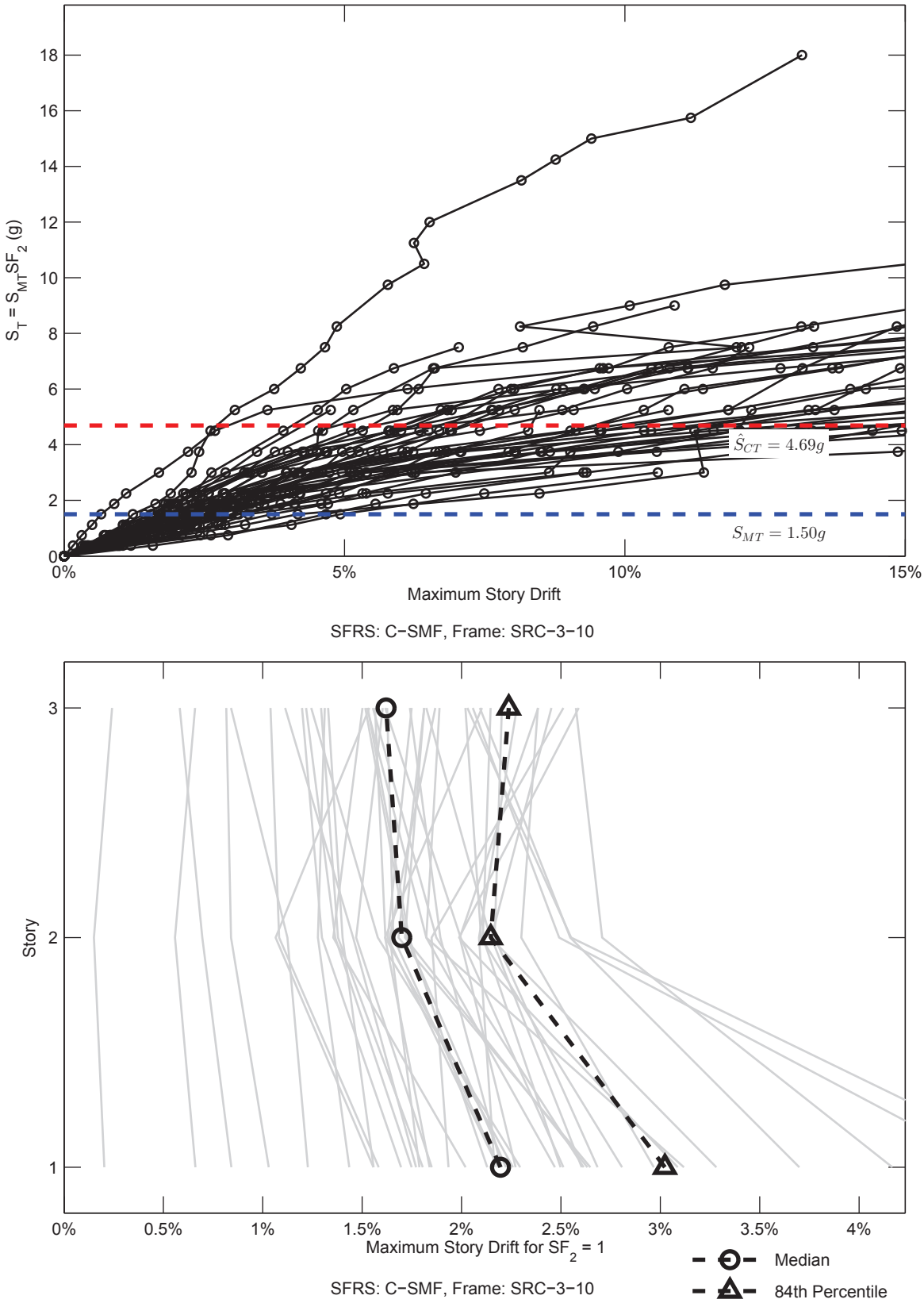

Figure C.90. Dynamic Response History Analysis Results: Frame SRC-3-10

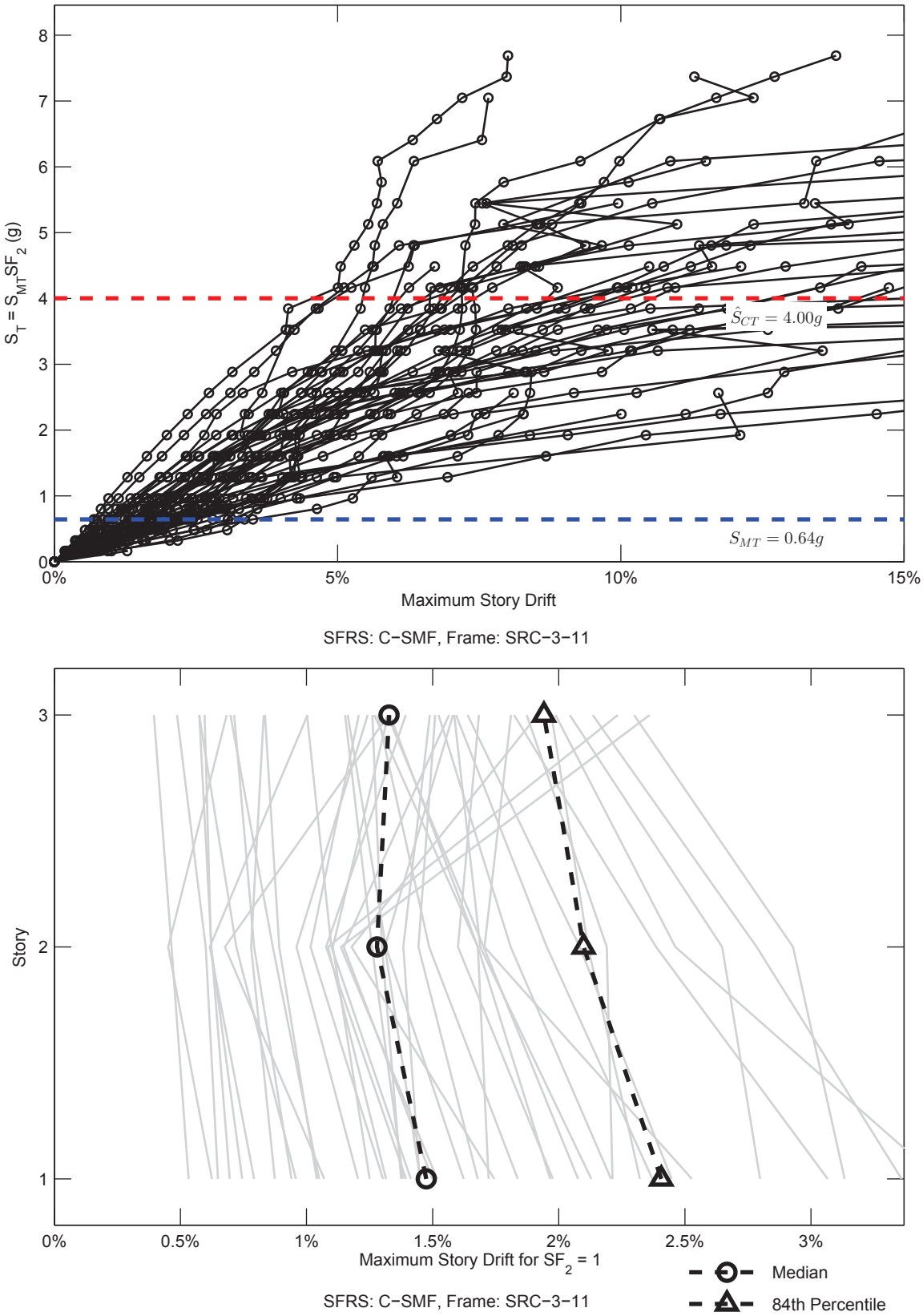

Figure C.91. Dynamic Response History Analysis Results: Frame SRC-3-11

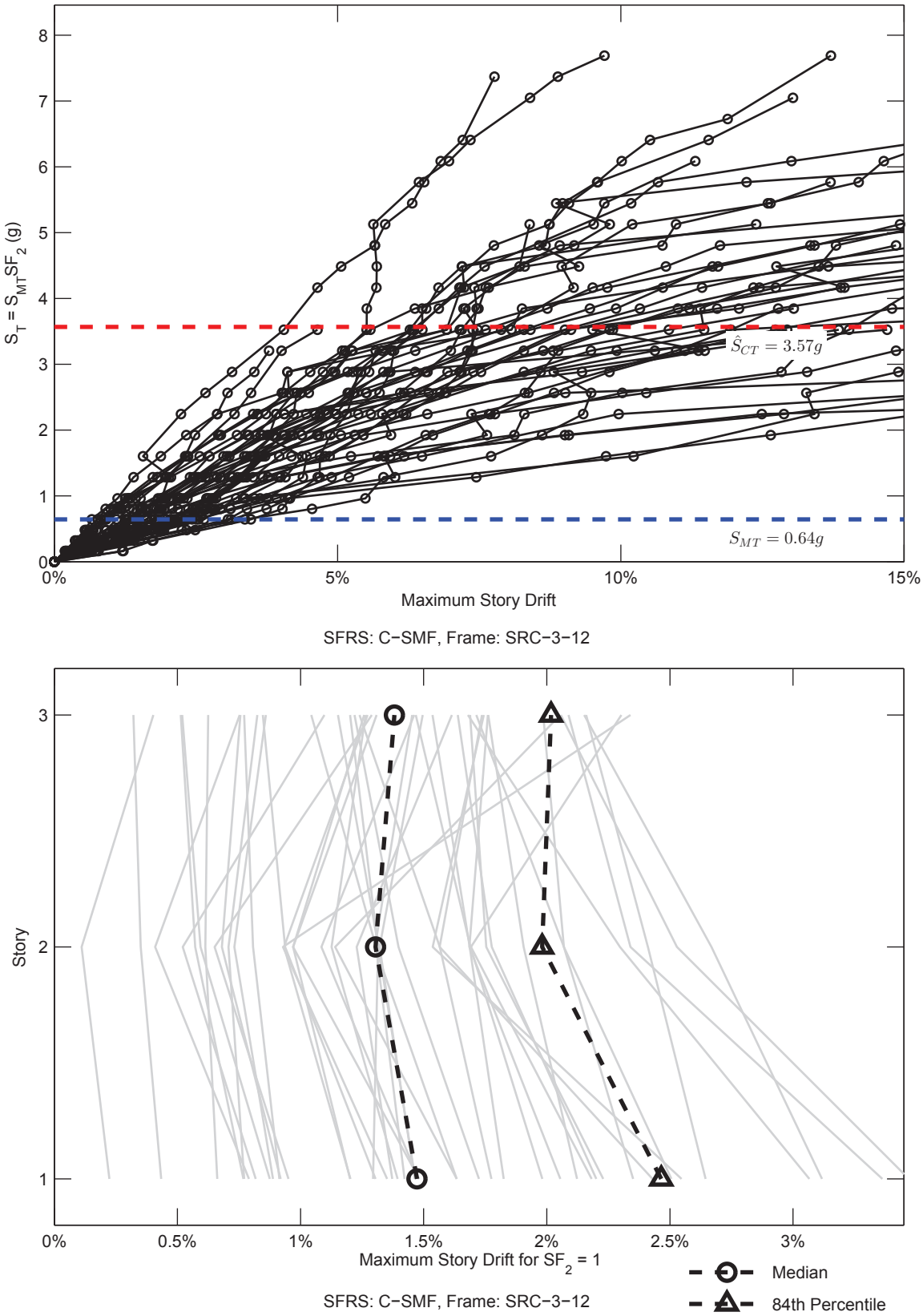

Figure C.92. Dynamic Response History Analysis Results: Frame SRC-3-12

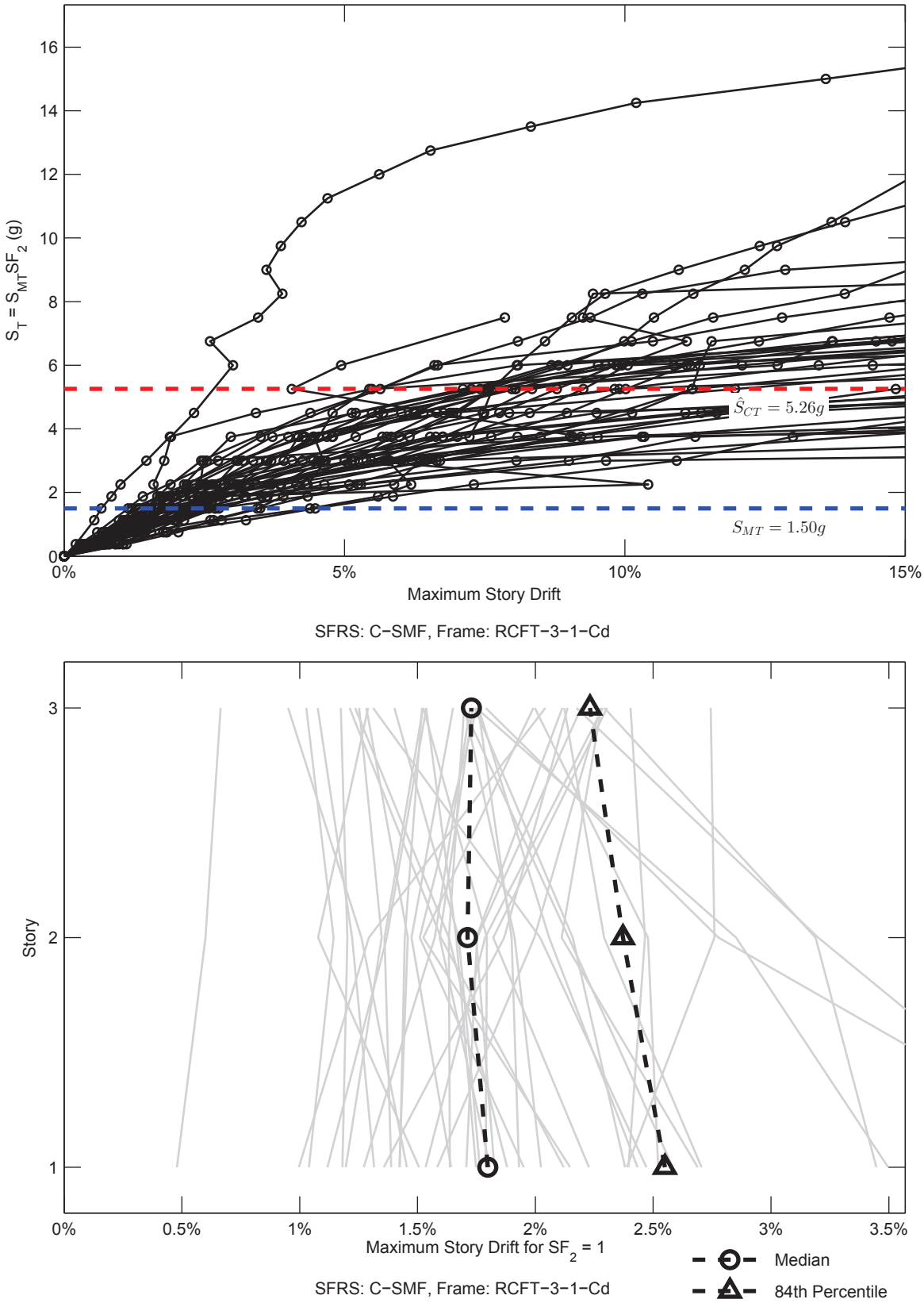

Figure C.93. Dynamic Response History Analysis Results: Frame RCFT-3-1-Cd

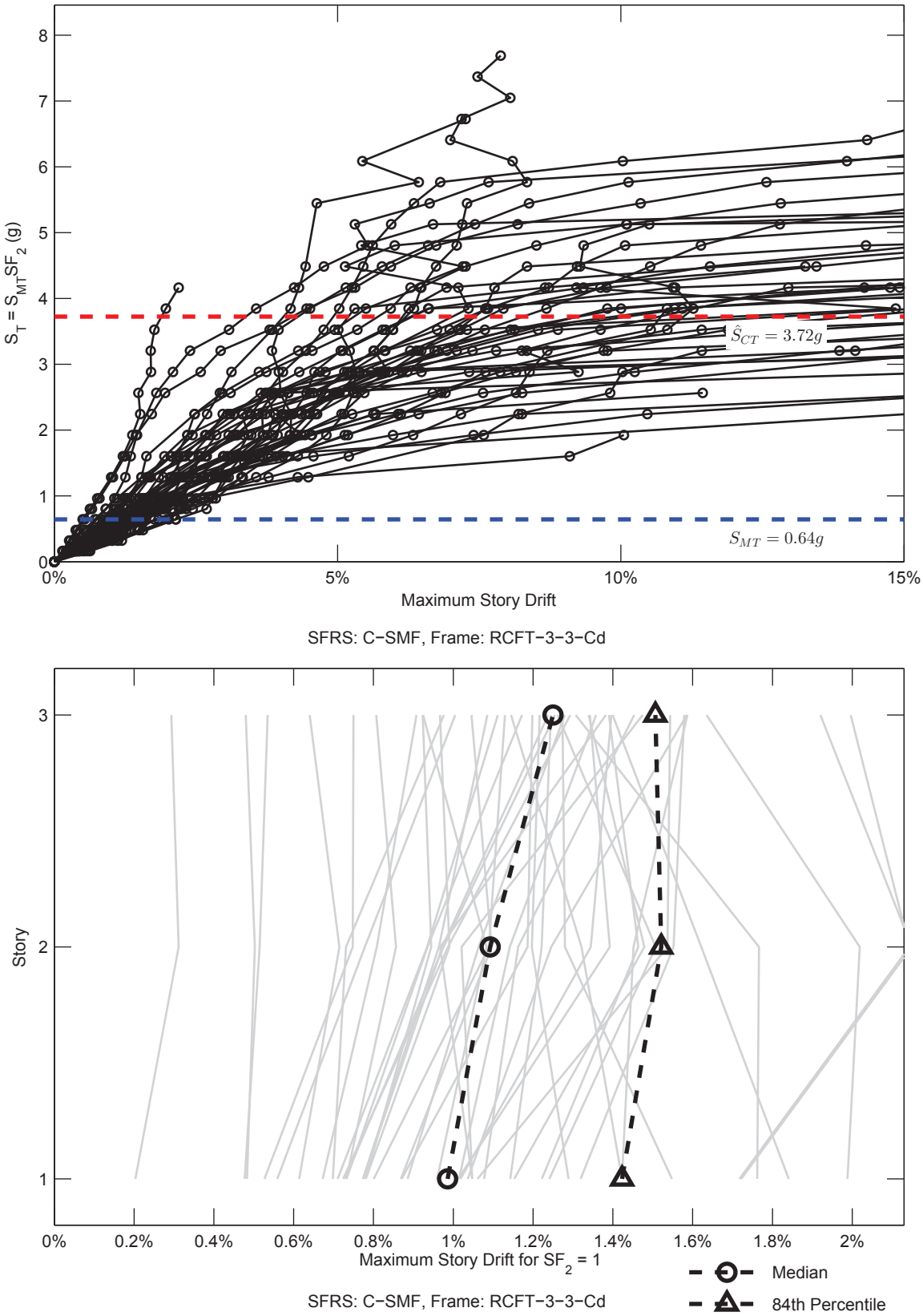

Figure C.94. Dynamic Response History Analysis Results: Frame RCFT-3-3-Cd

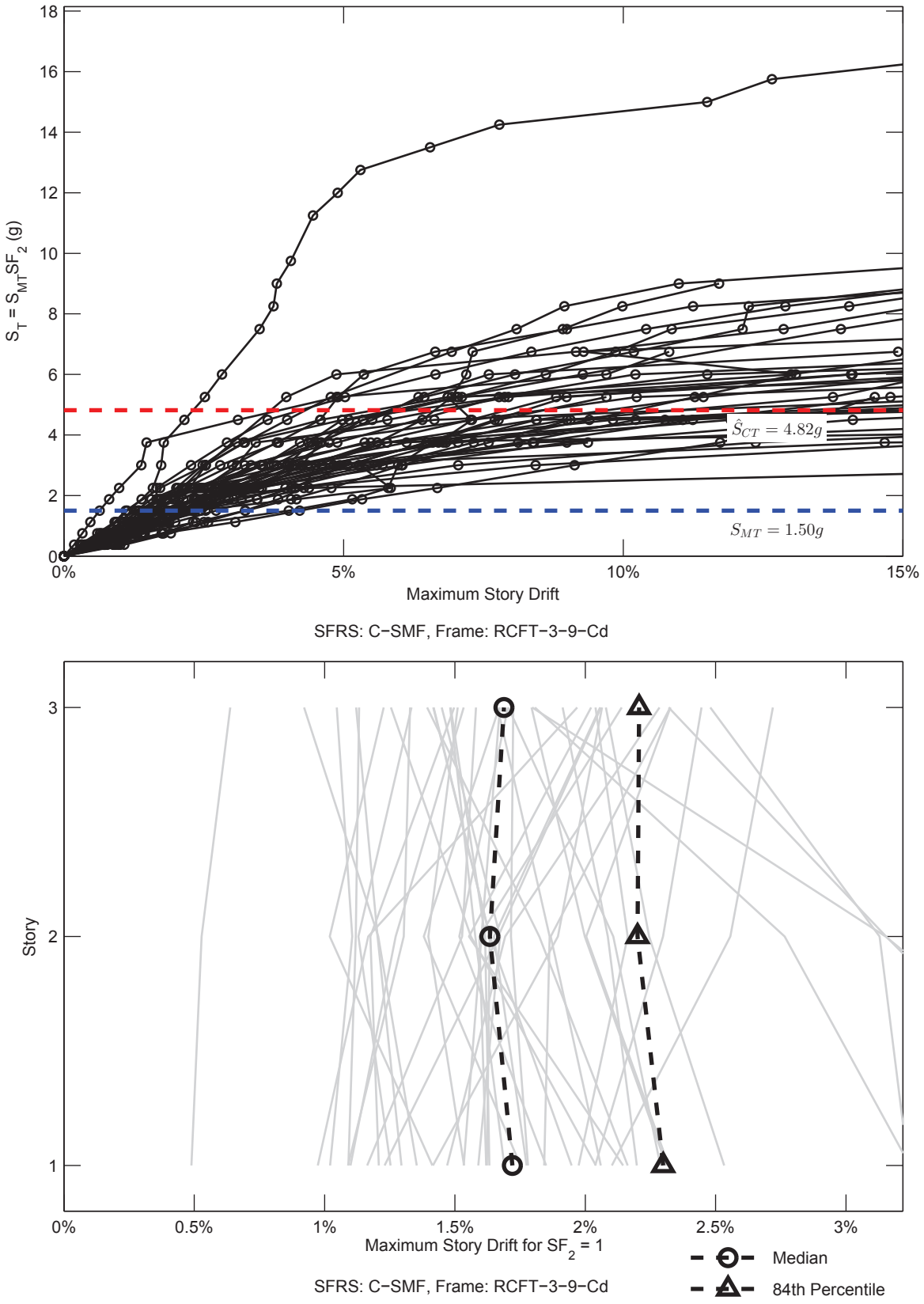

Figure C.95. Dynamic Response History Analysis Results: Frame RCFT-3-9-Cd

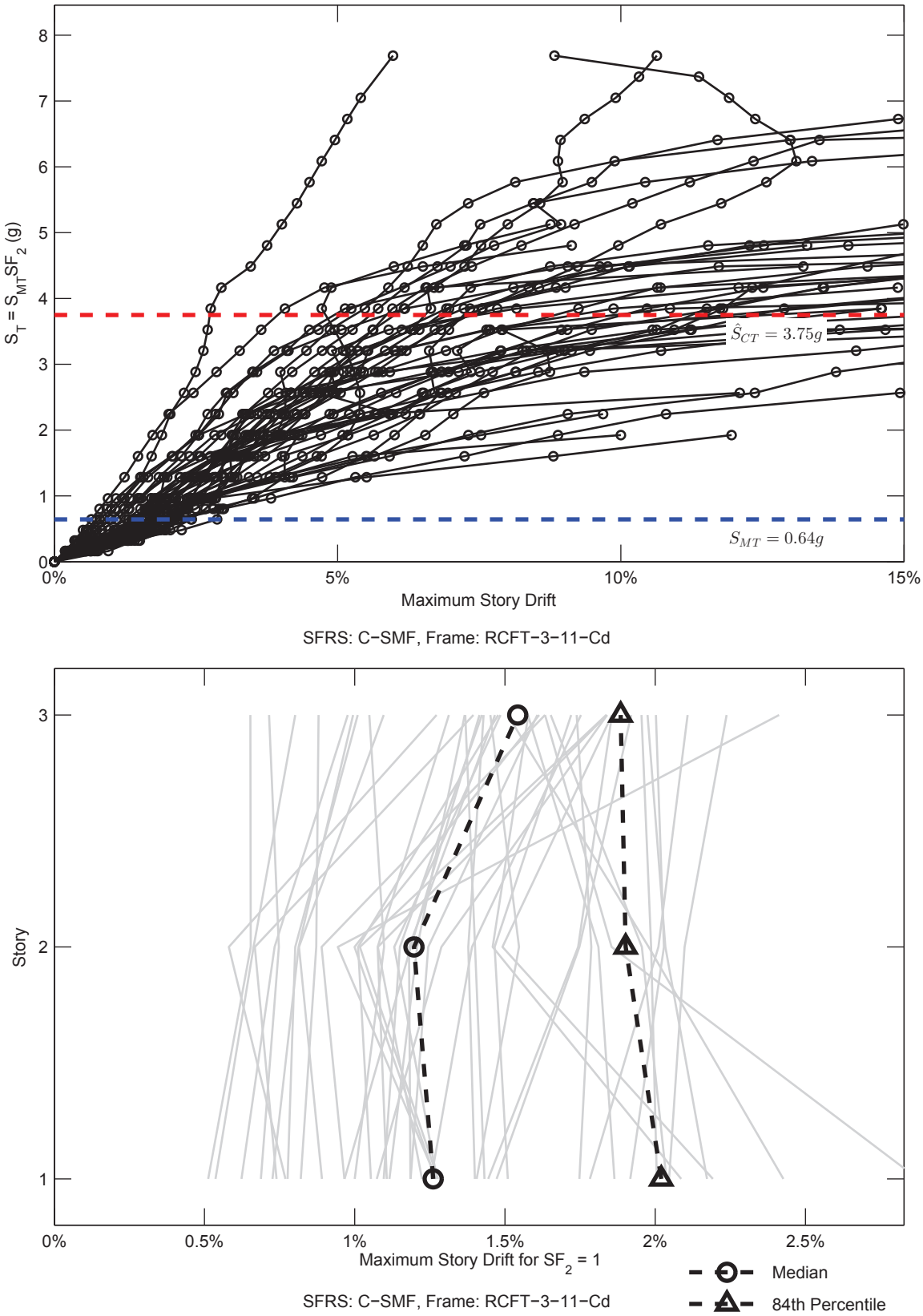

Figure C.96. Dynamic Response History Analysis Results: Frame RCFT-3-11-Cd

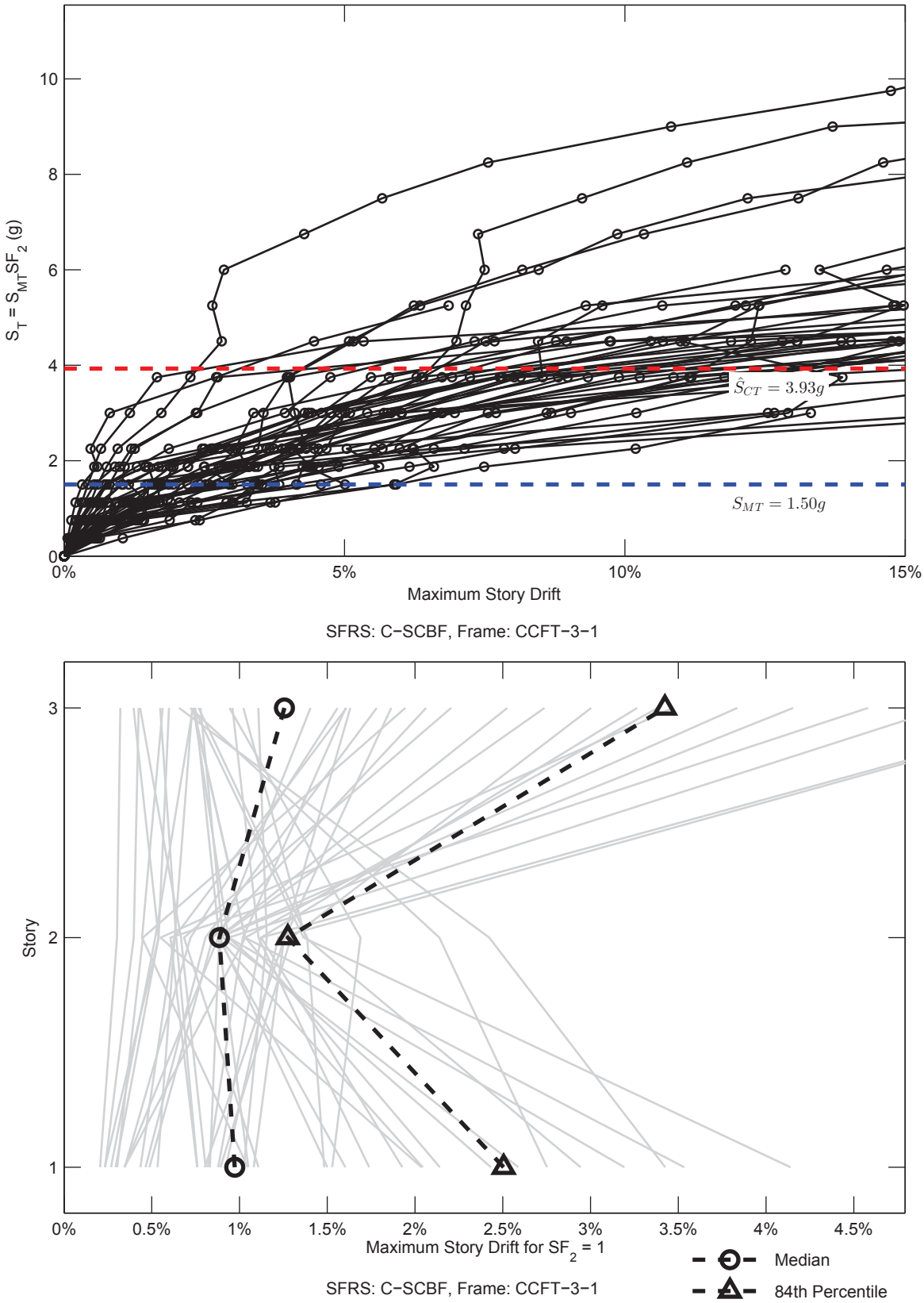

Figure C.97. Dynamic Response History Analysis Results: Frame CCFT-3-1

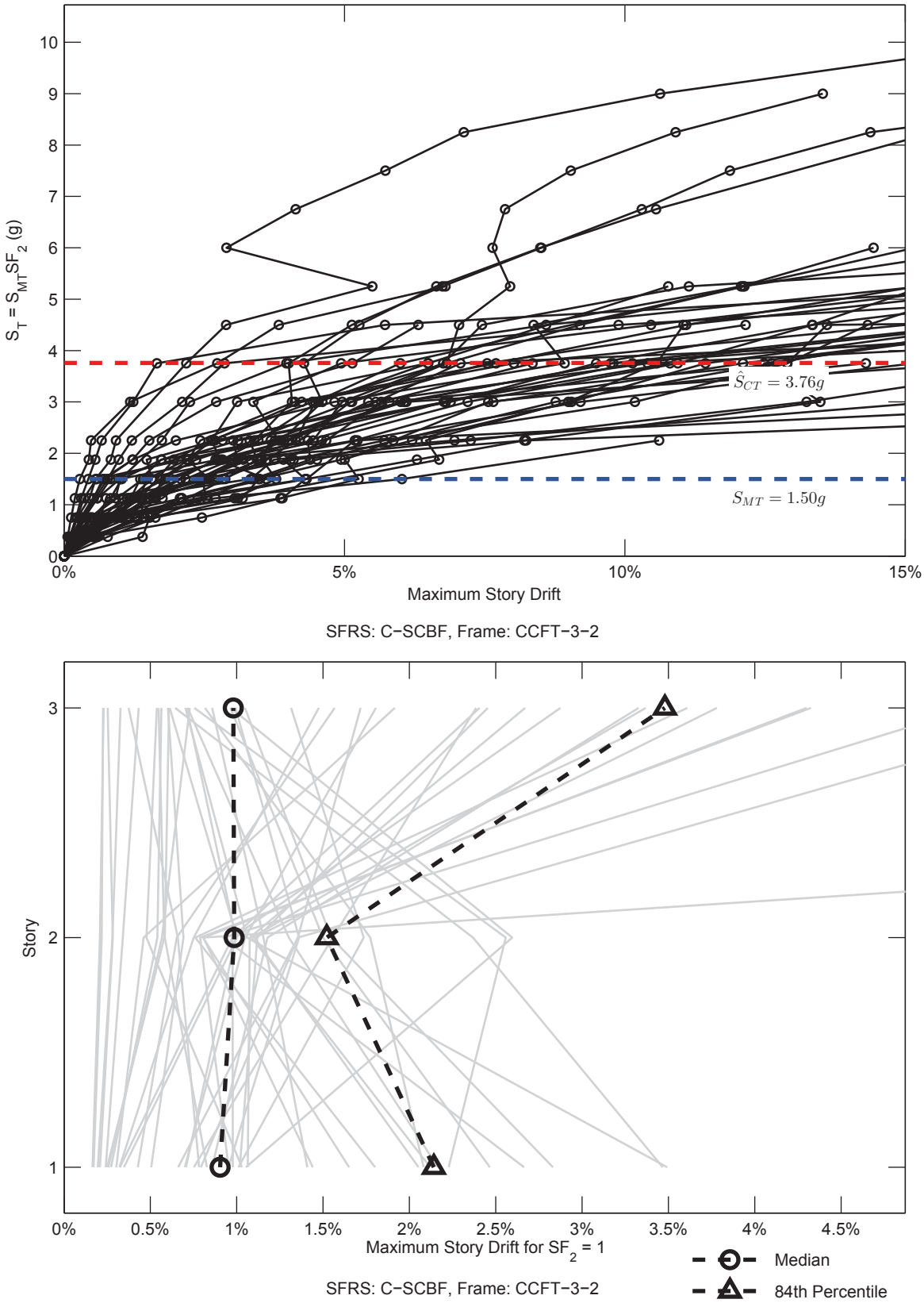

Figure C.98. Dynamic Response History Analysis Results: Frame CCFT-3-2

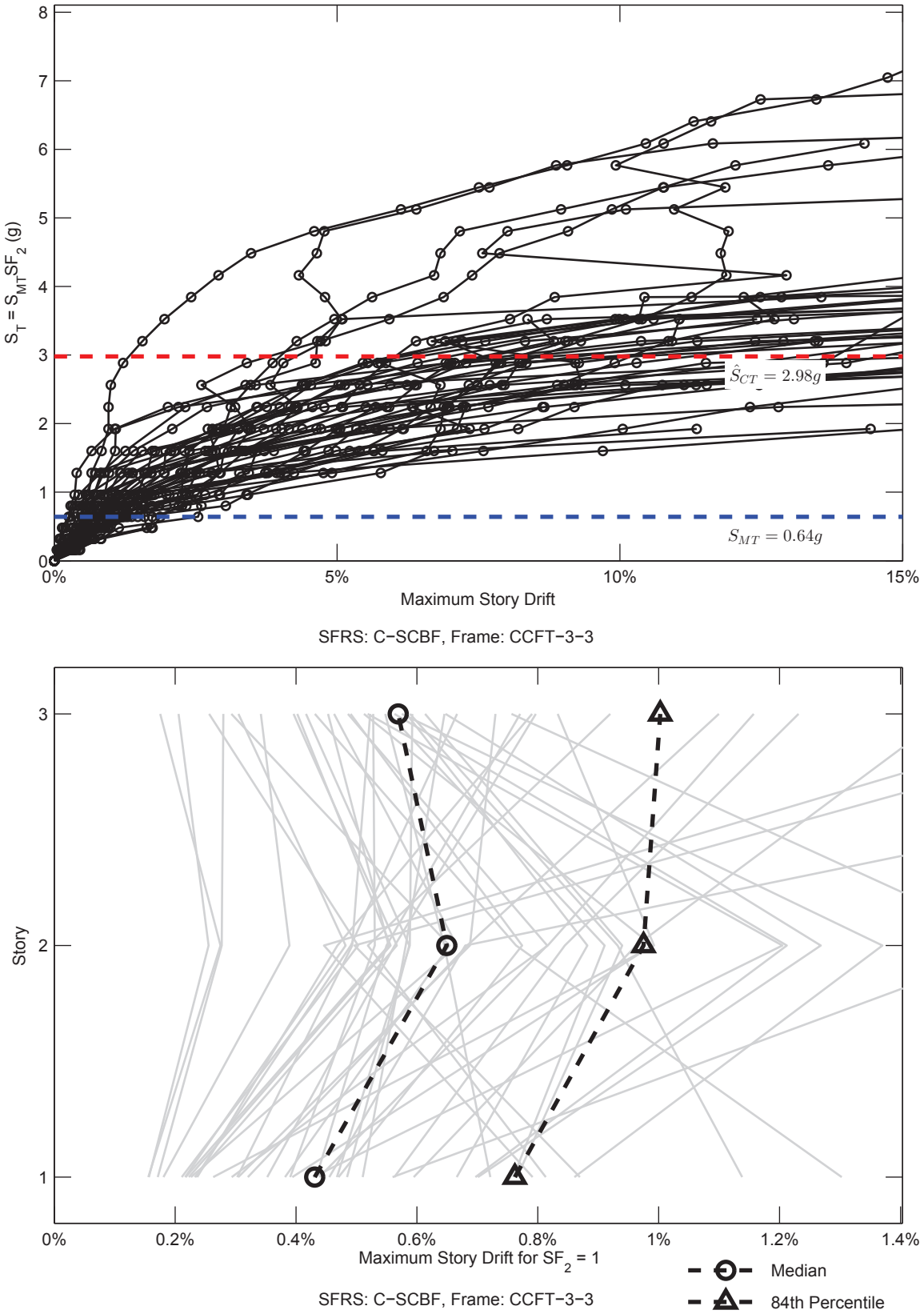

Figure C.99. Dynamic Response History Analysis Results: Frame CCFT-3-3

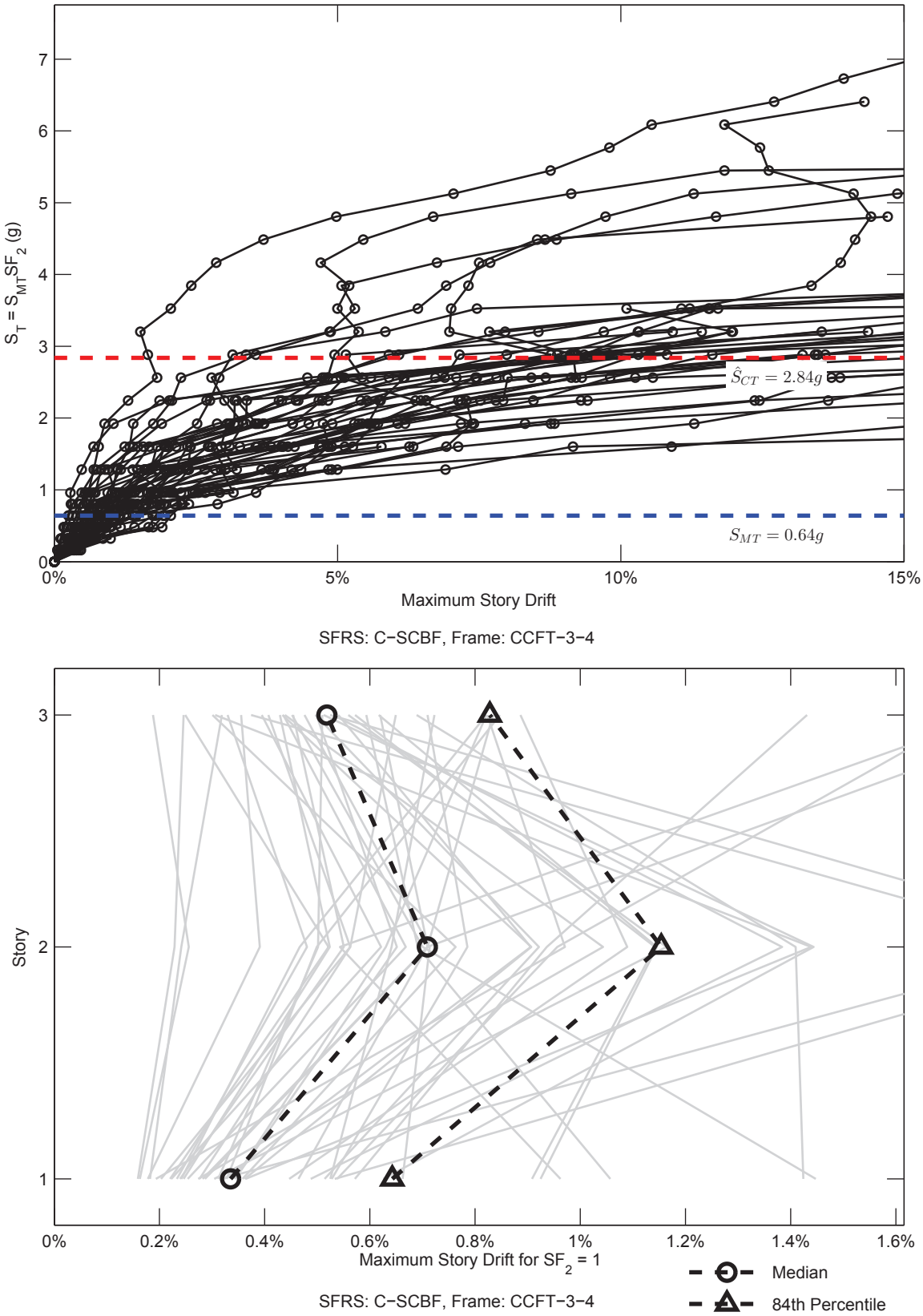

Figure C.100. Dynamic Response History Analysis Results: Frame CCFT-3-4

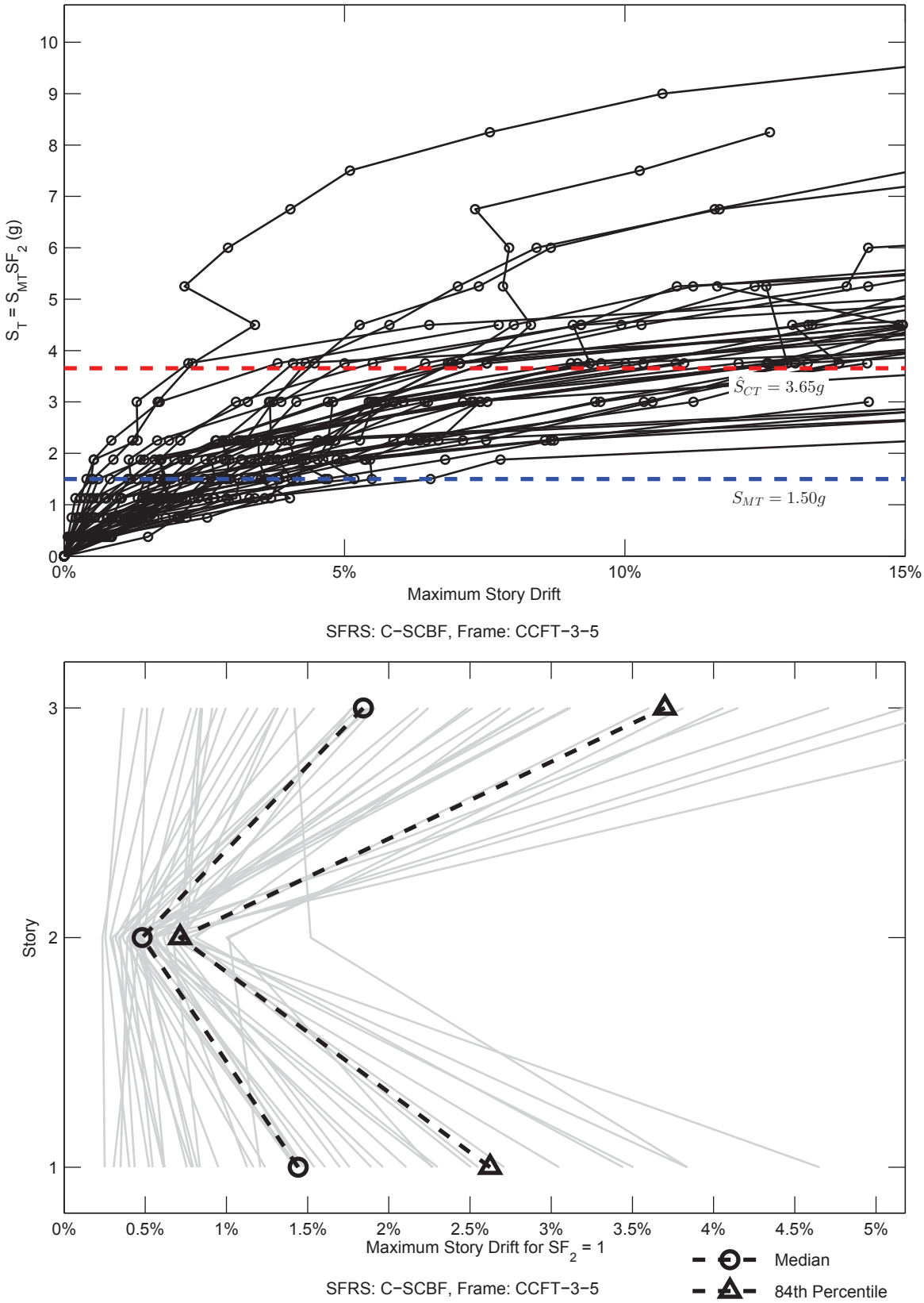

Figure C.101. Dynamic Response History Analysis Results: Frame CCFT-3-5

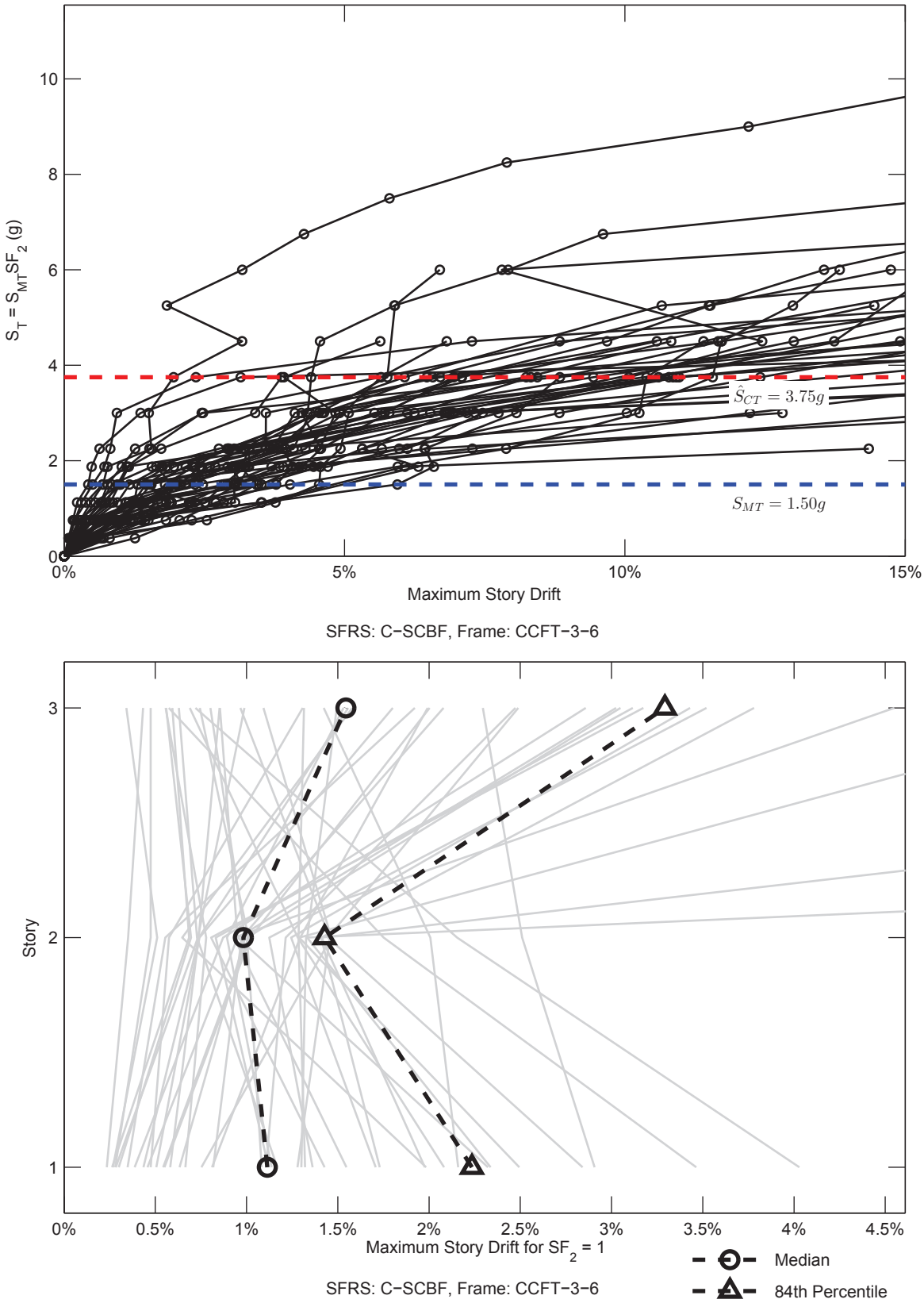

Figure C.102. Dynamic Response History Analysis Results: Frame CCFT-3-6

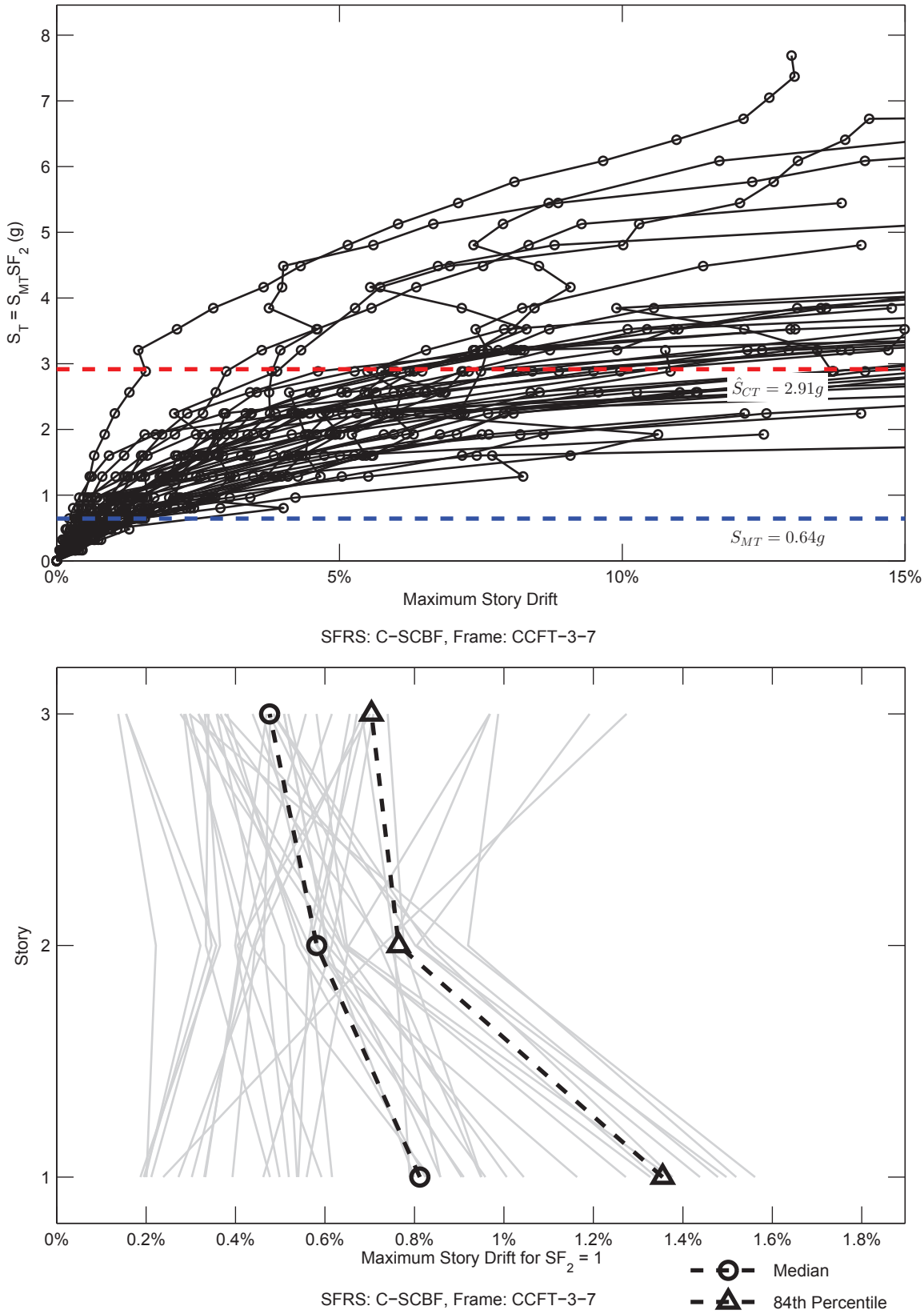

Figure C.103. Dynamic Response History Analysis Results: Frame CCFT-3-7

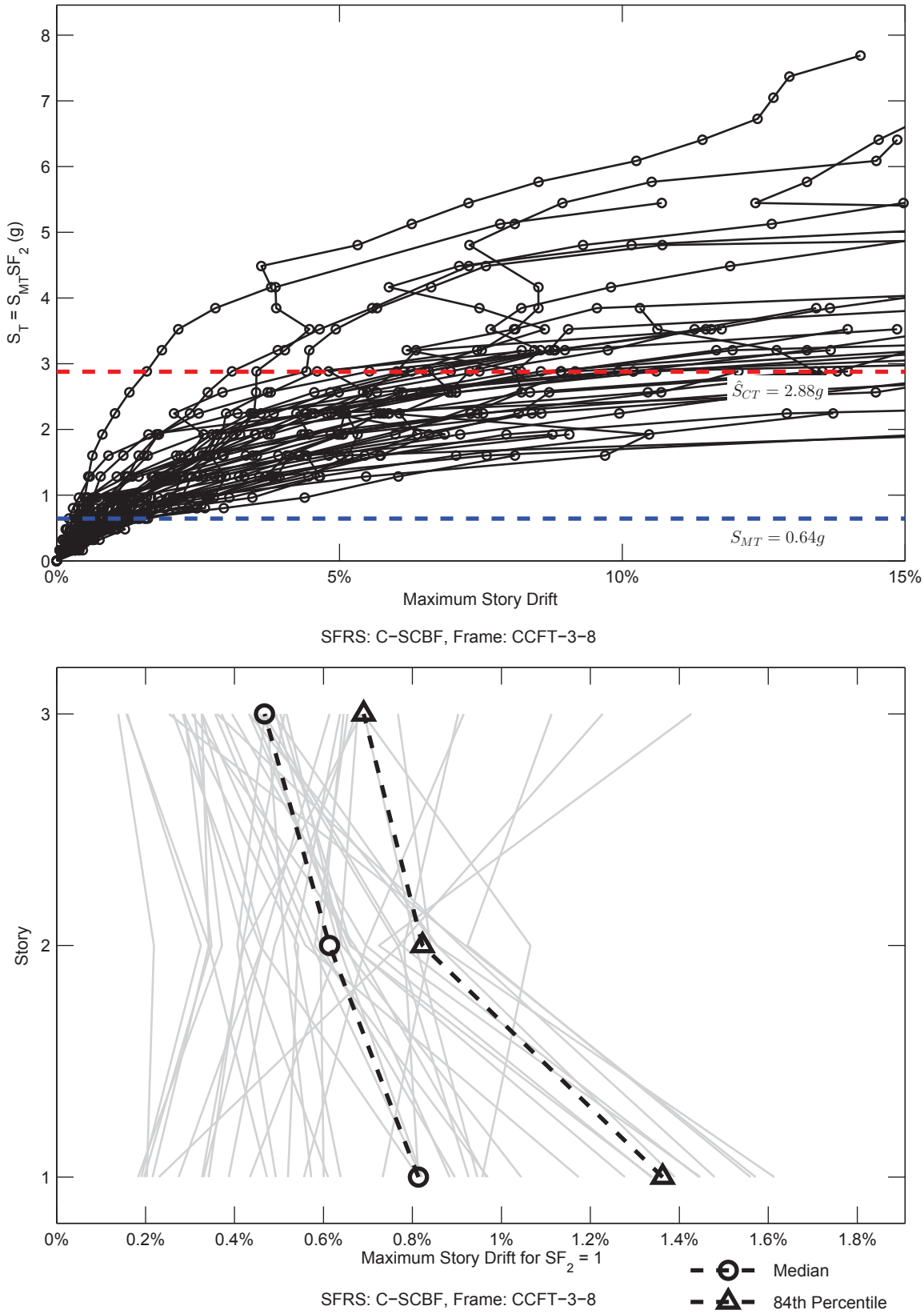

Figure C.104. Dynamic Response History Analysis Results: Frame CCFT-3-8

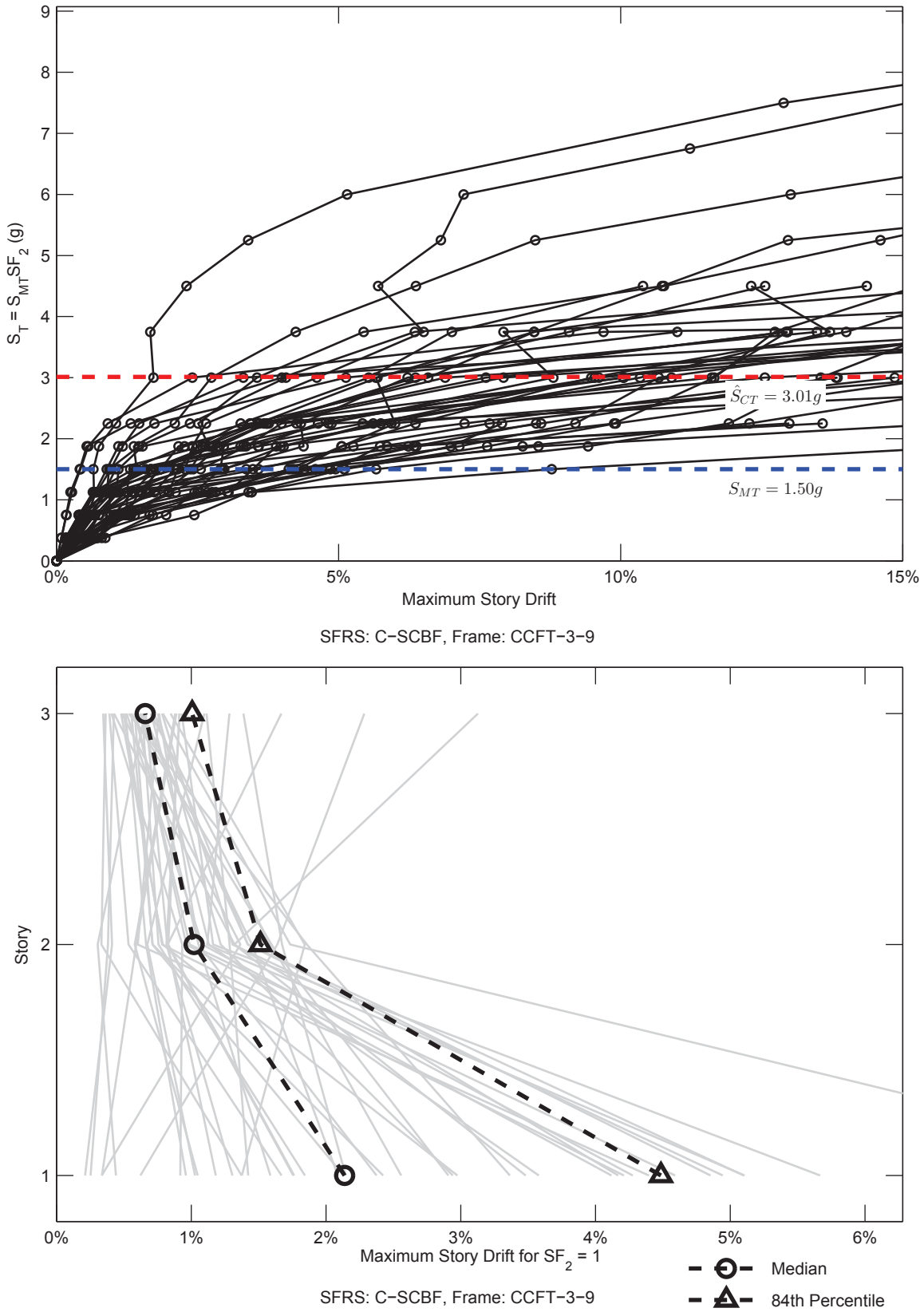

Figure C.105. Dynamic Response History Analysis Results: Frame CCFT-3-9

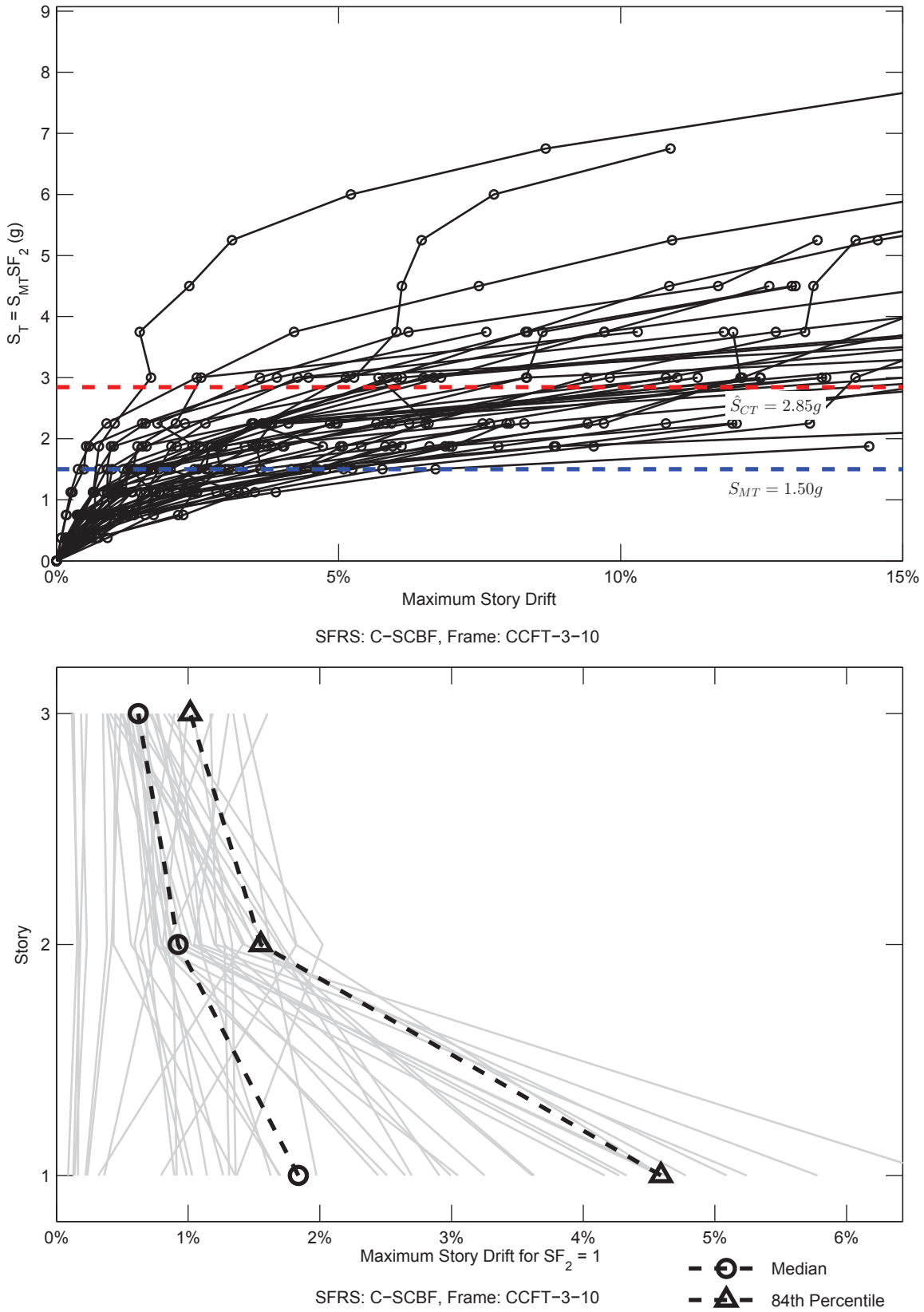

Figure C.106. Dynamic Response History Analysis Results: Frame CCFT-3-10

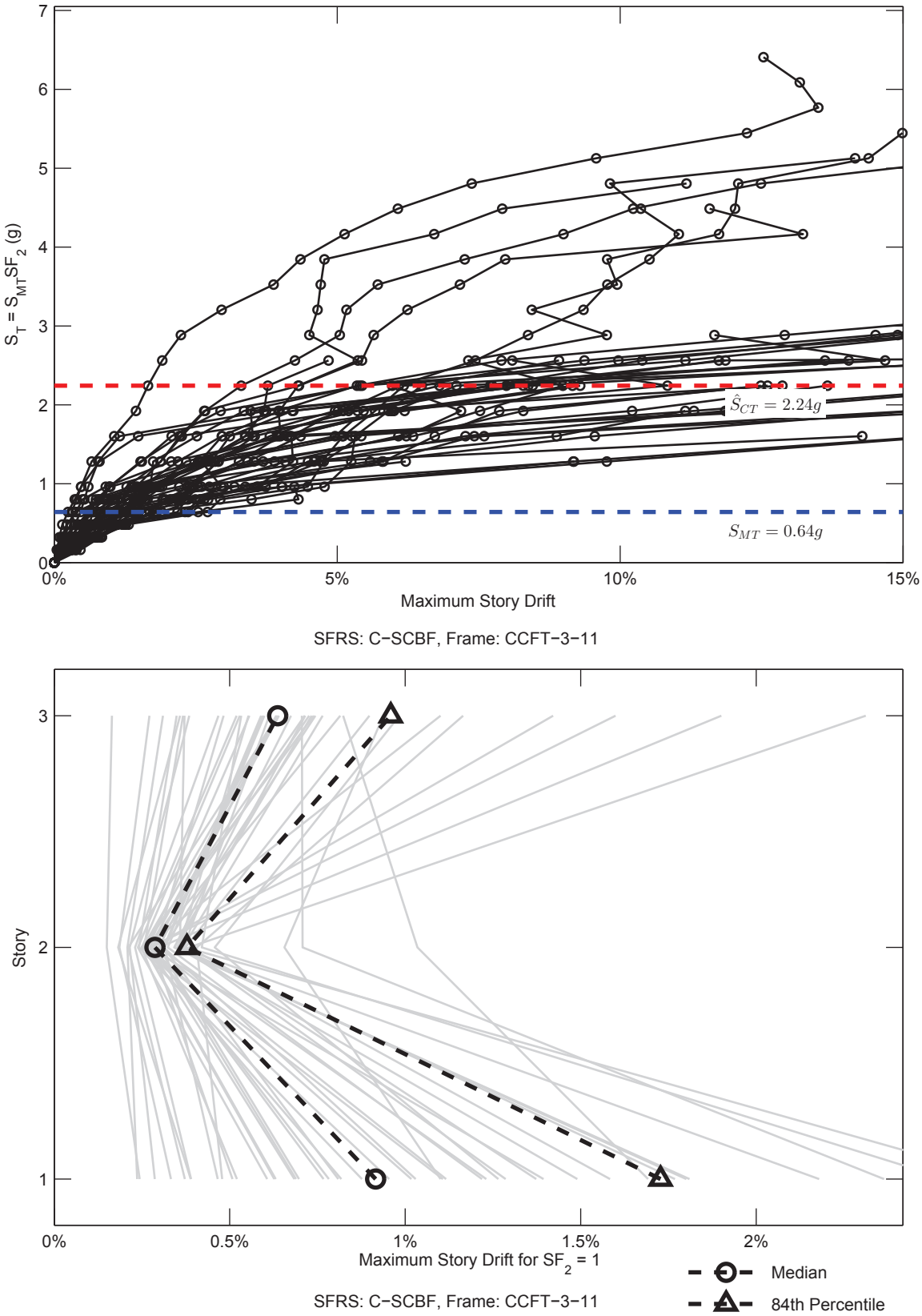

Figure C.107. Dynamic Response History Analysis Results: Frame CCFT-3-11

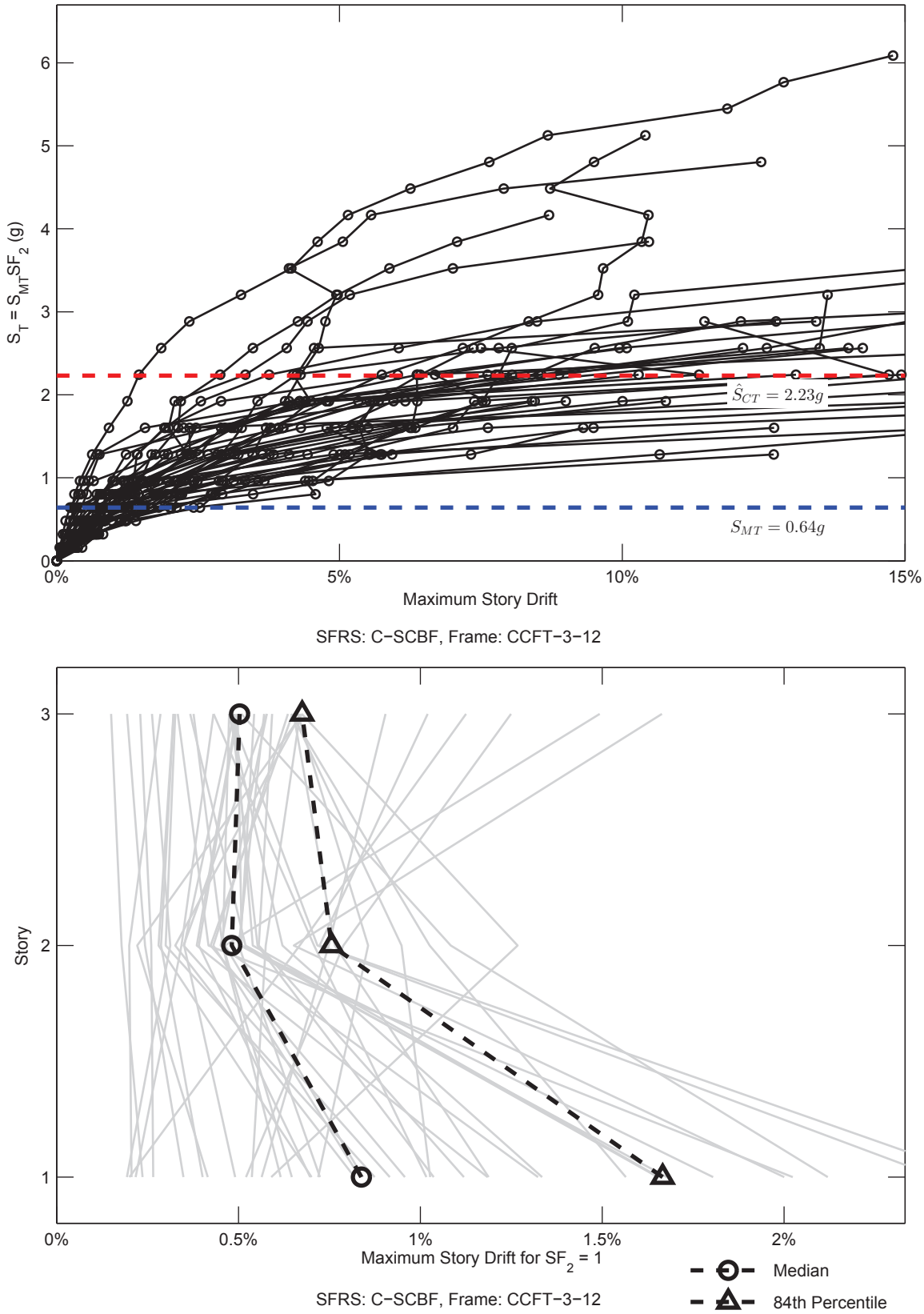

Figure C.108. Dynamic Response History Analysis Results: Frame CCFT-3-12

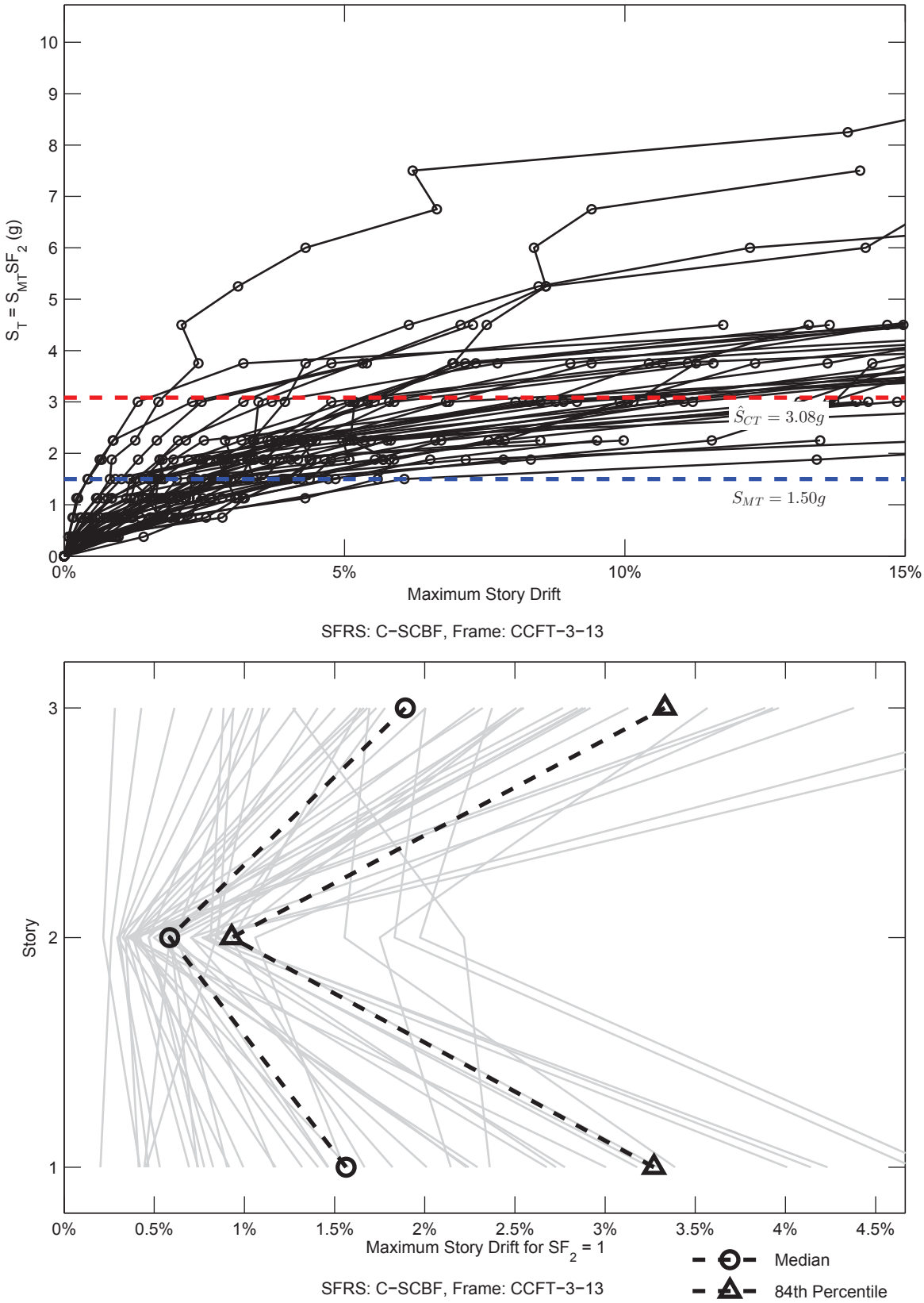

Figure C.109. Dynamic Response History Analysis Results: Frame CCFT-3-13

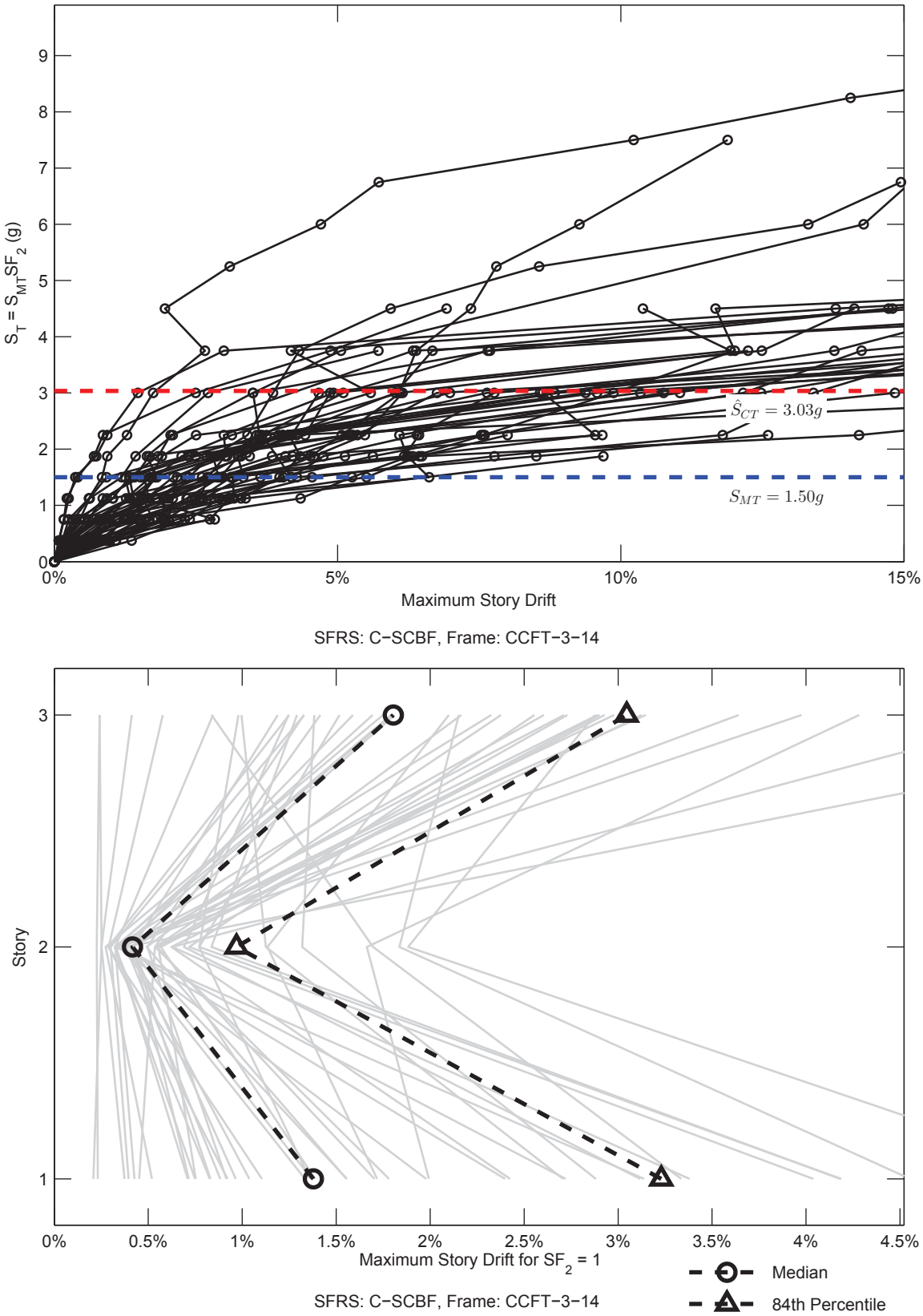

Figure C.110. Dynamic Response History Analysis Results: Frame CCFT-3-14

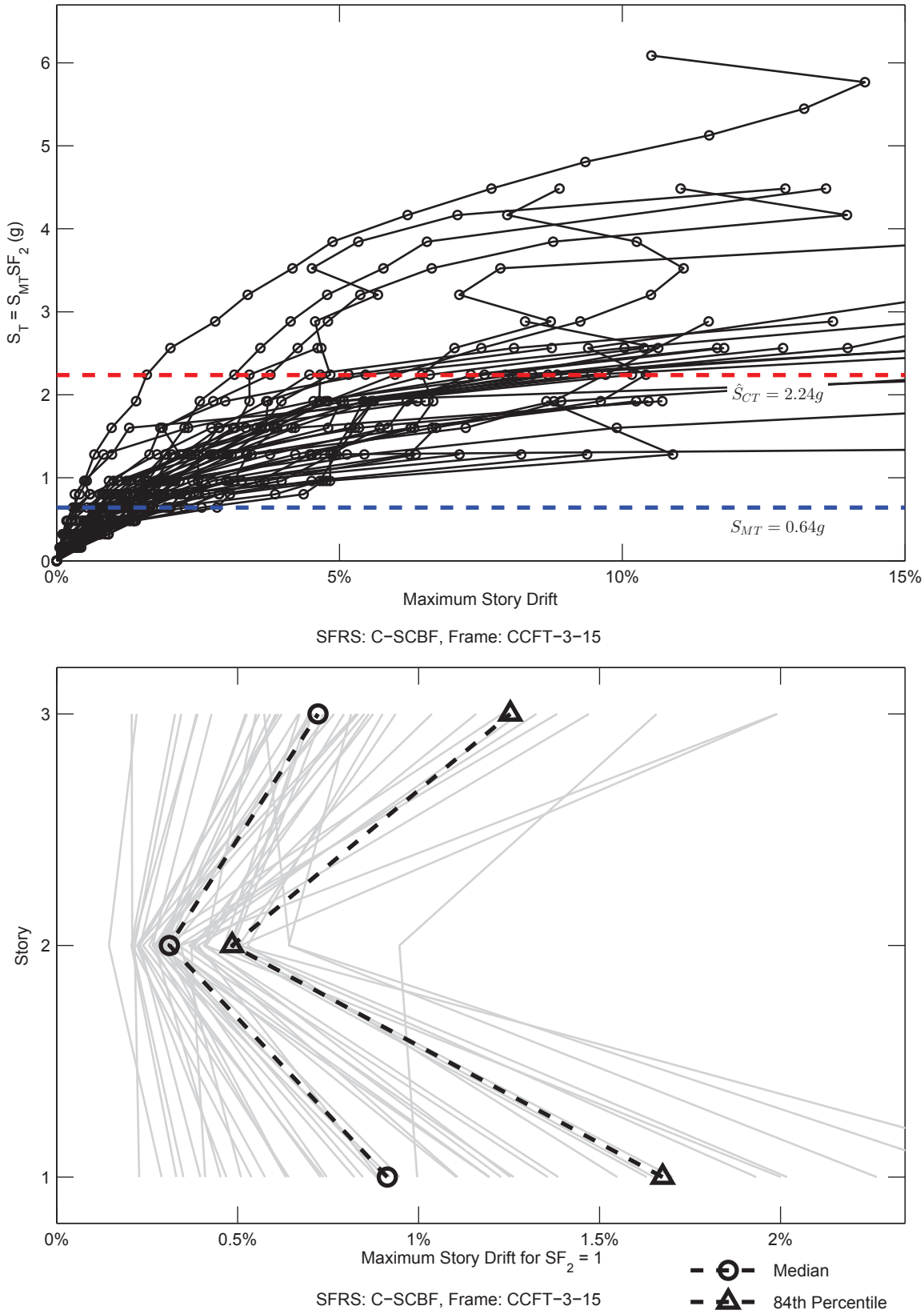

Figure C.111. Dynamic Response History Analysis Results: Frame CCFT-3-15

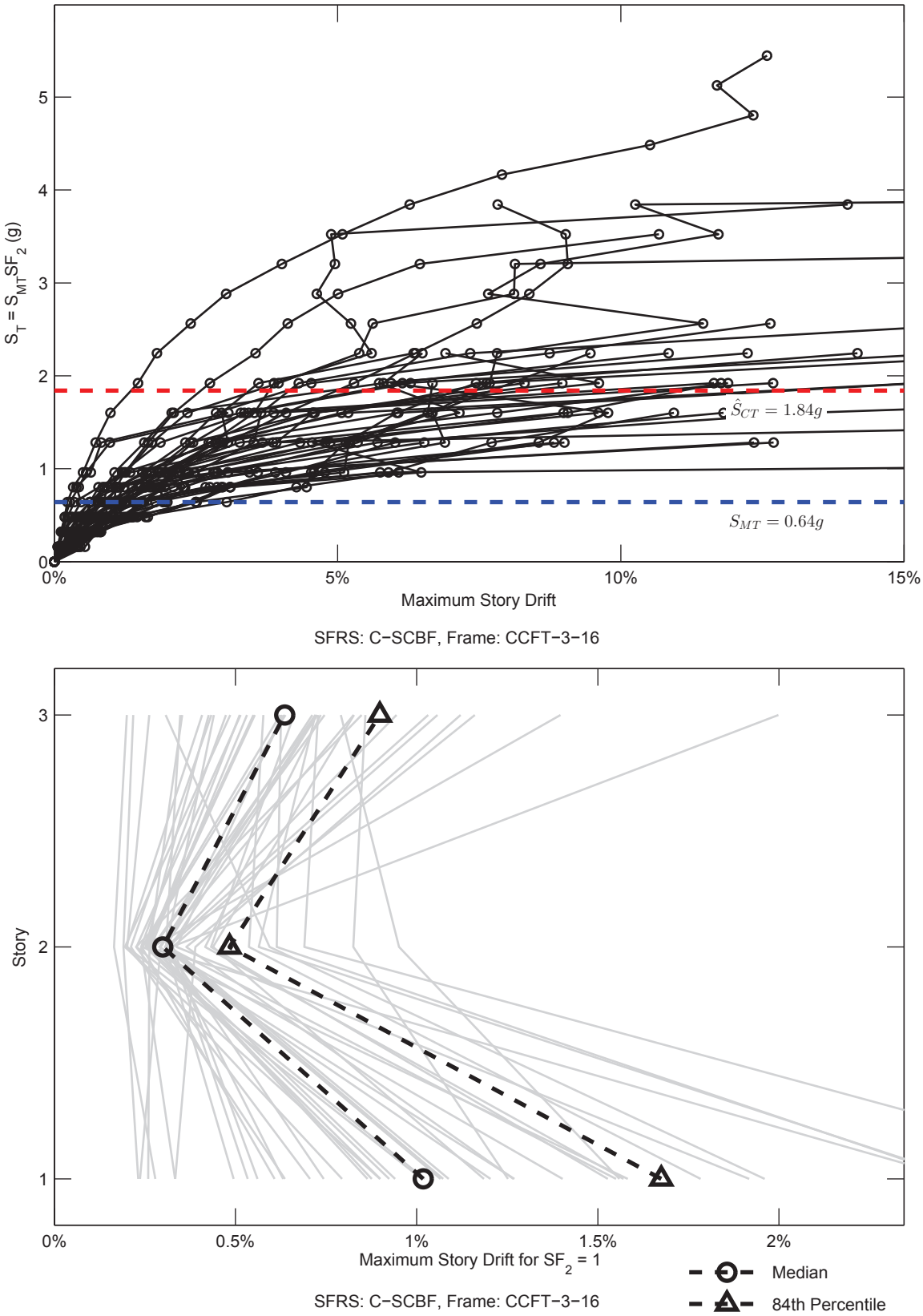

Figure C.112. Dynamic Response History Analysis Results: Frame CCFT-3-16

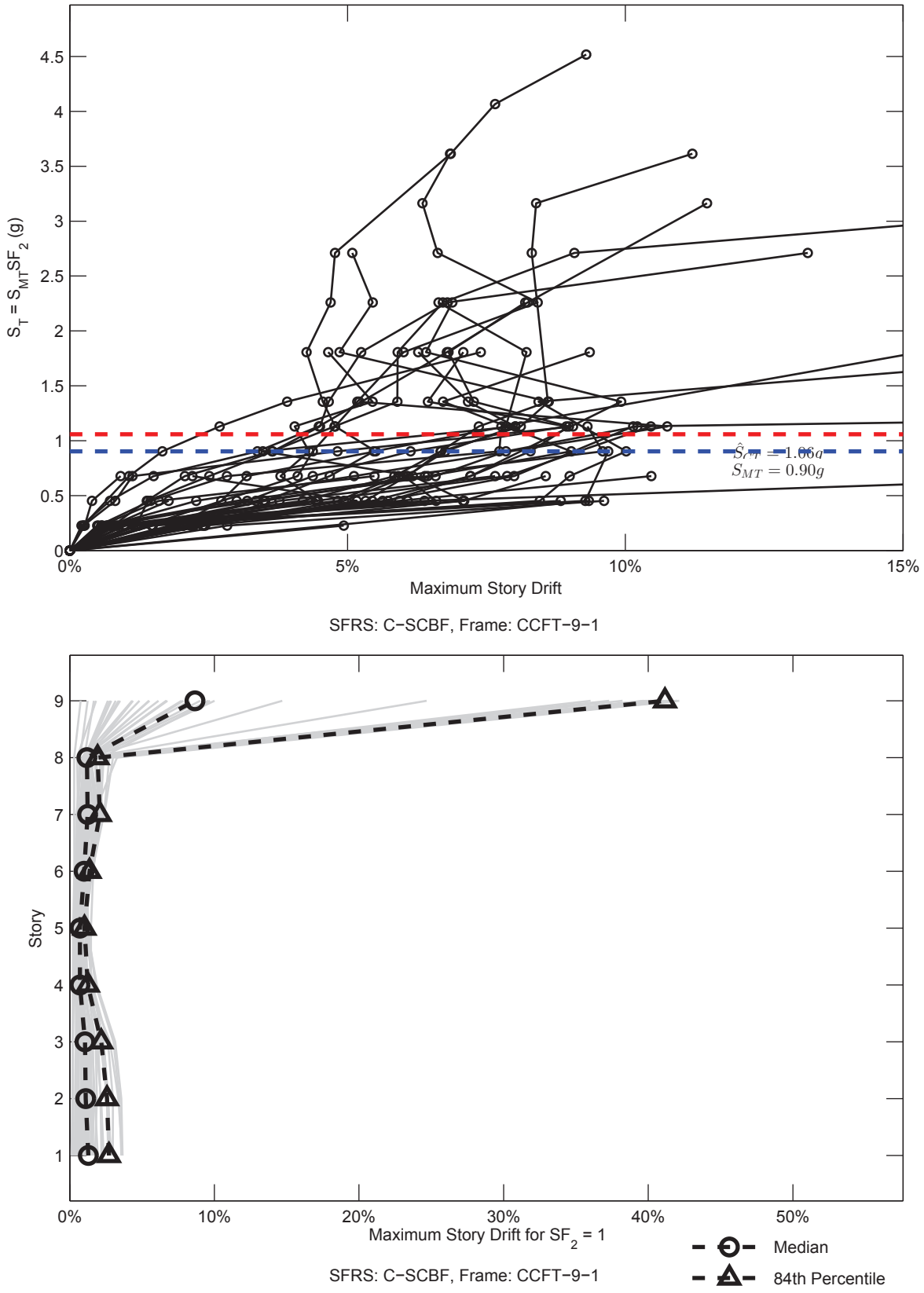

Figure C.113. Dynamic Response History Analysis Results: Frame CCFT-9-1

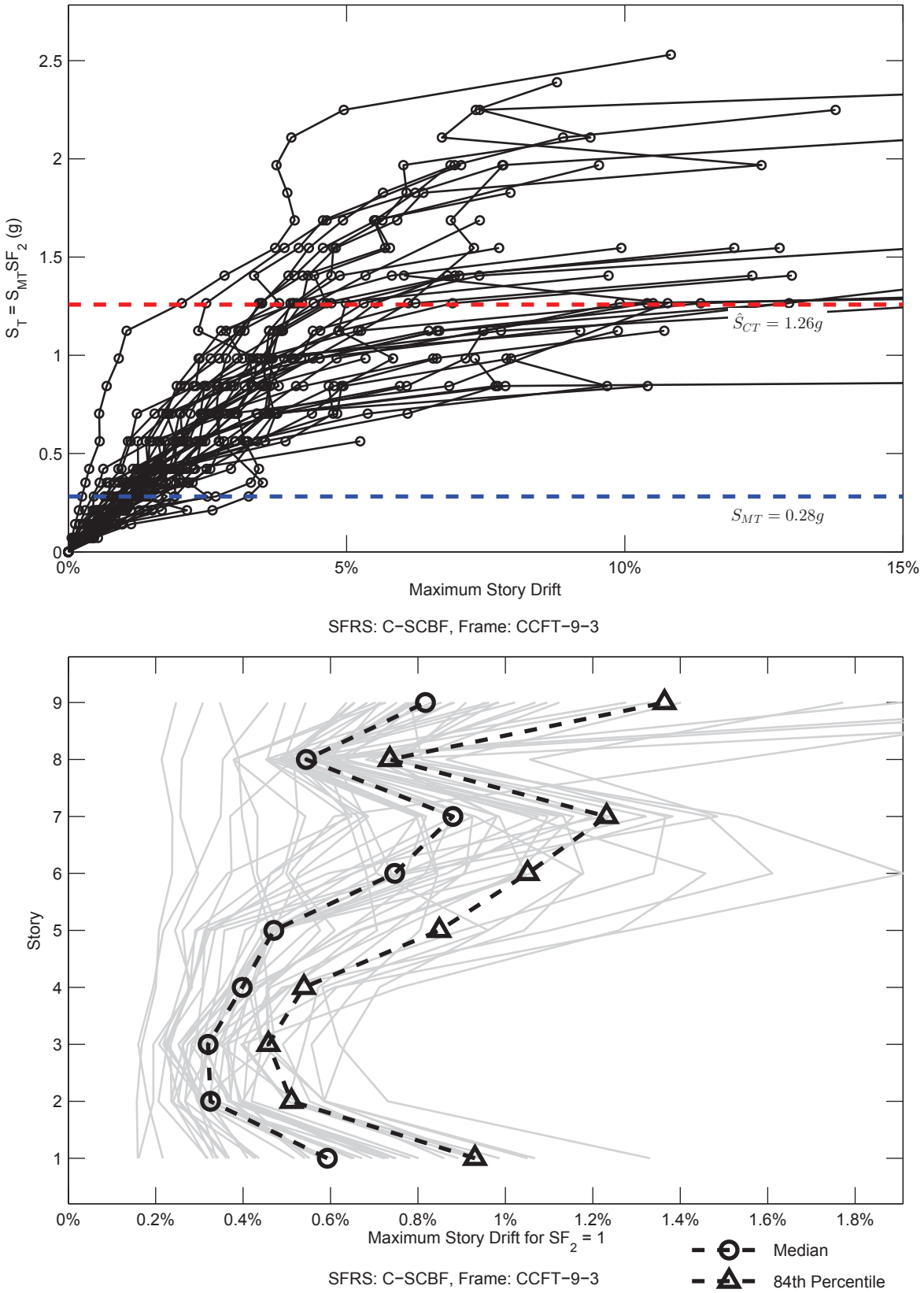

Figure C.114. Dynamic Response History Analysis Results: Frame CCFT-9-3

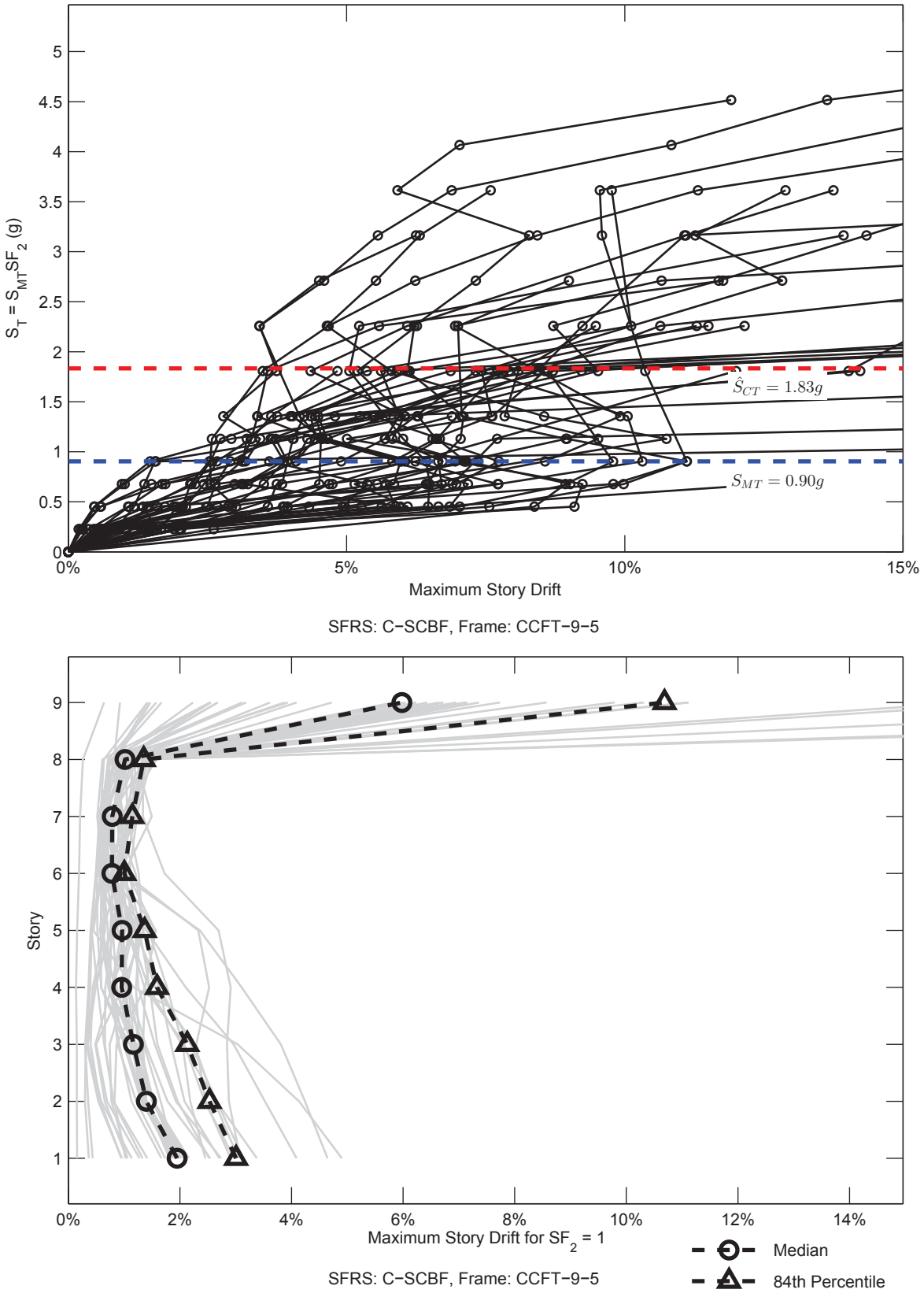

Figure C.115. Dynamic Response History Analysis Results: Frame CCFT-9-5

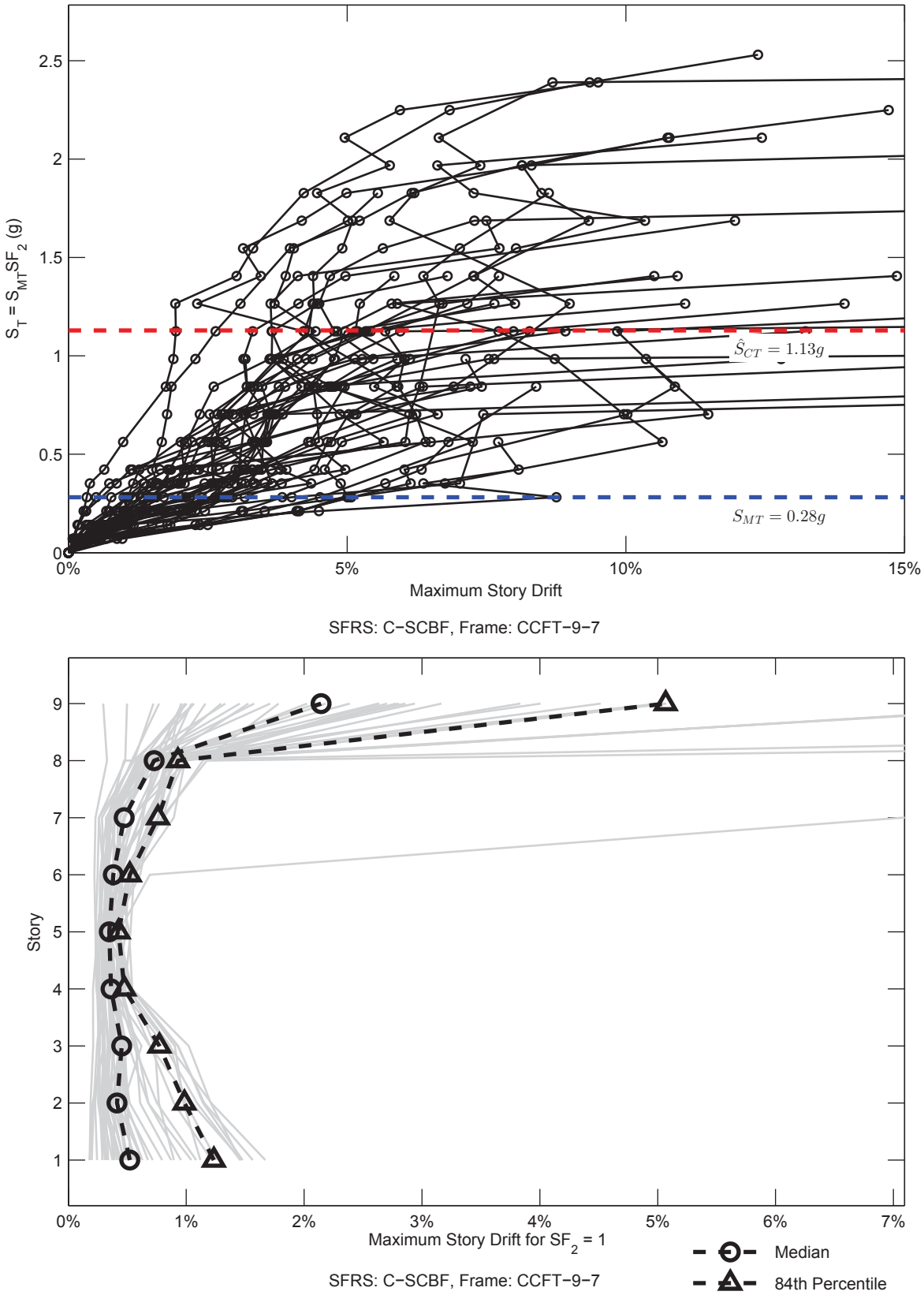

Figure C.116. Dynamic Response History Analysis Results: Frame CCFT-9-7

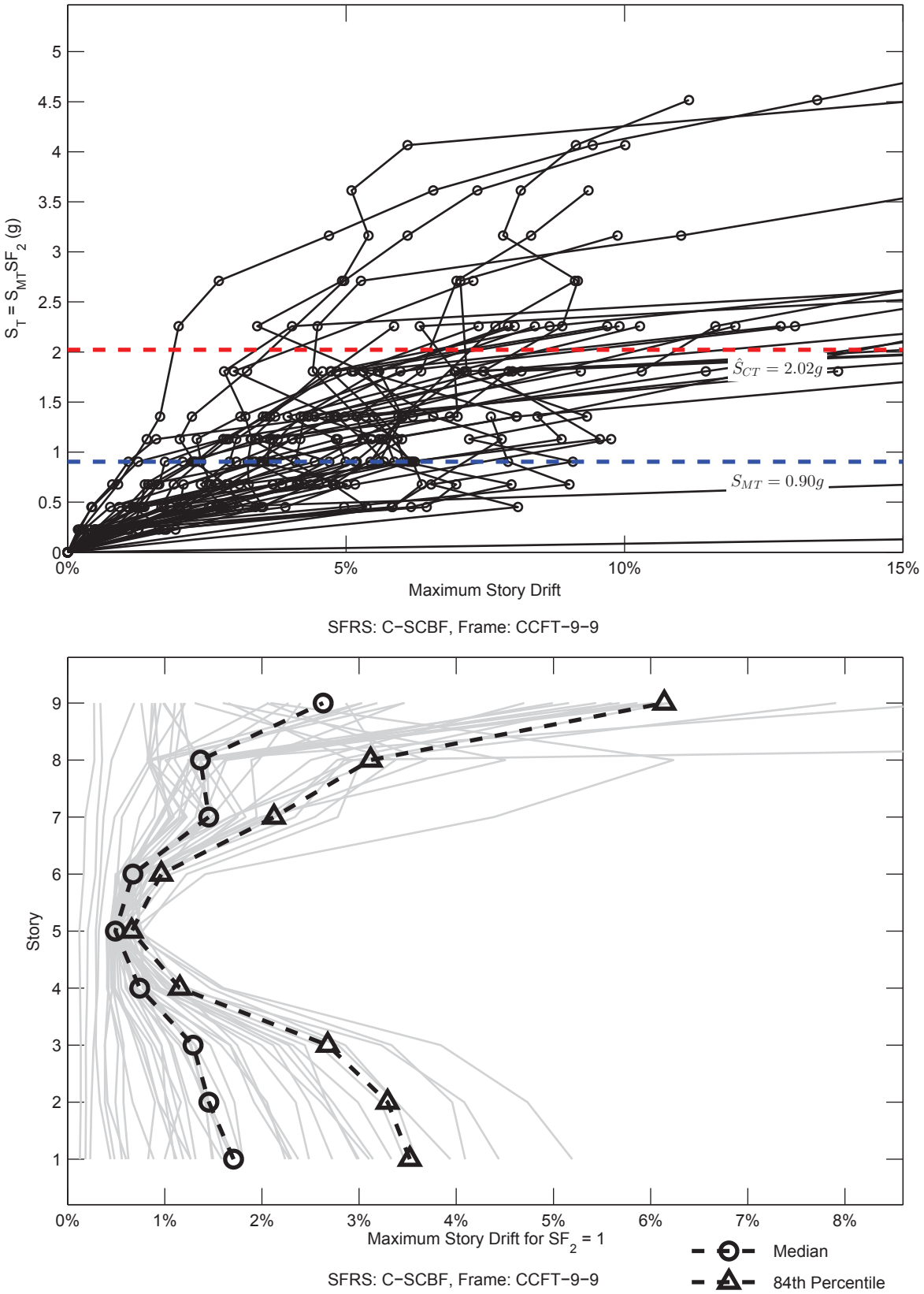

Figure C.117. Dynamic Response History Analysis Results: Frame CCFT-9-9

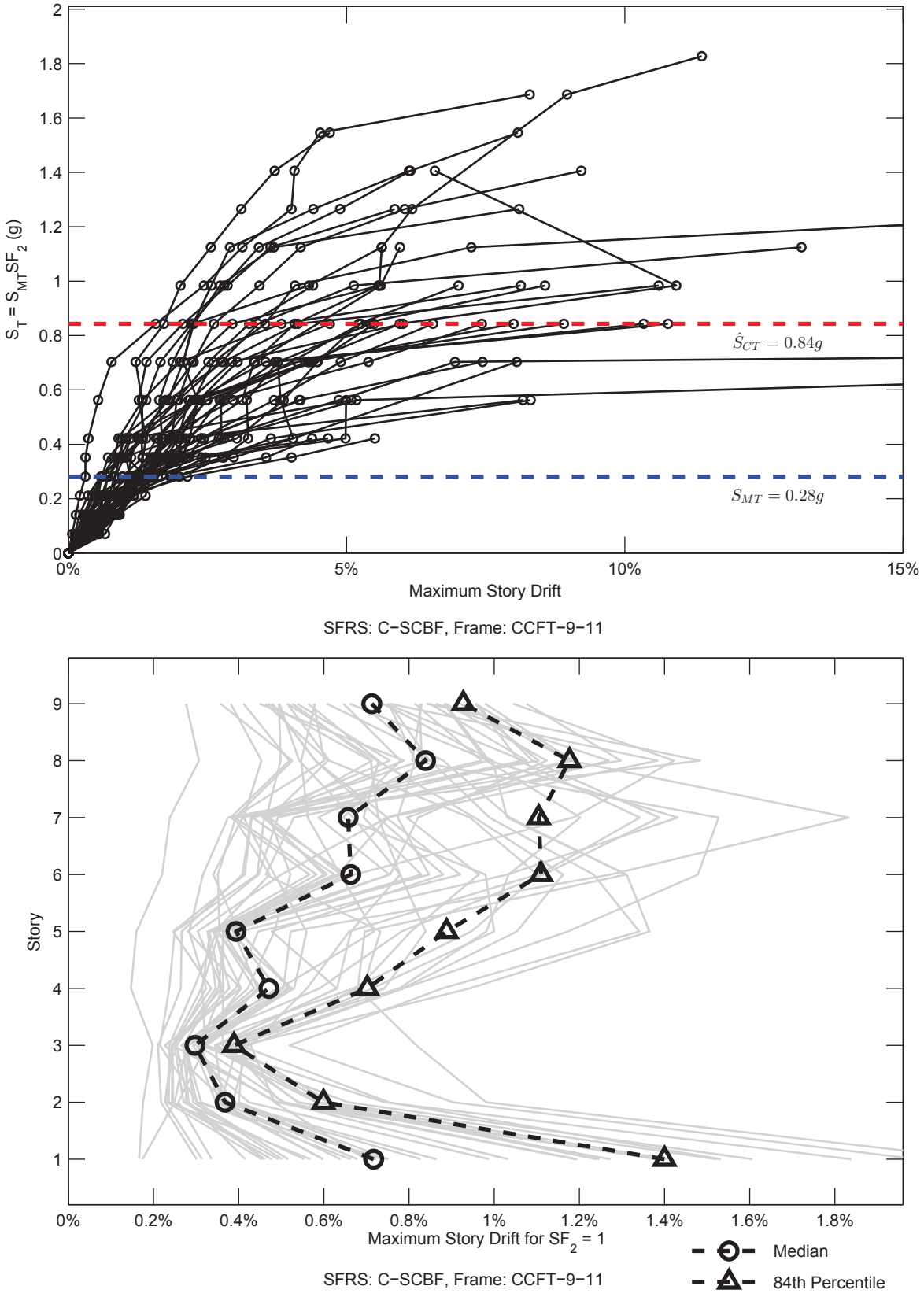

Figure C.118. Dynamic Response History Analysis Results: Frame CCFT-9-11

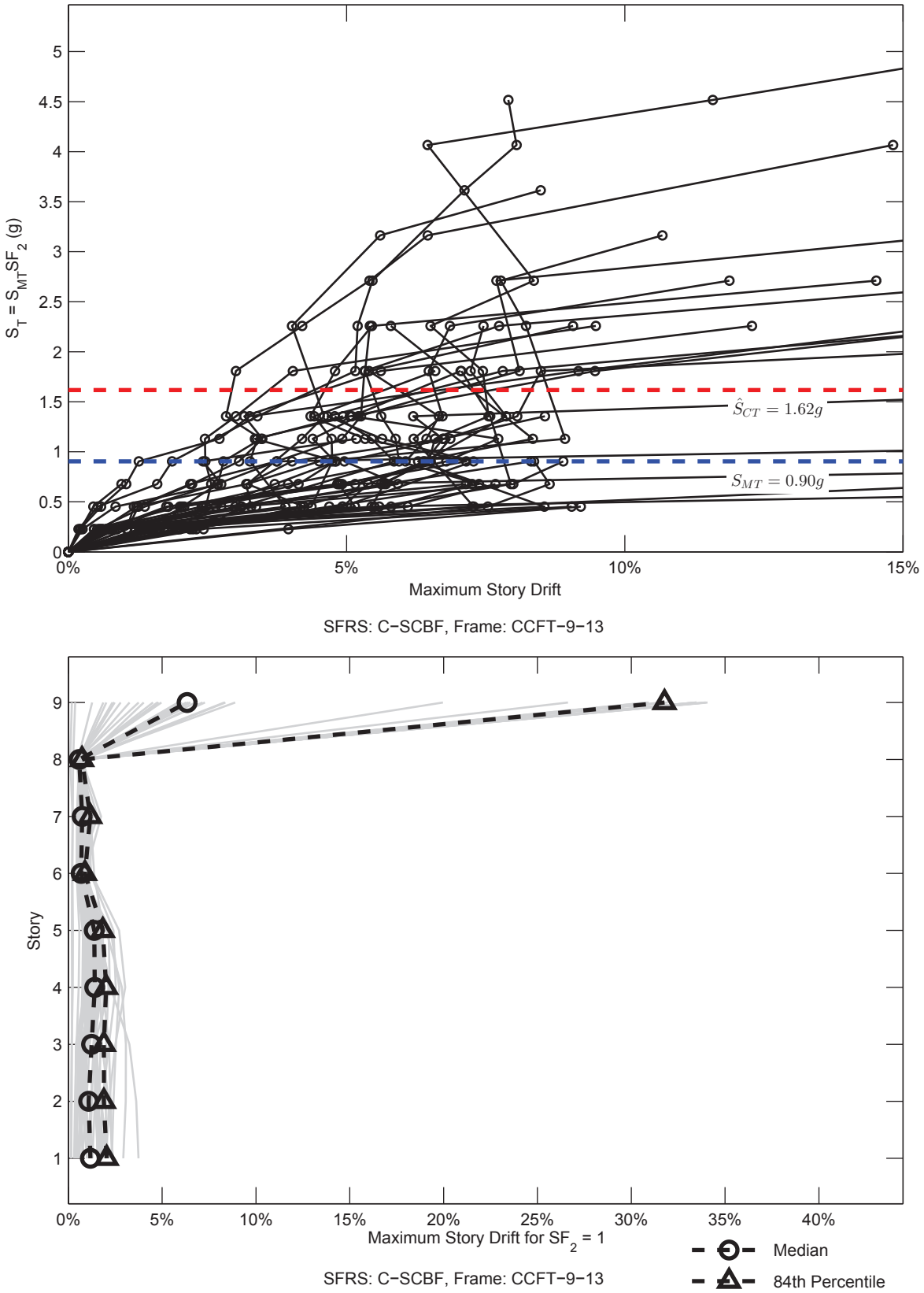

Figure C.119. Dynamic Response History Analysis Results: Frame CCFT-9-13

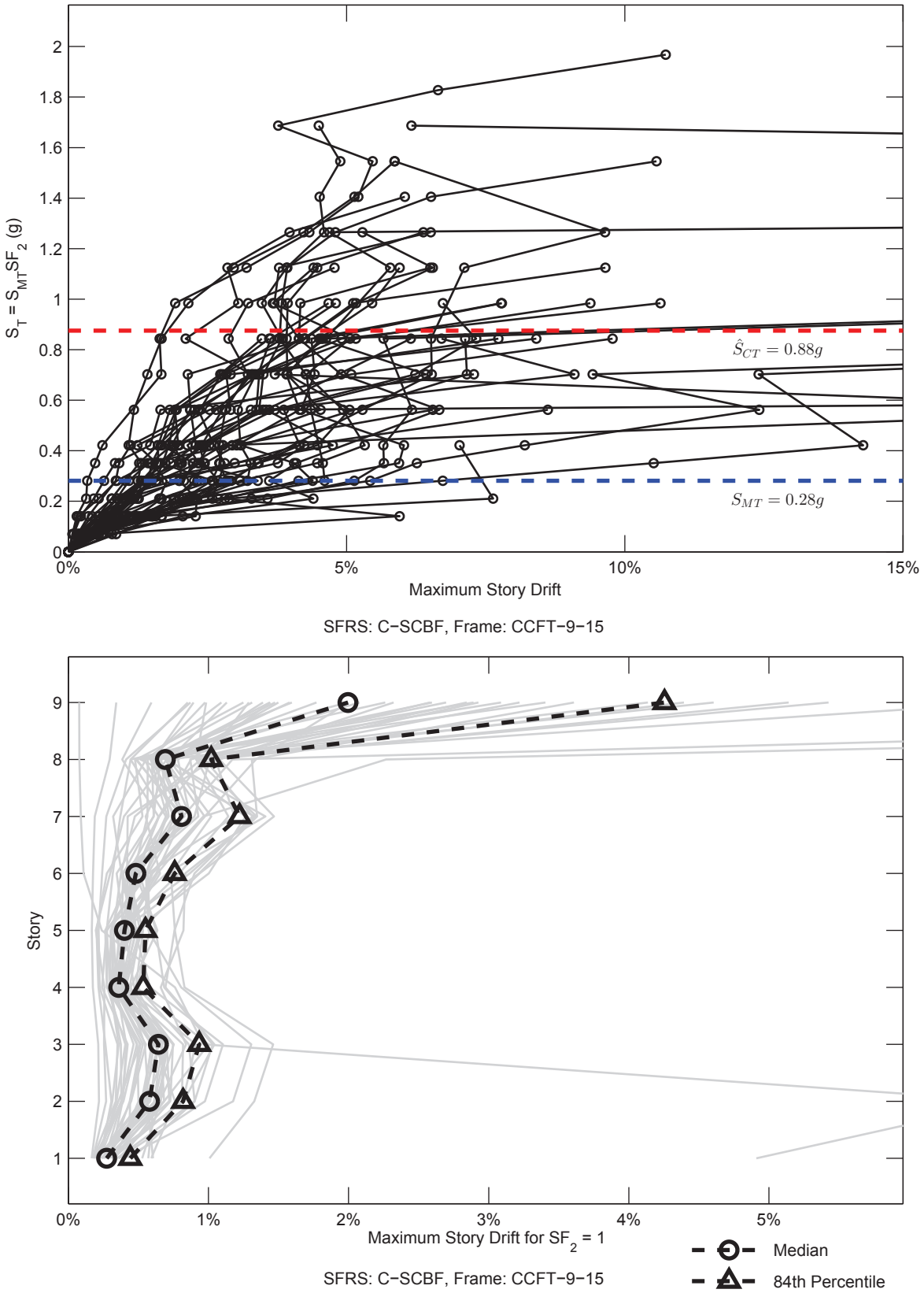

Figure C.120. Dynamic Response History Analysis Results: Frame CCFT-9-15

List of Recent NSEL Reports

No.	*Authors*	*Title*	*Date*
018	Rice, J.A. and Spencer, B.F.	Flexible Smart Sensor Framework for Autonomous Full-scale Structural Health Monitoring	Aug. 2009
019	Sim, S.-H. and Spencer, B.F.	Decentralized Strategies for Monitoring Structures using Wireless Smart Sensor Networks	Nov. 2009
020	Kim, J. and LaFave, J.M.	Joint Shear Behavior of Reinforced Concrete Beam-Column Connections subjected to Seismic Lateral Loading	Nov. 2009
021	Linderman, L.E., Rice, J.A., Barot, S., Spencer, B.F., and Bernhard, J.T.	Characterization of Wireless Smart Sensor Performance	Feb. 2010
.			
022	Miller, T.I. and Spencer, B.F.	Solar Energy Harvesting and Software Enhancements for Autonomous Wireless Smart Sensor Networks	March 2010
023	Denavit, M.D. and Hajjar, J.F.	Nonlinear Seismic Analysis of Circular Concrete-Filled Steel Tube Members and Frames	March 2010
024	Spencer, B.F. and Yun, C.-B. (Eds.)	Wireless Sensor Advances and Applications for Civil Infrastructure Monitoring	June 2010
025	Eatherton, M.R.. and Hajjar, J.F.	Large-Scale Cyclic and Hybrid Simulation Testing and Development of a Controlled-Rocking Steel Building System with Replaceable Fuses	Sept. 2010
026	Hall, K., Eatherton, M.R., and Hajjar, J.F.	Nonlinear Behavior of Controlled Rocking Steel-Framed Building Systems with Replaceable Energy Dissipating Fuses	Oct. 2010
027	Yeo, D. and Jones, N.P.	Computational Study on 3-D Aerodynamic Characteristics of Flow around a Yawed, Inclined, Circular Cylinder	Mar. 2011
028	Phillips, B.M. and Spencer, B.F.	Model-Based Servo-Hydraulic Control for Real-Time Hybrid Simulation	June 2011
029	Linderman, L.E., Mechitov, K.A., and Spencer, B.F.	Real-Time Wireless Data Acquisition for Structural Health Monitoring and Control	June 2011
030	Chang, C.-M. and Spencer, B.F.	Multi-axial Active Isolation for Seismic Protection of Buildings	May 2012
031	Phillips, B.M. and Spencer, B.F.	Model-Based Framework for Real-Time Dynamic Structural Performance Evaluation	August 2012
032	Moreu, F. and LaFave, J.M.	Current Research Topics: Railroad Bridges and Structural Engineering	October 2012
033	Linderman, L.E., Spencer, B.F.	Smart Wireless Control of Civil Structures	January 2014
034	Denavit, M.D. and Hajjar, J.F.	Characterization of Behavior of Steel-Concrete Composite Members and Frames with Applications for Design	July 2014